

Lecture Notes in Networks and Systems 666

Jagdev Singh
George A. Anastassiou
Dumitru Baleanu
Devendra Kumar *Editors*

Advances in Mathematical Modelling, Applied Analysis and Computation

Proceedings of ICMMAAC 2022

 Springer

Series Editor

Janusz Kacprzyk, *Systems Research Institute, Polish Academy of Sciences, Warsaw, Poland*

Advisory Editors

Fernando Gomide, *Department of Computer Engineering and Automation—DCA, School of Electrical and Computer Engineering—FEEC, University of Campinas—UNICAMP, São Paulo, Brazil*

Okay Kaynak, *Department of Electrical and Electronic Engineering, Bogazici University, Istanbul, Türkiye*

Derong Liu, *Department of Electrical and Computer Engineering, University of Illinois at Chicago, Chicago, USA*

Institute of Automation, Chinese Academy of Sciences, Beijing, China

Witold Pedrycz, *Department of Electrical and Computer Engineering, University of Alberta, Alberta, Canada*

Systems Research Institute, Polish Academy of Sciences, Warsaw, Poland

Marios M. Polycarpou, *Department of Electrical and Computer Engineering, KIOS Research Center for Intelligent Systems and Networks, University of Cyprus, Nicosia, Cyprus*

Imre J. Rudas, *Óbuda University, Budapest, Hungary*

Jun Wang, *Department of Computer Science, City University of Hong Kong, Kowloon, Hong Kong*

The series “Lecture Notes in Networks and Systems” publishes the latest developments in Networks and Systems—quickly, informally and with high quality. Original research reported in proceedings and post-proceedings represents the core of LNNS.

Volumes published in LNNS embrace all aspects and subfields of, as well as new challenges in, Networks and Systems.

The series contains proceedings and edited volumes in systems and networks, spanning the areas of Cyber-Physical Systems, Autonomous Systems, Sensor Networks, Control Systems, Energy Systems, Automotive Systems, Biological Systems, Vehicular Networking and Connected Vehicles, Aerospace Systems, Automation, Manufacturing, Smart Grids, Nonlinear Systems, Power Systems, Robotics, Social Systems, Economic Systems and other. Of particular value to both the contributors and the readership are the short publication timeframe and the world-wide distribution and exposure which enable both a wide and rapid dissemination of research output.

The series covers the theory, applications, and perspectives on the state of the art and future developments relevant to systems and networks, decision making, control, complex processes and related areas, as embedded in the fields of interdisciplinary and applied sciences, engineering, computer science, physics, economics, social, and life sciences, as well as the paradigms and methodologies behind them.

Indexed by SCOPUS, INSPEC, WTI Frankfurt eG, zbMATH, SCImago.

All books published in the series are submitted for consideration in Web of Science.

For proposals from Asia please contact Aninda Bose (aninda.bose@springer.com).

Jagdev Singh · George A. Anastassiou ·
Dimitru Baleanu · Devendra Kumar
Editors

Advances in Mathematical Modelling, Applied Analysis and Computation

Proceedings of ICMMAAC 2022

Editors

Jagdev Singh
Department of Mathematics
JECRC University
Jaipur, Rajasthan, India

George A. Anastassiou
Department of Mathematics
University of Memphis
Memphis, TN, USA

Dumitru Baleanu
Department of Mathematics
Cankaya University
Ankara, Türkiye

Devendra Kumar
Department of Mathematics
University of Rajasthan
Jaipur, India

Institute of Space Sciences
Bucharest, Romania

ISSN 2367-3370

ISSN 2367-3389 (electronic)

Lecture Notes in Networks and Systems

ISBN 978-3-031-29958-2

ISBN 978-3-031-29959-9 (eBook)

<https://doi.org/10.1007/978-3-031-29959-9>

© The Editor(s) (if applicable) and The Author(s), under exclusive license
to Springer Nature Switzerland AG 2023

This work is subject to copyright. All rights are solely and exclusively licensed by the Publisher, whether the whole or part of the material is concerned, specifically the rights of translation, reprinting, reuse of illustrations, recitation, broadcasting, reproduction on microfilms or in any other physical way, and transmission or information storage and retrieval, electronic adaptation, computer software, or by similar or dissimilar methodology now known or hereafter developed.

The use of general descriptive names, registered names, trademarks, service marks, etc. in this publication does not imply, even in the absence of a specific statement, that such names are exempt from the relevant protective laws and regulations and therefore free for general use.

The publisher, the authors, and the editors are safe to assume that the advice and information in this book are believed to be true and accurate at the date of publication. Neither the publisher nor the authors or the editors give a warranty, expressed or implied, with respect to the material contained herein or for any errors or omissions that may have been made. The publisher remains neutral with regard to jurisdictional claims in published maps and institutional affiliations.

This Springer imprint is published by the registered company Springer Nature Switzerland AG
The registered company address is: Gewerbestrasse 11, 6330 Cham, Switzerland

Contents

Multivariate Fuzzy-Random and Stochastic Arctangent, Algebraic, Gudermannian and Generalized Symmetric Activation Functions Induced Neural Network Approximations	1
<i>George A. Anastassiou</i>	
From Koeller's Idea to Modern Fractional Calculus: Fractional Polynomial Operators	33
<i>Jordan Hristov</i>	
On Weighted Fractional Operators with Applications to Mathematical Models Arising in Physics	53
<i>Muhammad Samraiz, Muhammad Umer, Saima Naheed, and Dumitru Baleanu</i>	
Numerical Solution of Eighth Order Boundary Value Problems by Using Vieta-Lucas Polynomials	69
<i>Rakesh Kumar, Shivani Aeri, and Poonam Sharma</i>	
The Mexican Hat Wavelet Transform on Generalized Quotients and Its Applications	82
<i>Abhishek Singh, Shubha Singh, and Devendra Kumar</i>	
Second-Order Nonlinearity of a Boolean Function Class with Low Spectra	100
<i>Kezia Saini and Manish Garg</i>	
On Semimonotone Z-Matrices	110
<i>Kumar Sunil and Ravindran Gomatam</i>	
Mathematical Analysis of Hall Effect and Hematocrit Dependent Viscosity on Au/GO-Blood Hybrid Nanofluid Flow Through a Stenosed Catheterized Artery with Thrombosis	121
<i>Umesh Khanduri and B. K. Sharma</i>	
A Computational Investigation of the Characteristics of Velocity Slips and Convective Boundary Conditions in Maxwell Nanofluid Flow over a Permeable Stretching Surface with Activation Energy	138
<i>Bidyasagar Kumbhakar, Manik Das, and Jagdev Singh</i>	

Modelling Pulsatile Blood Flow Using Casson Fluid Model Through an Overlapping Stenotic Artery with Au-Cu Hybrid Nanoparticles: Varying Viscosity Approach	155
<i>Rishu Gandhi and B. K. Sharma</i>	
Generalized Solitary Wave Approximate Analytical and Numerical Solutions for Generalized Damped Forced KdV and Generalized Damped Forced MKdV Equations	177
<i>Shruti Tomar, Naresh M. Chadha, and Santanu Raut</i>	
NIPG Method on Shishkin Mesh for Singularly Perturbed Convection-Diffusion Problem with Discontinuous Convection Coefficient	195
<i>Kumar Rajeev Ranjan and S. Gowrisankar</i>	
Simultaneous Action of Modulated Temperature and Third Diffusing Component on Natural Convection	209
<i>Pervinder Singh and Vinod K. Gupta</i>	
Approximate Numerical Solution of the Nonlinear Klein-Gordon Equation with Caputo-Fabrizio Fractional Operator	232
<i>Ajay Kumar, Haci Mehmet Baskonus, and Amit Prakash</i>	
On a Class of New q -Hypergeometric Expansions as Discrete Analogues of the Erdélyi Type q -Integrals	248
<i>Anand V. Bhatnagar and Yashoverdhan Vyas</i>	
Mathematical Modelling of an Incompressible, Newtonian Blood Flow for the Carotid Artery	259
<i>Damini Singh and Sarita Singh</i>	
The Effect of Peripheral Layer Thickness on Pulsatile Flow of Blood in Human Femoral Artery	273
<i>K. Gayathri and K. Shobika</i>	
A Computational Study of Local Fractional Helmholtz and Coupled Helmholtz Equations in Fractal Media	286
<i>Devendra Kumar, Hassan Kamil Jassim, Jagdev Singh, and Ved Prakash Dubey</i>	
Estimation of Software Reliability Using Lindley Distribution Based on MLE and UMVUE	299
<i>Kavita and Shiv Kumar Sharma</i>	

Solution of Fractional Order Foam Drainage Equation Using Shehu Transform 317
T. Pasayat and A. Patra

On a Class of MacRobert’s Type Finite Integrals Involving Generalized Hypergeometric Functions 332
Vidha Kulkarni, Yashoverdhan Vyas, and Arjun K. Rathie

Irreversibility Analysis in Micropolar Thermofluidics Involving Deforming Sheet 352
Paresh Vyas and Rajesh Kumar Kasana

A Variational Description to Modulational Instability Criterion 371
Ram Dayal Pankaj, Arun Kumar, and Chimam Lal

Applications of General Summation Formulas Contiguous to q -Kummer Theorems 380
Yashoverdhan Vyas, Shivani Pathak, and Kalpana Fatawat

MHD Radiative Casson Fluid Flow over a Non-linear Extending Surface with Cross-Diffusion Impact in the Presence of Buoyancy and Porous Impacts 391
Atiya Ali, Ruchika Mehta, Tripti Mehta, and Sanju Jangid

A Comparative Analysis of Different Basis Functions for Constructing Bézier Curves 413
Harmanjit Kaur and Meenu Rani Goyal

Study of Copper-Water Nanofluid Flow over an Isothermal Moving Sheet 424
Susheela Chaudhary

Thermal Instability of Rivlin-Ericksen Elastico-Viscous Nanofluid Saturated by a Porous Medium with Rotation 436
Ismail and B. S. Bhadauria

Study of the Convective-Radiative Moving Porous Fin with Temperature-Dependent Variables 456
Parvinder Kaur and Surjan Singh

Multi-objective Linear Fractional Transportation Problems Under Uncertainty 475
Rachana Saini, Vishwas Deep Joshi, and Jagdev Singh

Mathematical Model on the Effects of Environmental Pollution on Biological Populations	488
<i>Sanjay Bhattar, Nishant, and Shyamsunder</i>	
High Gain Calculation & Simulation for Antenna Design for 6G Wireless Applications	497
<i>Narayan Krishan Vyas and Mohammad Salim</i>	
Non-similarity Solutions of MHD Boundary Layer Flow	508
<i>Abhishek Neemawat and Sushila</i>	
Deferred (Δ_v^m, f) -Statistical Convergence of Order α in Normed Space	522
<i>A. K. Verma and Sudhanshu Kumar</i>	
Integral Formulae Associated with the S-Function, \overline{H} -Function and the Aleph Function	533
<i>Sapna Tyagi, Monika Jain, and Jagdev Singh</i>	
Air Quality Index: A Comparative Study of Air Quality in Jaipur When the Pre-lockdown and Post-lockdown Phases Are in Effect	552
<i>Ronak Khandelwal, Suraksha Grewal, Ashok K. Kakodia, and Kumud Tanwar</i>	
Mathematical Study on Corona-Virus (COVID-19) Disease Transmission and Its Stability Through SEIR Epidemic Model	562
<i>Krishna Pada Das, Sanjukta Pramanik, Partha Karmakar, and Seema Sarkar Mondal</i>	
Author Index	319



Multivariate Fuzzy-Random and Stochastic Arctangent, Algebraic, Gudermannian and Generalized Symmetric Activation Functions Induced Neural Network Approximations

George A. Anastassiou^(✉)

Department of Mathematical Sciences, University of Memphis,
Memphis, TN 38152, USA
ganastss@memphis.edu

Abstract. In this article we study the degree of approximation of multivariate pointwise and uniform convergences in the q -mean to the Fuzzy-Random unit operator of multivariate Fuzzy-Random Quasi-Interpolation arctangent, algebraic, Gudermannian and generalized symmetric activation functions based neural network operators. These multivariate Fuzzy-Random operators arise in a natural way among multivariate Fuzzy-Random neural networks. The rates are given through multivariate Probabilistic-Jackson type inequalities involving the multivariate Fuzzy-Random modulus of continuity of the engaged multivariate Fuzzy-Random function. The plain stochastic extreme analog of this theory is also met in detail for the stochastic analogs of the operators: the stochastic full quasi-interpolation operators, the stochastic Kantorovich type operators and the stochastic quadrature type operators.

Keywords: Fuzzy-Random analysis · Fuzzy-Random neural networks and operators · Fuzzy-Random modulus of continuity · Fuzzy-Random functions · Stochastic processes · Jackson type fuzzy and probabilistic inequalities

1 Fuzzy-Random Functions and Stochastic Processes Background

See also [18], Ch. 22, pp. 497–501.

We start with

Definition 1 (see [35]). Let $\mu : \mathbb{R} \rightarrow [0, 1]$ with the following properties:

- (i) is normal, i.e., $\exists x_0 \in \mathbb{R} : \mu(x_0) = 1$.
- (ii) $\mu(\lambda x + (1 - \lambda)y) \geq \min\{\mu(x), \mu(y)\}$, $\forall x, y \in \mathbb{R}$, $\forall \lambda \in [0, 1]$ (μ is called a convex fuzzy subset).

- (iii) μ is upper semicontinuous on \mathbb{R} , i.e., $\forall x_0 \in \mathbb{R}$ and $\forall \varepsilon > 0$, \exists neighborhood $V(x_0) : \mu(x) \leq \mu(x_0) + \varepsilon, \forall x \in V(x_0)$.
- (iv) the set $\text{supp}(\mu)$ is compact in \mathbb{R} (where $\text{supp}(\mu) := \{x \in \mathbb{R}; \mu(x) > 0\}$).

We call μ a fuzzy real number. Denote the set of all μ with $\mathbb{R}_{\mathcal{F}}$.

E.g., $\chi_{\{x_0\}} \in \mathbb{R}_{\mathcal{F}}$, for any $x_0 \in \mathbb{R}$, where $\chi_{\{x_0\}}$ is the characteristic function at x_0 .

For $0 < r \leq 1$ and $\mu \in \mathbb{R}_{\mathcal{F}}$ define $[\mu]^r := \{x \in \mathbb{R} : \mu(x) \geq r\}$ and $[\mu]^0 := \{x \in \mathbb{R} : \mu(x) > 0\}$.

Then it is well known that for each $r \in [0, 1]$, $[\mu]^r$ is a closed and bounded interval of \mathbb{R} . For $u, v \in \mathbb{R}_{\mathcal{F}}$ and $\lambda \in \mathbb{R}$, we define uniquely the sum $u \oplus v$ and the product $\lambda \odot u$ by

$$[u \oplus v]^r = [u]^r + [v]^r, \quad [\lambda \odot u]^r = \lambda [u]^r, \quad \forall r \in [0, 1],$$

where $[u]^r + [v]^r$ means the usual addition of two intervals (as subsets of \mathbb{R}) and $\lambda [u]^r$ means the usual product between a scalar and a subset of \mathbb{R} (see, e.g., [35]). Notice $1 \odot u = u$ and it holds $u \oplus v = v \oplus u, \lambda \odot u = u \odot \lambda$. If $0 \leq r_1 \leq r_2 \leq 1$ then $[u]^{r_2} \subseteq [u]^{r_1}$. Actually $[u]^r = [u_-^{(r)}, u_+^{(r)}]$, where $u_-^{(r)} < u_+^{(r)}, u_-^{(r)}, u_+^{(r)} \in \mathbb{R}, \forall r \in [0, 1]$.

Define

$$D : \mathbb{R}_{\mathcal{F}} \times \mathbb{R}_{\mathcal{F}} \rightarrow \mathbb{R}_+ \cup \{0\}$$

by

$$D(u, v) := \sup_{r \in [0, 1]} \max \left\{ \left| u_-^{(r)} - v_-^{(r)} \right|, \left| u_+^{(r)} - v_+^{(r)} \right| \right\},$$

where $[v]^r = [v_-^{(r)}, v_+^{(r)}]$; $u, v \in \mathbb{R}_{\mathcal{F}}$. We have that D is a metric on $\mathbb{R}_{\mathcal{F}}$. Then $(\mathbb{R}_{\mathcal{F}}, D)$ is a complete metric space, see [35], with the properties

$$\begin{aligned} D(u \oplus w, v \oplus w) &= D(u, v), \quad \forall u, v, w \in \mathbb{R}_{\mathcal{F}}, \\ D(k \odot u, k \odot v) &= |k| D(u, v), \quad \forall u, v \in \mathbb{R}_{\mathcal{F}}, \quad \forall k \in \mathbb{R}, \\ D(u \oplus v, w \oplus e) &\leq D(u, w) + D(v, e), \quad \forall u, v, w, e \in \mathbb{R}_{\mathcal{F}}. \end{aligned} \tag{1}$$

Let (M, d) metric space and $f, g : M \rightarrow \mathbb{R}_{\mathcal{F}}$ be fuzzy real number valued functions. The distance between f, g is defined by

$$D^*(f, g) := \sup_{x \in M} D(f(x), g(x)).$$

On $\mathbb{R}_{\mathcal{F}}$ we define a partial order by “ \leq ”: $u, v \in \mathbb{R}_{\mathcal{F}}, u \leq v$ iff $u_-^{(r)} \leq v_-^{(r)}$ and $u_+^{(r)} \leq v_+^{(r)}, \forall r \in [0, 1]$.

\sum^* denotes the fuzzy summation, $\tilde{0} := \chi_{\{0\}} \in \mathbb{R}_{\mathcal{F}}$ the neutral element with respect to \oplus . For more see also [36, 37].

We need

Definition 2 (see also [30], Definition 13.16, p. 654). Let (X, \mathcal{B}, P) be a probability space. A fuzzy-random variable is a \mathcal{B} -measurable mapping $g : X \rightarrow \mathbb{R}_{\mathcal{F}}$ (i.e., for any open set $U \subseteq \mathbb{R}_{\mathcal{F}}$, in the topology of $\mathbb{R}_{\mathcal{F}}$ generated by the metric D , we have

$$g^{-1}(U) = \{s \in X; g(s) \in U\} \in \mathcal{B}. \quad (2)$$

The set of all fuzzy-random variables is denoted by $\mathcal{L}_{\mathcal{F}}(X, \mathcal{B}, P)$. Let $g_n, g \in \mathcal{L}_{\mathcal{F}}(X, \mathcal{B}, P)$, $n \in \mathbb{N}$ and $0 < q < +\infty$. We say $g_n(s) \xrightarrow[n \rightarrow +\infty]{\text{"q-mean"}} g(s)$ if

$$\lim_{n \rightarrow +\infty} \int_X D(g_n(s), g(s))^q P(ds) = 0. \quad (3)$$

Remark 1 (see [30], p. 654). If $f, g \in \mathcal{L}_{\mathcal{F}}(X, \mathcal{B}, P)$, let us denote $F : X \rightarrow \mathbb{R}_+ \cup \{0\}$ by $F(s) = D(f(s), g(s))$, $s \in X$. Here, F is \mathcal{B} -measurable, because $F = G \circ H$, where $G(u, v) = D(u, v)$ is continuous on $\mathbb{R}_{\mathcal{F}} \times \mathbb{R}_{\mathcal{F}}$, and $H : X \rightarrow \mathbb{R}_{\mathcal{F}} \times \mathbb{R}_{\mathcal{F}}$, $H(s) = (f(s), g(s))$, $s \in X$, is \mathcal{B} -measurable. This shows that the above convergence in q -mean makes sense.

Definition 3 (see [30], p. 654, Definition 13.17). Let (T, \mathcal{T}) be a topological space. A mapping $f : T \rightarrow \mathcal{L}_{\mathcal{F}}(X, \mathcal{B}, P)$ will be called fuzzy-random function (or fuzzy-stochastic process) on T . We denote $f(t)(s) = f(t, s)$, $t \in T$, $s \in X$.

Remark 2 (see [30], p. 655). Any usual fuzzy real function $f : T \rightarrow \mathbb{R}_{\mathcal{F}}$ can be identified with the degenerate fuzzy-random function $f(t, s) = f(t)$, $\forall t \in T$, $s \in X$.

Remark 3 (see [30], p. 655). Fuzzy-random functions that coincide with probability one for each $t \in T$ will be considered equivalent.

Remark 4 (see [30], p. 655). Let $f, g : T \rightarrow \mathcal{L}_{\mathcal{F}}(X, \mathcal{B}, P)$. Then $f \oplus g$ and $k \odot f$ are defined pointwise, i.e.,

$$\begin{aligned} (f \oplus g)(t, s) &= f(t, s) \oplus g(t, s), \\ (k \odot f)(t, s) &= k \odot f(t, s), \quad t \in T, s \in X, k \in \mathbb{R}. \end{aligned}$$

Definition 4 (see also Definition 13.18, pp. 655–656, [30]). For a fuzzy-random function $f : W \subseteq \mathbb{R}^N \rightarrow \mathcal{L}_{\mathcal{F}}(X, \mathcal{B}, P)$, $N \in \mathbb{N}$, we define the (first) fuzzy-random modulus of continuity

$$\Omega_1^{(\mathcal{F})}(f, \delta)_{L^q} = \sup \left\{ \left(\int_X D^q(f(x, s), f(y, s)) P(ds) \right)^{\frac{1}{q}} : x, y \in W, \|x - y\|_{\infty} \leq \delta \right\},$$

$0 < \delta, 1 \leq q < \infty$.

Definition 5 [16]. Here $1 \leq q < +\infty$. Let $f : W \subseteq \mathbb{R}^N \rightarrow \mathcal{L}_{\mathcal{F}}(X, \mathcal{B}, P)$, $N \in \mathbb{N}$, be a fuzzy random function. We call f a (q -mean) uniformly continuous fuzzy

random function over W , iff $\forall \varepsilon > 0 \exists \delta > 0$: whenever $\|x - y\|_\infty \leq \delta$, $x, y \in W$, implies that

$$\int_X (D(f(x, s), f(y, s)))^q P(ds) \leq \varepsilon.$$

We denote it as $f \in C_{FR}^{U_q}(W)$.

Proposition 1 [16]. Let $f \in C_{FR}^{U_q}(W)$, where $W \subseteq \mathbb{R}^N$ is convex.

Then $\Omega_1^{(\mathcal{F})}(f, \delta)_{L^q} < \infty$, any $\delta > 0$.

Proposition 2 [16]. Let $f, g : W \subseteq \mathbb{R}^N \rightarrow \mathcal{L}_{\mathcal{F}}(X, \mathcal{B}, P)$, $N \in \mathbb{N}$, be fuzzy random functions. It holds

- (i) $\Omega_1^{(\mathcal{F})}(f, \delta)_{L^q}$ is nonnegative and nondecreasing in $\delta > 0$.
- (ii) $\lim_{\delta \downarrow 0} \Omega_1^{(\mathcal{F})}(f, \delta)_{L^q} = \Omega_1^{(\mathcal{F})}(f, 0)_{L^q} = 0$, iff $f \in C_{FR}^{U_q}(W)$.

We mention

Definition 6 (see also [6]). Let $f(t, s)$ be a random function (stochastic process) from $W \times (X, \mathcal{B}, P)$, $W \subseteq \mathbb{R}^N$, into \mathbb{R} , where (X, \mathcal{B}, P) is a probability space. We define the q -mean multivariate first modulus of continuity of f by

$$\Omega_1(f, \delta)_{L^q} := \sup \left\{ \left(\int_X |f(x, s) - f(y, s)|^q P(ds) \right)^{\frac{1}{q}} : x, y \in W, \|x - y\|_\infty \leq \delta \right\}, \quad (4)$$

$\delta > 0$, $1 \leq q < \infty$.

The concept of f being (q -mean) uniformly continuous random function is defined the same way as in Definition 5, just replace D by $|\cdot|$, etc. We denote it as $f \in C_{\mathbb{R}}^{U_q}(W)$.

Similar properties as in Propositions 1, 2 are valid for $\Omega_1(f, \delta)_{L^q}$.

Also we have

Proposition 3 [3]. Let $Y(t, \omega)$ be a real valued stochastic process such that Y is continuous in $t \in [a, b]$. Then Y is jointly measurable in (t, ω) .

According to [28], p. 94 we have the following

Definition 7. Let (Y, \mathcal{T}) be a topological space, with its σ -algebra of Borel sets $\mathcal{B} := \mathcal{B}(Y, \mathcal{T})$ generated by \mathcal{T} . If (X, \mathcal{S}) is a measurable space, a function $f : X \rightarrow Y$ is called measurable iff $f^{-1}(B) \in \mathcal{S}$ for all $B \in \mathcal{B}$.

By Theorem 4.1.6 of [28], p. 89 f as above is measurable iff

$$f^{-1}(C) \in \mathcal{S} \text{ for all } C \in \mathcal{T}.$$

We mention

Theorem 1 (see [28], p. 95). Let (X, \mathcal{S}) be a measurable space and (Y, d) be a metric space. Let f_n be measurable functions from X into Y such that for all $x \in X$, $f_n(x) \rightarrow f(x)$ in Y . Then f is measurable. I.e., $\lim_{n \rightarrow \infty} f_n = f$ is measurable.

We need also

Proposition 4 [16]. Let f, g be fuzzy random variables from \mathcal{S} into $\mathbb{R}_{\mathcal{F}}$. Then

- (i) Let $c \in \mathbb{R}$, then $c \odot f$ is a fuzzy random variable.
- (ii) $f \oplus g$ is a fuzzy random variable.

Proposition 5. Let $Y(\vec{t}, \omega)$ be a real valued multivariate random function (stochastic process) such that Y is continuous in $\vec{t} \in \prod_{i=1}^N [a_i, b_i]$. Then Y is jointly measurable in (\vec{t}, ω) and $\int_{\prod_{i=1}^N [a_i, b_i]} Y(\vec{t}, \omega) d\vec{t}$ is a real valued random variable.

Proof. Similar to Proposition 18.14, p. 353 of [7].

2 About Neural Networks Background

2.1 About the Arctangent Activation Function

We consider the

$$\arctan x = \int_0^x \frac{dz}{1+z^2}, \quad x \in \mathbb{R}. \quad (5)$$

We will be using

$$h(x) := \frac{2}{\pi} \arctan\left(\frac{\pi}{2}x\right) = \frac{2}{\pi} \int_0^{\frac{\pi x}{2}} \frac{dz}{1+z^2}, \quad x \in \mathbb{R}, \quad (6)$$

which is a sigmoid type function and it is strictly increasing. We have that

$$h(0) = 0, \quad h(-x) = -h(x), \quad h(+\infty) = 1, \quad h(-\infty) = -1,$$

and

$$h'(x) = \frac{4}{4 + \pi^2 x^2} > 0, \quad \text{all } x \in \mathbb{R}. \quad (7)$$

We consider the activation function

$$\psi_1(x) := \frac{1}{4} (h(x+1) - h(x-1)), \quad x \in \mathbb{R}, \quad (8)$$

and we notice that

$$\psi_1(-x) = \psi_1(x), \quad (9)$$

it is an even function.

Since $x + 1 > x - 1$, then $h(x + 1) > h(x - 1)$, and $\psi_1(x) > 0$, all $x \in \mathbb{R}$.

We see that

$$\psi_1(0) = \frac{1}{\pi} \arctan \frac{\pi}{2} \cong 0.319. \quad (10)$$

Let $x > 0$, we have that

$$\begin{aligned} \psi_1'(x) &= \frac{1}{4} (h'(x + 1) - h'(x - 1)) = \\ &= \frac{-4\pi^2 x}{(4 + \pi^2(x + 1)^2)(4 + \pi^2(x - 1)^2)} < 0. \end{aligned} \quad (11)$$

That is

$$\psi_1'(x) < 0, \text{ for } x > 0. \quad (12)$$

That is ψ_1 is strictly decreasing on $[0, \infty)$ and clearly is strictly increasing on $(-\infty, 0]$, and $\psi_1'(0) = 0$.

Observe that

$$\begin{aligned} \lim_{x \rightarrow +\infty} \psi_1(x) &= \frac{1}{4} (h(+\infty) - h(+\infty)) = 0, \\ \text{and} \\ \lim_{x \rightarrow -\infty} \psi_1(x) &= \frac{1}{4} (h(-\infty) - h(-\infty)) = 0. \end{aligned} \quad (13)$$

That is the x -axis is the horizontal asymptote on ψ_1 .

All in all, ψ_1 is a bell symmetric function with maximum $\psi_1(0) \cong 0.319$.

We need

Theorem 2 ([19], p. 286). *We have that*

$$\sum_{i=-\infty}^{\infty} \psi_1(x - i) = 1, \forall x \in \mathbb{R}. \quad (14)$$

Theorem 3 ([19], p. 287). *It holds*

$$\int_{-\infty}^{\infty} \psi_1(x) dx = 1. \quad (15)$$

So that $\psi_1(x)$ is a density function on \mathbb{R} .

We mention

Theorem 4 ([19], p. 288). *Let $0 < \alpha < 1$, and $n \in \mathbb{N}$ with $n^{1-\alpha} > 2$. It holds*

$$\begin{cases} \sum_{k=-\infty}^{\infty} \psi_1(nx - k) < \frac{2}{\pi^2(n^{1-\alpha} - 2)} =: c_1(\alpha, n). \\ : |nx - k| \geq n^{1-\alpha} \end{cases} \quad (16)$$

Denote by $\lfloor \cdot \rfloor$ the integral part of the number and by $\lceil \cdot \rceil$ the ceiling of the number.

We need

Theorem 5 ([19], p. 289). *Let $x \in [a, b] \subset \mathbb{R}$ and $n \in \mathbb{N}$ so that $\lceil na \rceil \leq \lfloor nb \rfloor$. It holds*

$$\frac{1}{\sum_{k=\lceil na \rceil}^{\lfloor nb \rfloor} \psi_1(nx - k)} < \frac{1}{\psi_1(1)} \cong \mathbf{4.9737} =: \alpha_1, \forall x \in [a, b]. \quad (17)$$

Note 1 ([19], pp. 290–291).

i) We have that

$$\lim_{n \rightarrow \infty} \sum_{k=\lceil na \rceil}^{\lfloor nb \rfloor} \psi_1(nx - k) \neq 1, \quad (18)$$

for at least some $x \in [a, b]$.

ii) For large enough $n \in \mathbb{N}$ we always obtain $\lceil na \rceil \leq \lfloor nb \rfloor$. Also $a \leq \frac{k}{n} \leq b$, iff $\lceil na \rceil \leq k \leq \lfloor nb \rfloor$.

In general, by Theorem 2, it holds

$$\sum_{k=\lceil na \rceil}^{\lfloor nb \rfloor} \psi_1(nx - k) \leq 1. \quad (19)$$

We introduce (see [24])

$$Z_1(x_1, \dots, x_N) := Z_1(x) := \prod_{i=1}^N \psi_1(x_i), \quad x = (x_1, \dots, x_N) \in \mathbb{R}^N, \quad N \in \mathbb{N}. \quad (20)$$

Denote by $a = (a_1, \dots, a_N)$ and $b = (b_1, \dots, b_N)$.

It has the properties:

- (i) $Z_1(x) > 0, \forall x \in \mathbb{R}^N$,
- (ii)

$$\sum_{k=-\infty}^{\infty} Z_1(x - k) := \sum_{k_1=-\infty}^{\infty} \sum_{k_2=-\infty}^{\infty} \dots \sum_{k_N=-\infty}^{\infty} Z_1(x_1 - k_1, \dots, x_N - k_N) = 1, \quad (21)$$

where $k := (k_1, \dots, k_n) \in \mathbb{Z}^N, \forall x \in \mathbb{R}^N$,

hence

(iii)

$$\sum_{k=-\infty}^{\infty} Z_1(nx - k) = 1, \quad (22)$$

$\forall x \in \mathbb{R}^N; n \in \mathbb{N}$,

and

(iv)

$$\int_{\mathbb{R}^N} Z_1(x) dx = 1, \tag{23}$$

that is Z_1 is a multivariate density function.

(v) It is clear that

$$\sum_{k=-\infty}^{\infty} Z_1(nx - k) < \frac{2}{\pi^2(n^{1-\beta} - 2)} = c_1(\beta, n), \tag{24}$$

$$\left\{ \begin{array}{l} k = -\infty \\ \left\| \frac{k}{n} - x \right\|_{\infty} > \frac{1}{n^{\beta}} \end{array} \right.$$

$0 < \beta < 1, n \in \mathbb{N} : n^{1-\beta} > 2, x \in \mathbb{R}^N.$

(vi) By Theorem 5 we get that

$$0 < \frac{1}{\sum_{k=\lceil na \rceil}^{\lfloor nb \rfloor} Z_1(nx - k)} < \frac{1}{(\psi_1(1))^N} \cong (4.9737)^N =: \gamma_1(N), \tag{25}$$

$$\forall x \in \left(\prod_{i=1}^N [a_i, b_i] \right), n \in \mathbb{N}.$$

Furthermore it holds

$$\lim_{n \rightarrow \infty} \sum_{k=\lceil na \rceil}^{\lfloor nb \rfloor} Z_1(nx - k) \neq 1, \tag{26}$$

for at least some $x \in \left(\prod_{i=1}^N [a_i, b_i] \right).$

Above it is $\|x\|_{\infty} := \max \{|x_1|, \dots, |x_N|\}, x \in \mathbb{R}^N,$ also set $\infty := (\infty, \dots, \infty), -\infty = (-\infty, \dots, -\infty)$ upon the multivariate context.

2.2 About the Algebraic Activation Function

Here see also [20].

We consider the generator algebraic function

$$\varphi(x) = \frac{x}{\sqrt[2m]{1 + x^{2m}}}, m \in \mathbb{N}, x \in \mathbb{R}, \tag{27}$$

which is a sigmoidal type of function and is a strictly increasing function.

We see that $\varphi(-x) = -\varphi(x)$ with $\varphi(0) = 0.$ We get that

$$\varphi'(x) = \frac{1}{(1 + x^{2m})^{\frac{2m+1}{2m}}} > 0, \forall x \in \mathbb{R}, \tag{28}$$

proving φ as strictly increasing over $\mathbb{R}, \varphi'(x) = \varphi'(-x).$ We easily find that $\lim_{x \rightarrow +\infty} \varphi(x) = 1, \varphi(+\infty) = 1,$ and $\lim_{x \rightarrow -\infty} \varphi(x) = -1, \varphi(-\infty) = -1.$

We consider the activation function

$$\psi_2(x) = \frac{1}{4} [\varphi(x+1) - \varphi(x-1)]. \quad (29)$$

Clearly it is $\psi_2(x) = \psi_2(-x)$, $\forall x \in \mathbb{R}$, so that ψ_2 is an even function and symmetric with respect to the y -axis. Clearly $\psi_2(x) > 0$, $\forall x \in \mathbb{R}$.

Also it is

$$\psi_2(0) = \frac{1}{2^{2m/\sqrt{2}}}. \quad (30)$$

By [20], we have that $\psi_2'(x) < 0$ for $x > 0$. That is ψ_2 is strictly decreasing over $(0, +\infty)$.

Clearly, ψ_2 is strictly increasing over $(-\infty, 0)$ and $\psi_2'(0) = 0$.

Furthermore we obtain that

$$\lim_{x \rightarrow +\infty} \psi_2(x) = \frac{1}{4} [\varphi(+\infty) - \varphi(+\infty)] = 0, \quad (31)$$

and

$$\lim_{x \rightarrow -\infty} \psi_2(x) = \frac{1}{4} [\varphi(-\infty) - \varphi(-\infty)] = 0. \quad (32)$$

That is the x -axis is the horizontal asymptote of ψ_2 .

Conclusion, ψ_2 is a bell shape symmetric function with maximum

$$\psi_2(0) = \frac{1}{2^{2m/\sqrt{2}}}, \quad m \in \mathbb{N}. \quad (33)$$

We need

Theorem 6 [20]. *We have that*

$$\sum_{i=-\infty}^{\infty} \psi_2(x-i) = 1, \quad \forall x \in \mathbb{R}. \quad (34)$$

Theorem 7 [20]. *It holds*

$$\int_{-\infty}^{\infty} \psi_2(x) dx = 1. \quad (35)$$

Theorem 8 [20]. *Let $0 < \alpha < 1$, and $n \in \mathbb{N}$ with $n^{1-\alpha} > 2$. It holds*

$$\begin{cases} k = -\infty \\ : |nx - k| \geq n^{1-\alpha} \end{cases} \psi_2(nx - k) < \frac{1}{4m(n^{1-\alpha} - 2)^{2m}} =: c_2(\alpha, n), \quad m \in \mathbb{N}. \quad (36)$$

We need

Theorem 9 [20]. Let $[a, b] \subset \mathbb{R}$ and $n \in \mathbb{N}$ so that $\lceil na \rceil \leq \lfloor nb \rfloor$. It holds

$$\frac{1}{\sum_{k=\lceil na \rceil}^{\lfloor nb \rfloor} \psi_2(nx - k)} < 2 \left(\sqrt[2m]{1 + 4^m} \right) =: \alpha_2, \quad (37)$$

$\forall x \in [a, b], m \in \mathbb{N}$.

Note 2. 1) By [20] we have that

$$\lim_{n \rightarrow \infty} \sum_{k=\lceil na \rceil}^{\lfloor nb \rfloor} \psi_2(nx - k) \neq 1, \quad (38)$$

for at least some $x \in [a, b]$.

2) Let $[a, b] \subset \mathbb{R}$. For large $n \in \mathbb{N}$ we always have $\lceil na \rceil \leq \lfloor nb \rfloor$. Also $a \leq \frac{k}{n} \leq b$, iff $\lceil na \rceil \leq k \leq \lfloor nb \rfloor$.

In general it holds that

$$\sum_{k=\lceil na \rceil}^{\lfloor nb \rfloor} \psi_2(nx - k) \leq 1. \quad (39)$$

We introduce (see also [25])

$$Z_2(x_1, \dots, x_N) := Z_2(x) := \prod_{i=1}^N \psi_2(x_i), \quad x = (x_1, \dots, x_N) \in \mathbb{R}^N, \quad N \in \mathbb{N}. \quad (40)$$

It has the properties:

(i) $Z_2(x) > 0, \forall x \in \mathbb{R}^N$,

(ii)

$$\sum_{k=-\infty}^{\infty} Z_2(x - k) := \sum_{k_1=-\infty}^{\infty} \sum_{k_2=-\infty}^{\infty} \dots \sum_{k_N=-\infty}^{\infty} Z_2(x_1 - k_1, \dots, x_N - k_N) = 1, \quad (41)$$

where $k := (k_1, \dots, k_n) \in \mathbb{Z}^N, \forall x \in \mathbb{R}^N$,

hence

(iii)

$$\sum_{k=-\infty}^{\infty} Z_2(nx - k) = 1, \quad (42)$$

$\forall x \in \mathbb{R}^N; n \in \mathbb{N}$,

and

(iv)

$$\int_{\mathbb{R}^N} Z_2(x) dx = 1, \quad (43)$$

that is Z_2 is a multivariate density function.

(v) It is clear that

$$\sum_{k=-\infty}^{\infty} Z_2(nx - k) < \frac{1}{4m(n^{1-\beta} - 2)^{2m}} = c_2(\beta, n), \quad (44)$$

$$\left\{ \begin{array}{l} k = -\infty \\ \left\| \frac{k}{n} - x \right\|_{\infty} > \frac{1}{n^{\beta}} \end{array} \right.$$

$0 < \beta < 1$, $n \in \mathbb{N} : n^{1-\beta} > 2$, $x \in \mathbb{R}^N$, $m \in \mathbb{N}$.

(vi) By Theorem 9 we get that

$$0 < \frac{1}{\sum_{k=\lceil na \rceil}^{\lfloor nb \rfloor} Z_2(nx - k)} < \frac{1}{(\psi_2(1))^N} \cong [2(\sqrt[2m]{1 + 4m})]^N := \gamma_2(N), \quad (45)$$

$\forall x \in \left(\prod_{i=1}^N [a_i, b_i] \right)$, $n \in \mathbb{N}$.

Furthermore it holds

$$\lim_{n \rightarrow \infty} \sum_{k=\lceil na \rceil}^{\lfloor nb \rfloor} Z_2(nx - k) \neq 1, \quad (46)$$

for at least some $x \in \left(\prod_{i=1}^N [a_i, b_i] \right)$.

2.3 About the Gudermannian Activation Function

See also [21, 34].

Here we consider $gd(x)$ the Gudermannian function [34], which is a sigmoid function, as a generator function:

$$\sigma(x) = 2 \arctan \left(\tanh \left(\frac{x}{2} \right) \right) = \int_0^x \frac{dt}{\cosh t} =: gd(x), \quad x \in \mathbb{R}. \quad (47)$$

Let the normalized generator sigmoid function

$$f(x) := \frac{2}{\pi} \sigma(x) = \frac{2}{\pi} \int_0^x \frac{dt}{\cosh t} = \frac{4}{\pi} \int_0^x \frac{1}{e^t + e^{-t}} dt, \quad x \in \mathbb{R}. \quad (48)$$

Here

$$f'(x) = \frac{2}{\pi \cosh x} > 0, \quad \forall x \in \mathbb{R},$$

hence f is strictly increasing on \mathbb{R} .

Notice that $\tanh(-x) = -\tanh x$ and $\arctan(-x) = -\arctan x$, $x \in \mathbb{R}$.

So, here the neural network activation function will be:

$$\psi_3(x) = \frac{1}{4} [f(x+1) - f(x-1)], \quad x \in \mathbb{R}. \quad (49)$$

By [21], we get that

$$\psi_3(x) = \psi_3(-x), \quad \forall x \in \mathbb{R}, \quad (50)$$

i.e. it is even and symmetric with respect to the y -axis. Here we have $f(+\infty) = 1$, $f(-\infty) = -1$ and $f(0) = 0$. Clearly it is

$$f(-x) = -f(x), \forall x \in \mathbb{R}, \tag{51}$$

an odd function, symmetric with respect to the origin. Since $x + 1 > x - 1$, and $f(x + 1) > f(x - 1)$, we obtain $\psi_3(x) > 0, \forall x \in \mathbb{R}$.

By [21], we have that

$$\psi_3(0) = \frac{1}{\pi}gd(1) \cong 0.2757. \tag{52}$$

By [21] ψ_3 is strictly decreasing on $(0, +\infty)$, and strictly increasing on $(-\infty, 0)$, and $\psi'_3(0) = 0$.

Also we have that

$$\lim_{x \rightarrow +\infty} \psi_3(x) = \lim_{x \rightarrow -\infty} \psi_3(x) = 0, \tag{53}$$

that is the x -axis is the horizontal asymptote for ψ_3 .

Conclusion, ψ_3 is a bell shaped symmetric function with maximum $\psi_3(0) \cong 0.551$.

We need

Theorem 10 [21]. *It holds that*

$$\sum_{i=-\infty}^{\infty} \psi_3(x - i) = 1, \forall x \in \mathbb{R}. \tag{54}$$

Theorem 11 [21]. *We have that*

$$\int_{-\infty}^{\infty} \psi_3(x) dx = 1. \tag{55}$$

So $\psi_3(x)$ is a density function.

Theorem 12 [21]. *Let $0 < \alpha < 1$, and $n \in \mathbb{N}$ with $n^{1-\alpha} > 2$. It holds*

$$\sum_{\substack{k=-\infty \\ : |nx - k| \geq n^{1-\alpha}}}^{\infty} \psi_3(nx - k) < \frac{2}{\pi e^{(n^{1-\alpha}-2)}} = \frac{2e^2}{\pi e^{n^{1-\alpha}}} =: c_3(\alpha, n). \tag{56}$$

Theorem 13 [21]. *Let $[a, b] \subset \mathbb{R}$ and $n \in \mathbb{N}$, so that $\lceil na \rceil \leq \lfloor nb \rfloor$. It holds*

$$\frac{1}{\sum_{k=\lceil na \rceil}^{\lfloor nb \rfloor} \psi_3(nx - k)} < \frac{2\pi}{gd(2)} \cong 4.824 =: \alpha_3, \tag{57}$$

$\forall x \in [a, b]$.

We make

Remark 5 [21].

(i) We have that

$$\lim_{n \rightarrow \infty} \sum_{k=\lceil na \rceil}^{\lfloor nb \rfloor} \psi_3(nx - k) \neq 1, \quad (58)$$

for at least some $x \in [a, b]$.

(ii) Let $[a, b] \subset \mathbb{R}$. For large n we always have $\lceil na \rceil \leq \lfloor nb \rfloor$. Also $a \leq \frac{k}{n} \leq b$, iff $\lceil na \rceil \leq k \leq \lfloor nb \rfloor$.

In general it holds

$$\sum_{k=\lceil na \rceil}^{\lfloor nb \rfloor} \psi_3(nx - k) \leq 1. \quad (59)$$

We introduce (see also [23])

$$Z_3(x_1, \dots, x_N) := Z_3(x) := \prod_{i=1}^N \psi_3(x_i), \quad x = (x_1, \dots, x_N) \in \mathbb{R}^N, \quad N \in \mathbb{N}. \quad (60)$$

It has the properties:

- (i) $Z_3(x) > 0, \quad \forall x \in \mathbb{R}^N,$
 (ii)

$$\sum_{k=-\infty}^{\infty} Z_3(x - k) := \sum_{k_1=-\infty}^{\infty} \sum_{k_2=-\infty}^{\infty} \dots \sum_{k_N=-\infty}^{\infty} Z_3(x_1 - k_1, \dots, x_N - k_N) = 1, \quad (61)$$

where $k := (k_1, \dots, k_n) \in \mathbb{Z}^N, \quad \forall x \in \mathbb{R}^N,$

hence

(iii)

$$\sum_{k=-\infty}^{\infty} Z_3(nx - k) = 1, \quad (62)$$

$\forall x \in \mathbb{R}^N; \quad n \in \mathbb{N},$

and

(iv)

$$\int_{\mathbb{R}^N} Z_3(x) dx = 1, \quad (63)$$

that is Z_3 is a multivariate density function.

(v) It is also clear that

$$\sum_{k=-\infty}^{\infty} Z_3(nx - k) < \frac{2e^2}{\pi e^{n^{1-\beta}}} = c_3(\beta, n), \quad (64)$$

$$\left\{ \begin{array}{l} k = -\infty \\ \left\| \frac{k}{n} - x \right\|_{\infty} > \frac{1}{n^{\beta}} \end{array} \right.$$

$0 < \beta < 1, n \in \mathbb{N} : n^{1-\beta} > 2, x \in \mathbb{R}^N, m \in \mathbb{N}.$

(vi) By Theorem 13 we get that

$$0 < \frac{1}{\sum_{k=\lceil na \rceil}^{\lfloor nb \rfloor} Z_3(nx - k)} < \left(\frac{2\pi}{gd(2)} \right)^N \cong (4.824)^N =: \gamma_3(N), \quad (65)$$

$\forall x \in \left(\prod_{i=1}^N [a_i, b_i] \right), n \in \mathbb{N}.$

Furthermore it holds

$$\lim_{n \rightarrow \infty} \sum_{k=\lceil na \rceil}^{\lfloor nb \rfloor} Z_3(nx - k) \neq 1, \quad (66)$$

for at least some $x \in \left(\prod_{i=1}^N [a_i, b_i] \right).$

2.4 About the Generalized Symmetrical Activation Function

Here we consider the generalized symmetrical sigmoid function [22, 29]

$$f_1(x) = \frac{x}{(1 + |x|^{\mu})^{\frac{1}{\mu}}}, \mu > 0, x \in \mathbb{R}. \quad (67)$$

This has applications in immunology and protection from disease together with probability theory. It is also called a symmetrical protection curve.

The parameter μ is a shape parameter controlling how fast the curve approaches the asymptotes for a given slope at the inflection point. When $\mu = 1$ f_1 is the absolute sigmoid function, and when $\mu = 2$, f_1 is the square root sigmoid function. When $\mu = 1.5$ the function approximates the arctangent function, when $\mu = 2.9$ it approximates the logistic function, and when $\mu = 3.4$ it approximates the error function. Parameter μ is estimated in the likelihood maximization [29]. For more see [29].

Next we study the particular generator sigmoid function

$$f_2(x) = \frac{x}{(1 + |x|^{\lambda})^{\frac{1}{\lambda}}}, \lambda \text{ is an odd number, } x \in \mathbb{R}. \quad (68)$$

We have that $f_2(0) = 0$, and

$$f_2(-x) = -f_2(x), \quad (69)$$

so f_2 is symmetric with respect to zero.

When $x \geq 0$, we get that [22]

$$f_2'(x) = \frac{1}{(1+x^\lambda)^{\frac{\lambda+1}{\lambda}}} > 0, \quad (70)$$

that is f_2 is strictly increasing on $[0, +\infty)$ and f_2 is strictly increasing on $(-\infty, 0]$. Hence f_2 is strictly increasing on \mathbb{R} .

We also have $f_2(+\infty) = f_2(-\infty) = 1$.

Let us consider the activation function [22]:

$$\begin{aligned} \psi_4(x) &= \frac{1}{4} [f_2(x+1) - f_2(x-1)] = \\ &= \frac{1}{4} \left[\frac{(x+1)}{\left(1+|x+1|^\lambda\right)^{\frac{1}{\lambda}}} - \frac{(x-1)}{\left(1+|x-1|^\lambda\right)^{\frac{1}{\lambda}}} \right]. \end{aligned} \quad (71)$$

Clearly it holds [22]

$$\psi_4(x) = \psi_4(-x), \quad \forall x \in \mathbb{R}. \quad (72)$$

and

$$\psi_4(0) = \frac{1}{2\sqrt[\lambda]{2}}, \quad (73)$$

and $\psi_4(x) > 0, \forall x \in \mathbb{R}$.

Following [22], we have that ψ_4 is strictly decreasing over $[0, +\infty)$, and ψ_4 is strictly increasing on $(-\infty, 0]$, by ψ_4 -symmetry with respect to y -axis, and $\psi_4'(0) = 0$.

Clearly it is

$$\lim_{x \rightarrow +\infty} \psi_4(x) = \lim_{x \rightarrow -\infty} \psi_4(x) = 0, \quad (74)$$

therefore the x -axis is the horizontal asymptote of $\psi_4(x)$.

The value

$$\psi_4(0) = \frac{1}{2\sqrt[\lambda]{2}}, \quad \lambda \text{ is an odd number}, \quad (75)$$

is the maximum of ψ_4 , which is a bell shaped function.

We need

Theorem 14 [22]. *It holds*

$$\sum_{i=-\infty}^{\infty} \psi_4(x-i) = 1, \quad \forall x \in \mathbb{R}. \quad (76)$$

Theorem 15 [22]. *We have that*

$$\int_{-\infty}^{\infty} \psi_4(x) dx = 1. \quad (77)$$

So that $\psi_4(x)$ is a density function on \mathbb{R} .

We need

Theorem 16 [22]. *Let $0 < \alpha < 1$, and $n \in \mathbb{N}$ with $n^{1-\alpha} > 2$. It holds*

$$\left\{ \begin{array}{l} \sum_{j=-\infty}^{\infty} \psi_4(nx - j) < \frac{1}{2\lambda(n^{1-\alpha} - 2)^\lambda} =: c_4(\alpha, n), \\ : |nx - j| \geq n^{1-\alpha} \end{array} \right. \quad (78)$$

where $\lambda \in \mathbb{N}$ is an odd number.

We also need

Theorem 17 [22]. *Let $[a, b] \subset \mathbb{R}$ and $n \in \mathbb{N}$ so that $\lceil na \rceil \leq \lfloor nb \rfloor$. Then*

$$\frac{1}{\sum_{k=\lceil na \rceil}^{\lfloor nb \rfloor} \psi_4(|nx - k|)} < 2 \sqrt[\lambda]{1 + 2^\lambda} =: \alpha_4, \quad (79)$$

where λ is an odd number, $\forall x \in [a, b]$.

We make

Remark 6 [22]. (1) We have that

$$\lim_{n \rightarrow \infty} \sum_{k=\lceil na \rceil}^{\lfloor nb \rfloor} \psi_4(nx - k) \neq 1, \text{ for at least some } x \in [a, b]. \quad (80)$$

(2) Let $[a, b] \subset \mathbb{R}$. For large enough n we always obtain $\lceil na \rceil \leq \lfloor nb \rfloor$. Also $a \leq \frac{k}{n} \leq b$, iff $\lceil na \rceil \leq k \leq \lfloor nb \rfloor$.

In general it holds that

$$\sum_{k=\lceil na \rceil}^{\lfloor nb \rfloor} \psi_4(nx - k) \leq 1. \quad (81)$$

We introduce (see also [26])

$$Z_4(x_1, \dots, x_N) := Z_4(x) := \prod_{i=1}^N \psi_4(x_i), \quad x = (x_1, \dots, x_N) \in \mathbb{R}^N, \quad N \in \mathbb{N}. \quad (82)$$

It has the properties:

(i) $Z_4(x) > 0, \forall x \in \mathbb{R}^N$,

(ii)

$$\sum_{k=-\infty}^{\infty} Z_4(x-k) := \sum_{k_1=-\infty}^{\infty} \sum_{k_2=-\infty}^{\infty} \dots \sum_{k_N=-\infty}^{\infty} Z_4(x_1 - k_1, \dots, x_N - k_N) = 1, \quad (83)$$

where $k := (k_1, \dots, k_n) \in \mathbb{Z}^N$, $\forall x \in \mathbb{R}^N$,
hence

(iii)

$$\sum_{k=-\infty}^{\infty} Z_4(nx-k) = 1, \quad (84)$$

$\forall x \in \mathbb{R}^N$; $n \in \mathbb{N}$,

and

(iv)

$$\int_{\mathbb{R}^N} Z_4(x) dx = 1, \quad (85)$$

that is Z_4 is a multivariate density function.

(v) It is clear that

$$\sum_{\substack{k=-\infty \\ \left\| \frac{k}{n} - x \right\|_{\infty} > \frac{1}{n^{\beta}}}^{\infty} Z_4(nx-k) < \frac{1}{2\lambda(n^{1-\beta}-2)^{\lambda}} = c_4(\beta, n), \quad (86)$$

$0 < \beta < 1$, $n \in \mathbb{N} : n^{1-\beta} > 2$, $x \in \mathbb{R}^N$, λ is odd.

(vi) By Theorem 17 we get that

$$0 < \frac{1}{\sum_{k=\lceil na \rceil}^{\lfloor nb \rfloor} Z_4(nx-k)} < \left(2\sqrt[\lambda]{1+2^{\lambda}}\right)^N =: \gamma_4(N), \quad (87)$$

$\forall x \in \left(\prod_{i=1}^N [a_i, b_i]\right)$, $n \in \mathbb{N}$, λ is odd.

Furthermore it holds

$$\lim_{n \rightarrow \infty} \sum_{k=\lceil na \rceil}^{\lfloor nb \rfloor} Z_4(nx-k) \neq 1, \quad (88)$$

for at least some $x \in \left(\prod_{i=1}^N [a_i, b_i]\right)$.

Set

$$\lceil na \rceil := (\lceil na_1 \rceil, \dots, \lceil na_N \rceil),$$

$$\lfloor nb \rfloor := (\lfloor nb_1 \rfloor, \dots, \lfloor nb_N \rfloor),$$

where $a := (a_1, \dots, a_N)$, $b := (b_1, \dots, b_N)$, $k := (k_1, \dots, k_N)$.

Let $f \in C\left(\prod_{i=1}^N [a_i, b_i]\right)$, and $n \in \mathbb{N}$ such that $\lceil na_i \rceil \leq \lfloor nb_i \rfloor$, $i = 1, \dots, N$.

We define the multivariate averaged positive linear quasi-interpolation neural network operators ($x := (x_1, \dots, x_N) \in \left(\prod_{i=1}^N [a_i, b_i]\right)$); $j = 1, 2, 3, 4$:

$${}_j A_n(f, x_1, \dots, x_N) := {}_j A_n(f, x) := \frac{\sum_{k=\lceil na \rceil}^{\lfloor nb \rfloor} f\left(\frac{k}{n}\right) Z_j(nx - k)}{\sum_{k=\lceil na \rceil}^{\lfloor nb \rfloor} Z_j(nx - k)} = \quad (89)$$

$$\frac{\sum_{k_1=\lceil na_1 \rceil}^{\lfloor nb_1 \rfloor} \sum_{k_2=\lceil na_2 \rceil}^{\lfloor nb_2 \rfloor} \dots \sum_{k_N=\lceil na_N \rceil}^{\lfloor nb_N \rfloor} f\left(\frac{k_1}{n}, \dots, \frac{k_N}{n}\right) \left(\prod_{i=1}^N \psi_j(nx_i - k_i)\right)}{\prod_{i=1}^N \left(\sum_{k_i=\lceil na_i \rceil}^{\lfloor nb_i \rfloor} \psi_j(nx_i - k_i)\right)}.$$

For large enough $n \in \mathbb{N}$ we always obtain $\lceil na_i \rceil \leq \lfloor nb_i \rfloor$, $i = 1, \dots, N$. Also $a_i \leq \frac{k_i}{n} \leq b_i$, iff $\lceil na_i \rceil \leq k_i \leq \lfloor nb_i \rfloor$, $i = 1, \dots, N$.

When $f \in C_B(\mathbb{R}^N)$ we define ($j = 1, 2, 3, 4$)

$${}_j B_n(f, x) := {}_j B_n(f, x_1, \dots, x_N) := \sum_{k=-\infty}^{\infty} f\left(\frac{k}{n}\right) Z_j(nx - k) := \quad (90)$$

$$\sum_{k_1=-\infty}^{\infty} \sum_{k_2=-\infty}^{\infty} \dots \sum_{k_N=-\infty}^{\infty} f\left(\frac{k_1}{n}, \frac{k_2}{n}, \dots, \frac{k_N}{n}\right) \left(\prod_{i=1}^N \psi_j(nx_i - k_i)\right),$$

$n \in \mathbb{N}$, $\forall x \in \mathbb{R}^N$, $N \in \mathbb{N}$, the multivariate full quasi-interpolation neural network operators.

Also for $f \in C_B(\mathbb{R}^N)$ we define the multivariate Kantorovich type neural network operators ($j = 1, 2, 3, 4$)

$${}_j C_n(f, x) := {}_j C_n(f, x_1, \dots, x_N) := \sum_{k=-\infty}^{\infty} \left(n^N \int_{\frac{k}{n}}^{\frac{k+1}{n}} f(t) dt \right) Z_j(nx - k) := \quad (91)$$

$$\sum_{k_1=-\infty}^{\infty} \sum_{k_2=-\infty}^{\infty} \dots \sum_{k_N=-\infty}^{\infty} \left(n^N \int_{\frac{k_1}{n}}^{\frac{k_1+1}{n}} \int_{\frac{k_2}{n}}^{\frac{k_2+1}{n}} \dots \int_{\frac{k_N}{n}}^{\frac{k_N+1}{n}} f(t_1, \dots, t_N) dt_1 \dots dt_N \right)$$

$$\cdot \left(\prod_{i=1}^N \psi_j(nx_i - k_i) \right),$$

$n \in \mathbb{N}$, $\forall x \in \mathbb{R}^N$.

Again for $f \in C_B(\mathbb{R}^N)$, $N \in \mathbb{N}$, we define the multivariate neural network operators of quadrature type ${}_j D_n(f, x)$, $n \in \mathbb{N}$, as follows. Let $\theta = (\theta_1, \dots, \theta_N) \in \mathbb{N}^N$, $\bar{r} = (r_1, \dots, r_N) \in \mathbb{Z}_+^N$, $w_{\bar{r}} = w_{r_1, r_2, \dots, r_N} \geq 0$, such that

$$\sum_{\bar{r}=0}^{\theta} w_{\bar{r}} = \sum_{r_1=0}^{\theta_1} \sum_{r_2=0}^{\theta_2} \dots \sum_{r_N=0}^{\theta_N} w_{r_1, r_2, \dots, r_N} = 1; k \in \mathbb{Z}^N \text{ and}$$

$$\delta_{nk}(f) := \delta_{n, k_1, k_2, \dots, k_N}(f) := \sum_{\bar{r}=0}^{\theta} w_{\bar{r}} f\left(\frac{k}{n} + \frac{\bar{r}}{n\theta}\right) :=$$

$$\sum_{r_1=0}^{\theta_1} \sum_{r_2=0}^{\theta_2} \cdots \sum_{r_N=0}^{\theta_N} w_{r_1, r_2, \dots, r_N} f \left(\frac{k_1}{n} + \frac{r_1}{n\theta_1}, \frac{k_2}{n} + \frac{r_2}{n\theta_2}, \dots, \frac{k_N}{n} + \frac{r_N}{n\theta_N} \right), \quad (92)$$

where $\frac{\bar{r}}{\theta} := \left(\frac{r_1}{\theta_1}, \frac{r_2}{\theta_2}, \dots, \frac{r_N}{\theta_N} \right); j = 1, 2, 3, 4.$

We put

$${}_j D_n(f, x) := {}_j D_n(f, x_1, \dots, x_N) := \sum_{k=-\infty}^{\infty} \delta_{nk}(f) Z_j(nx - k) := \quad (93)$$

$$\sum_{k_1=-\infty}^{\infty} \sum_{k_2=-\infty}^{\infty} \cdots \sum_{k_N=-\infty}^{\infty} \delta_{n, k_1, k_2, \dots, k_N}(f) \left(\prod_{i=1}^N \psi_j(nx_i - k_i) \right),$$

$\forall x \in \mathbb{R}^N.$

For the next we need, for $f \in C \left(\prod_{i=1}^N [a_i, b_i] \right)$ the first multivariate modulus of continuity

$$\omega_1(f, h) := \sup_{\substack{x, y \in \prod_{i=1}^N [a_i, b_i] \\ \|x - y\|_{\infty} \leq h}} |f(x) - f(y)|, \quad h > 0. \quad (94)$$

It holds that

$$\lim_{h \rightarrow 0} \omega_1(f, h) = 0. \quad (95)$$

Similarly it is defined for $f \in C_B(\mathbb{R}^N)$ (continuous and bounded functions on \mathbb{R}^N) the $\omega_1(f, h)$, and it has the property (95), given that $f \in C_U(\mathbb{R}^N)$ (uniformly continuous functions on \mathbb{R}^N).

We mention

Theorem 18 (see [23–26]). *Let $f \in C \left(\prod_{i=1}^N [a_i, b_i] \right)$, $0 < \beta < 1$, $x \in \left(\prod_{i=1}^N [a_i, b_i] \right)$, $N, n \in \mathbb{N}$ with $n^{1-\beta} > 2$; $j = 1, 2, 3, 4$. Then*

1)

$$|{}_j A_n(f, x) - f(x)| \leq \gamma_j(N) \left[\omega_1 \left(f, \frac{1}{n^\beta} \right) + 2c_j(\beta, n) \|f\|_{\infty} \right] =: \lambda_{j1}, \quad (96)$$

and

2)

$$\|{}_j A_n(f) - f\|_{\infty} \leq \lambda_{j1}. \quad (97)$$

We notice that $\lim_{n \rightarrow \infty} {}_j A_n(f) = f$, pointwise and uniformly.

In this article we extend Theorem 18 to the fuzzy-random level.

We mention

Theorem 19 (see [23–26]). *Let $f \in C_B(\mathbb{R}^N)$, $0 < \beta < 1$, $x \in \mathbb{R}^N$, $N, n \in \mathbb{N}$ with $n^{1-\beta} > 2$; $j = 1, 2, 3, 4$. Then*

1)

$$|{}_jB_n(f, x) - f(x)| \leq \omega_1\left(f, \frac{1}{n^\beta}\right) + 2c_j(\beta, n) \|f\|_\infty =: \lambda_{j2}, \quad (98)$$

2)

$$\|{}_jB_n(f) - f\|_\infty \leq \lambda_{j2}. \quad (99)$$

Given that $f \in (C_U(\mathbb{R}^N) \cap C_B(\mathbb{R}^N))$, we obtain $\lim_{n \rightarrow \infty} {}_jB_n(f) = f$, uniformly.

We also need

Theorem 20 (see [23–26]). Let $f \in C_B(\mathbb{R}^N)$, $0 < \beta < 1$, $x \in \mathbb{R}^N$, $N, n \in \mathbb{N}$ with $n^{1-\beta} > 2$; $j = 1, 2, 3, 4$. Then

1)

$$|{}_jC_n(f, x) - f(x)| \leq \omega_1\left(f, \frac{1}{n} + \frac{1}{n^\beta}\right) + 2c_j(\beta, n) \|f\|_\infty =: \lambda_{j3}, \quad (100)$$

2)

$$\|{}_jC_n(f) - f\|_\infty \leq \lambda_{j3}. \quad (101)$$

Given that $f \in (C_U(\mathbb{R}^N) \cap C_B(\mathbb{R}^N))$, we obtain $\lim_{n \rightarrow \infty} {}_jC_n(f) = f$, uniformly.

We also need

Theorem 21 (see [23–26]). Let $f \in C_B(\mathbb{R}^N)$, $0 < \beta < 1$, $x \in \mathbb{R}^N$, $N, n \in \mathbb{N}$ with $n^{1-\beta} > 2$; $j = 1, 2, 3, 4$. Then

1)

$$|{}_jD_n(f, x) - f(x)| \leq \omega_1\left(f, \frac{1}{n} + \frac{1}{n^\beta}\right) + 2c_j(\beta, n) \|f\|_\infty = \lambda_{j3}, \quad (102)$$

2)

$$\|{}_jD_n(f) - f\|_\infty \leq \lambda_{j3}. \quad (103)$$

Given that $f \in (C_U(\mathbb{R}^N) \cap C_B(\mathbb{R}^N))$, we obtain $\lim_{n \rightarrow \infty} {}_jD_n(f) = f$, uniformly.

In this article we extend Theorems 19, 20, 21 to the random level.

We are also motivated by [1–16] and continuing [17]. For general knowledge on neural networks we recommend [31–33].

3 Main Results

I) q -mean Approximation by Fuzzy-Random arctangent, algebraic, Gudermannian and generalized symmetric activation functions based Quasi-Interpolation Neural Network Operators

All terms and assumptions here as in Sects. 1, 2.

Let $f \in C_{\mathcal{FR}}^{U_q} \left(\prod_{i=1}^N [a_i, b_i] \right)$, $1 \leq q < +\infty$, $n, N \in \mathbb{N}$, $0 < \beta < 1$, $\vec{x} \in \left(\prod_{i=1}^N [a_i, b_i] \right)$, (X, \mathcal{B}, P) probability space, $s \in X$; $j = 1, 2, 3, 4$.

We define the following multivariate fuzzy random arctangent, algebraic, Gudermannian and generalized symmetric activation functions based quasi-interpolation linear neural network operators

$$({}_j A_n^{\mathcal{FR}}(f))(\vec{x}, s) := \sum_{\vec{k}=\lceil na \rceil}^{\lfloor nb \rfloor^*} f\left(\frac{\vec{k}}{n}, s\right) \odot \frac{Z_j(n\vec{x} - \vec{k})}{\sum_{\vec{k}=\lceil na \rceil}^{\lfloor nb \rfloor} Z_j(n\vec{x} - \vec{k})}, \quad (104)$$

(see also (89)).

We present

Theorem 22. Let $f \in C_{\mathcal{FR}}^{U_q} \left(\prod_{i=1}^N [a_i, b_i] \right)$, $0 < \beta < 1$, $\vec{x} \in \left(\prod_{i=1}^N [a_i, b_i] \right)$, $n, N \in \mathbb{N}$, with $n^{1-\beta} > 2$, $1 \leq q < +\infty$. Assume that $\int_X (D^*(f(\cdot, s), \tilde{\omega}))^q P(ds) < \infty$; $j = 1, 2, 3, 4$. Then

1)

$$\left(\int_X D^q(({}_j A_n^{\mathcal{FR}}(f))(\vec{x}, s), f(\vec{x}, s)) P(ds) \right)^{\frac{1}{q}} \leq \quad (105)$$

$$\gamma_j(N) \left\{ \Omega_1 \left(f, \frac{1}{n^\beta} \right)_{L^q} + 2c_j(\beta, n) \left(\int_X (D^*(f(\cdot, s), \tilde{\omega}))^q P(ds) \right)^{\frac{1}{q}} \right\} =: \lambda_{j1}^{(\mathcal{FR})},$$

2)

$$\left\| \left(\int_X D^q(({}_j A_n^{\mathcal{FR}}(f))(\vec{x}, s), f(\vec{x}, s)) P(ds) \right)^{\frac{1}{q}} \right\|_{\infty, \left(\prod_{i=1}^N [a_i, b_i] \right)} \leq \lambda_{j1}^{(\mathcal{FR})}, \quad (106)$$

where $\gamma_j(N)$ as in (25), (45), (65), (87) and $c_j(\beta, n)$ as in (24), (44), (64), (86).

Proof. We notice that

$$D \left(f \left(\frac{\vec{k}}{n}, s \right), f(\vec{x}, s) \right) \leq D \left(f \left(\frac{\vec{k}}{n}, s \right), \tilde{\omega} \right) + D(f(\vec{x}, s), \tilde{\omega}) \quad (107)$$

$$\leq 2D^*(f(\cdot, s), \tilde{o}).$$

Hence

$$D^q \left(f \left(\frac{\vec{k}}{n}, s \right), f(\vec{x}, s) \right) \leq 2^q D^{*q}(f(\cdot, s), \tilde{o}), \quad (108)$$

and

$$\left(\int_X D^q \left(f \left(\frac{\vec{k}}{n}, s \right), f(\vec{x}, s) \right) P(ds) \right)^{\frac{1}{q}} \leq 2 \left(\int_X (D^*(f(\cdot, s), \tilde{o}))^q P(ds) \right)^{\frac{1}{q}}. \quad (109)$$

We observe that

$$D(({}_j A_n^{\mathcal{FR}}(f))(\vec{x}, s), f(\vec{x}, s)) = \quad (110)$$

$$D \left(\sum_{\vec{k}=\lceil na \rceil}^{\lfloor nb \rfloor^*} f \left(\frac{\vec{k}}{n}, s \right) \odot \frac{Z_j(nx-k)}{\sum_{\vec{k}=\lceil na \rceil}^{\lfloor nb \rfloor} Z_j(nx-k)}, f(\vec{x}, s) \odot 1 \right) =$$

$$D \left(\sum_{\vec{k}=\lceil na \rceil}^{\lfloor nb \rfloor^*} f \left(\frac{\vec{k}}{n}, s \right) \odot \frac{Z_j(nx-k)}{\sum_{\vec{k}=\lceil na \rceil}^{\lfloor nb \rfloor} Z_j(nx-k)}, f(\vec{x}, s) \odot \frac{\sum_{\vec{k}=\lceil na \rceil}^{\lfloor nb \rfloor} Z_j(nx-k)}{\sum_{\vec{k}=\lceil na \rceil}^{\lfloor nb \rfloor} Z_j(nx-k)} \right) = \quad (111)$$

$$D \left(\sum_{\vec{k}=\lceil na \rceil}^{\lfloor nb \rfloor^*} f \left(\frac{\vec{k}}{n}, s \right) \odot \frac{Z_j(nx-k)}{\sum_{\vec{k}=\lceil na \rceil}^{\lfloor nb \rfloor} Z_j(nx-k)}, \sum_{\vec{k}=\lceil na \rceil}^{\lfloor nb \rfloor^*} f(\vec{x}, s) \odot \frac{Z_j(nx-k)}{\sum_{\vec{k}=\lceil na \rceil}^{\lfloor nb \rfloor} Z_j(nx-k)} \right) \\ \leq \sum_{\vec{k}=\lceil na \rceil}^{\lfloor nb \rfloor} \left(\frac{Z_j(nx-k)}{\sum_{\vec{k}=\lceil na \rceil}^{\lfloor nb \rfloor} Z_j(nx-k)} \right) D \left(f \left(\frac{\vec{k}}{n}, s \right), f(\vec{x}, s) \right). \quad (112)$$

So that

$$D(({}_j A_n^{\mathcal{FR}}(f))(\vec{x}, s), f(\vec{x}, s)) \leq$$

$$\sum_{\vec{k}=\lceil na \rceil}^{\lfloor nb \rfloor} \left(\frac{Z_j(nx-k)}{\sum_{\vec{k}=\lceil na \rceil}^{\lfloor nb \rfloor} Z_j(nx-k)} \right) D \left(f \left(\frac{\vec{k}}{n}, s \right), f(\vec{x}, s) \right) = \quad (113)$$

$$\begin{aligned} & \sum_{\substack{\vec{k}=\lceil na \rceil \\ \|\frac{\vec{k}}{n}-\vec{x}\|_\infty \leq \frac{1}{n^\beta}}}^{\lfloor nb \rfloor} \left(\frac{Z_j(nx-k)}{\sum_{\vec{k}=\lceil na \rceil}^{\lfloor nb \rfloor} Z_j(nx-k)} \right) D \left(f \left(\frac{\vec{k}}{n}, s \right), f(\vec{x}, s) \right) + \\ & \sum_{\substack{\vec{k}=\lceil na \rceil \\ \|\frac{\vec{k}}{n}-\vec{x}\|_\infty > \frac{1}{n^\beta}}}^{\lfloor nb \rfloor} \left(\frac{Z_j(nx-k)}{\sum_{\vec{k}=\lceil na \rceil}^{\lfloor nb \rfloor} Z_j(nx-k)} \right) D \left(f \left(\frac{\vec{k}}{n}, s \right), f(\vec{x}, s) \right). \end{aligned}$$

Hence it holds

$$\left(\int_X D^q \left(({}_j A_n^{\mathcal{FR}}(f))(\vec{x}, s), f(\vec{x}, s) \right) P(ds) \right)^{\frac{1}{q}} \leq \quad (114)$$

$$\begin{aligned} & \sum_{\substack{\vec{k}=\lceil na \rceil \\ \|\frac{\vec{k}}{n}-\vec{x}\|_\infty \leq \frac{1}{n^\beta}}}^{\lfloor nb \rfloor} \left(\frac{Z_j(nx-k)}{\sum_{\vec{k}=\lceil na \rceil}^{\lfloor nb \rfloor} Z_j(nx-k)} \right) \left(\int_X D^q \left(f \left(\frac{\vec{k}}{n}, s \right), f(\vec{x}, s) \right) P(ds) \right)^{\frac{1}{q}} + \\ & \sum_{\substack{\vec{k}=\lceil na \rceil \\ \|\frac{\vec{k}}{n}-\vec{x}\|_\infty > \frac{1}{n^\beta}}}^{\lfloor nb \rfloor} \left(\frac{Z_j(nx-k)}{\sum_{\vec{k}=\lceil na \rceil}^{\lfloor nb \rfloor} Z_j(nx-k)} \right) \left(\int_X D^q \left(f \left(\frac{\vec{k}}{n}, s \right), f(\vec{x}, s) \right) P(ds) \right)^{\frac{1}{q}} \leq \\ & \left(\frac{1}{\sum_{\vec{k}=\lceil na \rceil}^{\lfloor nb \rfloor} Z_j(nx-k)} \right) \cdot \left\{ \Omega_1^{(\mathcal{F})} \left(f, \frac{1}{n^\beta} \right)_{L^q} + \right. \quad (115) \\ & \left. 2 \left(\int_X (D^*(f(\cdot, s), \tilde{o}))^q P(ds) \right)^{\frac{1}{q}} \left(\sum_{\substack{\vec{k}=\lceil na \rceil \\ \|\frac{\vec{k}}{n}-\vec{x}\|_\infty > \frac{1}{n^\beta}}}^{\lfloor nb \rfloor} Z_j(nx-k) \right) \right\} \end{aligned}$$

(by (24), (25); (44), (45); (64), (65); (86), (87))

$$\leq \gamma_j(N) \left\{ \Omega_1^{(\mathcal{F})} \left(f, \frac{1}{n^\beta} \right)_{L^q} + 2c_j(\beta, n) \left(\int_X (D^*(f(\cdot, s), \tilde{o}))^q P(ds) \right)^{\frac{1}{q}} \right\}. \quad (116)$$

We have proved claim.

Conclusion 6. By Theorem 22 we obtain the pointwise and uniform convergences with rates in the q -mean and D -metric of the operator ${}_jA_n^{\mathcal{FR}}$ to the unit operator for $f \in C_{\mathcal{FR}}^{Uq} \left(\prod_{i=1}^N [a_i, b_i] \right)$, $j = 1, 2, 3, 4$.

II) 1-mean Approximation by Stochastic arctangent, algebraic, Gudermannian and generalized symmetric activation functions based full Quasi-Interpolation Neural Network Operators

Let $g \in C_{\mathcal{R}}^{U1}(\mathbb{R}^N)$, $0 < \beta < 1$, $\vec{x} \in \mathbb{R}^N$, $n, N \in \mathbb{N}$, with $\|g\|_{\infty, \mathbb{R}^N, X} < \infty$, (X, \mathcal{B}, P) probability space, $s \in X$.

We define

$${}_jB_n^{(\mathcal{R})}(g)(\vec{x}, s) := \sum_{\vec{k}=-\infty}^{\infty} g\left(\frac{\vec{k}}{n}, s\right) Z_j(n\vec{x} - \vec{k}), \quad j = 1, 2, 3, 4, \quad (117)$$

(see also (90)).

We give

Theorem 23. Let $g \in C_{\mathcal{R}}^{U1}(\mathbb{R}^N)$, $0 < \beta < 1$, $\vec{x} \in \mathbb{R}^N$, $n, N \in \mathbb{N}$, with $n^{1-\beta} > 2$, $\|g\|_{\infty, \mathbb{R}^N, X} < \infty$; $j = 1, 2, 3, 4$. Then

1)

$$\int_X \left| ({}_jB_n^{(\mathcal{R})}(g))(\vec{x}, s) - g(\vec{x}, s) \right| P(ds) \leq \left\{ \Omega_1 \left(g, \frac{1}{n^\beta} \right)_{L^1} + 2c_j(\beta, n) \|g\|_{\infty, \mathbb{R}^N, X} \right\} =: \mu_{j1}^{(\mathcal{R})}, \quad (118)$$

2)

$$\left\| \int_X \left| ({}_jB_n^{(\mathcal{R})}(g))(\vec{x}, s) - g(\vec{x}, s) \right| P(ds) \right\|_{\infty, \mathbb{R}^N} \leq \mu_{j1}^{(\mathcal{R})}. \quad (119)$$

Proof. Since $\|g\|_{\infty, \mathbb{R}^N, X} < \infty$, then

$$\left| g\left(\frac{\vec{k}}{n}, s\right) - g(\vec{x}, s) \right| \leq 2 \|g\|_{\infty, \mathbb{R}^N, X} < \infty. \quad (120)$$

Hence

$$\int_X \left| g\left(\frac{\vec{k}}{n}, s\right) - g(\vec{x}, s) \right| P(ds) \leq 2 \|g\|_{\infty, \mathbb{R}^N, X} < \infty. \quad (121)$$

We observe that

$$\begin{aligned} & \left({}_jB_n^{(\mathcal{R})}(g) \right) (\vec{x}, s) - g(\vec{x}, s) = \\ & \sum_{\vec{k}=-\infty}^{\infty} g\left(\frac{\vec{k}}{n}, s\right) Z_j(n\vec{x} - \vec{k}) - g(\vec{x}, s) \sum_{\vec{k}=-\infty}^{\infty} Z_j(n\vec{x} - \vec{k}) = \end{aligned} \quad (122)$$

$$\left(\sum_{\vec{k}=-\infty}^{\infty} g\left(\frac{\vec{k}}{n}, s\right) - g(\vec{x}, s) \right) Z_j(nx - k).$$

However it holds

$$\sum_{\vec{k}=-\infty}^{\infty} \left| g\left(\frac{\vec{k}}{n}, s\right) - g(\vec{x}, s) \right| Z_j(nx - k) \leq 2 \|g\|_{\infty, \mathbb{R}^N, X} < \infty. \quad (123)$$

Hence

$$\begin{aligned} & \left| \left({}_j B_n^{(\mathcal{R})}(g) \right) (\vec{x}, s) - g(\vec{x}, s) \right| \leq \\ & \sum_{\vec{k}=-\infty}^{\infty} \left| g\left(\frac{\vec{k}}{n}, s\right) - g(\vec{x}, s) \right| Z_j(nx - k) = \\ & \sum_{\vec{k}=-\infty}^{\infty} \left| g\left(\frac{\vec{k}}{n}, s\right) - g(\vec{x}, s) \right| Z_j(nx - k) + \\ & \left\| \frac{\vec{k}}{n} - \vec{x} \right\|_{\infty} \leq \frac{1}{n^\beta} \\ & \sum_{\vec{k}=-\infty}^{\infty} \left| g\left(\frac{\vec{k}}{n}, s\right) - g(\vec{x}, s) \right| Z_j(nx - k). \\ & \left\| \frac{\vec{k}}{n} - \vec{x} \right\|_{\infty} > \frac{1}{n^\beta} \end{aligned} \quad (124)$$

Furthermore it holds

$$\begin{aligned} & \left(\int_X \left| \left({}_j B_n^{(\mathcal{R})}(g) \right) (\vec{x}, s) - g(\vec{x}, s) \right| P(ds) \right) \leq \\ & \sum_{\vec{k}=-\infty}^{\infty} \left(\int_X \left| g\left(\frac{\vec{k}}{n}, s\right) - g(\vec{x}, s) \right| P(ds) \right) Z_j(nx - k) + \\ & \left\| \frac{\vec{k}}{n} - \vec{x} \right\|_{\infty} \leq \frac{1}{n^\beta} \\ & \sum_{\vec{k}=-\infty}^{\infty} \left(\int_X \left| g\left(\frac{\vec{k}}{n}, s\right) - g(\vec{x}, s) \right| P(ds) \right) Z_j(nx - k) \leq \\ & \left\| \frac{\vec{k}}{n} - \vec{x} \right\|_{\infty} > \frac{1}{n^\beta} \\ & \Omega_1 \left(g, \frac{1}{n^\beta} \right)_{L^1} + 2 \|g\|_{\infty, \mathbb{R}^N, X} \sum_{\substack{\vec{k}=-\infty \\ \left\| \frac{\vec{k}}{n} - \vec{x} \right\|_{\infty} > \frac{1}{n^\beta}}}^{\infty} Z_j(nx - k) \leq \\ & \Omega_1 \left(g, \frac{1}{n^\beta} \right)_{L^1} + 2c_j(\beta, n) \|g\|_{\infty, \mathbb{R}^N, X}, \end{aligned} \quad (125)$$

proving the claim.

Conclusion 7. By Theorem 23 we obtain pointwise and uniform convergences with rates in the 1-mean of random operators ${}_j B_n^{(\mathcal{R})}$ to the unit operator for $g \in C_{\mathcal{R}}^{U_1}(\mathbb{R}^N)$, $j = 1, 2, 3, 4$.

III) 1-mean Approximation by Stochastic arctangent, algebraic, Gudermannian and generalized symmetric activation functions based multivariate Kantorovich type neural network operator

Let $g \in C_{\mathcal{R}}^{U_1}(\mathbb{R}^N)$, $0 < \beta < 1$, $\vec{x} \in \mathbb{R}^N$, $n, N \in \mathbb{N}$, with $\|g\|_{\infty, \mathbb{R}^N, X} < \infty$, (X, \mathcal{B}, P) probability space, $s \in X$.

We define ($j = 1, 2, 3, 4$):

$${}_j C_n^{(\mathcal{R})}(g)(\vec{x}, s) := \sum_{\vec{k}=-\infty}^{\infty} \left(n^N \int_{\frac{\vec{k}}{n}}^{\frac{\vec{k}+1}{n}} g(\vec{t}, s) d\vec{t} \right) Z_j(n\vec{x} - \vec{k}), \quad (126)$$

(see also (91)).

We present

Theorem 24. Let $g \in C_{\mathcal{R}}^{U_1}(\mathbb{R}^N)$, $0 < \beta < 1$, $\vec{x} \in \mathbb{R}^N$, $n, N \in \mathbb{N}$, with $n^{1-\beta} > 2$; $j = 1, 2, 3, 4$, $\|g\|_{\infty, \mathbb{R}^N, X} < \infty$. Then

1)

$$\int_X \left| ({}_j C_n^{(\mathcal{R})}(g))(\vec{x}, s) - g(\vec{x}, s) \right| P(ds) \leq \left[\Omega_1 \left(g, \frac{1}{n} + \frac{1}{n^\beta} \right)_{L^1} + 2c_j(\beta, n) \|g\|_{\infty, \mathbb{R}^N, X} \right] =: \gamma_{j1}^{(\mathcal{R})}, \quad (127)$$

2)

$$\left\| \int_X \left| ({}_j C_n^{(\mathcal{R})}(g))(\vec{x}, s) - g(\vec{x}, s) \right| P(ds) \right\|_{\infty, \mathbb{R}^N} \leq \gamma_{j1}^{(\mathcal{R})}. \quad (128)$$

Proof. Since $\|g\|_{\infty, \mathbb{R}^N, X} < \infty$, then

$$\begin{aligned} \left| n^N \int_{\frac{\vec{k}}{n}}^{\frac{\vec{k}+1}{n}} g(\vec{t}, s) d\vec{t} - g(\vec{x}, s) \right| &= \left| n^N \int_{\frac{\vec{k}}{n}}^{\frac{\vec{k}+1}{n}} (g(\vec{t}, s) - g(\vec{x}, s)) d\vec{t} \right| \leq \\ n^N \int_{\frac{\vec{k}}{n}}^{\frac{\vec{k}+1}{n}} |g(\vec{t}, s) - g(\vec{x}, s)| d\vec{t} &\leq 2 \|g\|_{\infty, \mathbb{R}^N, X} < \infty. \end{aligned} \quad (129)$$

Hence

$$\int_X \left| n^N \int_{\frac{\vec{k}}{n}}^{\frac{\vec{k}+1}{n}} g(\vec{t}, s) d\vec{t} - g(\vec{x}, s) \right| P(ds) \leq 2 \|g\|_{\infty, \mathbb{R}^N, X} < \infty. \quad (130)$$

We observe that

$$({}_j C_n^{(\mathcal{R})}(g))(\vec{x}, s) - g(\vec{x}, s) =$$

$$\begin{aligned}
& \sum_{\vec{k}=-\infty}^{\infty} \left(n^N \int_{\frac{\vec{k}}{n}}^{\frac{\vec{k}+1}{n}} g(\vec{t}, s) d\vec{t} \right) Z_j(n\vec{x} - \vec{k}) - g(\vec{x}, s) = \\
& \sum_{\vec{k}=-\infty}^{\infty} \left(n^N \int_{\frac{\vec{k}}{n}}^{\frac{\vec{k}+1}{n}} g(\vec{t}, s) d\vec{t} \right) Z_j(n\vec{x} - \vec{k}) - g(\vec{x}, s) \sum_{\vec{k}=-\infty}^{\infty} Z_j(n\vec{x} - \vec{k}) = \\
& \sum_{\vec{k}=-\infty}^{\infty} \left[\left(n^N \int_{\frac{\vec{k}}{n}}^{\frac{\vec{k}+1}{n}} g(\vec{t}, s) d\vec{t} \right) - g(\vec{x}, s) \right] Z_j(n\vec{x} - \vec{k}) = \\
& \sum_{\vec{k}=-\infty}^{\infty} \left[n^N \int_{\frac{\vec{k}}{n}}^{\frac{\vec{k}+1}{n}} (g(\vec{t}, s) - g(\vec{x}, s)) d\vec{t} \right] Z_j(n\vec{x} - \vec{k}).
\end{aligned} \tag{131}$$

However it holds

$$\sum_{\vec{k}=-\infty}^{\infty} \left[n^N \int_{\frac{\vec{k}}{n}}^{\frac{\vec{k}+1}{n}} |g(\vec{t}, s) - g(\vec{x}, s)| d\vec{t} \right] Z_j(n\vec{x} - \vec{k}) \leq 2 \|g\|_{\infty, \mathbb{R}^N, X} < \infty. \tag{132}$$

Hence

$$\begin{aligned}
& \left| \left({}_j C_n^{(\mathcal{R})}(g) \right) (\vec{x}, s) - g(\vec{x}, s) \right| \leq \\
& \sum_{\vec{k}=-\infty}^{\infty} \left[n^N \int_{\frac{\vec{k}}{n}}^{\frac{\vec{k}+1}{n}} |g(\vec{t}, s) - g(\vec{x}, s)| d\vec{t} \right] Z_j(n\vec{x} - \vec{k}) = \tag{133}
\end{aligned}$$

$$\begin{aligned}
& \sum_{\vec{k}=-\infty}^{\infty} \left[n^N \int_{\frac{\vec{k}}{n}}^{\frac{\vec{k}+1}{n}} |g(\vec{t}, s) - g(\vec{x}, s)| d\vec{t} \right] Z_j(n\vec{x} - \vec{k}) + \\
& \left\| \frac{\vec{k}}{n} - \vec{x} \right\|_{\infty} \leq \frac{1}{n^\beta} \tag{134}
\end{aligned}$$

$$\begin{aligned}
& \sum_{\vec{k}=-\infty}^{\infty} \left[n^N \int_{\frac{\vec{k}}{n}}^{\frac{\vec{k}+1}{n}} |g(\vec{t}, s) - g(\vec{x}, s)| d\vec{t} \right] Z_j(n\vec{x} - \vec{k}) = \\
& \left\| \frac{\vec{k}}{n} - \vec{x} \right\|_{\infty} > \frac{1}{n^\beta} \\
& \sum_{\vec{k}=-\infty}^{\infty} \left[n^N \int_0^{\frac{1}{n}} \left| g\left(\vec{t} + \frac{\vec{k}}{n}, s\right) - g(\vec{x}, s) \right| d\vec{t} \right] Z_j(n\vec{x} - \vec{k}) + \\
& \left\| \frac{\vec{k}}{n} - \vec{x} \right\|_{\infty} \leq \frac{1}{n^\beta} \tag{135}
\end{aligned}$$

$$\begin{aligned}
& \sum_{\vec{k}=-\infty}^{\infty} \left[n^N \int_0^{\frac{1}{n}} \left| g\left(\vec{t} + \frac{\vec{k}}{n}, s\right) - g(\vec{x}, s) \right| d\vec{t} \right] Z_j(n\vec{x} - \vec{k}). \\
& \left\| \frac{\vec{k}}{n} - \vec{x} \right\|_{\infty} > \frac{1}{n^\beta}
\end{aligned}$$

Furthermore it holds

$$\begin{aligned}
 & \left(\int_X \left| ({}_j C_n^{(\mathcal{R})}(g))(\vec{x}, s) - g(\vec{x}, s) \right| P(ds) \right) \stackrel{\leq}{\text{(by Fubini's theorem)}} \\
 & \sum_{\vec{k}=-\infty}^{\infty} \left[n^N \int_0^{\frac{1}{n}} \left(\int_X \left| g\left(\vec{t} + \frac{\vec{k}}{n}, s\right) - g(\vec{x}, s) \right| P(ds) \right) d\vec{t} \right] Z_j(n\vec{x} - \vec{k}) + \\
 & \left\| \frac{\vec{k}}{n} - \vec{x} \right\|_{\infty} \leq \frac{1}{n^\beta} \\
 & \sum_{\vec{k}=-\infty}^{\infty} \left[n^N \int_0^{\frac{1}{n}} \left(\int_X \left| g\left(\vec{t} + \frac{\vec{k}}{n}, s\right) - g(\vec{x}, s) \right| P(ds) \right) d\vec{t} \right] Z_j(n\vec{x} - \vec{k}) \leq \\
 & \left\| \frac{\vec{k}}{n} - \vec{x} \right\|_{\infty} > \frac{1}{n^\beta} \\
 & \Omega_1\left(g, \frac{1}{n} + \frac{1}{n^\beta}\right)_{L^1} + 2\|g\|_{\infty, \mathbb{R}^N, X} \sum_{\vec{k}=-\infty}^{\infty} Z_j(n\vec{x} - \vec{k}) \leq \\
 & \left\| \frac{\vec{k}}{n} - \vec{x} \right\|_{\infty} > \frac{1}{n^\beta} \\
 & \Omega_1\left(g, \frac{1}{n} + \frac{1}{n^\beta}\right)_{L^1} + 2c_j(\beta, n)\|g\|_{\infty, \mathbb{R}^N, X}, \tag{137}
 \end{aligned}$$

proving the claim.

Conclusion 8. *By Theorem 24 we obtain pointwise and uniform convergences with rates in the 1-mean of random operators ${}_j C_n^{(\mathcal{R})}$ to the unit operator for $g \in C_{\mathcal{R}}^{U_1}(\mathbb{R}^N)$, $j = 1, 2, 3, 4$.*

IV) 1-mean Approximation by Stochastic arctangent, algebraic, Gudermannian and generalized symmetric activation functions based multivariate quadrature type neural network operator

Let $g \in C_{\mathcal{R}}^{U_1}(\mathbb{R}^N)$, $0 < \beta < 1$, $\vec{x} \in \mathbb{R}^N$, $n, N \in \mathbb{N}$, with $\|g\|_{\infty, \mathbb{R}^N, X} < \infty$, (X, \mathcal{B}, P) probability space, $s \in X$, $j = 1, 2, 3, 4$.

We define

$${}_j D_n^{(\mathcal{R})}(g)(\vec{x}, s) := \sum_{\vec{k}=-\infty}^{\infty} (\delta_{n\vec{k}}(g))(s) Z_j(n\vec{x} - \vec{k}), \tag{138}$$

where

$$(\delta_{n\vec{k}}(g))(s) := \sum_{\vec{r}=0}^{\vec{\theta}} w_{\vec{r}} g\left(\frac{\vec{k}}{n} + \frac{\vec{r}}{n\vec{\theta}}, s\right), \tag{139}$$

(see also (92), (93)).

We finally give

Theorem 25. *Let $g \in C_{\mathcal{R}}^{U_1}(\mathbb{R}^N)$, $0 < \beta < 1$, $\vec{x} \in \mathbb{R}^N$, $n, N \in \mathbb{N}$, with $n^{1-\beta} > 2$; $j = 1, 2, 3, 4$, $\|g\|_{\infty, \mathbb{R}^N, X} < \infty$. Then*

1)

$$\int_X \left| \left({}_j D_n^{(\mathcal{R})} (g) \right) (\vec{x}, s) - g(\vec{x}, s) \right| P(ds) \leq \left\{ \Omega_1 \left(g, \frac{1}{n} + \frac{1}{n^\beta} \right)_{L^1} + 2c_j(\beta, n) \|g\|_{\infty, \mathbb{R}^N, X} \right\} =: \gamma_{j1}^{(\mathcal{R})}, \quad (140)$$

2)

$$\left\| \int_X \left| \left({}_j D_n^{(\mathcal{R})} (g) \right) (\vec{x}, s) - g(\vec{x}, s) \right| P(ds) \right\|_{\infty, \mathbb{R}^N} \leq \gamma_{j1}^{(\mathcal{R})}. \quad (141)$$

Proof. Notice that

$$\begin{aligned} & |(\delta_{n\vec{k}} (g)) (s) - g(\vec{x}, s)| = \\ & \left| \sum_{\vec{r}=0}^{\vec{\theta}} w_{\vec{r}} \left(g \left(\frac{\vec{k}}{n} + \frac{\vec{r}}{n\theta}, s \right) - g(\vec{x}, s) \right) \right| \leq \\ & \sum_{\vec{r}=0}^{\vec{\theta}} w_{\vec{r}} \left| g \left(\frac{\vec{k}}{n} + \frac{\vec{r}}{n\theta}, s \right) - g(\vec{x}, s) \right| \leq 2 \|g\|_{\infty, \mathbb{R}^N, X} < \infty. \end{aligned} \quad (142)$$

Hence

$$\int_X |(\delta_{n\vec{k}} (g)) (s) - g(\vec{x}, s)| P(ds) \leq 2 \|g\|_{\infty, \mathbb{R}^N, X} < \infty. \quad (143)$$

We observe that

$$\begin{aligned} & \left({}_j D_n^{(\mathcal{R})} (g) \right) (\vec{x}, s) - g(\vec{x}, s) = \\ & \sum_{\vec{k}=-\infty}^{\infty} (\delta_{n\vec{k}} (g)) (s) Z_j (n\vec{x} - \vec{k}) - g(\vec{x}, s) = \\ & \sum_{\vec{k}=-\infty}^{\infty} ((\delta_{n\vec{k}} (g)) (s) - g(\vec{x}, s)) Z_j (n\vec{x} - \vec{k}). \end{aligned} \quad (144)$$

Thus

$$\begin{aligned} & \left| {}_j D_n^{(\mathcal{R})} (g) (\vec{x}, s) - g(\vec{x}, s) \right| \leq \\ & \sum_{\vec{k}=-\infty}^{\infty} |(\delta_{n\vec{k}} (g)) (s) - g(\vec{x}, s)| Z_j (n\vec{x} - \vec{k}) \leq 2 \|g\|_{\infty, \mathbb{R}^N, X} < \infty. \end{aligned} \quad (145)$$

Hence it holds

$$\begin{aligned} & \left| \left({}_j D_n^{(\mathcal{R})} (g) \right) (\vec{x}, s) - g(\vec{x}, s) \right| \leq \\ & \sum_{\vec{k}=-\infty}^{\infty} |(\delta_{n\vec{k}} (g)) (s) - g(\vec{x}, s)| Z_j (n\vec{x} - \vec{k}) = \end{aligned}$$

$$\sum_{\vec{k}=-\infty}^{\infty} |(\delta_{n\vec{k}}(g))(s) - g(\vec{x}, s)| Z_j(n\vec{x} - \vec{k}) + \sum_{\vec{k}=-\infty}^{\infty} |(\delta_{n\vec{k}}(g))(s) - g(\vec{x}, s)| Z_j(n\vec{x} - \vec{k}). \tag{146}$$

$\|\frac{\vec{k}}{n} - \vec{x}\|_{\infty} \leq \frac{1}{n^{\beta}}$ $\|\frac{\vec{k}}{n} - \vec{x}\|_{\infty} > \frac{1}{n^{\beta}}$

Furthermore we derive

$$\left(\int_X \left| ({}_j D_n^{(\mathcal{R})}(g))(\vec{x}, s) - g(\vec{x}, s) \right| P(ds) \right) \leq \sum_{\vec{k}=-\infty}^{\infty} \sum_{\vec{r}=0}^{\vec{\theta}} w_{\vec{r}} \left(\int_X \left| g\left(\frac{\vec{k}}{n} + \frac{\vec{r}}{n\theta}, s\right) - g(\vec{x}, s) \right| P(ds) \right) Z_j(n\vec{x} - \vec{k}) \tag{147}$$

$\|\frac{\vec{k}}{n} - \vec{x}\|_{\infty} \leq \frac{1}{n^{\beta}}$

$$+ \left(\sum_{\substack{\vec{k}=-\infty \\ \|\frac{\vec{k}}{n} - \vec{x}\|_{\infty} > \frac{1}{n^{\beta}}}^{\infty} Z_j(n\vec{x} - \vec{k}) \right) 2 \|g\|_{\infty, \mathbb{R}^N, X} \leq \Omega_1 \left(g, \frac{1}{n} + \frac{1}{n^{\beta}} \right)_{L^1} + 2c_j(\beta, n) \|g\|_{\infty, \mathbb{R}^N, X}, \tag{148}$$

proving the claim.

Conclusion 9. From Theorem 25 we obtain pointwise and uniform convergences with rates in the 1-mean of random operators ${}_j D_n^{(\mathcal{R})}$ to the unit operator for $g \in C_{\mathcal{R}}^{U_1}(\mathbb{R}^N)$, $j = 1, 2, 3, 4$.

References

1. Anastassiou, G.A.: Rate of convergence of fuzzy neural network operators, univariate case. J. Fuzzy Math. **10**(3), 755–780 (2002)
2. Anastassiou, G.A.: Higher order fuzzy approximation by fuzzy wavelet type and neural network operators. Comput. Math. **48**, 1387–1401 (2004)
3. Anastassiou, G.A.: Univariate fuzzy-random neural network approximation operators. Computers and Mathematics with Applications, Special issue Proceedings edited by G. Anastassiou of special session “Computational Methods in Analysis”, AMS meeting in Orlando. Florida, November 2002, vol. 48, pp. 1263–1283 (2004)
4. Anastassiou, G.A.: Higher order fuzzy Korovkin theory via inequalities. Commun. Appl. Anal. **10**(2), 359–392 (2006)

5. Anastassiou, G.A.: Fuzzy Korovkin theorems and inequalities. *J. Fuzzy Math.* **15**(1), 169–205 (2007)
6. Anastassiou, G.A.: Multivariate stochastic Korovkin theory given quantitatively. *Math. Comput. Model.* **48**, 558–580 (2008)
7. Anastassiou, G.A.: *Fuzzy Mathematics: Approximation Theory*. Springer, Heidelberg (2010)
8. Anastassiou, G.A.: *Intelligent Systems: Approximation by Artificial Neural Networks*. Springer, Heidelberg (2011)
9. Anastassiou, G.A.: Univariate hyperbolic tangent neural network approximation. *Math. Comput. Model.* **53**, 1111–1132 (2011)
10. Anastassiou, G.A.: Multivariate hyperbolic tangent neural network approximation. *Comput. Math.* **61**, 809–821 (2011)
11. Anastassiou, G.A.: Multivariate sigmoidal neural network approximation. *Neural Netw.* **24**, 378–386 (2011)
12. Anastassiou, G.A.: Higher order multivariate fuzzy approximation by multivariate fuzzy wavelet type and neural network operators. *J. Fuzzy Math.* **19**(3), 601–618 (2011)
13. Anastassiou, G.A.: Univariate sigmoidal neural network approximation. *J. Comput. Anal. Appl.* **14**(4), 659–690 (2012)
14. Anastassiou, G.A.: Rate of convergence of some multivariate neural network operators to the unit, revisited. *J. Comput. Anal. Appl.* **15**(7), 1300–1309 (2013)
15. Anastassiou, G.A.: Higher order multivariate fuzzy approximation by basic neural network operators. *CUBO* **16**(3), 21–35 (2014)
16. Anastassiou, G.A.: Multivariate fuzzy-random Quasi-interpolation neural network approximation operators. *J. Fuzzy Math.* **22**(1), 167–184 (2014)
17. Anastassiou, G.: Multivariate fuzzy-random error function based neural network approximation. *J. Fuzzy Math.* **23**(4), 917–935 (2015)
18. Anastassiou, G.A.: *Intelligent Systems II: Complete Approximation by Neural Network Operators*. SCI, vol. 608. Springer, Cham (2016). <https://doi.org/10.1007/978-3-319-20505-2>
19. Anastassiou, G.A.: *Intelligent Computations: Abstract Fractional Calculus, Inequalities, Approximations*. Springer, Heidelberg (2018). <https://doi.org/10.1007/978-3-319-66936-6>
20. Anastassiou, G.A.: Algebraic function based Banach space valued ordinary and fractional neural network approximations. *New Trends Math. Sci.* **10**(1), 100–125 (2022)
21. Anastassiou, G.A.: Gudermannian function activated Banach space valued ordinary and fractional neural network approximation. *Adv. Nonlinear Var. Inequal.* **25**(2), 27–64 (2022)
22. Anastassiou, G.A.: Generalized symmetrical sigmoid function activated Banach space valued ordinary and fractional neural network approximation. *Analele Universității Oradea, Fasc. Matematica* (2022, accepted for publication)
23. Anastassiou, G.A.: Abstract multivariate Gudermannian function activated neural network approximations. *Panamerican Math. J.* (2022, accepted)
24. Anastassiou, G.A.: General multivariate arctangent function activated neural network approximations (2022, submitted)
25. Anastassiou, G.A., Kozma, R.: Abstract multivariate algebraic function activated neural network approximations (2022, submitted)
26. Anastassiou, G.A.: Generalized symmetrical sigmoid function activated neural network multivariate approximation (2022, submitted)

27. Chen, Z., Cao, F.: The approximation operators with sigmoidal functions. *Comput. Math. Appl.* **58**, 758–765 (2009)
28. Dudley, R.M.: *Real Analysis and Probability*. Wadsworth & Brooks/Cole Mathematics Series. Pacific Grove, California (1989)
29. Dunning, A.J., Kensler, J., Goudeville, L., Bailleux, F.: Some extensions in continuous methods for immunological correlates of protection. *BMC Med. Res. Methodol.* **15**(107) (2015). <https://doi.org/10.1186/s12874-015-0096-9>
30. Gal, S.: Approximation theory in fuzzy setting, Chapter 13. In: Anastassiou, G. (ed.) *Handbook of Analytic-Computational Methods in Applied Mathematics*, pp. 617–666. Chapman & Hall/CRC, Boca Raton (2000)
31. Haykin, S.: *Neural Networks: A Comprehensive Foundation*, 2nd edn. Prentice Hall, New York (1998)
32. Mitchell, T.M.: *Machine Learning*. WCB-McGraw-Hill, New York (1997)
33. McCulloch, W., Pitts, W.: A logical calculus of the ideas immanent in nervous activity. *Bull. Math. Biophys.* **7**, 115–133 (1943)
34. Weisstein, E.W.: Gudermannian, MathWorld
35. Congxin, W., Zengtai, G.: On Henstock integral of interval-valued functions and fuzzy valued functions. *Fuzzy Sets Syst.* **115**(3), 377–391 (2000)
36. Wu, C., Gong, Z.: On Henstock integral of fuzzy-number-valued functions (I). *Fuzzy Sets Syst.* **120**(3), 523–532 (2001)
37. Wu, C., Ma, M.: On embedding problem of fuzzy number space: part 1. *Fuzzy Sets Syst.* **44**, 33–38 (1991)



From Koeller's Idea to Modern Fractional Calculus: Fractional Polynomial Operators

Jordan Hristov^(✉)

Department of Chemical Engineering, University of Chemical Technology
and Metallurgy, Sofia, Bulgaria
jordan.hristov@mail.bg, jyh@uctm.edu

Abstract. In this chapter, Koeller's original idea on polynomial fractional operators with singular (Riesz) kernels and solutions to a few viscoelasticity relaxation issues is highlighted. Now, we show how this concept can be directly related to how relaxation relationships are presented using fractional operators with non-singular kernels. Additionally, it shows that viscoelastic interactions that defy singular (power-law) behavior may be described by polynomial operators with non-singular memory.

Keywords: fractional calculus · polynomial operators · viscoelasticity

1 Introduction

The main idea of this study is to demonstrate the applicability of the so-called polynomial fractional operators which in general can be presented as

$$P_c(t) = \sum_0^N a_n D_t^{\alpha_n} [f(t)] \quad (1)$$

where $D_t^{\alpha_n} [f(t)]$ are fractional derivatives with any type of memory kernels relevant to modeled relaxation process. The concept of these polynomial fractional operators (PFOs) was inspired by research done by Bagley and Torvik [1] on the use of fractional calculus in viscoelastic models, although it is based on the work of Koeller [2] (see also [3,4], and [5]). The Bagley-Torvik equation will be covered in this chapter, but for now, to better understand the rationale behind how polynomial fractional operators are created, we had want to go over some key fractional calculus principles. The chapter addresses a new modelling philosophy allowing relaxation functions (memory kernels) to be expressed as finite sums (polynomial operators) of elementary kernels, either of singular (power-law) or non-singular (exponential) kernels. This gives an advantages in modelling when single kernel fractional operators are not applicable for modeling of real-world phenomena such as viscoelasticity and diffusions.

1.1 The Koeller Main Idea and Its Background

Now, following Koeller [2] we present step-by step his idea (in the original notations which to some extent may differ from the contemporary expressions in the literature).

N-Fold Iterated Integral and Its Consequences. The n -fold iterated integral can be presented as single integrals as [2]

$$\begin{aligned} D^{-n}x(t) &= \int_0^t \int_0^{t_{n-1}} \dots \int_0^{t_1} x(t_0) dt_0 dt_1 \dots dt_{n-2} dt_{n-1} \\ &= \int_0^t \frac{(t-\tau)^{n-1}}{(n-1)!}, \quad n = 0, 1, 2, \dots, N \end{aligned} \quad (2)$$

where $x(t)$ is a Heaviside function of class H^N if

$$x(t) = \begin{cases} x(t) = 0, & t \in (-\infty, 0] \\ x(t) \in C^N, & t \in (0, \infty) \end{cases} \quad (3)$$

where C^N is the class of all N time continuously differentiable functions on the open interval $(0, \infty)$ and N is appositive integer. The integral of fractional order n between the limits 0 and t is commonly defined by replacing the factorials by the Gamma function, that is [2]

$$D^{-n}x(t) = \int_0^t \frac{(t-\tau)^{n-1}}{\Gamma(n)} x(t) d\tau, \quad n \in [0, \infty) \quad (4)$$

This is the well-known as the Riemann-Liouville (RL) fractional integral [6].

The differentiation for $n = \alpha \in [0, 1]$ is defined as (in the original Koeller's notations) [2]

$$D^\alpha x(t) = DD^{\alpha-1}[x(t)] = D \int_0^t \frac{(t-\tau)^{-\alpha}}{\Gamma(1-\alpha)}, \quad D = \frac{d}{dt} \quad (5)$$

The Riesz Distribution. In linear viscoelasticity of the creep compliance is taken as

$$R_n(t) = \frac{t^n}{\Gamma(n+1)} \quad (6)$$

Then we have the so-called Riesz distribution [7] $R_n(t)$ is valid for all values of n , that is

$$R_n(t) = 0, \quad t \in (-\infty, 0) \quad (7)$$

and for $R_n(t) \equiv t^{-n}$ we have

$$R_n(t) = \frac{t^{-n}}{\Gamma(1-n)}, \quad t \in (0, \infty) \tag{8}$$

The integration of the Riesz distribution in order to obtain the Stieltjes integral representation of the fractional integral we may integrate the Riemann-Liouville integral (4) by parts. Then, for $\alpha \geq 0$ we get [2]

$$D^{-\alpha}x(t) = \int_0^t \frac{(t-\tau)^\alpha}{\Gamma(1+\alpha)} dx(\tau) + x(0) \frac{t^\alpha}{\Gamma(1+\alpha)} \tag{9}$$

In terms of Riesz distribution we may present this result as [2]

$$\begin{aligned} D^{-\alpha}x(t) &= \int_0^t R_{(-\alpha)}(t-\tau) dx(\tau) + x(0) R_{(-\alpha)}(t) \\ &= (R_{(-\alpha)} * dx)(t) + x(0) R_{(-\alpha)}(t), \quad \alpha \in [0, 1] \end{aligned} \tag{10}$$

where $(R_{(-\alpha)} * dx)(t)$ is a Stieltjes convolution. In a similar way, applying the Leibniz rule to the definition of the RL fractional derivative [6] we get [2]

$$\begin{aligned} D^\alpha x(t) &= \int_0^t \frac{(t-\tau)^{-\alpha}}{\Gamma(1-\alpha)} dx(\tau) + x(0) \frac{t^{-\alpha}}{\Gamma(1-\alpha)} \\ &= \int_0^t R_{(\alpha)}(t-\tau) dx(\tau) + x(0) \int_0^t R_{(\alpha)}(t) \\ &= \int_0^t (R_{(\alpha)} * dx)(t) + x(0) R_{(\alpha)}(t), \quad \alpha \in [0, 1] \end{aligned} \tag{11}$$

Further, since $D^{\lambda_1} D^{\lambda_2} = D^{\lambda_1+\lambda_2}$ then it follows that $R_{(-\lambda)}$ is Stieltjes inverse of $R_{(\lambda)}$, that is

$$R_{(\lambda)} * dR_{(-\lambda)} = R_{(-\lambda)} * dR_{(\lambda)} = h \tag{12}$$

In accordance with Koeller [2] both the fractional derivative (Riemann-Liouville) and fractional integral can be expressed as Stieltjes convolution in the form

$$D^\lambda = R_{(\lambda)} * dx, \quad \lambda \in (-\infty, \infty) \tag{13}$$

$$D^{-\lambda} = R^{-\lambda} * dx, \quad \lambda \in (-\infty, \infty) \tag{14}$$

1.2 The Koeller's Polynomial Operators

The examples developed by Koeller are from the area of linear viscoelasticity (following the works of Bagley and Torvik [1]) where the general form of the constitutive equations is

$$P(D)\sigma = Q(D)\varepsilon \quad (15)$$

where $P(D)$ and $Q(D)$ are polynomial operators defined as

$$P(D) = \sum_{n=0}^N p_n D^{\alpha_n}, \quad Q(D) = \sum_{n=0}^N q_n D^{\beta_n} \quad (16)$$

with fractional (memory) parameters (orders) α_n and β_n .

Note: When α_n and β_n are positive integers, then (15) is the standard differential operator constitutive law.

Further, when $\sigma(t)$ and $\varepsilon(t)$ are specified, then (15) is a fractional differential equation without jump initial conditions. Hence, the solutions of (15) for any action as input shear stress (or input shear strain) requires knowledge of the entire history of the shear stress (shear strain). The general formulation (15) can be developed as a linear hereditary law if we consider the properties of the Stieltjes convolution and the Riesz distribution [2], namely

$$\sum_{n=0}^N p_n R_{(\alpha_n)} * d\sigma = \sum_{n=0}^N q_n R_{(\beta_n)} * d\varepsilon \quad (17)$$

Then, we may define fractional polynomials $B(t)$ and $D(t)$ [2]

$$B(t) = \sum_{n=0}^N p_n R_{(\alpha_n)}(t) = \sum_{n=0}^N p_n \frac{t^{-\alpha_n}}{\Gamma(1-\alpha_n)} \quad (18)$$

$$D(t) = \sum_{n=0}^N q_n R_{(\beta_n)}(t) = \sum_{n=0}^N q_n \frac{t^{-\beta_n}}{\Gamma(1-\beta_n)} \quad (19)$$

and the constitutive law (15) can be presented in two forms [2]

$$B * d\sigma = D * d\varepsilon \quad (20)$$

$$\int_{-\infty}^t B(t-\tau) d\sigma(\tau) = \int_{-\infty}^t D(t-\tau) d\varepsilon(\tau) \quad (21)$$

If B^{-1} and D^{-1} are defined as Stieltjes inverse of B and D , then applying the associative property of the Stieltjes convolution we have

$$\sigma = G * d\varepsilon, \quad \varepsilon = J * d\sigma \quad (22)$$

where $G = B^{-1} * D$ and $J = D^{-1} * B$ are the *relaxation modulus* and the *creep compliance*, respectively.

1.3 Koeller Example of a Polynomial Operator

The Koeller example developed in [2] selects only one memory parameter β (which actually is violation of the causality principle [8], since *the input and output should have different time delays*). Anyway, the following expansion was considered (three component Kelvin-Voigt model)

$$(p_0 + p_1 D^\beta + p_2 D^{2\beta}) \sigma = (q_0 + q_1 D^\beta + q_2 D^{2\beta}) \varepsilon \quad (23)$$

which *possesses symmetry, that is no preference is given to the stress or strain*. The solution of (23) is [2] by Laplace transforms yields

$$J(t) = \frac{1}{E_0} + \frac{1}{E_1} \left\{ 1 - E_\beta \left[-\left(\frac{t}{t_1}\right)^\beta \right] \right\} + \frac{1}{E_2} \left\{ 1 - E_\beta \left[-\left(\frac{t}{t_2}\right)^\beta \right] \right\} \quad (24)$$

$$G(t) = E_0 - E_0 R_1 \left\{ 1 - E_\beta \left[-\left(\frac{t}{t_1}\right)^\beta \right] \right\} - E_0 R_2 \left\{ 1 - E_\beta \left[-\left(\frac{t}{t_2}\right)^\beta \right] \right\} \quad (25)$$

where E_0, E_1 and E_2 are the *moduli of the springs* and t_1, t_2 are *relaxation times*, and

$$E_\beta(x) = \sum_{n=0}^{\infty} (-1)^n \frac{x^n}{\Gamma(1 + \beta n)}, t > 0, \quad 0 < \beta \leq 1 \quad (26)$$

is the Mittag-Leffler function; When $\beta_n = 0, 1, \dots, N$ classical results are recovered.

After this example Koeller clearly stated [2] “*The final determination of whether fractional calculus is a valuable tool in the study of viscoelastic materials could be answered if specific data were taken over long periods of time and it (they) were fitted to one of these functions*”.

To complete this section let us turn on the formulation of the polynomial fractional operator. From the definitions (18) and (19) we may see that the memory functions can be presented as sums of Riesz distributions, namely

$$M_B = \sum_0^\infty p_n \frac{t^{-\alpha_n}}{\Gamma(1 - \alpha_n)}, \quad M_D = \sum_0^\infty q_n \frac{t^{-\beta_n}}{\Gamma(1 - \beta_n)} \quad (27)$$

Therefore, the relaxation functions, the **shear stress modulus** and the **shear strain compliance** are *decomposed as sums of elementary kernels* (Riesz distributions).

1.4 Outcomes of the Koeller’s Approach and Beyond

The findings of (27) provide a useful framework for decomposing response (relaxation) functions into sums of basic functions acting as memory kernels in relevant fractional operators. For instance, two possibilities are offered in the context of the fractional operators with the non-singular kernels, namely:

- A sums of exponential (Maxwell or Debay) memories which be easily obtained by applying the Prony's decomposition approach of experimental data [9] (see also [10] and [11]). That is

$$B_\beta(t) \equiv \sum_0^N b_n \exp\left(-\frac{t}{\tau_n}\right) \quad (28)$$

where τ_n are discrete relaxation times.

- Approximations as Mittag-Leffler functions [6]

$$B_\beta(t) \equiv E_\beta(-t^\beta) = \sum_{n=0}^{\infty} (-1)^n \frac{x^{-\beta n}}{\Gamma(1 + \beta n)} = 1 - \frac{x^{-\beta}}{\Gamma(1 + \beta)} + \frac{x^{-2\beta}}{\Gamma(1 + 2\beta)} \cdots \quad (29)$$

which actually resembles the idea of Koeller to present the operators as sums of Riesz distributions.

According to Koeller's remark above, the appropriate approximations of the experimental data by these sums have a significant impact on the choice of decomposition (approximation). We will now investigate how models, particularly the constitutive equations in the linear viscoelasticity, can be represented using polynomial fractional operators.

2 Fractional Calculus in Viscoelasticity

2.1 Stress-Strain Viscoelasticity Response and Hereditary Integral Construction

The superposition of the material's single-step reactions enables the creation of functional relationships between stress and strain while taking into account the fact that there is a temporal lag in both $G(t)$ and $J(t)$ following the application of the stress or strain. Convolution integrals, such as the stress integral (30), and creep integral (31), are effective in representing these interactions [12–14]

$$\sigma(t) = \int_0^t G(t-s) d\varepsilon(s) \quad (30)$$

$$\varepsilon(t) = \int_0^t J(t-s) d\sigma(s) \quad (31)$$

In the convolution integrals the lower limit is at $t = 0$ since both $\sigma(t)$ and $\varepsilon(t)$ are causal functions. Now, consider the application of the fading memory

concept applicable to stress and strain relationships which can be presented as [12, 14]

$$\sigma(t) = G_\infty + \int_0^t G(t-s) \frac{d\varepsilon}{ds} ds \quad (32)$$

$$\epsilon(t) = J_\infty + \int_0^t J(t-s) d\sigma(s) \quad (33)$$

The values of G_∞ and J_∞ are the instantaneous responses or in other words, the equilibrium values established for long time when the effects of the second terms in (32) and (33) disappear, that is when $G(t-s)$ and $J(t-s)$ will approach zero.

The relationships (32) and (33) contain Stieltjes integrals [12, 14] because

$$\sigma(t) = G_\infty + \int_{-\infty}^0 G(t-s) dk(s) + \int_0^t G(t-s) dk(s) \quad (34)$$

However, due the causality of $G(t)$ [8], i.e. $G(t) > 0$ for $0 < t < \infty$ and $G(t) = 0$ for $-\infty < t < 0$, the first integral is zero.

The appropriate viscoelastic kernel $G(t)$ should be able to account for short- and long-term strains to the applied stress and must satisfy the conditions for complete monotonicity following the general constraints set on the relaxation function.

$$(-1)^n \frac{\partial^n}{\partial t^n} G(t) \geq 0, \quad n = 1, 2, \dots \quad (35)$$

2.2 Discrete Spectra as Sums of Exponents

An exponential series (formerly cited as Prony's series) can be used to depict a non-linear monotonous response [9]

$$G(t) = G_\infty + \sum_{i=0}^N G_i \exp\left(-\frac{t}{\tau_i}\right) \quad (36)$$

The amount of molecular freedom in a material is measured by the number of independent relaxation periods, which may reach exceptionally high values for high polymers. When there are a lot of terms in (36), the total can be approximated by an integral that contains the distribution function $M_e(x)$ [15–17], namely

$$G(t) = G_\infty + \int_0^\infty \exp(-xt) M_e(x) dx, \quad M_e(x) \geq 0 \quad (37)$$

Prony's Series Decompositions: Discrete Relaxation Spectra. Through a decomposition into a Prony series, the viscoelastic relaxation function may be described as a discrete relaxation spectrum $\phi_P(t)$ with N^ϕ with rate constants β_i [15–17], namely

$$\phi_P(t) = \phi_\infty + \sum_{i=1}^{N^\phi} \phi_i e^{-\beta_i t} = \phi_\infty + \sum_{i=1}^{N^\phi} \phi_i e^{-\frac{t}{\tau_i}}, \quad \beta_i = \frac{1}{\tau_i} \geq 0 \quad (38)$$

Alternatively using weighted averages (amplitudes or normalized relaxation moduli) λ_i as

$$\lambda(t) = \frac{\phi_P(t)}{\phi_\infty} = 1 + \sum_{i=1}^{N^\phi} \lambda_i (e^{-\beta_i t} - 1), \quad \lambda_i = \frac{\phi_i}{\phi_\infty} \quad (39)$$

In (38) and (39) the parameters ϕ_∞ and ϕ_i are equilibrium (at large times) and relaxation moduli (stiffness), respectively, constrained according to [16, 17],

$$\phi_\infty + \sum_1^{N^\phi} \phi_i = 1 \quad (40)$$

The generalized Maxwell viscoelastic body, also known as the Maxwell-Wiechert model [16, 17, 20], is analogous to this popular Prony series expression. It consists of N^ϕ parallel spring-dashpot components, with a final parallel spring determining the equilibrium behavior. This formula takes into consideration dissipative effects, which appear as creep and stress relaxations that are load-rate dependent. Through its time-dependent shear and bulk moduli, the Prony series representation provides a crude method for representing any viscoelastic model [15–17, 20].

Polynomial Fractional Operators with the Caputo-Fabrizio Derivative.

Applying the Prony approximation of the relaxation curve and substituting in the convolution integral the following approximation is obtained [16, 17]

$$\sigma = \int_0^t E_i \exp\left(-\frac{t-s}{\tau_i}\right) \frac{d\varepsilon}{ds} ds \quad (41)$$

Since $\sigma(t)$ is assumed as a finite sum of elements it is possible to invert the summation and the integral that leads to the expression [16, 17]

$$\sigma(t) = \int_0^t \sum_{i=0}^N E_i e^{-\frac{(t-s)}{\tau_i}} \frac{d\varepsilon}{ds} ds = \sum_{i=0}^N E_i \left[\int_0^t e^{-\frac{(t-s)}{\tau_i}} \frac{d\varepsilon}{ds} ds \right] \quad (42)$$

This makes it simple to include the memory effect from the convolution integral in each term of the Prony series. This result's obvious physical meaning is that

the strain $\varepsilon_i(t)$ at a given time t is described as a convolution integral with an exponential kernel.

Through the relation $\alpha = 1/(1 - \tau/t_0)$, the fractional parameter α is related to the dimensionless relaxation time τ/t_0 , where t_0 is the whole duration of the experiment. With a spectrum of relaxation times then we get [15–17]

$$\alpha_i = \frac{1}{1 - \tau_i/t_0} \quad (43)$$

This allows to present $\varepsilon_i(t)$ in way close to the basic construction of the Caputo-Fabrizio operator [18], namely [15–17]

$$\varepsilon_i(t) = (1 - \alpha_i) \int_0^t e^{-\frac{\alpha_i}{1-\alpha_i}(\bar{t}-\bar{s})} \frac{d\varepsilon}{d\bar{s}} d\bar{s} = (1 - \alpha_i) D_t^{\alpha_i} \varepsilon(t) \quad (44)$$

Thus, the constitutive equation can be presented as [16,17]

$$\sigma(t) = \sum_{i=0}^N E_i (1 - \alpha_i) D_t^{\alpha_i} \varepsilon(t) \quad (45)$$

In the context of the initial definition of a polynomial fractional operators we may write

$$\sigma(t) = B_t^{\alpha_n} [\varepsilon(t)], \quad B_t^{\alpha_n} = \sum_{i=0}^N E_i (1 - \alpha_i) D_t^{\alpha_i} \quad (46)$$

and

$$\varepsilon(t) = P_t^{\beta_n} [\sigma(t)], \quad P_t^{\beta_n} = \sum_{i=0}^N E_i (1 - \beta_i) D_t^{\beta_i} \quad (47)$$

2.3 Viscoelastic Polynomial Fractional Model in Terms of Atangana-Baleanu Derivative

The Atangana-Baleanu derivative of Caputo sense (ABC) [19] can be rewritten (assuming for convenience of the explanations with $B(\alpha) = 1$) as

$${}^{ABC}D_{a+}^{\alpha} f(t) = \frac{1}{1 - \alpha} \int_0^z \frac{df(\bar{s})}{d\bar{s}} E_{\alpha} \left[-\left(\frac{\bar{t} - \bar{s}}{\bar{\tau}}\right)^{\alpha} \right] d\bar{s} \quad (48)$$

where $\frac{1-\alpha}{\alpha} = \left(\frac{\tau}{t_0}\right)^{\alpha} = (\bar{\tau})^{\alpha}$, $\bar{t} = \frac{t}{t_0}$.

That is through a nondimensionalization of the times [16,17] we get

$${}^{ABC}D_{a+}^{\alpha} f(t) = \frac{1}{1 - \alpha} \int_0^z \frac{df(\bar{s})}{d\bar{s}} \left\{ \sum_{j=0}^{\infty} \frac{1}{\Gamma(\alpha j + 1)} \left[-\left(\frac{\bar{t} - \bar{s}}{\bar{\tau}}\right)^{\alpha} \right]^j \right\} d\bar{s} \quad (49)$$

were the argument of the Mittag-Leffler kernel $E_\alpha(-z)$ is $z = [\alpha/(1-\alpha)](t-s)^\alpha$ and the following relationship exists [16, 17]

$$\left(\frac{1-\alpha}{\alpha}\right)^j = \left(\frac{\tau}{t_0}\right)^j \Rightarrow \alpha = \frac{1}{1+(\tau/t_0)} \quad (50)$$

which is the same as that established for the Caputo-Fabrizio operator.

Since the data fitting process practically requires a finite number in the series defining the Mittag-Leffler function, we obtain a discrete spectrum that approximates the relaxation (compliance) function made up of power-law terms $(t/\tau)^{\alpha_j}$. Further, with $f(\varepsilon) = \varepsilon(t)$, we have [16, 17]

$${}^{ABC}D_{a^+}^\alpha \varepsilon(t) = \frac{1}{1-\alpha} \int_0^z E_\alpha \left[-\left(\frac{\bar{t}-\bar{z}}{\bar{\tau}}\right)^\alpha \right] \frac{d\varepsilon(\bar{s})}{d\bar{s}} d\bar{s} \quad (51)$$

As a result, the stress-strain convolution integral has the following form [16, 17]

$$\begin{aligned} \sigma(t) &= \sum_{k=1}^N E_k(t) \int_0^t G_k(t-s) \frac{d}{ds} \varepsilon(s) \\ &= \sum_{k=1}^N E_k(t) (1-\alpha_k) \left[\frac{1}{1-\alpha_k} \int_0^z E_{\alpha_k} \left[-\left(\frac{\bar{t}-\bar{s}}{\bar{\tau}}\right)^{\alpha_k} \right] \frac{d\varepsilon(\bar{s})}{d\bar{s}} d\bar{s} \right] \end{aligned} \quad (52)$$

As commented above the values of N in the sum of relaxation kernels and J (the number of terms of E_α depends on the approximation approach accepted in data fitting. Hence, in a more compact form (52) can be expressed as

$$\sigma(t) = \sum_{k=1}^N E_k(t) [(1-\alpha_k) {}^{ABC}D_{a^+}^{\alpha_k} \varepsilon(t)] \quad (53)$$

because the, the relaxation spectrum is a sum of weighted ABC derivatives of $\varepsilon(t)$ [16, 17], namely

$$\frac{1-\alpha_k}{\alpha_k} = \bar{\tau}_k = \frac{\tau}{t_0} \Rightarrow \alpha_k = \frac{1}{1+\tau_k/t_0} \quad (54)$$

If only one term in the right-hand side of (52) is enough (that is $N = 1$ to approximate the stress relaxation function, then (53) takes the form

$$\sigma(t) = E(t) [(1-\alpha) {}^{ABC}D_t^\alpha \varepsilon(t)] \quad (55)$$

and α follows from $\alpha = 1/(1+\tau/t_0)$. Now, (55) defines a polynomial fractional operator with ABC derivatives, namely

$$\sigma(t) = {}^{ABC}B_t^\alpha [\varepsilon(t)], \quad {}^{ABC}B_t^\alpha = E(t) [(1-\alpha) {}^{ABC}D_t^\alpha] \quad (56)$$

If the simple case (55) (with $N = 1$ in the right-hand side of (52)) is not enough to fit the stress relaxation function, then a weighted sum of polynomials (truncated series of Mittag-Leffler function) should be used. Obviously, in this case the parameter estimation should need specific data.

3 Some Comments on the Bagley-Torvik Equation

3.1 The Initial Formulation and Assumed Approximations

Bagley and Torvik began their investigation using Rouse's idea [21] concerning the effective dynamic shear modulus of rarefied coiled polymers [1]. The sum of exponential decay modes (57) served as the Rouse model's representation [21] of the stress relaxation with decay times τ_i .

$$G(t) = \sum_{i=1}^N G_0 e^{-\frac{t}{\tau_i}} \quad (57)$$

It is simple to spot the Prony series decomposition in the context of the current investigation. However, if the distribution of τ_i is proportional to $t^{-\alpha-1}$, then we get (58) defining a fractional derivative (with singular kernel) from ε of order α (in the original notations of [1])

$$\sigma^\alpha = \int_a^t G(t-s) \frac{d}{ds} \varepsilon(s) ds \quad (58)$$

Hence, the total stress σ^α in the generalized Maxwell model, for instance, can be expressed as $\sigma^\alpha = \sum_{i=1}^N \sigma_i$ where σ_i is the stress in the i^{th} Maxwell element, namely

$$\sigma_i = k_i (\varepsilon - \varepsilon_i) = \eta_i \frac{d\varepsilon_i}{dt} \Rightarrow \frac{d\sigma_i}{dt} + \frac{1}{\tau_i} \sigma_i = \frac{d(k_i \varepsilon)}{dt}, \quad i = 1, \dots, N \quad (59)$$

As a result, if the material relaxes in a power-law fashion, a *fractional derivative model may be developed within the framework of weakly singular kernels*, that is $t^{-\alpha}$, which leads to

$$\sigma^\alpha(t) = \mu_A D_a^\alpha [k\varepsilon(t)], \quad \sigma^\alpha = \lim_{N \rightarrow \infty} \sum_{i=1}^N \sigma_i, \quad \sigma^\alpha = \lim_{N \rightarrow \infty} \sum_{i=1}^N k_i \quad (60)$$

where μ_A is a positive constant.

After this simple explanation let us see the original construction of Bagley and Torvik represented as [17]

$$\sigma(t) + \sum_{m=1}^N b_m D^{\beta_m} \sigma = E_0 \varepsilon(t) + \sum_{n=1}^N E_n D^{\alpha_n} \varepsilon(t) \quad (61)$$

In (61) the fractional derivatives are Riemann-Liouville derivatives (originally used by Bagley and Torvik) and in case of $N = 1$ this relationship reduces to a simple expression (see comments below)

$$\sigma(t) + bD^\beta\sigma(t) = E_0\varepsilon(t) + E_1D^\alpha\varepsilon(t) \quad (62)$$

containing two fractional derivatives with different orders.

Now, if the retardation spectrum corresponds to Riesz distribution and $\sigma(t) = G_1D^\alpha\varepsilon(t)$ then the stress relaxation modulus $G(t)$ and the creep compliance $J(t)$ are

$$G(t) = \frac{G_1}{\Gamma(1-\alpha)}t^{-\alpha}, \quad J(t) = \frac{1}{G_1} \frac{1}{\Gamma(1-\alpha)}t^\alpha \quad (63)$$

Therefore, *with a power-law relaxation* we get $\alpha = \beta$ in (62) thus making it a *single-fractional order equation*.

According to arguments made by Bagley and Torvik, the condition *alpha = beta*, which naturally results from the power-law stress relaxation kernel and the interconversion, is occasionally taken for granted as a norm. When the stress and strain relaxations in the model (60) are each represented by a single fractional derivative, correspondingly, we obtain a single-order equation in this instance, *which is an exception when only one power-law term models the entire stress relaxation*. This reduces the model to (61).

3.2 Bagley-Torvik Equation in Terms of Polynomial Caputo-Fabrizio Operators

It is normal to have concerns about properly simulating dynamic processes in non-power law media. Now, we could create a constitutive relationship in the manner of Bagley and Torvik and demonstrate how to reduce the relaxation (57) to (61), which naturally results in the application of the Caputo-Fabrizio operator [17].

$$\sigma(t) = E_0\varepsilon(t) + E_1D_t^\mu[\varepsilon(t)], \quad 0 < \mu < 1 \quad (64)$$

In (64) the fractional operator $D_t^\mu[\varepsilon(t)]$ is based on a memory kernel different from the power-law, in this specific case we use *exponential memory* [17].

$$\sigma(t) + \sum_{i=1}^N b_i [{}^{CF}D^{\beta_i}\sigma] = E_0\varepsilon(t) + \sum_{i=1}^N E_i [{}^{CF}D^{\alpha_i}\varepsilon(t)] \quad (65)$$

The Prony decomposition's fundamental principle is the source of the fractional order series, which has *an equal number of terms on both sides of the equation*. Moreover, the retardation times λ_i and the relaxation times τ_i obey the conditions [17, 20]

$$\tau_1 < \lambda_1 < \dots < \tau_i < \lambda_i < \dots < \tau_N < \lambda_N \quad (66)$$

In light of the connections between the relaxation (retardation) times and the fractional orders $\alpha_i = 1/(1 + \tau_i/t_0)$ and $\beta_i = 1/(1 + \lambda_i/t_0)$ we have the following requirement:

$$0 < \beta_1 < \alpha_1 < \dots < \beta_i < \alpha_i < \dots < \beta_N < \alpha_N < 1 \quad (67)$$

Further, a discrete relaxation spectrum (a series of exponents) with an accumulation point at zero, *behaves like a power-law for brief periods of time* in the context of polymer rheology [16,17,22], that is:

$$\sum_{i=0}^{\infty} \exp(-i^\gamma \xi) \rightarrow t^{-\frac{1}{\gamma}}, \quad t \rightarrow 0, \quad \gamma > 1 \quad (68)$$

Therefore, when for $t \rightarrow 0$ we may expect that (65) reduces to (68) and (62). This response explains how the model (65) reduces to the Bagley-Torvik equation with power-law-based derivatives and when this occurs: the discrete the relaxation spectrum asymptotic behaviour for short times. When $N = 1$, we get [17]

$$\sigma(t) + b [{}^{CF}D^\beta \sigma(t)] = E_0 \varepsilon(t) + E_1 [{}^{CF}D^\alpha \sigma(t)], \quad 1 > \beta > \alpha > 0 \quad (69)$$

Equation (69) contains *two fractional derivatives of different orders* as in (62) and this is the *generalized Zener type model*. Moreover, for $\alpha = \beta = 1$, this model reduces to

$$\sigma + \tau_\varepsilon \frac{d\sigma}{dt} = M_r \left(\varepsilon + \tau_\sigma \frac{d\varepsilon}{dt} \right), \quad \tau_\sigma / \tau_\varepsilon < 1 \quad (70)$$

with a relaxation modulus M_r . In general, $\tau < \lambda$ because this the basic causality requirement, meaning that the reaction occurs after the cause of it, but not the other way around, then the ratio τ/λ is always is less than 1.

4 Polynomial-Based Relationships Between Fractional Operators with Various Kernels

Now, the major goal of this section is to show that there are connections between popular fractional operators with single-memory kernels and the polynomial operator under discussion. The option to use various techniques (approximations) of the system responses (relations function) enables for showing the primary notion of this chapter because memory kernels in the hereditary integrals match (or approximate) the relaxation response of the system modelled.

4.1 Riemann-Liouville and Caputo Formulations as Fractional Caputo-Fabrizio Polynomials

Let us have a look at the Riemann construction for the integral (4) and derivative (5). The Riesz distributions, which act as memory kernels, (6) or (8), are the cores of these convolutions, that is, single power-law functions are used to model the system's relaxations (responses) based on this idea.

Since there is now a "competition" between the fractional operators with singular and those with non-singular kernels, the exponential sum approximation of the power-law function is quite an intriguing topic. The primary findings will be stated as follows after we quote McLean's study [23] (see also [24]) next.

Power-Law Function Approximation by a Sum of Exponentials. We can think about a convolution operator with a kernel of $k(t)$ [23] and specified points of time to address the power-law approximation by a sum exponentials [23,24].

$$K[u(t)] = \int_0^t k(t-s)u(s)ds \quad 0 = t_0 < t_1 < t_2 \cdots < t_{N_t} = T \quad (71)$$

Thus, allowing to attain a sufficient accuracy when only a moderate number of terms (moderate value of L) for a choice of δ that should be smaller than the time interval $(t_n - t_{n-1})$ between the sampling points. If $\Delta t_n \geq \delta$ it follows than $\delta \leq t_n - s \leq T$ when $0 \leq s \leq t_{n-1}$. With $k(t) = t^{-\beta}$, $\beta > 0$, the following transform is considered [23,24]

$$k(t) \approx \sum_{l=1}^L w_l \exp(b_l t) \quad (72)$$

As a result, it is possible to achieve an acceptable level of accuracy using just a moderate number of terms (moderate value of L) and a δ value that is chosen to be less than the time gap $(t_n - t_{n-1})$ between the sample points. If $\Delta t_n \geq \delta$, it is evident that $\delta \leq t_n - s \leq T$ occurs when $0 \leq s \leq t_{n-1}$. The following transform is said to [23] if $k(t) = t^{-\beta}$ and $\beta > 0$.

$$t^{-\beta} = \frac{1}{\Gamma(\beta)} \int_0^\infty e^{-pt} p^\beta \frac{dp}{p}, \quad t > 0, \quad \beta > 0 \quad (73)$$

By application the trapezoidal rule with a step $h > 0$ the following approximation can be obtained [23,24]

$$t^{-\beta} \approx \frac{1}{\Gamma(\beta)} \sum_{n=-\infty}^\infty w_n \exp(-a_n t), \quad a_n = e^{hn}, \quad w_n = h e^{\beta hn} \quad (74)$$

with a relative error [23,24]

$$\bar{\rho}(t) = 1 - \frac{t^\beta}{\Gamma(\beta)} \sum_{n=-\infty}^\infty w_n \exp(-a_n t), \quad 0 < t < \infty \quad (75)$$

When $t \in [\delta, t]$ with $\delta \in (0, T = \infty)$ and a finite number of terms we get [23,24]

$$t^{-\beta} \approx \frac{1}{\Gamma(\beta)} \sum_{n=-M}^N w_n \exp(-a_n t), \quad \delta \leq t \leq T \quad (76)$$

with a bounded error of approximation. In addition, the terms $a_n = \exp(nh)$ approach zero when $n \rightarrow -\infty$.

If $g(t) \approx \sum_{p=1}^N \tilde{w}_p \exp(-\tilde{a}_p t)$, $2N - 1 < L, \tilde{w}_l > 0$, $\tilde{a}_l > 0$ consequently $2N$ parameters from $2N$ conditions have to be determined, such that

$$g(t) \approx \sum_{p=1}^N \tilde{w}_p \exp(-\tilde{a}_p t), \quad 2N - 1 < L, \tilde{w}_l > 0, \quad \tilde{a}_l > 0 \quad (77)$$

The approximation (76) is a finite sum with many small exponents a_n . Now, the task is to develop more efficient approximations with as much as fewer N terms and acceptable accuracy, such that $g(t) \approx \sum_{p=1}^N \tilde{w}_p \exp(-\tilde{a}_p t)$, $2N - 1 < L, \tilde{w}_l > 0$, $\tilde{a}_l > 0$. The test for $\beta = 3/4$ (carried out with $\delta = 10^{-6}$ and $T = 10$) revealed that with $M = 65$ and $N = 36$ the relative error of approximation is $\leq 0.92 \times 10^{-8}$ ($\delta \leq t \leq T$). The data summarized in Table 1 of [23] indicate that for $L = 65$ and $N = 6$ the maximum relative error is about $1.66e^{-9}$. The same maximum relative error ($1.66e^{-9}$) appears when $L = 62$ and $N = 3$, as well as for $L = 56$ and $N = 2$ (two exponential terms). In all these cases the condition $2N - 1 < L$ is obeyed. Similar analysis was thoroughly performed in [10]. Further, if the appropriate coefficients in (72) are scaled as [25,26]

$$b_i = b_0/q^{i-1}, \quad w_l = C_\beta(q) k_\beta(t) \frac{b_l^\beta}{\Gamma(1-\beta)} \quad (78)$$

such as the inverse relaxation times b_l and the constants w_l , where q is a scaling parameters and $C_\beta(q)$ is a fitting dimensionless constant.

In this way, the power-law can be approximated over about $r = L \log_{10} q - 2$ temporal decades, where q is a scaling parameter related to the inverse relaxation time (rate constants) $b_l = b_0/q^{i-1}$, between two limits [25,26]: $\tau_l = 1/b_0 < t < \tau_h = \tau_l q^{L-1}$; and these restrictions always apply in physical situations. Hence, as mentioned by Goychuk [26] this approximation is not only natural but in some cases desirable (see comments in [27] where effects of fractional kernels on the type differentiable functions and emerging problems are discussed). As a result, as indicated by Goychuk in [26] this approximation is not only reasonable in some circumstances but also does so naturally (see the comments in [27] where the effects of fractional values on the type differentiable functions and new issues are examined). According to Goychuk [26], if the scaling parameter q is properly selected, even a decade scaling with $q = 10$, approximations with 1% accuracy can be developed. For instance, Goychuk's example [26] shows a nice fit of $t^{-0.5}$ over 14 time decades with a sum of 16 exponential terms.

Riemann-Liouville Operators Approximated by Fractional Caputo-Fabrizio Polynomials. Therefore, the Riemann-Liouville integral (4) can be approximated as fractional Caputo-Fabrizio polynomials if the kernel function $t^{-\beta}$, where $\beta = (1 - \alpha) < 1$, and therefore $\alpha = 1 - \beta$, is approximated as a series (76) or (76)), then we get an approximated Riemann-Liouville integral, namely

$$\begin{aligned}
 I^\alpha f(t) &= D^{-\alpha} f(t) \approx \frac{1}{\Gamma(\alpha)} \int_0^t g(t) f(s) ds \\
 &= \frac{1}{\Gamma(\alpha)} \int_0^t \left[\sum_{p=1}^N \tilde{\omega}_p \exp(-\tilde{a}_p(t-s)) \right] f(s) ds
 \end{aligned} \tag{79}$$

and an approximated Riemann-Liouville derivative, that is

$$\begin{aligned}
 {}^{RL}D_t^\alpha &\approx \frac{1}{\Gamma(\beta)} \frac{d}{dt} \int_0^t g(t) f(t) \\
 &= \frac{1}{\Gamma(\beta)} \frac{d}{dt} \int_0^t \left[\sum_{p=1}^N \tilde{\omega}_p \exp(-\tilde{a}_p(t-s)) \right] f(s) ds, \quad \beta = 1 - \alpha
 \end{aligned} \tag{80}$$

In both approximations, the discrete fractional orders are related to the rate coefficients \tilde{a}_p (having dimensions s^{-1}), which are the dimensionless inverse relaxation times, that is $\tilde{a}_p = 1/\bar{\tau}_{rp}$, where $\bar{\tau}_{rp} = \tau_{rp}/t_0$ (t_0 is macroscopic time scale) (see Eq. (43) as an example of this)

$$\tilde{a}_p = \frac{\alpha_p}{1 - \alpha_p} \tag{81}$$

Caputo Derivative Approximated by Fractional Caputo-Fabrizio Polynomials. Further, using the same approximation for the Caputo derivative we get

$${}^C D^\beta f(t) \approx \frac{1}{\Gamma(1-\beta)} \int_0^t \left[\sum_{p=1}^N \tilde{\omega}_p \exp(-\tilde{a}_p(t-s)) \right] \frac{df(s)}{ds} ds \tag{82}$$

where \tilde{a}_p are defined by (81). Changing the order of the integration and summation in (82) we get (see the same operation in (42))

$$\begin{aligned}
 {}^C D^\beta f(t) &\approx \frac{1}{\Gamma(1-\beta)} \sum_{p=1}^N \int_0^t [\tilde{\omega}_p \exp(-\tilde{a}_p(t-s))] \frac{df(s)}{ds} ds \\
 &= \frac{1}{\Gamma(1-\beta)} \sum_{p=1}^N {}^{CF}D_t^{\alpha_p} f(t)
 \end{aligned} \tag{83}$$

The essential principle of the fractional polynomial approximation, that we can approximate derivatives with the power-law kernel as a finite sum of Caputo-Fabrizio derivatives, is further illustrated by this conclusion. Regarding the Riemann-Liouville structures, the conclusion is not immediately apparent. It is straightforward to demonstrate the reasonableness of the polynomial approximations, though, because a simple integration by parts makes it possible to see the links between the Caputo and Riemann-Liouville derivatives [6].

Generally speaking, the Caputo construction, which is seen in other fractional operators with non-singular kernels, enables a more convincing demonstration of the rationality in approximation by fractional polynomials.

4.2 Fractional Operator with a Mittag-Leffler Kernel and Fractional Caputo-Fabrizio Polynomials

Mittag-Leffler Function Approximation by Exponential Sums. We shall now briefly discuss the exponential sums approach or the Mittag-Leffler function approximation method [28]

$$E_\alpha(-t^\alpha) = \sum_{k=0}^{\infty} \frac{(-1)^k t^{k\alpha}}{\Gamma(\alpha k + 1)}, \quad 0 < \alpha < 1, \quad t > 0 \quad (84)$$

as

$$E_\alpha(-t^\alpha) \approx \sum_{i=1}^N w_i \exp(-p_i t), \quad 0 < \alpha < 1, \quad t > 0 \quad (85)$$

Following Lam [28] (see more details in [24]) we have

$$E(-t^\alpha) = \int_0^{\infty} \frac{\sin(\alpha\pi)}{x^2 + 2 \cos(\alpha\pi)x + 1} \exp(-x^{1/\alpha}) dx \quad (86)$$

Then, expressing the integral in (86) as a sum of sub-integrals [28]

$$E_\alpha(-t^\alpha) = \int_0^{b^{-N}} + \sum_{j=1}^N \int_{b^{-j}}^{b^{-j+1}} + \sum_{j=1}^M \int_{b^{j-1}}^{b^j} + \int_{b^M}^{\infty} \quad (87)$$

allows in each sub-interval- the Gauss-Legendre quadrature to be applied. And, the result is [28]

$$E_\alpha(-t^\alpha) \approx S(t) = \sum_{j=1}^{N+M} \sum_{i=1}^{n_j} w_{ij} \exp(-s_{ij}t) \quad (88)$$

with

$$w_{ij} = \omega_{ij}^{(n_j)} \frac{\sin c(\alpha\pi)}{x_{ij}^2 + 2 \cos(\alpha\pi)x_{ij} + 1}, \quad s_{ij} = [x_{ij}^{(n_j)}]^{1/\alpha}, \quad \sin c(x) = \frac{\sin(x)}{x} \quad (89)$$

where and $\omega_{ij}^{(n_j)} x_{ij}^{(n_j)}$ are the Gauss-Legendre quadrature nodes and weights of order n_j of the j th interval $[b^{j-N}, b^{j-N+1}]$.

A Constitutive Equation with Mittag-Leffler Memory Approximated by Caputo-Fabrizio Polynomials. It is feasible to give a single convolution constitutive equation using the Mittag-Leffler function as a memory kernel, as an approximation, using the desired presentation (85) and the result (88), that is

$$G(t) = E_{\alpha_1} \left[\left(-\frac{t}{\tau_k} \right)^{\alpha_k} \right] \approx E_{\alpha}(-t^{\alpha}) \approx \sum_{j=1}^{N+M} \sum_{i=1}^{n_j} w_{ij} \exp(-s_{ij}t) \quad (90)$$

where simple relations link $\alpha_{ij} = 1/(1 + \tau_{ij}/t_0)$ terms of relaxation periods $s_{ij} = 1/\tau_{ij}$ to fractional orders α_{ij} of the Caputo-Fabrizio operators.

This replacement of the Mittag-Leffler kernel with a Prony's series in the convolution integral results in [24]

$$\begin{aligned} \sigma(t) &= G_{\infty} + \int_0^t E_{\alpha_1} \left(\frac{t-s}{\tau_k} \right)^{\alpha_k} \frac{d}{ds} \varepsilon(s) ds \Rightarrow \sigma(t) \\ &\approx G_{\infty} + \int_0^t \left[\sum_{j=1}^{N+M} \sum_{i=1}^{n_j} w_{ij} \exp(-s_{ij}t) \right] \frac{d}{ds} \varepsilon(s) ds \end{aligned} \quad (91)$$

As a result of the integration and summation orders being reversed in (91), [24] we get

$$\sigma(t) \approx G_{\infty} + \sum_{j=1}^{N+M} \sum_{i=1}^{n_j} \left[\int_0^t w_{ij} \exp(-s_{ij}t) \frac{d}{ds} \varepsilon(s) ds \right] \quad (92)$$

Now, we may express (92) in terms of Caputo-Fabrizio operators with fractional orders α_{ij} as [24]

$$G(t) \approx G_{\infty} + \sum_{j=1}^{N+M} \sum_{i=1}^{n_j} [(1 - \alpha_{ij}) D_t^{\alpha_{ij}} \varepsilon(t)] \quad (93)$$

This is comparable to the stress relaxation function that Prony's series directly approximates. Such an approach may facilitate the calculation techniques and avoid the problems with slow convergence of the Mittag-Leffler function. Moreover, from a practical point of view, when high precisions in the approximations requiring too many terms to be involved in the series (defined by the condition (89) are not attainable due to the experimental techniques restrictions, less accuracy in approximation results in less number of Prony's series approximating the Mittag-Leffler function. Thus this end, these comments only draw a perspective that needs thorough investigations. Such a method might simplify the calculation processes and prevent issues with the Mittag-Leffler function's sluggish convergence. Additionally, from a practical standpoint, reduced accuracy in approximation leads to fewer Prony's series approximating the Mittag-Leffler function when high precisions in approximations, indicated

by the condition (89), are not achievable due to the experimental procedure limitations. To that aim, these remarks just highlight a viewpoint that requires in-depth research.

5 Final Remarks

The author's view on fractional polynomial operators is presented in this chapter. It starts with Koeller's theory and is then expanded to include some recent advancements in fractional calculus, particularly the non-singular kernel operators. This initial step makes it possible to connect operators with singular and non-singular kernels, which in some situations with a practical orientation may ease with computation. However, the primary goal is to demonstrate that all new operators, like Mittag-Leffler (it is simple to develop this line also for Prabhakar, Rabotnov, and others functions, albeit they are not provided here), with memory kernels based on entire functions (of polynomial type converging completely at the complex plane), are in reality polynomial operators.

With satisfaction, we may mention the following from this vantage point and at the date and time that such a position is taken: *We may occasionally unearth inspired ideas by looking at what has already been done, even though they were not acknowledged in the original source. By having the ability to discern the invisible in previously seen results, science is being pushed into new frontiers.*

References

1. Baglet, R.L., Torvik, P.J.: On the fractional calculus model of viscoelastic behavior. *J. Rheol.* **30**, 133–155 (1986). <https://doi.org/10.1122/1.549887>
2. Koeller, R.C.: Polynomial operators, Stieltjes convolution and Fractional Calculus in hereditary mechanics. *Acta Mech.* **58**, 251–264 (1986). <https://doi.org/10.1007/BF01176603>
3. Koeller, R.C.: Application of fractional calculus to the theory of viscoelasticity. *J. Appl. Mech.* **51**, 299–307 (1984). <https://doi.org/10.1115/1.3167616>
4. Koeller, R.C.: A theory relating creep and relaxation for linear materials with memory. *J. Appl. Mech.* **77**, 031008 (2010). <https://doi.org/10.1115/1.4000415>
5. Koeller, R.C.: Toward an equation of state for solid materials with memory by use of the half-order derivative. *Acta Mech.* **191**, 125–133 (2007). <https://doi.org/10.1007/s00707-006-0411-y>
6. Podlubny, I.: *Fractional Differential Equations*. Academic, New York (1999)
7. Riesz, F., Sz.-Nagy, B.: *Functional Analysis*, Frederick Ungar Publishing, New York (1955)
8. Nussenzweig, H.: *Causality and Dispersion Relations*. Mathematics in Science and Engineering, vol. 95. Academic Press (1972)
9. de Prony, R.R.: *Essai Experimentale at analitique*. *J. Ecole Polytechnique* **1**, 24–76 (1795)
10. Beylkin, G., Monzon, L.: Approximation by exponential sums. *Appl. Comput. Harmon. Anal.* **28**, 17–48 (2005). <https://doi.org/10.1016/j.acha.2005.01.003>
11. Beylkin, G., Monzon, L.: Approximation by exponential sums revisited. *Appl. Comput. Harmon. Anal.* **28**, 131–149 (2010). <https://doi.org/10.1016/j.acha.2009.08.011>

12. Wineman, A.: Nonlinear viscoelastic solids-a Review. *Math. Mech. Solids* **14**, 300–366 (2009). <https://doi.org/10.1177/10812865091036>
13. Coleman, B., Noll, W.: Foundations of linear viscoelasticity. *Rev. Modern Phys.* **33**, 239–249 (1961). <https://doi.org/10.1103/RevModPhys.33.239>
14. Cristensen, R.M.: *Theory of Viscoelasticity. An Introduction*. Academic Press, New York (1982)
15. Hristov, J.: Response functions in linear viscoelastic constitutive equations and related fractional operators. *Math. Modell. Natur. Phenom.* **14**(3)(2019). <https://doi.org/10.1051/mmnp/2018067>
16. Hristov, J.: Linear viscoelastic responses: the Prony decomposition naturally leads into the Caputo-Fabrizio fractional operator. *Front. Phys.* (2018). <https://doi.org/10.3389/fphy.2018.00135>
17. Hristov, J.: Linear viscoelastic responses and constitutive equations in terms of fractional operators with non-singular kernels. *Eur. Phys. J. Plus* **134**(6), 1–31 (2019). <https://doi.org/10.1140/epjp/i2019-12697-7>
18. Caputo, M., Fabrizio, M.: A new definition of fractional derivative without singular kernel. *Progr. Fract. Differ. Appl.* **1**, 73–85 (2015). <https://doi.org/10.12785/pfda/010201>
19. Atangana, A., Baleanu, D.: New fractional derivatives with non-local and non-singular kernel: theory and application to Heat transfer model. *Therm. Sci.* **20**, 763–769 (2016). <https://doi.org/10.2298/TSCI160111018A>
20. Tschoegl, N.W.: *The Phenomenological Theory of Linear Viscoelastic Behaviour: An Introduction*. Springer, New Yorks (1989). <https://doi.org/10.2174/9789815051933122030007>
21. Rouse, P.E., Jr.: A theory of the linear viscoelastic properties of dilute solutions of coiling polymers. *J. Chem. Phys.* **21**, 1272–1280 (1953). <https://doi.org/10.1063/1.1699180>
22. Renardy, M.: Some remarks on the propagation and non-propagation of discontinuities in linearly viscoelastic liquids. *Rheol. Acta* **21**, 251–254 (1982). <https://doi.org/10.1007/BF01515713>
23. McLean, W.: Exponential sum approximations for $t^{-\beta}$. In: Dick, J., Kuo, F.Y., Woźniakowski, H. (eds.) *Contemporary Computational Mathematics - A Celebration of the 80th Birthday of Ian Sloan*, pp. 911–930. Springer, Cham (2018). https://doi.org/10.1007/978-3-319-72456-0_40
24. Hristov, J.: Prony's series and modern fractional calculus. In: Karaca, Y., Baleanu, D., Gervasi, O., Zhang, Y.-D.: (eds.) *Nonlinear Dynamical Models of Complex Systems*, pp. 187–200. Elsevier Inc. (2022). <https://doi.org/10.1016/B978-0-323-90032-4.00005-5>
25. Goychuk, I.: Viscoelastic subdiffusion: from anomalous to normal. *Phys. Rev. E* **80**, 046125 (2009). <https://doi.org/10.1103/PhysRevE.80.046125>
26. Goychuk, I.: Viscoelastic subdiffusion: generalized Langevin equation approach, In: Rice, S.A., Dinner, A.R. (eds.) *Advances in Chemical Physics*, vol. 150. Wiley (2012). <https://doi.org/10.1002/9781118197714.ch5>
27. Hristov, J.: The Duhamel Method in transient heat conduction: a rendezvous of classics and modern fractional calculus, In: Yavuz, M., Ozdemir, N. (eds.) *Current Developments in Mathematical Sciences, Fractional Calculus: New Applications in Understanding Nonlinear Phenomena*, vol. 3, pp. 85–107. Bentham Science Publishers (2022)
28. Lam, P.H., So, H.C., Chan, C.F.: Exponential sum approximation for the Mittag-Leffler function and its application to fractional Zener equation. *J. Comput. Phys.* **410**, 109389 (2020). <https://doi.org/10.1016/j.jcp.2020.109389>



On Weighted Fractional Operators with Applications to Mathematical Models Arising in Physics

Muhammad Samraiz¹(✉), Muhammad Umer¹, Saima Naheed¹,
and Dumitru Baleanu^{2,3}

¹ Department of Mathematics, University of Sargodha, Sargodha 40100, Pakistan
{muhammad.samraiz,saima.naheed}@uos.edu.pk, msamraizuos@gmail.com

² Department of Mathematics, Cankaya University, 06530 Ankara, Turkey

³ Institute of Space Sciences, 077125 Magurele, Romania

Abstract. In recent study, we develop the weighted generalized Hilfer-Prabhakar fractional derivative operator and explore its key properties. It unifies many existing fractional derivatives like Hilfer-Prabhakar and Riemann-Liouville. The weighted Laplace transform of the newly defined derivative is obtained. By involving the new fractional derivative, we modeled the free-electron laser equation and kinetic equation and then found the solutions of these fractional equations by applying the weighted Laplace transform.

Keywords: weighted Hilfer-Prabhakar fractional derivative · weighted Laplace transform · free-electron laser equation · fractional kinetic equation

1 Introduction

Fractional calculus is a natural development of classical calculus with a long mathematical history. The fractional calculus concept has been applied in numerous models. In a variety of domains, fractional models can be utilized to capture and comprehend complex processes (see related literature [1, 2]). Fractional calculus has progressed significantly as a result of its applications in practical mathematics such as chemistry, mechanics, physics, engineering, and biology [3–7]. In literature, several fractional operators exist with wide applications such as the Riemann-Liouville [8], the ψ -Hilfer fractional derivative and its properties [9], generalized Hilfer-Prabhakar fractional derivative with arising physical models [31], the fractional calculus iteration procedure on conformable derivatives [10], the Hadamard fractional calculus and Hadamard-type fractional differential equations [11], kernel Hilbert space method for nonlinear partial differential equations [12].

The generalization of fractional integral and derivative operators have achieved remarkable attention in recent decades [13–20]. Various special functions arise in the kernels of fractional operators, including the Wright function,

the Gauss hypergeometric function, Mittag-Leffler function, Fox H-function and Meijer G-function. The Hilfer-Prabhakar fractional derivative, which is an extension of the Caputo and the Riemann-Liouville fractional derivatives was presented by R. Hilfer in [13]. The fractional Prabhakar integral and derivative operators are established by involving the generalized Mittag-Leffler function in the kernel of the Riemann-Liouville fractional operators [14].

This research is inspired by the widespread use of fractional differential equations in engineering, economics, physics, and a variety of other fields of science [21–27]. The purpose of this work is to enhance the existing literature on fractional calculus and to provide the strong applicability in sciences.

We start this study by recalling some relevant definitions and notions.

Definition 1. [28] *The j -gamma function is defined as:*

$$\Gamma_j(\vartheta) = \int_0^\infty x^{\vartheta-1} e^{-\frac{x^j}{j}} dx, \Re(\vartheta) > 0, j > 0.$$

Note that $\Gamma(\vartheta) = \lim_{j \rightarrow 1} \Gamma_j(\vartheta)$ and $\Gamma_j(\vartheta) = j^{\frac{\vartheta}{j}-1} \Gamma(\frac{\vartheta}{j})$.

Definition 2. [28] *For $\Re(\vartheta) > 0, j > 0$ and $\Re(\varsigma) > 0$, the j -beta function is defined as*

$$B_j(\vartheta, \varsigma) = \frac{1}{j} \int_0^1 \tau^{\frac{\vartheta}{j}-1} (1-\tau)^{\frac{\varsigma}{j}-1} d\tau.$$

Γ_j and B_j functions are related as $B_j(\vartheta, \varsigma) = \frac{\Gamma_j(\vartheta)\Gamma_j(\varsigma)}{\Gamma_j(\vartheta+\varsigma)}$.

Definition 3. *For $F \in C^n[\hat{a}, \ell]$ and $F'(\varsigma) > 0$ on $[\hat{a}, \ell]$. Then*

$$AC_F^n[\hat{a}, \ell] = \left\{ \Psi : [\hat{a}, \ell] \rightarrow \mathbb{C} \ \Psi^{[n-1]} \in AC[\hat{a}, \ell] \right\},$$

where $\Psi^{[n-1]} = \left(\frac{1}{g'(\varsigma)} \frac{d}{d\varsigma} \right)^{n-1} \Psi$.

Definition 4. [29] *Let $n \in \mathbb{N}, j \in \mathbb{R}^+, \alpha, \varrho, \epsilon \in \mathbb{C}, \Re(\varrho) > 0, \Re(\alpha) > 0$, then j -Mittag-Leffler function is defined by*

$$E_{j,\varrho,\alpha}^\epsilon(\vartheta) = \sum_{n=0}^\infty \frac{(\epsilon)_{n,j} \vartheta^n}{\Gamma_j(\varrho n + \alpha) n!}.$$

Weighted generalized fractional integral operator involving j -Mittag-Leffler function introduced in [30] is described in the following definition.

Definition 5. *For $s \in \mathbb{R} \setminus \{-1\}, j \in \mathbb{R}^+, \alpha, \varrho, \omega, \epsilon \in \mathbb{C}, \Re(\varrho) > 0, \Re(\epsilon) > 0, \Re(\alpha) > 0$. Let Φ be a positive increasing function on $(\delta, \ell], \delta > 0$ having continuous derivative Φ' on $(0, \ell)$, and $\Psi \in L_1[\delta, \ell]$, then*

$$\begin{aligned} (\Phi, j \mathfrak{J}_{\delta^+, \varrho, \alpha}^{\omega, w, \epsilon} \Psi)(\vartheta) &= \frac{(s+1)^{1-\frac{\alpha}{j}}}{j} w^{-1}(\vartheta) \int_\delta^\vartheta (\Phi^{s+1}(\vartheta) - \Phi^{s+1}(\varsigma))^{\frac{\alpha}{j}-1} \Phi^s(\varsigma) \\ &\times E_{j,\varrho,\alpha}^\epsilon(\omega(\Phi^{s+1}(\vartheta) - \Phi^{s+1}(\varsigma))^{\frac{\varrho}{j}}) \Phi'(\varsigma) w(\varsigma) \Psi(\varsigma) d\varsigma. \end{aligned} \tag{1}$$

Definition 6. [31] Let $\Psi \in C^1[\delta, \ell]$, $\delta > 0$, $0 < \vartheta < \ell < \infty$, $s \in \mathbb{R} \setminus \{-1\}$, $j, \varrho > 0$, $\omega, \epsilon \in \mathbb{R}$, $\alpha \in (0, 1)$, $\mathbb{k} \in [0, 1]$ and $(\Psi * {}^s\mathfrak{J}_{0^+; \varrho, (1-\mathbb{k})(j-\alpha)}^{\omega, -\epsilon(1-\mathbb{k})})(\vartheta) \in AC^1[\delta, \ell]$, then generalized Hilfer-Prabhakar derivative is defined as

$${}^s\mathfrak{D}_{\delta^+; \varrho, \omega}^{\epsilon, \alpha, \varpi} \Psi(\vartheta) = j \left({}^s\mathfrak{J}_{\delta^+; \varrho, \varpi(j-\alpha)}^{\omega, -\epsilon\varpi} \left(\frac{1}{\vartheta^s} \frac{d}{d\vartheta} \right) {}^s\mathfrak{J}_{\delta^+; \varrho, (1-\varpi)(j-\alpha)}^{\omega, -\epsilon(1-\varpi)} \Psi \right)(\vartheta).$$

Weighted generalized Laplace transform introduced in [32] is defined as follows:

Definition 7. For the real valued functions Ψ , $w(x) \neq 0$ and Φ is such that $\Phi'(\xi) > 0$ on $[a, \infty)$, the weighted generalized Laplace transform of Ψ is given by

$$\mathfrak{L}_{\Phi}^w \{ \Psi(t) \}(u) = \int_a^{\infty} e^{-u(\Phi(t)-\Phi(a))} w(t) \Psi(t) \Phi'(t) dt, \tag{2}$$

for all values of u .

Definition 8. [33] For some $\alpha \in \mathbb{R}$, the Caputo derivative of non integer order α with $\Psi(x) \in AC^n([a, b])$ is given by

$$({}_a\mathfrak{D}_{a^+}^{\alpha} \Psi)(\vartheta) = \frac{1}{\Gamma(n-\alpha)} \int_a^{\vartheta} (\vartheta - x)^{n-\alpha-1} \Psi^{(n)}(x) dx, \quad n \in \mathbb{N} \tag{3}$$

where $n = [\alpha] + 1$.

Definition 9. [20] Let $\Psi, \psi \in C^1[\delta, \ell]$, $\delta > 0$, $0 < \vartheta < \ell < \infty$, $\varrho > 0$, $\epsilon \in \mathbb{R}$, $\alpha \in (0, 1)$, $\varpi \in [0, 1]$ and $(\Psi * {}^s\mathfrak{J}_{\delta^+; \varrho, (1-\varpi)(1-\alpha)}^{-\epsilon(1-\varpi)})(\vartheta) \in AC^1[\delta, \ell]$, then weighted generalized Hilfer-Prabhakar fractional derivative is defined as

$$\mathfrak{D}_{\delta^+; \varrho, \omega}^{\epsilon, \alpha, \varpi} \Psi(\vartheta) = \left({}^s\mathfrak{J}_{\delta^+; \varrho, \varpi(1-\alpha)}^{\omega, -\epsilon\varpi} \left(\frac{d}{d\vartheta} \right) {}^s\mathfrak{J}_{\delta^+; \varrho, (1-\varpi)(1-\alpha)}^{\omega, -\epsilon(1-\varpi)} \Psi \right)(\vartheta),$$

Samraiz et al. [34] proposed the modified weighted (j, s) -Riemann-Liouville fractional integral of order ρ , which is stated as follows:

Definition 10. Suppose that Ψ be a continuous function on $[a, b]$ and Φ is strictly increasing differentiable function. Then modified weighted (j, s) -Riemann-Liouville fractional integral of order ρ is given by

$$\begin{aligned} & (\Phi; {}^s\mathfrak{J}_{a^+; w}^{\rho} \Psi)(\vartheta) \\ &= \frac{(s+1)^{1-\frac{\rho}{j}} w^{-1}(\vartheta)}{j\Gamma_j(\rho)} \int_a^{\vartheta} (\Phi^{s+1}(\vartheta) - \Phi^{s+1}(t))^{\frac{\rho}{j}-1} \Phi^s(t) \Phi'(t) w(t) \Psi(t) dt, \quad \vartheta \in [a, b], \end{aligned}$$

where $\rho, j > 0$, $w(\vartheta) \neq 0$ and $s \in \mathbb{R} \setminus \{-1\}$.

Theorem 1. [32] Let $\mathfrak{D}_w^j \Psi$, $j = 0, 1, 2, \dots, m-1$ be weighted Φ -exponential order with $\Psi \in AC_w^{m-1}[a, \xi]$. Furthermore, if the function $\mathfrak{D}_w^n \Psi$ is piecewise continuous on an $[a, T]$, then the weighted Laplace transform of $\mathfrak{D}_w^n \Psi$ is defined by

$$\mathfrak{L}_{\Phi}^w \{ \mathfrak{D}_w^n \Psi \}(u) = u^n \mathfrak{L}_{\Phi}^w \{ \Psi(\xi) \}(u) - \sum_{j=0}^{n-1} u^{n-j-1} \Psi_j(a).$$

Definition 11. [32] The convolution of Ψ and Φ is defined by

$$(\Psi *_{\Phi}^w h)(\xi) = w^{-1}(\xi) \int_a^{\xi} w(\Phi^{-1}(\Phi(\xi) + \Phi(a) - \Phi(t))) \times \Psi(\Phi^{-1}(\Phi(\xi) + \Phi(a) - \Phi(t)))w(t)h(t)\Phi'(t)dt.$$

Theorem 2. [30] Let Ψ be a piecewise continuous w -weighted Φ -exponential order function on interval $[a, \vartheta]$. Then

$$\begin{aligned} & \mathfrak{L}_{\Phi}^w \{ \psi, {}_j^s \mathfrak{J}_{\delta^+; \varrho, \alpha}^{\omega, \omega, \epsilon} \Psi(\vartheta) \} (s) \\ &= (s + 1)^{1 - \frac{\varrho}{j}} (js)^{-\frac{\alpha}{k}} \left(1 - k\omega (ks)^{-\frac{\varrho}{k}} \right)^{-\frac{\epsilon}{k}} \mathfrak{L}_{\Phi}^w \{ \Psi(\vartheta) \} (s), \end{aligned}$$

with $|j\omega(js)^{-\frac{\varrho}{j}}| < 1$.

The present work is one in a sequence of studies starting by Garra et al. [20] in 2014, then modified by Samraiz et al. [31] in 2020.

2 Weighted Generalized Hilfer-Prabhakar Fractional Derivative and Weighted Laplace Transform

In the current section, we describe the weighted generalized Hilfer-Prabhakar fractional derivative. The weighted Laplace transform of the novel operator is also evaluated.

Definition 12. Let $\Psi, \psi \in C^1[\delta, \ell]$, $\delta > 0$, $0 < \vartheta < \ell < \infty$, $s \in \mathbb{R} \setminus \{-1\}$, $\eta, \varrho > 0$, $\omega, \epsilon \in \mathbb{R}$, $\alpha \in (0, 1)$, $\varpi \in [0, 1]$ and $(\Psi *_{\psi, \eta}^s \mathfrak{J}_{\delta^+; \varrho, (1-\varpi)(\eta-\alpha)}^{\omega, \omega, -\epsilon(1-\varpi)})(\vartheta) \in AC^1[\delta, \ell]$, then weighted generalized Hilfer-Prabhakar fractional derivative is defined as

$${}_{\psi, \eta}^s \mathfrak{D}_{\delta^+; \varrho, \omega}^{\epsilon, \omega, \alpha, \varpi} \Psi(\vartheta) = \eta \left({}_{\psi, \eta}^s \mathfrak{J}_{\delta^+; \varrho, \varpi(\eta-\alpha)}^{\omega, \omega, -\epsilon\varpi} \left(\frac{w^{-1}(\vartheta)}{\psi^s(\vartheta)\psi'(\vartheta)} \frac{d}{d\vartheta} \right) w(\vartheta) {}_{\psi, \eta}^s \mathfrak{J}_{\delta^+; \varrho, (1-\varpi)(\eta-\alpha)}^{\omega, \omega, -\epsilon(1-\varpi)} \Psi \right) (\vartheta), \quad (4)$$

where $\psi^s(\vartheta) = (\psi(\vartheta))^s$, $\psi^s(\vartheta) \neq 0$ and $w(\vartheta) \neq 0$.

We observe that, the generalized Hilfer-Prabhakar fractional derivative operator given in [31] can be achieved with choice of parameters $\psi(\vartheta) = \vartheta$ and $w(\vartheta) = 1$ in (4). The choice of the parameters $\psi(\vartheta) = \vartheta, w(\vartheta) = 1, \eta = 1, s = 0$, gives Hilfer-Prabhakar fractional derivative introduced by Garra et al. in [20] presented in Definition 9. If we set $\psi(\vartheta) = \vartheta, w(\vartheta) = 1, \varpi = 0$ and $\epsilon = 0$ in (4), we get (η, s) -Riemann-Liouville fractional derivative operator given in [35]. Corresponding to the choice of the parameters $\psi(\vartheta) = \vartheta, w(\vartheta) = 1$ and $\varpi = 0$ in (4), we obtain (η, s) -Prabhakar fractional derivative given in [36]. If we substitute $\psi(\vartheta) = \vartheta, w(\vartheta) = 1, \varpi = 0$, and $s = 0$ in (4), we get η -Prabhakar fractional derivative operator given in [8], the choice of the parameters $\psi(\vartheta) = \vartheta, w(\vartheta) = 1, \varpi = 0, s = 0$ and $\eta = 1$ in (4) gives Prabhakar fractional derivative operator presented in [14].

Proposition 1. Let $s \in \mathbb{R} \setminus \{-1\}$, $\eta \in \mathbb{R}^+$, $\alpha, \varrho, \omega, \epsilon \in \mathbb{C}$, $\Re(\varrho) > 0$, $\Re(\alpha) > 0$ and $\ell > 0$ then integral operator $\psi_{,\eta}^s \mathfrak{J}_{\delta^+; \varrho, \alpha}^{\omega, w, \epsilon}$ is bounded on $C[\delta, \ell]$, $\delta \geq 0$ i.e.,

$$|(\psi_{,\eta}^s \mathfrak{J}_{\delta^+; \varrho, \alpha}^{\omega, w, \epsilon} \Psi)(\vartheta)| \leq G \|w\Psi\|_{C[\delta, \ell]},$$

where

$$\|w\Psi\|_{C[\delta, \ell]} = \max\{|w\Psi| : 0 < x < \ell\}$$

and

$$\begin{aligned} G &= \frac{(s+1)^{-\frac{\alpha}{\eta}} (\psi^{s+1}(\ell) - \psi^{s+1}(\delta))^{\frac{\alpha}{\eta}}}{\eta} \sum_{m=0}^{\infty} \frac{|(\epsilon)_{m, \eta} \omega^m|}{|\Gamma_{\eta}(\varrho m + \alpha)| m!} \\ &\quad \times \frac{(\psi^{s+1}(\ell) - \psi^{s+1}(\delta))^{\frac{\varrho}{\eta} m}}{\left[\frac{m}{\eta}(\varrho + \alpha)\right]}. \end{aligned} \quad (5)$$

Proof. We first prove that the series in the Eq. (5) is convergent. Let b_m denotes the m^{th} term of the series, then we have

$$\begin{aligned} \frac{b_{m+1}}{b_m} &= \frac{|(\epsilon)_{m+1, \eta} \omega^{m+1} (\psi^{s+1}(\ell) - \psi^{s+1}(\delta))^{\frac{\varrho(m+1)}{\eta}}|}{|(\epsilon)_{m, \eta} \omega^m (\psi^{s+1}(\ell) - \psi^{s+1}(\delta))^{\frac{\varrho m}{\eta}}|} \\ &\quad \times \frac{\left[\frac{m\varrho + \alpha}{\eta}\right] |\Gamma_{\eta}(\varrho m + \alpha)| m!}{\left[\frac{(m+1)\varrho + \alpha}{\eta}\right] |\Gamma_{\eta}(\varrho(m+1) + \alpha)| (m+1)!} \\ &= \eta^{-\frac{\varrho}{\eta}} \frac{|m + \frac{\epsilon}{\eta}|}{m+1} \frac{\left|\Gamma\left(\frac{\varrho m}{\eta} + \frac{\alpha}{\eta}\right)\right|}{\left|\Gamma\left(\frac{\varrho m}{\eta} + \frac{\varrho}{\eta} + \frac{\alpha}{\eta}\right)\right|} \\ &\quad \times \frac{\left[\frac{m\varrho + \alpha}{\eta}\right]}{\left|\left[\frac{(m+1)\varrho + \alpha}{\eta}\right]\right|} \omega |(\psi^{s+1}(\ell) - \psi^{s+1}(\delta))^{\frac{\varrho}{\eta}}| \\ &\sim \frac{\omega |(\psi^{s+1}(\ell) - \psi^{s+1}(\delta))^{\frac{\varrho}{\eta}}|}{\left(\frac{\varrho}{\eta} m\right)^{\frac{\varrho}{\eta}}} \rightarrow 0 (m \rightarrow \infty). \end{aligned}$$

This implies that the series on the right side of (5) is convergent and hence G is finite.

Now, Consider

$$\begin{aligned} |(\psi_{,\eta}^s \mathfrak{J}_{\delta^+; \varrho, \alpha}^{\omega, w, \epsilon} \Psi)(\vartheta)| &\leq \frac{(s+1)^{1-\frac{\alpha}{\eta}}}{\eta} w^{-1}(\vartheta) \int_{\delta}^{\vartheta} (\psi^{s+1}(\vartheta) - \psi^{s+1}(\varsigma))^{\frac{\alpha}{\eta}-1} \psi^s(\varsigma) \\ &\quad \times |E_{\eta, \varrho, \alpha}^{\epsilon}(\omega(\psi^{s+1}(\vartheta) - \psi^{s+1}(\varsigma))^{\frac{\varrho}{\eta}}) w(\varsigma) \Psi(\varsigma)| \psi'(\varsigma) d\varsigma. \end{aligned} \quad (6)$$

Substitute $u = \psi^{s+1}(\vartheta) - \psi^{s+1}(\varsigma)$ on the right side of (6), we get

$$\begin{aligned}
 |(\psi, \eta^s \mathfrak{J}_{\delta^+; \varrho, \alpha}^{\omega, w, \epsilon} \Psi)(\vartheta)| &\leq \frac{(s+1)^{-\frac{\alpha}{\eta}}}{\eta} w^{-1}(\vartheta) \int_0^{\psi^{s+1}(\vartheta) - \psi^{s+1}(\delta)} u^{\frac{\alpha}{\eta} - 1} \\
 &\quad \times |E_{\eta, \varrho, \alpha}^{\epsilon}(\omega(u)^{\frac{\varrho}{\eta}})| \|w\Psi\|_{C[\delta, \ell]} du \\
 &\leq \|w\Psi\|_{C[\delta, \ell]} \frac{(s+1)^{-\frac{\alpha}{\eta}}}{\eta} w^{-1}(\ell) \int_0^{\psi^{s+1}(\ell) - \psi^{s+1}(\delta)} u^{\frac{\alpha}{\eta} - 1} \\
 &\quad \times |E_{\eta, \varrho, \alpha}^{\epsilon}(\omega(u)^{\frac{\varrho}{\eta}})| du \\
 &\leq \|w\Psi\|_{C[\delta, \ell]} \frac{(s+1)^{-\frac{\alpha}{\eta}}}{\eta} w^{-1}(\ell) \sum_{m=0}^{\infty} \frac{|(\epsilon)_{m, \eta} \omega^m|}{|\Gamma_{\eta}(\varrho m + \alpha)| m!} \\
 &\quad \times \int_0^{\psi^{s+1}(\ell) - \psi^{s+1}(\delta)} (u)^{\left(\frac{\varrho}{\eta} m + \left(\frac{\alpha}{\eta}\right) - 1\right)} du \\
 &\leq \|w\Psi\|_{C[\delta, \ell]} \frac{(s+1)^{-\frac{\alpha}{\eta}} (\psi^{s+1}(\ell) - \psi^{s+1}(\delta))^{\left(\frac{\alpha}{\eta}\right)}}{\eta} \sum_{m=0}^{\infty} \frac{|(\epsilon)_{m, \eta} \omega^m|}{|\Gamma_{\eta}(\varrho m + \alpha)| m!} \\
 &\quad \times \frac{(\psi^{s+1}(\ell) - \psi^{s+1}(\delta))^{\left(\frac{\varrho}{\eta}\right) m}}{\left[\frac{m}{\eta} (\varrho + \alpha)\right]},
 \end{aligned}$$

which gives

$$|(\psi, \eta^s \mathfrak{J}_{\delta^+; \varrho, \alpha}^{\omega, w, \epsilon} \Psi)(\vartheta)| \leq G \|w\Psi\|_{C[\delta, \ell]}.$$

This completes the proof of Proposition 1.

Theorem 3. *Let s be any real number except -1 , $\eta, \varrho > 0$, $\omega, \epsilon \in \mathbb{R}$, $\alpha \in (0, 1)$, $\varpi \in [0, 1]$. If $\Psi \in L_1[\delta, \ell]$, then the weighted generalized Hilfer-Prabhakar fractional derivative $\psi, \eta^s \mathfrak{D}_{\delta^+; \varrho, \omega}^{\epsilon, w, \alpha, \varpi}$ is bounded on $C[\delta, \ell]$*

$$\|\psi, \eta^s \mathfrak{D}_{\delta^+; \varrho, \omega}^{\epsilon, \alpha, \varpi} \Psi(\vartheta)\| \leq A_1 A_2 \|w\Psi\|_{[\delta, \ell]},$$

where

$$\begin{aligned}
 A_1 &= \frac{(s+1)^{-\frac{\varpi(\eta-\alpha)}{\eta}} (\psi^{s+1}(\ell) - \psi^{s+1}(\delta))^{\frac{\varpi(\eta-\alpha)}{\eta}}}{\eta} \\
 &\quad \times \sum_{n=0}^{\infty} \frac{|(-\epsilon \varpi)_{n, \eta} \omega^n|}{|\Gamma_{\eta}(\varrho n + \varpi(\eta - \alpha))| n!} \frac{(\psi^{s+1}(\ell) - \psi^{s+1}(\delta))^{\frac{\varrho n}{\eta}}}{\left[\frac{\varrho n}{\eta} + \frac{\varpi(\eta - \alpha)}{\eta}\right]}, \tag{7}
 \end{aligned}$$

and

$$\begin{aligned}
 A_2 &= \frac{(s+1)^{-\frac{(1-\varpi)(\eta-\alpha)-\eta}{\eta}} (\psi^{s+1}(\ell) - \psi^{s+1}(\delta))^{\frac{(1-\varpi)(\eta-\alpha)-\eta}{\eta}}}{\eta} \\
 &\quad \times \sum_{m=0}^{\infty} \frac{|(\epsilon(\varpi-1))_{m, \eta} \omega^m|}{|\Gamma_{\eta}(\varrho m + (1-\varpi)(\eta - \alpha))| m!} \frac{(\psi^{s+1}(\ell) - \psi^{s+1}(\delta))^{\frac{\varrho m}{\eta}}}{\left[\frac{\varrho m}{\eta} + \frac{(1-\varpi)(\eta - \alpha)}{\eta}\right]}. \tag{8}
 \end{aligned}$$

Proof. Using Proposition 1, we have

$$\begin{aligned}
 & \left\| \psi, {}^s \mathfrak{D}_{\delta^+; \varrho, \omega}^{\epsilon, w, \alpha, \varpi} \Psi(\vartheta) \right\| \\
 = & \left\| \eta \left(\psi, {}^s \mathfrak{J}_{\delta^+; \varrho, \varpi(\eta-\alpha)}^{\omega, w, -\epsilon\varpi} \left(\frac{w^{-1}(\vartheta)}{\psi^s(\vartheta)\psi'(\vartheta)} \frac{d}{d\vartheta} \right) w(\vartheta) \left(\psi, {}^s \mathfrak{J}_{\delta^+; \varrho, (1-\varpi)(\eta-\alpha)}^{\omega, w, -\epsilon(1-\varpi)} \Psi \right)(\vartheta) \right) \right\| \\
 & \leq \eta A_1 \left\| \left(\frac{w^{-1}(\vartheta)}{\psi^s(\vartheta)\psi'(\vartheta)} \frac{d}{d\vartheta} \right) w(\vartheta) \left(\psi, {}^s \mathfrak{J}_{\delta^+; \varrho, (1-\varpi)(\eta-\alpha)}^{\omega, w, -\epsilon(1-\varpi)} \Psi \right)(\vartheta) \right\| \\
 & = A_1 \left\| \left(\psi, {}^s \mathfrak{J}_{\delta^+; \varrho, (1-\varpi)(\eta-\alpha)-\eta}^{\omega, w, -\epsilon(1-\varpi)} \Psi \right)(\vartheta) \right\| \\
 & \leq A_1 A_2 \|\Psi\|_{[\delta, \ell]},
 \end{aligned}$$

where both A_1 and A_2 are given by (7) and (8).

Proposition 2. *Let $s \in \mathbb{R} \setminus -1$, $\eta, \varrho, \rho > 0$, $\omega, \epsilon, \sigma \in \mathbb{R}$, $\alpha \in (0, 1)$, $\varpi \in [0, 1]$, $\rho > \alpha + \varpi\eta - \alpha\varpi$ and $\Psi \in L_1[\delta, \ell]$, then*

$$\left(\psi, {}^s \mathfrak{D}_{\delta^+; \varrho, \omega}^{\epsilon, w, \alpha, \varpi} \left(\psi, {}^s \mathfrak{J}_{\delta^+; \varrho, \rho}^{\omega, w, \sigma} \Psi \right) \right)(\vartheta) = \left(\psi, {}^s \mathfrak{J}_{\delta^+; \varrho, \rho-\alpha}^{\omega, w, \sigma-\epsilon} \Psi \right)(\vartheta).$$

In particular

$$\left(\psi, {}^s \mathfrak{D}_{\delta^+; \varrho, \omega}^{\epsilon, w, \alpha, \varpi} \left(\psi, {}^s \mathfrak{J}_{\delta^+; \varrho, \alpha}^{\omega, w, \epsilon} \Psi \right) \right)(\vartheta) = \Psi(\vartheta).$$

Proof. Using the Definition 12 and semi group property of (5) given in [30], we have

$$\begin{aligned}
 & \left(\psi, {}^s \mathfrak{D}_{\delta^+; \varrho, \omega}^{\epsilon, w, \alpha, \varpi} \left(\psi, {}^s \mathfrak{J}_{\delta^+; \varrho, \rho}^{\omega, w, \sigma} \Psi \right) \right)(\vartheta) \\
 = & \eta \left(\psi, {}^s \mathfrak{J}_{\delta^+; \varrho, \varpi(\eta-\alpha)}^{\omega, w, -\epsilon\varpi} \left(\frac{w^{-1}(\vartheta)}{\psi^s(\vartheta)\psi'(\vartheta)} \frac{d}{d\vartheta} w(\vartheta) \right) \psi, {}^s \mathfrak{J}_{\delta^+; \varrho, (1-\varpi)(\eta-\alpha)}^{\omega, w, -\epsilon(1-\varpi)} \left(\psi, {}^s \mathfrak{J}_{\delta^+; \varrho, \rho}^{\omega, w, \sigma} \Psi \right) \right)(\vartheta) \\
 = & \eta \left(\psi, {}^s \mathfrak{J}_{\delta^+; \varrho, \varpi(\eta-\alpha)}^{\omega, w, -\epsilon\varpi} \left(\frac{w^{-1}(\vartheta)}{\psi^s(\vartheta)\psi'(\vartheta)} \frac{d}{d\vartheta} w(\vartheta) \right) \left(\psi, {}^s \mathfrak{J}_{\delta^+; \varrho, (1-\varpi)(\eta-\alpha)+\rho}^{\omega, w, -\epsilon(1-\varpi)+\sigma} \Psi \right) \right)(\vartheta) \\
 = & \left(\psi, {}^s \mathfrak{J}_{\delta^+; \varrho, \varpi(\eta-\alpha)}^{\omega, w, -\epsilon\varpi} \left(\psi, {}^s \mathfrak{J}_{\delta^+; \varrho, (1-\varpi)(\eta-\alpha)+\rho-\eta}^{\omega, w, -\epsilon(1-\varpi)+\sigma} \Psi \right) \right)(\vartheta) \\
 = & \left(\psi, {}^s \mathfrak{J}_{\delta^+; \varrho, \rho-\alpha}^{\omega, w, \sigma-\epsilon} \Psi \right)(\vartheta).
 \end{aligned}$$

The proof of the Proposition 2 is completed.

Theorem 4. *For $s \in \mathbb{R} \setminus \{-1\}$, $\eta, \varrho, \rho > 0$, $\omega, \epsilon \in \mathbb{R}$, $\alpha \in (0, 1)$, $\varpi \in [0, 1]$, $\rho > \alpha + \varpi\eta - \alpha\varpi$ and $\Psi \in L_1[\delta, \ell]$ then*

$$\left(\psi, {}^s \mathfrak{J}_{\delta^+; \omega}^{\rho} \left(\psi, {}^s \mathfrak{D}_{\delta^+; \varrho, \omega}^{\epsilon, w, \alpha, \varpi} \Psi \right) \right)(\vartheta) = \left(\psi, {}^s \mathfrak{J}_{\delta^+; \varrho, \rho-\alpha}^{\omega, w, -\epsilon} \Psi \right)(\vartheta).$$

Proof. Using the Definition 12 and Theorem 2.5 given in [36], we get

$$\begin{aligned}
 & \left(\psi, {}^s \mathfrak{J}_{\delta^+}^\rho, w \left(\psi, {}^s \mathfrak{D}_{\delta^+; \rho, \omega}^{\epsilon, w, \alpha, \varpi} \Psi \right) \right) (\vartheta) \\
 &= \eta \left(\psi, {}^s \mathfrak{J}_{\delta^+}^\rho, w \psi, {}^s \mathfrak{J}_{\delta^+; \rho, \varpi(\eta-\alpha)}^{\omega, w, -\epsilon \varpi} \left(\frac{w^{-1}(\vartheta)}{\psi^s(\vartheta) \psi'(\vartheta)} \frac{d}{d\vartheta} w(\vartheta) \right), \psi, {}^s \mathfrak{J}_{\delta^+; \rho, (1-\varpi)(\eta-\alpha)}^{\omega, w, -\epsilon(1-\varpi)} \Psi \right) (\vartheta) \\
 &= \eta \left(\psi, {}^s \mathfrak{J}_{\delta^+; \rho, \varpi(\eta-\alpha)}^{\omega, w, -\epsilon \varpi} \left(\frac{w^{-1}(\vartheta)}{\psi^s(\vartheta) \psi'(\vartheta)} \frac{d}{d\vartheta} w(\vartheta) \right), \psi, {}^s \mathfrak{J}_{\delta^+; \rho, (1-\varpi)(\eta-\alpha)}^{\omega, w, -\epsilon(1-\varpi)} \Psi \right) (\vartheta) \\
 &= \left(\psi, {}^s \mathfrak{J}_{\delta^+; \rho, \varpi(\eta-\alpha) + \rho}^{\omega, w, -\epsilon \varpi} \left(\psi, {}^s \mathfrak{J}_{\delta^+; \rho, (1-\varpi)(\eta-\alpha) - \eta}^{\omega, -\epsilon(1-\varpi)} \Psi \right) \right) (\vartheta) \\
 &= \left(\psi, {}^s \mathfrak{J}_{\delta^+; \rho, \rho - \alpha}^{\omega, -\epsilon} \Psi \right) (\vartheta).
 \end{aligned}$$

This completes the proof.

Theorem 5. *The weighted Laplace transform of generalized Hilfer-Prabhakar fractional derivative is given by*

$$\begin{aligned}
 \mathfrak{L}_\psi^w \{ \psi, {}^s \mathfrak{D}_{\delta^+; \rho, \omega}^{\epsilon, w, \alpha, \varpi} \Psi(\vartheta) \} (u) &= (s+1)^{\frac{\alpha-\eta}{\eta}} (\eta u)^{\frac{\alpha}{\eta}} \left(1 - \eta \omega (\eta u)^{-\frac{\rho}{\eta}} \right)^{\frac{\epsilon}{\eta}} \\
 &\quad \times \mathfrak{L}_\psi^w \{ \Psi(\vartheta) \} (u) - \eta (s+1)^{-\frac{\varpi(\eta-\alpha)}{\eta}} (\eta u)^{-\frac{\varpi(\eta-\alpha)}{\eta}} \\
 &\quad \times \left(1 - \eta \omega (\eta u)^{-\frac{\rho}{\eta}} \right)^{\frac{\epsilon \varpi}{\eta}} \psi, {}^s \mathfrak{J}_{\delta^+; \rho, (1-\varpi)(\eta-\alpha)}^{\omega, w, -\epsilon(1-\varpi)} \Psi(\delta^+).
 \end{aligned}$$

Proof. Using the Definition 12 and Theorem 1, we have

$$\begin{aligned}
 & \mathfrak{L}_\psi^w \{ \psi, {}^s \mathfrak{D}_{\delta^+; \rho, \omega}^{\epsilon, w, \alpha, \varpi} \Psi(\vartheta) \} (u) \\
 &= \eta (s+1)^{-\frac{\varpi(\eta-\alpha)}{\eta}} (\eta u)^{-\frac{\varpi(\eta-\alpha)}{\eta}} \left(1 - \eta \omega (\eta u)^{-\frac{\rho}{\eta}} \right)^{\frac{\epsilon \varpi}{\eta}} \\
 &\quad \times \mathfrak{L}_\psi^w \left\{ \psi, {}^s \mathfrak{J}_{\delta^+; \rho, (1-\varpi)(\eta-\alpha)}^{\omega, w, -\epsilon(1-\varpi)} \Psi(\vartheta) \right\}^{[1]} (u) \\
 &= \eta (s+1)^{-\frac{\varpi(\eta-\alpha)}{\eta}} (\eta u)^{-\frac{\varpi(\eta-\alpha)}{\eta}} \left(1 - \eta \omega (\eta u)^{-\frac{\rho}{\eta}} \right)^{\frac{\epsilon \varpi}{\eta}} \\
 &\quad \times \left[u \mathfrak{L}_\psi^w \{ \psi, {}^s \mathfrak{J}_{\delta^+; \rho, (1-\varpi)(\eta-\alpha)}^{\omega, w, -\epsilon(1-\varpi)} \Psi(\vartheta) \} (u) - \psi, {}^s \mathfrak{J}_{\delta^+; \rho, (1-\varpi)(\eta-\alpha)}^{\omega, w, -\epsilon(1-\varpi)} \Psi(\delta^+) \right] \\
 &= (\eta u) (s+1)^{-\frac{\varpi(\eta-\alpha)}{\eta}} (\eta u)^{-\frac{\varpi(\eta-\alpha)}{\eta}} \left(1 - \eta \omega (\eta u)^{-\frac{\rho}{\eta}} \right)^{\frac{\epsilon \varpi}{\eta}} \\
 &\quad \times \mathfrak{L}_\psi^w \{ \psi, {}^s \mathfrak{J}_{\delta^+; \rho, (1-\varpi)(\eta-\alpha)}^{\omega, w, -\epsilon(1-\varpi)} \Psi(\vartheta) \} (u) - \eta (s+1)^{-\frac{\varpi(\eta-\alpha)}{\eta}} (\eta u)^{-\frac{\varpi(\eta-\alpha)}{\eta}} \\
 &\quad \times \left(1 - \eta \omega (\eta u)^{-\frac{\rho}{\eta}} \right)^{\frac{\epsilon \varpi}{\eta}} \psi, {}^s \mathfrak{J}_{\delta^+; \rho, (1-\varpi)(\eta-\alpha)}^{\omega, w, -\epsilon(1-\varpi)} \Psi(\delta^+) \\
 &= (\eta u) (s+1)^{-\frac{\varpi(\eta-\alpha)}{\eta}} (\eta u)^{-\frac{\varpi(\eta-\alpha)}{\eta}} \left(1 - \eta \omega (\eta u)^{-\frac{\rho}{\eta}} \right)^{\frac{\epsilon \varpi}{\eta}} \\
 &\quad \times \left[(s+1)^{-\frac{(1-\varpi)(\eta-\alpha)}{\eta}} (\eta u)^{-\frac{(1-\varpi)(\eta-\alpha)}{\eta}} \left(1 - \eta \omega (\eta u)^{-\frac{\rho}{\eta}} \right)^{\frac{\epsilon(1-\varpi)}{\eta}} \right.
 \end{aligned}$$

$$\begin{aligned}
 & \times \mathfrak{L}_{\psi}^w \{ \Psi(\vartheta) \} (u) \Big] - \eta(s+1)^{-\frac{\varpi(\eta-\alpha)}{\eta}} (\eta u)^{-\frac{\varpi(\eta-\alpha)}{\eta}} \left(1 - \eta\omega(\eta u)^{-\frac{\varrho}{\eta}} \right)^{\frac{\epsilon\varpi}{\eta}} \\
 & \quad \times \psi, \eta^s \mathfrak{J}_{\delta^+; \varrho, (1-\varpi)(\eta-\alpha)}^{\omega, w, -\epsilon(1-\varpi)} \Psi(\delta^+) \\
 = & (s+1)^{\frac{\alpha-\eta}{\eta}} (\eta u)^{\frac{\alpha}{\eta}} \left(1 - \eta\omega(\eta u)^{-\frac{\varrho}{\eta}} \right)^{\frac{\epsilon}{\eta}} \mathfrak{L}_{\psi}^w \{ \Psi(\vartheta) \} (u) - \eta(s+1)^{-\frac{\varpi(\eta-\alpha)}{\eta}} \\
 & \quad \times (\eta u)^{-\frac{\varpi(\eta-\alpha)}{\eta}} \left(1 - \eta\omega(\eta u)^{-\frac{\varrho}{\eta}} \right)^{\frac{\epsilon\varpi}{\eta}} \psi, \eta^s \mathfrak{J}_{\delta^+; \varrho, (1-\varpi)(\eta-\alpha)}^{\omega, w, -\epsilon(1-\varpi)} \Psi(\delta^+),
 \end{aligned}$$

this proves the proof of the Theorem 5.

3 Free-Electron Laser Equation Involving Weighted Generalized Fractional Operators

In recent decades, several methods for tackling the generalized fractional integro-differential free-electron laser problem have been proposed. In the present section, we offer a more generalized model of the free-electron laser problem involving the newly defined operator.

Theorem 6. *The solution of free-electron laser problem*

$$\psi, \eta^s \mathfrak{D}_{\delta^+; \varrho, \omega, w}^{\epsilon, \alpha, \varpi} \Psi(\vartheta) = \rho \psi, \eta^s \mathfrak{J}_{\delta^+; \varrho, \alpha}^{\sigma, \omega, w} \Psi(\vartheta) + f(\vartheta), \quad (9)$$

$$\psi, \eta^s \mathfrak{J}_{\delta^+; \varrho, (1-\varpi)(\eta-\alpha), w}^{\omega, -\epsilon(1-\varpi)} \Psi(\delta^+) = D, \quad D \geq 0, \quad (10)$$

where $\vartheta \in (0, \infty)$, $f \in L_1[0, \infty)$, $\alpha \in (0, 1)$, $\varpi \in [0, 1]$, $\omega, \rho \in \mathbb{R}$, $\delta > 0$, $\varrho > 0$, $\epsilon, \sigma \geq 0$ is given by

$$\begin{aligned}
 \Psi(\vartheta) = & D \sum_{m=0}^{\infty} \rho^m (s+1)^{-\frac{\varpi(\eta-\alpha)+\alpha-\eta}{\eta}} (\psi^{s+1}(\vartheta) - \psi^{s+1}(\delta))^{\frac{\varpi(\eta-\alpha)+\alpha(1+2m)-1}{\eta}} \\
 & \times E_{\eta, \varrho, \varpi(\eta-\alpha)+\alpha(1+2m)}^{(\epsilon+\sigma)m-\epsilon(\varpi-1)} (\omega(\psi^{s+1}(\vartheta) - \psi^{s+1}(\delta))^{\frac{\varrho}{\eta}}) \\
 & + \sum_{m=0}^{\infty} \rho^m (s+1)^{2m} (\psi, \eta^s \mathfrak{J}_{\eta, \varrho, \alpha(1+2m)}^{\omega, w, (\epsilon+\sigma)m+\epsilon} f)(\vartheta).
 \end{aligned}$$

Proof. Applying weighted Laplace transform on both sides of (9) and using Theorems 2 and 5, we get

$$\mathfrak{L}_{\psi}^w \{ \psi, \eta^s \mathfrak{D}_{\delta^+; \varrho, \omega, w}^{\epsilon, \alpha, \varpi} \Psi(\vartheta) \} (u) = \rho \mathfrak{L}_{\psi}^w \{ \psi, \eta^s \mathfrak{J}_{\delta^+; \varrho, \alpha}^{\sigma, \omega, w} \Psi(\vartheta) \} (u) + \mathfrak{L}_{\psi}^w \{ f(\vartheta) \} (u). \quad (11)$$

The Eq. (11) can be presented as

$$\begin{aligned}
 \mathfrak{L}_{\psi}^w \{ \Psi(\vartheta) \} (u) = & \frac{D \eta (s+1)^{-\frac{\varpi(\eta-\alpha)}{\eta}} (\eta u)^{-\frac{\varpi(\eta-\alpha)}{\eta}} \left(1 - \eta\omega(\eta u)^{\frac{\varrho}{\eta}} \right)^{\frac{\epsilon\varpi}{\eta}}}{(s+1)^{\frac{\alpha-\eta}{\eta}} (\eta u)^{\frac{\alpha}{\eta}} \left(1 - \eta\omega(\eta u)^{-\frac{\varrho}{\eta}} \right)^{\frac{\epsilon}{\eta}}} \\
 & + \frac{\mathfrak{L}_{\psi}^w \{ f(\vartheta) \} (u)}{(s+1)^{\frac{\alpha-\eta}{\eta}} (\eta u)^{\frac{\alpha}{\eta}} \left(1 - \eta\omega(\eta u)^{-\frac{\varrho}{\eta}} \right)^{\frac{\epsilon}{\eta}}} \\
 & \times \left(1 - \rho(\eta u)^{-\frac{2\alpha}{\eta}} \left(1 - \eta\omega(\eta u)^{-\frac{\varrho}{\eta}} \right)^{-\frac{\epsilon+\sigma}{\eta}} \right)^{-1}.
 \end{aligned}$$

By using the binomial expansion, we get

$$\begin{aligned} & \mathfrak{L}_\psi^w \{ \Psi(\vartheta) \} (u) \\ &= \frac{D\eta(s+1)^{-\frac{\varpi(\eta-\alpha)}{\eta}} (\eta u)^{-\frac{\varpi(\eta-\alpha)}{\eta}} \left(1 - \eta\omega(\eta u)^{\frac{\varrho}{\eta}} \right)^{\frac{\epsilon+\varpi}{\eta}}}{(s+1)^{\frac{\alpha-\eta}{\eta}} (\eta u)^{\frac{\alpha}{\eta}} \left(1 - \eta\omega(\eta u)^{\frac{-\varrho}{\eta}} \right)^{\frac{\epsilon}{\eta}}} \\ & \quad + \frac{\mathfrak{L}_\psi^w \{ f(\vartheta) \} (u)}{(s+1)^{\frac{\alpha-\eta}{\eta}} (\eta u)^{\frac{\alpha}{\eta}} \left(1 - \eta\omega(\eta u)^{\frac{-\varrho}{\eta}} \right)^{\frac{\epsilon}{\eta}}} \\ & \quad \times \sum_{m=0}^\infty \rho^m (\eta u)^{-2\frac{\alpha m}{\eta}} \left(1 - \eta\omega(\eta u)^{\frac{-\varrho}{\eta}} \right)^{-\frac{(\epsilon+\sigma)}{\eta} m}, \\ & \quad = D\eta \sum_{m=0}^\infty \rho^m (s+1)^{-\frac{\varpi(\eta-\alpha)+\alpha-\eta}{\eta}} \\ & \quad \times (\eta u)^{-\frac{\varpi(\eta-\alpha)+\alpha(1+2m)}{\eta}} \left(1 - \eta\omega(\eta u)^{\frac{-\varrho}{\eta}} \right)^{-\frac{(\epsilon+\sigma)m-\epsilon(\varpi-1)}{\eta}} \\ & \quad \quad + \sum_{m=0}^\infty \rho^m (s+1)^{-\frac{\alpha-\eta}{\eta}} (\eta u)^{-\frac{\alpha(1+2m)}{\eta}} \\ & \quad \quad \times \left(1 - \eta\omega(\eta u)^{\frac{-\varrho}{\eta}} \right)^{-\frac{\epsilon+m(\epsilon+\sigma)}{\eta}} \mathfrak{L}_\psi^w \{ f(\vartheta) \} (u). \end{aligned}$$

Applying inverse Laplace transform, we obtain

$$\begin{aligned} \Psi(\vartheta) &= D \sum_{m=0}^\infty \rho^m (s+1)^{-\frac{\varpi(\eta-\alpha)+\alpha-\eta}{\eta}} (\psi^{s+1}(\vartheta) - \psi^{s+1}(\delta))^{\frac{\varpi(\eta-\alpha)+\alpha(1+2m)}{\eta}-1} \\ & \quad \times E_{\eta,\varrho,\varpi(\eta-\alpha)+\alpha(1+2m)}^{(\epsilon+\sigma)m-\epsilon(\varpi-1)} (\omega(\psi^{s+1}(\vartheta) - \psi^{s+1}(\delta))^{\frac{\varrho}{\eta}}) \\ & \quad + \sum_{m=0}^\infty \rho^m (s+1)^{2m} (\psi, \eta \mathfrak{J}_{\eta,\varrho,\alpha(1+2m)}^{\omega,w,(\epsilon+\sigma)m+\epsilon} f)(\vartheta). \end{aligned}$$

Hence the proof is completed.

Remark 1. Let $s = 0$, $\psi(\vartheta) = 1$, $w(\vartheta) = 1$, $\eta = 1$, $\epsilon = \varpi = 0$, $\sigma = \varrho = 1$, $\alpha \rightarrow 1$, $f(\vartheta) = 0$, $\omega = ir$, $\rho = -i\Pi p$ with $r, p \in \mathbb{R}$, then the Theorem 6 convert to the following free-electron laser equation

$$\frac{d}{d\vartheta} \Psi(\vartheta) = -ip\Pi \int_0^\vartheta (\vartheta - t) e^{ir(\vartheta-t)} \Psi(t) dt, \quad \Psi(0) = 1.$$

Corollary 1. Let $\psi(\vartheta) = 1$, $w(\vartheta) = 1$, $s = 0$ and $\eta = 1$, then we have the problem given in [20] is defined as follows:

$$\mathfrak{D}_{\delta^+; \varrho, \omega}^{\epsilon, \alpha, \varpi} \Psi(\vartheta) = \rho \mathfrak{J}_{\delta^+; \varrho, \alpha}^{\sigma, \omega} \Psi(\vartheta) + f(\vartheta), \tag{12}$$

$$\mathfrak{J}_{\delta^+; \varrho, (1-\varpi)(\eta-\alpha)}^{\omega, -(1-\varpi)} \Psi(\delta^+) = A, \quad A \geq 0,$$

where $\vartheta \in (0, \infty)$, $f \in L_1[0, \infty)$; $\alpha \in (0, 1)$, $\varpi \in [0, 1]$, $\omega, \rho \in \mathbb{R}$, $\varrho > 0$, $\epsilon, \sigma \geq 0$. The solution to the fractional equation is

$$\begin{aligned} \Psi(\vartheta) &= C \sum_{m=0}^\infty \rho^m (\vartheta)^{\varpi(1-\alpha)+\alpha(1+2m)-1} \\ & \quad \times E_{\varrho, \varpi(1-\alpha)+\alpha(1+2m)}^{(\epsilon+\sigma)m-\epsilon(\varpi-1)} (\omega(\vartheta)^\varrho) \\ & \quad + \sum_{m=0}^\infty \rho^m (\mathfrak{J}_{\delta^+; \varrho, \alpha(1+2m)}^{\omega, (\epsilon+\sigma)m+\epsilon} f)(\vartheta). \end{aligned}$$

4 Fractional Kinetic Equation Involving Weighted Generalized Fractional Operators

Physics, control systems, dynamic systems, and engineering have all become more interested in developing mathematical models of various physical phenomena due to their importance in the field of applied research. The fundamental equations of mathematical physics and the natural sciences known as the kinetic equations, define the continuation of a substance’s motion. In the present segment, we establish a generalization of the kinetic equation. The reader is referred to related literature [37–40].

Theorem 7. *Then solution to the Cauchy fractional problem*

$$c_{\psi,\eta} {}^s \mathfrak{D}_{\delta^+;\varrho,\omega}^{\epsilon,\alpha,\varpi} M(t) - M_0 f(t) = b_{\psi,\eta} {}^s \mathfrak{J}_{\delta^+;\varrho,q}^{\omega,w,\sigma} M(t), \quad f \in L_1[0, \infty); \quad (13)$$

subject to

$${}^s_{\psi,\eta} \mathfrak{J}_{\delta^+;\varrho,(1-\varpi)(\eta-\alpha)}^{\omega,w,-\epsilon(1-\varpi)} M(\delta) = d, \quad d \geq 0,$$

with $s \in [0, \infty)$, $\varpi \in [0, 1]$ $\omega \in \mathbb{C}$, $c, b \in \mathbb{R}(c \neq 0)$, $\alpha, \varrho, q, \eta > 0$, $\delta, \epsilon, \sigma \geq 0$ is given by

$$\begin{aligned} M(t) = & d \sum_{n=0}^{\infty} \left(\frac{b}{c}\right)^n (s+1)^{-\frac{\varpi(\eta-\alpha)+(\alpha-\eta)(n+1)+qn}{\eta}} (\psi^{s+1}(t) - \psi^{s+1}(\delta))^{\frac{\varpi(\eta-\alpha)+\alpha+(q+\alpha)n}{\eta}-1} \\ & \times E_{\eta,\varrho,\varpi(\eta-\alpha)+\alpha+(q+\alpha)n}^{(\epsilon+\sigma)n+\epsilon(1-\varpi)}(\omega(\psi^{s+1}(t) - \psi^{s+1}(\delta))^{\frac{\varrho}{\eta}}) \\ & + \frac{M_0}{c} \sum_{n=0}^{\infty} \left(\frac{b}{c}\right)^n (s+1)^{n+1} {}^s_{\psi,\eta} \mathfrak{J}_{\delta^+;\varrho,(q+\alpha)n+\alpha}^{\omega,(\epsilon+\sigma)n+\epsilon} f(t). \end{aligned}$$

Proof. Applying weighted generalized Laplace transform on both sides of (14), we have

$$c \mathfrak{L}_{\psi}^w \{ {}^s_{\psi,\eta} \mathfrak{D}_{\delta^+;\varrho,\omega}^{\epsilon,\alpha,\varpi} M(t) \}(u) - M_0 \mathfrak{L}_{\psi}^w \{ f(t) \}(u) = b \mathfrak{L}_{\psi}^w \{ {}^s_{\psi,\eta} \mathfrak{J}_{\delta^+;\varrho,q}^{\omega,\sigma} M(t) \}(u).$$

By considering the hypothesis of Theorems 2 and 5, we get

$$\begin{aligned} & c \left[(s+1)^{\frac{\alpha-\eta}{\eta}} (\eta u)^{\frac{\alpha}{\eta}} \left(1 - \eta \omega (\eta u)^{-\frac{\varrho}{\eta}} \right)^{\frac{\epsilon}{\eta}} \mathfrak{L}_{\psi}^w \{ M(t) \}(u) - \eta (s+1)^{-\frac{\varpi(\eta-\alpha)}{\eta}} (\eta u)^{\frac{-\varpi(\eta-\alpha)}{\eta}} \right. \\ & \times \left. \left(1 - \eta \omega (\eta u)^{-\frac{\varrho}{\eta}} \right)^{\frac{\epsilon\varpi}{\eta}} {}^s_{\psi,\eta} \mathfrak{J}_{\delta^+;\varrho,(1-\varpi)(\eta-\alpha)}^{\omega,-\epsilon(1-\varpi)} M(\delta^+) \right] - M_0 \mathfrak{L}_{\psi}^w \{ f(t) \}(u) = b (s+1)^{-\frac{\alpha}{\eta}} (\eta u)^{\frac{-\alpha}{\eta}} \\ & \times \left(1 - \eta \omega (\eta u)^{-\frac{\varrho}{\eta}} \right)^{\frac{-\sigma}{\eta}} \mathfrak{L}_{\psi}^w \{ M(t) \}. \end{aligned}$$

We can rewrite the above equations as

$$\begin{aligned} & \left[\frac{c-b(s+1)^{-\frac{\alpha-\eta+q}{\eta}} (\eta u)^{-\frac{\alpha+q}{\eta}} \left(1-\eta\omega(\eta u)^{-\frac{\rho}{\eta}}\right)^{-\frac{\epsilon+\sigma}{\eta}}}{(s+1)^{-\frac{\alpha-\eta}{\eta}} (\eta u)^{-\frac{\alpha}{\eta}} \left(1-\eta\omega(\eta u)^{-\frac{\rho}{\eta}}\right)^{-\frac{\epsilon}{\eta}}} \right] \mathfrak{L}_\psi^w \{M(t)\}(u) \\ &= c\eta d(s+1)^{-\frac{\varpi(\eta-\alpha)}{\eta}} (\eta u)^{-\frac{\varpi(\eta-\alpha)}{\eta}} \left(1-\eta\omega(\eta u)^{-\frac{\rho}{\eta}}\right)^{\frac{\epsilon\varpi}{\eta}} + M_0 \mathfrak{L}_\psi^w \{f(t)\}(u), \\ \mathfrak{L}_\psi^w \{M(t)\}(u) &= c\eta d \left[\frac{(s+1)^{-\frac{\varpi(\eta-\alpha)+(\alpha-\eta)}{\eta}} (\eta u)^{-\frac{\varpi(\eta-\alpha)+\alpha}{\eta}} \left(1-\eta\omega(\eta u)^{-\frac{\rho}{\eta}}\right)^{\frac{\epsilon(\varpi-1)}{\eta}}}{c-b(s+1)^{-\frac{\alpha-\eta+q}{\eta}} (\eta u)^{-\frac{\alpha+q}{\eta}} \left(1-\eta\omega(\eta u)^{-\frac{\rho}{\eta}}\right)^{-\frac{\epsilon+\sigma}{\eta}}} \right] \\ &+ \left[\frac{(s+1)^{-\frac{\alpha-\eta}{\eta}} (\eta u)^{-\frac{\alpha}{\eta}} \left(1-\eta\omega(\eta u)^{-\frac{\rho}{\eta}}\right)^{-\frac{\epsilon}{\eta}}}{c-b(s+1)^{-\frac{\alpha-\eta+q}{\eta}} (\eta u)^{-\frac{\alpha+q}{\eta}} \left(1-\eta\omega(\eta u)^{-\frac{\rho}{\eta}}\right)^{-\frac{\epsilon+\sigma}{\eta}}} \right] M_0 \mathfrak{L}_\psi^w \{f(t)\}(u). \end{aligned}$$

Taking $\left| \frac{b}{c}(s+1)^{-\frac{\alpha-\eta+q}{\eta}} (\eta u)^{-\frac{\alpha+q}{\eta}} \left(1-\eta\omega(\eta u)^{-\frac{\rho}{\eta}}\right)^{-\frac{\epsilon+\sigma}{\eta}} \right| < 1$, we get

$$\begin{aligned} \mathfrak{L}_\psi^w \{M(t)\}(u) &= \left[\eta d(s+1)^{-\frac{\varpi(\eta-\alpha)+(\alpha-\eta)}{\eta}} (\eta u)^{-\frac{\varpi(\eta-\alpha)+\alpha}{\eta}} \left(1-\eta\omega(\eta u)^{-\frac{\rho}{\eta}}\right)^{\frac{\epsilon(\varpi-1)}{\eta}} \right. \\ &\quad \left. + (s+1)^{-\frac{\alpha-\eta}{\eta}} (\eta u)^{-\frac{\alpha}{\eta}} \left(1-\eta\omega(\eta u)^{-\frac{\rho}{\eta}}\right)^{-\frac{\epsilon}{\eta}} c^{-1} M_0 \mathfrak{L}_\psi^w \{f(t)\}(u) \right] \\ &\quad \times \sum_{n=0}^\infty \left(\frac{b}{c}\right)^n (s+1)^{-\frac{(\alpha-\eta+q)n}{\eta}} (\eta u)^{-\frac{(\alpha+q)n}{\eta}} \left(1-\eta\omega(\eta u)^{-\frac{\rho}{\eta}}\right)^{-\frac{(\epsilon+\sigma)n}{\eta}} \\ &= d\eta \sum_{n=0}^\infty \left(\frac{b}{c}\right)^n (s+1)^{-\frac{\varpi(\eta-\alpha)+(\alpha-\eta)(n+1)+qn}{\eta}} (\eta u)^{-\frac{\varpi(\eta-\alpha)+\alpha+(\alpha+q)n}{\eta}} \\ &\quad \times \left(1-\eta\omega(\eta u)^{-\frac{\rho}{\eta}}\right)^{-\frac{(\epsilon+\sigma)n+\epsilon(1-\varpi)}{\eta}} + \frac{M_0}{c} \sum_{n=0}^\infty \left(\frac{b}{c}\right)^n (s+1)^{-\frac{(\alpha-\eta)(n+1)+qn}{\eta}} (\eta u)^{-\frac{\alpha+(\alpha+q)n}{\eta}} \\ &\quad \times \left(1-\eta\omega(\eta u)^{-\frac{\rho}{\eta}}\right)^{-\frac{(\epsilon+\sigma)n+\epsilon}{\eta}}. \end{aligned}$$

Applying inverse Laplace transform, we get

$$\begin{aligned} M(t) &= d \sum_{n=0}^\infty \left(\frac{b}{c}\right)^n (s+1)^{-\frac{\varpi(\eta-\alpha)+(\alpha-\eta)(n+1)+qn}{\eta}} (\psi^{s+1}(t) - \psi^{s+1}(\delta))^{\frac{\varpi(\eta-\alpha)+\alpha+(q+\alpha)n}{\eta}-1} \\ &\quad \times E_{\eta, \varrho, \varpi(\eta-\alpha)+\alpha+(q+\alpha)n}^{(\epsilon+\sigma)n+\epsilon(1-\varpi)} (\omega(\psi^{s+1}(t) - \psi^{s+1}(\delta))^{\frac{\rho}{\eta}}) \\ &\quad + \frac{M_0}{c} \sum_{n=0}^\infty \left(\frac{b}{c}\right)^n (s+1)^{n+1} \psi_{\eta, \varrho}^s \mathfrak{J}_{\delta^+; \varrho, (q+\alpha)n+\alpha}^{\omega, (\epsilon+\sigma)n+\epsilon} f(t). \end{aligned}$$

Hence the proof is done.

In next example, we establish the corresponding growth model and shows the behaviour by sketching its graph.

Example 1. The solution to the growth model

$$\psi_{\eta, \varrho}^s \mathfrak{D}_{\delta^+; \varrho, \omega, w}^{\epsilon, \alpha, \varpi} M(t) - M(t) = 0 \tag{14}$$

subject to

$$\psi, {}_s \mathfrak{J}_{\delta^+; \varrho, (1-\varpi)(\eta-\alpha)}^{\omega, w, -\epsilon(1-\varpi)} M(0) = d_0,$$

is

$$M(t) = \sum_{n=0}^{\infty} \frac{t^{2n}}{\Gamma 2(n+0.5)}, \quad 0 \leq t \leq 1. \tag{15}$$

Solution 1. By setting $c = b = 1, s = 0, \psi(t) = t, \varpi = 0, \eta = 1, \sigma = 0, \epsilon = 0, \delta = 0, \alpha = 1, q = 1, d = d_0 = 1, M_0 = 0$, we obtained Eq. (15). The graph of this equation is

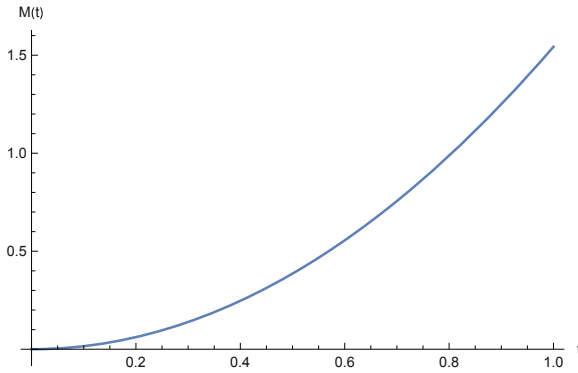


Fig. 1. For $\psi(t) = t$ the graph in Fig. 1 shows the increasing behaviour with $0^+ \leq t \leq 1$.

Remark 2. [37] If we take $s = 0, \psi(t) = 1, w(t) = 1, \eta = 1, \sigma = \epsilon = \varpi = 0, \alpha \rightarrow 0$, and $b = -c^p$, then we have

$$M(t) - M_0 f(t) = -c^p D_{\delta^+}^p M(t), \quad M(0) = d, \quad d \geq 0,$$

where $D_{\delta^+}^p$ is the Riemann-Liouville fractional derivative operator.

Corollary 2. Let $s = 0, \psi(t) = 1, w(t) = 1$ and $\varpi = 0$, then we obtain the Cauchy problem given in [40] and is defined by

$$\begin{aligned} c_\eta \mathfrak{D}_{\delta^+; \varrho, \omega}^{\epsilon, \alpha}(t) - M_0 f(t) &= b_\eta \mathfrak{J}_{\delta^+; \varrho, q}^{\omega, \sigma} M(t), \quad f \in L_1[0, \infty); \\ \eta \mathfrak{J}_{\delta^+; \varrho, \eta-\alpha}^{\omega, -\epsilon} M(0) &= d, \quad d \geq 0, \end{aligned}$$

with $\omega \in \mathbb{C}, c, b \in \mathbb{R}(c \neq 0), \alpha, \varrho, q, \eta > 0, \epsilon, \sigma \geq 0$. The resolution to the equation is given by

$$\begin{aligned} M(t) &= d \sum_{n=0}^{\infty} \left(\frac{b}{c}\right)^n t^{\frac{\alpha+(q+\alpha)n}{\eta}-1} E_{\eta, \varrho, \alpha+(q+\alpha)n}^{(\epsilon+\sigma)n+\epsilon}(\omega(t)^{\frac{\varrho}{\eta}}) \\ &\quad + \frac{M_0}{c} \sum_{n=0}^{\infty} \left(\frac{b}{c}\right)^n \eta \mathfrak{J}_{\delta^+; \varrho, (q+\alpha)n+\alpha}^{\omega, (\epsilon+\sigma)n+\epsilon} f(t). \end{aligned}$$

5 Conclusions

In this article, we introduced a new weighted generalized Hilfer-Prabhakar fractional derivative operator. This operator generalized many existing fractional derivatives. The novel operator was applied to the kinetic differintegral equation and the free-electron laser equation to create their fractional models as applications. The classical Laplace fails to find the solutions to these models, so we utilized a weighted Laplace transform. By using the specific values of the parameters the fractional growth model is presented that is strongly applicable in the field of science. The graph of the explored model is sketched that has increasing behaviour. We conclude, that the results presented in this article are more general and this idea may use to explore new weighted version of Furthermore, such fractional operators will be helpful to developed physical models. Then these new operators can be utilized to modeled physical problems like free electron laser equation and kinetic equation. The solutions to these models can be found by using Laplace transform of some other significant ways.

References

1. Mainardi, F., Gorenflo, R.: Time-fractional derivatives in relaxation processes: a tutorial survey. *Frac. Calc. Appl. Anal.* **10**(3), 269–308 (2007)
2. Wenchang, T., Wenxiao, P., Mingyu, X.: A note on unsteady flows of a viscoelastic fluid with the fractional Maxwell model between two parallel plates. *Inter. J. Nonlinear Mech.* **38**, 645–650 (2003)
3. Lozi, R., Abdelouahab, M.S., Chen, G.: Mixed-mode oscillations based on complex canard explosion in a fractional-order FitzHugh-Nagumo model. *Appl. Math. Nonlinear Sci.* **5**(2), 239–256 (2020)
4. Onal, M., Esen, A.: A Crank-Nicolson approximation for the time fractional Burgers equation. *Appl. Math. Nonlinear Sci.* **5**(2), 177–184 (2020)
5. Akin, L.: New principles of non-linear integral inequalities on time scales. *Appl. Math. Nonlinear Sci.* 535–555 (2021)
6. Ziane, D., Cherif, M.H., Cattani, C., Belghaba, K.: Yang-Laplace decomposition method for nonlinear system of local fractional partial differential equations. *Appl. Math. Nonlinear Sci.* **4**(2), 489–502 (2019)
7. Koca, I., Yaprakdal, P.: A new approach for nuclear family model with fractional order Caputo derivative. *Appl. Math. Nonlinear. Sci.* **5**(1), 393–404 (2020)
8. Dorrego, G.A.: Generalized Riemann-Liouville fractional operators associated with a generalization of the Prabhakar integral operator. *Progr. Fract. Differ. Appl.* **2**(2), 131–140 (2016)
9. Vanterler da, J., Sousa1, C., Capwlas de Oliveiral, E.: On The ψ -Hilfer fractional derivative. *Commun. Nonlinear Sci. Numer. Simul.* (2017)
10. Jarad, F., Uğurlu, E., Abdeljawad, T., Baleanu, D.: On a new class of fractional operators. *Adv. Differ. Equ.* **2017**(1), 1–16 (2017). <https://doi.org/10.1186/s13662-017-1306-z>
11. Li, M.A., Li, C.: On Hadamard fractional calculus. *Fractals* **25**(3), 1750033 (2017)
12. Attia, N., Akgül, A.: A reproducing kernel Hilbert space method for nonlinear partial differential equations: applications to physical equations. *Phys. Scripta.* **97**, 104001 (2022)

13. Hilfer, R.: *Threefold Introduction to Fractional Derivatives*. Anomalous Transport Foundations and Applications Publishing, Germany (2008)
14. Panchal, S.K., Pravinkumar, V.D., Khandagale, A.D.: k -Hilfer-Prabhakar fractional derivatives and its applications. *Indian J. Math.* **59**, 367–83 (2017)
15. Rahman, G., Nisar, K.S., Mubeen, S.: A new extension of extended Caputo fractional derivative operator. *Math. Eng. Sci. Aerospace.* **11**, 265–279 (2020)
16. Bohner, M., Rahman, G., Mubeen, S., Nisar, K.S.: A further extension of the extended Riemann-Liouville fractional derivative operator. *Turk. J. Math.* **42**, 2631–2642 (2018)
17. Nisar, K.S., Rahman, G., Tomovski, Z.: On a certain extension of the Riemann-Liouville fractional derivative operator. *Commun. Korean Math. Soc.* **34**, 507–522 (2018)
18. Rahman, G., Mubeen, S., Nisar, K.S., Choi, J.: Certain extended special functions and fractional integral and derivative operators via an extended beta functions. *Nonlinear Funct. Anal. Appl.* **24**, 1–13 (2020)
19. Rahman, G., Mubeen, S., Nisar, K.S.: On generalized k -fractional derivative operator. *AIMS Math.* **5**, 1936–1945 (2020)
20. Garra, R., Goreno, R., Polito, F., Tomovski, Ž.: Hilfer-Prabhakar derivative and some applications. *Appl. Math. Comput.* **242**, 576–89 (2014)
21. Hilfer, R.: *Applications of Fractional Calculus in Physics*. World Scientific Publishing Co. Pte. Ltd., Singapore (2000)
22. Kilbas, A., Srivastava, H.M., Trujillo, J.J.: *Theory and Application of Fractional Differential Equations*. North Holland Mathematics Studies, Amsterdam (2006)
23. Podlubny, I.: *Fractional Differential Equations*. Academic Press, San Diego (1999)
24. Diethelm, K.: *The Analysis of Fractional Differential Equations: An Application-Oriented Exposition Using Differential Operators of Caputo Type*. Springer, Cham (2010)
25. Dubey, V.P., Kumar D., Dubey S.: A modified computational scheme and convergence analysis for fractional order hepatitis E virus model. In: *Advanced Numerical Methods for Differential Equations: Applications in Science and Engineering*. CRC Press, Taylor & Francis Group, Boca Raton, pp. 279–312 (2021)
26. Dubey, V.P., Singh, J., Alshehri, A.M., Dubey, S., Kumar, D.: Forecasting the behavior of fractional order Bloch equations appearing in NMR flow via a hybrid computational technique. *Chaos Solitons Fractals* **164**, 112691 (2022)
27. Dubey, V.P., Singh, J., Alshehri, A.M., Dubey, S., Kumar, D.: An efficient analytical scheme with convergence analysis for computational study of local fractional Schrödinger equations. *Math. Comput. Simulation.* **196**, 296–318 (2022)
28. Diaz, R., Pariguan, E.: On hypergeometric functions and pochhammer k -symbol. *Divulg. Math.* **15**, 179–192 (2007)
29. Dorrego, G.A., Cerutti, R.A.: The k -Mittag-Leffler function. *Int. J. Contemp. Math. Sci.* **7**, 705–716 (2012)
30. Wu, S., Samraiz, M., Mehmood, A., Jarad, F., Naheed, S.: Some symmetric properties and applications of weighted fractional integral operator. Accepted
31. Samraiz, M., Perveen, Z., Rehman, G., Nisar, S.K., Kumar, D.: On the (k, s) -Hilfer-Prabhakar Fractional Derivative With Applications to Mathematical Physics. *Front. Phys.* **242**, 576–589 (2020)
32. Jarad, F., Abdeljawad, T.: Generalized fractional derivatives and Laplace transform. *Discrete Contin. Dyn. Syst.* **13**(3), 709–722 (2020)
33. Anastassiou, G.A.: *Fractional Differentiation Inequalities*. Springer Verlag, Berlin-New York (2009)

34. Samraiz, M., Umer, M., Abdeljawad, T., Naheed, S., Rahman, G., Shah, K.: On Riemann-type weighted fractional operators and solutions to cauchy problems. Accepted
35. Nisar, K.S., Rahman, G., Choi, J., Mubeen, S., Arshad, M.: Generalized hypergeometric k -functions via (k, s) -fractional calculus. *J. Nonlinear Sci. Appl.* **10**, 1791–1800 (2017)
36. Samraiz, M., Perveen, Z., Abdeljawad, T., Iqbal, S., Naheed, S.: On certain fractional calculus operators and thier applications. *Phys. Scripta.* **95** (2020)
37. Saxena, R.K., Kalla, S.L.: On the solutions of certain fractional kinetic equations. *Appl. Math. Comput.* **199**, 504–511 (2008)
38. Choi, J., Kumar, D.: Solutions of generalized fractional kinetic equations involving aleph functions. *Math. Commun.* **20**, 113–123 (2015)
39. Kumar, D., Choi, J.: Generalized fractional kinetic equations associated with aleph function. *Proce. Jangjeon Math. Soc.* **19**, 145–155 (2016)
40. Dorrego, G.A., Kumar, D.: A generalization of the kinetic equation using the Prabhakar-type operators. *Honam Math. J.* **39**, 401–416 (2017)



Numerical Solution of Eighth Order Boundary Value Problems by Using Vieta-Lucas Polynomials

Rakesh Kumar¹, Shivani Aeri^{1(✉)}, and Poonam Sharma²

¹ Srinivasa Ramanujan Department of Mathematics, Central University of Himachal Pradesh, Shahpur Campus, Shahpur 176206, H.P., India

shivvani.aeri@gmail.com

² Department of Mathematics, PGDC Hamirpur, Hamirpur, H.P., India

Abstract. In this paper, the eighth order boundary value problems (BVPs) are solved by utilizing the Vieta-Lucas polynomials based scheme. The operational matrix of derivative of shifted Vieta-Lucas polynomials is used. The corresponding algebraic equations are handled by taking the roots of Vieta-Lucas polynomials as collocation points. The illustrative examples provide the favorable comparison with other existing methods that demonstrates the efficiency and accuracy of the scheme.

Keywords: Vieta-Lucas polynomials · collocation method · Eighth order BVPs

1 Introduction

Higher-order BVPs have a variety of usage in engineering and sciences [1]. These kind of equations can be found in fluid dynamics, hydrodynamics, astrophysics, beam theory, astronomy, induction motors, and other fields [2]. The physics of various hydrodynamic stability issues are governed by eighth-order differential equations [3]. In this paper, we offer a strategy based on Vieta-Lucas polynomials for solving eighth order boundary value problems. Numerous scholars have worked on eighth order BVPs using diverse approaches. Using finite difference methods Boutayeb and Twizell [4] solved these kind of problems, Wazwaz [5] proposed a numerical technique that employed the Adomian decomposition method as well as a modified Adomian decomposition approach. Siddiqi and Twizell [6] introduced differential quadrature and generalised differential quadrature rules, Nonic spline and nonpolynomial nonic spline methods were utilised by Siddiqi and Akram [7], variational iteration decomposition was suggested by Noor and Mohyud-Din [8], and homotopy perturbation was employed by Golbabai and Javidi [9]. Costabile and Napoli [10] employed collocation techniques and particular classes of polynomials to solve ninth order BVPs, whereas Akram and Rehman [11] used the reproducing kernel space approach. Xu et al. [12] introduced a collocation approach based on second kind Chebyshev wavelets.

Elahi et al. [13] employed the Legendre Galerkin approach to solve eighth order boundary value problems, whereas Islam et al. [14] used the Galerkin method. Agarwal [1] investigated the existence and uniqueness of these equations.

Different kinds of differential equations are handled analytically [15–19] however it is not always possible to find the analytical solutions, thus the researchers are interested in the development of new numerical schemes that provide better approximations such as the operational matrix approach [20–24] has been widely used for the approximation purposes. Vieta-Lucas polynomials (VLPs) and their shifted forms have recently become popular for numerically solving several types of differential equations [25,26]. In this paper, we solved eighth order boundary value problems using a Vieta-Lucas polynomials based scheme.

This work is organised as follows: In Sect. 2, we discuss the necessary background and terminologies. Section 3 describes the mathematical model and the proposed method. Section 4 gives the estimates for convergence and error. Section 5 includes various illustrated examples to demonstrate the proposed approach's simplicity and applicability. In Sect. 6, the obtained results are compared to the approximate solutions of other known techniques. A reliable excellent degree of accuracy is achieved in all of the circumstances tested. The final remarks are found in Sect. 7.

2 Preliminaries

In this part, we will go through some of the fundamental definitions and properties of Vieta-Lucas polynomials, which are used in this study.

Definition 2.1. The Vieta-Lucas polynomials $VL_n(\zeta)$ of degree n ($n \in \mathbb{N} \cup \{0\}$) can be defined as [27]:

$$VL_n(\zeta) = 2 \cos(n\delta), \quad (1)$$

where $\delta = \arccos(\frac{\zeta}{2})$ and $|\zeta| \in [-2, 2]$, $\delta \in [0, \pi]$.

The recurrence relation for Vieta-Lucas polynomials $VL_n(\zeta)$ is given by [27]:

$$VL_n(\zeta) = \zeta VL_{n-1}(\zeta) - VL_{n-2}(\zeta), \quad m \geq 2, \quad (2)$$

with $VL_0(\zeta) = 2$ and $VL_1(\zeta) = \zeta$.

The first few Vieta-Lucas polynomials are given as:

$$\begin{aligned} VL_0(\zeta) &= 2, \\ VL_1(\zeta) &= \zeta, \\ VL_2(\zeta) &= \zeta^2 - 2, \\ VL_3(\zeta) &= \zeta^3 - 3\zeta, \\ VL_4(\zeta) &= \zeta^4 - 4\zeta^2 + 2, \\ VL_5(\zeta) &= \zeta^5 - 5\zeta^3 + 5\zeta, \\ VL_6(\zeta) &= \zeta^6 - 6\zeta^4 + 9\zeta^2 - 2. \end{aligned}$$

In terms of power series expansion, the Vieta-Lucas polynomials are expressed as [27]:

$$VL_n(\zeta) = \sum_{j=0}^{\lfloor n/2 \rfloor} (-1)^j \frac{n(n-j-1)!}{j!(n-2j)!} \zeta^{n-2j}, \quad n \geq 1. \tag{3}$$

The Vieta-Lucas polynomials $VL_n(\zeta)$ and $VL_m(\zeta)$ are orthogonal over $[-2, 2]$ with respect to weight function $w(\zeta) = \frac{1}{\sqrt{4-\zeta^2}}$ and satisfy the following condition [25]:

$$\langle VL_n(\zeta), VL_m(\zeta) \rangle_{w(\zeta)} = \int_{-2}^2 VL_n(\zeta) VL_m(\zeta) w(\zeta) d\zeta = \begin{cases} 4\pi, & n = m = 0, \\ 2\pi, & n = m \neq 0, \\ 0, & n \neq m. \end{cases} \tag{4}$$

Proposition 2.1. The basic properties of Vieta-Lucas polynomials are given as:

- (i) $VL_n(\zeta)(VL_m(\zeta)) = VL_{nm}(\zeta)$.
- (ii) $VL_n(\zeta) VL_m(\zeta) = VL_{n+m}(\zeta) + VL_{|n-m|}(\zeta)$.
- (iii) $\zeta VL_n(\zeta) = VL_{n+1}(\zeta) + VL_{n-1}(\zeta)$.
- (iv) $(4 - \zeta^2)VL_n(\zeta) = -VL_{n+2}(\zeta) + 2VL_n(\zeta) - VL_{n-2}(\zeta)$.

Proof. Omitted □

2.1 Shifted Vieta-Lucas Polynomials and Its Operational Matrix of Differentiation

Definition 2.2. The shifted VLPs $VL_n^*(\zeta)$ over $[0, 1]$ with degree $n \in \mathbb{N} \cup \{0\}$ can be defined as [25]:

$$VL_n^*(\zeta) = VL_n(4\zeta - 2). \tag{5}$$

The recurrence relation of shifted VLPs is [25]:

$$VL_n^*(\zeta) = (4\zeta - 2)VL_{n-1}^*(\zeta) - VL_{n-2}^*(\zeta), \tag{6}$$

provided $VL_0^*(\zeta) = 2$ and $VL_1^*(\zeta) = 4\zeta - 2$.

The power series expansion of shifted VLPs are [25]:

$$VL_n^*(\zeta) = 2n \sum_{j=0}^n (-1)^j \frac{4^{n-j}(2n-j-1)!}{j!(2n-2j)!} \zeta^{n-j}, \quad n \geq 1. \tag{7}$$

The shifted VLPs satisfy the following orthogonality property [25]:

$$\langle VL_n^*(\zeta), VL_m^*(\zeta) \rangle_{w^*(\zeta)} = \int_0^1 VL_n^*(\zeta) VL_m^*(\zeta) w^*(\zeta) d\zeta = \begin{cases} 4\pi, & n = m = 0, \\ 2\pi, & n = m \neq 0, \\ 0, & n \neq m, \end{cases} \tag{8}$$

where $w^*(\zeta) = \frac{1}{\sqrt{\zeta-\zeta^2}}$ is the weight function of shifted Vieta-Lucas polynomials. Assume $y(\zeta)$ defined on the interval $[0,1]$ be a Lebesgue square integrable function. So it can be written in terms of shifted VLPs as

$$y(\zeta) = \sum_{j=0}^{\infty} c_j \text{VL}_j^*(\zeta), \tag{9}$$

where c_j are unknown coefficients and can be obtained by following expressions

$$c_j = \frac{1}{\alpha_j \pi} \int_0^1 \frac{y(\zeta) \text{VL}_j^*(\zeta)}{\sqrt{\zeta-\zeta^2}} d\zeta, \tag{10}$$

where

$$\alpha_j = \begin{cases} 4, & j = 0, \\ 2, & j \geq 1. \end{cases}$$

Now, the truncated series can be written as

$$y_N(\zeta) = \sum_{j=0}^N c_j \text{VL}_j^*(\zeta) = C^T \Phi(\zeta),$$

where

$$C^T = [c_0, c_1, c_2, \dots, c_N], \quad \Phi(\zeta) = [\text{VL}_0^*(\zeta), \text{VL}_1^*(\zeta), \text{VL}_2^*(\zeta), \dots, \text{VL}_N^*(\zeta)].$$

The shifted VLPs operation matrix is defined as

$$\frac{dy_N}{d\zeta} = C^T D^{(1)} \Phi(\zeta), \tag{11}$$

where $D^{(1)}$ is the operation matrix of differentiation of shifted VLPs of order $(N + 1) \times (N + 1)$ are given as:

$$D^{(1)} = d_{ij} = \begin{cases} \frac{4i}{\alpha_j}, & j = i - h \begin{cases} h = 1, 3, \dots, N & \text{if } N \text{ even,} \\ h = 1, 3, \dots, N - 1 & \text{if } N \text{ odd,} \end{cases} \\ 0, & \text{otherwise.} \end{cases} \tag{12}$$

where $\alpha_0 = 2$ and $\alpha_k = 1(k \geq 1)$.

For any $n \in \mathbb{N}$, it can be generalized as:

$$\frac{d^n \Phi(\zeta)}{d\zeta^n} = (D^{(1)})^n \Phi(\zeta) = D^{(n)} \Phi(\zeta), \text{ where } n \in \mathbb{N}. \tag{13}$$

For example: for $N = 6$, we get

$$D^{(1)} = \begin{pmatrix} 0 & 0 & 0 & 0 & 0 & 0 \\ 2 & 0 & 0 & 0 & 0 & 0 \\ 0 & 8 & 0 & 0 & 0 & 0 \\ 6 & 0 & 12 & 0 & 0 & 0 \\ 0 & 16 & 0 & 16 & 0 & 0 \\ 10 & 0 & 20 & 0 & 20 & 0 \end{pmatrix}.$$

3 Mathematical Model and Numerical Scheme

This section includes the mathematical description of the model followed by the numerical scheme that describes the utility of differentiation matrix of shifted Vieta-Lucas polynomial to solve the eighth order BVPs. The eighth order differential equation is formulated as

$$\frac{d^8 y}{d\zeta^8} + \sum_{j=0}^7 a_j \frac{d^j y}{d\zeta^j} = f(\zeta), \quad \zeta \in [0, 1], \tag{14}$$

where $f(\zeta)$ and a_j are the continuous functions on the interval $[0, 1]$. Subject to supplementary conditions

$$\frac{d^i y}{d\zeta^i} \Big|_{\zeta=0} = u_i, \quad \frac{d^i y}{d\zeta^i} \Big|_{\zeta=1} = v_i, \quad i = 0, 1, 2, 3. \tag{15}$$

Let $y_N(\zeta)$ be the shifted Vieta-Lucas polynomials approximation given as

$$y_N(\zeta) = \sum_{j=0}^N c_j \text{VL}_j^*(\zeta) = C^T \Phi(\zeta), \tag{16}$$

where the unknowns are $C = [c_0, c_1, c_2, \dots, c_N]^T$.

Using shifted Vieta-Lucas polynomial operational matrix of derivative, Eq. (14) can be expressed as

$$C^T D^{(8)} \Phi(\zeta) + \sum_{j=0}^7 a_j C^T D^{(j)} \Phi(\zeta) = f(\zeta). \tag{17}$$

Thus, the residual term can be written as

$$R_N(\zeta) = C^T D^{(8)} \Phi(\zeta) + \sum_{j=0}^7 a_j C^T D^{(j)} \Phi(\zeta) - f(\zeta). \tag{18}$$

Now, by using collocation method, we get

$$R_N(\zeta_i) = 0, \quad i = 0, 1, 2, \dots, N - 8. \tag{19}$$

where collocation points are taken as

$$\zeta_i = \frac{1 + \cos\left(\frac{(2i+1)\pi}{2(N-8)}\right)}{2}, \quad i = 0, 1, \dots, N - 8. \tag{20}$$

The corresponding boundary conditions gives

$$\frac{d^i y}{d\zeta^i} \Big|_{\zeta=0} = C^T \Phi(0) = u_i, \quad \frac{d^i y}{d\zeta^i} \Big|_{\zeta=1} = C^T \Phi(1) = v_i, \quad i = 0, 1, 2, 3. \tag{21}$$

This yields N nonlinear equations. This nonlinear system can be solved to determine the values of coefficients of vector C . By substituting the value of C , we obtain the numerical solution $y_N(\zeta)$.

4 Convergence and Error Analysis

Theorem 4.1 [25]. Let $y(\zeta) \in L^2_\omega[0, 1]$ and $\frac{d^2 y}{d\zeta^2} \leq H$, where H is arbitrary constant. Then $y(\zeta)$ can be expressed as

$$y(\zeta) = \sum_{j=0}^{\infty} c_j VL_j^*(\zeta), \quad (22)$$

and $y_N(\zeta)$ is defined in (16). Furthermore, this numerical solution uniformly converges to $y(\zeta)$ ($y_N(\zeta) \rightarrow y(\zeta)$ as $N \rightarrow \infty$). Also, the coefficients c_i are bounded, i.e.,

$$|c_i| \leq \frac{H}{4i(i^2 - 1)}. \quad (23)$$

Lemma 4.2 [28]. Let $f(\zeta)$ be a function such that $f(k) = c_k$ and assume the following:

1. $f(\zeta)$ is a continuous, decreasing, positive function for $\zeta \geq N$.
2. $\sum c_N$ is convergent, and $R_N = \sum_{k=N+1}^{\infty} c_k$.

Then

$$R_N \leq \int_N^{\infty} f(\zeta) d\zeta. \quad (24)$$

Theorem 4.3 [25]. If Theorem (4.1) is satisfied by the function $y(\zeta)$, and $y_N(\zeta) = \sum_{i=0}^n c_i VL_i^*(\zeta)$, then the estimated error (in $\mathbb{L}^2[0, 1]$ norm) can be given as:

$$\|y(\zeta) - y_N(\zeta)\| < \frac{H}{12N^{\frac{3}{2}}}. \quad (25)$$

5 Numerical Examples

We provide the following test examples in this section to validate the accuracy and efficiency of the proposed method.

Example 5.1. Let us consider the eighth order differential equation as

$$\frac{d^8 y}{d\zeta^8} + \zeta y = -(48 + 15\zeta + \zeta^3)e^\zeta, \quad \zeta \in [0, 1]. \quad (26)$$

with

$$\begin{aligned} y|_{\zeta=0} &= 0, & \frac{dy}{d\zeta}|_{\zeta=0} &= 1, & \frac{d^2 y}{d\zeta^2}|_{\zeta=0} &= 0, & \frac{d^3 y}{d\zeta^3}|_{\zeta=0} &= -3, \\ y|_{\zeta=1} &= 0, & \frac{dy}{d\zeta}|_{\zeta=1} &= -e, & \frac{d^2 y}{d\zeta^2}|_{\zeta=1} &= -4e, & \frac{d^3 y}{d\zeta^3}|_{\zeta=1} &= -9e. \end{aligned}$$

Apply our proposed method as follows

$$y_N(\zeta) = \sum_{j=0}^9 c_j \text{VL}_j^*(\zeta) = C^T \Phi(\zeta). \tag{27}$$

Now using operational matrix of derivative approach

$$\frac{d^8 y_N}{d\zeta^8} = C^T D^{(8)} \Phi(\zeta), \tag{28}$$

where

$$D^{(1)} = \begin{pmatrix} 0 & 0 & 0 & 0 & 0 & 0 & 0 & 0 & 0 & 0 \\ 2 & 0 & 0 & 0 & 0 & 0 & 0 & 0 & 0 & 0 \\ 0 & 8 & 0 & 0 & 0 & 0 & 0 & 0 & 0 & 0 \\ 6 & 0 & 12 & 0 & 0 & 0 & 0 & 0 & 0 & 0 \\ 0 & 16 & 0 & 16 & 0 & 0 & 0 & 0 & 0 & 0 \\ 10 & 0 & 20 & 0 & 20 & 0 & 0 & 0 & 0 & 0 \\ 0 & 24 & 0 & 24 & 0 & 24 & 0 & 0 & 0 & 0 \\ 14 & 0 & 28 & 0 & 28 & 0 & 28 & 0 & 0 & 0 \\ 0 & 32 & 0 & 32 & 0 & 32 & 0 & 32 & 0 & 0 \end{pmatrix},$$

$$D^{(8)} = \begin{pmatrix} 0 & 0 & 0 & 0 & 0 & 0 & 0 & 0 & 0 & 0 \\ 0 & 0 & 0 & 0 & 0 & 0 & 0 & 0 & 0 & 0 \\ 0 & 0 & 0 & 0 & 0 & 0 & 0 & 0 & 0 & 0 \\ 0 & 0 & 0 & 0 & 0 & 0 & 0 & 0 & 0 & 0 \\ 0 & 0 & 0 & 0 & 0 & 0 & 0 & 0 & 0 & 0 \\ 0 & 0 & 0 & 0 & 0 & 0 & 0 & 0 & 0 & 0 \\ 0 & 0 & 0 & 0 & 0 & 0 & 0 & 0 & 0 & 0 \\ 0 & 0 & 0 & 0 & 0 & 0 & 0 & 0 & 0 & 0 \\ 1321205760 & 0 & 0 & 0 & 0 & 0 & 0 & 0 & 0 & 0 \end{pmatrix},$$

and

$$\Phi(\zeta) = \begin{pmatrix} 2 \\ 4\zeta - 2 \\ 2 - 16\zeta + 16\zeta^2 \\ -2 + 36\zeta - 96\zeta^2 + 64\zeta^3 \\ 2 - 64\zeta + 320\zeta^2 - 512\zeta^3 + 256\zeta^4 \\ -2 + 100\zeta - 800\zeta^2 + 2240\zeta^3 - 2560\zeta^4 + 1024\zeta^5 \\ 2 - 144\zeta + 1680\zeta^2 - 7168\zeta^3 + 13824\zeta^4 - 12288\zeta^5 + 4096\zeta^6 \\ -2 + 196\zeta - 3136\zeta^2 + 18816\zeta^3 - 53760\zeta^4 + 78848\zeta^5 - 57344\zeta^6 + 16384\zeta^7 \\ 2 - 256\zeta + 5376\zeta^2 - 43008\zeta^3 + 168960\zeta^4 - 360448\zeta^5 + 425984\zeta^6 - 262144\zeta^7 + 65536\zeta^8 \end{pmatrix}.$$

Substituting these values in Eq. (26), we get residual function as:

$$R_N(\zeta) = C^T D^{(8)} \Phi(\zeta) + \zeta(C^T \Phi(\zeta)) + (48 + 15\zeta + \zeta^3)e^\zeta. \tag{29}$$

Now using the collocation method, we get

$$c_0 - c_2 + c_4 - c_6 + 2642411521c_8 + \frac{445\sqrt{e}}{8} = 0. \tag{30}$$

and from the boundary conditions, we have

$$C^T \Phi(0) = 0, \quad C^T D^{(1)} \Phi(0) = 1, \quad C^T D^{(2)} \Phi(0) = 0, \quad C^T D^{(3)} \Phi(0) = -3, \quad (31)$$

$$C^T \Phi(1) = 0, \quad C^T D^{(1)} \Phi(1) = -e, \quad C^T D^{(2)} \Phi(1) = -4e, \quad C^T D^{(3)} \Phi(1) = -9e. \quad (32)$$

On solving Eqs. (30) together with (31) and (32), we get the values of unknown coefficients and which leads to the required solution as

$$y_N(\zeta) = 4.20 \times 10^{-17} + \zeta + 8.32 \times 10^{-17} \zeta^2 - 0.49 \zeta^3 + \dots - 0.002 \zeta^8. \quad (33)$$

Example 5.2. Consider the following eighth order differential equation

$$\begin{aligned} \frac{d^8 y}{d\zeta^8} + \frac{d^7 y}{d\zeta^7} + 2 \frac{d^6 y}{d\zeta^6} + 2 \frac{d^5 y}{d\zeta^5} + 2 \frac{d^4 y}{d\zeta^4} + 2\zeta \frac{d^3 y}{d\zeta^3} + 2 \frac{d^2 y}{d\zeta^2} + \zeta^2 \frac{dy}{d\zeta} + \zeta y(\zeta) \\ = -(\zeta^4 - 2\zeta^3 + 14\zeta - 27) \cos \zeta - (3\zeta^3 - 13\zeta^2 + 11\zeta + 17) \sin \zeta, \quad \zeta \in [0, 1]. \end{aligned}$$

with

$$\begin{aligned} y|_{\zeta=0} = 0, \quad \frac{dy}{d\zeta}|_{\zeta=0} = -1, \quad \frac{d^2 y}{d\zeta^2}|_{\zeta=0} = 0, \quad \frac{d^3 y}{d\zeta^3}|_{\zeta=0} = 7, \\ y|_{\zeta=1} = 0, \quad \frac{dy}{d\zeta}|_{\zeta=1} = 2 \sin 1, \quad \frac{d^2 y}{d\zeta^2}|_{\zeta=1} = 4 \cos 1 + 2 \sin 1, \quad \frac{d^3 y}{d\zeta^3}|_{\zeta=1} = 6 \cos 1 - 6 \sin 1. \end{aligned}$$

Similarly, using the approximation

$$y_N(\zeta) = \sum_{j=0}^9 c_j VL_j^*(\zeta) = C^T \Phi(\zeta). \quad (34)$$

which gives the required solution as

$$y_N(\zeta) = 3.95 \times 10^{-18} - \zeta - 5.50 \times 10^{-17} \zeta^2 + 1.16 \zeta^3 + \dots - 0.0006 \zeta^8. \quad (35)$$

Example 5.3. The eighth order differential equation is considered as

$$\begin{aligned} \frac{d^8 y}{d\zeta^8} + \frac{d^7 y}{d\zeta^7} + 2 \frac{d^6 y}{d\zeta^6} + 2 \frac{d^5 y}{d\zeta^5} + 2 \frac{d^4 y}{d\zeta^4} + 2\zeta \frac{d^3 y}{d\zeta^3} + 2 \frac{d^2 y}{d\zeta^2} + \frac{dy}{d\zeta} + y(\zeta) \\ = 14 \cos \zeta - 16 \sin \zeta - 4\zeta \sin \zeta, \quad \zeta \in [0, 1]. \end{aligned}$$

with conditions

$$\begin{aligned} y|_{\zeta=0} = 0, \quad \frac{dy}{d\zeta}|_{\zeta=0} = -1, \quad \frac{d^2 y}{d\zeta^2}|_{\zeta=0} = 0, \quad \frac{d^3 y}{d\zeta^3}|_{\zeta=0} = 7, \\ y|_{\zeta=1} = 0, \quad \frac{dy}{d\zeta}|_{\zeta=1} = 2 \sin 1, \quad \frac{d^2 y}{d\zeta^2}|_{\zeta=1} = 4 \cos 1 + 2 \sin 1, \quad \frac{d^3 y}{d\zeta^3}|_{\zeta=1} = 6 \cos 1 - 6 \sin 1. \end{aligned}$$

For

$$y_N(\zeta) = \sum_{j=0}^9 c_j VL_j^*(\zeta) = C^T \Phi(\zeta). \quad (36)$$

Hence, the required solution are obtained as

$$y_N(\zeta) = 1.73 \times 10^{-18} - \zeta - 1.94 \times 10^{-16} \zeta^2 + 1.16 \zeta^3 + \dots - 0.00082 \zeta^8. \quad (37)$$

Example 5.4. Assume the nonlinear eighth order differential equation as

$$\frac{d^8 y}{d\zeta^8} = e^{-\zeta} y^2(\zeta), \quad \zeta \in [0, 1].$$

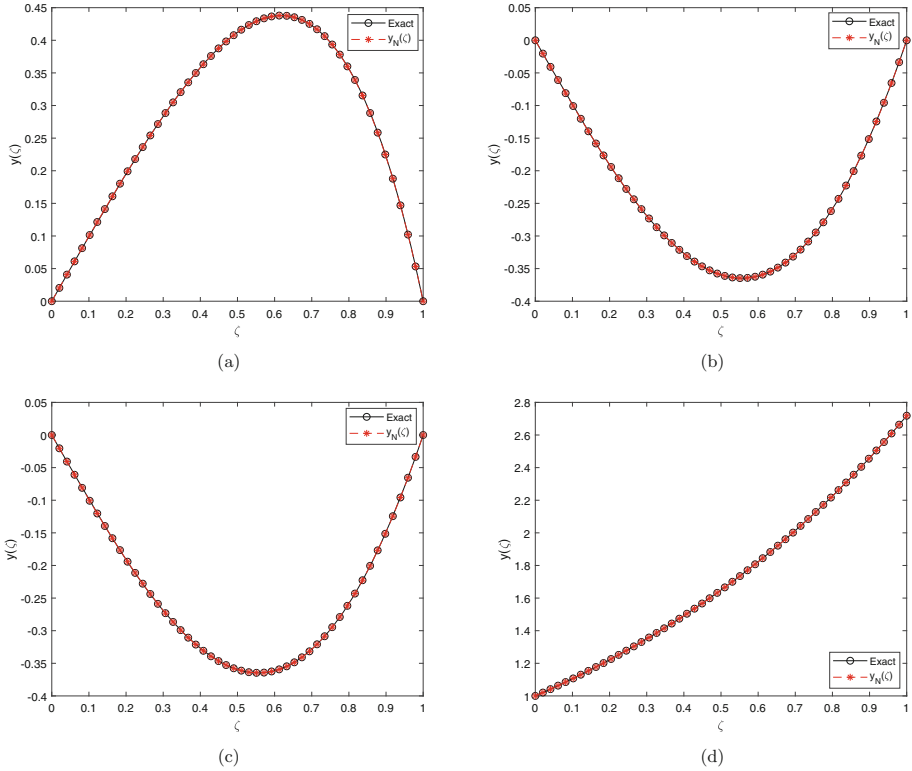


Fig. 1. Solution curves for (a) Example 5.1, (b) Example 5.2, (c) Example 5.3 and (d) Example 5.4.

with supplementary conditions

$$\begin{aligned}
 y|_{\zeta=0} &= 1, & \frac{dy}{d\zeta}|_{\zeta=0} &= 1, & \frac{d^2y}{d\zeta^2}|_{\zeta=0} &= 1, & \frac{d^3y}{d\zeta^3}|_{\zeta=0} &= 1, \\
 y|_{\zeta=1} &= e, & \frac{dy}{d\zeta}|_{\zeta=1} &= e, & \frac{d^2y}{d\zeta^2}|_{\zeta=1} &= e, & \frac{d^3y}{d\zeta^3}|_{\zeta=1} &= e.
 \end{aligned}$$

Let

$$y_N(\zeta) = \sum_{j=0}^{11} c_j \text{VL}_j^*(\zeta) = C^T \Phi(\zeta). \tag{38}$$

Which leads to the desired solution as

$$y_N(\zeta) = 5.58 \times 10^{-17} - 0.99\zeta - 1.14 \times 10^{-16}\zeta^2 - 0.49\zeta^3 + \dots - 0.000041\zeta^8. \tag{39}$$

6 Results and Discussions

Figure 1a, 1b, 1c and 1d demonstrates the solution plots of the exact solution and approximate solution ($y_N(\zeta)$) obtained from the proposed numerical scheme for Example 5.1, 5.2, 5.3 and 5.4 respectively. It is observed from the figure that the approximate solution is in good agreement with the exact solution. Which signifies that the proposed numerical scheme is capable to solve the problem effectively.

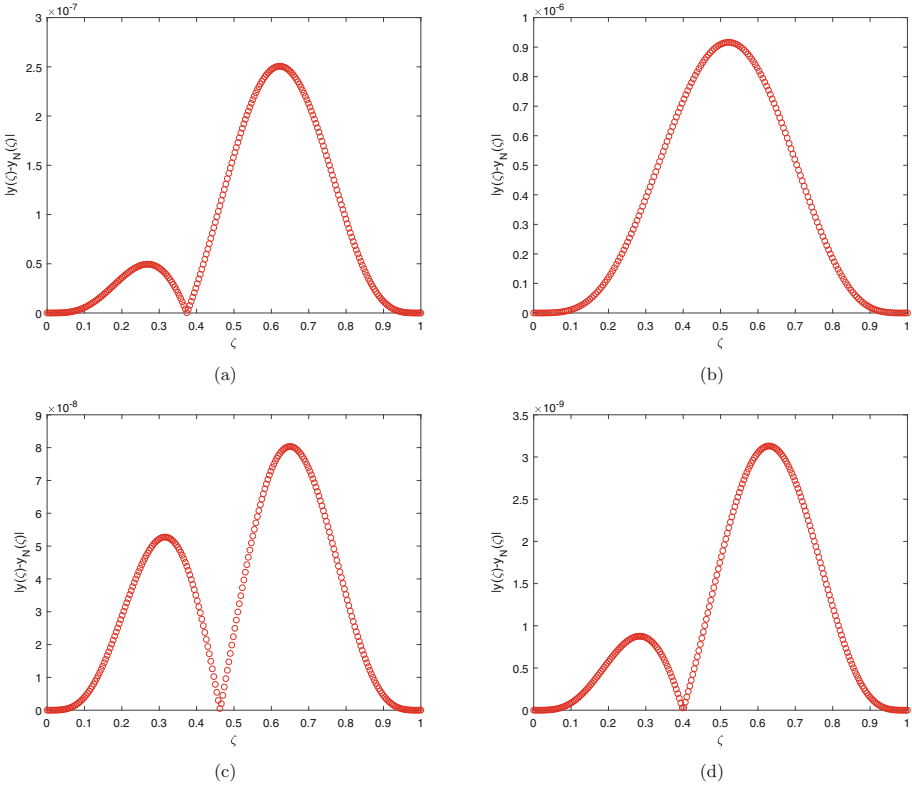


Fig. 2. Absolute error plots for (a) Example 5.1, (b) Example 5.2, (c) Example 5.3 and (d) Example 5.4.

Figure 2a, 2b, 2c and 2d depicts the absolute error plots on the interval $[0, 1]$ for Example 5.1, 5.2, 5.3 and 5.4 respectively. Which shows that the order of error is less and the error is bounded in the interval $[0, 1]$ that clearly represents the reliability of the proposed numerical scheme.

Table 1 compares the absolute errors obtained by the proposed method and from the other existing methods. From Table 1, it is observed that the proposed

Table 1. Absolute error comparisons for Example 5.1, Example 5.2, Example 5.3 and Example 5.4.

Example 5.1				
ζ	Exact Solution	Viswanadham [29]	Elahi et al. [13]	$ y(\zeta) - y_N(\zeta) $
0.1	0.09946	5.21×10^{-8}	1.44×10^{-7}	5.55×10^{-9}
0.2	0.19542	2.22×10^{-6}	1.45×10^{-6}	3.57×10^{-8}
0.3	0.28347	7.00×10^{-6}	4.38×10^{-6}	4.55×10^{-8}
0.4	0.35803	1.11×10^{-5}	7.59×10^{-6}	2.79×10^{-8}
0.5	0.41218	1.22×10^{-5}	9.06×10^{-6}	1.60×10^{-7}
0.6	0.43730	8.88×10^{-6}	7.81×10^{-6}	2.47×10^{-7}
0.7	0.42288	2.53×10^{-6}	4.64×10^{-6}	2.11×10^{-7}
0.8	0.35608	1.81×10^{-6}	1.58×10^{-6}	9.44×10^{-8}
0.9	0.22136	2.04×10^{-6}	1.61×10^{-7}	1.18×10^{-8}
Example 5.2				
0.1	-0.09883	4.23×10^{-6}	5.03×10^{-8}	1.08×10^{-8}
0.2	-0.19072	9.98×10^{-6}	5.14×10^{-7}	1.20×10^{-7}
0.3	-0.26892	5.09×10^{-6}	1.55×10^{-6}	3.88×10^{-7}
0.4	-0.32711	7.62×10^{-6}	2.71×10^{-6}	7.18×10^{-7}
0.5	-0.35956	1.49×10^{-5}	3.26×10^{-6}	9.09×10^{-7}
0.6	-0.36137	2.28×10^{-5}	2.82×10^{-6}	8.25×10^{-7}
0.7	-0.32855	2.27×10^{-5}	1.68×10^{-6}	5.14×10^{-7}
0.8	-0.25824	1.94×10^{-5}	5.77×10^{-7}	1.83×10^{-7}
0.9	-0.14883	1.32×10^{-5}	5.88×10^{-8}	1.93×10^{-8}
Example 5.3				
0.1	-0.09883	3.79×10^{-7}	5.03×10^{-8}	3.98×10^{-9}
0.2	-0.19072	2.14×10^{-6}	5.14×10^{-7}	2.86×10^{-8}
0.3	-0.26892	5.63×10^{-6}	1.55×10^{-6}	5.22×10^{-8}
0.4	-0.32711	9.74×10^{-6}	2.71×10^{-6}	3.40×10^{-8}
0.5	-0.35956	1.13×10^{-5}	3.26×10^{-6}	2.36×10^{-8}
0.6	-0.36137	1.01×10^{-5}	2.82×10^{-6}	7.32×10^{-8}
0.7	-0.32855	7.27×10^{-6}	1.68×10^{-6}	7.35×10^{-8}
0.8	-0.25824	3.87×10^{-6}	5.77×10^{-7}	3.48×10^{-8}
0.9	-0.14883	1.43×10^{-6}	5.88×10^{-8}	4.48×10^{-9}
Example 5.4				
ζ	Exact Solution	Bernstein poly. [14]	Legendre poly. [14]	$ y(\zeta) - y_N(\zeta) $
0.1	1.10517	5.43×10^{-7}	8.54×10^{-6}	8.57×10^{-11}
0.2	1.22140	7.34×10^{-7}	1.73×10^{-6}	5.75×10^{-10}
0.3	1.34986	9.54×10^{-7}	1.33×10^{-6}	8.60×10^{-10}
0.4	1.49182	1.73×10^{-7}	2.97×10^{-6}	8.45×10^{-12}
0.5	1.64872	4.99×10^{-8}	9.49×10^{-7}	1.78×10^{-9}
0.6	1.82212	2.40×10^{-7}	1.24×10^{-6}	3.05×10^{-9}
0.7	2.01375	4.30×10^{-8}	9.54×10^{-6}	2.70×10^{-9}
0.8	2.22554	7.75×10^{-7}	7.75×10^{-7}	1.22×10^{-9}
0.9	2.45960	3.20×10^{-7}	2.32×10^{-6}	1.55×10^{-10}

numerical method provides less error in comparison to the other existing methods. Thus, it clearly demonstrates the accuracy and efficiency of the proposed numerical scheme.

7 Conclusion

In this work, we presented a reliable strategy for solving eighth order boundary value problems numerically. Based on a class of shifted VLPs, this approach is developed. The operational matrix of derivative of shifted VLPs are used to formulate the numerical scheme. From the illustrative examples, it is observed that the method is efficient for solving linear/nonlinear eighth order BVPs effectively. The resulting findings are also compared to the previous results, which show good agreement. Which demonstrates the efficiency and reliability of the proposed approach.

References

1. Agarwal, R.P.: Boundary Value Problems from Higher Order Differential Equations. World Scientific (1986)
2. Wang, Y., Zhao, Y.B., Wei, G.: A note on the numerical solution of high-order differential equations. *J. Comput. Appl. Math.* **159**(2), 387–398 (2003)
3. Chandrasekhar, S.: Hydrodynamic and Hydromagnetic Stability. Courier Corporation (2013)
4. Boutayeb, A., Twizell, E.H.: Finite-difference methods for the solution of special eighth-order boundary-value problems. *Int. J. Comput. Math.* **48**(1–2), 63–75 (1993)
5. Wazwaz, A.M.: Approximate solutions to boundary value problems of higher order by the modified decomposition method. *Comput. Math. Appl.* **40**(6–7), 679–691 (2000)
6. Liu, G.R., Wu, T.Y.: Differential quadrature solutions of eighth-order boundary-value differential equations. *J. Comput. Appl. Math.* **145**(1), 223–235 (2002)
7. Akram, G., Siddiqi, S.S.: Nonic spline solutions of eighth order boundary value problems. *Appl. Math. Comput.* **182**(1), 829–845 (2006)
8. Noor, M.A., Mohyud-Din, S.T.: Variational iteration decomposition method for solving eighth-order boundary value problems. *Differential Equations and Nonlinear Mechanics* (2008)
9. Golbabai, A., Javidi, M.: Application of homotopy perturbation method for solving eighth-order boundary value problems. *Appl. Math. Comput.* **191**(2), 334–346 (2007)
10. Costabile, F.A., Napoli, A.: Collocation for high order differential equations with two-points Hermite boundary conditions. *Appl. Numer. Math.* **87**, 157–167 (2015)
11. Akram, G., Rehman, H.U.: Numerical solution of eighth order boundary value problems in reproducing Kernel space. *Numer. Algorithms* **62**(3), 527–540 (2013)
12. Xu, X., Zhou, F.: Numerical solutions for the eighth-order initial and boundary value problems using the second kind Chebyshev wavelets. *Advances in Mathematical Physics* (2015)

13. Elahi, Z., Akram, G., Siddiqi, S.S.: Numerical solution for solving special eighth-order linear boundary value problems using Legendre Galerkin method. *Math. Sci.* **10**(4), 201–209 (2016). <https://doi.org/10.1007/s40096-016-0194-9>
14. Islam, M.S., Hossain, M.B.: Numerical solutions of eighth order BVP by the Galerkin residual technique with Bernstein and Legendre polynomials. *Appl. Math. Comput.* **261**, 48–59 (2015)
15. Goswami, A., Rathore, S., Singh, J., Kumar, D.: Analytical study of fractional nonlinear Schrödinger equation with harmonic oscillator. *Discret. Continuous Dyn. Syst.-S.* **14**(10), 3589 (2021)
16. Goswami, A., Singh, J., Kumar, D., Gupta, S.: An efficient analytical technique for fractional partial differential equations occurring in ion acoustic waves in plasma. *J. Ocean Eng. Sci.* **4**(2), 85–99 (2019)
17. Goswami, A., Singh, J., Kumar, D.: An efficient analytical approach for fractional equal width equations describing hydro-magnetic waves in cold plasma. *Physica A* **524**, 563–575 (2019)
18. Goswami, A., Singh, J., Kumar, D.: Numerical simulation of fifth order KdV equations occurring in magneto-acoustic waves. *Ain Shams Eng. J.* **9**(4), 2265–2273 (2018)
19. Goswami, A., Singh, J., Kumar, D.: A reliable algorithm for KdV equations arising in warm plasma. *Nonlinear Eng.* **5**(1), 7–16 (2016)
20. Mohammadi, F., Hosseini, M.M.: A new Legendre wavelet operational matrix of derivative and its applications in solving the singular ordinary differential equations. *J. Franklin Inst.* **348**(8), 1787–1796 (2011)
21. Saadatmandi, A.: Bernstein operational matrix of fractional derivatives and its applications. *Appl. Math. Model.* **38**(4), 1365–1372 (2014)
22. Saadatmandi, A., Dehghan, M.: A new operational matrix for solving fractional-order differential equations. *Comput. Math. Appl.* **59**(3), 1326–1336 (2010)
23. Kumar, R., Koundal, R., Srivastava, K., Baleanu, D.: Normalized Lucas wavelets: an application to Lane-Emden and pantograph differential equations. *Eur. Phys. J. Plus* **135**(11), 1–24 (2020)
24. Koundal, R., Kumar, R., Kumar, R., Srivastava, K., Baleanu, D.: A novel collocated-shifted Lucas polynomial approach for fractional integro-differential equations. *Int. J. Appl. Comput. Math.* **7**(4), 1–19 (2021)
25. Agarwal, P., El-Sayed, A.A.: Vieta-Lucas polynomials for solving a fractional-order mathematical physics model. *Adv. Differ. Equ.* **2020**(1), 1–18 (2020)
26. Heydari, M.H., Avazzadeh, Z., Razzaghi, M.: Vieta-Lucas polynomials for the coupled nonlinear variable-order fractional Ginzburg-Landau equations. *Appl. Numer. Math.* **165**, 442–458 (2021)
27. Horadam, A.F.: Vieta polynomials. *Fibonacci Q.* **40**(3), 223–232 (2002)
28. Stewart, J.: *Single Variable Essential Calculus: Early Transcendentals*. Cengage Learning (2012)
29. Viswanadham, K.K., Ballem, S.: Numerical solution of tenth order boundary value problems by Galerkin method with Quintic B-splines. *Int. J. Appl. Sci. Eng.* **2**(3), 288–294 (2014)



The Mexican Hat Wavelet Transform on Generalized Quotients and Its Applications

Abhishek Singh^{1(✉)}, Shubha Singh², and Devendra Kumar³

¹ Department of Mathematics and Statistics, Banasthali Vidhyapith, Banasthali, India

abhisheksingh@banasthali.in

² Department of Physics, Banaras Hindu University, Varanasi, India

³ Department of Mathematics and Statistics, Rajasthan University, Jaipur, India

Abstract. The theory of wavelet analysis is used to characterize functions and distribution spaces intrinsically. It is a field that is constantly evolving and is a mathematical approach widely used for many applications. Recently, the theory of Mexican hat wavelet transform (MHWT) on distributions and its properties are derived by Pathak et al. [10]. Further, Singh et al. [18] constructed Representation theorems for the same transform with some applications.

In this chapter, we study the Mexican hat wavelet transform (MHWT) to the space of generalized quotients with its operational properties and applications. We extend MHWT as a continuous linear map between the spaces of generalized quotients. An inversion and a characterization theorem for the MHWT of generalized quotients are also discussed. Further, Mexican hat wavelet transformation is defined on the space of tempered generalized quotients by employing the structure of exchange property. We study the exchange property for the Mexican hat wavelet transform by applying the theory of the Mexican hat wavelet transform of distributions. Furthermore, different properties of Mexican hat wavelet transform are discussed on the space of tempered generalized quotients with applications.

Keywords: Fourier transform · Wavelet transform · Schwartz distributions · quotient spaces

Mathematics Subject Classification (2010): 44A15 · 46F12 · 54B15 · 46F99

1 Introduction

The field of wavelet has lately drawn a substantial amount of attention from mathematical scientists from domains of different subject areas. That is forming a generic bond among physicists, mathematicians, and electrical engineers.

The topic of wavelets has always been a prevalent cause of discussion in numerous engineering and scientific gatherings at present. Few considered wavelets as a unique basis for representing functions, others view it as a method for the analysis of time-frequency, and rest believe that it is an advanced topic of mathematics. Indeed, all of these theories are correct, given the fact that “wavelets” are flexible mechanisms that are extremely rich in mathematical scope and have a significant number of applications.

Wavelets are the latest area in the frontiers of mathematics, signal processing, image processing, and scientific computing. It is a versatile tool in every aspect of mathematical context and possesses great potential for applications, as wavelets can be viewed as a unique basis for representing functions for time-frequency analysis. The theory of Fourier analysis is well established and popular subject at the core of pure and applied mathematical analysis. The basic building blocks of the Fourier transform (complex exponentials: $e^{i2\pi tu}$) oscillate over all of the time ($-\infty < t < \infty$). As a result, it is difficult for the Fourier transform to represent signals that are localized in time. Thus, it fails to accumulate information that varies with time. As it does not provide the time at which frequency exists hence, it is only ideal for stationary signals. Hence, Fourier methods are not very effective in recapturing the non-smooth signal. In these cases, wavelet analysis is often very efficient, as it presents a simple approach for dealing with the local aspects of a signal. For the last two decades, the advancement of wavelet transform in the field of signal analysis is expanding making it an important mathematical tool. The main reason is wavelet transform can represent a function of the time domain in a time-frequency plane. Therefore, it works as a frequency and time localization operator. Also, wavelets can change according to time intervals to obtain high and low-frequency components. Hence, enhancing the study of signal analysis with localized impulses and oscillations. In particular, wavelet analysis is efficient in extracting noise from signals that complement the classical methods of Fourier analysis. Wavelet analysis has been one of the major research directions in both pure and applied mathematics and is still undergoing rapid growth.

The wavelets were developed mostly during the last three decades and are associated with the classical theories of different disciplines, including pure and applied mathematics and engineering. The theory of wavelets can be seen as syntheses of different ideas that started from various areas, including physics (coherent states formalism in quantum mechanics), mathematics (Calderón Zygmund operators and Littlewood - Paley theory), and engineering (in signal and image processing). The mathematical interpretation of the wavelet transform started in the year 1985 when Y. Meyer discovered the results given by Morlet and the Marseille group. He noticed a link of Morlet’s algorithm to the resolution of identity in the harmonic analysis due to A. Calderón in 1964. Therefore, Meyer built the mathematical foundation of wavelet analysis and hence may be regarded as the founder of it. He still actively promotes the field of wavelet analysis as an interdisciplinary area of research. Recently, applications of wavelet analysis have been extended across various fields of mathematics, physics, computer science,

and engineering. The term wavelet refers to a short wave. This indicates that every wavelet is localized and has to have at least some oscillations. Wavelets were introduced to represent functions more efficiently than the Fourier series. Further, wavelets comprise a family which contains functions indexed by two parameters, one for scaling and the other for positioning. They are developed from one single function called the mother wavelet. A function ψ is called wavelet if it satisfies

$$\int_{-\infty}^{\infty} \psi(t)dt = 0. \tag{1.1}$$

This condition indicates that ψ switches sign in $(-\infty, \infty)$, and it fades at $\pm\infty$. By applying position and scaling parameters on the basic function $\psi \in L^2(\mathbb{R})$, the wavelet $\psi_{b,a}(t)$ is defined by

$$\psi_{b,a}(t) = (\sqrt{a})^{-1}\psi\left(\frac{t-b}{a}\right), \quad t \in \mathbb{R}, \tag{1.2}$$

where the normalizing factor $(\sqrt{|a|})^{-1}$ ensures that $\|\psi_{b,a}(x)\|$ is independent of the position parameter b and scaling parameter a . Also, $\psi_{b,a}(t)$ is called the mother wavelet and it satisfies the admissibility condition given by [9] as follows:

$$C_\psi = \int_{-\infty}^{\infty} \frac{|\hat{\psi}(u)|^2}{|u|} du < \infty. \tag{1.3}$$

The wavelet is called admissible if $C_\psi < \infty$. Therefore,

$$\Psi(0) = \int_{-\infty}^{\infty} \psi(t)dt = 0. \tag{1.4}$$

The wavelet $\psi(t)$ acts as a impulse response of a band-pass filter that decays as fast as $|t|^{1-\epsilon}$. Practically, the wavelet $\psi(t)$ should decay much faster to provide good time-localization. The mother wavelet emerges as a local oscillation such that the energy of each oscillation in the physical space is discovered in the limited province. Then by the uncertainty principle, the positioning of the function in the physical space restricts the positioning in the frequency domain. The dilation or scaling parameter ‘a’controls the width and the frequency of $\psi_{b,a}(t)$. The position or translation parameter ‘b’relocates the wavelet across the whole domain and is beneficial for identifying the location of the wavelets.

The wavelet transform of $\phi \in L^2(\mathbb{R})$, with respect to (1.2), is defined by [9]

$$(W\phi)(b, a) = \int_{\mathbb{R}} \phi(t)\overline{\psi_{b,a}}(t)dt, \quad t, b \in \mathbb{R}, \quad a > 0. \tag{1.5}$$

and the inversion for (1.5) is given by

$$\phi(x) = \frac{2}{C_\psi} \int_0^\infty \left[\int_{-\infty}^\infty \frac{1}{\sqrt{a}} (W\phi)(b, a) \psi\left(\frac{x-b}{a}\right) db \right] \frac{da}{a^2}, \quad x \in \mathbb{R}, \tag{1.6}$$

where,

$$\frac{C_\psi}{2} = \int_0^\infty \frac{|\hat{\psi}(v)|^2}{|v|} dv = \int_0^\infty \frac{|\hat{\psi}(-v)|^2}{|v|} dv < \infty \quad [3, \text{ p. 64}]. \quad (1.7)$$

If (1.5) exists, then $(W\phi)(b, a)$ maps each square integrable function ϕ on \mathbb{R} to wavelet transform function W on $\mathbb{R} \times \mathbb{R}_+$. Therefore, from (1.5),

$$(W\phi)(b, a) = (\phi * h_{a,0})(b), \quad (1.8)$$

where $h(t) = \bar{\psi}(-t)$.

If $\phi \in L^p(\mathbb{R})$ and $\psi \in L^q(\mathbb{R})$, then

$$\phi * h_{a,0}(b) \in L^r(\mathbb{R}), \quad \frac{1}{p} + \frac{1}{q} = \frac{1}{r} + 1. \quad (1.9)$$

Now, applying Fourier transform to (1.8), we get

$$\begin{aligned} (W\phi)(b, a) &= \frac{|a|^{1/2}}{(2\pi)} \int_{\mathbb{R}} e^{i\omega b} \overline{\hat{\psi}(a\omega)} \hat{\phi}(\omega) d\omega \\ &= \frac{|a|^{1/2}}{(2\pi)} \mathcal{F}^{-1} \left[\hat{\phi}(\omega) \overline{\hat{\psi}(a\omega)} \right] (b, a). \end{aligned} \quad (1.10)$$

Hence,

$$\mathcal{F} [(W\phi)(b, a)] (\omega) = |a|^{1/2} \hat{\phi}(\omega) \overline{\hat{\psi}(a\omega)}. \quad (1.11)$$

This relation holds in general, for $\phi \in L^p(\mathbb{R})$ and $\psi \in L^q(\mathbb{R})$, where $\frac{1}{p} + \frac{1}{q} = \frac{1}{r} + 1$; $1 \leq p, q, r \leq 2$.

The Mexican hat wavelet is constructed by taking the negative normalized second derivative of a Gaussian function which, up to scale and normalization, is the second Hermite function. It is a special case of the family of continuous wavelets known as Hermitian wavelets and is defined by [10, 29]

$$\psi(t) = e^{-\left(\frac{t^2}{2}\right)} (1 - t^2) = -\frac{d^2}{dt^2} e^{-\left(\frac{t^2}{2}\right)} \quad (1.12)$$

such that

$$\psi_{b,a}(t) = -a^{\frac{3}{2}} D_t^2 e^{-\frac{(b-t)^2}{2a^2}}, \quad \left(D_t = \frac{d}{dt} \right). \quad (1.13)$$

Thus, the wavelet transform (1.5) can be written as:

$$(W\phi)(b, a) = -a^{\frac{3}{2}} \int_{\mathbb{R}} \phi(t) D_t^2 e^{-\frac{(b-t)^2}{2a^2}} dt, \quad a > 0 \quad (1.14)$$

which then, under certain conditions on ϕ is

$$(W\phi)(b, a) = -a^{\frac{3}{2}} \int_{\mathbb{R}} \phi^{(2)}(t) e^{-\frac{(b-t)^2}{2a^2}} dt, \quad a > 0. \quad (1.15)$$

From the above two equations, the MHWT can also be considered as the Weierstrass transform of $D_t^2 \phi(t) = \phi^{(2)}(t)$. Hence, we may infer various properties of MHWT from the known theory of the Weierstrass transform. The distributional Weierstrass transform has been studied in [8]. For a suitable space of generalized functions $(\mathscr{W}_{\alpha,\beta}^\gamma)'$ the generalized MHWT is given by [10]

$$(W\phi)(b, a) = -a^{\frac{3}{2}} \left\langle \phi(t), D_t^2 \exp\left(-\frac{(b-t)^2}{2a^2}\right) \right\rangle, \quad \frac{\alpha}{\gamma} < \operatorname{Re} b < \frac{\beta}{\gamma}. \quad (1.16)$$

A function $k(b, a)$ is defined by

$$k(b, a) = \frac{1}{\sqrt{2\pi a}} e^{\left(\frac{-b^2}{2a}\right)}, \quad (1.17)$$

where $a \in (0, \infty)$ and $b = \sigma + i\omega$. Then

$$D_t^2 k(b-t, a^2) = \frac{1}{\sqrt{2\pi a}} D_t^2 \left(e^{\frac{-(b-t)^2}{2a^2}} \right). \quad (1.18)$$

Therefore, by (1.13)

$$\psi_{b,a}(t) = -(2\pi)^{\frac{1}{2}} a^{\frac{5}{2}} D_t^2 k(b-t, a^2)$$

and
$$(W\phi)(b, a) = (2\pi)^{\frac{1}{2}} a^{\frac{5}{2}} \int_{\mathbb{R}} \phi(t) D_t^2 k(b-t, a^2) dt. \quad (1.19)$$

The most general theory of the MHWT is investigated on the generalized function space $(\mathscr{W}_{\alpha,\beta}^\gamma)'$ developed by Pathak *et al.* [10]. It is proved that the MHWT $(W\phi)(b, a)$ of $\phi \in (\mathscr{W}_{\alpha,\beta}^\gamma)'$, is given by $\langle \phi^{(2)}(t), k_{a^2}(b-t) \rangle$ is an analytic function in the strip $\frac{\alpha}{\gamma} < \operatorname{Re} b < \frac{\beta}{\gamma}$ for some $\alpha, \beta, \gamma \in \mathbb{R}$. Therefore, it follows that the MHWT of $\phi \in (\mathscr{W}_{\alpha,\beta}^\gamma)'$ is an entire function and hence its restriction to the real axis is in $C^\infty(\mathbb{R})$ and further this restriction uniquely determines the analytic function $(W\phi)(b, a)$. For our purposes the MHWT of ϕ denotes this restriction only.

1.1 Generalized Quotients

In recent years the theory of distributions or generalized functions is at its peak bringing a great revolution in mathematical analysis. In 1935, Sergei L. Sobolev derived the theory of generalized functions while working on the second-order hyperbolic partial differential equations. But in the 1950s, L. Schwartz introduced the concept of distributions that opened a new area of mathematical research [28]. This concept supported the development of several mathematical disciplines, such as transformation theory, operational calculus, ordinary and partial differential equations, and functional analysis. Another approach for this theory was given by S. Bochner around 1930s, to generalize the Fourier transformation for functions $f(t)$ that grow as t approaches infinity. The concept of

distribution gives a better mechanism for analysing various entities, such as the delta function, which arise naturally in several mathematical sciences and which can be corrected using distributions. The idea behind distribution is assigning a function not by its values but by its behaviour as a functional on some space of testing functions. Here the space of testing functions is represented by \mathcal{D} which contains all complex-valued functions that are infinitely smooth and have compact support. A continuous linear functional on the space \mathcal{D} is called a distribution and space of all distributions is dual of the space \mathcal{D} , denoted by \mathcal{D}' .

In the theory of distributional analysis, differentiation is a continuous operation as every distribution has derivatives of all orders. Consequently, distributional differentiation commutes with different limiting processes such as integration and infinite summation. This is the contrast to classical analysis wherein either such operations cannot be interchanged or the inversion of the order must be justified by an additional argument. Though not very recently, yet during the last five decades the theory of generalized functions and integral transforms has been combined, which gave rise to fruitful results in the theory of integral transforms associated with distributions, known as distributional transform analysis. Recently, there were many applications of wavelet and other transforms in distribution spaces [11–15, 17]. Further, the investigation of the wavelet transform of distributions, tempered distributions, and ultra-distributions has extended the applications of the wavelet transform [7, 19–21].

One of the recent generalizations of L. Schwartz's theory of distributions is the Mikusiński's algebraic approach or the sequential approach, used to define generalized quotient spaces (Boehmians). The theory of generalized quotients in 1973 by T. K. Boehme, brought a new change in the theory of applicable functional analysis [2]. The motivation for the development of the theory of generalized quotients lies in the core of regular operators, proposed by J. Mikusiński and P. Mikusiński in [4–6], which form a subalgebra of the field of Mikusiński operators.

The generalized quotients are defined by an abstract algebraic construction which is the same as the construction of the field of quotients. Instead of the normal quotients, here we use quotients of sequences where the numerator is a sequence of some set G and the denominator is a delta sequence. This space of generalized quotients includes all regular operators, all distributions, and some objects which are neither operators nor distributions. Also, it is possible to construct generalized quotients even if there are zero divisors, such as the space of all continuous functions, say C . Application of this construction to function spaces with the convolution product provides different spaces of generalized functions. Therefore, different integral transforms have been defined for various spaces of generalized quotients and their properties are investigated in [1, 16, 22–25].

In the next section, we discuss some of the basic results required for the investigation of MHWT on the generalized quotient space. Also we show the MHWT becomes a continuous linear map from one space of generalized quotient into another. The operational properties of MHWT and an inversion formula in the context of generalized quotients is also discussed in this section. In the

last section, we deals with Mexican hat wavelet transformation on the space of tempered generalized quotients by employing the structure of exchange property. Furthermore, different properties of Mexican hat wavelet transform are discussed on the space of tempered generalized quotients with applications.

2 The Mexican Hat Wavelet Transform (MHWT) on the Space \mathcal{H}

Now, we take suitable generalized quotient spaces on which the MHWT can be derived. The construction of the space $\mathcal{B}(C^\infty, \Delta)$ is given by Pathak [8] and the construction of $\mathcal{B}(\mathcal{H}, \Delta)$ is as follows:

Let the space \mathcal{H} consists of functions $\phi \in C^\infty$ such that

$$\sup_{x \in \mathbb{R}} e^{-\frac{x^2}{2}} \rho_{p,q}^{-1}(x) |\phi(x)| \leq M(p, q) \text{ for all } -\infty < p < 0 < q < \infty,$$

where
$$\rho_{p,q}(x) = \begin{cases} e^{-\frac{px}{2}}, & x < 0 \\ e^{-\frac{qx}{2}}, & x \geq 0 \end{cases}$$

and $M(p, q)$ is a constant which depends on p and q . The n^{th} semi norm for $N = 0, 1, 2, \dots$ on \mathcal{H} is defined as,

$$\|\phi\|_N = \sup_{x \in \mathbb{R}} |e^{-\frac{x^2}{2}} \rho_{-N,N}^{-1}(x)\phi(x)|, \tag{2.1}$$

where \mathcal{H} becomes a Fréchet space under the above mentioned family of semi norms. A sub semi group of \mathcal{H} , denoted by S is taken as a testing function space i.e., $S = \mathcal{D}$ and let Δ be a class of sequences (δ_n) from \mathcal{D} which satisfies the following conditions:

- (i) $\int_{\mathbb{R}} \delta_n = 1,$
- (ii) $\int_{\mathbb{R}} |\delta_n| \leq M,$
- (iii) $\text{supp } \delta_n \rightarrow 0 \text{ as } n \rightarrow \infty.$

The set of all continuous linear functionals defined on \mathcal{D} is denoted by \mathcal{D}' .

Now we consider the Mexican hat wavelet transform of the function $\phi(t)$ as the convolution of $\phi^{(2)}(t)$ with the function $k_{a^2}(b)$. Hence, the classical inverse wavelet transform will produce the second derivative of the function $\phi(t)$. If $\phi(t), \varphi(t) \in \mathcal{H}$, then the convolution product $\phi * \varphi$ is given by

$$(\phi * \varphi)(x) = \int_{\mathbb{R}} \phi(u)\varphi(x - u)du. \tag{2.2}$$

The MHWT of $\phi \in \mathcal{H}$, is given by,

$$\begin{aligned} (W\phi)(b, a) &= (2\pi)^{\frac{1}{2}} a^{\frac{5}{2}} (\phi^{(2)} * k_{a^2})(b) \\ &= (2\pi)^{\frac{1}{2}} a^{\frac{5}{2}} \int_{\mathbb{R}} \phi^{(2)}(t)k_{a^2}(b)dt, \quad b \in \mathbb{C}, a \in \mathbb{R}^+, \end{aligned} \tag{2.3}$$

where $k_{a^2}(b) = k(b - t, a^2) = \frac{1}{\sqrt{2\pi a}} e^{-\frac{(b-t)^2}{2a^2}}.$

Theorem 1. For a function $\phi \in \mathcal{H}$ and $t \in \mathbb{R}$,

$$(W\phi)(b, a) = (2\pi)^{\frac{1}{2}} a^{\frac{5}{2}} (\phi^{(2)} * k_{a^2})(b) = (2\pi)^{\frac{1}{2}} a^{\frac{5}{2}} \lim_{n \rightarrow \infty} ((\phi^{(2)} * k_{a^2}) e^{-\frac{t^2}{2n}})(b).$$

Proof. Consider,

$$\begin{aligned} (2\pi)^{\frac{1}{2}} a^{\frac{5}{2}} \lim_{n \rightarrow \infty} ((\phi^{(2)} * k_{a^2}) e^{-\frac{t^2}{2n}})(b) &= (2\pi)^{\frac{1}{2}} a^{\frac{5}{2}} \lim_{n \rightarrow \infty} \int_{\mathbb{R}} \phi^{(2)}(t) k(b-t, a^2) e^{-\frac{t^2}{2n}} dt \\ &= a^{\frac{3}{2}} \lim_{n \rightarrow \infty} \int_{\mathbb{R}} \phi^{(2)}(t) e^{-\frac{(b-t)^2}{2a^2}} e^{-\frac{t^2}{2n}} dt \\ &= a^{\frac{3}{2}} \int_{\mathbb{R}} \phi^{(2)}(t) e^{-\frac{(b-t)^2}{2a^2}} dt, \end{aligned}$$

(by Lebesgue dominated convergence theorem).

Therefore,

$$(W\phi)(b, a) = (2\pi)^{\frac{1}{2}} a^{\frac{5}{2}} \lim_{n \rightarrow \infty} ((\phi^{(2)} * k_{a^2}) e^{-\frac{t^2}{2n}})(b).$$

□

Theorem 2. For $\phi \in \mathcal{W}'(-\infty, \infty)$ and $\varphi \in \mathcal{D}$, we have

$$(W(\phi * \varphi))(b, a) = (W\phi)(b, a) * \varphi.$$

Theorem 3. Let $\phi_n^{(2)} \rightarrow \phi^{(2)}$ uniformly as $n \rightarrow \infty$ in \mathcal{H} , then $(W\phi_n)(b, 1) \rightarrow (W\phi)(b, 1)$ as $n \rightarrow \infty$, for $b = \sigma + i\omega$.

Lemma 1. Let $\phi, g \in \mathcal{H}$ such that $(W\phi)(b, a) = (Wg)(b, a)$, then $\phi^{(2)} = g^{(2)}$ in \mathcal{H} .

Proof. The proof is similar to [[27], Lemma 4.4.4], in the case of Weierstrass transform. □

Definition 1. Let $X = \left[\begin{array}{c} \phi_n \\ \varphi_n \end{array} \right] \in \mathcal{B}(\mathcal{H}, \Delta)$, then the MHWT of X as a generalized quotient is defined by,

$$Y = (WX)(b, a) = \left[\begin{array}{c} (W\phi_n)(b, a) \\ \varphi_n \end{array} \right].$$

It is well defined since, if $X = \left[\begin{array}{c} \phi_n \\ \varphi_n \end{array} \right] = Y = \left[\begin{array}{c} g_n \\ \psi_n \end{array} \right]$ in $\mathcal{B}(\mathcal{H}, \Delta)$, then

$$\begin{aligned} \phi_m * \psi_n &= g_n * \varphi_m \quad \forall m, n \in \mathbb{N} \\ (W(\phi_m * \psi_n))(b, a) &= (W(g_n * \varphi_m))(b, a) \\ (W\phi_m)(b, a) * \psi_n &= (Wg_n)(b, a) * \varphi_m \quad (\text{by Theorem 2}) \\ \left[\begin{array}{c} (W\phi_m)(b, a) \\ \varphi_n \end{array} \right] &= \left[\begin{array}{c} (Wg_n)(b, a) \\ \psi_n \end{array} \right]. \end{aligned}$$

Theorem 4. For $\phi \in \mathcal{W}'(-\infty, \infty)$, Definition 3 is consistent with the classical definition.

Proof. By considering the map $\phi \rightarrow \left[\frac{\phi * \delta_n}{\delta_n} \right]$, any $\phi \in \mathcal{W}'(-\infty, \infty)$ can be considered as an element of $\mathcal{B}(\mathcal{H}, \Delta)$ by [27, Theorem 4.3.9], i.e., if $X = \left[\frac{\phi * \delta_n}{\delta_n} \right]$, then

$$(WX)(b, a) = \left[\frac{W(\phi * \delta_n)(b, a)}{\delta_n} \right] = \left[\frac{(W\phi)(b, a) * \delta_n}{\delta_n} \right] = (W\phi)(b, a).$$

□

3 Operational Properties

This section introduces the operational properties of the MHWT on generalized quotient space. Further, through inversion it is shown that the generalized quotient in $\mathcal{B}(\mathcal{H}, \Delta)$ approximates to a function in C^∞ in a distributional sense.

Theorem 5. (i) For $X, Y \in \mathcal{B}(\mathcal{H}, \Delta)$, $X + Y \in \mathcal{B}(\mathcal{H}, \Delta)$ and $(W(X + Y))(b, a) = (WX)(b, a) + (WY)(b, a)$.

(ii) For $X \in \mathcal{B}(\mathcal{H}, \Delta)$ and $\alpha (\neq 0) \in \mathbb{C}$, $\alpha X \in \mathcal{B}(\mathcal{H}, \Delta)$ and $(W(\alpha X))(b, a) = \alpha(WX)(b, a)$.

Theorem 6. For $X \in \mathcal{B}(\mathcal{H}, \Delta)$ and $\psi \in \mathcal{D}$, $(W(X * \psi))(b, a) = (WX)(b, a) * \psi$.

Proof. Let $X = \left[\frac{\phi_n}{\varphi_n} \right] \in \mathcal{B}(\mathcal{H}, \Delta)$ and $\psi \in \mathcal{D}$, then

$$X * \psi = \left[\frac{\phi_n * \psi}{\varphi_n} \right] \in \mathcal{B}(\mathcal{H}, \Delta). \tag{3.1}$$

Thus,

$$\begin{aligned} (W(X * \psi))(b, a) &= \left[\frac{(W(\phi_n * \psi))(b, a)}{\varphi_n} \right] \\ &= \left[\frac{(W\phi_n)(b, a) * \psi}{\varphi_n} \right] \\ &= \left[\frac{(W\phi_n)(b, a)}{\varphi_n} \right] * \psi \\ &= (WX)(b, a) * \psi. \end{aligned}$$

□

Now, we show that the MHWT on $\mathcal{B}(\mathcal{H}, \Delta)$ is continuous in the sense that it carries δ -convergent sequences onto δ -convergent sequences.

Theorem 7. *Let (X_n) be a sequence of generalized quotients such that $X_n \xrightarrow{\delta} X$ in $\mathcal{B}(\mathcal{H}, \Delta)$, then $(WX_n)(b, 1) \xrightarrow{\delta} (WX)(b, 1)$ in $\mathcal{B}(C^\infty, \Delta)$.*

In the next theorem we show the inversion of the MHWT of generalized quotients belonging to the space $\mathcal{B}(\mathcal{H}, \Delta)$.

Theorem 8. *Let $Y = \left[\frac{g_n}{\varphi_n} \right] \in \mathcal{B}(C^\infty, \Delta)$ be such that $Y = (WX)(b, a)$ for some $X \in \mathcal{B}(\mathcal{H}, \Delta)$. Then $X = \left[\frac{\phi_n}{\varphi_n * \varphi_n} \right]$ where ϕ_n 's are defined as follows:*

$$\phi_{n,k}(t) = \frac{1}{\sqrt{2\pi}} \int_{-k}^k g_n(iy, a) k(y + it, a) dy$$

and $F_n^{(2)} = \lim_{k \rightarrow \infty} \phi_{n,k}$,

where the limit is taken in \mathcal{D}' , then $\phi_n = F_n * \varphi_n$.

The next theorem indicates the characterization of MHWT for generalized quotients on compact subsets of \mathbb{R} .

Theorem 9. *A generalized quotient $Y = \left[\frac{g_n}{\psi_n} \right]$ in $\mathcal{B}(C^\infty, \Delta)$ is the MHWT of a generalized quotient $X = \left[\frac{\phi_n}{\varphi_n} \right]$ in $\mathcal{B}(\mathcal{H}, \Delta)$ if and only if for each n , g_n can be extended as an entire function satisfying $|g_n(b, a)| \leq C_n e^{\frac{\omega^2}{2}} P_n(|\omega|)$, where $b = \sigma + i\omega$ as σ varies on compact subsets of \mathbb{R} and $P_n(|\omega|)$ is a polynomial in $|\omega|$ depending on both n and on the compact set in which σ varies.*

Proof. Let $Y = (WX)(b, a)$, then by applying Mexican hat wavelet transform on Theorem 1.3.15 of [27],

$$|g_n(b, a)| \leq C_n e^{\frac{\omega^2}{2}} P_n(|\omega|) \text{ for every } n \in \mathbb{N}. \tag{3.2}$$

Conversely, let g_n can be extended as an entire function which satisfies (3.2) for every $n \in \mathbb{N}$, and by the same Theorem there exists, $h_n \in \mathcal{W}'(-\infty, \infty)$ such that $(Wh_n)(b, a) = g_n$. Since $h_n \in \mathcal{W}'(-\infty, \infty)$ and $\psi_n \in \Delta$, therefore, by Lemma 4.3.8 of [27], $h_n * \psi_n \in G$.

Now, put $\phi_n = h_n * \psi_n$ and $\varphi_n = \psi_n * \psi_n$ so that $\phi_n \in \mathcal{H}$ and $(\varphi_n) \in \Delta$. Clearly, $\frac{\phi_n}{\varphi_n}$ is a quotient in $\mathcal{B}(\mathcal{H}, \Delta)$, as $\frac{g_n}{\psi_n}$ is a quotient in $\mathcal{B}(\mathcal{H}, \Delta)$.

Also, $g_n = (Wh_n)(b, a)$, i.e., $X = \left[\frac{\phi_n}{\varphi_n} \right] \in \mathcal{B}(\mathcal{H}, \Delta)$ and

$$\begin{aligned} (WX)(b, a) &= \left[\frac{(W\phi_n)(b, a)}{\varphi_n} \right] \\ &= \left[\frac{W(h_n * \psi_n)(b, a)}{\psi_n * \psi_n} \right] \\ &= \left[\frac{(Wh_n)(b, a) * \psi_n}{\psi_n * \psi_n} \right] \\ &= \left[\frac{g_n * \psi_n}{\psi_n * \psi_n} \right] \\ &= \left[\frac{g_n}{\psi_n} \right] \\ &= Y. \end{aligned}$$

□

4 The Exchange Property

In this section, the space of tempered generalized quotients is constructed by applying the exchange property. This construction for generalized quotients indicates that the role of convergence is not necessary.

Let the space of rapidly decreasing smooth functions on \mathbb{R}^n and $\mathbb{R}^n \times \mathbb{R}_+$ be denoted by $\mathcal{S}(\mathbb{R}^n)$ and $\mathcal{S}(\mathbb{R}^n \times \mathbb{R}_+)$. The dual of \mathcal{S} is the space of tempered distributions, represented by \mathcal{S}' . The spaces \mathcal{S} and \mathcal{S}' have been introduced and developed in [1]. The class \mathcal{S}' of tempered distributions is contained in $(\mathcal{W}_{\alpha, \beta}^\gamma)'$. Therefore the Mexican hat wavelet transform theory can be made applicable to \mathcal{S}' . Further, the Mexican hat wavelet transform can be expanded to the space of tempered generalized quotient, as the space is a natural expansion of tempered distributions. In this paper, we extend the Mexican hat wavelet transformation to a class of generalized quotient space that have quotients of sequences in the form of ϕ_n/φ_n , where the numerator contains terms of the sequence from some set \mathcal{S}' and the denominator is a delta sequence such that it satisfies the following condition

$$\phi_n * \varphi_m = \phi_m * \varphi_n, \quad \forall m, n \in \mathbb{N}. \tag{4.1}$$

Further, the delta sequences are defined as sequences of functions $\{\varphi_n\} \in \mathcal{S}$ such that

1. $\int_{\mathbb{R}^n} \varphi_n(x) dx = 1$ for all $n = 1, 2, 3, \dots$.
2. There exists a constant $C > 0$ such that

$$\int_{\mathbb{R}^n} |\varphi_n(x)| dx \leq C \text{ for all } n = 1, 2, 3, \dots$$

3. $\lim_{n \rightarrow \infty} \int_{\|x\| \geq \epsilon} \|x\|^k |(\varphi_j(x))| dx = 0$ for every $k \in \mathbb{N}$ and $\epsilon > 0$.

In particular, we extend the transformation to generalized quotient space by defining an exchange property for the Mexican hat wavelet transform. We discuss some of the basic results required for the investigation of MHWT on the generalized quotient space. Further, we describes some algebraic properties of MHWT in the context of tempered generalized quotients.

Theorem 10. For a function $\phi \in \mathcal{S}'$ and $t \in \mathbb{R}$,

$$(W\phi)(b, a) = (2\pi)^{\frac{1}{2}} a^{\frac{5}{2}} (\phi^{(2)} * k_{a^2})(b) = (2\pi)^{\frac{1}{2}} a^{\frac{5}{2}} \lim_{n \rightarrow \infty} ((\phi^{(2)} * k_{a^2})e^{-\frac{t^2}{2n}})(b).$$

Proof. Consider,

$$\begin{aligned} (2\pi)^{\frac{1}{2}} a^{\frac{5}{2}} \lim_{n \rightarrow \infty} ((\phi^{(2)} * k_{a^2})e^{-\frac{t^2}{2n}})(b) &= (2\pi)^{\frac{1}{2}} a^{\frac{5}{2}} \lim_{n \rightarrow \infty} \int_{\mathbb{R}} \phi^{(2)}(t)k_{a^2}(b)e^{-\frac{t^2}{2n}} dt \\ &= a^{\frac{3}{2}} \lim_{n \rightarrow \infty} \int_{\mathbb{R}} \phi^{(2)}(t)e^{-\frac{(b-t)^2}{2a^2}} e^{-\frac{t^2}{2n}} dt \\ &= a^{\frac{3}{2}} \int_{\mathbb{R}} \phi^{(2)}(t)e^{-\frac{(b-t)^2}{2a^2}} dt. \end{aligned}$$

Therefore,

$$(W\phi)(b, a) = (2\pi)^{\frac{1}{2}} a^{\frac{5}{2}} \lim_{n \rightarrow \infty} ((\phi^{(2)} * k_{a^2})e^{-\frac{t^2}{2n}})(b).$$

□

Theorem 11. For $\phi \in \mathcal{S}'$ and $\varphi \in \mathcal{S}$, we have

$$(W(\phi * \varphi))(b, a) = (Wf)(b, a) * \varphi.$$

Proof. By using [[27], Lemma 4.3.8], $(\phi * \varphi) \in \mathcal{S}'$ and hence $(W(\phi * \varphi))(b, a)$ is defined. Also, by Theorem 10

$$(W(\phi * \varphi))(b, a) = (2\pi)^{\frac{1}{2}} a^{\frac{5}{2}} \lim_{n \rightarrow \infty} (((\phi^{(2)} * \varphi) * k_{a^2})e^{-\frac{t^2}{2n}})(b).$$

Consider,

$$\begin{aligned} (2\pi)^{\frac{1}{2}} a^{\frac{5}{2}} (((\phi^{(2)} * \varphi) * k_{a^2})e^{-\frac{t^2}{2n}})(b) &= (2\pi)^{\frac{1}{2}} a^{\frac{5}{2}} \int_{\mathbb{R}} (\phi^{(2)} * \varphi)(t)k(b - t, a^2)e^{-\frac{t^2}{2n}} dt \\ &= a^{\frac{3}{2}} \int_{\mathbb{R}} (\phi^{(2)} * \varphi)(t)e^{-\frac{(b-t)^2}{2a^2}} e^{-\frac{t^2}{2n}} dt \\ &= a^{\frac{3}{2}} \int_{\mathbb{R}} \langle \phi^{(2)}(s), \varphi(t - s) \rangle e^{-\frac{(b-t)^2}{2a^2}} e^{-\frac{t^2}{2n}} dt \\ &= a^{\frac{3}{2}} \int_{\mathbb{R}} \langle \phi^{(2)}(s), \varphi(t - s) \rangle \psi_n(t) dt, \end{aligned} \tag{4.2}$$

where $\psi_n(t) = e^{-\frac{(b-t)^2}{2a^2}} e^{-\frac{t^2}{2n}}$.

By [10, Lemma 4.3], we have

$$a^{\frac{3}{2}} \int_{-m}^m \langle \phi^{(2)}(s), \varphi(t - s) \rangle \psi_n(t) dt = a^{\frac{3}{2}} \left\langle \phi^{(2)}(s), \int_{-m}^m \varphi(t - s) \psi_n(t) dt \right\rangle, \quad \forall m > 0,$$

which converges to

$$a^{\frac{3}{2}} \left\langle \phi^{(2)}(s), \int_{-m}^m \varphi(t-s) \psi_n(t) dt \right\rangle \text{ as } m \rightarrow \infty,$$

Therefore,

$$\begin{aligned} \int_{-\infty}^{\infty} \langle \phi^{(2)}(s), \varphi(t-s) \rangle e^{-\frac{(b-t)^2}{2a^2}} e^{-\frac{t^2}{2n}} dt &= \left\langle \phi^{(2)}(s), \int_{-\infty}^{\infty} \varphi(t-s) \psi_n(t) dt \right\rangle \\ &= \langle \phi^{(2)}(s), (\varphi * \psi_n)(s) \rangle. \end{aligned} \tag{4.3}$$

Let us now consider,

$$\begin{aligned} (2\pi)^{\frac{1}{2}} a^{\frac{5}{2}} ((\phi^{(2)} * k_{a^2}) * \varphi)(b) &= (2\pi)^{\frac{1}{2}} a^{\frac{5}{2}} \int_{\mathbb{R}} (\phi^{(2)} * k_{a^2})(b-t) \varphi(t) dt \\ &= (2\pi)^{\frac{1}{2}} a^{\frac{5}{2}} \int_{-M}^M \langle \phi^{(2)}(s), k_{a^2}(b-t-s) \rangle \varphi(t) dt, \end{aligned}$$

where $\text{supp } \varphi \subseteq [-P, P]$. Now by [10, Lemma 4.3],

$$\begin{aligned} (2\pi)^{\frac{1}{2}} a^{\frac{5}{2}} ((\phi^{(2)} * k_{a^2}) * \varphi)(b) &= (2\pi)^{\frac{1}{2}} a^{\frac{5}{2}} \int_{-M}^M \langle \phi^{(2)}(s), k_{a^2}(b-t-s) \rangle \varphi(t) dt \\ &= (2\pi)^{\frac{1}{2}} a^{\frac{5}{2}} \left\langle \phi^{(2)}(s), \int_{-\infty}^{\infty} k_{a^2}(b-t-s) \varphi(t) dt \right\rangle \\ &= (2\pi)^{\frac{1}{2}} a^{\frac{5}{2}} \left\langle \phi^{(2)}(s), \int_{-\infty}^{\infty} \frac{1}{\sqrt{2\pi a}} \psi(t-s) \varphi(t) dt \right\rangle \\ &= a^{\frac{3}{2}} \left\langle \phi^{(2)}(s), \int_{-\infty}^{\infty} \psi(t-s) \varphi(t) dt \right\rangle \\ &= a^{\frac{3}{2}} \langle \phi^{(2)}(s), (\varphi * \psi)(s) \rangle. \end{aligned} \tag{4.4}$$

From (4.3) and (4.4), we obtain

$$(W(\phi * \varphi))(b, a) = (W\phi)(b, a) * \varphi.$$

□

Definition 2. For a family $\{\varphi_j\}_{j \in J}$, where $\varphi_j \in \mathcal{S}$, we define

$$M\left(\{\varphi_j\}_J\right) = \{x \in \mathbb{R}^n : \varphi_j(x) = 0, \forall j \in J\}. \tag{4.5}$$

A family of pairs $\{(\phi_j, \varphi_j)\}_J$, where $\phi_j \in \mathcal{S}'$ and $\varphi_j \in \mathcal{S}$, have the exchange property if

$$\phi_j * \varphi_k = \phi_k * \varphi_j, \forall j, k \in J. \tag{4.6}$$

Let set \mathcal{A} denotes the collection of $\{(\phi_j, \varphi_j)\}_J$, where $\phi_j \in \mathcal{S}'(\mathbb{R}^n)$ and $\varphi_j \in \mathcal{S}(\mathbb{R}^n)$, $\forall j \in J$, with exchange property such that $M\left(\{\varphi_j\}_J\right) = \emptyset$.

Lemma 2. *If $M(\{\varphi_j\}_J) = \emptyset$ and $M(\{\lambda_k\}_K) = \emptyset$, then $M(\{\varphi_j * \lambda_k\}_{J \times K}) = \emptyset$.*

Theorem 12. *If $\{(\phi_j, \varphi_j)\}_J \in \mathcal{A}$, then there exists a unique $F \in \mathcal{S}'(\mathbb{R}^n \times \mathbb{R}_+)$ such that F is the Mexican hat wavelet transform of the family of functions $\{(\phi_j, \varphi_j)\}_J$, i.e., $F = (W\{(\phi_j, \varphi_j)\}_J)$.*

Proof. Let us consider family of sequences $\{(\phi_j, \varphi_j)\}_J \in \mathcal{A}$, where $\phi_j \in \mathcal{S}'(\mathbb{R}^n)$ and $\varphi \in \mathcal{S}$, $\forall j \in J$, with exchange property such that for some $\epsilon > 0$, we have $|\varphi(x)| > \epsilon$, $\forall x \in M(\{\varphi_j\}_J)^c$. Then, in some open neighborhood of x , we define

$$F = \frac{(W\phi_j)}{\varphi_j}. \tag{4.7}$$

Case 1: We show that for some open neighborhood of x we have a quotient F that is unique in that neighborhood, i.e., F does not depend on $j \in J$. Let U and V be some open neighborhood of x such that $|\varphi_j(x)| > \epsilon$, $\forall x \in U$ and $|\varphi_k(x)| > \epsilon$, $\forall x \in V$. Then since $\{(\phi_j, \varphi_j)\} \in \mathcal{A}$, hence it satisfy the exchange property and therefore,

$$\phi_j * \varphi_k = \phi_k * \varphi_j, \quad \forall j, k \in J. \tag{4.8}$$

Applying Mexican hat wavelet transform to (4.8), we get

$$\begin{aligned} (W(\phi_j * \varphi_k)) &= (W(\phi_k * \varphi_j)) \\ (W\phi_j) * \varphi_k &= (W\phi_k) * \varphi_j \quad (\text{by Theorem 11}) \\ \frac{(W\phi_j)}{\varphi_j} &= \frac{(W\phi_k)}{\varphi_k}. \end{aligned} \tag{4.9}$$

Hence, we get a unique quotient $F = \frac{(W\phi_j)}{\varphi_j}$ on $U \cap V$.

Case 2: We need to show that there exists a unique quotient $F \in \mathcal{S}'(\mathbb{R}^n \times \mathbb{R}_+)$. From (4.7) and (4.9), for any $j, k \in J$, we have

$$(W\phi_k) = F\varphi_k, \quad \forall k \in J \tag{4.10}$$

such that there exists a unique $F \in \mathcal{S}'(\mathbb{R}^n \times \mathbb{R}_+)$ which implies exchange property.

Clearly, for a total sequence, say $\{\varphi_j\}_{\mathbb{N}}$, where $\varphi_j \in \mathcal{S}(\mathbb{R}^n)$ for all $j \in \mathbb{N}$, there is an $\phi_j \in \mathcal{S}'(\mathbb{R}^n)$ such that $(W\phi_j) = \varphi_j F$. Hence, $\{(\phi_j, \varphi_j)\}_{\mathbb{N}} \in \mathcal{A}$ and $F = (W(\{(\phi_j, \varphi_j)\}_{\mathbb{N}}))$. □

Lemma 3. *For the family of pairs of sequences $\{(\phi_j, \varphi_j)\}_J$, $\{(g_k, \lambda_k)\}_K \in \mathcal{A}$ has an Equivalence Relation, i.e., $\{(\phi_j, \varphi_j)\}_J \sim \{(g_k, \phi_k)\}_K$ if*

$$\phi_j * \lambda_k = g_k * \varphi_j, \quad \forall j \in J, k \in K. \tag{4.11}$$

Theorem 13. Let $\{(\phi_j, \varphi_j)\}_J, \{(g_k, \lambda_k)\}_K \in \mathcal{A}$. Then $\{(\phi_j, \varphi_j)\}_J \sim \{(g_k, \lambda_k)\}_K$ iff $(W(\{(\phi_j, \varphi_j)\}_J)) = (W(\{(g_k, \lambda_k)\}_K))$.

Proof. Let $\{(\phi_j, \varphi_j)\}_J \sim \{(g_k, \lambda_k)\}_K$, hence, they satisfy the exchange property, defined as

$$\phi_j * \lambda_k = g_k * \varphi_k, \quad \forall j \in J, k \in K.$$

Let F and G denotes the Mexican hat wavelet transform of some family of sequences such that $F = (W(\{(\phi_j, \varphi_j)\}_J))$ and $G = (W(\{(g_k, \lambda_k)\}_K))$. Now, consider,

$$\begin{aligned} \varphi_j F * \lambda_k &= (W\phi_j) * \lambda_k \\ &= (W(\phi_j * \lambda_k)) \\ &= (W(g_k * \varphi_j)) \\ &= (Wg_k) * \varphi_j \\ &= \lambda_k G * \varphi_j. \end{aligned}$$

Now, by applying Lemma 2, we get $F = G$.

Conversely, we need to show that the family of sequences $\{(\phi_j, \varphi_j)\}_J$ and $\{(g_k, \lambda_k)\}_K$ are equivalent. Let us consider

$$\begin{aligned} F &= G \\ \implies (W\phi_j) * \lambda_k &= (Wg_k) * \varphi_j \\ \implies (W(\phi_j * \lambda_k)) &= (W(g_k * \varphi_j)) \\ \implies \phi_j * \lambda_k &= g_k * \varphi_j. \end{aligned} \tag{4.12}$$

Hence, $\{(\phi_j, \varphi_j)\}_J \sim \{(g_k, \lambda_k)\}_K$. □

From the above theorem it is shown that there is an equivalence relation on \mathcal{A} and hence splits \mathcal{A} into equivalence classes. The equivalence class contains the generalized quotient $\frac{\phi_n}{\varphi_n}$ and is denoted by $\left[\frac{\phi_n}{\varphi_n} \right]$. These equivalence classes are called generalized quotients or Boehmians and the space of all such generalized quotients is denoted by \mathcal{B} .

Definition 3. Let $X = \left[\frac{\phi_n}{\varphi_n} \right] \in \mathcal{B}$, then the MHWT of X as a generalized quotient is defined by,

$$Y = (WX)(b, a) = \left[\frac{(W\phi_n)(b, a)}{\varphi_n} \right].$$

It is well defined since, if $X = \left[\frac{\phi_n}{\varphi_n} \right] = Y = \left[\frac{g_n}{\psi_n} \right]$ in \mathcal{B} , then

$$\begin{aligned} \phi_m * \psi_n &= g_n * \varphi_m \quad \forall m, n \in \mathbb{N} \\ (W(\phi_m * \psi_n))(b, a) &= (W(g_n * \varphi_m))(b, a) \\ (W\phi_m)(b, a) * \psi_n &= (Wg_n)(b, a) * \varphi_m \quad (\text{by Theorem 11}) \\ \left[\frac{(W\phi_n)(b, a)}{\varphi_n} \right] &= \left[\frac{(Wg_n)(b, a)}{\psi_n} \right]. \end{aligned}$$

Further, by considering the map $\phi \rightarrow \left[\frac{\phi * \delta_n}{\delta_n} \right]$, any $\phi \in \mathcal{W}'(-\infty, \infty)$ can be considered as an element of \mathcal{B} by [27, Theorem 4.3.9], i.e., if $X = \left[\frac{f * \delta_n}{\delta_n} \right]$, then

$$(WX)(b, a) = \left[\frac{W(\phi * \delta_n)(b, a)}{\delta_n} \right] = \left[\frac{(W\phi)(b, a) * \delta_n}{\delta_n} \right] = (W\phi)(b, a).$$

This definition extends the theory of MHWT to more general spaces than $(\mathcal{W}'_{\alpha, \beta})'$.

From Theorem 12 and Theorem 13, it is clear that the Mexican hat wavelet transform is a bijection from the space of generalized quotients to the space of distributions.

Theorem 14. *For every $\mathcal{X} \in \mathcal{B}_{\mathcal{S}'(\mathbb{R}^n)}$ there exists a delta sequence (φ_n) such that $\mathcal{X} = [\{(\phi_n, \varphi_n)\}_{\mathbb{N}}]$ for some $\phi_n \in \mathcal{S}'(\mathbb{R}^n)$.*

Proof. Let $(\phi_n) \in \mathcal{S}'(\mathbb{R}^n)$, be a delta sequence and $X \in \mathcal{B}_{\mathcal{S}'(\mathbb{R}^n)}$. Then, $(WX) * \phi_n \in \mathcal{S}'$, since $(WX) \in \mathcal{S}'$. Consequently, $(WX) * \phi_n = (Wg_n)$ for some $g_n \in \mathcal{S}'$. Therefore, we have

$$X = \left[\frac{g_n * \phi_n}{\phi_n * \phi_n} \right]. \quad (4.13)$$

Hence, $\phi_n = (g_n * \phi_n) \in \mathcal{S}'$ and by using the property of delta sequences $\phi_n * \phi_n \in \mathcal{S}$ is a delta sequence. This completes the proof. \square

5 Conclusions

Wavelet analysis is a field that is constantly evolving and is a mathematical approach widely used for many applications. The Mexican hat wavelet transform (MHWT) is considered to have one of the most appropriate wavelet basis constructed by using Gaussian function. Therefore, it is symmetrical and satisfies the Gaussian decays in both space and frequency, which helps to extract data in the space-frequency window. The space of generalized quotients includes regular operators, distributions, ultra-distributions and also objects which are neither regular operators nor distributions. It may be concluded here that the

space of tempered generalized quotient is constructed in a simple way by using the exchange property.

In this chapter, the MHWT has been investigated explicitly on generalized quotient space and its operational properties are obtained with its inverse. The characterization of the MHWT for generalized quotients is also achieved. Further, the Mexican hat wavelet has one of the most appropriate wavelet basis functions which is localized in both space and frequency, hence it can give strong applications for the analysis of space-frequency and other digital modulation. This generalized quotient space can be used to examine Mexican hat wavelet transformation on various manifolds. Moreover, the results can be applied to solving ordinary and partial differential equations, Cauchy problem, mixed boundary value problems, approximation theory, mathematical modeling and computation. Moreover, the aforesaid analysis can be used to obtain approximation theory, mixed boundary value problems, and Paley-Wiener-Schwartz theorem for the MHWT.

Acknowledgement. The first author (AS) is supported by National Board for Higher Mathematics(DAE), Government of India, through sanction No. 02011/7/2022 NBHM(R.P.)/R&D-II/10010 and the Second author is supported by DST under WOS-A, Government of India.

References

1. Atanasiu, D., Mikusiński, P.: On the Fourier transform and the exchange property. *Int. J. Math. Math. Sci.* **2005**(16), 2579–2584 (2005)
2. Boehme, T.K.: The support of Mikusiński operators. *Trans. Am. Math. Soc.* **176**, 319–334 (1973)
3. Chui, C.K.: *An Introduction to Wavelets*. Academic Press, New York (1992)
4. Mikusiński, J.: Quotients de suites et leurs applications dans l'analyse fonctionnelle. *CR Acad. Sci. Paris* **293**, 463–464 (1981)
5. Mikusiński, P.: Tempered Boehmians and ultradistributions. *Proc. Am. Math. Soc.* **123**(3), 813–817 (1995)
6. Mikusiński, P.: Convergence of Boehmians. *Japan. J. Math.* **9**(1), 159–179 (1983)
7. Mala, A., Singh, A., Banerji, P.K.: Wavelet transform of $L_{c,d}$ -space. *Integral Transform. Spec. Funct.* **29**(6), 431–441 (2018)
8. Pathak, R.S.: *Integral Transforms of Generalized Functions and Their Applications*. Routledge, Oxfordshire (2017)
9. Pathak, R.S.: *The Wavelet Transform*, vol. 4. Springer, Atlantis Press, Paris (2009). <https://doi.org/10.2991/978-94-91216-24-4>
10. Pathak, R.S., Singh, A.: Mexican hat wavelet transform of distributions. *Integral Transforms Spec. Funct.* **27**(6), 468–483 (2016)
11. Pathak, R.S., Singh, A.: Distributional wavelet transform. *Proc. Natl. Acad. Sci., India, Sect. A* **86**(2), 273–277 (2016)
12. Pathak, R.S., Singh, A.: Wavelet transform of generalized functions in $K' \{M_p\}$ spaces. *Proc. Math. Sci.* **126**(2), 213–226 (2016)
13. Pathak, R.S., Singh, A.: Wavelet transform of Beurling-Björck type ultradistributions. *Rendiconti del Seminario Matematico della Università di Padova* **137**(1), 211–222 (2017)

14. Pathak, R.S., Singh, A.: Paley-Wiener-Schwartz type theorem for the wavelet transform. *Appl. Anal.* **98**(7), 1324–1332 (2019)
15. Rawat, A., Singh, A.: Mexican hat wavelet transform of generalized functions in \mathcal{G}' spaces. *Proc. Math. Sci.* **131**(2), 1–13 (2021)
16. Singh, A.: On the exchange property for the Hartley transform. *Italian J. Pure Appl. Math* **35**, 373–380 (2015)
17. Singh, A., Mala, A.: The continuous wavelet transform on ultradistribution spaces. *Colloq. Math.* **157**, 189–201 (2019)
18. Singh, A., Raghuthaman, N., Rawat, A., Singh, J.: Representation theorems for the Mexican hat wavelet transform. *Math. Methods Appl. Sci.* **43**(7), 3914–3924 (2020)
19. Singh, A.: Distributional Mexican hat wavelet transform. *J. Anal.* **28**(2), 533–544 (2020)
20. Singh, A., Raghuthaman, N., Rawat, A.: Paley-Wiener-Schwartz type theorem for ultradistributional wavelet transform. *Complex Anal. Oper. Theory* **15**(4), 1–11 (2021)
21. Singh, A.: Some characterizations of wavelet transform. *Natl. Acad. Sci. Lett.* **44**(2), 143–145 (2021)
22. Singh, A., Rawat, A., Dhawan, S.: On the exchange property for the wavelet transform. *J. Anal.* **30**, 1743–1751 (2022). <https://doi.org/10.1007/s41478-022-00428-8>
23. Singh, A., Rawat, A., Singh, S., Banerji, P.K.: On the wavelet transform for Boehmians. *Proc. Natl. Acad. Sci., India, Sect. A* **92**(3), 331–336 (2022). <https://doi.org/10.1007/s40010-021-00733-0>
24. Singh, A., Banerji, P.K., Kalla, S.L.: A uniqueness theorem for Mellin transform for quotient space. *Sci., Ser. A, Math. Sci. (NS)* **23**, 25–30 (2012)
25. Singh, A., Banerji, P.K.: Fractional integrals of fractional Fourier transform for integrable Boehmians. *Proc. Natl. Acad. Sci., India, Sect. A Phys. Sci.* **88**(1), 49–53 (2018). <https://doi.org/10.1007/s40010-016-0329-2>
26. Singh, A., Rawat, A.: Mexican hat wavelet transform of generalized quotient spaces (2022). Preprint
27. Kalpakam, N.V.: Topics in the theory of Boehmians and their integral transforms. Doctoral dissertation (1998)
28. Schwartz, L.: *Théorie des Distributions*. 2 Vols., Hermann, Paris (1950, 1951), Vol. I and II are republished by *Actualités Scientifiques et Industrielles*, Herman & Cie, Paris, (1957, 1959)
29. Srivastava, H.M., Singh, A., Rawat, A., Singh, S.: A family of Mexican hat wavelet transforms associated with an isometry in the heat equation. *Math. Methods Appl. Sci.* **44**(14), 11340–11349 (2021)



Second-Order Nonlinearity of a Boolean Function Class with Low Spectra

Kezia Saini^(✉) and Manish Garg

Department of Mathematics, The LNM Institute of Information Technology,
Jaipur 302031, Rajasthan, India
{18pmt001,manishgarg}@lnmiit.ac.in

Abstract. In 2015, Cao and Hu (Cao, X., Hu, L.: Two boolean functions with five-valued walsh spectra and high nonlinearity. *International Journal of Foundations of Computer Science*, pp. 537–556 (2015)) introduced a certain class of Boolean functions, possessing low Walsh spectra, high nonlinearity, and high algebraic degree. For this class of Boolean functions, computation of higher-order nonlinearities (even second-order) is a tedious task. Therefore, in this article, we study the lower bound on the second-order nonlinearity of the above-mentioned class of Boolean functions for $n = 4$. Also, we deduce that the bound, thus obtained is the maximum possible bound. We also demonstrated that our lower bound is greater than the lower bound on the second-order nonlinearity of other classes of cubic Boolean functions.

Keywords: Boolean Functions · Walsh Hadamard Transform · Trace Representation · Linearized Polynomial · Primitive Element

1 Introduction

For given $n \in \mathbb{N}$, an n -variable Boolean function is a function from the finite field \mathbb{F}_{2^n} to one of its subfield \mathbb{F}_2 , where \mathbb{F}_{2^n} denotes an n -degree field extension of a prime field of characteristic 2 i.e., \mathbb{F}_2 . The set \mathcal{B}_n collects all n -variable Boolean functions. The Hamming distance between two functions $f, g \in \mathcal{B}_n$, denoted by $d(f, g)$ is defined as $|\{x \in \mathbb{F}_{2^n} : f(x) \neq g(x)\}|$, where $|E|$ gives the cardinality of the set E . Further, the set or collection of n -variable Boolean functions of algebraic degree at most r is known as the Reed-Muller code of length 2^n and order r , denoted by $RM(r, n)$. For every integer r , $0 < r \leq n$, the r th-order nonlinearity of a given Boolean function $f \in \mathcal{B}_n$, $nl_r(f)$ is defined as the minimum Hamming distance of f from all the functions of $RM(r, n)$. For r ranging from 1 to $(n - 1)$, the sequence of values of $nl_r(f)$ is defined as the nonlinearity profile of f .

The Boolean functions having high r th-order nonlinearity is preferred over others when the security and design of symmetric cryptosystems are considered since the Boolean functions having high r th-order nonlinearity can resist several

known attacks like best affine approximation attacks and linear cryptanalytic attacks [4, 5, 18]. The nonlinearity of a Boolean function can be easily computed using the algorithm of Fast Fourier Transform (FFT). On the contrary, not much is known for $nl_r(f)$, for given $f \in \mathcal{B}_n$, even for $r = 2$ since, there is no efficient algorithm, for $n > 11$ for computing the second-order nonlinearities. Forquet and Tavernier [6] have given the most effective algorithm, which works for the case $r = 2$ and $n \leq 11$ (and up to $n \leq 13$ for some notable functions).

In the direction of computing the bounds on the second and third-order nonlinearities of different classes of cryptographic Boolean functions, several authors have played their part, some of them being [7–9, 11–15, 17]. Thus, identifying and studying the classes of Boolean functions possessing “good” nonlinearity profile is a salient problem.

In 2015, Cao and Hu [1] have introduced a new class of n -variable Boolean function with low Walsh spectra, high nonlinearity (near optimal) as well as high algebraic degree given by,

$$f_{\lambda, \mu}(x) = Tr(\lambda x^{2^m+1}) + Tr(x)Tr(\mu x^{2^m-1}) \tag{1}$$

with $n = 2m$, $\lambda \in \mathbb{F}_{2^n}$ satisfying $\lambda + \lambda^{2^m} = 1$ and $\mu \in \mathbb{F}_{2^m}^*$. Unlike other Boolean functions (i.e, functions with a single trace term or sum of multiple trace terms), computing the higher-order nonlinearity (even the second order nonlinearity) of functions possessing the product of trace terms is computationally a difficult task (even for a fixed number of variables n). In consideration of the importance of studying Boolean functions for their nonlinearity profile, we will further study functions (1) for their higher-order nonlinearity (in particular second-order nonlinearity) for the case $m = 2$ and prove that the computed value attains the maximum known Hamming distance, as mentioned in [6]. Also, we will compare the computed result with the bounds on the second-order nonlinearity of other cubic Boolean functions provided by Tang et al. [16], and Garg and Gangopadhyay [10], proving it to be better.

2 Preliminaries

In this section, we introduce some preliminary notations, definitions and results.

For $n \in \mathbb{N}$, \mathbb{F}_2^n denotes an n -dimensional vector space over the field \mathbb{F}_2 and $\mathbb{F}_{2^n}^*$, the multiplicative cyclic group consisting of invertible elements of \mathbb{F}_{2^n} . The Galois field \mathbb{F}_{2^n} can be identified with the vector space \mathbb{F}_2^n over \mathbb{F}_2 because of the natural \mathbb{F}_2 -vector space isomorphism between the two. Thus, an n -variable Boolean function can also be viewed as a mapping $\mathbb{F}_2^n \rightarrow \mathbb{F}_2$. The support of an n -variable Boolean function f can be defined as $\{(x_1, x_2, \dots, x_n) \in \mathbb{F}_2^n \mid f(x_1, x_2, \dots, x_n) = 1\}$, denoted by $supp(f)$. We define the Hamming weight of a Boolean function f as $wt(f) = |supp(f)|$. A given Boolean function $f \in \mathcal{B}_n$ can be uniquely expressed as a multivariate polynomial over \mathbb{F}_2 as follows

$$f(x_1, x_2, \dots, x_n) = \sum_{a=(a_1, a_2, \dots, a_n) \in \mathbb{F}_2^n} \nu_a \left(\prod_{i=1}^n x_i^{a_i} \right)$$

where, $\nu_a \in \mathbb{F}_2$. This form is known as the Algebraic Normal Form (ANF) of f and it is useful in studying the algebraic properties of a Boolean function for its cryptographic applications. Given ANF of a Boolean function f , its algebraic degree, $\text{deg}(f)$ is defined as $\text{deg}(f) = \max_{a \in \mathbb{F}_2^n} \{wt(a) | \nu_a \neq 0\}$, where $wt(a)$ represents weight of a binary vector $a \in \mathbb{F}_2^n$ and is defined as $wt(a) = |\{i | a_i \neq 0, 1 \leq i \leq n\}|$. Boolean functions with an algebraic degree at most 1 and, respectively 2 are said to be affine functions and, respectively quadratic functions. The set \mathcal{A}_n denotes the set of all affine functions in n -variables.

The trace function, $Tr_m^n : \mathbb{F}_{2^n} \rightarrow \mathbb{F}_{2^m}$ is given as

$$Tr_m^n(x) = x + x^{2^m} + x^{2^{2m}} + x^{2^{3m}} + \dots + x^{2^{n-m}} \text{ for all } x \in \mathbb{F}_{2^n}$$

where, m is a positive divisor of n . We will consider the case of $m = 1$. In such a case, the trace function is known as absolute trace function, which follows certain vital properties of linearity, surjectivity and $Tr_1^n(x^2) = Tr_1^n(x) \forall x \in \mathbb{F}_{2^n}$. For $x, y \in \mathbb{F}_2^n$, the inner product, denoted by $x \cdot y$ is given by $x \cdot y = \sum_{j=1}^n x_j y_j$. We can also identify \mathbb{F}_{2^n} with an inner product as $x \cdot y = Tr_1^n(xy)$. The Walsh Hadamard transform of $f \in \mathcal{B}_n$, $W_f : \mathbb{F}_{2^n} \rightarrow [-2^n, 2^n]$ is given by

$$W_f(\lambda) = \sum_{x \in \mathbb{F}_{2^n}} \chi(f(x) + Tr_1^n(\lambda x))$$

where, $\lambda \in \mathbb{F}_{2^n}$ and $\chi(f) = (-1)^f$ denotes the sign function of $f \in \mathcal{B}_n$. The multiset $\{W_f(\lambda) : \lambda \in \mathbb{F}_{2^n}\}$ is called the Walsh spectrum of f . Following we have the relation between Walsh spectrum and nonlinearity (i.e, r th-order nonlinearity for $r = 1$) of an n -variable Boolean function f

$$nl(f) = 2^{n-1} - \frac{1}{2} \max_{\lambda \in \mathbb{F}_{2^n}} |W_f(\lambda)|.$$

By Parseval's identity we have, $\sum_{\lambda \in \mathbb{F}_{2^n}} W_f(\lambda)^2 = 2^{2n}$, from which we can say that $\max\{W_f(\lambda) : \lambda \in \mathbb{F}_{2^n}\} \geq 2^{\frac{n}{2}}$ and, thus $nl(f) \leq 2^{n-1} - 2^{\frac{n}{2}-1}$. Let n be an even positive integer then the Boolean function f such that $nl(f) = 2^{n-1} - 2^{\frac{n}{2}-1}$ is said to be a bent function.

For given $f \in \mathcal{B}_n$, the derivative of f with respect to $b \in \mathbb{F}_2^n$ is the function $D_b f \in \mathcal{B}_n$ and is defined as $D_b f : x \rightarrow f(x) + f(x + b)$ for all $x \in \mathbb{F}_2^n$. Adding to the concept of derivative, suppose, V_k is a k -dimensional subspace of \mathbb{F}_2^n , generated by elements a_1, a_2, \dots, a_k then the k th-order derivative of $f \in \mathcal{B}_n$ with respect to V_k is defined as

$$D_{V_k} f(x) = D_{a_1} D_{a_2} \dots D_{a_k} f(x) \text{ for all } x \in \mathbb{F}_2^n.$$

A Boolean function $f \in \mathcal{B}_n$ is said to be affine equivalent to another function $g \in \mathcal{B}_n$ if there exist a matrix $A \in GL(n, \mathbb{F}_2)$ (where, $GL(n, \mathbb{F}_2)$ denotes the set

of all non-singular matrices of order $n \times n$ with entries 0 or 1), $b, \alpha \in \mathbb{F}_2^n$ and $\varepsilon \in \mathbb{F}_2$ such that

$$f(x) = g(Ax + b) + \alpha \cdot x + \varepsilon.$$

Suppose, q is any prime power, then a linearized polynomial over \mathbb{F}_{q^s} (an s degree field extension of \mathbb{F}_q) is

$$L(x) = \sum_{i=0}^s \beta_i x^{q^i}.$$

Given a quadratic function $f \in \mathcal{B}_n$, the associated bilinear form is defined as $\Omega(x, y) = f(0) + f(x) + f(y) + f(x + y)$. The kernel \mathcal{K} of the bilinear form $\Omega(x, y)$ associated with f forms a subspace of \mathbb{F}_2^n , given by

$$\mathcal{K} = \{x \in \mathbb{F}_2^n : \Omega(x, y) = 0 \ \forall y \in \mathbb{F}_2^n\}.$$

Following results, proved by Canteaut et al. [2] holds a significant role in determining the dimension k of the kernel and, hence the Walsh spectrum associated with a quadratic Boolean function.

Lemma 1. [2] *Let U be a vector space over a field \mathbb{F}_q of characteristic 2 and $Q : U \rightarrow \mathbb{F}_q$ be a quadratic form on U . Then the dimension of U and the dimension of the kernel of the bilinear form $\Omega(x, y)$ on U have the same parity.*

Lemma 2. [2] *Let $f : \mathbb{F}_2^n \rightarrow \mathbb{F}_2$ be a quadratic Boolean function, $\alpha \in \mathbb{F}_2^n$ and $\Omega(x, y)$ be the associated bilinear form with f . Then the Walsh spectrum of f depends only on the dimension d of the kernel of $\Omega(x, y)$ and the weight distribution of the Walsh spectrum of f is given by*

$W_f(\alpha)$	Number of α
0	$2^n - 2^{n-d}$
$2^{\frac{n+d}{2}}$	$2^{\frac{n-d-1}{2}} + (-1)^{f(0)} 2^{\frac{n-d-2}{2}}$
$-2^{\frac{n+d}{2}}$	$2^{\frac{n-d-1}{2}} - (-1)^{f(0)} 2^{\frac{n-d-2}{2}}$

For the first time, Carlet [3] has proposed lower bounds on the nonlinearity profile of a given Boolean function, recursively in terms of the nonlinearity profile of derivatives of that function.

Lemma 3. [3] *Let f be an n -variable Boolean function and r be a positive integer smaller than n . Then for every positive integer $k < r$ we have*

$$nl_r(f) \geq \frac{1}{2^k} \max_{a_1, a_2, \dots, a_k \in \mathbb{F}_2^n} nl_{r-k}(D_{a_1} D_{a_2} \dots D_{a_k} f).$$

Let, q be a prime power. Then, a generator of the multiplicative cyclic group \mathbb{F}_q^* is called a primitive element of \mathbb{F}_q . Moreover, for given $m \in \mathbb{N}$, a minimal polynomial $g \in \mathbb{F}_q[x]$ of degree $m \geq 1$, of a primitive element of \mathbb{F}_{q^m} over \mathbb{F}_q is known as a primitive polynomial over \mathbb{F}_q .

3 Main Result

Following we have our main result, which is based on obtaining the bounds for the second-order nonlinearity of functions, introduced by Cao and Hu [1], as mentioned in Eq. (1) for the case $m = 2$.

Theorem 1. *Define a class of Boolean functions on \mathbb{F}_{2^n} ($n = 4$) of the form*

$$f_{\lambda,\mu}(x) = Tr(\lambda x^{2^m+1}) + Tr(x)Tr(\mu x^{2^m-1})$$

with $m = n/2 = 2$, $\lambda \in \mathbb{F}_{2^n}$ and $\mu \in \mathbb{F}_{2^m} \setminus \mathbb{F}_2$. Then, $nl_2(f_{\lambda,\mu}) \geq 2$.

Proof. Suppose, a_0 is a zero of monic irreducible polynomial $x^4 + x + 1 \in \mathbb{F}_2[x]$, then we can say a_0 is a primitive element of \mathbb{F}_{2^4} such that $Tr(a_0) = 0$. Also, $\mu \in \mathbb{F}_{2^2} \setminus \mathbb{F}_2$ and \mathbb{F}_{2^2} is isomorphic to a subfield of \mathbb{F}_{2^4} . Therefore, μ can be considered as an element of \mathbb{F}_{2^4} . Moreover, since $\mu^3 = 1$ and $\mu \neq 1$, which implies that $\mu = a_0^5$ or $\mu = a_0^{10}$. Without loss of generality, we can assume that $\mu = a_0^5$.

Note that, algebraic degree of $f_{\lambda,\mu}$ is 3. Thus, by Lemma 3 we have

$$nl_2(f_{\lambda,\mu}) \geq \frac{1}{2} \max_{a \in \mathbb{F}_{2^4}} nl(D_a f_{\lambda,\mu}). \quad (2)$$

For $x, a \in \mathbb{F}_{2^4}$

$$\begin{aligned} D_a f_{\lambda,\mu}(x) &= f_{\lambda,\mu}(x) + f_{\lambda,\mu}(x+a) \\ &= Tr(\lambda x^{2^2+1}) + Tr(x)Tr(\mu x^{2^2-1}) + Tr(\lambda(x+a)^{2^2+1}) + Tr(x)Tr(\mu(x+a)^{2^2-1}) \\ &= Tr(\lambda(x^{2^2}a + xa^{2^2} + a^{2^2+1})) + Tr(x)Tr(\mu(xa^2 + x^2a + a^{1+2})) \\ &\quad + Tr(a)Tr(\mu(x^{1+2} + xa^2 + x^2a + a^{1+2})) \end{aligned} \quad (3)$$

which implies,

$$g_\mu(x) = Tr(x)Tr(\mu(xa^2 + x^2a)) + Tr(a)Tr(\mu x^{1+2})$$

where, the function g_μ is affine equivalent to $D_a f_{\lambda,\mu}$, obtained by eliminating affine part from Eq. (3), concluding that g_μ is a quadratic Boolean function. Hence from now, we need to work on the Walsh spectrum of g_μ so, according to Lemma 3, we first need to compute the associated Bilinear form $\Omega(x, y)$, given as

$$\begin{aligned} \Omega(x, y) &= g_\mu(0) + g_\mu(x) + g_\mu(y) + g_\mu(x+y) \\ &= Tr(x)Tr(\mu(xa^2 + x^2a)) + Tr(a)Tr(\mu x^{1+2}) + Tr(y)Tr(\mu(ya^2 + y^2a)) + Tr(a)Tr(\mu y^{1+2}) \\ &\quad + Tr(x+y)Tr(\mu(xa^2 + ya^2 + x^2a + y^2a)) + Tr(a)Tr(\mu(x^{1+2} + xy^2 + x^2y + y^{1+2})) \\ &= Tr(x)Tr(\mu(ya^2 + y^2a)) + Tr(y)Tr(\mu(xa^2 + x^2a)) + Tr(a)Tr(\mu(xy^2 + x^2y)) \\ &= Tr(x)Tr(y(\mu a^2 + \mu^2 a^{2^3})) + Tr(y)Tr(\mu(xa^2 + x^2a)) + Tr(a)Tr(y(\mu^2 x^{2^3} + \mu x^2)) \\ &= Tr(x)Tr(by) + Tr(y)Tr(bx) + Tr(a)Tr(y(\mu x^2 + \mu^2 x^8)) \end{aligned}$$

where, $b = \mu a^2 + \mu^2 a^3$. The associated kernel \mathcal{K} is given by

$$\mathcal{K} = \{x \in \mathbb{F}_{2^4} | \Omega(x, y) = 0 \forall y \in \mathbb{F}_{2^4}\}.$$

To get the result, we need to find the lowest possible cardinality (or dimension) of \mathcal{K} . We shall discuss it in further two cases.

Case 1: When $Tr(a) = 0$

In this case, we have

$$\Omega(x, y) = Tr(x)Tr(by) + Tr(y)Tr(bx)$$

Subcase 1: When $b = 0$ (possible case for $a = 0$)

Thus, $\Omega(x, y) = 0$ for all $x, y \in \mathbb{F}_{2^4}$, which implies $\mathcal{K} = \mathbb{F}_{2^4}$, which is a trivial case.

Subcase 2: When $b = 1$

Then, $\Omega(x, y) = 0$ for all $x, y \in \mathbb{F}_{2^4}$, which gives $\mathcal{K} = \mathbb{F}_{2^4}$. Again, a trivial case.

Subcase 3: When $b \neq 0, 1$ (possible for many values of $a \in \mathbb{F}_{2^4}$, in particular holds for $a = a_0$)

Here, $\Omega(x, y) = 0$ for all $y \in \mathbb{F}_{2^4}$, holds with the following three possibilities.

(a₁) $Tr(x)Tr(by) = 0$ and $Tr(y)Tr(bx) = 0$ for all $y \in \mathbb{F}_{2^4}$.

(a₂) $Tr(x)Tr(by) = 1$ and $Tr(y)Tr(bx) = 1$ for all $y \in \mathbb{F}_{2^4}$.

(a₃) There exist $\emptyset \neq B_1, B_2 \subseteq \mathbb{F}_{2^4}$ such that $B_1 \cap B_2 = \emptyset, B_1 \cup B_2 = \mathbb{F}_{2^4}$ for which

$Tr(x)Tr(by) = 0, Tr(y)Tr(bx) = 0$ for all $y \in B_1$

and, $Tr(x)Tr(by) = 1, Tr(y)Tr(bx) = 1$ for all $y \in B_2$, holds simultaneously.

Let,

$$K_{a_1} = \{x \in \mathbb{F}_{2^4} | Tr(x)Tr(by) = 0 \text{ and } Tr(y)Tr(bx) = 0 \forall y \in \mathbb{F}_{2^4}\}$$

$$K_{a_2} = \{x \in \mathbb{F}_{2^4} | Tr(x)Tr(by) = 1 \text{ and } Tr(y)Tr(bx) = 1 \forall y \in \mathbb{F}_{2^4}\}$$

$$K_{a_3} = \{x \in \mathbb{F}_{2^4} | Tr(x)Tr(by) = 0, Tr(y)Tr(bx) = 0 \forall y \in B_1 \tag{4}$$

and, $Tr(x)Tr(by) = 1, Tr(y)Tr(bx) = 1 \forall y \in B_2$, holds simultaneously}

Then, $\mathcal{K} = \bigcup_{i=1}^3 K_{a_i}$.

For K_{a_1} : Let $A = \{x \in \mathbb{F}_{2^4} | Tr(x) = 0\}$ and $B = \{x \in \mathbb{F}_{2^4} | Tr(bx) = 0\}$.

It is easy to observe that $K_{a_1} = A \cap B$. Also, A and B being the set of zeroes of linearized polynomials $x^8 + x^4 + x^2 + x$ and $b^8x^8 + b^4x^4 + b^2x^2 + bx$ respectively, becomes the subspaces of \mathbb{F}_{2^4} , when observed as a vector space over \mathbb{F}_2 . Moreover, $K_{a_1} = A \cap B$ forms a subspace, being the intersection of subspaces.

Therefore, $dim(K_{a_1})$ can be 0, 1, 2, 3. However, $dim(K_{a_1}) = 3$ if and only if $A = B$ if only if $b = 1$, which is not so.

Hence, $dim(K_{a_1}) \leq 2$, which implies $|K_{a_1}| \leq 4$.

Remark 1. In fact, $|A \cap B| = 4$, which can be verified for each $a \in \mathbb{F}_{2^4}$ such that $b \neq 0, 1$.

For K_{a_2} : Since, $Tr(y)$ is an onto function therefore, there exist some $y_0 \in \mathbb{F}_{2^4}$ such that $Tr(y_0) = 0$. Thus, equations in K_{a_2} fails for all $x \in \mathbb{F}_{2^4}$. Hence, $K_{a_2} = \emptyset$

For K_{a_3} : By definition of K_{a_3} , one can observe that $A, B \subseteq \mathbb{F}_{2^4} \setminus K_{a_3}$, which implies that $A \cup B \subseteq \mathbb{F}_{2^4} \setminus K_{a_3}$ i.e., $K_{a_3} \subseteq \mathbb{F}_{2^4} \setminus (A \cup B)$.

Hence, $|K_{a_3}| \leq |\mathbb{F}_{2^4} \setminus (A \cup B)| = 16 - 12 = 4$ i.e., $|K_{a_3}| \leq 4$.

Collecting all we get,

$$|\mathcal{K}| \leq |K_{a_1}| + |K_{a_2}| + |K_{a_3}| \leq 8 = 2^3.$$

Case 2: When $Tr(a) = 1$ then,

$$\Omega(x, y) = Tr(x)Tr(by) + Tr(y)Tr(bx) + Tr(y(\mu x^2 + \mu^2 x^8))$$

where, $b = \mu a^2 + \mu^2 a^8$.

Claim: $b \neq 0, 1$

If $b = 0$ then, $\mu a^2 + \mu^2 a^8 = 0$ i.e., $\mu a^2(1 + \mu a^6) = 0$, which implies $a = 0$ or $a^6 = \mu^2$. But $Tr(0) = 0$ and we are in the case $Tr(a) = 1$ therefore, $a^6 = \mu^2$. Cubing both sides and using $\mu^3 = 1$ and $a^{15} = 1$ we have, $a^3 = 1$. Hence, any $a \in \mathbb{F}_{2^4}^*$ for which $b = 0$ must satisfy $a^3 = 1$. Therefore, possibilities of a are $1, \mu, \mu^2$. However, $Tr(a) = 0$ for $a = 1, \mu, \mu^2$. Hence, b cannot be 0.

Also, by putting values of each a such that $Tr(a) = 1$, we verified that $b \neq 1$. Thus, from now onwards, we will assume that $b \neq 0, 1$.

Now, $\Omega(x, y) = 0$ for all $y \in \mathbb{F}_{2^4}$ hold with the following possibilities.

- (b₁) $Tr(x)Tr(by) = Tr(y)Tr(bx) = Tr(y(\mu x^2 + \mu^2 x^8)) = 0 \forall y \in \mathbb{F}_{2^4}$.
- (b₂) $Tr(x)Tr(by) = Tr(y)Tr(bx) = 1 \forall y \in \mathbb{F}_{2^4}$ and, $Tr(y(\mu x^2 + \mu^2 x^8)) = 0 \forall y \in \mathbb{F}_{2^4}$.
- (b₃) $Tr(x)Tr(by) = Tr(y(\mu x^2 + \mu^2 x^8)) = 1 \forall y \in \mathbb{F}_{2^4}$ and, $Tr(y)Tr(bx) = 0 \forall y \in \mathbb{F}_{2^4}$.
- (b₄) $Tr(y)Tr(bx) = Tr(y(\mu x^2 + \mu^2 x^8)) = 1 \forall y \in \mathbb{F}_{2^4}$ and, $Tr(x)Tr(by) = 0 \forall y \in \mathbb{F}_{2^4}$.
- (b₅) There exist $\emptyset \neq B_3, B_4 \subseteq \mathbb{F}_{2^4}$ such that $B_3 \cap B_4 = \emptyset, B_3 \cup B_4 = \mathbb{F}_{2^4}$ for which
 - $Tr(x)Tr(by) = Tr(y)Tr(bx) = 0$ for all $y \in B_3$,
 - $Tr(x)Tr(by) = Tr(y)Tr(bx) = 1$ for all $y \in B_4$ and
 - $Tr(y(\mu x^2 + \mu^2 x^8)) = 0$ for all $y \in \mathbb{F}_{2^4}$.
- (b₆) There exist $\emptyset \neq B_5, B_6 \subseteq \mathbb{F}_{2^4}$ such that $B_5 \cap B_6 = \emptyset, B_5 \cup B_6 = \mathbb{F}_{2^4}$ for which
 - $Tr(x)Tr(by) = Tr(y(\mu x^2 + \mu^2 x^8)) = 0$ for all $y \in B_5$,
 - $Tr(x)Tr(by) = Tr(y(\mu x^2 + \mu^2 x^8)) = 1$ for all $y \in B_6$ and
 - $Tr(y)Tr(bx) = 0$ for all $y \in \mathbb{F}_{2^4}$.
- (b₇) There exist $\emptyset \neq B_7, B_8 \subseteq \mathbb{F}_{2^4}$ such that $B_7 \cap B_8 = \emptyset, B_7 \cup B_8 = \mathbb{F}_{2^4}$ for which
 - $Tr(y)Tr(bx) = Tr(y(\mu x^2 + \mu^2 x^8)) = 0$ for all $y \in B_7$,
 - $Tr(y)Tr(bx) = Tr(y(\mu x^2 + \mu^2 x^8)) = 1$ for all $y \in B_8$ and
 - $Tr(x)Tr(by) = 0$ for all $y \in \mathbb{F}_{2^4}$.

For convenience, let us denote

$$K_{b_i} = \{x \in \mathbb{F}_{2^4} | x \text{ satisfies the condition}(b_i)\}.$$

for $1 \leq i \leq 7$. Then, clearly $\mathcal{K} = \bigcup_{i=1}^7 K_{b_i}$ or $|\mathcal{K}| \leq \sum_{i=1}^7 |K_{b_i}|$.

Now, $Tr(y(\mu x^2 + \mu^2 x^8)) = 0$ for all $y \in \mathbb{F}_{2^4}$ if and only if $\mu x^2 + \mu^2 x^8 = 0$ if and only if $x = 0$. Further, $x = 0$ satisfies the other two equations in (b_1) therefore, $|K_{b_1}| = 1$. But $x = 0$ does not satisfies $Tr(x)Tr(by) = 1 \forall y \in \mathbb{F}_{2^4}$, which gives $K_{b_5} = \emptyset$ and hence, $|K_{b_5}| = 0$.

Following, the similar arguments as in *Case 1, Subcase 2* we get, $K_{b_2} = K_{b_3} = K_{b_4} = \emptyset$ i.e., $|K_{b_2}| = |K_{b_3}| = |K_{b_4}| = 0$.

Also, the equation $Tr(x)Tr(by) = 0$ for all $y \in \mathbb{F}_{2^4}$ holds if and only if $Tr(x) = 0$ if and only if $x \in A = \{x \in \mathbb{F}_{2^4} | Tr(x) = 0\}$. As already mentioned, $B = \{x \in \mathbb{F}_{2^4} | Tr(bx) = 0\}$. Note that, if $x \in B$ then, the equation $Tr(y)Tr(bx) = 1$ for all $y \in B_8$ fails. Hence, we can conclude that $K_{b_7} \subseteq A \cap B^c = A \setminus (A \cap B)$, which means $|K_{b_7}| \leq |A| - |A \cap B| = 8 - 4 = 4$. Similarly, we can prove that $|K_{b_6}| \leq 4$.

Hence, $|\mathcal{K}| \leq \sum_{i=1}^7 |K_{b_i}| = 9$.

Thus, from *Case 1* and *Case 2*, we can say that there exist $a \in \mathbb{F}_{2^4}$ such that $\mathcal{K} \leq 8$, which implies that $dim(\mathcal{K}) = k \leq 3$.

Since, n is even, thus in view of Lemma 1 and Lemma 2, we can say $k \leq 2$ and, hence $W_{D_a f_{\lambda, \mu}}(x) \leq 2^{\frac{n+k}{2}} = 8$ for any $x \in \mathbb{F}_{2^4}$.

So, $nl(D_a f_{\lambda, \mu}) \geq 2^{n-1} - \frac{1}{2}(8) = 4$.

Finally, Eq. (2) concludes the required result i.e., $nl_2(f_{\lambda, \mu}) \geq 2$.

Further, we will provide the comparison among the computed lower bound on the second-order nonlinearity of the considered cubic Boolean function obtained in Theorem 1 with the maximum noted Hamming distance, as given in [6], concluding that the obtained bound attains the maximum known Hamming distance. We will also show that the results obtained is better than the ones, given by Garg and Gangopadhyay [10], and Tang et al. [16] on the second-order nonlinearity of other cubic Boolean functions.

Table 1. Comparison of lower bounds on the second-order nonlinearity

$n = 2m$	4
Order of nonlinearity ($r = m$)	2
Lower bound obtained in Theorem 1	2
Lower bound obtained by Tang et al. (for $k = n/2 = 2$) [16]	0
Lower bound obtained by Garg and Gangopadhyay (for $e = n/2 = 2$) [10]	1.272
Maximum noted Hamming distance [6]	2

4 Conclusion

The computation of the r th-order nonlinearity ($r > 1$), theoretically as well as computationally is a difficult task. It becomes more complicated when the Boolean function contains the product of two or more trace terms. Here, we considered the boolean function class from [1] for $n = 4$ and computed the lower bound for second-order nonlinearity of these Boolean functions, given by Theorem 1. However, for $n = 4$, the functions in Eq. (1) become cubic. Therefore, we compared our bounds with already available bounds of other cubic Boolean functions and found them to be better, as mentioned in Table 1. Moreover, we are also working on the higher-order nonlinearity of this class of functions for general values of n , where n is an even positive integer. Further, we encourage other researchers to study this class of Boolean functions for general values of n to get more interesting results on higher-order nonlinearity.

Acknowledgment. The author would like to thank the Council of Scientific and Industrial Research for providing the financial support.

References

1. Cao, X., Hu, L.: Two Boolean functions with five-valued Walsh spectra and high nonlinearity. *Int. J. Found. Comput. Sci.* **26**, 537–556 (2015)
2. Canteaut, A., Charpin, P., Kyureghyan, G.M.: A new class of monomial bent functions. *Finite Fields Appl.* **14**, 221–241 (2008)
3. Carlet, C.: Recursive lower bounds on the nonlinearity profile of Boolean functions and their applications. *IEEE Trans. Inf. Theory* **54**, 1262–1272 (2008)
4. Carlet, C.: Vectorial Boolean functions for cryptography. In: *Boolean Models and Methods in Mathematics, Computer Science, and Engineering*, vol. 134, pp. 398–469 (2010)
5. Carlet, C.: Boolean functions for cryptography and error correcting codes. In: *Boolean Models and Methods in Mathematics, Computer Science, and Engineering*, vol. 2, pp. 257–397 (2010)
6. Fourquet, R., Tavernier, C.: An improved list decoding algorithm for the second order reed-muller codes and its applications. *Des. Codes Crypt.* **49**, 323–340 (2008)
7. Gangopadhyay, S., Sarkar, S., Telang, R.: On the lower bounds of the second order nonlinearities of some Boolean functions. *Inf. Sci.* **180**, 266–273 (2010)
8. Gao, Q., Tang, D.: A lower bound on the second-order nonlinearity of the generalized Maiorana-McFarland Boolean functions. *IEICE Trans. Fundam. Electron. Commun. Comput. Sci.* **101**, 2397–2401 (2018)
9. Garg, M., Gangopadhyay, S.: A lower bound of the second-order nonlinearities of Boolean bent functions. *Fund. Inform.* **111**, 413–422 (2011)
10. Garg, M., Gangopadhyay, S.: On lower bounds on second-order nonlinearities of bent functions obtained by using Niho power functions. *Cryptology ePrint Archive* (2011)
11. Gode, R., Gangopadhyay, S.: On higher order nonlinearities of Monomial Partial Spreads type Boolean functions. *J. Comb. Inf. Syst. Sci.* **35**, 341–360 (2010)
12. Gode, R., Gangopadhyay, S.: Third-order nonlinearities of a subclass of Kasami functions. *Cryptogr. Commun.* **2**, 69–83 (2010). <https://doi.org/10.1007/s12095-009-0017-z>

13. Singh, B.K.: On third-order nonlinearity of biquadratic monomial Boolean functions. *Int. J. Eng. Math.* **2014**, 1–7 (2014)
14. Sun, G., Wu, C.: The lower bounds on the second order nonlinearity of three classes of Boolean functions with high nonlinearity. *Inf. Sci.* **179**, 267–278 (2009)
15. Sun, G., Wu, C.: The lower bound on the second-order nonlinearity of a class of Boolean functions with high nonlinearity. *Appl. Algebra Eng. Commun. Comput.* **22**, 37–45 (2011). <https://doi.org/10.1007/s00200-010-0136-y>
16. Tang, D., Carlet, C., Tang, X.: On the second-order nonlinearities of some bent functions. *Inf. Sci. Elsevier* **223**, 322–330 (2013)
17. Tang, D., Yan, H., Zhou, Z., Zhang, X.: A new lower bound on the second-order nonlinearity of a class of monomial bent functions. *Cryptogr. Commun.* **12**, 77–83 (2020). <https://doi.org/10.1007/s12095-019-00360-y>
18. Wang, Qichun, Johansson, Thomas: A note on fast algebraic attacks and higher order nonlinearities. In: Lai, Xuejia, Yung, Moti, Lin, Dongdai (eds.) *Inscrypt 2010*. LNCS, vol. 6584, pp. 404–414. Springer, Heidelberg (2011). https://doi.org/10.1007/978-3-642-21518-6_28



On Semimonotone Z -Matrices

Kumar Sunil^(✉) and Ravindran Gomatam

Indian Statistical Institute, Chennai 600029, TN, India

Sunny061193@gmail.com

Abstract. In 1981, Stone conjectured that a fully semimonotone Q_0 matrix is contained in P_0 . In 1995, Murthy proved that for $n = 5$, if $A \in \mathbb{R}^{n \times n} \cap E_0^f \cap Q_0$ and $a_{ii} > 0$, then $A \in P_0$. Here, we show that for matrices with some specific sign patterns this conjecture is true. Murthy showed that fully semimonotone Z -matrices are P_0 , that is $E_0^f \cap Z \subseteq P_0$. Here, we show that semimonotone Z -matrices are contained in P_0 , that is, we exempt the condition of fully semimonotone with semimonotone. Further, we show the equivalency of E_0 -matrices and E_0^f -matrices for Z -matrices. Precisely, we are characterizing the matrices in $P_0 \cap Q_0$. These classes have been found to be interesting in view of the fact that these are processable by Lemke's algorithm.

Keywords: Q_0 -matrices · E_0 -matrices · Two-person finite game · Completely mixed game · Principal Pivot Transform

MSC(2010): 91A05 · 90C33

1 Introduction

Given a matrix $A \in \mathbb{R}^{n \times n}$. Let $q \in \mathbb{R}^n$ be a vector. The linear complementarity problem, $LCP(q, A)$ can be described as follows:

We want to find $x \in \mathbb{R}^n$ such that

$$x \geq 0, \tag{1}$$

$$Ax + q = w \geq 0, \tag{2}$$

$$x^t w = 0. \tag{3}$$

If such a vector exists, we call this x as a solution to the $LCP(q, A)$. For a given $q \in \mathbb{R}^n$, if some vector $x \in \mathbb{R}^n$ satisfies (1) and (2), we call it as a feasible solution for $LCP(q, A)$. We call a matrix Q_0 if for all q , whenever $LCP(q, A)$ has a feasible solution, it also has a solution satisfying (1), (2), and (3). We call A to be a Q -matrix if $LCP(q, A)$ has a solution for every q . We call A to be an R_0 -matrix, if $LCP(0, A)$ has a unique solution. If all the principal minors of a matrix A are positive (nonnegative), then we call A to be a P (P_0)-matrix. We call A to be a Z -matrix, if $a_{ij} \leq 0$ for $i \neq j$. We denote the classes of matrices in each of the above cases by Q , Q_0 , R_0 , P , P_0 , and Z respectively. For further references, the reader may refer to [3, 5, 10] and the results therein.

Characterizing the number of solutions to an LCP has been found to be interesting among the researchers. LCP associated to a P -matrix has a unique solution for every vector q . In 1983, Cottle and Stone introduced a new class U known as the class of U -matrices. We say a matrix U if $LCP(q, A)$ has a unique solution whenever q is in the interior of the union of complementary cones. Further, the class is expanded for the unique solution of $LCP(q, A)$ for q in the interior of any non-degenerate complementary cone. This class is known as the class of fully semimonotone matrices, denoted by E_0^f . The class of E_0^f was introduced by Stone. For further results refer to [9].

In [4], Cottle and Stone proved $P \subseteq U \subseteq E_0^f$. In [13], Stone proved that $U \cap Q_0 \subseteq P_0$. Further, he raised the conjecture $E_0^f \cap Q_0 \subseteq P_0$. For matrices with some specific sign patterns, we show that this conjecture is true. In particular, we show that semimonotone Z -matrices are contained in P_0 . In addition, we also prove that fully semimonotone matrices having specific sign patterns are P_0 .

In proving some of our results we use the concept from the Completely mixed matrix games. A two person zero-sum game may be described as following:

Let Player 1 and player 2 choose integers $i \in \bar{m}$ and $j \in \bar{n}$ respectively. Then Player 2 receives an amount a_{ij} from Player 1. This amount a_{ij} may be negative, positive, or zero. A mixed strategy for Player 1 and 2 are the probability vectors $x = (x_1, x_2, \dots, x_m)^t$, and $y = (y_1, y_2, \dots, y_n)^t$, respectively, where $x_i \geq 0$ for all i and $\sum_{i=1}^m x_i = 1$ and $y_j \geq 0$ for all j and $\sum_{j=1}^n y_j = 1$. We call (x^*, y^*) to be the optimal strategies for Player 1 and Player 2 respectively, if the following conditions hold

$$\sum_i x_i^* a_{ij} \leq v \quad \text{for } j = 1, 2, \dots, n, \tag{4}$$

$$\sum_j y_j^* a_{ij} \geq v \quad \text{for } i = 1, 2, \dots, m. \tag{5}$$

It is known that such a v exists and is unique. We denote $v = val(A)$ and call it the value of the matrix game $A = (a_{ij})$. In describing (4) and (5), we assumed Player 1 to be the minimizer where Player 2 to be the maximizer. If each entry of the vector $x = (x_1, x_2, \dots, x_m)^t$ is positive, then we call such a vector x as a completely mixed strategy for player 1. Similarly, if each entry of the vector $y = (y_1, y_2, \dots, y_n)^t$ is positive, then we call such a vector y as a completely mixed strategy for player 2. If each of the optimal pair (x^*, y^*) is completely mixed for a game associated with A , then we call it a completely mixed game.

Kaplansky [7] has characterized a completely mixed (c.m.) matrix game. He showed the following:

Consider a game associated with matrix $A \in \mathbb{R}^{m \times n}$ and suppose $val(A) = 0$, then the game associated with matrix A is c.m. if and only if $m = n$, $r(A) = n - 1$, and each of the cofactor of A is nonzero and have same sign.

The organisation of this manuscript is as following: In Sect. 2, we present a few basic results that are used in further sections. In Sect. 3, we provide our main theorem regarding the Z -matrices. Section 4 contains some more results related

to E_0^f . In Sect. 5, we provide some open problem for future work and conclude the paper.

2 Preliminaries

Notation: In this manuscript, we used signs at many places instead of a fix value. The meaning for these signs is as following: $+$ implies positive, \ominus means nonpositive, $-$ denotes negative, \oplus means nonnegative, and $*$ denotes any real value.

$A \in \mathbb{R}^{m \times n} = (a_{ij}); i = 1, 2, \dots, m$ and $j = 1, 2, \dots, n$ denotes a matrix. \bar{n} denotes the set $\{1, 2, \dots, n\}$. Let $\alpha, \beta \subseteq \bar{n}$ and the complements are $\bar{\alpha} = \bar{n} \setminus \alpha$ and $\bar{\beta} = \bar{n} \setminus \beta$. If we delete rows of A corresponding to $\bar{\alpha}$ and columns of A corresponding to $\bar{\beta}$, then the resulting matrix is a submatrix of A , denoted by $A_{\alpha\beta}$. We call $A_{\alpha\beta}$ to be a principal submatrix of A if $\alpha = \beta$. $|\alpha|$ denotes the cardinality of the set α . The determinant of the matrix A is denoted as $|A| = \det(A)$. We say a vector $x \geq 0$ ($x > 0$), if every coordinate of x is nonnegative (positive). Similarly, we say a matrix $A \geq 0$ ($A > 0$), if each entry of A is nonnegative (positive). $r(A)$ denotes the rank of matrix A .

This section contains some basic definitions and results from the literature. These results are used in the next sections.

A.W. Tucker introduced the concept of PPTs. PPTs (principal pivot transforms) play a crucial role in the consideration of LCP. A detailed treatment of PPT was given by Tsatsomeros [14].

Let $A \in \mathbb{R}^{n \times n}$ and $\alpha \subseteq \bar{n}$.

$$A = \begin{pmatrix} A_{\alpha\alpha} & A_{\alpha\bar{\alpha}} \\ A_{\bar{\alpha}\alpha} & A_{\bar{\alpha}\bar{\alpha}} \end{pmatrix}$$

If $A_{\alpha\alpha}^{-1}$ exists, then for such an α , the PPT is defined. We denote such a PPT of A as $\text{ppt}(A, \alpha)$.

$$\text{ppt}(A, \alpha) = \begin{pmatrix} A_{\alpha\alpha}^{-1} & -A_{\alpha\alpha}^{-1}A_{\alpha\bar{\alpha}} \\ A_{\bar{\alpha}\alpha}A_{\alpha\alpha}^{-1} & A/A_{\alpha\alpha} \end{pmatrix},$$

where $A/A_{\alpha\alpha} = A_{\bar{\alpha}\bar{\alpha}} - A_{\bar{\alpha}\alpha}A_{\alpha\alpha}^{-1}A_{\alpha\bar{\alpha}}$ is known as the Schur complement. For any α , if $A_{\alpha\alpha}$ is invertible, then PPT exists for the corresponding α . We call all those PPTs as legitimate PPTs.

Semimonotone matrices were first initiated by Eaves [5], and initially these are denoted by L_1 . Later, in [3], this class was denoted by E_0 . The name ‘‘semimonotone’’ was initiated by Karamardian. It is known that $P_0 \subseteq E_0$.

Definition 1. We call $A \in \mathbb{R}^{n \times n}$ to be a semimonotone matrix if, for any nonzero nonnegative vector x , there is some k in such a manner that x_k is positive and $(Ax)_k$ is nonnegative. We call A as a fully semimonotone matrix, denoted by E_0^f , if A and all its legitimate principal pivot transforms are in E_0 .

Some of the useful properties of semimonotone matrices from [3, 10] are stated below.

Theorem 1. *If $A \in \mathbb{R}^{n \times n} \cap E_0$, then we can conclude the following:*

1. $A_{\alpha\alpha} \in E_0$ for all $\alpha \subseteq \bar{n}$.
2. $A^t \in E_0$.
3. a_{ii} are nonnegative for all $i = 1, 2, \dots, n$.
4. For any vector $q > 0$, there is a unique solution for $LCP(q, A)$, that is $x = 0$.
5. $\text{val}(A) \geq 0$.

Tsatsomeros and Wendler [15] provided the following result:

Theorem 2. *Let $A \in \mathbb{R}^{2 \times 2}$ and $a_{ii} > 0$. Then $A \in E_0$ if and only if either $A \geq 0$ or $\det(A) \geq 0$.*

Definition 2. We call $A \in \mathbb{R}^{n \times n}$ to be a copositive matrix if for any nonnegative vector x , $x^t Ax \geq 0$. We denote the class of such matrices by C_0 . A matrix A is called fully copositive matrix, denoted by C_0^f , if A and each of its legitimate PPTs is in C_0 .

The class E_0^f includes the class C_0^f . In [8], Murthy and Parthasarathy provide a result for C_0^f .

Theorem 3. *Let $A \in C_0^f \cap Q_0 \cap \mathbb{R}^{n \times n}$. Then $A \in P_0$.*

Next we state a few known results for fully semimonotone Q_0 matrices from [11].

Theorem 4. *Let $A \in E_0^f \cap Q_0 \cap \mathbb{R}^{n \times n}$. Further, assume $\det(A_{\alpha\alpha}) \geq 0$ for all $|\alpha| = n - 1$. Then $A \in P_0$.*

Theorem 5. *Let $A \in \mathbb{R}^{n \times n} \cap E_0^f \cap R_0$. Then A is a P_0 -matrix.*

The following corollary is proved already. Here we provide another proof.

Corollary 1. *Let $A \in \mathbb{R}^{n \times n} \cap E_0^f \cap Q_0$. Further, suppose that $A_{\alpha\alpha} \in P$ for $|\alpha| \leq (n - 2)$. Then $A \in P_0$.*

Proof. Let $B = A_{\alpha\alpha}$ where $|\alpha| = n - 1$. We claim that $\det(B) \geq 0$.

Suppose $\det(B) < 0$. Since $A_{\alpha\alpha} \in P$ for $|\alpha| \leq (n - 2)$, that is each proper principal submatrix of B is also a P -matrix. Hence, the diagonal entries of B^{-1} are negative.

Since $A \in E_0^f$, observe that $B \in E_0$ and $B^{-1} \in E_0$. It is not possible for E_0 -matrix to have negative diagonal entry. Hence, $\det(B) \geq 0$. Therefore, using Theorem 4, $A \in P_0$. □

Remark 1. We have used the fact that if $A \in E_0^f$, then any proper principal submatrix is E_0 . If some proper principal submatrix (say B) is non-singular, then $B^{-1} \in E_0$.

The result given below is the Theorem 4.1.2 in [3]. This result is useful in proving next theorem.

Theorem 6. [3] Let $M = ppt(A, \alpha)$. Then for any submatrix $M_{\beta\beta}$ of M

$$\det(M_{\beta\beta}) = \frac{\det(A_{\gamma\gamma})}{\det(A_{\alpha\alpha})}$$

where $\gamma = \alpha \triangle \beta$.

We need the following result.

Theorem 7. Let A be a P_0 -matrix. Then any PPT of A is also a P_0 -matrix.

Proof. Let $A \in \mathbb{R}^{n \times n} \cap P_0$ and $\alpha \subseteq \bar{n}$ such that $\det(A_{\alpha\alpha}) \neq 0$. Therefore, $ppt(A, \alpha)$ exists. Let us call it M . Now for any $\beta \subseteq \{1, 2, \dots, n\}$, using Theorem 6, we have

$$\det(M_{\beta\beta}) = \frac{\det(A_{\gamma\gamma})}{\det(A_{\alpha\alpha})} \tag{6}$$

where $\gamma = \alpha \triangle \beta$. Observe that $A_{\alpha\alpha}$ and $A_{\gamma\gamma}$ are principal submatrices of A . Since $A \in P_0$. Hence, $\det(A_{\alpha\alpha}) > 0$, $\det(A_{\gamma\gamma}) \geq 0$. Therefore, on putting these in 6, we have $\det(M_{\beta\beta}) \geq 0$. Since β was arbitrary, hence $M \in P_0$. Therefore, ppt of a P_0 -matrix is also a P_0 -matrix. \square

Remark 2 [3]. It is known that $P \subseteq P_0 \subseteq E_0^f \subseteq E_0$. In the next section we show that for the Z -matrices, P_0, E_0^f and E_0 are equal.

The following two results of game theory are used in proving our results.

Theorem 8 [2]. Let $A \in \mathbb{R}^{n \times n} \cap Z$. Consider a game is associated with matrix A . Suppose $val(A) > 0$. Then A has to be a P -matrix.

Theorem 9 [7]. Consider a game associated with matrix $A \in \mathbb{R}^{m \times n}$ and $val(A) = 0$. Then A is c.m. if and only if $m = n$, $r(A) = n - 1$, and each of the cofactor of A is nonzero and have same sign.

The next two results are known for Q and R_0 matrices.

Theorem 10 [1]. Let $A \in \mathbb{R}^{n \times n} \cap P_0$. Then $A \in Q$ if and only if $A \in R_0$.

Theorem 11 [6]. Let $A \in R_0 \cap \mathbb{R}^{n \times n}$ and $LCP(q, A)$ has a unique solution, for some $q > 0$. Then $A \in Q$.

3 Main Results

Murthy and Parthasarathy [9] showed that $E_0^f \cap Z \subseteq P_0$. In this section, we show that the condition of fully semimonotone is not necessary. In particular, we show that the semimonotone, Z -matrices are P_0 .

Theorem 12. Let $A \in \mathbb{R}^{n \times n} \cap E_0 \cap Z$, then $A \in P_0$.

Proof. This proof is done using the mathematical induction. For $n = 1$, it is obvious.

For $n = 2$, the sign pattern would be

$$\begin{pmatrix} \oplus & \ominus \\ \ominus & \oplus \end{pmatrix}.$$

Since the diagonal entries are nonnegative, both proper principal minors are nonnegative. If any of the off-diagonal entry is zero, then the determinant would be nonnegative. Hence, $A \in P_0$. If both the off-diagonal entries are negative, then using Theorem 2, the determinant of the matrix A is nonnegative. Hence, $A \in P_0$.

Now for $n = 3$. Since $A \in E_0$, using Theorem 1, each of its principal sub-matrix is E_0 and the diagonal entries are nonnegative. From Theorem 2, either $A_{\alpha\alpha} \geq 0$ for $|\alpha| = 2$ or $\det(A) \geq 0$. That means $A_{\alpha\alpha} \in P_0$ for all $|\alpha| = 2$. Consider $x \geq 0$ be an optimal for A , so $Ax \geq 0$,

$$\begin{pmatrix} \oplus & \ominus & \ominus \\ \ominus & \oplus & \ominus \\ \ominus & \ominus & \oplus \end{pmatrix} \begin{pmatrix} x_1 \\ x_2 \\ x_3 \end{pmatrix} \geq \begin{pmatrix} 0 \\ 0 \\ 0 \end{pmatrix}$$

- a) If exactly one coordinate of x is non-zero (say x_1), then $A \in E_0$ implies that A must be of the type

$$A = \begin{pmatrix} \oplus & \ominus & \ominus \\ 0 & \oplus & \ominus \\ 0 & \ominus & \oplus \end{pmatrix}.$$

Here, $\det(A) \geq 0$. Hence, $A \in P_0$.

- b) If exactly two coordinates of x are non-zero (say x_1, x_2), then $A \in E_0$ implies that A must be of the type

$$A = \begin{pmatrix} \oplus & \ominus & \ominus \\ \ominus & \oplus & \ominus \\ 0 & 0 & \oplus \end{pmatrix}.$$

Since, $A \in E_0$, using 1, the submatrix B of A , on omitting last row and last column, is also E_0 . Using the Theorem 2, either $B \geq 0$ or $\det(B) \geq 0$. Hence, $\det(A) \geq 0$. Therefore, $A \in P_0$.

- c) Let $x > 0$. Then the game associated with A is c.m. We have the hypothesis that A is a semimonotone matrix, hence using Theorem 1, $val(A) \geq 0$. Now, we will check for both the cases when the value is zero or the value is positive. If $val(A) > 0$, then by Theorem 8, $A \in P$. Therefore, $A \in P_0$. Now for $val(A) = 0$, from Theorem 9, $rank(A) = n - 1$. That means one of the row is linear combination of others. Hence $\det(A) = 0$ and therefore $A \in P_0$.

Hence, it is true for $n = 3$. Now for the induction hypothesis, let it is true up to any $n - 1$ order. Now we will show that it is true for n .

- a) Let all the coordinates of x be positive, that is, the game is completely mixed. Since $A \in E_0$, hence $val(A) \geq 0$. If $val(A) > 0$, then by Theorem 8, $A \in P$. Therefore, $A \in P_0$. If $val(A) = 0$, then using Theorem 9, $rank(A) = n - 1$. That means one of the row is linear combination of others. Hence $det(A) = 0$ and therefore $A \in P_0$.
- b) Let x has k non-zero coordinates such that $k \leq n - 1$. We can partition our given matrix as

$$A = \begin{pmatrix} C & B \\ 0 & D \end{pmatrix}$$

where $C \in \mathbb{R}^{k \times k}$, $B \in \mathbb{R}^{k \times n-k}$, $D \in \mathbb{R}^{n-k \times n-k}$ and 0 is null matrix of order $n - k \times k$. From partitioned matrix properties, we know that $det(A) = det(C).det(D)$. Since from induction we know that for any $k \leq n - 1$, $det(C) \geq 0, det(D) \geq 0$. Hence, $det(A) \geq 0$. Therefore, $A \in P_0$.

Hence, for any n , $A \in \mathbb{R}^{n \times n} \cap E_0 \cap Z$ implies $A \in P_0$. □

In the above theorem, both the conditions of A being E_0 and Z are necessary. We can see this by the following two examples.

Example 1. Let

$$A = \begin{pmatrix} 1 & -2 \\ -1 & 0 \end{pmatrix}.$$

It can be seen that $A \in Z$ and A is not an E_0 -matrix (since $Ax < 0$ for some vector $x = (1, 1)^t$). Notice that $det(A) = -2$. Therefore, it is not a P_0 -matrix. □

Example 2. Let

$$A = \begin{pmatrix} 1 & 2 \\ 1 & 1 \end{pmatrix}$$

Since A is a nonnegative matrix, it can be easily verified that $A \in E_0$. Since off-diagonal entries are positive, $A \notin Z$. But the determinant of A is negative, hence A is not a P_0 -matrix. □

Remark 3. It is known that $P_0 \subseteq E_0$. From Theorem 12, we can conclude that within Z -matrices, P_0 is equivalent to E_0 . From Example 2, it can be seen that the Z -property is necessary for the equivalence to hold. From this result, we can conclude the next two theorems.

In [12], Parthasarathy, Ravindran and Sunil showed that within the class of E_0 , R_0 -matrices and Q -matrices are equivalent for matrices up to order 3. They provided counter examples of matrices which are $E_0 \cap Q$ but not R_0 for order 4 and above. But here we prove the equivalence with the additional assumption of Z for any order of matrices.

Theorem 13. *Let $A \in \mathbb{R}^{n \times n} \cap E_0 \cap Z$. Then $A \in Q$ iff $A \in R_0$.*

Proof. Let $A \in \mathbb{R}^{n \times n} \cap E_0 \cap Z$. Using Theorem 12, $A \in P_0$. Then Theorem 10 states that within P_0 , Q is equivalent to R_0 . Hence, $A \in Q$ if and only if $A \in R_0$. Therefore, within the class of E_0 and Z -matrices, R_0 is equivalent to Q □

Theorem 14. *Let $A \in \mathbb{R}^{n \times n} \cap Z$. Then $A \in E_0$ if and only if $A \in E_0^f$.*

Proof. Whenever $A \in E_0^f$, it is obvious A is an E_0 -matrix. Now for the converse part let us assume $A \in E_0$. Since $A \in Z$, by Theorem 12, $A \in P_0$. Using remark 2, it is known that $P_0 \subseteq E_0^f$. Therefore, $A \in E_0^f$.

Hence, within the class of Z -matrices, E_0 is equivalent to E_0^f . □

In general, E_0 -matrix are not equivalent to E_0^f . Hence, in the above theorem, the condition of matrix being a Z -matrix is necessary. It can be seen by the example below.

Example 3. Let

$$A = \begin{pmatrix} 1 & 2 & 0 \\ 1 & 1 & 1 \\ 1 & 0 & 0 \end{pmatrix}.$$

Since A is a nonnegative matrix, it can be easily verified that $A \in E_0$. Let $\alpha = \{1, 2\}$. Consider $ppt(A, \alpha)$.

$$ppt(A, \alpha) = \begin{pmatrix} -1 & 2 & -2 \\ 1 & -1 & 1 \\ -1 & 2 & -2 \end{pmatrix}.$$

Observe that the diagonal entries of the ppt corresponding to the above α are negative. Using Theorem 1, $ppt(A, \alpha)$ is not an E_0 -matrix. Therefore, $A \notin E_0^f$. □

4 Results for Matrices with Specific Sign Patterns

In this section, we consider matrices with some specific sign patterns and show some properties of such matrices.

Theorem 15. *Let $A \in \mathbb{R}^{n \times n}$ and $a_{ii} > 0$. Further suppose that all the entries below the diagonal are nonnegative. Then $A \in Q$.*

Proof. First we show that $A \in R_0$ for the given sign pattern of A . On the contrary, suppose $A \notin R_0$. That is, there is a non-zero vector $x \geq 0$ such that $Ax = w \geq 0$ and $x^t w = 0$.

$$Ax = \begin{pmatrix} + & * & * & \dots & * \\ \oplus & + & * & \dots & * \\ \oplus & \oplus & + & \dots & * \\ \vdots & \vdots & \vdots & \ddots & \vdots \\ \oplus & \oplus & \oplus & \dots & + \end{pmatrix} \begin{pmatrix} x_1 \\ \vdots \\ x_k \\ 0 \\ 0 \end{pmatrix} = \begin{pmatrix} w_1 \\ \vdots \\ w_k \\ \vdots \\ w_n \end{pmatrix} = w$$

WLOG, let $x_k > 0$ for any $1 \leq k \leq n$, and $x_m = 0$ for $m > k$. Then it is easy to observe that w_k is positive. Hence, $x_k w_k \neq 0$. Hence, x_k cannot be positive for any k . Therefore, $A \in R_0$.

Let $d \in \mathbb{R}^n$ be any positive vector. Similarly, we can show that $x = 0$ is the only solution for $LCP(d, A)$. Hence, using Theorem 11, it can be concluded that $A \in Q$. \square

Theorem 16. *Let $A \in \mathbb{R}^{n \times n}$ and $a_{ii} > 0$. Further suppose that all the entries below the diagonal are nonnegative and all the entries above the diagonal are non-positive. Then $A \in P_0$.*

Proof. Since A has all its diagonal entries positive. Hence, for $n = 1$, $A \in P_0$.
 Now for $n = 2$,

$$A = \begin{pmatrix} + & \ominus \\ \oplus & + \end{pmatrix}$$

Here, $\det(A) > 0$, hence $A \in P$ as well as $A \in P_0$.

For $n = 3$, every proper principal submatrix have the same sign pattern. Since we have seen such a matrix is P_0 up to $n = 2$, that is, proper principal minor are nonnegative. Hence, from Theorem 4, $A \in P_0$.

Assume it is true for the matrices up to order $n - 1$, that is, every matrix of the given sign pattern up to order $n - 1$ is P_0 . For n , every proper principal minor is nonnegative. Therefore, using Theorem 4, such a matrix A is always a P_0 -matrix. \square

Remark 4. Since we know that $P_0 \subseteq E_0^f$, the matrices with given sign pattern in the above theorem are E_0^f . Therefore, Stone’s conjecture holds for the matrices with all its diagonal entries positive, all the entries below the diagonal are nonnegative, and all the entries above the diagonal are non-positive.

Next, we show another sign pattern such that the conjecture holds for that pattern too. This pattern is almost similar to the above. But for the sake of completeness we are also giving an another way of proving it.

Theorem 17. *Let $A \in \mathbb{R}^{n \times n}$ and $a_{ii} > 0$. Further suppose that all the entries above the diagonal are nonnegative. Then $A \in R_0$.*

Proof. For given A , consider $LCP(0, A)$.

$$Ax = \begin{pmatrix} + \oplus \oplus \dots \oplus \\ * + \oplus \dots \oplus \\ * * + \dots \oplus \\ \vdots \vdots \vdots \ddots \vdots \\ * * * \dots + \end{pmatrix} \begin{pmatrix} 0 \\ \vdots \\ x_k \\ \vdots \\ x_n \end{pmatrix} = w$$

where $*$ is any real number and $w \in \mathbb{R}^n$. Here for least value of k such that $x_k > 0$, $(Ax)_k = w_k$ is also positive. It contradicts the condition of complementarity. Hence, no x_k is positive. Therefore, $A \in R_0$. \square

Remark 5. In the above theorem, if we further assume that A is fully semimonotone, then $A \in P_0$.

Theorem 18. *Let $A \in \mathbb{R}^{n \times n} \cap E_0^f$ and $a_{ii} > 0$. Further suppose that all the entries above the diagonal are nonnegative. Then $A \in P_0$.*

Proof. Let $A \in \mathbb{R}^{n \times n}$ and $a_{ii} > 0$. All the entries above the diagonal are nonnegative. Theorem 17 implies that $A \in R_0$. Since $A \in E_0^f$, Theorem 5 implies that $A \in P_0$. \square

5 Conclusions

We have proved that a fully semimonotone and Q_0 -matrix with specific sign patterns is a P_0 -matrix. We also have proved that a matrix that is semimonotone and Z is contained in the class of P_0 -matrices. Further, we have shown that for Z -matrices, the semimonotone matrices are the fully semimonotone matrices. Observe that these classes are subsets of $P_0 \cap Q_0$, and hence these classes are processable by Lemke's algorithm, that is, for each q , either Lemke's algorithm gives a solution or terminates in a ray.

Open Problem: Now, we state an open problem. The following conjecture is due to R.E. Stone.

Let $A \in \mathbb{R}^{n \times n}$. Further assume that A is a fully semimonotone Q_0 -matrix. Can we say A is a P_0 -matrix?

Acknowledgements. The author would like to thank the referees for their suggestions and comments. We also thank Professor T. Parthasarathy for making several valuable suggestions that resulted in improving the presentation of this manuscript.

References

1. Aganagic, M., Cottle, R.W.: A note on Q -matrices. *Math. Program.* **16**, 374–377 (1979)
2. Berman, A., Plemmons, R.J.: *Nonnegative Matrices in the Mathematical Sciences*. Society for Industrial and Applied Mathematics (1994)
3. Cottle, R.W., Pang, J.S., Stone, R.E.: *The Linear Complementarity Problem*. Academic Press, New York (1992)
4. Cottle, R.W., Stone, R.E.: On the uniqueness of solutions to linear complementarity problems. *Math. Program.* **27**, 191–213 (1983)
5. Eaves, B.C.: The linear complementarity problem. *Manage. Sci.* **17**, 621–634 (1971)
6. Ingleton, A.W.: The linear complementarity problem. *J. London Math. Soc.* **2**, 330–336 (1970)
7. Kaplansky, I.: A contribution to von Neumann's theory of games. *Ann. Math.* **46**, 474–479 (1945)
8. Murthy, G.S.R., Parthasarathy, T.: Fully copositive matrices. *Math. Program.* **82**, 401–411 (1998)
9. Murthy, G.S.R., Parthasarathy, T.: Some properties of fully semimonotone, $\$Q_0$ $\$$ -matrices. *SIAM J. Matrix Anal. App.* **16**, 1268–1286 (1995)
10. Murthy, G.S.R., Parthasarathy, T., Ravindran, G.: On copositive Semimonotone Q -matrices. *Math. Program.* **68**, 187–203 (1995)

11. Murthy, G.S.R.: Some Contributions to Linear Complementarity Problem, PhD Thesis, SQC & OR Unit, ISI Madras (1994)
12. Parthasarathy, T., Ravindran, G., Kumar, S.: On semimonotone matrices, R_0 -matrices and Q -matrices. *J. Optim. Theory App.* **195**, 131–147 (2022)
13. Stone, R.E.: Geometric aspects of the linear complementarity problem. Stanford University of CA System Optimization Lab (1981)
14. Tsatsomeris, M.J.: Principal pivot transforms: properties and applications. *Linear Algebra Appl.* **307**, 151–165 (2000)
15. Tsatsomeris, M.J., Wendler, M.: Semimonotone matrices. *Linear Algebra Appl.* **578**, 207–224 (2019)



Mathematical Analysis of Hall Effect and Hematocrit Dependent Viscosity on Au/GO-Blood Hybrid Nanofluid Flow Through a Stenosed Catheterized Artery with Thrombosis

Umesh Khanduri^(✉) and B. K. Sharma

Department of Mathematics, Birla Institute of Technology and Science Pilani,
Pilani, Rajasthan, India
umeshkhanduri09@gmail.com

Abstract. The present paper addresses the rheological perspective of blood flow with the suspension of Au/GO nanoparticles through the curved artery with multiple stenosis and thrombosis. The influences of hematocrit-dependent viscosity and Hall effects are taken into account. The flow is subjected to a strong radial magnetic field. Using the mild stenosis and axi-directional flow assumptions, the governing equations are simplified and then the reduced equations are discretize using the Crank-Nicholson technique to get the tridiagonal systems of equations which are further solved by employing the Tri-diagonal Matrix Algorithm (TDMA) at each time step. The flow patterns are also shown by plotting velocity contours. It has been observed that raising the Hall parameter induces an increase in fluid velocity owing to an increase in collision time or electron frequency, hence assisting fluid flow. Further, Au-GO/blood hybrid nanoparticles have a higher velocity profile than pure blood and unitary nanoparticles. Current findings may have applications in the biomedical field, particularly in imaging techniques like magnetic resonance angiography (MRA), which analyses an image of an artery to detect problems. The current findings are consistent with recent findings in earlier blood flow research studies.

Keywords: Stenosis · Hybrid nanoparticles · Hall effect · Clot

1 Introduction

Among the various cardiovascular diseases, arteriosclerosis/stenosis is the major cause of morbidity and mortality worldwide [1]. Arteriosclerosis is a condition in which plaque gets deposited at the arterial wall and constricts the blood flow. The plaque is the composition of fats/lipids, cholesterol, greasy substances, and other cellular wastes. The constriction may trigger thrombosis (blood clot) upon rupture and lead to a heart attack. Doffin et al. [2] experimented with

studying the oscillatory flow between the clot and stenosis model. The oscillation is produced by the two pistons moving in the oscillate phase. They determined the velocity and streamlined pattern by visualising the suspended aluminium particles in water glycerol fluid. Strony et al. [3] investigated the high shear stress effect and hemodynamic factors for the thrombus deposition in the stenotic region. According to their study, the shear stress would be higher in the stenotic region, which causes the platelets to get aggregated at the vessel wall damage and from the occlusive thrombosis. Elnaqeeb et al. [4] explored the copper blood model due to its application in biomedicine. They also discovered the blood tapering phenomenon in catheterised stenosis arteries. The time-variant stenosis with an aneurysm was numerically explored by Sultan et al. [5]. They considered the non-Newtonian Eyring Powell fluid model and curvilinear coordinate system to study the blood flow through the curved artery. Akthar et al. [6] developed a mathematical model to simulate the blood flow through multiple thromboses with the Peristaltic wall.

In the magnetic field, moving conducting fluids experience a resistive force known as Lorentz force. When the moving fluid is ionised gas, or the strong magnetic field is applied, the conductivity normal to the magnetic field is reduced. This reduction is due to the free spinning of the electrons. Thus, it induces the electric current normal to the magnetic and electric field. This phenomenon is known as Hall current. Mekheimer et al. [7] studied the Hall effect with viscous dissipation on the micropolar fluid through the stenosis artery. Mishra et al. [8] experimented to understand the Hall and magnetic field effect on the MHD flow through the rotating channel. Das et al. [9] conducted theoretical research to investigate peristaltic blood pumping. They examined the Hall and ion slip effects by using Casson fluid to mimic the rheological properties of blood.

Nanotechnology advancements and designing techniques help researchers probe into the nanoscale particles' properties and features. In the biomedical field, the advancement of nanotechnology helps design nanomedicine to diagnose and treat diseases. Nanoparticles are small tiny particles, and with the suspension in the base fluid, they enhance the characteristics and properties of the base fluid. In this study, we have considered the hybrid nanofluid by the suspension of Graphene Oxide and Gold nanoparticles in the base fluid (blood). Elnaqeeb et al. [10] studied the gold nanoparticle's blood flow through the tapered artery and did a comparative study for gold, Cu, and TiO₂ nanoparticles. They looked at temperature-dependent viscosity and observed that the velocity of gold nanoparticles in a stenosed blood artery is greater than the other two nanoparticles. Thus, explaining the enhancement in the hemodynamic performance of blood in the diseased artery. Changdar et al. developed a single and discrete phase model to observe the effect of gold, Cu, and silver nanoparticles as drug carriers. They have considered multiple stenoses and spherical-shaped nanoparticles. According to their findings, cylindrical nanoparticles are more effective than spherical nanoparticles in drug delivery. Mekheimer et al. [11] examined the gold nanoparticles in the peristaltic flow between the two coaxial tubes. They contemplated the gold nanoparticles due to their application in treating cancerous cells. Seo Kyung et al. [12] formed the hybrid sheet of Au-GO nanoparticles to enhance the photothermic

effect helpful in cancer therapy. Further, Liu et al. [13] studied graphene-based nanoparticles in their work. They considered graphene nanoparticles due to their photothermal effect beneficial in cancer treatment. Khazayinejad et al. [14] analytically solved the mathematical model portraying graphene nanoparticles' suspension in a tube with wavy walls. Through the use of particle shape factor, slip, and convective regime, Sindhu et al. [15] analysed the flow of a hybrid nanoliquid in a microchannel. Rishu et al. [16] considered the bell-shaped artery with temperature-dependent viscosity to explore the effect of hybrid nanoparticles (Au-Al₂O₃) on blood flow. Furthermore, they [17] investigated the entropy analysis of the MHD slip flow with tapered multiple-stenosis artery.

Blood flow is greatly influenced by pressure, viscosity, and other external and internal elements in the human circulatory system. Blood's hemodynamic properties are constantly changing due to its shear-thinning feature. As a result, blood viscosity cannot be assumed to be constant. Singh et al. [18] explored the Jeffery-Hamel flow in the non-parallel walls by adopting the hybrid computational approach. By employing a hybrid analytical approach, Sushila et al. [19] examined the thin film flow issue. Bhavya et al. [20] studied the inclination and hematocrit dependent viscosity effect on the MHD blood flow. Further, Chandan et al. [21] developed the model by considering the two phase blood flow. Their findings show that radial curvature increases the risk of atherosclerosis whereas heat radiation decreases it. Khanduri and Sharma [22] investigated the entropy generation on the MHD flow by considering the variable viscosity and thermal conductivity. Several other researchers [23–29] developed a mathematical model to illustrate the effect of variable viscosity on MHD flow.

From a bioengineering perspective, it is crucial to research the behaviour of hybrid nanoparticles (Au-GO) suspended by streaming blood flow on the curved stenosed artery in the presence of a strong radial magnetic field; however, no such study has yet been published. The multiple stenosis and thrombosis at the catheter walls hinder the hemodynamic flow. The curvilinear coordinate is customised to simulate blood flow. The current study may be beneficial in radiological examinations such as magnetic resonance angiography (MRA) to detect vascular abnormalities. The hybrid nanoparticles Au-GO/blood have been studied due to their potential applicability in nanomedicine and biomedicine. The inert nature, stability, and anti-bacterial capabilities makes the Au nanoparticles to have the wide range of applications. As a result, the current study sheds light on the treatment of stenosis and other anomalies without surgery while also reducing post-surgical problems. In the future work, the researchers can explore the effect of nanoparticle shapes with the permeable arterial walls along with the different shapes of stenosis (example, triangular and elliptical shapes) with tapering effects can be explored.

The novelty of the present work includes:

- The influence of (Au-GO/blood) hybrid nanoparticles on diseased segments characterized by multiple stenosis and thrombosis.
- To analyze the hematocrit-dependent viscosity model with the combined effect of Hall and body acceleration in the porous medium.

2 Mathematical Formulation

Considered the unsteady, laminar, incompressible, two-dimensional blood flow with suspension of Au/GO nanoparticles through the two coaxial tube forming the constriction due to the thromosis and stenosis. The blood flow is assumed to be Newtonian and axisymmetric. The (r_1, θ_1, z_1) curvilinear coordinate is chosen to mimic the blood flow through a diseased artery. The r and z represent the radial and axial direction respectively. Figure 1 represent the pictorial representation of diseased artery in which the outer tube has the multiple stenosis with radius η and the inner tube has the clot on the catheter with radius ψ .

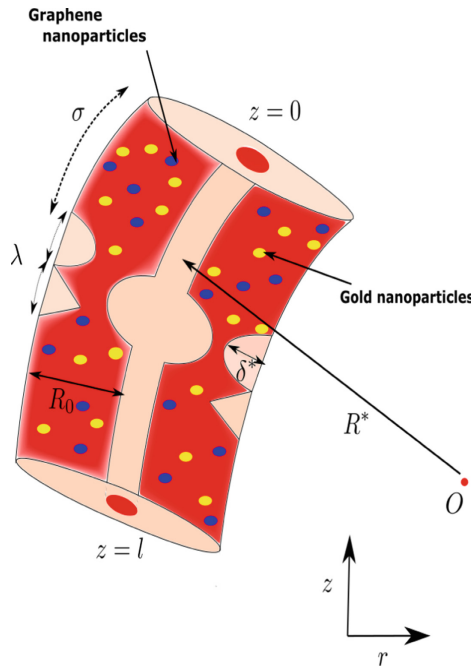


Fig. 1. Diseased artery segment

The mathematical representation of diseased segment [17]:

Stenosis:

$$\eta(z_1^*) = \begin{cases} R_0 - 2\frac{\delta}{\lambda}(z_1^* - d), & d \leq z_1^* \leq d + \frac{\lambda}{2} \\ R_0 + 2\frac{\delta}{\lambda}(z_1^* - d - \lambda), & d + \frac{\lambda}{2} \leq z_1^* \leq d + \lambda \\ R_0 + \frac{\delta}{\lambda} \text{Sin}(\pi(z_1^* - d)), & d + \lambda \leq z_1^* \leq d + 2\lambda \\ R_0 & \text{otherwise.} \end{cases} \quad (1)$$

Clot:

$$\epsilon(z_1^*) = \begin{cases} R_0(c + \sigma \exp(-\frac{\pi^2}{\lambda}(z_1^* - z_d^* - 0.5\lambda)^2)), & d < z_1^* < d + \frac{3\lambda}{2}, \\ cR_0, & \text{otherwise.} \end{cases} \quad (2)$$

where, σ is the maximum height of the clot at the axial position z_d^* , cR_0 is the radius of the inner tube with $c \ll 1$. In Eq. (1), δ represents the maximum height of the stenosis, d is the location of diseased segment.

Blood is assumed to be the suspension of red blood cells(RBCs), platelets, white blood cells, and plasma, etc. The migration of RBCs towards the center of the tube due to fluid shear resulted in the variation of viscosity and increase the fluid velocity towards the center resulting in more variation of RBCs distribution in the tube. To account for this variation of the blood viscosity due to spatial variation of RBCs, we proposed the hematocrit-dependent viscosity model:

$$\mu_f = \mu_0[1 + \gamma_1 h(r_1^*)], \quad (3)$$

where, $h(r_1^*) = h_m[1 - (\frac{r_1^*}{R_0})^m]$, h_m represent the maximum hematocrit at center with γ_1 as constant and $m \geq 2$ represent the exact shape of velocity profile.

2.1 Governing Equations

A uniform radial magnetic field B is applied on the diseased segment. The induced magnetic field is assumed to be negligible as it is very small as compared to the applied magnetic field. Subject to the above mention assumption with the MHD flow interaction, the resultant governing equations becomes [30]:

Continuity

$$\frac{\partial u_1^*}{\partial r_1^*} + \frac{u_1^*}{r_1^* + R^*} + \frac{R^*}{r_1^* + R^*} \frac{\partial w_1^*}{\partial z_1^*} = 0. \quad (4)$$

Momentum (in r_1^* -direction)

$$\begin{aligned} \rho_{hnf} \left[\frac{\partial u_1^*}{\partial t_1^*} + u_1^* \frac{\partial u_1^*}{\partial r_1^*} + \frac{w_1^* R^*}{r_1^* + R^*} \frac{\partial u_1^*}{\partial z_1^*} - \frac{w_1^{*2}}{r_1^* + R^*} \right] &= -\frac{\partial p}{\partial r_1^*} + \mu_{hnf} \left(\frac{\partial^2 u_1^*}{\partial r_1^{*2}} + \frac{1}{r_1^* + R^*} \frac{\partial u_1^*}{\partial r_1^*} \right. \\ &+ \left. \left(\frac{R^*}{r_1^* + R^*} \right)^2 \frac{\partial^2 u_1^*}{\partial z_1^{*2}} - \frac{u_1^*}{(r_1^* + R^*)^2} - \frac{2R^*}{r_1^* + R^*} \frac{\partial w_1^*}{\partial z_1^*} \right) - \frac{\sigma_{hnf} B_0 (-u_1^* + \beta_e w_1^*)}{(1 + \beta_e^2)} \left(\frac{R^*}{r_1^* + R^*} \right)^2 \\ &+ \left(\frac{4}{3} \frac{\partial u_1^*}{\partial r_1^*} - \frac{2}{3} \left(\frac{R^*}{R^* + r_1^*} \frac{\partial w_1^*}{\partial z_1^*} + \frac{u_1^*}{R^* + r_1^*} \right) \right) \frac{\partial \mu_{hnf}}{\partial r_1^*}. \end{aligned} \quad (5)$$

Momentum (in z_1^* -direction)

$$\begin{aligned} \rho_{hnf} \left[\frac{\partial w_1^*}{\partial t_1^*} + u_1^* \frac{\partial w_1^*}{\partial r_1^*} + \frac{R^*}{r_1^* + R^*} \frac{\partial w_1^*}{\partial z_1^*} + \frac{u_1^* w_1^*}{r_1^* + R^*} \right] &= - \left(\frac{R^*}{r_1^* + R^*} \right) \frac{\partial p}{\partial z_1^*} \\ + \mu_{hnf} \left(\frac{\partial^2 w_1^*}{\partial r_1^{*2}} + \frac{1}{r_1^* + R^*} \frac{\partial w_1^*}{\partial r_1^*} + \left(\frac{R^*}{r_1^* + R^*} \right)^2 \frac{\partial^2 w_1^*}{\partial z_1^{*2}} - \frac{w_1^*}{(r_1^* + R^*)^2} + \frac{2R^*}{r_1^* + R^*} \frac{\partial u_1^*}{\partial z_1^*} \right) \\ + \left(\frac{R^*}{R^* + r_1^*} \frac{\partial u_1^*}{\partial z_1^*} + \frac{\partial w_1^*}{\partial r_1^*} - \frac{w_1^*}{R^* + r_1^*} \right) \frac{\partial \mu_{hnf}}{\partial r_1^*} + G(t_1^*) - \frac{\mu_{hnf}}{K} w_1^* \\ - \frac{\sigma_{hnf} B_0^2 (\beta_e u_1^* + w_1^*)}{(1 + \beta_e^2)} \left(\frac{R^*}{r_1^* + R^*} \right)^2. \end{aligned} \tag{6}$$

where, the velocity (u,w) represent the velocity along the radial and axial direction respectively. The flow is independent in θ_1^* direction due to axi-symmetry blood flow in the artery. R^* represent the radius of curvature, t_1^* represent the time, β_e represent the Hall parameter, and K represent the permeability.

The associate dimensional boundary conditions are:

$$\begin{cases} w_1^* = 0 & \text{at} & t_1^* = 0, \\ w_1^* = 0 & \text{at} & r_1^* = \eta(z_1^*) \quad \text{and} \quad r_1^* = \epsilon(z_1^*). \end{cases} \tag{7}$$

The arterial hemodynamic involves the analysis of pressure and waveform that are continuously changing due to the propagation of blood flow from central to peripheral arteries. The expression for axial pressure gradient is represented as [30]:

$$- \frac{\partial p}{\partial z_1^*} = A_0 + A_1 \cos(2\pi\omega_p t_1^*), t > 0. \tag{8}$$

where, $\omega_p t_1^* = 2\pi f_p$ with frequency f_p , A_0 and A_1 represents the mean and pulsatile component of pressure gradient, respectively. The extrinsic periodic body acceleration applied on the axial direction is given as [30]:

$$G(t_1^*) = B_0 \cos(\omega_q t_1^* + \psi), \tag{9}$$

where, ψ is the phase angle, $\omega_q t_1^* = 2\pi f_q$ with f_q as frequency and B_0 as the amplitude for body acceleration, respectively. Table 1 represents the thermophysical parameters for nanofluid and hybrid nanofluid.

2.2 Non-dimensionalization of Governing Equations

Apply the non-dimensional variables into Eqs.1-2, one can obtain non-dimensionalize form of diseased artery:

Stenosis region:

$$\eta(z_1^*) = \begin{cases} 1 - 2\delta^*(z_1^* - d), & d \leq z_1^* \leq d + \frac{1}{2} \\ 1 + 2\delta^*(z_1^* - d - 1), & d + \frac{1}{2} \leq z_1^* \leq d + 1 \\ 1 + \delta^* \text{Sin}(\pi(z_1^* - d)), & d + 1 \leq z_1^* \leq d + 2 \\ 1 & \text{otherwise.} \end{cases} \tag{10}$$

Clot region:

$$\epsilon(z_1^*) = \begin{cases} c + \sigma \exp(-\pi^2(z_1^* - z_d^* - 0.5)^2), & d < z_1^* < d + 3/2, \\ c, & \text{otherwise,} \end{cases} \quad (11)$$

Table 1. Properties & Mathematical expression for nanofluid and hybrid nanofluid

Viscosity	$\mu_{nf} = \frac{\mu_f}{(1-\phi_1)^{2.5}}$ $\mu_{hnf} = \frac{\mu_{nf}}{(1-\phi_1)^{2.5}(1-\phi_2)^{2.5}}$
Density	$\rho_{nf} = (1 - \phi_1)\rho_f + \phi_1\rho_{s_1}$ $\rho_{hnf} = [(1 - \phi_2)\{(1 - \phi_1)\rho_f + \phi_1\rho_{s_1}\}] + \phi_2\rho_{s_2}$
Electrical Conductivity	$\frac{\sigma_{nf}}{\sigma_f} = \frac{\sigma_{s_1} + (m-1)\sigma_f - (m-1)\phi_1(\sigma_f - \sigma_{s_1})}{\sigma_{s_1} + (m-1)\sigma_f + \phi_1(\sigma_f - \sigma_{s_1})}$ $\frac{\sigma_{hnf}}{\sigma_{nf}} = \frac{\sigma_{s_2} + (m-1)\sigma_f - (m-1)\phi_2(\sigma_f - \sigma_{s_2})}{\sigma_{s_2} + (m-1)\sigma_f + \phi_2(\sigma_f - \sigma_{s_2})}$

Table 2. Non-dimensional parameters

$\bar{r}_1^* = \frac{r_1^*}{R_0}$	$\bar{z}_1^* = \frac{z_1^*}{\lambda}$	$\bar{u}_1^* = \frac{\lambda u_1^*}{\delta^* U_0}$	$\bar{w}_1^* = \frac{w_1^*}{U_0}$
$\delta = \frac{\delta^*}{R_0}$	$\bar{t}_1^* = \frac{U_0 t_1^*}{R_0}$	$\bar{R}_c = \frac{R_c}{R_0}$	$\bar{p} = \frac{R_0^2 p}{\mu_0 U_0 \lambda}$
$Re = \frac{U_0 \rho_f R_0}{\mu_f}$	$M^2 = \frac{\sigma_f B_0^2 R_0^2}{\mu_0}$	$Z = \frac{K}{R_0^2}$	$\beta_e = \omega_e \tau_e$

Again, use the non-dimensionalize parameters into Eqs. 4–6, neglecting the bar, and assuming the assumption of fully developed flow, mild stenosis ($\delta^* \ll 1$) with $O(1) = \alpha = \frac{R_0}{\lambda}$, the governing equations become:

$$\frac{dp}{dr_1^*} = 0, \quad (12)$$

$$\begin{aligned} \frac{\rho_{hnf}}{\rho_f} Re \frac{\partial w_1^*}{\partial t_1^*} = & -\frac{R_c}{R_c + r_1^*} \frac{\partial p}{\partial z_1^*} + \frac{\mu_{hnf}}{\mu_0} \left(\frac{\partial^2 w_1^*}{\partial r_1^{*2}} + \frac{1}{r_1^* + R_c} \frac{\partial w_1^*}{\partial r_1^*} \right. \\ & \left. - \frac{w_1^*}{(r_1^* + R_c)^2} \right) - \left(\frac{\partial w_1^*}{\partial r_1^*} + \frac{\partial w}{R_c + r_1^*} \right) \frac{m\beta_1 h_m r_1^{*m-1}}{(1 - \phi_1)^{2.5}(1 - \phi_2)^{2.5}} \\ & + G(t_1^*) - \frac{\mu_{hnf}}{\mu_0} \frac{w_1^*}{Z} - \frac{\sigma_{hnf}}{\sigma_f} \left(\frac{R_c}{r_1^* + R_c} \right)^2 \left(\frac{1}{1 + \beta_e^2} \right) M^2 w_1^*, \end{aligned} \quad (13)$$

The associate boundary conditions are:

$$\begin{cases} w_1^* = 0 & \text{at } t_1^* = 0, \\ w_1^* = 0, & \text{at } r_1^* = \eta(z_1^*) \text{ and } r_1^* = \epsilon(z_1^*). \end{cases} \quad (14)$$

The non-dimensionalize formed for pressure gradient and body acceleration are given as follows:

$$\frac{\partial p}{\partial z_1^*} = B_1(1 + e \cos c_1 t_1^*), \quad G(t_1^*) = B_2 \cos(c_2 t_1^* + \chi), \quad \text{where } B_1 = \frac{A_0 R_0^2}{\mu_0 U_0}, e = \frac{A_1}{A_0}, B_2 = \frac{\bar{A}_0 R_0^2}{\mu_0 U_0}, c_2 = \frac{\bar{\omega}_2 R_0}{U_0}.$$

In hemodynamic flow, the progression of arterial diseases can easily be understood by studying the basic hemodynamic factors like flow rate, impedance and wall shear stress. The mathematical expression for important hemodynamical factors such as wall shear stress, flow rate and resistive impedance are illustrated as [17,21]:

$$\tau_{w_1^*} = \left(\frac{\partial w_1^*}{\partial r_1^*} \right)_{r_1^* = \eta}, \quad (15)$$

$$Q = \int_{\epsilon}^{\eta} w_1^* r_1^* dr_1^*, \quad (16)$$

$$\lambda = \frac{L \left(\frac{\partial p}{\partial z_1^*} \right)}{Q}. \quad (17)$$

3 Solution Process

The governing equations are highly non-linear and coupled, so a robust technique is used to solve these equations. To solve these equations, we employed the Crank-Nicholson method, which is unconditionally stable and second-order convergent in space and time. The partial and spatial derivatives are given as:

$$\frac{\partial w}{\partial r} = \frac{w_{i+1}^k - w_{i-1}^k}{2\Delta r}, \quad \frac{\partial^2 w}{\partial^2 r} = \frac{w_{i+1}^k - 2w_i^k + w_{i-1}^k}{(\Delta x)^2}, \quad \frac{\partial w}{\partial t} = \frac{w_i^{k+1} - w_i^k}{\Delta t}. \quad (18)$$

The flow chart of the schematic representation of the work plan is depicted in Fig. 2. The domain is divided into $N + 1 \times M + 1$ grid points, where N denotes the grid point in the spatial direction and M denotes the grid point in the time direction. The subscript i and j -designate for the nodal point in spatial and time direction, respectively. The value of w at initial time $t = 0$ is known due to the given condition. Every nodal point in the i^{th} level constitutes the tridiagonal system, which is solved using the Tri-diagonal Matrix Algorithm (TDMA). Thus, the value of w is known for each $(j + 1)^{th}$ time level. Default values of parameters and thermodynamical properties of nanoparticles used in the present study are depicted in Table 3 and the Table 4 respectively.

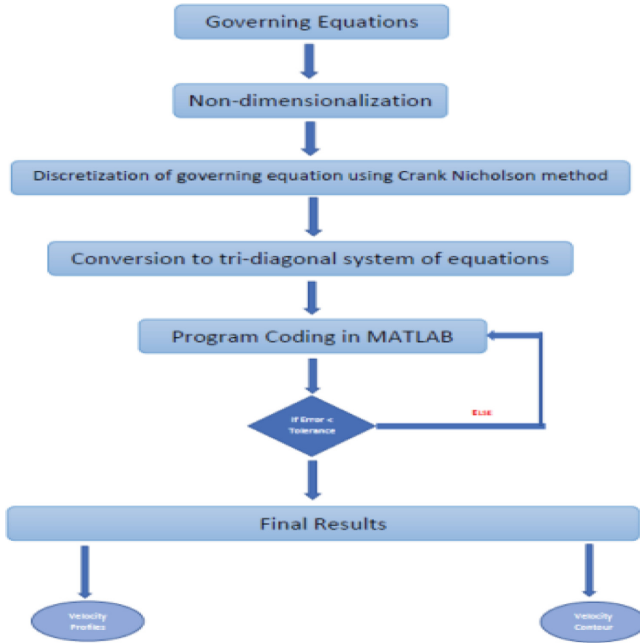


Fig. 2. Flow chart

Table 3. Dimensionless parameters

Parameter	ϕ_1	ϕ_2	δ	h_m	Re	M	R_c	β_e	e	B_1	B_2	Z
Value	0.02	0.02	0.1	1	2	1	3	0.5	0.2	0.25	5	3

Table 4. Thermophysical Properties

Thermophysical Properties	Blood	Gold	Graphene
Density [$\rho(Kg/m^3)$]	1063	19320	1800
Electrical Conductivity [$\sigma(S/m)$]	6.67×10^{-1}	4.52×10^7	6.3×10^7

4 Result and Discussion

The current study is validated using the published work of Elnaqeeb et al. [4], as shown in Fig. 3. To validate the result of present study with [4], we have reduced our model by considering straight artery assumption $R_c = 0$. The Copper blood flow model is considered instead of (Au-GO). We ignore the multiple stenosis and used the stenosis model for $n = 2$ used by [4]. The velocity profile is drawn by assuming the same set of values as in [4]. There is a good agreement between velocity trend in our research work and trend of velocity profile in ref. [4]. In the present model, we have considered the curved artery as in more generalized cases,

the artery is not straight. Furthermore, we have included hematocrit dependent viscosity model on which very researchers published their work. It is one of the most essential parameter as its depict the picture of the spatial distribution of RBCs. The influence of hematocrit parameter on the velocity profile is depicted in the Fig. 4.

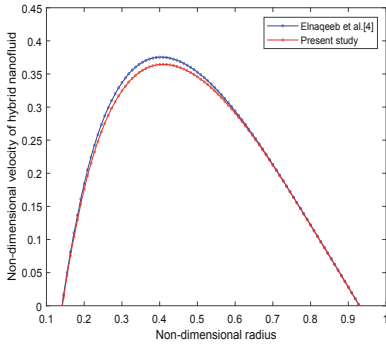


Fig. 3. Velocity profile for stenosis shape parameter $n = 2$

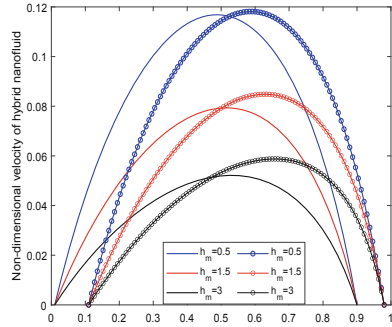


Fig. 4. Velocity profile for varying h_m

4.1 Velocity Profile

Blood undergoes a significant electromotive force when an external magnetic field is present. Haemoglobin contains magnetic iron ions, which significantly react to the surrounding magnetic field and affect blood flow. Red blood cells (RBCs) are magnetically repelled due to their inherent paramagnetic composition. From Fig. 4, we can infer that the velocity profile decreases as the hematocrit parameter h_m enhances. The reduction in velocity profile is due to the increase in the blood viscosity. Figure 5 depicts the relationship between velocity profiles and magnetic field parameter M for clot and stenotic regions. The graph shows that the velocity profile in both cases will be higher in the absence of a magnetic field. As the value of the M increases from 0 to 4, the fluid velocity decreases as it experiences a resistive force known as Lorentz force. Figure 6 illustrates the effect of Hall parameter β_e on the velocity profile. The hall currents are induced due to the collision of the electrons under the action of a strong magnetic field that generates electromagnetic forces resulting in the modifying nature of the current density. It is observed from the figure that the velocity increases with an increase in the Hall parameter. This has happened because an upsurge in the Hall parameter signifies escalation in collision time or electron frequency, thus, assisting in the fluid velocity.

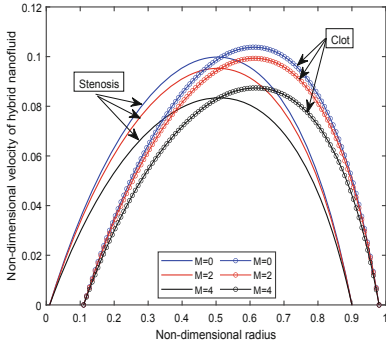


Fig. 5. Velocity profile for varying M

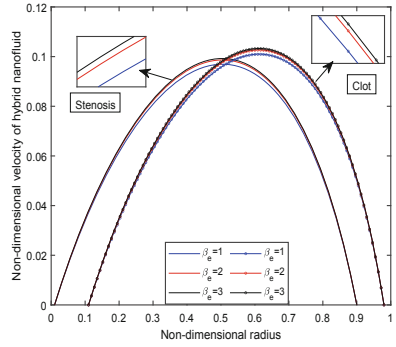


Fig. 6. Velocity profile for varying β_e

4.2 Flow Rate, Wall Shear Stress and Impedance

Figure 7 depicts the increment in flow rate with an upsurge in the radius of curvature parameter R_c . This increase may be explained by the fact that when the parameter R_c increases, the curved channel shrinks to a straight tube. The higher the value of R_c , the less obstruction comes in the fluid path, resulting in an upsurge in velocity profile with an increase in R_c . This study is helpful as it shows that for smaller value of R_c , there is a significant growth in fear of deposition of plaque (lipid). A very less study has been conducted to show the radius of curvature effect, as in more generalised cases the artery is not always straight. Thus, it is essential to consider this effect into the model. It is noted from the Fig. 8 that the flow rate decreases as the magnetic field parameter M increases from 0 to 4. The non-dimensional velocity profile for M follows the same pattern as that of [28, 29]. The flow rate is constant till $z = 2$; afterwards, the flow rate varies due to clot and stenosis, and it again attains its constant values after $z = 4$.

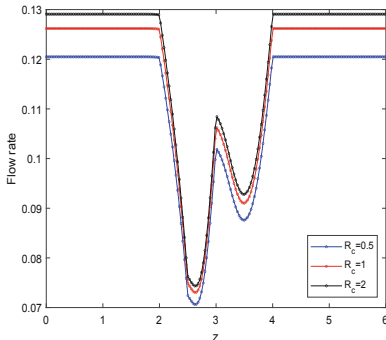


Fig. 7. Flow rate for varying R_c

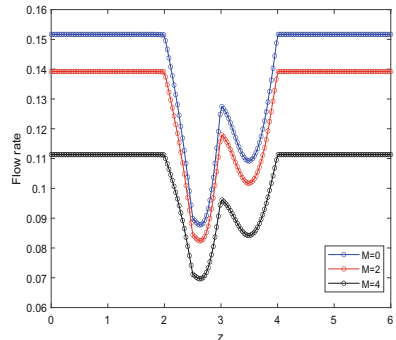


Fig. 8. Flow rate for varying M

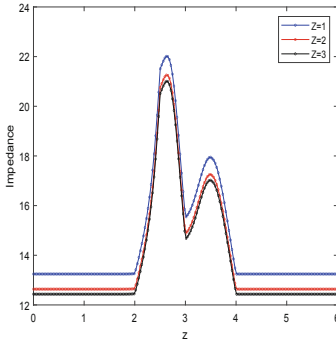


Fig. 9. Impedance for varying Z

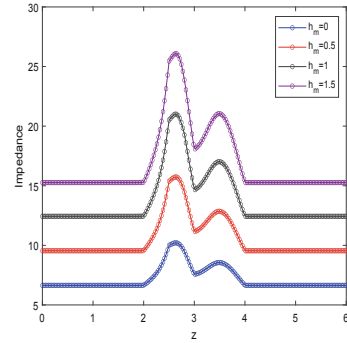


Fig. 10. Impedance for varying h_m

The existence of haemoglobin and magnetic iron oxide particles makes the blood to be profoundly impacted by a magnetic field. When a magnetic field is applied to an artery carrying blood, a strong electromotive field is generated known as the Lorentz force that results in the slowing down of the blood’s flow. Thus, the fluid experiences the retarding force with an increment in parameter M , which resists the fluid flow, as observed in Fig. 8. The effect of the permeability parameter Z on the Impedance profile is demonstrated in Fig. 9. The ratio of the empty space to the total volume of the fluid medium is the porosity of the material [31]. Due to the dispersion of artery-clogging fatty cholesterol, blood clots, and plaques in the arterial lumen, blood is thought of as a porous medium. Increases in porosity result in more empty space, which in turn leads to less resistance to flow and increased blood velocity. As a result, the fluid velocity increases with the rise in the permeability parameter due to the less obstruction in its path. Thus, the impedance profile shows the declining nature as the permeability parameter Z increases. Figure 10 is plotted to see the variation of impedance profile with hematocrit dependent viscosity h_m . From these plots, it can be inferred that the impedance profile also increases with an increase in h_m . This has happened due to increases in fluid viscosity that resist the fluid motion and amplify the impedance profile. In arterial blood flow, the term “wall shear stress” refers to the force exerted per unit area on the fluid by the arterial wall (and vice versa) in a direction that is parallel to the local tangent plane. It is generally known that regions of arteries with either low or fluctuating wall shear stress seem more susceptible to atherosclerosis. The influence of the pressure gradient parameter B_1 on the WSS profile is seen in Fig. 11. The figure demonstrates the periodic nature and enhances with an increment in the B_1 parameter. The role of WSS with body acceleration parameter B_2 is depicted in Fig. 12. It is observed that the WSS profile varies periodically with time. As the magnitude of B_2 increases, the fluid velocity also increases, which leads to an enhancement in the amplitude of B_2 .

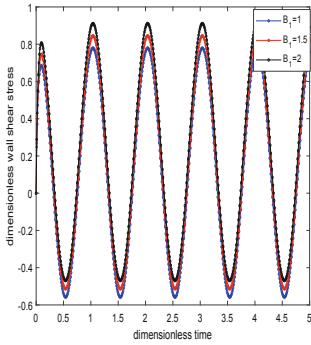


Fig. 11. Variation in WSS with varying B_1

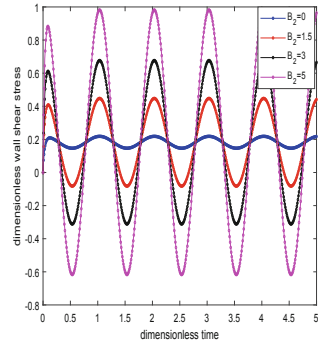


Fig. 12. Variation in WSS with varying B_2

4.3 Velocity Contour

Figure 13 illustrates the velocity contour for the varying height of stenosis and clot. It can be noted from the figure that the velocity decreases with an increase in the clot and stenosis height. There is a difference in the centre area that is occupied by the clot and the stenosis, despite the fact that the greatest velocity that can be achieved in each of the three scenarios being the same, which is 16×10^{-4} . As shown in the figure, the amplitude of the fluid velocity falls as the height of the clot and stenosis grows, which makes the flow of fluid more difficult to navigate.

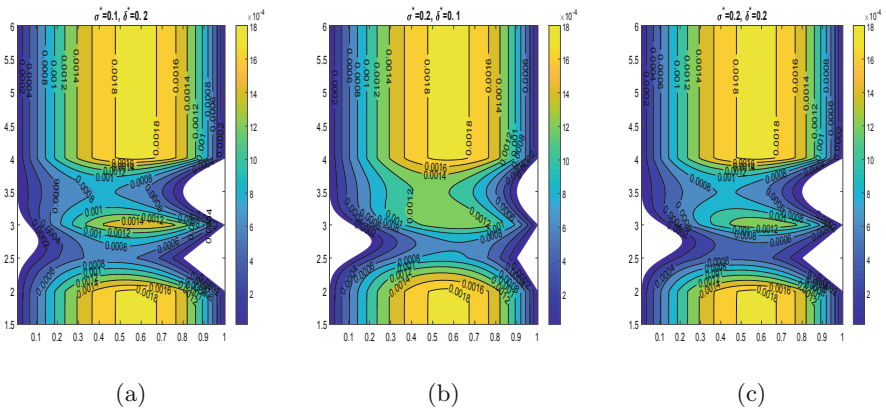


Fig. 13. Variation in blood flow patterns for diseased artery segment (a) $\sigma^* = 0.1, \delta^* = 0.2$, (b) $\sigma^* = 0.2, \delta^* = 0.1$ (c) $\sigma^* = 0.2, \delta^* = 0.2$.

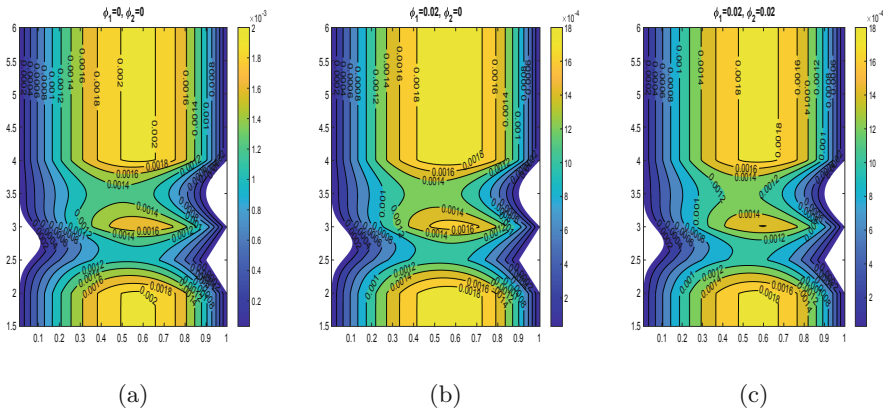


Fig. 14. Variation in blood flow patterns for different volume fractions of nanoparticles, (a) $\phi_1 = 0, \phi_2 = 0$, (b) $\phi_1 = 0.02, \phi_2 = 0$, (c) $\phi_1 = 0.02, \phi_2 = 0.02$.

Figure 14 highlights the effect of nanoparticles concentration ϕ_1 and ϕ_2 on the velocity contour. Figure 14a signifies the situation of pure blood when no nanoparticle is added. As we insert the gold nanoparticles into the blood, the fluid velocity decreases, as depicted in Fig. 14b. Further, the magnitude of the fluid velocity in the core area of the diseased artery is reduced as a result of the incorporation of graphene oxide with gold nanoparticles. Therefore, it could be beneficial for surgeons to manage the flow of blood.

5 Conclusion

A detailed study has been carried out to study the multiple stenotic arteries with thrombosis. The flow is subjected to the strong radial magnetic field, and the curvilinear coordinate is adapted to mimic the blood flow. There has been some thought given to the possibility of using a hybrid nanofluid created by suspending Au-GO nanoparticles in blood. Because of the extreme non-linearity of the governing equations, the robust implicit Crank-Nicholson method has been used. Starting with a discretization of the governing equations, a tridiagonal system is constructed for each nodal point on the $(i + 1)^{th}$ level, and then the Tri-diagonal Matrix Algorithm (TDMA) is used to solve it. The velocity w at each mesh point may be calculated by using this method again for every $(j + 1)^{th}$ time step. The effect of different pertinent parameters on velocity, temperature, wall shear stress, Impedance and velocity contour is displayed. The significant outcomes of the study are summarised below:

- The significant decline in flow velocity is observed for an increase in the stenosis and clot height.
- It has been observed that raising the Hall parameter induces an increase in fluid velocity owing to an increase in collision time or electron frequency, hence assisting fluid flow.

- Au-GO/blood hybrid nanoparticles have a higher velocity profile than pure blood and unitary nanoparticles.
- Increasing the permeability parameter Z allows the fluid to travel more freely, aiding the flow and decreasing the impedance profile.

The findings of this research may be useful in diagnostic imaging techniques for identifying vascular anomalies, such as magnetic resonance angiography (MRA). The hybrid nanoparticles Au-GO/blood have been studied due to their potential applicability in nanomedicine and biomedicine. Various stenosis forms (such as triangular and elliptical) and their tapering effects may be investigated in future studies, as can the interaction of nanoparticle shapes with permeable artery walls.

References

1. Prakash, O., Makinde, O.D., Singh, S.P., Jain, N., Kumar, D.: Effects of stenoses on non-Newtonian flow of blood in blood vessels. *Int. J. Biomath.* **8**(01), 1550010 (2015)
2. Doffin, J., Chagneau, F.: Oscillating flow between a clot model and a stenosis. *J. Biomech.* **14**(3), 143–148 (1981)
3. Stroy, J., Beaudoin, A., Brands, D., Adelman, B.: Analysis of shear stress and hemodynamic factors in a model of coronary artery stenosis and thrombosis. *Am. J. Physiol. Heart Circ.* **265**(5), H1787–H1796 (1993)
4. Elnaqeeb, T., Mekheimer, K.S., Alghamdi, F.: Cu-blood flow model through a catheterized mild stenotic artery with a thrombosis. *Math. Biosci.* **282**, 135–146 (2016)
5. Sultan, F., Khan, N.A., Qasim, M., Afridi, M.I.: Numerical simulation of the flow of nano-Eyring-Powell fluid through a curved artery with time-variant stenosis and aneurysm. *Nihon Reorogi Gakkaishi* **47**(2), 75–85 (2019)
6. Akhtar, S., McCash, L.B., Nadeem, S., Saleem, A.: Scientific breakdown for physiological blood flow inside a tube with multi-thrombosis. *Sci. Rep.* **11**(1), 6718 (2021)
7. Mekheimer, K.S., El Kot, M.A.: Influence of magnetic field and Hall currents on blood flow through a stenotic artery. *Appl. Math. Mech.* **29**(8), 1093–1104 (2008)
8. Mishra, A., Sharma, B.K.: MHD mixed convection flow in a rotating channel in the presence of an inclined magnetic field with the Hall effect. *J. Eng. Phys. Thermophys.* **90**(6), 1488–1499 (2017)
9. Das, S., Barman, B., Jana, R.N., Makinde, O.D.: Hall and ion slip currents' impact on electromagnetic blood flow conveying hybrid nanoparticles through an endoscope with peristaltic waves. *BioNanoScience* **11**(3), 770–792 (2021)
10. Changdar, S., De, S.: Investigation of nanoparticle as a drug carrier suspended in a blood flowing through an inclined multiple stenosed artery. *Bionanoscience* **8**(1), 166–178 (2018)
11. Mekheimer, K.S., Hasona, W.M., Abo-Elkhair, R.E., Zaher, A.Z.: Peristaltic blood flow with gold nanoparticles as a third grade nanofluid in catheter: application of cancer therapy. *Phys. Lett. A* **382**(2–3), 85–93 (2018)
12. Kang, S., et al.: Gold nanoparticle/graphene oxide hybrid sheets attached on mesenchymal stem cells for effective photothermal cancer therapy. *Chem. Mater.* **29**(8), 3461–3476 (2017)

13. Liu, J., Dong, J., Zhang, T., Peng, Q.: Graphene-based nanomaterials and their potentials in advanced drug delivery and cancer therapy. *J. Control. Release* **286**, 64–73 (2018)
14. Khazayinejad, M., Hafezi, M., Dabir, B.: Peristaltic transport of biological graphene-blood nanofluid considering inclined magnetic field and thermal radiation in a porous media. *Powder Technol.* **384**, 452–465 (2021)
15. Sindhu, S., Gireesha, B.J., Sowmya, G., Makinde, O.D.: Hybrid nanoliquid flow through a microchannel with particle shape factor, slip and convective regime. *Int. J. Numer. Methods Heat Fluid Flow* **32**(10), 3388–3410 (2022)
16. Gandhi, R., Sharma, B.K., Kumawat, C., Bég, O.A.: Modeling and analysis of magnetic hybrid nanoparticle (Au-Al₂O₃/blood) based drug delivery through a bell-shaped occluded artery with joule heating, viscous dissipation and variable viscosity effects. *Proc. Inst. Mech. Eng. Part E: J. Process Mech. Eng.* **236**(5), 2024–2043 (2022)
17. Sharma, B.K., Gandhi, R., Bhatti, M.M.: Entropy analysis of thermally radiating MHD slip flow of hybrid nanoparticles (Au-Al₂O₃/Blood) through a tapered multi-stenosed artery. *Chem. Phys. Lett.* **790**, 139348 (2022)
18. Singh, J., Rashidi, M.M., Kumar, D., et al.: A hybrid computational approach for Jeffery–Hamel flow in non-parallel walls. *Neural Comput. Appl.* **31**, 2407–2413 (2019). <https://doi.org/10.1007/s00521-017-3198-y>
19. Singh, J., Kumar, D., Baleanu, D., et al.: A hybrid analytical algorithm for thin film flow problem occurring in non-Newtonian fluid mechanics. *Ain Shams Eng. J.* **12**(2), 2297–2302 (2021)
20. Tripathi, B., Sharma, B.K.: Effect of variable viscosity on MHD inclined arterial blood flow with chemical reaction. *Int. J. Appl. Mech. Eng.* **23**(3), 767–785 (2018)
21. Kumawat, C., Sharma, B.K., Mekheimer, K.S.: Mathematical analysis of two-phase blood flow through a stenosed curved artery with hematocrit and temperature dependent viscosity. *Phys. Scr.* **96**(12), 125277 (2021)
22. Khanduri, U., Sharma, B.K.: Entropy analysis for MHD flow subject to temperature-dependent viscosity and thermal conductivity. In: Banerjee, S., Saha, A. (eds.) *Nonlinear Dynamics and Applications*. Springer Proceedings in Complexity, pp. 457–471. Springer, Cham (2022). https://doi.org/10.1007/978-3-030-99792-2_38
23. Prakash, J., Makinde, O.D.: Radiative heat transfer to blood flow through a stenotic artery in the presence of magnetic field. *Lat. Am. Appl. Res.* **41**(3), 273–277 (2011)
24. Sharma, B.K., Khanduri, U., Mishra, N.K., Chamkha, A.J.: Analysis of Arrhenius activation energy on magnetohydrodynamic gyrotactic microorganism flow through porous medium over an inclined stretching sheet with thermophoresis and Brownian motion. *Proc. Inst. Mech. Eng. Part E: J. Process Mech. Eng.* 09544089221128768 (2022)
25. Khanduri, U., Sharma, B.K.: Hall and ion slip effects on hybrid nanoparticles (Au-GO/blood) flow through a catheterized stenosed artery with thrombosis. *Proc. Inst. Mech. Eng., Part C: J. Mech. Eng. Sci.* 09544062221136710 (2022)
26. Sharma, B.K., Kumar, A., Gandhi, R., Bhatti, M.M.: Exponential space and thermal-dependent heat source effects on electro-magneto-hydrodynamic Jeffrey fluid flow over a vertical stretching surface. *Int. J. Mod. Phys. B* **36**(30), 2250220 (2022)
27. Gupta, S., Kumar, D., Singh, J.: Analytical study for MHD flow of Williamson nanofluid with the effects of variable thickness, nonlinear thermal radiation and

- improved Fourier's and Fick's Laws. SN Appl. Sci. **2**(3), 1–12 (2020). <https://doi.org/10.1007/s42452-020-1995-x>
28. Tassaddiq, A., Khan, I., Nisar, K.S., Singh, J.: MHD flow of a generalized Casson fluid with Newtonian heating: a fractional model with Mittag-Leffler memory. Alex. Eng. J. **59**(5), 3049–3059 (2020)
 29. Sheikh, N.A., Ching, D.L.C., Khan, I., Kumar, D., Nisar, K.S.: A new model of fractional Casson fluid based on generalized Fick's and Fourier's laws together with heat and mass transfer. Alex. Eng. J. **59**(5), 2865–2876 (2020)
 30. Sharma, B.K., Kumawat, C., Vafai, K.: Computational biomedical simulations of hybrid nanoparticles (Au-Al₂O₃/blood-mediated) transport in a stenosed and aneurysmal curved artery with heat and mass transfer: Hematocrit dependent viscosity approach. Chem. Phys. Lett. **800**, 139666 (2022)
 31. Sharma, B.K., Khanduri, U., Mishra, N.K., Mekheimer, K.S.: Combined effect of thermophoresis and Brownian motion on MHD mixed convective flow over an inclined stretching surface with radiation and chemical reaction. Int. J. Mod. Phys. B **2350095** (2022)



A Computational Investigation of the Characteristics of Velocity Slips and Convective Boundary Conditions in Maxwell Nanofluid Flow over a Permeable Stretching Surface with Activation Energy

Bidyasagar Kumbhakar¹, Manik Das^{1(✉)}, and Jagdev Singh²

¹ Department of Mathematics, National Institute of Technology Meghalaya,
Shillong 793003, India
manikdas@nitm.ac.in

² Department of Mathematics, JECRC University, Jaipur 303905, Rajasthan, India

Abstract. In this study, we analyze the effects of velocity slips and convective boundary conditions in the flow and heat transfer of Maxwell nanofluid across a stretching sheet considering magnetic field, thermal radiation, chemical reaction, and activation energy. The influence of Brownian diffusion and thermophoresis are considered using Buongiorno's nanofluid model. By applying suitable similarity variables, the governing Maxwell nanofluid flow equations, which include the momentum, energy, and nanoparticle volume fraction are simplified to nonlinear differential equations. MATLAB's *bvp4c* finite difference tool is used to solve the nondimensionalized differential equations. In order to illustrate the influence of physical factors on velocity, temperature, and nanoparticle volume fraction, the numerical solutions are shown graphically. In addition, the skin friction, rate of heat transmission, and mass transfer are all given physical interpretations. The current analysis demonstrates that the velocity slip and suction parameters significantly reduce the velocity. Increased thermal radiation and Biot number for temperature raise the temperature profile. Further, the activation energy and thermophoresis factors lead to a decrease in the mass transfer rate, while the Lewis number and Biot number due to concentration contribute to an increase.

Keywords: Hall effect · Radiation absorption · Thermal radiation · Chemical reaction · Convective heating · Activation energy

Nomenclature

T	Temperature	K_1	Chemical reaction parameter
c	Velocity ratio parameter	h_2	Convective mass transfer coefficient
u, v, w	Velocity components	k_r^2	Chemical reaction coefficient
M	Magnetic parameter	B_0	Constant magnetic field
x, y, z	Space coordinates	D_T	Coefficient of thermal diffusion
K	Deborah number	Bi_1	Biot number for temperature
n	Fitted rate constant	Bi_2	Biot number for concentration
Le	Lewis number	w_0	Suction velocity
u_w, v_w	Stretching velocities	Greek Symbols	
E	Dimensionless activation energy	α_1	Velocity slip parameter
k	Thermal conductivity	μ	Dynamic viscosity
k^*	Mean absorption coefficient	θ_w	Temperature ratio parameter
T_∞, C_∞	Ambient temperature and concentration	κ	Boltzmann constant
S	Suction parameter	ρ	Density
Rd	Thermal radiation parameter	θ	Dimensionless temperature
Pr	Prandtl number	λ	Fluid relaxation time
c_p	Specific heat	α	Thermal diffusivity
C	Concentration	ν	Kinematic viscosity
Nt	Thermophoresis parameter	ϕ	Dimensionless concentration
T_w, C_w	Surface temperature and concentration	σ^*	Stefan-Boltzmann constant
Nb	Brownian motion parameter	β	Slip coefficient
E_a	Activation energy	σ	Electrical conductivity
D_B	Mass diffusivity	τ	Ratio between effective heat capacity of nanoparticles and base fluid
h_1	Convective heat transfer coefficient		

1 Introduction

In the petroleum industry and engineering applications, non-Newtonian fluid flow coupled with heat and mass transfer is of significant interest. Desalination, refrigeration and air conditioning, compact heat exchangers, chemical processing equipment, solid matrix heat exchangers, solar power collectors, and other applications [1, 2] are examples. The Laplace and Hankel transforms were used to calculate the velocity field and shear stress field of a generalised Maxwell fluid that flows between two infinite coaxial circular cylinders [3]. By employing the multi-step differential transform approach, Keimanesh et al. [4] investigated third grade non-Newtonian fluid flow between two parallel plates. Nadeem et al. [5] presented a model of a two-dimensional Williamson fluid past a stretched sheet that they had developed. Seyedi et al. [6] investigated effect of natural convection on non-Newtonian fluid flow between two vertical plates using Galerkin interpolation scaling functions.

Thermal radiation effects on nanofluid flow and heat transfer are becoming increasingly popular because nanofluids have a variety of characteristics. In addition, the influence of radiative heat transfer has increased dramatically in the design of modern energy conversion systems [7], plasma studies, agriculture, and petroleum industries [8,9]. Numerous research have been conducted in this area to investigate the impacts of heat radiation in various areas. A two-dimensional MHD mixed convection viscoelastic fluid flow across a porous wedge with heat radiation was investigated by Rashidi et al. [10], who sought an analytical solution. Daniel and Daniel [11] did research on the theoretical impact of buoyancy and heat radiation on MHD flow past a stretched porous sheet. Pal and Mandal [12] discussed the influence of thermal radiation, non-uniform heat source/sink and suction on MHD micropolar nanofluid flow across a stretched sheet. MHD viscous fluid was flowed over a horizontally rotating disc, and Shah et al. [13] explored the effect of non-linear thermal radiations on the unsteady flow of the fluid. Effect of thermal radiation on MHD stagnation-point flow over a nonlinearly moving sheet was described by Jamaludin et al. [14] with mathematical solutions. Tarakaramu et al. [15] investigated the impact of non-linear thermal radiation and Joule heating on the flow of a three-dimensional viscoelastic nanofluid via a stretched surface.

In various physical scenarios involving suspensions, foams and polymer solutions [16], the assumption of slip flow boundary condition is necessary. The no-slip boundary condition is involved in the research listed above. With the Soret and Dufoué effect, Babu and Sandeep [17] investigated multiple slip effects on the magnetohydrodynamic Williamson fluid flow past a variable thickness stretching sheet. Using a non-isothermal radiate wedge submerged in ferrofluid, Rashad [18] analysed the impact of partial slip and thermal radiation on MHD boundary layer flow in his research. With entropy analysis, Ellahi et al. [19] looked at the combined impact of MHD and slip on a flat moving plate over a wide range of physical factors. Das et al. [20] examined multiple slips as well as nonlinearly changing thermal radiation on a 3D MHD nonlinear convective tangent hyperbolic nanofluid flow generated by a bidirectional stretching surface with Soret and Dufour impacts.

In the investigation of a number of physical phenomena, including engineering and oil storage, activation energy is often taken into consideration. A few theoretical studies that discuss the function of activation energy in fluid dynamics are currently available. Numerous uses of Arrhenius activation energy, as well as chemical reactions, have made fluid dynamics an appealing area for researchers. The least amount of energy required to stimulate the particles or molecules in which physical transit occurs is known as activation energy. This is due to the fact that different chemical processes need some amount of energy merely to begin. Other uses of activation energy include atomic processes, the discovery of compounds, and thermal lubricant recovery [21–23]. Fayyadh et al. [24] investigated the magneto-flow and heat transfer of the Carreau nanofluids model in the presence of Arrhenius activation energy and chemical reaction toward a stretching/shrinking surface. Akbar et al. [25] studied the effects of gyrotactic motile

microorganisms and Arrhenius activation on the bioconvection peristaltic transport of nanofluid. They also considered variable viscosity, Brownian diffusion, porous medium, mixed convection, nonuniform heat absorption/generation, viscous dissipation, and thermophoresis diffusion. Shoaib et al. [26] examined the significance of activation energy during chemical reactions, temperature gradient, and thermal radiations of 3-D steady magnetite Casson nanofluid flow over an oscillating disk.

Convective heating is very common in engineering practises such as nuclear reactors, gas turbines and thermal energy storage [27,28]. These activities generate a high temperature, which is transferred to the flow via the convective boundary condition. To better understand the impact of convective boundary conditions on the MHD flow of nanofluids near a stretching rotating disc with partial slip effects, Mustafa and Khan [29] carried out a numerical study. On mixed convection MHD micropolar fluid with non-linear stretched sheet, Patel and Singh [30] investigated the impacts of convective heat boundary condition, viscous dissipation and Joule heating, among other things. MHD Casson fluid flow across an exponentially extending curved sheet was studied by Kumar et al. [31] and shown to be affected by convective heating, thermal radiation and Joule heating. Das et al. [32] explored effects of convective heating, velocity slips, and activation energy on unsteady MHD 3D Carreau nanofluid flow over a stretching sheet. Mandal et al. [33] examined the convective heat transfer and entropy generation of magnetohydrodynamic Maxwell nanofluid flow including gyrotactic microorganisms along a stretching cylinder with heat source and chemical reaction.

To the best of the authors' knowledge, no studies have reported the impacts of velocity slip, activation energy, and convective heating on Maxwell nanofluid to this day. Hence, the purpose of this study is to investigate the effects of velocity slip, activation energy, and convective heating on MHD Maxwell nanofluid flow via a permeable stretching surface when thermal radiation is present. The problem of non Newtonian nanofluid flow across a stretched surface is extremely helpful in gas turbines, aerodynamic heating, food processes, biomedicines, polymer processing, and other fields. In order to convert the dimensional governing equations into their dimensionless counterparts, proper similarity transformations have been used. The *bvp4c* solver in MATLAB is applied to simulate reduced highly nonlinear ordinary differential equations. The effects of significant factors on the momentum, temperature, concentration, and skin friction coefficients, as well as the Nusselt and Sherwood numbers, are graphically depicted.

2 Mathematical Modelling

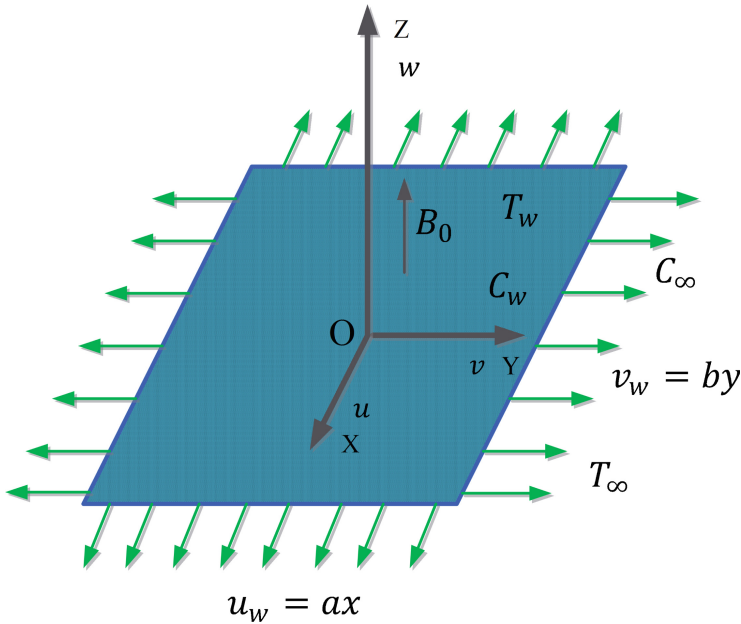


Fig. 1. Geometry of the flow problem

Consider a 3D Maxwell nanofluid flow across a stretched surface in the xy -plane, with the fluid at $z \geq 0$. In the x -direction, the sheet is stretched with a linear velocities of $u_w = ax$ and $v_w = by$ (a and b being positive constants). We'll call these two values T_w and C_w , the surface temperatures and concentrations. T_∞ and C_∞ , on the other hand, represent the temperature and concentration far away from the surface, as illustrated in Fig. 1. The stretched surface is subjected to a magnetic force of strength B_0 , which is applied normal to the surface. Thermal radiation and activation energy are considered to study the fluid flow. Another consideration is that the flow field does not have any polarization of charges since no external electric field is applied, which corresponds to the condition when no energy is injected or withdrawn from the fluid by electrical methods. Furthermore, a fluid with a low magnetic Reynolds number is thought to be a metallic liquid or partly ionized. So fluid motion's effect on the induced magnetic field is minuscule in compared to the applied magnetic field. The governing equations may be reconstructed on the basis of the aforementioned flow assumptions [34,35]:

$$\frac{\partial u}{\partial x} + \frac{\partial v}{\partial y} + \frac{\partial w}{\partial z} = 0, \tag{1}$$

$$\begin{aligned}
 u \frac{\partial u}{\partial x} + v \frac{\partial u}{\partial y} + w \frac{\partial u}{\partial z} + \lambda \left(u^2 \frac{\partial^2 u}{\partial x^2} + v^2 \frac{\partial^2 u}{\partial y^2} + 2uv \frac{\partial^2 u}{\partial x \partial y} + 2uw \frac{\partial^2 u}{\partial x \partial z} + 2vw \frac{\partial^2 u}{\partial y \partial z} \right) \\
 = \nu \frac{\partial^2 u}{\partial z^2} - \frac{\sigma B_0^2}{\rho_f} \left(u + \lambda w \frac{\partial u}{\partial z} \right), \tag{2}
 \end{aligned}$$

$$\begin{aligned}
 u \frac{\partial v}{\partial x} + v \frac{\partial v}{\partial y} + w \frac{\partial v}{\partial z} + \lambda \left(u^2 \frac{\partial^2 v}{\partial x^2} + v^2 \frac{\partial^2 v}{\partial y^2} + 2uv \frac{\partial^2 v}{\partial x \partial y} + 2vw \frac{\partial^2 v}{\partial y \partial z} + 2uw \frac{\partial^2 v}{\partial x \partial z} \right) \\
 = \nu \frac{\partial^2 v}{\partial z^2} - \frac{\sigma B_0^2}{\rho_f} \left(v + \lambda w \frac{\partial v}{\partial z} \right), \tag{3}
 \end{aligned}$$

$$u \frac{\partial T}{\partial x} + v \frac{\partial T}{\partial y} + w \frac{\partial T}{\partial z} = \alpha \frac{\partial^2 T}{\partial z^2} + \tau \left\{ D_B \frac{\partial T}{\partial z} \frac{\partial C}{\partial z} + \frac{D_T}{T_\infty} \left(\frac{\partial T}{\partial z} \right)^2 \right\} - \frac{1}{(\rho c_p)_f} \frac{\partial q_r}{\partial z}, \tag{4}$$

$$u \frac{\partial C}{\partial x} + v \frac{\partial C}{\partial y} + w \frac{\partial C}{\partial z} = D_B \frac{\partial^2 C}{\partial z^2} + \frac{D_T}{T_\infty} \frac{\partial^2 T}{\partial z^2} - k_r^2 (C - C_\infty) \left(\frac{T}{T_\infty} \right)^n e^{\left(\frac{-E_a}{\kappa T} \right)}. \tag{5}$$

The following are the physical boundary conditions for the present problem [36–38]:

$$\left. \begin{aligned}
 u - ax + \lambda \left(u \frac{\partial u}{\partial x} - au + v \frac{\partial u}{\partial y} + w \frac{\partial u}{\partial z} \right) &= \beta \frac{\partial u}{\partial z}, \quad v - by + \lambda \left(u \frac{\partial v}{\partial x} - bv + v \frac{\partial v}{\partial y} + w \frac{\partial v}{\partial z} \right) = \beta \frac{\partial v}{\partial z}, \quad w = w_0, \\
 -k \frac{\partial T}{\partial z} &= h_1 (T_w - T), \quad -D_B \frac{\partial C}{\partial z} = h_2 (C_w - C), \quad \text{at } z = 0, \\
 u \rightarrow 0, \quad v \rightarrow 0, \quad T \rightarrow T_\infty, \quad C \rightarrow C_\infty &\quad \text{as } z \rightarrow \infty.
 \end{aligned} \right\} \tag{6}$$

The following Rosseland's estimate for an optically thick fluid is used to approximate the radiative heat flux q_r [39]:

$$q_r = - \frac{16\sigma^* T^3}{3k^*} \frac{\partial T}{\partial z}. \tag{7}$$

The energy equation has the following form when expression (7) is applied to Eq. (4):

$$u \frac{\partial T}{\partial x} + v \frac{\partial T}{\partial y} + w \frac{\partial T}{\partial z} = \alpha \frac{\partial^2 T}{\partial z^2} + \tau \left\{ D_B \frac{\partial T}{\partial z} \frac{\partial C}{\partial z} + \frac{D_T}{T_\infty} \left(\frac{\partial T}{\partial z} \right)^2 \right\} + \frac{16\sigma^* T^2}{(3\rho c_p)_f k^*} \left\{ T \frac{\partial^2 T}{\partial z^2} + 3 \left(\frac{\partial T}{\partial z} \right)^2 \right\}. \tag{8}$$

The following similarity variables are included in order to achieve similar solutions for Eqs. (2), (3), (8), and (5), subject to the boundary constraints (6):

$$u = axf'(\eta), \quad v = ayg(\eta), \quad w = -\sqrt{av}(f(\eta) + g(\eta)), \quad \theta(\eta) = \frac{T - T_\infty}{T_w - T_\infty}, \quad \phi(\eta) = \frac{C - C_\infty}{C_w - C_\infty}, \quad \eta = z\sqrt{\frac{a}{\nu}}. \tag{9}$$

The following ordinary differential equations result from substituting the aforementioned similarity variables in Eqs. (2), (3), (8), and (5):

$$f'''' - f'^2 + (MK + 1)(f + g)f'' + K(2f'(f + g)f'' - (f + g)^2 f''') - Mf' = 0, \tag{10}$$

$$g'''' - g'^2 + (MK + 1)(f + g)g'' + K(2g'(f + g)g'' - (f + g)^2 g''') - Mg' = 0, \tag{11}$$

$$\theta'' + Pr(f + g)\theta' + PrNb\theta'\phi' + PrNt(\theta')^2 + \frac{4}{3}Rd\{1 + \theta(\theta_w - 1)\}^2\left[3(\theta')^2(\theta_w - 1) + \{1 + \theta(\theta_w - 1)\}\theta''\right] = 0, \tag{12}$$

$$\phi'' + PrLe(f + g)\phi' + \frac{Nt}{Nb}\theta'' - PrLeK_1(1 + (\theta_w - 1)\theta)^n e^{\left(-\frac{E}{1+(\theta_w-1)\theta}\right)}\phi = 0. \tag{13}$$

The dimensionless boundary conditions are written as follows:

$$\left. \begin{aligned} f'(0) &= 1 - K\{f'^2 - f' - (f + g)f''\} + \alpha_1 f'', & g'(0) &= c - K\{g'^2 - cg' - (f + g)g''\} + \alpha_1 g'', \\ f(0) &= S, & g(0) &= 0, & \theta'(0) &= -Bi_1(1 - \theta(0)), & \phi'(0) &= -Bi_2(1 - \phi(0)), \\ f'(\infty) &\rightarrow 0, & g(\infty) &\rightarrow 0, & \theta(\infty) &\rightarrow 0, & \phi(\infty) &\rightarrow 0. \end{aligned} \right\} \tag{14}$$

where

$$\begin{aligned} K &= \lambda a, & Pr &= \frac{\nu}{\alpha}, & M &= \frac{\sigma B_0^2}{a\rho_f}, & Nb &= \frac{\tau D_B(C_w - C_\infty)}{\nu}, & Nt &= \frac{\tau D_T(T_w - T_\infty)}{\nu T_\infty}, \\ \alpha_1 &= \beta\sqrt{\frac{a}{\nu}}, & S &= -\frac{w_0}{\sqrt{a\nu}}, & K_1 &= \frac{k_r^2}{a}, & \theta_w &= \frac{T_w}{T_\infty}, & E &= \frac{E_a}{\kappa T_\infty}, \\ Bi_1 &= \frac{h_1}{k}\sqrt{\frac{\nu}{a}}, & Rd &= \frac{4\sigma^* T_\infty^3}{k^* k}, & c &= \frac{b}{a}, & Le &= \frac{\alpha}{D_B}, & Bi_2 &= \frac{h_2}{D_B}\sqrt{\frac{\nu}{a}}. \end{aligned}$$

3 Local Skin-Friction Coefficients, Nusselt Number and Sherwood Number

In this fluid flow problem, the local skin-friction coefficients (C_{fx} , C_{fy}), Nusselt number (Nu_x), and Sherwood number (Sh_x) are the relevant physical quantities, and their expressions are as follows:

$$C_{fx} = \frac{\nu}{u_w^2} \left[(1 + K) \frac{\partial u}{\partial z} \right]_{z=0}, \tag{15}$$

$$C_{fy} = \frac{\nu}{v_w^2} \left[(1 + K) \frac{\partial v}{\partial z} \right]_{z=0}, \tag{16}$$

$$Nu_x = -\frac{x}{k(T_w - T_\infty)} \left[\left(k + \frac{16\sigma^* T^3}{3k^*} \right) \frac{\partial T}{\partial z} \right]_{z=0}, \tag{17}$$

$$Sh_x = -\frac{x D_B}{D_B(C_w - C_\infty)} \left(\frac{\partial C}{\partial z} \right)_{z=0}. \tag{18}$$

Using the dimensionless variables provided in (9), the aforementioned physical quantities may be stated in non-dimensional form

$$C_{fx}\sqrt{Re_x} = (1 + K)f''(0), \tag{19}$$

$$C_{fy}\sqrt{Re_y} = (c)^{-\frac{3}{2}}(1 + K)g''(0), \tag{20}$$

$$\frac{Nu_x}{\sqrt{Re_x}} = -\left[1 + \frac{4}{3}Rd\{1 + (\theta_w - 1)\theta(0)\}^3 \right] \theta'(0), \tag{21}$$

$$\frac{Sh_x}{\sqrt{Re_x}} = -\phi'(0), \tag{22}$$

where $Re_x = \frac{u_w x}{\nu}$ and $Re_y = \frac{v_w y}{\nu}$ are the local Reynolds numbers.

4 Implementation of Numerical Technique

4.1 Solution Procedure

MATLAB’s bvp4c code is used to solve the nonlinear ordinary differential equations (ODE) that govern flow Eqs. (10–13) with boundary conditions 14. Other researchers have extensively implemented this code to tackle the boundary value issue. The MATLAB routine is a representation of a finite difference algorithm that achieves fourth-order precision. For the solver to work, the equations need to be rewritten as a system of equivalent first-order differential equations.

4.2 Results Validation

To validate the employed technique, we got $-f''(0)$ and $-g''(0)$ values and compared them to earlier reported results by Hayat and Awais [40] and Kumar et al. [8] in Tables 1 and 2 where $M = K = \alpha_1 = S = 0.0$ for a variety of c values. It is recognized that the comparison is realistic, which provides assurance of the accuracy of the numerical results presented in this study.

Table 1. Comparison of $-f''(0)$ ’s numerical findings with previously published data

c	$-f''(0)$		
	Hayat and Awais [40]	Kumar et al. [8]	Present result
0	1	1.000003	1
0.2	1.039495	1.039498	1.039498
0.4	1.075788	1.075789	1.075789
0.6	1.109946	1.109948	1.109947
0.8	1.142488	1.142490	1.142488
1.0	1.173720	1.173722	1.173720

Table 2. Comparison of $-g''(0)$ ’s numerical findings with previously published data

c	$-g''(0)$		
	Hayat and Awais [40]	Kumar et al. [8]	Present result
0	0	0	0
0.2	0.148736	0.148738	0.148738
0.4	0.349208	0.349209	0.349210
0.6	0.590528	0.590526	0.590529
0.8	0.866682	0.866679	0.866683
1.0	1.173720	1.173717	1.173720

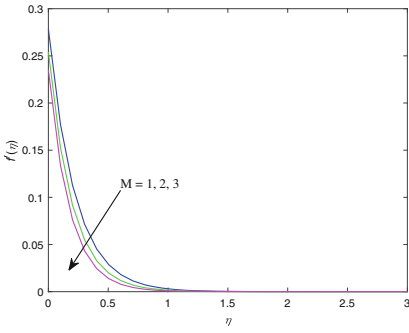


Fig. 2. Impact of M on $f'(\eta)$

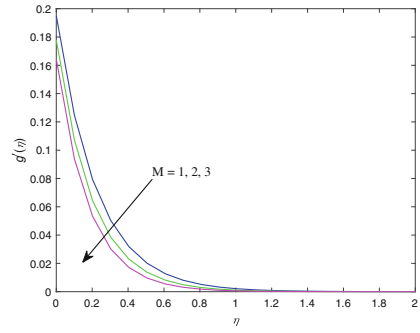


Fig. 3. Impact of M on $g'(\eta)$

5 Results and Discussion

Many important factors have been looked at in this section. They have an effect on velocities, temperature, concentration, skin friction, rate of heat transfer, and rate of mass transfer. To do the calculations, we chose $K = 0.1$, $Pr = S = 2.0$, $Nt = n = 0.5$, $M = 1$, $Rd = K_1 = 0.2$, $Nb = \alpha_1 = 0.4$, $Le = 1$, $\theta_w = 1.3$, $Bi_1 = Bi_2 = 0.3$, $E = 0.6$ and $c = 0.7$.

Figures 2 and 3 demonstrate the non-dimensional velocities $f'(\eta)$ and $g'(\eta)$ for different magnetic field parameter values M . The velocities $f'(\eta)$ and $g'(\eta)$ decrease as the magnetic parameter M increases. The physical explanation for this behavior is that increasing the magnetic parameter operating transverse to the flow enhances the Lorentz force, which tends to resist the fluid motion. The velocity slip parameter α_1 has a significant impact on fluid flow, as seen in Figs. 4 and 5. By raising the velocity parameter α_1 , the velocities $f'(\eta)$ and $g'(\eta)$ decrease. The slip between the fluid and the sheet surface increases as the velocity slip parameters rise. As a result, a partial slip velocity is transferred to the flow-field that tends to minimize fluid velocities. Figures 6 and 7 express that enhanced values of S imply the decreasing nature of flow velocities. Suction is

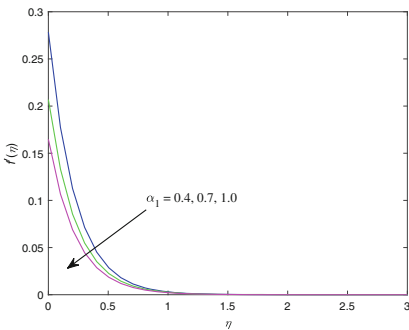


Fig. 4. Impact of α_1 on $f'(\eta)$

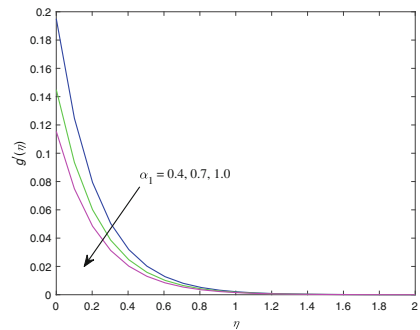


Fig. 5. Impact of α_1 on $g'(\eta)$

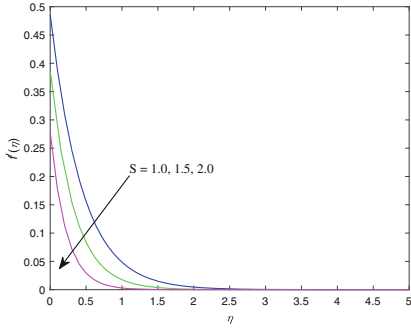


Fig. 6. Impact of S on $f'(\eta)$

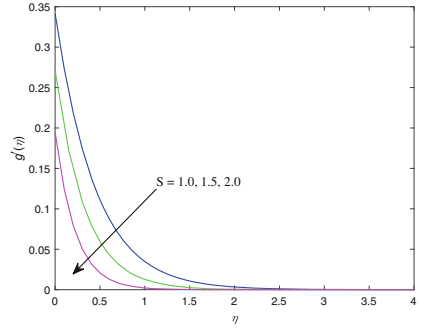


Fig. 7. Impact of S on $g'(\eta)$

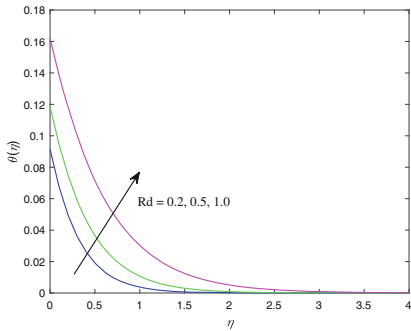


Fig. 8. Impact of Rd on $\theta(\eta)$

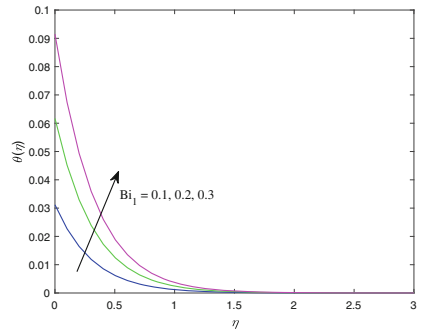


Fig. 9. Impact of Bi_1 on $\theta(\eta)$

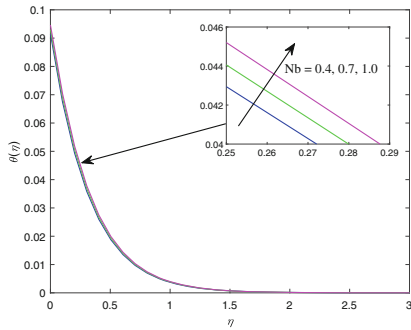


Fig. 10. Impact of Nb on $\theta(\eta)$

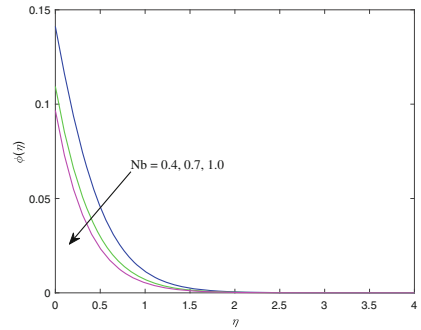


Fig. 11. Impact of Nb on $\phi(\eta)$

utilized to regulate the nanofluid flow physically, with the purpose of reducing velocities by minimizing drag on nanoparticles in an external flow.

Figure 8 illustrates the effect of the thermal radiation parameter Rd on the temperature distribution. The graphic clearly shows that with increasing Rd values, $\theta(\eta)$ is upsurged. In general, increasing radiative characteristics promote

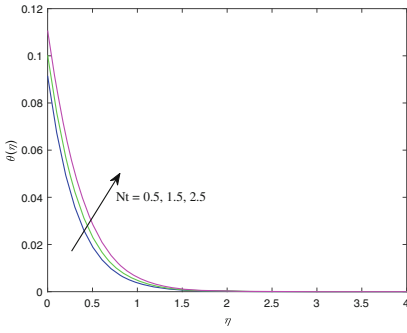


Fig. 12. Impact of Nt on $\theta(\eta)$

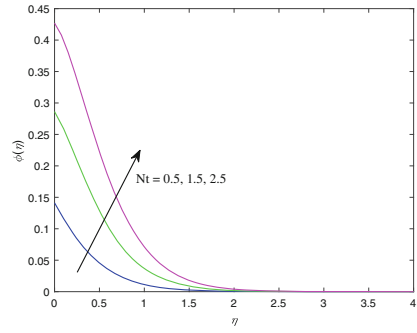


Fig. 13. Impact of Nt on $\phi(\eta)$

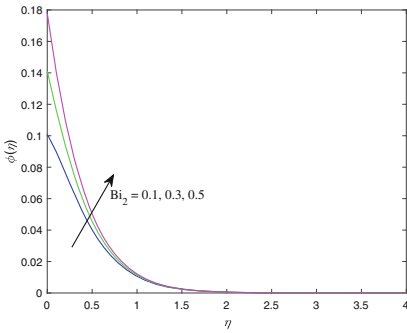


Fig. 14. Impact of Bi_2 on $\phi(\eta)$

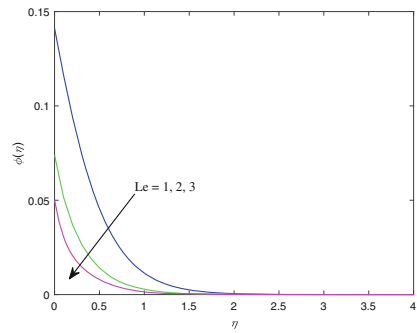


Fig. 15. Impact of Le on $\phi(\eta)$

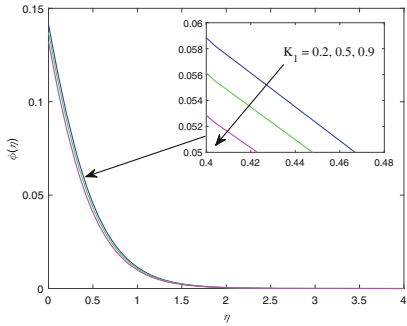


Fig. 16. Impact of K_1 on $\phi(\eta)$

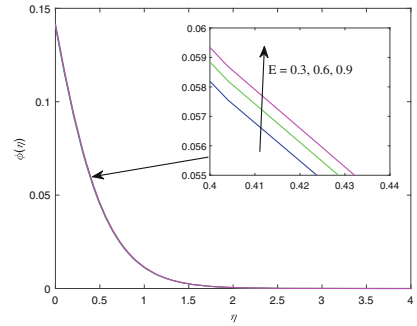


Fig. 17. Impact of E on $\phi(\eta)$

molecular mobility within the system, resulting in frequent collisions between particles that convert to heat energy. As a result, the temperature has risen. The effect of Biot number for temperature on the temperature field is explored in Fig. 9. The increase in Bi_1 indicates that conduction dominates convection heat transfer at the surface. Consequently, for higher Bi_1 values, temperature

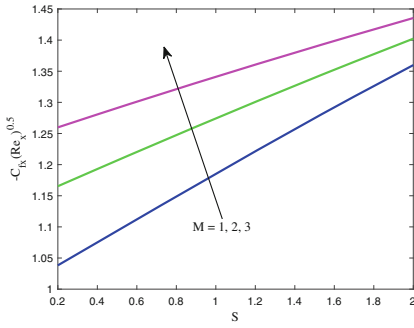


Fig. 18. Impact of M and S on $-C_{fx}\sqrt{Re_x}$

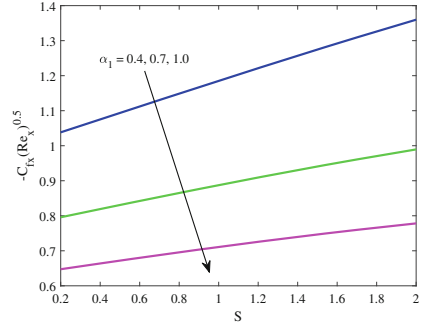


Fig. 19. Impact of α_1 and S on $-C_{fx}\sqrt{Re_x}$

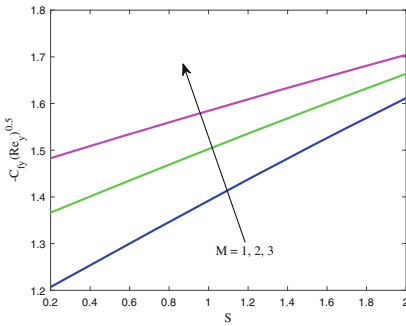


Fig. 20. Impact of M and S on $-C_{fy}\sqrt{Re_y}$

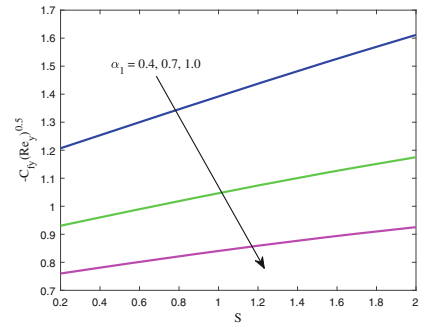


Fig. 21. Impact of α_1 and S on $-C_{fy}\sqrt{Re_y}$

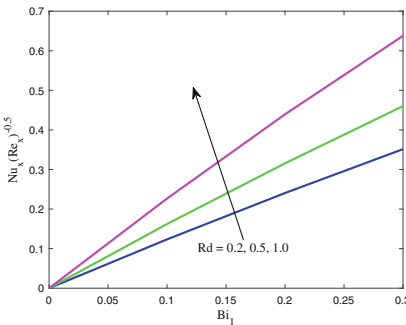


Fig. 22. Impact of Rd and Bi_1 on $\frac{Nu_x}{\sqrt{Re_x}}$

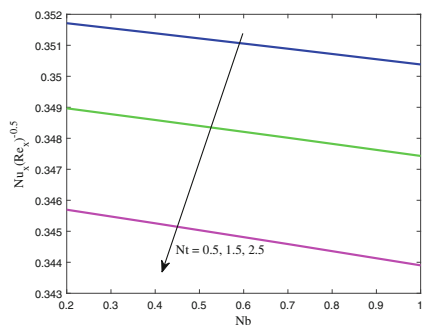


Fig. 23. Impact of Nt and Nb on $\frac{Nu_x}{\sqrt{Re_x}}$

curves are accelerated. According to Figs. 10 and 11, an increase in Nb results in an increase in $\theta(\eta)$ and a decrease in $\phi(\eta)$ over the boundary layer area. When microscopic particles in the flow field come into contact with one other, they

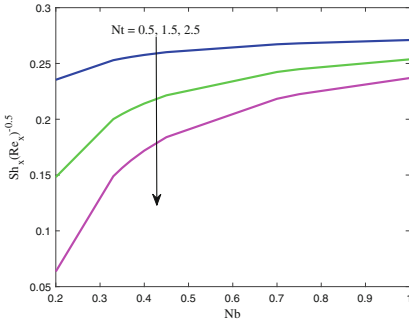


Fig. 24. Impact of Nt and Nb on $\frac{Sh_x}{\sqrt{Re_x}}$

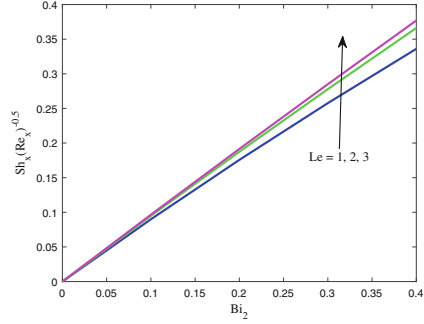


Fig. 25. Impact of Le and Bi_2 on $\frac{Sh_x}{\sqrt{Re_x}}$

create thermal energy, raising the fluid temperature. As a result of Brownian diffusion, the volume fraction of nanoparticles in the boundary layer decreases as they recede from the sheet’s surface. It is clear from Figs. 12 and 13 that when Nt grows, $\theta(\eta)$ and $\phi(\eta)$ rise with it. When a nanoparticle in touch with a stretched sheet is heated by the sheet’s temperature, it exhibits a thermophoretic force that causes it to push back other nanoparticles in its vicinity. An increase in Nt raises the thermophoretic force, which drives the nanoparticles from a hot location to a cool one inside the boundary layer, increasing the temperature of the nanofluid and the volume fraction of the nanoparticles. Figure 14 shows the influence of Bi_2 on the dispersion of concentration. The graphic demonstrates that there is a direct relationship between $\phi(\eta)$ and Bi_2 . As the Brownian diffusivity coefficient is inversely proportional to the Bi_2 , this means the velocity-dependent diffusion of momentum is more powerful than the temperature-dependent diffusion. So, $\phi(\eta)$ is amplified. Figure 15 depicts the relationship between the Lewis number Le and the concentration profile. $\phi(\eta)$ decelerates as Le increases throughout the boundary layer area. The Lewis number is the ratio of heat diffusivity to mass diffusivity, according to its definition. Increasing the Lewis number means that there is more thermal diffusion and less mass diffusion, which makes the concentration boundary layer thinner. The influence of the chemical reaction parameter K_1 on species concentration is depicted in Fig. 16. We can observe from this graph that as K_1 increases, $\phi(\eta)$ falls. This is because there is more thermal energy available to obtain the activation energy required to compensate for the breakdown of atoms’ bonds. The activation energy parameter E has been displayed in Fig. 17 to show how it affects concentration distribution. This diagram clearly shows that $\phi(\eta)$ and E have a direct relationship. As E increases, the pace of a chemical reaction physically increases. Hence, $\phi(\eta)$ is heightened.

The differences in the local surface drag coefficients $-C_{fx}\sqrt{Re_x}$ and $-C_{fy}\sqrt{Re_y}$ scatterings of Maxwell nanofluid as a function of M , α_1 , and S are depicted in Figs. 18, 19, 20 and 21. The figures demonstrate that $-C_{fx}\sqrt{Re_x}$ and $-C_{fy}\sqrt{Re_y}$ degrade with increasing α_1 values, but M and S exhibit the opposite pattern. Figures 22 and 23 illustrate the effects of Rd , Bi_1 , Nt and

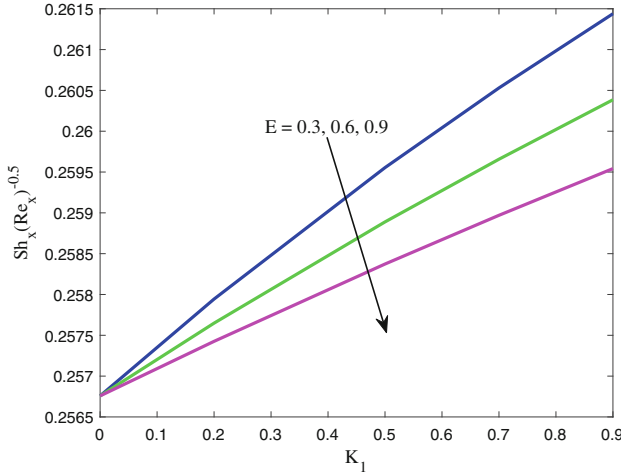


Fig. 26. Impact of E and K_1 on $\frac{Sh_x}{\sqrt{Re_x}}$

Nb on the local Nusselt number $\frac{Nu_x}{\sqrt{Re_x}}$. On the basis of the figures, it can be concluded that $\frac{Nu_x}{\sqrt{Re_x}}$ is directly proportional to Rd and Bi_1 , however an inverse relationship can be noticed between Nt and Nb . The effects of Nt , Nb , Le , Bi_2 , K_1 , and E on local mass transfer rate $\frac{Sh_x}{\sqrt{Re_x}}$ scattering are displayed in Figs. 24, 25 and 26. Figures show that $\frac{Sh_x}{\sqrt{Re_x}}$ is heightened with increasing amounts of Nb , Le , Bi_2 , and K_1 , whereas an inverse association is noticed with Nt and E .

6 Conclusions

The effects of velocity slip, activation energy, and convective heating on MHD Maxwell nanofluid flow across a permeable stretched surface heated by thermal radiation are examined computationally in this study using MATLAB's *bvp4c* solver. The following conclusions are made from the findings:

- For increasing levels of the velocity slip and suction parameters, the velocity decreases in magnitude.
- Increasing the Biot number for temperature and thermal radiation can enhance temperature profiles.
- Concentration field increases with an elevation in the Biot number for concentration and the activation energy parameter.
- Increases in the magnetic field and suction parameter augment the shear stress function, whilst velocity slip lowers it.
- The combination of radiation absorption, thermal radiation, and convection heating can all help to boost the heat transmission rate.
- Activation energy can uplift mass transfer rate while chemical reaction slows it down.

References

1. Dogonchi, A.S., Ganji, D.D.: Investigation of heat transfer for cooling turbine disks with a non-Newtonian fluid flow using DRA. *Case Stud. Therm. Eng.* **6**, 40–51 (2015)
2. Rashidi, M.M., Bagheri, S., Momoniat, E., Freidoonimehr, N.: Entropy analysis of convective MHD flow of third grade non-Newtonian fluid over a stretching sheet. *Ain Shams Eng. J.* **8**(1), 77–85 (2017)
3. Mahmood, A., Parveen, S., Ara, A., Khan, N.A.: Exact analytic solutions for the unsteady flow of a non-Newtonian fluid between two cylinders with fractional derivative model. *Commun. Nonlinear Sci. Numer. Simul.* **14**, 3309–3319 (2009)
4. Keimanesh, M., Rashidi, M.M., Chamkha, A.J., Jafari, R.: Study of a third grade non-newtonian fluid flow between two parallel plates using the multi-step differential transform method. *Comput. Math. Appl.* **62**(8), 2871–2891 (2011)
5. Nadeem, S., Hussain, S.T., Lee, C.: Flow of a Williamson fluid over a stretching sheet. *Braz. J. Chem. Eng.* **30**(3), 619–625 (2013)
6. Seyedi, S.H., Saray, B.N., Nobari, M.R.H.: Using interpolation scaling functions based on Galerkin method for solving non-Newtonian fluid flow between two vertical at plates. *Appl. Math. Comput.* **269**, 488–496 (2015)
7. Nandi, S., Kumbhakar, B.: Hall current and thermo-diffusion effects on magneto-hydrodynamic convective flow near an oscillatory plate with ramped type thermal and solutal boundary conditions. *Indian J. Phys.* **96**, 763–776 (2022)
8. Kumar, S.G., Varma, S.V.K., Prasad, P.D., Raju, C.S.K., Makinde, O.D., Sharma, R.: MHD reacting and radiating 3-D flow of Maxwell fluid past a stretching sheet with heat source/sink and Soret effects in a porous Medium. *Defect Diffus. Forum* **384**, 145–156 (2018)
9. Makinde, O.D., Mabood, F., Ibrahim, M.S.: Chemically reacting on MHD boundary-layer flow of nanofluids over a non-linear stretching sheet with heat source/sink and thermal radiation. *Therm. Sci.* **22**(1), 495–506 (2018)
10. Rashidi, M.M., Ali, M., Freidoonimehr, N., Rostami, B., Hossain, M.A.: Mixed convective heat transfer for MHD viscoelastic fluid flow over a porous wedge with thermal radiation. *Adv. Mech. Eng.* **2014**, 735939 (2014)
11. Daniel, Y.S., Daniel, S.K.: Effects of buoyancy and thermal radiation on MHD flow over a stretching porous sheet using homotopy analysis method. *Alex. Eng. J.* **54**(3), 705–712 (2015)
12. Pal, D., Mandal, G.: Thermal radiation and MHD effects on boundary layer flow of micropolar nanofluid past a stretching sheet with non-uniform heat source/sink. *Int. J. Mech. Sci.* **126**, 307–318 (2017)
13. Shah, Z., Dawar, A., Kumam, P., Khan, W., Islam, S.: Impact of nonlinear thermal radiation on MHD nanofluid thin film flow over a horizontally rotating disk. *Appl. Sci.* **9**(8), 1533 (2019)
14. Jamaludin, A., Naganthran, K., Nazar, R., Pop, I.: Thermal radiation and MHD effects in the mixed convection flow of Fe_3O_4 -Water ferrofluid towards a nonlinearly moving surface. *Processes* **8**(1), 95 (2020)
15. Tarakaramu, N., Narayana, P.V.S., Babu, D.H., Sarojamma, G., Makinde, O.D.: Joule heating and dissipation effects on magnetohydrodynamic couple stress nanofluid flow over a bidirectional stretching surface. *Int. J. Heat Technol.* **39**(1), 205–212 (2021)
16. Mahanthesh, B., Gireesha, B.J., Gorla, R.S.R., Makinde, O.D.: Magnetohydrodynamic three-dimensional flow of nanofluids with slip and thermal radiation over a

- nonlinear stretching sheet: a numerical study. *Neural Comput. Appl.* **30**, 1557–1567 (2018)
17. Babu, M.J., Sandeep, N.: MHD non-Newtonian fluid flow over a slendering stretching sheet in the presence of cross-diffusion effects. *Alex. Eng. J.* **55**, 2193–2201 (2016)
 18. Rashad, A.M.: Impact of thermal radiation on MHD slip flow of a ferrofluid over a non-isothermal wedge. *J. Magn. Magn. Mater.* **422**, 25–31 (2017)
 19. Ellahi, R., Alamri, S.Z., Basit, A., Majeed, A.: Effects of MHD and slip on heat transfer boundary layer flow over a moving plate based on specific entropy generation. *J. Taibah Univ. Sci.* **12**(4), 476–482 (2018)
 20. Das, M., Nandi, S., Kumbhakar, B., Seth, G.S.: Soret and Dufour effects on MHD nonlinear convective flow of tangent hyperbolic nanofluid over a bidirectional stretching sheet with multiple slips. *J. Nanofluids* **10**, 200–213 (2021)
 21. Ullah, I., et al.: Theoretical analysis of activation energy effect on Prandtl-Eyring nanoliquid flow subject to melting condition. *J. Non-Equilib. Thermodyn.* **47**(1), 1–12 (2022)
 22. Uddin, I., Ullah, I., Ali, R., Khan, I., Nisar, K.S.: Numerical analysis of nonlinear mixed convective MHD chemically reacting flow of prandtl-eyring nanofluids in the presence of activation energy and joule heating. *J. Therm. Anal. Calorim.* **145**, 495–505 (2021)
 23. Khan, U., Zaib, A., Khan, I., Nisar, K.S.: Activation energy on MHD flow of titanium alloy (Ti6Al4V) nanoparticle along with a cross flow and streamwise direction with binary chemical reaction and non-linear radiation: dual solutions. *J. Mater. Res. Technol.* **9**(1), 188–199 (2020)
 24. Fayyadh, M.M., Basavarajappa, M., Hashim, I., Mackolil, J., Nisar, K.S., Roslan, R., Allaw, D.: The mathematical model for heat transfer optimization of Carreau fluid conveying magnetized nanoparticles over a permeable surface with activation energy using response surface methodology. *ZAMM* **102**(11), e202100185 (2022)
 25. Akbar, Y., Alotaibi, H., Iqbal, J., Nisar, K.S., Alharbi, K.A.M.: Thermodynamic analysis for bioconvection peristaltic transport of nanofluid with gyrotactic motile microorganisms and arrhenius activation energy. *Case Stud. Therm. Eng.* **34**, 102055 (2022)
 26. Shoaib, M., Naz, S., Nisar, K.S., Raja, M.A.Z., Aslam, S., Ahmad, I.: MHD casson nanofluid in darcy-forchheimer porous medium in the presence of heat source and arrhenious activation energy: applications of neural networks. *Int. J. Model. Simul.* (2022). <https://doi.org/10.1080/02286203.2022.2091973>
 27. Das, M., Kumbhakar, B., Singh, J.: Analysis of unsteady MHD Williamson nanofluid flow past a stretching sheet with nonlinear mixed convection, thermal radiation and velocity slips. *J. Comput. Anal. Appl.* **30**(1), 176–195 (2022)
 28. Das, M., Kumbhakar, B.: Hall and ion slip effects on MHD bioconvective eyring-powell nanofluid flow past a slippery sheet under a porous medium considering Joule heating and activation energy. *J. Porous Media* **25**(5), 17–32 (2022)
 29. Mustafa, M., Khan, J.A.: Numerical study of partial slip effects on MHD flow of nanofluids near a convectively heated stretchable rotating disk. *J. Mol. Liq.* **234**, 287–295 (2017)
 30. Patel, H.R., Singh, R.: Thermophoresis, Brownian motion and non-linear thermal radiation effects on mixed convection MHD micropolar fluid flow due to nonlinear stretched sheet in porous medium with viscous dissipation, joule heating and convective boundary condition. *Int. Commun. Heat Mass Transf.* **107**, 68–92 (2019)

31. Kumar, K.A., Sugunamma, V., Sandeep, N.: Effect of thermal radiation on MHD casson fluid flow over an exponentially stretching curved sheet. *J. Therm. Anal. Calorim.* **140**, 2377–2385 (2020)
32. Das, M., Nandi, S., Kumbhakar, B.: Hall effect on unsteady MHD 3D Carreau nanofluid flow past a stretching sheet with Navier's slip and nonlinear thermal radiation. *Palestine J. Math.* **11**(I), 95–108 (2022)
33. Mandal, S., Shit, G.C., Shaw, S., Makinde, O.D.: Entropy analysis of thermo-solutal stratification of nanofluid flow containing gyrotactic microorganisms over an inclined radiative stretching cylinder. *Therm. Sci. Eng. Prog.* **34**, 101379 (2022)
34. Bilal, M., Sagheer, M., Hussain, S.: Three dimensional MHD upper-convected Maxwell nanofluid flow with nonlinear radiative heat flux. *Alex. Eng. J.* **57**, 1917–1925 (2018)
35. Reddy, M.V., Lakshminarayana, P.: Cross-diffusion and heat source effects on a three-dimensional MHD flow of Maxwell nanofluid over a stretching surface with chemical reaction. *Eur. Phys. J. Spec. Top.* **230**(5), 1371–1379 (2021). <https://doi.org/10.1140/epjs/s11734-021-00037-9>
36. Sajid, M., Abbas, Z., Ali, N., Javed, T., Ahmad, I.: Slip flow of a maxwell fluid past a stretching sheet. *Walailak J. Sci. Technol.* **11**(12), 1093–1103 (2014)
37. Shehzad, S.A., Hayat, T., Alsaedi, A.: MHD flow of jeffrey nanofluid with convective boundary conditions. *J. Braz. Soc. Mech. Sci. Eng.* **37**, 873–883 (2015)
38. Khan, M.I., Waqas, M., Hayat, T., Khan, M.I., Alsaedi, A.: Chemically reactive flow of upper-convected Maxwell fluid with cattaneo christov heat flux model. *J. Braz. Soc. Mech. Sci. Eng.* **39**, 4571–4578 (2017)
39. Fatunmbi, E.O., Adeniyani, A.: Nonlinear thermal radiation and entropy generation on steady flow of magneto-micropolar fluid passing a stretchable sheet with variable properties. *Results Eng.* **6**, 100142 (2020)
40. Hayat, T., Awais, M.: Three-dimensional flow of upper-convected Maxwell (UCM) fluid. *Int. J. Numer. Methods Fluids* **66**, 875–884 (2011)



Modelling Pulsatile Blood Flow Using Casson Fluid Model Through an Overlapping Stenotic Artery with Au-Cu Hybrid Nanoparticles: Varying Viscosity Approach

Rishu Gandhi^(✉) and B. K. Sharma

Department of Mathematics, Birla Institute of Technology and Science, Pilani,
Pilani, Rajasthan, India
I.rishugandhi155@gmail.com

Abstract. The present study aims to perform computer simulations of two-dimensional hemodynamics of blood flow through an overlapping stenosed artery considering the non-Newtonian Casson fluid model to simulate the arterial region's hemorheological properties and hematocrit-dependent viscosity to mimic the realistic behavior of blood with a uniform magnetic field applied in the radial direction of the blood flow, motivated by magneto-hemodynamics effects. This study is influenced by drug delivery applications and proposes a mathematical model for unsteady blood flow using hybrid biocompatible nanoparticles (Gold and Copper). The Crank-Nicolson method solves the transformed governing equations with accompanying boundary conditions. For a given critical height of the stenosis, key hemodynamic variables such as velocity, wall shear stress, temperature, and flow rate are computed. The velocity and temperature profiles show enhancement as the Casson fluid parameter (β) increases. The velocity, wall shear stress, and flow rate of the fluid (blood) decline with an increment in the hematocrit parameter (h_m). A comparative study with published work is done to validate the current model, which is in good accord with the previous work. The findings may act as a benchmark for formulating the best regimens for the targeted treatment of atherosclerosis, obstructed hemodynamics, nano-hemodynamics, nano-pharmacology, blood purification systems, and treatment of hemodynamic ailments.

Keywords: Hematocrit-dependent viscosity · Overlapping stenosis · Au-Cu/Blood hybrid nanofluid · Pulsatile blood flow

1 Introduction

Nanofluids have gained popularity as a significant development in biomedical engineering in recent years. Theoretical and practical studies on the possible applications of nanoparticles in blood flow issues have significantly influenced

Nomenclature

r_1^*	Radial direction	d	location of stenosis
z_1^*	Axial direction	L_0	length of stenosis
t_1^*	Time	M^2	Magnetic Number
u_1^*	Velocity component in radial direction	Re	Reynold's Number
w_1^*	Velocity component in axial direction	Gr	Grashof Number
U_0	Reference velocity	Pr	Prandtl Number
R	Radius of artery in stenotic region	Q_1	Flow Rate
R_0	Radius of artery in non-stenotic region	Greek Letters	
g	Acceleration by virtue of gravity	δ	Stenosis depth
$h(r_1^*)$	volume fraction of RBCs	β	Casson Fluid Parameter
h_m	maximum hematocrit at artery's center	σ	Electrical conductivity
\tilde{T}^*	Temperature of the base fluid	$\tilde{\theta}$	Non-dimensional temperature
\tilde{T}_1^*	Reference temperature	ρ	Density
\tilde{T}_w^*	Temperature at the wall	ϕ_1	Volume fraction of Au-NPs
B_0	Uniform Magnetic Field	ϕ_2	Volume fraction of Cu-NPs
\tilde{C}_p^*	Specific heat at constant pressure	γ	Thermal expansion coefficient
k_f	Thermal conductivity	τ_w	Shear stress at the wall
p_1^*	Pressure	μ_0	coefficient of viscosity of plasma
w_s	Wall slip velocity	μ_f	Blood's viscosity

current bio-science literature. Many nanoparticle applications include gene therapy, MRI, tracking agents, and surgical tools for treating hyperthermia. Gold nanoparticles transport and unload drugs using their unique physical and chemical properties. Ghosh et al. [1] investigated the role of gold nanoparticles in drug administration. Gentile et al. [2] investigated the effects of vascular permeability on blood transport with nanoparticle suspension via blood vessels. The impact of the slip condition on blood flow through a tapering stenosed artery in the presence of nanoparticles was examined by Nadeem and Ijaz [3]. Using nanoparticles, Bahrami et al. [4] studied cancer therapy through targeted drug delivery. They found that nanoparticles have proven to be a successful technique that can lessen the side effects of current anti-cancer drugs. Gupta et al. [5] examined the MHD 2D-flow of Williamson-type nanofluid using nonlinear thermal radiation, Cattaneo-Christov heat and mass flux models. Under the influence of the magnetic field, Umadevi et al. [6] examined the blood flow suspended with Cu-nanoparticles via an inclined artery having overlapping stenosis. Gandhi et al. [7] constructed a mathematical model for drug delivery using Au-Al₂O₃/Blood hybrid nanoparticles via a bell-shaped stenosed artery. Gandhi and Sharma [8] studied the influence of hybrid nanoparticles on two-dimensional pulsatile blood flow through a vertical artery with irregular stenosis with an inclined external magnetic field. Using Au and GO nanoparticles, Khanduri and Sharma [9] investigated the influence of Hall and ion slips on MHD blood flow through a catheterized multi-stenosis artery with thrombosis.

A frequent cause of cardiovascular disease in coronary arteries is the buildup of fatty substances inside the artery wall lumen. This mechanism limits the amount of oxygenated blood that may leave the heart and travel to the rest of the body by decreasing the radius of blood arteries while raising blood flow resistance. The hemodynamical study in stenosed arteries is a crucial field of research because of its vital applications in cardiovascular illnesses like angina, heart attacks, atherosclerosis, and aneurysms, which are among the world's top causes of death. Numerous theoretical and practical research efforts have been conducted to gain a deeper understanding of the factors contributing to stenosis formation and its effects on blood flow dynamics. Several researchers [10–13] have mathematically explored the blood flow via arteries with overlapping stenosis. Sharma et al. [14] utilized blood as biomagnetic fluid to explore Soret and Dufour's effects via a stenosed artery having tapering effects. Under the impact of a uniform magnetic field, Das et al. [15] investigated the physical repercussions of suspension of hybrid nanoparticles in blood moving via porous artery with inclination having minor stenosis. Using a two-phase mixing approach, Zhang et al. [16] studied the impacts of nanoparticle volume fraction on plaque disintegration during transit. Basha et al. [17] investigated the fluid transport behavior of Au-Cu/Blood hybrid nanofluid via an artery having the inclination and irregular stenosis. Gandhi et al. [18] performed entropy generation analysis for blood flow through an irregular stenosed artery utilizing hybrid nanoparticles of different shapes. Using hematocrit-dependent viscosity, Sharma et al. [19] examined the effects of heat transfer and body acceleration on unsteady MHD blood flow in a curved artery in the presence of stenosis and aneurysm.

Most of the research described above examined the connection between artery stenosis and blood flow dynamics while treating blood as a Newtonian fluid. The blood behaves in the larger-diameter arteries with an assertive Newtonian behavior when shear rates are greater than 100 s^{-1} . However, because blood is a suspension of cells, it is widely known that arteries with smaller diameters and lower shear rates exhibit greater non-Newtonian blood behavior. The Casson fluid flow model has acquired popularity recently due to its fascinating application in human life. In today's science, the Casson fluid flow model has significant demand. Casson fluid demonstrates yield stress features. When the yield stress is high enough, the Casson fluid transforms into the Newtonian fluid. Sarifuddin et al. [20] explored the effect of two-dimensional blood flow, considering blood to be Casson fluid via an irregular stenosed artery employing the Marker and Cell approach for solving the equations numerically. Debnath et al. [21] studied the influence of a 1^{st} -order homogeneous-heterogeneous chemical reaction in an annular pipe, using the Casson model to characterize the liquid's non-Newtonian viscosity. Ali et al. [22] used Darcy's law to investigate the flow behavior of Casson fluid via a 2-D porous channel employing a vorticity-stream function approach. Tassaddiq et al. [23] examined the Newtonian heating effects for the generalized Casson fluid flow utilizing a Mittag-Leffler fractional operator. Using the Elzaki transform method and Elzaki decomposition approach, Sushila et al. [24] studied the thin film flow of a third-grade fluid down an inclined plane. Das et al. [25] investigated solute dispersion through a stenotic tube with

an absorptive wall, and Casson fluid describes the rheology of blood. Padma et al. [26] aimed to investigate how yield stress affected the EMHD motion of Casson fluid and nanoparticles as they flow via a mildly blocked inclined tapering artery.

The present research is inspired by the potential for nanoparticles to serve as efficient drug delivery and transport systems, given their capacity to hold significant quantities of therapeutic substances. Since blood is considered a non-Newtonian fluid, small-sized nanoparticles are becoming increasingly common in biomedical applications. Therefore, nanoparticles can either stimulate or inhibit blood vessel formation. Although some medications can increase or decrease blood-capillary expansion in some conditions, they only work for a short duration. Recently, researchers found that using these nanoparticles might resolve previously identified medication administration problems. Based on the literature survey performed above, no effort has been yet made to study the two-dimensional pulsatile hybrid nanofluid flow through an overlapping stenosed artery incorporating gold and copper nanoparticles considering blood as non-Newtonian Casson fluid with variable viscosity dependent on hematocrit under the influence of radiation and magnetic field effects. The present study seeks to perform computer simulations of two-dimensional hemodynamics of blood flow through an overlapping stenosed artery using the non-Newtonian Casson fluid model to simulate the arterial region's hemorheological properties and hematocrit-dependent viscosity to mimic the realistic behavior of blood with a uniform magnetic field applied in the radial direction of the blood flow. The pulsatile pressure gradient effects portray actual blood flow in unsteady flow situations. The novelty of the mathematical model formulated in the present analysis is as follows:

- To evaluate the impact of hybrid nanoparticles (Au + Cu) through an overlapping stenotic artery influenced by an external magnetic field and radiation, considering wall slip effects.
- Utilizing the Casson fluid model to address the non-Newtonian features of blood along with the hematocrit-dependent viscosity model to analyze the variable viscosity.

2 Mathematical Formulation

An unsteady, laminar, incompressible, viscous electrically conducting MHD blood flow through an inclined artery with overlapping stenosis is considered. A cylindrical coordinate system (r_1^*, θ, z_1^*) is employed with r_1^* and z_1^* as radial and axial directions respectively. The axial symmetry of the artery corresponds to the independence of flow in the azimuthal (θ) direction. The blood behavior is assumed non-Newtonian and is represented using Casson fluid model. The variable viscosity which is dependent on hematocrit is employed. A uniform magnetic field B_0 is applied to the blood flow in the radial direction. The magnetic Reynold's number is assumed very small ($Re \ll 1$); therefore, the induced magnetic field is neglected compared to the applied magnetic field.

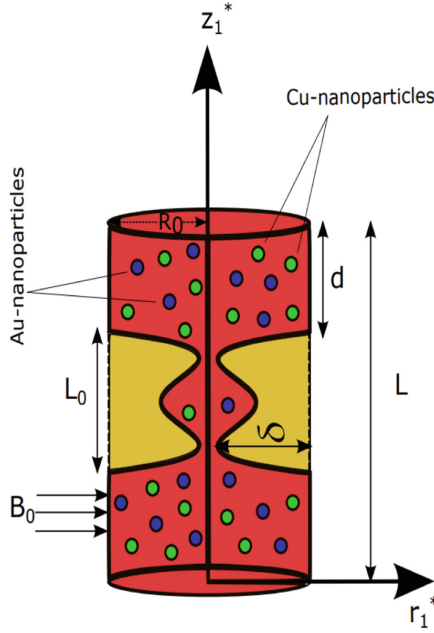


Fig. 1. The overlapping stenotic artery doped with hybrid nanoparticles

The geometry of the overlapping stenosis is assumed as [13]:

$$R(z_1^*) = \begin{cases} R_0 \left[1 - \frac{64}{10} \eta_1 \left(\frac{11}{32} L_0^3 (z_1^* - d) + \frac{47}{48} L_0^2 (z_1^* - d)^2 - L_0 (z_1^* - d)^3 \right. \right. \\ \qquad \qquad \qquad \left. \left. + \frac{1}{3} (z_1^* - d)^4 \right) \right], & d \leq z_1^* \leq d + 3L_0/2, \\ R_0, & \text{otherwise.} \end{cases} \quad (1)$$

The parameter η_1 is defined as:

$$\eta_1 = \frac{4\delta}{R_0 L_0^4}$$

where δ is the critical height of the stenosis occurring at two different positions, i.e.,

$$z_1^* = d + \frac{8L_0}{25}, \quad \text{and} \quad z_1^* = d + \frac{61L_0}{50}$$

The blood viscosity is affected by several parameters, including plasma viscosity, protein level, red blood cell concentration, strain rate and temperature. The concentration of red blood cells or hematocrit is one of these factors that significantly impact blood viscosity. Blood viscosity at a distance of r_1^* from an artery's axis can be described as

$$\mu_f = \mu_0[1 + \beta_1 h(r_1^*)], \tag{2}$$

and the expression for the hematocrit, $h(r_1^*)$ is given as -

$$h(r_1^*) = h_m \left[1 - \left(\frac{r_1^*}{R_0} \right)^m \right] \tag{3}$$

where β_1 has value 2.5 for blood and m is the control parameter for the shape of the blood velocity profile ($m \geq 2$).

2.1 Governing Equations

The blood flow through an inclined overlapping stenosed artery (Fig.1) is assumed to be bidirectional. Therefore, the velocity and temperature fields are represented as:

$$\tilde{V}^* = \tilde{V}^*[u_1^*(r_1^*, z_1^*, t_1^*), 0, w_1^*(r_1^*, z_1^*, t_1^*)] , \quad \tilde{T}^* = \tilde{T}^*(r_1^*, z_1^*, t_1^*)$$

The Casson fluid model’s rheological equation of state for an incompressible flow is as follows:

$$\tau_{ij}^* = \begin{cases} 2 \left(\mu_b^* + \frac{p_y^*}{\sqrt{2\pi^*}} \right) e_{ij}^*, & \pi^* > \pi_c^* \\ 2 \left(\mu_b^* + \frac{p_y^*}{\sqrt{2\pi_c^*}} \right) e_{ij}^*, & \pi^* \leq \pi_c^* \end{cases} \tag{4}$$

where $\pi^* = e_{ij}^* \cdot e_{ij}^*$ is the product of deformation rate with itself, π_c^* is a critical value based on the non-Newtonian model, μ_b^* is the plastic dynamic viscosity of the non-Newtonian fluid, and p_y^* is the yield stress of the fluid.

When $\pi^* \leq \pi_c^*$, Eq. (4) can be expressed as:

$$\tau_{ij}^* = 2\mu_b^* \left(1 + \frac{1}{\beta} \right) e_{ij}^* \tag{5}$$

where $\beta = \frac{\mu_b^* \sqrt{2\pi_c^*}}{p_y^*}$ is the Casson fluid parameter.

Under the above assumptions and invoking the Boussinesq approximation, the continuity equation, momentum equation and energy equation are represented as:

Continuity Equation:

$$\frac{\partial u_1^*}{\partial r_1^*} + \frac{u_1^*}{r_1^*} + \frac{\partial w_1^*}{\partial z_1^*} = 0, \quad (6)$$

Momentum Equation:
r-direction:

$$\begin{aligned} \rho_{hnf} \left[\frac{\partial u_1^*}{\partial t_1^*} + u_1^* \frac{\partial u_1^*}{\partial r_1^*} + w_1^* \frac{\partial u_1^*}{\partial z_1^*} \right] &= -\frac{\partial p_1^*}{\partial r_1^*} + \frac{1}{r_1^*} \frac{\partial}{\partial r_1^*} \left[\mu_{hnf} \left(1 + \frac{1}{\beta} \right) r_1^* \frac{\partial u_1^*}{\partial r_1^*} \right] \\ &+ \frac{1}{2} \frac{\partial}{\partial z_1^*} \left[\mu_{hnf} \left(1 + \frac{1}{\beta} \right) \left(\frac{\partial w_1^*}{\partial r_1^*} + \frac{\partial u_1^*}{\partial z_1^*} \right) \right] - \mu_{hnf} \left(1 + \frac{1}{\beta} \right) \frac{u_1^*}{r_1^{*2}}, \end{aligned} \quad (7)$$

z-direction:

$$\begin{aligned} \rho_{hnf} \left[\frac{\partial w_1^*}{\partial t_1^*} + u_1^* \frac{\partial w_1^*}{\partial r_1^*} + w_1^* \frac{\partial w_1^*}{\partial z_1^*} \right] &= -\frac{\partial p_1^*}{\partial z_1^*} + \frac{1}{2} \frac{1}{r_1^*} \frac{\partial}{\partial r_1^*} \left[\mu_{hnf} \left(1 + \frac{1}{\beta} \right) r_1^* \left(\frac{\partial u_1^*}{\partial z_1^*} + \frac{\partial w_1^*}{\partial r_1^*} \right) \right] \\ &+ \frac{\partial}{\partial z_1^*} \left[\mu_{hnf} \left(1 + \frac{1}{\beta} \right) \frac{\partial w_1^*}{\partial z_1^*} \right] + (\rho\gamma)_{hnf} g(\tilde{T}^* - \tilde{T}_1^*) - \sigma_{hnf} B_0^2 w_1^*, \end{aligned} \quad (8)$$

Energy Equation:

$$(\rho C_p)_{hnf} \left[\frac{\partial \tilde{T}^*}{\partial t_1^*} + u_1^* \frac{\partial \tilde{T}^*}{\partial r_1^*} + w_1^* \frac{\partial \tilde{T}^*}{\partial z_1^*} \right] = k_{hnf} \left[\frac{\partial^2 \tilde{T}^*}{\partial r_1^{*2}} + \frac{1}{r_1^*} \frac{\partial \tilde{T}^*}{\partial r_1^*} + \frac{\partial^2 \tilde{T}^*}{\partial z_1^{*2}} \right] - \frac{\partial q_r^*}{\partial r_1^*}, \quad (9)$$

where

$$q_r^* = -\frac{4\sigma_e}{3k_e} \frac{\partial T^4}{\partial r_1^*}, \quad (10)$$

It is assumed that there are minimal temperature changes within the blood flow. Therefore, \tilde{T}^4 in Eq. (10) is linearized by disregarding higher-order terms and is expanded using Taylor series around \tilde{T}_1^* :

$$\tilde{T}^{*4} = 4\tilde{T}_1^{*3}\tilde{T} - 3\tilde{T}_1^{*4},$$

Hence, Eq. (10) becomes

$$q_r^* = -\frac{16\tilde{T}_1^{*3}\sigma_e}{3k_e k_f} \frac{\partial \tilde{T}}{\partial r_1^*}.$$

The boundary conditions are:

$$\frac{\partial w_1^*}{\partial r_1^*} = 0, \quad \frac{\partial \tilde{T}^*}{\partial r_1^*} = 0 \quad \text{at } r_1^* = 0, \quad (11)$$

$$w_1^* = w_s, \quad \tilde{T}^* = \tilde{T}_w^* \quad \text{at } r_1^* = -R, R, \quad (12)$$

The initial assumptions regarding velocity and temperature are considered as:

$$w_1^* = 0, \quad \tilde{T}^* = 0 \quad \text{at } t_1^* = 0. \quad (13)$$

Table 1. Thermophysical parameters of nanofluid and hybrid nanofluid [18,27]

Properties	Mathematical expression for nanofluid and hybrid nanofluid
Viscosity	$\mu_{hnf} = \frac{\mu_{nf}}{(1-\phi_1)^{2.5}(1-\phi_2)^{2.5}}$
Density	$\rho_{hnf} = [(1-\phi_2)\{(1-\phi_1)\rho_f + \phi_1\rho_{s1}\}] + \phi_2\rho_{s2}$
Heat Capacity	$(\rho C_p)_{hnf} = [(1-\phi_2)\{(1-\phi_1)(\rho C_p)_f + \phi_1(\rho C_p)_{s1}\}]$
Thermal Conductivity	$\frac{k_{hnf}}{k_{bf}} = \frac{k_{s2} + (m-1)k_f - (m-1)\phi_2(k_f - k_{s2})}{k_{s2} + (m-1)k_f + \phi_2(k_f - k_{s2})}$ where $\frac{k_{bf}}{k_f} = \frac{k_{s1} + (m-1)k_f - (m-1)\phi_1(k_f - k_{s1})}{k_{s1} + (m-1)k_f + \phi_1(k_f - k_{s1})}$
Electrical Conductivity	$\frac{\sigma_{hnf}}{\sigma_{bf}} = \frac{\sigma_{s2} + (m-1)\sigma_f - (m-1)\phi_2(\sigma_f - \sigma_{s2})}{\sigma_{s2} + (m-1)\sigma_f + \phi_2(\sigma_f - \sigma_{s2})}$ where $\frac{\sigma_{bf}}{\sigma_f} = \frac{\sigma_{s1} + (m-1)\sigma_f - (m-1)\phi_1(\sigma_f - \sigma_{s1})}{\sigma_{s1} + (m-1)\sigma_f + \phi_1(\sigma_f - \sigma_{s1})}$
Thermal Expansion Coefficient	$\gamma_{hnf} = [(1-\phi_2)\{(1-\phi_1)\gamma_f + \phi_1\gamma_{s1}\}] + \phi_2\gamma_{s2}$

Table 2. Default Values of emerging parameters

Parameters	ϕ_1	ϕ_2	d	B_1	c_1	e	δ	β	w_s	β_1	h_m
Value	0.03	0.03	1	1.41	1	0.2	0.1	2	0.1	2.5	0.5

Table 3. Thermophysical properties of nanoparticles

Thermophysical Properties	Blood	Gold	Copper
Density [$\rho(kg/m^3)$]	1063	19320	8933
Thermal Conductivity [K(W/mK)]	0.492	314	400
Electrical Conductivity [$\sigma(S/m)$]	0.667	4.10×10^7	5.96×10^7
Thermal Expansion Coefficient [$\gamma \times 10^{-5}(K^{-1})$]	0.18	1.4	1.67
Heat Capacitance [$C_p(J/kgK)$]	3594	129	385

2.2 Non-dimensionalization

The governing equations given by (6)–(9) need to be transformed into dimensionless form so that a numerical solution for these equations can be obtained. The following dimensionless variables are introduced:

$$\begin{aligned} \bar{r}_1^* &= \frac{r_1^*}{R_0}, \bar{w}_1^* = \frac{w_1^*}{U_0}, \bar{u}_1^* = \frac{L_0 u_1^*}{\delta^* U_0}, \bar{t}_1^* = \frac{U_0 t_1^*}{R_0}, \bar{z}_1^* = \frac{z_1^*}{L_0}, \bar{p}_1^* = \frac{R_0^2 p_1^*}{U_0 L_0 \mu_f}, \bar{\theta} = \frac{\tilde{T}^* - \tilde{T}_1^*}{\tilde{T}_w^* - \tilde{T}_1^*}, \\ \bar{R} &= \frac{R}{R_0}, \alpha = \frac{\alpha^* L_0}{R_0}, \bar{d} = \frac{d}{L_0}, \bar{w}_s = \frac{w_s}{U_0}, Re = \frac{U_0 \rho_f R_0}{\mu_f}, M^2 = \frac{\sigma_f B_0^2 R_0^2}{\mu_f}, \\ Gr &= \frac{\rho_f R_0^2 g \gamma_f (\tilde{T}_w^* - \tilde{T}_1^*)}{\mu_f U_0}, Pr = \frac{\mu_f C_p}{k_f}, Nr = \frac{16 \sigma_e \tilde{T}_1^{*3}}{3 k_f k_e}. \end{aligned} \tag{14}$$

The insertion of the above non-dimensional parameters mentioned in (14), disregarding the bars and using the mild stenotic hypotheses that the maximal stenosis height is less than the artery’s radius, i.e., $\delta(= \delta^*/R_0) \ll 1$, and the artery’s radius and the stenotic region’s length are proportionate, i.e., $\epsilon(=$

$R_0/L_0) = O(1)$ leads to the modified form of governing Eqs. (6)–(9), which are as follows:

Continuity Equation:

$$\frac{\partial w_1^*}{\partial z_1^*} = 0, \quad (15)$$

Momentum Equation:

r-direction:

$$\frac{\partial p_1^*}{\partial r_1^*} = 0, \quad (16)$$

z-direction:

$$Re \frac{\rho_{hnf}}{\rho_f} \frac{\partial w_1^*}{\partial t_1^*} = -\frac{\partial p_1^*}{\partial z_1^*} + \frac{1}{2r_1^*} \frac{\partial}{\partial r_1^*} \left[\frac{\mu_{hnf}}{\mu_f} \left(1 + \frac{1}{\beta} \right) r_1^* \frac{\partial w_1^*}{\partial r_1^*} \right] + \frac{(\rho\gamma)_{hnf}}{(\rho\gamma)_f} Gr\tilde{\theta} - \frac{\sigma_{hnf}}{\sigma_f} M^2 w_1^*, \quad (17)$$

Energy Equation:

$$\frac{(\rho C_p)_{hnf}}{(\rho C_p)_f} \frac{\partial \tilde{\theta}}{\partial t_1^*} = \frac{1}{RePr} \frac{k_{hnf}}{k_f} \left[\frac{\partial^2 \tilde{\theta}}{\partial r_1^{*2}} + \frac{1}{r_1^*} \frac{\partial \tilde{\theta}}{\partial r_1^*} \right] + \frac{Nr}{RePr} \frac{\partial^2 \tilde{\theta}}{\partial r_1^{*2}}. \quad (18)$$

The geometry of stenosis in the dimensionless form can be described as:

$$R(z_1^*) = \begin{cases} 1 - \frac{64}{10} \eta_1 \left(\frac{11}{32} (z_1^* - d) + \frac{47}{48} (z_1^* - d)^2 - (z_1^* - d)^3 + \frac{1}{3} (z_1^* - d)^4 \right), & d \leq z_1^* \leq d + 3/2, \\ 1, & \text{otherwise.} \end{cases} \quad (19)$$

where

$$\eta_1 = 4\delta, \quad \delta = \frac{\delta^*}{R_0}.$$

Blood flows through the cardiovascular system due to the heart's pumping motion, causing a pressure gradient across the vascular network. The pressure gradient is separated into two parts: non-fluctuating (continuous) and fluctuating (pulsatile) [28] as given below:

$$-\frac{\partial p_1^*}{\partial z_1^*} = A_0 + A_1 \cos(w_p t_1^*), \quad t_1^* > 0, \quad (20)$$

where, A_0 and A_1 signify the amplitudes of the steady-state and pulsatile pressure gradient components, respectively, and $w_p = 2\pi f_p$, f_p depicts the heart pulse frequency.

On the substitution of dimensionless variables given in (14), the modified equation for the pressure gradient becomes:

$$-\frac{\partial p_1^*}{\partial z_1^*} = B_1 [1 + e \cos(c_1 t_1^*)], \quad (21)$$

where

$$e = \frac{A_1}{A_0}, B_1 = \frac{A_0 R_0^2}{\mu_0 U_0}, c_1 = \frac{2\pi R_0 f_p}{U_0}. \quad (22)$$

Using Eq. (21) in Eq. (17), we have:

$$\begin{aligned} Re \frac{\rho_{hnf}}{\rho_f} \frac{\partial w_1^*}{\partial t_1^*} &= B_1 [1 + e \cos(c_1 t_1^*)] - \frac{1}{2} \left(1 + \frac{1}{\beta}\right) \frac{m \beta_1 h_m (r_1^*)^{m-1}}{(1 - \phi_1)^{2.5} (1 - \phi_2)^{2.5}} \frac{\partial w_1^*}{\partial r_1^*} \\ &+ \frac{1}{2} \frac{\mu_{hnf}}{\mu_f} \left(1 + \frac{1}{\beta}\right) \frac{1}{r_1^*} \frac{\partial}{\partial r_1^*} \left(r_1^* \frac{\partial w_1^*}{\partial r_1^*}\right) + \frac{(\rho\gamma)_{hnf}}{(\rho\gamma)_f} Gr \tilde{\theta} - \frac{\sigma_{hnf}}{\sigma_f} M^2 w_1^*. \end{aligned} \quad (23)$$

2.3 Radial Coordinate Transformation

The physical geometry taken into account in the formulated problem is cylindrical, i.e., a cylindrical coordinate system is considered. However, in order to use the computational approach, the considered geometry needs to be transformed into a rectangular domain by employing the transformation $\left(x_1^* = \frac{r_1^*}{R(z_1^*)}\right)$. On applying this transformation, the Eqs. (23) and (18) become:

$$\begin{aligned} Re \frac{\rho_{hnf}}{\rho_f} \frac{\partial w_1^*}{\partial t_1^*} &= B_1 [1 + e \cos(c_1 t_1^*)] - \frac{1}{2} \left(1 + \frac{1}{\beta}\right) \frac{m \beta_1 h_m R^{m-2} (x_1^*)^{m-1}}{(1 - \phi_1)^{2.5} (1 - \phi_2)^{2.5}} \frac{\partial w_1^*}{\partial x_1^*} \\ &+ \frac{1}{2} \frac{1 + \beta_1 h_m [1 - R^m (x_1^*)^m]}{(1 - \phi_1)^{2.5} (1 - \phi_2)^{2.5}} \left(1 + \frac{1}{\beta}\right) \left(\frac{1}{R^2}\right) \left[\frac{\partial^2 \tilde{w}_1^*}{\partial x_1^{*2}} + \frac{1}{x_1^*} \frac{\partial \tilde{w}_1^*}{\partial x_1^*}\right] + \frac{(\rho\gamma)_{hnf}}{(\rho\gamma)_f} Gr \tilde{\theta} \\ &\quad - \frac{\sigma_{hnf}}{\sigma_f} M^2 w_1^*, \end{aligned} \quad (24)$$

$$\frac{(\rho C_p)_{hnf}}{(\rho C_p)_f} \frac{\partial \tilde{\theta}}{\partial t_1^*} = \frac{1}{Re Pr} \frac{k_{hnf}}{k_f} \left(\frac{1}{R^2}\right) \left[\frac{\partial^2 \tilde{\theta}}{\partial x_1^{*2}} + \frac{1}{x_1^*} \frac{\partial \tilde{\theta}}{\partial x_1^*}\right] + \left(\frac{1}{R^2}\right) \frac{Nr}{Re Pr} \frac{\partial^2 \tilde{\theta}}{\partial x_1^{*2}}. \quad (25)$$

The boundary conditions mentioned in Eq. (11) and (12) are reduced as follows:

$$\left. \frac{\partial w_1^*}{\partial x_1^*} \right|_{x_1^*=0} = 0, \quad w_1^*|_{x_1^*=-1,1} = w_s, \quad \left. \frac{\partial \tilde{\theta}}{\partial x_1^*} \right|_{x_1^*=0} = 0, \quad \tilde{\theta}|_{x_1^*=-1,1} = 1. \quad (26)$$

The wall shear stress (WSS) and volumetric flow rate are expressed as:

$$\tau_w = -\frac{1}{R} \left(1 + \frac{1}{\beta}\right) \left(\frac{\partial w_1^*}{\partial x_1^*}\right)_{x_1^*=1} \quad (27)$$

$$Q_1 = 2\pi R^2 \int_0^1 w_1^* x_1^* dx_1^*, \quad (28)$$

3 Solution Process

The partial differential Eqs. (24) and (25) are coupled differential equations; therefore, obtaining an analytic solution is too difficult. On the other hand, numerical approaches can yield a highly accurate solution. An unconditionally stable implicit finite difference (Crank-Nicolson) approach is used in this case. The subscripts and superscripts in Eqs. (24) and (25) are ignored for discretization.

3.1 Discretization

On employing the values of thermophysical parameters of hybrid nanofluid from Table 1 and discretizing the governing Eqs. (24) and (25) using the Crank-Nicolson scheme, the desired form of equations is:

$$\begin{aligned}
 & \left[(1 - \phi_2) \left[(1 - \phi_1) + \phi_1 \frac{\rho_{s1}}{\rho_f} \right] + \phi_2 \frac{\rho_{s2}}{\rho_f} \right] Re \left[\frac{w_i^{k+1} - w_i^k}{dt} \right] = B_1 [1 + \text{ecos}(c_1 t^k)] \\
 & - \frac{1}{2} \left(1 + \frac{1}{\beta} \right) \frac{m\beta_1 h_m R^{m-2} (x(i))^{m-1}}{(1 - \phi_1)^{2.5} (1 - \phi_2)^{2.5}} \left[\frac{1}{2} \left(\frac{w_{i+1}^{k+1} - w_{i-1}^{k+1}}{2dx} + \frac{w_{i+1}^k - w_{i-1}^k}{2dx} \right) \right] \\
 & + \frac{1}{2} \left(1 + \frac{1}{\beta} \right) \frac{1 + \beta_1 h_m [1 - R^m (x(i))^m]}{(1 - \phi_1)^{2.5} (1 - \phi_2)^{2.5}} \left(\frac{1}{R^2} \right) \left[\frac{1}{2} \left(\frac{w_{i+1}^{k+1} - 2w_i^{k+1} + w_{i-1}^{k+1}}{dx^2} \right. \right. \\
 & \left. \left. + \frac{w_{i+1}^k - 2w_i^k + w_{i-1}^k}{dx^2} \right) + \frac{1}{2x(i)} \left(\frac{w_{i+1}^{k+1} - w_{i-1}^{k+1}}{2dx} + \frac{w_{i+1}^k - w_{i-1}^k}{2dx} \right) \right] \\
 & + \left[(1 - \phi_2) \left[(1 - \phi_1) + \phi_1 \frac{(\rho\gamma)_{s1}}{(\rho\gamma)_f} \right] + \phi_2 \frac{(\rho\gamma)_{s2}}{(\rho\gamma)_f} \right] Gr \tilde{\theta}_i^k - \frac{1}{2} \frac{\sigma_{hnf}}{\sigma_f} M^2 (w_i^k + w_i^{k+1}), \tag{29}
 \end{aligned}$$

$$\begin{aligned}
 & \left[(1 - \phi_2) \left[(1 - \phi_1) + \phi_1 \frac{(\rho C_p)_{s1}}{(\rho C_p)_f} \right] + \phi_2 \frac{(\rho C_p)_{s2}}{(\rho C_p)_f} \right] \left[\frac{\tilde{\theta}_i^{k+1} - \tilde{\theta}_i^k}{dt} \right] \\
 & = \frac{1}{RePr} \left(\frac{k_{hnf}}{k_f} + Nr \right) \left(\frac{1}{R^2} \right) \left[\frac{1}{2} \left(\frac{\tilde{\theta}_{i+1}^{k+1} - 2\tilde{\theta}_i^{k+1} + \tilde{\theta}_{i-1}^{k+1}}{dx^2} + \frac{\tilde{\theta}_{i+1}^k - 2\tilde{\theta}_i^k + \tilde{\theta}_{i-1}^k}{dx^2} \right) \right. \\
 & \left. + \frac{1}{2x(i)} \left(\frac{\tilde{\theta}_{i+1}^{k+1} - \tilde{\theta}_{i-1}^{k+1}}{2dx} + \frac{\tilde{\theta}_{i+1}^k - \tilde{\theta}_{i-1}^k}{2dx} \right) \right]. \tag{30}
 \end{aligned}$$

The Crank-Nicolson scheme employed in the current analysis is, however, stable for all values for dt and dx still, a minimal value is considered with great precision as $dt = 10^{-4}$ and $dx = 10^{-4}$. It is noticed that no further change occurs in the values of hemodynamical parameters studied in the research with decreasing values of dt and dx . A total of $N + 1$ grid points have been considered in the spatial direction, with $x = 1/N + 1$ being the step size, whereas $M + 1$

grid points are considered temporal. The value at any time instant t^k is given as $t^k = (k - 1)dt$, dt being a small increment in time. As the scheme employed is an implicit one; therefore a system of equations is obtained, and it is in the form of a tri-diagonal system which can be solved with the Tri-diagonal Matrix Algorithm (TDMA) [29].

The tri-diagonal system corresponding to Eq. (29) is given by

$$A_i^k w_{i-1}^{k+1} + B_i^k w_i^{k+1} + C_i^k w_{i+1}^{k+1} = A_i'^k w_{i-1}^k + B_i'^k w_i^k + C_i'^k w_{i+1}^k + D_i^k, \quad (31)$$

where

$$A_i^k = -\frac{1+\beta_1 h_m [1-R^m(x(i))^m]}{(1-\phi_1)^{2.5}(1-\phi_2)^{2.5}} \left(\frac{1}{4R^2}\right) \left(\frac{dt}{dx^2} - \frac{1}{2x(i)} \frac{dt}{dx}\right) - \frac{dt}{8dx} \left(1 + \frac{1}{\beta}\right) \frac{m\beta_1 h_m R^{m-2}(x(i))^{m-1}}{(1-\phi_1)^{2.5}(1-\phi_2)^{2.5}},$$

$$B_i^k = Re \left[(1-\phi_2) \left[(1-\phi_1) + \phi_1 \frac{\rho_{s1}}{\rho_f} \right] + \phi_2 \frac{\rho_{s2}}{\rho_f} \right] + \frac{1+\beta_1 h_m [1-R^m(x(i))^m]}{(1-\phi_1)^{2.5}(1-\phi_2)^{2.5}} \frac{1}{2R^2} \frac{dt}{dx^2} + \frac{dt}{2} \frac{\sigma_{hnf}}{\sigma_f} M^2,$$

$$C_i^k = -\frac{1+\beta_1 h_m [1-R^m(x(i))^m]}{(1-\phi_1)^{2.5}(1-\phi_2)^{2.5}} \left(\frac{1}{4R^2}\right) \left(\frac{dt}{dx^2} + \frac{1}{2x(i)} \frac{dt}{dx}\right) + \frac{dt}{8dx} \left(1 + \frac{1}{\beta}\right) \frac{m\beta_1 h_m R^{m-2}(x(i))^{m-1}}{(1-\phi_1)^{2.5}(1-\phi_2)^{2.5}},$$

$$A_i'^k = \frac{1+\beta_1 h_m [1-R^m(x(i))^m]}{(1-\phi_1)^{2.5}(1-\phi_2)^{2.5}} \left(\frac{1}{4R^2}\right) \left(\frac{dt}{dx^2} - \frac{1}{2x(i)} \frac{dt}{dx}\right) + \frac{dt}{8dx} \left(1 + \frac{1}{\beta}\right) \frac{m\beta_1 h_m R^{m-2}(x(i))^{m-1}}{(1-\phi_1)^{2.5}(1-\phi_2)^{2.5}},$$

$$B_i'^k = Re \left[(1-\phi_2) \left[(1-\phi_1) + \phi_1 \frac{\rho_{s1}}{\rho_f} \right] + \phi_2 \frac{\rho_{s2}}{\rho_f} \right] - \frac{1+\beta_1 h_m [1-R^m(x(i))^m]}{(1-\phi_1)^{2.5}(1-\phi_2)^{2.5}} \frac{1}{2R^2} \frac{dt}{dx^2} - \frac{dt}{2} \frac{\sigma_{hnf}}{\sigma_f} M^2,$$

$$C_i'^k = \frac{1+\beta_1 h_m [1-R^m(x(i))^m]}{(1-\phi_1)^{2.5}(1-\phi_2)^{2.5}} \left(\frac{1}{4R^2}\right) \left(\frac{dt}{dx^2} + \frac{1}{2x(i)} \frac{dt}{dx}\right) - \frac{dt}{8dx} \left(1 + \frac{1}{\beta}\right) \frac{m\beta_1 h_m R^{m-2}(x(i))^{m-1}}{(1-\phi_1)^{2.5}(1-\phi_2)^{2.5}},$$

$$D_i^k = dt B_1 [1 + \text{ecos}(c_1 t^k)] + dt \left[(1-\phi_2) \left[(1-\phi_1) + \phi_1 \frac{(\rho\gamma)_{s1}}{(\rho\gamma)_f} \right] + \phi_2 \frac{(\rho\gamma)_{s2}}{(\rho\gamma)_f} \right] Gr \hat{\theta}_i^k.$$

The tri-diagonal system corresponding to Eq. (30) is given by

$$P_i^k \theta_{i-1}^{k+1} + Q_i^k \theta_i^{k+1} + S_i^k \theta_{i+1}^{k+1} = P_i'^k \theta_{i-1}^k + Q_i'^k \theta_i^k + S_i'^k \theta_{i+1}^k + F_i^k, \quad (32)$$

where

$$P_i^k = -\frac{1}{RePr} \left(\frac{1}{2R^2}\right) \left(\frac{k_{hnf}}{k_f} + Nr\right) \left(\frac{dt}{dx^2} - \frac{1}{2x(i)} \frac{dt}{dx}\right),$$

$$Q_i^k = \left[(1-\phi_2) \left[(1-\phi_1) + \phi_1 \frac{(\rho C_p)_{s1}}{(\rho C_p)_f} \right] + \phi_2 \frac{(\rho C_p)_{s2}}{(\rho C_p)_f} \right] + \frac{1}{RePr} \frac{1}{R^2} \frac{dt}{dx^2} \left(\frac{k_{hnf}}{k_f} + Nr\right),$$

$$S_i^k = -\frac{1}{RePr} \left(\frac{1}{2R^2}\right) \left(\frac{k_{hnf}}{k_f} + Nr\right) \left(\frac{dt}{dx^2} + \frac{1}{2x(i)} \frac{dt}{dx}\right),$$

$$P_i'^k = \frac{1}{RePr} \left(\frac{1}{2R^2}\right) \left(\frac{k_{hnf}}{k_f} + Nr\right) \left(\frac{dt}{dx^2} - \frac{1}{2x(i)} \frac{dt}{dx}\right),$$

$$Q_i'^k = \left[(1-\phi_2) \left[(1-\phi_1) + \phi_1 \frac{(\rho C_p)_{s1}}{(\rho C_p)_f} \right] + \phi_2 \frac{(\rho C_p)_{s2}}{(\rho C_p)_f} \right] - \frac{1}{RePr} \frac{1}{R^2} \frac{dt}{dx^2} \left(\frac{k_{hnf}}{k_f} + Nr\right),$$

$$S_i'^k = \frac{1}{RePr} \left(\frac{1}{2R^2}\right) \left(\frac{k_{hnf}}{k_f} + Nr\right) \left(\frac{dt}{dx^2} + \frac{1}{2x(i)} \frac{dt}{dx}\right),$$

$$F_i^k = 0.$$

4 Results and Graphical Analysis

The effect of various flow-related parametric parameters, including the hematocrit parameter (h_m), wall slip velocity (w_s), Casson fluid parameter (β), volume fractions of both nanoparticles (ϕ_1, ϕ_2), radiation parameter (Nr), and Prandtl number (Pr), on non-dimensional velocity, non-dimensional temperature, wall shear stress, and flow rate, are covered in this section. Au-Blood, a unitary nanofluid, and Au-Cu/Blood, a hybrid nanofluid, have been compared. The values of the emergent parameters employed in the analysis are shown in Table 2. Table 3 lists the values for the thermophysical characteristics of the blood, Au, and Cu nanoparticles.

To validate the study conducted, the numerical scheme (Crank-Nicolson) used must be verified. In the absence of a few physical parameters, the current model reduces the ones published in the literature. As the Casson fluid parameter in the current work approaches infinity ($\beta \rightarrow \infty$), the current model approaches the Newtonian model in [27]. The hematocrit parameter (h_m) in the present analysis and viscosity parameter (β_0) in [27] have been neglected to verify the results. The numerical scheme has also been validated for Au-nanoparticles used in both research works. The effect of inclination of the magnetic field, Joule heating, and viscous dissipation in [27] has been ignored. Figure 2a & 2b have been plotted for verification. The findings of comparison with existing literature results [27] indicate good agreement, which supports the validity of the current solutions.

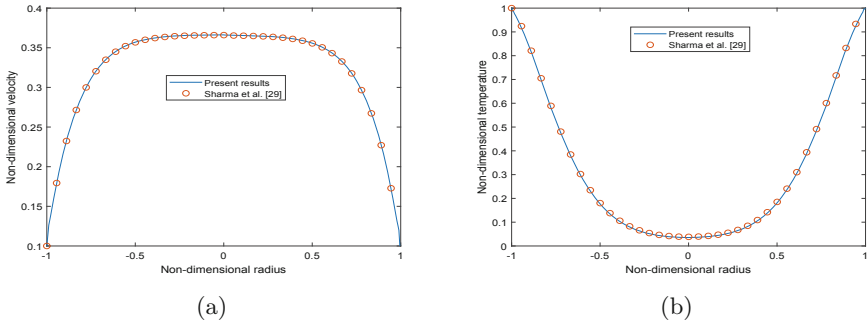


Fig. 2. Comparative study (a) velocity profile ($M^2 = 1$), (b) temperature profile ($Ec = 0.2$).

The effect of various flow parameters such as hematocrit parameter (h_m), wall slip velocity (w_s), Casson fluid parameter (β), and volume fractions of both the nanoparticles (ϕ_1, ϕ_2) on non-dimensional velocity profiles is portrayed in Fig. 3. A comparative analysis has been performed between unitary nanofluid (Au-Blood) and hybrid nanofluid (Au-Cu/Blood). Blood velocity distribution

for various h_m values is shown in a radial direction in Fig. 3a. Blood viscosity is significantly influenced by the hematocrit measure (h_m). Both the hematocrit-dependent ($h_m \neq 0$) and constant ($h_m = 0$) scenarios have been studied. The hybrid blood velocity is larger when $h_m = 0$ and falls as h_m increases, according to Fig. 3a. With an increase in h_m levels, the viscosity of the blood increases, which impedes blood flow; a drop in velocity profiles is examined with h_m . Additionally, greater magnitudes of the hybrid nanofluid (Au-Cu/Blood) have been observed than those of the unitary nanofluid (Au-Blood). The velocity is at its peak near the artery's centerline, gradually decreasing until it approaches the vessel wall, reaching the wall slip velocity (w_s). Figure 3b depicts the effect of w_s on non-dimensional velocity profiles. With an increase in the slip parameter w_s , the axial flow accelerates significantly as the hydrodynamic wall slip effect increases. No-slip velocity is typically considered at the artery wall, which has the least significance. As a result, the wall slip has been introduced at the arterial wall in the current investigation using boundary conditions. The artery's core region exhibits the highest flow velocity, which decreases as it gets closer to the arterial wall. Figure 3c shows how β affects the non-dimensional velocity profile. The velocity field rises as the β expands since the velocity field's boundary layer thickness decreases. It is so because HNF becomes more viscous, and its elasticity increases as the value of β rise. Figure 3d displays the non-dimensional velocity profiles for various values of ϕ_1, ϕ_2 . The volume fraction of both Au- and Cu-nanoparticles rises along with the velocity profiles. When $\phi_1 = 0.01, \phi_2 = 0.01$, the velocity value is the lowest, and when $\phi_1 = 0.05, \phi_2 = 0.05$, the velocity value is the highest.

Figure 4 illustrates the impact of several flow parameters, including the radiation parameter (Nr), Prandtl number (Pr), Casson fluid parameter (β), and volume fractions of both the nanoparticles (ϕ_1, ϕ_2) on non-dimensional temperature profiles. The effect of Nr on non-dimensional temperature profiles is depicted in Fig. 4a. With rising values of Nr, there is an increase in temperature profiles. Additionally, Au-Cu/Blood hybrid nanofluid reaches higher magnitudes than Au-Blood nanofluid. The system emits the most heat due to the inverse effect of Nr on thermal conductivity. Radiation serves as a heat source within the bloodstream. Hence an increase in radiation exposure elevates body temperature. When light with the proper wavelength interacts with nanoparticles, the free electrons within the nanoparticles vibrate. These oscillations generate heat that kills malignant cells by spreading over the surrounding environment. This discovery has extensive thermal therapeutic applications. Figure 4b highlights how Pr affects the non-dimensional temperature profile. An increase in Pr values accompanies the declination of the temperature profiles since the thermal boundary layer thickness decreases with Pr. The viscosity and thermal diffusivity of the fluid determine Pr. The momentum transport is linked to heat transport through this dimensionless quantity. The Prandtl number tells us how heat diffuses faster, i.e., whether heat conduction or convection is more prominent in a fluid. The physical importance of the Prandtl number is that when it is smaller than 1, conductive heat transfer becomes the more prominent process,

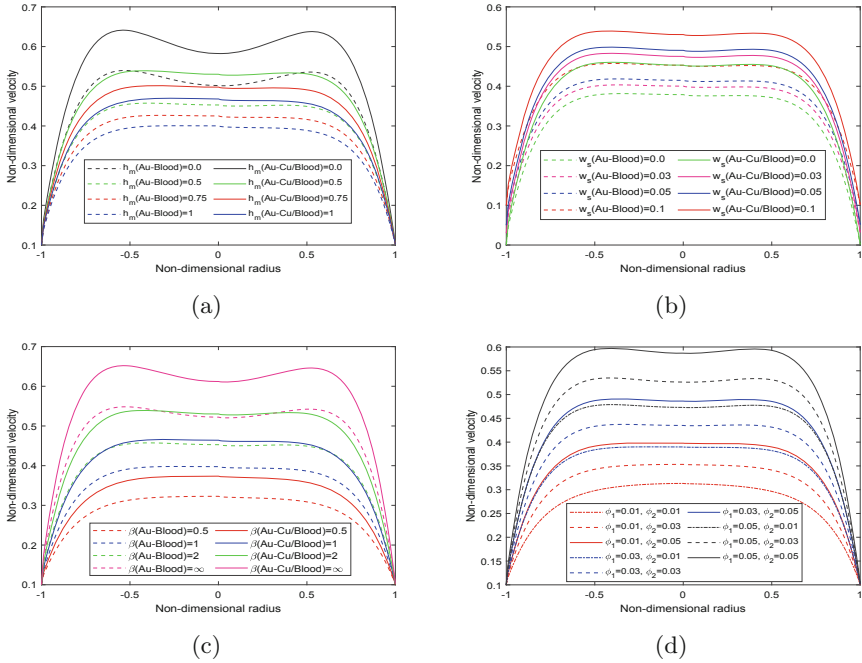


Fig. 3. Effect of (a) hematocrit parameter (h_m), (b) wall slip velocity (w_s), (c) Casson fluid parameter (β), (d) volume fractions of both nanoparticles (ϕ_1, ϕ_2) on non-dimensional velocity at $z_1^* = 1.31$ and $t_1^* = 1.2$

i.e., conduction transfers a higher proportion of heat than convection. Convective heat transfer is more significant than conduction when the Prandtl value is greater than 1. The effect of β on the temperature profile is illustrated in Fig. 4c. The fluid’s temperature increases with an increase in β because the thickness of the thermal boundary layer increases with an increment in values of β . Figure 4d shows the impact of ϕ_1, ϕ_2 on non-dimensional temperature profiles. When the volume percentage of both nanoparticles increases, the temperature profiles also show enhancement. The temperature demonstrates minimal value for $\phi_1 = 0.01, \phi_2 = 0.01$, and a maximum value for $\phi_1 = 0.05, \phi_2 = 0.05$, highlighting the importance of both nanoparticles in regulating the temperature.

The time series plots for wall shear stress (WSS) and volumetric flow rate at the stenosis region are shown in Fig. 5. These graphs depict the oscillating character of blood flow in the stenotic zone as time passes. The graphs demonstrate that the magnitude initially declines before exhibiting an ascending trend sustained throughout time after a crucial point in time. The influence of w_s on WSS and flow rate is represented in Fig. 5a and 5b. Figure 5a depicts that WSS decreases dramatically with increment in w_s values, with minor backflow. As a result, as w_s rises, the beginning value of WSS profiles lowers by a certain amount. Figure 5b illustrates that raising the wall slip parameter causes a

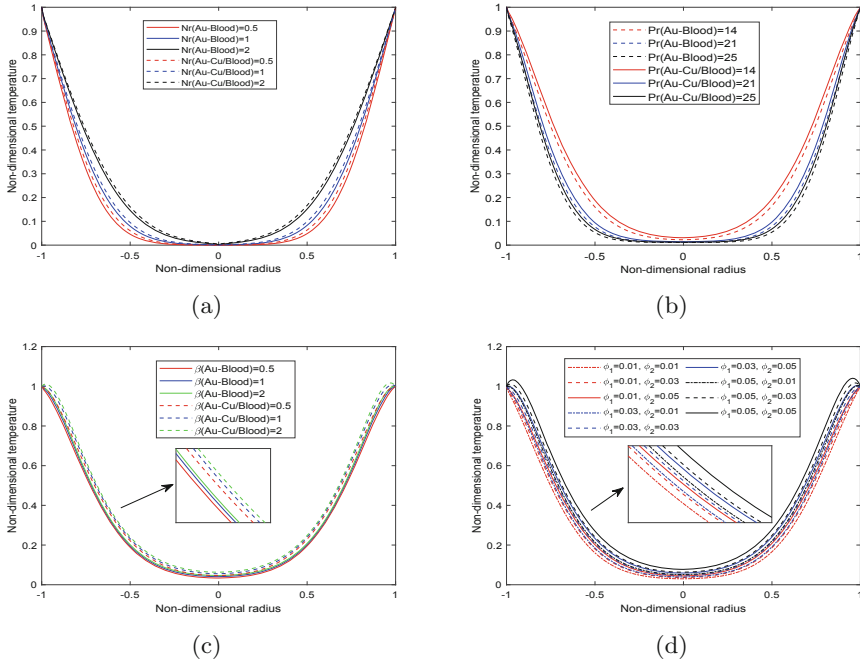


Fig. 4. Effect of (a) Radiation parameter (Nr), (b) Prandtl number (Pr), (c) Casson fluid parameter (β), (d) different concentrations of both nanoparticles (ϕ_1, ϕ_2) on temperature profiles at $z_1^* = 1.31$ and $t_1^* = 1.2$

significantly more pronounced increase in volumetric flow rate, implying that significant growth in flux is driven by increasing wall slip. The impact of the volume fraction of Au-nanoparticles (ϕ_1) on WSS and volumetric flow rate is depicted in Fig. 5c and 5d. It is analyzed that there is a decrement in WSS and flow rate initially up to a certain point of time with increasing values of ϕ_1 , but then it rises over time. Figures 5e and 5f highlight the variations of WSS and flow rate profiles for various hybrid nanoparticle combinations. The patterns show that when the nanoparticles' volume fraction rises simultaneously, the oscillatory wall shear stress profiles reduce in magnitude up to a certain threshold, increasing with time. The profiles for flow rate exhibit the same trend as that of WSS, as presented in Fig. 5f.

The influence of the hematocrit parameter (h_m) and stenotic depth (δ) on wall shear stress and flow rate concerning arterial length is highlighted in Fig. 6. The WSS profiles for h_m are depicted in Fig. 6a. A declination in WSS values is analyzed with increasing h_m values since the fluid's viscosity is enhanced. Moreover, Fig. 6b manifests that the flow rate profiles also decline with an increment in h_m values since the increased viscosity hinders the flow of the fluid (blood). Figure 6c depicts the influence of δ on WSS profiles. According to Zhang et al. [30], the WSS reduces as δ increases, indicating that lower shear stress levels are

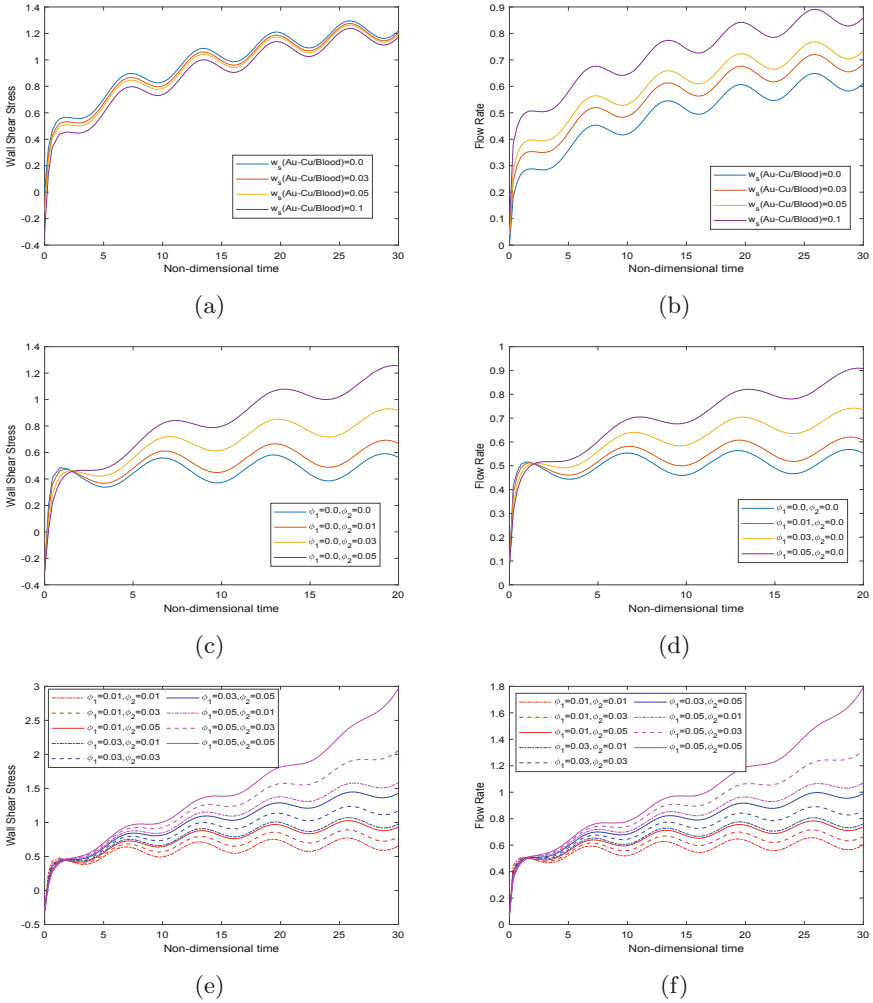


Fig. 5. Effect of (a, b) wall slip velocity (w_s), (c, d) volume fraction of Au-nanoparticles (ϕ_1) (e,f) volume fraction of both nanoparticles (ϕ_1, ϕ_2) on wall shear stress and flow rate with respect to time

more harmful. The effect of δ on flow rate profiles is presented in Fig. 6d. It is seen that flow rate profiles decline with an increase in δ values.

This section aims to analyze how the blood flows in the stenotic zone and how it behaves in other parts of the artery. Also, hybrid nanoparticles are inserted to boost drug delivery and treat atherosclerosis. The impact of flow parameters such as hematocrit parameter (h_m), Casson fluid parameter (β), and volume fraction of both the nanoparticles (ϕ_1, ϕ_2) is illustrated via velocity contours in Fig. 7, 8, 9. The effect of h_m is highlighted in Fig. 7. Figure 7a depicts the constant viscosity case ($h_m=0$), and the maximum velocity value is observed in this case.

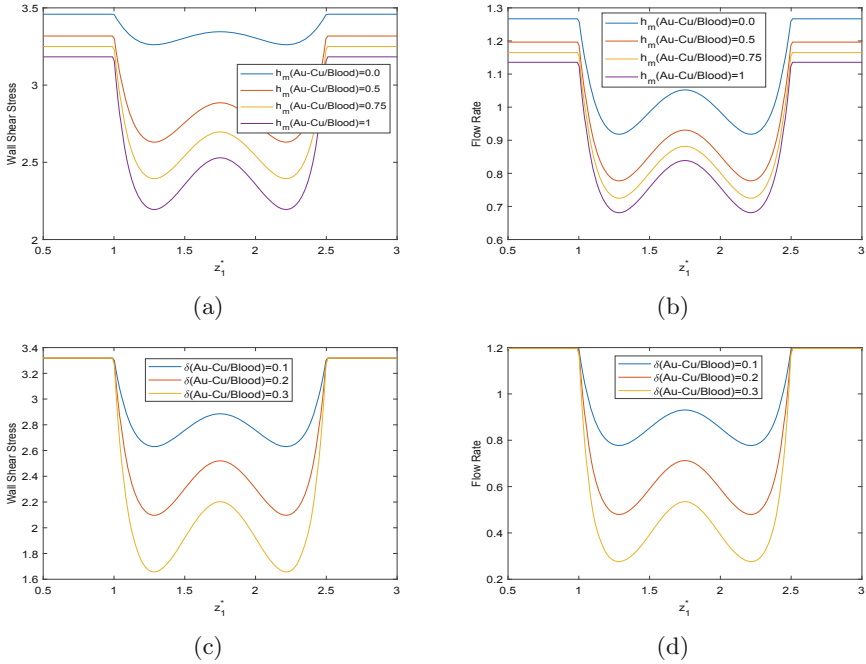


Fig. 6. Effect of Effect of (a, b) hematocrit parameter (h_m), and (c, d) stenotic depth (δ) on wall shear stress and flow rate at $t_1^* = 1.2$

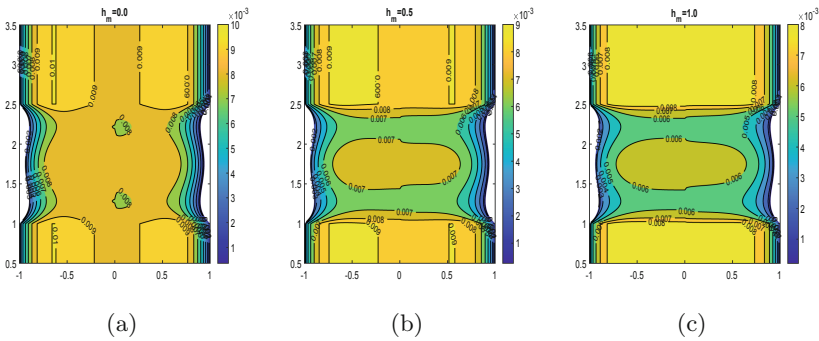


Fig. 7. Velocity contours for (a) $h_m = 0.0$, (b) $h_m = 0.5$, (c) $h_m = 1.0$

The velocity profiles decline with increasing h_m values since viscosity enhances and flow retardation occurs. The velocity contours for β are represented by Fig. 8. As β increases, the boundary layer thickness of the velocity field decreases, increasing velocity. Figure 9 highlights the velocity contours for different combinations of ϕ_1 and ϕ_2 . It is analyzed that the velocity increases with an increase in the volume fraction of both nanoparticles. Figure 9a shows the contour for the pure-blood case, i.e., when no nanoparticle is injected into the bloodstream. The

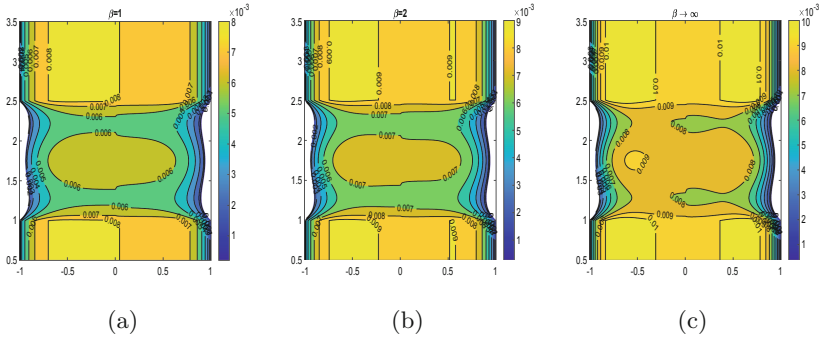


Fig. 8. Velocity contours for (a) $\beta = 1$, (b) $\beta = 2$, (c) $\beta \rightarrow \infty$

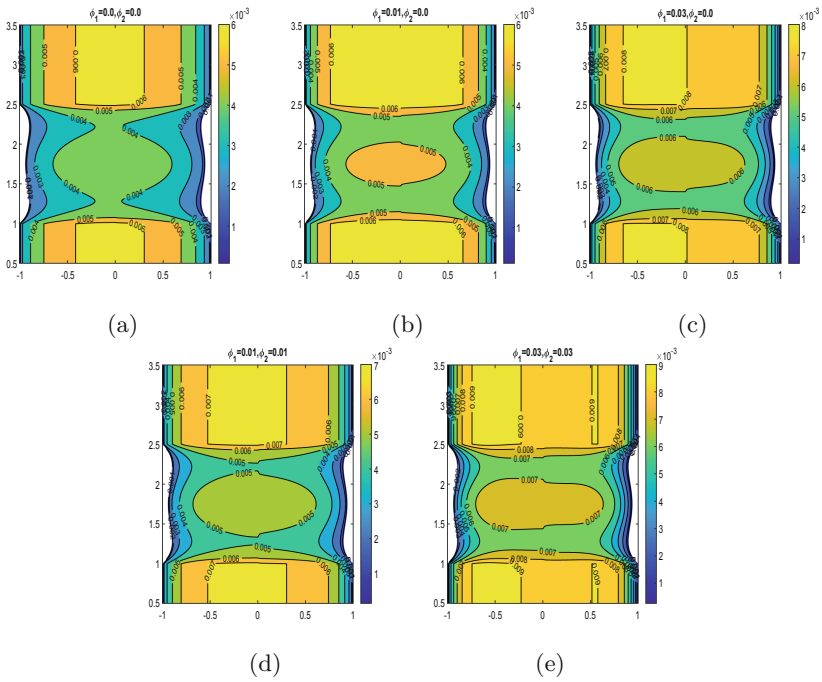


Fig. 9. Velocity contours for (a) $\phi_1 = 0.0, \phi_2 = 0.0$, (b) $\phi_1 = 0.01, \phi_2 = 0.0$, (c) $\phi_1 = 0.03, \phi_2 = 0.0$, (d) $\phi_1 = 0.01, \phi_2 = 0.01$, (e) $\phi_1 = 0.03, \phi_2 = 0.03$

formation of the trapped bolus is visible in the stenotic zone when comparing the pure-blood and nanoparticle cases. Also, the trapped bolus's size increases with an increase in the volume fraction of both nanoparticles.

5 Conclusions

In this study, hybrid nanoparticles (Au+Cu) of various shapes are used to evaluate the impacts of wall slip effects on blood flow through an overlapping stenosed artery. It is assumed that the blood viscosity varies with hematocrit. Additionally, as blood is thought to be non-Newtonian, it is modeled using the Casson fluid model, which accurately captures the properties of real blood. The Crank-Nicolson approach is used to discretize the governing equations before MATLAB is used to solve them. Graphical representations of the results, including contour plots, are used. According to the findings mentioned above, the following observations are made:

- The Au-Cu/Blood hybrid nanofluid reaches constantly higher magnitudes than Au-Blood nanofluid for the velocity and temperature profiles.
- The velocity profile show declination with h_m whereas the opposite trend is noticed for β .
- The WSS profiles elevate with w_s while the reverse trend is analyzed for flow rate profiles.
- WSS and flow rate profiles show elevation with ϕ_1 .
- The temperature profiles show enhancement with β and Nr.
- There is an increment in velocity and temperature profile with increase in ϕ_1 and ϕ_2 simultaneously.

Future Work. The current study may be extended to include a permeable bifurcated artery with stenosis in the parent and daughter artery while considering the shape and size of the nanoparticles influenced by external factors such as an applied electric field, Joule heating, heat source, and viscous dissipation.

References

1. Ghosh, P., Han, G., De, M., Kim, C.K., Rotello, V.M.: Gold nanoparticles in delivery applications. *Adv. Drug Deliv. Rev.* **60**(11), 1307–1315 (2008)
2. Gentile, F., Ferrari, M., Decuzzi, P.: The transport of nanoparticles in blood vessels: the effect of vessel permeability and blood rheology. *Ann. Biomed. Eng.* **36**(2), 254–261 (2008). <https://doi.org/10.1007/s10439-007-9423-6>
3. Ijaz, S., Nadeem, S.: Slip examination on the wall of tapered stenosed artery with emerging application of nanoparticles. *Int. J. Therm. Sci.* **109**, 401–412 (2016)
4. Bahrami, B., et al.: Nanoparticles and targeted drug delivery in cancer therapy. *Immunol. Lett.* **190**, 64–83 (2017)
5. Gupta, S., Kumar, D., Singh, J.: Analytical study for MHD flow of Williamson nanofluid with the effects of variable thickness, nonlinear thermal radiation and improved Fourier's and Fick's laws. *SN Appl. Sci.* **2**(3), 1–12 (2020). <https://doi.org/10.1007/s42452-020-1995-x>
6. Umadevi, C., Dhange, M., Haritha, B., Sudha, T.: Flow of blood mixed with copper nanoparticles in an inclined overlapping stenosed artery with magnetic field. *Case Stud. Thermal Eng.* **25**, 100947 (2021)

7. Ghandi, R., Sharma, B.K., Kumawat, C., Beg, O.A.: Modeling and analysis of magnetic hybrid nanoparticle (Au–Al₂O₃/blood) based drug delivery through a bell-shaped occluded artery with Joule heating, viscous dissipation and variable viscosity effects. *Proc. Inst. Mech. Eng., Part E: J. Process Mech. Eng.* 09544089221080273 (2022)
8. Gandhi, R., Sharma, B.K.: Unsteady MHD hybrid nanoparticle (Au–Al₂O₃/blood) mediated blood flow through a vertical irregular stenosed artery: Drug delivery applications. In: Banerjee, S., Saha, A. (eds.) *Nonlinear Dynamics and Applications*. Springer Proceedings in Complexity, pp. 325–337. Springer, Cham (2022). https://doi.org/10.1007/978-3-030-99792-2_28
9. Khanduri, U., Sharma, B.K.: Hall and ion slip effects on hybrid nanoparticles (au-go/blood) flow through a catheterized stenosed artery with thrombosis. *Proc. Inst. Mech. Eng., Part C: J. Mech. Eng. Sci.* 09544062221136710 (2022)
10. Layek, G.C., Mukhopadhyay, S., Gorla, R.S.R.: Unsteady viscous flow with variable viscosity in a vascular tube with an overlapping constriction. *Int. J. Eng. Sci.* **47**(5–6), 649–659 (2009)
11. Riahi, D.N., Roy, R., Cavazos, S.: On arterial blood flow in the presence of an overlapping stenosis. *Math. Comput. Model.* **54**(11–12), 2999–3006 (2011)
12. GC Sait and Sreeparna Majee: Pulsatile flow of blood and heat transfer with variable viscosity under magnetic and vibration environment. *J. Magn. Magn. Mater.* **388**, 106–115 (2015)
13. Zaman, A., Ali, N., Sajid, M.: Numerical simulation of pulsatile flow of blood in a porous-saturated overlapping stenosed artery. *Math. Comput. Simul.* **134**, 1–16 (2017)
14. Sharma, M., Sharma, B.K., Gaur, R.K., Tripathi, B.: Soret and Dufour effects in biomagnetic fluid of blood flow through a tapered porous stenosed artery. *J. Nanofluids* **8**(2), 327–336 (2019)
15. Das, S., Pal, T.K., Jana, R.N.: Outlining impact of hybrid composition of nanoparticles suspended in blood flowing in an inclined stenosed artery under magnetic field orientation. *BioNanoScience* **11**(1), 99–115 (2021). <https://doi.org/10.1007/s12668-020-00809-y>
16. Zhang, X., Wang, E., Ma, L., Shu, C., Zheng, L.: Analysis of hemodynamics and heat transfer of nanoparticle-injected atherosclerotic patient: considering the drag force and slip between phases of different particle shapes and volume fractions. *Int. J. Therm. Sci.* **159**, 106637 (2021)
17. Basha, H.T., Rajagopal, K., Ahammad, N.A., Sathish, S., Gunakala, S.R.: Finite difference computation of Au-Cu/magneto-bio-hybrid nanofluid flow in an inclined uneven stenosis artery. *Complexity* **2022**, 1–18 (2022)
18. Gandhi, R., Sharma, B.K., Makinde, O.D.: Entropy analysis for MHD blood flow of hybrid nanoparticles (Au–Al₂O₃/blood) of different shapes through an irregular stenosed permeable walled artery under periodic body acceleration: Hemodynamical applications. *ZAMM-J. Appl. Math. Mecha./Zeitschrift für Angewandte Mathematik und Mechanik* e202100532 (2022)
19. Sharma, B.K., Poonam, Chamkha, A.J.: Effects of heat transfer, body acceleration and hybrid nanoparticles (Au–Al₂O₃/blood) on MHD blood flow through a curved artery with stenosis and aneurysm using hematocrit-dependent viscosity. *Waves Random Complex Media* 1–31 (2022)
20. Chakravarty, S., Mandal, P.K., et al.: Numerical simulation of Casson fluid flow through differently shaped arterial stenoses. *Zeitschrift angewandte Math. Phys.* **65**(4), 767–782 (2014)

21. Debnath, S., Saha, A.K., Mazumder, B.S., Roy, A.K.: Transport of a reactive solute in a pulsatile non-Newtonian liquid flowing through an annular pipe. *J. Eng. Math.* **116**(1), 1–22 (2019). <https://doi.org/10.1007/s10665-019-09999-1>
22. Ali, A., Farooq, H., Abbas, Z., Bukhari, Z., Fatima, A.: Impact of Lorentz force on the pulsatile flow of a non-Newtonian Casson fluid in a constricted channel using Darcy's law: a numerical study. *Sci. Rep.* **10**(1), 1–15 (2020)
23. Tassaddiq, A., Khan, I., Nisar, K.S., Singh, J.: MHD flow of a generalized Casson fluid with Newtonian heating: a fractional model with Mittag-Leffler memory. *Alexandria Eng. J.* **59**(5), 3049–3059 (2020)
24. Singh, J., Kumar, D., Baleanu, D., et al.: A hybrid analytical algorithm for thin film flow problem occurring in non-Newtonian fluid mechanics. *Ain Shams Eng. J.* **12**(2), 2297–2302 (2021)
25. Das, P., Sarifuddin, Rana, J., Mandal, P.K. Solute dispersion in transient Casson fluid flow through stenotic tube with exchange between phases. *Phys. Fluids* **33**(6), 061907 (2021)
26. Padma, R., Tamil Selvi, R., Ponalagusamy, R.: Electromagnetic control of non-Newtonian fluid (blood) suspended with magnetic nanoparticles in the tapered constricted inclined tube. In: *AIP Conference Proceedings*, vol. 2336, p. 020008. AIP Publishing LLC (2021)
27. Sharma, B.K., Gandhi, R., Bhatti, M.M.: Entropy analysis of thermally radiating MHD slip flow of hybrid nanoparticles (Au-Al₂O₃/blood) through a tapered multi-stenosed artery. *Chem. Phys. Lett.* **790**, 139348 (2022)
28. Burton, A.C.: Physiology and biophysics of the circulation. *Acad. Med.* **40**(8), xxx–xxxvi (1965)
29. Anderson, J.D., Wendt, J.: *Computational Fluid Dynamics an Introduction*, vol. 206 (1995)
30. Zhang, B., Junyi, G., Qian, M., Niu, L., Zhou, H., Ghista, D.: Correlation between quantitative analysis of wall shear stress and intima-media thickness in atherosclerosis development in carotid arteries. *Biomed. Eng. Online* **16**(1), 1–17 (2017)



Generalized Solitary Wave Approximate Analytical and Numerical Solutions for Generalized Damped Forced KdV and Generalized Damped Forced MKdV Equations

Shruti Tomar^{1(✉)}, Naresh M. Chadha¹, and Santanu Raut²

¹ Department of Mathematics, School of Physical Sciences, DIT University, Dehradun 248009, Uttarakhand, India
tomar05shruti@gmail.com

² Department of Mathematics, Mathabhanga College, Coochbehar 736146, India

Abstract. In this article, we study the non-linear partial differential equation given by $u_t + Pu^k u_x + Qu_{xxx} + Su = f(t)$, where P, Q, S denote non-linear coefficient, dispersion coefficient, and damping coefficient, respectively; $f(t)$ denotes external hyperbolic forcing term, $f_0 \cosh(\omega t)$. The parameter ' k ' denotes the non-linear exponent. For $k = n$, where $n \in \mathbb{N}$, the equation represents the Generalized Damped Forced KdV (GDFKdV) equation, and for $k = n/2$, it can be referred to as the Generalized Modified Damped Forced KdV (GMDFKdV) equation. Initially, analytical solution of the Generalized KdV (GKdV) equation and the Generalized modified KdV (GMKdV) equation are derived employing sine-cosine method. Further, we obtain the solitary wave analytical solutions to the GDFKdV and GMDFKdV equations by using the direct assumption technique. We construct the generalized forms of the solutions, which involve two new parameters, ' a ' and ' b '. In the first instance, the solutions to GDFKdV, and GMDFKdV may look very similar. However, in this article, it has been shown that the nature of solitons and their topological structures emerging from these two equations are very different. Using the method of dynamical systems, we analyse the bifurcation and nature of the solutions. Finally, the pseudo-spectral method, which we employed to approximate the solutions, is proven to be ineffective concerning time and the increasing value of exponent power n . Our theoretical results are supported by our numerical experiments.

Keywords: GDFKdV · GDFMKdV · the sine-cosine method · Bifurcation analysis · the basic Pseudo-spectral method

1 Introduction

Nonlinear evolution equations (NLEEs) can be used to represent a wide range of complicated physical processes and have applications in many areas of research,

including physics, chemistry, biology, astronomy, and others [1, 3, 8, 10, 15, 20]. Several researchers have suggested different approaches to find its analytical solutions, e.g., the Hirota bilinear method [22], the generalized exponential rational function technique [6], the local fractional natural homotopy analysis method [4], the semi analytical method [19], the simple equation method [9], the Exp $(-\phi(\xi))$ expansion method [11, 12], the sine-cosine method [21] to name a few. Finding approximate analytical solutions to NLEEs may present some difficulties if a highly nonlinear term appears in these equations. For example, the scenario may become more complicated if damping or forcing terms are present [13, 17].

Recently, enormous interest began to investigate the NLEEs under a localized disturbance in the dynamic system [14, 16]. Actually, some excellent observations in the astronomical space plasma environment motivated the researchers for examining the NLEEs under the influence of external forces [2, 18]. Again, damping is a common phenomenon that exists in all real physical systems. Thus, the non-autonomous system containing damping and forcing terms is much more realistic than its autonomous counterpart.

In this paper, we take into account a highly nonlinear evolution equation and use the direct assumption method to generate approximate analytical solutions that contain both damping and forcing terms, and we study the bifurcation analysis while considering the forcing and the damping terms equal to zero. For this generalized setting, it exhibits different-different topological structures for a range of values of the parameters which are supported by the numerical technique, the Pseudo-spectral method [5]. The spectral approach can be used to approximately correlate the numerical results to the analytical results. Accuracy is provided using spectral approaches with an exponential convergence rate. With this approach, the partial differential equation can be represented as a linear combination of basis functions, with the coefficient chosen so that the resulting linear combination closely approximates the solution. This approach has a number of constraints, including boundary conditions. To support our theoretical findings in this study, we are using the fundamental Pseudo-spectral approach.

We consider the non-linear evolution equation

$$u_t + Pu^k u_x + Qu_{xxx} + Su = f(t), \quad (1.1)$$

where $f(t)$ stands for the external hyperbolic forcing term and P , Q , and S stand for the non-linear coefficients, dispersion coefficient, and damping coefficient, respectively. The non-linear exponent is denoted by the parameter k , for which if $k = n$, it represents the GDFKdV equation and if $k = n/2$, it is the GMDFKdV equation, where $n \in N$. equal to zero.

In this paper, Sect. 2 represents the analytical solutions for $k = n$, and $k = n/2$ which are obtained by the sine-cosine method for the simplified case i.e. $u_t + Pu^k u_x + Qu_{xxx} = 0$. It appears that there is no significant difference in the solution profile except for varied values of P . However, when this equation is transformed into a dynamical system, it becomes clear that the solutions of GKdV and GMKdV behave very differently near their equilibrium points

for the same value of the parameters, which is investigated by the standard tools of the bifurcation analysis in Sect. 3. By using the direct assumption technique, an approximative analytical solution for a generalized situation Eq. (1.1) is obtained. It can be seen that the parameters have a dramatically different effect on the solutions of GDFKdV and GMDFKdV, which are displayed using contour plots and three-dimensional surface graphs. This is the subject matter of Sect. 4. In Sect. 5, we extend the study by introducing two new parameters, a and b in the solution of Eq. (1.1), which is referred to as the generalized solution of the GDFKdV and the GMDFKdV here. It is observed that for the different values of these parameters, one can obtain multiple types of solitons which may depict Gaussian-type pulses, multiple humps, and twisted curved sheet-like topological structures. These results are supported by the Pseudo-spectral method, described in Sect. 6. The conclusion of this study is summarized in Sect. 7.

2 Approximate Analytical Solutions of GKdV and GMKdV Equations

Consider the case of a general non-linear partial differential equation with an unknown $u = u(x, t)$ as,

$$\mathcal{N}(u, u_t, u_x, u_{xx}, u_{tx}, u_{xxx}, \dots) = 0. \tag{2.1}$$

Now introducing a new stretching variable ζ by combining the real variables x and t such that,

$$u(x, t) = V(\zeta), \quad \zeta = \omega_0(x - ct). \tag{2.2}$$

Eq. (2.1) is converted into an ordinary differential equation (ODE) with the help of the above transformation,

$$\mathcal{M}(V, V', V'', V''', \dots) = 0, \tag{2.3}$$

where $(')$ signifies a derivative with respect to ζ and \mathcal{M} is a polynomial in terms of V and its derivatives.

The sine-cosine approach suggests that the solutions could take the following form of

$$V = \lambda_0 \sin^\gamma(\zeta), \tag{2.4}$$

or in the form

$$V = \lambda_0 \cos^\gamma(\zeta). \tag{2.5}$$

where λ_0 , γ and ζ are included parameters to be determined. Substituting Eq.(2.4) or Eq.(2.5) into Eq.(2.3), and solving the system of equations to obtain all possible values of the parameters λ_0 , γ , and ζ . Put the values into Eq.(2.4) or Eq.(2.5), will present a new solutions of Eq.(2.3).

We employ sine-cosine method to find the analytical solutions of GKdV and GMKdV equation. Here, a suitable transform is chosen to reduced the partial

differential equation into an ordinary differential equation (ODE). We consider a generalized form of KdV equation given by

$$u_t + Pu^k u_x + Qu_{xxx} = 0. \tag{2.6}$$

Using the wave transformation $u(x, t) = V(\zeta)$, $\zeta = w_0(x - ct)$, and taking integration, we find

$$-cV' + \frac{PV^{k+1}}{k+1} + Qw_0^2 V'' = 0. \tag{2.7}$$

According to the sine-cosine method the solutions of Eq. (2.7) can be expressed in the form

$$V = \lambda_0 \cos^\gamma(\zeta). \tag{2.8}$$

By substituting Eq.(2.8) into Eq.(2.7) gives the system of algebraic equations

$$\begin{aligned} \gamma - 2 &= \gamma(k + 1), \\ Qw^2\gamma^2\lambda_0(k + 1) - c\lambda_0(k + 1) &= 0, \\ Qw_0^2\lambda_0\gamma^2k - Qw_0^2\lambda_0\gamma n - Qw_0^2\lambda_0\gamma + Qw_0^2\lambda_0\gamma^2 + P\lambda_0^{k+1} &= 0. \end{aligned} \tag{2.9}$$

Solving this system, we have

$$\gamma = -\frac{2}{n}, w_0 = \frac{k}{2}\sqrt{-\frac{c}{Q}}, \lambda_0 = \left(\frac{c(k+1)(k+2)}{2P}\right)^{\frac{1}{k}}. \tag{2.10}$$

From Eq. (2.10),the analytical solution of Eq.(2.6) is obtained and given by

$$V(\zeta) = u(x, t) = \left[\frac{c(k+1)(k+2)}{2P} \operatorname{sech}^2\left(\frac{k}{2}\sqrt{\frac{c}{Q}}(x - ct)\right)\right]^{\frac{1}{k}}. \tag{2.11}$$

Now, we have two cases: for (a) $k = n$, and $k = n/2$; they correspond to GKdV and GMKdV equations, respectively. Their solutions are as follows

– **Case 1** $k = n$ (GKdV equation), the solution is

$$u(x, t) = \left[\frac{c(n+1)(n+2)}{2P} \operatorname{sech}^2\left(\frac{n}{2}\sqrt{\frac{c}{Q}}(x - ct)\right)\right]^{\frac{1}{n}}. \tag{2.12}$$

– **Case 2** $k = n/2$ (mGKdV equation), the solution is

$$u(x, t) = \left[c\frac{(n+2)(n+4)}{8P} \operatorname{sech}^2\left(\frac{n}{4}\sqrt{\frac{c}{Q}}(x - ct)\right)\right]^{\frac{2}{n}}. \tag{2.13}$$

These solutions are plotted in Fig. 1 for the parameters $P = 0.5, Q = 2.5, t = 0.5, c = 0.5$. For Fig. 1 (a), (e), n is varied and rest of the figures $n = 3$ is kept fixed and P , and Q are varied. From the comparison of these figures, it seems there is no significant difference in the analytical behaviour of the solitons obtained for both GKdV and GMKdV except for the parameter P . In the next section, we employ certain tools such as eigenvalues and phase portraits from bifurcation analysis to investigate the impact of the parameters on the solution profiles.

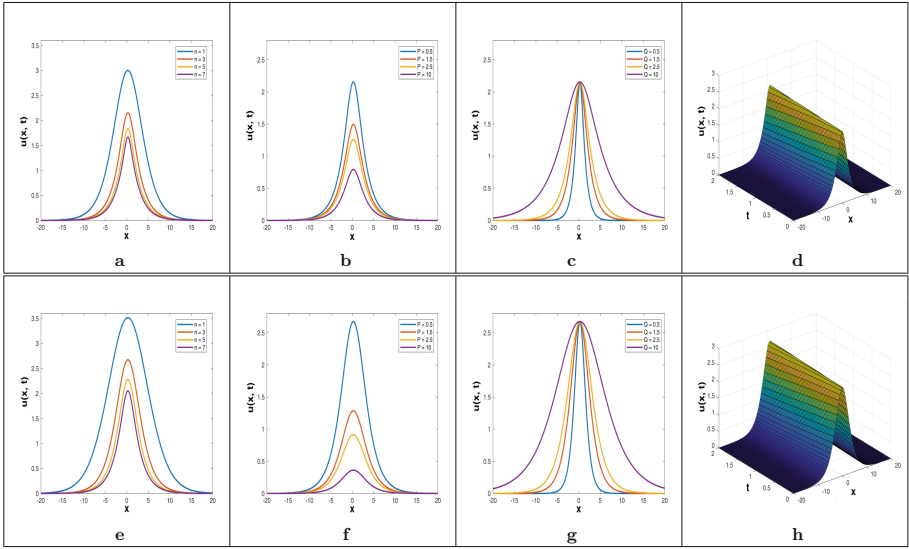


Fig. 1. The solutions of GKdV and Modified KdV are compared. The parameters used are: $P = 0.5, Q = 2.5, t = 0.5, c = 0.5,$ and $n = 3$ is fixed except for the figure where n is varied.

3 Bifurcation Analysis of GKdV Equation and GMKdV Equation

By following the [7], the dynamical system corresponding to Eq.(2.7) is as follows

$$u' = v, v' = \frac{1}{Qw_0^2} \left(cu - P \frac{u^{k+1}}{k+1} \right). \tag{3.1}$$

The determinant of Jacobian matrix is $|J| = -\frac{1}{Qw_0^2} (c - Pu^k)$, we have two equilibrium points for this system: $(0, 0)$ and $\left(\left(\frac{(k+1)c}{P} \right)^{1/k}, 0 \right), n \in N$. The corresponding eigenvalues are

$$\lambda_{1,2} = \pm \sqrt{\frac{c - Pu^k}{Qw_0^2}}. \tag{3.2}$$

In the dynamical system given by Eq. (3.1), we have a exponent k , different values of $k = n$ or $n/2$ will produce different sets of equilibrium points. In this study, we are considering $n = [1, 3, 5]$.

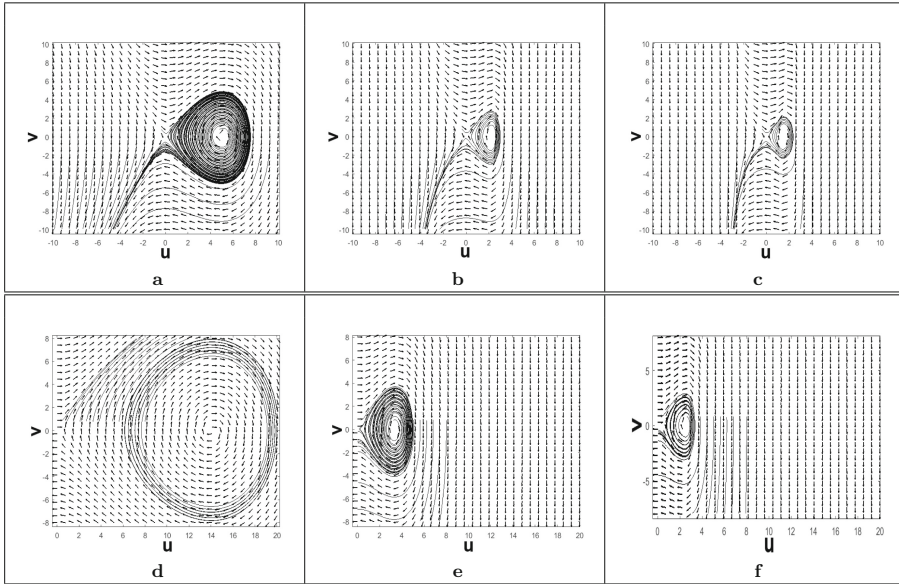


Fig. 2. Behaviour of Dynamical system (3.1) for GKdV and GMKdV equation. For odd values of $n = [1, 3, 5]$ and other parameter are $c = 1$; $P = 0.4$; $Q = 0.35$; $w_0 = 1$.

Let us consider two cases:

- **For $k = n$,** the dynamical system corresponds to GKdV equation. The phase portraits corresponding to $n = [1, 3, 5]$ are shown in Fig. 2 a, b, c for fixed value of the parameters $P = 0.4$, $Q = 0.35$, $c_0 = 1$, and $w_0 = 1$. For $n = 1$, the system will have two equilibrium points $(0, 0)$ and $(\frac{2c}{P}, 0)$. There is a center in the vicinity of point $(\frac{2c}{P}, 0)$, and trajectories show periodic behaviour around this center. These trajectories move away from each other when they move further towards $(0, 0)$ which implies that the system becomes unstable in the neighborhood of $(0, 0)$ and enters into unbounded open orbits. For fixed values of the parameters, the system will always remain unstable in this orbit. Similar conclusions can be drawn for $n = 3, 5$.
- **For $k = \frac{n}{2}$,** the dynamical system will correspond to the GMKdV equation. For $n = [1, 3, 5]$, we will have a fractional exponent. The phase portraits are shown in Fig. 2 d, e, f corresponding to these values of n , considering the same values of the parameters used to plot phase portraits Fig. 2 a, b, c. This system will have one saddle point at $(0, 0)$ and one centre point at $\left(\left(\frac{(\frac{n}{2} + 1)c}{P} \right)^{2/n}, 0 \right)$. In the neighborhood of the center point, these trajectories show periodic behaviour. Proceeding further, the system becomes unstable near the saddle point, and trajectories stop moving forward at this unstable point. For the higher value of n i.e., $n = [3, 5]$, these trajectories are showing compressive behaviour and moving towards an unstable point.

For GKdV and GMKdV, the equilibrium point, corresponding eigenvalues, and expected topological properties are summarized in Table 1 and Table 2. Complex equilibrium points are omitted here as they may not be very useful for practical purposes.

Table 1. Behaviour of equilibrium points and corresponding eigenvalues with respect to values of $n = [1, 3, 5]$ for GKdV.

k	Equilibrium points	Eigenvalues	Nature	Topological property
1	$(0, 0), (\frac{2c}{P}, 0)$	$\lambda_{1,2} = \pm i\sqrt{\frac{c}{Qw_0^2}}, \lambda_{1,2} = \pm\sqrt{\frac{c}{Qw_0^2}}$	1-SADDLE 1-CENTRE	1-unstable, 1-stable
3	$(0, 0), (\sqrt[3]{\frac{4c}{P}}, 0)$	$\lambda_{1,2} = \pm i\sqrt{\frac{3c}{2Qw_0^2}}, \lambda_{1,2} = \pm\sqrt{\frac{c}{Qw_0^2}}$	1-SADDLE 1-CENTRE	1-unstable, 1-stable
5	$(0, 0), (\sqrt[5]{\frac{6c}{P}}, 0)$	$\lambda_{1,2} = \pm i\sqrt{\frac{5c}{2Qw_0^2}}, \lambda_{1,2} = \pm\sqrt{\frac{c}{Qw_0^2}}$	1-SADDLE 1-CENTRE	1-unstable, 1-stable

Table 2. Behaviour of equilibrium points and corresponding eigenvalues with respect to values of $n = [1, 3, 5]$ for GMKdV equations.

k	Equilibrium points	Eigenvalues	Nature	Topological property
$\frac{1}{2}$	$(0, 0), ((\frac{3c}{P})^2, 0)$	$\lambda_{1,2} = \pm i\sqrt{\frac{c}{2Qw_0^2}}, \lambda_{1,2} = \pm\sqrt{\frac{c}{Qw_0^2}}$	1-SADDLE 1-CENTRE	1-unstable, 1-stable
$\frac{3}{2}$	$(0, 0), ({}^2\sqrt[3]{\frac{5c}{2P}}, 0)$	$\lambda_{1,2} = \pm i\sqrt{\frac{3c}{2Qw_0^2}}, \lambda_{1,2} = \pm\sqrt{\frac{c}{Qw_0^2}}$	1-SADDLE 1-CENTRE	1-unstable, 1-stable
$\frac{5}{2}$	$(0, 0), ({}^2\sqrt[5]{\frac{7c}{2P}}, 0)$	$\lambda_{1,2} = \pm i\sqrt{\frac{5c}{2Qw_0^2}}, \lambda_{1,2} = \pm\sqrt{\frac{c}{Qw_0^2}}$	1-SADDLE 1-CENTRE	1-unstable, 1-stable

4 Approximate Analytical Solutions of GDFKDV and GMDFKDV Equations

In this section, we shall derive approximate analytical solutions of GDFKDV and GMDFKDV equations by using direct assumption technique. Recall, a generalized form of equation as

$$u_t + Pu^k u_x + Qu_{xxx} + Su = f(t), \tag{4.1}$$

where S is damping coefficient, and $f(t)$ denotes the forcing term. We take the solution for the above equation as

$$u = \left[\frac{c(t)(k+1)(k+2)}{2P} \operatorname{sech}^2 \left(\frac{k}{2} \sqrt{\frac{c(t)}{Q}} (x - c(t)t) \right) \right]^{\frac{1}{k}}. \tag{4.2}$$

We know that $I = \int_{-\infty}^{\infty} u^2 dx$ is conserved. Thus, we have

$$I = \int_{-\infty}^{\infty} u(x, t)^2 dx = \frac{2^{\frac{4}{k}+1} c(t)^{\frac{2}{k}-\frac{1}{2}} \beta \left(\frac{2}{k}, \frac{2}{k} \right) \left(\sqrt[2k]{\frac{(k+1)(k+2)}{2P}} \right)^2}{k \sqrt{\frac{1}{Q}}}. \tag{4.3}$$

Differentiating the Eq. (4.3) with respect to t and taking Eq. (4.1) and Eq. (4.3) together with differential value as,

$$\begin{aligned} \frac{dI}{dt} &= 2 \int_{-\infty}^{\infty} u(x, t) \frac{\partial u}{\partial t} dx = -2 \int_{-\infty}^{\infty} u (P u^k u_x + Q u_{xxx} + S u - f(t)) dx \\ &= -2S \frac{2^{\frac{4}{k}+1} c(t)^{\frac{2}{k}-\frac{1}{2}} \beta \left(\frac{2}{k}, \frac{2}{k}\right) \left(\sqrt[k]{\frac{(k+1)(k+2)}{2P}}\right)^2}{k\sqrt{\frac{1}{Q}}} + 2f(t) \frac{\left[c(t)^{\frac{1}{k}-\frac{1}{2}} \left(\sqrt[k]{\frac{(k+1)(k+2)}{2P}}\right)^{2^{\frac{2}{k}+1}} \beta \left(\frac{1}{k}, \frac{1}{k}\right) \right]}{k\sqrt{\frac{1}{Q}}}. \end{aligned} \tag{4.4}$$

(Since $\int_{-\infty}^{\infty} u^k u u_x dx = 0$ and $\int_{-\infty}^{\infty} u u_{xxx} dx = 0$ both holds true.)

By simplifying the Eq. (4.4), we obtain following differential equation for $c(t)$ as

$$\frac{1}{k} c(t)^{\frac{1}{k}-1} \frac{dc(t)}{dt} + \frac{4S}{(4-k)} c(t)^{\frac{1}{k}} = \frac{4\beta \left(\frac{1}{k}, \frac{1}{k}\right)}{(4-k) \left(\sqrt[k]{\frac{(k+1)(k+2)}{2P}}\right)^{2^{\frac{2}{k}}}} \beta \left(\frac{2}{k}, \frac{2}{k}\right) f(t). \tag{4.5}$$

For the forcing term $f(t) = f_0 \cosh(\omega t)$, the solution is

$$u(x, t) = \left[\frac{c(t)(n+1)(n+2)}{2P} \operatorname{sech}^2 \left(\frac{n}{2} \sqrt{\frac{c(t)}{Q}} (x - c(t)t) \right) \right]^{\frac{1}{n}}, \tag{4.6}$$

where

$$c(t)^{\frac{1}{k}} = \frac{2\beta \left(\frac{1}{k}, \frac{1}{k}\right) f_0}{2^{\frac{2}{k}} \beta \left(\frac{2}{k}, \frac{2}{k}\right) \sqrt[k]{\frac{(k+1)(k+2)}{2P}}} \left[\frac{8S \cosh(\omega t) - 2\omega(4-k) \sinh(\omega t)}{16S^2 - \omega^2(4-k)^2} \right] + c_1 e^{-\frac{4S}{(4-k)}t},$$

and the constant

$$c_1 = c_0^{1/k} - \frac{2\beta \left(\frac{1}{k}, \frac{1}{k}\right) f_0}{2^{\frac{2}{k}} \beta \left(\frac{2}{k}, \frac{2}{k}\right) \sqrt[k]{\frac{(k+1)(k+2)}{2P}}} \frac{8S}{16S^2 - \omega^2(4-k)^2}.$$

– **Case1.** $k = n$, **Solitary Wave Solution of GDFKDV** For the forcing term $f(t) = f_0 \cosh(\omega t)$, the solution is

$$u = \left[\frac{c(t)(n+1)(n+2)}{2P} \operatorname{sech}^2 \left(\frac{n}{2} \sqrt{\frac{c(t)}{Q}} (x - c(t)t) \right) \right]^{\frac{1}{n}}, \tag{4.7}$$

where

$$c(t)^{\frac{1}{n}} = \frac{2\beta \left(\frac{1}{n}, \frac{1}{n}\right) f_0}{2^{\frac{2}{n}} \beta \left(\frac{2}{n}, \frac{2}{n}\right) \sqrt[n]{\frac{(n+1)(n+2)}{2P}}} \left[\frac{8S \cosh(\omega t) - 2\omega(4-n) \sinh(\omega t)}{16S^2 - \omega^2(4-n)^2} \right] + c_1 e^{-\frac{4S}{(4-n)}t},$$

and the constant

$$c_1 = c_0^{1/n} - \frac{2\beta \left(\frac{1}{n}, \frac{1}{n}\right) f_0}{2^{\frac{2}{n}} \beta \left(\frac{2}{n}, \frac{2}{n}\right) \sqrt[n]{\frac{(n+1)(n+2)}{2P}}} \frac{8S}{16S^2 - \omega^2(4-n)^2}.$$

– **Case2.** $k = n/2$, **Solitary Wave Solution of GMDFKDV** For the forcing term $f(t) = f_0 \cosh(\omega t)$, the solution is

$$u = \left[\frac{c(t)(n+2)(n+4)}{8P} \operatorname{sech}^2 \left(\frac{n}{4} \sqrt{\frac{c(t)}{Q}} (x - c(t)t) \right) \right]^{\frac{2}{n}}, \quad (4.8)$$

where

$$c(t)^{\frac{2}{n}} = \frac{4f\beta \left(\frac{2}{n}, \frac{2}{n}\right)}{2^{\frac{4}{n}} \beta \left(\frac{4}{n}, \frac{4}{n}\right) \left(\sqrt{\frac{(n+2)(n+4)}{8P}} \right)^2} \left[\frac{16S \cosh(\omega t) - 2\omega(8-n) \sinh(\omega t)}{64S^2 - \omega^2(8-n)^2} \right] + c_1 e^{-\frac{8S}{(8-n)}t},$$

and the constant

$$c_1 = c_0^{2/n} - \frac{4f\beta \left(\frac{2}{n}, \frac{2}{n}\right)}{2^{\frac{4}{n}} \beta \left(\frac{4}{n}, \frac{4}{n}\right) \left(\sqrt{\frac{(n+2)(n+4)}{8P}} \right)^2} \frac{16S}{64S^2 - \omega^2(8-n)^2}.$$

The impact of the damping coefficient on the solutions of GDFKdV and GMDFKdV is shown in Fig. 3. The damping coefficient is considered for these discrete values $S = [0.1, 0.2, 0.5, 0.8]$, and the rest of the parameters are kept fixed as $c_0 = 0.5, P = 0.5, Q = 2.5, \omega = 0.5, n = 3, f = 0.01$. It is very clear from the plots that the profiles corresponding to GDFKdV and GMDFKdV are very different. For GDFKdV, with an increase in damping coefficient, the soliton, which has a Gaussian-pulse type structure, tends to flatten down from the backside. The impact is clearly visible in the contour plots also. A similar impact can also be observed for GMDFKdV. The impact of frequency coefficient ω on the solution profiles of GDFKdV and GMDFKdV is shown in Fig. 4. The values of ω are $\omega = [0.05, 2.0, 2.5, 3.0]$, and rest of the parameters are $c_0 = 0.5, P = 0.5, Q = 2.5, f = 0.02, n = 3, S = 0.01$. For both GDFKdV and GMDFKdV, it can be seen that with an increase in frequency coefficient, the soliton acquires curvature, which is visible in surface plots and corresponding contour plots.

5 Generalized Solutions of GDFKDV and GMDFKDV Equations

For our generalized problem

$$u_t + Pu^k u_x + Qu_{xxx} + Su = f(t), \quad (5.1)$$

we consider the solution in more generalized form given as follows

$$u = c^a(t) \left[\frac{(k+1)(k+2)}{2P} \operatorname{sech}^2 \left(\left(\frac{k}{2} \sqrt{\frac{1}{Q}} (x - c(t)t) \right) c^b(t) \right) \right]^{\frac{1}{k}}. \quad (5.2)$$

For the hyperbolic forcing term of the form, $f(t) = f \cosh(\omega t)$, the generalized solution is as follows:

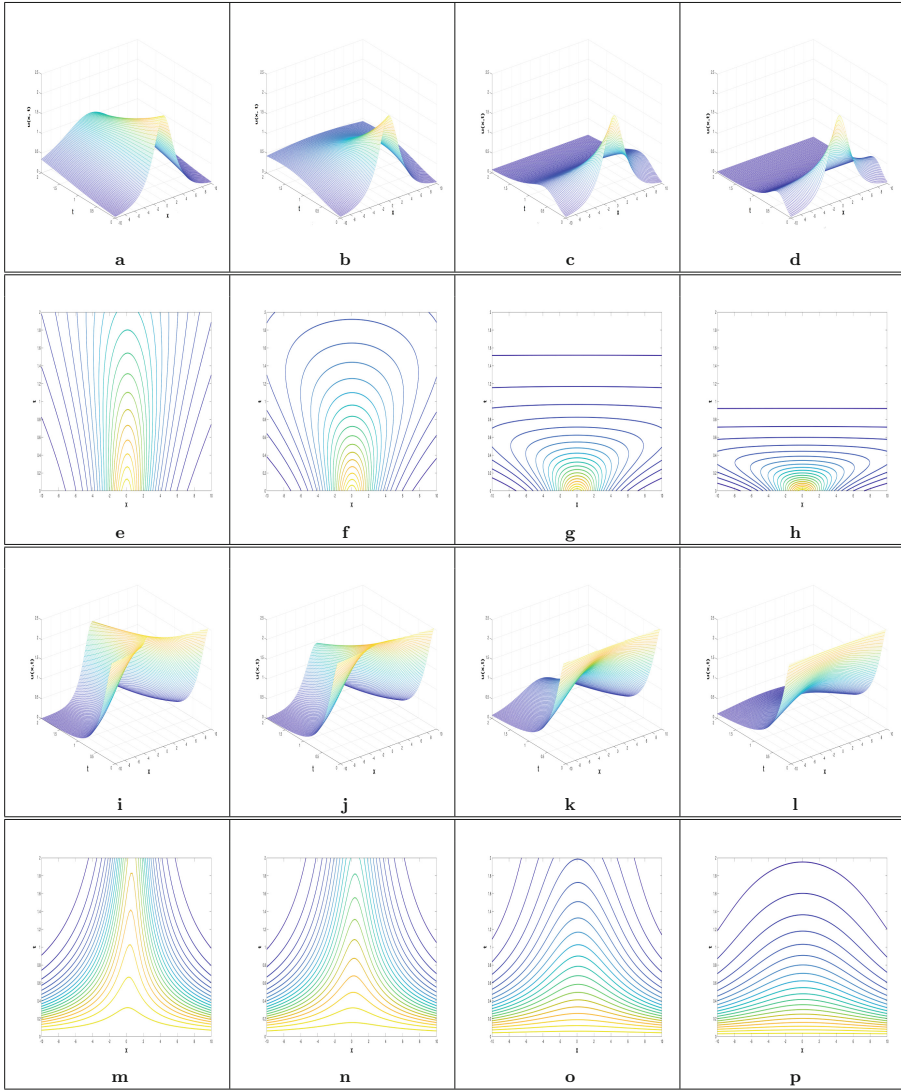


Fig. 3. The solutions of GDFKdV and GMDFKdV are compared for different values of damping parameter $S = [0.1, 0.2, 0.5, 0.8]$. Other parameters used are: $c_0 = 0.5, P = 0.5, Q = 2.5, \omega = 0.5, n = 3, f = 0.01$.

– **Case1. $k = n$, Solitary Wave Solution of GDFKdV**

$$u = c^a(t) \left[\frac{(n+1)(n+2)}{2P} \operatorname{sech}^2 \left(\left(\frac{n}{2} \sqrt{\frac{1}{Q}} (x - c(t)t) \right) c^b(t) \right) \right]^{\frac{1}{n}}. \quad (5.3a)$$

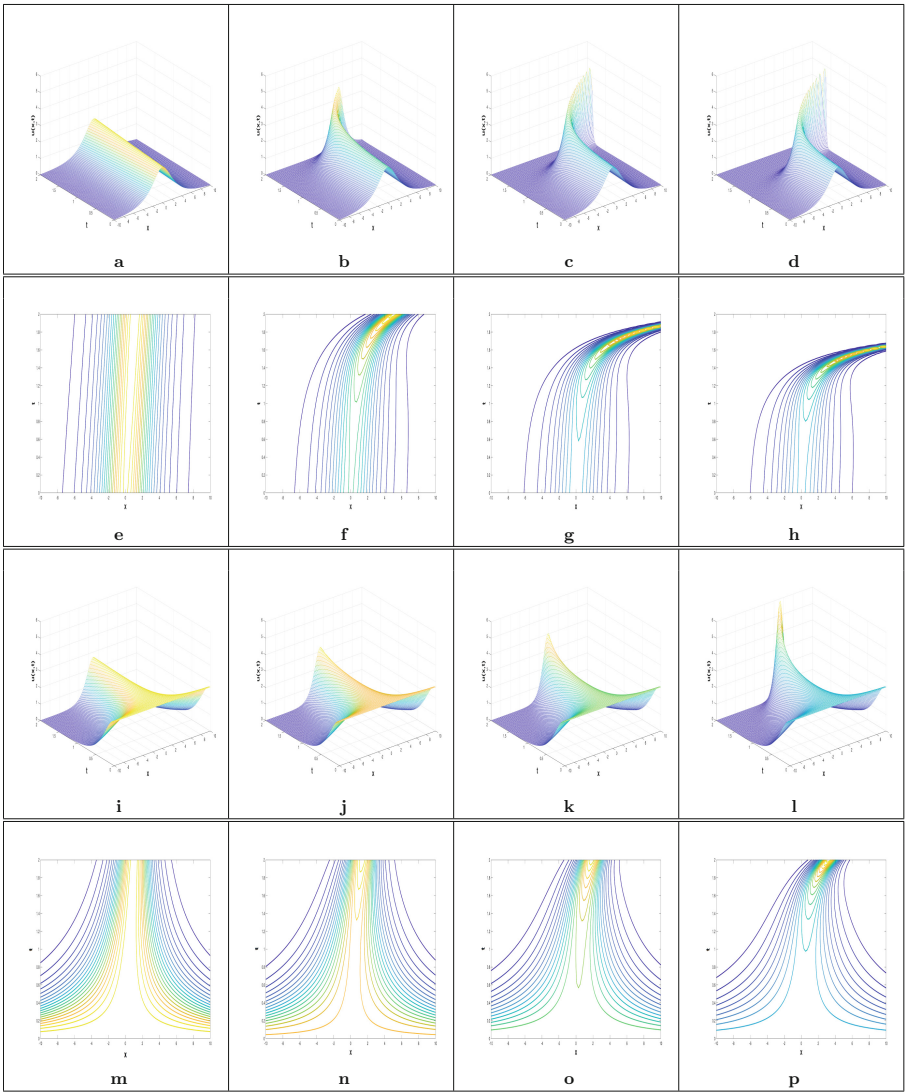


Fig. 4. The solutions of the GDFKdV and GMDFKdV are compared for different values of frequency coefficient $\omega = [0.05, 2.0, 2.5, 3.0]$. Other parameters used are: $c_0 = 0.5, P = 0.5, Q = 2.5, f = 0.02, n = 3, S = 0.01$.

where

$$c^a(t) = \frac{a\beta \left(\frac{1}{n}, \frac{1}{n}\right) f}{2^{\frac{2}{n}} \beta \left(\frac{2}{n}, \frac{2}{n}\right) n \sqrt{\frac{(n+1)(n+2)}{2P}}} \left[\frac{4aS \cosh(\omega t) - 2\omega(2a-b) \sinh(\omega t)}{4a^2 S^2 - \omega^2(2a-b)^2} \right] + c_1 e^{-\frac{2aS}{(2a-b)} t}, \tag{5.3b}$$

and the constant

$$c_1 = c_0^a - \frac{a\beta \left(\frac{1}{n}, \frac{1}{n}\right) f}{2^{\frac{2}{n}} \beta \left(\frac{2}{n}, \frac{2}{n}\right) \sqrt[n]{\frac{(n+1)(n+2)}{2P}}} \frac{4aS}{4a^2S^2 - \omega^2(2a - b)^2}. \tag{5.3c}$$

– **Case2.** $k = n/2$, **Solitary Wave Solution of GMDFKDV**

$$u = c^a(t) \left[\frac{(n+2)(n+4)}{8P} \operatorname{sech}^2 \left(\left(\frac{n}{4} \sqrt{\frac{1}{Q}} (x - c(t)t) \right) c^b(t) \right) \right]^{\frac{2}{n}}. \tag{5.4}$$

where

$$c^a(t) = \frac{a\beta \left(\frac{2}{n}, \frac{2}{n}\right) f}{2^{\frac{4}{n}} \beta \left(\frac{4}{n}, \frac{4}{n}\right) \left(\sqrt[n]{\frac{(n+2)(n+4)}{8P}} \right)^2} \left[\frac{4aS \operatorname{cosh}(\omega t) - 2\omega(2a - b) \sinh(\omega t)}{4a^2S^2 - \omega^2(2a - b)^2} \right] + c_1 e^{-\frac{2aS}{(2a-b)}t},$$

and the constant

$$c_1 = c_0^a - \frac{a\beta \left(\frac{2}{n}, \frac{2}{n}\right) f}{2^{\frac{4}{n}} \beta \left(\frac{4}{n}, \frac{4}{n}\right) \left(\sqrt[n]{\frac{(n+2)(n+4)}{8P}} \right)^2} \frac{4aS}{4a^2S^2 - \omega^2(2a - b)^2}.$$

Various topological structures within the framework of solitons corresponding to various combinations of a , and b are shown in Fig. 5 and Fig. 6. The value of other parameters are kept fixed as $c_0 = 0.5, P = 0.5, Q = 2.5, f = 0.01, \omega = 0.5, S = 0.05, n = 3$ to generate these plots.

6 Analysis of GKdV and GMKdV Equation with the Help of Pseudo-spectral Method

Consider a Generalized nonlinear evolution equation

$$u_t + Pu^k u_x + Qu_{xxx} = 0, \\ u(x, 0) = \left(\frac{c(k+1)(k+2)}{2P} \operatorname{sech} \left(\frac{k}{2} \sqrt{\frac{c}{Q}} (x - x_0) \right) \right)^{1/n}, u(-L, t) = u(L, t). \tag{6.1}$$

To apply Fourier transformation and employ inverse Fourier transformation, let us consider: $x = Xb$, and $u(x, t) = v(x/b, t) = v(X, t)$, where $b = L_1/L$. Then, the GKdV equation becomes

$$v_t + \frac{P}{b} v^k v_x + \frac{Q}{b^3} v_{xxx} = 0. \tag{6.2}$$

Let the Fourier function is

$$\mathcal{F}(f(a)) = \hat{f}(k) = \int_{-\infty}^{\infty} f(a) e^{-2\pi ika} dt. \tag{6.3}$$

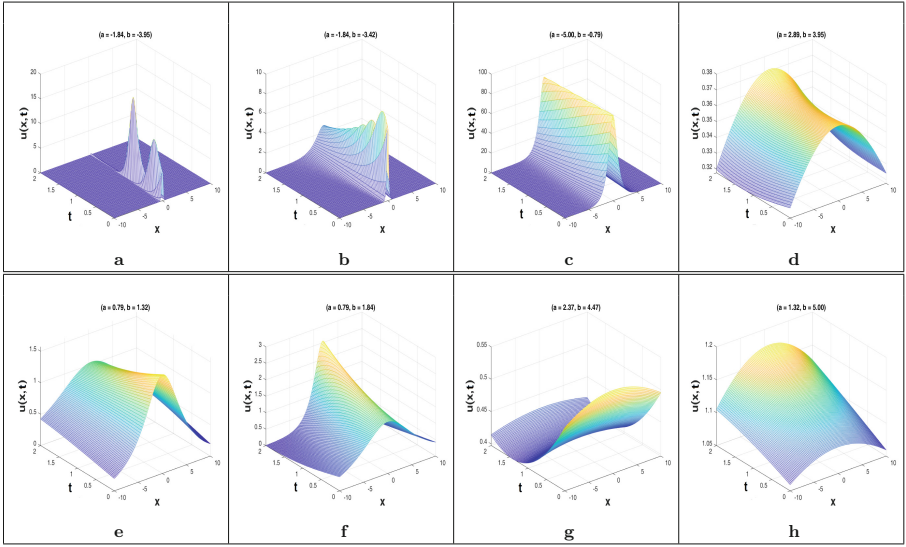


Fig. 5. Analytical solution of the Generalized KdV Equation for different combinations of a and b . Other parameters are: $c_0 = 0.5, P = 0.5, Q = 2.5, f = 0.01, \omega = 0.5, S = 0.05, n = 3$.

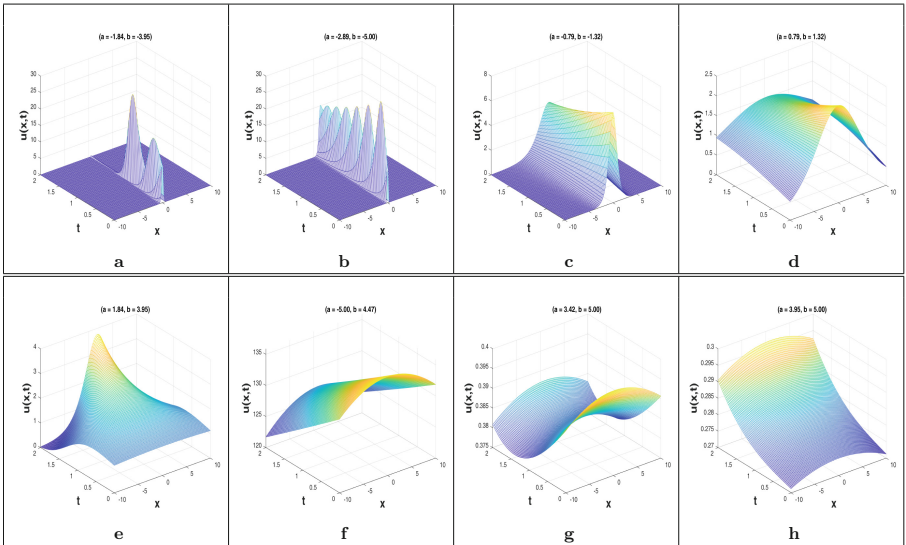


Fig. 6. Analytical solution of the Generalized Modified KdV Equation for different combinations of a and b . Other parameters are: $c_0 = 0.5, P = 0.5, Q = 2.5, f = 0.01, \omega = 0.5, S = 0.05, n = 3$.

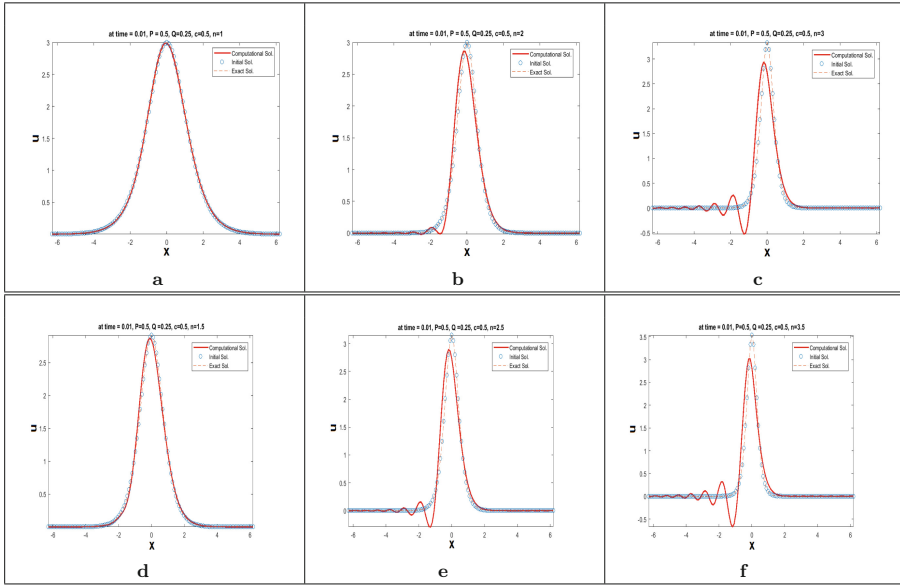


Fig. 7. Pseudo-spectral method with $k = n$ i.e. the GKdV equation, and $k = n/2$ i.e. the GMKdV equation where $n = [1, 2, 3]$ on the Eq. (6.1).

Taking Fourier transformation on Eq. (6.2), we get

$$v_x = ik\mathcal{F}(v); v_{xxx} = -ik^3\mathcal{F}(v). \tag{6.4}$$

Taking inverse FFT on Eq. (6.4) and using the RK4 method for the Eq. (6.1) is given by

$$u_{n+1} = u_n + \frac{1}{6}(a + 2b + 2c + d), \tag{6.5}$$

where $a = -dtf(u)$, $b = -dtf(u + 0.5a)$, $c = -dtf(u + 0.5b)$, $d = -dtf(u + c)$.

In this Sect. 6, with the help of the Pseudo-spectral method, we are comparing the results between the exact solution, the initial solution, and the computational solution concerning the time and various included parameters P , Q , and k . For $k = n$, and $k = n/2$, the Eq. (6.1) represents the GKdV and GMKdV equations respectively. In Fig. 7 for $n = [1, 2, 3]$, $P = 0.5$, $Q = 0.25$, $c = 0.5$, and $t = 0.01$, we have seen that solitons of both the equations show oscillating behaviour with respect to the computational scheme and for higher value of n this scheme will break, Fig. 7 a, b, and c represents for GKdV and d, e, and f represents for GMKdV equations. The effect of time t and included rest parameters P , and Q are also shown in Fig. 8. The soliton will move smoothly with regard to time up until it reaches $t = 0.05$, as shown by Fig. 8 a, b, and c. At this time, oscillations occur in the soliton with respect to the computational scheme and

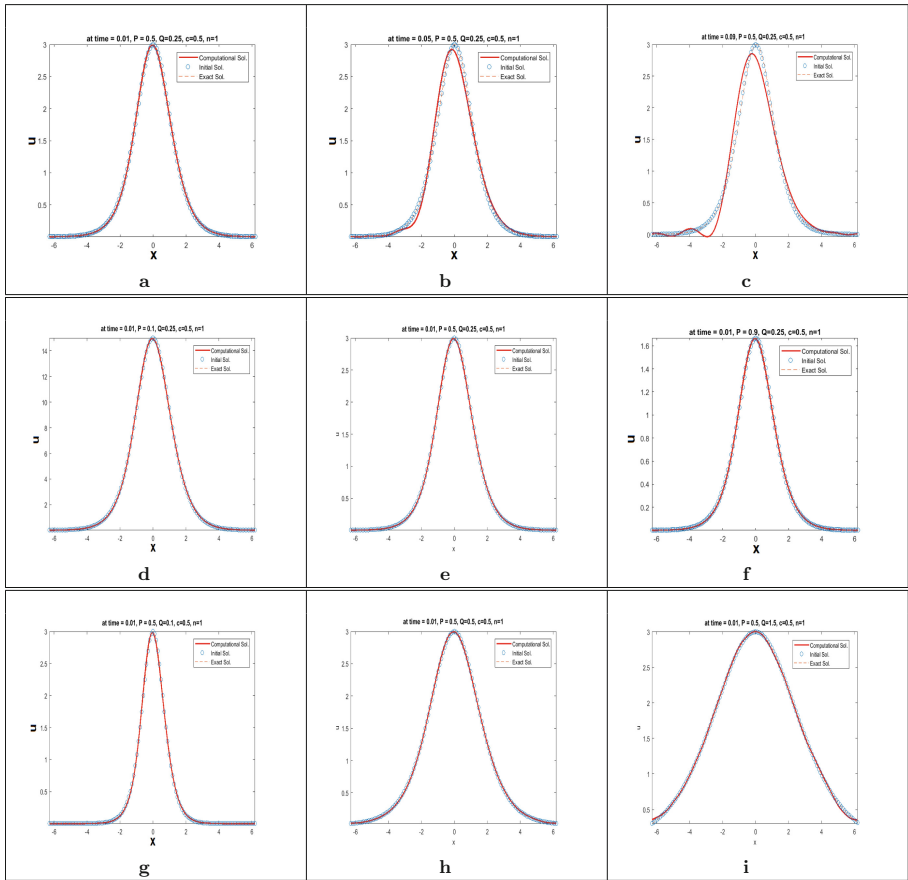


Fig. 8. Comparison of the exact solution, the initial solution, and the computational solution with respect to the time t , and the range of the parameters P and Q of Eq. (6.1) at fixed time $t = 0.01$. Parameters values are $t = [0.01, 0.05, 0.09]$, $P = [0.1, 0.5, 0.9]$, and $Q = [0.1, 0.5, 1.5]$.

breaks down but in case of P , this scheme will move smoothly and the amplitude of the soliton will decrease while increasing the value of the nonlinear coefficient $P = [0.1, 0.5, 0.9]$, shown in Fig. 8 d, e, and f. Figure 8 g, h, and i represent the behaviour of soliton with respect to the dispersion parameter Q and we observed that for $Q = [0.1, 0.5, 1.5]$, $P = 0.5$, $c = 0.5$, $n = 1$, and $t = 0.01$, the width of the soliton will increase, but at $Q = 1.5$ there exists a small oscillation in the soliton and for this value this scheme will fail. Hence overall, we have observed that with respect to time, k , and dispersion parameters this scheme will fail.

Remark 1. We have observed that this pseudo-spectral scheme will fail with time. To improve the accuracy, we need to move to a better scheme, which may be the modified exponential time differencing method (mETDRK4). This can be the further research work with this problem.

7 Conclusions and Future Work

In this article, to investigate the autonomous GKDV and GMKDV system, the sine cosine method is employed; further, the analytical solution of the non-autonomous part of the said system is derived using the direct assumption technique. Finally, the reliability of the solutions is achieved by numerical investigation. In this connection, it is important to mention that the analytical techniques mentioned here, are not able to find more complex solutions such as rouge wave, breather, etc. Finding such solutions using Hirota's bi-linear techniques, Darboux transformation remains for a future project. The main outcomes of our investigation can be stated below:

- We have compared the soliton behaviours of the generalized KDV and generalized Modified KDV equations.
- In the absence of forcing and damping terms, there is no significant difference between the behaviours except for the non-linear parameter.
- Visible effects are shown in the behaviour of dynamical systems of GKdV and GMKdV equations. For $k = n$, the system will always remain unstable and move in an unbounded open orbit. Again, for $k = \frac{n}{2}$, the system becomes unstable, but the trajectories do not move into open orbit and exhibit compressive behaviour.
- In the case of GDFKdV and GDFMKdV equations, the Effect of forcing parameters and damping parameters is shown with the help of surface and contour plots. The graphs for the damping parameter make it evident that as the damping coefficient increases, the soliton tends to flatten out from the back. Similarly for the case of forcing term parameter, the soliton acquires the curvature.
- A visible effect in the behaviour of generalized solutions of both equations is shown with the help of two newly introduced parameters, a , and b . This may represent topological structures such as multiple humps, twisted curved sheets, and pulses of the Gaussian type.
- With the help of the pseudo-spectral approach, we provide additional support for all of these findings.
- We have observed that this pseudo-spectral scheme will fail with time and increasing value of exponent parameter n . To improve the accuracy, we need to move to a better scheme, which may be the modified exponential time differencing method (mETDRK4) [5]. This can be the subject of further research work on this problem.

References

1. Ablowitz, M.J., Clarkson, P.A.: *Solitons, Nonlinear Evolution Equations and Inverse Scattering*. Cambridge University Press, Cambridge (1991)
2. Aslanov, V.S., Yudintsev, V.V.: Dynamics, analytical solutions and choice of parameters for towed space debris with flexible appendages. *Adv. Space Res.* **55**, 660–667 (2015)
3. Debnath, L., Basu, K.: Nonlinear water waves and nonlinear evolution equations with applications. *Encycl. Complex. Syst. Sci.* 1–59 (2014)
4. Dubey, V.P., Singh, J., Alshehri, A.M., Dubey, S., Kumar, D.: Analysis of local fractional coupled Helmholtz and coupled Burgers' equations in fractal media. *AIMS Math.* **7**(5), 8080–1111 (2022)
5. Fabien, M.S.: Spectral methods for partial differential equations that model shallow water wave phenomena. Ph.D. Dissertation (2014)
6. Ghanbari, B., Kumar, D., Singh, J.: Exact solutions of local fractional longitudinal wave equation in a magneto-electro-elastic circular rod in fractal media. *Indian J. Phys.* **96**(3), 787–94 (2022)
7. Guckenheimer, J., Holmes, P.: Nonlinear oscillations, dynamical systems and bifurcations of vector fields. *J. Appl. Mech.* **51**(4), 947 (1984)
8. Hirota, R.: Exact Solution of the Korteweg-de Vries Equation for Multiple Collisions of Solitons. *Phys. Rev. Lett.* **27**(18), 1192–1194 (1971). <https://doi.org/10.1103/physrevlett.27.1192>
9. Jawad, A.J.M., Petković, M.D., Biswas, A.: Modified simple equation method for nonlinear evolution equations. *Appl. Math. Comput.* **217**(2), 869–877 (2010)
10. Kudryashov, N.A.: Exact solutions of the generalized Kuramoto-Sivashinsky equation. *Phys. Lett. A* **147**(5–6), 287–291 (1990). [https://doi.org/10.1016/0375-9601\(90\)90449-x](https://doi.org/10.1016/0375-9601(90)90449-x)
11. Pankaj, R.D., Kumar, A., Singh, B., Meena, M.L.: Exp $(-\phi(\xi))$ expansion method for soliton solution of nonlinear Schrödinger system. *J. Interdisc. Math.* **25**(1), 89–97 (2022)
12. Pankaj, R.D., Lal, C., Kumar, A.: New expansion scheme to solitary wave solutions for a model of wave-wave interactions in plasma. *Sci. Technol. Asia* 49–59 (2021)
13. Raut, S., Roy, S., Kairi, R.R., Chatterjee, P.: Approximate analytical solutions of generalized zakharov-kuznetsov and generalized modified zakharov-kuznetsov equations. *Int. J. Appl. Comput. Math.* **7**(4), 1–25 (2021)
14. Raut, S., Roy, A., Mondal, K.K., et al.: Non-stationary solitary wave solution for damped forced kadomtsev-petviashvili equation in a magnetized dusty plasma with q-nonextensive velocity distributed electron. *Int. J. Appl. Comput. Math.* **7**, 223 (2021). <https://doi.org/10.1007/s40819-021-01168-2>
15. Rogers, C., Shadwick, W.R.: *Bäcklund Transformations and Their Application Mathematics in Science and Engineering*, vol. 161. Academic Press, New York (1982)
16. Roy, S., Raut, S., Kairi, R.R., et al.: Integrability and the multi-soliton interactions of non-autonomous Zakharov-Kuznetsov equation. *Eur. Phys. J. Plus* **137**, 579 (2022). <https://doi.org/10.1140/epjp/s13360-022-02763-y>
17. Roy, S., Raut, S., Kairi, R.R., et al.: Bilinear Bäcklund, lax pairs, breather waves, lump waves and soliton interaction of (2+1)-dimensional non-autonomous Kadomtsev-Petviashvili equation. *Nonlinear Dyn.* **111**, 5721–5741 (2022). <https://doi.org/10.1007/s11071-022-08126-7>
18. Sen, A., Tiwari, S., Mishra, S., Kaw, P.: Nonlinear wave excitations by orbiting charged space debris objects. *Adv. Space Res.* **56**(3), 429 (2015)

19. Singh, J., Gupta, A., Baleanu, D.: On the analysis of an analytical approach for fractional Caudrey-Dodd-Gibbon equations. *Alex. Eng. J.* **61**(7), 5073–82 (2022)
20. Wazwaz, A.M.: The tanh-coth method for solitons and kink solutions for nonlinear parabolic equations. *Appl. Math. Comput.* **188**(2), 1467–1475 (2007). <https://doi.org/10.1016/j.amc.2006.11.013>
21. Wazwaz, A.M.: A sine-cosine method for handling nonlinear wave equations. *Math. Comput. Model.* **40**, 499–508 (2004)
22. Zuo, J.M., Zhang, Y.M.: The Hirota bilinear method for the coupled Burgers equation and the high-order Boussinesq-Burgers equation. *Chin. Phys. B* **20**(1), 010205 (2011)



NIPG Method on Shishkin Mesh for Singularly Perturbed Convection-Diffusion Problem with Discontinuous Convection Coefficient

Kumar Rajeev Ranjan and S. Gowrisankar^(✉)

Department of Mathematics, National Institute of Technology Patna,
Patna 800005, India

kumarr.phd18.ma@nitp.ac.in, s.gowri@nitp.ac.in

Abstract. In this paper, we investigate the convergence of discontinuous Galerkin finite element method (DGFEM) for singularly perturbed convection-diffusion problem with discontinuous convection coefficient. Due to the discontinuity in the convection coefficient, the problem typically shows a weak interior layer. We develop a kind of DGFEM, the non-symmetric discontinuous Galerkin finite element method with interior penalties (NIPG) to handle the layer setbacks. With the use of a typical Shishkin mesh, the domain is discretized and uniform error estimate is obtained and theoretically we have obtained the convergence of order $\mathcal{O}(N^{-1} \ln N)$. The numerical outcome backs up our theoretical conclusions.

Keywords: Convection-diffusion problem · The NIPG methods · Shishkin mesh · Interior layers · Uniform convergence

Classification: AMS 65L70 · AMS 65L20 · AMS 65L6

1 Introduction

In this article we consider a singularly perturbed convection-diffusion problem of the type

$$\begin{cases} \mathcal{L}u(x) := -\varepsilon u'' + b(x)u'(x) + c(x)u(x) = f(x), & \text{in } x \in \Omega = (0, 1), \\ u(0) = u(1) = 0, \end{cases} \quad (1)$$

where, ε is the perturbation parameter satisfies $0 < \varepsilon \ll 1$ and $b(x)$ has jump discontinuity at $x = d \in \Omega$. We define $\Omega_1 = (0, d)$ and $\Omega_2 = (d, 1)$ where d is a point of discontinuity of $b(x)$. Let us assume b, c and f belong to the class $C^2(\Omega_1 \cup \Omega_2)$ and the function satisfy

$$c(x) - \frac{1}{2}b'(x) \geq \gamma^2 > 0. \quad \text{on } \Omega_1 \cup \Omega_2 \quad (2)$$

Here, γ is some fixed positive constant. Moreover the following conditions hold good,

$$\beta_1^* > b(x) > \beta_1 > 0, \quad x < d, \quad -\beta_2^* < b(x) < -\beta_2 < 0, \quad x > d, \quad c(x) \geq 0 \quad x \in \overline{\Omega},$$

and

$$|[b](d)| \leq C, \quad |[c](d)| \leq C, \quad |[f](d)| \leq C, \quad (3)$$

where, $\beta_1, \beta_1^*, \beta_2$ and β_2^* are positive constants. In the close vicinity of $x = d$ in the solution $u(x)$ of problem (1), exhibits layer of width $\mathcal{O}(\varepsilon \ln(1/\varepsilon))$. We refer the layer as an interior layer.

There is a large number of papers in the literature dealing with a singular perturbation problem with continuous coefficients and source terms, see [10, 12] for a survey. Problem of type (1) with discontinuous right hand side are considered in [1, 12], whereas problem with discontinuous coefficient is considered in [3, 20]. In these articles, authors have proved second order and first order convergence, respectively. In [8] authors have proved first order ε -uniform convergence on Shishkin mesh of finite difference scheme for reaction-diffusion problem with discontinuous source term.

Except these literature review some of these are [16] in which, Singh *et al.* presented an algorithms for approximate solution of nonlinear Lane-Emden type equations. Convergence analysis and stability result are also provided. Also Singh has applied Chebyshev's spectral collocation method for Bratu's type, Troesch's and nonlocal elliptic boundary value problems in [14]. Moreover, Majid *et al.* has established the convergence result for solution of nonlinear Lane-Emden type equations. Pandey *et al.* has established the convergence of Bratu's equation by means of Chebyshev polynomials [15]. Some other equations and physical models are investigated numerically in [4–6]. In these articles authors established the existence using Banach fixed point theory and convergence of numerical schemes are also investigated.

The idea to use non-symmetric Galerkin method with interior penalty (NIPG) method is not new in the literature. The interest in the non-symmetric Galerkin method with interior penalty (NIPG) method and singular perturbation problem is beneficial due to the presence of penalty terms which fulfill the requirement of additional stabilization. The non-symmetric Galerkin method with interior penalty (NIPG) method has the advantage to be very flexible in the sense of adaptivity; moreover it can be applied for the case $\varepsilon = 0$ if the solution is not smooth. In [10, 21] authors have proved first order convergence for convection-diffusion problem with turning point and continuous coefficients, respectively. This method is preferred like streamline diffusion finite element method (SDFEM) [17] over the classical finite element methods because of their potential in approximating globally rough solutions, their possible definition (additionally jump and penalization parameter) on unstructured meshes, their potential for error control and mesh adaptation, etc. There are other variants of DGFEM like symmetric interior penalty Galerkin (SIPG) method and incomplete interior penalty Galerkin (IIPG) method in which, we have to choose penalty parameters so that the method could be stable and convergent, besides

these properties establishment of coercivity property is not an easy task. In addition to the aforementioned privilege to non-symmetric interior penalty Galerkin (NIPG) method. Drawbacks of this method is its much larger number of degree of freedom as compared to standard Galerkin finite element method. Another disadvantage of the method is adjoint consistency which is better in SIPG technique that appears in sketching optimal L^2 error or to apply dual weighted residual (DWR) technique.

In this paper, we adopt to the non-symmetric Galerkin method with interior penalty (NIPG) method for problem (1). As a result of discontinuity in convection coefficient, interior layer is present in the solution. Interior layer usually present due to turning point or discontinuity in the coefficients. In [11], authors have established the first order convergence up to logarithmic factor for non-symmetric interior penalty Galerkin (NIPG) method for one dimensional singular perturbation problem with discontinuous source term. We have shown the uniform convergence of the method on usual Shishkin mesh. Simplifying our analysis and using piecewise linear element on Ω , in Theorem 4 we prove that the finite element method (FEM) leads to the convergence result $\mathcal{O}(N^{-1} \ln N)$ and finally we get the result of same order in Theorem 5.

The article is arranged in the following way: Sect. 2 describes the existence, stability properties of the solution, opportunistically we have included decomposition of the solution in this section too. In Sect. 3, we have discussed the Shishkin mesh, the non-symmetric Galerkin method with interior penalty (NIPG) method and existence of solution. Section 4 dealt with the error analysis on the given mesh. Uniform convergence of the given FEM is described in Sect. 5 and the last Sect. 6 provides the numerical result that supports our theoretical findings. Section 7 is all about the summary of the article and last but not the least the original contribution in this article is described in Sect. 8.

2 Stability and Solution Decomposition

We propose some necessary notations. For any function $v(x)$, the jump at d is denoted by $[v](d)$ and defined by $[v](d) = v(d^+) - v(d^-)$. C is a generic constant (sometimes subscripted) is free from perturbation parameter ε and mesh parameter N . An arbitrary subinterval $[x_{j-1}, x_j]$ is represented by I_j with interval height $h_j = x_j - x_{j-1}$.

Now the theorem given below guarantees the existence of solution to the problem (1).

Theorem 1. *Let $u(x)$ is the solution of (1) that belongs to the class of function $C^0(\overline{\Omega}) \cap C^1(\Omega) \cap C^2(\Omega_1 \cup \Omega_2)$.*

Proof. The detailed proof can be similar as in [20]. ■

Lemma 1. *Suppose the problem (1) has a solution $u(x)$ that belongs to the class of functions $C^0(\overline{\Omega}) \cap C^1(\Omega) \cap C^2(\Omega_1 \cup \Omega_2)$, which satisfies the bound*

$$\|u(x)\|_{L^\infty(\Omega)} \leq \frac{1}{\lambda} \|f(x)\|_{L^\infty(\Omega)},$$

where $\lambda = \min\{\beta_1/d, \beta_2/(1-d)\}$.

Proof. Put $\psi(x) = -\frac{x\|f(x)\|_{L^\infty(\Omega)}}{\lambda d} + u(x)$, $x < d$ and $\psi(x) = -\frac{(1-x)\|f(x)\|_{L^\infty(\Omega)}}{\lambda(1-d)} + u(x)$, $x > d$.

Therefore, we have $\psi(x) \in C^0(\overline{\Omega})$ and $\psi(0) \leq 0$, $\psi(1) \leq 0$.

For each $x \in \Omega_1 \cup \Omega_2$,

$$\mathcal{L}\psi(x) \geq 0.$$

Furthermore, since $u(x) \in C^1(\Omega)$

$$[\psi](d) = [u](d) = 0 \quad \text{and} \quad [\psi'](d) = \frac{\|f\|_{L^\infty(\Omega)}}{\lambda d} + \frac{\|f\|_{L^\infty(\Omega)}}{\lambda(1-d)} \geq 0.$$

Hence, following comparison principle in Lemma 2 [7] that $\psi(x) \leq 0$ for all $x \in \overline{\Omega}$. Which determines the desired bound for the solution $u(x)$.

Let us consider the decomposition $u = v + w$ into smooth component v and interior layer component w . We take two discontinuous function v_0 and v_1 such that

$$\begin{aligned} bv'_0 &= f, & x \in \Omega_1 \cup \Omega_2 \\ v_0(0) &= u(0), & v_0(1) = u(1), \\ bv'_1 &= -v''_0, \\ v_1(0) &= 0, & v_1(1) = 0. \end{aligned}$$

Now we define smooth component of the solution v such that

$$\mathcal{L}v = f, \quad x \in \Omega_1 \cup \Omega_2 \tag{4a}$$

$$v(0) = u(0), \quad v(d^-) = v_0(d^-) + \varepsilon v_1(d^-), \tag{4b}$$

$$v(d^+) = v_0(d^+) + \varepsilon v_1(d^+), \quad v(1) = u(1). \tag{4c}$$

Note that it is discontinuous function. Further, we have layer part of the solution w which is also discontinuous and given by the set of following equation

$$\mathcal{L}w = 0, \quad x \in \Omega_1 \cup \Omega_2 \tag{5a}$$

$$w(0) = w(1) = 0, \quad [w](d) = -[v](d), \quad [w'](d) = -[v'](d). \tag{5b}$$

Hence, we get $w(d^-) = u(d^-) - v(d^-)$ and $w(d^+) = u(d^+) - v(d^+)$. We note that the solution $u = v + w$ is unique to the problem (1). It is merited consideration that v and w are discontinuous at $x = d$, but their sum u is in $C^1(\Omega)$ by (5b). It is called stability property for the exact solution of (1). ■

It is crucial to deduce the bounds for different components of the solution in order to obtain the convergence result in the finite element method. The same is addressed in the below mentioned theorem.

Theorem 2. *Let (3) holds true. Assume that $b, c, f \in C^2(\Omega_1 \cup \Omega_2)$, we have*

$$\|b^m(x)\|_{L^\infty(\Omega_1 \cup \Omega_2)} \leq C, \quad \|c^m(x)\|_{L^\infty(\Omega_1 \cup \Omega_2)} \leq C, \quad \|f^m(x)\|_{L^\infty(\Omega_1 \cup \Omega_2)} \leq C,$$

$m = 0, 1, 2$ and we are able to derive the decomposition of solution to the problem (1) and in this way we find the smooth part S and layer part E satisfy $\mathcal{L}S = f$ and $\mathcal{L}E = 0$, respectively and their bound could be

$$\begin{aligned} \|S^i(x)\|_{L^\infty(\Omega_1 \cup \Omega_2)} \leq C, \quad |[S](d)| \leq C, \quad |[S'](d)| \leq C. \\ |E^i(x)| \leq \begin{cases} C\varepsilon^{-i}e^{(x-d)\beta_1/\varepsilon}, & x \in \Omega_1, \\ C\varepsilon^{-i}e^{-(x-d)\beta_2/\varepsilon}, & x \in \Omega_2. \end{cases} \end{aligned} \tag{6}$$

$i = 0, 1, 2$.

Proof. The proof is same as it has been done in [20], so we omit the proof here. ■

3 Piecewise Equidistant Mesh and NIPG Method

3.1 Shishkin Mesh

For the domain discretization, a most practicable Shishkin mesh is considered. Let $N \in \mathbb{N}$, where $N \geq 4$ and N is a multiple of 4. Layer in the vicinity of d has been considered and any possibility of layer at the boundary is completely ruled out. Therefore the mesh can be generated in the following way: Following [19], we take transition points $\lambda_1 = d - \frac{\rho\varepsilon}{\beta_1} \ln N$ and $\lambda_2 = d + \frac{\rho\varepsilon}{\beta_2} \ln N$ where $\rho \geq 2$, with the help of these two transition points we make the division of $\overline{\Omega}$ into four subintervals

$$\overline{\Omega} = [0, \lambda_1] \cup [\lambda_1, d] \cup [d, \lambda_2] \cup [\lambda_2, 1]$$

such that $d - \lambda_1 \leq d/2$ and $\lambda_2 - d \leq (1 - d)/2$. Furthermore we assume that each subintervals are distributed into $N/4$ intervals, where grid points satisfy $x_{N/4} = \lambda_1$, $x_{N/2} = d$ and $x_{3N/4} = \lambda_2$.

Remark 1. Throughout our analysis we take $\varepsilon \leq CN^{-1}$, which is reasonable in practice.

3.2 The NIPG Method: Procedure and Properties

The Shishkin mesh defined in Subsect. 3.1 partitioning the domain Ω into subintervals $I_j = [x_{j-1}, x_j]$, $j = 1, 2, \dots, N$. Denote these collections by \mathcal{T}_N . We introduce with some essential notations: For every $I_j \in \mathcal{T}_N$, define broken Sobolev space of order k

$$H^k(\Omega, \mathcal{T}_N) = \{v \in L^2(\Omega) : v|_{I_j} \in H^k(I_j), \forall I_j \in \mathcal{T}_N\}$$

and corresponding broken Sobolev norm and seminorm defined by

$$\|v\|_{s, \mathcal{T}_N} = \left(\sum_{j=1}^N \|v\|_{s, I_j}^2 \right)^{1/2}, \quad |v|_{s, \mathcal{T}_N} = \left(\sum_{j=1}^N |v|_{s, I_j}^2 \right)^{1/2},$$

respectively. Define V^N as a finite element space related to the collection \mathcal{T}_N of Shishkin meshes

$$V^N = \{v \in L^2(\Omega) : v|_{I_j} \in P^1(I_j), \forall I_j \in \mathcal{T}_N\},$$

where $P^1(I_j)$ denotes the space of polynomial of degree at most one in each I_j . Moreover, the functions in V^N are completely discontinuous on the boundaries of the subintervals in \mathcal{T}_N . That is we are considering the non-confirming finite element.

The NIPG formulation [10] of (1) reads as: Find $u_N \in V^N$ such that

$$B(u_N, v_N) = L(v_N), \quad \text{for all } v_N \in V^N \tag{7}$$

where

$$B(u, v) = B_1(u, v) + B_2(u, v), \tag{8a}$$

$$B_1(u, v) = \sum_{j=1}^N \int_{I_j} \varepsilon u' v' dx + \sum_{j=0}^N \varepsilon \left([u(x_j)] \{v'(x_j)\} - [v(x_j)] \{u'(x_j)\} \right) + \sum_{j=0}^N \sigma_j [u(x_j)] [v(x_j)], \tag{8b}$$

$$B_2(u, v) = \sum_{j=1}^N \int_{I_j} (bu' + cu)v dx + \sum_{j=0}^{N-1} b(x_j) [u(x_j)] v(x_j^+), \tag{8c}$$

$$L(v) = \sum_{j=1}^N \int_{I_j} f v dx. \tag{8d}$$

Here $\sigma_j (j = 0, 1, \dots, N)$ are the discontinuous-penalization parameters that are closely related to each nodes x_j . These are user-defined parameters, in the sequel, we will provide the exact choice of these parameters. The construction of bilinear form inspired us to introduce the DG norm as follows: For any $v \in H^2(\Omega, \mathcal{T}_N)$,

$$\|v\|_{DG}^2 = \sum_{j=1}^N (\varepsilon \|v'\|_{L^2(I_j)}^2 + \|\gamma v\|_{L^2(I_j)}^2) + \sum_{j=0}^N \left(\frac{1}{2} b(x_j) + \sigma_j \right) [v(x_j)]^2. \tag{9}$$

Lemma 2. *Let u and u_N are the exact solution to the problem (1) and discretized solution to the weak formulation (7), respectively. Then the bilinear form provided by (7) satisfies,*

$$B(u - u_N, v_N) = 0 \quad \text{for all } v_N \in V^N, \quad (\text{Galerkin orthogonality}) \tag{10a}$$

$$B(v_N, v_N) = \|v_N\|_{DG}^2 \quad \text{for all } v_N \in V^N, \quad (\text{coercivity}) \tag{10b}$$

Proof. Both the properties in (10a) and (10b) in the above Lemma 2 can be followed from [10] in Lemma 3.1 and equation (3.5). ■

4 Error Estimations: Sharp Bound on Shishkin Mesh

In this section, we present piecewise linear interpolation u^I of the exact solution u and their properties. There are numerous results on interpolation error in the literature (see [2]). We introduce an estimation on interpolation error which is useful in the derivation of error estimation.

Lemma 3. [18]: *The special interpolant has the following properties:*

$$|u - u^I|_{m,\mathcal{N}} \leq Ch_{\mathcal{N}}^{j+1-m} |u|_{j+1,\mathcal{N}}, \quad m = 0, 1, \dots, j+1, \quad \forall u \in H^{j+1}(\mathcal{N}), \quad (11a)$$

$$\|u\|_{L^\infty(\mathcal{N})} \leq Ch_{\mathcal{N}}^{j+1} |u|_{j+1,\infty,\mathcal{N}}, \quad \forall u \in W^{j+1,\infty}(\mathcal{N}), \quad (11b)$$

where \mathcal{N} is an element in the partition \mathcal{T}_N of the domain Ω and $h_{\mathcal{N}}$ is the length of element \mathcal{N} .

4.1 Interpolation Error

Lemma 4. *On the Shishkin mesh, we have the following properties:*

$$\|S - S^I\|_{L^2[0,\lambda_1]} + \|u - u^I\|_{L^2[0,\lambda_1]} \leq CN^{-2}, \quad (12a)$$

$$\|E - E^I\|_{L^2[\lambda_1,d]} + \|u - u^I\|_{L^2[\lambda_1,d]} \leq C\varepsilon^{1/2}(N^{-1} \ln N)^2, \quad (12b)$$

$$\|(E - E^I)'\|_{L^2[0,d]} + \|(u - u^I)'\|_{L^2[0,d]} \leq C\varepsilon^{-1/2}N^{-1} \ln N. \quad (12c)$$

Proof. To estimate $\|S - S^I\|_{L^2[0,\lambda_1]}$, we use classical interpolation theory given by (11a) with $m = 0$ and $j = 1$

$$\|S - S^I\|_{L^2(I_j)} \leq Ch_{\mathcal{N}}^2 \|S''\|_{L^2(I_j)} \leq CN^{-2}.$$

Now

$$\|E - E^I\|_{L^2(I_j)} \leq C \|E\|_{L^2(I_j)} + \|E^I\|_{L^2(I_j)} \leq CN^{-2}.$$

combining the above two estimates, we get (12a). For (12b), we use the interpolation result from (11a).

Now we will estimate (12c)

$$\begin{aligned} \|(E - E^I)'\|_{L^2[0,\lambda_1]} &\leq \|E'\|_{L^2[0,\lambda_1]} + \|(E^I)'\|_{L^2[0,\lambda_1]}, \\ &\leq \|E'\|_{L^2[0,\lambda_1]} + CN \|(E^I)\|_{L^2[0,\lambda_1]}. \end{aligned} \quad (13)$$

Here we have used inverse inequality and stability property for interpolant (see Lemma 3.3, [21]).

$$\|E'\|_{L^2[0,\lambda_1]} \leq C\varepsilon^{-1/2}N^{-2}, \quad \|E^I\|_{L^2[0,\lambda_1]} \leq C\varepsilon^{1/2}N^{-2}. \quad (14)$$

(11a) give us

$$\|(E - E^I)'\|_{L^2[\lambda_1, d]} \leq C\varepsilon^{-1/2}N^{-1} \ln N \tag{15}$$

and finally

$$\|(S - S^I)'\|_{L^2[0, d]} \leq C\varepsilon N^{-1} \ln N. \tag{16}$$

Combining (13)–(16), we get (12c). ■

Remark 2. Bound for the estimations in Lemma 4 on the interval $[d, 1]$ can be achieved easily. Hence, we have

$$\begin{aligned} \|S - S^I\|_{L^2[\lambda_2, 1]} + \|u - u^I\|_{L^2[\lambda_2, 1]} &\leq CN^{-2}, \\ \|E - E^I\|_{L^2[d, \lambda_2]} + \|u - u^I\|_{L^2[d, \lambda_2]} &\leq C\varepsilon^{1/2}(N^{-1} \ln N)^2, \\ \|(E - E^I)'\|_{L^2[d, 1]} + \|(u - u^I)'\|_{L^2[d, 1]} &\leq C\varepsilon^{-1/2}N^{-1} \ln N. \end{aligned}$$

To cover error analysis we need multiplicative trace inequality which is referred as

Lemma 5. [9]. For $w \in H^1(I_j)$

$$|w(x_s)|^2 \leq 2(h_j^{-1} \|w\|_{L^2(I_j)}^2 + \|w\|_{L^2(I_j)} \|w'\|_{L^2(I_j)}), \quad s \in \{j - 1, j\}. \tag{17}$$

Proof. For any $w \in H^1(0, 1)$, we set $v(t) = w^2(t)(t - 1/4)$. Now we just verify the inequality in (17) for $t = 3/4$ and proof at another point will be similar,

$$v'(t) = w^2(t) + 2w(t)w'(t)(t - 1/4).$$

Using the definition of $v(t)$ we see that $v(3/4) = \int_{1/4}^{3/4} v'(t)dt$.

$$\begin{aligned} |v(3/4)| &\leq \int_{1/4}^{3/4} |v'(t)|dt, \\ &\leq \int_{1/4}^{3/4} |w^2(t)|dt + \int_{1/4}^{3/4} |2w(t)w'(t)(t - 1/4)|dt. \end{aligned}$$

Therefore,

$$\begin{aligned} |v(3/4)| &\leq \int_0^{3/4} |w^2(t)|dt + \int_0^{3/4} |2w(t)w'(t)(t - 1/4)|dt, \\ &\leq \|w(t)\|_{L^2[0, 3/4]}^2 + 2 \max_{t \in [0, 3/4]} |t - 1/4| \|w(t)\|_{L^2[0, 3/4]} \|w'(t)\|_{L^2[0, 3/4]}, \\ &\leq \|w(t)\|_{L^2[0, 3/4]}^2 + \|w(t)\|_{L^2[0, 3/4]} \|w'(t)\|_{L^2[0, 3/4]}. \end{aligned}$$

Hence for all the points it can be shown similarly by changing in the definition of $v(t)$. So, scaling argument tells us the consequences leads to the validation of the result given in the Lemma 5. ■

Lemma 6. *On the Shishkin mesh given in Subsect. 3.1, take $\rho = 2$ and $\eta = u - u^I$, we have the following bounds for $\{\eta'\}$*

$$\{\eta'(x_j)\}^2 \leq \begin{cases} C\varepsilon^{-2}(N^{-1} \ln N)^2 & j = N/4 + 1, \dots, N/2 \text{ and } j = 3N/4 + 1, \dots, N, \\ C\varepsilon^{-2}N^{-3} & j = 0, \dots, N/4 \text{ and } j = N/2 + 1, \dots, 3N/4. \end{cases} \quad (18)$$

Proof. The proof of this lemma is quite similar as the Lemma 3.6 has been proved in [21]. So we leave the steps of the proof. ■

Theorem 3. *Let the assumption in Remark 1 holds, then the following result on Interpolation error holds true*

$$\|u - u^I\|_{DG} \leq CN^{-1} \ln N \quad (19)$$

Proof. Recall that η is continuous on interelement boundaries we have, $\{\eta(x_j)\} = 0$. Using coercivity property in Lemma 2, we have

$$\|\eta\|_{DG}^2 = \sum_{j=1}^N \left(\varepsilon \|\eta'\|_{L^2(I_j)}^2 + \gamma^2 \|\eta\|_{L^2(I_j)}^2 \right)$$

Now bounds can be obtained from the estimations in Lemma 3 and Remark 2. ■

5 Uniform Convergence

In this section, we deduce bound for error $u - u_N$, which will be free from ε . The obtained bound in this section relies on a priori estimate of the exact solution u and an special interpolant first introduced in [18].

Theorem 4. *We introduce $\chi = u^I - u_N$. Applying Galerkin orthogonality and coercivity properties from (10a) and (10b) of Lemma 2, respectively, we have*

$$\|\chi\|_{DG} \leq CN^{-1} \ln N. \quad (20)$$

Proof. Consider,

$$\begin{aligned} \|\chi\|_{DG}^2 &= B(\chi, \chi) = B(\eta, \chi), \\ &= B_1(\eta, \chi) + B_2(\eta, \chi). \end{aligned}$$

Since η is continuous on Ω which implies that $[\eta]_j = 0$, for $j = 0, 1, \dots, N$. Therefore,

$$B_1(\eta, \chi) = \sum_{j=1}^N \int_{I_j} \varepsilon \eta' \chi' dx - \sum_{j=0}^N \varepsilon([\chi(x_j)]\{\eta'(x_j)\}) = I_1 + I_2,$$

and

$$B_1(\eta, \chi) = \sum_{j=1}^N \int_{I_j} (b\eta' + c\eta)\chi dx.$$

Making the use of Cauchy-Schwarz inequality, Eq. (12c) and Remark 2, we obtain,

$$|I_1| \leq \left(\sum_{j=1}^N \int_{I_j} \varepsilon(\eta')^2 dx \right)^{1/2} \left(\sum_{j=1}^N \int_{I_j} \varepsilon(\chi')^2 dx \right)^{1/2} \leq CN^{-1} \ln N \|\chi\|_{DG}. \quad (21)$$

Now we have to make a bound for I_2 . In this case the path of approach will be different,

$$\begin{aligned} |I_2| &\leq \left(\sum_{j=0}^N \frac{\varepsilon^2}{\sigma_j} \{\eta'(x_j)\}^2 \right)^{1/2} \left(\sum_{j=0}^N \sigma_j [\chi(x_j)]^2 \right)^{1/2}, \\ &\leq \left(\sum_{j=0}^{N/4} \frac{\varepsilon^2}{\sigma_j} \varepsilon^{-2} N^{-3} + \sum_{j=N/4+1}^{N/2} \frac{\varepsilon^2}{\sigma_j} \varepsilon^{-2} N^{-2} \ln^2 N \right. \\ &\quad \left. + \sum_{j=N/2+1}^{3N/4} \frac{\varepsilon^2}{\sigma_j} \varepsilon^{-2} N^{-3} + \sum_{j=3N/4+1}^N \frac{\varepsilon^2}{\sigma_j} \varepsilon^{-2} N^{-2} \ln^2 N \right)^{1/2} \|\chi\|_{DG}. \end{aligned}$$

In this procedure we take the exact choice of discontinuity-penalization parameter,

$$\sigma_j = N \quad \text{for all } j = 0, 1, \dots, N$$

Meanwhile, I_2 can be estimated as,

$$|I_2| \leq CN^{-1} \ln N \|\chi\|_{DG}. \quad (22)$$

Collecting (21) and (22), we get

$$B_1(\eta, \chi) \leq CN^{-1} \ln N \|\chi\|_{DG}. \quad (23)$$

It only remains to bound $B_2(\eta, \chi)$ and our purpose will be served. To bound the estimation one can refer [20] which also gives the bound

$$|B_2(\eta, \chi)| \leq CN^{-1} \ln N \|\chi\|_{DG}. \quad (24)$$

Therefore (23) and (24) together gives us (20) in Theorem 4. ■

Theorem 5. *Let u is the exact solution of (1) and u_N is the discretized solution of the NIPG formulation 7 on the Shishkin mesh introduced in Subsect. 3.1. Then the discretization error obeys the following bound*

$$\|u - u_N\|_{DG} \leq CN^{-1} \ln N.$$

Proof. From the estimations obtained in Theorem 3, Theorem 4 followed by triangular inequality we get the desired result. ■

6 Numerical Result and Implementation

In this section, we present numerical result for a test problem to illustrate the theoretical results that has been established in Sect. 5.

Example 1.

$$\begin{aligned}
 -\varepsilon u'' + b(x)u'(x) + 7u(x) &= x, \\
 u(0) = u(1) &= 0.
 \end{aligned}$$

where

$$b(x) = \begin{cases} 3x^2 + 2 & x \leq d, \\ 0.5x & x > d, \end{cases}$$

and $d = 0.7$.

The test problem in Example 1 is taken similar to the test problems in Example 7.1 and 7.2 in [11]. Solution of the test problem given in Example 1 exhibits an interior layer at $x = d$. The curve of computed solution along with exact solution is sketched in Fig. 1 with $N = 1024$ and $\varepsilon = 10^{-7}$ for Example 1. The solution curve is showing interior layer at $x = d$ where d is a point of discontinuity of convection coefficient b inside the domain depends on the user choice. The exact choice of discontinuous-penalization parameters σ_j 's has been presented in Sect. 5.

Error and convergence rate are examined for various value of N and ε with respect to DG-norm, $\|\cdot\|_{\text{DG}}$. In the present Example (1) do not have exact solution, so we apply double mesh principle to find out errors in the numerical solution and their convergence rates. We determine errors for DG-norm by $\|u_N - u_{2N}\|_{\text{DG}}$. The rate of convergence using double mesh principle can be calculated by the following expression

$$R_\varepsilon^N = \log_2 \left(\frac{\|u_N - u_{2N}\|_{\text{DG}}}{\|u_{2N} - u_{4N}\|_{\text{DG}}} \right)$$

The error and rate of convergence calculated in DG-norm for the above example are provided by Table 1 and Table 2, respectively. It can be easily seen that the solution converges with desired order, which is free from perturbation parameter ε . It is presented in Table 2, which reflects the first order convergence in ε weighted norm introduced by the bilinear form (9) that supports our theoretical findings. Hence, the numerical solution approximates the exact solution very well. All the calculations have been performed using FENICS library for finite element method and CPU run time was approximately two minutes.

Table 1. $\|u_N - u_{2N}\|_{DG}$ errors for Example 1.

ε	Number of Intervals (N)					
	32	64	128	256	512	1024
10^{-1}	9.844E-03	3.084E-03	9.963E-04	3.344E-04	1.110E-04	3.995E-05
10^{-2}	4.0731E-02	2.0132E-02	8.873E-03	3.571E-03	1.410E-03	5.314E-04
10^{-3}	4.180E-02	2.044E-02	8.844E-03	3.589E-03	1.384E-03	5.383E-04
10^{-4}	4.184E-02	2.0351E-02	8.834E-03	3.587E-03	1.423E-03	5.262E-04
10^{-5}	4.184E-02	2.0351E-02	8.838E-03	3.587E-03	1.408E-03	5.327E-04
10^{-6}	4.184E-02	2.0351E-02	8.838E-03	3.586E-03	1.411E-03	5.328E-04
10^{-7}	4.184E-02	2.035E-02	8.838E-03	3.586E-03	1.411E-03	5.327E-04

Table 2. Convergence rates R_ε^N for Example 1.

ε	Number of Intervals (N)				
	32	64	128	256	512
10^{-1}	1.6742	1.6303	1.5748	1.5901	1.4751
10^{-2}	1.0166	1.1819	1.3128	1.3401	1.4083
10^{-3}	1.0320	1.2089	1.3009	1.3739	1.3630
10^{-4}	1.0397	1.2039	1.3000	1.3333	1.4359
10^{-5}	1.0399	1.2032	1.3008	1.3486	1.4027
10^{-6}	1.0399	1.2032	1.3010	1.3458	1.4050
10^{-7}	1.0399	1.2031	1.3011	1.3454	1.4057

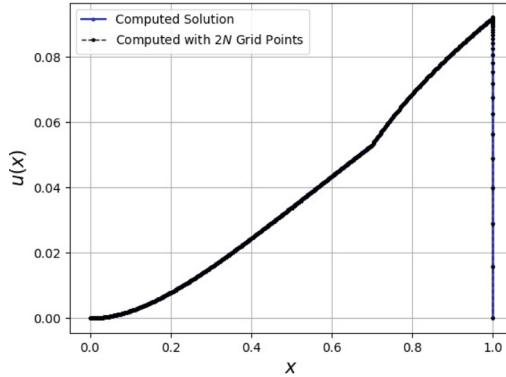


Fig. 1. Computed and Exact solution for Example 1 for $N = 1024$ and $\varepsilon = 10^{-7}$.

7 Conclusion

The singularly perturbed convection-diffusion problem with discontinuous coefficient is investigated in this paper. In order to find the numerical approximation

when the perturbation parameter ε goes to zero, we apply NIPG method on piecewise uniform Shishkin mesh and convergence result is established. Numerical results are provided to defend our analytical findings. It is a singular perturbation problem with single perturbation parameter with discontinuities. We can extend this work to two parametric perturbation problem with discontinuities caused layer phenomenon at both boundaries points and some of the interior points as well. Not only this, but these problems can be extended to its $2 - D$ limitations, in which we can discuss the uniform convergence of continuous/discontinuous Galerkin methods in ε -weighted norm and usual L^2 -norm. So many cases can be there, like discontinuous coefficients, problem with two perturbation parameters and turning point, etc. In these conditions, solution may have boundary and interior layers simultaneously. Domain discretization also matter for these problem, for ex; if one discretize the domain by Bakhvalov mesh or more than that by exponential mesh gives the sharper convergence than the mesh discretization by Shishkin mesh.

8 Discussion

The literature contains a large number of studies that discuss the continuous/discontinuous Galerkin technique for singular perturbation problem (SPP). There are several papers in the literature which discussed the convergence of NIPG method for instance, one can see ([10, 11, 13, 21]). In first three papers authors deduced the first order convergence, while the last one reflects super-convergence of the solution. Except [11] all other deals with the discontinuous Galerkin method for SPP with continuous coefficients and source term but the former has convergence result for the problem with discontinuous source term. Furthermore, so many articles in the literature which we have already discussed in Sect. 1 that have analysis of SPP with discontinuous coefficient or source term. But there are not a single paper that analyze NIPG method for SPP with discontinuous source term ever before. That's why this paper is elaboration of first order convergence up to logarithmic factor of NIPG method on usual Shishkin mesh where discontinuity of jump type occurs in convection coefficient.

References

1. Babu, A.R., Ramanujam, N.: The SDFEM for singularly perturbed convection-diffusion problems with discontinuous source term arising in the chemical reactor theory. *Int. J. Comput. Math.* **88**(8), 1664–1680 (2011)
2. Brenner, S.C., Scott, L.R., Scott, L.R.: The mathematical theory of finite element methods, vol. 3, pp. 263–291. Springer, New York (2008). <https://doi.org/10.1007/978-1-4757-4338-8>
3. Cen, Z.: A hybrid difference scheme for a singularly perturbed convection-diffusion problem with discontinuous convection coefficient. *Appl. Math. Comput.* **169**(1), 689–699 (2005)

4. Dubey, V.P., Kumar, D., Dubey, S.: A modified computational scheme and convergence analysis for fractional order hepatitis E virus model. In: *Advanced Numerical Methods for Differential Equations*, pp. 279–312. CRC Press (2021)
5. Dubey, V.P., Singh, J., Alshehri, A.M., Dubey, S., Kumar, D.: Forecasting the behavior of fractional order Bloch equations appearing in NMR flow via a hybrid computational technique. *Chaos Solit. Fractals* **164**, 112691 (2022)
6. Dubey, V.P., Singh, J., Alshehri, A.M., Dubey, S., Kumar, D.: Numerical investigation of fractional model of Phytoplankton-toxic Phytoplankton-Zooplankton system with convergence analysis. *Int. J. Biomath.* **15**(04), 2250006 (2022)
7. Farrell, P.A., Hegarty, A.F., Miller, J.J., O’Riordan, E., Shishkin, G.I.: Global maximum norm parameter-uniform numerical method for a singularly perturbed convection-diffusion problem with discontinuous convection coefficient. *Math. Comput. Model.* **40**(11–12), 1375–1392 (2004)
8. Farrell, P.A., Miller, J.J.H., Shishkin, G.I.: Singularly perturbed differential equations with. In: *Analytical and Numerical Methods for Convection-Dominated and Singularly Perturbed Problems*, p. 23 (2000)
9. Peng, Z., Ziqing, X., Shuzi, Z.: A coupled continuous-discontinuous fem approach for convection diffusion equations. *Acta Math. Sci.* **31**(2), 601–612 (2011)
10. Ranjan, K.R., Gowrisankar, S.: Uniformly convergent NIPG method for singularly perturbed convection diffusion problem on Shishkin type meshes. *Appl. Numer. Math.* **179**(4), 125–148 (2022)
11. Ranjan, K.R., Gowrisankar, S.: NIPG method on Shishkin mesh for singularly perturbed convection–diffusion problem with discontinuous source term. *Int. J. Comput. Methods* 2250048 (2022)
12. Roos, H.G., Zarin, H.: The streamline-diffusion method for a convection-diffusion problem with a point source. *J. Comput. Appl. Math.* **150**(1), 109–128 (2003)
13. Singh, G., Natesan, S.: Study of the NIPG method for two-parameter singular perturbation problems on several layer adapted grids. *J. Appl. Math. Comput.* **63**(1), 683–705 (2020). <https://doi.org/10.1007/s12190-020-01334-7>
14. Singh, H.: Chebyshev spectral method for solving a class of local and nonlocal elliptic boundary value problems. *Int. J. Nonlinear Sci. Numer. Simul.* (2021)
15. Singh, H., Singh, A.K., Pandey, R.K., Kumar, D., Singh, J.: An efficient computational approach for fractional Bratu’s equation arising in electrospinning process. *Math. Methods Appl. Sci.* **44**(13), 10225–10238 (2021)
16. Singh, H., Srivastava, H.M., Kumar, D.: A reliable algorithm for the approximate solution of the nonlinear Lane-Emden type equations arising in astrophysics. *Numer. Methods Partial Differ. Equ.* **34**(5), 1524–1555 (2018)
17. Teofanov, L., Brdar, M., Franz, S., Zarin, H.: SDFEM for an elliptic singularly perturbed problem with two parameters. *Calcolo* **55**(4), 1–20 (2018). <https://doi.org/10.1007/s10092-018-0293-0>
18. Tobiska, L.: Analysis of a new stabilized higher order finite element method for advection-diffusion equations. *Comput. Methods Appl. Mech. Eng.* **196**(1), 538–550 (2006)
19. Zarin, H., Gordic, S.: Numerical solving of singularly perturbed boundary value problems with discontinuities. *Novi Sad J. Math.* **42**, 01 (2012)
20. Zhang, J., Ma, X., Lv, Y.: Finite element method on Shishkin mesh for a singularly perturbed problem with an interior layer. *Appl. Math. Lett.* **121**, 107509 (2021)
21. Zhu, P., Yang, Y., Yin, Y.: Higher order uniformly convergent NIPG methods for 1-d singularly perturbed problems of convection-diffusion type. *Appl. Math. Model.* **39**(22), 6806–6816 (2015)



Simultaneous Action of Modulated Temperature and Third Diffusing Component on Natural Convection

Pervinder Singh and Vinod K. Gupta^(✉)

Department of Mathematics, DIT University, Dehradun 248009, India
vinodguptabhu@gmail.com

Abstract. The modulated temperature and triple diffusive convection play significant contribution in regulating the heat and mass transports inducing some applications in industry. The weakly non-linear stability analysis is performed to depict the rate of heat and mass transport due to the third diffusing component on Rayleigh-Bénard convection. The Newtonian fluid layer is heated from below and solutes are concentrated from opposite boundaries, i.e. one of the solute is concentrated from below and other is concentrated from above. The fluid layer is extended infinitely in x - direction and between two parallel plates at $z = 0$ and $z = d$ for this study. The time dependent temperature consists a constant basic temperature and a time-dependent sinusoidal part. The Asymptotic expansion method is applied to determine the solution of system of non-linear differential equations. The Ginzburg-Landau differential equation is extracted by applying the Fredholm solvability condition and is solved numerically by the software MATHEMATICA 12. The impact of various dimensionless parameters; Prandtl number (Pr), Lewis numbers (Le_{S_1} and Le_{S_2}), solute Rayleigh numbers (Ra_{S_1} , Ra_{S_2}), amplitude of modulation (δ) and frequency of modulation (ω) on heat and mass transport are shown graphically. The parameters δ and ω increase the heat and mass transport. Also, It is found that heat and mass transports can be controlled by a suitable choice of range of parameters.

Keywords: Newtonian liquid · Triple diffusive convection · Temperature Modulation · Thermal Rayleigh Number · Solute Rayleigh Number

1 Introduction

The Rayleigh - Bénard convection in Newtonian liquid is very interesting topic among the researchers due to its significant applications in engineering, science and technology. Some of them are in food processing, oil recovery techniques, geophysics, oceanography, biological system, underground water flow, rain effects, nuclear reactors and many more. The subsequent developments on the problems based on Rayleigh - Bénard convection in fluid layers as well as in porous media are reported by Chandrasekhar [1], Nield and Bejan [2], Drazin and Reid [3].

The Rayleigh - Bénard convection due to one concentrated species and a temperature gradient is known as double diffusive convective problem. The instability problems of double diffusive convection problems attract researcher's attention due to their numerous applications in industry, science and technology like material processing, food processing, oil reservoirs oceanography and nuclear reactors. The external regulatory forces like concentration modulation, gravity modulation, rotational modulation are the topics of discussion among the researchers from last two decades. The time-dependent boundaries allow us to control the convective heat and mass transports. Some of the reports available on different types of modulations are; Gershuni *et al.* [4], Davis [5], Mehta [6], Gupta *et al.* [7], Gupta [8], Kumar *et al.* [9,10] and keshri *et al.* [11]. Gershuni *et al.* [4] examined the effect of vertical temperature modulation for free and rigid surface. The effect of temperature modulation on double diffusive convection is reported by Mehta [6]. The critical thermal Rayleigh number was obtained with correction factor associated with modulated boundaries and it was found that thermal Rayleigh number depends on the amplitude and the phase difference between them. Gupta *et al.* [7] analysed the effect of concentration modulation as well as gravitational modulation in a rotating layer and the report revealed that the frequency of modulation and Taylor number stabilize the convection process. Further, Gupta [8] extended the study of Gupta *et al.* [7] for couple stress liquid.

Although, double diffusive convection has its own importance due to its large number of applications in geophysics, oceanography and binary mixture's solidification but there exist some real life situations in which the convective system contains more than one solute and so the problem of double diffusion becomes a limited case. Degens *et al.* [12] documented a report on multi-diffusive convection. The topological nature of neutral curves in the presence of multicomponent convection in porous media is analysed by Tracey [13]. Further, Rionero [14] derived a sufficient condition for inhibiting the onset of convection and the global non-linear stability of the thermal conduction in a porous media due to triple diffusive convection. Raghunatha *et al.* [15] scrutinized the impact of triple diffusive convection in Maxwell fluid saturated porous layer and showed that the rate of heat and mass transport increases with an increase in relaxation parameter. Shivkumara *et al.* [16] established condition for existence of oscillatory convection in terms of diffusivity ratios. Some more available documents on the onset of convection in Newtonian and non-Newtonian fluids under third diffusing component are reported by Awasthi *et al.* [17], Zhao *et al.* [18], Patil *et al.* [19], Khan *et al.* [20], Pearlstein *et al.* [21] and Straughan and Walker [22].

In aforesaid literature, the authors have investigated the effect of various parameters on convective system due to third diffusing component under spatial coordinates dependent boundary conditions. In real life scenario, there are some physical situations occur in industry in which boundary conditions are dependent on spatial coordinates as well as time. So, the study of time-periodic boundary conditions become important due to its need. Nothing is found for deliberation on the effect of time-periodic boundary conditions on Rayleigh-Bénard convec-

tion due to third diffusing component. It has numerous applications in material science, oceanography, medical sciences, oil reservoirs, Biological systems and many more. With these motivations, the present study has been carried-out. A weakly non-linear stability analysis in terms of asymptotic expansion of perturbation parameter is performed to extract the Ginzburg-Landau equation (Landau [23]). Dubey *et al.* [24–27], Singh *et al.* [28] and Singh [29, 30] discussed on the convergence of the methods for solving non-linear equations.

2 Governing Equations

The present study is carried out to examine the efficacy of time dependent thermal boundaries and solute concentrations on heat and mass transports. The problem is formulated mathematically under the assumptions that the Newtonian fluid is incompressible and confined between two parallel plates at $z = 0$ and $z = d$, which is extended infinitely in x -direction. The first solute is concentrated from lower plate while second solute is concentrated from upper plate. An adverse concentration gradients $\Delta S_i/d$ are maintained between the boundaries. The Boussinessq approximation is also incorporated in mathematical model which assumes that the density varies linearly with temperature and solute concentrations. A graphical representation of considered problem is shown by Fig. 1.

In view of above assumptions, a mathematical representation of considered problem may be written as

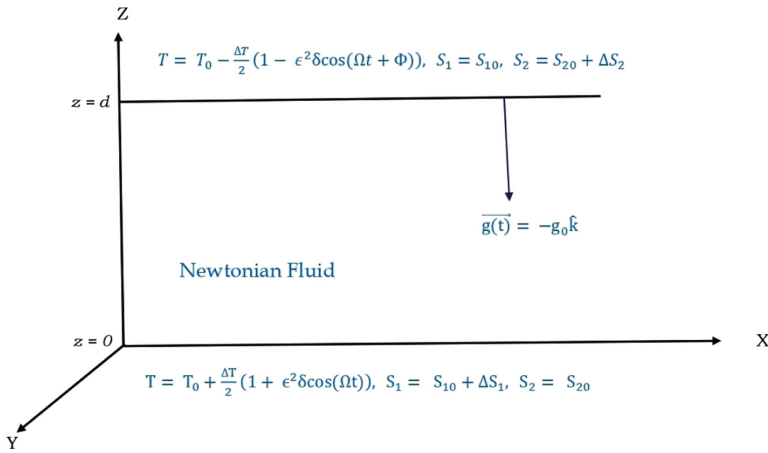


Fig. 1. Physical Presentation

$$\rho_0 \left[\frac{\partial \mathbf{q}}{\partial t} + (\mathbf{q} \cdot \nabla) \mathbf{q} \right] = -\nabla p + \rho \mathbf{g} + \mu \nabla^2 \mathbf{q}, \tag{1}$$

$$\frac{\partial T}{\partial t} + (\mathbf{q} \cdot \nabla)T = k_T \nabla^2 T, \tag{2}$$

$$\frac{\partial S_1}{\partial t} + (\mathbf{q} \cdot \nabla)S_1 = k_{s_1} \nabla^2 S_1, \tag{3}$$

$$\frac{\partial S_2}{\partial t} + (\mathbf{q} \cdot \nabla)S_2 = k_{s_2} \nabla^2 S_2. \tag{4}$$

The Boussinesq approximation is given as

$$\rho = \rho_0 [1 - \alpha_T(T - T_0) + \beta_{S_1}(S_1 - S_{10}) + \beta_{S_2}(S_2 - S_{20})]. \tag{5}$$

The equation of continuity for incompressible fluid is taken as

$$\nabla \cdot \mathbf{q} = 0. \tag{6}$$

The thermal and concentrations boundary conditions are given by

$$T = T_0 + \frac{\Delta T}{2} [1 + \epsilon^2 \delta \cos(\Omega t)] \text{ at } z = 0, \tag{7}$$

$$T = T_0 - \frac{\Delta T}{2} [1 - \epsilon^2 \delta \cos(\Omega t + \phi)] \text{ at } z = d, \tag{8}$$

$$S_1 = S_{10} + \Delta S_1 \text{ at } z = 0 \text{ and } S_1 = S_{10} \text{ at } z = d, \tag{9}$$

$$S_2 = S_{20} \text{ at } z = 0 \text{ and } S_2 = S_{20} + \Delta S_2 \text{ at } z = d, \tag{10}$$

where $\mathbf{q} = (u, v, w)$ is the fluid velocity, p is the pressure, ρ is the fluid density, ρ_0 is the reference density, $\mathbf{g} = (0, 0, -g)$ is the gravitational acceleration, μ is the viscosity of the fluid, T, S_1, S_2 are the temperature, concentration of first solute and concentration of second solute respectively, and k_T, k_{S_1}, k_{S_2} are respective diffusivity ratios.

3 Basic State

Initially, fluid is assumed to be quiescent so the fluid velocity, pressure, density, temperature and solute concentrations at basic state are defined as $q_b = (0, 0, 0)$, $p = p_b(z)$, $\rho = \rho_b(z)$, $T = T_b(z, t)$, $S_1 = S_{1b}(z)$, $S_2 = S_{2b}(z)$. Using these values in Eqs. (1)–(6), we get

$$\frac{\partial T_b(z, t)}{\partial t} = \kappa_T \frac{\partial^2 T_b(z, t)}{\partial z^2}, \tag{11}$$

$$\frac{d^2 S_{1b}}{dz^2} = 0, \tag{12}$$

$$\frac{d^2 S_{2b}}{dz^2} = 0. \tag{13}$$

The solution of Eqs. (11)–(17) under the thermal and solutes boundary conditions may be obtained as

$$p_b = -\rho_b g_0 z, \quad (14)$$

$$T_b = -\left(\frac{\Delta T}{d}\right)z + \left(T_0 + \frac{\Delta T}{2}\right) + \epsilon^2 \frac{\Delta T}{2} f(z, t), \quad (15)$$

where,

$$f(z, t) = \text{Re} \left[a(\lambda) e^{\frac{\lambda z}{d}} + a(-\lambda) e^{-\frac{\lambda z}{d}} \right] e^{-i\Omega t}, \quad (16)$$

and

$$a(\lambda) = \frac{\lambda e^{-i\phi} + e^{-\lambda}}{2 e^{\lambda} - e^{-\lambda}} \text{ and } \lambda = \pm(1-i) \sqrt{\frac{\omega d}{2\kappa_T}}, \quad (17)$$

$$S_{1b}(z) = S_{10} - \frac{\Delta S_1}{d} z, \quad (18)$$

$$S_{2b}(z) = S_{20} + \frac{\Delta S_2}{d} z. \quad (19)$$

4 Perturbation

To perform stability analysis, an infinitesimal perturbation in variables are taken in account. Thus, the variables at perturbed state are defined as:

$$p = \bar{p}_b + p', \mathbf{q} = \bar{\mathbf{q}}_b + \mathbf{q}', \rho = \bar{\rho}_b + \rho', S_1 = S_{1b} + S'_1, S_2 = S_{2b} + S_2, T = T_b + T', \quad (20)$$

where ' denotes the perturbed state of variables.

In Rayleigh - Bénard convection, convective rolls are parallel to the y - axis so study restricts us for two dimensional study and the velocity component in x - z and z - direction are defined in terms of stream function as $\mathbf{q}' = (u', v', z') = (\frac{\partial \psi}{\partial z}, 0, -\frac{\partial \psi}{\partial x})$. Further to eliminate the pressure term from Eq. (1), we take its curl and rewrite the governing equations in terms of stream function as

$$\rho_0 \left[\frac{\partial}{\partial t} (\nabla^2 \psi) - \frac{\partial(\psi, \nabla^2 \psi)}{\partial(x, z)} \right] = \rho g_0 \left[-\alpha_T \frac{\partial T'}{\partial x} + \beta_{S_1} \frac{\partial S'_1}{\partial x} + \beta_{S_2} \frac{\partial S'_2}{\partial x} \right] + \nabla^4 \psi, \quad (21)$$

$$\frac{\partial T'}{\partial t} - \frac{\partial(\psi, T')}{\partial(x, z)} - \frac{\partial T_b}{\partial x} \frac{\partial \psi}{\partial x} = \kappa_T \nabla^2 T', \quad (22)$$

$$\frac{\partial S'_1}{\partial t} - \frac{\partial(\psi, S'_1)}{\partial(x, z)} - \frac{\partial S_{1b}}{\partial x} \frac{\partial \psi}{\partial x} = \kappa_{S_1} \nabla^2 S'_1, \quad (23)$$

$$\frac{\partial S'_2}{\partial t} - \frac{\partial(\psi, S'_2)}{\partial(x, z)} - \frac{\partial S_{2b}}{\partial x} \frac{\partial \psi}{\partial x} = \kappa_{S_2} \nabla^2 S'_2. \quad (24)$$

5 Non Dimensionalised Parameter

The following variables are used to obtain the dimensionless form of Eqs. (5)–(27)

$$(x, y, z) = d(x^*, y^*, z^*), \quad t = \frac{d^2(t^*)}{\kappa_T}, \quad \psi' = \kappa_T(\psi^*), \quad T' = (\Delta T)T^*, \quad T_b = (\Delta T)T_b^*,$$

$$(S'_1, S_{1b}) = (\Delta_1)(S_1^*, S_{1b}^*), \quad (S'_2, S_{2b}) = (\Delta T)(S_2^*, S_{2b}^*). \quad (25)$$

By using non dimensional variables in Eq. (5) to (27) and remove the asterisks for simplicity, we get the following set of equations:

$$\frac{1}{Pr} \left[\frac{\partial}{\partial t} \nabla^2(\psi) - \frac{\partial(\psi, \nabla^2 \psi)}{\partial(x, z)} \right] = [-R_{T_0} \frac{\partial T}{\partial x} + Ra_{S_1} \frac{\partial S_1}{\partial x} + Ra_{S_2} \frac{\partial S_2}{\partial x}] + \nabla^4 \psi, \quad (26)$$

$$\frac{\partial T}{\partial t} - \frac{\partial(\psi, T)}{\partial(x, z)} - \frac{\partial \psi}{\partial x} \frac{\partial T_b}{\partial z} = \kappa_T \nabla^2 T, \quad (27)$$

$$\frac{\partial S_1}{\partial t} - \frac{\partial(\psi, S_1)}{\partial(x, z)} - \frac{\partial \psi}{\partial x} \frac{\partial S_{1b}}{\partial z} = Le_{S_1} \nabla^2 S_1, \quad (28)$$

$$\frac{\partial S_2}{\partial t} - \frac{\partial(\psi, S_2)}{\partial(x, z)} - \frac{\partial \psi}{\partial x} \frac{\partial S_{2b}}{\partial z} = Le_{S_2} \nabla^2 S_2, \quad (29)$$

where, $Pr = \frac{\nu}{\kappa_T}$ is Prandtl number, $\nu = \frac{\mu}{\rho_0}$ is the kinematic viscosity, $R_{T_0} = \frac{\alpha_T g \Delta T d^3}{\nu \kappa_T}$ is the thermal Rayleigh number, $Ra_{S_1} = \frac{\beta_{S_1} g \Delta S_1 d^3}{\nu \kappa_T}$ and $Ra_{S_2} = \frac{\beta_{S_2} g \Delta S_2 d^3}{\nu \kappa_T}$ are solute Rayleigh number for solute one and two respectively, $Le_{S_1} = \frac{\kappa_{S_1}}{\kappa_T}$ and $Le_{S_2} = \frac{\kappa_{S_2}}{\kappa_T}$ are the Lewis numbers corresponding to two solutes respectively.

6 Weakly Non-linear Stability Analysis

For temporal time scale, time t is rescaled as $\tau = \epsilon^2 t$. Therefore, matrix form of system of Eqs. (26)–(29) is obtained as

$$\begin{bmatrix} \nabla^4 & -R_{T_0} \frac{\partial}{\partial x} & Ra_{S_1} \frac{\partial}{\partial x} & Ra_{S_2} \frac{\partial}{\partial x} \\ -\frac{\partial}{\partial x} & \nabla^2 & 0 & 0 \\ -\frac{\partial}{\partial x} & 0 & \frac{1}{Le_{S_1}} \nabla^2 & 0 \\ \frac{\partial}{\partial x} & 0 & 0 & \frac{1}{Le_{S_2}} \nabla^2 \end{bmatrix} \begin{bmatrix} \psi \\ T \\ S_1 \\ S_2 \end{bmatrix} = \begin{bmatrix} \frac{1}{Pr} [\epsilon^2 \frac{\partial}{\partial \tau} \nabla^2 \psi - J(\psi, \nabla^2 \psi)] \\ \epsilon^2 \frac{\partial T}{\partial \tau} - J(\psi, T) - \epsilon^2 \frac{\delta}{2} f'(z, \tau) \\ \epsilon^2 \frac{\partial S_1}{\partial \tau} - J(\psi, S_1) \\ \epsilon^2 \frac{\partial S_2}{\partial \tau} - J(\psi, S_2) \end{bmatrix}, \quad (30)$$

where, J denotes the Jacobian and $f(z, \tau) = \frac{\delta}{2} Re [a(\lambda) e^{\lambda z} + a(-\lambda) e^{-\lambda z}] e^{-i\omega \tau}$.

6.1 Expansion of Variables

In order to determine the solution of Eq. (30), the asymptotic analysis method is used. For that, we have introduced a small perturbation parameter ϵ to expand the variables ψ , T , R_T , S_1 and S_2 .

$$\begin{aligned}\psi &= \sum_{m=1}^{\infty} \epsilon^m \psi_m, \quad T = \sum_{m=1}^{\infty} \epsilon^m T_m, \quad R_T = \sum_{m=1}^{\infty} \epsilon^{2m-2} R_{2m-2}, \\ S_1 &= \sum_{m=1}^{\infty} \epsilon^m S_m, \quad S_2 = \sum_{m=1}^{\infty} \epsilon^n S_{2m},\end{aligned}\tag{31}$$

Using the expression of ψ , T , S_1 and S_2 defined by Eq. (31) in Eq. (30), the solution can be determined by equating the coefficient of various order of ϵ on both the sides.

6.2 First-Order Solution

To find the solution at first-order of Eq. (30), the coefficients of ϵ on both sides are compared which gives the following system of equations.

$$\begin{bmatrix} \nabla^4 & -R_0 \frac{\partial}{\partial x} & Ra_{S_1} \frac{\partial}{\partial x} & Ra_{S_2} \frac{\partial}{\partial x} \\ -\frac{\partial}{\partial x} & \nabla^2 & 0 & 0 \\ -\frac{\partial}{\partial x} & 0 & \frac{1}{Le_{S_1}} \nabla^2 & 0 \\ \frac{\partial}{\partial x} & 0 & 0 & \frac{1}{Le_{S_2}} \nabla^2 \end{bmatrix} \begin{bmatrix} \psi_1 \\ T_1 \\ S_{11} \\ S_{21} \end{bmatrix} = \begin{bmatrix} 0 \\ 0 \\ 0 \\ 0 \end{bmatrix}.\tag{32}$$

As the Rayleigh-Bénard convective cells are periodic, therefore we may assume the periodic solutions which satisfy the boundary conditions given by Eqs. (7)–(10) as

$$\begin{aligned}\psi_1 &= \mathcal{A}(\tau) \sin(kx) \sin(\pi z), \quad T_1 = \mathcal{B}(\tau) \cos(kx) \sin(\pi z), \\ S_{11} &= \mathcal{D}(\tau) \cos(kx) \sin(\pi z), \quad S_{21} = \mathcal{E}(\tau) \cos(kx) \sin(\pi z),\end{aligned}\tag{33}$$

where $\mathcal{A}(\tau)$, $\mathcal{B}(\tau)$, $\mathcal{D}(\tau)$ and $\mathcal{E}(\tau)$ are undetermined coefficients. Making use of Eq. (33) in Eq. (32), we get the following expressions:

$$\psi_1 = \mathcal{A}(\tau) (\sin(kx) \sin(\pi z)),\tag{34}$$

$$T_1 = -\frac{k}{p^2} \mathcal{A}(\tau) \cos(kx) \sin(\pi z),\tag{35}$$

$$S_{11} = -\frac{k}{p^2 \tau_1} \mathcal{A}(\tau) \cos(kx) \sin(\pi z),\tag{36}$$

$$S_{21} = \frac{k}{p^2 \tau_2} \mathcal{A}(\tau) \cos(kx) \sin(\pi z),\tag{37}$$

where

$$p^2 = k^2 + \pi^2.\tag{38}$$

The value of $\mathcal{A}(\tau)$ will be obtained at the third order stage by using Fredholm-solvability condition. For the onset of stationary convection, the critical value of thermal Rayleigh number (R_0) and corresponding wave number (k_c) are given by

$$R_0 = \frac{p^6}{k^2} + Ra_{S_1} \cdot Le_{S_1} - Ra_{S_2} \cdot Le_{S_2} \quad \text{and} \quad k_c = \frac{\pi}{\sqrt{2}}, \tag{39}$$

which coincides with the result obtained by Shivkumara *et al.* [16] for couple stress parameter ($\Lambda_c = 0$).

6.3 Second-Order Solution

To find the solution of second-order system, the coefficient of ϵ^2 in Eq. (30) are compared and the following system of equations are obtained:

$$\begin{bmatrix} \nabla^4 & -R_0 \frac{\partial}{\partial x} & Ra_{S_1} \frac{\partial}{\partial x} & Ra_{S_2} \frac{\partial}{\partial x} \\ -\frac{\partial}{\partial x} & \nabla^2 & 0 & 0 \\ -\frac{\partial}{\partial x} & 0 & \frac{1}{Le_{S_1}} \nabla^2 & 0 \\ \frac{\partial}{\partial x} & 0 & 0 & \frac{1}{Le_{S_2}} \nabla^2 \end{bmatrix} \begin{bmatrix} \psi_2 \\ T_2 \\ S_{12} \\ S_{22} \end{bmatrix} = \begin{bmatrix} R_{21} \\ R_{22} \\ R_{23} \\ R_{24} \end{bmatrix}, \tag{40}$$

where,

$$R_{21} = 0, \quad R_{22} = \frac{\pi k^2}{2p^2} \mathcal{A}^2(\tau) \sin(2\pi z), \tag{41}$$

$$R_{23} = \frac{\pi k^2}{2\tau_1 p^2} \mathcal{A}^2(\tau) \sin(2\pi z), \tag{42}$$

$$R_{24} = -\frac{\pi k^2}{2\tau_2 p^2} \mathcal{A}^2(\tau) \sin(2\pi z). \tag{43}$$

At second-order solution of Eq. (45) is obtained as

$$\psi_2 = 0, \tag{44}$$

$$T_2 = -\frac{k^2}{8\pi p^2} \mathcal{A}^2(\tau) \sin(2\pi z), \tag{45}$$

$$S_{12} = -\frac{k^2}{8\pi \tau_1^2 p^2} \mathcal{A}^2(\tau) \sin(2\pi z), \tag{46}$$

$$S_{22} = \frac{k^2}{8\pi \tau_2^2 p^2} \mathcal{A}^2(\tau) \sin(2\pi z). \tag{47}$$

The horizontally averaged Nusselt number and Sherwood numbers are given by

$$Nu(\tau) = \frac{\left[\frac{k}{2\pi} \int_0^{\frac{2\pi}{k}} (1 + T_2 - z) dx \right]_{z=0}}{\left[\frac{k}{2\pi} \int_0^{\frac{2\pi}{k}} (1 - z) dx \right]_{z=0}}, \tag{48}$$

$$Sh_1(\tau) = \frac{\left[\frac{k}{2\pi} \int_0^{\frac{2\pi}{k}} (1 + S_{12} - z) dx \right]_{z=0}}{\left[\frac{k}{2\pi} \int_0^{\frac{2\pi}{k}} (1 - z) dx \right]_{z=0}}, \quad (49)$$

$$Sh_2(\tau) = \frac{\left[\frac{k}{2\pi} \int_0^{\frac{2\pi}{k}} (S_{22} + z) dx \right]_{z=1}}{\left[\frac{k}{2\pi} \int_0^{\frac{2\pi}{k}} z dx \right]_{z=1}}, \quad (50)$$

using the value of T_2 , S_{12} and S_{22} from the Eqs. (45)–(47) in the Eqs. (48)–(50), we have the following expressions for Nusselt and Sherwood numbers:

$$Nu(\tau) = 1 + \frac{k^2}{4p^2} \mathcal{A}^2(\tau), \quad (51)$$

$$Sh_1(\tau) = 1 + \frac{k^2 \cdot Le_{S_1}^2}{4p^2} \mathcal{A}^2(\tau), \quad (52)$$

$$Sh_2(\tau) = 1 - \frac{k^2 \cdot Le_{S_2}^2}{4p^2} \mathcal{A}^2(\tau). \quad (53)$$

6.4 Third-Order Solution

For third-order solution, we compare the coefficient of ϵ^3 in Eq. (30) on both the sides which gives following systems of equations:

$$\begin{bmatrix} \nabla^4 & -R_0 \frac{\partial}{\partial x} & Ra_{S_1} \frac{\partial}{\partial x} & Ra_{S_2} \frac{\partial}{\partial x} \\ -\frac{\partial}{\partial x} & \nabla^2 & 0 & 0 \\ -\frac{\partial}{\partial x} & 0 & \frac{1}{Le_{S_1}} \nabla^2 & 0 \\ \frac{\partial}{\partial x} & 0 & 0 & \frac{1}{Le_{S_2}} \nabla^2 \end{bmatrix} \begin{bmatrix} \psi_3 \\ T_3 \\ S_{13} \\ S_{23} \end{bmatrix} = \begin{bmatrix} R_{31} \\ R_{32} \\ R_{33} \\ R_{34} \end{bmatrix}, \quad (54)$$

where

$$R_{31} = \left[-\frac{p^2}{P_r} \frac{d}{d\tau} \mathcal{A}(\tau) + Ra_{T_2} \frac{k^2}{p^2} \right] \sin kx \sin(\pi z), \quad (55)$$

$$R_{32} = \left[-\frac{k}{p^2} \frac{d}{d\tau} \mathcal{A}(\tau) + \frac{k^3 \mathcal{A}^3(\tau)}{4p^2} \cos 2\pi z - k \delta f'(z, \tau) \mathcal{A}(\tau) \right] \cos kx \sin(\pi z), \quad (56)$$

$$R_{33} = \left[-\frac{k \cdot Le_{S_1}}{p^2} \frac{d}{d\tau} \mathcal{A}(\tau) + \frac{k^3 \cdot Le_{S_1}^2 \mathcal{A}^3(\tau)}{4p^2} \cos(2\pi z) \right] \cos kx \sin(\pi z), \quad (57)$$

$$R_{34} = \left[\frac{k \cdot Le_{S_1}}{2p^2} \frac{d}{d\tau} \mathcal{A}(\tau) - \frac{k^3 \cdot Le_{S_2}^2 \mathcal{A}^3(\tau)}{4p^2} \cos(2\pi z) \right] \cos kx \sin(\pi z), \quad (58)$$

using the value of R_{31} , R_{32} , R_{33} and R_{34} and apply the solvability condition for the existence of third-order solution, we have

$$\int_{z=0}^{z=1} \int_{x=0}^{x=\frac{2\pi}{k}} [\hat{\psi}_1 R_{31} + A \hat{T}_1 R_{32} + B \hat{S}_{11} R_{33} + C \hat{S}_{21} R_{34}] dx dz = 0. \quad (59)$$

After solving the above equation we get, $A = 1$, $B = R_0$, $C = -Ra_{S_1}$, $D = Ra_{S_2}$, putting these values in Eq. (59), we obtain the Ginzburg-Landau equation as

$$\left[\frac{p^2}{Pr} + \frac{k^2 R_0}{p^4} - \frac{Ra_{S_1} k^2 Le_{S_1}^2}{p^4} + \frac{Ra_{S_2} k^2 Le_{S_2}^2}{p^4} \right] \frac{d}{d\tau} \mathcal{A}(\tau) = \frac{k^2}{p^2} \left[R_2 - R_0 \frac{\delta k^2}{p^2} F(\tau) \right] \mathcal{A}(\tau) + \frac{k^4}{8p^4} \left[-R_0 + Ra_{S_1} Le_{S_1}^3 - Ra_{S_2} Le_{S_2}^3 \right] \mathcal{A}^3(\tau), \quad (60)$$

where,

$$F(\tau) = \int_{z=0}^{z=1} f'(z, \tau) \sin^2(\pi z) dz. \quad (61)$$

The above Ginzburg-Landau differential equation is solved by fourth order Runge-Kutta method with initial condition $a_0 = A(0)$, where a_0 is the amplitude of the convection at initial stage.

7 Results and Discussion

The current study emphasis on the impact of modulated temperature and third diffusing component on heat and mass transport in Newtonian liquid. The linear stability analysis is not sufficient to explore the nature of mass and heat transports therefore, a weakly non-linear analysis has been used in terms of the method of asymptotic expansion. By this method, Ginzburg-Landau equation has been extracted to depict the rate of heat and mass transports. Moreover, to perform stability analysis, the amplitude of modulation and asymptotic expansion parameter ϵ are considered to be small. In this section, we analyse the effect of dimensionless parameters on heat transport (Nu) and mass transports (Sh_1) and (Sh_2) graphically under the influence of temperature modulation. In this investigation, the values of parameters are assumed as follows $\delta = 0.05$, $Le_{S_1} < Le_{S_2}$, $Ra_{S_1} < Ra_{S_2}$ and taking the fixed values as $\omega = 1$, $Le_{S_1} = 1.5$, $Le_{S_2} = 2.0$, $Ra_{S_1} = 10$, $Ra_{S_2} = 20$, $Pr = 0.71$. Moreover, for the present problem we consider the three different types of temperature modulation as

- 1) In Phase modulation(IPM) ($\phi = 0$)
- 2) Out phase modulation(OPM) ($\phi = \pi$), and
- 3) Modulation of only the lower boundary (MOLB) ($\phi = -i\omega$)

The effect of parameters in all the above three cases are shown in the Figs. 2, 3, 4, 5, 6, 7, 8, 9 and 10.

In Phase Modulation (IPM)

From Fig. 2(a), it can be easily observed that the rate of heat transport become constant after a very short time of interval for each value of δ . Thus, the different amplitudes of modulation do not affect the rate of heat transport. Figures 2(b)–(c) depict the effect of Lewis numbers Le_{S_1} and Le_{S_2} on heat transport. From these figures, it is found that on increase the value of Lewis numbers the rate of heat transport increases. Further, from the Figs. 2(d)–(e), it is found that

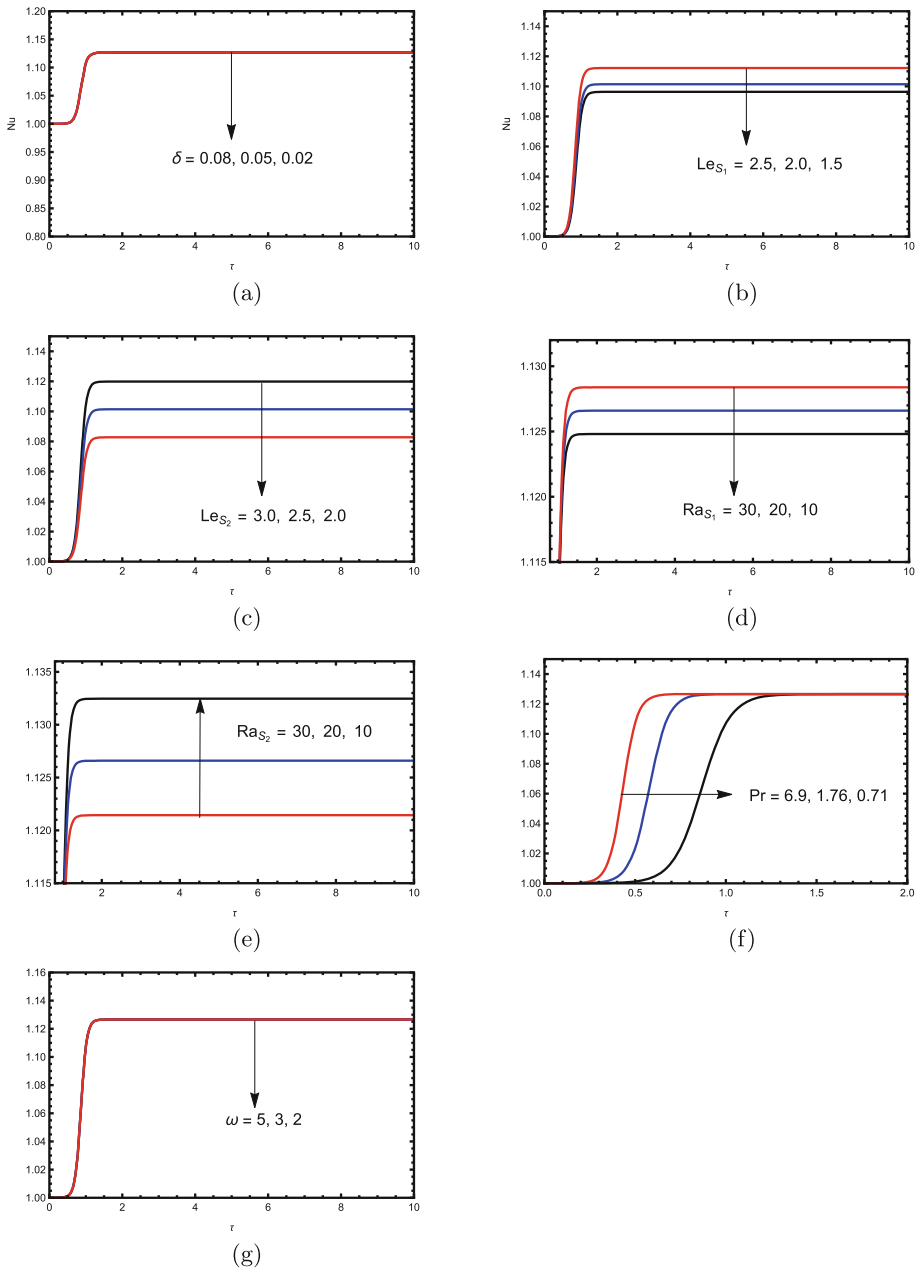


Fig. 2. IPM: Nu versus slow time for different values of (a) δ , (b) Le_{S_1} , (c) Le_{S_2} , (d) Ra_{S_1} , (e) Ra_{S_2} , (f) Pr , (g) ω

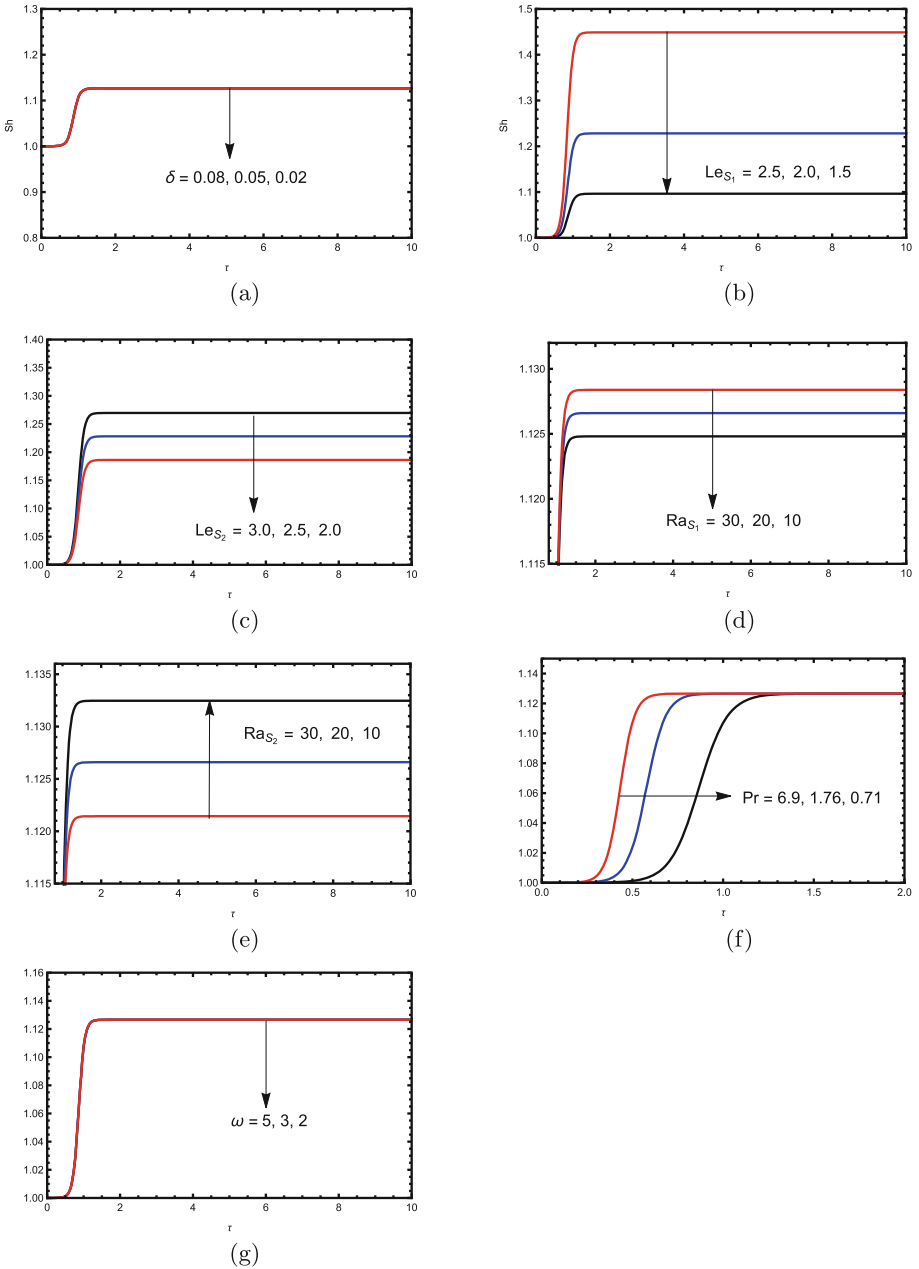


Fig. 3. IPM: Sh_1 versus slow time for different values of (a) δ , (b) Le_{S_1} , (c) Le_{S_2} , (d) Ra_{S_1} , (e) Ra_{S_2} , (f) Pr , (g) ω

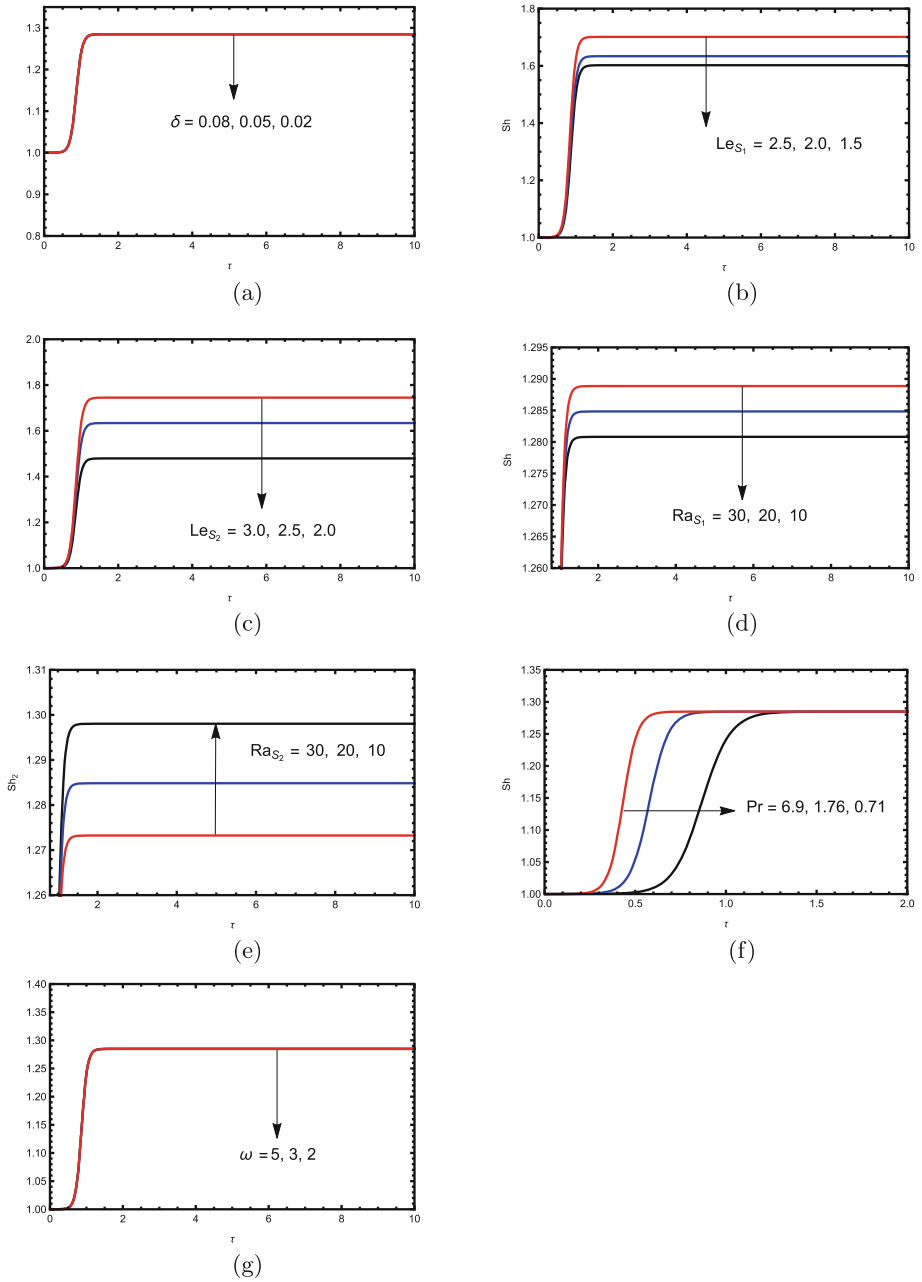


Fig. 4. IPM: Sh_2 versus slow time for different values of (a) δ , (b) Le_{S_1} , (c) Le_{S_2} , (d) Ra_{S_1} , (e) Ra_{S_2} , (f) Pr , (g) ω

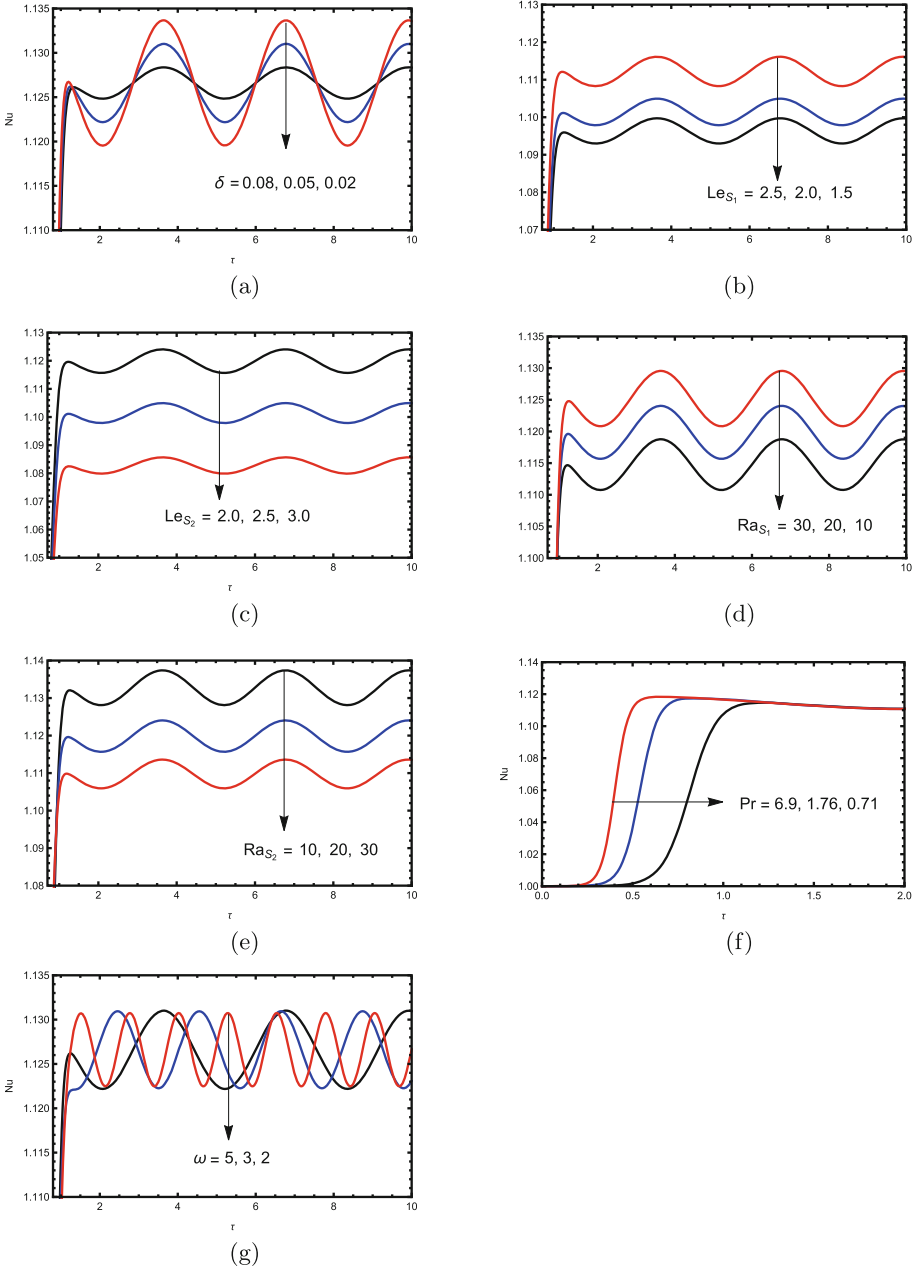


Fig. 5. OPM: Nu versus slow time for different values of (a) δ , (b) Le_{S_1} , (c) Le_{S_2} , (d) Ra_{S_1} , (e) Ra_{S_2} , (f) Pr , (g) ω

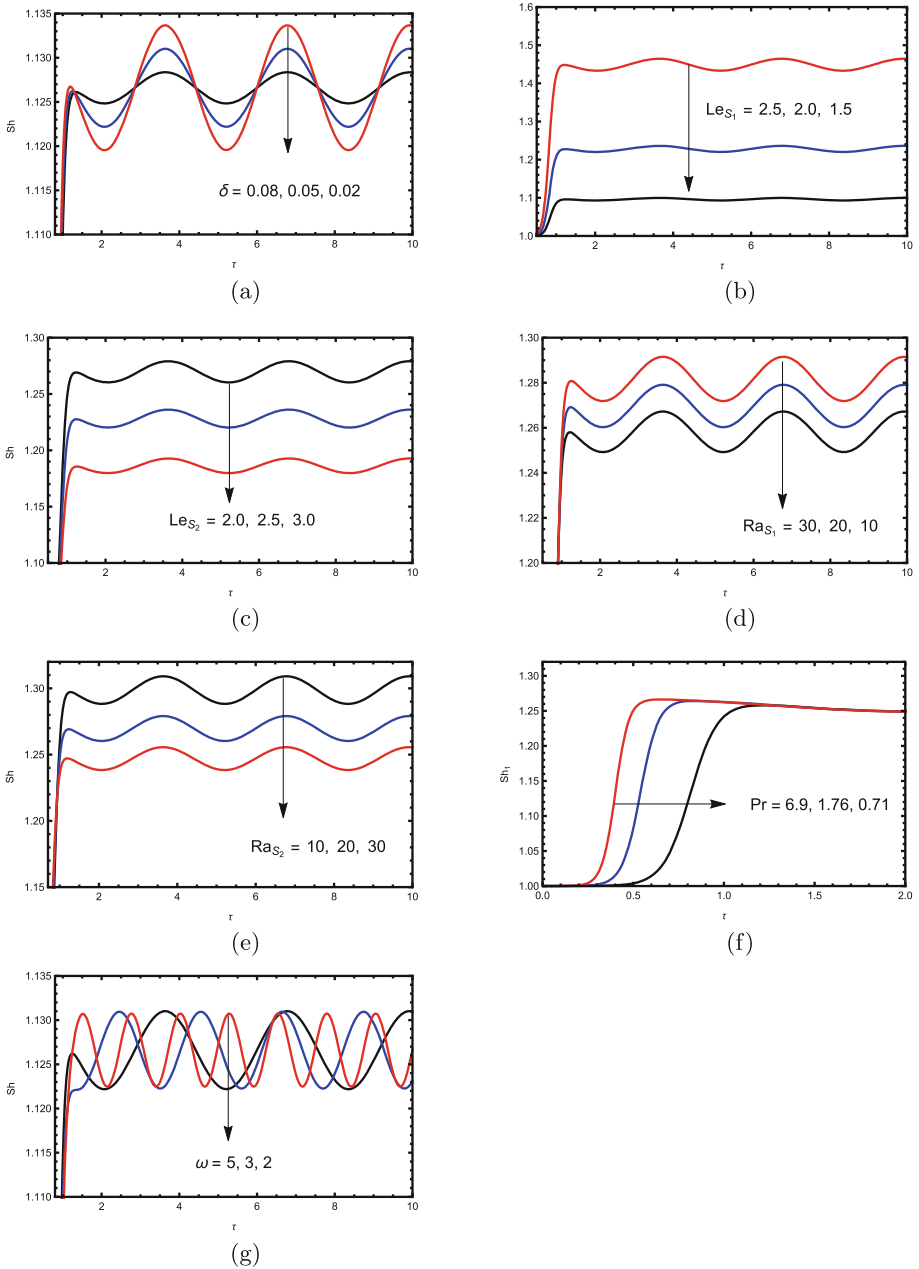


Fig. 6. OPM: Sh_1 versus slow time for different values of (a) δ , (b) Le_{S_1} , (c) Le_{S_2} , (d) Ra_{S_1} , (e) Ra_{S_2} , (f) Pr , (g) ω

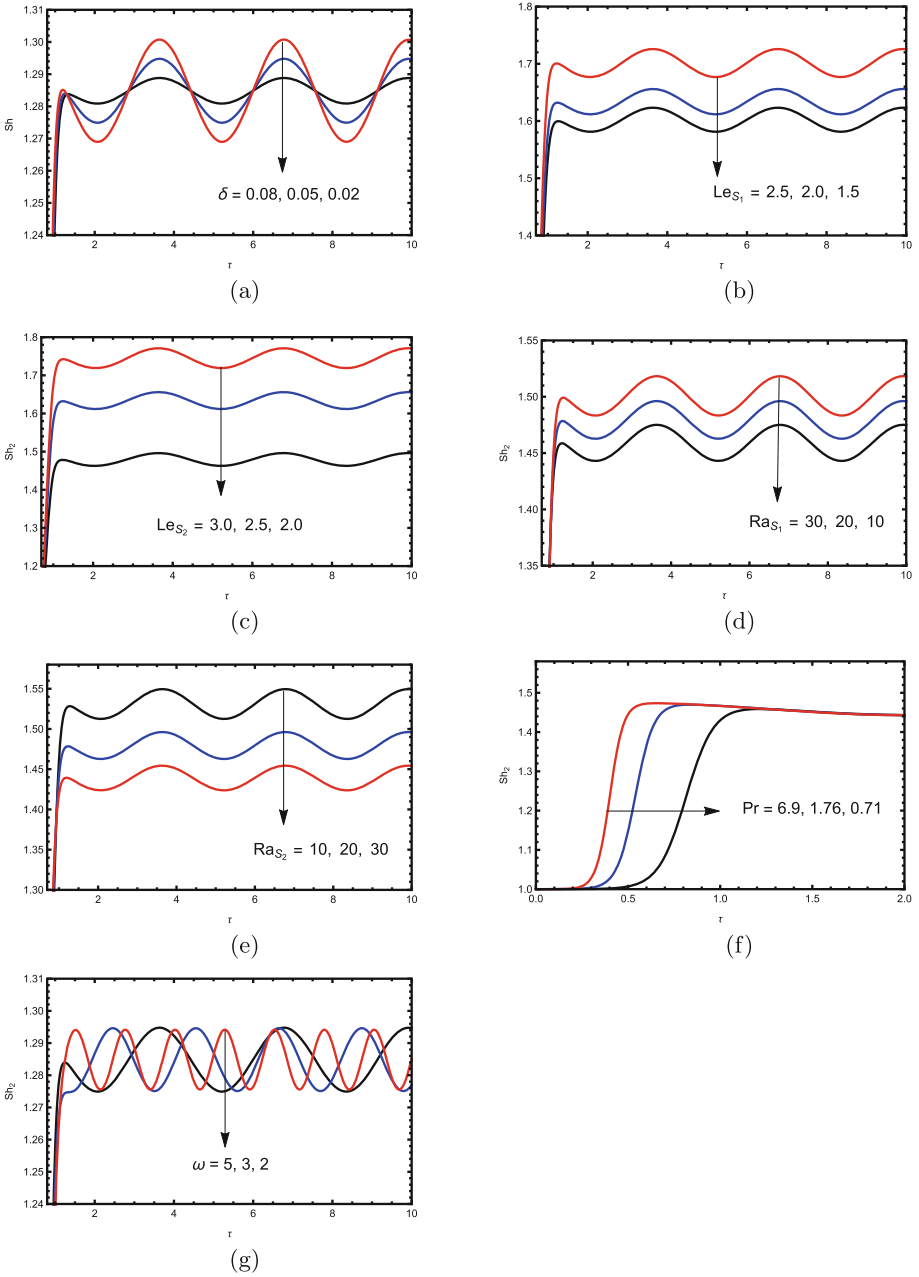


Fig. 7. OPM: Sh_2 versus slow time for different values of (a) δ , (b) Le_{S_1} , (c) Le_{S_2} , (d) Ra_{S_1} , (e) Ra_{S_2} , (f) Pr , (g) ω

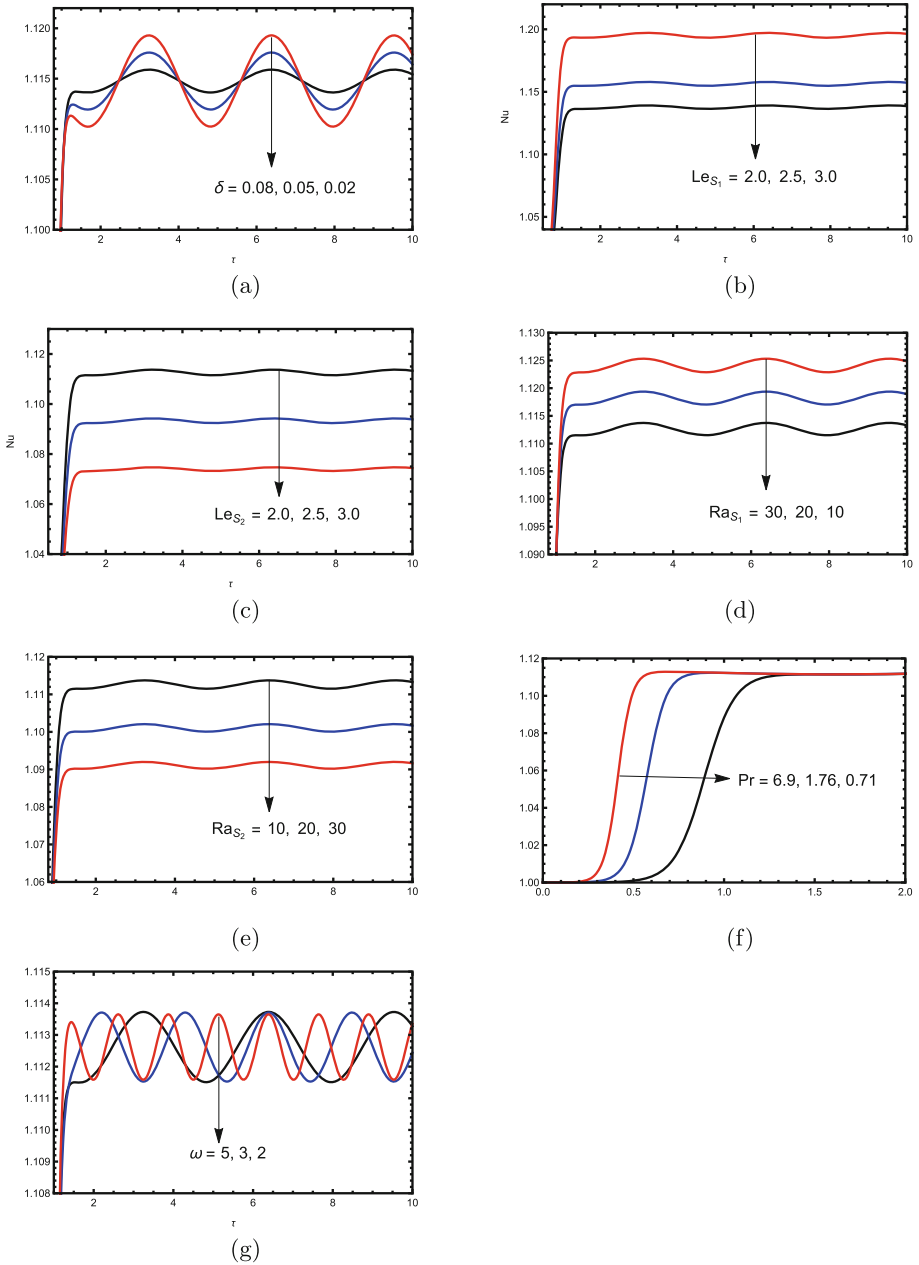


Fig. 8. MOLB: Nu versus slow time for different values of (a) δ , (b) Le_{S_1} , (c) Le_{S_2} , (d) Ra_{S_1} , (e) Ra_{S_2} , (f) Pr , (g) ω

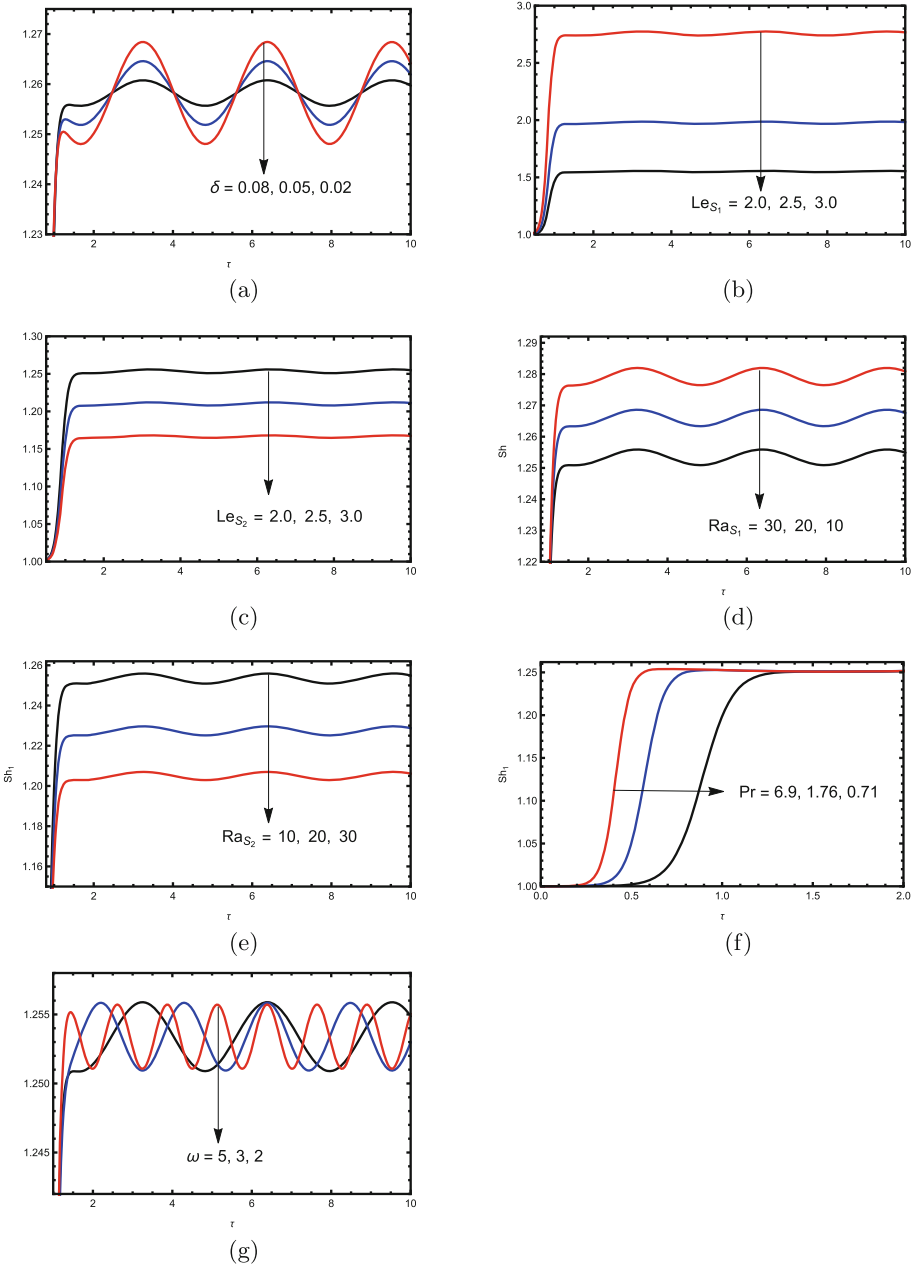


Fig. 9. MOLB: Sh_1 versus slow time for different values of (a) δ , (b) Le_{S_1} , (c) Le_{S_2} , (d) Ra_{S_1} , (e) Ra_{S_2} , (f) Pr , (g) ω

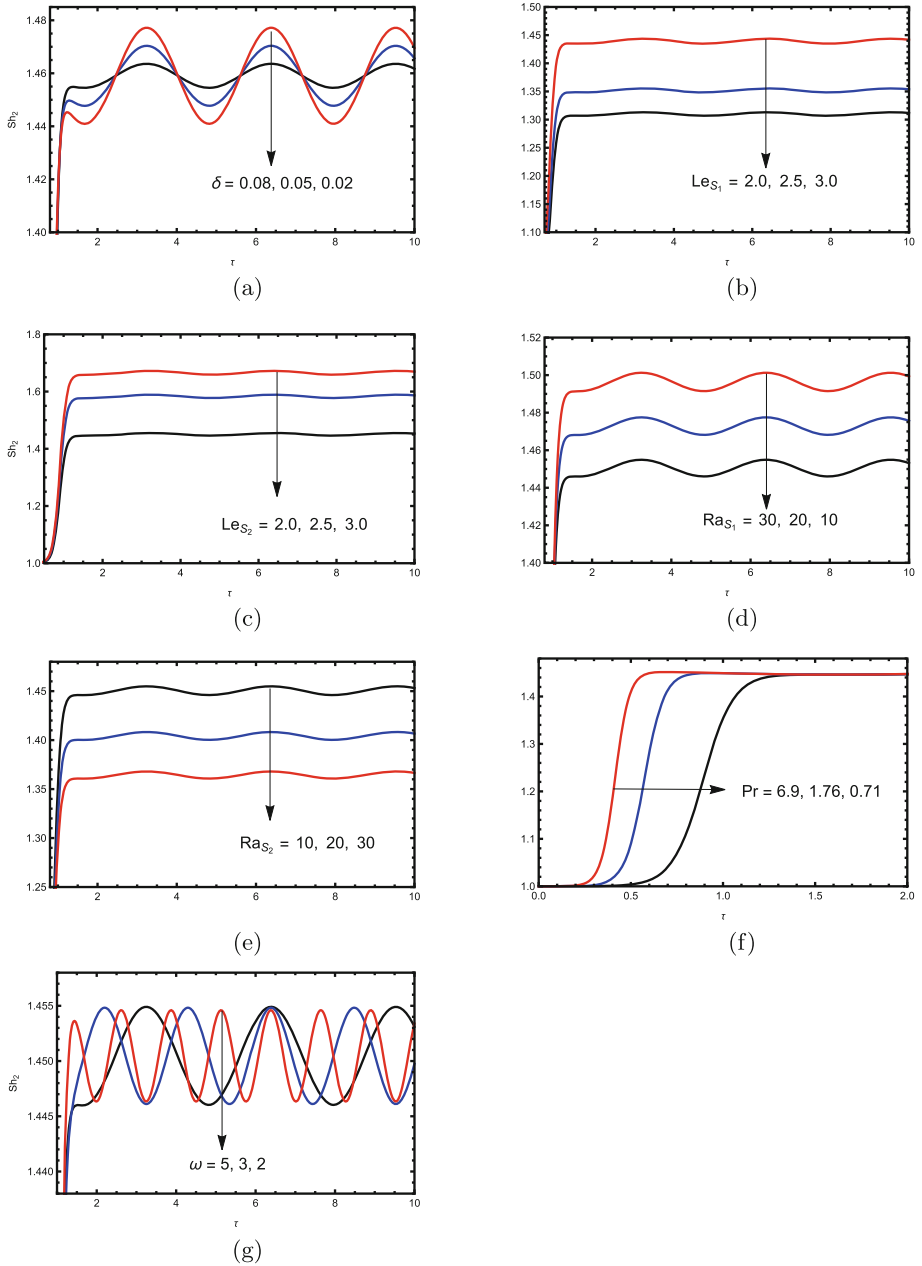


Fig. 10. MOLB: Sh_2 versus slow time for different values of (a) δ , (b) Le_{S_1} , (c) Le_{S_2} , (d) Ra_{S_1} , (e) Ra_{S_2} , (f) Pr , (g) ω

the value of Nu increases as the value of solute Rayleigh numbers Ra_{S_1} and Ra_{S_2} increase. The effect of Prandtl number Pr on Nu is displayed by Fig. 2(f). This figure shows that the magnitude of heat transport remains same as the value of Pr increases. Moreover, the heat transport taken place rapidly when we increase the value of Prandtl number. Figure 2(f) shows the effect of frequency of modulation on heat transport. Figure 2(f) reveals that frequency of modulation has negligible effect on Nu . Figure 3(a)–(f) and Figs. 4(a)–(f) are plotted to examine the behavior of mass transports for in phase modulation. We found a similar behavior of parameters on rate of mass transports Sh_1 and Sh_2 as we found for Nusselt number.

Out Phase Modulation (OPM)

Figure 5 is plotted to see the behavior of dimensionless parameters on rate of heat transport (Nu) for the case of out phase modulation. Figure 5(a) shows the effect of amplitude of modulation on Nu . This figure shows that the value of Nu increases as we increase the value of δ . Thus, the amplitude of modulation increases the heat transport. The effect of Lewis numbers Le_{S_1} and Le_{S_2} are displayed by Figs. 5(b)–(c). It is found that Le_{S_1} increases the rate of heat transport while an increase in the value of Le_{S_2} decreases the magnitude of Nu . It may happen because solute one is concentrated from lower boundary while solute two concentrated from upper boundary. Figures 5(d)–(e) exhibit the efficacy of solute Rayleigh numbers Ra_{S_1} and Ra_{S_2} on Nu . A similar trend has been observed as we found for Le_{S_1} and Le_{S_2} respectively. The effect of Pr is depicted by Fig. 5(f). From the figure, it is found that Pr has negligible effect on heat transport. In Fig. 5(g), the effect of ω on Nu is displayed. From the figure, it is found that increasing value of ω shorten the wavelength of oscillation. Figures 6 and 7 are plotted to depict the behavior of parameters on mass transports Sh_1 and Sh_2 in case of out phase modulation. From the Figs. 6 and 7, we found that behavior of parameters on rate of mass transports are similar as we found their effects on rate of heat transport.

Modulation of Lower Boundary (MOLB)

Figures 8, 9 and 10 are plotted to see the nature of parameters on rate of heat and mass transports when lower boundary in modulated. Figure 8(a) depicts the behavior of δ on Nu . It shows that an increment in the value of δ increases the value of Nu . The effect of parameters Le_{S_1} and Le_{S_2} on rate of heat and mass transports are same as we found for OPM. From the Figs. 8, 9 and 10, we found that the effect of various parameters on heat and mass transports are similar as we obtained for OPM.

8 Conclusion

The combined effect of third diffusing component and temperature modulation on Rayleigh-Bénard convection is presented through this article. A usual Cartesian coordinate system extended infinitely in x - direction is chosen for the study. The fluid layer is heated from below and salted from both the plates

$z = 0$ and $z = d$. The asymptotic expansion method is applied to obtain the Ginzburg-Landau equation. The triple diffusive convection plays significant role in material science, food processing, oil reservoirs, biological system and many others. The following are the finding of this study:

1. The Nusselt Number and Sherwood number are the directly proportional to the of Le_{S_1} and Ra_{S_1} means that Le_{S_1} and Ra_{S_1} increase the rate of heat and mass transports for all three cases.
2. The magnitude of Nusselt Number and Sherwood numbers decrease as the value of Le_{S_2} and Ra_{S_2} increases for all three cases.
3. Pr does not affect the magnitude of Nu , Sh_1 and Sh_2 but it plays a role to start the convection. The convection takes place more rapidly when we increase the value of Pr .
4. Frequency of modulation(ω) and amplitude of modulation (δ) both increase the rate of heat and mass transports.

For all three cases IPM, OPM and MOLB, we can summarize the above results as:

- $Nu/\delta=0.02 < Nu/\delta=0.05 < Nu/\delta=0.08$
- $Nu/Le_{S_1}=1.5 < Nu/Le_{S_1}=2 < Nu/Le_{S_1}=2.5$
- $Nu/Le_{S_2}=2 > Nu/Le_{S_2}=2.25 > Nu/Le_{S_2}=2.5$
- $Nu/Ra_{S_1}=10 < Nu/Ra_{S_1}=20 < Nu/Ra_{S_1}=30$
- $Nu/Ra_{S_2}=20 > Nu/Ra_{S_2}=30 > Nu/Ra_{S_2}=40$
- $Nu/\omega=1 < Nu/\omega=3 < Nu/\omega=5$ only for OPM and MOLB.
- $Nu^{IPM} < Nu^{MOLB} < Nu^{OPM}$ except for Le_{S_2} and Ra_{S_2}
- $Sh_1/\delta=0.02 < Sh_1/\delta=0.02 < Sh_1/\delta=0.02$
- $Sh_1/Le_{S_1}=1.5 < Sh_1/Le_{S_1}=2 < Sh_1/Le_{S_1}=2.5$
- $Sh_1/Ra_{S_1}=10 > Sh_1/Ra_{S_1}=20 > Sh_1/Ra_{S_1}=30$
- $Sh_1/Ra_{S_2}=20 < Sh_1/Ra_{S_2}=30 < Sh_1/Ra_{S_2}=40$
- $Sh_1/\omega=1 < Sh_1/\omega=1 < Sh_1/\omega=1$ only for OPM and MOLB.
- $Sh_1^{IPM} < Sh_1^{OPM} < Sh_1^{MOLB}$

The similar effect are found for Sh_2 except for the values of Le_{S_2} .

References

1. Chandrasekhar, S.: Hydrodynamic and Hydromagnetic Stability. Dover Publication, New York (1981)
2. Nield, D.A., Bejan, A.: Convection in Porous Media, 3rd edn. Springer, New York (2006)
3. Drazin, P.G., Reid, W.H.: Hydrodynamic Stability, 2nd edn. Cambridge University Press, Cambridge (2004)
4. Gershuni, G.Z., Zhukhovitskii, E.M., Jurkov, I.S.: On convective stability in the presence of periodically varying parameter. J. Appl. Math. Mech. **34**, 442–452 (1970)
5. Davis, S.H.: The stability of time-periodic flows. Annu. Rev. Fluid Mech. **8**, 57–74 (1976)

6. Mehta, J.M.: Analysis of double-diffusive convection with temperature modulations at the boundaries. *Int. J. Heat Fluid Flow* **13**, 160–167 (1992)
7. Gupta, V.K., Kumar, A., Singh, A.K.: Analytical study of weakly nonlinear mass transfer in rotating fluid layer under time-periodic concentration/gravity modulation. *Int. J. Non-Linear Mech.* **97**, 22–29 (2017)
8. Gupta, V.K.: Study of mass transport in rotating couple stress liquid under concentration modulation. *Chin. J. Phys.* **56**, 911–921 (2018)
9. Kumar, A., Hashim, I., Singh, A.K., Gupta, V.K., Saini, N.: Combined effect of internal heating and G-Jitter on Walter-B Viscoelastic fluid in highly permeable porous media. *J. Porous Med.* **24**(3), 21–33 (2021)
10. Kumar, A., Keshri, O.P., Gupta, V.K.: G-Jitter effect on mass transport in electrically conducting Newtonian fluid. *Chin. J. Phys.* **71**, 224–234 (2021)
11. Keshri, O.P., Kumar, A., Gupta, V.K.: Effect of internal heat Source on magneto-stationary convection of couple stress fluid under magnetic field modulation. *Chin. J. Phys.* **57**, 105–115 (2019)
12. Degens, E.T., et al.: Structure, chemistry and biology of an East African Rift lake. *Geol. Rundschau* **62**, 245–277 (1973)
13. Tracey, J.: Multi-component convection-diffusion in a porous medium. *Cont. Mech. Therm.* **8**, 316–381 (1996)
14. Rionero, S.: Triple diffusive convection in porous media. *Acta Mech.* **224**, 447–458 (2013)
15. Raghunatha, K.R., Shivakumara, I.S., Shankar, B.M.: Weakly nonlinear stability analysis of triple diffusive convection in a Maxwell fluid saturated porous layer. *Appl. Math. Mech.* **39**(2), 1–16 (2018). <https://doi.org/10.1007/s10483-018-2298-6>
16. Shivakumara, I.S., Kumar, S.B.: Linear and weakly nonlinear triple diffusive convection in a couple stress fluid layer. *Int. J. Heat Mass Trans.* **68**, 542–553 (2014)
17. Awasthi, M.K., Kumar, V., Patel, R.K.: Onset of triply diffusive convection in a Maxwell fluid saturated porous layer with internal heat source. *Ain Shams Eng. J.* **9**, 1591–1600 (2018)
18. Zhao, M., Wang, S., Zhang, Q.: Onset of triply diffusive convection in a Maxwell fluid saturated porous layer. *Appl. Math. Model.* **38**, 2345–2352 (2014)
19. Patil, P.M., Roy, M., Sashikant, A., Roy, S., Momoniat, E.: Triple diffusive mixed convection from an exponentially decreasing mainstream velocity. *Int. J. Heat Mass Transfer* **124**, 298–306 (2018)
20. Khan, Z.H., Khan, W.A., Sheremet, M.A.: Enhancement of heat and mass transfer rates through various porous cavities for triple convective-diffusive free convection. *Energy* **201**, 1177021–11770211 (2020)
21. Pearlstein, A.J., Harris, R.M., Terrones, G.: The onset of convective instability in a triply diffusive fluid layer. *J. Fluid Mech.* **202**, 443–465 (1989)
22. Straughan, B., Walker, D.W.: Multi component diffusion and penetrative convection. *Fluid Dyn. Res.* **19**, 77–89 (1997)
23. Landau, L.D.: On the problem of turbulence. *Dokl. Akad. Nauk SSSR* **44**(8), 339–349 (1944)
24. Dubey, V.P., Singh, J., Alshehri, A.M., Dubey, S., Kumar, D.: Numerical investigation of fractional model of Phytoplankton-Toxic Phytoplankton-Zooplankton system with convergence analysis. *Int. J. Biomath.* **15**(4), 2250006 (2022)
25. Dubey, V.P., Singh, J., Alshehri, A.M., Dubey, S., Kumar, D.: Forecasting the behavior of fractional order Bloch equations appearing in NMR flow via a hybrid computational technique. *Chaos Solitons Fract.* **164**, 112691 (2022)

26. Dubey, V.P., Kumar, D., Dubey, S.: A modified computational scheme and convergence analysis for fractional order hepatitis E virus model. In: *Advanced Numerical Methods for Differential Equations: Applications in Science and Engineering*, pp. 279-312. CRC Press, Taylor & Francis Group, Boca Raton (2021)
27. Dubey, V.P., Singh, J., Alshehri, A.M., Dubey, S., Kumar, D.: Analytical scheme with convergence analysis for computational study of local fractional Schrödinger equations. *Math. Comput. Simul.* **196**, 296–318 (2022)
28. Singh, H., Srivastava, H.M., Kumar, D.: A reliable algorithm for the approximate solution of the nonlinear Lane-Emden type equations arising in astrophysics. *Num. Methods for Partial Diff. Eq.* **34**(5), 1524–1555 (2018)
29. Singh, H.: Chebyshev spectral method for solving a class of local and non local elliptic boundary value problems. *Int. J. Non-linear Sci. Num. Sim.* (2021)
30. Singh, H., Wazwaz, A.-M.: Computational method for reaction diffusion-model arising in a spherical catalyst. *Int. J. Appl. Comput. Math.* **7**(3), 1–11 (2021). <https://doi.org/10.1007/s40819-021-00993-9>



Approximate Numerical Solution of the Nonlinear Klein-Gordon Equation with Caputo-Fabrizio Fractional Operator

Ajay Kumar¹, Haci Mehmet Baskonus², and Amit Prakash³✉

¹ Department of Mathematics, Bakhtiyarpur College of Engineering, Champapur, Dedaur, Bakhtiyarpur 803212, India

² Department of Mathematics and Science Education, Faculty of Education, Harran University, Sanliurfa, Turkey

³ Department of Mathematics, National Institute of Technology, Kurukshetra 136119, India
amitmath0185@gmail.com

Abstract. This work analyze the linear and nonlinear fractional Klein-Gordon equation using fractional homotopy perturbation transform method (FHPTM) via Caputo-Fabrizio derivative. The proposed technique is used to solve fractional model without any restrictive assumptions. The acquired results ratify that the proposed method is acceptable and credible for approximate analytic treatment of the extensive types of nonlinear physical processes.

Keywords: FHPTM · Fractional Klein-Gordon equation (FKGE) · Caputo-Fabrizio (CF) derivative · Laplace transform (LT) · Approximate solution

2010 AMS Subject Classification: 44A99 · 35Q99

1 Introduction

Nonlinear fractional differential equation (NFDEs), which is one of the emerging area that can be classified as an applied model, for example, physics, computational fluid dynamic, chemical science, natural science, optics, plasma physics etc. The difficulty to search exact solution for the NFDEs has led researchers to explore the approximate and numerical methods to find the solution of these systems [1–7]. There are various numerical methods like projective Riccati equation method [8], HPTM is used to solve the NFDEs [9], Collocation method [10], reduced differential transform method [11], Laplace transform method [12], q-homotopy analysis Sumudu transform technique [13–16], Sine-Gordon expansion method [17, 18], Caputo-Fabrizio fractional derivative [19, 20, 25], Homotopy perturbation technique [21–23], Atangana-Baleanu fractional derivative [24], FVIM [26], and many others [27–54].

The aim of this paper is to analyze the nonlinear fractional KGE with CF derivative by FHPTM. Let us assume the fractional KGE [27, 30] as:

$$h_{tt}(x, t) - h_{xx}(x, t) + ah(x, t) = r(x, t), \quad (1)$$

having initial conditions

$$h(x, 0) = f(x), \text{ and } h_t(x, 0) = g(x). \tag{2}$$

where a is real constant, $h(x, t)$ is a complex valued function, t is a time variable and x is a space variable. The fractional KGE appear in physics. The KGE is solved by modified Adomian decomposition method by Yokchoo et al. (2020) [27] and HATM by Kumar et al. (2014) [30].

The present manuscript is organized as follows: Some definitions are given in Sect. 2, in Sect. 3 general description of FHPTM using CF derivative is discussed, in Sect. 4 test example is presented and in Sect. 5, we conclude our work.

2 Basic Tools

In this section, we present some fundamental notion of fractional calculus and Laplace transform, which are essential in the present framework.

Definition 2.1. The Caputo fractional derivative of order $\alpha \geq 0$ and $n \in N \cup \{0\}$ is define as:

$${}_0^{CF}D_t^\alpha h(t) = \frac{1}{\Gamma(n - \alpha)} \int_0^t (t - \xi)^{(n-\alpha-1)} \frac{d^n}{dt^n} h(\xi) d\xi, \tag{3}$$

where $n - 1 \leq \alpha < n$.

Definition 2.2. Let $h \in K^1(a, b)$, $b > a$, then the Caputo-Fabrizio fractional differential operator is defined as:

$${}_0^{CF}D_t^\alpha h(t) = \frac{M(\alpha)}{(1 - \alpha)} \int_a^t \exp\left[-\frac{\alpha(1 - \xi)}{1 - \alpha}\right] h'(\xi) d\xi, t \geq 0, 0 < \alpha < 1, \tag{4}$$

where $M(\alpha)$ is a normalisation function which satisfies $M(0) = M(1) = 1$.

${}_0^{CF}D_t^\alpha h(t) = 0$, if h is a constant function.

Definition 2.3. The CF integral of order $0 < \alpha < 1$ is given by

$${}_0^{CF}I_t^\alpha h(t) = \frac{2(1 - \alpha)}{(2 - \alpha)M(\alpha)} u(t) + \frac{2\alpha}{(2 - \alpha)M(\alpha)} \int_0^t h(\xi) d\xi, t \geq 0, \tag{5}$$

Definition 2.4. The Laplace transform (LT) for the CF fractional operator of order $0 < \alpha \leq 1$ for $m \in N$ is given as:

$$\begin{aligned} L\left[{}_0^{CF}D_t^{(m+\alpha)} h(t)\right](s) &= \frac{1}{1 - \alpha} L\left[h^{(m+1)}(t)\right] L\left[\exp\left(\frac{-\alpha}{(1 - \alpha)} t\right)\right] \\ &= \frac{s^{(m+1)} L[h(t)] - s^m h(0) - s^{(m-1)} h'(0) \dots \dots \dots - h^{(m)}(0)}{s + \alpha(1 - s)}. \end{aligned} \tag{6}$$

In particular, we have

$$\begin{aligned} L\left({}_0^{CF}D_t^\alpha h(t)\right)(s) &= \frac{sL(h(t)) - h(0)}{s + \alpha(1 - s)}, \quad m = 0, \\ L\left({}_0^{CF}D_t^{\alpha+1} h(t)\right)(s) &= \frac{s^2 h(f(t)) - sh(0) - h'(0)}{s + \alpha(1 - s)}, \quad m = 1. \end{aligned}$$

3 General Description of FHPTM Using CF Operator

We have considered the following nonlinear partial differential equation in the CF sense as:

$${}_0^{CF}D_t^{(m+\alpha)}h(x, t) + \rho h(x, t) + \sigma h(x, t) = k(x, t), n - 1 < \alpha + m \leq n, \tag{7}$$

with initial conditions:

$$\frac{\partial^j h(x,0)}{\partial t^j} = f_j(k), j = 0, 1, 2, \dots, m - 1. \tag{8}$$

Applying the LT on both Eq. (7) and Eq. (8), we get

$$L[h(x, t)] = \eta(x, s) - \left(\frac{s + \alpha(1 - s)}{s^{(m+1)}} \right) L[\rho h(x, t) + \sigma h(x, t)], \tag{9}$$

where

$$\eta(x, s) = \frac{1}{s^{(m+1)}} \left[s^m f_0(x) + s^{m-1} f_1(x) + \dots + f_m(x) \right] + \frac{s + \alpha(1 - s)}{s^{(m+1)}} \tilde{h}(x, s). \tag{10}$$

Taking the inverse LT the Eq. (9) yields

$$h(x, t) = \eta(x, s) - L^{-1} \left[\left(\frac{s + \alpha(1 - s)}{s^{(m+1)}} \right) L[\rho h(x, t) + \sigma h(x, t)] \right]. \tag{11}$$

where $\eta(x, s)$ arises from the source term.

Now, we apply the FHPTM to obtain the solution of Eq. (11) starting by the hypothesis that $h(x, t)$ expressed below is a solution of this equation.

$$h(x, t) = \sum_{n=0}^{\infty} z^n h_n(x, t), \tag{12}$$

where, $h_n(x, t)$ are known functions, the nonlinear term can be decomposed as:

$$\sigma h(x, t) = \sum_{n=0}^{\infty} z^n H_n(x, t). \tag{13}$$

The polynomials $H_m(x, t)$ [28] are

$$H_n(h_0, h_1, h_2, \dots, h_m) = \frac{1}{m!} \frac{\partial^m}{\partial p^m} \left[\sigma \left(\sum_{i=0}^{\infty} z^i h_i \right) \right]_{z=0}, m = 0, 1, 2, \dots \tag{14}$$

Substituting Eq. (12) and Eq. (13) into (11), we get

$$\sum_{n=0}^{\infty} z^n h_n(x, t) = \eta(x, s) - zL^{-1} \left[\left(\frac{s + \alpha(1 - s)}{s^{(m+1)}} \right) L \left[\rho \sum_{m=0}^{\infty} z^m h_m(x, t) + \sigma \sum_{m=0}^{\infty} z^m H_m \right] \right], \tag{15}$$

comparing the coefficients of z^0 , z^1 , z^2 , and z^3 , we get

$$\begin{aligned}
 z^0 : h_0(x, t) &= \eta(x, s), \\
 z^1 : h_1(x, t) &= -L^{-1} \left[\left(\frac{s + \alpha(1-s)}{s^{(m+1)}} \right) L[\rho h_0(x, t) + H_0(u)] \right], \\
 z^2 : h_2(x, t) &= -L^{-1} \left[\left(\frac{s + \alpha(1-s)}{s^{(m+1)}} \right) L[\rho h_1(x, t) + H_1(u)] \right], \\
 z^3 : h_3(x, t) &= -L^{-1} \left[\left(\frac{s + \alpha(1-s)}{s^{(m+1)}} \right) L[\rho h_2(x, t) + H_2(u)] \right], \\
 z^{m+1} : h_{m+1}(x, t) &= -L^{-1} \left[\left(\frac{s + \alpha(1-s)}{s^{(m+1)}} \right) L[\rho h_{m+1}(x, t) + H_{m+1}(u)] \right].
 \end{aligned}
 \tag{16}$$

4 Applications

In this segment, four different examples are solved by FHPTM.

Example 4.1. Let us assume the linear fractional KGE as [27, 30]:

$$D_t^\alpha h(x, t) - h_{xx}(x, t) + h(x, t) = 0,
 \tag{17}$$

having initial conditions

$$h(x, 0) = f(x), \quad h_t(x, 0) = g(x).
 \tag{18}$$

Taking the LT on Eq. (17) both sides and from Eq. (18), we get

$$L[h(x, t)] = \frac{1}{s^2} x + \left(\frac{s + \alpha(1-s)}{s^2} \right) L[h_{xx} + h].
 \tag{19}$$

Applying the inverse of the LT to Eq. (19), we get

$$h(x, t) = xt + L^{-1} \left[\left(\frac{s + \alpha(1-s)}{s^2} \right) L[h_{xx} + h] \right].
 \tag{20}$$

Now, we apply the HPTM, we have

$$\sum_{m=0}^{\infty} h_m(x, t) = xt + zL^{-1} \left[\left(\frac{s + \alpha(1-s)}{s^2} \right) L \left[\sum_{m=0}^{\infty} z^m h_m(x, t) - \sum_{m=0}^{\infty} z^m h_m(x, t) \right] \right], \tag{21}$$

$$z^0 : h_0(x, t) = xt,$$

$$z^1 : h_1(x, t) = xt \left[t(1 - \alpha) + \frac{t^2 \alpha}{2} \right], \tag{22}$$

$$z^2 : h_2(x, t) = xt \left[\frac{t^2}{2} (1 - 2\alpha + \alpha^2) - \frac{t^3}{3} (-\alpha + \alpha^2) + \frac{t^4 \alpha}{24} \right].$$

Example 4.2. Let us assume the linear fractional KGE as [27, 30]:

$$D_{tt}^\alpha h(x, t) - h_{xx}(x, t) + h(x, t) = 2 \sin x, \tag{23}$$

having initial conditions

$$h(x, 0) = \sin x, \quad \text{and} \quad h_t(x, 0) = 1. \tag{24}$$

Taking the LT on Eq. (22) both sides and from Eq. (23), we have

$$L[h(x, t)] = \frac{1}{s^2} \sin x + \frac{1}{s^2} + \frac{s + \alpha(1-s)}{s^2} 2 \sin x + \left(\frac{s + \alpha(1-s)}{s^2} \right) L[h_{xx} - h]. \tag{25}$$

Applying inverse LT to Eq. (24), we get

$$h(x, t) = 2t \sin x - 2t\alpha \sin x + t^2 \alpha \sin x + t + L^{-1} \left[\left(\frac{s + \alpha(1-s)}{s^2} \right) L[h_{xx} - h] \right]. \tag{26}$$

Now, we apply the HPTM, we have

$$\sum_{m=0}^{\infty} h_m(x, t) = 2t \sin x - 2t\alpha \sin x + t^2 \alpha \sin x + t + zL^{-1} \left[\left(\frac{s + \alpha(1-s)}{s^2} \right) L \left[\sum_{n=0}^{\infty} z^n h_m(x, t) - \sum_{n=0}^{\infty} z^n h_n(x, t) \right] \right], \tag{27}$$

$$z^0 : h_0(x, t) = 2t \sin x - 2t\alpha \sin x + t^2 \alpha \sin x + t,$$

$$z^1 : h_1(x, t) = \frac{t^2}{2} (-1 + \alpha - 4 \sin x + 8\alpha \sin x - 4\alpha^2 \sin x)$$

$$+ \frac{t^3}{2} (-\alpha - 8\alpha \sin x + 8\alpha^2 \sin x) - \frac{t^2 \alpha^2}{6} \sin x,$$

$$z^2 : h_2(x, t) = \frac{t^3}{6} (-1 + 2\alpha + \alpha^2 + 8 \sin x - 24\alpha \sin x + 24\alpha^2 \sin x - 8\alpha^3 \sin x)$$

$$+ \frac{t^4}{12} (\alpha - \alpha^2 + 12\alpha \sin x + 8\alpha^2 \sin x)$$

$$+ \frac{t^5}{120} (\alpha^2 + 24\alpha^2 \sin x - 24\alpha^3 \sin x) - \frac{t^6 \alpha^3}{90} \sin x.$$

(28)

Example 4.3. Let us assume the linear fractional KGE as [27, 30]:

$$D_t^\alpha h(x, t) - h_{xx}(x, t) + h^2(x, t) = x^2 t^2, \tag{29}$$

having initial conditions

$$h(x, 0) = 0, \text{ and } h_t(x, 0) = x. \tag{30}$$

Taking the LT on Eq. (29) both sides and from Eq. (30), we have

$$L[h(x, t)] = \frac{1}{s^2}x + \frac{s + \alpha(1 - s)}{s^2} \left(\frac{2x^2}{s^3} \right) + \left(\frac{s + \alpha(1 - s)}{s^2} \right) L[h_{xx} - h^2]. \tag{31}$$

Applying the inverse of the LT to Eq. (31), we have

$$h(x, t) = xt + 2x^2 \left[\frac{1}{6}t^3(1 - \alpha) + \frac{t^4\alpha}{24} \right] + L^{-1} \left[\left(\frac{s + \alpha(1 - s)}{s^2} \right) L[h_{xx} - h^2] \right]. \tag{32}$$

Now, we apply the HPTM, we have

$$\begin{aligned} \sum_{m=0}^\infty h_m(x, t) &= xt + 2x^2 \left[\frac{1}{6}t^3(1 - \alpha) + \frac{t^4\alpha}{24} \right] \\ &+ zL^{-1} \left[\left(\frac{s + \alpha(1 - s)}{s^2} \right) L \left[\sum_{m=0}^\infty z^m h_m(x, t) - \sum_{m=0}^\infty z^m H_m(x, t) \right] \right]. \end{aligned} \tag{33}$$

where $H_m(h)$ is the He's polynomial used to decomposed the nonlinear term is defined as:

$$\begin{aligned} H_0(h) &= h_0^2, \\ H_1(h) &= \frac{\partial}{\partial z} \left[(h_0 + zh_1)^2 \right]_{z=0} = 2h_0h_1. \end{aligned} \tag{34}$$

Comparing the coefficient of z in Eq. (33), we get

$$\begin{aligned} z^0 : h_0(x, t) &= xt + \frac{x^2 t^2}{3}(1 - \alpha) + \frac{t^4 \alpha x^2}{12}, \\ z^1 : h_1(x, t) &= \frac{t^3}{3}(-x^2 + x^4 \alpha) - \frac{t^4}{12}(-2 + 4\alpha^2 x^2 - 2\alpha^2) \\ &- \frac{t^5}{15}(2x^3 - \alpha - 4x^3 \alpha + \alpha^2 + 2x^3 \alpha^2) + \frac{t^6}{180}(-9x^3 \alpha + \alpha^2 + 9x^3 \alpha^2) \\ &+ \frac{t^7}{252}(-4x^2 + 12x^4 \alpha - x^3 \alpha^2 - 12x^4 \alpha^2 + 4x^2 \alpha^3) \\ &- \frac{t^8}{112}(x^4 \alpha - 2x^4 \alpha^2 + x^4 \alpha^3) + \frac{t^9}{648}(-x^4 \alpha^2 + x^4 \alpha^3) - \frac{x^4 \alpha^3 t^{10}}{12960}, \\ z^2 : h_2(x, t) &= \frac{t^4}{16}(-1 + 2\alpha + \alpha^2) + \frac{t^5}{15}(2x^3 - \alpha - 4x^3 \alpha + \alpha^2 + 2x^3 \alpha^2) \\ &- \frac{t^6}{180}(34x - 102x\alpha - 9x^3 \alpha + \alpha^2 + 102x\alpha^2 + 9x^3 \alpha^2 - 34x\alpha^3) \\ &- \frac{t^7}{1260}(-88x^4 + 112x\alpha + 264x^4 \alpha - 224x\alpha^2 - 5x^3 \alpha^2 - 264x^4 \alpha^2 + 112x\alpha^3 + 88x^4 \alpha^3) + \dots \end{aligned} \tag{35}$$

Example 4.4. Let us assume the linear fractional KGE as [27, 30]:

$$D_t^\alpha h(x, t) - h_{xx}(x, t) + h^2(x, t) = 2x^2 - 2t^2 + x^4 t^4, \tag{36}$$

having initial conditions

$$h(x, 0) = 0, \text{ and } h_t(x, 0) = 0. \tag{37}$$

Taking the LT on Eq. (36) both sides and from Eq. (37), we have

$$L[h(x, t)] = \frac{s + \alpha(1 - s)}{s^2} \left(\frac{-4}{s^3} + \frac{2x^2}{s} + \frac{2x^4}{s^3} \right) + \left(\frac{s + \alpha(1 - s)}{s^2} \right) L[h_{xx} - h^2]. \tag{38}$$

Applying the inverse of the LT to Eq. (38), we have

$$h(x, t) = t^2 x^2 \alpha - 2t(-x^2 + x^2 \alpha) + \frac{t^4}{12}(-2\alpha + x^4 \alpha) - \frac{t^3}{3}(2 - x^4 - 2\alpha + x^4 \alpha) + L^{-1} \left[\left(\frac{s + \alpha(1 - s)}{s^2} \right) L[h_{xx} - h^2] \right]. \tag{39}$$

Now, we apply the HPTM, we have

$$\sum_{m=0}^\infty h_m(x, t) = t^2 x^2 \alpha - 2t(-x^2 + x^2 \alpha) + \frac{t^4}{12}(-2\alpha + x^4 \alpha) - \frac{t^3}{3}(2 - x^4 - 2\alpha + x^4 \alpha) + z L^{-1} \left[\left(\frac{s + \alpha(1 - s)}{s^2} \right) L \left[\sum_{m=0}^\infty z^m h_m(x, t) - \sum_{m=0}^\infty z^m H_m(x, t) \right] \right]. \tag{40}$$

where $H_m(h)$ is the He’s polynomial used to decomposed the nonlinear term is defined as:

$$H_0(h) = h_0^2, \\ H_1(h) = \frac{\partial}{\partial z} \left[(h_0 + z h_1)^2 \right]_{z=0} = 2h_0 h_1. \tag{41}$$

Comparing the coefficient of z in Eq. (40), we get

$$\begin{aligned}
z^0 : h_0(x, t) &= t^2 x^2 \alpha - 2t(-x^2 + x^2 \alpha) + \frac{t^4}{12}(-2\alpha + x^4 \alpha) \\
&\quad - \frac{t^3}{3}(2 - x^4 - 2\alpha + x^4 \alpha), \\
z^1 : h_1(x, t) &= 2t^2(1 - 2\alpha + \alpha^2) + \frac{4t^3}{3}(-x^4 + \alpha + 3x^4 \alpha - \alpha^2 - 3x^4 \alpha^2 + x^4 \alpha^3) \\
&\quad - \frac{2t^5}{15}(4x^2 - 2x^6 - 9x^2 \alpha + 6x^6 \alpha + 9x^2 \alpha^2 - 3x^4 \alpha^2 - 6x^6 \alpha^2 - 4x^2 \alpha^3 \\
&\quad + 3x^4 \alpha^3 + 2x^6 \alpha^3) \\
&\quad - \frac{t^6}{90}(-38x^2 \alpha + 19x^6 \alpha + 73x^2 \alpha^2 - 38x^6 \alpha^2 + 3x^4 \alpha^3 + 19x^6 \alpha^3) \\
&\quad + \frac{t^7}{63}(-4 + 4x^4 - x^8 + 12\alpha - 12x^4 \alpha + 3x^8 \alpha - 12\alpha^2 + 6x^2 \alpha^2 + 12x^4 \alpha^2 \\
&\quad - 3x^6 \alpha^2 - 3x^8 \alpha^2 + 4\alpha^3 - \dots) \\
&\quad - \frac{t^8}{648}(12\alpha - 12x^4 \alpha + 3x^8 \alpha - 24\alpha^2 + 24x^4 \alpha^2 - 6x^8 \alpha^2 + 12\alpha^3 - 2x^2 \alpha^3 \\
&\quad - 12x^4 \alpha^3 + x^6 \alpha^3 + 3x^8 \alpha^3) \\
&\quad + \frac{t^9}{648}(-4\alpha^2 + 4x^4 \alpha^2 - x^8 \alpha^2 + 4\alpha^3 - 4x^4 \alpha^3 + x^8 \alpha^3) \\
&\quad - \frac{t^{10}}{12960}(4\alpha^3 - 4x^4 \alpha^3 + x^8 \alpha^3), \\
z^2 : h_2(x, t) &= -6t^4(x^4 - 4x^2 \alpha + 6x^2 \alpha^2 - 4x^2 \alpha^3 + x^2 \alpha^4) - \frac{2t^5}{15}(-3 - 8x^6 + 9\alpha \\
&\quad + 47x^2 \alpha + 40x^6 \alpha - 9\alpha^2 - 141x^2 \alpha^2 - 80x^6 \alpha^2 + 3\alpha^2 + 141x^2 \alpha^3 + 80x^6 \alpha^3 - \dots) \\
&\quad + \frac{t^6}{45}(28 - 100x^4 - 103\alpha + 400x^4 \alpha + 68x^6 \alpha + 150\alpha^2 - 99x^2 \alpha^2 - 600x^4 \alpha^2 - 272x^6 \alpha^2 - 103\alpha^3 + \dots) \\
&\quad - \frac{t^7}{315}(176x^4 - 88x^8 - 176\alpha - 2778x^4 \alpha + 440x^8 \alpha + 519\alpha^2 \\
&\quad - 46x^4 \alpha^2 - 252x^6 \alpha^2 - 880x^8 \alpha^2 - \dots) + \dots
\end{aligned} \tag{42}$$

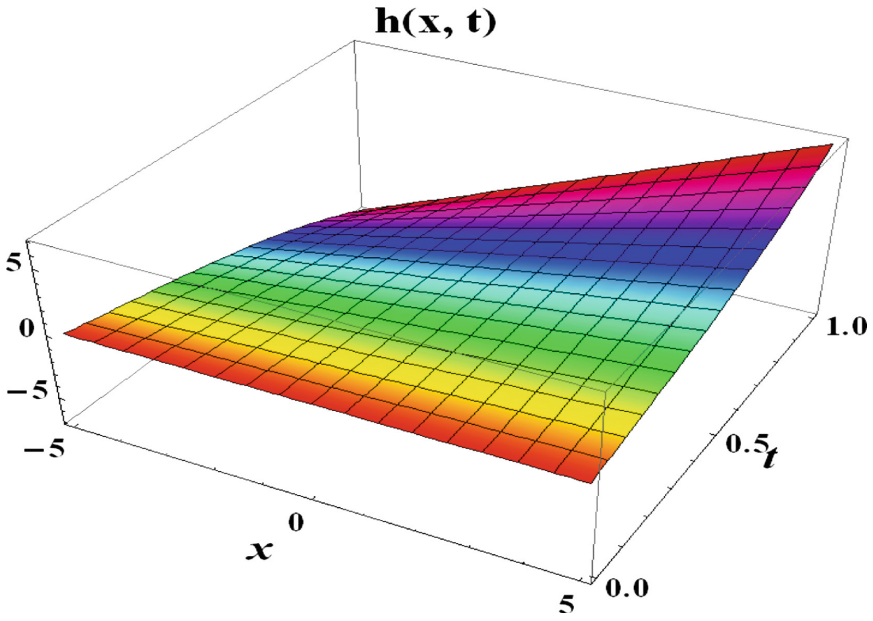


Fig. 1. FHPTM solution $h(x, t)$ at $\alpha = 2$ for Ex.4.1.

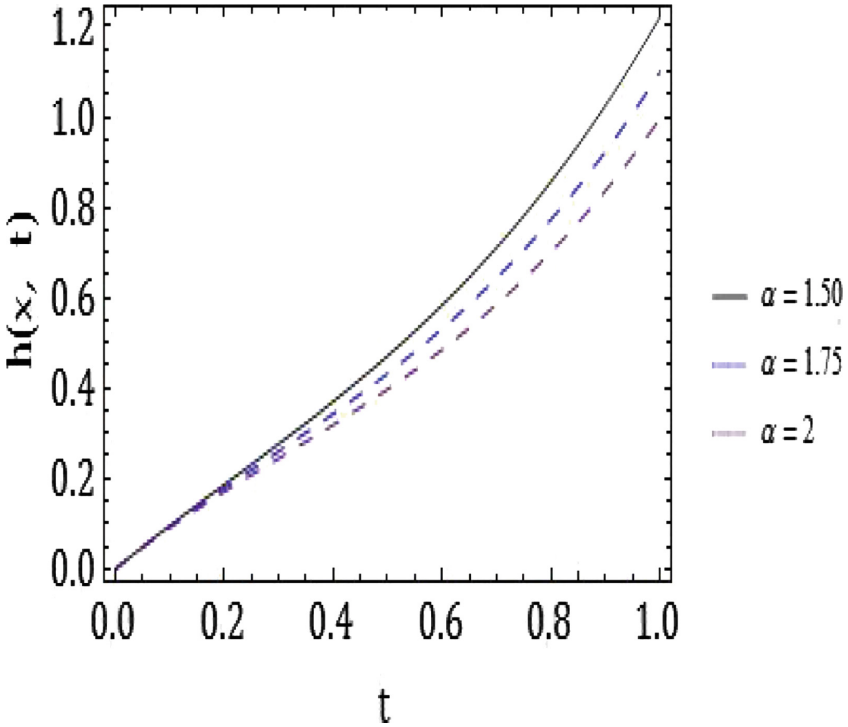


Fig. 2. FHPTM solution $h(x, t)$ for different values of $\alpha = 1.50, 1.75, 2$ for Ex.4.1.

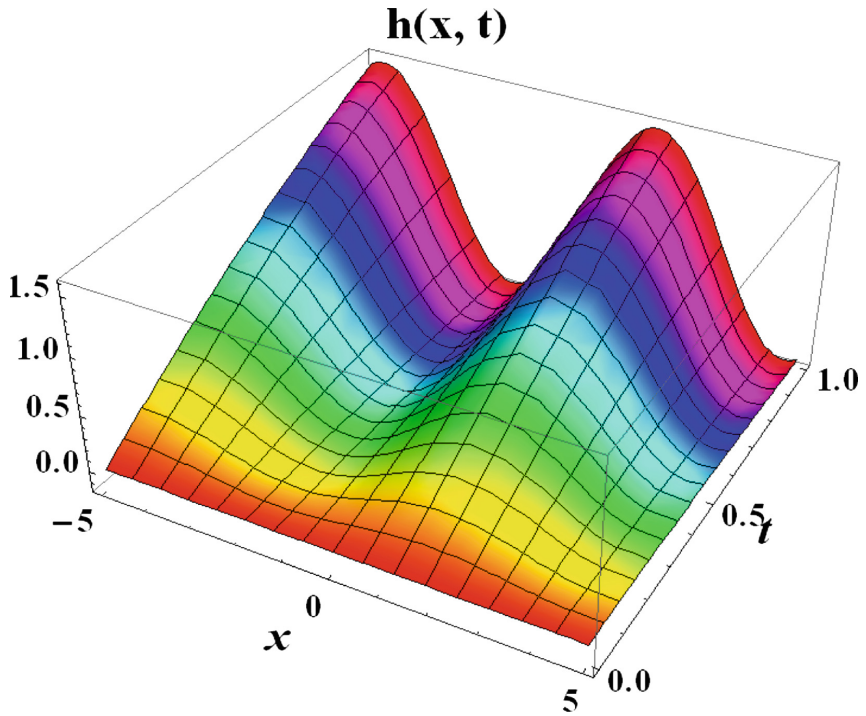


Fig. 3. FHPTM solution $h(x,t)$ at $\alpha = 2$ for Ex.4.2.

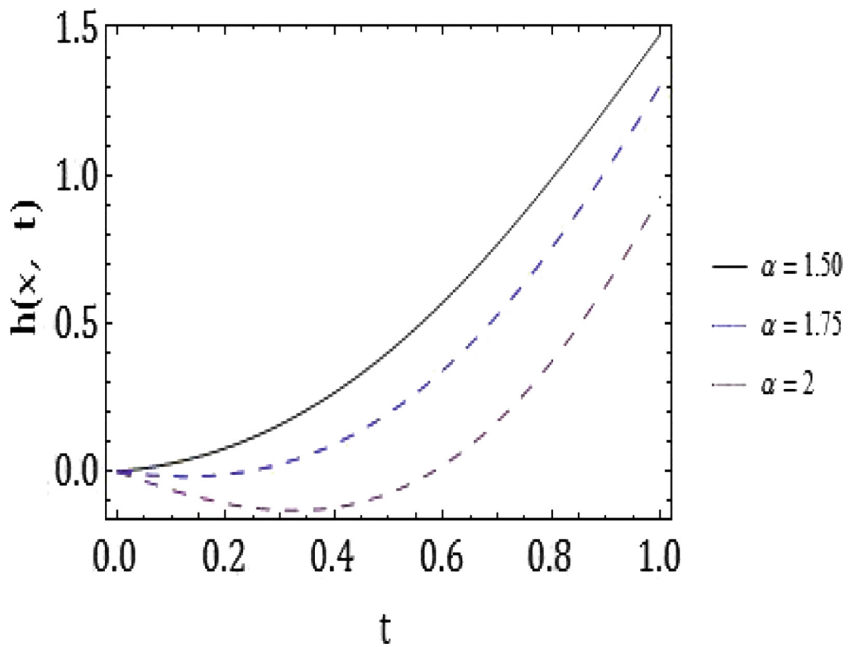


Fig. 4. FHPTM solution $h(x,t)$ for distinct values of $\alpha = 1.50, 1.75, 2$ for Ex.4.2.

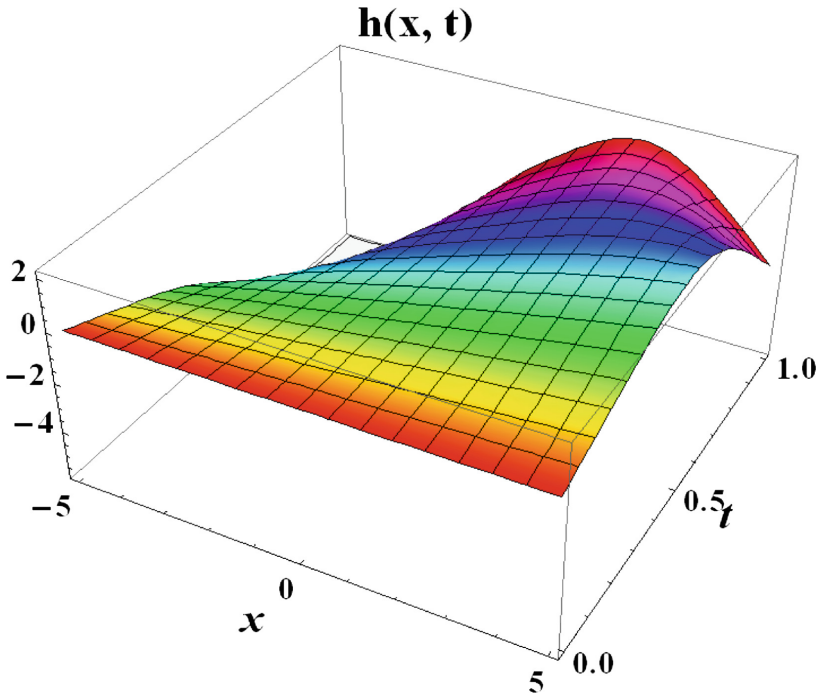


Fig. 5. FHPTM solution $h(x,t)$ at $\alpha = 2$ for Ex.4.3.

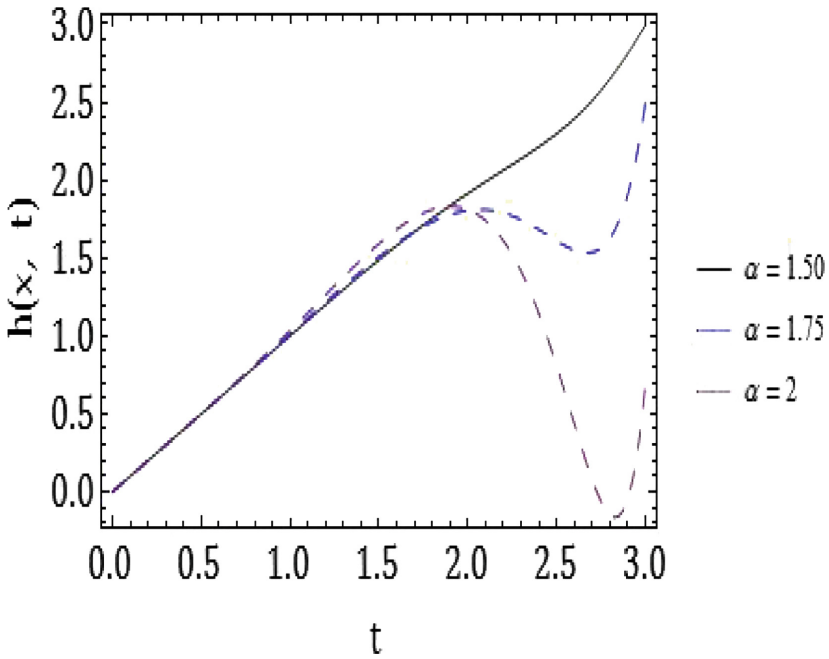


Fig. 6. FHPTM solution $h(x,t)$ for distinct values of $\alpha = 1.50, 1.75, 2$ for Ex.4.3.

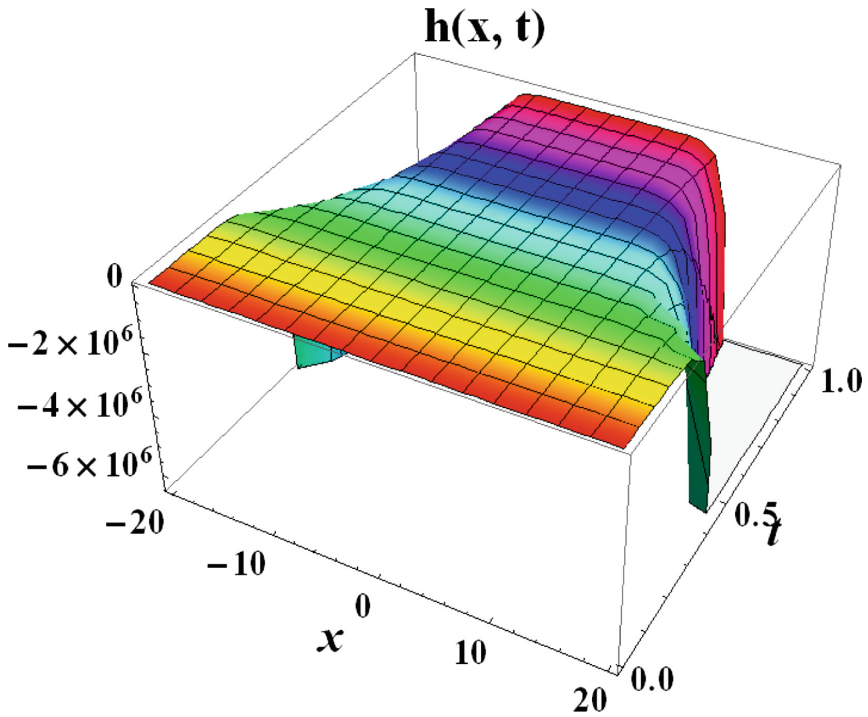


Fig. 7. FHPTM solution $h(x,t)$ at $\alpha = 2$ for Ex.4.4.

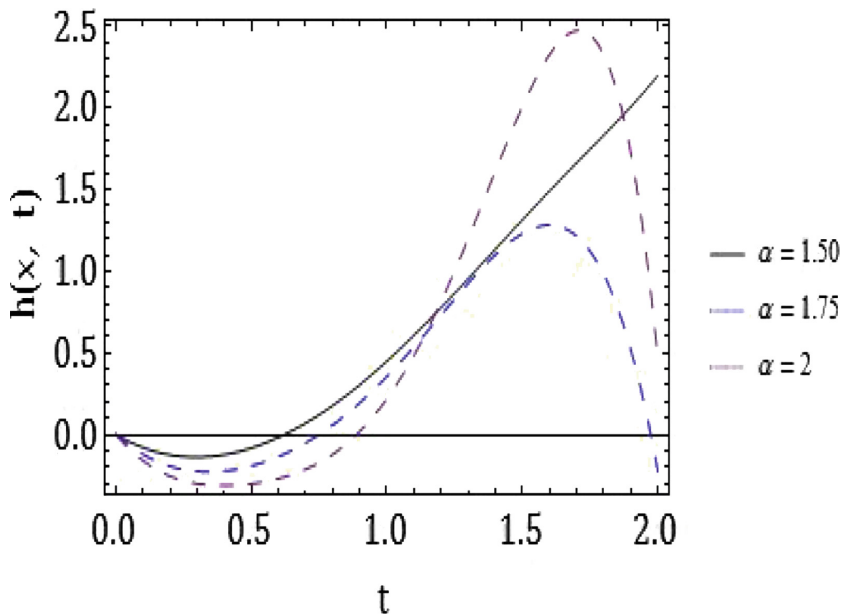


Fig. 8. FHPTM solution $h(x,t)$ for distinct values of $\alpha = 1.50, 1.75, 2$ for Ex.4.4.

5 Conclusion

In this present work, the FHPTM is applied on the fractional linear and nonlinear KGE via CF derivative (Figs. 1, 2, 3, 4, 5, 6, 7 and 8). We note that the approximate series solutions acquired for the first three terms is very suitable and converges very strongly with solutions to real physical problems. The above method is reliable, simple and dominant in seeking approximate solution to different nonlinear Klein-Gordon fractional order equation. Finally, we can draw the conclusion that the proposed FHPTM is highly expressive and can be used to analyze broad class of the fractional order linear and nonlinear models to perceive the behavior of the phenomena that emerged in linked sciences and engineering areas.

References

1. Golshan, A.N., Nourazar, S.S., G-Fard, H.A., Yildirim, A., Campo, A.: A modified homotopy perturbation method coupled with the Fourier transform for nonlinear and singular Lane-Emden equations. *Appl. Math. Lett.* **26**(10), 1018–1025 (2013)
2. Prakash, A., Verma, V.: Numerical solution of nonlinear fractional Zakharov-Kuznetsov equation arising in ion-acoustic waves. *Pram. J. Phy.* **93**(66), 1–19 (2019)
3. Prakash, A., Kumar, M.: Numerical solution of time-fractional order Fokker-Planck equation. *TWMSJ. App. Eng. Math.* **9**(3), 446–454 (2019)
4. Prakash, A.: Analytical method for space-fractional telegraph equation by Homotopy perturbation transform method. *Nonlinear Eng. Model. Appl.* **5**(2), 123–128 (2016)
5. Prakash, A., Kaur, H.: q-homotopy analysis transform method for space and time-fractional KdV- Burgers equation. *Nonlinear Sci. Lett. A.* **9**(1), 44–61 (2018)
6. Rahul, P.A.: Numerical simulation of SIR childhood diseases model with fractional Adams–Bashforth method. *Math. Method Appl. Sci.* 1–21 (2022). <https://doi.org/10.1002/mma.8785>
7. Prakash, A.R.: Analysis and numerical simulation of fractional biological population model with singular and non-singular kernels. *Proc. Inst. Math. Mech.* **48**, 178–193 (2022). <https://doi.org/10.30546/2409-4994.48.2022.178193>
8. Rezazadeh, H., Korkmaz, A., Eslami, M., Vahidi, J., Asghari, R.: Traveling wave solution of conformable fractional generalized reaction Duffing model by generalized projective Riccati equation method. *Opt. Quant. Electron.* **50**(3), 1–13 (2018). <https://doi.org/10.1007/s11082-018-1416-1>
9. Jleli, M., Kumar, S., Kumar, R., Samet, B.: Analytical approach for time fractional wave equations in the sense of Yang-Abdel-Aty-Cattani via the homotopy Perturbation transform method. *Alex. Eng. J.* **59**(5), 2859–2863 (2020)
10. Prakash, A., Veerasha, P., Prakasha, D.G., Goyal, M.: A homotopy technique for a fractional order multi-dimensional telegraph equation via the Laplace transform. *Eur. Phys. J. Plus* **134**(1), 1–18 (2019). <https://doi.org/10.1140/epjp/i2019-12411-y>
11. Gupta, P.K.: Approximate analytical solutions of fractional Benney-Lin equation by reduced differential transform method and the homotopy perturbation method. *Comput. Math. Appl.* **61**(9), 2829–2842 (2011)
12. Abbasbandy, S.: Application of He’s homotopy perturbation method for Laplace transform. *Chaos Solit. Fract.* **30**, 1206–1212 (2006)
13. Prakash, A., Goyal, M., Baskonus, H.M., Gupta, S.: A reliable hybrid numerical method for a timedependent vibration model of arbitrary order. *AIMS. Math.* **5**(2), 979–1000 (2020)

14. Goyal, M., Baskonus, H.M., Prakash, A.: Regarding new positive, bounded and convergent numerical solution of nonlinear time fractional HIV/AIDS transmission model. *Chaos. Solit. Fract.* **139**, 1–12 (2020)
15. Baskonus, H.M., Kumar, A., Gao, W.: Deeper investigations of the (4+1)-dimensional Fokas and (2+1)-dimensional Breaking soliton equations. *Int. J. Mod. Phys. B* **34**(17), 1–16 (2020)
16. Guirao, J.L.G., Baskonus, H.M., Kumar, A., Rawat, M.S., Yel, G.: Complex patterns to the (3+1)-dimensional B-type Kadomtsev-Petviashvili-Boussinesq equation. *Symmetry* **12**(1), 1–10 (2020)
17. Guirao, J.L.G., Baskonus, H.M., Kumar, A., Causanilles, F.S.V., Bermudez, G.R.: Complex mixed dark bright wave patterns to the modified α and modified Vakhnenko-Parkes equations. *Alex. Eng. J.* **59**(4), 2149–2160 (2020)
18. Guirao, J.L.G., Baskonus, H.M., Kumar, A.: Regarding new wave patterns of the newly extended nonlinear (2+1)-dimensional Boussinesq equation with fourth order. *Mathematics* **8**(341), 1–9 (2020)
19. Gong, X., Fatmawati, K.M.A.: A new numerical solution of the competition model among bankdata in Caputo-Fabrizio derivative. *Alex. Eng. J.* **59**(4), 2251–2259 (2020)
20. Martoinez, H.Y., Gomez-Aguilar, J.F.: A new modified definition of Caputo-Fabrizio fractional order derivative and their applications to the multistep homotopy analysis method. *J. Comput. Appl. Math.* **346**(15), 247–260 (2020)
21. He, J.H.: Homotopy perturbation technique. *Comput. Meth. Appl. Mech. Eng.* **178**(3–4), 257–262 (1999)
22. Prakash, A., Kaur, H.: Numerical solution for fractional model of Fokker-Planck equation by using q-HATM. *Chaos Solit. Fract.* **105**, 99–110 (2017)
23. Goyal, M., Baskonus, H.M., Prakash, A.: An efficient technique for a time-fractional model of Lassa hemorrhagic fever spreading in pregnant women. *Europ. Phys. J. Plus.* **134**(482), 1–10 (2019)
24. Algahtani, O.J.J.: Comparing the Atangana-Baleanu and Caputo-Fabrizio derivative with fractional order: Allen Cahn model. *Chaos Solit. Fract.* **89**, 552–559 (2016)
25. Zhenga, X., Wang, H., Fu, H.: Well-posedness of fractional differential equations with variable-order Caputo-Fabrizio derivative. *Chaos Solit. Fract.* **138**, 1–7 (2020)
26. Prakash, A., Goyal, M., Gupta, S.: Fractional variational iteration method for solving time-fractional Newell-Whitehead-Segel equation. *Nonlinear Eng. Model. Appl.* **8**, 164–171 (2019)
27. Saelao, J., Yokchoo, N.: The solution of Klein-Gordon equation by using modified Adomian de-composition method. *Math. Comput. Simul.* **171**, 94–102 (2020)
28. Baleanu, D., Aydogan, S.M., Mohammadi, H., Rezapour, S.: On modelling of epidemic childhood diseases with the Caputo-Fabrizio derivative by using the Laplace Adomian decomposition method. *Alex. Eng. J.* **59**(5), 3029–3039 (2020)
29. Prakash, A., Kaur, H.: A reliable numerical algorithm for fractional model of Fitzhugh-Nagumo equation arising in the transmission of nerve impulses. *Nonlinear Eng. Model. Appl.* **8**, 719–727 (2019)
30. Kumar, D., Singh, J., Kumar, S.S.: Numerical computation of Klein-Gordon equations arising in quantum field theory by using homotopy analysis transform method. *Alex. Eng. J.* **53**(2), 469–474 (2014)
31. Verma, V., Prakash, A., Kumar, D., Singh, J.: Numerical study of fractional model of multi-dimensional dispersive partial differential equation. *J. Ocean Eng. Sci.* **4**, 338–351 (2019)
32. Prakash, A., Kaur, H.: Analysis and numerical simulation of fractional order Cahn-Allen model with Atangana-Baleanu derivative. *Chaos Solit. Fract.* **124**, 134–142 (2019)
33. Prakash, A.K.: Numerical method for space- and time-fractional telegraph equation with generalized lagrange multipliers. *Prog. Fract. Differ. Appl.* **5**(2), 111–123 (2019)

34. Prakash, A., Kumar, A., Baskonus, H.M., Kumar, A.: Numerical analysis of nonlinear fractional Klein-Fock-Gordon equation arising in quantum field theory via Caputo-Fabrizio fractional operator. *Math. Sci.* **15**, 269–281 (2021)
35. Kala, B.S., Rawat, M.S., Kumar, A.: Numerical analysis of the flow of a Casson fluid in magnetic field over an inclined nonlinearly stretching surface with velocity slip in a Forchheimer porous medium. *Asian Res. J. Math.* **16**(7), 34–58 (2020)
36. Kumar, A., Ilhan, E., Ciancio, A., Yel, G., Baskonus, H.M.: Extractions of some new travelling wave solutions to the conformable Date-Jimbo-Kashiwara-Miwa equation. *AIMS. Math.* **6**(5), 4238–4264 (2021)
37. Nisar, K.S., Ilhan, O.A., Manafian, J., Shahriari, M., Soybas, D.: Analytical behavior of the fractional Bogoyavlenskii equations with conformable derivative using two distinct reliable methods. *Res. Phys.* **22**, 1–14 (2021)
38. Dubey, V.P., Dubey, S., Kumar, D., Singh, J.: A computational study of fractional model of atmospheric dynamics of carbon dioxide gas. *Chaos Solit. Frac.* **142**, 1–10 (2021)
39. Yadav, S., Kumar, D., Singh, J., Baleanu, D.: Analysis and dynamics of fractional order Covid-19 model with memory effect. *Res. Phys.* **24**, 1–16 (2021)
40. Goswami, A., Rathore, S., Singh, J., Kumar, D.: Analytical study of fractional nonlinear Schrödinger equation with harmonic oscillator. *AIMS Math.* **14**(10), 3589–3610 (2021)
41. Ravichandran, C., Trujillo, J.J.: Controllability of impulsive fractional functional integro-differential equations in Banach spaces. *J. Funct. Space* **2013**, 1–8 (2013)
42. Yel, G., Kayhan, M., Ciancio, A.: A new analytical approach to the (1+1)-dimensional conformable Fisher equation. *Math. Model. Numer. Simul. Appl.* **2**(4), 211–220 (2022)
43. Baskonus, H.M., Mahmud, A.A., Muhamad, K.A., Tanriverdi, T.: A study on Caudrey–Dodd–Gibbon–Sawada–Kotera partial differential equation. *Math. Method Appl. Sci.* **45**(14), 8737–8753 (2022)
44. Isah, M.A., Yokuş, A.: The investigation of several soliton solutions to the complex Ginzburg-Landau model with Kerr law nonlinearity. *Math. Model. Numer. Simul. Appl.* **2**(3), 147–163 (2022)
45. Tao, L., Xu, L., Sulaimani, H.J.: Nonlinear differential equations based on the BSM model in the pricing of derivatives in financial markets. *Appl. Math. Nonlinear Sci.* **7**(2), 91–102 (2021)
46. Yadav, A.K.S., Sora, M.: An optimized deep neural network-based financial statement fraud detection in text mining. *3c Empresa: investigación y pensamiento crítico* **10**(4), 77–105 (2021)
47. Yan, L., Sabir, Z., Ilhan, E., Raja, M.A.Z., Gao, W., Baskonus, H.M.: Design of a computational heuristic to solve the nonlinear Liénard differential model: nonlinear Liénard differential model. *Comput. Model Eng. Sci.* 1–10 (2023)
48. Guo, H.: Nonlinear strategic human resource management based on organisational mathematical model. *Appl. Math. Nonlinear Sci.* **7**(2), 163–170 (2022)
49. Wang, Y., Veerasha, P., Prakasha, D.G., Baskonus, H.M., Gao, W.: Regarding deeper properties of the fractional order Kundu-Eckhaus equation and massive thirring model. *CMES-Comput. Model. Eng. Sci.* **133**(3), 697–717 (2022)
50. Veerasha, P., Ilhan, E., Prakasha, D.G., Baskonus, H.M., Gao, W.: Regarding on the fractional mathematical model of Tumour invasion and metastasis. *Comput. Model. Eng. Sci.* **127**(3), 1013–1036 (2021)
51. Yel, G., Bulut, H.: New wave approach to the conformable resonant nonlinear Schrödinger’s equation with Kerr-law nonlinearity. *Opt. Quant. Electron.* **54**(4), 1–13 (2022). <https://doi.org/10.1007/s11082-022-03655-2>
52. Alam, M.N., Islam, S., Ilhan, O.A., Bulut, H.: Some new results of nonlinear model arising in incompressible visco-elastic Kelvin-Voigt fluid. *Math. Method Appl. Sci.* **45**(16), 10347–10362 (2022). <https://doi.org/10.1002/mma.8372>

53. Baskonus, H.M., Mahmud, A.A., Muhamad, K.A., Tanriverdi, T., Gao, W.: Studying on Kudryashov-Sinelshchikov dynamical equation arising in mixtures liquid and gas bubbles. *Therm. Sci.* **26**(2 Part B), 1229–1244 (2022)
54. Tanriverdi, T., Baskonus, H.M., Mahmud, A.A., Muhamad, K.A.: Explicit solution of fractional order atmosphere-soil-land plant carbon cycle system. *Ecol. Complex.* **48**, 100966 (2021)



On a Class of New q -Hypergeometric Expansions as Discrete Analogues of the Erdélyi Type q -Integrals

Anand V. Bhatnagar and Yashoverdhan Vyas^(✉)

Department of Mathematics, School of Engineering, Sir Padampat Singhanian University,
Bhatewar, Udaipur 313601, Rajasthan, India
{anand.bhatnagar, yashoverdhan.vyas}@spsu.ac.in

Abstract. Recently, Vyas et al. have developed an alternative way of proof for the Gasper's discrete analogue of an Erdélyi integral and inspired from this new type of derivation they resolved the problem of finding the discrete extensions of all the Erdélyi type integrals in the form of several new hypergeometric expansions for certain ${}_{q+1}F_q$. Motivated from the above-mentioned work, here in this paper, our objective is to resolve the problem of finding the discrete extensions of the Erdélyi type q -integrals in the form of several new q -hypergeometric expansions for certain ${}_{r+1}\Phi_r$. The motivation behind this work is the fact that the q -series and basic q -polynomials, specifically the q -gamma and basic q -hypergeometric functions and basic q -hypergeometric polynomials, are applicable particularly in several diverse areas of science and engineering, viz. Statistics, number theory, combinatorial analysis, nonlinear electric circuit theory, combinatorial generating functions, quantum mechanics, mechanical engineering, lie theory, theory of heat conduction, particle physics and cosmology.

Keywords: Erdélyi integrals · Erdélyi type q -integrals · Basic q -hypergeometric functions · classical summation theorem · Basic q -hypergeometric expansions

2010 AMS Subject Classification: 33D05 · 33D15 · 33D45

1 Introduction

Heine [7, 8] first developed the idea of basic analogue or q -analogue of the Gauss hypergeometric function ${}_2F_1$ as an infinite series.

The q -shifted factorials are described in the literature for arbitrary (real or complex) q , a and $|q| < 1$ as:

$$(\alpha; q)_n = \begin{cases} 1, & n = 0 \\ (1 - \alpha)(1 - \alpha q)(1 - \alpha q^2) \dots (1 - \alpha q^{n-1}), & n \in \mathbb{N} \end{cases} \quad (1.1)$$

Using this notation, we can write the Heine’s series analogous to the notation for Gauss’ series as:

$${}_2\Phi_1(\alpha, \beta; \gamma; q, z) \equiv {}_2\Phi_1 \left[\begin{matrix} \alpha, \beta; \\ \gamma; \end{matrix} q, z \right] = \sum_{k=0}^{\infty} \frac{(\alpha; q)_k (\beta; q)_k z^k}{(\gamma; q)_k (q; q)_k}. \tag{1.2}$$

A generalized q -hypergeometric series [24, p. 347], see also [2] and [5] with ν numerator parameters $\alpha_1, \alpha_2, \dots, \alpha_\nu$ and u denominator parameters $\beta_1, \beta_2, \dots, \beta_u$ is defined by

$${}_\nu\Phi_u(\alpha_1, \dots, \alpha_\nu; \beta_1, \dots, \beta_u; q, z) \equiv {}_\nu\Phi_u \left[\begin{matrix} \alpha_1, \dots, \alpha_\nu; \\ \beta_1, \dots, \beta_u; \end{matrix} q, z \right] = \sum_{k=0}^{\infty} \frac{(\alpha_1; q)_k \dots (\alpha_\nu; q)_k z^k}{(\beta_1; q)_k \dots (\beta_u; q)_k (q; q)_k} \left[(-1)^k q^{\binom{k}{2}} \right]^{1+u-\nu} \tag{1.3}$$

where $\binom{k}{2} = k(k - 1)/2$.

For the convergence conditions of the above hypergeometric series, please see [5]. A complete list of important properties and formulas for q -shifted factorial, to be used frequently while deriving the q -hypergeometric expansion of Sect. 3, can be found in [5, Appendix 1, pp. 351–352].

The Euler’s integral representation of Gauss hypergeometric function is given in [19, p. 47, Theorem 16] and its Thomae’s q -analogue is mentioned in [5].

In 1939, Erdélyi [1] used fractional calculus method to develop three integrals [4, Eqs. (1.3)–(1.5)], known as “Erdélyi integrals” in the literature, which extend Euler’s integral for ${}_2F_1(z)$ [19, p. 47, Theorem 16] and Bateman’s integral [4, Eq. (1.2)]. Gasper [3] derived the discrete extension of one of the Erdélyi integrals [4, Eq. (1.6)] as stated below [6, Eq. (26)]:

$${}_3F_2 \left(\begin{matrix} \alpha, \beta, -n; \\ \gamma, \delta; \end{matrix} 1 \right) = \sum_{k=0}^n \binom{n}{k} \frac{(\mu)_k (\lambda + \delta - \alpha - \beta)_k (\gamma - \mu)_{n-k}}{(\gamma)_n (\delta)_k} \times {}_3F_2 \left(\begin{matrix} \lambda - \alpha, \lambda - \beta, -k; \\ \mu, \lambda + \delta - \alpha - \beta; \end{matrix} 1 \right) {}_3F_2 \left(\begin{matrix} \alpha + \beta - \lambda, \lambda - \mu, k - n; \\ \gamma - \mu, \delta + k; \end{matrix} 1 \right). \tag{1.4}$$

Gasper [3] proved (1.4) by following the steps analogous to Erdélyi’s fractional calculus proof of [4, Eq. (1.3)].

Later, Gasper [4] motivated from the proof of the above-mentioned discrete analogue, developed three expansions identities for the terminating balanced ${}_4\Phi_3$ series and obtained the q -analogues of Erdélyi’s integrals [4, Eqs. (1.8), (1.9), (1.13) and (1.14)] and corresponding discrete analogues and discrete q -extensions, see [3, Eqs. (1.6), (1.7), (2.9), (3.4), (1.11) and (1.12)].

The discrete extensions of the q -analogue of Erdélyi’s integrals [4, Eq. (1.8)] or q -analogue of (1.4), developed by [4] is as given below:

$$\begin{aligned}
 {}_3\Phi_2\left(\begin{matrix} \alpha, \beta, q^{-n}; \\ \gamma, \delta; \end{matrix} q, q\right) &= \sum_{k=0}^n \binom{n}{k}_q \frac{(\mu; q)_k \left(\frac{\lambda\delta}{\alpha\beta}; q\right)_k \left(\frac{\gamma}{\mu}; q\right)_{n-k} \mu^n \left(\frac{\alpha\beta}{\lambda\mu}\right)^k}{(\gamma; q)_n (\delta; q)_k} \\
 &\times {}_3\Phi_2\left(\begin{matrix} \frac{\lambda}{\alpha}, \frac{\lambda}{\beta}, q^{-k}; \\ \mu, \frac{\lambda\delta}{\alpha\beta}; \end{matrix} q, q\right) {}_3\Phi_2\left(\begin{matrix} \frac{\alpha\beta}{\lambda}, \frac{\lambda}{\mu}, q^{k-n}; \\ \frac{\gamma}{\mu}, \delta q^k; \end{matrix} q, q\right). \quad (1.5)
 \end{aligned}$$

The two expansions [4, Eqs. (2.8) and (2.9)] were further applied to obtain expansion formulas for the orthogonal polynomials like Racah polynomials, Askey-Wilson polynomials and their q -analogues. The application of q -Erdélyi integral [4, Eq. (1.12)] in driving the q -analogue of a Kampé de Fériet summation; conjectured by Joris Ven der Jeugt in his work on the evaluation of the $9 - j$ recoupling coefficients appearing in the quantum theory of angular momentum, are also discussed in [4].

The recent research papers [22, 23] and many others, cited therein, are examples of ongoing trend and interest in the field of q -analysis and q -calculus. Srivastava [22] presents an excellent set of discussion and comments on the study of post-quantum or (p, q) -version of the classical q -analysis.. In a review article by Srivastava [23], the overview and recent developments in the theory of several extensively studied higher transcendental functions along with their applications in widely investigated areas of various sciences have been nicely presented. For some recent developments in the field of special functions, we refer to the following research paper [14, 15, 20, 21, 27] and [28]. Further, the inspiration to work on q -hypergeometric functions and basic q -hypergeometric polynomials, is because of their vast applicability in several diverse areas of science and engineering (see, for details, [29, p. 235]). The above-mentioned analysis and observations motivate us to study q -discrete expansions of Erdélyi’s type integrals investigated by [26].

2 Motivation and Objective

Several researchers, for example, [6, 17, 18, 26] and [30] have studied and investigated the expansions which involve integrals and represent the hypergeometric functions because of the several applications of such integrals (see, for example, [4, 5]). In this context, Joshi and Vyas [9] gave an alternative way to prove Erdélyi’s integrals by utilizing the classical series rearrangement techniques [19, 25] and some classical hypergeometric summation theorems. This kind of proof motivated them to establish seven Erdélyi type integrals including a generalization and unification of Erdélyi integrals [9, Eqs. (3.1) to (3.7) and Eq. (4.1)] for certain ${}_{q+1}F_q(z)$. Taking this work forward, Joshi and Vyas [11] investigated two different classes of the q -integrals in the form of basic q -extensions of all Erdélyi type integrals due to [9], along with various special cases and applications. Further, following [4], Joshi and Vyas [12] obtained two q -hypergeometric expansions for ${}_{12}\Phi_{11}(q)$ and ${}_r\Phi_s(q)$. As applications, these expansion formulas were set to give some ${}_{10}\Phi_9(q)$ expansions applicable to the top class ${}_{10}\Phi_9(q)$ biorthogonal rational functions which on specialization lead us to the gasper’s ${}_4\Phi_3(q)$ expansion formulas.

Recently, Vyas et al. [26] investigated the discrete analogues of the Erdélyi type integrals due to [9] and Luo and Raina [16], along the lines of a triple series manipulation-based derivation of the Erdélyi's integrals due to [9]. A careful investigation of the papers [10–13, 16] and [26] depicts that classical series rearrangement technique is a versatile technique which helps in deriving the higher order hypergeometric identities and q -hypergeometric expansions which are not available in the literature.

Motivated from the above-mentioned work and an analysis of the method of proof discussed in [26], here, in this research paper we establish new q -hypergeometric expansions as q -discrete analogues of the Erdélyi type integrals. Inline to [11], we obtain two types of q -analogues of Erdélyi type of integrals. It may be noted from [11] that all Erdélyi type of integrals possesses first type of q -analogues (having t^{-1} in the numerator), while some possess the second type of q -analogue (do not have t^{-1} in the numerator). To derive these q -expansion formulas, we express the right side of each of the q -expansion formulas as a triple series and then apply the double series manipulation lemma [21, p. 57, Lemma 10] or [24, p. 100, Eq. (2)]:

$$\sum_{n_2=0}^{\infty} \sum_{n_1=0}^{n_2} \Omega(n_1, n_2) = \sum_{n_2=0}^{\infty} \sum_{n_1=0}^{\infty} \Omega(n_1, n_2 + n_1), \tag{2.1}$$

and ${}_3\Phi_2$ transformation formula [5, p. 212, Eq. (III.12)]

$${}_3\Phi_2 \left[\begin{matrix} -n, b, c \\ d, e \end{matrix}; q, q \right] = \frac{\left(\frac{e}{c}, q\right)_n}{\left(e, q\right)_n} c^n {}_3\Phi_2 \left[\begin{matrix} q^{-n}, c, \frac{d}{b} \\ d, \frac{c}{e} q^{1-n} \end{matrix}; q, \frac{qb}{e} \right]. \tag{2.2}$$

At the end, the application of triple series manipulation lemma [9, p. 128]:

$$\sum_{n_3=0}^{\infty} \sum_{n_2=0}^{\infty} \sum_{n_1=0}^{\infty} \Omega(n_3, n_2, n_1) = \sum_{n_3=0}^{\infty} \sum_{n_2=0}^{n_3} \sum_{n_1=0}^{n_3-n_2} \Omega(n_3 - n_2 - n_1, n_2, n_1), \tag{2.3}$$

and use of two appropriate q -classical summation theorems to solve the involved inner series, lead us to the desired discrete q -extensions.

In Sect. 3, we state all of the investigated new q -hypergeometric expansions. All the q -hypergeometric expansions stated in Sect. 3 include terminating series only, hence the question of convergence doesn't arise because terminating series are always convergent. Further, to convert the results of Sect. 3 into their corresponding Erdélyi type q -integrals, the procedure mentioned in [26, p. 2 and p. 5 (Remark 2)] can be applied in a straight forward manner. In Sects. 4 and 5, we give the brief outline of the derivations of the new q -hypergeometric expansions, to illustrate the difference between the derivations of the discrete extensions or the new q -hypergeometric expansions corresponding to the Erdélyi type q -integrals with and without the presence t^{-1} as one of the numerator parameters in one of the involved hypergeometric functions.

3 Discrete Extensions of Erdélyi Type q -Integrals or New q -Hypergeometric Expansions

The results from (3.1) to (3.11) provide the basic (or q -) expansion formulas or the discrete analogue of the Erdélyi type q -integrals given [11, Eqs. (1.2) to (1.12)], respectively. The

usual condition for the convergence of q -hypergeometric series that is the denominator parameters are non negative integers. This condition is applied to all the following q -hypergeometric expansions:

$$\begin{aligned}
 {}_4\Phi_3 \left[\begin{matrix} -N, v, \xi, \lambda; \\ \varepsilon, \gamma, \delta; \end{matrix} q; q \right] &= \frac{(q^{\gamma-\mu}; q)_N}{(q^\gamma; q)_N} \sum_{k=0}^{\infty} \frac{(q^{-N}; q)_k (q^\mu; q)_k (q^{\varepsilon-v-\xi+\delta}; q)_k}{(q^\varepsilon; q)_k (q^{1+\mu-\gamma-N}; q)_k (q; q)_k} (q^{1+v+\xi-\delta-\gamma})^k q^{\mu N} \\
 {}_3\Phi_2 \left[\begin{matrix} \frac{v\xi}{\delta}, \frac{\lambda}{\mu}, q^{-N+k}; \\ \frac{\gamma}{\mu}, q^{\varepsilon+k}; \end{matrix} q; q \right] & {}_4\Phi_3 \left[\begin{matrix} \frac{\delta}{\xi}, \frac{\delta}{v}, \lambda, q^{-k}; \\ \frac{\varepsilon\delta}{v\xi}, \mu, \delta; \end{matrix} q; q \right] \tag{3.1}
 \end{aligned}$$

$$\begin{aligned}
 {}_4\Phi_3 \left[\begin{matrix} -N, v, \xi, \lambda; \\ \varepsilon, \gamma, \delta; \end{matrix} q; \frac{q\mu}{\lambda} \right] &= \frac{(q^{\gamma-\mu}; q)_N}{(q^\gamma; q)_N} \sum_{k=0}^{\infty} \frac{(q^{-N}; q)_k (q^\mu; q)_k (q^{\varepsilon-v-\xi+\delta}; q)_k q^{\mu N}}{(q^\varepsilon; q)_k (q^{1+\mu-\gamma-N}; q)_k (q; q)_k} (q^{1+v+\xi-\delta-\gamma})^k \\
 {}_3\Phi_2 \left[\begin{matrix} \frac{\lambda}{\mu}, \frac{v\xi}{\delta}, q^{-N+k}; \\ \frac{\gamma}{\mu}, q^{\varepsilon+k}; \end{matrix} q; \frac{q}{\lambda} \right] & {}_4\Phi_3 \left[\begin{matrix} \frac{\delta}{\xi}, \frac{\delta}{v}, \lambda, q^{-k}; \\ \frac{\varepsilon\delta}{v\xi}, \mu, \delta; \end{matrix} q; \frac{q\mu}{\lambda} \right] \tag{3.2}
 \end{aligned}$$

$${}_6\Phi_5 \left[\begin{matrix} -N, q^\alpha, \sqrt{\frac{\gamma}{\beta}}, -\sqrt{\frac{\gamma}{\beta}}, \sqrt{\frac{q\gamma}{\beta}}, -\sqrt{\frac{q\gamma}{\beta}}; \\ \varepsilon, \sqrt{\gamma} - \sqrt{\gamma}, \sqrt{q\gamma}, -\sqrt{q\gamma}; \end{matrix} q, \frac{q\beta}{\alpha} \right] = \frac{(q^{\alpha+\beta}; q)_N}{(q^\gamma; q)_N}$$

$$\begin{aligned}
 \sum_{k=0}^{\infty} \frac{(q^{-N}; q)_k (q^{\gamma-\alpha-\beta}; q)_k (q^{\varepsilon-\beta}; q)_k}{(q^\varepsilon; q)_k (q^{1-\alpha-\beta-N}; q)_k (q; q)_k} (q^{1+\beta-\gamma})^k {}_3\Phi_2 \left[\begin{matrix} \frac{\alpha}{\beta}, \frac{\gamma}{\beta}, q^{-k}; \\ \frac{\gamma}{\alpha\beta}, \frac{\varepsilon}{\beta}; \end{matrix} q, \frac{q}{\alpha} \right] \\
 {}_8\Phi_7 \left[\begin{matrix} \alpha, \sqrt{\beta}, -\sqrt{\beta}, \sqrt{\beta}q, -\sqrt{\beta}q, \frac{q\beta}{\varepsilon m}, \frac{\alpha q^{-N+k}}{\beta}, q^{-N+k}; \\ \sqrt{\alpha\beta}, -\sqrt{\alpha\beta}, \sqrt{\alpha\beta}q, -\sqrt{\alpha\beta}q, \frac{q\beta}{\varepsilon k}, \gamma q^N, q^{\varepsilon+k}; \end{matrix} q, q \right] \tag{3.3}
 \end{aligned}$$

$${}_4\Phi_3 \left[\begin{matrix} -N, \alpha, \beta, \frac{q\gamma}{\lambda\mu}; \\ \varepsilon, \frac{q\gamma}{\lambda}, \frac{q\gamma}{\mu}; \end{matrix} q, \frac{q\mu}{\alpha} \right] = \frac{(q^{1+\gamma-\beta}; q)_N}{(q^{1+\gamma}; q)_N} \sum_{k=0}^{\infty} \frac{(q^{-N}; q)_k (q^\beta; q)_k (q^{\varepsilon-\mu}; q)_k q^{\beta N}}{(q^\varepsilon; q)_k (q^{\beta-\gamma-N}; q)_k (q; q)_k} (q^{\mu-\gamma})^k$$

$${}_4\Phi_3 \left[\begin{matrix} \frac{\alpha}{\mu}, \beta q^k, \frac{\varepsilon q^k}{\mu}, q^{-N+k}; \\ \varepsilon q^k, \frac{\varepsilon}{\mu}, \frac{\beta q^{-N+k}}{\gamma}; \end{matrix} q, \frac{q\mu}{\alpha\gamma} \right]$$

$${}_8\Phi_8 \left[\begin{matrix} \gamma, q\sqrt{\gamma}, -q\sqrt{\gamma}, \mu, \lambda, \alpha, \frac{q\gamma q^N}{\beta q^k}, q^{-k}; \\ \sqrt{\gamma}, -\sqrt{\gamma}, \frac{q\gamma}{\beta}, \frac{q\gamma}{\lambda}, \frac{q\gamma}{\mu}, \frac{\mu q^{1-k}}{\varepsilon}, \gamma q^{1-k}, 0; \end{matrix} q, \frac{q\lambda}{\varepsilon\alpha\gamma} \right] \tag{3.4}$$

$${}_4\Phi_3 \left[\begin{matrix} -N, \alpha, \beta, \frac{q\gamma}{\lambda\mu}; \\ \varepsilon, \frac{q\gamma}{\lambda}, \frac{q\gamma}{\mu}; \end{matrix} q, q \right] = \frac{(q^{1+\gamma-\beta}; q)_N}{(q^{1+\gamma}; q)_N} \sum_{k=0}^{\infty} \frac{(q^{-N}; q)_k (q^\beta; q)_k (q^{\varepsilon-\mu}; q)_k q^{\beta N}}{(q^\varepsilon; q)_k (q^{\beta-\gamma-N}; q)_k (q; q)_k} (q^{\mu-\gamma})^k$$

$${}_4\Phi_3 \left[\begin{matrix} \frac{\alpha}{\mu}, q^{-N+k}, \beta q^k, \frac{\varepsilon q^k}{\mu}; \\ \frac{\varepsilon}{\mu}, q^{\varepsilon+k}, \frac{\beta q^k}{\gamma q^N}; \end{matrix} q, \frac{q}{\gamma} \right]$$

$${}_8\Phi_8 \left[\begin{matrix} \gamma, q\sqrt{\gamma}, -q\sqrt{\gamma}, \mu, \lambda, \alpha, \frac{\gamma q^{1-k+N}}{\beta}, q^{-k}; \\ \sqrt{\gamma}, -\sqrt{\gamma}, \frac{q\gamma}{\mu}, \frac{q\gamma}{\lambda}, \frac{q\gamma}{\beta}, \gamma q^{1-N}, \frac{\mu q^{1-k}}{\varepsilon}, 0; \end{matrix} q, \frac{q\lambda}{\varepsilon\mu} \right] \tag{3.5}$$

$$\begin{aligned}
 {}_4\Phi_3 \left[\begin{matrix} -N, \alpha, \beta, \frac{q\gamma}{\lambda\mu}; \\ \varepsilon, \frac{q\gamma}{\lambda}, \frac{q\gamma}{\mu}; \end{matrix} ; q, q \right] &= \frac{(q^{1+\gamma-\beta}; q)_N}{(q^{1+\gamma}; q)_N} \sum_{k=0}^{\infty} \frac{(q^{-N}; q)_k (q^{\beta}; q)_k (q^{\varepsilon-\mu}; q)_k}{(q^{\varepsilon}; q)_k (q^{\beta-\gamma-N}; q)_k (q; q)_k} (q^{\mu-\gamma})^k q^{\beta N} \\
 {}_3\Phi_2 \left[\begin{matrix} \frac{\alpha}{\mu}, \frac{\varepsilon q^k}{\mu}, q^{-N+k}; \\ \frac{\varepsilon}{\mu}, \varepsilon q^k; \end{matrix} ; q, q \right] &{}_9\Phi_7 \left[\begin{matrix} \alpha, \mu, \gamma, \lambda, q^{-k}, \beta q^k, q\sqrt{\gamma}, -q\sqrt{\gamma}, 0; \\ \frac{q\gamma}{\mu}, \frac{q\gamma}{\lambda}, \frac{q\gamma}{\beta}, \frac{q\gamma}{N}, q^{\varepsilon+k}, \sqrt{\gamma}, -\sqrt{\gamma}; \end{matrix} ; q, \frac{q^{1+N}\gamma}{\lambda\mu\beta} \right] \tag{3.6}
 \end{aligned}$$

$$\begin{aligned}
 {}_7\Phi_6 \left[\begin{matrix} -N, \alpha, \beta, \sqrt{\frac{\gamma}{\mu}}, -\sqrt{\frac{\gamma}{\mu}}, \sqrt{\frac{q\gamma}{\mu}}, -\sqrt{\frac{q\gamma}{\mu}}; \\ \varepsilon, \frac{\gamma}{\mu}, \sqrt{\gamma}, -\sqrt{\gamma}, \sqrt{q\gamma}, -\sqrt{q\gamma}; \end{matrix} ; q, q \right] &= \frac{(q^{\gamma-\beta}; q)_N}{(q^{\gamma}; q)_N} \\
 &\sum_{k=0}^{\infty} \frac{(q^{-N}; q)_k (q^{\beta}; q)_k (q^{\varepsilon-\mu}; q)_k q^{\beta N}}{(q^{\varepsilon}; q)_k (q^{1+\beta-\gamma-N}; q)_k (q; q)_k} (q^{1+\mu-\gamma})^k \\
 {}_4\Phi_3 \left[\begin{matrix} \alpha, \mu, \beta q^k, q^{-N+k}; \\ \frac{\gamma}{\beta}, \gamma N, q^{\varepsilon+k}; \end{matrix} ; q, \frac{\gamma q^{1+N}}{\alpha\beta} \right] &{}_2\Phi_1 \left[\begin{matrix} \frac{\alpha}{\mu}, q^{-k}; \\ \frac{\varepsilon}{\mu}; \end{matrix} ; q, \frac{q}{\alpha} \right] \tag{3.7}
 \end{aligned}$$

$$\begin{aligned}
 {}_5\Phi_4 \left[\begin{matrix} -N, \alpha, \beta, \gamma, \frac{\alpha q \mu}{\beta \gamma}; \\ \varepsilon, \frac{\alpha q}{\beta}, \frac{\alpha q}{\gamma}, \frac{\beta \gamma}{\mu}; \end{matrix} ; q, \frac{q\lambda}{\alpha} \right] &= \frac{(q^{1+\alpha-\mu-\lambda}; q)_N}{(q^{1+\alpha-\mu}; q)_N} \sum_{k=0}^{\infty} \frac{(q^{-N}; q)_k (q^{\lambda}; q)_k (q^{\varepsilon-\mu}; q)_k}{(q^{\varepsilon}; q)_k (q^{\mu-\alpha+\lambda-N}; q)_k (q; q)_k} (q^{2\mu-\alpha})^k \\
 {}_4\Phi_3 \left[\begin{matrix} \mu, \frac{\alpha}{\lambda}, \frac{\alpha q^{1-k+N}}{\mu\lambda}, q^{-k}; \\ \frac{q\alpha}{\lambda\mu}, \frac{q\mu}{\varepsilon}, \frac{q^{1-k}}{\lambda}; \end{matrix} ; q, \frac{q^{2-N}}{\alpha\varepsilon} \right]
 \end{aligned}$$

$$\begin{aligned}
 {}_{12}\Phi_{11} \left[\begin{matrix} \frac{\alpha}{\mu}, q\sqrt{\frac{\alpha}{\mu}}, -q\sqrt{\frac{\alpha}{\mu}}, \frac{\beta}{\mu}, \frac{\gamma}{\mu}, \frac{q\alpha}{\beta\gamma}, \sqrt{\alpha}, -\sqrt{\alpha}, \\ \sqrt{\frac{\alpha}{\mu}}, -\sqrt{\frac{\alpha}{\mu}}, \frac{q\alpha}{\beta}, \frac{\alpha\beta}{\gamma}, \frac{\beta\gamma}{\mu}, \sqrt{\gamma}, -\sqrt{\gamma}, \\ q\sqrt{\alpha}, -q\sqrt{\alpha}, \frac{\varepsilon q^k}{\mu}, q^{-N+k}; \\ q\sqrt{\lambda}, -q\sqrt{\lambda}, \frac{q^{1+N}\alpha}{\mu}, q^{\varepsilon+k}; \end{matrix} ; q, \frac{q^{1+N}\gamma\mu}{\alpha} \right] \tag{3.8}
 \end{aligned}$$

$$\begin{aligned}
 {}_5\Phi_4 \left[\begin{matrix} -N, \alpha, \beta, \gamma, \frac{\alpha q}{\beta \gamma}; \\ \varepsilon, \frac{\alpha q}{\beta}, \frac{\alpha q}{\gamma}, \frac{\beta \gamma}{\mu}; \end{matrix} ; q, q \right] &= \frac{(q^{1+\alpha-\mu-\lambda}; q)_N}{(q^{1+\alpha-\lambda}; q)_N} \sum_{k=0}^{\infty} \frac{(q^{-N}; q)_k (q^{\lambda}; q)_k (q^{\varepsilon-\mu}; q)_k}{(q^{\varepsilon}; q)_k (q^{\mu-\alpha+\lambda-N}; q)_k (q; q)_k} (q^{2\mu-\alpha})^k \\
 {}_4\Phi_3 \left[\begin{matrix} \mu, \frac{\alpha}{\lambda}, \frac{\alpha q^{1-k+N}}{\mu\lambda}, q^{-k}; \\ \frac{q\alpha}{\lambda\mu}, \frac{q^{1-k}}{\lambda}, \frac{\mu q^{1-k}}{\varepsilon}; \end{matrix} ; q, \frac{q^{2-N}}{\varepsilon} \right]
 \end{aligned}$$

$$\begin{aligned}
 {}_{13}\Phi_{12} \left[\begin{matrix} \frac{\alpha}{\beta}, q\sqrt{\frac{\alpha}{\mu}}, -q\sqrt{\frac{\alpha}{\mu}}, \frac{\beta}{\mu}, \frac{\gamma}{\mu}, \frac{q\alpha}{\beta\gamma}, \sqrt{\alpha}, -\sqrt{\alpha}, \\ \sqrt{\frac{\alpha}{\mu}}, -\sqrt{\frac{\alpha}{\mu}}, \frac{q\alpha}{\beta}, \frac{q\alpha}{\gamma}, \frac{\beta\gamma}{\mu}, \sqrt{\lambda}, -\sqrt{\lambda}, \\ q\sqrt{\alpha}, -q\sqrt{\alpha}, \frac{\varepsilon q^k}{\mu}, \lambda q^k, q^{-N+k}; \\ q\sqrt{\lambda}, -q\sqrt{\lambda}, \frac{\mu\lambda q^k}{\alpha}, \frac{q^{1+N}\alpha}{\mu}, q^{\varepsilon+k}; \end{matrix} ; q, \frac{q^{1+N}\mu}{\alpha} \right] \tag{3.9}
 \end{aligned}$$

$${}_8\Phi_7 \left[\begin{matrix} -N, \beta, \gamma, \frac{\alpha q}{\mu\lambda}, q\sqrt{\mu}, -q\sqrt{\mu}, \sqrt{q\alpha}, -\sqrt{q\alpha}; \\ \varepsilon, \frac{\alpha q}{\lambda}, \frac{\beta\gamma}{\mu}, \sqrt{\beta\gamma}, -\sqrt{\beta\gamma}, \sqrt{q\beta\gamma}, -\sqrt{q\beta\gamma}; \end{matrix} ; q, q \right] = \frac{(q^{2\gamma+\beta-\alpha-1}; q)_N}{(q^{\gamma+\beta}; q)_N}$$

$$\begin{aligned}
 & \sum_{k=0}^{\infty} \frac{(q^{-N}; q)_k (q^{1+\alpha-\gamma}; q)_k (q^{\varepsilon-\gamma}; q)_k}{(q^{\varepsilon}; q)_k (q^{2+\alpha-2\gamma-N-\beta}; q)_k (q; q)_k} (q^{1-\beta})^k \\
 & {}_4\Phi_3 \left[\begin{matrix} \frac{2\gamma\beta q^{1+n+N}}{\alpha}, \frac{\beta\gamma}{\alpha q}, \gamma, -k; \\ \frac{\lambda q^{-m}}{\alpha}, \frac{\mu\gamma q^{1+n}}{\varepsilon}, \frac{2\gamma\beta q^{2n-1}}{\alpha}; \end{matrix} q, \frac{q^{1-N}}{\varepsilon} \right] \\
 & {}_9\Phi_8 \left[\begin{matrix} \alpha, q\sqrt{\mu}, -q\sqrt{\mu}, \beta, \mu, \lambda, \frac{2\gamma\beta q^{N-1}}{\alpha}, \gamma q^{2m}, q^{-N+k}; \\ \sqrt{\alpha}, -\sqrt{\alpha}, \frac{q\alpha}{\mu}, \frac{q\alpha}{\lambda}, \frac{2\gamma\beta}{\alpha q}, q^{\varepsilon+k}; \end{matrix} q, \frac{q\varepsilon}{\alpha\mu} \right] \\
 & {}_9\Phi_8 \left[\begin{matrix} -N, \varepsilon, \beta, \gamma, \frac{q\alpha^2}{\beta\gamma\mu}, q\sqrt{\mu}, -q\sqrt{\mu}, \sqrt{q\mu}, -\sqrt{q\mu}; \\ \varepsilon, \frac{q\alpha}{\beta}, \frac{q\alpha}{\gamma}, \frac{\beta\gamma\mu}{\alpha}\sqrt{\lambda}, -\sqrt{\lambda}, \sqrt{q\lambda}, -\sqrt{q\lambda}; \end{matrix} q, q \right] = \frac{(q^{\lambda-\alpha}; q)_N}{(q^{\lambda}; q)_N} \\
 & \sum_{k=0}^{\infty} \frac{(q^{-N}; q)_k (q^{\alpha}; q)_k (q^{\varepsilon-\alpha+\mu}; q)_k}{(q^{\varepsilon}; q)_k (q^{1+\alpha-\lambda-N}; q)_k (q; q)_k} (q^{1+\alpha-\lambda-\mu})^k
 \end{aligned} \tag{3.10}$$

$${}_4\Phi_3 \left[\begin{matrix} \frac{\alpha}{\mu}, \frac{\lambda}{q\mu}, \alpha q^k, q^{-N+k}; \\ \frac{\lambda}{\alpha}, \lambda q^N, q^{\varepsilon+k}; \end{matrix} q, \frac{q^2\mu}{\alpha} \right] \tag{3.11}$$

4 Proof of q -Hypergeometric Expansion (3.1) Corresponding to Erdélyi Type Integrals with t^{-1} as One of the Numerator Parameters

Denoting the right hand side of (3.1) by Δ and replacing the hypergeometric series by their series form and then using the double series manipulation (2.1), we get

$$\begin{aligned}
 \Delta &= \frac{\left(\frac{\gamma}{\mu}; q\right)_N q^{\mu N}}{(\gamma; q)_N} \sum_{k=0}^{\infty} \sum_{n=0}^{\infty} \sum_{m=0}^k \frac{(q^{-N}; q)_{k+m+n} (\mu; q)_{k+m} \left(\frac{\varepsilon\delta}{v\xi}; q\right)_{k+m} \left(\frac{qv\xi}{\delta\gamma}\right)^{k+m}}{(\varepsilon; q)_{k+m+n} \left(\frac{\mu q^{1-N}}{\gamma}; q\right)_{k+m} (q; q)_k} \\
 & \times \frac{\left(\frac{v\xi}{\delta}; q\right)_n \left(\frac{\lambda}{\mu}; q\right)_n \left(\frac{\delta}{\xi}; q\right)_m \left(\frac{\delta}{v}; q\right)_m (\lambda; q)_m (-q)^m q^n q^{\binom{m}{2} - m^2 - mk}}{\left(\frac{\gamma}{\mu}; q\right)_n \left(\frac{\varepsilon\delta}{\gamma\xi}; q\right)_m (\mu; q)_m (\delta; q)_m (q; q)_m (q; q)_n}. \tag{4.1}
 \end{aligned}$$

Taking inner series in above equation, we obtain the following equation:

$$\begin{aligned}
 \Delta &= \frac{\left(\frac{\gamma}{\mu}; q\right)_N q^{\mu N}}{(\gamma; q)_N} \sum_{m=0}^{\infty} \sum_{n=0}^{\infty} \frac{(q^{-N}; q)_{m+n} (\mu; q)_m \left(\frac{qv\xi}{\delta\gamma}\right)^m}{(\varepsilon; q)_{m+n} \left(\frac{\mu q^{1-N}}{\gamma}; q\right)_m} \\
 & \times \frac{\left(\frac{v\xi}{\delta}; q\right)_n \left(\frac{\lambda}{\mu}; q\right)_n \left(\frac{\delta}{\xi}; q\right)_m \left(\frac{\delta}{v}; q\right)_m (\lambda; q)_m (-q)^m q^n q^{\binom{m}{2} - m^2}}{\left(\frac{\gamma}{\mu}; q\right)_n (\mu; q)_m (\delta; q)_m (q; q)_m (q; q)_n}
 \end{aligned}$$

$$\times {}_3\Phi_2 \left[\begin{matrix} q^{-(N-m-n)}, \mu q^m, \frac{\varepsilon \delta}{v \xi} q^m; & qv\xi q^{-m} \\ \varepsilon q^{m+n}, \frac{\mu q^{1-N+m}}{\gamma}; & \delta \gamma \end{matrix} \right]. \tag{4.2}$$

Now, applying the formula (2.2) (reversed) on the ${}_3\Phi_2$ of above equation, we can write

$$\begin{aligned} \Delta &= \sum_{k=0}^{\infty} \sum_{m=0}^{\infty} \sum_{n=0}^{\infty} \frac{(q^{-N}; q)_{k+m+n} (\mu; q)_{k+m} \left(\frac{v\xi}{\delta}; q\right)_{n+k} \left(\frac{v\xi}{\delta\gamma}\right)^m}{(\varepsilon : q)_{k+m+n} (\gamma : q)_{k+m+n}} \\ &\times \frac{\left(\frac{\lambda}{\mu}; q\right)_n \left(\frac{\delta}{\xi}; q\right)_m \left(\frac{\delta}{v}; q\right)_m (\lambda; q)_m q^{k+m+n} \mu^n q^{mn} \gamma^m}{(\mu; q)_m (\delta; q)_m (q; q)_k (q; q)_m (q; q)_n}. \end{aligned} \tag{4.3}$$

Next, applying the triple series manipulation (2.3) on the above equation and then taking an inner series in n gives:

$$\begin{aligned} \Delta &= \sum_{k=0}^{\infty} \sum_{m=0}^{\infty} \frac{(q^{-N}; q)_k (\mu; q)_k \left(\frac{v\xi}{\delta}; q\right)_k}{(\varepsilon : q)_k (\gamma : q)_k (q; q)_k} \\ &\times \frac{\left(\frac{\delta}{\xi}; q\right)_m \left(\frac{\delta}{v}; q\right)_m (\lambda; q)_m (q^{-k}; q)_m q^{m+k}}{\left(\frac{\delta q^{1-k}}{v\xi}; q\right)_m (\mu; q)_m (\delta; q)_m (q; q)_m} {}_2\Phi_1 \left[\begin{matrix} q^{m-k}, \frac{\lambda}{\mu}; \\ \frac{q^{1-k} \mu}{\mu}; \end{matrix} q \right]. \end{aligned} \tag{4.4}$$

Now, applying Chu-Vandermonde summation theorem [5, p. 354, Eq. (II.6)] and then taking an inner series in m leads us to the following equation:

$$\Delta = \sum_{k=0}^{\infty} \frac{(q^{-N}; q)_k \left(\frac{v\xi}{\delta}; q\right)_k q^k}{(\varepsilon : q)_k (\gamma : q)_k (q; q)_k} {}_3\Phi_2 \left[\begin{matrix} \frac{\delta}{\xi}, \frac{\delta}{v}, q^{-k}; \\ \delta, \frac{\delta q^{1-k}}{v\xi}; \end{matrix} q \right]. \tag{4.5}$$

The application of q -Pfaff-Saalschütz summation theorem [5, p. 355, Eq. (II.12)] leads to the left side of (3.1).

5 Proof of the New q -hypergeometric Expansion (3.2) Corresponding to Erdélyi Type Integrals Without t^{-1} as One of the Numerator Parameters

Denoting the right hand side of (3.2) by Δ and replacing the hypergeometric series by their series form and then using the double series manipulation (2.1), we get

$$\Delta = \frac{\left(\frac{\gamma}{\mu}; q\right)_N q^{\mu N}}{(\gamma; q)_N} \sum_{k=0}^{\infty} \sum_{n=0}^{\infty} \sum_{m=0}^k \frac{(q^{-N}; q)_{k+m+n} (\mu; q)_{k+m} \left(\frac{\varepsilon \delta}{v \xi}; q\right)_{k+m} \left(\frac{qv\xi}{\delta\gamma}\right)^{k+m}}{(\varepsilon : q)_{k+m+n} \left(\frac{\mu q^{1-N}}{\gamma}; q\right)_{k+m} (q; q)_k}$$

$$\times \frac{\left(\frac{v\xi}{\delta}; q\right)_n \left(\frac{\lambda}{\mu}; q\right)_n \left(\frac{\delta}{\xi}; q\right)_m \left(\frac{\delta}{v}; q\right)_m (\lambda; q)_m \left(-\frac{\mu}{\lambda} q^{1-n}\right)^m \left(\frac{q}{\lambda}\right)^n q^{\binom{m}{2}}}{\left(\frac{\gamma}{\mu}; q\right)_n \left(\frac{\varepsilon\delta}{\gamma\xi}; q\right)_m (\mu; q)_m (\delta; q)_m (q; q)_m (q; q)_n} \tag{5.1}$$

Taking inner series in above equation, we obtain the following equation:

$$\begin{aligned} \Delta &= \frac{\left(\frac{\gamma}{\mu}; q\right)_N q^{\mu N}}{(\gamma; q)_N} \sum_{m=0}^{\infty} \sum_{n=0}^{\infty} \frac{(q^{-N}; q)_{m+n} (\mu; q)_m \left(\frac{qv\xi}{\delta\gamma}\right)^m}{(\varepsilon; q)_{m+n} \left(\frac{\mu q^{1-N}}{\gamma}; q\right)_m} \\ &\times \frac{\left(\frac{v\xi}{\delta}; q\right)_n \left(\frac{\lambda}{\mu}; q\right)_n \left(\frac{\delta}{\xi}; q\right)_m \left(\frac{\delta}{v}; q\right)_m (\lambda; q)_m \left(-\frac{\mu}{\lambda} q^{1-n}\right)^m \left(\frac{q}{\lambda}\right)^n q^{\binom{m}{2}}}{\left(\frac{\gamma}{\mu}; q\right)_n (\mu; q)_m (\delta; q)_m (q; q)_m (q; q)_n} \\ &\times {}_3\Phi_2 \left[\begin{matrix} q^{-(N-m-n)}, \mu q^m, \frac{\varepsilon\delta}{v\xi} q^m; & qv\xi q^{-m} \\ \varepsilon q^{m+n}, \frac{\mu q^{1-N+m}}{\gamma} & : & \delta\gamma \end{matrix} \right]. \end{aligned} \tag{5.2}$$

Now, applying the formula (2.2) (reversed) on the ${}_3\Phi_2$ of above equation, we can obtain

$$\begin{aligned} \Delta &= \sum_{k=0}^{\infty} \sum_{m=0}^{\infty} \sum_{n=0}^{\infty} \frac{(q^{-N}; q)_{k+m+n} (\mu; q)_{k+m} \left(\frac{v\xi}{\delta}; q\right)_{n+k} \left(\frac{v\xi}{\delta\lambda}\right)^m}{(\varepsilon; q)_{k+m+n} (\gamma; q)_{k+m+n}} \\ &\times \frac{\left(\frac{\lambda}{\mu}; q\right)_n \left(\frac{\delta}{\xi}; q\right)_m \left(\frac{\delta}{v}; q\right)_m (\lambda; q)_m q^{k+m+n} \mu^{m+n}}{(\mu; q)_m (\delta; q)_m (q; q)_k (q; q)_m (q; q)_n}. \end{aligned} \tag{5.3}$$

Next, applying the triple series manipulation (2.3) on Eq. (5.3) and then taking an inner series in n gives:

$$\begin{aligned} \Delta &= \sum_{k=0}^{\infty} \sum_{m=0}^{\infty} \frac{(q^{-N}; q)_k (\mu; q)_k \left(\frac{v\xi}{\delta}; q\right)_k}{(\varepsilon; q)_k (\gamma; q)_k (q; q)_k} \\ &\times \frac{\left(\frac{\delta}{\xi}; q\right)_m \left(\frac{\delta}{v}; q\right)_m (\lambda; q)_m (q^{-k}; q)_m \mu^m q^{m+k}}{\left(\frac{\delta q^{1-k}}{v\xi}; q\right)_m (\mu; q)_m (\delta; q)_m (q; q)_m} {}_2\Phi_1 \left[\begin{matrix} q^{m-k}, \frac{\lambda}{\mu}; & q^{1-m} \\ \frac{q^{1-k}}{\mu}; & : & \lambda \end{matrix} \right]. \end{aligned} \tag{5.4}$$

Now, applying Chu-Vandermonde summation theorem [5, p. 354, Eq. (II.7)] and then taking an inner series in m , we can write

$$\Delta = \sum_{k=0}^{\infty} \frac{(q^{-N}; q)_k \left(\frac{v\xi}{\delta}; q\right)_k (\lambda; q)_k q^k \left(\frac{\mu}{\lambda}\right)^k}{(\varepsilon; q)_k (\gamma; q)_k (q; q)_k} {}_3\Phi_2 \left[\begin{matrix} \frac{\delta}{\xi}, \frac{\delta}{v}, q^{-k}; \\ \delta, \frac{\delta q^{1-k}}{v\xi}; & : & q \end{matrix} \right]. \tag{5.5}$$

The application of q -Pfaff-Saalschütz summation theorem [5, p. 355, Eq. (II.12)] leads to the left side of (3.1).

6 Conclusion

In conclusion, this paper shows the superiority of the series manipulation method discussed by Vyas et al. [26], in deriving the discrete analogues of the Erdélyi type q -integrals in the form of the new q -hypergeometric expansions. More significantly, the main results, Eqs. (3.1) to (3.11), provide the generalizations and a set of different q -analogues (in some cases) and thus lead to many of the ordinary hypergeometric expansions derived in [26], on setting $q \rightarrow 1$. The Eqs. (3.1) and (3.2) provide two q -analogues of the result [26, Theorem 2, p.5], the Eq. (3.3) is a q -analogue of [26, Theorem 5, p. 6], the Eqs. (3.4) to (3.6) are q -analogues of [26, Theorem 6, p. 6], the Eq. (3.7) is a q -analogue of [26, Theorem 7, p. 6], the Eqs. (3.8) to (3.9) are q -analogues of [26, Theorem 8, p. 7], the Eq. (3.10) is a q -analogue of [26, Theorem 9, p. 7] and the Eq. (3.11) is a q -analogue of [26, Theorem 10, p. 8]. However, the q -analogues of [26, Theorems 1, 3 and 4, p. 5] can't be developed until the required q -analogue of the extended Saalschütz theorem (see [26, Eq. (17), p. 3]) is determined, and hence it remains an open problem. Some future directions for further research for the q -hypergeometric expansions obtained in this paper may be to discover the further generalizations of the expansions along the line of [4, 12] and in addition, these results may also be specialized along the line of [11] to produce known and new q -hypergeometric transformations, which will form the subject matter of our subsequent paper in the foreseeable future. Moreover, in [22], the $(p; q)$ -calculus was exposed to be a rather trivial and inconsequential variation of the classical q -calculus, the additional parameter p being redundant. This observation by Srivastava [22] will indeed apply also to any future attempt to produce the rather straightforward $(p; q)$ -variants of the results of this paper.

References

1. Erdélyi, A.: Transformation of hypergeometric integrals by means of fractional integration by parts. *J. Math. (Oxford)* **10**, 176–189 (1939)
2. Exton, H.: q -Hypergeometric Functions and Applications. Ellis Horwood Series: Mathematics and Its Applications. Ellis Horwood (1983)
3. Gasper, G.: Formulas of the dirichlet-mehler type. In: Ross, B. (ed.) *Fractional Calculus and its Applications. Lecture Notes in Mathematics*, vol. 457, pp. 207–215. Springer, Berlin, Heidelberg (1975). <https://doi.org/10.1007/BFb0067105>
4. Gasper, G.: q -extensions of Erdélyi's fractional integral representations for hypergeometric functions. In: q -Series from a Contemporary Perspective. AMS-IMS-SIAM Joint Summer Research Conference on q -Series. Combinatorics, and Computer Algebra, p. 254. American Mathematical Society. Mount Holyoke College, South Hadley (2000)
5. Gasper, G., Rahman, M.: *Basic Hypergeometric Series. Encyclopedia of Mathematics and its Applications*, 2nd edn., vol. 96, Cambridge University Press (2004)
6. Gradshteyn, I.S., Ryzhik, I.M.: *Table of Integrals, Series, and Products (Corrected and Enlarged Ed. prepared by A. Jeffrey and D. Zwillinger)*. Academic Press, California (2014)
7. Heine E.: *Untersuchungen über die Reihe \dots* . *J. Reine Angewandte Math.* **34**, 285 (1847)
8. Heine, E.: *Handbuch der Kugelfunctionen. Theorie und Anwendungen*, vol. I. Reimer, Berlin (1878)
9. Joshi, C.M., Vyas, Y.: Extensions of certain classical integrals of Erdélyi for Gauss hypergeometric functions. *J. Comput. Appl. Math.* **160**(1–2), 125–138 (2003)

10. Joshi, C.M., Vyas, Y.: Extensions of Bailey's transform and applications. *Int. J. Math. and Math. Sci.* **2005**(12), 1909–1923 (2005)
11. Joshi, C.M., Vyas, Y.: q -extensions of certain Erdélyi type integrals. *J. Math. Anal. Appl.* **320**(2), 642–648 (2006)
12. Joshi, C.M., Vyas, Y.: Extensions of two q -series expansions with applications to biorthogonal rational functions. *Appl. Math. Comput.* **187**(1), 219–222 (2007)
13. Joshi, C.M., Vyas, Y.: Bailey type transforms and applications. *Jñānābha* **45**, 53–80 (2015)
14. Kumar, B.M., Kumar, D., Singh, J., Sooppy, N.K.: On the solutions of a class of integral equations pertaining to incomplete H-function and incomplete H-function. *Math.* **8**(5), 819 (2020)
15. Kumar, B.M., Kumar, D., Nisar, K.S., Singh, J.: Certain fractional calculus and integral transform results of incomplete \aleph -functions with applications. *Math. Methods Appl. Sci.* **43**(8), 5602–5614 (2020)
16. Luo, M.J., Raina, R.K.: Erdélyi-type integrals for generalized hypergeometric functions with integral parameter differences. *Integr. Transf. Spec. Funct.* **28**(6), 476–487 (2017)
17. Orlik, P., Terao, H.: Arrangements and Hypergeometric Integrals, vol. 9. Mathematical Society of Japan, Tokyo (2001)
18. Prudnikov, A.P., Brychkov, Yu.A., Marichev, O.L.: Integrals and Series, vols. I, II, III. Gordon and Breach Publication, New York (1990)
19. Rainville, E.D.: Special Functions. MacMillan Co., New York (1967)
20. Sharma, R., Singh, J., Kumar, D., Singh, Y.: Certain unified integrals associated with product of the general class of polynomials and incomplete I-functions. *Int. J. Appl. Comput. Math.* **8**(1), 1–11 (2022)
21. Singh, Y., Gill, V., Singh, J., Kumar, D., Khan, I.: Computable generalization of fractional kinetic equation with special functions. *J. King Saud Univ. Science.* **33**(1), 101221 (2021)
22. Srivastava, H.M.: A survey of some recent developments on higher transcendental functions of analytic number theory and applied mathematics. *Symmetry.* **13**(12), 1–22 (2021)
23. Srivastava, H.M.: Some parametric and argument variations of the operators of fractional calculus and related special functions and integral transformations. *J Nonlinear Convex Anal.* **22**(8), 1501–1520 (2021)
24. Srivastava, H.M., Karlsson, P.W.: Multiple Gaussian Hypergeometric Series. Ellis Horwood Ltd., New York (1985)
25. Srivastava, H.M., Manocha, H.L.: A Treatise on Generating Functions. Ellis Horwood Series. Mathematical Applications. Ellis Horwood Ltd. Chichester (1984).
26. Vyas, Y., Bhatnagar, A.V., Fatawat, K., Suthar, D.L., Purohit, S.D.: Discrete analogues of the Erdélyi type integrals for hypergeometric functions. *J. Math.* **2022**, 1 (2022)
27. Vyas, Y., Fatawat, K.: Summations and transformations for very well-poised hypergeometric functions and with arbitrary integer parameter difference. *Miskolc Math. Notes* **23**(2), 957–973 (2022)
28. Vyas, Y., Srivastava, H.M., Pathak, S., Fatawat, K.: General summation formulas contiguous to the q -Kummer summation theorems and their applications. *Symmetry* **13**(6), 1102 (2021)
29. Vyas, Y., Pathak, S., Fatawat, K.: Andrews' type WP-lemma and its applications. *Jñānābha.* **52**(1), 234–245 (2022)
30. Yakubovich, S.B., Luchko, Y.: The Hypergeometric Approach to Integral Transforms and Convolutions. Springer, Netherlands (2012)



Mathematical Modelling of an Incompressible, Newtonian Blood Flow for the Carotid Artery

Damini Singh and Sarita Singh^(✉)

Department of Mathematics, School of Physical Sciences, Doon University,
Dehradun 248001, Uttarakhand, India

saritamath@gmail.com

Abstract. This research aims to analyse the complex blood flow pattern in the 2D model of the human carotid artery. The steady blood flow in a 2D bifurcation model of the human carotid artery is described through the computer software ANSYS 19.1 and numerically simulated using the finite volume method on a staggered grid using the control volume method. This structural model in two dimensions is obtained to investigate the behaviour of hemodynamic parameters like blood velocity, considering blood as Newtonian, and incompressible. The incompressible 2D Navier-Stokes equation is used as the governing equation to determine the blood flow pattern. The blood flow in this model is examined by separating the flow analysis into two distinct patterns. Because of the regular design, laminar flow was obtained before the artery bifurcation. However, turbulent flow or reverse flow was achieved following the artery bifurcation because an irregular flow pattern is generated by a change in shape.

Keywords: 2D modeling · ANSYS 19.1 · Finite volume method · Navier-Stokes equation

1 Introduction

Cardiovascular diseases are undergoing a rapid increase in the death of humans all over the world, according to the WHO updated risk chart, an estimated 17.9 million people died from CVDs (due to some risk factors such as diabetes, hypertension, blockage, thinning, and dilations of the blood cells) [1]. According to hematology, the blood vessels, including arteries, capillaries, and arterioles, execute some biotic functions such as supplying oxygen, waste products, and some essential nutrients to all the parts of the body and removing catabolic products [2–4]. Hence, the research works in the numerical simulation of blood rheology growing continuously for diagnosis, prevention, and the cure of cardiovascular diseases with the increase of computational power, for deeper study of the complexity of hemodynamic of blood and geometric parameters effect of CVDs [5–9].

The motivation behind this is to exert more and more effort in the development of these physiological methods and blood flow simulations because a computational tool could enable the development of alternative methods for clinical doctors to obtain some detection of cardiovascular disease in a non-invasive way.

The function of the carotid artery is to supply blood as well as other nutrients to the brain, face, and neck of the human body. The carotid arteries are located on both sides of the neck. Internal carotid artery (ICA) and external carotid artery (ECA) are the two divisions that may be used to categorize carotid artery [10–13]. Figure 1 shows that the internal carotid artery is larger in diameter than the external carotid artery. The internal carotid artery supplies blood to the brain, whereas the external carotid artery supplies blood to the face and neck.

When predicting the flow pattern within an artery and monitoring the onset and evolution of plaque on the arterial wall, a computational fluid dynamics (CFD) model is a useful tool [14–16]. The application of CFD to 2-D artery geometries with plaque forms offers a priceless simulation of complicated geometry. The results produced by computational approaches are more accurate and cost-effective, and they are simple to mimic. In this current study, we use the methods that necessitated the foundations for the development of convoluted mathematics and physics. Consequently, the cardiovascular system modelling is limited to the parameters and boundary conditions that are available. So the computationally finite volume method for this system is prohibitive, and hence we used the coupled parameters to compromise. Therefore, this research simplified the area of interest for the 2D cardiovascular system model. Although only a few researchers have conducted a comprehensive study of hemodynamics on the 2D cardiovascular system model, [17–19].

In this study, we analyse the velocity of fluid in the constructed carotid artery by using the Navier-Stokes equation (NSE) as the governing equation of the motion of the fluid. The Navier-Stokes equation is a sequence of continuity and momentum equations that describe the flow in the large vascular domain and is coupled with the structural equation for simulation with the multi-dimensional structure. The objective of this research is to develop a simple simulation implementation that realistically describes the hemodynamics 2D constructed geometry of the vascular system using the axisymmetric Navier-Stokes equation.

2 Material and Methods

2.1 Elastic Model

Blood is a suspension of cells-red blood cells, white blood cells, platelets, and plasma-in a liquid solution, which consists of about 7% of protein and 90% of water. The elastic properties of the red blood cell membrane are responsible for the viscoelastic fluid behaviour of blood. The nature of the flow of blood determines whether the blood is Newtonian or non-Newtonian [20, 21]. Usually, the flow of blood is considered Newtonian in the large blood vessels. In this study, Blood is considered as the Newtonian fluid with the blood properties density and dynamic viscosity of 1060 kg/m^3 and 0.04 Pa.s respectively. [22].

This section of the study dealt with the spatial discretization of the Navier-Stokes equations for incompressible Newtonian fluids as the governing equations. The two-dimensional Navier-Stokes equations for incompressible Newtonian fluids consist of the momentum equation and the continuity equation with Ω as the reference domain and the τ as the boundary of the domain. The Cartesian form of the 2D Navier-stokes equation is given as follows [1, 11, 22, 23];

$$\frac{\partial u(x, t)}{\partial t} + u(x, t) \frac{\partial u(x, t)}{\partial x} + v(x, t) \frac{\partial u(x, t)}{\partial y} = -\frac{1}{\rho} \frac{\partial p}{\partial x} + \frac{\mu}{\rho} \left(\frac{\partial^2 u(x, t)}{\partial x^2} + \frac{\partial^2 u(x, t)}{\partial y^2} \right) \quad (1)$$

$$\frac{\partial v(y, t)}{\partial t} + u(x, t) \frac{\partial v(y, t)}{\partial x} + v(x, t) \frac{\partial v(y, t)}{\partial y} = -\frac{1}{\rho} \frac{\partial p}{\partial y} + \frac{\mu}{\rho} \left(\frac{\partial^2 v(y, t)}{\partial x^2} + \frac{\partial^2 v(y, t)}{\partial y^2} \right) \quad (2)$$

And the continuity equation,

$$\frac{\partial u(x, t)}{\partial x} + \frac{\partial v(x, t)}{\partial y} = 0 \quad (3)$$

Where ρ is the density of fluid, u and v are velocity components along the x -axis and y -axis respectively with the pressure p and μ is the dynamic viscosity [24]. Taking into account the fluid velocity and pressure, Eq. (1) and (2) 2D the Navier-Stokes equations are discretized with the explicit method, as stated by the following equation:

$$\begin{aligned} \frac{u_{i,j}^{n+1} - u_{i,j}^n}{\Delta t} + u \frac{u_{i,j}^n - u_{i-1,j}^n}{\Delta x} + v \frac{u_{i,j}^n - u_{i-1,j}^n}{\Delta y} &= -\frac{1}{\rho} \frac{p_{i,j}^{n+1} - p_{i-1,j}^n}{\Delta x} \\ + \frac{\mu}{\rho} \left(\frac{u_{i+1,j}^n - 2u_{i,j}^n + u_{i-1,j}^n}{\Delta x^2} + \frac{u_{i+1,j}^n - 2u_{i,j}^n + u_{i-1,j}^n}{\Delta y^2} \right) & \quad (4) \end{aligned}$$

$$\begin{aligned} \frac{v_{i,j}^{n+1} - v_{i,j}^n}{\Delta t} + u \frac{v_{i,j}^n - v_{i-1,j}^n}{\Delta x} + v \frac{v_{i,j}^n - v_{i-1,j}^n}{\Delta y} &= -\frac{1}{\rho} \frac{p_{i,j}^{n+1} - p_{i-1,j}^n}{\Delta y} \\ + \frac{\mu}{\rho} \left(\frac{v_{i+1,j}^n - 2v_{i,j}^n + v_{i-1,j}^n}{\Delta x^2} + \frac{v_{i+1,j}^n - 2v_{i,j}^n + v_{i-1,j}^n}{\Delta y^2} \right) & \quad (5) \end{aligned}$$

2.2 Spatial Discretization

On the staggered grid space, the spatial discretization is performed with the velocity u on the horizontal cell interfaces, velocity v placed on the vertical cell interfaces, and the pressure p in the cell midpoint. For the staggered grid taking,

$$\Delta x = \Delta y = h \quad (6)$$

and

$$\frac{\mu}{\rho} = \gamma, \text{ and } \frac{p}{\rho} = P \quad (7)$$

Using the Eq. (6), and (7), discrete form of Navier-stokes Eq. (4), and (5) are generalized to,

$$\frac{u_{i,j}^{n+1} - u_{i,j}^n}{\Delta t} = -\frac{1}{h}((u^2)_{i,j}^n - (u^2)_{i-1,j}^n + (uv)_{i,j}^n - (uv)_{i,j-1}^n) - \frac{1}{h}(P_{i,j}^n - P_{i-1,j}^n) + \frac{\gamma}{h^2}(u_{i+1,j}^n + u_{i-1,j}^n + u_{i,j+1}^n + u_{i,j-1}^n - 4u_{i,j}^n) \tag{8}$$

$$\frac{v_{i,j}^{n+1} - v_{i,j}^n}{\Delta t} = -\frac{1}{h}((v^2)_{i,j}^n - (v^2)_{i,j-1}^n + (uv)_{i,j}^n - (uv)_{i-1,j}^n) - \frac{1}{h}(P_{i,j}^n - P_{i-1,j}^n) + \frac{\gamma}{h^2}(v_{i+1,j}^n + v_{i-1,j}^n + v_{i,j+1}^n + v_{i,j-1}^n - 4v_{i,j}^n) \tag{9}$$

or,

$$\frac{u_{i,j}^{n+1} - u_{i,j}^n}{\Delta t} = -(a_1) - \frac{1}{h}(P_{i,j}^n - P_{i-1,j}^n) + (a_2 + a_3) \tag{10}$$

$$\frac{v_{i,j}^{n+1} - v_{i,j}^n}{\Delta t} = -(b_1) - \frac{1}{h}(P_{i,j}^n - P_{i-1,j}^n) + (b_2 + b_3) \tag{11}$$

where,

$$\begin{aligned} a_1 &= \frac{1}{h} \left((u^2)_{i,j}^n - (u^2)_{i-1,j}^n + (uv)_{i,j}^n - (uv)_{i,j-1}^n \right); & b_1 &= \frac{1}{h} \left((v^2)_{i,j}^n - (v^2)_{i,j-1}^n + (uv)_{i,j}^n - (uv)_{i-1,j}^n \right); \\ a_2 &= \frac{\gamma}{h^2} \left(u_{i+1,j}^n + u_{i-1,j}^n - 2u_{i,j}^n \right); & b_2 &= \frac{\gamma}{h^2} \left(v_{i+1,j}^n + v_{i-1,j}^n - 2v_{i,j}^n \right); \\ a_3 &= \frac{\gamma}{h^2} \left(u_{i,j+1}^n + u_{i,j-1}^n - 2u_{i,j}^n \right); & b_3 &= \frac{\gamma}{h^2} \left(v_{i,j+1}^n + v_{i,j-1}^n - 2v_{i,j}^n \right); \end{aligned}$$

In vector notation to the velocity correction equation read as,

$$\frac{U_{i,j}^{n+1} - U_{i,j}^n}{\Delta t} = -G_{i,j}^n - \nabla h P_{i,j} + F_{i,j}^n \tag{12}$$

where,

$$U_{i,j}^{n+1} = \begin{bmatrix} u_{i,j}^{n+1} \\ u_{i,j}^{n+1} \end{bmatrix}, U_{i,j}^n = \begin{bmatrix} u_{i,j}^n \\ u_{i,j}^n \end{bmatrix}$$

$$G_{i,j}^n = \begin{bmatrix} a_1 \\ a_1 \end{bmatrix}, P_{i,j} = \begin{bmatrix} P_{i,j}^n - P_{i-1,j}^n \\ P_{i,j}^n - P_{i,j-1}^n \end{bmatrix}, F_{i,j}^n = \begin{bmatrix} b_1 \\ 2b_1 \end{bmatrix},$$

The spatial discretize form of continuity Eq. (3) as,

$$\frac{u_{i,j}^n - u_{i-1,j}^n}{\Delta x} + \frac{v_{i,j}^n - v_{i,j-1}^n}{\Delta y} = 0 \tag{13}$$

As grid space is, $\Delta x = \Delta y = h$

$$u_{i,j}^n - u_{i-1,j}^n + v_{i,j}^n - v_{i,j-1}^n \tag{14}$$

Write Eq. (14) as one vector equation for constraint on velocity,

$$\Delta_h \mathbf{u}_{i,j}^{n+1} = \mathbf{0} \quad (15)$$

Split the Eq. (12) with adding the temporary velocity into,

$$\frac{U_{i,j}^t - U_{i,j}^n}{\Delta t} = -G_{i,j}^n + F_{i,j}^n \quad (16)$$

$$U_{i,j}^t = U_{i,j}^n + \Delta t(-G_{i,j}^n + F_{i,j}^n) \quad (17)$$

Evaluating $U_{i,j}^{n+1}$ from Eq. (17) with the advection and the diffusion terms.

$$\frac{U_{i,j}^{n+1} - U_{i,j}^t}{\Delta t} = -\nabla_h P_{i,j} \quad (18)$$

On applying the divergence on the both side of Eq. (18),its becomes

$$\nabla_h U_{i,j}^{n+1} = \nabla_h U_{i,j}^t - \Delta t \nabla_h \cdot \nabla_h P_{i,j} \quad (19)$$

From Eq. (15) the right-hand side of (19) become vanish and the pressure needed to enforce the velocity becomes incompressible. Hence, it is obtained by solving the linear system.

$$\nabla_h^2 P_{i,j} = \frac{1}{\Delta_h} \nabla_h U_{i,j}^t \quad (20)$$

Update the velocity field by adding the pressure

$$U_{i,j}^{n+1} = U_{i,j}^t - \Delta t \nabla_h \cdot P_{i,j} \quad (21)$$

2.3 Boundary Conditions for the Tangential Velocity

Wall velocity is,

$$U_w = 0 \quad (22)$$

i.e. have no slip condition. Then, interpolate the U_w velocity linearly by adding the ghost $u_{i,2}$,

$$\frac{u_{i,2} + u_{j,1}}{2} = U_w \quad (23)$$

$$u_{i,2} = 2U_w - u_{j,1} \quad (24)$$

If $U_w = 0$, then Eq. (24) becomes,

$$u_{i,1} = -u_{i,2} \quad (25)$$

This represents the reflection technique.

2.4 Solve for the Pressure

Here, the pressure at the boundary of the domain is obtained through solving the continuity Eq. (14) and Eq. (21), then using the presented method, rearranging for pressure, obtain a numerical scheme for boundary condition exactly in the form presented in [23].

$$P_{i+1,j} + P_{i-1,j} + P_{i,j+1} + P_{i,j-1} - 4P_{i,j} = \frac{h}{\Delta x} (u_{i+1,j}^t - u_{i-1,j}^t + v_{i,j+1}^t - v_{i,j-1}^t) \quad (26)$$

For the pressure at the boundary, the velocity $v_{i,j-1}^t$ become vanish at the boundary of the domain, therefore Eq. (26)

$$P_{i+1,j} + P_{i-1,j} + P_{i,j+1} + P_{i,j-1} - 3P_{i,j} = \frac{h}{\Delta x} (u_{i+1,j}^t - u_{i-1,j}^t + v_{i,j+1}^t) \quad (27)$$

where, for the boundary nodes except corner (Table 1),
 $i = 2; i = nx;$ and $j = 2; j = ny;$

Table 1. Array dimension

Field quantity	Interior nodes	Boundary nodes
Velocity U	$(nx - 2) \times (ny)$	$(nx) \times (ny + 1)$
Velocity V	$(nx) \times (ny - 2)$	$(nx + 1) \times (ny)$
Pressure P	$(nx - 1) \times (ny - 1)$	$(nx + 1) \times (ny + 1)$

3 Result and Discussions

In this section, we discussed the numerical results of the regular and irregular flow patterns of fluid in a constructed carotid artery and bifurcation area. Fluid was incompressible, Newtonian, laminar flow having the blood properties density and dynamic viscosity 1060 kg/m^3 and 0.04 Pa. s respectively. An analysis of the result, the time impedance was considered $t = 0$. At the inlet, the initial time-averaged reference velocity, v_0 , was assumed to be 0.3 m/s . At the carotid bifurcation area, where there is a narrowing of the artery, the fluid velocities were found to be relatively high. In the tubular area before the bifurcation, the flow pattern of blood is regular, while after the bifurcation, with the change in dimensions near the sinus from dilation, the blood flow pattern is irregular.

The anatomical pathologies of the carotid artery shown in Fig. 1 are highly receptive due to bifurcation, high turbulence, or reverse flow. Because anatomical pathologies can affect blood flow, they contribute to the development of atherosclerosis. The spline and center-line geometry descriptions of the standard carotid artery are shown in Table 2 and is created using the outline listed in the literature [5, 6, 24, 25].

The meshing of the carotid artery is shown in Fig. 3 and the number of nodes and elements is given in Table 2, the size of elements being 0.2 m/s (Fig. 2),

Table 2. Meshing details

Number of node	24431
Number of element	23809
Size of element	0.2 m/s

The blood velocity was found to be lower in the enlargement area while reaching a maximum velocity field of 0.4556 m/s in the narrowing area. The flow pattern of continuity was obtained alternately between the internal and external carotid artery models. The wall and boundaries where the velocity was found to be at its maximum indicate the deformation of the wall of the reference geometry (Figs. 4 and 5).

The flow pattern of the blood is regular in the tubular areas while irregular in areas with changes in dimensions, as in the sinus, i.e., turbulent flow. More recirculation of blood flow is found in the sinus area (Table 3).

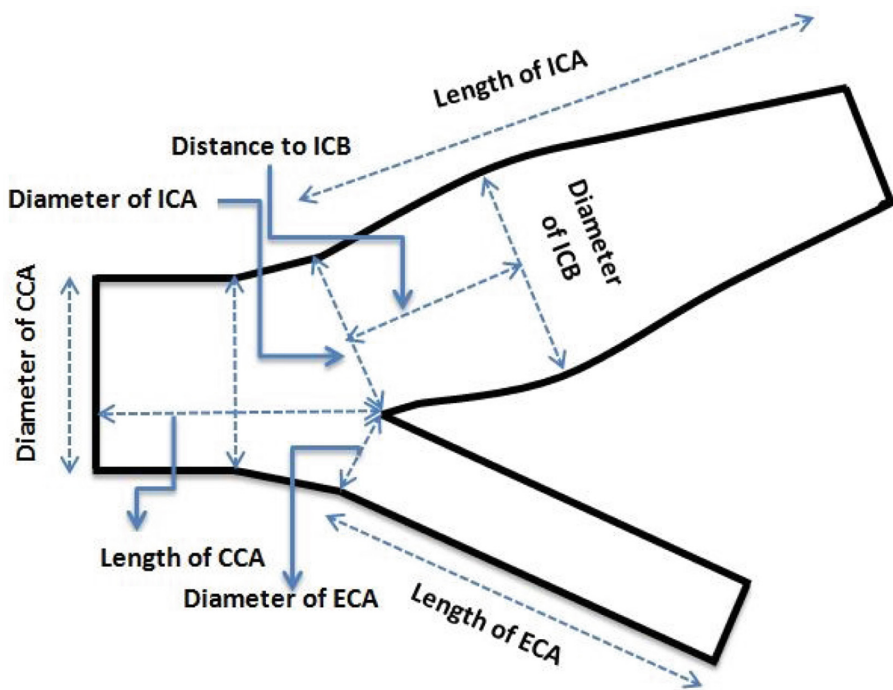


Fig. 1. Two-dimensional idealized geometric specification of Carotid artery: CAA, ICA and ECA

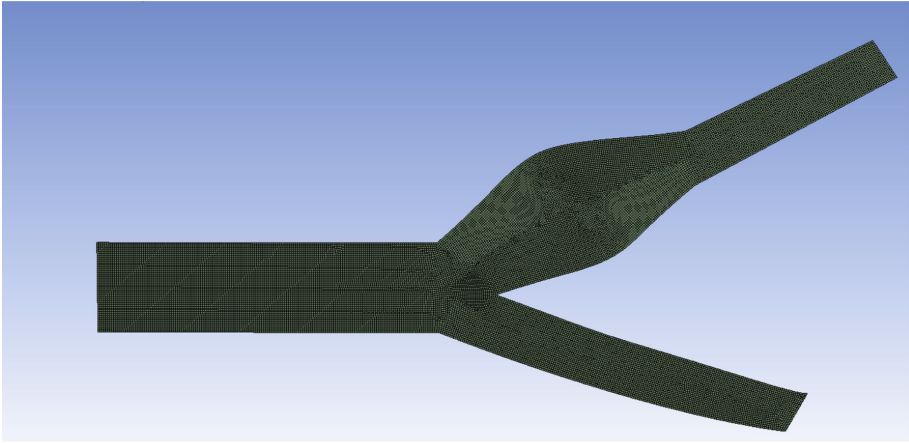


Fig. 2. Two-dimensional idealized geometric specification of Carotid artery: CAA, ICA and ECA

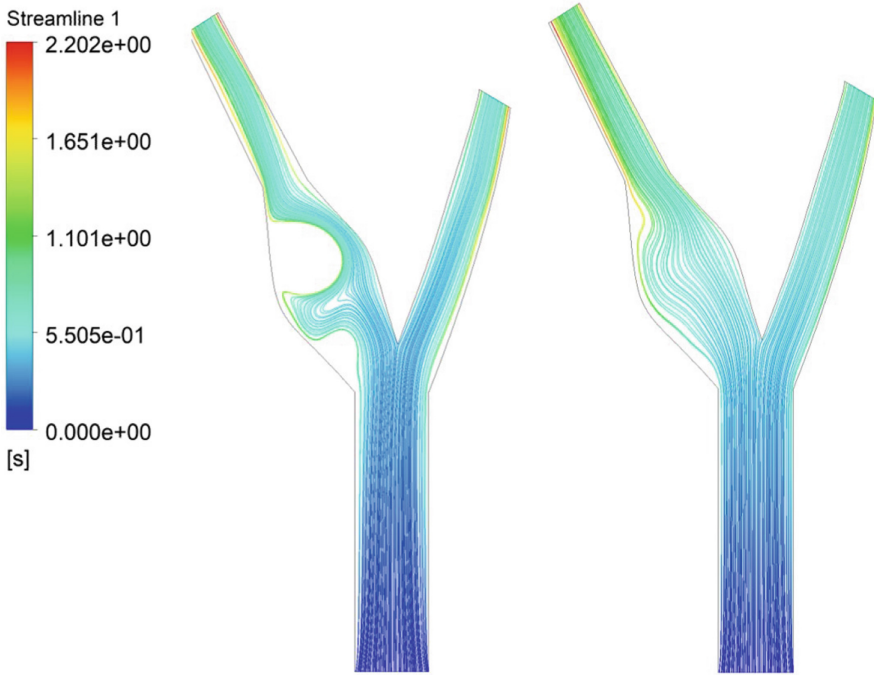


Fig. 3. Streamline simulated blood velocity field around the bifurcation of carotid artery at different time steps at $t = 0.2$ and $t = 0.4$

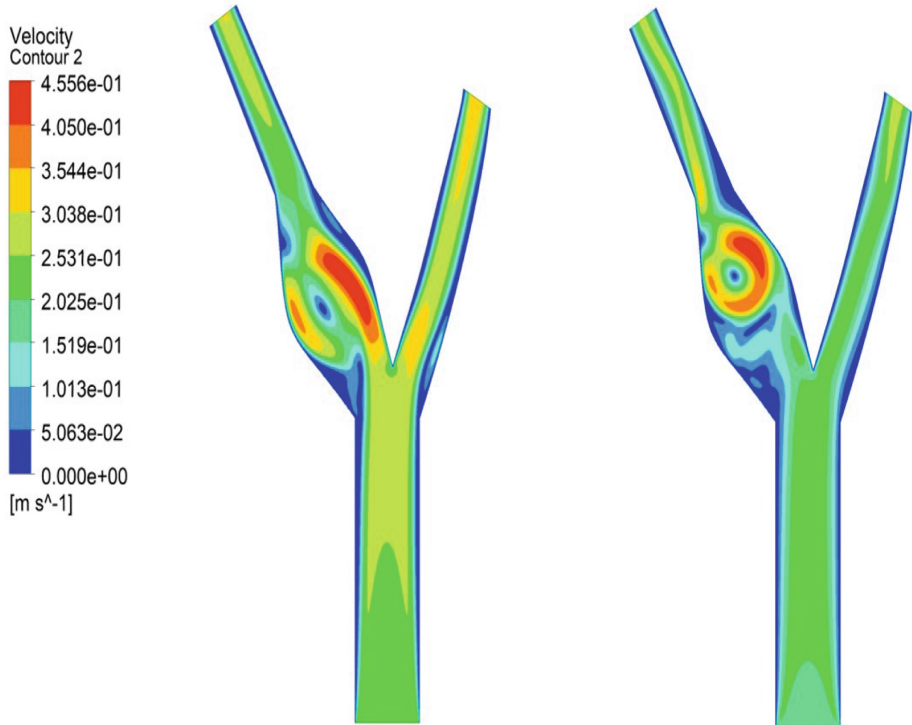


Fig. 4. Contour velocity field around the bifurcation of carotid artery at different time steps at $t = 0.2$ and $t = 0.4$

Arteries with maximum pressures of 20.88 Pa.s are more widely recirculated in the region. At the dividing wall of an artery, pressure is higher than at the non-dividing wall, and at the point of bifurcation, pressure is at its maximum, due to the force exerted by the blood on the artery.

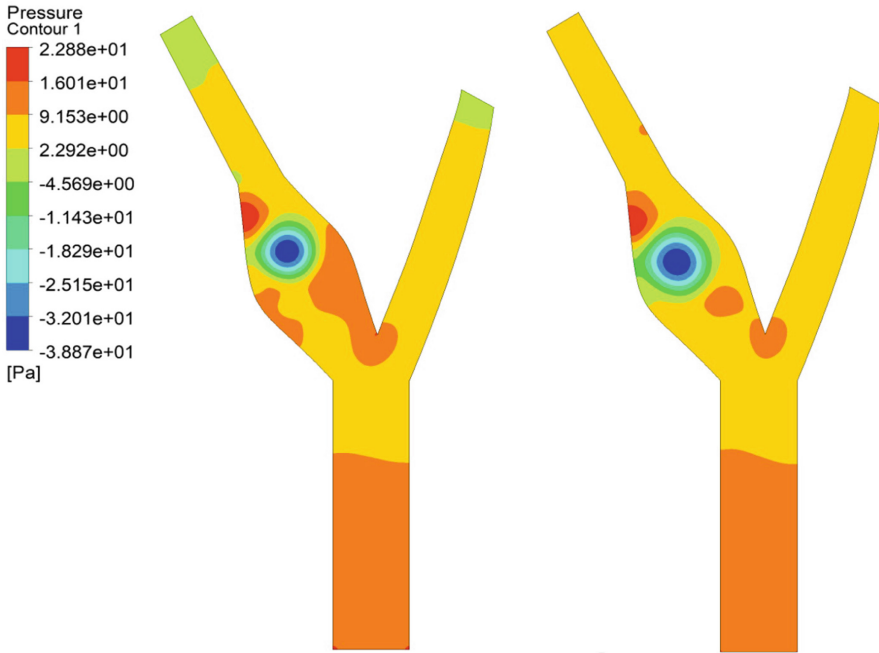


Fig. 5. Pressure Contour around the bifurcation of carotid artery at different time steps at $t = 0.2$ and $t = 0.4$

Table 3. Geometry specification of vessel diameter and the location

GEOMETRY SPECIFICATION	DIMENSION (MM)
Length of the CCA	41
Diameter of CCA	8
Length of ICA	36
Diameter of ICA	5.6
Diameter of ECA	4.6
Length of ECA	30
Diameter of ICB	8.9
Wall thickness	0.2

The regular and irregular blood flow patterns were analysed in the rectangular tube and in vasodilation, respectively, for incompressible fluid in the subparts of the carotid artery. This regular and irregular have been done to determine the behaviour of blood flow patterns in the uniform and dilation areas. The density and the dynamic viscosity of blood were used as 1060 kg/m^3 and 0.04 Pa.s respectively. The inflow boundary condition was considered as parabolic, and the outlet boundary condition was set to zero external force. Laminar flow occurs

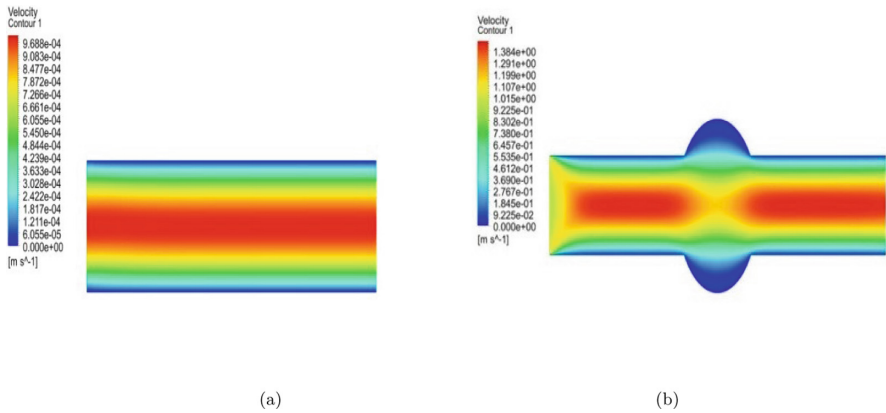


Fig. 6. Blood velocity profile with regular and irregular flow pattern (6a) Laminar flow in Tubular domain, (6b) vasodilation

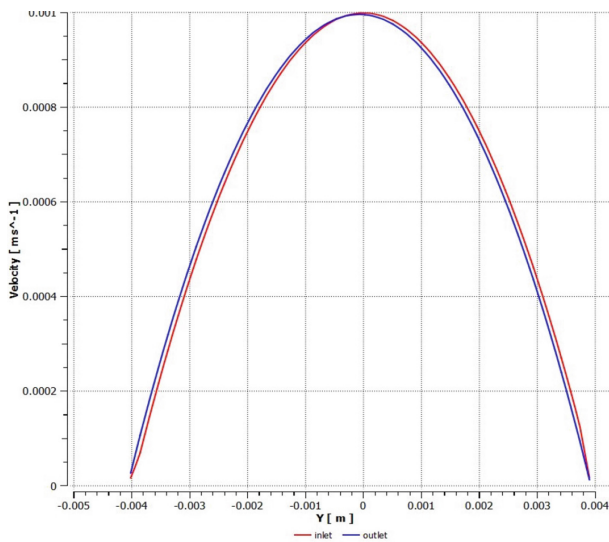


Fig. 7. Parabolic velocity profile at inlet and out of Tubular domain

where there is a uniform flow, as shown in Fig. 6a. The turbulent flow occurs in the area where there is an irregular flow due to the blockage and constrictions. The turbulent flow generally produces a non-parabolic velocity profile because, in turbulent flow, the stream of fluid mixes both types radially and axially. These flow models were analysed using the same parameters and presented in Fig. 6 (Fig 7).

4 Conclusion

The objective of this research is to present a simplified model for the cardiovascular system. The analysis of the blood flow profile in 2D using the Navier-Stokes equation as the governing equations for the incompressible Newtonian fluid. The blood flow pattern was computed in the idealised geometry of tubular and dilation, which leads to analysis in the carotid artery's idealised 2D geometry. The idealised 2D carotid artery geometry parameters were taken from [11, 26]. Based on the results, we concluded that the numerical study of the generalised Newtonian 2D model of blood flow can be solved very well. In this model, the blood flow is determined by dividing the flow analysis into two different patterns, which are regular and irregular blood flow patterns analysed in the rectangular tube and in vasodilation, respectively, and the existence of reverse flow in the area of the internal carotid artery near the non-dividing wall. In the simulation of flow velocity in a rectangular tube domain, laminar flow was obtained, with a maximum velocity field of 9.688×10^{-4} m/s. In the simulation of vasodilation, we obtained the irregular flow pattern, and the maximum velocity was found 1.384 m/s for the vasodilation prototype simulation. The blood flow pattern simulation about the bifurcation in the carotid artery was done at the inlet by using the same fluid quantities of blood, parabolic velocity profile, and boundary conditions. There was no external force considered at the outlet of the both external carotid artery and the internal carotid artery. The determination of the convergence of the solution was crucial on account of the boundary value problem and the complexity of the equation. In general, this paper shows quite good qualitative agreement with the nonlinearity of the problem and the multi-scale modelling based on the initial point. The modeling around the bifurcation of the carotid artery was done using ANSYS 19.1 CAD software and numerically solved to produce a valid simulation of flow. This research work is only the initial point for the bigger project with the biological parameters and 3D realistic geometry reconstructed from the patient-specific medical images. We could also work on the detection of possible multiplaque formation regions by computing the WSS and the blood flow behaviour.

References

1. Avolio, A.P.: Multi-branched model of the human arterial system. *Med. Biol. Eng. Comput.* **18**, 709–18 (1980)
2. Milner, J.S., Moore, J.A., Rutt, B.K., Steinman, D.A.: Hemodynamics of human carotid artery bifurcations: computational studies in models reconstructed from magnetic resonance imaging of normal subjects. *J. Vasc. Surg.* **28**, 143–156 (1998). official publication, the Society for Vascular Surgery [and] International Society for Cardiovascular Surgery, North American Chapter
3. Gijsen, F.J., van de Vosse, F.N., Janssen, J.D.: The influence of the non-Newtonian properties of blood on the flow in large arteries: steady flow in a carotid bifurcation model. *J. Biomech.* **32**, 601–608 (1999)
4. Formaggia, L., Quarteroni, A., Veneziani, A.: *Cardiovascular Mathematics: Modeling and Simulation of the Circulatory System*, vol. 1 (2009)

5. Bharadvaj, B.K., Mabon, R.F., Giddens, D.P.: Steady flow in a model of the human carotid bifurcation. part I-flow visualization. *J. Biomech.* **15**, 349–62 (1982)
6. Bharadvaj, B.K., Mabon, R.F., Giddens, D.P.: Steady flow in a model of the human carotid bifurcation part 2 - laser-doppler anemometer measurements. *J. Biomech.* **15**, 363–78 (1982)
7. Cardamone, L., Valentin, A., Eberth, J.F., Humphrey, J.D.: Modelling carotid artery adaptations to dynamic alterations in pressure and flow over the cardiac cycle. *Math. Med. Biol. J. IMA* **27**, 343–71 (2010)
8. Chen, J., Lu, X.-Y.: Numerical investigation of the non-Newtonian pulsatile blood flow in a bifurcation model with a non-planar branch. *J. Biomech.* **39**, 818–32 (2006)
9. Xu, X.Y., Collins, M.W., Jones, C.J.H.: Flow studies in canine artery bifurcations using a numerical simulation method. *J. Biomech. Eng.* **114**, 504–11 (1992)
10. Marshall, I., Zhao, S., Papathanasopoulou, P., Hoskins, P., Xu, X.Y.: MRI and CFD studies of pulsatile flow in healthy and stenosed carotid bifurcation models. *J. Biomech.* **37**, 679–87 (2004)
11. Perktold, K., Rappitsch, G.: Computer simulation of local blood flow and vessel mechanics in a compliant carotid artery bifurcation model. *J. Biomech.* **28**, 845–56 (1995)
12. Nosovitsky, V.A., Ilegbusi, O.J., Jiang, J., Stone, P.H., Feldman, C.L.: Effects of curvature and stenosis-like narrowing on wall shear stress in a coronary artery model with phasic flow. *Comput. Biomed. Res.* **30**, 61–82 (1997)
13. Myers, J.G., Moore, J.A., Ojha, M., Johnston, K.W., Ethier, C.R.: Factors influencing blood flow patterns in the human right coronary artery. *Ann. Biomed. Eng.* **29**, 109–120 (2001)
14. Yadav, R., Vashisth, S., Varma, R., Kumar, K.: Effect of flow velocity and pressure on carotid artery due to deposition of different shapes of plaque (2021)
15. Vashisth, S., Yadav, R., Verma, R.: Computer based methods to analyze carotid stenosis, pp. 267–269 (2017)
16. Sun, Z., Mwapatayi, B., Chaichana, T., Ng, C.: Hemodynamic effect of calcified plaque on blood flow in carotid artery disease: a preliminary study, pp. 1 – 4 (2009)
17. Puritipati, C., Keri, V., Kumar, N.: Hemodynamics of idealized carotid artery. In: MATEC Web of Conferences, vol. 144, p. 01020 (2018)
18. Smith, B.W., Andreassen, S., Shaw, G.M., Jensen, P.L., Rees, S.E., Chase, J.G.: Simulation of cardiovascular system diseases by including the autonomic nervous system into a minimal model. *Comput. Methods Programs Biomed.* **86**, 153–160 (2007)
19. Silva, T., Sequeira, A., Santos, R.F., Tiago, J.: Mathematical modeling of atherosclerotic plaque formation coupled with a non-Newtonian model of blood flow. In: Conference Papers in Mathematics, pp. 1–14 (2013)
20. Pedley, T.: The fluid mechanics of large blood vessels. SERBIULA (sistema Librum 2.0) (1982)
21. Berger, S.A., Jou, L.-D.: Flows in stenotic vessels. *Annu. Rev. Fluid Mech.* **32**, 347–382 (2000)
22. Kapur, J.: Mathematical models in biology and medicine. The Mathematics Student (2022)
23. De Hart, J., Peters, G.W.M., Schreurs, P.J.G., Baaijens, F.P.T.: A three-dimensional computational analysis of fluid-structure interaction in the aortic valve. *J. Biomech.* **36**, 103–12 (2003)

24. Fojas, J.J.R., De Leon, R.L.: Carotid artery modeling using the Navier-stokes equations for an incompressible, Newtonian and axisymmetric flow. *APCBEE Procedia* **7**, 86–92 (2013)
25. PZ. Annual review of fluid mechanics. *Environ. Softw.* **1**, 60 (1986)
26. Perktold, K., Resch, M.: Numerical flow studies in human carotid artery bifurcations: basic discussion of the geometric factor in atherogenesis. *J. Biomed. Eng.* **12**, 111–23 (1990)



The Effect of Peripheral Layer Thickness on Pulsatile Flow of Blood in Human Femoral Artery

K. Gayathri^(✉) and K. Shobika

Department of Mathematics, Amrita School of Physical Sciences, Amrita Vishwa Vidyapeetham, Coimbatore, India
K_gayathri@cb.amrita.edu

Abstract. Peripheral artery disease is one among the circulatory problems in the cardiovascular system in which narrowed artery reduces blood to limbs. This paper focus on the effect of peripheral layer thickness on velocity of blood and on the hemodynamic parameters such as wall shear stress and oscillatory shear index in human femoral artery using two-layered model. Owing to the necessity of clinically reliable estimates for hemodynamic parameters, at the time of prognosis and diagnosis of peripheral diseases, in this investigation the physiological pressure gradient of human femoral artery was taken from cardiology literature and is described using McDonalds model. To the best of our knowledge, this is the first primitive study of this kind. Governing equations are solved analytically. Velocity, wall shear stress and oscillatory shear index for different peripheral layer thicknesses are obtained. Dimensional graphs for velocity and wall shear stress are plotted using MATLAB. Quantitative and qualitative analysis shows that the velocity as well as oscillatory shear index in the core region increases as the peripheral layer thickness decreases. Results are interpreted medically which helps to improve the understanding of the state of artery. Comparison of our results with that of single layer model in the literature indicates that single layer model overestimates core region velocity by approximately 65% and underestimates wall shear stress and oscillatory shear index by 84% and 88% respectively. Primitive model employed in the current investigation recommends for more number of subject specific studies before benchmarking the thresholds for the clinically crucial hemodynamic parameters.

Keywords: Hemodynamic Wall Parameter · Wall Shear Stress · Oscillatory Shear Index · Femoral Pressure Gradient

1 Introduction

Peripheral Artery Disease (PAD) is a chronic disease of peripheral vasculature [1]. PAD is the indication of systemic atherosclerosis in which the lumen of the lower extremity arteries gradually gets occluded resulting in the limb associated complications such as reduction of blood flow to the limbs [1, 2]. Furthermore, occlusion of arterial lumen in

one segment should not be understood as a localized or isolated disorder/disease but as a marker for possibly insidious diseases in other vascular regions [3, 4]. PAD is underdiagnosed, undertreated and poorly understood among other cardiovascular diseases [1, 5, 6]. Indeed, subjects with PAD have an increased rate of myocardial infarction, stroke and cardiovascular death [1, 5, 6]. However, symptoms of PAD may range from intermittent claudication to ulceration and gangrene [2, 5]. Skau and Jonsson [4] in their epidemiologic studies concluded that nearly 1% to 2% of women and 2% to 3% of men of 60 + years had mild to moderate symptoms of claudication. Also, it is worth noticing here that the pathology of PAD is continuously increasing among the younger people due to population ageing, though it was reasonably infrequent in this cluster [6]. The three most common lower extremity artery in human beings which are prone to PAD are iliac, femoral and infrapopliteal artery. This motivated us to investigate the hemodynamics in the human femoral artery in the present study. One can refer to the critical review on PAD by Weitz et al. [5] and epidemiological inference on PAD by Shu and Santulli [6] and Skau and Jonsson [7] to gain knowledge in this aspect in a broader perspective.

Incidentally, in 1989, Texon [8] concluded that the hemodynamic factors were the main causative factors in localization, inception and progressive development of atherosclerosis. Numerous hemodynamic near wall parameters have been introduced in last decades to measure the risk of vascular diseases such as atherosclerosis and aneurysm [9, 10]. Two such medically relevant near wall parameters are Wall Shear Stress (WSS) and Oscillatory Shear Index (OSI) whose significance are rendered in Sect. 3. The former helps quantifying the magnitude change in the WSS vector whereas the later, tells how much WSS vector fluctuates near the arterial wall in a cardiac cycle.

In 2001, Chaturani and Bharathiya [11] modelled blood flow through hemodialysers as a flow through uniform parallel plate as two-layered model. Further, they had observed that the flow of suspensions has the tendency to leave a particle free layer near the wall. In addition, they inferred that their results might help reducing the cell injury and the dialysis time. In their model, the physiological pressure gradient was taken as constant [12]. It is worth recalling the fact here that the pressure gradient, the driving force for the blood, is periodic in nature because of the rhythmic pumping mechanism of the heart in each cardiac cycle [12]. Although the modeling of pressure gradient waveform was not suitable, Chaturani and Bharathiya [11] have established the importance of two layered model approximation in the hemodynamic studies.

Hemodynamics eventually instigates with the heart that supplies blood throughout the cardiovascular system. Thus, the real challenge in hemodynamic studies depends on modeling the pressure gradient waveform more appropriately in such a way that it captures the pulsatility in a less unrealistic manner. It is a real challenge owing to the fact that the pressure gradient is not only pulsatile in nature but also it varies subject to subject and furthermore it varies from artery to artery within a subject. On the other hand, Womersely and McDonald in 1955, categorically established that reproducing the physiological pressure gradient waveform as a Fourier series with adequate number of harmonic describes the waveform less unrealistic [13, 14, 18, 19]. Following Womersely and McDonald [12], Gayathri and Shailendhran 2014, made a comparative study among the existing models employed in the mathematical literature to describe the pressure gradient waveform using single layered model and established that McDonalds model

captures pulsatility in a more appropriate way. In addition, they estimated hemodynamic wall parameters such as WSS and OSI for the human arteries such as the femoral, the brachial and the pulmonary artery and rendered inferences, which are clinically valuable [17].

Thus, in the present study a maiden attempt is made to investigate the effect of peripheral layer thickness on the velocity of blood in the lumen of the human femoral artery and on the hemodynamic wall parameters such as WSS and OSI. Blood flow in the human femoral artery is assumed to be laminar pulsatile flow through a uniform two layered channel. Further, no-slip condition is employed at the lumen wall interface. Owing to the necessity of clinically reliable estimates for hemodynamic wall parameters during the prognosis and diagnosis of peripheral artery diseases, in this investigation the physiological pressure gradient of the human femoral artery was taken from cardiology literature and is described using McDonald's model. McDonald's model captures the pulsatility in the waveform in a less unrealistic manner. Governing equations are solved analytically for velocity and WSS. Dimensional graphs are plotted using MATLAB. The obtained results are compared with the results reported in the hemodynamic literature and are interpreted in such a way that it can be useful for clinicians during the assessment of vascular diseases.

2 Mathematical Formulation and Solution

Consider a laminar pulsatile flow of blood in a two-layered uniform channel of width $2h$ bounded by the rigid walls at $y = \pm h$ with δ as the thickness of the peripheral layer. Blood flow in the lumen of the artery is approximated as a flow through a two layered uniform channel. Further, blood is assumed to be Newtonian. Consider the vector form of continuity and Navier-Stokes equations in the core and peripheral region as

$$\nabla \cdot \bar{q}_c = 0; \nabla \cdot \bar{q}_p = 0 \quad (1)$$

$$\rho \left(\frac{\partial \bar{q}_c}{\partial t} + (\bar{q}_c \cdot \nabla) \bar{q}_c \right) = -\nabla p + \mu_c \nabla^2 \bar{q}_c \quad (2)$$

$$\rho \left(\frac{\partial \bar{q}_p}{\partial t} + (\bar{q}_p \cdot \nabla) \bar{q}_p \right) = -\nabla p + \mu_p \nabla^2 \bar{q}_p \quad (3)$$

where \bar{q}_c and \bar{q}_p denote the velocity of blood in the core and peripheral region respectively. μ_c, μ_p denote the viscosity in the core and peripheral region respectively.

Womersley and McDonald [12] established that the arterial system could be considered as a linear system and that any harmonic component of pressure wave could be related to the same harmonic of another pressure or flow wave recorded at the same time and to no other harmonic. The physiological pressure gradient of the human femoral artery is approximated by McDonald's model [12, 15] as

$$\begin{aligned} -\frac{\partial p}{\partial x} &= A_0 + \sum_{n=1}^m (A_n \cos(n\omega t) + B_n \sin(n\omega t)) \\ &= a_0 + \sum_{n=1}^m (a_n \cos(n\omega t - \alpha_n)) \end{aligned}$$

$$= a_0 + Re\left(\sum_{n=1}^m a_n e^{i(n\omega t - \alpha_n)}\right) \tag{4}$$

where $a_0 = A_0$, $a_n = \sqrt{A_n^2 + B_n^2}$, $\alpha_n = \arctan \frac{B_n}{A_n}$ and “ m ” denotes the number of harmonics.

Accordingly, the velocities and $u_c(y, t)$ and $u_p(y, t)$ in the core and peripheral region can be modelled respectively as follows:

$$u_c(y, t) = \bar{u}_c(y) + Re\left(\sum_{n=1}^m \tilde{u}_{c_n}(y) e^{i(n\omega t - \alpha_n)}\right) \tag{5}$$

$$u_p(y, t) = \bar{u}_p(y) + Re\left(\sum_{n=1}^m \tilde{u}_{p_n}(y) e^{i(n\omega t - \alpha_n)}\right) \tag{6}$$

where the symbol “ $-$ ” denotes the steady part and the symbol “ \sim ” denotes the unsteady part. By plugging in the Eqs. (4)–(6) in the vector form of governing Eqs. (1)–(3) and expressing in Cartesian coordinates, we get the dimensional form of steady part and the n^{th} harmonic of the unsteady part of the governing equation of the flow in the core and the peripheral region as follows

$$0 = -\frac{\partial \bar{p}}{\partial x} + \mu_c \frac{\partial^2 \bar{u}_c}{\partial y^2} \tag{7}$$

$$0 = -\frac{\partial \bar{p}}{\partial x} + \mu_p \frac{\partial^2 \bar{u}_p}{\partial y^2} \tag{8}$$

$$\rho \frac{\partial \tilde{u}_{c_n}}{\partial t} = -\frac{\partial \tilde{p}}{\partial x} + \mu_c \frac{\partial^2 \tilde{u}_{c_n}}{\partial y^2} \tag{9}$$

$$\rho \frac{\partial \tilde{u}_{p_n}}{\partial t} = -\frac{\partial \tilde{p}}{\partial x} + \mu_p \frac{\partial^2 \tilde{u}_{p_n}}{\partial y^2} \tag{10}$$

with no-slip boundary [20] conditions

$$u_p = 0 \text{ when } y = h \tag{11}$$

$$u_p = 0 \text{ when } y = -h \tag{12}$$

$$u_p = u_c \text{ when } y = h - \delta \tag{13}$$

$$u_p = u_c \text{ when } y = -(h - \delta) \tag{14}$$

The characteristic length (h), time ($1/\omega$), and velocity ($h\omega$) are used for non-dimensionalization. Accordingly, the Eqs. (7)–(14) takes the non-dimensional form as in the Eqs. (15)–(26). Further, the steady part of velocity in the peripheral and core region in the non-dimensional forms are

$$\frac{\partial^2 \bar{u}_p^*}{\partial y^{*2}} = E_0 \text{ where } E_0 = -a_0 \frac{h}{\mu_p \omega} \tag{15}$$

$$\frac{\partial^2 \bar{u}_c^*}{\partial y^{*2}} = F_0 \text{ where } F_0 = -a_0 \frac{h}{\mu_c \omega} \quad (16)$$

with the steady part boundary conditions in the non-dimensional form

$$\bar{u}_p^* = 0 \text{ when } y^* = 1 \quad (17)$$

$$\bar{u}_p^* = 0 \text{ when } y^* = -1 \quad (18)$$

$$\bar{u}_p^* = \bar{u}_c^* \text{ when } y^* = 1 - \frac{\delta}{h} \quad (19)$$

$$\bar{u}_p^* = \bar{u}_c^* \text{ when } y^* = -\left(1 - \frac{\delta}{h}\right) \quad (20)$$

Similarly, the n^{th} harmonic of unsteady part of velocity in peripheral and core region in the non-dimensional forms are

$$\frac{\partial^2 \tilde{u}_{p_n}^*}{\partial y^{*2}} - G_n^2 \tilde{u}_{p_n}^* = E_n \quad (21)$$

$$\frac{\partial^2 \tilde{u}_{c_n}^*}{\partial y^{*2}} - I_n^2 \tilde{u}_{c_n}^* = F_n \quad (22)$$

with the n^{th} harmonic of unsteady part boundary conditions in the non-dimensional form

$$\tilde{u}_{p_n}^* = 0 \text{ when } y^* = 1 \quad (23)$$

$$\tilde{u}_{p_n}^* = 0 \text{ when } y^* = -1 \quad (24)$$

$$\tilde{u}_{p_n}^* = \tilde{u}_{c_n}^* \text{ when } y^* = 1 - \frac{\delta}{h} \quad (25)$$

$$\tilde{u}_{p_n}^* = \tilde{u}_{c_n}^* \text{ when } y^* = -\left(1 - \frac{\delta}{h}\right) \quad (26)$$

where $E_n = -\frac{a_n h}{\mu_p \omega}$, $F_n = -\frac{a_n h}{\mu_c \omega}$, $G_n = \sqrt{i n \alpha_p^2}$, $I_n = \sqrt{i n \alpha_c^2}$; $\alpha_p = h \sqrt{\frac{\omega \rho}{\mu_p}}$, $\alpha_c = h \sqrt{\frac{\omega \rho}{\mu_c}}$ are known as Womersley number.

On solving the above equations analytically, we arrive at the velocity of blood in the peripheral and core region as

$$u_p(y^*, t) = \frac{E_0(y^{*2} - 1)}{2} + Re \sum_{n=1}^m [\tilde{\chi}_{p_n}(y^*) e^{i(n\omega t - \alpha_n)}] \quad (27)$$

$$u_c(y^*, t) = \frac{1}{2} \left(F_0 y^{*2} - E_0 + \left(\frac{h - \delta}{h} \right)^2 (E_0 - F_0) \right) + Re \sum_{n=1}^m [\tilde{\chi}_{c_n}(y^*) e^{i(n\omega t - \alpha_n)}] \quad (28)$$

where

$$\tilde{\chi}_{p_n}(y^*) = \frac{E_n}{G_n^2} \operatorname{sech}(G_n) \cosh(G_n y^*) - \frac{E_n}{G_n^2}$$

$$\tilde{\chi}_{c_n}(y^*) = \left(\frac{F_n}{I_n^2} \operatorname{sech} \left[I_n \left(\frac{h-\delta}{h} \right) \right] - \frac{\dot{E}_n}{G_n^2} \operatorname{sech} \left[I_n \left(\frac{h-\delta}{h} \right) \right] + \frac{E_n}{G_n^2} \operatorname{sech}(G_n) \right) \cosh[I_n(y^*)] - \frac{F_n}{I_n^2}$$

3 Significance of Hemodynamic Near Wall Parameters

Hemodynamics caused by blood flow generates multiple mechanical forces that directly act on the endothelial surface of vessel walls [18, 19]. Normal hemodynamic conditions guide development during embryogenesis and remodelling to optimize the blood flow to tissues throughout postnatal and adult life. However, disorder in hemodynamics leads to the exacerbation or acceleration of cardiovascular diseases [1]. It is to be noted that the vital hemodynamic near wall parameters whose accurate measures are crucial during the clinical assessment of vascular diseases are wall shear stress and oscillatory shear index [18, 19]. Elaborate discussion on the significance of these parameters are rendered in this section.

3.1 Wall Shear Stress

WSS is the frictional force exerted by the moving blood on the arterial wall and is defined as the viscosity times the shear rate $\partial u/\partial y$ near the wall. Quantification of WSS can be made by computing the time averaged WSS over the cardiac cycle. The segments of unidirectional to mild fluctuation in the direction of WSS vector results in elongated and aligned endothelial cells, which form tight intracellular junctions. Any deviations from this situation can be risky [18, 19]. The arterial segment for which time averaged WSS value less than $0.04 Pa$ is atherogenic and is classified as atherosclerotic prone region whereas in the disease free zone, this value ranges between $1 Pa$ to $7 Pa$ [9, 17]. One can refer to the review articles by Perter F Davis [18] and Ku [19] for more details.

3.2 Oscillatory Shear Index

The dimensionless quantity OSI has been developed to characterize the areas of fluctuating shear direction in a cardiac cycle. The original mathematical definition for OSI developed by He and Ku in 1986 was modified by He and in 1996 [10]. However, the widely used alternative definition for OSI is

$$OSI = 0.5 \times \left(1 - \frac{\frac{1}{T} \left| \int_0^T \tau dt \right|}{\frac{1}{T} \int_0^T |\tau| dt} \right) \tag{29}$$

This ratio varies between 0 and 0.5 [10]. The region where the OSI is greater than 0.3 is considered atherogenic and leaky to atherogenic particles. In the low shear region, high OSI indicates high vulnerability to wall rupture [10]. This metric captures the directional change in WSS vector in a cardiac cycle. The estimated value of OSI helps to characterize the regions of varying shear direction which in turn helps to gain better knowledge on the endothelial wall functionality [10].

4 Result

The parameter values used during the computation are as follows: density of the blood $\rho = 1050 \text{ kg m}^{-3}$, viscosity of the blood in peripheral and core regions are $0.0012 \text{ kg m}^{-1} \text{ s}^{-1}$ [11] and $0.004 \text{ kg m}^{-1} \text{ s}^{-1}$ and the heart frequency is 1.2 Hz which are often used in hemodynamic studies [17]. The geometry of the human femoral artery is approximated as the flow through two parallel plates and hence the height of the channel is chosen to be the radius of the femoral artery $h = 0.0033 \text{ m}$ [17]. McDonald model is used to reproduce the physiological pressure gradient waveform of human femoral artery which was taken from cardiology literature. The adequate number of harmonics in Fourier series expansion to reproduce the original waveform is $m = 50$ [17]. The thickness of the peripheral layer is denoted by δ and is varied from 10% of height (h) to 40% of the height (h) throughout the discussion. The estimated center line velocity, minimum and maximum velocity in core region for various peripheral layer thickness are tabulated in Table 1. Further, the mean WSS, minimum and maximum value of WSS and OSI in core and peripheral region for various peripheral layer thickness are tabulated in Table 2. and Table 3. respectively. The dimensional graphs for the center line velocity and WSS of the human femoral artery in core and peripheral region for various peripheral layer thicknesses are depicted in Fig. 1, Fig. 2 and 3.

Table 1. Mean center line velocity, Minimum and Maximum velocity of human femoral artery in Core region for various peripheral layer thickness.

Thickness of Peripheral Layer	Mean Centerline Velocity (m/s)	Maximum Velocity (m/s)	Minimum Velocity (m/s)
40% of h	0.0631	0.8004 (0.00168 sec)	-0.5291 (0.4477 sec)
30% of h	0.0632	0.0632 (0.00084 sec)	-0.4087 (0.4477 sec)
20% of h	0.0634	0.4782 (0.00168 sec)	-0.2696 (0.4486 sec)
10% of h	0.0636	0.0636 (0.00084 sec)	-0.1121 (0.4477 sec)

Table 2. Mean WSS, Minimum and Maximum WSS, OSI of human femoral artery in Core region for various peripheral layer thickness.

Thickness of Peripheral Layer	Mean WSS (Pa)	Maximum WSS (Pa)	Minimum WSS (Pa)	OSI
40% of h	-0.0386	0.2205 (0.6661 sec)	-0.2517 (0.07476 sec)	0.3633
30% of h	-0.0386	0.2639 (0.6653 sec)	-0.2876 (0.07392 sec)	0.3819
20% of h	-0.0386	0.3501 (0.6619 sec)	-0.3602 (0.06804 sec)	0.3961
10% of h	-0.0386	0.3509 (0.6602 sec)	-0.3605 (0.07056 sec)	0.4073

Table 3. Mean WSS, Minimum and Maximum WSS, OSI of human femoral artery in peripheral region for various peripheral layer thickness.

Thickness of Peripheral Layer	Mean WSS (Pa)	Maximum WSS (Pa)	Minimum WSS (Pa)	OSI
40% of h	-0.0383	0.2372 (0.4267 <i>sec</i>)	-0.3367 (0.7972 <i>sec</i>)	0.3168
30% of h	-0.0383	0.2841 (0.4242 <i>sec</i>)	-0.3884 (0.7988 <i>sec</i>)	0.3422
20% of h	-0.0383	0.3315 (0.4225 <i>sec</i>)	-0.4392 (0.7988 <i>sec</i>)	0.3617
10% of h	-0.0383	0.3793 (0.4192 <i>sec</i>)	-0.4882 (0.7997 <i>sec</i>)	0.3772

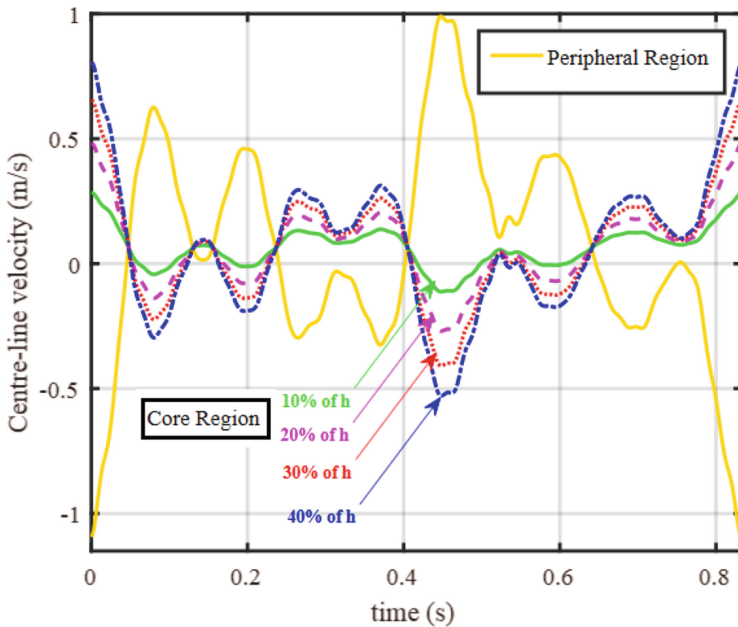


Fig. 1. Center line velocity of blood in the peripheral and core region of human femoral artery for various peripheral layer thickness.

5 Discussion

PAD is an atherosclerotic peripheral vascular disease of the lower extremities associated with high cardiovascular mortality [1–3]. To the best of our knowledge, this is the first elaborate study investigating the hemodynamics in the human femoral artery by describing the physiological pressure gradient using McDonald’s model in two layered blood flow model. All the results obtained in the present investigation reduces to the results reported by Chaturani and Bhraithiya [11] when the pressure gradient is taken as constant. At the same time, the single layer approximation of the present study provides all the results reported by Gayathri and Shaiendhra [17]. This validates our present model.

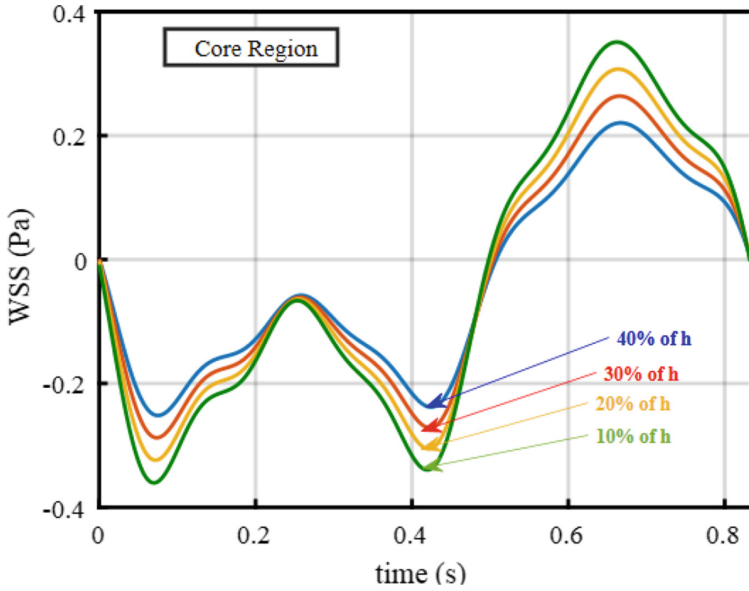


Fig. 2. WSS in core region of human femoral artery for various peripheral layer thickness.

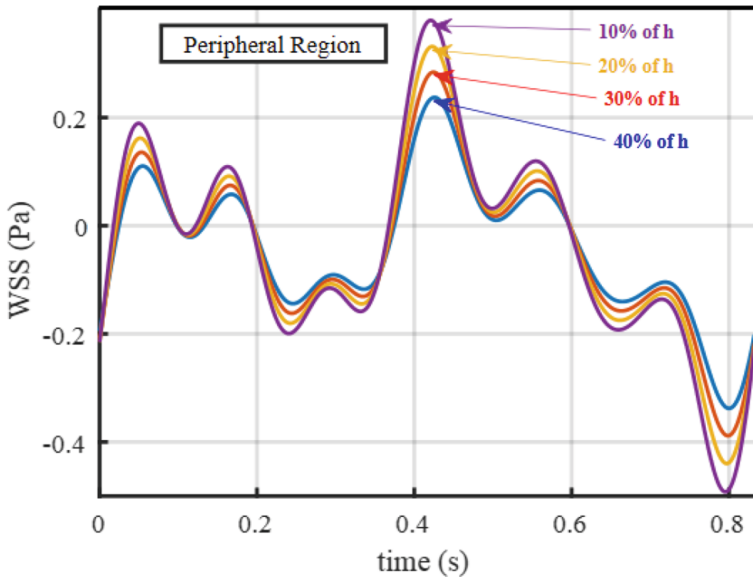


Fig. 3. WSS in peripheral region of human femoral artery for various peripheral layer thickness.

In the peripheral region, the estimated mean center line velocity of the human femoral artery is 0.0651 ms^{-1} and the maximum and minimum velocities are respectively 0.9907 ms^{-1} at 0.4477 s and -1.082 ms^{-1} at 0.00168 s whatever be the peripheral

layer thickness (Fig. 1). At the same time, in the core region, as the peripheral layer thickness decreases from 40% of h to 10% of h , the mean center line velocity of the femoral artery increases from 0.0631 ms^{-1} to 0.0636 ms^{-1} (ref Table 1.). It is approximately 0.79% increase in the velocity.

It is worth recalling here that the mean center line velocity of the human femoral artery in a single layer model reported in the literature is 0.1050 ms^{-1} [17]. Comparing the results obtained in the two layered model in the present study with that of the single layer model in [17] shows that the single layer model overestimates the core region velocity approximately by 65%. The estimated value of the average mass flux in the single layer model is approximately 0.0038 kgs^{-2} . At the same time, in the two layered model, the average mass flux is approximately 0.0023 kgs^{-2} . It is inferred from the obtained results that the presence of peripheral layer decreases the average mass flux by approximately 39%.

Further, the pulsatile velocity profiles for the two layered flow model depicted in Fig. 1 are much different from that of the one depicted for single layered flow model of the human femoral artery investigated by Gayathri and Shailendra [17]. In addition, it is inappropriate to compare the velocity profile given in [11] with the present study due to the fact that the pressure gradient is pulsatile in nature and is not constant as was chosen in [11]. Once again, the physiological pressure gradient is not only artery specific but also subject specific [17]. Furthermore, for estimating the near wall parameter, the WSS, it is necessary to measure the blood flow velocity gradient near the vessel wall (wall shear rate). As a consequence, a small change in the velocity can significantly affect the WSS and hence the metric OSI.

The estimated value of mean WSS is -0.0383 Pa in the peripheral region whereas it is -0.0386 Pa in the core region of the human femoral artery in the two-layered model. It is observed that the mean WSS of femoral artery is unchanged as the peripheral layer thickness decreases from 40% of h to 10% of h both in peripheral and core region. Unlike the mean WSS, the maximum and minimum values of mean WSS in peripheral and core region shows decreasing trend as the peripheral layer thickness decreases as is tabulated in Table 2. and in Table 3. respectively. Further, Fig. 2 and Fig. 3 depicts the dimensional graphs of WSS in peripheral and core region of human femoral artery for various peripheral layer thickness respectively.

Indeed, Malek [9] documented that $|WSS| < \pm 0.4 \text{ Pa}$ is atherosclerotic prone zone. Moreover, Gayathri and Shailendra [17] in their hemodynamic study pertaining to single layered model reported that the mean WSS of the human femoral artery was -0.2545 Pa . This value is approximately 84% of decrease in the mean WSS when compared to the estimated mean WSS value in the core region of two-layered model. This justifies the need for two-layered model in the hemodynamic studies. Furthermore, the obtained value of WSS in the present study indicates that the femoral segment of the subject with whom the pressure gradient waveform was measured is prone to atherosclerosis. In order to improve the understanding of severity of the damage caused to the arterial wall due to the low WSS range, the non-dimensional measure OSI has to be computed.

He and Ku [10] developed a metric to capture the directional changes in the WSS vector in a cardiac cycle termed as OSI. Once again, zero OSI value indicates the unidirectional alignment of WSS vector in a cardiac cycle whereas the OSI value of 0.5 indicates substantially high fluctuation in the direction of WSS vector near the wall in a cardiac cycle. In the peripheral region, the value of OSI increases from 0.3168(40% of h) to 0.3772(10% of h) as the peripheral layer thickness decreases from 40% of h to 10% of h . This is approximately 19% of increase in the value of OSI in peripheral region. At the same time, in the core region of the femoral artery, the value of OSI increases from 0.3633(40% of h) to 0.4073(10% of h) as the peripheral layer thickness decreases, which is approximately an increase by 12%. Since $|WSS| < \pm 0.4 Pa$ and $OSI > 0.3$, the femoral segment of the subject with whom the pressure gradient waveform was measured is more atherogenic.

It is also evident from Fig. 2 and Fig. 3 that the graph of WSS is changing the sign from negative to positive thrice in the peripheral region whereas it is only once in the core region as the peripheral layer thickness decreases from 40% of h to 10% of h in a cardiac cycle. It is worth recalling here that increase in the OSI value indicates the increase in the fluctuation of WSS vector near the wall in a cardiac cycle. In addition, the endothelial cell alignment may get modify as the WSS vector changes its direction quite often and this may widen up the endothelial junction gap. This may increase the chance for the lingering atherogenic particles near the wall to penetrate and getting deposited inside the wall resulting in the formation of plaque. However, Gayathri and Shailendra [17] in their hemodynamic study using single layered model reported that the value of OSI in the human femoral artery as 0.0454. OSI value reported by them [17] for single layer model is 88% lesser than the one obtained in the present analysis. This establishes the importance of two-layered model in hemodynamic studies.

In summary, all the results obtained in the present investigation reduces to the results reported by Chaturani and Bhrathiya [11] when the pressure gradient is assumed as constant and reduces to the results reported by Gayathri and Shailendra [17] when the two-layered model is approximated to the single layer model. As the peripheral layer thickness decreases, the mean center line velocity and OSI shows increasing trend. In addition, the presence of peripheral layer decreases the average mass flux by approximately 39% in comparison with the single layer model. Numerically insignificant changes in the estimated values of the near wall parameter as the peripheral layer thickness varies cannot be overlooked medically. More number of subject specific studies are recommended before benchmarking the results reported in this primitive study to practice it as clinical thresholds.

6 Conclusion

The drive for improvising the knowledge both biologically and medically on the hemodynamics in human vascular system is increasing over the years. To the best of our knowledge, this is the first elaborate study investigating the hemodynamics in the human femoral artery by describing the physiological pressure gradient using McDonald's model in two-layered blood flow model. The following are the main conclusions arrived in this study:

- Mean center line velocity in the core region increases by 0.79% as the peripheral layer thickness decreases from 40% of h to 10% of h . Although, no significant changes are noticed in the peripheral region.
- Estimated value of the average mass flux in the two layer model is approximately 0.0023 kgs^{-2} . Comparing the average mass flux with that of the single layer model, it is inferred that the presence of peripheral layer decreases the average mass flux by approximately 39%.
- Maximum and minimum values of mean WSS in the core and peripheral regions are not the same as though mean WSS is unaltered as the peripheral layer thickness decreases from 40% of h to 10% of h .
- OSI increases by 12% in the core region as peripheral layer thickness decreases from 40% of h to 10% of h whereas it increases by 19% in the peripheral region.
- Single layer model overestimates core velocity by 65%, underestimates core WSS and OSI by 84% and 88% respectively.

Primitive model employed in the current investigation recommends for more number of subject specific studies before benchmarking the thresholds for the clinically crucial hemodynamic near wall parameters.

References

1. Bevan, G.H., White Solaru, K.T.: Evidence based medical management of peripheral artery disease. *Arterioscler. Thromb. Vasc. Biol.* **40**(3), 541–553 (2020)
2. Mohler, E.R.: Peripheral arterial disease – identification and implications. *Arch. Intern. Med.* **163**, 2306–2314 (2003)
3. Dormandy, J., Heeck, L., Vig, S.: Lower extremity arteriosclerosis as a reflection of a systemic process: implications for concomitant coronary and carotid disease. *Semin. Vasc. Surg.* **12**, 118–122 (1999)
4. Criui, K.H., Denenberg, J.O.: The generalized nature of atherosclerosis: how peripheral arterial disease may predict adverse events from coronary artery disease. *Vasc. Med.* **3**, 241–245 (1998)
5. Weitz, J.I., et al.: Diagnosis and treatment of chronic arterial insufficiency of the lower extremities: a critical review. *Circulation* **94**(11), 3026–3049 (1996)
6. Shu, J., Santulli, G.: Update on peripheral artery disease: epidemiology and evidence-based facts. *Atherosclerosis* **275**, 379–381 (2018)
7. Skau, T., Jonsson, H.: Prevalence of symptomatic leg ischaemic in a swedish community – an epidemiological study. *Eur. J. Vasc. Surg.* **7**, 432–437 (1993)
8. Texon, M.: The cholesterol-heart disease hypothesis (critique) – time to change course? *Bull. N. Y. Acad. Med.* **65**, 836–841 (1989)
9. Malek, A.M., Alper, S.L., Izumo, S.: Hemodynamic shear stress and its role in atherosclerosis. *J. Am. Med. Assoc.* **282**, 2035–2042 (1999)
10. He, X., Ku, D.N.: Pulsatile flow in the human left coronary artery bifurcation: average conditions. *J. Biomech. Eng.* **118**, 74–82 (1996)
11. Chaturani, P., Saxena Bharathiya, S.: Two layered Magnetohydrodynamic flow through parallel plates with applications. *Indian J. Pure Appl. Math.* **32**(1), 55–68 (2001)
12. Burton, A.C.: *Physiology and Biophysics of the Circulation*. Book Medical Publisher, Chicago (1966)

13. Nichols, W.W., O'Rourke, M.F.: *McDonald's Blood Flow in Arteries, Theoretical Experimental and Clinical Principles*. Oxford University Press, New York (2005)
14. Chaturani, P., Saxena Bharatiya, S.: Magnetic fluid model for two phase pulsatile flow of blood. *Acta Mech.* **149**, 97–114 (2001)
15. Tabassum, M.F., Saeed, M., Akgul, A., Farman, M., Akram, S.: Solution of chemical dynamic optimization systems using novel differential gradient evolution algorithm. *Phys. Scr.* **96**(3), 035212 (2021)
16. Ali, R., Akgül, A., Asjad, M.I.: Power law memory of natural convection flow of hybrid nanofluids with constant proportional caputo fractional derivative due to pressure gradient. *Pramana* **94**(1), 1–11 (2020). <https://doi.org/10.1007/s12043-020-01997-8>
17. Gayathri, K., Shailendra, K.: Pulsatile blood flow in large arteries: comparative study of Burton's and McDonald's models. *Appl. Math. Mech.* **35**(5), 575–590 (2014). <https://doi.org/10.1007/s10483-014-1814-7>
18. Davis, P.F.: Flow mediated endothelial mechanotransduction. *Physiol. Rev.* **75**, 519–560 (1995)
19. Ku, D.N.: Blood flow in arteries. *Annu. Rev. Fluid Mech.* **29**, 399–435 (1997)
20. Thiagarajan, V., Purushothaman, R.K., Shailendra, K., Gayathri, K.: Pulsatile blood flow through large arteries with BJR slip condition. In: *International Conference on Electrical Electronics, and Optimization Technique* (2016)



A Computational Study of Local Fractional Helmholtz and Coupled Helmholtz Equations in Fractal Media

Devendra Kumar¹(✉), Hassan Kamil Jassim², Jagdev Singh³,
and Ved Prakash Dubey⁴

¹ Department of Mathematics, University of Rajasthan, Jaipur 302004, Rajasthan, India
devendra.maths@gmail.com

² Department of Mathematics, Faculty of Education for Pure Sciences, University of Thi-Qar,
Nasiryah, Iraq
hassankamil@utq.edu.iq

³ Department of Mathematics, JECRC University, Jaipur, Rajasthan, India

⁴ Faculty of Mathematical and Statistical Sciences, Shri Ramswaroop Memorial University,
Barabanki 225003, Uttar Pradesh, India

Abstract. In this manuscript, an approximate analytical solution of the Helmholtz and coupled Helmholtz equations of fractional order is obtained using local fractional Sumudu decomposition method (LFSDM). The Helmholtz equations play an important role in the study of various physical problems such as seismology, tsunamis, optics, acoustics, medical imaging, electrostatics and quantum mechanics. To validate the efficiency and reliability of the employed scheme, the Helmholtz and coupled Helmholtz equations are considered. The results obtained with this scheme are in a good agreement with previous works. Moreover, the graphical presentations for obtained solutions are also illustrated for distinct values of order of a partial derivative.

Keywords: Helmholtz equations · Local fractional derivative · Fractal media · Sumudu transform

1 Introduction

In last decades, fractional calculus has been applied very frequently in the field of applied sciences and technology. Actually, the area of fractional calculus is concerned with integral and derivatives of real order and it significantly handles scientific and engineering problems by formulating them in the form of fractional differential equations such as the diffusion equations [1], the gas dynamic equation [2], telegraph equation [3], wave equation [4–7], Fokker-Planck equation [8, 9], Laplace equation [10], Klein-Gordon equations [11], Helmholtz equation [12], and Burger's equations [13].

Various local fractional schemes have been used to solve the local fractional PDEs (LFPDEs) such as the local fractional decomposition method [13–15], local fractional variational iteration method [16–22], local fractional differential transform method [23, 24], local fractional series expansion method [25, 26], local fractional Sumudu decomposition method [27], local fractional reduce differential transform method [28], local fractional Laplace variational iteration method [29], local fractional Laplace decomposition method [30], and local fractional Laplace homotopy perturbation method [31, 32]. This paper presents the copulation of LFST and LFADM, which is called as LFSDM, to solve the local fractional Helmholtz and coupled Helmholtz equations.

The paper is arranged in the following way: The basic definitions for calculus and fractional integration are presented in Sect. 2, the method used are analyzed in Sect. 3, illustrative examples are given that explain the effectiveness of the method proposed in Sect. 4, the numerical results and discussion are described in the Sect. 5 and finally, the conclusion is provided in Sect. 6.

2 Mathematical Fundamentals

Definition 2.1. The LF derivative of $\varphi(\mu)$ of order ε at μ_0 is [14–16]:

$$\varphi^{(\varepsilon)}(\mu_0) = \lim_{\mu \rightarrow \mu_0} \frac{\Gamma(1 + \varepsilon)[\varphi(\mu) - \varphi(\mu_0)]}{(\mu - \mu_0)^\varepsilon}, \quad 0 < \varepsilon \leq 1 \tag{1}$$

Definition 2.2. The Mittag-Leffler function is defined by [14]:

$$E_\varepsilon(\mu^\varepsilon) = \sum_{k=0}^{\infty} \frac{\mu^{k\varepsilon}}{\Gamma(1 + k\varepsilon)}, \quad \mu \in R, \quad 0 < \varepsilon \leq 1 \tag{2}$$

Definition 2.3. The LFST of $\varphi(\mu)$ given by [26]

$$ST_\varepsilon\{\varphi(\mu)\} = \frac{1}{\Gamma(1 + \varepsilon)} \int_0^\infty E_\varepsilon(-w^\varepsilon \mu^\varepsilon) \frac{\varphi(\mu)}{w^\varepsilon} (d\mu)^\varepsilon. \tag{3}$$

Following (4), its inverse formula is defined by

$$ST_\varepsilon^{-1}(ST_\varepsilon\{\varphi(\mu)\}) = \varphi(\mu), \quad 0 < \varepsilon \leq 1. \tag{4}$$

The properties for LFST are:

1. $ST_\varepsilon\left\{\frac{\mu^\varepsilon}{\Gamma(1+\varepsilon)}\right\} = w^\varepsilon.$
2. $ST_\varepsilon\left\{\frac{\partial^{m\varepsilon}\varphi(\mu,\tau)}{\partial\mu^{m\varepsilon}}\right\} = \frac{1}{w^{m\varepsilon}}\left[ST_\varepsilon\{\varphi(\mu,\tau)\} - \sum_{k=0}^{m-1} w^{k\varepsilon} \frac{\partial^{k\varepsilon}\varphi(0,\tau)}{\partial\tau^{k\varepsilon}}\right].$

3 Analysis of LFSDM

Let us consider the PDE with LFDOs:

$$L_\varepsilon \varphi(\mu, \tau) + R_\varepsilon \varphi(\mu, \tau) = g(\mu, \tau), \quad 0 < \varepsilon \leq 1 \tag{5}$$

where $L_\varepsilon \varphi(\mu, \tau) = \frac{\partial^{m\varepsilon}}{\partial \mu^{m\varepsilon}} \varphi(\mu, \tau)$, R_ε denotes linear LFDO, and $g(\mu, \tau)$ is the non-differentiable source term.

Applying the LFST on Eq. (5), and using the property of the LFST, we get

$$ST_\varepsilon \{\varphi(\mu, \tau)\} = \sum_{k=0}^{m-1} w^{k\varepsilon} \frac{\partial^{k\varepsilon} \varphi(0, \tau)}{\partial \tau^{k\varepsilon}} + w^{m\varepsilon} ST_\varepsilon \{g(\mu, \tau)\} - w^{m\varepsilon} ST_\varepsilon \{R_\varepsilon \varphi(\mu, \tau)\}. \tag{6}$$

Taking the inverse of LFST on Eq. (6), we have

$$\begin{aligned} \varphi(\mu, \tau) &= \sum_{k=0}^{m-1} w^{k\varepsilon} \frac{\partial^{k\varepsilon} \varphi(0, \tau)}{\partial \tau^{k\varepsilon}} \frac{\mu^{k\varepsilon}}{\Gamma(1 + k\varepsilon)} + ST_\varepsilon^{-1} [w^{m\varepsilon} ST_\varepsilon \{g(\mu, \tau)\}] \\ &\quad - ST_\varepsilon^{-1} [w^{m\varepsilon} ST_\varepsilon \{R_\varepsilon \varphi(\mu, \tau)\}]. \end{aligned} \tag{7}$$

Now, procedure of ADM suggests the decomposition of the unknown function $\varphi(\mu, \tau)$ as an infinite series in the following way

$$\varphi(\mu, \tau) = \sum_{n=0}^{\infty} \varphi_n(\mu, \tau). \tag{8}$$

By making use of the Eq. (8) in Eq. (7), it yields the following result:

$$\begin{aligned} \sum_{n=0}^{\infty} \varphi_n(\mu, \tau) &= \sum_{k=0}^{m-1} w^{k\varepsilon} \frac{\partial^{k\varepsilon} \varphi(0, \tau)}{\partial \tau^{k\varepsilon}} \frac{\mu^{k\varepsilon}}{\Gamma(1 + k\varepsilon)} + ST_\varepsilon^{-1} [w^{m\varepsilon} ST_\varepsilon \{g(\mu, \tau)\}] \\ &\quad - ST_\varepsilon^{-1} \left[w^{m\varepsilon} ST_\varepsilon \left\{ R_\varepsilon \sum_{n=0}^{\infty} \varphi_n(\mu, \tau) \right\} \right]. \end{aligned} \tag{9}$$

Matching both sides of (9) provides

$$\begin{aligned} \varphi_0(\mu, \tau) &= \sum_{k=0}^{m-1} w^{k\varepsilon} \frac{\partial^{k\varepsilon} \varphi(0, \tau)}{\partial \tau^{k\varepsilon}} \frac{\mu^{k\varepsilon}}{\Gamma(1 + k\varepsilon)} + ST_\varepsilon^{-1} [w^{m\varepsilon} ST_\varepsilon \{g(\mu, \tau)\}] \\ \varphi_1(\mu, \tau) &= -ST_\varepsilon^{-1} [w^{m\varepsilon} ST_\varepsilon \{R_\varepsilon [\varphi_0(\mu, \tau)]\}], \\ \varphi_2(\mu, \tau) &= -ST_\varepsilon^{-1} [w^{m\varepsilon} ST_\varepsilon \{R_\varepsilon [\varphi_1(\mu, \tau)]\}], \\ \varphi_3(\mu, \tau) &= -ST_\varepsilon^{-1} [w^{m\varepsilon} ST_\varepsilon \{R_\varepsilon [\varphi_2(\mu, \tau)]\}], \\ &\vdots \end{aligned} \tag{10}$$

The general form of above obtained local fractional recursive relations is

$$\begin{aligned} \varphi_0(\mu, \tau) &= \sum_{k=0}^{m-1} w^{k\varepsilon} \frac{\partial^{k\varepsilon} \varphi(0, \tau)}{\partial \tau^{k\varepsilon}} \frac{\mu^{k\varepsilon}}{\Gamma(1 + k\varepsilon)} + ST_\varepsilon^{-1} [w^{m\varepsilon} ST_\varepsilon \{g(\mu, \tau)\}], \\ \varphi_n(\mu, \tau) &= -ST_\varepsilon^{-1} [w^{m\varepsilon} ST_\varepsilon \{R_\varepsilon [\varphi_{n-1}(\mu, \tau)]\}], \quad n \geq 1, 0 < \varepsilon \leq 1 \end{aligned} \tag{11}$$

4 Application of LFSDM

Example 4.1. Consider the Helmholtz equation with LFDO:

$$\frac{\partial^{2\varepsilon} \varphi(\mu, \tau)}{\partial \mu^{2\varepsilon}} + \frac{\partial^{2\varepsilon} \varphi(\mu, \tau)}{\partial \tau^{2\varepsilon}} + \varphi(\mu, \tau) = \frac{\mu^\varepsilon}{\Gamma(1 + \varepsilon)} \frac{\tau^\varepsilon}{\Gamma(1 + \varepsilon)}, \tag{12}$$

with

$$\varphi(0, \tau) = 0, \quad \varphi^{(\varepsilon)}(0, \tau) = \frac{\tau^\varepsilon}{\Gamma(1 + \varepsilon)}. \tag{13}$$

Taking LFST of (12), we get

$$\begin{aligned} ST_\varepsilon\{\varphi(\mu, \tau)\} &= \sum_{k=0}^1 w^{k\varepsilon} \frac{\partial^{k\varepsilon} \varphi(0, \tau)}{\partial \mu^{k\varepsilon}} + w^{2\varepsilon} ST_\varepsilon \left\{ \frac{\mu^\varepsilon}{\Gamma(1 + \varepsilon)} \frac{\tau^\varepsilon}{\Gamma(1 + \varepsilon)} \right\} \\ &\quad - w^{2\varepsilon} ST_\varepsilon \left\{ \frac{\partial^{2\varepsilon} \varphi(\mu, \tau)}{\partial \tau^{2\varepsilon}} + \varphi(\mu, \tau) \right\} \\ &= w^\varepsilon \frac{\tau^\varepsilon}{\Gamma(1 + \varepsilon)} + w^{3\varepsilon} \frac{\tau^\varepsilon}{\Gamma(1 + \varepsilon)} - w^{2\varepsilon} ST_\varepsilon \left\{ \frac{\partial^{2\varepsilon} \varphi(\mu, \tau)}{\partial \tau^{2\varepsilon}} + \varphi(\mu, \tau) \right\}. \end{aligned}$$

The inversion of LFST implies that

$$\begin{aligned} \varphi(\mu, \tau) &= \frac{\mu^\varepsilon}{\Gamma(1 + \varepsilon)} \frac{\tau^\varepsilon}{\Gamma(1 + \varepsilon)} + \frac{\mu^{3\varepsilon}}{\Gamma(1 + 3\varepsilon)} \frac{\tau^\varepsilon}{\Gamma(1 + \varepsilon)} \\ &\quad - ST_\varepsilon^{-1} \left[w^{2\varepsilon} ST_\varepsilon \left\{ \frac{\partial^{2\varepsilon} \varphi(\mu, \tau)}{\partial \tau^{2\varepsilon}} + \varphi(\mu, \tau) \right\} \right]. \end{aligned} \tag{14}$$

Now, procedure of ADM suggests the decomposition of the unknown function $\varphi(\mu, \tau)$ as an infinite series in the following way

$$\varphi(\mu, \tau) = \sum_{n=0}^{\infty} \varphi_n(\mu, \tau). \tag{15}$$

Substituting (15) in (14), it yields the following result:

$$\begin{aligned} \sum_{n=0}^{\infty} \varphi_n(\mu, \tau) &= \frac{\mu^\varepsilon}{\Gamma(1 + \varepsilon)} \frac{\tau^\varepsilon}{\Gamma(1 + \varepsilon)} + \frac{\mu^{3\varepsilon}}{\Gamma(1 + 3\varepsilon)} \frac{\tau^\varepsilon}{\Gamma(1 + \varepsilon)} \\ &\quad - ST_\varepsilon^{-1} \left[w^{2\varepsilon} ST_\varepsilon \left\{ \frac{\partial^{2\varepsilon}}{\partial \tau^{2\varepsilon}} \sum_{n=0}^{\infty} \varphi_n(\mu, \tau) + \sum_{n=0}^{\infty} \varphi_n(\mu, \tau) \right\} \right]. \end{aligned} \tag{16}$$

On comparing both sides of (16), we have:

$$\begin{aligned} \varphi_0(\mu, \tau) &= \frac{\mu^\varepsilon}{\Gamma(1 + \varepsilon)} \frac{\tau^\varepsilon}{\Gamma(1 + \varepsilon)} + \frac{\mu^{3\varepsilon}}{\Gamma(1 + 3\varepsilon)} \frac{\tau^\varepsilon}{\Gamma(1 + \varepsilon)}, \\ \varphi_1(\mu, \tau) &= -ST_\varepsilon^{-1} \left[w^{2\varepsilon} ST_\varepsilon \left\{ \frac{\partial^{2\varepsilon} \varphi_0(\mu, \tau)}{\partial \tau^{2\varepsilon}} + \varphi_0(\mu, \tau) \right\} \right] \\ &= -\frac{\mu^{3\varepsilon}}{\Gamma(1 + 3\varepsilon)} \frac{\tau^\varepsilon}{\Gamma(1 + \varepsilon)} - \frac{\mu^{5\varepsilon}}{\Gamma(1 + 5\varepsilon)} \frac{\tau^\varepsilon}{\Gamma(1 + \varepsilon)}, \\ \varphi_2(\mu, \tau) &= -ST_\varepsilon^{-1} \left[w^{2\varepsilon} ST_\varepsilon \left\{ \frac{\partial^{2\varepsilon} \varphi_1(\mu, \tau)}{\partial \tau^{2\varepsilon}} + \varphi_1(\mu, \tau) \right\} \right] \\ &= \frac{\mu^{5\varepsilon}}{\Gamma(1 + 5\varepsilon)} \frac{\tau^\varepsilon}{\Gamma(1 + \varepsilon)} + \frac{\mu^{7\varepsilon}}{\Gamma(1 + 7\varepsilon)} \frac{\tau^\varepsilon}{\Gamma(1 + \varepsilon)}, \\ \varphi_3(\mu, \tau) &= -ST_\varepsilon^{-1} \left[w^{2\varepsilon} ST_\varepsilon \left\{ \frac{\partial^{2\varepsilon} \varphi_2(\mu, \tau)}{\partial \tau^{2\varepsilon}} + \varphi_2(\mu, \tau) \right\} \right] \\ &= -\frac{\mu^{7\varepsilon}}{\Gamma(1 + 7\varepsilon)} \frac{\tau^\varepsilon}{\Gamma(1 + \varepsilon)} - \frac{\mu^{9\varepsilon}}{\Gamma(1 + 9\varepsilon)} \frac{\tau^\varepsilon}{\Gamma(1 + \varepsilon)}, \\ &\vdots \end{aligned}$$

Therefore, the approximate solution $\varphi(\mu, \tau)$ of Eq. (12) is expressed by

$$\varphi(\mu, \tau) = \sum_{n=0}^{\infty} \varphi_n(\mu, \tau) = \frac{\mu^\varepsilon}{\Gamma(1 + \varepsilon)} \frac{\tau^\varepsilon}{\Gamma(1 + \varepsilon)}. \tag{17}$$

The result is the same as the one which is obtained by the LFLADM [12] and LFLHPM [31].

Example 4.2. Now we examine the coupled Helmholtz equations with LFDOS:

$$\begin{aligned} \frac{\partial^{2\varepsilon} \varphi(\mu, \tau)}{\partial \mu^{2\varepsilon}} + \frac{\partial^{2\varepsilon} \psi(\mu, \tau)}{\partial \tau^{2\varepsilon}} - \varphi(\mu, \tau) &= 0, \\ \frac{\partial^{2\delta} \psi(\mu, \tau)}{\partial \mu^{2\delta}} + \frac{\partial^{2\delta} \varphi(\mu, \tau)}{\partial \tau^{2\delta}} - \psi(\mu, \tau) &= 0, \end{aligned} \tag{18}$$

with

$$\begin{aligned} \varphi(0, \tau) &= 0, \varphi^{(\varepsilon)}(0, \tau) = E_\varepsilon(\tau^\varepsilon), \\ \psi(0, \tau) &= 0, i\psi^{(\delta)}(0, \tau) = E_\delta(\tau^\delta). \end{aligned} \tag{19}$$

Taking LFLT of (18), we obtain

$$\begin{aligned}
 ST_\varepsilon\{\varphi(\mu, \tau)\} &= w^\varepsilon E_\varepsilon(\tau^\varepsilon) + w^{2\varepsilon} ST_\varepsilon\left\{\varphi(\mu, \tau) - \frac{\partial^{2\varepsilon}\psi(\mu, \tau)}{\partial\tau^{2\varepsilon}}\right\}, \\
 ST_\varepsilon\{\psi(\mu, \tau)\} &= -w^\varepsilon E_\varepsilon(\tau^\varepsilon) + w^{2\varepsilon} ST_\varepsilon\left\{\psi(\mu, \tau) - \frac{\partial^{2\varepsilon}\varphi(\mu, \tau)}{\partial\tau^{2\varepsilon}}\right\},
 \end{aligned}
 \tag{20}$$

The inversion of LFST implies that

$$\begin{aligned}
 \varphi(\mu, \tau) &= \frac{\mu^\varepsilon}{\Gamma(1 + \varepsilon)} E_\varepsilon(\tau^\varepsilon) + ST_\varepsilon^{-1}\left[w^{2\varepsilon} ST_\varepsilon\left\{\varphi(\mu, \tau) - \frac{\partial^{2\varepsilon}\psi(\mu, \tau)}{\partial\tau^{2\varepsilon}}\right\}\right], \\
 \psi(\mu, \tau) &= -\frac{\mu^\varepsilon}{\Gamma(1 + \varepsilon)} E_\varepsilon(\tau^\varepsilon) + ST_\varepsilon^{-1}\left[w^{2\varepsilon} ST_\varepsilon\left\{\psi(\mu, \tau) - \frac{\partial^{2\varepsilon}\varphi(\mu, \tau)}{\partial\tau^{2\varepsilon}}\right\}\right].
 \end{aligned}
 \tag{21}$$

Now, we compose the unknown functions $\varphi(\mu, \tau)$ and $\psi(\mu, \tau)$ in the form of infinite series as

$$\begin{aligned}
 \varphi(\mu, \tau) &= \sum_{n=0}^{\infty} \varphi_n(\mu, \tau), \\
 \psi(\mu, \tau) &= \sum_{n=0}^{\infty} \psi_n(\mu, \tau).
 \end{aligned}
 \tag{22}$$

On making use of (22) in (21), it yields the following result:

$$\begin{aligned}
 \sum_{n=0}^{\infty} \varphi_n(\mu, \tau) &= \frac{\mu^\varepsilon}{\Gamma(1 + \varepsilon)} E_\varepsilon(\tau^\varepsilon) \\
 &+ ST_\varepsilon^{-1}\left[w^{2\varepsilon} ST_\varepsilon\left\{\sum_{n=0}^{\infty} \varphi_n(\mu, \tau) - \frac{\partial^{2\varepsilon}}{\partial\tau^{2\varepsilon}}\left(\sum_{n=0}^{\infty} \psi_n(\mu, \tau)\right)\right\}\right], \\
 \sum_{n=0}^{\infty} \psi_n(\mu, \tau) &= -\frac{\mu^\varepsilon}{\Gamma(1 + \varepsilon)} E_\varepsilon(\tau^\varepsilon) \\
 &+ ST_\varepsilon^{-1}\left[w^{2\varepsilon} ST_\varepsilon\left\{\sum_{n=0}^{\infty} \psi_n(\mu, \tau) - \frac{\partial^{2\varepsilon}}{\partial\tau^{2\varepsilon}}\left(\sum_{n=0}^{\infty} \varphi_n(\mu, \tau)\right)\right\}\right].
 \end{aligned}
 \tag{23}$$

Now, comparison of both sides of (23) yields

$$\varphi_0(\mu, \tau) = \frac{\mu^\varepsilon}{\Gamma(1 + \varepsilon)} E_\varepsilon(\tau^\varepsilon),$$

$$\psi_0(\mu, \tau) = -\frac{\mu^\varepsilon}{\Gamma(1 + \varepsilon)} E_\varepsilon(\tau^\varepsilon),$$

$$\varphi_1(\mu, \tau) = ST_\varepsilon^{-1} \left[w^{2\varepsilon} ST_\varepsilon \left\{ \varphi_0(\mu, \tau) - \frac{\partial^{2\varepsilon}}{\partial \tau^{2\varepsilon}} \psi_0(\mu, \tau) \right\} \right]$$

$$\psi_1(\mu, \tau) = ST_\varepsilon^{-1} \left[w^{2\varepsilon} ST_\varepsilon \left\{ \psi_0(\mu, \tau) - \frac{\partial^{2\varepsilon}}{\partial \tau^{2\varepsilon}} \varphi_0(\mu, \tau) \right\} \right]$$

$$= \frac{2\mu^{3\varepsilon}}{\Gamma(1 + 3\varepsilon)} E_\varepsilon(\tau^\varepsilon),$$

$$= -\frac{2\mu^{3\varepsilon}}{\Gamma(1 + 3\varepsilon)} E_\varepsilon(\tau^\varepsilon),$$

$$\varphi_2(\mu, \tau) = ST_\varepsilon^{-1} \left[w^{2\varepsilon} ST_\varepsilon \left\{ \varphi_1(\mu, \tau) - \frac{\partial^{2\varepsilon}}{\partial \tau^{2\varepsilon}} \psi_1(\mu, \tau) \right\} \right]$$

$$\psi_2(\mu, \tau) = ST_\varepsilon^{-1} \left[w^{2\varepsilon} ST_\varepsilon \left\{ \psi_1(\mu, \tau) - \frac{\partial^{2\varepsilon}}{\partial \tau^{2\varepsilon}} \varphi_1(\mu, \tau) \right\} \right]$$

$$= \frac{4\mu^{5\varepsilon}}{\Gamma(1 + 5\varepsilon)} E_\varepsilon(\tau^\varepsilon),$$

$$= -\frac{4\mu^{5\varepsilon}}{\Gamma(1 + 5\varepsilon)} E_\varepsilon(\tau^\varepsilon),$$

$$\varphi_3(\mu, \tau) = ST_\varepsilon^{-1} \left[w^{2\varepsilon} ST_\varepsilon \left\{ \varphi_2(\mu, \tau) - \frac{\partial^{2\varepsilon}}{\partial \tau^{2\varepsilon}} \psi_2(\mu, \tau) \right\} \right]$$

$$\psi_3(\mu, \tau) = ST_\varepsilon^{-1} \left[w^{2\varepsilon} ST_\varepsilon \left\{ \psi_2(\mu, \tau) - \frac{\partial^{2\varepsilon}}{\partial \tau^{2\varepsilon}} \varphi_2(\mu, \tau) \right\} \right]$$

$$= \frac{8\mu^{7\varepsilon}}{\Gamma(1 + 7\varepsilon)} E_\varepsilon(\tau^\varepsilon),$$

$$= -\frac{8\mu^{7\varepsilon}}{\Gamma(1 + 7\varepsilon)} E_\varepsilon(\tau^\varepsilon),$$

⋮

Hence, the solutions are expressed as

$$\begin{aligned} \varphi(\mu, \tau) &= \sum_{n=0}^{\infty} \varphi_n(\mu, \tau) = E_\varepsilon(\tau^\varepsilon) \frac{\sinh_\varepsilon(\sqrt{2}\mu^\varepsilon)}{\sqrt{2}}. \\ \psi(\mu, \tau) &= \sum_{n=0}^{\infty} \psi_n(\mu, \tau) = -E_\varepsilon(\tau^\varepsilon) \frac{\sinh_\varepsilon(\sqrt{2}\mu^\varepsilon)}{\sqrt{2}}. \end{aligned} \tag{24}$$

The result (24) is the same as the one which is obtained by the LFADM [12] and LFHPM [31].

5 Numerical Results and Discussion

In this segment, the numerical simulations for solution of Helmholtz and coupled Helmholtz equations obtained via LFSDM are presented. The numerical investigation of Helmholtz and coupled Helmholtz equations considers different values of $\varepsilon = 1, \frac{\log 2}{\log 3}$. Here, the Matlab software is utilized to draw all the 3D plots. Figures 1 & 2 show the 3D surface plot for solution $\varphi(\mu, \tau)$ for Example 1 for $\varepsilon = 1.0$ and $\varepsilon = \frac{\log 2}{\log 3}$, respectively. Figure 2 represents the variation of $\varphi(\mu, \tau)$ in fractal dimension. Similarly, the 3D surface plots for solution $\varphi(\mu, \tau)$ for Example 2 are depicted in Figs. 3 and 4 for $\varepsilon = 1.0$ and $\varepsilon = \frac{\log 2}{\log 3}$, respectively. Figures 5 & 6 represent the 3D variation for solution

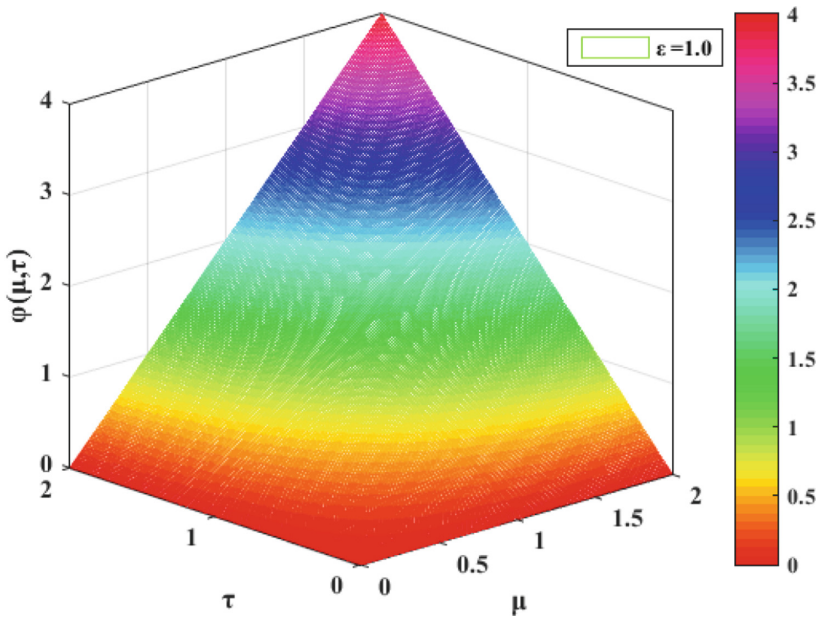


Fig. 1. 3D behaviour of $\varphi(\mu, \tau)$ for Example 1 w.r.t. μ and τ for $\varepsilon = 1.0$

$\psi(\mu, \tau)$ for Example 2 for $\varepsilon = 1, \frac{\log 2}{\log 3}$, respectively. Figure 6 represents the variation of $\varphi(\mu, \tau)$ on Cantor set.

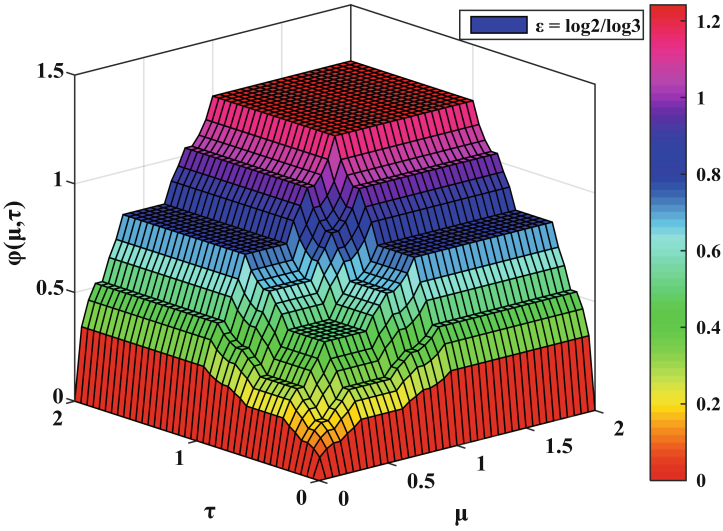


Fig. 2. 3D behaviour of $\varphi(\mu, \tau)$ for Example 1 w.r.t. μ and τ for $\varepsilon = \frac{\log 2}{\log 3}$

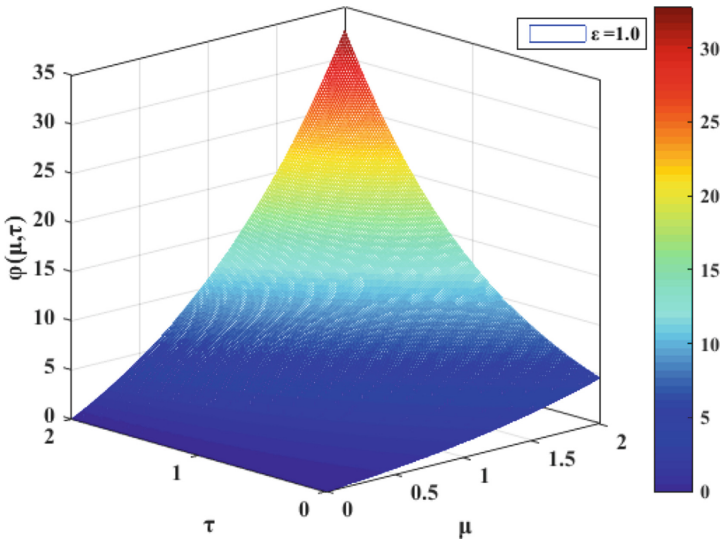


Fig. 3. 3D variation of $\varphi(\mu, \tau)$ for Example 2 w.r.t. μ and τ for $\varepsilon = 1.0$

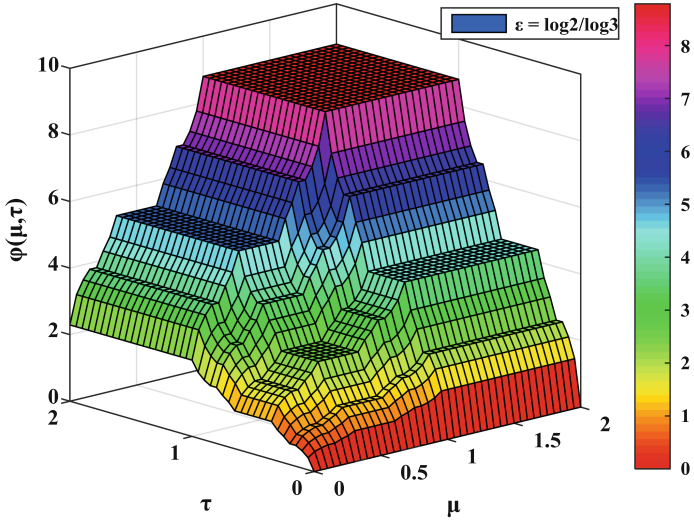


Fig. 4. 3D variation of $\varphi(\mu, \tau)$ for Example 2 w.r.t. μ and τ for $\varepsilon = \frac{\log 2}{\log 3}$

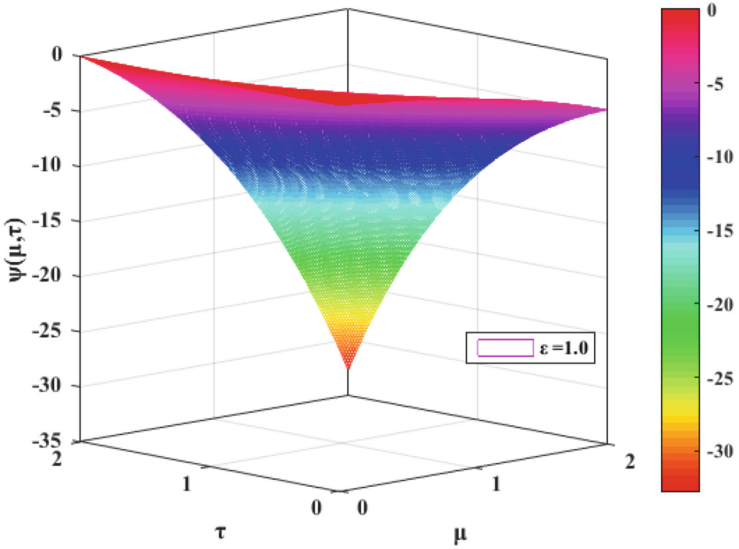


Fig. 5. 3D behaviour of $\psi(\mu, \tau)$ for Example 2 w.r.t. μ and τ for $\varepsilon = 1.0$

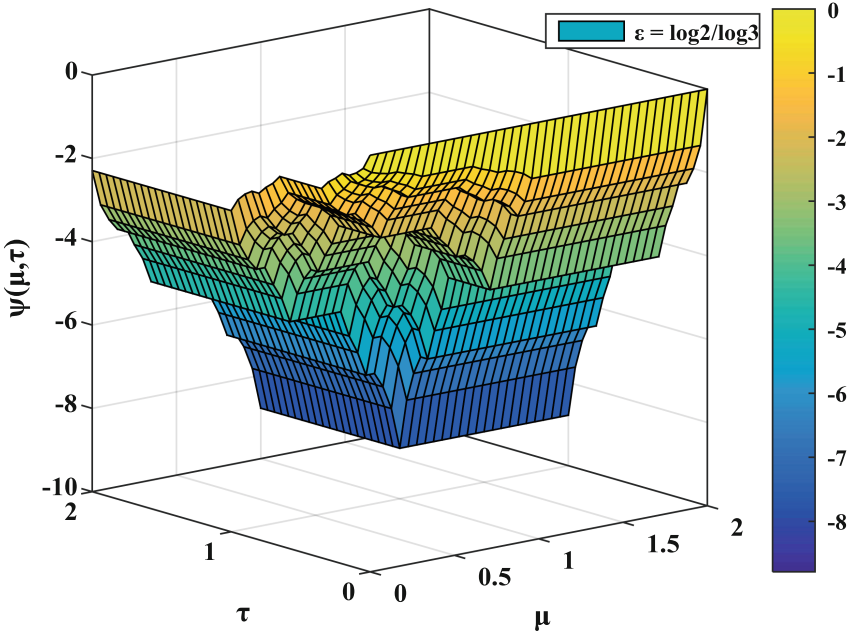


Fig. 6. 3D behaviour of $\psi(\mu, \tau)$ for Example 2 w.r.t. μ and τ for $\varepsilon = \frac{\log 2}{\log 3}$

6 Conclusions

In this work, the LFSM is conveniently employed to obtain the approximate solution of Helmholtz and coupled Helmholtz equations within LFDs. The proposed algorithm provides a solution in a series form that converges rapidly to an exact solution if it exists. From the obtained results, it is clear that the FSDM yields very accurate solutions using only a few iterates. The method is very powerful and efficient in finding semi-analytical solutions for wide classes of LFPDEs.

References

1. Jafari, H., Jassim, H.K., Vahidi, J.: Reduced differential transform and variational iteration methods for 3D diffusion model in fractal heat transfer within local fractional operators. *Therm. Sci.* **22**, S301–S307 (2018)
2. Baleanu, D., Jassim, H.K.: A modification fractional variational iteration method for solving nonlinear gas dynamic and coupled KdV equations involving local fractional operators. *Therm. Sci.* **22**, S165–S175 (2018)
3. Jafari, H., Jassim, H.K.: Application of the local fractional adomian decomposition and series expansion methods for solving telegraph equation on cantor sets involving local fractional derivative operators. *J. ZankoySulaimani-Part A* **17**, 15–22 (2015)
4. Jassim, H.K., Ünlü, C., Moshokoa, S.P., KhaliqC.M.: Local fractional Laplace variational iteration method for solving diffusion and wave equations on cantor sets within local fractional operators. *Math. Probl. Eng.* **2015**, 1–9 (2015)

5. Baleanu, D., Jassim, H.K.: Approximate solutions of the damped wave equation and dissipative wave equation in fractal strings. *Fractal Fract.* **3**(26), 1–12 (2019)
6. Jassim, H.K.: The approximate solutions of three-dimensional diffusion and wave equations within local fractional derivative operator. *Abstr. Appl. Anal.* **2016**, 1–5 (2016)
7. Wang, S.Q., Yang, Y.J., Jassim, H.K.: Local fractional function decomposition method for solving inhomogeneous wave equations with local fractional derivative. *Abstr. Appl. Anal.* **2014**, 1–7 (2014)
8. Yang, X.J., et al.: Local fractional variational iteration method for Fokker-Planck equation on a Cantor set. *Acta Universitaria* **23**, 3–8 (2013)
9. Jassim, H.K.: New approaches for solving fokker planck equation on cantor sets within local fractional operators. *J. Math.* **2015**, 1–8 (2015)
10. Yan, S.P., Jafari, H., Jassim, H.K.: Local fractional Adomian decomposition and function decomposition methods for solving Laplace equation within local fractional operators. *Adv. Math. Phys.* **2014**, 1–7 (2014)
11. Yang, A.M., et al.: Application of local fractional series expansion method to solve Klein-Gordon equations on Cantor sets. *Abstr. Appl. Anal.* **2014**, 1–6 (2014)
12. Jassim, H.K.: The approximate solutions of Helmholtz and coupled Helmholtz equations on cantor sets within local fractional operator. *J. Zankoy Sulaimani-Part A* **17**, 19–25 (2015)
13. Jassim, H.K.: A new approach to find approximate solutions of Burger's and coupled Burger's equations of fractional order. *TWMS J. Appl. Eng. Math.* **11**(2), 415–423 (2021)
14. Baleanu, D., Jassim, H.K.: Approximate analytical solutions of goursat problem within local fractional operators. *J. Nonlinear Sci. Appl.* **9**, 4829–4837 (2016)
15. Jafari, H., et al.: Local fractional adomian decomposition method for solving two dimensional heat conduction equations within local fractional operators. *J. Adv. Math.* **9**, 2574–2582 (2014)
16. Jassim, H.K., Khafif, S.A.: SVIM for solving Burger's and coupled Burger's equations of fractional order. *Prog. Fract. Differ. Appl.* **7**(1), 1–6 (2021)
17. Jafari, H., et al.: Local Fractional variational iteration method for nonlinear partial differential equations within local fractional operators. *Appl. Appl. Math.* **10**, 1055–1065 (2015)
18. Xu, S., Ling, X., Zhao, Y., Jassim, H.K.: A novel schedule for solving the two-dimensional diffusion in fractal heat transfer. *Therm. Sci.* **19**, S99–S103 (2015)
19. Yang, X.J.: *Advanced Local Fractional Calculus and Its Applications*. World Science Publisher, New York (2012)
20. Yang, X.J.: *Local Fractional Functional Analysis and Its Applications*. Asian Academic Publisher Limited, Hong Kong (2011)
21. Jafari, H, Jassim, H.K., Vahidi V.: Reduced differential transform and variational iteration methods for 3D diffusion model in fractal heat transfer within local fractional operators. *Therm. Sci.* **22**, S301–S307 (2018)
22. Jassim, H.K., Shahab, W.A.: Fractional variational iteration method to solve one dimensional second order hyperbolic telegraph equations. *J. Phys. Conf. Ser.* **1032**(1), 1–9 (2018)
23. Yang, X.J., Machad, J.A., Srivastava, H.M.: A new numerical technique for solving the local fractional diffusion equation: two-dimensional extended differential transform approach. *Appl. Math. Comput.* **274**, 143–151 (2016)
24. Jafari, H., Jassim, H.K., Tchier, F., Baleanu, D.: On the approximate solutions of local fractional differential equations with local fractional operator. *Entropy* **18**, 1–12 (2016)
25. Jassim, H.K., Baleanu, D.: A novel approach for Korteweg-de Vries equation of fractional order. *J. Appl. Comput. Mech.* **5**(2), 192–198 (2019)
26. Singh, J., Jassim, H.K., Kumar, D.: An efficient computational technique for local fractional Fokker-Planck equation. *Phys. A* **555**(124525), 1–8 (2020)
27. Baleanu, D., Jassim, H.K.: Exact solution of two-dimensional fractional partial differential equations. *Fractal Fract.* **4**(21), 1–9 (2020)

28. Jafari, H., Jassim, H.K., Moshokoa, S.P., Ariyan, V.M., Tchier, F.: Reduced differential transform method for partial differential equations within local fractional derivative operators. *Adv. Mech. Eng.* **8**, 1–6 (2016)
29. Baleanu, D., Jassim, H.K., Al Qurashi, M.: Solving Helmholtz equation with local fractional derivative operators. *Fractal Fract.* **3**(43), 1–13 (2019)
30. Jassim, H.K.: Analytical approximate solutions for local fractional wave equations. *Math. Methods Appl. Sci.* **43**(2), 939–947 (2020)
31. Baleanu, D., Jassim, H.K.: A modification fractional homotopy perturbation method for solving Helmholtz and coupled Helmholtz equations on cantor sets. *Fractal Fract.* **3**(30), 1–8 (2019)
32. Singh, J., et al.: On the local fractional wave equation in fractal strings. *Math. Method Appl. Sci.* **2019**, 1–8 (2019)



Estimation of Software Reliability Using Lindley Distribution Based on MLE and UMVUE

Kavita and Shiv Kumar Sharma^(✉)

Department of Mathematics, Chandigarh University,
Gharuan, 140413 SAS Nagar, Punjab, India
shivksharma2005@gmail.com

Abstract. Today's world is computerized in every field. Reliable software is the most important concern for every software developers. Software reliability is defined as the probability of a failure-free operation in a specified environment for a given period of time. To measure the reliability of software, various models of reliability that are based upon Exponential Distribution have been proposed. One of the most common methods to estimate reliability is Maximum Likelihood Estimation but it is not effective in some of the cases. Two reliability estimation of Lindley Distribution have been discussed in this paper. One is Maximum Likelihood Estimator and other is Uniform Minimum Variance Unbiased Estimator. Lindley Distribution is also the family of Exponential Distribution. In this paper, we have compared Maximum Likelihood Estimator(MLE) and Uniform Minimum Variance Unbiased Estimator(UMVUE) of reliability estimation of different data sets.

Keywords: Software Reliability Model · Maximum Likelihood Estimator · Uniform Minimum Variance Unbiased Estimator · Lindley Distribution

1 Introduction

Every software developer must understand the concept of software reliability. Various software reliability models based on Exponential, Gamma, Weibull, Logistic Distributions etc. have been developed. Quality, value and schedule are the most significant features of software product. For the last two features Quantitative measurement exists, but quality quantification is more challenging. It is utmost significant, however, due to the non-explore measure for quality of software generally means that feature will fail when it resists over concern with cost and time. Software Reliability is an essential factor for its worth. Software Reliability is concerned with how properly the software performs in meeting needs of consumer. Reliability is defined as probability of a failure free operation in a given environment for a certain time period [1]. The time of failures is unpredictable in nature. If T indicates the time of software failure, then its reliability

is given by $R(t) = P(T > t)$. There are several ways for estimating the software reliability, Maximum Likelihood Estimator(MLE) is most commonly used method [2], but it is not as operational as UMVUE. Nozer D. Singpurwalla, *et al.* [3] defined concisely, various models to analysis reliability of software. Harpreet Kaur, *et al.* [22] explained the concept of Software Reliability Growth Modeling. Using the MVUE approach Roopashri and Murulidhar [4] calculated reliability estimates of Exponential Class Models. Chris Dale [5] describes the current and possible usages of numerical approach in the evaluation of Software Reliability. R.Kumar, *et al.* [19,20] describes the concept of Least Square Estimation. Roopashri and Murulidhar [6] used MLE and MVUE approaches to estimate the reliability of Gamma Class Models. Tapan Nayak [7] provided an outline of statistical methods and methods for Software Reliability Estimation. M.E. Ghitany *et al.* [8] estimated various reliability parameters by using Lindley Distribution. Priyanka Thakur *et al.* [23] provided the consistent performance in software reliability and complexity of software. Roopashri and Murulidhar [9] obtained reliability estimates of Exponential Class Models based on Littlewood Pareto Failure Time Model by using MVUE approach. Sudhansu S. Maiti & Indrani Mukherjee calculated PDF and CDF of Lindley Distribution [10]. D.Laxmi *et al.* [21] explained the various concept of Software Reliability.

Variou reliability estimators have been developed like MLE, UMVUE and Least Square Estimation. Estimator is used to calculate the value of unknown parameters using sample data. A good estimator follows four properties consistency, efficiency, sufficiency, unbiasedness [11].

This paper discusses the reliability estimation of Lindley Distribution. This model has probability distribution given by

$$f(x) = \frac{\theta^2}{\theta + 1} (1 + x) e^{-\theta x}; x > 0, \theta > 0 \text{ with parameter } \theta$$

In this paper, we calculated MLE of $R(t)$ and compared it with UMVUE of reliability. We calculated MLE of $R(t)$ by using Invariance Property. Blackwellization Method is used for calculating UMVUE [2, 12]. Failure time data given by MUSA [13], Lyu [2], J.LIU [14], H.joe and N.Reid [15], J.F. Flawless [16] have been used to compare Maximum Likelihood Estimator of reliability and Uniform Minimum Variance Unbiased Estimator of reliability and to decide better estimate amongst these two estimators.

2 Methods to Estimate Reliability

Various methods to estimate software reliability are available. Few methods to estimate reliability are: Moments Method, Least Square Method, Mean Square Error, Maximum Likelihood Estimation Method, Uniform Minimum Variance Unbiased Estimator etc. All of these estimators must satisfy the above described features. Best estimator is considered as which satisfies all of above four properties. From these different estimators, two methods are discussed below namely the Method of MLE and Method of UMVUE.

2.1 Maximum Likelihood Estimation Method

Let $x_1, x_2, x_3, \dots, x_n$ be a random sample of size n from the population of probability function $f(x, \theta)$. Then likelihood function is defined as [11]

$$L = \prod_{i=1}^n f(x_i, \theta)$$

We have to maximize this likelihood function L which will give an estimator. Now $\frac{\partial L}{\partial \theta} = 0$ which implies that $\frac{\partial^2 L}{\partial \theta^2} < 0$. As we know that $L > 0$, the above equation can be written as

$$\frac{1}{L} \frac{\partial L}{\partial \theta} = 0 \text{ i.e. } \frac{\partial(\ln L)}{\partial \theta} = 0$$

We will get the solution of θ by solving $\frac{\partial(\ln L)}{\partial \theta} = 0$.

2.2 Uniform Minimum Variance Unbiased Estimator Method (UMVUE)

If a statistic T which is created on sample size n such that T is unbiased Estimator of θ that has lowest variance between all unbiased estimators of θ then T is known as UMVUE of θ and T is always unique. With the help of Blackwellization, UMVUE can be obtained and that method is explained below: First find unbiased estimator U then find complete sufficient estimator S [8]. UMVUE is then obtained as $E(U/S)$. UMVUE gives more efficiency than any other estimators.

3 Reliability Estimations of Lindley Distribution Model

Commonly used method for reliability is MLE which is always reliable and sufficient but it is not balanced and efficient. UMVUE is always unbiased and efficient which is known as best class for all estimators [17].

We will find Maximum Likelihood Estimator and Uniform Minimum Variance Unbiased Estimator of $R(t)$ and both of the estimators will compare.

3.1 MLE of $R(t)$

Using 2.1, We obtain

$$\hat{\theta} = \frac{-(\bar{t}-1) \pm \sqrt{(\bar{t}-1)^2 + 8\bar{t}}}{2\bar{t}} \tag{1}$$

where

$$\bar{t} = \frac{x_1 + x_2 + x_3 + \dots + x_n}{n}$$

By using MLE property of Invariance [18], we find MLE of R(t) as below:

$$\widehat{R}(t) = \frac{\left[\frac{-(\bar{t}-1) \pm \sqrt{(\bar{t}-1)^2 + 8\bar{t}}}{2\bar{t}} \right] (t+1) + 1}{\left[\frac{-(\bar{t}-1) \pm \sqrt{(\bar{t}-1)^2 + 8\bar{t}}}{2\bar{t}} \right] + 1} e^{\left[\frac{-(\bar{t}-1) \pm \sqrt{(\bar{t}-1)^2 + 8\bar{t}}}{2\bar{t}} \right] t} \tag{2}$$

3.2 UMVUE of R(t)

UMVUE of R(t) = P(T ≥ t)

First state a function U (t₁, t₂, t₃ , t_n) such that U(t₁) = {1 if t₁ ≥ t and 0 otherwise }

Then

$$E[U(t_1)] = 1 \cdot P(T_1 \geq t) + 0 \cdot P(T_1 \leq t) \\ = P(T_1 \geq t) = R(t)$$

Which proves U(t₁) is an unbiased estimator for R(t)

$$L = \prod_{i=1}^n f(t_i) \\ = \frac{\theta^{2n}}{(\theta+1)^n} \prod_{i=1}^n [1 + t_i] e^{-\theta(t_1+t_2+\dots+t_n)}$$

By Theorem of Factorization,

$$S = \sum_{i=1}^n t_i \text{ is complete sufficient estimator for } \theta$$

UMVUE of R(t) is obtained as

$$\widetilde{R}(t) = E(U(t_1/S)) = \int_t^\infty f(t_1/S) dt_1 \tag{3}$$

Conditional Probability Function is

$$f(t_1/S) = \frac{n\theta}{\theta+1} \frac{(1+t_1)(\sum_{i=1}^n t_i - t_1)^{n-2}}{(\sum_{i=1}^n t_i)^{n-1}} \tag{4}$$

UMVUE of reliability is

$$\widehat{R}(t) = \int_t^\infty f(t_1/S) dt_1 \\ = \frac{n\theta}{(\theta+1)(2-n)} \left[\left\{ (1+t) \left(1 + \frac{t}{z} \right)^{2-n} - 1 \right\} + \frac{z}{3-n} \left\{ 1 - \left(1 + \frac{t}{z} \right)^{3-n} \right\} \right] \text{ where } z = \sum_{i=2}^n t_i \tag{5}$$

4 Datasets

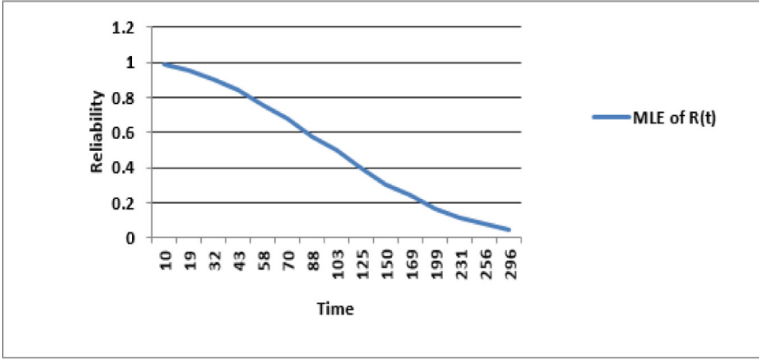
Various data sets of failure times of different failures obtained by Lyu [2], MUSA [13], and J.LIU [11], H. Joe and N. Reid [15], J.F. Flawless [16] have been considered below. Comparison of two reliability estimates and their analysis has been carried out for these datasets.

4.1 Data Set I

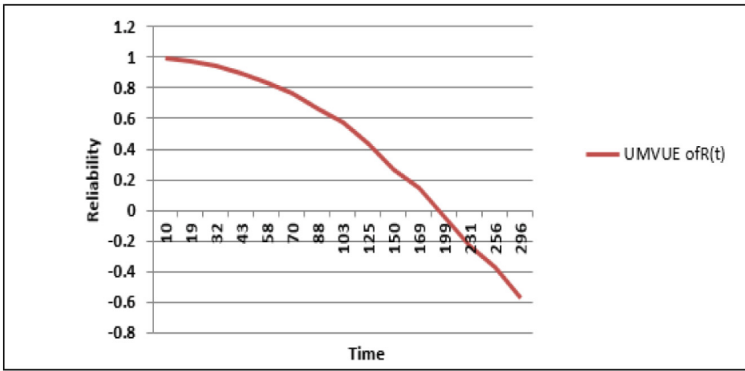
Failure data for 15 samples given by Musa [13] is calculated below. For this data, we will consider $\hat{\theta} = \frac{-(\bar{t}-1)+\sqrt{(\bar{t}-1)^2+8\bar{t}}}{2\bar{t}} = 0.0161$ obtained using Eq. (1). Table 1 gives reliability estimates $\hat{R}(t)$ and $\tilde{R}(t)$ for different values of failure time t, obtained using Eqs. (2) and (5) respectively. In these figures, we have taken failure time on x-axis and reliability is taken on y-axis.

Table 1. MLE and UMVUE of R(t)

Failure No	Time(t)	R(t)-MLE	R(t)-UMVUE
1	10	0.9862	0.9926
2	19	0.9582	0.9765
3	32	0.9003	0.9399
4	43	0.8414	0.8987
5	58	0.7544	0.8305
6	70	0.6835	0.7681
7	88	0.5807	0.6650
8	103	0.5014	0.5730
9	125	0.3985	0.4323
10	150	0.3019	0.2695
11	169	0.2422	0.1465
12	199	0.1687	-0.0420
13	231	0.1131	-0.2318
14	256	0.0821	-0.3704
15	296	0.0485	-0.5725



(a) Reliability curve of MLE



(b) Reliability curve of UMVUE

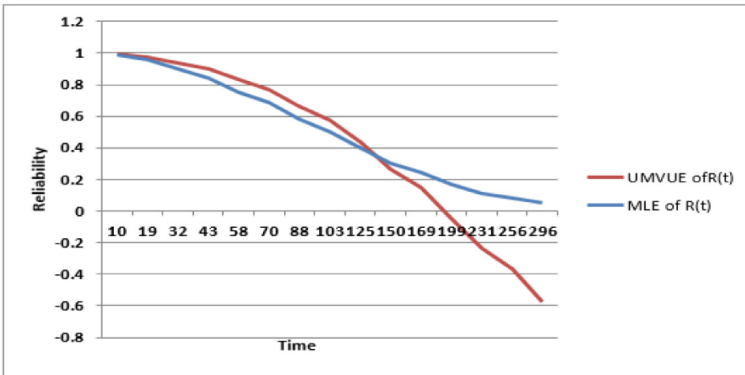


Fig. 1. Reliability curves of MLE and UMVUE of $R(t)$

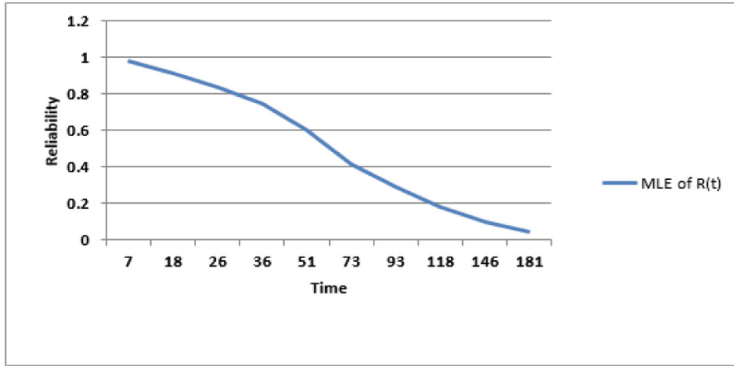
From the above Fig. 1, we observed that as failure time increases reliability of MLE decreases but reliability of UMVUE decreases rapidly as compare to MLE with increasing failure time.

4.2 Data Set II

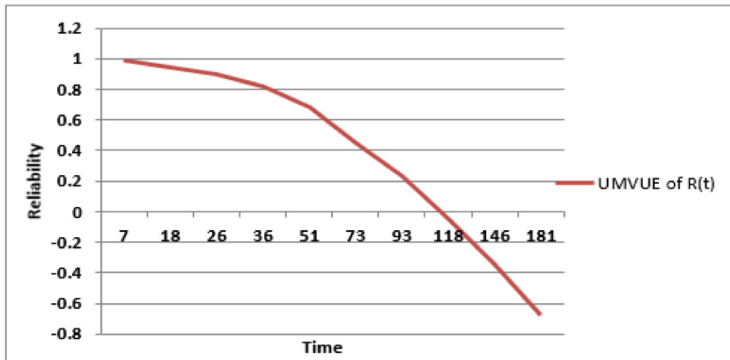
Failure data for 10 samples given by Lyu [2] is calculated below. For this data, we will consider $\hat{\theta} = \frac{-(\bar{t}-1)+\sqrt{(\bar{t}-1)^2+8\bar{t}}}{2\bar{t}} = 0.0263$ obtained using Eq. (1). Table 2 gives reliability estimates $\hat{R}(t)$ and $\tilde{R}(t)$ for different values of failure time t, obtained using Eq. (2) and (5) respectively. In these figures, we have taken failure time on x-axis and reliability is taken on y-axis.

Table 2. MLE and UMVUE of R(t)

Failure No.	Time(t)	R(t)-MLE	R(t)-UMVUE
1	7	0.9809	0.9896
2	18	0.9098	0.9459
3	26	0.8404	0.8972
4	36	0.7450	0.8210
5	51	0.6021	0.6836
6	73	0.4196	0.4524
7	93	0.2919	0.2296
8	118	0.1796	-0.0474
9	146	0.1012	-0.3414
10	181	0.0478	-0.6721



(a) Reliability curve of MLE



(b) Reliability curve of UMVUE

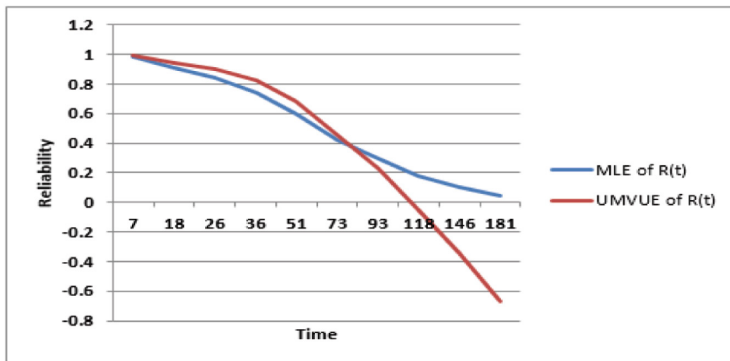


Fig. 2. Reliability curves of MLE and UMVUE of $R(t)$

From the above Fig. 2, we observed that as failure time increases reliability of MLE decreases but reliability of UMVUE decreases rapidly as compare to MLE with increasing failure time.

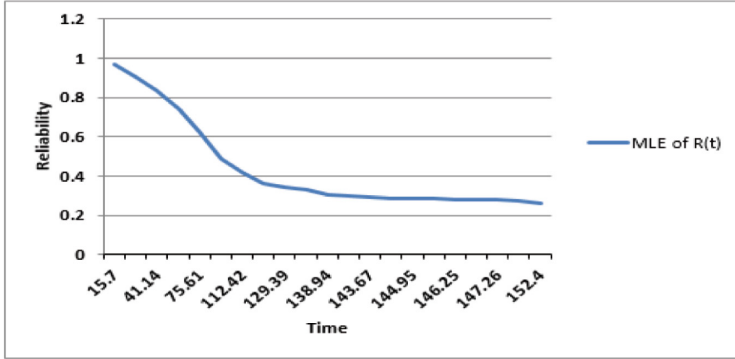
4.3 Data Set III

Failure data for 21 samples given by H. Joe and N. Reid [15] is calculated below.

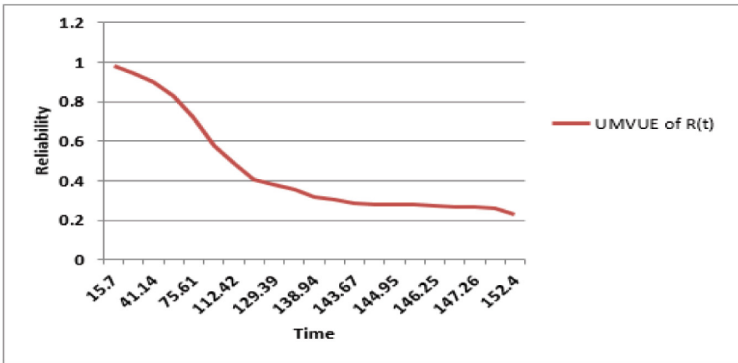
For this data, we will consider $\hat{\theta} = \frac{-(\bar{t}-1)+\sqrt{(\bar{t}-1)^2+8\bar{t}}}{2\bar{t}} = 0.0172$ obtained using Eq. (1). Table 3 gives reliability estimates $\hat{R}(t)$ and $\tilde{R}(t)$ for different values of failure time t, obtained using Eqs. (2) and (5) respectively. In these figures, we have taken failure time on x-axis and reliability is taken on y-axis.

Table 3. MLE and UMVUE of R(t)

Failure No	Time(t)	R(t)-MLE	R(t)-UMVUE
1	15.7	0.9659	0.9818
2	29.39	0.9027	0.9439
3	41.14	0.8353	0.8986
4	56.47	0.7396	0.8261
5	75.61	0.6200	0.7202
6	98.83	0.4872	0.5776
7	112.42	0.4187	0.4904
8	125.61	0.3593	0.4048
9	129.39	0.3435	0.3802
10	133.45	0.3272	0.3538
11	138.94	0.3062	0.3183
12	141.41	0.2971	0.3023
13	143.67	0.2890	0.2877
14	144.63	0.2856	0.2815
15	144.95	0.2845	0.2795
16	145.16	0.2837	0.2781
17	146.25	0.2799	0.2711
18	146.7	0.2784	0.2682
19	147.26	0.2764	0.2646
20	148.15	0.2734	0.2589
21	152.4	0.2593	0.2317



(a) Reliability curve of MLE



(b) Reliability curve of UMVUE

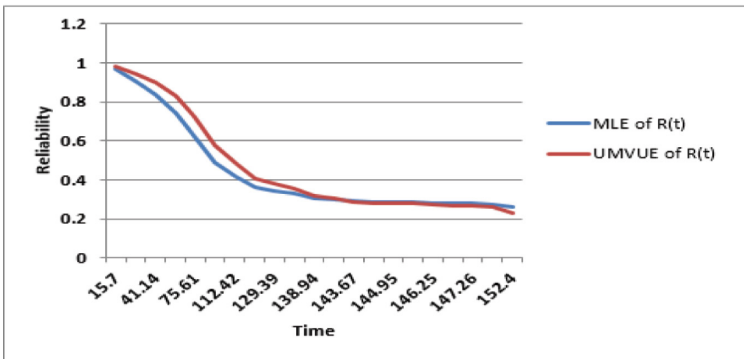


Fig. 3. Reliability curves of MLE and UMVUE of R(t)

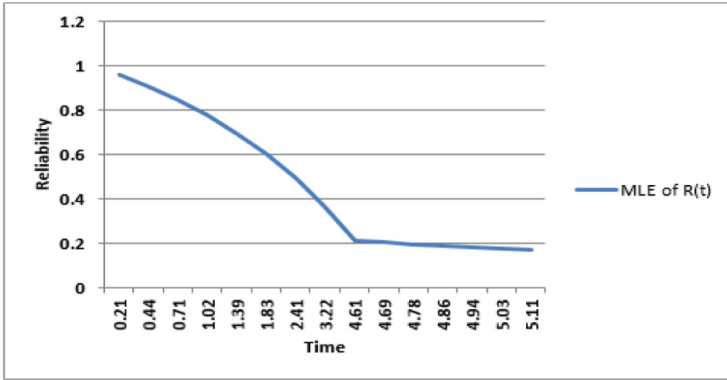
From the above Fig. 3, we observed that as failure time increases reliability of MLE decreases but reliability of UMVUE also decreases with increasing failure time.

4.4 Data Set IV

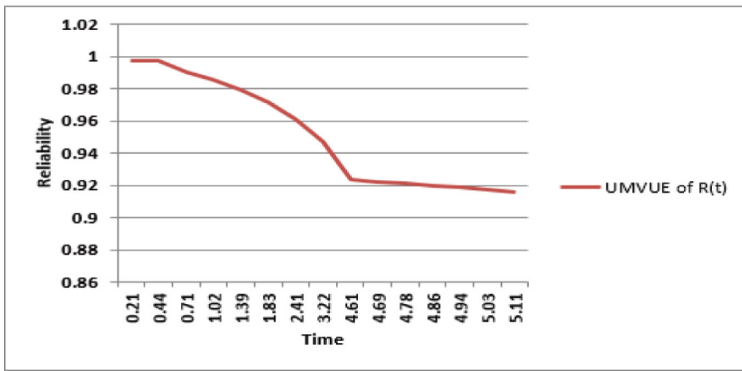
Failure data for 15 samples given by MUSA [14] is calculated below. For this data, we will consider $\hat{\theta} = \frac{-(\bar{t}-1)+\sqrt{(\bar{t}-1)^2+8\bar{t}}}{2\bar{t}} = 0.034$ obtained using Eq. (1). Table 4 gives reliability estimates $\hat{R}(t)$ and $\tilde{R}(t)$ for different values of failure time t, obtained using Eqs. (2) and (5) respectively. In these figures, we have taken failure time on x-axis and reliability is taken on y-axis.

Table 4. MLE and UMVUE of R(t)

Failure No.	Time(t)	R(t)-MLE	R(t)-UMVUE
1	0.21	0.9578	0.9975
2	0.44	0.9087	0.9971
3	0.71	0.8488	0.9905
4	1.02	0.7794	0.9857
5	1.39	0.6980	0.9795
6	1.83	0.6062	0.9718
7	2.41	0.4966	0.9614
8	3.22	0.3685	0.9469
9	4.61	0.2121	0.9237
10	4.69	0.2053	0.9224
11	4.78	0.1978	0.9211
12	4.86	0.1913	0.9198
13	4.94	0.1850	0.9186
14	5.03	0.1782	0.9173
15	5.11	0.1723	0.9161



(a) Reliability curve of MLE



(b) Reliability curve of UMVUE

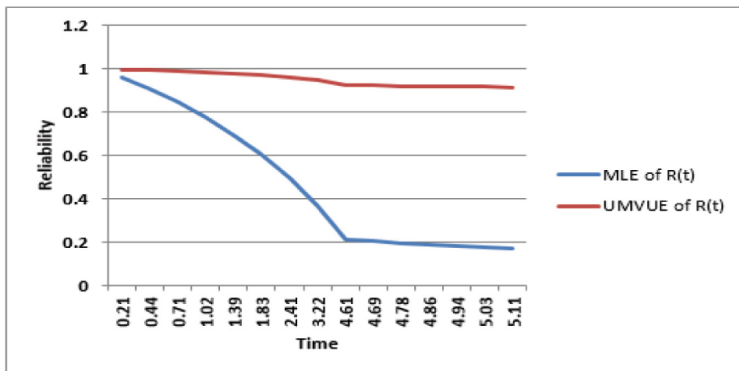


Fig. 4. Reliability curves of MLE and UMVUE of R(t)

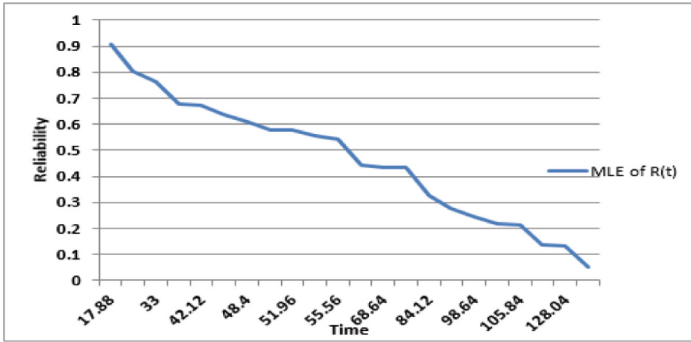
From the above Fig. 4, we observed that as failure time increases reliability of MLE decreases but reliability of UMVUE decreases very slowly as compare to MLE with increasing failure time. We have seen that due to less variation in failure time in the above data UMVUE has greater value as compare to MLE.

4.5 Data Set V

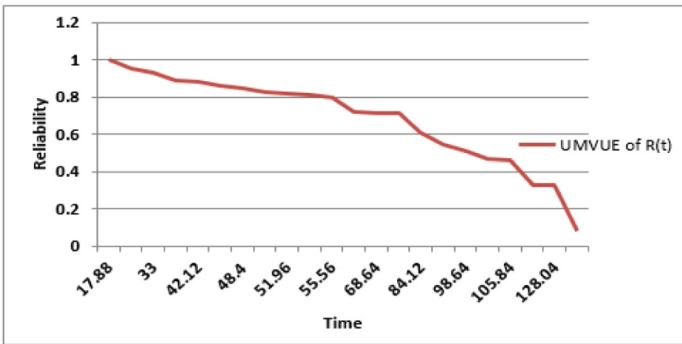
Failure data for 22 samples given by J.F. Flawless [16] is calculated below. For this data, we will consider $\hat{\theta} = \frac{-(\bar{t}-1)+\sqrt{(\bar{t}-1)^2+8\bar{t}}}{2\bar{t}} = 0.0272$ obtained using Eq. (1). Table 5 gives reliability estimates $\hat{R}(t)$ and $\tilde{R}(t)$ for different values of failure time t, obtained using Eqs. (2) and (5) respectively. In these figures, we have taken failure time on x-axis and reliability is taken on y-axis.

Table 5. MLE and UMVUE of R(t)

Failure No.	Time(t)	R(t)-MLE	R(t)-UMVUE
1	17.88	0.9056	1.0011
2	28.92	0.8034	0.9543
3	33.0	0.7629	0.9338
4	41.52	0.6776	0.8864
5	42.12	0.6717	0.8829
6	45.60	0.6375	0.8620
7	48.40	0.6105	0.8448
8	51.84	0.5781	0.8232
9	51.96	0.5770	0.8224
10	54.12	0.5571	0.8086
11	55.56	0.5441	0.7992
12	67.80	0.4408	0.7180
13	68.64	0.4343	0.7123
14	68.88	0.4324	0.7107
15	84.12	0.3262	0.6071
16	93.12	0.2741	0.5464
17	98.64	0.2458	0.5097
18	105.12	0.2157	0.4672
19	105.84	0.2126	0.4625
20	127.92	0.1344	0.3251
21	128.04	0.1340	0.3244
22	173.4	0.0496	0.0845



(a) Reliability curve of MLE



(b) Reliability curve of UMVUE

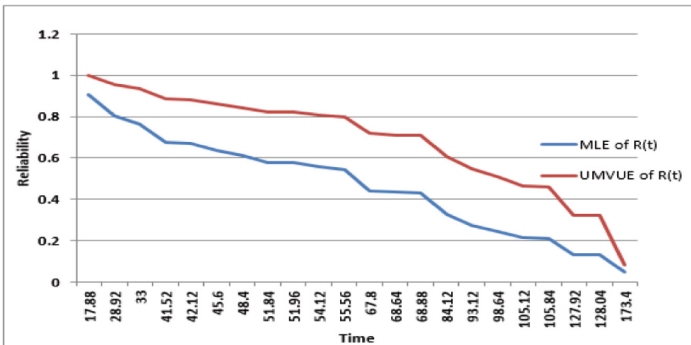


Fig. 5. Reliability curves of MLE and UMVUE of $R(t)$

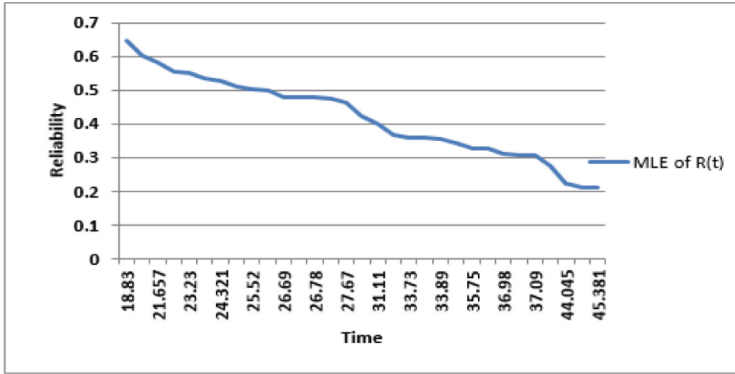
From the above Fig. 5, we observed that as failure time increases reliability of MLE decreases but reliability of UMVUE decreases very slowly as compare to MLE with increasing failure time. We have seen that due to less variation in failure time in the above data UMVUE has greater value as compare to MLE.

4.6 Data Set VI

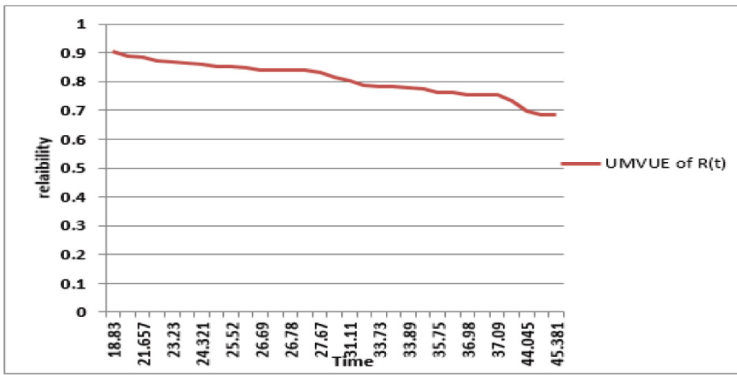
Failure data for 31 samples given by J.F. Flawless [16] is calculated below. For this data, we will consider $\hat{\theta} = \frac{-(\bar{t}-1)+\sqrt{(\bar{t}-1)^2+8\bar{t}}}{2\bar{t}} = 0.0629$ obtained using Eq. (1). Table 6 gives reliability estimates $\hat{R}(t)$ and $\tilde{R}(t)$ for different values of failure time t, obtained using Eqs. (2) and (5) respectively. In these figures, we have taken failure time on x-axis and reliability is taken on y-axis.

Table 6. MLE and UMVUE of R(t)

Failure No	Time(t)	R(t)-MLE	R(t)-UMVUE
1	18.83	0.6461	0.9051
2	20.8	0.6021	0.8897
3	21.657	0.5835	0.8828
4	23.03	0.5542	0.8717
5	23.23	0.5500	0.8700
6	24.05	0.5330	0.8633
7	24.321	0.5274	0.8611
8	25.5	0.5097	0.8512
9	25.52	0.5033	0.8511
10	25.8	0.4977	0.8487
11	26.69	0.4804	0.8413
12	26.77	0.4789	0.8406
13	26.78	0.4787	0.8405
14	27.05	0.4735	0.8382
15	27.67	0.4618	0.8330
16	29.9	0.4214	0.8141
17	31.11	0.4005	0.8038
18	33.2	0.3664	0.7861
19	33.73	0.3581	0.7816
20	33.76	0.3577	0.7813
21	33.89	0.3557	0.7802
22	34.76	0.3425	0.7728
23	35.75	0.3279	0.7645
24	35.91	0.3256	0.7631
25	36.98	0.3106	0.7541
26	37.08	0.3092	0.7533
27	37.09	0.3090	0.7532
28	39.58	0.2764	0.7325
29	44.045	0.2251	0.6961
30	45.29	0.2124	0.6862
31	45.381	0.2115	0.6855



(a) Reliability curve of MLE



(b) Reliability curve of UMVUE

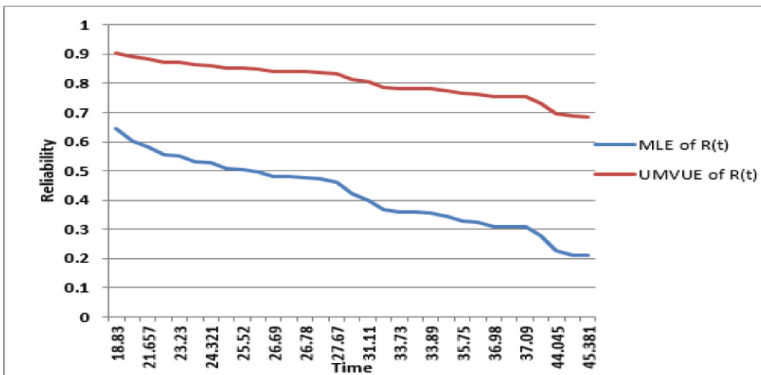


Fig. 6. Reliability curves of MLE and UMVUE of R(t)

From the above Fig. 6, we observed that as failure time increases reliability of MLE decreases but reliability of UMVUE decreases very slowly as compare to MLE with increasing failure time. We have seen that due to less variation in failure time in the above data UMVUE has greater value as compare to MLE.

5 Conclusion

Quality of software is the best measures for reliability. Reliability helps customers to have an idea about stability of the software in the long run and to adopt whether or not to take this software. The data which is obtained during testing of software can be used to estimate the reliability. Statistical estimataion of reliability is considered in this paper. Two reliability estimation have been derived for Lindley Distribution which is MLE and UMVUE. Six different datasets have been taken to compare these reliability estimates. It is observed from first three datasets that Reliability of MLE decreases as failure time increases but Reliability of UMVUE decreases fastly as compare to MLE with increasing failure time so we can conclude that reliability of UMVUE is more efficient as compare to Reliability of MLE. In dataset fourth, fifth and sixth we observed that as there is less difference in failure time then reliability of MLE decreases with time but reliability of UMVUE decreases very slowly due to less difference in failure time and UMVUE has higher values than MLE. If we constrain to select only unbiased class of estimators for reliability, Uniform Minimum Variance Unbiased Estimator is the best in case of smallest variance.

References

1. Trivedi, K.S.: Probability and Statistics with Reliability Queuing and Computer Science Applications (2nd ed.) (2008)
2. Lyu, M.R.: Hand book of Software Reliability Engineering, IEEE Computer Society Press, McGraw Hill Trans. (2004)
3. Singpurwalla, N.D., Soyer, R.: Reliability and Maintenance of Complex Systems. In: NATO ASI Series, vol. 154, pp. 345–367. Springer, Berlin, Heidelberg (1996). <https://doi.org/10.1007/978-3-662-03274-9>
4. Shetty, N.R., Patnaik, L.M., Nagaraj, H.C., Hamsavath, P.N., Nalini, N. (eds.): LNEE, vol. 790. Springer, Singapore (2022). <https://doi.org/10.1007/978-981-16-1342-5>
5. Dale, C.: The assessment of software reliability. Reliab. Eng. Syst. Saf. **34**(1), 91–103 (1991)
6. Tantri, B.R., Murulidhar, N.N.: Software reliability estimation of gamma failure time models. In: Proceedings of the IEEE International Conference on System Reliability and Science, pp. 105–109, Paris, France (2016)
7. Nayak, T.K.: Frontiers in reliability - series on quality. Reliab. Eng. Stat. **4**, 271–281 (1998)
8. Ghitany, M.E., Atieh, B., Nadarajah, S.: Lindley distribution and its application. Math. Comput. Simul. **78**(4), 493–506 (2008)

9. Tantri, B.R.: Estimation of Software Reliability for Littlewood Pareto Failure Time Model Estimation of Software Reliability for Littlewood Pareto Failure Time Model (2018). <https://doi.org/10.14257/ijseia.2017.11.6.03>
10. Maiti, S.S., Mukherjee, I.: On estimation of the PDF and CDF of the Lindley distribution. *Commun. Stat. Simul. Comput.* **47**(5), 1370–1381 (2018)
11. Gupta, S.C., Kapoor, V.K.: *Theory of Estimation and Fundamentals of Mathematical Statistics*, 9th ed. Sultan Chand & Sons, Darya Ganj (1996)
12. Musa, J.D.: *Software Reliability Engineering*, 2nd ed. Tata McGraw Hill, Noida (2004)
13. Musa, J.D., Iannino, A., Okumoto, K.: *Software Reliability: Measurement, Prediction, Application*. McGraw-Hill, Bengaluru (1987)
14. Liu, J., Liu, Y., Xu, M.: Parameter Estimation of Jelinski-Moranda Model Based on Weighted Nonlinear Least Squares and Heteroscedasticity, pp. 1–17, arXiv preprint [arXiv:1503.00094](https://arxiv.org/abs/1503.00094) (2015)
15. Joe, H., Reid, N.: On the software reliability models of jelinski-moranda and littlewood. *IEEE Trans. Reliab.* **34**(3), 216–218 (1985)
16. Francis, B., Lawless, J.F.: *Statistical Models and Methods for Lifetime Data*, 2nd edn. John Wiley & Sons Inc., Hoboken, New Jersey (2003)
17. Tantri, B.R.: An Efficient Estimator of Reliability for Exponential Class Software Reliability Models (2014). <https://doi.org/10.7763/LNSE.2014.V2.123>
18. Sinha, S., Sinha, S.K., Kale, B.K.: *Exponential Failure Model, Life Testing & Reliability Estimation*. Wiley Eastern Limited, Mumbai, (1980)
19. Kumar, R., Koundal, R., Shehzad, S.A.: Generalized least square homotopy perturbation solution of fractional telegraph equations. *Comput. Appl. Math.* **38**(4), 1–20 (2019). <https://doi.org/10.1007/s40314-019-0943-0>
20. Kumar, R., Koundal, R., Shehzad, S.A.: Least square homotopy solution to hyperbolic telegraph equations: multi-dimension analysis *International Journal of. Appl. Comput. Math.* **6**, 1–19 (2020)
21. Laxmi, D., Sharma, S.K.: Testing of $n+1$ Parameter from unlike load sharing system. *Int. J. Emerg. Technol.* **10**(2b), 83–87 (2019)
22. Kaur, H., Sharma, S.K.: Exploration on reliability theory using LGCM model in neural network. *Adv. Math. Sci. J.* **8**, 5349–5359 (2020)
23. Thakur, P., Sharma, S.K.: Estimation of complexity in software reliability growth modeling. *Adv. Appl. Math. Sci.* **19**(6), 563–572 (2020)



Solution of Fractional Order Foam Drainage Equation Using Shehu Transform

T. Pasayat and A. Patra^(✉)

School of Mathematics, Gangadhar Meher University,
Sambalpur 768004, Odisha, India
ashrita.patra@gmail.com

Abstract. Foaming arises in many processes of absorption and distillation. The drainage of liquid foams involves the interplay of gravity, surface tension and viscous forces. For the foam density the drainage of liquid can be represented as a nonlinear partial differential equation as a function of time and vertical position. In this paper, Combined Shehu Accelerated Adomian Decomposition method is applied to solve fractional order foam drainage equation. The powerful Shehu Transform(ST) combined with Accelerated Adomian decomposition method (AADM) evaluates the approximate solution in the form of infinite series which converges very rapidly.

Keywords: Foam drainage equation · Shehu transform · Accelerated Adomian decomposition method · Fractional derivatives

1 Introduction

The concept of Fractional calculus(FC) has been generalized by the theory of classical calculus perturbed with the operations of differentiation and integration of arbitrary order. Podlubny [14], Kilbas et al. [9], Miller and Ross [11], Oldham and Spanier [12], Samko et al. [16] and others are the trailblazer in this field; from their work it is easy to understand about the theory of fractional calculus, also the uniqueness and existence to the solution of fractional differential equations. The application of FC has been manifolded in widespread fields of engineering and science such as biological population models, signal processing, viscoelasticity, electromagnetics, optics, electrochemistry, fluid mechanics etc. By using FC it becomes very easy to describe the physical and mathematical models. Various numerical and analytical techniques has been proposed in recent years to solve the partial differential equations(PDEs) in these fields such as Sumudu Homotopy perturbation transform method [1, 2], Homotopy Perturbation method [5, 6, 18], Natural transform decomposition method [15], fractional complex transform method [17], Adomian decomposition method [24, 25] etc. Therefore it enhance with all established and newly developed techniques for solving arbitrary order PDEs.

The system of Foam drainage(FD) is a natural process, is described in [8, 10]. Many industrial and technological approach has been formed for foams because of its significance in real life which includes purification of water, mineral extraction and cleansing as shown in [8, 10]. More than ten years ago, the main features of both forced drainage, and free drainage were described by Verbist and Weaire. Due to gravity liquid drains out in free drainage and liquid is introduced in forced drainage [7, 19–23]. Then at a constant rate when some liquid is added a solitary wave of constant velocity is generated. So particularly for the solitary wave, the best example for certain general circumstances might be the forced foam drainage described by nonlinear PDEs.

2 The Model

The model is constructed on account of nearly dry foam and thus consider best in this limit. The size of the bubble and sample are in such a manner that the equilibrium foam is very dry in many practical cases. Some chief assumptions are made; such as in the film allowance of liquid flow is neglected completely. Further we take all the flow at the boundaries with zero velocity. We studied the flow only along the plateau borders which forms a web of passage gathering in bipyramidal confluence as a set of N identical pipes of cross section B , which is a function of position and time and below

$$\frac{\partial B(\phi, t)}{\partial t} + \frac{\partial}{\partial \phi} \left(B(\phi, t)^2 - \frac{\sqrt{B(\phi, t)}}{2} \frac{\partial B(\phi, t)}{\partial \phi} \right) = 0 \quad (2.1)$$

and the exact solution of (2.1) is

$$B(\phi, t) = \begin{cases} c \tanh(\sqrt{c}(\phi - ct))^2, & \phi \leq ct, \\ 0, & \phi \geq ct, \end{cases} \quad (2.2)$$

where ϕ , t and c denotes location, time and velocity of the wave front respectively.

If we take $B(\phi, t) = \mathcal{V}(\phi, t)^2$ and rearranging Eq. (2.1) it can be defined as below

$$\mathcal{V}_t(\phi, t) + 2\mathcal{V}^2(\phi, t)\mathcal{V}_\phi(\phi, t) - \mathcal{V}_\phi^2(\phi, t) - \frac{1}{2}\mathcal{V}(\phi, t)\mathcal{V}_{\phi\phi}(\phi, t) = 0 \quad (2.3)$$

with initial condition $\mathcal{V}(\phi, 0) = g(\phi)$

Here, we consider the nonlinear FD equation to solve by using ST and AADM which is more reliable to get an analytical approximation with rapid convergence with the exact solution.

3 Preliminaries

3.1 Some Important Definitions of Fractional Order Derivative

Let $\tau \in R^+$ such that $n = [\tau] + 1$ and $\psi \in AC^{[\tau]}([m, b])$ (the space of functions which have continuous derivatives up to order τ). Then some familiar definitions of arbitrary order derivatives of order τ can be described as below ([13–16]):

(i) *Riemann-Liouville derivative:*

$${}^{RL}D_m^\tau \psi(t) = \frac{d^n}{dt^n} \int_m^t \frac{(t - \phi)^{n-\tau-1}}{\Gamma(n - \tau)} \psi(\phi) d\phi, \quad (t > m), \tag{3.1}$$

(ii) *Caputo derivative:*

$${}^C D_m^\tau \psi(t) = \int_m^t \frac{(t - \phi)^{n-\tau-1}}{\Gamma(n - \tau)} \psi^{(n)}(\phi) d\phi, \quad (t > m). \tag{3.2}$$

(iii) *Grunwald-Letnikov derivative:*

$$D^\tau \psi(t) = \lim_{h \rightarrow 0} \frac{1}{h^\tau} \sum_{j=0}^{[\frac{t-\tau}{h}]} (-1)^j \binom{\tau}{j} \psi(t - jh). \tag{3.3}$$

where $\Gamma(\cdot)$ is the Euler gamma function, $\psi^{(n)}(x) = \frac{d^n}{d\phi^n} \psi(\phi)$, $[\tau]$ is the integral part of τ . Then the correlation between arbitrary order derivatives in view of Riemann-Liouville and Caputo can be described as below:

Remark 3.1. If $n = [\tau] + 1$ and $\psi \in AC^{[\tau]}([m, b])$, then

$${}^{RL}D_m^\tau \psi(t) = {}^C D_m^\tau \psi(t) + \sum_{k=0}^{n-1} \frac{(t - m)^{k-\tau}}{\Gamma(k - \tau + 1)} \psi^{(k)}(m),$$

and in specific if $\psi(t) = (t - m)^\delta$, and $\delta \notin \mathbb{Z}^-$, then

$${}^{RL}D_m^\tau \psi(t) = {}^C D_m^\tau \psi(t) = D_m^\tau \psi(t) = \frac{\Gamma(\delta + 1)}{\Gamma(\delta + 1 - \tau)} (t - m)^{\delta - \tau}.$$

Remark 3.2. If $\tau > 0$, and $\psi(t) = (t - m)^\delta$ with $\tau - \delta - 1 \in \mathbb{N}_0$ (the set of all nonnegative integers), then

$${}^{RL}D_m^\tau \psi(t) = {}^C D_m^\tau \psi(t) = D^\tau \psi(t) = 0.$$

3.2 Shehu Transform

The ST of the function $f(t)$ of exponential order can be described over the set of the functions:

$$G = \left\{ f(t) : \exists M, \mu_1, \mu_2 > 0, |f(t)| < M e^{\left(\frac{|t|}{\mu_j}\right)}, \text{ if } t \in (-1)^j \times [0, \infty) \right\}, \tag{3.4}$$

by the following integral

$$\mathbb{S}\{f(t)\} = [H(s, u)] = \int_0^\infty f(t)e^{-\frac{st}{u}} dt = \lim_{\delta \rightarrow \infty} \int_0^\delta f(t)e^{-\frac{st}{u}} dt, \quad s > 0, u > 0 \tag{3.5}$$

where operator \mathbb{S} is called the Shehu transform operator.

The inverse ST of $H(s, u)$ is given as

$$\mathbb{S}^{-1}\{H(s, u)\} = f(t), \quad \text{for } t \geq 0. \tag{3.6}$$

Equivalently

$$f(t) = \mathbb{S}^{-1}\{H(s, u)\} = \frac{1}{2\pi i} \int_{\delta-i\infty}^{\delta+i\infty} \frac{1}{u} e^{\frac{st}{u}} H(s, u) ds \tag{3.7}$$

where the operator \mathbb{S}^{-1} is called the inverse Shehu transform operator, s and u are the variables of Shehu transform, the integral in Eq. (3.7) is taken along $s = \delta$ in the complex plane $s = x + iy$ and $\delta \in R$.

Theorem 3.8. *The sufficient conditions for the existence of ST:*

If the function $f(t)$ is piecewise continuous in every finite interval $0 \leq t \leq \alpha$ and of exponential order δ for $t > \alpha$, then its ST $H(s, u)$ exists.

Theorem 3.9. *ST of the derivatives of the function $f(t)$:*

If the function $f(t) \in G$ and $f^{(n)}(t)$ is the n th order derivative of $f(t)$ with respect to t then its ST is defined as:

$$\mathbb{S} \left[f^{(n)}(t) \right] = \frac{s^n}{u^n} H(s, u) - \sum_{k=0}^{n-1} \left(\frac{s}{u}\right)^{n-(k+1)} f^{(k)}(0) \tag{3.10}$$

Taking $n = 1, 2$ and 3 in Eq. (3.10), we get

$$\begin{aligned} \mathbb{S}\{f'(t)\} &= \frac{s}{u} H(s, u) - f(0) \\ \mathbb{S}\{f''(t)\} &= \frac{s^2}{u^2} H(s, u) - \frac{s}{u} f(0) - f'(0) \\ \mathbb{S}\{f'''(t)\} &= \frac{s^3}{u^3} H(s, u) - \frac{s^2}{u^2} f(0) - \frac{s}{u} f'(0) - f''(0) \end{aligned} \tag{3.11}$$

Shehu Transform of Some Fundamental Functions

S N	$f(t)$	$\mathbb{S}\{f(t)\} = H(s, u)$
1	1	$\frac{u}{s}$
2	t	$(\frac{u}{s})^2$
3	t^2	$2!(\frac{u}{s})^3$
4	$t^n, n \in N$	$n!(\frac{u}{s})^{(n+1)}$
5	$t^n > -1$	$\Gamma(n+1)(\frac{u}{s})^{(n+1)}$
6	e^{at}	$\frac{u}{s-au}$
7	sinat	$\frac{au^2}{s^2+a^2u^2}$
8	cosat	$\frac{us}{s^2+a^2u^2}$
9	sinhat	$\frac{au^2}{s^2-a^2u^2}$
10	coshat	$\frac{us}{s^2-a^2u^2}$

3.3 The Combined Shehu Accelerated Adomian Decomposition Method

To exemplify the elementary idea of ST combined with AADM [24], we consider a general nonlinear nonhomogeneous PDE

$$\frac{\partial^\alpha \mathcal{V}(\phi, t)}{\partial t^\alpha} + R[\mathcal{V}(\phi, t)] + N[\mathcal{V}(\phi, t)] = g(\phi, t) \tag{3.12}$$

where $\frac{\partial^\alpha \mathcal{V}(\phi, t)}{\partial t^\alpha}$ is the partial derivative of the function $\mathcal{V}(\phi, t)$ of order α , R and N are the general linear and nonlinear differential operators and $g(\phi, t)$ is the source term.

Applying the ST on both sides of Eq. (3.12), we obtain

$$\mathbb{S} \left[\frac{\partial^\alpha \mathcal{V}(\phi, t)}{\partial t^\alpha} \right] + \mathbb{S}[R\mathcal{V}(\phi, t) + N\mathcal{V}(\phi, t)] = \mathbb{S}[g(\phi, t)] \tag{3.13}$$

Using properties of ST, we obtain

$$\frac{s^\alpha}{u^\alpha} \mathbb{S}[\mathcal{V}(\phi, t)] = \sum_{k=0}^{\alpha-1} \left(\frac{s}{u}\right)^{\alpha-(k+1)} \frac{\partial^k \mathcal{V}(\phi, 0)}{\partial t^k} + \mathbb{S}[g(\phi, t)] - \mathbb{S}[R\mathcal{V}(\phi, t) + N\mathcal{V}(\phi, t)] \tag{3.14}$$

Thus we have

$$\mathbb{S}[\mathcal{V}(\phi, t)] = \sum_{k=0}^{\alpha-1} \left(\frac{u}{s}\right)^{k+1} \frac{\partial^k \mathcal{V}(\phi, 0)}{\partial t^k} + \frac{u^\alpha}{s^\alpha} \mathbb{S}[g(\phi, t)] - \frac{u^\alpha}{s^\alpha} \mathbb{S}[R\mathcal{V}(\phi, t) + N\mathcal{V}(\phi, t)] \tag{3.15}$$

taking inverse ST on both sides of Eq. (3.15), we obtain

$$\mathcal{V}(\phi, t) = G(\phi, t) - \mathbb{S}^{-1} \left(\frac{u^\alpha}{s^\alpha} \mathbb{S}[R\mathcal{V}(\phi, t) + N\mathcal{V}(\phi, t)] \right) \tag{3.16}$$

where $G(\phi, t)$ arises from the stipulated initial conditions and the source term.

Then the solution can be represented as an infinite series as follows

$$\mathcal{V}(\phi, t) = \sum_{n=0}^{\infty} \mathcal{V}_n(\phi, t). \tag{3.17}$$

and the nonlinear term can be decomposed as:

$$N\mathcal{V}(\phi, t) = \sum_{n=0}^{\infty} \overline{A}_n(\mathcal{V}_0, \mathcal{V}_1, \dots, \mathcal{V}_n), \tag{3.18}$$

here

$$\overline{A}_n = f(S_n) - \sum_{i=0}^{n-1} \overline{A}_i \tag{3.19}$$

and

$$A_n = \frac{1}{n!} \frac{d^n}{d\lambda^n} \left[N \left(\sum_{k=0}^{\infty} \lambda^k \mathcal{V}_k \right) \right]_{\lambda=0}, \quad n = 0, 1, 2, \dots \tag{3.20}$$

where \overline{A}_n are Adomian polynomials of $\mathcal{V}_0, \mathcal{V}_1, \dots, \mathcal{V}_n$ [25] \overline{A}_n are El-kalla polynomials $\overline{A}_0, \overline{A}_1, \overline{A}_2 \dots$ and $f(S_n)$ represents the substitution of the summation of dependent variable in the nonlinear term.

putting Eq. (3.17) and (3.18) in Eq. (3.16), we obtain

$$\sum_{n=0}^{\infty} \mathcal{V}_n(\phi, t) = G(\phi, t) - \mathbb{S}^{-1} \left[\frac{u^\alpha}{s^\alpha} \mathbb{S} \left[R \sum_{n=0}^{\infty} \mathcal{V}_n(\phi, t) + \sum_{n=0}^{\infty} \overline{A}_n(\mathcal{V}_0, \mathcal{V}_1, \dots, \mathcal{V}_n) \right] \right] \tag{3.21}$$

on comparing both sides of the Eq. (3.21), we obtain

$$\mathcal{V}_0(\phi, t) = G(\phi, t) \tag{3.22}$$

$$\mathcal{V}_1(\phi, t) = -\mathbb{S}^{-1} \left[\frac{u^\alpha}{s^\alpha} \mathbb{S}[R\mathcal{V}_0(\phi, t) + \overline{A}_0\mathcal{V}] \right] \tag{3.23}$$

$$\mathcal{V}_2(\phi, t) = -\mathbb{S}^{-1} \left[\frac{u^\alpha}{s^\alpha} \mathbb{S}[R\mathcal{V}_1(\phi, t) + \overline{A}_1\mathcal{V}] \right] \tag{3.24}$$

$$\mathcal{V}_3(\phi, t) = -\mathbb{S}^{-1} \left[\frac{u^\alpha}{s^\alpha} \mathbb{S}[R\mathcal{V}_2(\phi, t) + \overline{A}_2\mathcal{V}] \right] \tag{3.25}$$

⋮
⋮
⋮

In general, the recursive relation can be written as

$$\mathcal{V}_{n+1}(\phi, t) = -\mathbb{S}^{-1} \left[\frac{u^\alpha}{s^\alpha} \mathbb{S} [R\mathcal{V}_n(\phi, t) + \overline{A}_n \mathcal{V}] \right], \quad n \geq 0 \tag{3.26}$$

Then, the analytical solution $\mathcal{V}(\phi, t)$ can be approximated as below

$$\mathcal{V}(\phi, t) = \lim_{N \rightarrow \infty} \sum_{n=0}^N \mathcal{V}_n(\phi, t), \tag{3.27}$$

4 Results and Discussion

In this section, we discuss three exemplars to explore the proficiency and applicability of the proposed method. We have implemented Shehu Transform on fractional order foam drainage equation.

Exemplar 1 :

Let us consider the one-dimensional time dependent FD equation of arbitrary order α as follows

$$D_t^\alpha \mathcal{V}(\phi, t) = \frac{1}{2} \mathcal{V}(\phi, t) \mathcal{V}_{\phi\phi}(\phi, t) + \mathcal{V}_\phi^2(\phi, t) - 2\mathcal{V}^2(\phi, t) \mathcal{V}_\phi(\phi, t), \quad 0 < \alpha \leq 1 \tag{4.1}$$

with initial source

$$\mathcal{V}(\phi, 0) = \sqrt{c} \tanh(\sqrt{c}\phi) \tag{4.2}$$

Applying ST and then inverse ST to both sides of Eq. (4.1) we get

$$\mathcal{V}(\phi, t) = \mathcal{V}(\phi, 0) - \mathbb{S}^{-1} \left(\frac{u^\alpha}{s^\alpha} \mathbb{S} \left[\frac{1}{2} \mathcal{V}(\phi, t) \mathcal{V}_{\phi\phi}(\phi, t) + \mathcal{V}_\phi^2(\phi, t) - 2\mathcal{V}^2(\phi, t) \mathcal{V}_\phi(\phi, t) \right] \right) \tag{4.3}$$

to decompose the nonlinear term, we apply Accelerated Adomian polynomial to Eq. (4.7) we get,

$$\sum_{n=0}^{\infty} \mathcal{V}_n(\phi, t) = \mathcal{V}(\phi, 0) - \mathbb{S}^{-1} \left[\frac{u^\alpha}{s^\alpha} \mathbb{S} \left[\frac{1}{2} \sum_{n=0}^{\infty} \overline{A}_n + \sum_{n=0}^{\infty} \overline{B}_n - 2 \sum_{n=0}^{\infty} \overline{C}_n \right] \right] \tag{4.4}$$

where

$$\begin{aligned} \overline{A}_0 &= \mathcal{V}_{0\phi\phi} \mathcal{V}_0 \\ \overline{A}_1 &= \mathcal{V}_{0\phi\phi} \mathcal{V}_1 + \mathcal{V}_0 \mathcal{V}_{1\phi\phi} + \mathcal{V}_1 \mathcal{V}_{1\phi\phi} \\ \overline{A}_2 &= \mathcal{V}_1 \mathcal{V}_{2\phi\phi} + \mathcal{V}_{0\phi\phi} \mathcal{V}_2 + \mathcal{V}_0 \mathcal{V}_{2\phi\phi} + \mathcal{V}_2 \mathcal{V}_{1\phi\phi} + \mathcal{V}_2 \mathcal{V}_{2\phi\phi} \\ &\vdots \end{aligned}$$

$$\begin{aligned} \bar{B}_0 &= \mathcal{V}_{0\phi}^2 \\ \bar{B}_1 &= \mathcal{V}_{1\phi}^2 + 2\mathcal{V}_{0\phi}\mathcal{V}_{1\phi} \\ \bar{B}_2 &= \mathcal{V}_{2\phi}^2 + 2\mathcal{V}_{1\phi}\mathcal{V}_{2\phi} + \mathcal{V}_{2\phi}\mathcal{V}_{0\phi} \\ &\vdots \end{aligned}$$

$$\begin{aligned} \bar{C}_0 &= \mathcal{V}_0^2\mathcal{V}_{0\phi} \\ \bar{C}_1 &= \mathcal{V}_1^2\mathcal{V}_{0\phi} + 2\mathcal{V}_0\mathcal{V}_1\mathcal{V}_{0\phi} + \mathcal{V}_0^2\mathcal{V}_{1\phi} + \mathcal{V}_1^2\mathcal{V}_{1\phi} + 2\mathcal{V}_0\mathcal{V}_1\mathcal{V}_{1\phi} \\ \bar{C}_2 &= \mathcal{V}_2^2\mathcal{V}_{0\phi} + 2\mathcal{V}_1\mathcal{V}_2\mathcal{V}_{0\phi} + 2\mathcal{V}_0\mathcal{V}_2\mathcal{V}_{0\phi} + \mathcal{V}_2^2\mathcal{V}_{1\phi} + 2\mathcal{V}_1\mathcal{V}_2\mathcal{V}_{1\phi} + 2\mathcal{V}_0\mathcal{V}_2\mathcal{V}_{1\phi} + \mathcal{V}_0^2\mathcal{V}_{2\phi} + \mathcal{V}_1^2\mathcal{V}_{2\phi} \\ &\quad + \mathcal{V}_2^2\mathcal{V}_{2\phi} + 2\mathcal{V}_0\mathcal{V}_1\mathcal{V}_{2\phi} + 2\mathcal{V}_1\mathcal{V}_2\mathcal{V}_{2\phi} + 2\mathcal{V}_0\mathcal{V}_2\mathcal{V}_{2\phi} \end{aligned}$$

from Eq. (4.8) we get,
for $n = 0$,

$$\mathcal{V}_0(\phi, t) = \mathcal{V}(\phi, 0) = \sqrt{c} \tanh(\sqrt{c}\phi)$$

for $n = 1$,

$$\begin{aligned} \mathcal{V}_1(\phi, t) &= -\mathbb{S}^{-1} \left[\frac{u^\alpha}{s^\alpha} \mathbb{S} \left[\frac{1}{2} \sum_{n=0}^\infty \bar{A}_0 + \sum_{n=0}^\infty \bar{B}_0 - 2 \sum_{n=0}^\infty \bar{C}_0 \right] \right] \\ &= \frac{t^\alpha}{\Gamma(1 + \alpha)} \left[c^2 (\operatorname{sech} \sqrt{c}\phi)^4 - 3c^2 (\operatorname{sech} \sqrt{c}\phi)^2 (\tanh \sqrt{c}\phi)^2 \right] \end{aligned}$$

for $n = 2$,

$$\begin{aligned} \mathcal{V}_2(\phi, t) &= -\mathbb{S}^{-1} \left[\frac{u^\alpha}{s^\alpha} \mathbb{S} \left[\frac{1}{2} \sum_{n=0}^\infty \bar{A}_1 + \sum_{n=0}^\infty \bar{B}_1 - 2 \sum_{n=0}^\infty \bar{C}_1 \right] \right] \\ &= \frac{t^{2\alpha}}{\Gamma(1 + 2\alpha)} \left(4c^{\frac{3}{2}} \frac{t^\alpha}{\Gamma(1 + \alpha)} (\operatorname{sech} \sqrt{c}\phi)^2 (\tanh \sqrt{c}\phi) \left(c^2 (\operatorname{sech} \sqrt{c}\phi)^4 - 3c^2 (\operatorname{sech} \sqrt{c}\phi)^2 (\tanh \sqrt{c}\phi)^2 \right) \right. \\ &\quad \left. + \frac{2ct^\alpha}{\Gamma(1 + \alpha)} (\operatorname{sech} \sqrt{c}\phi)^2 \left(-10c^{\frac{5}{2}} (\operatorname{sech} \sqrt{c}\phi)^4 (\tanh \sqrt{c}\phi) + 6c^{\frac{5}{2}} (\operatorname{sech} \sqrt{c}\phi)^2 (\tanh \sqrt{c}\phi)^3 \right) + \dots \right. \end{aligned}$$

Exemplar 2 :

To check the accuracy, efficiency and reliability of SDM we have considered the fractional order FD Eq. (2.3) with a different initial condition as follows

$$D_t^\alpha \mathcal{V}(\phi, t) = \frac{1}{2} \mathcal{V}(\phi, t) \mathcal{V}_{\phi\phi}(\phi, t) + \mathcal{V}_\phi^2(\phi, t) - 2\mathcal{V}^2(\phi, t) \mathcal{V}_\phi(\phi, t), \quad 0 < \alpha \leq 1 \quad (4.5)$$

with initial source

$$\mathcal{V}(\phi, 0) = -\frac{1}{2} + \frac{1}{1 + e^\phi} \quad (4.6)$$

Applying ST and then inverse ST to both sides of Eq. (4.1) we get

$$\mathcal{V}(\phi, t) = \mathcal{V}(\phi, 0) - \mathbb{S}^{-1} \left(\frac{u^\alpha}{s^\alpha} \mathbb{S} \left[\frac{1}{2} \mathcal{V}(\phi, t) \mathcal{V}_{\phi\phi}(\phi, t) + \mathcal{V}_\phi^2(\phi, t) - 2\mathcal{V}^2(\phi, t) \mathcal{V}_\phi(\phi, t) \right] \right) \quad (4.7)$$

to decompose the nonlinear term, we apply Accelerated Adomian polynomial to Eq. (4.7) we get,

$$\sum_{n=0}^{\infty} \mathcal{V}_n(\phi, t) = \mathcal{V}(\phi, 0) - \mathbb{S}^{-1} \left[\frac{u^\alpha}{s^\alpha} \mathbb{S} \left[\frac{1}{2} \sum_{n=0}^{\infty} \overline{A}_n + \sum_{n=0}^{\infty} \overline{B}_n - 2 \sum_{n=0}^{\infty} \overline{C}_n \right] \right] \quad (4.8)$$

where

$$\begin{aligned} \overline{A}_0 &= \mathcal{V}_{0\phi\phi} \mathcal{V}_0 \\ \overline{A}_1 &= \mathcal{V}_{0\phi\phi} \mathcal{V}_1 + \mathcal{V}_0 \mathcal{V}_{1\phi\phi} + \mathcal{V}_1 \mathcal{V}_{1\phi\phi} \\ \overline{A}_2 &= \mathcal{V}_1 \mathcal{V}_{2\phi\phi} + \mathcal{V}_{0\phi\phi} \mathcal{V}_2 + \mathcal{V}_0 \mathcal{V}_{2\phi\phi} + \mathcal{V}_2 \mathcal{V}_{1\phi\phi} + \mathcal{V}_2 \mathcal{V}_{2\phi\phi} \\ &\vdots \\ \overline{B}_0 &= \mathcal{V}_{0\phi}^2 \\ \overline{B}_1 &= \mathcal{V}_{1\phi}^2 + 2\mathcal{V}_{0\phi} \mathcal{V}_{1\phi} \\ \overline{B}_2 &= \mathcal{V}_{2\phi}^2 + 2\mathcal{V}_{1\phi} \mathcal{V}_{2\phi} + \mathcal{V}_{2\phi} \mathcal{V}_{0\phi} \\ &\vdots \end{aligned}$$

$$\begin{aligned} \overline{C}_0 &= \mathcal{V}_0^2 \mathcal{V}_{0\phi} \\ \overline{C}_1 &= \mathcal{V}_1^2 \mathcal{V}_{0\phi} + 2\mathcal{V}_0 \mathcal{V}_1 \mathcal{V}_{0\phi} + \mathcal{V}_0^2 \mathcal{V}_{1\phi} + \mathcal{V}_1^2 \mathcal{V}_{1\phi} + 2\mathcal{V}_0 \mathcal{V}_1 \mathcal{V}_{1\phi} \\ \overline{C}_2 &= \mathcal{V}_2^2 \mathcal{V}_{0\phi} + 2\mathcal{V}_1 \mathcal{V}_2 \mathcal{V}_{0\phi} + 2\mathcal{V}_0 \mathcal{V}_2 \mathcal{V}_{0\phi} + \mathcal{V}_2^2 \mathcal{V}_{1\phi} + 2\mathcal{V}_1 \mathcal{V}_2 \mathcal{V}_{1\phi} + 2\mathcal{V}_0 \mathcal{V}_2 \mathcal{V}_{1\phi} + \mathcal{V}_0^2 \mathcal{V}_{2\phi} + \mathcal{V}_1^2 \mathcal{V}_{2\phi} + \mathcal{V}_2^2 \mathcal{V}_{2\phi} \\ &\quad + 2\mathcal{V}_0 \mathcal{V}_1 \mathcal{V}_{2\phi} + 2\mathcal{V}_1 \mathcal{V}_2 \mathcal{V}_{2\phi} + 2\mathcal{V}_0 \mathcal{V}_2 \mathcal{V}_{2\phi} \\ &\vdots \end{aligned}$$

from Eq. (4.8) we get,
for n = 0,

$$\mathcal{V}_0(\phi, t) = \mathcal{V}(\phi, 0) = -\frac{1}{2} + \frac{1}{1 + e^\phi}$$

for n = 1,

$$\begin{aligned} \mathcal{V}_1(\phi, t) &= -\mathbb{S}^{-1} \left[\frac{u^\alpha}{s^\alpha} \mathbb{S} \left[\frac{1}{2} \sum_{n=0}^{\infty} \overline{A}_0 + \sum_{n=0}^{\infty} \overline{B}_0 - 2 \sum_{n=0}^{\infty} \overline{C}_0 \right] \right] \\ &= \frac{t^\alpha}{\Gamma(1 + \alpha)} \left[\frac{e^{2\phi}}{(1 + e^\phi)^4} + \frac{1}{2} \left(\frac{2e^{2\phi}}{(1 + e^\phi)^3} - \frac{e^\phi}{(1 + e^\phi)^2} \right) \left(\frac{-1}{2} + \frac{1}{1 + e^\phi} \right) + \frac{2e^\phi \left(\frac{-1}{2} + \frac{1}{1 + e^\phi} \right)^2}{(1 + e^\phi)^2} \right] \end{aligned}$$

for n = 2,

$$\begin{aligned} \mathcal{V}_2(\phi, t) &= -\mathbb{S}^{-1} \left[\frac{u^\alpha}{s^\alpha} \mathbb{S} \left[\frac{1}{2} \sum_{n=0}^{\infty} \overline{A}_1 + \sum_{n=0}^{\infty} \overline{B}_1 - 2 \sum_{n=0}^{\infty} \overline{C}_1 \right] \right] \\ &= \frac{t^{2\alpha}}{\Gamma(1 + 2\alpha)} \left[\frac{1}{2} \frac{t^\alpha}{\Gamma(1 + \alpha)} \left(\frac{2e^{2\phi}}{(1 + e^\phi)^3} - \frac{e^\phi}{(1 + e^\phi)^2} \right) \left(\frac{e^{2\phi}}{(1 + e^\phi)^4} + \frac{1}{2} \left(\frac{2e^{2\phi}}{(1 + e^\phi)^3} - \frac{e^\phi}{(1 + e^\phi)^2} \right) \right) \right. \\ &\quad \left(\frac{-1}{2} + \frac{1}{1 + e^\phi} \right) + \frac{2e^\phi \left(\frac{-1}{2} + \frac{1}{1 + e^\phi} \right)^2}{(1 + e^\phi)^2} + \left(\frac{-1}{2} + \frac{1}{1 + e^\phi} \right) \left(-\frac{16e^{3\phi}}{(1 + e^\phi)^5} + \frac{4e^{2\phi}}{(1 + e^\phi)^4} \right) \\ &\quad \left. + e^{2\phi} \left(\frac{20e^{2\phi}}{(1 + e^\phi)^6} - \frac{4e^\phi}{(1 + e^\phi)^5} \right) + \dots \right] \end{aligned}$$

Exemplar 3 :

Here we have consider another problem of fractional order foam drainage equation as follows

$$D_t^\alpha \mathcal{V}(\phi, t) = \frac{1}{4\sqrt{\mathcal{V}(\phi, t)}} (\mathcal{V}_\phi(\phi, t))^2 \frac{\sqrt{\mathcal{V}(\phi, t)}}{2} \mathcal{V}_{\phi\phi}(\phi, t) - 2\mathcal{V}(\phi, t)\mathcal{V}_\phi(\phi, t), \quad 0 < \alpha \leq 1 \tag{4.9}$$

with initial condition

$$\mathcal{V}(\phi, 0) = 3\tanh^2(\sqrt{3}\phi) \tag{4.10}$$

Applying ST and then inverse ST to both sides of Eq. (4.9) we get

$$\mathcal{V}(\phi, t) = \mathcal{V}(\phi, 0) - \mathbb{S}^{-1} \left(\frac{u^\alpha}{s^\alpha} \mathbb{S} \left[\frac{1}{4\sqrt{\mathcal{V}(\phi, t)}} (\mathcal{V}_\phi(\phi, t))^2 + \frac{\sqrt{\mathcal{V}(\phi, t)}}{2} \mathcal{V}_{\phi\phi}(\phi, t) - 2\mathcal{V}(\phi, t)\mathcal{V}_\phi(\phi, t) \right] \right) \tag{4.11}$$

to decompose the nonlinear term, we apply Accelerated Adomian polynomial to Eq. (4.11) we get,

$$\sum_{n=0}^\infty \mathcal{V}_n(\phi, t) = \mathcal{V}(\phi, 0) - \mathbb{S}^{-1} \left[\frac{u^\alpha}{s^\alpha} \mathbb{S} \left[\frac{1}{4} \sum_{n=0}^\infty \overline{A}_n + \frac{1}{2} \sum_{n=0}^\infty \overline{B}_n - 2 \sum_{n=0}^\infty \overline{C}_n \right] \right] \tag{4.12}$$

where

$$\begin{aligned} \overline{A}_0 &= \frac{1}{\sqrt{\mathcal{V}_0}} \mathcal{V}_{0\phi}^2 \\ \overline{A}_1 &= \frac{(\mathcal{V})_{0\phi}^2 + (\mathcal{V})_{1\phi}^2 + 2\mathcal{V}_{0\phi}\mathcal{V}_{1\phi}}{\sqrt{\mathcal{V}_0 + \mathcal{V}_1}} - \frac{1}{\sqrt{\mathcal{V}_0}} (\mathcal{V})_{0\phi}^2 \\ &\vdots \\ \overline{B}_0 &= \sqrt{\mathcal{V}_0} \mathcal{V}_{0\phi\phi} \\ \overline{B}_1 &= \sqrt{\mathcal{V}_0 + \mathcal{V}_1} (\mathcal{V}_{0\phi\phi} + \mathcal{V}_{1\phi\phi}) - \sqrt{\mathcal{V}_0} \mathcal{V}_{0\phi\phi} \\ &\vdots \\ \overline{C}_0 &= \mathcal{V}_0 \mathcal{V}_{0\phi} \\ \overline{C}_1 &= \mathcal{V}_0 \mathcal{V}_{1\phi} + \mathcal{V}_1 \mathcal{V}_{0\phi} + \mathcal{V}_1 \mathcal{V}_{1\phi} \\ &\vdots \end{aligned}$$

from Eq. (4.12) we get,
for n = 0,

$$\mathcal{V}_0(\phi, t) = \mathcal{V}(\phi, 0) = 3\tanh^2(\sqrt{3}\phi)$$

for $n = 1$,

$$\begin{aligned} \nu_1(\phi, t) &= -s^{-1} \left[\frac{u^\alpha}{s^\alpha} s \left[\frac{1}{4} \sum_{n=0}^{\infty} \overline{A_0} + \frac{1}{2} \sum_{n=0}^{\infty} \overline{B_0} - 2 \sum_{n=0}^{\infty} \overline{C_0} \right] \right] \\ &= \frac{t^\alpha}{\Gamma(1 + \alpha)} \left(-18\sqrt{3} \operatorname{sech}[\sqrt{3}\phi]^2 \left(2 \operatorname{tanh}[\sqrt{3}\phi]^3 + \sqrt{\operatorname{tanh}[\sqrt{3}\phi]^2} \left(-\operatorname{sech}[\sqrt{3}\phi]^2 + \operatorname{tanh}[\sqrt{3}\phi]^2 \right) \right) \right) \end{aligned}$$

Table 1. The comparative study of absolute errors for Exemplar-1 at $t = 0.2$, $\alpha = 1$ and $c=1$

ϕ	\mathcal{V}_{Exact}	\mathcal{V}_{SDM}	$ \mathcal{V}_{Exact} - \mathcal{V}_{SDM} $
0	0.197375	0.2	0.0026468
1	0.664037	0.654206	0.00983052
2	0.946806	0.922295	0.0245109
3	0.992632	0.98854	0.00409162
4	0.999	0.99843	0.000569282
5	0.999865	0.999787	0.0000773322
6	0.999982	0.999971	0.0000104711
7	0.999998	0.999996	1.4172×10^{-6}
8	1	0.999999	1.91799×10^{-7}
9	1	1	2.59572×10^{-8}
10	1	1	3.51293×10^{-9}

Table 2. The absolute errors between Exact and SDM solution for different value of c at $t = 0.5$ and $\alpha = 1$ for Exemplar-1

ϕ	$ \mathcal{V}_{Exact} - \mathcal{V}_{SDM} $ at $c = 1$	$ \mathcal{V}_{Exact} - \mathcal{V}_{SDM} $ at $c = 2$
0	0.0378828	0.743633
1	0.0768653	0.121464
2	0.0892258	0.0973875
3	0.0166811	0.00614685
4	0.00235412	0.000364663
5	0.000320397	0.0000215584
6	0.0000433941	1.27424×10^{-6}
7	5.87336×10^{-6}	7.53151×10^{-8}
8	7.94883×10^{-7}	4.45156×10^{-9}
9	1.07576×10^{-7}	2.63113×10^{-10}
10	1.45588×10^{-8}	1.55513×10^{-11}

We have presented the graphs and tables for arbitrary order foam drainage equation for distinct values of α , ϕ and t . In Fig. 1 2D plot for exact and analytical solution are represented which reveals that the value of \mathcal{V} increases with the value

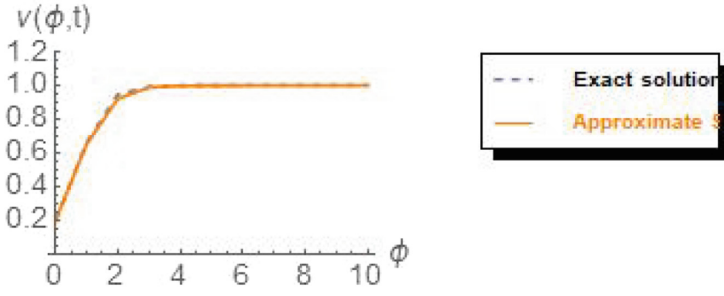


Fig. 1. 2D plot for Exact and SDM solution at $c = 1$ of Exemplar-1

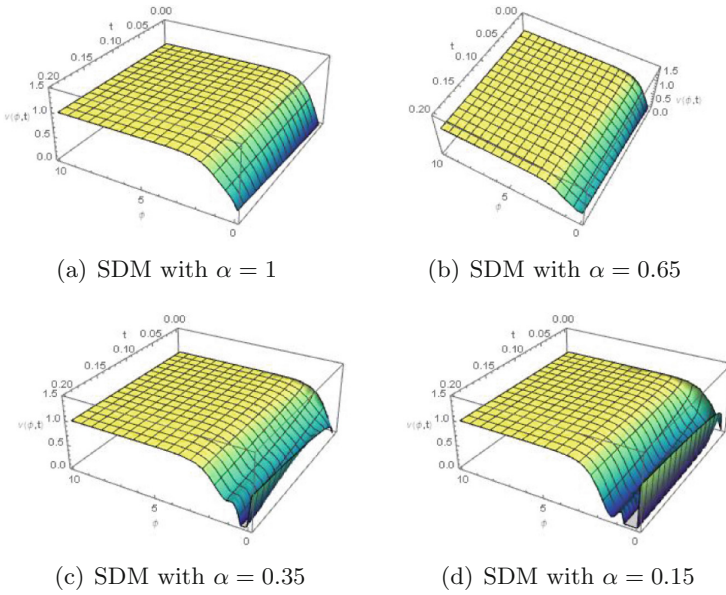


Fig. 2. 3D plots for arbitrary α with $c=1$ of exemplar-1

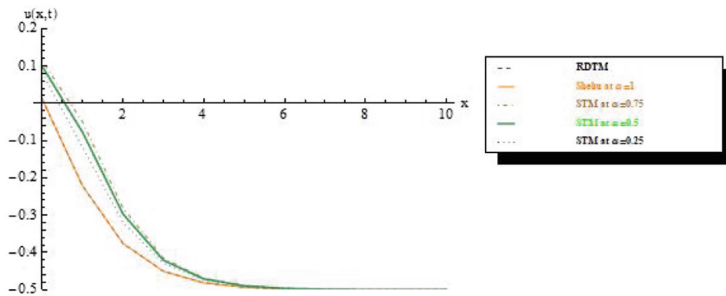


Fig. 3. comparative 2D plot of RDTM and SDM for arbitrary α of exemplar 2

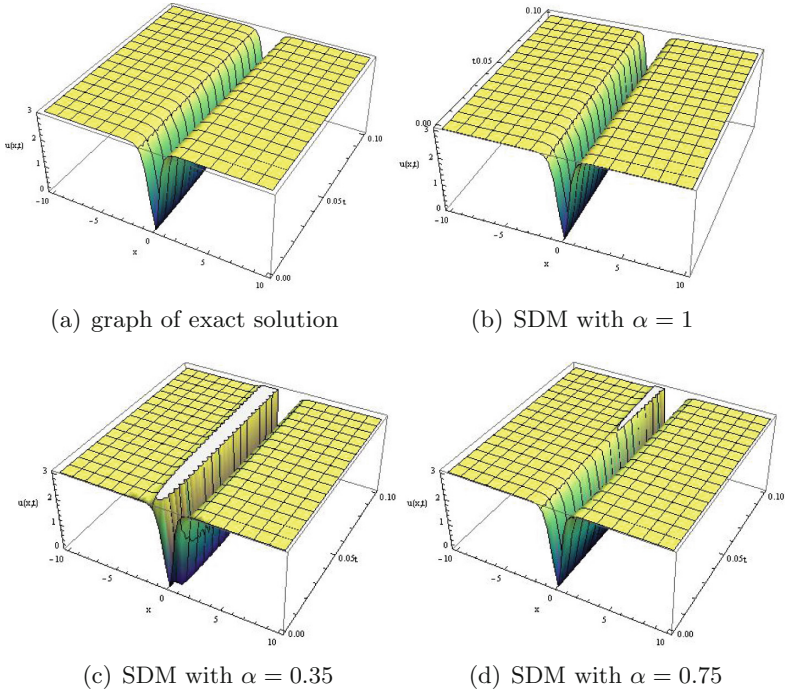


Fig. 4. 3D plots of Exemplar-3 for arbitrary α

of ϕ upto certain limit then it stabilizes, in Fig. 2 the behaviour of the analytical solution with distinct α are presented for exemplar-1 where it can be seen that as the value of α decreases the nature of solitary waves becomes folded. In Fig. 3 a comparative 2D plot is presented between RDTM [7] and SDM with different values of α for exemplar-2. Here it is shown that the result acquired by the proposed method is getting nearer to the solution obtained by RDTM as the value of α decreases. In Fig. 4 the behaviour of the exact and analytical solution for distinct α are presented for exemplar-3 which reveals that the gap between the solitary waves increases as the value of α decreases. To show the algorithm is systematic and accurate we have presented two tables for exemplar-1. In Table-1 a comparative study between exact and analytical solution has been shown and absolute error has been calculated. In Table-2 by taking different values of c the absolute errors has been calculated between exact solution and the proposed method (SDM).

5 Conclusion

We have applied the analytical technique SDM to find approximate solution for fractional order Foam Drainage equation. The proposed method is perceived to

be more genuine in comparison with the other techniques. Also the methodology is easy to understand to the readers as Shehu Transform is directly implemented to the given equation and to decompose the nonlinear terms we have used Accelerated Adomian polynomials. Then inverse Shehu Transform is applied to acquire the analytical solution. To exemplify the methodology illustrative exemplars also taken. We have presented two tables which shows the study of absolute errors between the exact and analytical solutions and the comparative study between the two analytical techniques i.e. SDM and RDTM [7] using different α . The solitary wave solutions represents the distinct nonlinear waves which have the astounding characteristic that retain its specification upon interrelate with other. Some comparative study is done for showing the analytical results which are analogous with the exact solutions of the nonlinear problems. It provides enough accuracy to obtain the approximate solution. Thus to solve the fractional order as well as classical order nonlinear PDEs we can consider the proposed method is more suitable and reliable technique.

Acknowledgement. This research work was financially supported by Minor Research Project under OHEPEE (World Bank), Govt. of Odisha with grant no.- 753/GMU, Sambalpur.

References

1. Goswami, A., Rathore, S., Singh, J., Kumar, D.: Analytical study of fractional nonlinear Schrödinger equation with harmonic oscillator. *Discret. Contin. Dyn. Syst. S* **14**(10), 3589–3610 (2021)
2. Goswami, A., Sushila., Singh, J., Kumar, D.: Numerical computation of fractional Kersten-Krasil'shchik coupled KdV-mKdV system arising in multi-component plasmas. *AIMS Math.* **5**(3), 2346–2368 (2020)
3. Goswami, A., Singh, J., Kumar, D., Rathore, S.: An efficient analytical approach for fractional equal width equations describing hydro-magnetic waves in cold plasma. *Phys. A* **524**, 563–575 (2019)
4. Goswami, A., Singh, J., Kumar, D., Rathore, S.: An efficient analytical technique for fractional partial differential equations occurring in ion acoustic waves in plasma. *J. Ocean Eng. Sci.* **4**, 85–99 (2019)
5. Goswami, A., Singh, J., Kumar, D.: Numerical simulation of fifth order KdV equations occurring in magneto-acoustic waves. *Ain Shams Eng. J.* **9**, 2265–2273 (2018)
6. Goswami, A., Singh, J., Kumar, D.: A reliable algorithm for KdV equations arising in warm plasma. *Nonlinear Eng.* **5**(1), 7–16 (2016)
7. Gubes, M., Keskin, Y., Oturanç, G.: Numerical solution of time-dependent foam drainage equation (FDE). *Comput. Methods Differ. Equ.* **3**, 111–122 (2015)
8. Hilgenfeldt, S., Koehler, S.A., Stone, H.A.: Dynamics of coarsening foams: accelerated and self-limiting drainage. *Phys. Rev. Lett.* **20**, 4704–4707 (2001)
9. Kilbas, A.A., Srivastava, H.M., Trujillo, J.J.: *Theory and Applications of Fractional Differential Equations*. Elsevier, Amsterdam (2006)
10. Koehler, S.A., Stone, H.A., Brenner, M.P., Eggers, J.: Dynamics of foam drainage. *Phys. Rev. E* **58**, 2097–2106 (1998)
11. Miller, K., Ross, B.: *An Introduction to the Fractional Calculus and Fractional Differential Equations*. Wiley, New York (1993)

12. Oldham, K.B., Spanier, J.: *The Fractional Calculus: Theory and Application of Differentiation and Integration to Arbitrary order*. Academic Press, California (1974)
13. Patra, A., Baliarsingh, P., Dutta, H.: Solution to fractional evolution equation using Mohand transform. *Math. Comput. Simul.* **200**, 557–570 (2022)
14. Podlubny, I.: *Fractional Differential Equations*. Academic Press, New York (1999)
15. Sahoo, M., Patra, A.: Modified decomposition method based on natural transform for solving nonlinear differential equations using Newton-Raphson scheme. *Int. J. Appl. Comput. Math* **7**, 91 (2021)
16. Samko, S.G., Kilbas, A.A., Marichev, O.I.: *Fractional integrals and Derivatives Theory and Applications*, vol. 1993. Gordon and Breach, Yverdon (1993)
17. Shone, T.T., Patra, A.: Solution for non-linear fractional partial differential equations using fractional complex transform. *Int. J. Appl. Comput. Math.* **5**(3), 1–8 (2019). <https://doi.org/10.1007/s40819-019-0673-4>
18. Shone, T.T., Patra, A., Mishra, B.B.: Solution of nonlinear fractional quadratic Riccati differential equations using perturbation method. *Int. J. Appl. Comput. Math.* **6**(3), 1–11 (2020). <https://doi.org/10.1007/s40819-020-00837-y>
19. Verbist, G., Weaire, D., Kraynik, A.M.: The foam drainage equation. *J. Phys. Condens. Matter* **83**, 715–731 (1996)
20. Verbist, G., Weaire, D.: Soluble model for foam drainage. *Europhys. Lett.* **26**, 631–641 (1994)
21. Weaire, D., Hutzler, S., Cox, S., Alonso, M.D., Drenckhan, D.: The fluid dynamics of foams. *J. Phys. Condens. Matter* **15**, 65–72 (2003)
22. Weaire, D., Hutzler, S.: *The Physics of Foams*, Oxford University Press, Oxford (2000)
23. Weaire, D., Hutzler, S., Verbist, G., Peters, E.A.J.: A review of foam drainage. *Adv. Chem. Phys.* **102**, 315–374 (1997)
24. Ziane, D., Belgacem, R., Bokhari, A.: A new modified Adomian decomposition method for nonlinear partial differential equations. *Open J. Math. Anal.* **3**, 81–90 (2019)
25. Zhu, Y., Chang, Q., Wu, S.: A new algorithm for calculating Adomian polynomials. *Appl. Math. Comput.* **169**, 402–416 (2005)



On a Class of MacRobert's Type Finite Integrals Involving Generalized Hypergeometric Functions

Vidha Kulkarni^{1(✉)}, Yashoverdhan Vyas¹, and Arjun K. Rathie²

¹ Department of Mathematics, School of Engineering, Sir Padampat Singhania University, Bhatewar, Udaipur 313601, Rajasthan, India

kvidha@gmail.com, yashoverdhan.vyas@spsu.ac.in

² Department of Mathematics, Vedant College of Engineering and Technology (Rajasthan Technical University), Bundi 323021, Rajasthan, India

Abstract. The classical hypergeometric summation theorems have a significant role in the theory of generalized hypergeometric functions. Over the years generalization and extension of classical summation theorems for the series ${}_qF_q$, and their applications have been the predominant area of research. Notably, Masjed-Jamei and Koepf (2018) extended these classical summation theorems for the series ${}_{q+1}F_q$ for $q = 1, 2, 3, 4, 5$, and explored a variety of provocative instances of their key discoveries. These findings were recently applied by Jun et al. (2019) in the evaluation of single integrals, double integrals, and Laplace-type integrals. The main aim of this paper is to elucidate eleven Eulerian's integrals of MacRobert's type involving generalized hypergeometric functions. This is accomplished by combining an intriguing integral given by MacRobert with the extended summation theorems due to Masjed-Jamei and Koepf (2018). Additionally, there are a few interesting specific illustrations of our main findings which are based on prior findings derived by Jun et al. (2019). The results are clear, appealing, and logical along with the potential for further applications.

Keywords: Generalized hypergeometric function · Classical summation theorems generalization · Eulerian's-type integral · MacRobert's integral

Classification: Primary 33C05, 33C20 · Secondary 33C99, 65B10

1 Overview

The well-known generalized hypergeometric function with r numerator and s denominator parameters is defined [2, 20, 24] by:

$${}_rF_s \left[\begin{matrix} u_1, u_2, \dots, u_r \\ v_1, v_2, \dots, v_s \end{matrix}; w \right] = 1 + \sum_{n=1}^{\infty} \frac{\prod_{i=1}^r (u_i)_n}{\prod_{i=1}^s (v_i)_n} \frac{w^n}{n!}. \quad (1)$$

Also, no denominator parameter v_i is supposed to be zero or a negative integer. If any parameter u_i is zero or a negative integer, the series terminates. The power series (1) could be examined using the elementary ratio test, which confirms that [12]:

- (i) If $r \leq s$, the series is convergent for all finite w .
- (ii) If $r = s + 1$, the series is convergent, for $|w| < 1$ and diverges for $|w| > 1$.
- (iii) If $r \geq s + 1$, the series diverges for $w \neq 0$.
- (iv) If $r = s + 1$, the series is absolutely convergent on the circle $|w| = 1$ if

$$Re\left(\sum_{i=1}^s v_i - \sum_{i=1}^r u_i\right) > 0$$

Moreover $(u)_n$ in series (1) is widely known as the shifted factorial for any complex number and is defined by [20, p. 22]:

$$(u)_n = \frac{\Gamma(u+n)}{\Gamma(u)} = \begin{cases} 1 & (n = 0, u \in \mathbb{C} \setminus \{0\}) \\ u(u+1)\dots(u+n-1) & (n \in \mathbb{N}, u \in \mathbb{C}) \end{cases} \quad (2)$$

Also, when a generalized hypergeometric function ${}_qF_q$ is transformed into a gamma function, the results are highly relevant and beneficial from applications perspective. We will discuss the following classical summation theorems, so the work should stand on its own [1, 2, 20, 24]:

- Gauss's summation theorem [13, p. 108]:

$${}_2F_1\left[\begin{matrix} a, & b \\ & c \end{matrix}; 1\right] = \frac{\Gamma(c-a-b)\Gamma(c)}{\Gamma(c-a)\Gamma(c-b)}. \quad (3)$$

provided $Re(c-a-b) > 0$.

- Kummer's summation theorem [13, p. 108]:

$${}_2F_1\left[\begin{matrix} a, & b \\ 1+a-b \end{matrix}; -1\right] = \frac{\Gamma(1+a-b)\Gamma(1+\frac{a}{2})}{\Gamma(1-b+\frac{a}{2})\Gamma(1+a)}. \quad (4)$$

- Gauss's second summation theorem [13, p. 108]:

$${}_2F_1\left[\begin{matrix} a, & b \\ \frac{1}{2}(a+b+1) \end{matrix}; \frac{1}{2}\right] = \frac{\sqrt{\pi}\Gamma(\frac{1}{2}(a+b+1))}{\Gamma(\frac{1}{2}(a+1))\Gamma(\frac{1}{2}(b+1))}. \quad (5)$$

- Bailey's summation theorem [13, p. 108]:

$${}_2F_1\left[\begin{matrix} a, & 1-a \\ & b \end{matrix}; \frac{1}{2}\right] = \frac{\Gamma(\frac{1}{2}b)\Gamma(\frac{1}{2}(b+1))}{\Gamma(\frac{1}{2}(a+b))\Gamma(\frac{1}{2}(b-a+1))}. \quad (6)$$

- Dixon's summation theorem [13, p. 108]:

$$\begin{aligned} & {}_3F_2\left[\begin{matrix} a, & b, & c \\ 1+a-b, & 1+a-c \end{matrix}; 1\right] \\ &= \frac{\Gamma(1+\frac{1}{2}a)\Gamma(1+a-b)\Gamma(1+a-c)\Gamma(1-b-c+\frac{1}{2}a)}{\Gamma(1+a)\Gamma(1-b+\frac{1}{2}a)\Gamma(1-c+\frac{1}{2}a)\Gamma(1+a-b-c)}. \end{aligned} \quad (7)$$

provided $Re(a-2b-2c) > -2$.

- Watson’s summation theorem [13, p. 108]:

$$\begin{aligned}
 & {}_3F_2 \left[\begin{matrix} a, & b, & c \\ \frac{1}{2}(a+b+1), & 2c \end{matrix}; 1 \right] \\
 &= \frac{\sqrt{\pi} \Gamma(c + \frac{1}{2}) \Gamma(\frac{1}{2}(a+b+1)) \Gamma(c - \frac{1}{2}(a+b-1))}{\Gamma(\frac{1}{2}(a+1)) \Gamma(\frac{1}{2}(b+1)) \Gamma(c - \frac{1}{2}(a-1)) \Gamma(c - \frac{1}{2}(b-1))}.
 \end{aligned} \tag{8}$$

provided $Re(2c - a - b) > -1$.

- Whipple’s summation theorem [13, p. 108]:

$$\begin{aligned}
 & {}_3F_2 \left[\begin{matrix} a, & 1-a, & b \\ c, & 2b-c+1 \end{matrix}; 1 \right] \\
 &= \frac{\pi 2^{1-2b} \Gamma(c) \Gamma(2b-c+1)}{\Gamma(\frac{a}{2} + \frac{c}{2}) \Gamma(b + \frac{a}{2} - \frac{c}{2} + \frac{1}{2}) \Gamma(\frac{1}{2} - \frac{a}{2} + \frac{c}{2}) \Gamma(b+1 - \frac{1}{2}(a+c))}.
 \end{aligned} \tag{9}$$

- Pfaff-Saalschütz’s summation theorem [13, p. 108]:

$${}_3F_2 \left[\begin{matrix} a, & b, & -n \\ c, & 1+a+b-c-n \end{matrix}; 1 \right] = \frac{(c-a)_n (c-b)_n}{(c)_n (c-a-b)_n}. \tag{10}$$

- Second Whipple’s summation theorem [13, p. 108]:

$${}_4F_3 \left[\begin{matrix} a, & 1 + \frac{1}{2}a, & b, & c \\ \frac{1}{2}a, & a-b+1, & a-c+1 \end{matrix}; -1 \right] = \frac{\Gamma(a-b+1) \Gamma(a-c+1)}{\Gamma(a+1) \Gamma(a-b-c+1)}. \tag{11}$$

- Dougall’s summation theorem [13, p. 108]:

$$\begin{aligned}
 & {}_5F_4 \left[\begin{matrix} a, & 1 + \frac{1}{2}a, & c, & d, & e \\ \frac{1}{2}a, & a-c+1, & a-d+1, & a-e+1 \end{matrix}; 1 \right] \\
 &= \frac{\Gamma(a-c+1) \Gamma(a-d+1) \Gamma(a-e+1) \Gamma(a-c-d-e+1)}{\Gamma(a+1) \Gamma(a-d-e+1) \Gamma(a-c-e+1) \Gamma(a-c-d+1)}.
 \end{aligned} \tag{12}$$

- Second Dougall’s summation theorem [13, p. 108]:

$$\begin{aligned}
 & {}_7F_6 \left[\begin{matrix} a, & 1 + \frac{1}{2}a, & b, & c, & d, & 1+2a-b-c-d+n, & -n \\ \frac{1}{2}a, & a-b+1, & a-c+1, & a-d+1, & b+c+d-a-n, & a+1+n \end{matrix}; 1 \right] \\
 &= \frac{(a+1)_n (a-b-c+1)_n (a-b-d+1)_n (a-c-d+1)_n}{(a+1-b)_n (a+1-c)_n (a+1-d)_n (a+1-b-c-d)_n}.
 \end{aligned} \tag{13}$$

Masjed-Jamei and Koepf [11, p. 5] created a detailed relationship lately in order to expand classical summation theorems:

$$\begin{aligned}
 & {}_pF_q \left[\begin{matrix} a_1, \dots, a_{p-1}, 1 \\ b_1, \dots, b_{q-1}, m \end{matrix}; z \right] \\
 &= \frac{\Gamma(b_1)\dots\Gamma(b_{q-1}) \Gamma(a_1 - m + 1)\dots\Gamma(a_{p-1} - m + 1) (m - 1)!}{\Gamma(a_1)\dots\Gamma(a_{p-1}) \Gamma(b_1 - m + 1)\dots\Gamma(b_{q-1} - m + 1) z^{m-1}} \\
 &\times \left\{ {}_{p-1}F_{q-1} \left[\begin{matrix} a_1 - m + 1, \dots, a_{p-1} - m + 1 \\ b_1 - m + 1, \dots, b_{q-1} - m + 1 \end{matrix}; z \right] \right. \\
 &\quad \left. - {}_{p-1}F_{q-1} \left[\begin{matrix} a_1 - m + 1, \dots, a_{p-1} - m + 1 \\ b_1 - m + 1, \dots, b_{q-1} - m + 1 \end{matrix}; z \right] \right\}.
 \end{aligned} \tag{14}$$

Using above Eq. (14) classical summation theorems (3) to (13) are generalized as follows:

(a) Generalization of Gauss's summation theorem (3) [11, p. 5]:

$$\begin{aligned}
 & {}_3F_2 \left[\begin{matrix} a, b, 1 \\ c, m \end{matrix}; 1 \right] \\
 &= \frac{\Gamma(m) \Gamma(c) \Gamma(a - m + 1) \Gamma(b - m + 1)}{\Gamma(a) \Gamma(b) \Gamma(c - m + 1)} \\
 &\times \left\{ \frac{\Gamma(c - m + 1) \Gamma(c - a - b + m - 1)}{\Gamma(c - a) \Gamma(c - b)} - {}_2F_1 \left[\begin{matrix} a - m + 1, b - m + 1 \\ c - m + 1 \end{matrix}; 1 \right] \right\} \\
 &= \gamma_1.
 \end{aligned} \tag{15}$$

(b) Generalization of Kummer's summation theorem (4) [11, p. 5]:

$$\begin{aligned}
 & {}_3F_2 \left[\begin{matrix} a, b, 1 \\ m + a - b, m \end{matrix}; -1 \right] \\
 &= (-1)^{m-1} \frac{\Gamma(m) \Gamma(a - b + m) \Gamma(a - m + 1) \Gamma(b - m + 1)}{\Gamma(a) \Gamma(b) \Gamma(a - b + 1)} \\
 &\times \left\{ \frac{\Gamma(a - b + 1) \Gamma(1 + \frac{1}{2}(a - m + 1))}{\Gamma(2 + a - m) \Gamma(m - b + \frac{1}{2}(a - m + 1))} - {}_2F_1 \left[\begin{matrix} a - m + 1, b - m + 1 \\ 1 + a - b \end{matrix}; -1 \right] \right\} \\
 &= \gamma_2.
 \end{aligned} \tag{16}$$

(c) Generalization of Gauss's second summation theorem (5) [11, p. 6]:

$$\begin{aligned}
 & {}_3F_2 \left[\begin{matrix} a, b, 1 \\ \frac{1}{2}(1 + a + b), m \end{matrix}; \frac{1}{2} \right] \\
 &= 2^{m-1} \frac{\Gamma(m) \Gamma(\frac{1}{2}(a + b + 1)) \Gamma(a - m + 1) \Gamma(b - m + 1)}{\Gamma(a) \Gamma(b) \Gamma(-m + 1 + \frac{1}{2}(a + b + 1))} \\
 &\times \left\{ \frac{\sqrt{\pi} \Gamma(-m + 1 + \frac{1}{2}(a + b + 1))}{\Gamma(1 + \frac{1}{2}(a - m)) \Gamma(1 + \frac{1}{2}(b - m))} - {}_2F_1 \left[\begin{matrix} a - m + 1, b - m + 1 \\ -m + 1 + \frac{1}{2}(a + b + 1) \end{matrix}; \frac{1}{2} \right] \right\} \\
 &= \gamma_3.
 \end{aligned} \tag{17}$$

(d) Generalization of Bailey’s summation theorem (6) [11, p. 6]:

$$\begin{aligned}
 & {}_3F_2 \left[\begin{matrix} a, & 2m - a - 1, & 1 \\ & b, & m \end{matrix} ; \frac{1}{2} \right] \\
 &= 2^{m-1} \frac{\Gamma(m) \Gamma(b) \Gamma(a - m + 1) \Gamma(m - a)}{\Gamma(a) \Gamma(2m - a - 1) \Gamma(b - m + 1)} \\
 &\times \left\{ \frac{\Gamma(\frac{1}{2}(b - m + 1)) \Gamma(\frac{1}{2}(b - m + 2))}{\Gamma(-m + 1 + \frac{1}{2}(a + b)) \Gamma(\frac{1}{2}(b - a + 1))} - {}_2F_1^{(m-2)} \left[\begin{matrix} a - m + 1, m - a \\ b - m + 1 \end{matrix} ; \frac{1}{2} \right] \right\} \\
 &= \gamma_4.
 \end{aligned} \tag{18}$$

(e) Generalization of Dixon’s summation theorem (7) [11, p. 7]:

$$\begin{aligned}
 & {}_4F_3 \left[\begin{matrix} a, & b, & c, & 1 \\ a - b + m, & a - c + m, & m \end{matrix} ; 1 \right] \\
 &= \frac{\Gamma(m) \Gamma(a - b + m) \Gamma(a - c + m) \Gamma(a + 1 - m) \Gamma(b + 1 - m) \Gamma(c + 1 - m)}{\Gamma(a) \Gamma(b) \Gamma(c) \Gamma(a - b + 1) \Gamma(a - c + 1)} \\
 &\times \left\{ \frac{\Gamma(\frac{1}{2}(a + 3 - m)) \Gamma(a - b + 1) \Gamma(a - c + 1) \Gamma(-b - c + \frac{1}{2}(a + 3m - 1))}{\Gamma(a + 2 - m) \Gamma(-b + \frac{1}{2}(a + m + 1)) \Gamma(-c + \frac{1}{2}(a + m + 1)) \Gamma(a - b - c + m)} \right. \\
 &\quad \left. - {}_3F_2^{(m-2)} \left[\begin{matrix} a - m + 1, b - m + 1, c - m + 1 \\ a - b + 1, a - c + 1 \end{matrix} ; 1 \right] \right\} \\
 &= \gamma_5.
 \end{aligned} \tag{19}$$

(f) Generalization of Watson’s summation theorem (8) [11, p. 7]:

$$\begin{aligned}
 & {}_4F_3 \left[\begin{matrix} a, & b, & c, & 1 \\ \frac{1}{2}(a + b + 1), & 2c + 1 - m, & m \end{matrix} ; 1 \right] \\
 &= \frac{\Gamma(m) \Gamma(\frac{1}{2}(a + b + 1)) \Gamma(2c + 1 - m) \Gamma(a + 1 - m) \Gamma(b + 1 - m) \Gamma(c + 1 - m)}{\Gamma(a) \Gamma(b) \Gamma(c) \Gamma(-m + \frac{1}{2}(a + b + 3)) \Gamma(2c - 2m + 2)} \\
 &\times \left\{ \frac{\sqrt{\pi} \Gamma(c - m + \frac{3}{2}) \Gamma(-m + \frac{1}{2}(a + b + 3)) \Gamma(c - \frac{1}{2}(a + b - 1))}{\Gamma(1 + \frac{1}{2}(a - m)) \Gamma(1 + \frac{1}{2}(b - m)) \Gamma(c + 1 - \frac{1}{2}(a + m)) \Gamma(c + 1 - \frac{1}{2}(b + m))} \right. \\
 &\quad \left. - {}_3F_2^{(m-2)} \left[\begin{matrix} a - m + 1, b - m + 1, c - m + 1 \\ -m + 1 + \frac{1}{2}(a + b + 1), 2c - 2m + 2 \end{matrix} ; 1 \right] \right\} \\
 &= \gamma_6.
 \end{aligned} \tag{20}$$

(g) Generalization of Whipple’s summation theorem (9) [11, p. 8]:

$$\begin{aligned}
 & {}_4F_3 \left[\begin{matrix} a, & 2m - 1 - a, & b, & 1 \\ & c, & 2b - c + 1, & m \end{matrix} ; 1 \right] \\
 &= \frac{\Gamma(m) \Gamma(c) \Gamma(2b - c + 1) \Gamma(m - a) \Gamma(a + 1 - m) \Gamma(b + 1 - m)}{\Gamma(a) \Gamma(b) \Gamma(2m - 1 - a) \Gamma(c + 1 - m) \Gamma(2b - c - m + 2)} \\
 &\times \left\{ \frac{\pi 2^{2m-2b-1} \Gamma(c - m + 1)}{\Gamma(-m + 1 + \frac{1}{2}(a + c)) \Gamma(-m + 1 + b + \frac{1}{2}(a - c + 1)) \Gamma(\frac{1}{2}(1 - a + c))} \right. \\
 &\quad \left. \times \frac{\Gamma(2b - c - m + 2)}{\Gamma(b + 1 - \frac{1}{2}(a + c))} - {}_3F_2^{(m-2)} \left[\begin{matrix} a - m + 1, b - m + 1, m - a \\ c - m + 1, 2b - c - m + 2 \end{matrix} ; 1 \right] \right\} \\
 &= \gamma_7.
 \end{aligned} \tag{21}$$

(h) Generalization of Pfaff-Saalschütz's summation theorem (10) [11, p. 9]:

$$\begin{aligned}
 & {}_4F_3 \left[\begin{matrix} a, & b, & -n+m-1, & 1 \\ c, & 1+a+b-c-n, & m \end{matrix} ; 1 \right] \\
 &= \frac{(m-1)! (1-c)_{m-1}}{(1-a)_{m-1} (1-b)_{m-1}} \frac{(c-a-b+n)_{m-1}}{(n+2-m)_{m-1}} \\
 &\times \left\{ \frac{(c-a)_n (c-b)_n}{(c+1-m)_n (c-a-b+m-1)_n} - {}_3F_2^{(m-2)} \left[\begin{matrix} a-m+1, b-m+1, -n \\ c-m+1, 2+a+b-c-m-n \end{matrix} ; 1 \right] \right\} \\
 &= \gamma_8.
 \end{aligned} \tag{22}$$

(i) Generalization of Second Whipple's summation theorem (11) [11, p. 10]:

$$\begin{aligned}
 & {}_5F_4 \left[\begin{matrix} a, & \frac{1}{2}(a+m+1), & b, & c, & 1 \\ \frac{1}{2}(a+m-1), & a-b+m, & a-c+m, & m \end{matrix} ; -1 \right] = (-1)^{m-1} \Gamma(m) \\
 &\times \frac{\Gamma(\frac{1}{2}(a+m-1)) \Gamma(a-b+m) \Gamma(a-c+m) \Gamma(\frac{1}{2}(a-m+3)) \Gamma(a-m+1)}{\Gamma(a) \Gamma(b) \Gamma(c) \Gamma(\frac{1}{2}(a+m+1)) \Gamma(\frac{1}{2}(a-m+1))} \\
 &\times \frac{\Gamma(b-m+1) \Gamma(c-m+1)}{\Gamma(a-b+1) \Gamma(a-c+1)} \times \left\{ \frac{\Gamma(1+a-b) \Gamma(1+a-c)}{\Gamma(2-m+a) \Gamma(m+a-b-c)} \right. \\
 &\quad \left. - {}_4F_3^{(m-2)} \left[\begin{matrix} a-m+1, b-m+1, \frac{1}{2}(a-m+3), c-m+1 \\ \frac{1}{2}(a-m+1), a-b+1, a-c+1 \end{matrix} ; -1 \right] \right\} \\
 &= \gamma_9.
 \end{aligned} \tag{23}$$

(j) Generalization of Dougall's summation theorem (12) [11, p. 10]:

$$\begin{aligned}
 & {}_6F_5 \left[\begin{matrix} a, & \frac{1}{2}(a+m+1), & c, & d, & e, & 1 \\ \frac{1}{2}(a+m-1), & a-c+m, & a-d+m, & a-e+m, & m \end{matrix} ; 1 \right] \\
 &= \frac{\Gamma(m) \Gamma(\frac{1}{2}(a+m-1)) \Gamma(a-c+m) \Gamma(a-d+m) \Gamma(a-e+m)}{\Gamma(a-c+1) \Gamma(a-d+1) \Gamma(a-e+1)} \\
 &\times \frac{\Gamma(a-m+1) \Gamma(\frac{1}{2}(a-m+3)) \Gamma(c+1-m) \Gamma(d+1-m) \Gamma(e+1-m)}{\Gamma(a) \Gamma(c) \Gamma(d) \Gamma(e) \Gamma(\frac{1}{2}(a+m+1)) \Gamma(\frac{1}{2}(a-m+1))} \\
 &\times \left\{ \frac{\Gamma(a-c+1) \Gamma(a-d+1) \Gamma(a-e+1) \Gamma(a-c-d-e+2m-1)}{\Gamma(2-m+a) \Gamma(a-c-e+m) \Gamma(a-d-e+m) \Gamma(a-c-d+m)} \right. \\
 &\quad \left. - {}_5F_4^{(m-2)} \left[\begin{matrix} a-m+1, c-m+1, \frac{1}{2}(a-m+3), d-m+1, e-m+1 \\ \frac{1}{2}(a-m+1), a-c+1, a-d+1, a-e+1 \end{matrix} ; 1 \right] \right\} \\
 &= \gamma_{10}.
 \end{aligned} \tag{24}$$

(k) Generalization of Second Dougall’s summation theorem (13) [11, p. 11]:

$$\begin{aligned}
 & {}_8F_7 \left[\begin{matrix} a, \frac{1}{2}(a+m+1), b, c, d, 2a-b-c-d+2m-1+n, m-n-1, 1 \\ \frac{1}{2}(a+m-1), a-b+m, a-c+m, a-d+m, b+c+d-a+1-m-n, a+n+1, m \end{matrix} ; 1 \right] \\
 &= (-1)^{m-1} (m-1)! \times \frac{(\frac{1}{2}(3-a-m))_{m-1} (1-a+b-m)_{m-1}}{(\frac{1}{2}(1-a-m))_{m-1} (1-a)_{m-1}} \\
 &\times \frac{(1-a+c-m)_{m-1} (1-a+d-m)_{m-1} (m+n+a-b-c-d)_{m-1} (-a-n)_{m-1}}{(1-b)_{m-1} (1-c)_{m-1} (1-d)_{m-1} (b+c+d-2a+2-2m-n)_{m-1} (n+2-m)_{m-1}} \\
 &\times \left\{ \frac{(a-m+2)_n (a-b-c+m)_n (a-b-d+m)_n (a-c-d+m)_n}{(a-b+1)_n (a-c+1)_n (a-d+1)_n (a-b-c-d+2m-1)_n} \right. \\
 &\quad \left. - \frac{(m-2)}{7F_6} \left[\begin{matrix} a-m+1, \frac{1}{2}(a-m+3), b-m+1, c-m+1, d-m+1, \\ 2a-b-c-d+m+n, -n \\ \frac{1}{2}(a-m+1), a-b+1, a-c+1, a-d+1, \\ b+c+d-a+2-2m-n, a-m+n+2 \end{matrix} ; 1 \right] \right\} \\
 &= \gamma_{11}.
 \end{aligned} \tag{25}$$

It is important to note that for $m = 1$, the results (15) to (25) reduce to the results (3) to (13) respectively. We refer to [14–17, 21] for various generalizations and extensions of the results (3) to (13).

Many researchers have examined integral representations of hypergeometric functions in various forms [10, 19] in the last several years. The current work is primarily driven by the fact that integral representations of hypergeometric functions are crucial because they can be utilized to derive various relations between hypergeometric functions as well as to investigate their applications [8]. The goal of this work is to develop eleven Eulerian’s type integrals involving generalized hypergeometric functions using the summation theorems (15) to (25), as well as an intriguing integral due to MacRobert [18]:

$$\int_0^1 x^{\alpha-1} (1-x)^{\beta-1} [1+px+q(1-x)]^{-\alpha-\beta} dx = \frac{1}{(1+p)^\alpha (1+q)^\beta} \frac{\Gamma(\alpha) \Gamma(\beta)}{\Gamma(\alpha+\beta)}. \tag{26}$$

where $Re(\alpha) > 0, Re(\beta) > 0$ and the constants p, q are such that no one of the expressions $1+p, 1+q, 1+px+q(1-x)$, where $0 \leq x \leq 1$, are zero.

There are several prominent specific instances of our key findings. Jun’s results [12] are specific examples of our main findings. The discoveries of the paper are uncomplicated, timely, transparent and they have the capability to be significant.

2 Eulerian’s Type Integrals

The eleven different categories of Eulerian’s type integrals incorporating generalized hypergeometric functions that will be developed in the paper are established by the underlying theorems:

Theorem 1. For $m \in \mathbb{N}, Re(b) > 0, Re(c-b) > 0, Re(c-a-b+m) > 1$ and the constants p, q are such that no one of the expressions $1+p, 1+q, 1+px+q(1-x)$, where $0 \leq x \leq 1$, are zero. As a result, the following conclusion is correct:

$$\int_0^1 x^{b-1}(1-x)^{c-b-1}[1+px+q(1-x)]^{-c} {}_2F_1\left[\begin{matrix} a, 1 \\ m \end{matrix}; \frac{(1+p)x}{1+px+q(1-x)}\right] dx$$

$$= \frac{1}{(1+p)^b(1+q)^{c-b}} \frac{\Gamma(b)\Gamma(c-b)}{\Gamma(c)} \gamma_1. \tag{27}$$

where γ_1 is the same as given in (15).

Proof. In order to establish Theorem 1, we indicated the left-hand side of (27) by I , presented ${}_2F_1$ as a series, reversed the order of integration and summation as a series, and determined the beta integral employing (26). The outcomes were as follows:

$$I = \sum_{n=0}^{\infty} \frac{(a)_n(1)_n}{(m)_n n!} \frac{\Gamma(b+n)\Gamma(c-b)}{\Gamma(c+n)} \frac{1}{(1+p)^b(1+q)^{c-b}}$$

After further modification and utilizing (2), we obtained:

$$I = \frac{\Gamma(b)\Gamma(c-b)}{\Gamma(c)} \frac{1}{(1+p)^c(1+q)^{c-b}} \sum_{n=0}^{\infty} \frac{(a)_n(b)_n(1)_n}{(c)_n(m)_n n!}$$

By concluding the series, the result obtained by us is as follows:

$$I = \frac{1}{(1+p)^c(1+q)^{c-b}} \frac{\Gamma(b)\Gamma(c-b)}{\Gamma(c)} {}_3F_2\left[\begin{matrix} a, b, 1 \\ c, m \end{matrix}; 1\right]$$

Now, we observe that the result (15) can be employed to assess ${}_3F_2$, and we can simply reach the correct side of (27). This complete explanation of the Theorem 1.

Corollary 1. *In theorem (27), if we take $m = 2, 3$ (excluding the trivial case of $m = 1$). We subsequently get following result:*

$$\int_0^1 x^{b-1}(1-x)^{c-b-1}[1+px+q(1-x)]^{-c} {}_2F_1\left[\begin{matrix} a, 1 \\ 2 \end{matrix}; \frac{(1+p)x}{1+px+q(1-x)}\right] dx$$

$$= \frac{1}{(1+p)^b(1+q)^{c-b}} \frac{\Gamma(b-1)}{(a-1)\Gamma(c-1)} \left\{ \frac{\Gamma(c-1)\Gamma(c-a-b+1) - \Gamma(c-a)\Gamma(c-b)}{\Gamma(c-a)} \right\},$$

and

$$\int_0^1 x^{b-1}(1-x)^{c-b-1}[1+px+q(1-x)]^{-c} {}_2F_1\left[\begin{matrix} a, 1 \\ 3 \end{matrix}; \frac{(1+p)x}{1+px+q(1-x)}\right] dx$$

$$= \frac{1}{(1+p)^b(1+q)^{c-b}} \frac{2\Gamma(b-2)\Gamma(c-b)}{\Gamma(c-2)(a-2)_2}$$

$$\times \left\{ \frac{\Gamma(c-2)\Gamma(c-a-b+2)}{\Gamma(c-a)\Gamma(c-b)} - \frac{ab+c-2a-2b+2}{c-2} \right\}.$$

Further, if we put $p = q$ in theorem (27), it gives result obtained earlier by Jun et al. [12].

$$\int_0^1 x^{b-1}(1-x)^{c-b-1} {}_2F_1 \left[\begin{matrix} a, 1 \\ m \end{matrix}; x \right] dx = \frac{\Gamma(b)\Gamma(c-b)}{\Gamma(c)} \gamma_1.$$

where γ_1 is the same as given in (15).

The following theorems and the corresponding corollaries can be obtained by employing the results (16) to (25). Hence they are given here without proof.

Theorem 2. For $m \in \mathbb{N}$, $Re(b) > 0$, $Re(a-2b+m) > 0$ and the constants p, q are such that no one of the expressions $1+p, 1+q, 1+px+q(1-x)$, where $0 \leq x \leq 1$, are zero. As a result, the following conclusion is correct:

$$\int_0^1 x^{b-1}(1-x)^{a-2b+m-1} [1+px+q(1-x)]^{b-a-m} {}_2F_1 \left[\begin{matrix} a, 1 \\ m \end{matrix}; \frac{-(1+p)x}{1+px+q(1-x)} \right] dx \tag{28}$$

$$= \frac{1}{(1+p)^b(1+q)^{a-2b+m}} \frac{\Gamma(b)\Gamma(a-2b+m)}{\Gamma(a-b+m)} \gamma_2.$$

where γ_2 is the same as given in (16).

Corollary 2. In Theorem 2, if we take $m = 2, 3$ (excluding the trivial case of $m = 1$). We subsequently gain following conclusion:

$$\int_0^1 x^{b-1}(1-x)^{a-2b+1} [1+px+q(1-x)]^{b-a-2} {}_2F_1 \left[\begin{matrix} a, 1 \\ 2 \end{matrix}; \frac{-(1+p)x}{1+px+q(1-x)} \right] dx$$

$$= \frac{1}{(1+p)^b(1+q)^{a-2b+2}} \frac{\Gamma(b-1)\Gamma(a-2b+2)}{(a-1)\Gamma(a-b+1)} \left\{ 1 - \frac{\Gamma(1+a-b)\Gamma(\frac{1}{2}(a+1))}{\Gamma(a)\Gamma(\frac{1}{2}(a+3)-b)} \right\},$$

and

$$\int_0^1 x^{b-1}(1-x)^{a-2b+2} [1+px+q(1-x)]^{b-a-3} {}_2F_1 \left[\begin{matrix} a, 1 \\ 3 \end{matrix}; \frac{-(1+p)x}{1+px+q(1-x)} \right] dx$$

$$= \frac{1}{(1+p)^b(1+q)^{a-2b+3}} \frac{2\Gamma(b-2)\Gamma(a-2b+3)}{\Gamma(a-b+1)(a-2)_2}$$

$$\times \left\{ \frac{\Gamma(a-b+1)\Gamma(\frac{a}{2})}{\Gamma(a-1)\Gamma(-b+2+\frac{a}{2})} - \frac{3a+b-ab-3}{a-b+1} \right\}.$$

Further, if we put $p = q$ in Theorem 2, it gives result obtained earlier by Jun et al. [12].

$$\int_0^1 x^{b-1}(1-x)^{a-2b+m-1} {}_2F_1 \left[\begin{matrix} a, 1 \\ m \end{matrix}; -x \right] dx = \frac{\Gamma(b)\Gamma(a-2b+m)}{\Gamma(a-b+m)} \gamma_2.$$

where γ_2 is the same as given in (16).

Theorem 3. For $m \in \mathbb{N}$, $Re(b) > 0$, $Re(a - b + 1) > 0$ and the constants p, q are such that no one of the expressions $1 + p$, $1 + q$, $1 + px + q(1 - x)$, where $0 \leq x \leq 1$, are zero. As a result, the following conclusion is correct:

$$\int_0^1 x^{b-1}(1-x)^{\frac{1}{2}(a-b-1)}[1+px+q(1-x)]^{-\frac{1}{2}(a+b+1)} {}_2F_1\left[\begin{matrix} a, 1 \\ m \end{matrix}; \frac{1}{2} \frac{(1+p)x}{[1+px+q(1-x)]}\right] dx$$

$$= \frac{1}{(1+p)^b(1+q)^{\frac{1}{2}(a-b+1)}} \frac{\Gamma(b)\Gamma(\frac{1}{2}(a-b+1))}{\Gamma(\frac{1}{2}(a+b+1))} \gamma_3. \tag{29}$$

where γ_3 is the same as given in (17).

Corollary 3. In Theorem 3, if we take $m = 2, 3$ (excluding the trivial case of $m = 1$). We subsequently gain following conclusion:

$$\int_0^1 x^{b-1}(1-x)^{\frac{1}{2}(a-b-1)}[1+px+q(1-x)]^{-\frac{1}{2}(a+b+1)} {}_2F_1\left[\begin{matrix} a, 1 \\ 2 \end{matrix}; \frac{1}{2} \frac{(1+p)x}{[1+px+q(1-x)]}\right] dx$$

$$= \frac{1}{(1+p)^b(1+q)^{\frac{1}{2}(a-b+1)}} \frac{\Gamma(b)\Gamma(\frac{1}{2}(a-b+1))}{\Gamma(\frac{1}{2}(a+b+1))} \frac{a+b-1}{(a-1)(b-1)}$$

$$\times \left\{ \frac{\sqrt{\pi}\Gamma(\frac{1}{2}(a+b-1))}{\Gamma(\frac{a}{2})\Gamma(\frac{b}{2})} - 1 \right\},$$

and

$$\int_0^1 x^{b-1}(1-x)^{\frac{1}{2}(a-b-1)}[1+px+q(1-x)]^{-\frac{1}{2}(a+b+1)} {}_2F_1\left[\begin{matrix} a, 1 \\ 3 \end{matrix}; \frac{1}{2} \frac{(1+p)x}{[1+px+q(1-x)]}\right] dx$$

$$= \frac{1}{(1+p)^b(1+q)^{\frac{1}{2}(a-b+1)}} \frac{\Gamma(b)\Gamma(\frac{1}{2}(a-b+1))}{\Gamma(\frac{1}{2}(a+b+1))} \frac{2(a+b-1)(a+b-3)}{(a-2)_2(b-2)_2}$$

$$\times \left\{ \frac{\sqrt{\pi}\Gamma(\frac{1}{2}(a+b-3))}{\Gamma(\frac{a-1}{2})\Gamma(\frac{b-1}{2})} - \frac{ab-a-b+1}{a+b-3} \right\}.$$

Further, if we put $p = q$ in Theorem 3, it gives result obtained earlier by Jun et al. [12].

$$\int_0^1 x^{b-1}(1-x)^{\frac{1}{2}(a-b-1)} {}_2F_1\left[\begin{matrix} a, 1 \\ m \end{matrix}; \frac{1}{2}x\right] dx = \frac{\Gamma(b)\Gamma(\frac{1}{2}(a-b+1))}{\Gamma(\frac{1}{2}(a+b+1))} \gamma_3.$$

where γ_3 is the same as given in (17).

Theorem 4. For $m \in \mathbb{N}$, $Re(b) > 0$, $Re(b - a) > 0$ and the constants p, q are such that no one of the expressions $1 + p$, $1 + q$, $1 + px + q(1 - x)$, where $0 \leq x \leq 1$, are zero. As a result, the following conclusion is correct:

$$\int_0^1 x^{a-1}(1-x)^{b-a-1}[1+px+q(1-x)]^{-b} {}_2F_1\left[\begin{matrix} 2m-a-1, 1 \\ m \end{matrix}; \frac{1}{2} \frac{(1+p)x}{[1+px+q(1-x)]}\right] dx$$

$$= \frac{1}{(1+p)^a(1+q)^{b-a}} \frac{\Gamma(a)\Gamma(b-a)}{\Gamma(b)} \gamma_4. \tag{30}$$

where γ_4 is the same as given in (18).

Corollary 4. *In Theorem 4, if we take $m = 2, 3$ (excluding the trivial case of $m = 1$). We subsequently gain following conclusion:*

$$\int_0^1 x^{a-1}(1-x)^{b-a-1}[1+px+q(1-x)]^{-b} {}_2F_1\left[\begin{matrix} 3-a, 1 \\ 2 \end{matrix}; \frac{1}{2} \frac{(1+p)x}{[1+px+q(1-x)]}\right] dx$$

$$= \frac{1}{(1+p)^a(1+q)^{b-a}} \frac{\Gamma(a)\Gamma(b-a)}{\Gamma(b)} \frac{2(1-b)}{(1-a)_2}$$

$$\times \left\{ \frac{\Gamma(\frac{b-1}{2})\Gamma(\frac{b}{2})}{\Gamma(\frac{1}{2}(a+b)-1)\Gamma(\frac{1}{2}(b-a+1))} - 1 \right\},$$

and

$$\int_0^1 x^{a-1}(1-x)^{b-a-1}[1+px+q(1-x)]^{-b} {}_2F_1\left[\begin{matrix} 5-a, 1 \\ 3 \end{matrix}; \frac{1}{2} \frac{(1+p)x}{[1+px+q(1-x)]}\right] dx$$

$$= \frac{1}{(1+p)^a(1+q)^{b-a}} \frac{\Gamma(a)\Gamma(b-a)}{\Gamma(b)} \frac{8(b-2)_2}{(a-4)_4}$$

$$\times \left\{ \frac{\Gamma(\frac{1}{2}(b-1))\Gamma(\frac{1}{2}(b-2))}{\Gamma(\frac{1}{2}(a+b)-2)\Gamma(\frac{1}{2}(b-a+1))} - \frac{5a-a^2+2b-10}{2(b-2)} \right\}.$$

Further, if we put $p = q$ in Theorem 4, it gives result obtained earlier by Jun et al. [12].

$$\int_0^1 x^{a-1}(1-x)^{b-a-1} {}_2F_1\left[\begin{matrix} 2m-a-1, 1 \\ m \end{matrix}; \frac{1}{2}x\right] dx = \frac{\Gamma(a)\Gamma(b-a)}{\Gamma(b)} \gamma_4.$$

where γ_4 is the same as given in (18).

Theorem 5. *For $m \in \mathbb{N}$, $Re(c) > 0$, $Re(a-2c+m) > 0$ and the constants p, q are such that no one of the expressions $1+p, 1+q, 1+px+q(1-x)$, where $0 \leq x \leq 1$, are zero. As a result, the following conclusion is correct:*

$$\int_0^1 x^{c-1}(1-x)^{a-2c+m-1}[1+px+q(1-x)]^{c-a-m} {}_3F_2\left[\begin{matrix} a, b, 1 \\ a-b+m, m \end{matrix}; \frac{(1+p)x}{[1+px+q(1-x)]}\right] dx$$

$$= \frac{1}{(1+p)^c(1+q)^{a-2c+m}} \frac{\Gamma(c)\Gamma(a-2c+m)}{\Gamma(a-c+m)} \gamma_5. \tag{31}$$

where γ_5 is the same as given in (19).

Corollary 5. *In Theorem 5, if we take $m = 1, 2, 3$, we subsequently gain following conclusion:*

$$\int_0^1 x^{c-1}(1-x)^{a-2c}[1+px+q(1-x)]^{c-a-1} {}_2F_1\left[\begin{matrix} a, b \\ a-b+1 \end{matrix}; \frac{(1+p)x}{[1+px+q(1-x)]}\right] dx$$

$$= \frac{1}{(1+p)^c(1+q)^{a-2c+1}}$$

$$\times \frac{\Gamma(c)\Gamma(1+a-2c)\Gamma(1+\frac{a}{2})\Gamma(1+a-b)\Gamma(1+\frac{a}{2}-b-c)}{\Gamma(1+a)\Gamma(1+\frac{a}{2}-b)\Gamma(1+\frac{a}{2}-c)\Gamma(1+a-b-c)},$$

$$\int_0^1 x^{c-1}(1-x)^{a-2c+1}[1+px+q(1-x)]^{c-a-2} {}_3F_2 \left[\begin{matrix} a, & b, & 1 \\ a-b+2, & 2 \end{matrix}; \frac{(1+p)x}{[1+px+q(1-x)]} \right] dx$$

$$= \frac{1}{(1+p)^c(1+q)^{a-2c+2}} \frac{\Gamma(c-1)\Gamma(a-2c+2)(a-b+1)}{\Gamma(a-c+1)(a-1)(b-1)}$$

$$\times \left\{ \frac{\Gamma(\frac{1}{2}(a+1))\Gamma(1+a-b)\Gamma(1+a-c)\Gamma(\frac{a}{2}-b-c+\frac{5}{2})}{\Gamma(a)\Gamma(\frac{a}{2}-b+\frac{3}{2})\Gamma(\frac{a}{2}-c+\frac{3}{2})\Gamma(2+a-b-c)} - 1 \right\},$$

and

$$\int_0^1 x^{c-1}(1-x)^{a-2c+2}[1+px+q(1-x)]^{c-a-3} {}_3F_2 \left[\begin{matrix} a, & b, & 1 \\ a-b+3, & 3 \end{matrix}; \frac{(1+p)x}{[1+px+q(1-x)]} \right] dx$$

$$= \frac{1}{(1+p)^c(1+q)^{a-2c+3}} \frac{\Gamma(c)\Gamma(a-2c+3)}{\Gamma(a-c+3)} \frac{2(a-b+1)_2(a-c+1)_2}{(a-2)_2(b-2)_2(c-2)_2}$$

$$\times \left\{ \frac{\Gamma(\frac{a}{2})\Gamma(1+a-b)\Gamma(1+a-c)\Gamma(\frac{a}{2}-b-c+4)}{\Gamma(a-1)\Gamma(\frac{a}{2}-b+2)\Gamma(\frac{a}{2}-c+2)\Gamma(3+a-b-c)} - \frac{(a-2)(b-2)(c-2)}{(a-b+1)(a-c+1)} - 1 \right\}.$$

Further, if we put $p = q$ in Theorem 5, it gives result obtained earlier by Jun et al. [12].

$$\int_0^1 x^{c-1}(1-x)^{a-2c+m-1} {}_3F_2 \left[\begin{matrix} a, & b, & 1 \\ a-b+m, & m \end{matrix}; x \right] dx = \frac{\Gamma(c)\Gamma(a-2c+m)}{\Gamma(a-c+m)} \gamma_5.$$

where γ_5 is the same as given in (19).

Theorem 6. For $m \in \mathbb{N}$, $Re(c) > 0$ and the constants p, q are such that no one of the expressions $1 + p, 1 + q, 1 + px + q(1 - x)$, where $0 \leq x \leq 1$, are zero. As a result, the following conclusion is correct:

$$\int_0^1 x^{c-1}(1-x)^{c-m}[1+px+q(1-x)]^{m-2c-1} {}_3F_2 \left[\begin{matrix} a, & b, & 1 \\ \frac{1}{2}(a+b+1), & m \end{matrix}; \frac{(1+p)x}{[1+px+q(1-x)]} \right] dx$$

$$= \frac{1}{(1+p)^c(1+q)^{c-m+1}} \frac{\Gamma(c)\Gamma(c-m+1)}{\Gamma(2c-m+1)} \gamma_6. \tag{32}$$

where γ_6 is the same as given in (20).

Corollary 6. In Theorem 6, if we take $m = 1, 2, 3$, we subsequently gain following conclusion:

$$\int_0^1 x^{c-1}(1-x)^{c-1}[1+px+q(1-x)]^{-2c} {}_2F_1 \left[\begin{matrix} a, & b \\ \frac{1}{2}(a+b+1) \end{matrix}; \frac{(1+p)x}{[1+px+q(1-x)]} \right] dx$$

$$= \frac{1}{(1+p)^c(1+q)^c} \frac{\Gamma(c)\Gamma(c)}{\Gamma(2c)}$$

$$\times \frac{\sqrt{\pi}\Gamma(c+\frac{1}{2})\Gamma(\frac{1}{2}(a+b+1))\Gamma(c-\frac{1}{2}(a+b-1))}{\Gamma(\frac{1}{2}(a+1))\Gamma(\frac{1}{2}(b+1))\Gamma(c-\frac{1}{2}(a-1))\Gamma(c-\frac{1}{2}(b-1))},$$

$$\int_0^1 x^{c-1}(1-x)^{c-2}[1+px+q(1-x)]^{1-2c} {}_3F_2 \left[\begin{matrix} a, & b, & 1 \\ \frac{1}{2}(a+b+1), & 2 \end{matrix}; \frac{(1+p)x}{[1+px+q(1-x)]} \right] dx$$

$$= \frac{1}{(1+p)^c(1+q)^{c-1}} \frac{\Gamma(c)\Gamma(c-1)}{\Gamma(2c-1)} \frac{a+b-1}{(a-1)(b-1)}$$

$$\times \left\{ \frac{\sqrt{\pi}\Gamma(c-\frac{1}{2})\Gamma(\frac{1}{2}(a+b-1))\Gamma(c-\frac{1}{2}(a+b-1))}{\Gamma(\frac{a}{2})\Gamma(\frac{b}{2})\Gamma(c-\frac{a}{2})\Gamma(c-\frac{b}{2})} - 1 \right\},$$

and

$$\int_0^1 x^{c-1}(1-x)^{c-3}[1+px+q(1-x)]^{2-2c} {}_3F_2 \left[\begin{matrix} a, & b, & 1 \\ \frac{1}{2}(a+b+1), & 3 \end{matrix}; \frac{(1+p)x}{[1+px+q(1-x)]} \right] dx$$

$$= \frac{1}{(1+p)^c(1+q)^{c-2}} \frac{\Gamma(c)\Gamma(c-2)}{\Gamma(2c-2)} \frac{(2c-3)(a+b-1)(a+b-3)}{(a-2)_2(b-2)_2(c-1)}$$

$$\times \left\{ \frac{\sqrt{\pi}\Gamma(c-\frac{3}{2})\Gamma(\frac{1}{2}(a+b-3))\Gamma(c-\frac{1}{2}(a+b-1))}{\Gamma(\frac{a-1}{2})\Gamma(\frac{b-1}{2})\Gamma(c-\frac{a+1}{2})\Gamma(c-\frac{b+1}{2})} - \frac{(a-2)(b-2)}{a+b-3} - 1 \right\}.$$

Further, if we put $p = q$ in Theorem 6, it gives result obtained earlier by Jun et al. [12].

$$\int_0^1 x^{c-1}(1-x)^{c-m} {}_3F_2 \left[\begin{matrix} a, & b, & 1 \\ \frac{1}{2}(a+b+1), & m \end{matrix}; x \right] dx = \frac{\Gamma(c)\Gamma(c-m+1)}{\Gamma(2c-m+1)} \gamma_6.$$

where γ_6 is the same as given in (20).

Theorem 7. For $m \in \mathbb{N}$, $Re(a) > 0$, $Re(c-a) > 0$ and the constants p, q are such that no one of the expressions $1+p, 1+q, 1+px+q(1-x)$, where $0 \leq x \leq 1$, are zero. As a result, the following conclusion is correct:

$$\int_0^1 x^{a-1}(1-x)^{c-a-1}[1+px+q(1-x)]^{-c} {}_3F_2 \left[\begin{matrix} 2m-1-a, & b, & 1 \\ 2b-c+1, & m \end{matrix}; \frac{(1+p)x}{[1+px+q(1-x)]} \right] dx$$

$$= \frac{1}{(1+p)^a(1+q)^{c-a}} \frac{\Gamma(a)\Gamma(c-a)}{\Gamma(c)} \gamma_7. \tag{33}$$

where γ_7 is the same as given in (21).

Corollary 7. In Theorem 7, if we take $m = 1, 2, 3$, we subsequently gain following conclusion:

$$\int_0^1 x^{a-1}(1-x)^{c-a-1}[1+px+q(1-x)]^{-c} {}_2F_1 \left[\begin{matrix} 1-a, & b \\ 2b-c+1 \end{matrix}; \frac{(1+p)x}{[1+px+q(1-x)]} \right] dx$$

$$= \frac{1}{(1+p)^a(1+q)^{c-a}} \frac{\pi 2^{1-2b} \Gamma(a)\Gamma(c-a)\Gamma 2b-c+1}{\Gamma(\frac{1}{2}(a+c))\Gamma(b+\frac{1}{2}(a-c+1))\Gamma(\frac{1}{2}(1-a+c))\Gamma(b+1-\frac{1}{2}(a+c))},$$

$$\int_0^1 x^{a-1}(1-x)^{c-a-1}[1+px+q(1-x)]^{-c} {}_3F_2 \left[\begin{matrix} 3-a, & b, & 1 \\ 2b-c+1, & 2 \end{matrix}; \frac{(1+p)x}{[1+px+q(1-x)]} \right] dx$$

$$= \frac{1}{(1+p)^a(1+q)^{c-a}} \frac{\Gamma(a)\Gamma(c-a)}{\Gamma(c)} \frac{(c-1)(c-2b)}{(a-2)_2(b-1)}$$

$$\times \left\{ \frac{\pi 2^{3-2b} \Gamma(c-1)\Gamma(2b-c)}{\Gamma(\frac{1}{2}(a+c)-1)\Gamma(b+\frac{1}{2}(a-c+1))\Gamma(\frac{1}{2}(1+a-c))\Gamma(b+1-\frac{1}{2}(a+c))} - 1 \right\},$$

and

$$\int_0^1 x^{a-1}(1-x)^{c-a-1}[1+px+q(1-x)]^{-c} {}_3F_2 \left[\begin{matrix} 5-a, & b, & 1 \\ 2b-c+1, & 3 \end{matrix}; \frac{(1+p)x}{[1+px+q(1-x)]} \right] dx$$

$$= \frac{1}{(1+p)^a(1+q)^{c-a}} \frac{\Gamma(a)\Gamma(c-a)}{\Gamma(c)} \frac{2(c-2)_2}{(a-4)_2(b-2)_2} \frac{2b-c+1_2}{2}$$

$$\times \left\{ \frac{\pi 2^{5-2b} \Gamma(c-2)\Gamma(2b-c-1)}{\Gamma(\frac{1}{2}(a+c)-2)\Gamma(b+\frac{1}{2}(a-c-3))\Gamma(\frac{1}{2}(1-a+c))\Gamma(b+1-\frac{1}{2}(a+c))} \right.$$

$$\left. - \frac{(a-2)(3-a)(b-2)}{(c-2)(2b-c-1)} - 1 \right\}.$$

Further, if we put $p = q$ in Theorem 7, it gives result obtained earlier by Jun et al. [12].

$$\int_0^1 x^{a-1}(1-x)^{c-a-1} {}_3F_2 \left[\begin{matrix} 2m-1-a, & b, & 1 \\ 2b-c+1, & m \end{matrix}; x \right] dx = \frac{\Gamma(a)\Gamma(c-a)}{\Gamma(c)} \gamma_7.$$

where γ_7 is the same as given in (21).

Theorem 8. For $m \in \mathbb{N}$, $Re(a) > 0$, $Re(c-a) > 0$ and the constants p, q are such that no one of the expressions $1+p, 1+q, 1+px+q(1-x)$, where $0 \leq x \leq 1$, are zero. As a result, the following conclusion is correct:

$$\int_0^1 x^{a-1}(1-x)^{c-a-1} [1+px+q(1-x)]^{-c} {}_3F_2 \left[\begin{matrix} -n+m-1, & b, & 1 \\ 1+a+b-c-n, & m \end{matrix}; \frac{(1+p)x}{1+px+q(1-x)} \right] dx$$

$$= \frac{1}{(1+p)^a(1+q)^{c-a}} \frac{\Gamma(a)\Gamma(c-a)}{\Gamma(c)} \gamma_8. \tag{34}$$

where γ_8 is the same as given in (22).

Corollary 8. In Theorem 8, if we take $m = 1, 2, 3$, we subsequently gain following conclusion:

$$\int_0^1 x^{a-1}(1-x)^{c-a-1} [1+px+q(1-x)]^{-c} {}_2F_1 \left[\begin{matrix} -n, & b \\ 1+a+b-c-n \end{matrix}; \frac{(1+p)x}{1+px+q(1-x)} \right] dx$$

$$= \frac{1}{(1+p)^a(1+q)^{c-a}} \frac{\Gamma(a)\Gamma(c-a)}{\Gamma(c)} \frac{(c-a)_n(c-b)_n}{(c)_n(c-a-b)_n},$$

$$\int_0^1 x^{a-1}(1-x)^{c-a-1} [1+px+q(1-x)]^{-c} {}_3F_2 \left[\begin{matrix} -n+1, & b, & 1 \\ 1+a+b-c-n, & 2 \end{matrix}; \frac{(1+p)x}{1+px+q(1-x)} \right] dx$$

$$= \frac{1}{(1+p)^a(1+q)^{c-a}} \frac{\Gamma(a)\Gamma(c-a)}{\Gamma(c)} \frac{(1-c)(c-a-b+n)}{n(1-a)(1-b)}$$

$$\times \left\{ \frac{(c-a)_n(c-b)_n}{(c-1)_n(c-a-b+1)_n} - 1 \right\},$$

and

$$\int_0^1 x^{a-1}(1-x)^{c-a-1} [1+px+q(1-x)]^{-c} {}_3F_2 \left[\begin{matrix} -n+2, & b, & 1 \\ 1+a+b-c-n, & 3 \end{matrix}; \frac{(1+p)x}{1+px+q(1-x)} \right] dx$$

$$= \frac{1}{(1+p)^a(1+q)^{c-a}} \frac{\Gamma(a)\Gamma(c-a)}{\Gamma(c)} \frac{2(1-c)_2(c-a-b+n)_2}{n(1-a)_2(1-b)_2}$$

$$\times \left\{ \frac{(c-a)_n(c-b)_n}{(c-2)_n(c-a-b+2)_n} + \frac{n(a-2)(b-2)}{(c-2)(a+b-c-n-1)} - 1 \right\}.$$

Further, if we put $p = q$ in Theorem 8, it gives result obtained earlier by Jun et al. [12].

$$\int_0^1 x^{a-1}(1-x)^{c-a-1} {}_3F_2 \left[\begin{matrix} -n+m-1, & b, & 1 \\ 1+a+b-c-n, & m \end{matrix}; x \right] dx = \frac{\Gamma(a)\Gamma(c-a)}{\Gamma(c)} \gamma_8.$$

where γ_8 is the same as given in (22).

Theorem 9. For $m \in \mathbb{N}$, $Re(a) > 0$, $Re(a - 2b + m) > 0$ and the constants p, q are such that no one of the expressions $1 + p, 1 + q, 1 + px + q(1 - x)$, where $0 \leq x \leq 1$, are zero. As a result, the following conclusion is correct:

$$\begin{aligned} & \int_0^1 x^{b-1}(1-x)^{a-2b+m-1}[1+px+q(1-x)]^{b-a-m} \\ & \times {}_4F_3 \left[\begin{matrix} a, & \frac{1}{2}(a+m+1), & c, & 1 \\ \frac{1}{2}(a+m-1), & a-c+m, & m, & \frac{-(1+p)x}{[1+px+q(1-x)]} \end{matrix} \right] dx \quad (35) \\ & = \frac{1}{(1+p)^b(1+q)^{a-2b+m}} \frac{\Gamma(b)\Gamma(a-2b+m)}{\Gamma(a-b+m)} \gamma_9. \end{aligned}$$

where γ_9 is the same as given in (23).

Corollary 9. In Theorem 9, if we take $m = 1, 2, 3$, we subsequently gain following conclusion:

$$\begin{aligned} & \int_0^1 x^{b-1}(1-x)^{a-2b}[1+px+q(1-x)]^{b-a-1} {}_3F_2 \left[\begin{matrix} a, & \frac{1}{2}(a+2), & c \\ \frac{a}{2}, & a-c+1 \end{matrix} ; \frac{-(1+p)x}{[1+px+q(1-x)]} \right] dx \\ & = \frac{1}{(1+p)^b(1+q)^{a-2b+1}} \frac{\Gamma(b)\Gamma(a-2b+1)\Gamma(1+a-c)}{\Gamma(1+a)\Gamma(1+a-b-c)}, \end{aligned}$$

$$\begin{aligned} & \int_0^1 x^{b-1}(1-x)^{a-2b+1}[1+px+q(1-x)]^{b-a-2} \\ & \times {}_4F_3 \left[\begin{matrix} a, & \frac{1}{2}(a+3), & c, & 1 \\ \frac{a+1}{2}, & a-c+2, & 2 \end{matrix} ; \frac{-(1+p)x}{[1+px+q(1-x)]} \right] dx \\ & = \frac{1}{(1+p)^b(1+q)^{a-2b+2}} \frac{\Gamma(b)\Gamma(a-2b+2)}{\Gamma(a-b+2)} \frac{(1+a-b)(1+a-c)}{(a+1)(b-1)(c-1)} \\ & \times \left\{ 1 - \frac{\Gamma(1+a-b)\Gamma(1+a-c)}{\Gamma(a)\Gamma(2+a-b-c)} \right\}, \end{aligned}$$

and

$$\begin{aligned} & \int_0^1 x^{b-1}(1-x)^{a-2b+2}[1+px+q(1-x)]^{b-a-3} \\ & \times {}_4F_3 \left[\begin{matrix} a, & \frac{1}{2}(a+4), & c, & 1 \\ \frac{a+2}{2}, & a-c+3, & 3 \end{matrix} ; \frac{-(1+p)x}{[1+px+q(1-x)]} \right] dx \\ & = \frac{1}{(1+p)^b(1+q)^{a-2b+3}} \frac{\Gamma(b)\Gamma(a-2b+3)}{\Gamma(a-b+3)} \frac{2(1+a-b)_2(1+a-c)_2}{(a+2)(a-1)(b-2)_2(c-2)_2} \\ & \times \left\{ \frac{\Gamma(1+a-b)\Gamma(1+a-c)}{\Gamma(a-1)\Gamma(3+a-b-c)} + \frac{a(b-2)(c-2)}{(1+a-b)(1+a-c)} - 1 \right\}. \end{aligned}$$

Further, if we put $p = q$ in Theorem 9, it gives result obtained earlier by Jun et al. [12].

$$\int_0^1 x^{b-1}(1-x)^{a-2b+m-1} {}_4F_3 \left[\begin{matrix} a, & \frac{1}{2}(a+m+1), & c, & 1 \\ \frac{1}{2}(a+m-1), & a-c+m, & m \end{matrix}; -x \right] dx$$

$$= \frac{\Gamma(a)\Gamma(a-2b+m)}{\Gamma(a-b+m)} \gamma_9.$$

where γ_9 is the same as given in (23).

Theorem 10. For $m \in \mathbb{N}$, $Re(b) > 0$, $Re(a-2c+m) > 0$ and the constants p, q are such that no one of the expressions $1+p, 1+q, 1+px+q(1-x)$, where $0 \leq x \leq 1$, are zero. As a result, the following conclusion is correct:

$$\int_0^1 x^{c-1}(1-x)^{a-2c+m-1} [1+px+q(1-x)]^{c-a-m}$$

$$\times {}_5F_4 \left[\begin{matrix} a, & \frac{1}{2}(a+m+1), & d, & e, & 1 \\ \frac{1}{2}(a+m-1), & a-d+m, & a-e+m, & m \end{matrix}; \frac{(1+p)x}{[1+px+q(1-x)]} \right] dx$$

$$= \frac{1}{(1+p)^c(1+q)^{a-2c+m}} \frac{\Gamma(c)\Gamma(a-2c+m)}{\Gamma(a-c+m)} \gamma_{10}. \tag{36}$$

where γ_{10} is the same as given in (24).

Corollary 10. In Theorem 10, if we take $m = 1, 2, 3$, we subsequently gain following conclusion:

$$\int_0^1 x^{c-1}(1-x)^{a-2c} [1+px+q(1-x)]^{c-a-1}$$

$$\times {}_4F_3 \left[\begin{matrix} a, & \frac{1}{2}(a+2), & d, & e \\ \frac{a}{2}, & a-d+1, & a-e+1 \end{matrix}; \frac{(1+p)x}{[1+px+q(1-x)]} \right] dx$$

$$= \frac{1}{(1+p)^c(1+q)^{a-2c}}$$

$$\times \frac{\Gamma(c)\Gamma(a-2c)\Gamma(a-2c+1)\Gamma(1+a-d)\Gamma(1+a-e)\Gamma(1+a-c-d-e)}{\Gamma(1+a)\Gamma(1+a-d-e)\Gamma(1+a-c-e)\Gamma(1+a-c-d)},$$

$$\int_0^1 x^{c-1}(1-x)^{a-2c+1} [1+px+q(1-x)]^{c-a-2}$$

$$\times {}_5F_4 \left[\begin{matrix} a, & \frac{1}{2}(a+3), & d, & e, & 1 \\ \frac{1}{2}(a+1), & a-d+2, & a-e+2, & 2 \end{matrix}; \frac{(1+p)x}{[1+px+q(1-x)]} \right] dx$$

$$= \frac{1}{(1+p)^c(1+q)^{a-2c+2}} \times \frac{\Gamma(c)\Gamma(a-2c+2)}{\Gamma(a-c+2)} \frac{(1+a-c)(1+a-d)(1+a-e)}{(1+a)(c-1)(d-1)(e-1)}$$

$$\times \left\{ \frac{\Gamma(1+a-c)\Gamma(1+a-d)\Gamma(1+a-e)\Gamma(3+a-c-d-e)}{\Gamma(a)\Gamma(2+a-d-e)\Gamma(2+a-c-e)\Gamma(2+a-c-d)} - 1 \right\},$$

and

$$\begin{aligned} & \int_0^1 x^{c-1}(1-x)^{a-2c+2}[1+px+q(1-x)]^{c-a-3} \\ & \times {}_5F_4 \left[\begin{matrix} a, & \frac{1}{2}(a+4), & d, & e, & 1 \\ \frac{1}{2}(a+2), & a-d+3, & a-e+3, & 3, & \end{matrix} ; \frac{(1+p)x}{[1+px+q(1-x)]} \right] dx \\ & = \frac{1}{(1+p)^c(1+q)^{a-2c+3}} \times \frac{\Gamma(c)\Gamma(a-2c+3)}{\Gamma(a-c+3)} \frac{2(1+a-c)_2(1+a-d)_2(1+a-e)_2}{(a-1)(a+2)(c-2)_2(d-2)_2(e-2)_2} \\ & \times \left\{ \frac{\Gamma(1+a-c)\Gamma(1+a-d)\Gamma(1+a-e)\Gamma(5+a-c-d-e)}{\Gamma(a-1)\Gamma(3+a-d-e)\Gamma(3+a-c-e)\Gamma(3+a-c-d)} \right. \\ & \left. - \frac{a(c-2)(d-2)(e-2)}{(1+a-c)(1+a-d)(1+a-e)} - 1 \right\}. \end{aligned}$$

Further, if we put $p = q$ in Theorem 10, it gives result obtained earlier by Jun et al. [12].

$$\begin{aligned} & \int_0^1 x^{c-1}(1-x)^{a-2c+m-1} {}_5F_4 \left[\begin{matrix} a, & \frac{1}{2}(a+m+1), & d, & e, & 1 \\ \frac{1}{2}(a+m-1), & a-d+m, & a-e+m, & m, & \end{matrix} ; x \right] dx \\ & = \frac{\Gamma(c)\Gamma(a-2c+m)}{\Gamma(a-c+m)} \gamma_{10}. \end{aligned}$$

where γ_{10} is the same as given in (24).

Theorem 11. For $m \in \mathbb{N}$, $Re(b) > 0$, $Re(a - 2b + m) > 0$ and the constants p, q are such that no one of the expressions $1 + p$, $1 + q$, $1 + px + q(1 - x)$, where $0 \leq x \leq 1$, are zero. As a result, the following conclusion is correct:

$$\begin{aligned} & \int_0^1 x^{b-1}(1-x)^{a-2b+m-1}[1+px+q(1-x)]^{b-a-m} \\ & \times {}_7F_6 \left[\begin{matrix} A, & B, & C, & D, & E, & F, & 1 \\ G, & H, & I, & J, & K, & m, & \end{matrix} ; \frac{(1+p)x}{[1+px+q(1-x)]} \right] dx \quad (37) \\ & = \frac{1}{(1+p)^b(1+q)^{a-2b+m}} \frac{\Gamma(b)\Gamma(a-2b+m)}{\Gamma(a-b+m)} \gamma_{11}. \end{aligned}$$

where $A = a$, $B = \frac{1}{2}(a + m + 1)$, $C = c$, $D = d$, $E = 2a - b - c - d + 2m + n - 1$, $F = m - n - 1$, $G = \frac{1}{2}(a + m - 1)$, $H = a - c + m$, $I = a - d + m$, $J = b + c + d - a - m - n + 1$, $K = a + n + 1$ and γ_{11} is the same as given in (25).

Corollary 11. In Theorem 11, if we take $m = 1, 2, 3$, we subsequently gain following conclusion:

$$\begin{aligned} & \int_0^1 x^{b-1}(1-x)^{a-2b}[1+px+q(1-x)]^{b-a-1} \\ & \times {}_6F_5 \left[\begin{matrix} a, & \frac{1}{2}(a+2), & c, & d, & 2a-b-c-d+n+1, & -n \\ \frac{a}{2}, & a-c+1, & a-d+1, & b+c+d-a-n, & a+n+1, & \end{matrix} ; \frac{(1+p)x}{[1+px+q(1-x)]} \right] dx \\ & = \frac{1}{(1+p)^b(1+q)^{a-2b+1}} \times \frac{\Gamma(b)\Gamma(a-2b+1)}{\Gamma(a-b+1)} \\ & \times \frac{(1-a)_n(a-b-c+1)_n(a-b-d+1)_n(a-c-d+1)_n}{(1+a-b)_n(1+a-c)_n(1+a-d)_n(1+a-b-c-d)_n}, \end{aligned}$$

$$\int_0^1 x^{b-1}(1-x)^{a-2b+1}[1+px+q(1-x)]^{b-a-2} \times {}_7F_6 \left[\begin{matrix} a, \frac{1}{2}(a+3), c, d, 2a-b-c-d+n+3, 1-n, 1 \\ \frac{1}{2}(a+1), a-c+2, a-d+2, b+c+d-a-n-1, a+n+1, 2 \end{matrix}; \frac{(1+p)x}{[1+px+q(1-x)]} \right] dx$$

$$= \frac{1}{(1+p)^b(1+q)^{a-2b+2}} \frac{\Gamma(b)\Gamma(a-2b+2)}{\Gamma(a-b+2)}$$

$$\times \frac{(b-a-1)(c-a-1)(d-a-1)(n+2+a-b-c-d)(a+n)}{n(1+a)(1-b)(1-c)(1-d)(b+c+d-2a-2-n)}$$

$$\times \left\{ 1 - \frac{(a)_n(a-b-c+2)_n(a-b-d+2)_n(a-c-d+2)_n}{(1+a-b)_n(1+a-c)_n(1+a-d)_n(3+a-b-c-d)_n} \right\},$$

and

$$\int_0^1 x^{b-1}(1-x)^{a-2b+2}[1+px+q(1-x)]^{b-a-3} \times {}_7F_6 \left[\begin{matrix} a, \frac{1}{2}(a+4), c, d, 2a-b-c-d+n+5, 2-n, 1 \\ \frac{1}{2}(a+2), a-c+3, a-d+3, b+c+d-a-n-2, a+n+1, 3 \end{matrix}; \frac{(1+p)x}{[1+px+q(1-x)]} \right] dx$$

$$= \frac{1}{(1+p)^b(1+q)^{a-2b+3}} \frac{\Gamma(b)\Gamma(a-2b+3)}{\Gamma(a-b+3)}$$

$$\times \frac{(a-2)(b-a-2)_2(c-a-2)_2(d-a-2)_2(-a-n)_2(3+n+a-b-c-d)_2}{(a+2)(1-a)_2(1-b)_2(1-c)_2(1-d)_2(n-1)_2(b+c+d-2a-4-n)_2}$$

$$\times \left\{ \frac{(a-1)_n(a-b-c+3)_n(a-b-d+3)_n(a-c-d+3)_n}{(a-b+1)_n(a-c+1)_n(a-d+1)_n(a-b-c-d+5)_n} \right.$$

$$\left. + \frac{na(b-2)(c-2)(d-2)(2a-b-c+n-3)}{(a-b+1)(a-c+1)(a-d+1)(b+c+d-a-n-4)(n+a-1)} - 1 \right\}.$$

Further, if we put $p = q$ in Theorem 11, it gives result obtained earlier by Jun et al. [12].

$$\int_0^1 x^{b-1}(1-x)^{a-2b+m-1} \times {}_7F_6 \left[\begin{matrix} a, \frac{1}{2}(a+m+1), c, d, 2a-b-c-d+2m+n-1, m-n-1, 1 \\ \frac{1}{2}(a+m-1), a-c+m, a-d+m, b+c+d-a-m-n+1, a+n+1, m \end{matrix}; x \right] dx$$

$$= \frac{\Gamma(b)\Gamma(a-2b+m)}{\Gamma(a-b+m)} \gamma_{11}.$$

where γ_{11} is the same as given in (25).

Remark: For other recent interesting papers, we refer to [3–7, 9, 22, 23].

Conclusion

We have evaluated eleven Eulerian's type integrals involving generalized hypergeometric functions in terms of gamma function by implementing recently obtained summation theorems by Masjed-Jamei and Koepf. The specific instance of our primary results is the conclusion that Jun et al. [12] previously achieved. The results are straightforward, intriguing, and simple to prove. They might be helpful in the fields of mathematical physics and classical analysis for modelling and computation.

Possible Applications and Future work

It has already been pointed that in the year 2018, Jamei and Koepf have generalized several classical summation theorem for the series ${}_2F_1$, ${}_3F_2$, ${}_4F_3$, ${}_5F_4$ and ${}_6F_5$. Therefore, in near future, by employing the above mentioned general summation theorems, we are planning to establish interesting results related to Double integrals, Laplace-type integrals and Convolution-type of integrals involving generalized hypergeometric functions in the form of a series of research papers in this direction.

Acknowledgements. The authors are highly thankful to learned reviewers for providing the references [3–7, 9, 22, 23].

References

1. Andrews, G.E., Askey, R., Roy, R.: Special Functions, In Encyclopedia of Mathematics and its Applications, vol. 71. Cambridge University Press, Cambridge (1999)
2. Bailey, W.N.: Generalized Hypergeometric Series. Cambridge University Press, Cambridge (1935). Reprinted by Stechert-Hafner, Inc., New York (1964)
3. Bansal, M.K., Jain, R.: A study of unified fractional integral operators involving S-generalized Gauss's hypergeometric function as it's kernel. Palest. J. Math. **6**(1), 142–152 (2017)
4. Bansal, M.K., Kumar, D., Jain, R., Khan, I., Singh, J., Nisar, K.S.: Certain unified integrals associated with product of M-series and incomplete H-functions. Mathematics **7**(12), 1191 (2019)
5. Bansal, M.K., Kumar, D., Jain, R.: A study of Marichev-Saigo - Maeda fractional integral operators associated with S-generalized Gauss hypergeometric function. Kyungpook Math. J. **59**(3), 433–443 (2019)
6. Bansal, M.K., Kumar, D., Singh, J., Nisar, K.S.: On the solutions of a class of integral equations pertaining to incomplete H - function and incomplete \bar{H} - function. Mathematics **8**(5), 819 (2020). <https://doi.org/10.3390/math8050819>
7. Bansal, M.K., Kumar, D., Sing, J.: Finite and infinite integral formulas involving the family of incomplete H - functions. Appl. Appl. Math. **6**, 15–28 (2020)
8. Bell, W.W.: Special Functions for Scientists and Engineers. Oxford University Press, London (1968)
9. Bhattar, S., Mathur, A., Kumar, D., Singh, J.: On certain new results of fractional calculus involving product of generalized special functions. Int. J. Appl. Comput. Math. **8**(3), 135 (2022). <https://doi.org/10.1007/s40819-022-01253-0>
10. Choi, J., Rathie, A.K.: A new class of integrals involving generalized hypergeometric functions. Far East J. Math. Sci. **102**(7), 1559–1570 (2017). <https://doi.org/10.17654/MS102071559>
11. Jamei, M.M., Koepf, W.: Some summation theorems for generalized hypergeometric functions. Axioms **7**(2), 38 (2018)
12. Jun, S., Kim, I., Rathie, A.K.: On a new class of Eulerian's type integrals involving generalized hypergeometric functions. Aust. J. Math. Anal Appl. **16**(10) (2019)
13. Koepf, W.: Hypergeometric Summation: An Algorithmic Approach to Summation and Special Function Identities, 2nd edn. Springer, London (2014). <https://doi.org/10.1007/978-1-4471-6464-7>

14. Kim, Y.S., Rakha, M.A., Rathie, A.K.: Extension of certain classical summation theorems for the series ${}_2F_1$, ${}_3F_2$ and ${}_4F_3$ with applications in Ramanujan's summations. *Int. J. Math. Sci.* **2010**(28) (2010). <https://doi.org/10.1155/2010/309503>
15. Lavoie, J., Gordin, F., Rathie, A.K.: Generalization of Watson's theorem on the sum of a ${}_3F_2$. *Indian J. Math.* **34**(2) (1992)
16. Lavoie, J., Gordin, F., Rathie, A.K., Arora, A.K.: Generalization of Dixon's theorem on the sum of a ${}_3F_2$. *Math. comp.* **62**, 267–276 (1994)
17. Lavoie, J., Gordin, F., Rathie, A.K.: Generalization of Whipple's theorem on the sum of a ${}_3F_2$. *J. Comput. Appl. Math.* **72**(2), 293–300 (1996)
18. MacRobert, T.M.: Beta function formulae and integrals involving E-functions. *Math. Annalen* **142**(5), 450–452 (1961)
19. Prudnikov, A., Brychkov, Y.A., Marichev, O.: *More Special Functions and Series*, vol. 3. Gordon and Breach Science Publishers, Amsterdam (1990)
20. Rainville, E.D.: *Special Functions*. Macmillan Company, New York (1960). Reprinted by Chelsea Publishing Company, New York (1971)
21. Rakha, M.A., Rathie, A.K.: Generalizations of classical summation theorems for the series ${}_2F_1$ and ${}_3F_2$ with applications. *Integral Transf. Spec. Funct.* **22**(11), 823–840 (2011)
22. Sharma, R., Singh, J., Kumar, D., Singh, Y.: Certain unified integrals associated with product of the general class of polynomials and incomplete I - functions. *Int. J. Appl. Comput. Math.* **8**, 7 (2022)
23. Singh, J., Kumar, D., Kumar, M.: Solution of nonlinear differential equation and special functions. *Math. Method. Appl. Sci.* **43**(5), 2106–2116 (2020)
24. Slater, L.J.: *Generalized Hypergeometric Functions*. Cambridge University Press, Cambridge (1966)



Irreversibility Analysis in Micropolar Thermofluidics Involving Deforming Sheet

Paresh Vyas and Rajesh Kumar Kasana^(✉)

Department of Mathematics, University of Rajasthan, Jaipur, India
rkasanamaths@gmail.com

Abstract. This communication presents the micropolar thermo-fluidics and associated irreversibility confronted in a setup involving a sheet shrinking in an exponential fashion. The sheet placed at the bottom of fluid saturated porous medium bears non uniform prescribed temperature. A suction is applied transverse to the flow direction for containing the vorticity to facilitate laminar motion. The thermo-fluidics involved is governed by the PDE boundary value problem. To change the governing PDEs into ODEs, a similarity transformation is invoked. The resulting BVP is solved numerically by shooting technique. The strategy yields a dual solution system for the momentum, micropolar, and energy equations. The quantities thus obtained are prerequisite to compute entropy. The effects of embedded parameters on quantities of interest are depicted in tabular form/graphs and discussed.

Keywords: Micropolar Fluid · Heat Transfer · Entropy · Dual Solution · Deforming Sheet · Porous Medium

1 Introduction

Thermo-fluidics due to stretching or shrinking surfaces is significant in technological applications [1–3]. Recent research conducted by Liao [4, 5] investigated a variety of potential solutions for the flow in presence of both permeable and impermeable stretched surfaces. The flow configurations involving exponentially stretching surfaces have been treated analytically and numerically [6–9]. Fang [10] described flow across a constantly shrinking sheet with mass transfer and a low-power surface. Chauhan and Agarwal [11] investigated MHD flow and heat transfer in a channel bounded by a contracting sheet and a porous plate. Liu et al. [12] investigated the flow and heat transmission of a viscous fluid across an exponentially stretched sheet in 3-D flow. Bhattacharya [13] investigated the steady boundary layer flow and reactive mass transfer in the presence of an exponentially advancing free stream. Shah et al. [14] explored dual solution of MHD mixed convection flow and heat transfer across a shrinking sheet susceptible to thermal radiation. Hamid et al. [15] examined dual solutions and stability analysis of Casson fluid flow and heat transmission across a stretched sheet. Suction/injection effects and dufour number, together with chemical reaction impacts of mhd casson nanofluid in convectively heated non-linear extending surface were explored by Gangid et al.

[16]. Analytical investigation for MHD flow of Williamson nanofluid including impacts of changing thickness, nonlinear thermal radiation, and enhanced Fourier's and Fick's Laws was described by Gupta et al. [17]. Tassaddiq et al. [18] examined MHD flow of a generalized Casson fluid with Newtonian heating by employing fractional model with Mittag-Leffler memory. Many scholars recently reported important studies spanning a wide range of topics [19–25].

Micropolar fluid theory [26] treats microfluidics with an elegant mathematical basis to account for local effects arising from the microstructure. The concept of micropolar fluid and its extension to thermal micropolar fluids has the potential to build acceptable non-Newtonian fluid models, which may be used to examine the behavior of shear flow, exotic lubricants, and liquid crystals [27–34]. Aurangaib et al. [35] investigated the flow and heat transmission in the boundary layer of a micropolar fluid over a sheet that was rapidly shrinking. Bhattacharyya et al. [36] investigated how thermal radiation affected the flow of micropolar fluid and the transport of heat over a shrinking sheet placed in a porous medium. El-dawy and Gorla [37] studied micropolar nanofluid flow over a stretched and shrinking wedge surface with absorption. The present paper attempts to peep into inherent thermodynamic irreversibility in a boundary-layer micropolar flow system that involves a shrinking sheet and porous medium.

The motivation behind the study comes straight from its technological applications wherein quantification of entropy is requisite for devising optimal thermo-fluidic system. Quantifying entropy in fluidics is possible for devising an entropy minimization strategy as pioneered by Bejan [38]. Makinde [39] looked into the effects of varying viscosity and the entropy generation number on the flow of the hydromagnetic boundary layer when thermal radiation was present. In the presence of nonlinear thermal radiation, Bhatti and Rashidi [40] numerically investigated the entropy generation in MHD boundary layer flow over a permeable shrinking/stretching sheet. Ibáñez et al. [41] conducted research on the entropy production and heat transfer of a nanofluid flow via an MHD porous microchannel while accounting for hydrodynamic slip and thermal radiation. Studying the entropy production of micropolar fluid flow through a concentric cylinder annulus with slip and convective boundary conditions was the focus of Srinivasacharya and Hima Bindu's [42]. Asha and Deepa [43] reported entropy distribution for peristaltic blood flow of magneto-micropolar fluid with thermal radiation using an asymmetric channel with tapering. Chauhan and Rastogi [44] investigated the entropy production and heat transfer in a MHD boundary layer over a stretched sheet. Yusuf et al. [45] analyzed irreversibility of a Cu-TiO₂-H₂O hybrid nanofluid impinging on a three-dimensional stretched sheet in a porous media with nonlinear radiation using the Darcy-Forchheimer model. Yusuf et al. [37] studied entropy formation in MHD Williamson nanofluid over a convectively heated stretched plate with chemical reaction. Vyas and his co-authors conducted irreversibility analysis for a variety of thermo fluidic topologies [46–54]. Many others have also focused on the issue [55–58].

The present work is expected to be a basis for future explorations.

2 Mathematical Formulation of the Problem

Let us consider a steady 2-D radiative micropolar fluid flow over an exponentially permeable sheet placed in a fluid saturated porous material. The sheet shrinks with a velocity

$\tilde{U}_w(X) = ce^{X/2L}$ ($c > 0$ is a shrinking constant). To keep the vorticity in check for ensuring laminar flow, a normal suction is applied. The fluid’s thermal conductivity has dependence on temperature. Rosseland approximation is involved to account for radiative transfer. The model is applicable to fluids that do not undergo a phase transition, have optical density, and absorb/emit light, and are non scattering media. To model the problem mathematically a Cartesian coordinate system is called for where the \tilde{X} -axis is along the sheet, and the \tilde{Y} -axis is normal to the sheet (Fig. 1).

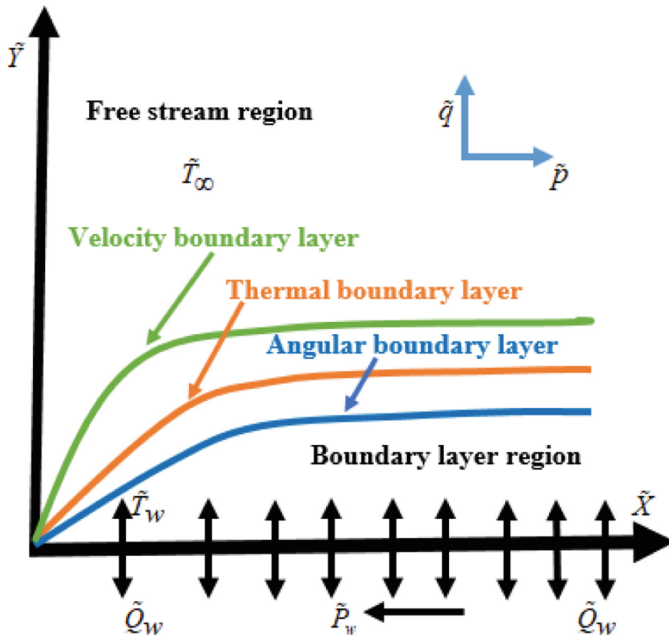


Fig. 1. Physical sketch and Coordinate space

The equations that govern the boundary layer flow are as follows:

$$\frac{\partial \tilde{p}}{\partial \tilde{X}} + \frac{\partial \tilde{q}}{\partial \tilde{Y}} = 0 \tag{1}$$

$$\tilde{p} \left(\frac{\partial \tilde{p}}{\partial \tilde{X}} \right) + \tilde{q} \left(\frac{\partial \tilde{q}}{\partial \tilde{Y}} \right) = \left(\vartheta + \frac{\kappa}{\rho} \right) \left(\frac{\partial^2 \tilde{p}}{\partial \tilde{Y}^2} \right) + \left(\frac{\kappa}{\rho} \right) \left(\frac{\partial \tilde{M}}{\partial \tilde{Y}} \right) - \left(\frac{\vartheta}{\tilde{k}} \right) \tilde{p} \tag{2}$$

$$\tilde{p} \left(\frac{\partial \tilde{M}}{\partial \tilde{X}} \right) + \tilde{q} \left(\frac{\partial \tilde{M}}{\partial \tilde{Y}} \right) = \left(\frac{\gamma}{\rho j^*} \right) \left(\frac{\partial^2 \tilde{M}}{\partial \tilde{Y}^2} \right) - \left(\frac{\kappa}{\rho j^*} \right) \left(2\tilde{M} + \frac{\partial \tilde{M}}{\partial \tilde{Y}} \right) \tag{3}$$

$$\tilde{p} \left(\frac{\partial \tilde{T}}{\partial \tilde{X}} \right) + \tilde{q} \left(\frac{\partial \tilde{T}}{\partial \tilde{Y}} \right) = \left(\frac{\kappa^*}{c_p \rho} \right) \left(\frac{\partial^2 \tilde{T}}{\partial \tilde{Y}^2} \right) - \left(\frac{1}{c_p \rho} \right) \left(\frac{\partial \tilde{q}_r}{\partial \tilde{Y}} \right) \tag{4}$$

Subject to the following conditions:

$$\left. \begin{aligned} \tilde{Y} = 0: \quad \tilde{P}_w(\tilde{X}) = \tilde{p} = -ce^{\tilde{X}/L}, \quad \tilde{Q}_w(\tilde{X}) = \tilde{q} = q_0e^{\tilde{X}/2L}, \\ \tilde{M} = -m\left(\frac{\partial \tilde{p}}{\partial \tilde{Y}}\right), \quad \tilde{T}_w(\tilde{X}) = \tilde{T} = \tilde{T}_\infty + \tilde{T}_0e^{\tilde{X}/2L} \\ \tilde{Y} \rightarrow \infty: \quad \tilde{p} \rightarrow 0, \quad \tilde{M} \rightarrow 0, \quad \tilde{T} \rightarrow \tilde{T}_\infty \end{aligned} \right\} \quad (5)$$

where \tilde{p} and \tilde{q} are the \tilde{X} - and \tilde{Y} -directional velocity components, respectively. $\bar{k}, c_p, \vartheta, \rho, \tilde{M}, j^*, \gamma, \kappa$ are permeability, specific heat at constant pressure, kinematic viscosity, density, microrotation, microinertia per unit mass, spin gradient viscosity, vortex viscosity, respectively. And also, $\tilde{T}, \kappa^*, L, \tilde{T}_w, \tilde{T}_0, \tilde{T}_\infty$ are temperature, thermal conductivity of the fluid, reference length, variable wall temperature and temperature uniformity in the free stream, respectively. $\tilde{P}_w(\tilde{X}) = -Ce^{\tilde{X}/L}$ and $\tilde{Q}_w(\tilde{X}) = q_0e^{\tilde{X}/2L}$ are the sheet's shrinking velocity and suction velocity, respectively, where $C > 0$ is the shrinking constant and q_0 is a constant (where $q_0 < 0$ corresponds to mass suction). The parameter 'm' is micro gyration associated with shear stress that takes values between 0 and 1 i.e. $0 \leq m \leq 1$. We recall that in the case $m = 0$, the angular or microrotation velocity will be zero at the surface i.e. inability of microelements to rotate. Additionally, $m = 0.5$ refers to the scenario in which the anti-symmetric portion of the stress tensor disappears and weak concentrations are indicated. However, for turbulent boundary layer flows, $m = 1$ is true. The spin gradient viscosity γ is taken as

$$\gamma = \left(\mu + \frac{\kappa}{2}\right)j^* = \mu\left(1 + \frac{\beta}{2}\right) \quad (6)$$

where $\beta\left(= \frac{\kappa}{\mu}\right)$ is the material parameter. In addition, we take $\lambda\left(= \frac{j^*c}{L\vartheta}e^{X/L}\right)$ as the micro inertia parameter

3 The Transformation

Here, we consider the stream function $\tilde{\omega}(\tilde{X}, \tilde{Y})$ as

$$\tilde{p} = \frac{\partial \tilde{\omega}}{\partial \tilde{Y}}, \quad \tilde{q} = -\frac{\partial \tilde{\omega}}{\partial \tilde{X}} \quad (7)$$

We note that the equation of continuity (1) is identically satisfied. Now we take the following similarity transformation

$$\tilde{\omega} = \sqrt{2CL\vartheta}f(\eta)e^{\tilde{X}/2L}, \quad \tilde{M} = C\sqrt{\frac{C}{2L\vartheta}}h(\eta)e^{3\tilde{X}/2L}, \quad \theta = \frac{\tilde{T} - \tilde{T}_\infty}{\tilde{T}_w - \tilde{T}_\infty}, \quad \eta = \tilde{Y}\sqrt{\frac{C}{2L\vartheta}}e^{\tilde{X}/2L} \quad (8)$$

On using Eqs. (7) and (8) we obtain the velocity expression in non-dimensional form as

$$\tilde{p} = Cf'(\eta)e^{\tilde{X}/L}, \quad \tilde{q} = -\sqrt{\frac{C\vartheta}{2L}}\{\eta f'(\eta) + f(\eta)\}e^{\tilde{X}/L} \quad (9)$$

In order to obtain the similar solution, the permeability $\bar{\kappa}$ of the porous medium is taken of the form

$$\bar{\kappa}(\tilde{X}) = 2k_0e^{-\tilde{X}/L} \tag{10}$$

where, k_0 being reference permeability.

The radiative heat flux \tilde{q}_r is defined following Rosseland approximation as follows:

$$\tilde{q}_r = -\left(\frac{4\sigma_1}{3\kappa_1}\right)\left(\frac{\partial \tilde{T}^4}{\partial \tilde{Y}}\right) \tag{11}$$

where the Stephan–Boltzman constant is σ_1 , and the mean absorption constant is κ_1 , respectively.

Noting that there is only a little fluctuation in temperature throughout the fluid system, one may represent \tilde{T}^4 as a linear function of temperature ‘ \tilde{T} ’ by the use of a Taylor series expansion of \tilde{T}^4 around \tilde{T}_∞ , which gives one the result:

Making a remark that small temperature variation in the fluid system allows \tilde{T}^4 to be expressed as a linear function of temperature ‘ \tilde{T} ’ by a Taylor series expansion of \tilde{T}^4 about \tilde{T}_∞ to yield

$$\tilde{T}^4 = -\left(3\tilde{T}_\infty^4 - 4\tilde{T}_\infty^3\tilde{T}\right) \tag{12}$$

In light of the Eqs. (11) and (12), we have

$$\tilde{q}_r = -\frac{16\sigma_1\tilde{T}_\infty^3}{3\kappa_1}\left(\frac{\partial \tilde{T}}{\partial \tilde{Y}}\right) \tag{13}$$

Further, the governing system of equations reduce to:

$$K\left\{(1 + \beta)f''' - 2f'^2 + ff'' + \beta h'\right\} - f' = 0 \tag{14}$$

$$\left(1 + \frac{\beta}{2}\right)h'' + fh' - 3hf' - \frac{2\beta}{\lambda}(f'' + 2h) = 0 \tag{15}$$

$$\left(1 + \frac{4R}{3}\right)\theta'' - \text{Pr}(f'\theta - f\theta') = 0 \tag{16}$$

With the boundary conditions:

$$\left. \begin{aligned} \eta = 0: & \quad f' = -1, \quad f = -q_0\sqrt{\frac{2L}{C\vartheta}} = -S, \quad h = -mf''(0), \quad \theta = 1 \\ \eta \rightarrow \infty: & \quad f' \rightarrow 0, \quad h \rightarrow 0, \quad \theta \rightarrow 0 \end{aligned} \right\} \tag{17}$$

where, $\text{Pr}\left(= \frac{\mu c_p}{k^*}\right)$; $\beta\left(= \frac{k}{\mu}\right)$; $S\left(= q_0\sqrt{\frac{2L}{C\vartheta}}\right)$; $K\left(= \frac{Ck_0}{\vartheta L}\right)$; and $R\left(= \frac{4\sigma_1 T_\infty^3}{k^* \kappa_1}\right)$ denote the Prandtl number, the material parameter, the wall mass suction/injection parameter ($S < 0$ for mass injection parameter and $S > 0$ for mass suction parameter), the permeability parameter, and radiation parameter, respectively. The prime (') denotes differentiation with respect to η .

4 Quantities of Interest

Besides the velocity and temperature distributions, the physical quantities of interest are the local skin friction coefficient C_f , the dimensionless wall couple stress M_x and the local Nusslet number Nu_x which are defined as follows

$$C_f = \frac{\tau_w}{\frac{1}{2}\rho U_w^2}, M_x = \frac{m_w}{\rho U_w^2 H}, \text{ and } Nu_x = \frac{xq_w}{qH}$$

where wall Shear Stress τ_w wall couple stress m_w and heat transfer at lower plate q_x are defined by

$$\tau_w = \left[\left(\vartheta + \frac{\kappa}{\rho} \right) \frac{\partial \tilde{p}}{\partial \tilde{Y}} + \frac{\kappa}{\rho} \tilde{M} \right]_{\tilde{Y}=0}, m_w = \left[\gamma \frac{\partial \tilde{M}}{\partial \tilde{Y}} \right]_{\tilde{Y}=0}, \text{ and } q_w = -\kappa^* \left[\frac{\partial \tilde{T}}{\partial \tilde{Y}} \right]_{\tilde{Y}=0} \quad (18)$$

Which yield,

$$\frac{1}{2} \text{Re} C_f = (1 + \beta) f''(0) + \beta h(0), \text{ Re } M_x = \frac{1}{\lambda} \left(1 + \frac{\beta}{2} \right) h'(0), \text{ and } Nu_x = -\theta'(0) \quad (19)$$

where $\text{Re} = \frac{\tilde{U}_w H}{\vartheta}$ Reynold number.

5 Numerical Solution Methodology

The governing BVP being nonlinear does not admit analytical solution hence require numerical treatment. We invoked the shooting method equipped with 4th order RK scheme. In order to apply the shooting method, the BVP is converted into a system of initial value problems. in the present case by making some transformations, we set the following system of initial value problems as

$$f' = \tilde{u}, f'' = \tilde{u}' = \tilde{v}, f''' = \tilde{v}' = \frac{1}{(1 + \beta)} \left(-\tilde{v}f + 2\tilde{u}^2 - \beta h' - \frac{\tilde{u}}{K} \right) \quad (20)$$

$$h' = \tilde{g}, h'' = \tilde{g}' = \frac{2}{(2 + \beta)} \left\{ -\tilde{g}f + 3h\tilde{u} + \frac{\beta}{\lambda} (2h + \tilde{v}) \right\} \quad (21)$$

$$\theta' = \tilde{z}, \theta'' = \tilde{z}' = \left(\frac{3 \text{Pr}}{3 + 4R} \right) (\tilde{u}\theta - \tilde{z}f) \quad (22)$$

The associated initial conditions are

$$f(0) = S, \tilde{u}(0) = -1, h(0) = -m r_1, \tilde{g}(0) = r_2, \theta(0) = 1, \tilde{z}(0) = r_3 \quad (23)$$

Here $r_1 = f''(0) = \tilde{q}(0)$, $r_2 = h'(0)$ and $r_3 = \theta'(0)$ are unknowns.

For the solution of the IVP (20)–(22) with (23), the values for r_1, r_2 and r_3 are needed but not readily available. We start with some initial guess values of r_1, r_2 and r_3 , and find the solution by fourth-order Runge-Kutta method. We experienced two difficulties throughout the calculating process. The first was figuring out the maximum value of η i.e. η_∞ for which $f' \rightarrow 0, h \rightarrow 0$ and $\theta \rightarrow 0$ at $\eta \rightarrow \infty$ and secondly, accurate predictions for the unknown quantities r_1, r_2 and r_3 . The first predictions were determined using a hit-and-trial method, and from there, refining was accomplished using iterative interpolation while maintaining the specified error tolerance. For these guesses, we compared the calculated $f'(\eta), h(\eta)$ and $\theta(\eta)$ at η_∞ with the given boundary conditions $f'(\eta_\infty) \rightarrow 0, h(\eta_\infty) \rightarrow 0$ and $\theta(\eta_\infty) \rightarrow 0$. We then used the “secant approach” to alter the values of $f''(0), h'(0)$, and $\theta'(0)$ to offer a better approximations. The step size $\eta = 0.01$ was found to be sufficient to ensure error tolerance of magnitude 10^{-7} .

6 Entropy Generation Analysis

Following, Bejan [37] the entropy production per unit volume ‘ S_G ’ for incompressible micropolar fluid flow can be expressed as

$$S_G = \left. \begin{aligned} & \frac{k}{\tilde{T}_\infty^2} \left(\frac{\partial \tilde{T}}{\partial \tilde{Y}} \right)^2 + \left(\frac{\mu + \mu_r}{T_\infty} \right) \left(\frac{\partial \tilde{p}}{\partial \tilde{Y}} \right)^2 + \left(\frac{2\mu_r}{T_\infty} \right) \left(\tilde{M}^2 + \tilde{M} \frac{\partial \tilde{M}}{\partial \tilde{Y}} \right) \\ & + \frac{\gamma}{T_\infty} \left(\frac{\partial \tilde{M}}{\partial \tilde{Y}} \right)^2 + \left(\frac{\mu}{T_\infty k_0} \right) \tilde{p}^2 - \frac{1}{T_\infty^2} \left(\frac{\partial \tilde{T}}{\partial \tilde{Y}} \right) \tilde{q}_r \end{aligned} \right\} \quad (24)$$

On prescribing the following characteristic quantities $S_{G_0} = \frac{c k(T_w - T_\infty)^2 e^{-x/L}}{2 T_\infty^2 \theta L}$ and $\Omega = \frac{T_\infty}{T_w - T_\infty}$.

The entropy generation number N_S is given by

$$N_S = \frac{S_G}{S_{G_0}} = \left(1 + \frac{4R}{3} \right) \theta'^2 + Br \Omega \left(f''^2 (1 + \beta) + 2\beta h^2 + 2\beta h f'' + \frac{\lambda}{2} (1 + \beta) h'^2 + \frac{f'^2}{K} \right) \left. \begin{aligned} & \\ & = H_1 + H_2 = HTI + FFI \end{aligned} \right\} \quad (25)$$

where, the first and the second terms stand for heat transfer (with radiative) irreversibility and the fluid friction irreversibility respectively. In addition, we determine the irreversibility distribution parameter known as Be (the Bejan number), which is the ratio of the entropy generation caused by heat transfer to the total entropy production. This ratio is defined as follows:

$$Be = \frac{H_1}{N_S} = \frac{HTI}{HTI + FFI} \quad (26)$$

Table 1. The $\frac{1}{2} \text{Re } C_f$ (Local Skin Friction), $\text{Re } M_x$ (dimensionless wall couple stress) and Nu_x (Local Nusselt Number) at $\eta = 0$.

β	S	K	m	R	Pr	λ	$\frac{1}{2} \text{Re } C_f$		$\text{Re } M_x$		Nu_x					
							1 st Sol ⁿ	2 nd Sol ⁿ	1 st Sol ⁿ	2 nd Sol ⁿ	1 st Sol ⁿ	2 nd Sol ⁿ				
0.0							-1.00000	-1.00000	1.69731	4.12103	0.44920	0.09270				
0.1	2.4	10	0.5	1.0	0.7	0.5	-1.17062	-1.11117	1.35114	-2.08295	0.42857	0.10993				
0.2							-1.32621	-1.23394	0.99773	-1.38751	0.40342	0.14222				
0.1	2.4	10	0.5	1.0	0.7	0.5	-1.17062	-1.11117	1.35114	-2.08295	0.42857	0.10993				
		20					-1.16722	-1.11734	1.20543	-1.35055	0.41835	0.15846				
		1000					-1.16317	-1.12337	1.03214	-0.88017	0.40534	0.20388				
β	S	K	m	R	Pr	λ	$\frac{1}{2} \text{Re } C_f$		$\text{Re } M_x$		Nu_x					
							1 st Sol ⁿ	2 nd Sol ⁿ	1 st Sol ⁿ	2 nd Sol ⁿ	1 st Sol ⁿ	2 nd Sol ⁿ				
0.1	2.3	10	0.5	1.0	0.7	0.5	-1.15881	-1.12349	0.64890	-1.20081	0.35521	0.16022				
	2.5						-1.17972	-1.09871	1.95578	-3.78123	0.48591	0.06763				
	2.7						-1.19495	-1.08223	3.10627	-0.34457	0.58269	0.05225				
0.1	2.4	10	0.0	1.0	0.7	0.5	-1.10000	-1.10000	-0.29883	-1.21362	0.40482	0.13210				
			0.5				-1.17062	-1.11117	1.35114	-2.08295	0.42857	0.10993				
			1.0				-1.25637	-1.11640	3.63261	-2.93309	0.45053	0.09395				
0.1	2.4	10	0.5	1.0	0.7	0.5	-1.17062	-1.11117	1.35114	-2.08295	0.42857	0.10993				
			2.0								0.26740	0.07048				
			3.0								0.20513	0.06808				
0.1	2.4	10	0.5	1.0	1.0	0.5	-1.17062	-1.11117	1.35114	-2.08295	0.42857	0.10993				
				1.0							0.64799	0.22038				
				1.5							1.05361	0.53688				
0.1	2.4	10	0.5	1.0	0.7	0.7	-1.17062	-1.11117	1.35114	-2.08295	0.42857	0.10993				
					0.8						-1.17061	-1.11205	0.84864	-1.11175	0.42851	0.11369
					1.2						-1.17061	-1.11253	0.56892	-0.67270	0.42846	0.11574

7 Results and Discussion

Table 1 displays the results of our investigation into the fluctuations in the local skin friction, the dimensionless wall couple stress, and the local Nusselt number as a parameter of the various aspects.

We can observe that the skin friction values drop from -1.00000 to -1.32621 and -1.00000 to -1.23394 for the first and second solutions, respectively. When all the numbers stay the same as $S = 2.4$, $K = 10$, $m = 0.5$, $R = 1.0$, $Pr = 0.7$, $\lambda = 0.5$ and material parameter β are increased from 0.0 to 0.2 . For the same variety of units, the dimensionless wall couple stress changes from 1.69731 to 0.99773 and from 4.12103 to -1.38751 for both solutions. For the same alteration, the Nusselt number for both solutions ranges from 0.44920 to 0.40342 for one solution and from 0.09270 to 0.14222 for the other.

When the values are considered to be, $\beta = 0.1$, $S = 2.4$, $m = 0.5$, $R = 1.0$, $Pr = 0.7$, $\lambda = 0.5$ and permeability parameter K goes from 10 to 1000 , For both solutions, the skin friction changes from -1.17062 to -1.16317 and from -1.11117 to -1.12337 , while the wall couple stress changes from -2.08295 to -0.88017 and from 1.35114 to 1.03214 . In response to the same alteration, the Nusselt number for both solutions changes from 0.42857 to 0.40534 and from 0.10993 to 0.20388 , respectively.

When the amounts are taken as $\beta = 0.1$, $K = 10$, $m = 0.5$, $R = 1.0$, $Pr = 0.7$, $\lambda = 0.5$ and When the value of the wall mass suction/injection parameter S is raised from 2.3 to 2.7 , the value of the skin friction for the first solution shifts from -1.15881 to -1.19495 , while the value of the skin friction for the second solution shifts from -1.12349 to -1.08223 .

In the first solution, the wall pair stress shifts from 0.64890 to 3.10627 , whereas in the second solution, it shifts from -1.20081 to -0.34457 . The value of the Nusselt number for the first solution shifts from 0.35521 to 0.58269 whereas the value of the Nusselt number for the second solution shifts from 0.16022 to 0.05225 when subjected to the same variation.

For the predetermined values $\beta = 0.1$, $S = 2.4$, $K = 10$, $R = 1.0$, $Pr = 0.7$, $\lambda = 0.5$, if the micro gyration vector m is raised from 0.0 to 1.0 . Then, it is seen that the skin friction of the first solution drops from -1.10000 to -1.25637 , but the skin friction of the second solution of it records a change from -1.10000 to -1.11640 . The wall couple stress for both solutions shifts from its previous value of -0.29883 to 3.63261 and from its previous value of -1.21362 to -2.93309 when subjected to the same variation. In addition, the values of the Nusselt number for both solutions move from 0.40482 to 0.45053 and from 0.13210 to 0.09395 , respectively, during the course of the study.

When the quantities are fixed as $\beta = 0.1$, $S = 2.4$, $K = 10$, $m = 0.5$, $Pr = 0.7$, $\lambda = 0.5$ and the value of the radiation parameter R goes from 1.0 to 3.0 , the skin friction and wall couple stress of the first and second solutions are always -1.17062 , -1.11117 and 1.35114 , -2.08295 , respectively. For the same change, the Nusselt number for the first solution goes from 0.42857 to 0.20513 and the Nusselt number for the second solution goes from 0.10993 to 0.06808 .

When the Prandtl number Pr is increased from 0.7 to 1.5 , but the other parameters are maintained constant as $\beta = 0.1$, $S = 2.4$, $K = 10$, $m = 0.5$, $R = 1.0$, $\lambda = 0.5$, the skin friction and local wall couple stress for first solutions are observed to have constant values of -1.17062 and 1.35114 , respectively. At the same time, the skin friction and wall couple stress of the second solution both have a value that is constant, and that value is -1.11117 and -2.08295 respectively. For the same variation, the Nusselt number of

the 1st solution changes from 0.42857 to 1.05361 while the Nusselt number of the 2nd solution changes from 0.10993 to 0.53688.

When the micro inertia number λ is increased from 0.5 to 1.2 while the other quantities remain unchanged as $\beta = 0.1, S = 2.4, K = 10, m = 0.5, R = 1.0, Pr = 0.7$, it is observed that the skin friction of the 1st solution is increases from a value of -1.17062 to -1.17061 , whereas the skin friction of the 2nd solution registers a change from -1.11117 to -1.11253 . For the same variation, the wall couple stress for the first solution goes from 1.35114 to 0.56892, and for the second solution, it goes from -2.0829 to -0.67270 . In addition, the value of the Nusselt number for the first solution shifts from 0.42857 to 0.42846, whereas the Nusselt number for the second solution shifts from 0.10993 to 0.11574 (Figs. 2, 3, 4, 5, 6, 7, 8, 9, 10, 11, 12, 13, 14, 15).

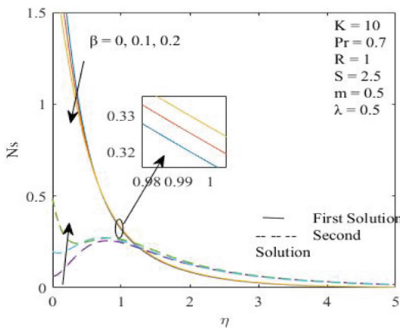


Fig. 2. Influence of β on N_s when $K = 10, Pr = 0.7, R = 1, S = 2.4, m = 0.5, \lambda = 0.5, \Omega = 0.5, Ec = 10.5$

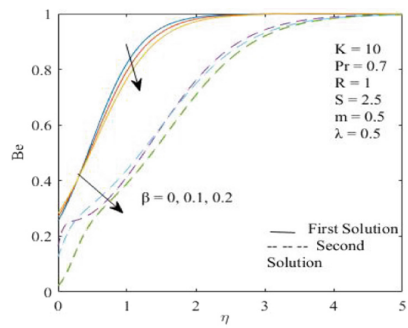


Fig. 3. Influence of β on Be when $K = 10, Pr = 0.7, R = 1, S = 2.4, m = 0.5, \lambda = 0.5, \Omega = 0.5, Ec = 10.5$

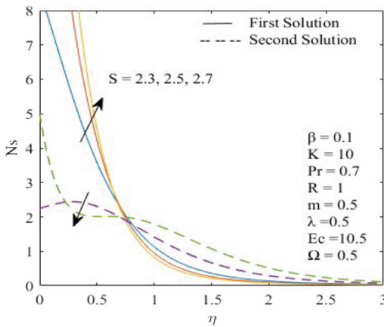


Fig. 4. Influence of S on N_s when $\beta = 0.1, K = 10, Pr = 0.7, R = 1, m = 0.5, \lambda = 0.5, \Omega = 0.5, Ec = 10.5$

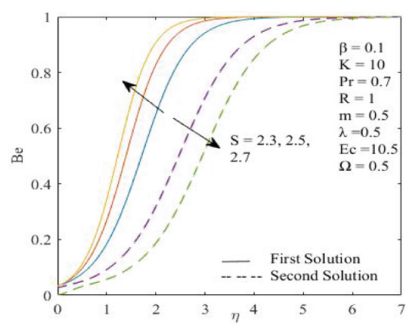


Fig. 5. Influence of S on Be when $\beta = 0.1, K = 10, Pr = 0.7, R = 1, m = 0.5, \lambda = 0.5, \Omega = 0.5, Ec = 10.5$

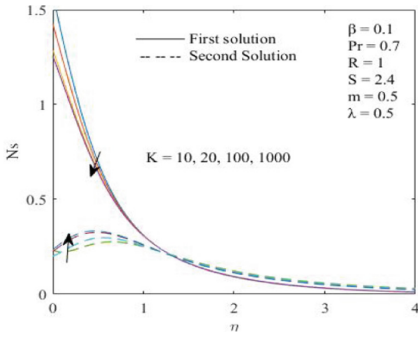


Fig. 6. Influence of K on N_s when $\beta = 0.1$, $Pr = 0.7$, $R = 1$, $S = 2.4$, $m = 0.5$, $\lambda = 0.5$, $\Omega = 0.5$, $Ec = 10.5$

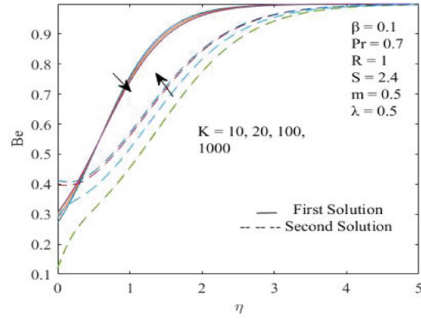


Fig. 7. Influence of K on Be when $\beta = 0.1$, $Pr = 0.7$, $R = 1$, $S = 2.4$, $m = 0.5$, $\lambda = 0.5$, $\Omega = 0.5$, $Ec = 10.5$

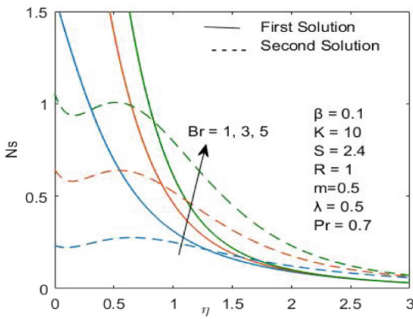


Fig. 8. Influence of Br on N_s when $\beta = 0.1$, $K = 10$, $R = 1$, $S = 2.4$, $m = 0.5$, $\lambda = 0.5$, $\Omega = 0.5$, $Pr = 0.7$

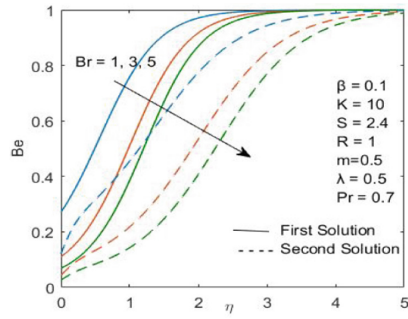


Fig. 9. Influence of Br on Be when $\beta = 0.1$, $K = 10$, $R = 1$, $S = 2.4$, $m = 0.5$, $\lambda = 0.5$, $\Omega = 0.5$, $Pr = 0.7$

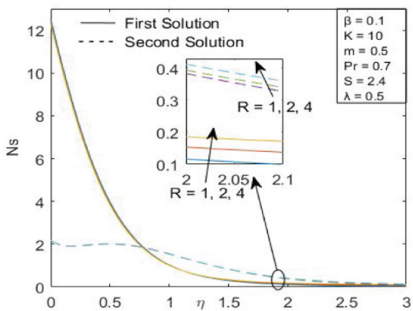


Fig. 10. Influence of R on N_s when $\beta = 0.1$, $K = 10$, $R = 1$, $S = 2.4$, $m = 0.5$, $\lambda = 0.5$, $\Omega = 0.5$, $Ec = 10.5$, $Pr = 0.7$

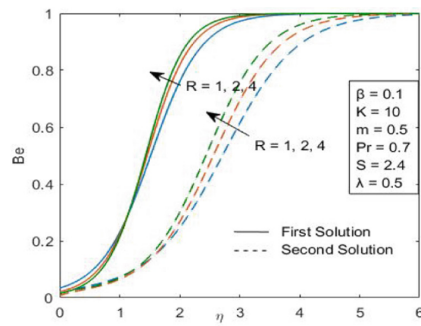


Fig. 11. Influence of R on Be when $\beta = 0.1$, $K = 10$, $S = 2.4$, $m = 0.5$, $\lambda = 0.5$, $\Omega = 0.5$, $Pr = 0.7$, $Ec = 10.5$

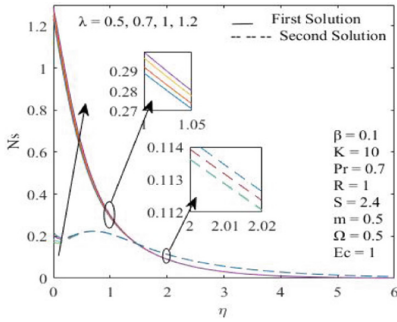


Fig. 12. Influence of λ on N_s when $\beta = 0.1$, $K = 10$, $Pr = 0.7$, $R = 1$, $S = 2.4$, $m = 0.5$, $\Omega = 0.5$, $Ec = 10.5$

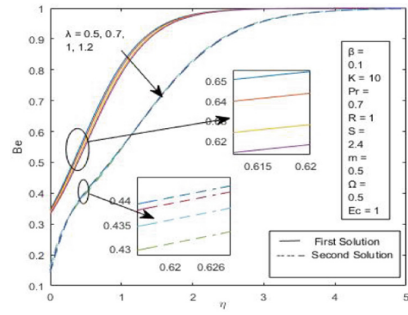


Fig. 13. Influence of λ on Be when $\beta = 0.1$, $K = 10$, $Pr = 0.7$, $R = 1$, $S = 2.4$, $m = 0.5$, $\Omega = 0.5$, $Ec = 10.5$

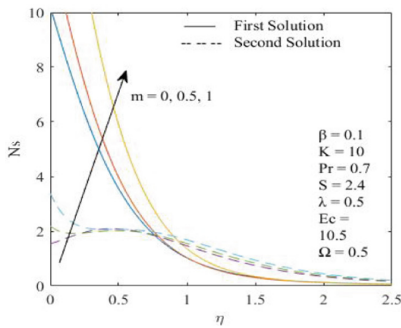


Fig. 14. Influence of m on N_s when $\beta = 0.1$, $K = 10$, $Pr = 0.7$, $R = 1$, $S = 2.4$, $\lambda = 0.5$, $\Omega = 0.5$, $Ec = 10.5$

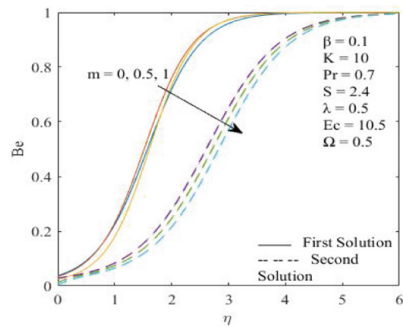


Fig. 15. Influence of m on Be when $\beta = 0.1$, $K = 10$, $Pr = 0.7$, $R = 1$, $S = 2.4$, $\lambda = 0.5$, $\Omega = 0.5$, $Ec = 10.5$

The thermos-fluidic system admits dual solutions for momentum, microrotation and energy regime. This ultimately leads to a dual system of entropy also. The findings have been portrayed graphically. We restrict our analysis to entropy only. However, velocity, microrotation, and temperature profiles have been appended for ready reference.

The figures reveal striking features that for a dual regime of entropy generation, the impact of parameters on the two branches of solution bear the same/distinct trends.

These unique patterns can also be seen in the Bejan number profiles, where we can see that, in contrast to the second solution, the first solution's Bejan number ' Be ' achieves unity at a location that is substantially closer to the surface. This indicates that in the case of the first solution, the contribution of dissipative losses to entropy weakens "far sooner spatially."

The figures show that contrary to the case of the second solution, entropy production for first solution increases with an increase in S , and it increases with a decaying values of β and K . However, we observe that entropy for both solutions exhibits a uniform trend in as much as that it increases with rising microrotation parameter m , microinertia parameter λ , Brinkman number Br and radiation parameter R . The trends reported above persist

in a region adjacent to the shrinking sheet i.e. for a finite value of η in respective cases, beyond which first and second solutions may switch to the opposite trends. Physically it happens as we approach towards the edge of the boundary layers (momentum and thermal).

8 Conclusion

The skin friction coefficient, wall stress and Nusselt number for both solutions exhibit qualitative and quantitative response to variations in embedded parameters. The presented dataset should be of pertinent value for future studies. The setup explored a dual regime for entropy generation that is found responsive, both qualitatively and quantitatively, to the embedded parameters.

Appendix

(See Figs. 16, 17, 18, 19, 20, 21, 22, 23, 24, 25, 26, 27, 28, 29, 30, 31, 32).

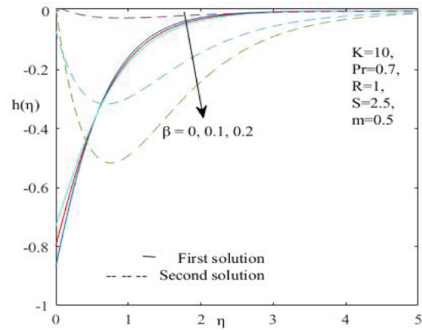
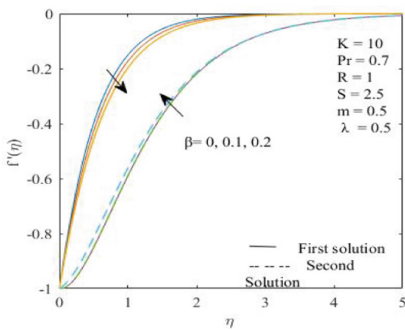


Fig. 16. Influence of β on $f'(\eta)$ when $K = 10, Pr = 0.7, R = 1, S = 2.5, m = 0.5, \lambda = 0.5$

Fig. 17. Influence of β on $h(\eta)$ when $K = 10, Pr = 0.7, R = 1, S = 2.5, m = 0.5, \lambda = 0.5$

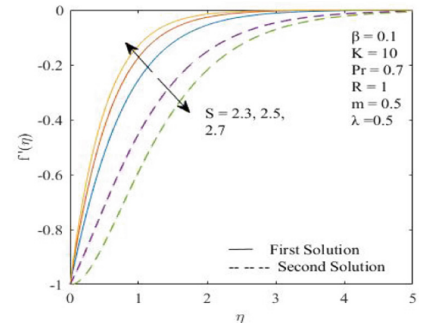
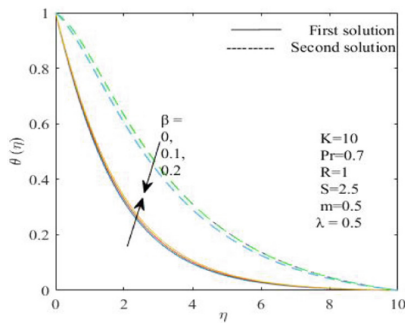


Fig. 18. Influence of β on $\theta(\eta)$ when $K = 10, Pr = 0.7, R = 1, S = 2.5, m = 0.5, \lambda = 0.5$

Fig. 19. Influence of S on $f'(\eta)$ when $\beta = 0.1, K = 10, Pr = 0.7, R = 1, m = 0.5, \lambda = 0.5$

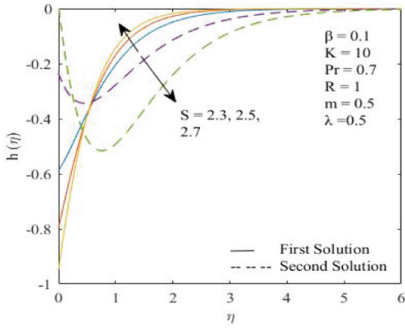


Fig. 20. Influence of S on $h(\eta)$ when $\beta = 0.1$, $K = 10$, $Pr = 0.7$, $R = 1$, $m = 0.5$, $\lambda = 0.5$

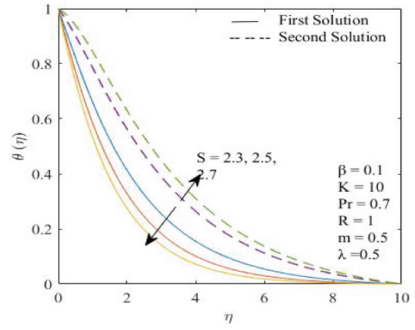


Fig. 21. Influence of S on $\theta(\eta)$ when $\beta = 0.1$, $K = 10$, $Pr = 0.7$, $R = 1$, $m = 0.5$, $\lambda = 0.5$

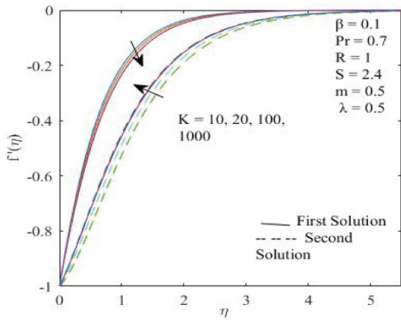


Fig. 22. Influence of K on $f'(\eta)$ when $\beta = 0.1$, $Pr = 0.7$, $R = 1$, $S = 2.4$, $m = 0.5$, $\lambda = 0.5$

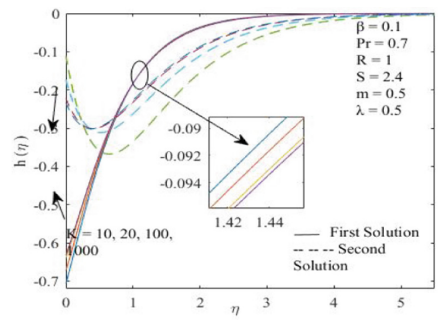


Fig. 23. Influence of K on $h(\eta)$ when $\beta = 0.1$, $Pr = 0.7$, $R = 1$, $S = 2.4$, $m = 0.5$, $\lambda = 0.5$

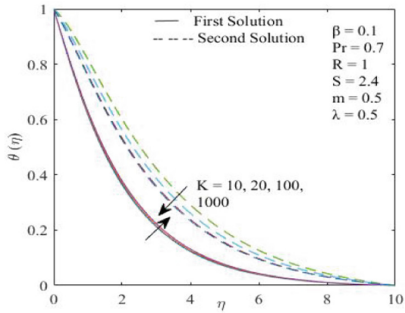


Fig. 24. Influence of K on $\theta(\eta)$ when $\beta = 0.1$, $Pr = 0.7$, $R = 1$, $S = 2.4$, $m = 0.5$, $\lambda = 0.5$

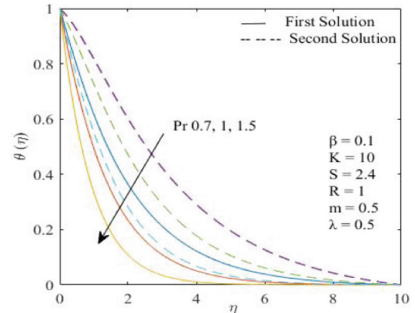


Fig. 25. Influence of Pr on $\theta(\eta)$ when $\beta = 0.1$, $K = 10$, $R = 1$, $S = 2.4$, $m = 0.5$, $\lambda = 0.5$

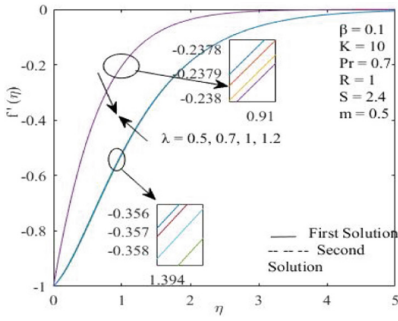


Fig. 26. Influence of λ on $f'(\eta)$ when $\beta = 0.1, K = 10, Pr = 0.7, R = 1, S = 2.4, m = 0.5$

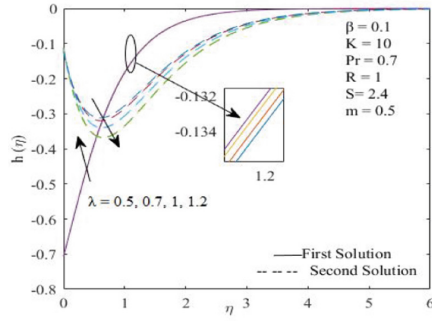


Fig. 27. Influence of λ on $h(\eta)$ when $\beta = 0.1, K = 10, Pr = 0.7, R = 1, S = 2.4, m = 0.5$

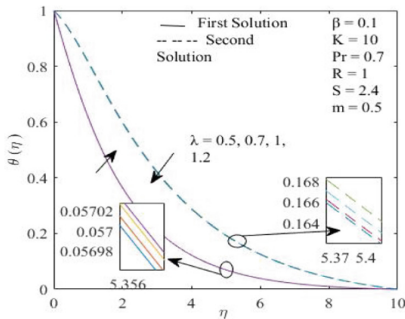


Fig. 28. Influence of λ on $\theta(\eta)$ when $\beta = 0.1, K = 10, Pr = 0.7, R = 1, S = 2.4, m = 0.5$

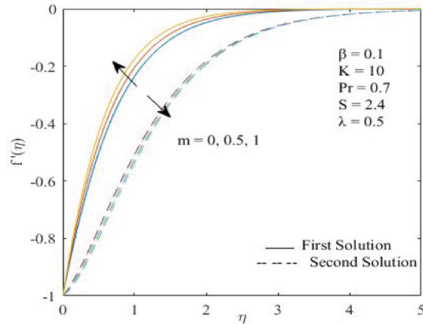


Fig. 29. Influence of m on $f'(\eta)$ when $\beta = 0.1, K = 10, Pr = 0.7, R = 1, S = 2.4, \lambda = 0.5$

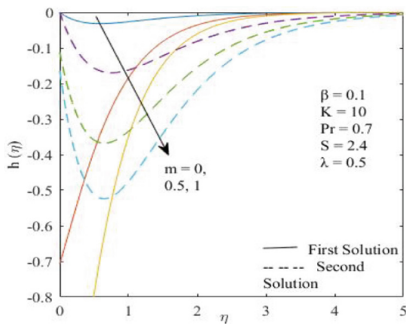


Fig. 30. Influence of m on $h(\eta)$ when $\beta = 0.1, K = 10, Pr = 0.7, R = 1, S = 2.4, \lambda = 0.5$

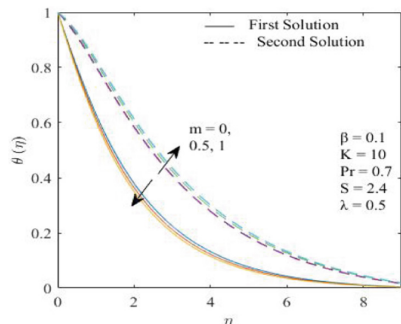


Fig. 31. Influence of m on $\theta(\eta)$ when $\beta = 0.1, K = 10, Pr = 0.7, R = 1, S = 2.4, \lambda = 0.5$

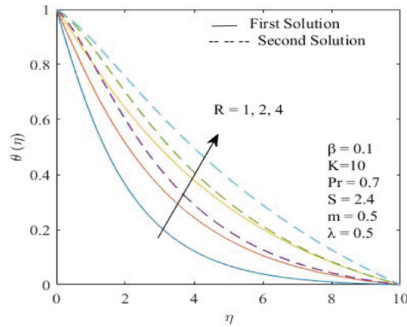


Fig. 32. Influence of R on $\theta(\eta)$ when $\beta = 0.1$, $K = 10$, $Pr = 0.7$, $S = 2.4$, $m = 0.5$, $\lambda = 0.5$

References

1. Crane, L.J.: Flow past a stretching plate. *Zeitschrift für Angewandte Mathematik und Physik ZAMP* **21**(4), 645–647 (1970)
2. Gupta, P.S., Gupta, A.S.: Heat and mass transfer on a stretching sheet with suction and blowing. *Can. J. Chem. Eng.* **55**, 744–746 (1977)
3. Khan, W.A., Pop, I.: Boundary-layer flow of a nanofluid past a stretching sheet. *Int. J. Heat Mass Transf.* **53**(11–12), 2477–2483 (2010)
4. Liao, S.: A new branch of solutions of boundary-layer flows over an impermeable stretched plate. *Int. J. Heat Mass Transf.* **48**(12), 2529–2539 (2005)
5. Liao, S.J.: A new branch of solutions of boundary-layer flows over a permeable stretching plate. *Int. J. Non-Linear Mech.* **42**(6), 819–830 (2007)
6. Magyari, E., Keller, B.: Heat and mass transfer in the boundary layers on an exponentially stretching continuous surface. *J. Phys. D Appl. Phys.* **32**(5), 577–585 (1999)
7. Elbashbeshy, E.M.A.: Heat transfer over an exponentially stretching continuous surface with suction. *Arch. Mech.* **53**(6), 643–651 (2001)
8. Al-Odat, M.Q., Damseh, R.A., Al-Azab, T.A.: Thermal boundary layer on an exponentially stretching continuous surface in the presence of magnetic field effect. *Int. J. Appl. Mech. Eng.* **11**(2), 289–299 (2006)
9. Sajid, M., Hayat, T.: Influence of thermal radiation on the boundary layer flow due to an exponentially stretching sheet. *Int. Commun. Heat Mass Transf.* **35**(3), 347–356 (2008)
10. Fang, T.: Boundary layer flow over a shrinking sheet with power-law velocity. *Int. J. Heat Mass Transf.* **51**, 5838–5843 (2008)
11. Chauhan, D.S., Agrawal, R.: MHD flow and heat transfer in a channel bounded by a shrinking sheet and a plate with a porous substrate. *J. Eng. Phys. Thermophys.* **84**(5), 1034–1046 (2011)
12. Liu, I.C., Wang, H.H., Peng, Y.F.: Flow and heat transfer for three-dimensional flow over an exponentially stretching surface. *Chem. Eng. Commun.* **200**, 253–268 (2013)
13. Bhattacharyya, K.: Steady boundary layer flow and reactive mass transfer past an exponentially stretching surface in an exponentially moving free stream. *J. Egypt. Math. Soc.* **20**, 223–228 (2012)
14. Shah, S.H.A.M., Suleman, M., Khan, U.: Dual solution of MHD mixed convection flow and heat transfer over a shrinking sheet subject to thermal radiation. *Partial Differ. Equ. Appl. Math.* **6**, 100412 (2022)
15. Hamid, M., Usman, M., Khan, Z.H., Ahmad, R., Wang, W.: Dual solutions and stability analysis of flow and heat transfer of casson fluid over a stretching sheet. *Phys. Lett. A* **383**(20), 2400–2408 (2019)

16. Jangid, S., Mehta, R., Kumar, D.: Suction/injection effects and dufour number also with chemical reaction impacts of MHD Casson nanofluid in convectively heated non-linear extending surface. *J. Comput. Anal. Appl.* **30**(1), 290–311 (2022)
17. Gupta, S., Kumar, D., Singh, J.: Analytical study for MHD flow of Williamson nanofluid with the effects of variable thickness, nonlinear thermal radiation and improved Fourier's and Fick's Laws. *SN Appl. Sci.* **2**(3), 1–12 (2020). <https://doi.org/10.1007/s42452-020-1995-x>
18. Tassaddiq, A., Khan, I., Nisar, K.S., Singh, J.: MHD flow of a generalized Casson fluid with Newtonian heating: A fractional model with Mittag–Leffler memory. *Alexandria Eng. J.* **59**(5), 3049–3059 (2020). <https://doi.org/10.1016/j.aej.2020.05.033>
19. Vyas, P., Rai, A.: Radiative flow with variable thermal conductivity over a non-isothermal Stretching sheet in a porous medium. *Int. J. Contemp. Math. Sci.* **5**, 2685–2698 (2010)
20. Vyas, P., Srivastava, N.: Radiative MHD flow over a nonisothermal stretching sheet in a porous medium. *Appl. Math. Sci.* **4**(49–52), 2475–2484 (2010)
21. Vyas, P., Ranjan, A.: Dissipative MHD boundary-layer flow in a porous medium over a sheet stretching nonlinearly in the presence of radiation. *Appl. Math. Sci.* **4**(61–64), 3133–3142 (2010)
22. Chauhan, D.S., Kumar, V.: Radiation effects on unsteady flow through a porous medium channel with velocity and temperature slip boundary conditions. *Appl. Math. Sci.* **6**(33–36), 1759–1769 (2012)
23. Mukhopadhyay, S., Bhattacharyya, K., Layek, G.C.: Mass transfer over an exponentially stretching porous sheet embedded in a stratified medium. *Chem. Eng. Commun.* **201**, 272–286 (2014)
24. Ene, R.D., Marinca, V.: Approximate solutions for steady boundary layer MHD viscous flow and radiative heat transfer over an exponentially porous stretching sheet. *Appl. Math. Comput.* **269**, 389–401 (2015)
25. Raju, C.S.K., Sandeep, N., Sugunamma, V., Babu, M.J., Reddy, J.V.R.: Heat and mass transfer in magnetohydrodynamic Casson fluid over an exponentially permeable stretching surface. *Eng. Sci. Technol. Int. J.* **19**(1), 45–52 (2016)
26. Eringen, A.C.: Theory of micropolar fluids. *J. Math. Mech.* **16**, 1–18 (1966)
27. Peddieson, J., McNitt, R.P.: Boundary-layer theory for a micropolar fluid. *Recent Adv. Eng. Sci.* **5**, 405–426 (1977)
28. Peddieson, J.: An application of the micropolar fluid model to the calculation of turbulent shear flow. *Int. J. Eng. Sci.* **10**, 23–32 (1972)
29. Sankara, K.K., Watson, L.T.: Micropolar flow past a stretching sheet. *Z. Angew. Math. Phys.* **36**(6), 845–853 (1985). <https://doi.org/10.1007/BF00944898>
30. Heruska, M.W., Watson, L.T., Sankara, K.K.: Micropolar flow past a porous stretching sheet. *Comput. Fluids* **14**, 117–129 (1986)
31. Hassanien, I.A., Gorla, R.S.R.: Heat transfer to a micropolar fluid from a non isothermal stretching sheet with suction and blowing. *Acta Mech.* **84**, 191–199 (1990)
32. Eringen, A.C.: Theory of thermomicrofluids. *J. Math. Anal. Appl.* **38**, 480–496 (1966)
33. Khonsari, M.M., Brewster, D.: On the performance of finite journal bearing lubricated with micropolar fluids. *STLE Tribol. Transm.* **32**, 155–160 (1989)
34. Hadimoto, B., Tokioka, T.: Two-dimensional shear flows of linear micropolar fluids. *Int. J. Eng. Sci.* **7**, 515–522 (1969)
35. Aurangzaib, Uddin, Md.S., Bhattacharyya, K., Shafie, S.: Miropolar fluid flow and heat transfer over an exponentially shrinking sheet. *Propul. Power Res.* **5**(4), 310–317 (2016)
36. Bhattacharyya, K., Mukhopadhyay, S., Layek, G.C., Pop, I.: Effects of thermal radiation on micropolar fluid flow and heat transfer over a porous shrinking sheet. *Int. J. Heat Mass Transf.* **55**, 2945–2952 (2012)
37. El-dawy, H.A., Gorla, R.S.R.: The flow of a micropolar nanofluid past a stretched and shrinking wedge surface with absorption. *Case Stud. Thermal Eng.* **26**, 101005 (2021)

38. Bejan, A.: A study of entropy generation in fundamental convective heat transfer. *ASME J. Heat Transf.* **101**(4), 718–725 (1979)
39. Makinde, O.D.: Second law analysis for variable viscosity hydromagnetic boundary layer flow with thermal radiation and Newtonian heating. *Entropy* **13**, 1446–1464 (2011)
40. Bhatti, M.M., Rashidi, M.M.: Entropy generation with nonlinear thermal radiation in MHD boundary layer flow over a permeable shrinking/stretching sheet: numerical solution. *J. Nanofluids* **5**(4), 1–6 (2016)
41. Ibáñez, G., López, A., Pantoja, J., Moreira, J.: Entropy generation analysis of a nanofluid flow in MHD porous microchannel with hydrodynamic slip and thermal radiation. *Int. J. Heat Mass Transfer* **100**, 89–97 (2016)
42. Srinivasacharya, D., Bindu, K.H.: Entropy generation due to micropolar fluid flow between concentric cylinders with slip and convective boundary conditions. *Ain Shams Eng. J.* **9**, 245–255 (2018)
43. Asha, S.K., Deepa, C.K.: Entropy generation for peristaltic blood flow of a magneto-micropolar fluid with thermal radiation in a tapered asymmetric channel. *Results Eng.* **3**, 100024 (2019)
44. Chauhan, D.S., Rastogi, P.: Heat transfer and entropy generation in MHD flow through a porous medium past a stretching sheet. *Int. J. Energy Technol.* **3**(15), 1–13 (2011)
45. Yusuf, T.A., Mabood, F., Khan, W.A., Gbadeyan, J.A.: Irreversibility analysis of Cu-TiO₂-H₂O hybrid-nanofluid impinging on a 3-D stretching sheet in a porous medium with nonlinear radiation: Darcy-Forchheimer's model. *Alex. Eng. J.* **59**, 5247–5261 (2020)
46. Vyas, P., Khan, S., Gajanand: Micropolar couple stress thermofluidics and entropy in Forchheimer channel. *Heat Transf.* **50**(5), 4382–4416 (2021). <https://doi.org/10.1002/hjt.22080>
47. Vyas, P., Khan, S., Gajanand: Cattaneo–Christov flux and entropy in thermofluidics involving shrinking surface. *Heat Transf.* **50**(6), 6210–6236 (2021). <https://doi.org/10.1002/hjt.22169>
48. Vyas, P., Gajanand, Khan, S.: Irreversibility analysis for Casson thermo-fluidics inside a cone: Cattaneo–Christov heat flux. *Heat Transf.* **51**(5), 4584–4619 (2022). <https://doi.org/10.1002/hjt.22514>
49. Vyas, P., Kasana, R.K., Khan, S.: Entropy analysis for boundary layer micropolar fluid flow. *AIMS Math.* **5**(3), 2009–2026 (2020). <https://doi.org/10.3934/math.2020133>
50. Vyas, P., Khan, S.: Entropy analysis for MHD dissipative Casson fluid flow in porous medium due to stretching cylinder. *Acta Tech.* **61**, 299–315 (2016)
51. Vyas, P., Srivastava, N.: Entropy analysis for magnetohydrodynamic fluid flow in porous medium due to a non-isothermal stretching sheet. *J. Rajasthan Acad. Phys. Sci.* **14**, 323–336 (2015)
52. Vyas, P., Soni, S.: On entropy generation in radiative MHD boundary layer flow with partial slip due to a melting surface stretching in porous medium. *J. Raj. Acad. Phys. Sci.* **16**(1), 93–111 (2017)
53. Vyas, P., Ranjan, A.: Entropy analysis of radiative MHD forced convection flow with weakly temperature dependent convection coefficient in porous medium channel. *Acta Technica* **60**(1), 1–14 (2015)
54. Vyas, P., Srivastava, N.: Entropy analysis of generalized MHD Couette flow inside a composite duct with asymmetric convective cooling. *Arab. J. Sci. Eng.* **40**(2), 603–614 (2015)
55. Shit, G.C., Mandal, S.: Entropy analysis on unsteady MHD flow of Casson nanofluid over a stretching vertical plate with thermal radiation effect. *Int. J. Appl. Comput. Math.* **6**(2), 1–22 (2020)
56. Tlili, I., Ramzan, M., Kadry, S., Kim, H., Nam, Y.: Radiative MHD nanofluid flow over a moving thin needle with entropy generation in a porous medium with dust particles and Hall current. *Entropy* **22**, 1–17 (2020)

57. Shahsavar, A., Sardari, P.T., Toghraie, D.: Free convection heat transfer and entropy generation analysis of water-Fe₃O₄/CNT hybrid nanofluid in a concentric annulus. *Int. J. Numer. Meth. Heat Fluid Flow* **424**, 0961–5539 (2018)
58. Seth, G.S., Bhattacharyya, A., Kumar, R., Chamkha, A.J.: Entropy generation in hydro-magnetic nanofluid flow over a non-linear stretching sheet with Navier's velocity slip and convective heat transfer. *Phys. Fluids* **30**, 1–16 (2018)



A Variational Description to Modulational Instability Criterion

Ram Dayal Pankaj¹ (✉), Arun Kumar², and Chiman Lal¹

¹ Department of Mathematics, J.N.V. University, Jodhpur, India
drrrdpankaj@yahoo.com

² Department of Mathematics, Government College, Kota, Kota, India

Abstract. In this article, the variational method (time dependent) is carried out for the parameterization of the evolved modulation instability (MI) in the coupled nonlinear Schrödinger equation (CNLS). The classical modulation instability criterion is obtained due to the pervasive dispersion relation. Will also investigate the case where the limits of the solution depend on time. Graphical sketch is also represented of the obtained solution.

Keywords: Coupled 1D Non-Linear Schrödinger System (CNLS) · Modulational Instability (MI) · And Variational Method (time dependent)

1 Introduction

Nonlinearity is a mesmerizing component of nature, with nonlinear wave phenomena appearing in one way or another in nearly all scientific and engineering fields. This phenomenon can be well explained by the Non-Linear Evolution Equations (NLEEs). Many physical phenomena can be explained by the interlinking of physical and biological systems on the basis of modulational instability (MI). MI obtainable, due to the establish relation between the nonlinearity and diffraction/dispersion special effects. It has been applied to produce train Soliton-like pulses, which is a predecessor to Soliton's configuration [1–7, 18]. A paradigm of wave-wave interaction as.

$$\begin{aligned} iE_t + E_{xx} + \frac{\alpha}{2} [|\eta|^2 + |E|^2] E &= 0 \\ i\eta_t + \eta_{xx} + \frac{\alpha}{2} [|\eta|^2 + |E|^2] \eta &= 0 \end{aligned} \quad (1)$$

called coupled 1D nonlinear Schrödinger (CNLS) system. $E(x, t)$ and $\eta(x, t)$ are complex-valued scalar field with space x and time t coordinate. Its application can be found in many areas of mathematics and physics, including nonlinear optics and plasma physics [9–14, 17]. The nonlinear Schrödinger (NLS) equation arises naturally as an envelope equation in physical wave systems where the propagation is governed by an asymptotic balance between the effects of dispersion and nonlinearity [19]

2 Criterion of Modulational Instability (MI)

We consider the exact solution of equation Eq. (1) in the plane wave - constant amplitude, exponential wave train.

$$E(x, t) = E_0 e^{i(kx - \omega t)}, \eta(x, t) = \eta_0 e^{i(-kx - \omega t)}$$

where wave number k and frequency ω , then

$$\omega = k^2 - \frac{\alpha}{2} [|\eta_0|^2 + |E_0|^2] \tag{2}$$

for MI examination Let

$$\begin{aligned} E(x, t) &= E_0(1 + A(x, t))e^{i(kx - \omega t)} \\ \eta(x, t) &= \eta_0(1 + B(x, t))e^{i(-kx - \omega t)} \end{aligned} \tag{3}$$

put in Eq. (1), we get

$$\begin{aligned} i(A_t + 2kA_x) + A_{xx} + \frac{\alpha}{2}|E_0|^2[A + A^*] + \frac{\alpha}{2}|\eta_0|^2[B + B^*] &= 0 \\ i(B_t + 2kB_x) + B_{xx} + \frac{\alpha}{2}|E_0|^2[A + A^*] + \frac{\alpha}{2}|\eta_0|^2[B + B^*] &= 0 \end{aligned} \tag{4}$$

Let $A(x, t)$ and $B(x, t)$ be two functions as

$$\begin{aligned} A(x, t) &= f_+ e^{i(qx - \Omega t)} + f_-^* e^{i(qx - \Omega^* t)} \\ B(x, t) &= g_+ e^{i(qx - \Omega t)} + g_-^* e^{i(qx - \Omega^* t)} \end{aligned} \tag{5}$$

Where f_{\pm} and g_{\pm} Fourier amplitude, E_0, η_0 parameters, superscript * denotes complex conjugation. Put these values in Eq. (4), we have the dispersion relation connecting the wave number q and frequency Ω of the perturbation,

$$\left[(\Omega - 2k)^2 + (\alpha|E_0|^2 - q^2) \right] \left[(\Omega + 2k)^2 + (\alpha|\eta_0|^2 - q^2) \right] - |\eta_0|^2 |E_0|^2 = 0 \tag{6}$$

Its quadratic polynomial and has complex frequency $\Omega(q)$ in term of disturbance wave number $q > 0$ and amplitudes. The polynomial has real coefficient for real value of q , therefore $\Omega(q)$ has complex roots. Both (conjugate pair) imaginary part is nonzero corresponds to linearly unstable modes, with growth rate $|\text{Im}(\Omega(q))|$. The coupled system will be shown to possess an additional instability that occurs even with the defocusing nonlinearity, i.e., an instability due to the nonlinear coupling.

We now endeavor to classify the interval of unstable wave numbers by means of the variational method (time dependent) [8, 11, 16 and 20].

3 Implement of Method for Solving the Model Equation

In special, the Lagrangian of the Eq. (1) is

$$L = \int_{-\infty}^{\infty} \left\{ \frac{i}{2} [EE_t^* - E^*E_t] + |E_x|^2 - \frac{\alpha}{4}|E|^4 + \frac{i}{2} [\eta\eta_t^* - \eta^*\eta_t] \right. \\ \left. + |\eta_x|^2 - \frac{\alpha}{4}|\eta|^4 - \frac{\alpha}{2}|E|^2|\eta|^2 \right\} dx \quad (7)$$

and consider a modulation of the plane wave form, where A (x, t) and B (x, t) are a generalized function of a(t), b(t), c(t) and d(t);

$$E = [E_0 + a(t)e^{i(\Phi_a(t)+qx)} + b(t)e^{i(\Phi_b(t)-qx)}] e^{i(kx-\omega t)} \\ \eta = [\eta_0 + c(t)e^{i(\Phi_c(t)+qx)} + d(t)e^{i(\Phi_d(t)-qx)}] e^{i(-kx-\omega t)} \quad (8)$$

Here we think about the integration limit $0 \leq x \leq 2\pi$ in Eq. and wave number $k, q = \pm 1, \pm 2, \pm 3, \dots$. Put the equation Eq. (8) into Eq. (7), using Dispersion relation (2), we get

$$L = \left\{ \begin{aligned} & 2(a^2\Phi'_a(t) + b^2\Phi'_b(t) + c^2\Phi'_c(t) + d^2\Phi'_d(t)) \\ & -\alpha(E_0^2(a^2 + b^2) + \eta_0^2(c^2 + d^2)) + \frac{\alpha}{2}(E_0^4 + \eta_0^4 + 2E_0^2\eta_0^2) \\ & + 2q^2(a^2 + b^2 + c^2 + d^2) + 2kq(a^2 - b^2 - c^2 + d^2) \\ & + \frac{\alpha}{2}(a^4 + b^4 + 4a^2b^2 + 4E_0^2ab \cos(\phi_a(t) + \phi_b(t))) \\ & - \frac{\alpha}{2}(c^4 + d^4 + 4c^2d^2 + 4\eta_0^2cd \cos(\Phi_c(t) + \Phi_d(t))) \\ & -\alpha \left\{ (a^2 + b^2)(c^2 + d^2) + 2abcd \cos(\phi_a(t) - \phi_b(t) - \phi_c(t) + \phi_d(t)) \right\} \\ & + 2E_0\eta_0ac \cos(\Phi_a(t) - \Phi_c(t)) + 2E_0\eta_0ad \cos(\Phi_a(t) + \Phi_d(t)) \\ & + 2E_0\eta_0bc \cos(\Phi_b(t) + \Phi_c(t)) + 2E_0\eta_0bd \cos(\Phi_b(t) - \Phi_d(t)) \end{aligned} \right\} \pi \quad (9)$$

The equation of motion by Lagrangian equations:

$$\frac{d}{dt} \left\{ \frac{\partial L}{\partial \Phi'_a} \right\} = \frac{\partial L}{\partial \Phi_a} \\ \Rightarrow a'(t) = \frac{1}{2} \left[\begin{aligned} & E_0^2\alpha b \sin(\Phi_a(t) + \Phi_b(t)) \\ & + \alpha acd \sin(\phi_a(t) - \phi_b(t) - \phi_c(t) + \phi_d(t)) \\ & + E_0\eta_0\{c \sin(\phi_a(t) - \phi_c(t)) + d \sin(\phi_a(t) + \phi_d(t))\} \end{aligned} \right] \quad (10)$$

$$\frac{d}{dt} \left\{ \frac{\partial L}{\partial \Phi'_b} \right\} = \frac{\partial L}{\partial \Phi_b}$$

$$\Rightarrow b'(t) = \frac{1}{2} \left[\begin{array}{l} E_0^2 \alpha a \sin(\Phi_a(t) + \Phi_b(t)) \\ + \alpha bcd \sin(\phi_a(t) - \phi_b(t) - \phi_c(t) + \phi_d(t)) \\ + E_0 \eta_0 \{c \sin(\phi_b(t) + \phi_c(t)) + d \sin(\phi_b(t) - \phi_d(t))\} \end{array} \right] \quad (11)$$

$$\frac{d}{dt} \left\{ \frac{\partial L}{\partial \Phi'_c} \right\} = \frac{\partial L}{\partial \Phi_c}$$

$$\Rightarrow c'(t) = \frac{1}{2} \left[\begin{array}{l} E_0^2 \alpha d \sin(\Phi_c(t) + \Phi_d(t)) \\ + \alpha abc \sin(\phi_a(t) - \phi_b(t) - \phi_c(t) + \phi_d(t)) \\ + E_0 \eta_0 \{-a \sin(\phi_a(t) - \phi_c(t)) + b \sin(\phi_b(t) + \phi_c(t))\} \end{array} \right] \quad (12)$$

$$\frac{d}{dt} \left\{ \frac{\partial L}{\partial \Phi'_d} \right\} = \frac{\partial L}{\partial \Phi_d}$$

$$\Rightarrow d'(t) = \frac{1}{2} \left[\begin{array}{l} E_0^2 \alpha c \sin(\Phi_c(t) + \Phi_d(t)) \\ + \alpha abd \sin(\phi_a(t) - \phi_b(t) - \phi_c(t) + \phi_d(t)) \\ + E_0 \eta_0 \{a \sin(\phi_a(t) + \phi_d(t)) - b \sin(\phi_b(t) - \phi_d(t))\} \end{array} \right] \quad (13)$$

$$\frac{d}{dt} \left\{ \frac{\partial L}{\partial a'} \right\} = \frac{\partial L}{\partial a}$$

$$\Rightarrow a(t)\Phi'_a(t) = \frac{1}{2} \left[\begin{array}{l} E_0^2 \alpha a - 2aq^2 - 4akq + \alpha \{a^3 + 2ab^2 + E_0^2 a \cos(\Phi_a(t) + \Phi_b(t))\} \\ + \alpha \{a(c^2 + d^2) + bcd \cos(\Phi_a(t) - \Phi_b(t) - \Phi_c(t) + \Phi_d(t))\} \\ + \alpha E_0 \eta_0 \{c \cos(\Phi_a(t) - \phi_c(t)) + d \cos(\Phi_a(t) + \Phi_d(t))\} \end{array} \right] \quad (14)$$

$$\frac{d}{dt} \left\{ \frac{\partial L}{\partial b'} \right\} = \frac{\partial L}{\partial b}$$

$$\Rightarrow b(t)\Phi'_b(t) = \frac{1}{2} \left[\begin{array}{l} E_0^2 \alpha b - 2bq^2 + 4bkq + \alpha \{b^3 + 2a^2b + E_0^2 a \cos(\Phi_a(t) + \Phi_b(t))\} \\ + \alpha \{b(c^2 + d^2) + acd \cos(\Phi_a(t) - \Phi_b(t) - \Phi_c(t) + \Phi_d(t))\} \\ + \alpha E_0 \eta_0 \{c \cos(\Phi_b(t) + \phi_c(t)) + d \cos(\Phi_b(t) - \Phi_d(t))\} \end{array} \right] \quad (15)$$

$$\frac{d}{dt} \left\{ \frac{\partial L}{\partial c'} \right\} = \frac{\partial L}{\partial c}$$

$$\Rightarrow c(t)\Phi'_c(t) = \frac{1}{2} \left[\begin{array}{l} \eta_0^2 \alpha c - 2cq^2 + 4ckq + \alpha \{c^3 + 2cd^2 + \eta_0^2 d \cos(\Phi_c(t) + \Phi_d(t))\} \\ + \alpha \{c(a^2 + b^2) + abd \cos(\Phi_a(t) - \Phi_b(t) - \Phi_c(t) + \Phi_d(t))\} \\ + \alpha E_0 \eta_0 \{a \cos(\Phi_a(t) - \phi_c(t)) + b \cos(\Phi_b(t) + \Phi_c(t))\} \end{array} \right] \quad (16)$$

$$\frac{d}{dt} \left\{ \frac{\partial L}{\partial d'} \right\} = \frac{\partial L}{\partial d}$$

$$\Rightarrow d(t)\Phi'_d(t) = \frac{1}{2} \left[\begin{aligned} &\eta_0^2 \alpha d - 2dq^2 - 4dkq + \alpha \{d^3 + 2c^2d + \eta_0^2 c \cos(\Phi_c(t) + \Phi_d(t))\} \\ &+ \alpha \{d(a^2 + b^2) + abc \cos(\Phi_a(t) - \Phi_b(t) - \Phi_c(t) + \Phi_d(t))\} \\ &+ \alpha E_0 \eta_0 \{a \cos(\Phi_a(t) + \phi_d(t)) + b \cos(\Phi_b(t) - \Phi_d(t))\} \end{aligned} \right] \quad (17)$$

Now, Let

$$\left. \begin{aligned} a(t) &= -b(t) = -c(t) = d(t), \\ \Phi_a(t) &= -\Phi_b(t) = -\Phi_c(t) = \Phi_d(t) \text{ and } |E_0|^2 = |\eta_0|^2 \end{aligned} \right\} \quad (18)$$

Now by putting the values from Eq. (18) into Eq. (14), we have

$$a(t)\Phi'_a(t) = \frac{1}{2} \left[\begin{aligned} &E_0^2 \alpha a - 2q^2 a - 4kqa + \alpha \{a^3 + 2a^3 - E_0^2 a \cos(0)\} \\ &+ \alpha \{2a^3 + a^3 \cos(4\phi_a(t))\} \\ &- E_0^2 \{-a \cos(2\Phi_a(t)) + a \cos(2\Phi_a(t))\} \end{aligned} \right]$$

$$\Rightarrow a(t)\Phi'_a(t) = \frac{1}{2} \left[\begin{aligned} &E_0^2 \alpha a - 2q^2 a - 4kqa \\ &+ \alpha \{5a^3 - E_0^2 a + a^3 \cos(4\Phi_a(t))\} \end{aligned} \right] \quad (19)$$

Similarly, by putting the values from Eq. (18) into Eq. (15), Eq. (16) and Eq. (17) respectively, we have

$$\Rightarrow b(t)\Phi'_b(t) = \frac{1}{2} \left[-E_0^2 \alpha a + 2q^2 a - 4kqa + \alpha \{-5a^3 + E_0^2 a - a^3 \cos(4\Phi_a(t))\} \right] \quad (20)$$

$$\Rightarrow c(t)\Phi'_c(t) = \frac{1}{2} \left[-E_0^2 \alpha a + 2q^2 a - 4kqa + \alpha \{-5a^3 + E_0^2 a + a^3 \cos(4\Phi_a(t))\} \right] \quad (21)$$

$$\Rightarrow d(t)\Phi'_d(t) = \frac{1}{2} \left[\begin{aligned} &-E_0^2 \alpha a(t) + 2q^2 a(t) - 4kqa(t) \\ &+ \alpha \{-5a^3(t) + E_0^2 a(t) - a^3(t) \cos(4\Phi_a(t))\} \end{aligned} \right] \quad (22)$$

After adding Eq. (19) and Eq. (20), we have,

$$a(t) \left[\Phi'_a(t) - \Phi'_b(t) \right] = -4kqa(t)$$

$$\Rightarrow \int d\Phi_a(t) - \int d\Phi_b(t) = -4kq \int dt$$

$$\Rightarrow \Phi_a(t) = -2kqt \quad (23)$$

Now by Eq. (18) and Eq. (10), We get

$$\begin{aligned}
 a'(t) &= \frac{1}{2} \left[\begin{array}{l} -\alpha E_0^2 a(t) \sin(0) + \alpha a^3(t) \sin(4\Phi_a(t)) \\ -E_0^2 \{-a(t) \sin(2\Phi_a(t) + a(t) \sin(2\Phi_a(t))\} \end{array} \right] \\
 \Rightarrow a'(t) &= \frac{1}{2} \alpha a^3(t) \sin(4\Phi_a(t)) \Rightarrow \int \frac{da}{a^3(t)} = \frac{1}{2} \alpha \int \sin(-8kqt) dt \\
 &\Rightarrow a^2(t) = \frac{-8kq}{\alpha} \sec(4\Phi_a(t)) \tag{24}
 \end{aligned}$$

if $k > 0, q < 0$; or $k < 0, q > 0$ then by Eq. (18),

$$\begin{aligned}
 \Rightarrow a(t) = -b(t) = -c(t) = d(t) &= \sqrt{\frac{8kq}{\alpha} \sec(8kqt)} \\
 \Rightarrow \Phi_a(t) = -\Phi_b(t) = -\Phi_c(t) = \Phi_d(t) &= -2kqt
 \end{aligned}$$

Now put these values in Eq. (8), We get

$$\begin{aligned}
 E &= E_0 + \sqrt{\frac{8kq}{\alpha} \sec(8kqt)} \left\{ e^{i(-2kqt+qx)} - e^{i(2kqt-qx)} \right\} e^{i(kx-\omega t)} \\
 \Rightarrow E &= \left\{ E_0 + \sqrt{\frac{8kq}{\alpha} \sec(8kqt)} 2i \sin(-2kqt + qx) \right\} e^{i(kx-\omega t)} \tag{25}
 \end{aligned}$$

and

$$\begin{aligned}
 \eta &= E_0 + \sqrt{\frac{8kq}{\alpha} \sec(8kqt)} \left\{ e^{i(-2kqt-qx)} - e^{-i(-2kqt-qx)} \right\} e^{i(-kx-\omega t)} \\
 \Rightarrow \eta &= \left\{ E_0 + \sqrt{\frac{8kq}{\alpha} \sec(8kqt)} 2i \sin(-2kqt - qx) \right\} e^{i(kx-\omega t)} \tag{26}
 \end{aligned}$$

4 Graphical Sketch

Numerical presentation for the solution of systems with $\frac{-k}{|E_0|} = \frac{q}{|\eta_0|} = 0.4, \alpha = -1, 0 \leq x \leq 6$ and $0 \leq t \leq 70$. (Fig. 3)

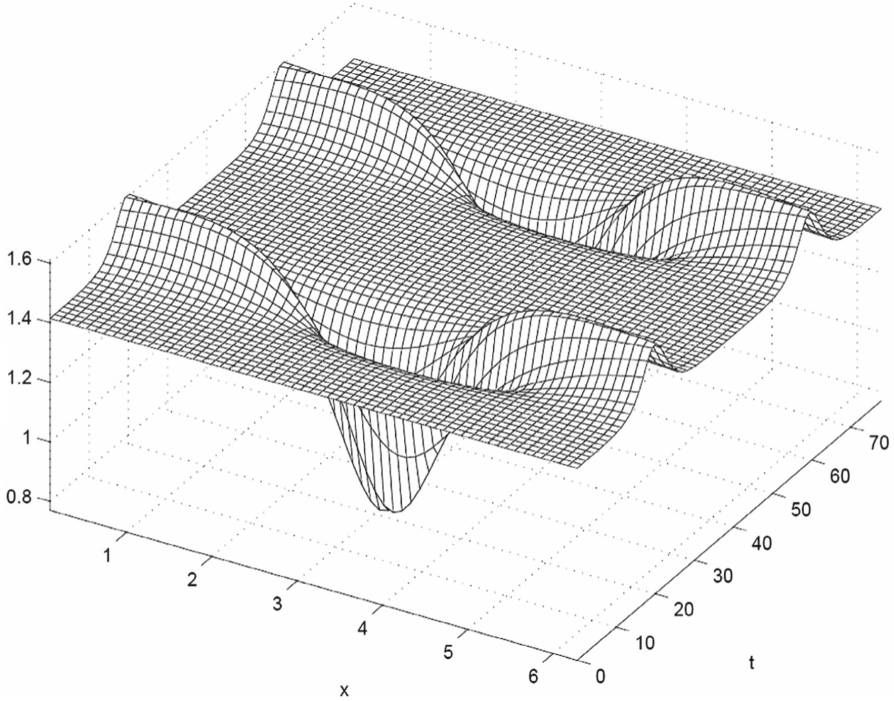


Fig. 1. The modulational instability of $|E|$

5 Result and Discussion

This scheme has been effectively executed to achieve new comprehensive region for the modulational stable/unstable wave numbers in the system of equation, also obtain Euler-Lagrange equation of motion and nonlinear dispersion relation (NDR). We analyze their strength for different amplitude (wave number and frequency) of perturbation of the wave solution. It is implied that some circumstances lead to a new ordinary differential equation, whose optimal condition is intimate to the instability/stability criterion, which is obtained.

Furthermore, the polynomial Eq. (6) only contains q^2 , which reflects the conjugate symmetry of the eigenmodes, so it is sufficient to consider only $q \geq 0$. Since the polynomial Eq. (6) neglects direct multiplication, this linear dispersion relation is analyzed in various asymptotic limits and the results are assembled to form a complete stability picture for the plane wave.

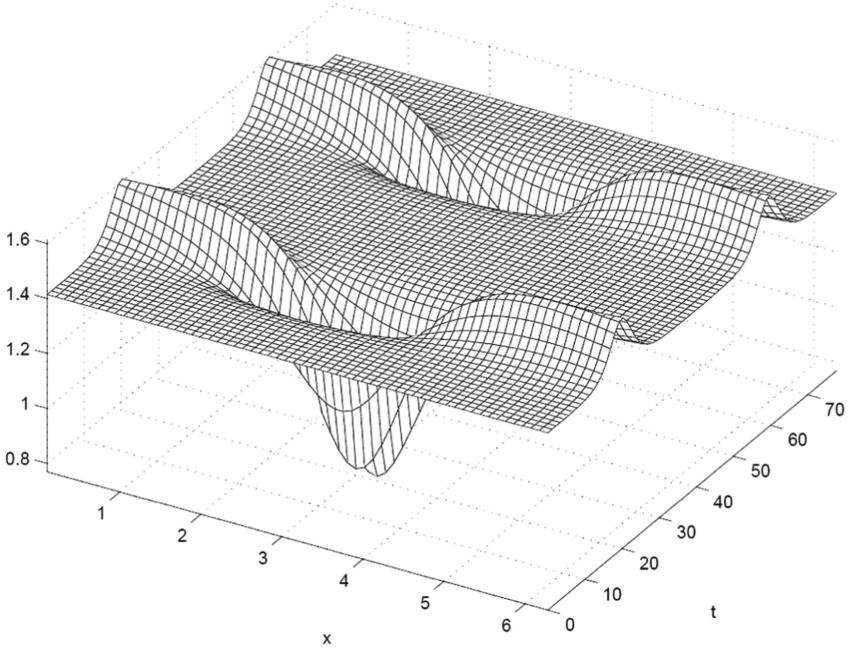


Fig. 2. The modulational instability of $|\eta|$

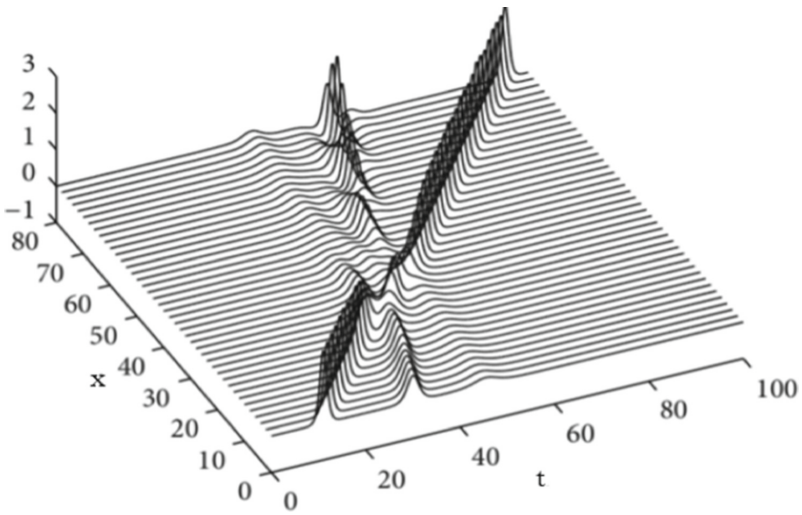


Fig. 3. Interaction of the two waves $|E|^2 + |\eta|^2$ with $\alpha = 2, q = k, E_0 = 2.5$

Figures: - 1 Modulational instabilities show in numerically. Figure-3 Interaction of the two waves same as [15].

References

1. Dhar, A.K., Das, K.P.: Fourth order nonlinear evolution equation for two Stokes wave trains in deep water physics of fluids A. *Fluid Dyn.* **3**, 3021 (1991)
2. Menyuk, C.R.: Stability of solitons in birefringent optical fibers. II. Arbitrary amplitudes. *J. Opt. Soc. Am. B Opt. Phys.* **5**, 392 (1988)
3. Hasegawa, A.: Springer Tracts in Modern Physics, Optical Solitons in Fibers. Springer, Heidelberg, vol. 116 (1989). <https://doi.org/10.1007/BFb0108677>
4. Yang, J.: Multi soliton perturbation theory for the Manakov equations and its applications to nonlinear optics. *Phys. Rev. E* **59**(2), 2393 (1999)
5. Ablowitz, M.J., Segur, H.: Solitons and the Inverse Scattering Transform, vol. 4. SIAM, Philadelphia (1981)
6. Millot, G., Seve, E., Wabnitz, S., Haelterman, M.: Observation of induced modulational polarization instabilities and pulse-train generation in the normal-dispersion regime of a birefringent optical fibers. *J. Opt. Soc. Am. B Opt. Phys.* **15**(4), 1266 (1998)
7. Agarwal, G.P.: Nonlinear Fiber Optics, 3rd edn. Academic Press, San Diego (2001)
8. Malomed, B.A.: Variational methods in nonlinear fibers optics and related fields. *Progr. Opt.* **43**, 69–75 (2002)
9. Kumar, A., Pankaj, R.D., Gaur, M.: Finite difference scheme of the model for non-linear wave-wave interaction in ionic media. *Comput. Math. Model.* **22**(3), 255–265 (2011)
10. Pankaj, R.D., Kumar, A., Singh, B.: Multi-symplectic integrator for complex nonlinear system. *J. Chem. Biolo. Phys. Sci. C* **7**(3), 631–637 (2018)
11. Pankaj, R.D., Kumar, A., Singh, B.: Evolution of modulational instability in non-linear Hirota types equation. *Sci. Technol. Asia* **25**(1), 123–127 (2019)
12. Kumar, A.: An analytical solution for a coupled partial differential equation. *Appl. Math. Comput.* **212**, 245–250 (2009)
13. Pankaj, R.D., Kumar, A., Sindhi, C.: Evolution of modulational instability in travelling wave solution of non-linear partial differential equation. *Int. J. Eng. Technol. Manage. Res.* **5**(1), 1–7 (2018)
14. Kumar, A., Pankaj, R.D.: Some solitary and periodic solutions of the nonlinear wave equation by variational approach. *J. Rajasthan Acad. Phys. Sci.* **11**(2), 133–139 (2012)
15. Pankaj, R.D., Kumar, A.: Multisymplectic structure of a finite difference scheme for a complex nonlinear system. *Int. J. Math. Trends Technol (IJMTT)* **52**(8), 552–557 (2018)
16. Pankaj, R.D.: Variational Method and Its Application. Lap Lambert academic publication, Germany (2022)
17. Goswami, A., Singh, J., Kumar, D., et al.: An efficient analytical approach for fractional equal width equations describing hydro-magnetic waves in cold plasma. *Phys. A* **524**, 563–575 (2019)
18. Goswami, A., Rathore, S., Singh, J., Kumar, D.: Analytical study of fractional nonlinear Schrödinger equation with harmonic oscillator. *Discrete Continuous Dyn. Syst. Ser. S* **14**(10), 3589–3610 (2021)
19. Newell, A.C.: Solitons in Mathematics and Physics. S.I.A.M, Philadelphia (1985)
20. Pankaj, R.D., Kumar, A., Lal, C.: A novel narration for two long waves interaction through the elaboration scheme. *J. Interdisc. Math.* **25**(1), 79–88 (2022). <https://doi.org/10.1080/09720502.2021.2010768>



Applications of General Summation Formulas Contiguous to q -Kummer Theorems

Yashoverdhan Vyas¹, Shivani Pathak¹, and Kalpana Fatawat²(✉)

¹ Department of Mathematics, School of Engineering, Sir Padampat Singhania University, Bhatewar, Udaipur 313601, Rajasthan, India

{yashoverdhan.vyas, shivani.bhatt}@spsu.ac.in

² Techno India NJR Institute of Technology, Plot SPL-T, Bhamashah (RIICO) Industrial Area, Kaladwas, Udaipur 313003, Rajasthan, India

kalpana.fatawat@technonjr.org

Abstract. This work is motivated essentially by the fact that the applications of basic (or q -) hypergeometric functions are frequently needed in the form of summations, transformations, expansions, reductions, and integral formulas. The objective of this research paper is to study the applications of the general summation formulas contiguous to q -Kummer theorems in deriving several presumably new q -integral evaluations involving the basic (or q -) hypergeometric functions of type ${}_3\Phi_3$ and ${}_3\Phi_2$. The results are further particularized to give specific integral evaluations in the form of summations to show the importance and utilizations of our main findings. We also derive the summation theorems for certain basic (or q -) Appell double hypergeometric functions, basic (or q -) Lauricella multiple hypergeometric functions, and certain basic (or q -) Laplace transforms by applying general summation formulas contiguous to q -Kummer theorems.

Keywords: Basic (or q -) hypergeometric functions · q -beta function · q -gamma function · q -Kummer summation theorems · General contiguous summation theorems · q -Appell functions · q -Lauricella functions · q -Laplace transforms · q -integrals

2010 AMS Subject Classification: 33D05 · 33D15 · 33D60 · 33C65

1 Introduction and Motivation

A natural generalization of Gauss's functions having arbitrary number of numerator (a_p) and denominator (b_q) parameters can be found in [28, p. 19, Eq. (23)].

The generalized basic (or q -) hypergeometric series [10, p. 4], see also [3, 9], with r numerator parameters a_1, \dots, a_r and s denominator parameters b_1, \dots, b_s ($\forall s, b_s$ is neither 0 nor a negative integer) is defined by

$${}_r\Phi_s(a_1, \dots, a_r; b_1, \dots, b_s; q, z) \equiv {}_r\Phi_s \left[\begin{matrix} a_1, \dots, a_r; \\ b_1, \dots, b_s; \end{matrix} q, z \right]$$

$$= \sum_{k=0}^{\infty} \frac{(a_1, \dots, a_r; q)_k z^k}{(q, b_1, \dots, b_s; q)_k} \left((-1)^k q^{\binom{k}{2}} \right)^{1+s-r}, \quad (1.1)$$

The series in Eq. (1.1) converges absolutely for

$$\begin{cases} \forall z & \text{if } 0 \leq |q| \leq 1, \quad r \leq s \\ |z| < 1 & \text{if } 0 \leq |q| \leq 1, \quad r = s + 1 \\ |z| < |b_1 \dots b_s| / |a_1 \dots a_r| & \text{if } |q| > 1 \end{cases} \quad (1.2)$$

These convergence conditions with suitable modifications are applicable to the results derived in Sects. 2 and 3.

For $0 < q < 1$, the q -gamma function [10] is defined as:

$$\Gamma_q(x) = \frac{(q; q)_{\infty}}{(q^x; q)_{\infty}} (1 - q)^{1-x}, \Re(x) > 0 \quad (1.3)$$

which was first introduced by Thomae and later by Jackson.

A key property of the beta function is close relationship to the gamma function: one has that

$$B_q(x, y) = \frac{\Gamma_q(x)\Gamma_q(y)}{\Gamma_q(x+y)}, 0 < q < 1, \Re(x) > 0, \Re(y) > 0. \quad (1.4)$$

For further such relations, we refer to [27, pp. 239–240, Appendix I].

Lavoie et al. [21–23] have obtained generalization of classical summation theorems for series ${}_2F_1$ and obtained a large number of contiguous results. Choi et al. [6] obtained general summation formulas contiguous to the Kummer's theorem by applying Euler's integral representation formula for ${}_2F_1$. Recently, several new results involving product of generalized special functions are investigated by [5, 19, 29].

The three q -Kummer contiguous summation theorems were given by Kummer in 1836, and we refer to these three theorems as Kummer's first summation theorem, Kummer's second summation theorem and Kummer's third summation theorem. Andrews [2] was the first to give the q -analogue of Kummer's second summation theorem and q -analogue of Kummer's third summation theorem. In the context of the three q -Kummer's theorems, Kim et al. [16], Harsh et al. [12, 13] derived some particular contiguous extensions. Recently, Vyas et al. [31] derived remarkably worthwhile, general summation theorem contiguous to the three q -Kummer summation theorems by using three different techniques. The present paper provides a set of applications of the results due to Vyas et al. [31].

Although, the integrals involving and representing hypergeometric functions have several applications in pure and applied mathematics, not all such integrals have been collected in tables or are readily available in the mathematical literature. The integral formulas for various special functions and polynomials can be found in [4] and references therein. The use of various summation formulas in deriving the integral formulas can be found in [4, 20, 25, 34] and references therein. Specifically, Joshi and Vyas [14] derived

extensions of certain classical integrals of Erdélyi for Gauss hypergeometric functions by applying well-known summation formulas. Recently, Vyas et al. [32] derived the discrete extensions of the Erdélyi-type integrals in the form of new hypergeometric expansions with the help of classical summation formulas and an extended Saalschütz summation theorem [18].

This research paper aims to utilize the general summation theorems contiguous to the q -Kummer summation theorems investigated by Vyas et al. [31] in deriving the integral formulas involving the q -hypergeometric functions of type ${}_3\Phi_3$ and ${}_3\Phi_2$, see Sect. 2. In Sect. 3, we obtain some specific integral formulas by specializing the main results obtained in Sect. 2. In Sect. 4, we provide presumably new summations for q -Lauricella functions with the help of general summation theorem contiguous to the q -Kummer summation theorems.

It is well-known that the Laplace transform has wide applications in the fields of science and engineering. Specifically, Laplace transform is applied to analyze the electric circuit. Laplace transform of various hypergeometric functions as well as q -polynomials can be found in [1, 10, 17, 24, 30, 33].

Hahn [11] (see also [1]) derived the q -analogue of well-known classical Laplace transform with the help of q -integral equations [25, p. 1, Eq. (2) and (3)]. Yadav and Purohit [25] derived a general q -Laplace transform and used it to identify several well-known q -polynomials. Kim et al. [17] derived a general Laplace transform of ${}_1F_1$ into ${}_2F_1$; where ${}_1F_1$ is Kummer's confluent hypergeometric function and ${}_2F_1$ is the Gauss hypergeometric function and then applying generalized Kummer's summation, Gauss's second and Bailey summation (see [21–23]) three new Laplace transforms for general ${}_1F_1$ Kummer confluent hypergeometric functions was investigated. Motivating from the work done by the Yadav and Purohit [25, p. 238, Eq. (31)] work, in Sect. 5, we establish the q -Laplace transforms involving q -hypergeometric functions, by applying the results due to Vyas et al. [31].

It is worthwhile to mention here that the kind of q -integral formulas investigated here, in this paper, involving q -hypergeometric series are comparatively very less in the literature than the integrals involving ordinary hypergeometric series.

2 Main Results

Here we present several integral formulas involving a generalized basic (or q -) hypergeometric functions ${}_3\Phi_3$ and ${}_3\Phi_2$ which are asserted in Theorems 2.1 to 2.6. The convergence conditions can easily be derived using Eq. (1.2).

Theorem 2.1. For $k \in \mathbb{N}_0$, the following assertion holds true:

$$\int_0^1 t^{d-1} \frac{(tq; q)_\infty}{(tq^{c-d}; q)_\infty} {}_3\Phi_2 \left[\begin{matrix} a, b, c; \\ d, \frac{aq^{1+k}}{b}; \end{matrix} \quad q, -\frac{qt}{b} \right] d_q t$$

$$= \frac{\Gamma_q(d)\Gamma_q(c-d)}{\Gamma_q(c)} \frac{\left(a, \frac{q^{1+k}}{b}, -q; q\right)_\infty}{\left(\frac{q^2}{b^2}; q\right)_\infty \left(\frac{aq^{1+k}}{b}; q^2\right)_\infty}$$

$$\cdot \sum_{j=0}^k \frac{(q^{-k}; q)_j}{(q; q)_j} \left(\frac{q^{1+k}}{b}\right)^j \frac{\left(\frac{aq^{j+2}}{b^2}; q^2\right)_\infty}{(aq^j; q^2)_\infty},$$
(1.5)

provided $|\frac{q}{b}| < 1, 0 < q < 1, \Re(d) > 0, \Re(c-d) > 0$.

Proof: In order to establish the integral (1.5), we proceed as follows:

Let us denote the left-hand side of Theorem 2.1 by I_1 .

$$I_1 = \int_0^1 t^{d-1} \frac{(tq; q)_\infty}{(tq^{c-d}; q)_\infty} {}_3\Phi_2 \left[\begin{matrix} a, b, c; \\ d, \frac{aq^{1+k}}{b}; \end{matrix} \quad q, -\frac{qt}{b} \right] d_q t.$$
(1.6)

In the above Eq. (1.6), replacing the generalized q -hypergeometric function ${}_3\Phi_2$ by its series form, we get

$$I_1 = \sum_{r \geq 0} \int_0^1 t^{d+r-1} \frac{(tq; q)_\infty}{(tq^{c-d}; q)_\infty} \frac{(a, b, c; q)_r \left(-\frac{q}{b}\right)^r}{\left(d, \frac{aq^{1+k}}{b}, q; q\right)_r r!} d_q t.$$
(1.7)

On evaluating the involved q -beta integral from [10, p. 19, Eq. (1.11.7)] and applying the key property of the q -beta function [8, p.18, Eq. (1.10.13)], the Eq. (1.7) becomes:

$$I_1 = \sum_{r \geq 0} \frac{\Gamma_q(d+r)\Gamma_q(c-d)}{\Gamma_q(c+r)} \frac{(a, b, c; q)_r \left(-\frac{q}{b}\right)^r}{\left(d, \frac{aq^{1+k}}{b}, q; q\right)_r r!}$$
(1.8)

After applying the definition of q -gamma function [10, p. 20, Eq. (1.10.1)] in Eq. (1.8), we can write,

$$I_1 = \sum_{r \geq 0} \frac{\Gamma_q(d)\Gamma_q(c-d)}{\Gamma_q(c)} \frac{(a, b, c, d; q)_r \left(-\frac{q}{b}\right)^r}{\left(c, d, \frac{aq^{1+k}}{b}, q; q\right)_r r!}$$
(1.9)

Now, on simplifying Eq. (1.9), we obtain

$$I_1 = \frac{\Gamma_q(d)\Gamma_q(c-d)}{\Gamma_q(c)} {}_2\Phi_2 \left[\begin{matrix} a, b; \\ \frac{aq^{1+k}}{b}; \end{matrix} \quad q, -\frac{q}{b} \right].$$
(1.10)

Finally, on evaluating ${}_2\Phi_1$ series by the general contiguous q -Kummer first summation theorem [31, p. 6, Eq. (16)], followed by some simplifications, would lead to the right hand side of Theorem 2.1. This completes the proof of Theorem 2.1.

Theorem 2.2. For $k \in \mathbb{N}_0$, the following assertion holds true:

$$\int_0^1 t^{d-1} \frac{(tq; q)_\infty}{(tq^{c-d}; q)_\infty} {}_3\Phi_2 \left[\begin{matrix} a, b, c; \\ d, \frac{aq^{1-k}}{b}; \end{matrix} \middle| q, -\frac{qt}{b} \right] dqt = \frac{\Gamma_q(d)\Gamma_q(c-d)}{\Gamma_q(c)} \cdot \frac{(a, -q; q)_\infty}{\left(\frac{aq^{1-k}}{b}, -\frac{q^{1-k}}{b}; q\right)_\infty} \sum_{j=0}^k \frac{(q^{-k}; q)_j}{(q; q)_j} \left(-\frac{q}{b}\right)^j \frac{\left(\frac{aq^{j+2(1-k)}}{b^2}; q^2\right)_\infty}{(aq^j; q^2)_\infty}, \tag{1.11}$$

provided that $\left|\frac{q}{b}\right| < 1, 0 < q < 1, \Re(d) > 0, \Re(c-d) > 0$.

Theorem 2.3. For $k \in \mathbb{N}_0$, the following assertion holds true:

$$\int_0^1 t^{d-1} \frac{(tq; q)_\infty}{(tq^{c-d}; q)_\infty} {}_3\Phi_2 \left[\begin{matrix} a, bq^{-k}, c; \\ d, \frac{aq}{b}; \end{matrix} \middle| q, -\frac{qt}{b} \right] dqt = \frac{\Gamma_q(d)\Gamma_q(c-d)}{\Gamma_q(c)} \cdot \frac{(a, -q; q)_\infty}{\left(\frac{aq}{b}, -\frac{q}{b}; q\right)_\infty} \sum_{j=0}^k \frac{(q^{-k}; q)_j}{(q; q)_j} (-q)^j \frac{\left(\frac{aq^{j+2}}{b^2}; q^2\right)_\infty}{(aq^j; q^2)_\infty}, \tag{1.12}$$

provided that $\left|\frac{q}{b}\right| < 1, 0 < q < 1, \Re(d) > 0, \Re(c-d) > 0$.

Proofs of Theorem 2.2 and 2.3: The proofs of the above two integrals Theorem 2.2 and Theorem 2.3 follow the similar steps as we discussed in the proof of Theorem 2.1, by utilizing general contiguous q -Kummer first summation theorem [31, p. 6, Eq. (16)].

Theorem 2.4. For $k \in \mathbb{N}_0$, the following assertion holds true:

$$\int_0^1 t^{d-1} \frac{(tq; q)_\infty}{(tq^{c-d}; q)_\infty} {}_3\Phi_3 \left[\begin{matrix} a, b, c; \\ d, \sqrt{abq^{1-k}}, -\sqrt{abq^{1-k}}; \end{matrix} \middle| q, -\frac{qt}{k} \right] dqt = \frac{\Gamma_q(d)\Gamma_q(c-d)}{\Gamma_q(c)} \frac{(a, -q; q)_\infty}{(abq^{1-k}; q^2)_\infty} \sum_{j=0}^k \frac{(q^{-k}; q)_j (-q)^j (bq^{1+j-k}; q^2)_\infty}{(q; q)_j (aq^j; q^2)_\infty}. \tag{1.13}$$

provided that $\Re(d) > 0, \Re(c-d) > 0$.

Theorem 2.5. For $k \in \mathbb{N}_0$, the following assertion holds true:

$$\int_0^1 t^{d-1} \frac{(tq; q)_\infty}{(tq^{c-d}; q)_\infty} {}_3\Phi_3 \left[\begin{matrix} a, \frac{q^{1+k}}{a}, c; \\ b, -q, d; \end{matrix} \middle| q, -tbq^{-k} \right] dqt = \frac{\Gamma_q(d)\Gamma_q(c-d)}{\Gamma_q(c)} \cdot \frac{\left(\frac{q^{1+k}}{a}; q\right)_\infty \left(\frac{ab}{q^{1+k}}; q\right)_\infty}{\left(\frac{q}{a}; q\right)_\infty} \sum_{j=0}^k \frac{(q^{-k}; q)_j \left(\frac{q^{1+k}}{a}\right)^j \left(\frac{bq^{1-k+j}}{a}; q^2\right)_\infty}{(q; q)_j (abq^{j-k-1}; q^2)_\infty}. \tag{1.14}$$

provided that $\Re(d) > 0, \Re(c-d) > 0$.

Theorem 2.6. For $k \in \mathbb{N}_0$, the following assertion holds true:

$$\int_0^1 t^{d-1} \frac{(tq;q)_\infty}{(tq^{c-d};q)_\infty} {}_3\Phi_3 \left[\begin{matrix} a, \frac{q^{1-k}}{a}, c; \\ b, -q, d; \end{matrix} \middle| q, -tbq^k \right] dqt = \frac{\Gamma_q(d)\Gamma_q(c-d)}{\Gamma_q(c)} \frac{\left(-\frac{q}{a};q\right)_\infty \left(\frac{ab}{q^{1-k}};q\right)_\infty}{\left(-\frac{q^{1-k}}{a};q\right)_\infty (b;q)_\infty} \sum_{j=0}^k \frac{(q^{-k};q)_j \left(-\frac{q}{a}\right)^j \left(\frac{bq^{1-k+j}}{a};q^2\right)_\infty}{(q;q)_j (abq^{j+k-1};q^2)_\infty}. \tag{1.15}$$

provided that $\Re(d) > 0, \Re(c - d) > 0$.

Proofs of Theorem 2.4, Theorem 2.5 and Theorem 2.6: Following the method explained in proof of Theorem 2.1 and utilizing the general contiguous q -Kummer second summation theorem [31, p. 10, Eq. (30)] and q -Kummer third summation theorem [31, pp. 10–11, Eq. (32) and (34)] respectively, we get the desired integrals (1.13), (1.14) and (1.15).

3 Applications

Several additional q -integrals as applications of main results (Theorems 2.1 to 2.6) are presented in this Section.

3.1. In addition, for $k = 1, 2, 3, 4 \dots$, Theorem 2.1 gives a number of additional q -integrals. For instance, taking $k = 1$ in Theorem 2.1, yields

$$\int_0^1 t^{d-1} \frac{(tq;q)_\infty}{(tq^{c-d};q)_\infty} {}_3\Phi_2 \left[\begin{matrix} a, b, c; \\ d, \frac{aq^2}{b}; \end{matrix} \middle| q, -\frac{qt}{b} \right] dqt = \frac{\Gamma_q(d)\Gamma_q(c-d)}{\Gamma_q(c)} \frac{\left(a, -q, \frac{q^2}{b};q\right)_\infty}{\left(\frac{aq^2}{b};q\right)_\infty \left(\frac{q^2}{b^2};q^2\right)_\infty} \sum_{j=0}^1 \frac{(q^{-1};q)_j \left(\frac{q^2}{b}\right)^j \left(\frac{aq^{2+j}}{b^2};q^2\right)_\infty}{(q;q)_j (aq^j;q^2)_\infty} \tag{1.16}$$

On applying the identity (1.3), followed by further simplification, leads to the following presumably new result:

$$\int_0^1 t^{d-1} \frac{(tq;q)_\infty}{(tq^{c-d};q)_\infty} {}_3\Phi_2 \left[\begin{matrix} a, b, c; \\ d, \frac{aq^2}{b}; \end{matrix} \middle| q, -\frac{qt}{b} \right] dqt = \frac{\Gamma_q(d)\Gamma_q(c-d)}{\Gamma_q(c)} \frac{(-q;q)_\infty}{(1-\frac{q}{b})\left(\frac{aq^2}{b};q\right)\left(-\frac{q}{b};q\right)_\infty} \left[(aq; q^2)_\infty \left(\frac{aq^2}{b^2}; q^2\right)_\infty - \left(\frac{q}{b}\right)(a; q^2)_\infty \left(\frac{aq^3}{b^2}; q^2\right)_\infty \right]. \tag{1.17}$$

3.2. In addition, for $k = 1, 2, 3, 4 \dots$, Theorem 2.2 gives a number of additional q -integrals. For instance, taking $k = 1$ in Theorem 2.2, yields

$$\int_0^1 t^{d-1} \frac{(tq;q)_\infty}{(tq^{c-d};q)_\infty} {}_3\Phi_2 \left[\begin{matrix} a, b, c; \\ d, \frac{a}{b}; \end{matrix} \middle| q, -\frac{tq}{b} \right] dqt = \frac{\Gamma_q(d)\Gamma_q(c-d)}{\Gamma_q(c)} \frac{(-q;q)_\infty}{\left(\frac{a}{b}, -\frac{1}{b};q\right)_\infty} \cdot \left[(aq; q^2)_\infty \left(\frac{a}{b^2}; q^2\right)_\infty + \frac{1}{b}(a; q^2)_\infty \left(\frac{aq}{b^2}; q^2\right)_\infty \right]. \tag{1.18}$$

3.3. In addition, for $k = 1, 2, 3, 4 \dots$, Theorem 2.3 gives a number of additional q -integrals. For instance, taking $k = 1$ in Theorem 2.3, yields

$$\int_0^1 t^{d-1} \frac{(tq; q)_\infty}{(tq^{c-d}; q)_\infty} {}_3\Phi_2 \left[\begin{matrix} a, b, c; \\ d, \frac{aq}{b}; \end{matrix} q, -\frac{tq}{b} \right] dqt = \frac{\Gamma_q(d)\Gamma_q(c-d)}{\Gamma_q(c)} \cdot \frac{(-q; q)_\infty}{\left(\frac{aq}{b}, -\frac{q}{b}; q\right)_\infty} \left[(aq; q^2)_\infty \left(\frac{aq^2}{b^2}; q^2\right)_\infty + (a; q^2)_\infty \left(\frac{aq^3}{b^2}; q^2\right)_\infty \right]. \tag{1.19}$$

3.4. In addition, for $k = 1, 2, 3, 4 \dots$, Theorem 2.4 gives a number of additional q -integrals. For instance, taking $k = 1$ in Theorem 2.4, yields

$$\int_0^1 t^{d-1} \frac{(tq; q)_\infty}{(tq^{c-d}; q)_\infty} {}_3\Phi_3 \left[\begin{matrix} a, b, c; \\ d, \sqrt{ab}, -\sqrt{ab}; \end{matrix} q, -t \right] dqt = \frac{\Gamma_q(d)\Gamma_q(c-d)}{\Gamma_q(c)} \cdot \frac{(-q; q)_\infty}{(ab; q^2)_\infty} \left[(aq; q^2)_\infty (b; q^2)_\infty + (a; q^2)_\infty (bq; q^2)_\infty \right]. \tag{1.20}$$

3.5. In addition, for $k = 1, 2, 3, 4 \dots$, Theorem 2.5 gives a number of additional q -integrals. For instance, taking $k = 1$ in Theorem 2.5, yields

$$\int_0^1 t^{d-1} \frac{(tq; q)_\infty}{(tq^{c-d}; q)_\infty} {}_3\Phi_3 \left[\begin{matrix} a, \frac{q^2}{a}, c; \\ b, d, -q; \end{matrix} -tbq^{-1} \right] dqt = \frac{\Gamma_q(d)\Gamma_q(c-d)}{\Gamma_q(c)} \cdot \frac{1}{(1-\frac{q}{a})(b; q)_\infty} \left[\left(\frac{ab}{q}; q^2\right)_\infty \left(\frac{b}{a}; q^2\right)_\infty - \frac{q}{a} \left(\frac{bq}{a}; q^2\right)_\infty \left(\frac{ab}{q^2}; q^2\right)_\infty \right]. \tag{1.21}$$

3.6 In addition, for $k = 1, 2, 3, 4 \dots$, Theorem 2.6 gives a number of additional q -integrals. For instance, taking $k = 1$ in Theorem 2.6, yields

$$\int_0^1 t^{d-1} \frac{(tq; q)_\infty}{(tq^{c-d}; q)_\infty} {}_3\Phi_3 \left[\begin{matrix} a, \frac{1}{a}, c; \\ b, d, -q; \end{matrix} q, -tbq \right] dqt = \frac{\Gamma_q(d)\Gamma_q(c-d)}{\Gamma_q(c)} \cdot \frac{a}{(1+a)(b; q)_\infty} \left[(abq; q^2)_\infty \left(\frac{b}{a}; q^2\right)_\infty + \frac{1}{a} (ab; q^2)_\infty \left(\frac{bq}{a}; q^2\right)_\infty \right]. \tag{1.22}$$

4 Summations of q -Lauricella Functions

Several summation formulas for q -Lauricella functions are presented here by using q -Kummer contiguous summation theorems investigated by Vyas et al. [31].

Theorem 4.1. For $k \in \mathbb{N}_0$, the following assertion holds true:

$$\begin{aligned} & \Phi_{1:0; \dots; 0}^{1:1; \dots; 1} \left[\begin{matrix} a : v_1; v_2; \dots; v_n; \\ \frac{aq^{1+k}}{b} : -; \dots; -; \end{matrix} q, -\frac{q}{v_1}, -\frac{q}{v_1 v_2}, \dots, -\frac{q}{v_1 v_n} \right] \\ &= \frac{(a; q)_\infty \left(-q, \frac{q^{1+k}}{v_1 v_2 \dots v_n}; q\right)_\infty}{\left(\frac{aq^{1+k}}{v_1 v_2 \dots v_n}; q\right)_\infty \left(\frac{q^2}{v_1^2 v_2^2 \dots v_n^2}; q^2\right)_\infty} \\ & \cdot \sum_{j=0}^k \frac{(q^{-k}; q)_j}{(q; q)_j} \left(\frac{q^{1+k}}{v_1 v_2 \dots v_n}\right)^j \frac{\left(\frac{aq^{2+j}}{v_1^2 v_2^2 \dots v_n^2}; q^2\right)_\infty}{(aq^j; q^2)_\infty}. \end{aligned} \tag{1.23}$$

Proof: The q -analogue of a generalized q -Kampé de Fériet reduction formula [28, p. 39, Eq. (32)] is given by:

$$\begin{aligned} \Phi_{q:0;\dots;0}^{p:1;\dots;1} \left[\begin{matrix} (a_p) : v_1; v_2; \dots; v_n; q, x, \frac{x}{v_2}, \dots, \frac{x}{v_n} \\ (b_q) : -; \dots; - \end{matrix} \right] \\ = {}_{p+1}\Phi_q \left[\begin{matrix} (a_p), v_1 v_2 \dots v_n; q, \frac{x}{v_2 v_3 \dots v_n} \\ (b_q) \end{matrix} \right]. \end{aligned} \quad (1.24)$$

Taking $x = -\frac{q}{v_1}$, $p = 1$, $q = 1$, $a_1 = a$, $b_1 = \frac{aq^{1+k}}{b}$ and $v_1 v_2 \dots v_n = b$ in Eq. (1.24), and then by applying q -Kummer first summation theorem [31, p. 6, Eq. (16)], we get required result for Theorem 4.1.

Further, for $n = 2$, the Eq. (1.23) yields the following summation for q -Appell hypergeometric function $\Phi^{(1)}$:

$$\begin{aligned} \Phi^{(1)} \left[a : v_1, v_2; \frac{aq^{1+k}}{b}; -\frac{q}{v_1}, -\frac{q}{v_1 v_2} \right] \\ = \frac{(a; q)_\infty \left(-q, \frac{q^{1+k}}{v_1 v_2}; q \right)_\infty}{\left(\frac{aq^{1+k}}{v_1 v_2}; q \right)_\infty \left(\frac{q^2}{v_1^2 v_2^2}; q^2 \right)_\infty} \\ \cdot \sum_{j=0}^k \frac{(q^{-k}; q)_j}{(q; q)_j} \left(\frac{q^{1+k}}{v_1 v_2} \right)^j \frac{\left(\frac{aq^{2+j}}{v_1^2 v_2^2}; q^2 \right)_\infty}{(aq^j; q^2)_\infty}. \end{aligned} \quad (1.25)$$

In the similar manner, we can compute more summation theorems for q -Lauricella multiple hypergeometric functions by utilizing the general contiguous q -Kummer first summation theorem [31, p. 9, Eq. (28) and Eq. (29)], q -Kummer second summation theorem [31, p. 9, Eq. (30)] and q -Kummer third summation theorem [31, pp. 10–11, Eq. (32) and (34)] and corresponding summations for q -Appell hypergeometric functions.

5 q -Laplace Transform

In this Section, we shall show that how, a general q -Laplace transform of basic (or q -) generalized hypergeometric function given by Yadav and Purohit, see [25, p. 238, Eq. (31)] and the results due to Vyas et al. [31], can be utilized to derive many presumably new q -Laplace transforms evaluations.

This general q -Laplace transform in Gasper's notation can be written as follows:

$${}_q L_s \left\{ t_r^{b-1} \Phi_s \left[\begin{matrix} a_1, \dots, a_r; \\ b_1, \dots, b_s; \end{matrix} q; wt \right] \right\} = \frac{(q; q)_\infty}{s^b (b; q)_\infty} {}_r \Phi_s \left[\begin{matrix} a_1, \dots, a_r, b; \\ b_1, \dots, b_s; \end{matrix} q; \frac{w}{s} \right]. \quad (1.26)$$

Taking $r = 2$ and $s = 1$ in the above Eq. (1.25) we obtain the following results:

$${}_q L_s \left\{ t_2^{b-1} \Phi_1 \left[\begin{matrix} a, 0; \\ c; \end{matrix} q; wt \right] \right\} = \frac{(q; q)_\infty}{s^b (b; q)_\infty} {}_2 \Phi_1 \left[\begin{matrix} a, b; \\ c; \end{matrix} q; \frac{w}{s} \right]. \quad (1.27)$$

Taking $r = 2$ and $s = 2$ in the above Eq. (1.25) we obtain the following results:

$${}_qL_s \left\{ t_2^{b-1} \Phi_2 \left[\begin{matrix} a, 0; \\ c, d; \end{matrix} q; wt \right] \right\} = \frac{(q; q)_\infty}{s^b(b; q)_\infty} {}_2\Phi_2 \left[\begin{matrix} a, b; \\ c, d; \end{matrix} q; \frac{w}{s} \right]. \tag{1.28}$$

Theorem 5.1. For $k \in \mathbb{N}_0$, the following assertion holds true:

$${}_qL_s \left\{ t_2^{b-1} \Phi_1 \left[\begin{matrix} a, 0; \\ aq^{1+k}, q; \end{matrix} -\frac{qts}{b} \right] \right\} = \frac{(q; q)_\infty \left(a, \frac{q^{1+k}}{b}, -q; q \right)_\infty}{s^b(b; q)_\infty \left(\frac{aq^{1+k}}{b}; q \right)_\infty \left(\frac{q^2}{b^2}; q^2 \right)_\infty} \cdot \sum_{j=0}^k \frac{(q^{-k}; q)_j}{(q; q)_j} \left(\frac{q^{1+k}}{b} \right)^j \frac{\left(\frac{aq^{j+2}}{b^2}; q^2 \right)_\infty}{(aq^j; q^2)_\infty}. \tag{1.29}$$

Proof: By taking $c = \frac{aq^{1+k}}{b}$ and $\frac{w}{s} = -\frac{q}{b}$ in Eq. (1.27) and applying general q -Kummer first summation theorem [31, p. 6, Eq. (16)], we get Theorem 5.1.

Furthermore, we can derive two more series of contiguous q -Laplace transforms by using Eq. (1.27) and by applying general contiguous q -Kummer first summation theorem [31, p. 9, Eq. (28) and Eq. (29)].

Theorem 5.2. For $k \in \mathbb{N}_0$, the following assertion holds true:

$${}_qL_s \left\{ t_2^{b-1} \Phi_2 \left[\begin{matrix} a, 0; \\ \sqrt{abq^{1-k}}, -\sqrt{abq^{1-k}}; \end{matrix} q; -q^{1-k}s \right] \right\} = \frac{(a, -q; q)_\infty (q; q)_\infty}{s^b(b; q)_\infty (abq^{1-k}; q^2)_\infty} \sum_{j=0}^k \frac{(q^{-k}; q)_j}{(q; q)_j} (-q)^j \frac{(bq^{1+j-k}; q^2)_\infty}{(aq^j; q^2)_\infty} \tag{1.30}$$

Proof: By taking $c = \sqrt{abq^{1-k}}$, $d = -\sqrt{abq^{1-k}}$ and $\frac{w}{s} = -q^{1-k}$ in Eq. (1.28) and applying general q -Kummer second summation theorem [31, p. 9, Eq. (30)], we get Theorem 5.2.

Theorem 5.3. For $k \in \mathbb{N}_0$, the following assertion holds true:

$${}_qL_s \left\{ t_2^{b-1} \Phi_2 \left[\begin{matrix} a, 0; \\ b, -q; \end{matrix} q, -q^{b-k}s \right] \right\} = \frac{(q; q)_\infty \left(\frac{ab}{q^{1+k}}, \frac{q^{1+k}}{a}; q \right)_\infty}{s^b(b; q)_\infty \left(\frac{q}{a}; q \right)_\infty} \sum_{j=0}^k \frac{(q^{-k}; q)_j}{(q; q)_j} \left(\frac{q^{1+k}}{a} \right)^j \frac{\left(\frac{bq^{1+j-k}}{a}; q^2 \right)_\infty}{(abq^{j-1-k}; q^2)_\infty} \tag{1.31}$$

Proof: By taking $c = b$, $d = -q$ and $\frac{w}{s} = -q^{b-k}$ in Eq. (1.28) and applying general q -Kummer third summation theorem [31, p. 10, Eq. (32)], we get Theorem 5.3.

Similarly, we can derive one more q -Laplace transform by using the Eq. (1.28) and applying the general contiguous q -Kummer third summation theorem [31, pp. 10–11, Eq. (34)].

It may be noted that, the kind of general q -Laplace transforms given in Eq. (1.29), Eq. (1.30), Eq. (1.31) and other pointed out similar results, provide the corresponding series of contiguous q -Laplace transform evaluations for $k = 0, 1, 2, \dots$.

6 Conclusion

The literature has a prodigious large number of integral formulae involving a range of special functions. Many researchers have used different summation formulas to derive various integral formulas, for example [15]. In conclusion, this research paper illustrates the application part of the newly investigated general summation formula contiguous to q -Kummer theorems in deriving presumably new integral formulas (Theorems 2.1 to 2.6). We also deduce summation formulas for generalized q -Lauricella functions and q -Laplace transforms. We remark in passing that the results obtained in this paper are useful in the study of various special functions.

References

1. Abdi, W.H.: Application of q -Laplace transform to the solution of certain q -integral equations. *Rend. Circ. Mat. Palermo* **11**(3), 245–257 (1962)
2. Andrews, G.E.: On the q -analogue of Kummer's theorem and applications. *Duke Math. J.* **40**(3), 525–528 (1973)
3. Andrews, G.E., Askey, R., Roy, R.: *Special Functions*. Cambridge University Press, Cambridge (1999)
4. Bhatner, S., Jangid, K., Meena, S., Purohit, S.D.: Certain integral formulae involving incomplete I-functions. *Sci. Tech. Asia*. **26**(4), 84–95 (2021)
5. Bhatner, S., Mathur, A., Kumar, D., Singh, J.: On certain new results of fractional calculus involving product of generalized special functions. *Int. J. Appl. Comput. Math.* **8**(3), 1–9 (2022)
6. Choi, J., Rathie, A.K., Malani, S.: Kummer's theorem and its contiguous identities. *Taiwanese J. Math.* **11**(5), 1521–1527 (2007)
7. Exton, H.: *Multiple Hypergeometric Functions and Applications*. Ellis Horwood Ltd. (1976)
8. Exton, H.: *q -Hypergeometric Functions and Applications*. Ellis Horwood Series: Mathematics and Its Applications. Ellis Horwood (1983)
9. Gasper, G., Rahman, M.: *Basic Hypergeometric Series*. Encyclopedia of Mathematics and its Applications, 2nd edn. Cambridge University Press (2004)
10. Hahn, W.: *Math. Nachr.* Uber orthogonalpolynome, die q -differenzgleichungen. **2**, 4–34 (1949)
11. Harsh, H.V., Kim, Y.S., Rakha, M.A., Rathie, A.K.: A study of q -contiguous function relations. *Comm. Kor. Math. Soc.* **31**(1), 65–94 (2016)
12. Harsh, H.V., Kim, Y.S., Rathie, A.K., Purohit, S.D.: On basic analogue of classical summation theorems due to Andrews. *Honam Math. J.* **38**(1), 25–37 (2016)
13. Joshi, C.M., Vyas, Y.: Extensions of certain classical integrals of Erdélyi for Gauss hypergeometric functions. *J. Comput. Appl. Math.* **160**(1), 125–138 (2003)

14. Joshi, C.M., Vyas, Y.: q -Extensions of certain Erdélyi type integrals. *J. Math. Anal. Appl.* **320**(2), 642–648 (2006)
15. Kim, Y.S., Rathie, A.K., Lee, C.H.: On q -analogue of Kummer's theorem and its contiguous results. *Commun. Korean Math. Soc.* **18**(1), 151–157 (2003)
16. Kim, Y.S., Rathie, A.K., Cvijović, D.: New laplace transforms of Kummer's confluent hypergeometric functions. *Math. Comput. Model.* **55**(3–4), 1068–1071 (2012)
17. Kim, Y.S., Rathie, A.K., Paris, R.B.: An extension of Saalschütz's summation theorem for the series. *Integr. Transf. Spec. Funct.* **24**(11), 916–921 (2013)
18. Kumar Bansal, M., Kumar, D., Singh, J., Sooppy Nisar, K.: On the solutions of a class of integral equations pertaining to incomplete H-function and incomplete H-function. *Math.* **8**(5), 819 (2020)
19. Karthikeyan, K.R., Murugusundaramoorthy, G., Purohit, S.D., Suthar, D.L.: Certain class of analytic functions with respect to symmetric points defined by Q -calculus. *J. Math.* **2021** (2021)
20. Lavoie, J.L., Grondin, F., Rathie, A.K.: Generalizations of Watson's theorem on the sum of a . *Indian J. Math.* **34**(2), 23–32 (1992)
21. Lavoie, J.L., Grondin, F., Rathie, A.K., Arora, K.: Generalizations of Dixon's theorem on the sum of A . *Math. Comp.* 267–76 (1994)
22. Lavoie, J.L., Grondin, F., Rathie, A.K.: Generalizations of Whipple's theorem on the sum of a . *J. Comp. Appl. Math.* **72**(2), 293–300 (1996)
23. López-Bonilla, J., Rathie, A.K., Vázquez-Álvarez, D.: On an integral involving the hypergeometric function . *Prespacetime J.* **6**(11) (2015)
24. Purohit, S.D., Gour, M.M., Joshi, S., Suthar, D.L.: Certain classes of analytic functions bound with kober operators in q -calculus. *J. Math.* **2021** (2021)
25. Slater, L.J.: *Generalized Hypergeometric Functions*. Cambridge University Press (1966)
26. Srivastava, H.M., Karlson, P.W.: *Multiple Gaussian Hypergeometric Series*. Ellis Horwood Ltd. (1985)
27. Singh, Y., Gill, V., Singh, J., Kumar, D., Khan I.: Computable generalization of fractional kinetic equation with special functions. *J. King Saud Univ. Sci.* **33**(1) (2021)
28. Vyas, V., Al-Jarrah, A., Purohit, S.D., Araci, S., Nisar, K.: q -Laplace transform for product of general class of q -polynomials and q -analogue of I-function. *J. Inequal. Spec. Funct.* **11**(3), 21–28 (2020)
29. Vyas, Y., Srivastava, H.M., Pathak, S., Fatawat, K.: General summation formulas contiguous to the q -Kummer summation theorems and their applications. *Symmetry* **13**(6), 1102 (2021)
30. Vyas, Y., Bhatnagar, A.V., Fatawat, K.: Discrete analogues of the Erdélyi type integrals for hypergeometric functions. *J. Math.* **2022**, 1 (2022)
31. Yadav, R.K., Purohit, S.D.: On q -Laplace transforms of certain q -hypergeometric polynomials. *Proc.-Natl. Acad. Sci. India Sect. A* **76**(3), 235 (2006)
32. Zhou, H., Selvakumaran, K.A., Sivasubramanian, S., Purohit, S.D., Tang, H.: Subordination problems for a new class of Bazilevič functions associated with k -symmetric points and fractional q -calculus operators. *AIMS Math.* **6**(8), 8642–8653 (2021)



MHD Radiative Casson Fluid Flow over a Non-linear Extending Surface with Cross-Diffusion Impact in the Presence of Buoyancy and Porous Impacts

Atiya Ali¹, Ruchika Mehta¹(✉), Tripti Mehta², and Sanju Jangid¹

¹ Department of Mathematics and Statistics, Manipal University Jaipur, Jaipur, India
ruchika.mehta1981@gmail.com

² Department of Mathematics, S.S. Jain Subodh P.G. College, Jaipur, India

Abstract. This research uses MHD Casson fluid flow with radiation, buoyancy, and joule heating impression over a non-linear extending surface. It also included the impressions of thermal diffusion—the Casson fluid's flow characteristics in a transverse magnetic field. Partial differential equations change into an ordinary differential coupled system through appropriate similarity modification. Diagrams and tables are used to analyze the impacts of numerous non-dimensional parameters on velocity, temperature, and concentration with the help of the BVP4C technique and MATLAB software. The temperature and concentration profiles decline with increasing Dufour and Soret impressions, respectively. Velocity profile increases with increasing local thermal Grashof number while the reverse impression shows growing local concentration Grashof number. The skin friction rises with the local thermal Grashof parameter but falloff with the local concentration Grashof number. The Nusselt number increases with the Soret, Dufour, and radiation impacts. The skin friction coefficient, Nusselt number, and Sherwood number are also shown in the table with validation.

Keywords: Casson fluid · Porous Medium · Radiation · Double diffusion · Buoyancy · Brownian motion

List of Symbols

B_0	Magnetic induction
Sr	Soret number
Sc	Schmidt parameter
C	Concentration
C_∞	Ambient concentration as y tends to infinity
C_{fx}	Skin-friction coefficient
C_p	Specific heat capacity
D_B	Brownian diffusion coefficient
D_T	Thermophoretic diffusion coefficient
D_m	Mass diffusivity
F	Dimensionless stream function

K	parameter of the Porous media
k	Permeability of the porous medium
M	Magnetic field parameter
n	viscosity factor (Constant)
Pr	Prandtl number
Q_0	The dimensional heat Source/sink coefficient
q	Radiative heat flux
Nr	Radiation parameter
Nb	Brownian motion parameter
N_T	Thermophoresis parameter
Nu_x	Local Nusselt number
Ec	Eckert number
G_T	Grashof number for local temperature
G_C	Grashof number for local concentration
Du	Dufour number
R	Chemical reaction parameter
R_0	Chemical reaction coefficient
Re	Local Reynolds number
Sh_x	Local Sherwood number
T	Temperature of the nanofluid within the boundary layer
T_w	Reference temperature
T_∞	Temperature of the ambient fluid
u; v	Velocity components along x- and y-directions, respectively
u_w	Reference velocity
x; y	Cartesian coordinates along the plate and normal to it, respectively

Greek Symbols

θ	Dimensionless temperature
ϕ	Dimensionless concentration
ν	Kinematic coefficient of viscosity
α	Thermal Diffusivity
β	Casson Fluid parameter
σ	The electrical conductivity
λ	The heat source or sink parameter
η	variable of Similarity
τ	Heat capacity ratio
μ_B	Non-Newtonian plastic dynamic viscosity
τ_w	wall shear stress of the fluid
π	deformation rate Multiple factors
π_c	Critical value of π founded on non-Newtonian model
e_{ij}	(i, j) th deformation rate factor

Subscripts

w	Surface conditions
∞	Conditions far away from the surfaces

Superscripts

- ' Differentiation with respect to η

1 Introduction

Non-Newtonian materials have drawn the attention of researchers over the past century due to their transdisciplinary character and intriguing rheology. A wide range of sectors, including processing, metals, chemical engineering, plastics, and food, can benefit from non-Newtonian fluids. Applications for non-Newtonian liquids include glassmaking, biological fluids, cosmetics, artificial fiber, pharmaceuticals, meals, metal spinning, shampoos, and many more. Non-Newtonian fluids can be classified as shear-thickening, dilatant, shear-thinning, and thixotropic. They all have different characteristics. Numerous fluid models, including Maxwell, Casson, Williamson, Burgers, Oldroyd-B, micropolar, Jeffrey, Sutterby Cross, and Sisko, among others, have been observed by rheologists. However, there are specific circumstances in which second-grade liquid, which exhibits shear thickening, shear thinning, and Newtonian flow properties, behaves. Due to its dynamic properties, second-grade fluid is renowned and deserving among researchers.

The study of electrically conducting flow in a magnetic field is known as MHD. The design of nuclear reactors, MHD generators, flow meters, and other industrial and technical applications depends on MHD fluxes. Liquids with exceptional thermal properties are required as commercial and industrial processes expand. As the thermal conductivity of liquids is used to quantify their heat transfer properties, empirical estimates indicate that the thermal conductance of common fluids is intrinsically low and should be enhanced via any technique. Researchers considered methods for increasing the thermal conductance of common liquids and discovered that adding particles with high conductivity magnitudes can do this. In this regard, it is found that nano-sized particles are ideal for achieving the desired result. Bachok et al. [5] examined the uniform free stream, a time-independent boundary-layer flow of a nano-fluid departed a dynamic semi-infinite flat sheet over a moving plate. Shehzad et al. [21] studied the mass transfer effect in the MHD Casson fluid flow across a porous stretched sheet in the presence of the suction parameter and chemical reaction. Haritha and Sarojamma [8] investigated the mass and heat transfer in the MHD radiative Casson fluid flow over a porous stretched sheet.

The effect of the buoyant force brought on by the stretching sheets could not be disregarded, aside from the flow created by an unstable or steady extending/shrinking sheet. The subject of thermal radiation with mixed convective boundary layer (BL) flow has become more popular due to its crucial applications in geothermal engineering, space technology, and cooling nuclear reactors. Mabood et al. [12] studied the effects of thermal radiation and chemical reaction of MHD Casson in a porous media. Reddy et al. [17] found the impacts of Joule heating, viscous dissipation, and Soret in a vertical channel of free convection electrically conducting Casson fluid. Singh et al. [24] presented an efficient hybrid computational technique, i.e., homotopy analysis transform method (HATM), to inspect Jeffery–Hamel flow. Sumalatha and Bandari [25] focused on radiative Casson fluid flow over a nonlinearly extending sheet with heat source/sink

effects into account. Kataria and Patel [10] examined the impact of heat generation and thermal diffusion on the MHD Chemical reactive Casson fluid flow past an oscillating erect plate inserted through a porous mode.

The phenomenon of energy or heat transmitted by electromagnetic waves is known as thermal radiation. When there is a considerable temperature variance between the boundary surface and the ambient fluid, thermal radiation plays a significant role. Radiative influences are crucial in physics and engineering. In operations involving high temperatures and space technology, the effects of radiation heat transfer on diverse flows are crucial. For example, in the polymer industries, where heat regulating factors somewhat impact the final product quality, the impacts of radiation are crucial for monitoring heat transfer. The effects of radiation on missiles, airplanes, gas turbines, solar radiation, spacecraft, liquid metal fluids, MHD accelerators, and nuclear power plants are also relevant. Waqas et al. [30] presented mixed convective MHD micropolar fluid flow toward a nonlinear stretched surface with various effects of viscous dissipation, Joule heating, and convective boundary conditions. Reddy [18] investigated a Casson fluid flow in a two-dimensional MHD convective boundary layer over an exponentially inclined stretched surface with a chemical reaction. Reddy and Janardhan [19] studied the Casson MHD fluid flow across a vertical plate with a heat source/sink, chemical reaction, radiation, Dufour, and Soret effects. Muthamilselvan [14] examined the heat radiation and buoyant effects of a grimy Casson fluid flowing across a stretchy sheet at its stagnation point. Singh et al. [23] investigated thin film flow of a third-grade fluid down an inclined plane derived by using an effective well organized computational scheme namely homotopy perturbation Elzaki transform method. Ramudu et al. [28] investigated the suction/bowing properties of MHD Casson fluid flow over an erect straightened sheet. Vijaya et al. [29] studied the Soret impact on steady 2D free convective MHD Casson fluid flow departed an erect moving plate when thermal radiation and chemical reactions are present.

The Dufour effect is connected to the energy flux produced by the solute difference, whereas the Soret effect is linked to mass flux phenomena brought on by heat diffusion. To deal with gas concentrations with lighter and medium molecular masses, the Soret impact is applied. Numerous industrial and engineering applications, including multicomponent melts in geosciences, groundwater pollutant migration, solidification of binary alloys, chemical reactors, space cooling, isotope separation, oil reservoirs, and mixtures of gases, benefit from heat and mass transfer via the Soret and Dufour phenomena. Ahmed and Arafa [2] analyzed the fractional derivatives methodologies to mathematically formulate and numerically simulate steady MHD non-Newtonian nanofluid flow with entropy creation over an erect plate with Caputo term. Khan et al. [11] examined a mixed convective Casson fluid flow along a stretching and contracting sheet in an unstable radiative two-dimensional stagnation point flow with Joule heating and heat source impact. Abo-Dahab et al. [1] experimented on MHD Casson nanofluid flow over nonlinearly porous extending surfaces with suction/injection.

Boundary slip fluid can clean mechanical heart valves and interior chambers, among other things. El-Shorbagy et al. [6] explored how porous media affects mixed convection of nano-fluid flow in a trapezoidal channel with two distinct aspect ratios. Additionally, a filled channel with porous media produces favorable outcomes for the upper wall. Awais

M et al. [4] explained the heat and mass transfer assets on the MHD Casson fluid flow via porous material under the influence of heat generation effects and absorption. Mondal et al. [13] addressed the convective heat transfer characteristics in a two-sided partly driven cavity (PDC) under the umbrella of foundations of flow physics and examined the effects of the pertinent parameters on fluid flow and heat transmission. Rao et al. [15] investigated the thermal radiative MHD free convection Casson fluid flow via a rapidly infinite erect plate through porous media. Reddy et al. [20] discussed MHD Casson fluid flow, the radiation impact across a rapidly stretched sheet set in the presence of a heat source/sink, and viscous dissipation. Finally, Akinshilo et al. [3] Considered the Casson nano-fluid flow departs a fine porous needle with the effects of nonlinear thermal radiation.

Gupta et al. [7] analyzed the MHD 2D Williamson nanofluid flow in the manifestation of nonlinear thermal radiation, Cattaneo–Christov heat and mass flux models, and varying thicker surfaces. Tassaddiq et al. [26] studied the generalized Casson fluid flow involving the Mittag–Leffler function in the presence of Newtonian heating effects. Sheikh et al. [22] studied the MHD Casson fluid flow with the generalized Fick’s and Fourier’s laws in a channel by analyzing the Caputo fractional model. Samrat et al. [27] considered the effects of the Brownian motion and thermophoresis in the MHD-free convection flow of the revolution paraboloid. Rasheed et al. [16] researched the effects of heat transfer with MHD Casson flow from a permeable straightened surface by considering the heat source, chemical reaction, and viscosity dissipation effects.

However, a thorough examination of the previously mentioned literature reveals several gaps. The authors have taken every precaution to ensure the accuracy of the information in this document, and no prior studies have examined the steady MHD radiative Casson fluid flow caused by a convectively heated nonlinear extending surface with double diffusion impact, Joule heating and buoyancy impact with suction/blowing impacts in their study outline. Additionally, the effects of viscous dissipation, heat source/sink, Brownian motion, and thermophoresis with zero mass flow are studied. By using a correspondence transformation, the boundary layer’s controlling PDEs are changed into ODEs. The BVP4C solver calculates the serious solutions of the velocity, heat, and concentration fields. The graphs and table provide detailed illustrations and descriptions of the many embedded flow parameters affecting skin friction and heat transfer rates.

2 Problem Structure

MHD Casson nanofluid flow in a 2D time-independent flow in the area ($y > 0$) with power-law along nonlinearly high extended sheet with velocity distribution $u_w(x) = ax^n$ and wall temperature $T_w(x) = T_\infty + Ax^n$ is taken, here $A > 0$ is constant, the pervasive fluid temperature is T_∞ and the pervasive nanoparticle concentration is C_∞ . In the transverse flow direction variable magnetic field with strength $B(x) = B_0x^{(n-1)/2}$ is applied. The electric field is missing, whereas by imaging a small magnetic Reynolds number, the induced magnetic field is ignored. The flow model is the same as the coordinate system in Fig. 1.

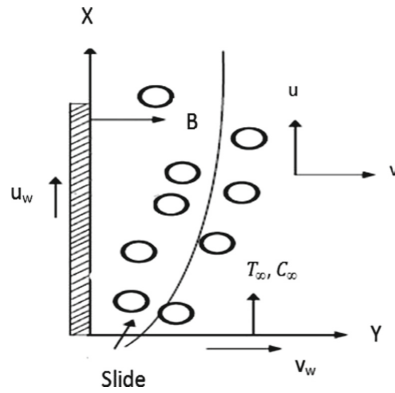


Fig. 1. Physical Diagram

For a Casson fluid isotropic flow, the rheological state equation is used Ref. [1, 3, 4, 9]:

$$\tau_{ij} = \begin{cases} 2\left(\mu_B + \tau_y / \sqrt{2\pi}\right)e_{ij}, & \pi > \pi_c \\ 2\left(\mu_B + \tau_y / \sqrt{(2\pi_c)}\right)e_{ij}, & \pi < \pi_c \end{cases} \tag{1}$$

where, $\pi = e_{ij}e_{ij}$ and e_{ij} denotes the $(i, j)^{th}$ factor, and π is the compound of the elements of the deformation rate, the critical rate of several built using a non-Newtonian model represented by π_c , the plastic dynamic viscidness represented by μ_B , τ_y is known as share stress and the non-Newtonian fluid yield stress represent by τ_y .

The current flow, mass, and heat transfer governing equations are stated by Ref. [1, 4, 9]

$$\frac{\partial u}{\partial x} + \frac{\partial v}{\partial y} = 0, \tag{2}$$

$$u \frac{\partial u}{\partial x} + v \frac{\partial u}{\partial y} = v \left(1 + \frac{1}{\beta}\right) \left(\frac{\partial^2 u}{\partial y^2}\right) - \frac{v}{\kappa} \left(1 + \frac{1}{\beta}\right) u - \frac{\sigma B^2(x)}{\rho_f} u + g_0 \beta_T (T - T_\infty) + g_0 \beta_c (C - C_\infty), \tag{3}$$

$$u \frac{\partial T}{\partial x} + v \frac{\partial T}{\partial y} = \alpha \left(\frac{\partial^2 T}{\partial y^2}\right) + \frac{Q_0}{\rho C_p} (T - T_\infty) - \frac{1}{\rho c_p} \frac{\partial q_r}{\partial y} + \frac{D_m K_T}{C_s C_p} \frac{\partial^2 c}{\partial y^2} + \frac{\sigma B^2(x) u^2}{\rho C_p} + \tau \left[D_B \left(\frac{\partial T}{\partial y} \frac{\partial C}{\partial y}\right) + \frac{D_T}{T_\infty} \left(\frac{\partial T}{\partial y}\right)^2 \right] + \frac{v}{C_p} \left(1 + \frac{1}{\beta}\right) \left(\frac{\partial u}{\partial y}\right)^2, \tag{4}$$

$$u \frac{\partial C}{\partial x} + v \frac{\partial C}{\partial y} = D_B \left(\frac{\partial^2 C}{\partial y^2}\right) + \frac{D_T}{T_\infty} \left(\frac{\partial^2 T}{\partial y^2}\right) - R_0 (C - C_\infty) + \frac{D_m K_T}{T_\infty} \left(\frac{\partial^2 T}{\partial y^2}\right), \tag{5}$$

where, the velocities are u and v in the directions x and y , the boundary condition for the problem is Ref. [1]:

$$\begin{cases} u = u_w(x) = ax^n, v = v_w, T = T_w(x) = T_\infty + Ax^n, D_B\left(\frac{\partial c}{\partial y}\right) + \frac{D_T}{T_\infty} \frac{\partial T}{\partial y}; & \text{at } y = 0 \\ u \rightarrow 0, T \rightarrow T_\infty, C \rightarrow C_\infty; & \text{at } y \rightarrow \infty \end{cases} \tag{6}$$

Through Rosseland approximation, using the radiative heat flux phrase Ref. [3, 7], we have

$$q_r = \frac{4\sigma^*}{3k^*} \frac{\partial T^4}{\partial y}, \tag{7}$$

The Stefan–Boltzmann constant is σ^* , and the Rosseland mean absorption coefficient is k^* . To get higher terms by using the Taylor series expansion and ignoring higher terms. We get

$$T^4 \approx 4T_\infty^3 T - 3T_\infty^4, \tag{8}$$

Equation (1) and significant equations are collected with References [1, 2, 18, 21].

Convert the leading PDEs into ODEs introduces the non-dimensional parameters Ref. [1]

$$\begin{cases} u = ax^n f'(\eta), v = -ax^{\frac{n-1}{2}} \sqrt{\frac{\nu}{a}} \left(\frac{n+1}{2} f(\eta) + \frac{n-1}{2} \eta f'(\eta)\right) \\ \eta = \sqrt{\frac{a}{\nu}} x^{\frac{n-1}{2}} y, \theta(\eta) = \frac{T-T_\infty}{T_w-T_\infty}, \phi(\eta) = \frac{C-C_\infty}{C_w-C_\infty}. \end{cases} \tag{9}$$

Using the above non-dimensional parameters, the equations came out in the nondimensional form, which is:

$$\left(1 + \frac{1}{\beta}\right) f''' - n f'^2 + \frac{n+1}{2} f f'' - M \left(1 + \frac{1}{\beta}\right) f' - K \left(1 + \frac{1}{\beta}\right) f' + G_T \theta + G_c \phi = 0 \tag{10}$$

$$\left(\frac{1}{Pr} + \frac{Nr}{Pr}\right) \theta'' - n f' \theta + \left(\frac{n+1}{2}\right) f \theta' + Nb \theta' \phi' + Nt \theta'^2 + \left(1 + \frac{1}{\beta}\right) Ec f'^2 + \lambda \theta + MEc f'^2 + Du \phi'' = 0 \tag{11}$$

$$\phi'' + \left(\frac{n+1}{2}\right) f \phi' Sc + \frac{Nb}{Nt} \theta'' - RSc \phi + SrSc \theta'' = 0 \tag{12}$$

The boundary conditions are:

$$\begin{cases} f(0) = f_w, f'(0) = 1, Nb\phi'(0) + Nt\theta'(0) = 0; & \text{at } \eta = 0 \\ f'(\infty) \rightarrow 0, \theta(\infty) \rightarrow 0, \phi(\infty) \rightarrow 0; & \text{at } \eta \rightarrow \infty \end{cases} \quad (13)$$

where,

Brownian Motion Parameter (Nb) = $\frac{\tau D_B(C_W - C_\infty)}{\nu}$	Radiation parameter (Nr) = $\frac{16\sigma^* T_\infty^3}{3kk^*}$
Thermophoresis Diffusion (Nt) = $\frac{\tau D_T(T_W - T_\infty)}{\nu T_\infty}$	Schmidt number (Sc) = $\frac{\nu}{D_B}$
Heat Generation/Absorption Parameter (λ) = $\frac{Q_0}{u_w \rho C_p x^{-1}}$	Eckert number (Ec) = $\frac{u_w^2}{(T_W - T_\infty) C_p}$
Magnetic parameter (M) = $\frac{\sigma B_0^2}{\alpha \rho x^{n-1}}$	Dufour number (Du) = $\frac{D_m K_T (C_W - C_\infty)}{C_S C_p \nu (T_W - T_\infty)}$
Local temperature Grashof number (G_T) = $\frac{g_0 \beta_T (T_W - T_\infty)}{a^2 x^{2n-1}}$	Porous media parameter (K) = $\frac{\nu}{ak_0}$
Local Concentration Grashof number (G_C) = $\frac{g_0 \beta_C (C_W - C_\infty)}{a^2 x^{2n-1}}$	Prandtl number (Pr) = $\frac{\nu}{\alpha}$
Injection/Suction Parameter $f_w = \frac{-2\nu_w}{(n+1)a^{1/n} \nu_w^{(2n-1)/2n}}$	Soret number (Sr) = $\frac{D_m K_T (T_W - T_\infty)}{T_m \nu (C_W - C_\infty)}$

The coefficient of skin friction (C_{fx}), local Nusselt number (Nu_x), and local Sherwood number (Sh_x) are the quantities of beneficial interest. They are as follows Ref. [1, 4]:

$$C_{fx} = \frac{\tau_w}{\rho u_w^2}, \quad Nu_x = \frac{xq_w}{\alpha_f (T_w - T_\infty)}, \quad Sh_x = \frac{xq_w}{D_B (C_w - C_\infty)}, \quad (14)$$

where, q_w, q_m are the wall heat and mass flux, τ_w is the shear stress of the wall, and α_f is the nano-fluid conductivity.

$$q_w = -\alpha_f \left(1 + Nr\right) \left(\frac{\partial T}{\partial y}\right)_{y=0}, \quad q_m = -D_B \left(\frac{\partial C}{\partial y}\right)_{y=0}, \quad \tau_w = \mu_B \left(1 + \frac{1}{\beta}\right) \left(\frac{\partial u}{\partial y}\right)_{y=0} \quad (15)$$

Using Eq. (9) in Eq. (14), we get

$$Re_x^{1/2} C_{fx} = \left(1 + \frac{1}{\beta}\right) f''(0), \quad Re_x^{-1/2} Nu_x = -\theta'(0), \quad Re_x^{-1/2} Sh_x = -\phi'(0), \quad (16)$$

where, $Re_x = \frac{u_w x}{\nu}$ is known as the local Reynolds number.

3 Results and Discussion

The effects of the porous medium’s physical constant on temperature $\theta(\eta)$, concentration $\phi(\eta)$, and velocity $f'(\eta)$ during a Casson nanofluid flow over a convectively heated nonlinear via a porous medium with injection/suction due to an extended surface. Table 1 calculated the value of velocity, temperature, and concentration with various parameters and try to find the Casson fluid flow behavior as per the submitted values of different parameters. Additionally, for comparison, it was made between the outcomes of earlier

Table 1. The rate of skin friction coefficient, mass transfer coefficient, and heat transfer coefficient for various dimension-less parameters

N	K	R	β	M	λ	Ec	fw	Sr	Sc	Du	Nr	Nb	Nt	GT	GC	Pr	$f'(0)$	$-\theta'(0)$	$-\phi'(0)$
0.5																	-0.63980	0.602351	-0.60235
1	0.1	0.1	0.5	0.5	0.1	0.1	0.1	0.1	2	0.1	0.1	0.1	0.1	0.1	0.1	0.7	-0.75147	0.856046	-0.85604
1.5																	-0.84655	1.05839	-1.05839
	-0.5																-0.60331	0.910742	-0.91074
1	0.5	0.1	0.5	0.5	0.1	0.1	0.1	0.1	2	0.1	0.1	0.1	0.1	0.1	0.1	0.7	-0.83636	0.823285	-0.82328
	1																-0.93163	0.785749	-0.78574
	2																-1.09726	0.71956	-0.71956
		0.2															-0.74880	0.856844	-0.856844
1	0.1	1.2	0.5	0.5	0.1	0.1	0.1	0.1	2	0.1	0.1	0.1	0.1	0.1	0.1	0.7	-0.73780	0.860293	-0.86029
		2.2															-0.73438	0.861402	-0.861402
			1														-0.92432	0.818015	-0.818015
1	0.1	0.1	1.5	0.5	0	0.1	0.1	0.1	2	0.1	0.1	0.1	0.1	0.1	0.1	0.7	-1.01487	0.797052	-0.79705
			2														-1.07123	0.783844	-0.783844
				1													-0.855621	0.7978	-0.7978
1	0.1	0.1	0.5	1.5	0.1	0.1	0.1	0.1	2	0.1	0.1	0.1	0.1	0.1	0.1	0.7	-0.94834	0.745555	-0.745555
				2													-1.03263	0.697952	-0.697952
					-0.1												-0.755612	0.9569	-0.9569
1	0.1	0.1	0.5	0.5	0	0.1	0.1	0.1	2	0.1	0.1	0.1	0.1	0.1	0.1	0.7	-0.753654	0.908476	-0.908476
					0.1												-10.751475	0.856046	-0.85604
						-0.1											-0.755612	0.9569	-0.9569
1	0.1	0.1	0.5	0.5	0.1	0	0.1	0.1	2	0.1	0.1	0.1	0.1	0.1	0.1	0.7	-0.754714	0.94073	-0.94073
						0.1											-0.75147	0.856046	-0.856046
							-0.2										-0.72462	0.724625	-0.72462
1	0.1	0.1	0.5	0.5	0.1	0.1	-0.1	0.1	2	0.1	0.1	0.1	0.1	0.1	0.1	0.7	-0.72077	0.766871	-0.766871
							0.1										-0.75147	0.856046	-0.85604
							0.2										-0.76772	0.902918	-0.90291
								-0.1									-0.74574	0.825242	-0.82524
1	0.1	0.1	0.5	0.5	0.1	0.1	0.1	0	2	0.1	0.1	0.1	0.1	0.1	0.1	0.7	-0.74854	0.840271	-0.84027
								0.1									-0.75147	0.856046	-0.85604
									1								-0.773347	0.837973	-0.837973
1	0.1	0.1	0.5	0.5	0.1	0.1	0.1	0.1	1.5	0.1	0.1	0.1	0.1	0.1	0.1	0.7	-0.758714	0.848893	-0.848893
									7								-0.736726	0.907046	-0.907046
										-0.5							-0.741751	0.654331	-0.654331
1	0.1	0.1	0.5	0.5	0.1	0.1	0.1	0.1	2	0	0.1	0.1	0.1	0.1	0.1	0.7	-0.73939	0.739396	-0.73939
										0.1							-0.75147	0.856046	-0.85604
											-0.1						-0.757853	1.00358	-1.00358
1	0.1	0.1	0.5	0.5	0.1	0.1	0.1	0.1	2	0.1	0	0.1	0.1	0.1	0.1	0.7	-0.75440	0.922509	-0.922509
											0.1						-0.751475	0.856046	-0.856046
												0.1					-0.75147	0.856046	-0.856046
1	0.1	0.1	0.5	0.5	0.1	0.1	0.1	0.1	2	0.1	0.1	0.2	0.1	0.1	0.1	0.7	-762231	0.942119	-0.942119

(continued)

Table 1. (continued)

N	K	R	β	M	λ	Ec	f_w	Sr	Sc	Du	Nr	Nb	Nt	GT	GC	Pr	$f'(0)$	$-\theta'(0)$	$-\phi'(0)$
												0.3					-0.783734	1.11557	-1.11557
													0.1				-0.751475	0.856046	-0.856046
1	0.1	0.1	0.5	0.5	0.1	0.1	0.1	0.1	2	0.1	0.1	0.1	0.5	0.1	0.1	0.7	-0.79266	0.969144	-0.969144
													1				-0.912053	1.37446	-1.37446
														-0.5			-0.876199	0.808341	-0.808
1	0.1	0.1	0.5	0.5	0.1	0.1	0.1	0.1	2	0.1	0.1	0.1	0.1	0	0.1	0.7	-0.77138	0.849181	-0.849181
														0.5			-0.674349	0.880643	-0.880643
															-0.5		-0.61306	0.895894	-0.895894
1	0.1	0.1	0.5	0.5	0.1	0.1	0.1	0.1	2	0.1	0.1	0.1	0.1	0.1	0	0.7	-0.728335	0.863243	-0.863243
															0.5		-0.824617	0.824617	-0.824617
																1	-0.763428	1.141	-1.141
1	0.1	0.1	0.5	0.5	0.1	0.1	0.1	0.1	2	0.1	0.1	0.1	0.1	0.1	0.1	1.5	0.782083	1.64413	-1.64413
																2	-0.802715	2.24733	-2.24733

Table 2. Comparative study of Heat Transfer rate at the sheet for frequent values of n, Nt, Nb, Pr, Sc, β and M , When $f_w = Ec = \lambda = 0 = K = R$ between Abo-Dahab et al. [1] and the present work.

Constant							Ref. [1]	Present work
n	M	β	Nt	Nb	Pr	Sc	$(-\theta'(0))$	$(-\theta'(0))$
0.5	3	0.6	0.1	0.1	7	20	2.12064	2.12066
0.5	3	0.6	0.5	0.5	7	20	1.63865	1.63863
0.5	3	0.6	0.9	0.9	7	20	1.37929	1.37925
1	3	0.6	0.5	0.5	7	5	2.69158	2.69151
1	3	0.6	0.5	0.5	7	10	2.51355	2.51353
1	3	0.6	0.5	0.5	7	20	2.31559	2.31551
1.5	3	0.6	0.5	0.5	7	5	2.43075	2.43074
1.5	3	0.6	0.5	0.5	7	5	2.85266	2.85263
1.5	3	0.6	0.5	0.5	9	5	3.21451	3.21446

studies, as indicated in Table 2 which displays the thermal characteristics of a Casson nano-fluid. The nano-fluid flows direction is shown in Fig. 1. Figures show the effects of all outer parameters, including the viscosity factor n , the suction/blowing factor f_w for suction ($f_w > 0$) and for blowing ($f_w < 0$), the magnetic field M , the chemical reaction parameter R , Porous media parameter K and the heat source λ , ($\lambda > 0$) or sink parameter ($\lambda < 0$), Radiation Parameter Nr , Brownian Motion Parameter Nb , Dufour number Du , Thermophoresis Diffusion Nt , Soret number Sr , Schmidt number Sc , Eckert number Ec , Local temperature Grashof number G_T , Local concentration Grashof number G_C , about η are displayed in the Figs. 2, 3, 4, 5, 6, 7, 8, 9, 10, 11, 12, 13, 14, 15, 16, 17, 18, 19, 20, 21, 22, 23, 24, 25, 26, 27, 28, 29, 30, 31, 32, 33, 34, 35, 36, 37, 38, 39, 40, 41, 42, 43, 44, 45, 46.

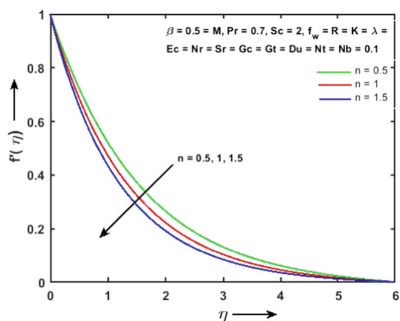


Fig. 2. Change in $f'(\eta)$ with various values of n (viscosity factor)

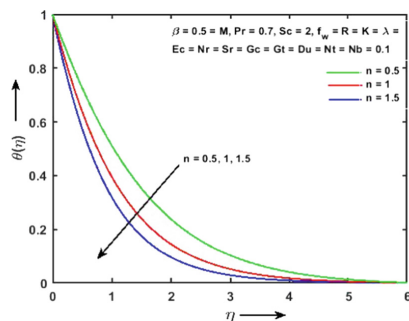


Fig. 3. Change in $\theta(\eta)$ with various values of n (viscosity factor)

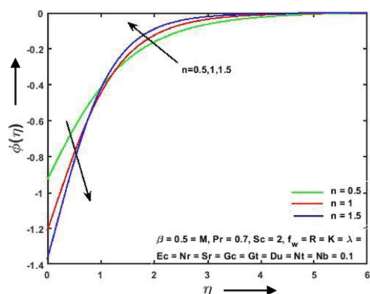


Fig. 4. Change in $\phi(\eta)$ with various values of n (viscosity factor)

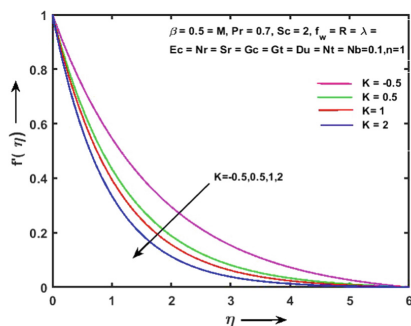


Fig. 5. Change in $f'(\eta)$ with various values of K (Porous Media parameter).

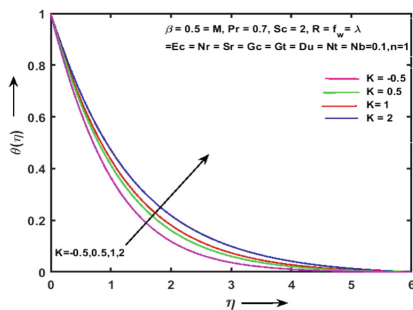


Fig. 6. Change in $\theta(\eta)$ with various values of K (Porous Media parameter).

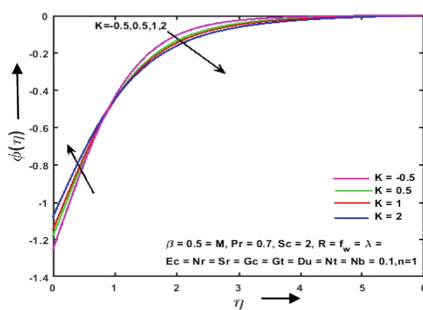


Fig. 7. Change in $\phi(\eta)$ with various values of K (Porous Media parameter).

Figure 2 shows the velocity f' variation about η with different values of n , as increased the value of viscosity factor n and the value of η the velocity decreased. Figure 3 shows the variation of temperature θ about η with different value of n , the temperature starts from unity at $\eta = 0$ the wall and eventually reaches zero as $\eta \rightarrow \infty$ (the fluid flows

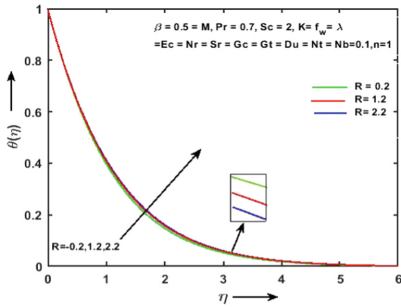


Fig. 8. Change in $\theta(\eta)$ with various values of R (Chemical Reaction Parameter)

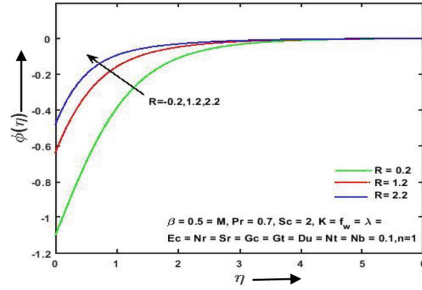


Fig. 9. Change in $\phi(\eta)$ with various values of R (Chemical Reaction Parameter)

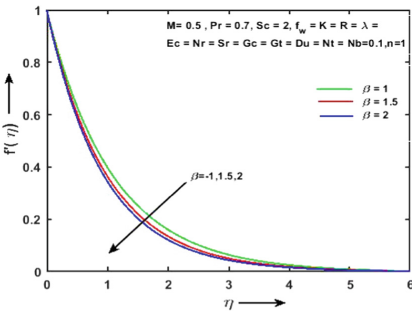


Fig. 10. Change in $f'(\eta)$ with various values of β (Casson fluid parameter)

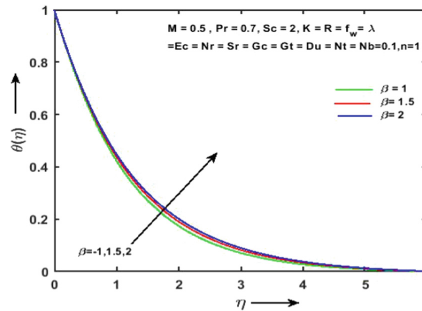


Fig. 11. Change in $\theta(\eta)$ with various values of β (Casson fluid parameter)

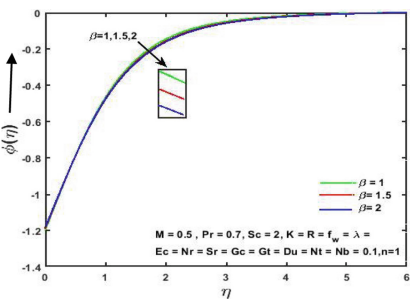


Fig. 12. Change in $\phi(\eta)$ with various values of β (Casson fluid parameter)

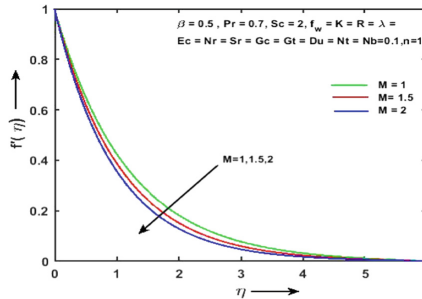


Fig. 13. Change in $f'(\eta)$ with various values of M (Magnetic Field)

away from the wall) as increased the values of n and the value of η then the temperature decreased. Figure 4 displays the concentration ϕ about η with different value of n , in the graph if η increased then ϕ increased as its max. Value imminent to zero $\eta \rightarrow \infty$ but decreased if η has great values. Figure 5 holds the graph mid between velocity f' and η with different values of porous media parameter K , arising the value of K then

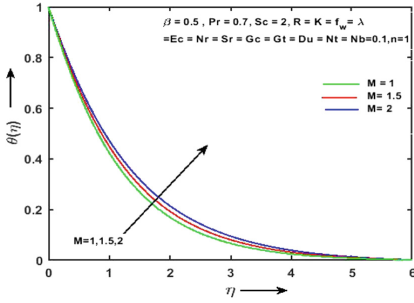


Fig. 14. Change in $\theta(\eta)$ with various values of M (Magnetic Field)

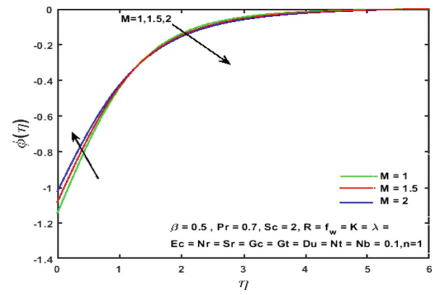


Fig. 15. Change in $\phi(\eta)$ with various values of M (Magnetic Field).

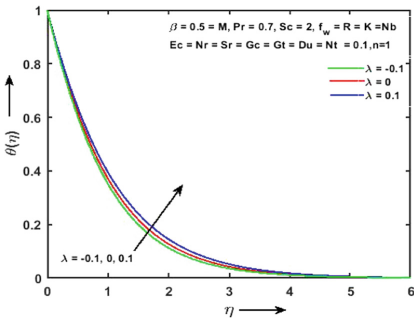


Fig. 16. Change in $\theta(\eta)$ with various values of λ (Heat Source/sink Parameter)

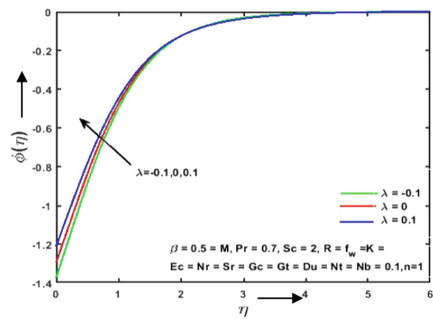


Fig. 17. Change in $\phi(\eta)$ with various values of λ (Heat Source/sink Parameter)

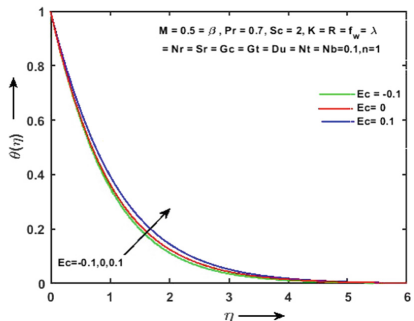


Fig. 18. Change in $\theta(\eta)$ with various values of Ec (Eckert number)

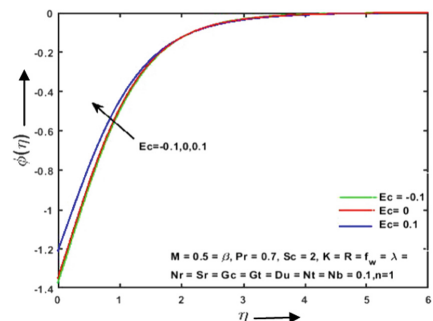


Fig. 19. Change in $\phi(\eta)$ with various values of Ec (Eckert number)

velocity profile decreased. Figure 6 indicates the graph of temperature and η with various values of K and notice that as per increasing K values the temperature increased as well. Figure 7 shows the concentration profile with respect to η with a distinct value of K, initially if increased the value of K then ϕ increased but after a point ($\eta = 1$) the behavior of the graph is changed and the concentration graph decreased. Figure 8 and Fig. 9 are

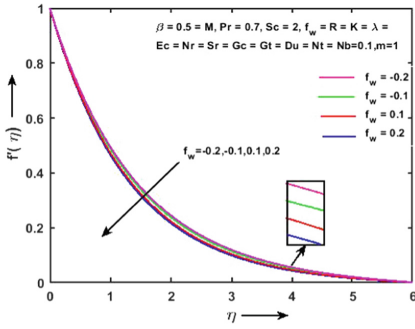


Fig. 20. Change in $f'(\eta)$ with various values of f_w (Injection/Suction Parameter)

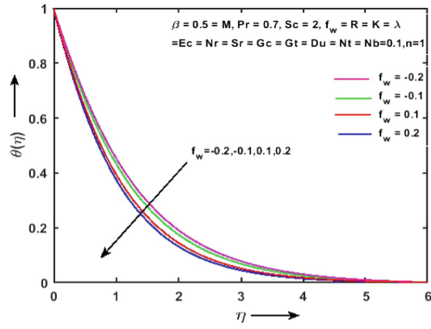


Fig. 21. Change in $\theta(\eta)$ with various values of f_w (Injection/Suction Parameter)

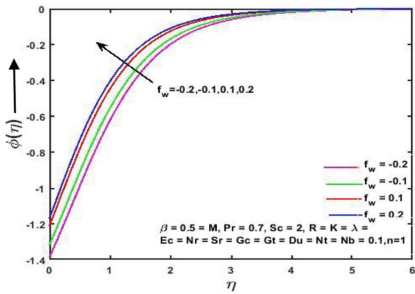


Fig. 22. Change in $\phi(\eta)$ with various values of f_w (Injection/Suction Parameter)

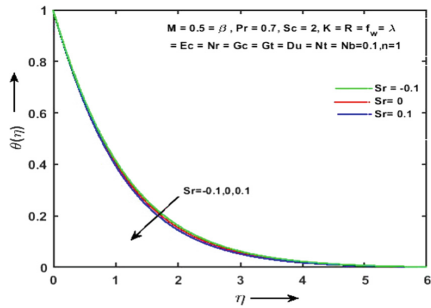


Fig. 23. Change in $\theta(\eta)$ with various values of Sr (Soret number)

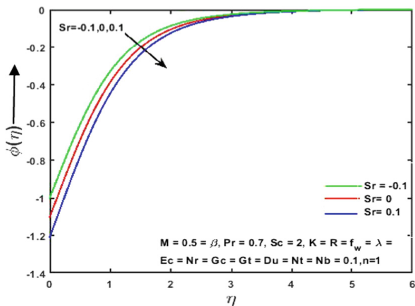


Fig. 24. Change in $\phi(\eta)$ with various values of Sr (Soret number)

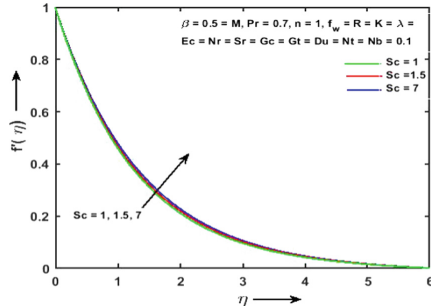


Fig. 25. Change in $f'(\eta)$ with various values of Sc (Schmidt number)

the graphs of temperature and concentration with a distinct value of chemical reaction parameter R about η , in this section concludes that increase the R then the temperature θ increased as well but the concentration ϕ decreased.

Figure 10, 11, and 12 are the graph of the velocity f' , temperature θ , and concentration ϕ with respect to η with different values of the Casson fluid parameter β , as increased

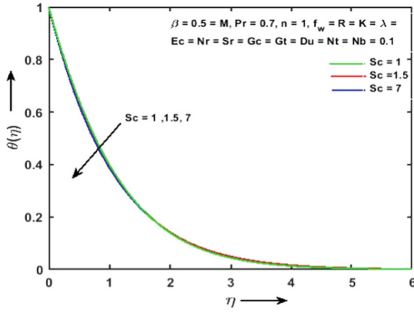


Fig. 26. Change in $\theta(\eta)$ with various values of Sc (Schmidt number)

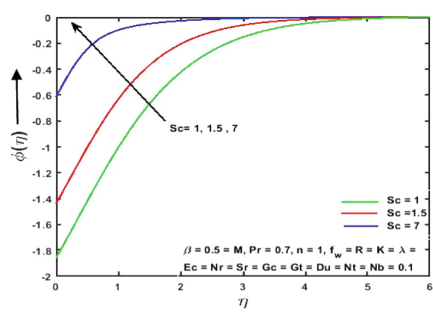


Fig. 27. Change in $\phi(\eta)$ with various values of Sc (Schmidt number)

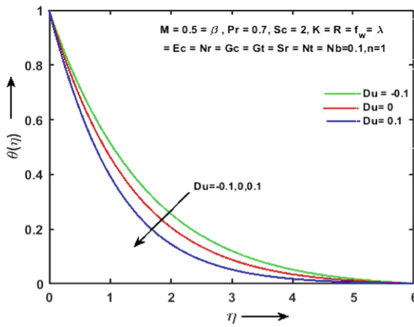


Fig. 28. Change in $\theta(\eta)$ with various values of Du (Dufour number)

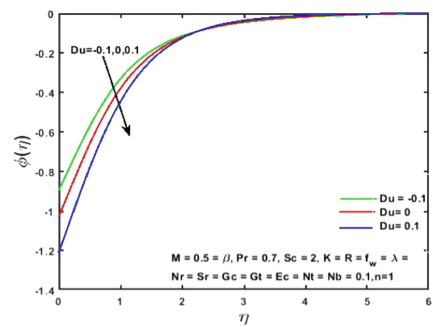


Fig. 29. Change in $\phi(\eta)$ with various values of Du (Dufour number)

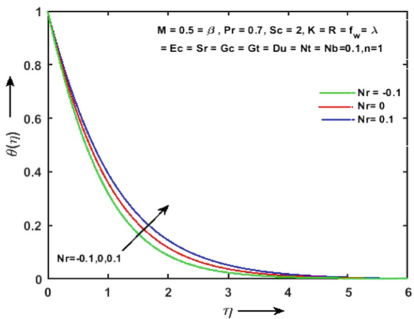


Fig. 30. Change in $\theta(\eta)$ with various values of Nr (Radiation Parameter)

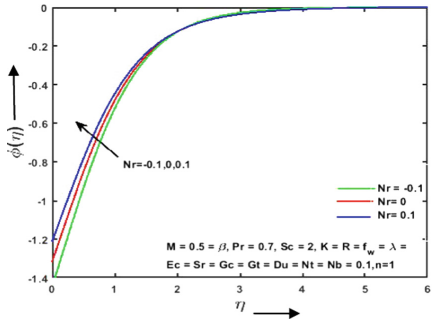


Fig. 31. Change in $\phi(\eta)$ with various values of Nr (Radiation Parameter)

the β , velocity is decreased, but temperature increased, and in the favor of concentration profile, it decreased as β increased. Since when the β growths, then the plastic dynamic viscosity is also increasing that produces the resistance in the fluid flow. That's why velocity declines with growing Casson fluid parameter. Figure 13, 14, and 15 are the

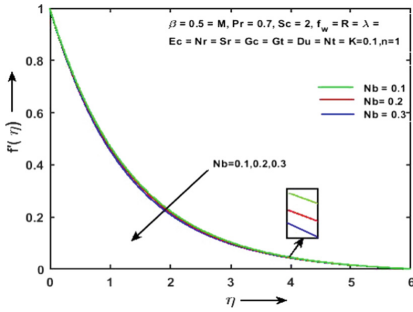


Fig. 32. Change in $f'(\eta)$ with various values of Nb (Brownian Motion Parameter)

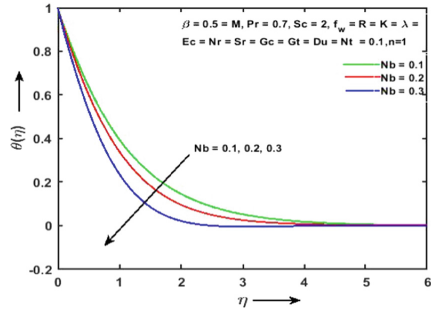


Fig. 33. Change in $\theta(\eta)$ with various values of Nb (Brownian Motion Parameter)

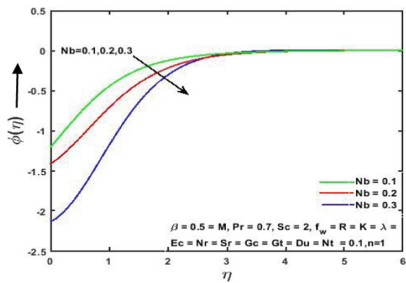


Fig. 34. Change in $\phi(\eta)$ with various values of Nb (Brownian Motion Parameter)

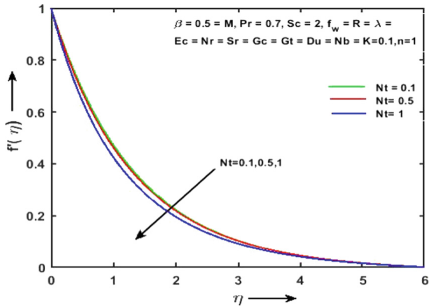


Fig. 35. Change in $f'(\eta)$ with various values of Nt (Thermophoresis Diffusion)

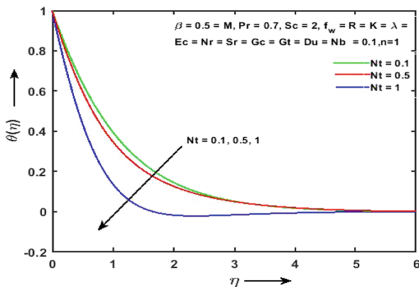


Fig. 36. Change in $\theta(\eta)$ with unlike values of Nt (Thermophoresis Diffusion)

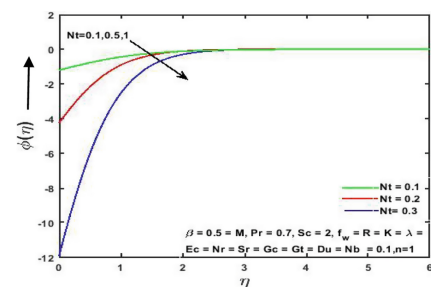


Fig. 37. Change in $\phi(\eta)$ with unlike values of Nt (Thermophoresis Diffusion)

graph for numerous values of M , for velocity f' , temperature θ , and concentration profile ϕ about η , if M increased then velocity is decreased, temperature θ increased, and concentration ϕ increases but for a short path of η , after ($\eta < 1$) the graph of concentration decreased as per M increased. In Fig. 13, we detected that the velocity declines when the Magnetic parameter Mn increases in the presence of powerful Lorentz forces in the fluid flow field because Lorentz force creates more resistance in the flow. In Fig. 14, the

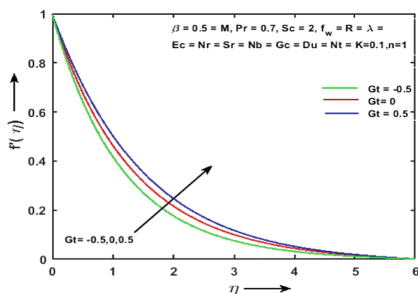


Fig. 38. Change in $f'(\eta)$ with various values of Gt (Local temperature Grashof number)

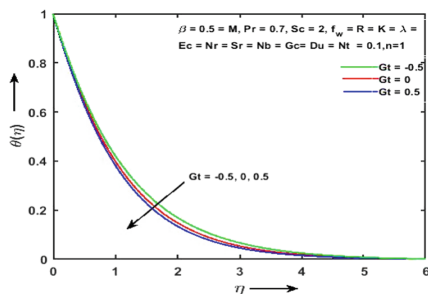


Fig. 39. Change in $\theta(\eta)$ with various values of Gt (Local temperature Grashof number)

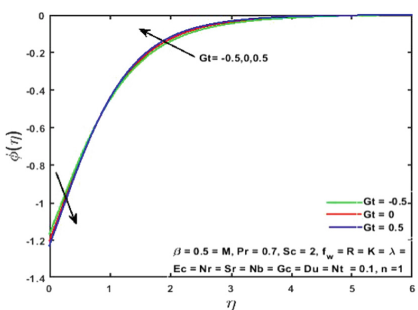


Fig. 40. Change in $\phi(\eta)$ with various values of Gt (Local temperature Grashof number)

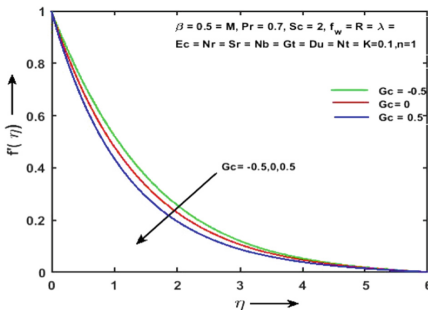


Fig. 41. Change in $f'(\eta)$ with various values of Gc (Local concentration Grashof number)

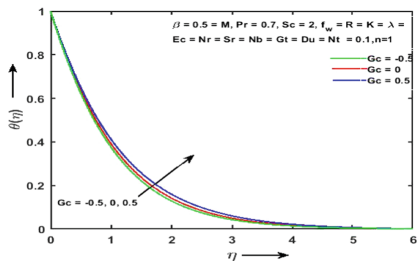


Fig. 42. Change in $\theta(\eta)$ with various values of Gc (Local concentration Grashof number)

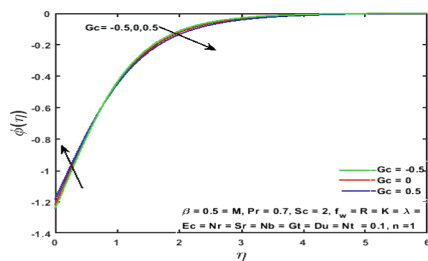


Fig. 43. Change in $\phi(\eta)$ with various values of Gc (Local concentration Grashof number)

temperature enhances with growing magnetic parameter Mn in the company of Joule and viscous dissipative impacts in the thermal equation. Figure 16 and 17 are the graph for various values of λ graphs credited in temperature θ and concentration ϕ profiles about η , and the disclaimer of the graph increased the value of λ then the temperature and the concentration profile ϕ increased. As seen in Fig. 16, temperature rises with growing heat source/sink parameter because heat source/sink produces heat in fluid flow. Figure 18 and 19 show the effect of the temperature and concentration profile with different values

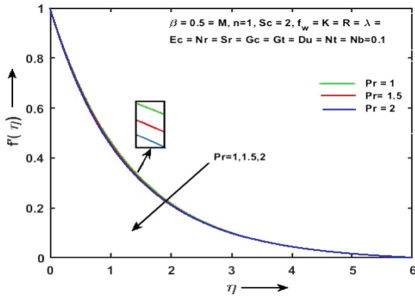


Fig. 44. Change in $f'(\eta)$ with various values of Pr(Prandtl number)

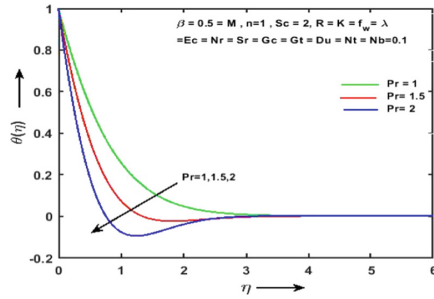


Fig. 45. Change in $\theta(\eta)$ with various values of Pr(Prandtl number)

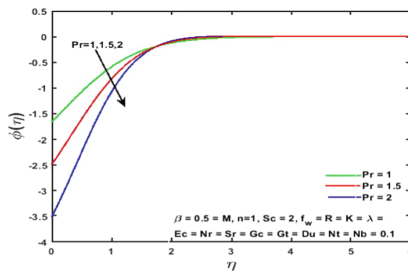


Fig. 46. Change in $\phi(\eta)$ with various values of Pr (Prandtl number)

of Eckert number Ec with concerning η , the temperature and the concentration profiles both are increased as increased the value of Ec . The temperature trends are illustrated in Fig. 18 as the Eckert number Ec grows. It has been discovered that as the Eckert number climbs, so does the temperature profile. The Eckert number represents the relationship between kinetic energy and enthalpy in a flow. It depicts the labour required to convert kinetic energy into internal energy in the face of viscous fluid forces. The greater the Eckert number, the higher the fluid's kinetic energy, resulting in more fluid vibration and more fluid-molecule collisions. Heat dissipation in the boundary layer region is aided by enhanced molecular collisions, increasing temperature profile. Figure 20, 21 and 22 display the variation of velocity f' , temperature θ and concentration profile ϕ with concerning η with numerous values of fw . It appears that from injection to suction with an arising fw , the velocity f' decreased but with a rising of fw , the temperature decreased, here concentration ϕ and temperature θ profile behave opposite to each other so the graph of concentration ϕ increases as fw increasing. Figure 23 and 24 state the graph for numerous values of Soret number Sr , graphs plots for temperature θ about η and concentration ϕ about η , which clarify that in the account of Soret number, the temperature and the concentration profile both behaved in the same manner when we consider Sr is increased then θ and ϕ both are increased. Figure 25 is the graph of the velocity profile f' concerning η with different values of Schmidt number Sc , this inducted that enlarges the Sc then the velocity profile f' increases. Figure 26 and 27 are made for temperature θ and concentration ϕ profile about η for multiple values of Sc , explained

that when Sc is involved the temperature θ and the concentration ϕ behavior are opposite to each other. If Sc increased, then the graph of θ is decreased slightly but the graph of ϕ grows rapidly. Figure 28 and 29 plotted for the temperature and the concentration profile concerning η with the distinct value of Dufour number Du , if increased the Du then both profiles are decreased, which means both profiles behave in the same manner. Figure 30 and 31 are manufactured for various values of the Radiation parameter Nr for temperature θ and concentration ϕ about η , it describes that both temperature and concentration are increased with a rising value of Nr . Because the thermal boundary layer grows with Nr , the temperature also rises.

Figure 32, 33, and 34 include the profiles of velocity, temperature, and concentration with η for various values of Brownian motion parameter Nb . It states that the behaviors of all profiles in these graphs are the same i.e., if increased the Nb then all profiles are decreased as well. Figure 35, 36, and 37 are plotted for different values of Thermophoresis diffusion Nt , these are for velocity, temperature, and concentration profiles with respect to η . These show that if Nb increased then all of the profiles decreased. Behavior of the graphs with Thermophoresis diffusion Nt and with the parameter of Brownian motion Nb is the same. Figure 38 is for velocity profile for η with numerous values of local temperature Grashof number G_T , as per increased G_T the velocity also increased. Since the Grashof number is the ratio amid the buoyancy force to the restraining force. Here buoyancy force is because of spatial disparity in density of fluid (produced by temperature differences) and the restraining force due to the viscosity of the fluid. Figure 39 is for temperature profile with η for various values of G_T . Here increased the G_T then the temperature decreased. Figure 40 have the concentration profile with η for numerous values of G_T , when G_T increased then concentration decreased (for $\eta < 1$), and the concentration increased (for $\eta > 1$) slightly. Figure 41 displayed the velocity profile for η with distinguishing values of Concentration Grashof number G_C , it shows that the velocity decreases if the value of G_C arises. The velocity declines with the local concentration Grashof number due to falling momentum boundary layer. Figure 42 is made for a temperature about η with the distinct value of G_C , the temperature increased if G_C is raised. Figure 43 holds the concentration profile concerning η with different values of G_C , If G_C increased then the concentration profile arises slightly (for $\eta < 1$), and ($\eta > 1$) concentration ϕ decreased slightly. To compare the graphs (all the profiles) of both of the parameter's G_T and G_C behave opposite to each other.

Figure 44, 45, and 46 state the graphs of velocity f' , temperature θ , and concentration ϕ profiles about η with various values of Prandtl number Pr . The value of Prandtl number Pr is increased then graphs of velocity f' , temperature θ , and concentration ϕ , all of the streams are decreased. Figure 45 describes the outcome of Prandtl on the temperature field for various Prandtl values. By reason of a high Pr -value, very viscid fluid with limited thermal conductivity is present as Pr values grow and diminish the temperature distribution. In terms of physics, the Prandtl number is the relationship between velocity and thermal diffusivities; greater Pr values have lesser conduction, whereas lower Pr amounts have higher thermal conductivity. The temperature declines due to This is evident that the different parameters have an impact on the MHD Casson nano-fluid flow above a non-linearly heated porous medium when an extended surface is present.

4 Conclusion

The current study provides that a Casson fluid flow with MHD and presence of suction/injection with radiation, porous medium, Grashof parameter for temperature and concentration, thermophoresis diffusion and Dufour number included then results get analytically and numerically, and we can deduce the following conclusions. This problem can be solved for future purpose if sheet is inclined at some angle. The boundary conditions and fluids can also be changed.

- The Radiation parameter N_r and the Magnetic parameter M affect the temperature and concentration profiles, both of the profiles increases if N_r and M increased.
- The behavior of the temperature Grashof number G_T has a vice versa behavior with the Concentration Grashof number G_C , which is applicable for all velocity, temperature, and concentration profiles.
- The heat transfer coefficient increases with the double diffusion thermo impression.
- Thermophoresis diffusion N_t and Brownian motion N_b both behave the same for the velocity, temperature, and concentration profiles.
- The skin friction increases with local thermal Grashof number while declines with local concentration Grashof number.
- Analyzing that the Dufour number Du effects same on Concentration and Temperature profile, if Du increased then they both profiles decreased.
- An increasing impact of growing radiation parameter is showing for the Nusselt number.
- When Prandtl number Pr added then Velocity, Concentration and Temperature profile affected, if Pr increased then all profiles decreased.

References

1. Abo-Dahab, S.M., Abdelhafez, M.A., Mebarek-Oudina, F., Bilal, S.M.: MHD Casson nanofluid flow over nonlinearly heated porous medium in presence of extending surface effect with suction/injection. *Indian J. Phys.* **95**(12), 2703–2717 (2021). <https://doi.org/10.1007/s12648-020-01923-z>
2. Ahmed, S.E., Arafa, A.A.: Impacts of the fractional derivatives on unsteady magnetohydrodynamics radiative Casson nanofluid flow combined with Joule heating. *Phys. Scr.* **95**(9), 095206 (2020)
3. Akinshilo, A.T., Mabood, F., Ilegbusi, A.O.: Heat generation and nonlinear radiation effects on MHD Casson nanofluids over a thin needle embedded in porous medium. *Int. Commun. Heat Mass Transfer* **127**, 105547 (2021)
4. Awais, M., Raja, M.A.Z., Awan, S.E., Shoaib, M., Ali, H.M.: Heat and mass transfer phenomenon for the dynamics of Casson fluid through porous medium over shrinking wall subject to Lorentz force and heat source/sink. *Alex. Eng. J.* **60**(1), 1355–1363 (2021)
5. Bachok, N., Ishak, A., Pop, I.: Boundary-layer flow of nanofluids over a moving surface in a flowing fluid. *Int. J. Therm. Sci.* **49**(9), 1663–1668 (2010)
6. El-Shorbagy, M.A., Eslami, F., Ibrahim, M., Barnoon, P., Xia, W.F., Toghraie, D.: Numerical investigation of mixed convection of nanofluid flow in a trapezoidal channel with different aspect ratios in the presence of porous medium. *Case Stud. Therm. Eng.* **25**, 100977 (2021)

7. Gupta, S., Kumar, D., Singh, J.: Analytical study for MHD flow of Williamson nanofluid with the effects of variable thickness, nonlinear thermal radiation and improved Fourier's and Fick's Laws. *SN Appl. Sci.* **2**(3), 1–12 (2020). <https://doi.org/10.1007/s42452-020-1995-x>
8. Haritha, A., Sarojamma, G.: Radiation effect on heat and mass transfer in MHD flow of a Casson fluid over a stretching surface. *Int. J. Sci. Innov. Math. Res.* **2**(6), 546–553 (2014)
9. Kataria, H.R., Patel, H.R.: Soret and heat generation effects on MHD Casson fluid flow past an oscillating vertical plate embedded through porous medium. *Alex. Eng. J.* **55**(3), 2125–2137 (2016)
10. Kataria, H.R., Patel, H.R.: Radiation and chemical reaction effects on MHD Casson fluid flow past an oscillating vertical plate embedded in porous medium. *Alex. Eng. J.* **55**(1), 583–595 (2016)
11. Khan, M.R., Elkotb, M.A., Matoog, R.T., Alshehri, N.A., Abdelmohimen, M.A.: Thermal features and heat transfer enhancement of a Casson fluid across a porous stretching/shrinking sheet: analysis of dual solutions. *Case Stud. Therm. Eng.* **28**, 101594 (2021)
12. Mabood, F., Khan, W.A., Ismail, A.M.: Multiple slips effects on MHD Casson fluid flow in porous media with radiation and chemical reaction. *Can. J. Phys.* **94**(1), 26–34 (2015)
13. Mondal, M.K., Biswas, N., Manna, N.K., Chamkha, A.J.: Enhanced magnetohydrodynamic thermal convection in a partially driven cavity packed with a nanofluid-saturated porous medium. *Math. Methods Appl. Sci.* (2021)
14. Muthamilselvan, M.: Stagnation point flow of dusty Casson fluid with thermal radiation and buoyancy effects. *J. Appl. Anal. Comput.* **9**(2), 615–627 (2019)
15. Rao, S.R., Vidyasagar, G., Deekshitulu, G.V.S.R.: Unsteady MHD free convection Casson fluid flow past an exponentially accelerated infinite vertical porous plate through porous medium in the presence of radiation absorption with heat generation/absorption. *Mater. Today: Proc.* **42**, 1608–1616 (2021)
16. Rasheed, H.U., Islam, S., Zeeshan, Abbas, T., Khan, J.: Analytical treatment of MHD flow and chemically reactive Casson fluid with Joule heating and variable viscosity effect. *Waves Random Complex Media* 1–17 (2022)
17. Reddy, C.R., Rao, C.V., Surender, O.: Soret, joule heating and hall effects on free convection in a Casson fluid saturated porous medium in a vertical channel in the presence of viscous dissipation. *Procedia Eng.* **127**, 1219–1226 (2015)
18. Reddy, P.B.A.: Magnetohydrodynamic flow of a Casson fluid over an exponentially inclined permeable stretching surface with thermal radiation and chemical reaction. *Ain Shams Eng. J.* **7**(2), 593–602 (2016)
19. Reddy, N.A., Janardhan, K.: Soret and Dufour effects on MHD Casson fluid over a vertical plate in presence of chemical reaction and radiation. *Int. J. Curr. Res. Rev.* **9**, 55–61 (2017)
20. Reddy, S.J., Valsamy, P., Reddy, D.S.: Radiation and heat source/sink effects on MHD Casson fluid flow over a stretching sheet with slip conditions. *J. Math. Comput. Sci.* **11**(5), 6541–6556 (2021)
21. Shehzad, S.A., Hayat, T., Qasim, M., Asghar, S.: Effects of mass transfer on MHD flow of Casson fluid with chemical reaction and suction. *Braz. J. Chem. Eng.* **30**, 187–195 (2013)
22. Sheikh, N.A., Ching, D.L.C., Khan, I., Kumar, D., Nisar, K.S.: A new model of fractional Casson fluid based on generalized Fick's and Fourier's laws together with heat and mass transfer. *Alex. Eng. J.* **59**(5), 2865–2876 (2020)
23. Singh, J., Kumar, D., Baleanu, D.: A hybrid analytical algorithm for thin film flow problem occurring in non-Newtonian fluid mechanics. *Ain Shams Eng. J.* **12**(2), 2297–2302 (2021)
24. Singh, J., Rashidi, M.M., Kumar, D.: A hybrid computational approach for Jeffery-Hamel flow in non-parallel walls. *Neural Comput. Appl.* **31**(7), 2407–2413 (2019)
25. Sumalatha, C., Bandari, S.: Effects of radiations and heat source/sink on a Casson fluid flow over nonlinear stretching sheet. *World J. Mech.* **5**(12), 257 (2015)

26. Tassaddiq, A., Khan, I., Nisar, K.S., Singh, J.: MHD flow of a generalized Casson fluid with Newtonian heating: a fractional model with Mittag-Leffler memory. *Alex. Eng. J.* **59**(5), 3049–3059 (2020)
27. Samrat, S.P., Reddy, M.G., Sandeep, N.: Buoyancy effect on magnetohydrodynamic radiative flow of Casson fluid with Brownian moment and thermophoresis. *Eur. Phys. J. Spec. Top.* **230**(5), 1273–1281 (2021). <https://doi.org/10.1140/epjs/s11734-021-00043-x>
28. Venkata Ramudu, A.C., Anantha Kumar, K., Sugunamma, V., Sandeep, N.: Influence of suction/injection on MHD Casson fluid flow over a vertical stretching surface. *J. Therm. Anal. Calorim.* **139**(6), 3675–3682 (2019). <https://doi.org/10.1007/s10973-019-08776-7>
29. Vijaya, K., Reddy, G.V.R., Makinde, O.D.: Soret effect on MHD Casson fluid flow past a moving vertical plate in the presence of radiation and chemical reaction. In: *Diffusion Foundations*, vol. 26, pp. 86–103. Trans Tech Publications Ltd. (2020)
30. Waqas, M., Farooq, M., Khan, M.I., Alsaedi, A., Hayat, T., Yasmeen, T.: Magnetohydrodynamic (MHD) mixed convection flow of micropolar liquid due to nonlinear stretched sheet with convective condition. *Int. J. Heat Mass Transf.* **102**, 766–772 (2016)



A Comparative Analysis of Different Basis Functions for Constructing Bézier Curves

Harmanjit Kaur^(✉) and Meenu Rani Goyal

School of Mathematics, Thapar Institute of Engineering and Technology,
Patiala 147004, India
{hkaur_phd21,meenu_rani}@thapar.edu

Abstract. In this paper, comparison among four distinct basis functions is conducted to generate trigonometric Bézier curves. The procedure calls for the use of the programming tool MATLAB to plot curves. Cubic trigonometric (T-Bézier) Bézier curves are compared to cubic Bézier curves at first. Same techniques are applied to generalized trigonometric (GT) Bézier curves and generalized blended trigonometric (GBT) Bézier curves to draw the conclusion. The features acquired by Bézier curves are investigated while curves are produced for various intervals. T-Bézier curves were found to be the closest to control polygon. These curves have been employed in a variety of applications, each of which required the use of a separate suitable basis functions. . . .

Keywords: Parametric curves · Bézier curves · Trigonometric Bézier curves · Curve modelling

1 Introduction

When it comes to dealing with the computational elements of geometric objects, the theory of Bézier curves has proven to be a significant turning point in Computer Aided Geometric Design (CAGD). CAGD encourages the use of simple designs, stark colour schemes, and an emphasis on visual functionality in anything from cereal boxes to gallery settings, for which Bézier curves prove to be of great help. Farin [2] gives an introduction to the Bernstein-Bézier methods and delivers topics in an approachable tone. Bézier curves have a wide range of uses in science, engineering, and technology due to their computational simplicity and stability, including networks, animation, computer-aided design systems, robotics, environment design, communications, and many other domains. The curves you've been tracing are Bézier curves if you've ever used vector graphics software like Flash or Inkscape or created Photoshop "paths".

Despite being the most often used option for curve tracing, classic Bézier curves lacked flexibility. It is necessary to adjust control points in order to change the curve's shape, which is a laborious operation when working with complex

curves that have numerous control points. Hence the shape parameters were added to the traditional Bézier curves as a fix for this issue. In [10], Wen-Tao et al. introduced a shape parameter λ ($\lambda \in (-\infty, -2) \cup (-2, 1)$) by an integral approach and researchers started working upon Bézier curves with shape parameters. Without a doubt, the shape parameters made it possible to change the curve's shape without changing the control points. However, even with these specifications, several of the shapes could not be drawn using Bézier curves. In order to support the curve tracing of shapes like helix, cycloid, ellipses, and other circular arcs, a switch to trigonometric Bézier curves with shape parameters occurred. To study the importance of these trigonometric Bézier curves, one can refer to [3]. Bézier-variant of Durrmeyer modification of the Bernstein operators has been studied by Tuncar et al. in [1]. The authors used usual modulus of continuity to examine the rate of approximation. Kajla et al. presented the Bézier variant of Srivastava-Gupta operators in [6] and Bézier variant of Bernstein-Durrmeyer type operators in [7] and studied direct approximation theorem corresponding to Ditzian-Totik modulus of smoothness.

In 2009, Han et al. [4] introduced cubic trigonometric Bézier curves with two shape parameters parallel to classical cubic Bézier curves. The authors concluded that it better approximated the shapes as compared to cubic Bézier curves and successfully represented ellipse. In [5], the shape analysis of the basis functions proposed in [4] has been illustrated by substituting $\mu = \lambda$. As the study of these curves gained pace, numerous researchers stepped up to introduce different trigonometric Bernstein like basis functions with shape parameters varying over different intervals. Maqsood et al. in [8,9] generalized the trigonometric Bézier curves using recursive technique and introduced two shape parameters. In this paper, we have compared the cubic Bézier curves with the Bézier curves formed corresponding to the basis functions suggested in [4,8,9].

The need to assess the accuracy, computational complexity and ability to better approximate the curves leads to the necessity for a direct comparison of cubic Bézier curves and trigonometric Bézier curves corresponding to varied basis functions. Each basis function is compared in both a simple and a complex figure construction to ascertain its benefits and drawbacks. To the writers' knowledge, this kind of comparison has never been made, hence it can be regarded as novel. The paper is organized in a manner that Sect. 2 gives a summary of the basis functions that are being thought about. Section 3 covers the mechanics of how these curves are applied. The final section compares distinct bases with an emphasis on the variations between these methods.

2 Theoretical Foundation

The fundamentals of these definitions are well-known, however to make this article self-sufficient, a number of recalls have been added.

2.1 Bézier Curves

[2] A Bézier curve is defined as a parametric curve which forms the basis of the Bernstein polynomials. Bézier curve of degree n , on an interval $[0,1]$ is defined by:

$$s(t) = \sum_{i=0}^n B_{i,n}(t)P_i, \quad t \in [0, 1]. \tag{2.1}$$

Coefficients P_i represent the control points and $B_{i,n}(t)$ are the Bernstein basis polynomials given by:

$$B_{i,n}(t) = \binom{n}{i} t^i (1-t)^{n-i}, \tag{2.2}$$

where $\binom{n}{i} = \frac{n!}{i!(n-i)!}$ and $i = 0, 1, \dots, n$. The polynomials $B_{i,n}(t) \in P_n$, $i = 0, 1, \dots, n$, where P_n denotes the space of all polynomials of degree at most n and $B_{i,n}(x) = 0$ if $i < 0$ or $i > n$. The cubic Bézier curve is obtained for $n = 3$ in Eq. (2.1). The polygon formed by connecting the sequence of control points is known as control polygon.

2.2 Cubic Trigonometric Bézier Curves

Han et al. [4] in 2009, developed a basis for cubic trigonometric Bézier curves, parallel to cubic Bézier curves.

Definition 1. [4] For two arbitrarily selected real values of λ and μ , where $\lambda, \mu \in [-2, 1]$; the following four functions of $t \in [0, 1]$; are defined as cubic trigonometric Bézier (i.e. T-Bézier) basis functions with two shape parameters λ and μ :

$$\left\{ \begin{array}{l} b_0(t) = (1 - \sin \frac{\pi}{2}t)^2 (1 - \lambda \sin \frac{\pi}{2}t), \\ b_1(t) = \sin \frac{\pi}{2}t (1 - \sin \frac{\pi}{2}t) (2 + \lambda - \lambda \sin \frac{\pi}{2}t), \\ b_2(t) = \cos \frac{\pi}{2}t (1 - \cos \frac{\pi}{2}t) (2 + \mu - \mu \cos \frac{\pi}{2}t), \\ b_3(t) = (1 - \cos \frac{\pi}{2}t)^2 (1 - \mu \cos \frac{\pi}{2}t). \end{array} \right. \tag{2.3}$$

For $\lambda = \mu = 0$, the basis functions are quadratic trigonometric polynomials. For $\lambda, \mu \neq 0$, the basis functions are cubic trigonometric polynomials. Corresponding to the above mentioned basis functions, cubic trigonometric Bézier curves are defined as:

$$r(t) = \sum_{i=0}^n b_i(t)P_i, \quad t \in [0, 1], \quad \lambda, \mu \in [-2, 1]. \tag{2.4}$$

Coefficients P_i represent the control points and $b_i(t)$ are the basis polynomials as defined in Eq. (2.3).

2.3 Properties of T-Bézier Curves

The T-Bézier curves satisfy the following properties which have been listed by Han et al. [4].

1. End point interpolation: The T-Bézier curve passes through the initial and final control points i.e.

$$\begin{aligned} r(0) &= P_0 \\ r(1) &= P_3 \end{aligned}$$

Here P_0 & P_3 are initial and final points respectively.

2. Convex hull property: The curve formed with the help of control points assigned, will always lie within the convex hull of the control polygon.

3. Geometric in-variance: The shape of the T-Bézier curve doesn't depend upon the coordinates chosen, i.e. the following equations are satisfied:

$$r(t; P_0 + v, P_1 + v, P_2 + v, P_3 + v) = r(t; P_0, P_1, P_2, P_3) + v.$$

4. Symmetry: $b_i(t; \lambda, \mu) = b_{3-i}(1 - t; \lambda, \mu)$ for $i = 0, 1, 2, 3$.

5. Derivative at the end points: T-Bézier curves at end points are given by:

$$\begin{cases} r'(0) = \frac{\pi}{2}(\lambda + 2)(P_1 - P_0), \\ r'(1) = \frac{\pi}{2}(\mu + 2)(P_3 - P_2), \end{cases} \tag{2.5}$$

$$\begin{cases} r''(0) = \frac{\pi^2}{2}(2\lambda + 1)(P_1 - P_0) + (P_2 - P_1), \\ r''(1) = \frac{\pi^2}{2}(2\mu + 1)(P_3 - P_2) + (P_2 - P_1), \end{cases} \tag{2.6}$$

$$\begin{cases} r'''(0) = \frac{\pi^3}{8}(5\lambda - 2)(P_1 - P_0), \\ r'''(1) = \frac{\pi^3}{8}(5\mu - 2)(P_3 - P_2), \end{cases} \tag{2.7}$$

3 Composition of T-Bézier Curves

In order to compose two T-Bézier curves, following conditions of continuity need to be followed. Let

$$\begin{aligned} r(t) &= \sum_{i=0}^3 b_i(t) * P_i, t \in [0, 1], \lambda, \mu \in [-2, 1] \\ \text{and} \\ s(t) &= \sum_{i=0}^3 b_i(t) * Q_i, t \in [0, 1], \lambda, \mu \in [-2, 1], \end{aligned} \tag{3.1}$$

where P_i and Q_i are control points for the T-Bézier curves $r(t)$ & $s(t)$ respectively and $b_i(t)$ represent the basis functions.

Also, we have

$$r(0) = P_0, r(1) = P_3$$

and

$$s(0) = Q_0, s(1) = Q_3$$

where p_0 & q_0 are initial control points of the first curve $r(t)$ and second curve $s(t)$ respectively and P_3 & Q_3 are final control points of the first curve $r(t)$ and second curve $s(t)$ respectively.

3.1 Parametric Continuity Constraints of T-Bézier Curves

In this section, we have worked upon the required parametric continuity constraints.

Theorem 3.1: The necessary and adequate constraints for parametric continuity between two T-Bézier curves as defined in Eq. (3.1) are given by:

1. Conditions for C^0 continuity: The value of first curve at “ $t = 1$ ” must be equal to the value of second curve at “ $t = 0$ ” *i.e.* $r(1) = s(0)$. Which means that beginning of the second curve marks the ending of the first curve. Since $r(1) = P_3$ and $s(0) = Q_0$ due to the end point interpolation property of T-Bézier curves, this leads to the constraint for C^0 continuity as:

$$Q_0 = P_3 \tag{3.2}$$

2. Conditions for C^1 continuity: Along with the constraints of C^0 continuity, the curve has to follow additional condition that the 1^{st} derivative of first curve at “ $t = 1$ ” must be equal to the 1^{st} derivative of the second curve at “ $t = 0$ ” *i.e.* $r(1) = s(0)$ and $r'(1) = s'(0)$. Thus, we get the conditions for C^1 continuity as:

$$\begin{cases} Q_0 = P_3 \\ Q_1 = P_3 + \frac{\mu+2}{\lambda+2}(P_3 - P_2) \end{cases} \tag{3.3}$$

3. Conditions for C^2 continuity: C^2 continuity provides a smooth transition between the curves by flattening them at the point of confluence. These constraints are obtained by using $r(1) = s(0)$, $r'(1) = s'(0)$ and $r''(1) = s''(0)$ leading to the following conditions:

$$\begin{cases} Q_0 = P_3 \\ Q_1 = P_3 + \frac{\mu+2}{\lambda+2}(P_3 - P_2) \\ Q_2 = P_3 + (P_2 - P_1) + \frac{4\mu-3\lambda+2}{\lambda+2}(P_3 - P_2) \end{cases} \tag{3.4}$$

3.2 GT-Bézier Curves

Maqsood et al. in 2020, introduced new basis functions for trigonometric Bézier curves as defined below.

Definition 2. [8] For $\alpha, \beta \in [-1, 1]$ and $z \in [0, 1]$, the functions

$$\begin{cases} w_{0,2}(z) = (1 - \sin(\frac{\pi}{2}z))(1 - \alpha \sin(\frac{\pi}{2}z)), \\ w_{1,2}(z) = (1 - w_{0,2}(z) - w_{2,2}(z)), \\ w_{2,2}(z) = (1 - \cos(\frac{\pi}{2}z))(1 - \beta \cos(\frac{\pi}{2}z)), \end{cases} \tag{3.5}$$

are called the second order GT-basis functions. In order to define basis function $w_{i,m}(z)$ ($i = 0, 1, \dots, m$) for degree $m \geq 3$, recursive technique has been used as below:

$$w_{i,m}(z) = (1 - \sin(\frac{\pi}{2}z))w_{i,m-1}(z) + \sin(\frac{\pi}{2}z)w_{i-1,m-1}(z), \tag{3.6}$$

where $w_{i,m}(z) = 0$ when $i = -1$ or $i > m$. For given control points P_i , the curves

$$S(z) = \sum_{i=0}^n w_{i,m}(z)P_i, \quad z \in [0, 1], \alpha, \beta \in [-1, 1], \tag{3.7}$$

are termed as the GT-Bézier curves of order m .

3.3 GBT-Bézier Curves

The basis functions formulated in [8] were further improved by blending the trigonometric and polynomial functions.

Definition 3. [9] For $\mu, \nu \in [-1, 1]$ and $z \in [0, 1]$, the functions

$$\begin{cases} f_{0,2}(z) = (1 - \sin(\frac{\pi}{2}z))(1 - \mu \sin(\frac{\pi}{2}z)), \\ f_{1,2}(z) = (1 - f_{0,2}(z) - f_{2,2}(z)), \\ f_{2,2}(z) = (1 - \cos(\frac{\pi}{2}z))(1 - \nu \cos(\frac{\pi}{2}z)), \end{cases} \tag{3.8}$$

are called the second order GBT-basis functions. Basis function $f_{i,m}(z)$ ($i = 0, 1, \dots, m$) for degree $m \geq 3$ is defined by using recursive technique as below:

$$f_{i,m}(z) = (1 - z)f_{i,m-1}(z) + zf_{i-1,m-1}(z), \tag{3.9}$$

where $f_{i,m}(z) = 0$ when $i = -1$ or $i > m$. Corresponding to these basis functions for the control points Q_i , GBT-Bézier curves of degree m are defined as follows:

$$F(z) = \sum_{i=0}^n f_{i,m}(z)Q_i, \quad z \in [0, 1], \alpha, \beta \in [-1, 1]. \tag{3.10}$$

3.4 Properties

The classical, cubic trigonometric, generalized trigonometric and generalized blended trigonometric Bézier curves, these all satisfy the following properties:

1. Geometric in-variance
2. Convex hull property
3. Symmetry
4. End point interpolation

To study these properties and continuity conditions in detail, readers can refer to [4, 8, 9].

4 Comparative Analysis

This section deals with the formations of shapes by comparing the curves generated by using different bases. In figure [1 - 5], T-Bézier ($\lambda = \mu = 1$), GT-Bézier ($\alpha = \beta = 1$), GBT-Bézier ($\mu = \nu = 1$) and cubic Bézier curves are represented by the colour red, black, blue and green respectively.

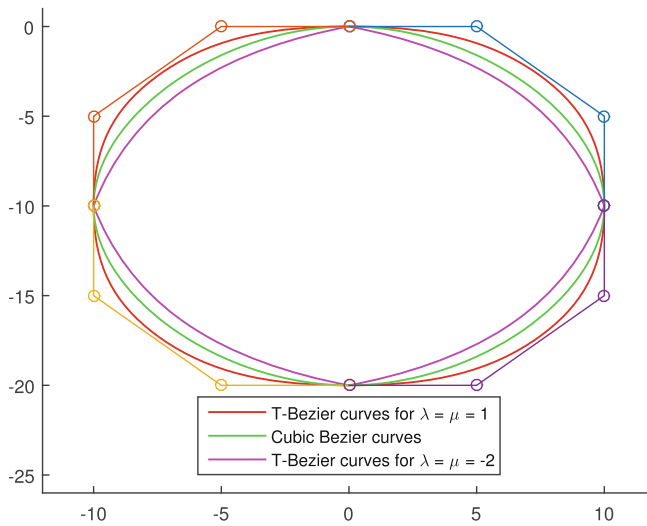


Fig. 1. Comparison between cubic Bézier curves and T-Bézier curves

4.1 Cubic Bézier Curves vs Cubic Trigonometric Bézier Curves

Figure 1 is generated by joining set of four arcs to get the final result. Red colour indicates the T-Bézier curves, which are closer to the control polygon as compared to the cubic Bézier curves in green colour. It is to be observed that T-Bézier curves can show variation in the shape just by altering the values of the

parameter. Magenta colour is used to trace the curves for $\lambda = \mu = -2$ and hence tracing generating the curves for the extreme values of $\lambda, \mu \in [-2, 1]$. The curves thus formed, interpolate at the end points and verify the convex hull property graphically.

4.2 Cubic Bézier Curves vs Other Basis Functions

We can observe a particular behaviour of the curves through Fig. 2. Four different sets of curves are composed together, corresponding to four bases functions. Here the colour red, black, blue and green indicate T, GT, GBT and cubic Bézier curves respectively. In Fig. 2(a) the control polygons ABCD, DEFG, GHID, DJKA form the corresponding set of four curves in the order mentioned. It is to be noted that as we move from initial point “A” to second control point “B” of control polygon ABCD, maximum pull is demonstrated by T-Bézier curves. Contrary to this, GT-Bézier curves are pulled towards the third control point “C”, exceeding T-Bézier curves as we approach the last control point “D”. Similar conduct is shown by the curves for control polygons DEFG, GHID and DJKA. Figure 2(b) shows how the spiral pattern formation looks once the control polygons are removed.

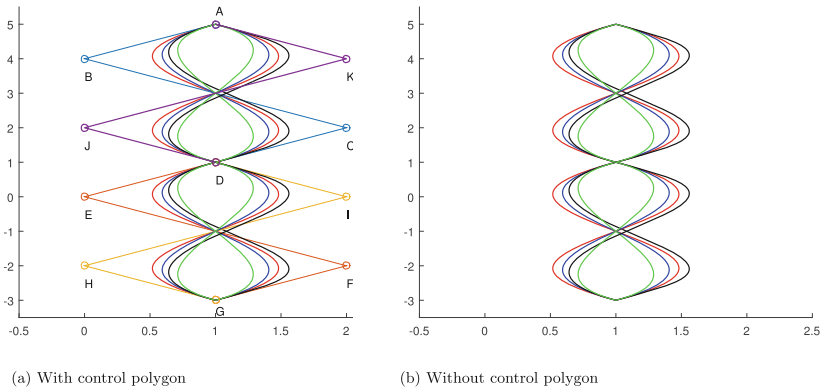


Fig. 2. Spiral patterns

Figure 3(a)-(d) represent the formation of a fish, using basis functions taken under account. It is interestingly observed that T-Bézier curves (in red colour) are closest to the control polygon ABCD only till the mid of the segment BC. As we approach towards the third control point, which in this case is “C”, GT-Bézier curves move closer to the control polygon once we cross the mid of segment BC as compared to the remaining curves. Similarly, for the control polygon EFGH the curves traced corresponding to it in Fig. 3(a) are closest to the control polygon for T-Bézier until the curve approaches the third point “G” and GT-Bézier curves are closer to the segment of the control polygon EFGH that approximates tail of the fish.

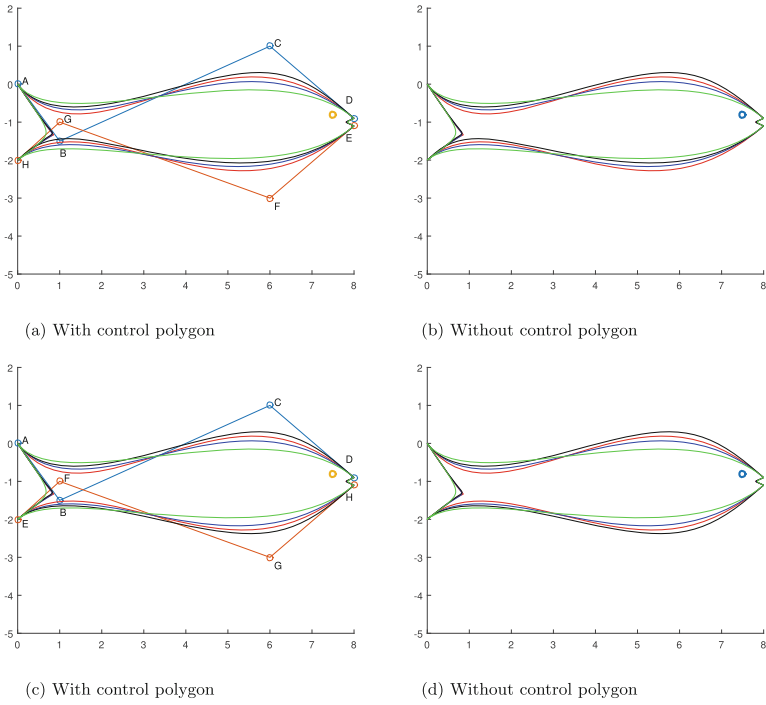


Fig. 3. Formation of a fish

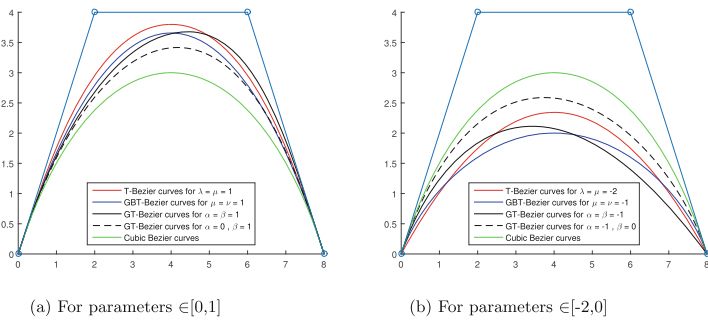


Fig. 4. Variation of parameters

Where as in Fig. 3(d), the orientation of the curve is reversed (left to right) and hence the tail is better approximated by the T-Bézier curves. GT-Bézier curves are closer to the control polygon as compared to the rest, for the segment beyond the mid of control polygon EFGH in Fig. 3(d). Therefore, we conclude that the cubic GT-Bézier curves are the most suitable when the shape to be modeled, requires higher pull towards the second last point of the control poly-

gon. On the other hand, T-Bézier curves supersede the cubic Bézier curves if $\alpha = 0$ and $\beta \in [-1, 1]$. Figure 4(a) can be referred for the same.

Figure 4 demonstrates the impact of changing parameters. We extract from Fig. 4(b) that the shapes concerning flattened curves at the conjunctures can be traced by using GBT-Bézier curves for lower values of shape parameters. As we set $\beta = -1$ and $\alpha \in [-1, 1]$, it can be seen that the most flattened arc is provided by GBT-Bézier curve and hence making it more suitable for circular shapes.

5 Conclusion

It is evident from Fig. 5 that basis functions suggested by Han et al. in [4] approximate the curves better as compared to the remaining bases.

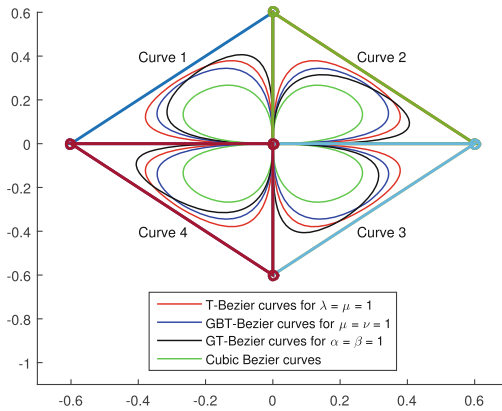


Fig. 5. Comparison between cubic Bézier curves formed by using different basis functions

Different basis functions have been used to compare the floral formation of cubic Bézier curves. To indicate cubic Bézier curves, green colour is used. Black and blue colours represent the basis functions formulated in [8,9] respectively. To trace the curves formed by using the basis functions suggested in [4], red colour has been used. It can be seen that the curves are closest to the control polygon for the basis formulated in [4]. Although GT-Bernstein basis [8] exceeds T-Bézier curves after a certain stage for $\alpha > 0$, but the long-range impact of [4] depicts the curves more effectively. Hence a recursive technique thus formulated to generate trigonometric curves of higher order will give better approximated curves, improve the computational time and reduce the cost of algorithms.

On the top of that, T-Bézier curves have identical structural formation with classical cubic Bézier curves. Therefore, adapting T-Bézier curve to a CAD/CAM system that already uses the cubic Bézier curves becomes an easy task. The parametric and geometric continuity conditions can be developed accordingly, to combine multiple curves of higher orders for constructing complex structures.

The only drawback, identified till now to this technique would be its inability to form curves of degree two. Whereas this was not the case with other bases under consideration since the recursive formula depends up on the basis functions of degree two.

References

1. Acar, T., Agrawal, P.N., Neer, T.: Bézier variant of the Bernstein-Durrmeyer type operators. *Results Math.* **72**(3), 1341–1358 (2017). <https://doi.org/10.1007/s00025-016-0639-3>
2. Farin, G.E., Farin, G.: *Curves and Surfaces for CAGD: A Practical Guide*. Morgan Kaufmann, Burlington (2002)
3. Hoschek J., Lasser D.: *Fundamentals of Computer Aided Geometric Design*. AK Peters, Wellesley, MA, translated by L.L. Schumaker (1993). <http://113.161.98.146/jspui/handle/123456789/299>
4. Han, X.A., Ma, Y., Huang, X.: The cubic trigonometric Bézier curve with two shape parameters. *Appl. Math. Lett.* **22**(2), 226–231 (2009). <https://doi.org/10.1016/j.aml.2008.03.015>
5. Han, X.A., Huang, X., Ma, Y.: Shape analysis of cubic trigonometric Bézier curves with a shape parameter. *Appl. Math. Comput.* **217**(6), 2527–2533 (2010). <https://doi.org/10.1016/j.amc.2010.07.065>
6. Kajla, A.: On the Bézier variant of the Srivastava-Gupta operators. *Constr. Math. Anal.* **1**, 99–107 (2018). <https://doi.org/10.33205/cma.465073>
7. Kajla, A., Acar, T.: Bézier-Bernstein-Durrmeyer type operators. *RACSAM* **114**(1), 1–11 (2020). <https://doi.org/10.1007/s13398-019-00759-5>
8. Maqsood, S., Abbas, M., Hu, G., Ramli, A.L.A., Miura, K.T.: A novel generalization of trigonometric Bézier curve and surface with shape parameters and its applications. *Math. Probl. Eng.* **2020**, 1–25 (2020). <https://doi.org/10.1155/2020/4036434>
9. Maqsood, S., Abbas, M., Miura, K.T., Majeed, A., Iqbal, A.: Geometric modeling and applications of generalized blended trigonometric Bézier curves with shape parameters. *Adv. Differ. Equ.* **2020**(1), 1–18 (2020). <https://doi.org/10.1186/s13662-020-03001-4>
10. Wen-tao, W., Guo-zhao, W.: Bézier curves with shape parameter. *J. Zhejiang Univ.-Sci. A* **6**(6), 497–501 (2005). <https://doi.org/10.1631/jzus.2005.A0497>



Study of Copper-Water Nanofluid Flow over an Isothermal Moving Sheet

Susheela Chaudhary^(✉)

Department of Mathematics, Shri Kalyan Rajkiya Kanya Mahavidyalaya, Sikar 332001, India
susheelamaths@gmail.com

Abstract. Subscription of copper–water nanofluid flow over an isothermal moving sheet has been inspected. Standard models of spherical, cubic, tetrahedron, cylindrical and lamina shapes of nanoparticle have been taken into consideration. Utilizing similarity transformation, boundary layer equations of the problem reduce to a set of nonlinear equations. Numerical solutions are achieved by implementing the MATLAB’s boundary layer problem solver (bvp4c). Consequences of relevant specifications on velocity and temperature have been compared graphically, while the influence on heat flux and shear stress has been collated in tables. Remarkable managing parameters of the problem are moving parameters, sphericity and shape of copper nanoparticles. It is noticeably detected that velocity improves with accrue in λ and reduces with ϕ . Temperature increases with fall off λ and rises with ϕ . The temperature continuously increases with nanoparticle shape changes from sphere to regular hexahedron to the tetrahedron, then further from tetrahedron to cylinder, and finally to lamina.

Keywords: Copper–water · Nanofluid · Isothermal · Moving Sheet

1 Introduction

Nanofluid is a scientific term of fluids containing ultrafine nanoparticles in a base fluid. The nanoparticle is usually distinguished as a particle with a diameter smaller than 100 nm. Nanofluid is encouraging in various applications, and the production depends on the dispersion and stability of nanoparticles. Nanoparticles are predominantly carbon nanotubes, metal oxides, and metal carbides made of metals. Ethylene glycol, oils, and water are popular base fluids. Nanofluid flow problems enhance an exciting theme to its many applications in the field of industrial and biomedical; the development of energy-efficient, lower thermal conductivity is the primary process of controlling heat transfer fluids. Choi [1] estimated the potential benefits of nanofluids and presented the thermal conductivity of nanofluids with nanoparticles. Its wide-ranging application in industrial and engineering was the attention of many scientific communities. Xuan and Li [2] introduced the thermal conductivity of nanofluids with heat transfer and used a hot-wire instrument to calculate nanofluids’ thermal conductivity with attached copper nanophase powders. Chein and Chuang [3] studied microchannel heat sink (MCHS) presentation by applying nanofluids experimentally. For low flow rate variations, in accord with the

theoretical forecast, on other hand, wall temperature is only partially admitted for high flow rate. Due to enormous applications such as heat exchanger technology, industrial cooling, computer technology, geothermal energy storage, and next-generation solar film collectors, nanofluids attracted the attention of researchers. Part of popular explorations regarding nanofluids is done by various researchers such as Rana and Bhargava [4], Pal and Mandal [5], Vanaki and Mohammed [6], Reddy and Chamkha [7], Gupta et al. [8], and Chaudhary and Kanika [9]. Nanofluid flow has become a hot issue for researchers due to its numerous applications in the pharmaceutical task, food processing, hybrid-powered engines, biological materials, nuclear reactor coolant, and space technology. Medical technologies acting as cancer therapy and safer surgery by cooling are useful applications of nanofluids. Recently, Mishra et al. [10] worked on the explorations with temperature-dependent heat source related to MHD nanofluid flow, and Chetteti and Srivastav [11] determined nanofluid flow over the vertical frustum of a cone.

Sakiadis [12] was the first to examine boundary layer flow behavior on moving solid surface. Further, Mahmoud and Mahmoud [13] extended the work and obtained a numerical solution of MHD boundary layer flow and compared analytical solutions with numerical solutions. Chaudhary and Kumar [14] considered MHD boundary layer flow over a continuously moving flat plate. In the polymer industry, the extrusion of plastic sheets, lamination and melt spinning processes, and spinning of fibers are some critical applications of this concept. Chaudhary and Choudhary [15] gave an interesting analysis of MHD boundary layer flow over a flat surface. Due to notable applications in a different area, a fractional model of Casson fluid with heat and mass transfer was developed by Tassaddiq et al. [16] and Sheikh et al. [17]. The problems of nanofluid flow with stretchable plates have consideration by several researchers; one of them is Chaudhary and Kanika [18]. Yousef et al. [19] recently studied nanofluid flow in porous medium. Malvandi et al. [20] observed thermodynamic fluid flow over a moving plate.

The novelty of present survey is to draw out the above research work by applying nanofluids and examining different shapes of nanoparticles in fluid nature. The current research work gives out original studies not published out to the best of author's knowledge.

2 Mathematical Analysis

Consider a two-dimensional boundary layer viscous incompressible copper-water nanofluid flow with numerous nanoparticle shapes over a moving sheet. The physical model is displayed in Fig. 1. Assume x -axis is onwards moving sheet, y -axis is at right angles to it and restricted flow area is $y > 0$. The moving sheet has velocity U_w and the free stream velocity U_∞ is taken as positive constant ($U_\infty > 0$). Along with $U_w > 0$ or $U_w < 0$ implies the sheet is moving in the positive x -direction or in the negative x -direction, respectively. Suppose, wall temperature T_w is constant and temperature of the nanofluid far away from the sheet is T_∞ such that $T_w > T_\infty$. The governing equations under these assumptions are exhibit as

$$\frac{\partial u}{\partial x} + \frac{\partial v}{\partial y} = 0 \quad (1)$$

$$\left(\frac{1}{\nu_{nf}}\right)\left(u\frac{\partial u}{\partial x} + v\frac{\partial v}{\partial y}\right) = \frac{\partial^2 u}{\partial y^2} \tag{2}$$

$$\left(\frac{1}{\alpha_{nf}}\right)\left(u\frac{\partial T}{\partial x} + v\frac{\partial T}{\partial y}\right) = \frac{\partial^2 T}{\partial y^2} \tag{3}$$

with boundary conditions

$$\begin{aligned} y = 0 & : u = U_w, v = 0, T = T_w \\ y \rightarrow \infty & : u \rightarrow U_\infty, T \rightarrow T_\infty \end{aligned} \tag{4}$$

The subscript *nf* mean features of nanofluid, *u* and *v* are flow components of velocity in *x*- axes direction and *y*- axes direction, respectively, $\nu (= \mu\rho^{-1})$ is the kinematic viscosity, $\alpha \{= \kappa(\rho C_p)^{-1}\}$ is the thermal diffusivity, μ is the coefficient of viscosity, ρ is the density, κ is the thermal conductivity and C_p is the specific heat at constant pressure, *T* is the nanofluid temperature.

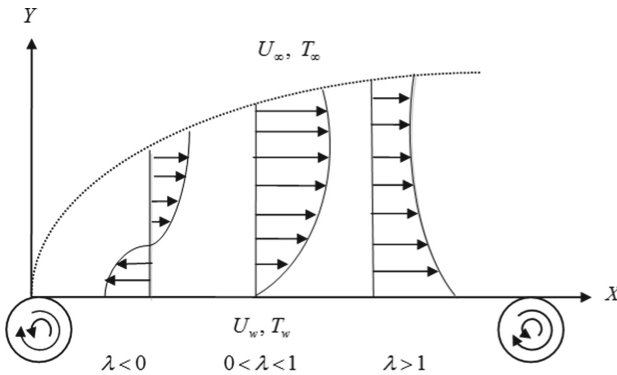


Fig. 1. Flow geometry.

Table 1 shows thermophysical properties of base fluid water and copper nanoparticles (Oztop and Abu-Nada [21]). Table 2 presented the thermophysical models for density, viscosity, heat capacity (ρC_p) and thermal conductivity of nanofluid (Mohammad and Kandasamy [22]). In this table the subscripts *f* and *s* are used for base fluid water and solid nanoparticles, respectively, ϕ is the solid volume fraction, $m (= 3\zeta^{-1})$ is the experimental shape factor and ζ is the sphericity of the particles. In the present investigation considered 5 different copper nanoparticles shapes. The values of sphericity of copper nanoparticles along with corresponding shapes (Lin et al. [23]) are illustrated in Table 3. The value of sphericity of the particle is one for sphere and less than one for non-uniform shapes.

Table 1. Thermophysical properties.

Themophysical properties	Base fluid Water	Copper Nanoparticles
$\kappa (W/mK)$	0.613	400
$\rho (Kg/m^3)$	997.1	8933
$C_p (J/Kg K)$	4179	385

Table 2. Thermophysical models.

Physical Quantities	Nanofluid
ρ	$\rho_{nf} = (1 - \phi) \left[\rho_f + \left\{ \frac{\phi}{(1-\phi)} \right\} \rho_s \right]$
μ	$\mu_{nf} = \mu_f (1 - \phi)^{-5/2}$
ρC_p	$(\rho C_p)_{nf} = (\rho C_p)_f - \phi \left[(\rho C_p)_f - (\rho C_p)_s \right]$
κ	$\kappa_{nf} = \left[\frac{(m-1) \{ \kappa_f - \phi (\kappa_f - \kappa_s) \} + \kappa_s}{(m-1) \kappa_f + \phi (\kappa_f - \kappa_s) + \kappa_s} \right] \kappa_f$

3 Comparability Variables

Introducing dimensionless stream function (ψ), similarity variable (η) and temperature (T) of nanofluid (Malvandi et al. [20]) given by

$$\left. \begin{aligned} \psi &= \sqrt{(2\nu_f U_\infty x)} F(\eta) \\ \eta &= \sqrt{\left(\frac{U_\infty}{2\nu_f x}\right)} y \\ T &= (T_w - T_\infty)\theta(\eta) + T_\infty \end{aligned} \right\} \quad (5)$$

In Eq. (5), dimensionless quantities F and θ are stream function, and temperature, respectively. Obviously $u = \frac{\partial \psi}{\partial y}$ and $v = -\frac{\partial \psi}{\partial x}$ satisfies Eq. (1). The following nonlinear equations are obtained by using Eq. (5) and the formulation given in Table 2, in Eqs. (2) to (4), we have

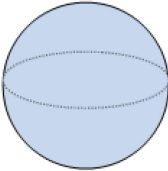
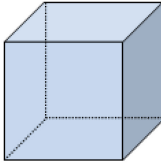
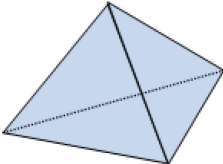
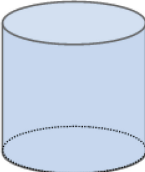

$$F''' + (1 - \phi)^{7/2} \left[1 + \left(\frac{\phi}{1 - \phi} \right) \left(\frac{\rho_s}{\rho_f} \right) \right] FF'' = 0 \quad (6)$$

$$\left(\frac{\kappa_{nf}}{\kappa_f} \right) \theta'' + \text{Pr}(1 - \phi) \left[1 + \left(\frac{\phi}{1 - \phi} \right) \left(\frac{\rho C_p}_s}{\rho C_p}_f \right) \right] F\theta' = 0 \quad (7)$$

boundary conditions

$$\eta = 0 : F = 0, \quad F' = \lambda = \frac{U_w}{U_\infty}, \quad \theta = 1$$

Table 3. Nanoparticle shapes and their sphericity.

Shape	Model	ζ
Sphere		1.0000
Regular Hexahedron		0.8060
Tetrahedron		0.7387
Cylinder		0.4710
Lamina		0.1857

$$\eta \rightarrow \infty : F' \rightarrow 1, \theta \rightarrow 0 \quad (8)$$

Here, primes (') stand for derivative with respect to η , $Pr (= \nu\alpha^{-1})$ is the Prandtl number and λ is the moving parameter (velocity ratio parameter).

4 Manifesto of Investigation

Experimental interested quantities are skin friction coefficient (C_f) and Nusselt number (Nu_x) with surface shear stress $\tau_w \left\{ = \mu_{nf} \left(\frac{\partial u}{\partial y} \right)_{y=0} \right\}$ and surface heat flux

$q_w \left[= - \left\{ \kappa_{nf} \left(\frac{\partial T}{\partial y} \right)_{y=0} \right\} \right]$ are expressed as

$$\left. \begin{aligned} C_f &= \frac{2\tau_w}{\rho_f U_\infty^2} = \left(\frac{2\mu_{nf}}{\rho_f U_\infty^2} \right) \left(\frac{\partial u}{\partial y} \right)_{y=0} \\ Nu_x &= \frac{xq_w}{\kappa_f (T_w - T_\infty)} = - \left\{ \frac{x\kappa_{nf}}{\kappa_f (T_w - T_\infty)} \right\} \left(\frac{\partial T}{\partial y} \right)_{y=0} \end{aligned} \right\} \quad (9)$$

Using Eq. (5) in Eq. (9), obtained the following

$$\left. \begin{aligned} C_f &= \left(\frac{1}{(1-\phi)^{5/2}} \right) \sqrt{\left(\frac{2}{Re_x} \right)} F''(0), \\ Nu_x &= - \sqrt{\left(\frac{Re_x}{2} \right)} \left(\frac{\kappa_{nf}}{\kappa_f} \right) \theta'(0) \end{aligned} \right\} \quad (10)$$

In Eq. (10), $Re_x \left[= \left\{ U_\infty (v_f)^{-1} \right\} x \right]$ is the local Reynolds number, $F''(0)$ is surface shear stress and $\theta'(0)$ is surface heat flux.

5 Validation of Solution Methodology

For based fluid water, keeping the fixed Prandtl number ($Pr = 5.2$), selected values of the velocity ratio parameter, nanoparticle volume fraction, and different shapes of the copper nanoparticles implementing the MATLAB's boundary layer problem solver (bvp4c), achieve the solution of Eqs. (6) and (7) with boundary conditions (8). The finite value of boundary conditions as $\eta \rightarrow \infty = 5$ and $\eta \rightarrow \infty = 6$ occupied for computational with step size $\Delta\eta (= 0.001)$ to carry out a convergence test of 10^{-6} asymptotically. Table 4 presented surface shear stress at $\lambda = 0$ and $\phi = 0$ and compared numerical results with published literature by Yacob et al. [24]. Obtained results and solution methodology used for the present obstacle are accurate.

Table 4. Outcome of $F''(0)$ at $\lambda = 0$ and $\phi = 0$

$F''(0)$	Present studies		Yacob et al. [24]	
	$\eta \rightarrow \infty = 5$	0.46968		0.46960
	$\eta \rightarrow \infty = 6$	0.46960		

6 Results Analysis

Results for particular values of physical quantities of shear stress and heat flux with $Pr = 5.2$ are cataloged in Table 5. It observed that $F''(0)$ reduces for more significant nanoparticle volume fraction and positive velocity ratio parameter. After that, for negative velocity ratio parameter, both λ and $F''(0)$ rise correspondingly. The drag force

utilized by nanofluid on a moving sheet implies a positive sign $F''(0)$, whereas a negative sign indicates the opposite. Also, the Nusselt number dwindles with improvement of volume fraction. In comparison, heat transfer rate is noticed to smaller with increasing moving parameters and sphericity of various shapes of nanoparticles utilized. For each parameter inspected value, the heat flux values are negative.

Table 5. Outcome of $F''(0)$ and $\theta'(0)$ with $Pr = 5.2$ for particular values of physical quantities

Solids shape of nanoparticles	λ	ϕ	$-F''(0)$	$-\theta'(0)$
Sphere	-0.3	0.04	-0.42870	0.33256
	-0.1		-0.54200	0.71417
	0.1		-0.54329	0.98004
	0.5		-0.38900	1.38141
	1.5		0.53764	2.08705
	2.3		1.62270	2.51731
	1.5	0.02	0.48054	2.28881
		0.06	0.49943	2.21465
		0.08	0.52500	2.14817
	0.10	0.53773	2.01217	
Regular Hexahedron		0.04	0.53764	2.02614
Tetrahedron				2.00421
Cylinder				1.87647
Lamina				1.49681

Figures 2, 3, 4, 5 and 6 convey the effect of dominating specification on fluid velocity and temperature. The supervising parameters considered in the problem are the velocity ratio parameter, nanoparticle volume fraction, and numerous shapes of the copper nanoparticles.

Figures 2 and 3 elaborated the effect of λ on $F'(\eta)$ and $\theta(\eta)$, respectively. It is eminent that velocity distribution grow with rising values of λ , while the reverse result is notice on thermal boundary layer. The nanofluid flow is analyzed for different values of velocity ratio parameter such as $\lambda < 0$, $0 < \lambda < 1$ and $\lambda > 1$ as draw in Fig. 1. It is also noteworthy that Fig. 2 has inadequate concurrence with the symbolic boundary layers exhibited in Fig. 1.

Figures 4 and 5 have shown the effects of spherical nanoparticles on velocity and temperature, respectively. Improving solid volume fraction leads to decreasing momentum boundary layer as an outcome of inconvenience in defying nanofluid flow. Nanoparticles push the thermal boundary layer and occur in the gain of the temperature with increased nanoparticle volume fraction. The temperature difference is presented in Fig. 6, determinable by the distinct nanoparticle shapes with the same base fluid. It is distinguished from the graph that the temperature increases with the value of sphericity dwindling or observational shape factor increases.

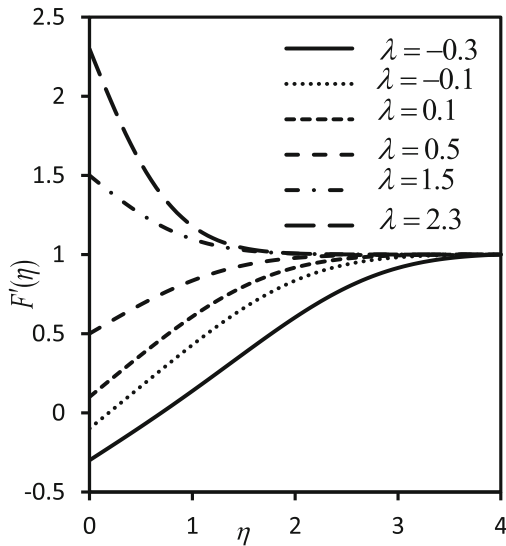


Fig. 2. Influence of λ on velocity $F'(\eta)$ with $m = 3$ and $\phi = 0.04$.

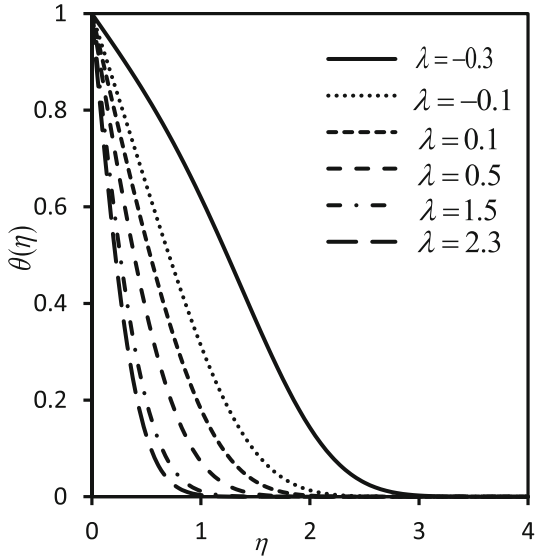


Fig. 3. Influence of λ on temperature $\theta(\eta)$ with $m = 3$, $\phi = 0.04$ and $\text{Pr} = 5.2$.

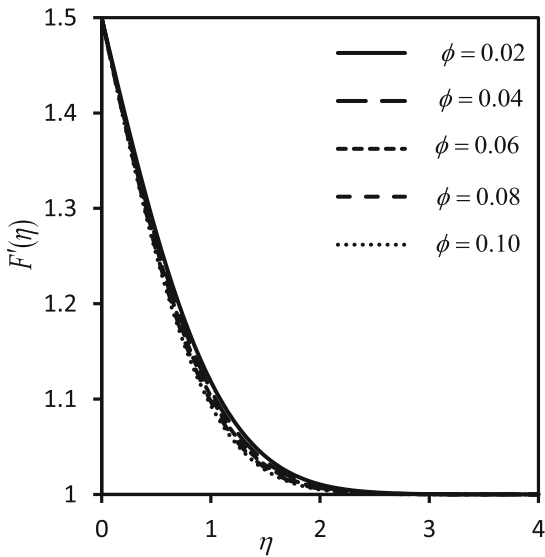


Fig. 4. Influence of ϕ on velocity profiles $F'(\eta)$ with $m = 3$ and $\lambda = 1.5$.

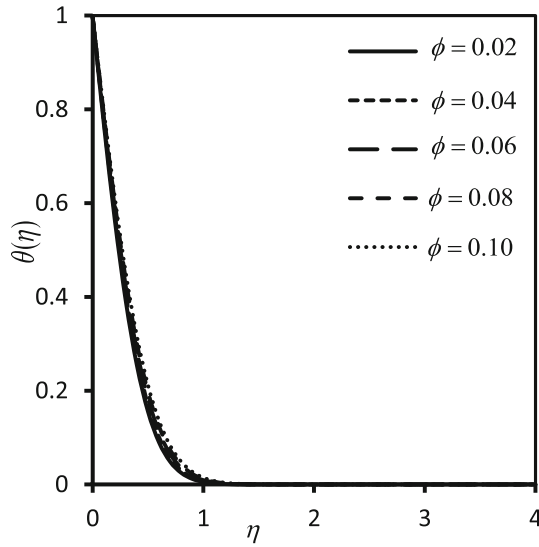


Fig. 5. Influence of ϕ on temperature $\theta(\eta)$ with $m = 3$, $\lambda = 1.5$ and $Pr = 5.2$.

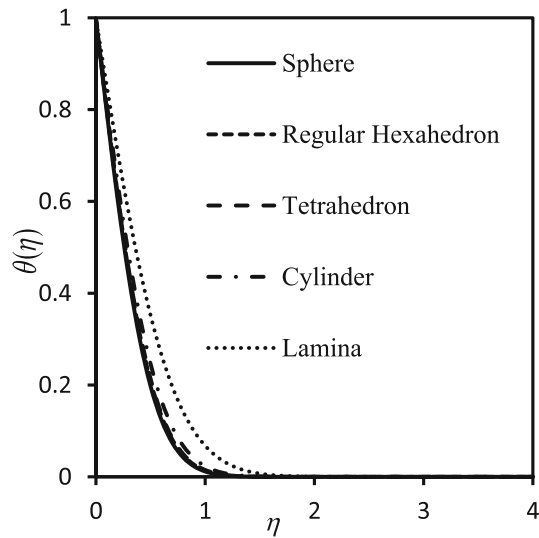


Fig. 6. Influence of nanoparticle shapes on temperature $\theta(\eta)$ with $\lambda = 1.5$, $\phi = 0.04$ and $Pr = 5.2$.

7 Conclusions

The consideration of the flow effects of copper-water nanofluid over an isothermal moving sheet is specified in the module. Utilizing similarity transformation, the governing

equations reduce to a set of ordinary equations. Solving ordinary equations by MATLAB and summarized the numerical results as follows.

- Velocity boundary layer thickness was raised, and thermal boundary layer thickness decreased with increasing moving parameters.
- Step down of the velocity and rise of the temperature with the rising value of solid volume fraction.
- Superior effect found on upgrade nanofluid temperature of nanoparticle-shaped Lamina compared to the rest of nanoparticle shape.
- In the case of $\lambda < 0$, shear stress is raised, while in the case of $\lambda > 0$, shear stress and heat flux rate fell with growing moving parameters.
- Reduce skin friction coefficient and rise of the Nusselt number with increasing value of solid volume fraction.

References

1. Choi, S.U.S.: Enhancing thermal conductivity of fluids with nanoparticles. In: Siginer, D.A., Wang, H.P. (eds.) *Developments and Applications of Non-Newtonian Flows*, vol. 66, pp. 99–105. ASME, New York (1995)
2. Xuan, Y., Li, Q.: Heat transfer enhancement of nanofluids. *Int. J. Heat Fluid Flow* **21**(1), 58–64 (2000)
3. Chein, R., Chuang, J.: Experimental microchannel heat sink performance studies using nanofluids. *Int. J. Therm. Sci.* **46**(1), 57–66 (2007)
4. Rana, P., Bhargava, R.: Numerical study of heat transfer enhancement in mixed convection flow along a vertical plate with heat source/sink utilizing nanofluids. *Commun. Nonlinear Sci. Numer. Simul.* **16**(11), 4318–4334 (2011)
5. Pal, D., Mandal, G.: Influence of thermal radiation on mixed convection heat and mass transfer stagnation-point flow in nanofluids over stretching/shrinking sheet in a porous medium with chemical reaction. *Nucl. Eng. Des.* **273**, 644–652 (2014)
6. Vanaki, S.M., Mohammed, H.A.: Numerical study of nanofluid forced convection flow in channels using different shaped transverse ribs. *Int. Commun. Heat Mass Transf.* **67**, 176–188 (2015)
7. Reddy, P.S., Chamkha, A.J.: Heat and mass transfer characteristics of Al_2O_3 -water and Ag-water nanofluid through porous media over a vertical cone with heat generation/absorption. *J. Porous Media* **20**(1), 1–17 (2017)
8. Gupta, S., Kumar, D., Singh, J.: Analytical study for MHD flow of Williamson nanofluid with the effects of variable thickness, nonlinear thermal radiation and improved Fourier's and Fick's Laws. *SN Appl. Sci.* **2**(3), 1–12 (2020). <https://doi.org/10.1007/s42452-020-1995-x>
9. Chaudhary, S., Kanika, K.M.: Heat generation/absorption and radiation effects on hydromagnetic stagnation point flow of nanofluids toward a heated porous stretching/shrinking sheet with suction/injection. *J. Porous Media* **23**(1), 27–49 (2020)
10. Mishra, P., Acharya, M.R., Panda, S.: Mixed convection MHD nanofluid flow over a wedge with temperature-dependent heat source. *Pramana* **95**(2), 1–12 (2021). <https://doi.org/10.1007/s12043-021-02087-z>
11. Chetteti, R., Srivastav, A.: Numerical study and error estimation in power-law nanofluid flow over vertical frustum of a cone. *Indian J. Phys.* **96**(4), 1167–1179 (2021). <https://doi.org/10.1007/s12648-021-02055-8>

12. Sakiadis, B.C.: Boundary-layer behavior on continuous solid surfaces: I. Boundary-Layer equations for two-dimensional and axisymmetric flow. *Am. Inst. Chem. Eng. J.* **7**(1), 26–28 (1961)
13. Mahmoud, M.A.A., Mahmoud, M.A.E.: Analytical solutions of hydromagnetic boundary-layer flow of a non-Newtonian power-law fluid past a continuously moving surface. *Acta Mech.* **181**(1), 83–89 (2006)
14. Chaudhary, S., Kumar, P.: MHD forced convection boundary layer flow with a flat plate and porous substrate. *Meccanica* **49**(1), 69–77 (2013). <https://doi.org/10.1007/s11012-013-9773-0>
15. Chaudhary, S., Choudhary, M.K.: Finite element analysis of magnetohydrodynamic flow over flat surface moving in parallel free stream with viscous dissipation and Joule heating. *Eng. Comput.* **35**(4), 1675–1693 (2018)
16. Tassaddiq, A., Khan, I., Nisar, K.S., Singh, J.: MHD flow of a generalized Casson fluid with Newtonian heating: a fractional model with Mittag-Leffler memory. *Alex. Eng. J.* **59**(5), 3049–3059 (2020)
17. Sheikh, N.A., Ching, D.L.C., Khan, I., Kumar, D., Nisar, K.S.: A new model of fractional Casson fluid based on generalized Fick's and Fourier's laws together with heat and mass transfer. *Alex. Eng. J.* **59**(5), 2865–2876 (2020)
18. Chaudhary, S., Kanika, K.M.: Galerkin finite-element numerical analysis of the effects of heat generation and thermal radiation on MHD SWCNT–water nanofluid flow with a stretchable plate. *Pramana – J. Phys.* **94**, Article ID 38 (2020)
19. Yousef, N.S., Megahed, A.M., Ghoneim, N.I., Elsafi, M., Fares, E.: Chemical reaction impact on MHD dissipative Casson-Williamson nanofluid flow over a slippery stretching sheet through porous medium. *Alex. Eng. J.* **61**(12), 10161–10170 (2022)
20. Malvandi, A., Hedayati, F., Ganji, D.D.: Thermodynamic optimization of fluid flow over an isothermal moving plate. *Alex. Eng. J.* **52**(3), 277–283 (2013)
21. Oztop, H.F., Abu-Nada, E.: Numerical study of natural convection in partially heated rectangular enclosures filled with nanofluids. *Int. J. Heat Fluid Flow* **29**(5), 1326–1336 (2008)
22. Mohammad, R., Kandasamy, R.: Nanoparticle shapes on electric and magnetic force in water, ethylene glycol and engine oil based Cu, Al₂O₃ and SWCNTs. *J. Mol. Liq.* **237**, 54–64 (2017)
23. Lin, Y., Li, B., Zheng, L., Chen, G.: Particle shape and radiation effects on Marangoni boundary layer flow and heat transfer of copper-water nanofluid driven by an exponential temperature. *Powder Technol.* **301**, 379–386 (2016)
24. Yacob, N.A., Ishak, A., Pop, I.: Falkner-Skan problem for a static or moving wedge in nanofluids. *Int. J. Therm. Sci.* **50**(2), 133–139 (2011)



Thermal Instability of Rivlin-Ericksen Elastico-Viscous Nanofluid Saturated by a Porous Medium with Rotation

Ismail^(✉) and B. S. Bhadauria

Department of Mathematics, Babasaheb Bhimrao Ambedkar University,
Lucknow 226025, India
ismailkoree786@gmail.com

Abstract. The current article examines the thermal instability of a rotating porous layer saturated by a Rivlin-Ericksen elastico-viscous nanofluid using both nonlinear and linear ways. Nonlinear stability analysis is carried out using the truncated Fourier series method while normal mode methodology is utilized to perform to evaluation of linear stability analytically. The outcomes are all displayed graphically. The findings show that the concentration Rayleigh number, Lewis number, and modified diffusivity ratio promote the commencement of convective motion within the system. On the other hand, porosity, Darcy number, and rotation stabilize the system. The variation of the kinematic viscoelasticity parameter is found to have a substantial effect on the heat/mass transfer when Nusselt numbers are evaluated as a function of time. It has been determined that for stationary convection, the Rivlin-Ericksen elastico-viscous nanofluid fluid conducts just like a typical Newtonian nanofluid. The Taylor number affects the behaviour of heat/mass transfer, as increase the value of Taylor number mass and heat transfer decrease in the system, and found that Rivlin-Ericksen elastico-viscous nanofluid delays the commencement of convection.

Keywords: Porous medium · Rivlin-Ericksen nanofluid · rotation · linear and non-linear analysis

Nomenclature

Latin symbols

- (x, y, z) cartesian or euclidian coordinates.
- Da the Brinkman-Darcy number.
- Rn Concentration Rayleigh Number.
- h horizontal layer thickness.
- Va Vadasz Number.
- Le Lewis Number.
- Ra Thermal Rayleigh-Darcy number.

- k_m effective thermal conductivity.
 p pressure. ($kgm^{-1}s^{-2}$)
 Nb Modified Particle-Density Increment.
 Na modified diffusivity ratio.
 g Gravitational acceleration. (ms^{-2})
 Ta Taylor's number.
 Rm Density Rayleigh Number.
 t Time.
 Nu Nusselt Number.
 T Temperature.
 \mathbf{q} Nanofluid velocity.
 s Growth rate of Disturbance.
 a wave number (m^{-1}).
 F Kinematic Viscoelasticity Parameter.
 σ Thermal Capacity Ratio.
 κ Thermal Diffusivity.
 k_1 permeability.
 T_L temperature at the lower wall.
 D_B Brownian diffusion coefficient.
 T_U temperature at the upper wall.
 D_T thermophoretic diffusion coefficient.
 (u, v, w) Velocity Components.

Greek symbols

- ϵ Porosity. ($0 < \epsilon < 1$).
 μ viscosity.
 ρ_f Density of Fluid (kgm^{-3}).
 $(\rho c)_p$ heat capacity in nanoparticles.
 α thermal expansion coefficient.
 ϕ nanoparticle-volume fraction.
 μ' Kinematic Viscoelasticity.
 ρ_p Density of Nanoparticles (kgm^{-3}).
 $(\rho c)_m$ heat capacity in porous medium.

Subscripts and superscripts

- $'$ Non-dimensional Variables.
 \sim Perturbed Quantity.

Operators

$$\nabla^2 = \frac{\partial^2}{\partial x^2} + \frac{\partial^2}{\partial y^2} + \frac{\partial^2}{\partial z^2}$$

1 Introduction

We have observed a significant class of fluid called as non-Newtonian fluids in mechanical areas, which is widely employed due to its practical use. Non-Newtonian fluids, such as pulps, emulsions, aqueous solutions of polyisobutylene and polyacrylamide, etc., are useful as chemical products and raw materials in a variety of industrial processes, which has inspired researchers to investigate at non-Newtonian fluids and the transport mechanisms that move them. Many researcher has worked on ordinary nanofluid to check the behaviour of heat and mass transfer. However, in this manuscript, we wish to find the effect of Rivlin-Ericksen elastico-viscous nanofluid on heat and mass transfer. One of these fluids is Rivlin-Ericksen. Rivlin-Ericksen [1] is a type of elastico-viscous fluid that was the first study to offer a theoretical and rheological model for elastico-viscous fluids. The erratic flow of Rivlin-Ericksen fluid with different cross sections was observed by Srivastva [2] when the pressure gradient is time-dependent and the dust particle dispersion between the channels is uniform. Kumar and Sharma [3] investigate at the Rivlin-Ericksen fluid's thermal instability when both magnetic field and rotation are present. The fluid layer is stabilised by kinematic viscoelasticity, according to Chand and Parkash [5] investigation of the effect of Rivlin-Ericksen fluid's instability due to kinematic viscoelasticity in porous media. Sharma et al. [6] observed the Rivlin-Ericksen fluid's Rayleigh-Taylor instability through a porous medium. Pardeep et al. [7] investigate how a magnetic field affects a rotating Rivlin-Ericksen fluid's thermal instability. Thermal instability was investigated in Sheu [8] by a viscoelastic nanofluid-saturated layer of porous material. Sharma and Rana [9] and Rana and Thakur [10] observed the convection initiation in a Rivlin-Ericksen fluid filling a Brinkman porous medium and heated from below. According to Rana and Chand [11] The thermal instability of Rivlin-Ericksen was investigated. By porous medium nanofluid is saturated, with nanoparticle flow on the borders controlled similarly to temperature. Although Nield and Kuznetsov [12] construct that managing the volume percentage of nanoparticles at the borders could be challenging. As a result, they expand a more practical boundary condition by assuming that the nanoparticle flux value is suitably accommodated and that there is no flux at the plate. The improved model of thermal instability in a porous media was developed by Chand et al. [13] of Rivlin-Ericksen Nanofluid. The thermal instabilities saturated in dracy-Brinkman porous media are observed by Rana et al. [14] of Rivlin-Ericksen nanofluid. Saini and Sharma [15] investigated in a porous medium was vertical throughflow's impact on Rivlin-Ericksen nanofluid. Malleswari [16] when the double diffusion effect and a transverse magnetic field were both present, a vertical plate brimming with porous media was used to test free convective flow. Salawu et al. [17] looked at the Trasient Rivlin-Ericksen fluid recently. Before reaching a steady condition, they noticed a small rise in both heat and momentum.

Choi introduced the concept of nanofluid and developed a nanofluid with excellent thermal conductivity [18]. Nanofluid research has gotten a lot of interest in recent years. They have evolved into modern materials utilised in thermal

engineering, energy conservation, the automotive industry, nuclear reactors, and other fields. Furthermore, nanoparticle suspensions are being used in medicinal applications such as cancer treatment. Choi et al. [19] observed that a modest quantity of (<1% volume fraction) copper (Cu) nanoparticles or carbon nanotubes suspended in ethylene glycol or oil increased the liquid's intrinsically low thermal conductivity by 40% and 150%, respectively. Das et al. [20] revealed a 5%–21% rise in water with nanoparticle diameter (10–20) nm for gold nanoparticles, as well as a 7%–14% increase in effective thermal conductivity. Buongiorno [21] proposed the formulation of convective transport equations in nanofluids. Tzou [22] and Kuznetsov and Nield [23] analysed when a nanofluid layer started convecting. The thermal instability of nanofluids has been investigated by numerous authors, including Agarwal and Bhadauria [26], Bhadauria et al. [27]. Nield and Kuznetsov [28] The Darcy model was utilized to examine natural convection for flow through a porous media containing a nanofluid. Agarwal and Bhadauria [29] for the Brinkman and Darcy models respectively. The same issue of thermal instability for bottom-heavy and top-heavy suspensions in a rotating porous layer saturated by a nanofluid was investigated. When nanofluid is employed, Rashidi et al. [30] research the heat transfer increasing and increases higher heat flux densities. Rawat et al. [31] evaluated the effects of suction and thermal radiation into the flow of silver and copper water nanofluids over a vertical Riga and plate. Garia et al. [32] to compare hybrid nanofluid flow through a wedge and a cone, it was done using the Cattaneo-Christov heat flux model. They observed that heat transfer rises as the thermal time lag increases. Gumber et al. [33] looked into the micropolar nature of hybrid nanofluid flow across a vertically positioned plate in the presence of heat radiation.

A rotating system's fluid flow occurs naturally. In reality, when fluid starts moving, this rotation becomes more pronounced among the fluid particles internally. Rotation therefore exists in fluid flow as a natural phenomenon to some extent. Taylor and Geoffrey [35] presented the experimental notion of the viscous fluid motion in a rotating apparatus. Greenspan [36] has conducted a thorough investigation on the fluid movement in rotating systems. Many researcher such as Pardeep et al. [37], Sunil et al. [38], Kirillov et al. [39] are work with magnetic and rotation. Yadav et al. [40] investigated the magneto-convection in a rotating layer of nanofluid. It is observed by Ramesh et al. [41] the thermal instability in a rotating porous layer of nanofluid contained in a Hele-Shaw cell. Manjula et al. [42] studied the complex ginzburg landau model for an oscillatory convection in a rotating fluid layer, and currently Manjula et al. [43] examined the influence of rotation speed modulation on weak nonlinear Rayleigh-Benard convection.

In this paper, we focus on combine effect of rotation, porous medium on Rivlin-Ericksen elastico-viscous nanofluid. Also, study the linear as well as non-linear (or mass/heat transfer) in the system. Due to the significance of the magnetic field, porous medium, and Non-Newtonian fluid in contemporary society for technical purposes, many works using porous medium, magnetic field, and rotation on Rivlin-Ericksen elastico-viscous nanofluid individually have been presented in the literature. This kind of research is essential if we want to understand

the behaviour of magnetic fields, porous medium and the rotation influence on Rivlin-Ericksen elastico-viscous nanofluid. According to our knowledge, no study that addresses these significant factors concurrently has been conducted in literature.

2 Governing Equations

An elastico-viscous Rivlin-Ericksen nanofluid saturated in a porous layer, the idea of being heated from below and restricted between two horizontal barriers at $z = h$ and $z = 0$ is considered (see Fig. 1). The porous layer rotates with a uniform rotational velocity Ω around the z -axis. It is assumed that the boundary wall is impermeable and perfectly thermally conductive. Force of gravity $\mathbf{g}(0, 0, -g)$ acts on the fluid layer. Temperatures T_U at $z = h$ and T_L at $z = 0$ were used to represent the upper and lower walls, respectively, with $(T_L > T_U)$. The dimensional governing equations in view of the above assumptions are (Chand and Rana [11] and Bhadauria and Agarwal [29]):

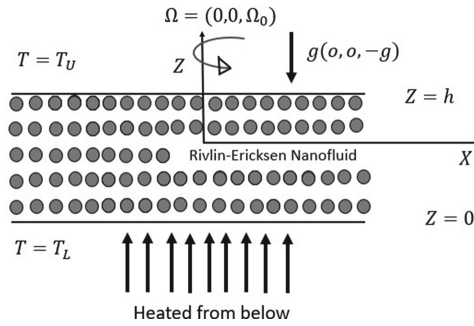


Fig. 1. Schematic diagram

$$\nabla \cdot \mathbf{q} = 0 \tag{1}$$

$$\frac{\rho_f}{\epsilon} \frac{d\mathbf{q}}{dt} = -\nabla p + \mu \nabla^2 \mathbf{q} - \frac{1}{k_1} (\mu + \mu' \frac{\partial}{\partial t}) \mathbf{q} + \frac{2\rho_0}{\epsilon} \mathbf{q} \times \Omega + [\phi \rho_p + (1 - \phi) \rho_f (1 - \alpha(T - T_U))] \mathbf{g} \tag{2}$$

$$(\rho c)_m \frac{\partial T}{\partial t} + (\rho c)_f \mathbf{q} \cdot \nabla T = k_m \nabla^2 T + \frac{D_T}{T_U} \nabla T \cdot \nabla T + \epsilon (\rho c)_p [D_B \nabla \phi \cdot \nabla T] \tag{3}$$

$$\frac{\partial \phi}{\partial t} + \frac{1}{\epsilon} (\mathbf{q} \cdot \nabla) \phi = \frac{D_T}{T_U} \nabla^2 T + D_B \nabla^2 \phi \tag{4}$$

where $\frac{d}{dt} \equiv \frac{\partial}{\partial t} + \frac{1}{\epsilon}(\mathbf{q} \cdot \nabla)$

where, q represent the velocity, g is gravity, μ denotes the viscosity, The volumetric fraction of the nanoparticles is represented by ϕ , ρ_p denotes the density of nanoparticles, ρ_f denotes the fluid density, μ' represent the kinematic viscoelasticity, ϵ is porosity, $(\rho c)_m$ is the heat capacity of porous medium, α denotes the thermal expansion, $(\rho c)_p$ is the volumetric heat capacity of nanoparticles, k_1 is medium of permeability and k_m is the thermal conductivity of the porous medium.

The above governing Eqs. (1)–(4) are governed by the following boundary criteria (Chand et al. [34]):

$$\left. \begin{aligned} w = 0, T = T_L, \quad D_B \frac{\partial \phi}{\partial z} + \frac{D_T}{T_U} \frac{\partial T}{\partial z} = 0, \quad \text{at } z = 0 \\ w = 0, T = T_U, \quad D_B \frac{\partial \phi}{\partial z} + \frac{D_T}{T_U} \frac{\partial T}{\partial z} = 0, \quad \text{at } z = 1 \end{aligned} \right\} \quad (5)$$

The following Non-dimensionalizing parameters have been used:

$$\begin{aligned} (x', y', z') &= \frac{(x, y, z)}{h}, \quad \mathbf{q}' = \frac{\mathbf{q}h}{\kappa}, \quad t' = \frac{\kappa t}{\sigma h^2}, p' = \frac{pk_1}{\mu\kappa}, \\ \phi' &= \frac{\phi - \phi_0}{\phi_1 - \phi_0}, \quad T' = \frac{T - T_U}{T_L - T_U}, \kappa = \frac{k_m}{(\rho c)_f}, \sigma = \frac{(\rho c)_m}{(\rho c)_f} \end{aligned}$$

After the non-dimensionalization process is completed and the dashes (') are removed, Eqs. (1)–(4) become:

$$\nabla \cdot \mathbf{q} = 0 \quad (6)$$

$$\frac{1}{V_a} \frac{d\mathbf{q}}{dt} = -\nabla p + Da \nabla^2 \mathbf{q} - (1 + F \frac{\partial}{\partial t}) \mathbf{q} + \sqrt{(Ta)(ve_x - ue_y)} + RaTe_z - Rme_z - Rn\phi e_z \quad (7)$$

$$\frac{\partial T}{\partial t} + \mathbf{q} \cdot \nabla T = \nabla^2 T + \epsilon \frac{Nb}{Le} \nabla \phi \cdot \nabla T + \epsilon \frac{Na Nb}{Le} \nabla T \cdot \nabla T \quad (8)$$

$$\frac{1}{\sigma} \frac{\partial \phi}{\partial t} + \frac{1}{\epsilon} \mathbf{q} \cdot \nabla \phi = \frac{1}{Le} \nabla^2 \phi + \frac{Na}{Le} \nabla^2 T \quad (9)$$

Non-dimensional boundary situations

$$\left. \begin{aligned} w = 0, T = 1, \quad \frac{\partial \phi}{\partial z} + Na \frac{\partial T}{\partial z} = 0, \quad \text{at } z = 0 \\ w = 0, T = 0, \quad \frac{\partial \phi}{\partial z} + Na \frac{\partial T}{\partial z} = 0, \quad \text{at } z = 1 \end{aligned} \right\} \quad (10)$$

where,

$$\begin{aligned}
 Va &= \frac{\epsilon\mu\sigma h^2}{\rho_f\kappa}, \text{ is the Vadasz number.} \\
 Rm &= \frac{(\rho_p\phi_0 + \rho_f(1 - \phi_0))\mathbf{g}k_1h}{\mu\kappa}, \text{ is the Rayleigh density number.} \\
 Ra &= \frac{(\rho_f\alpha(T_L - T_U)\mathbf{g}hk_1}{\mu\kappa}, \text{ known as Rayleigh number.} \\
 Na &= \frac{D_T(T_L - T_U)}{D_B T_U(\phi_1 - \phi_0)}, \text{ known as modified diffusivity ratio.} \\
 Le &= \frac{\kappa}{D_B}, \text{ known as Lewis number} \\
 Rn &= \frac{(\rho_p - \rho_f)(1 - \phi_0)\mathbf{g}hk_1}{\mu\kappa}, \text{ known as concentration Rayleigh number.} \\
 Nb &= \frac{\epsilon((\rho c)_P)(\phi_1 - \phi_0)}{(\rho c)_f}, \text{ known as modified thermal density increment.} \\
 \sqrt{Ta} &= \left(\frac{2\rho_0 h^2 \Omega k_1}{\epsilon\mu}\right)^2, \text{ known as Taylor number,} \\
 Da &= \frac{k_1}{h^2}, \text{ known as Darcy number,}
 \end{aligned}$$

2.1 Basic Solution

The temperature of the fluid, the nanoparticle and volume fraction are all functions of z :

$$\phi = \phi_b(z), \quad p = p_b(z), \quad T = T_b(z), \quad \mathbf{q} = 0 \tag{11}$$

With the use of Eq. (11) into Eqs. (8) and (9) we get:

$$\frac{d^2 T_b}{dz^2} + \epsilon \frac{Nb}{Le} \frac{dT_b}{dz} \left(\frac{d\phi_b}{dz} + Na \frac{dT_b}{dz} \right) = 0 \tag{12}$$

$$\frac{d^2 \phi_b}{d(z^2)} + Na \frac{d^2 T_b}{d(z^2)} = 0 \tag{13}$$

Solve Eq. (12) and Eq. (13) with boundary condition we get.

$$T_b = 1 - z \tag{14}$$

Solve Eq. (13) and using Eq. (14) with boundary condition we get.

$$\phi_b = Na(z) + \phi_1 \tag{15}$$

Perturbation Solution. Small perturbations are imposed to the conduction state:

$$p = p_b + \tilde{p}, \quad \phi = \phi_b + \tilde{\phi}, \quad \mathbf{q} = \mathbf{0} + \tilde{\mathbf{q}}, \quad T = T_b + \tilde{T}. \tag{16}$$

We use the above expressions (16) in the Eqs. (6)–(9), we have:

$$\nabla \cdot \tilde{\mathbf{q}} = 0 \tag{17}$$

$$\frac{1}{Va} \frac{d\tilde{\mathbf{q}}}{dt} = -\nabla \tilde{P} + Da \nabla^2 \tilde{\mathbf{q}} - (1 + F \frac{\partial}{\partial t}) \tilde{\mathbf{q}} + \sqrt{(Ta)}(ve_x - ue_y) + Ra \tilde{T} e_z - Rn \tilde{\phi} e_z \tag{18}$$

$$\frac{\partial \tilde{T}}{\partial t} - \tilde{w} = \nabla^2 \tilde{T} + \epsilon \frac{Nb}{Le} (\frac{Na \partial \tilde{T}}{\partial z} - \frac{\partial \tilde{\phi}}{\partial z}) - \frac{2\epsilon Na Nb}{Le} \frac{\partial \tilde{T}}{\partial z} \tag{19}$$

$$\frac{1}{\sigma} \frac{\partial \tilde{\phi}}{\partial t} + \frac{1}{\epsilon} Na \tilde{w} = \frac{1}{Le} \nabla^2 \tilde{\phi} + \frac{Na}{Le} \nabla^2 \tilde{T} \tag{20}$$

Taking curl operators on Eq. (18) we obtain.

$$(Da \nabla^2 - \frac{1}{Va} \frac{\partial}{\partial t} - (1 + F \frac{\partial}{\partial t})) \nabla \times \tilde{\mathbf{q}} + \sqrt{(Ta)} \nabla \times (ve_x - ue_y) + Ra \nabla \times \tilde{T} e_z - Rn \nabla \times \tilde{\phi} e_z = 0 \tag{21}$$

Again taking curl operators on Eq. (21) and taking z-component.

$$(Da \nabla^2 - \frac{1}{Va} \frac{\partial}{\partial t} - (1 + F \frac{\partial}{\partial t})) \nabla^2 \tilde{w} - \sqrt{(Ta)} \frac{\partial \zeta}{\partial z} + Ra \nabla_H^2 \tilde{T} - Rn \nabla_H^2 \tilde{\phi} = 0 \tag{22}$$

Taking z-component of Eq. (21) we get.

$$(Da \nabla^2 - \frac{1}{Va} \frac{\partial}{\partial t} - (1 + F \frac{\partial}{\partial t})) \zeta + \sqrt{(Ta)} \frac{\partial w}{\partial z} = 0 \tag{23}$$

Eliminating ζ from Eq. (22) and (23) we obtain.

$$\begin{aligned} (Da \nabla^2 - \frac{1}{Va} \frac{\partial}{\partial t} - (1 + F \frac{\partial}{\partial t}))^2 \nabla^2 \tilde{w} + (Ta) \frac{\partial^2 \tilde{w}}{\partial z^2} + Ra \nabla_H^2 \tilde{T} (Da \nabla^2 - \frac{1}{Va} \frac{\partial}{\partial t} - (1 + F \frac{\partial}{\partial t})) \\ - Rn \nabla_H^2 \tilde{\phi} (Da \nabla^2 - \frac{1}{Va} \frac{\partial}{\partial t} - (1 + F \frac{\partial}{\partial t})) = 0 \end{aligned} \tag{24}$$

where $\nabla_H^2 = \frac{\partial^2}{\partial x^2} + \frac{\partial^2}{\partial y^2}$, and $\nabla \times \tilde{\mathbf{q}} = \zeta$.

2.2 Linear Analysis

3 Normal Mode Method

$$\left. \begin{aligned} \tilde{w} &= \exp[i(lx + my) + st] W(z) \\ \tilde{T} &= \exp[i(lx + my) + st] \theta(z) \\ \tilde{\phi} &= \exp[i(lx + my) + st] \phi(z) \end{aligned} \right\} \tag{25}$$

where s is taken to be the growth rate of disturbances, lx and my are defined as the x and y-directional wave numbers, respectively.

Using Eq. (25) the Eqs. (24), (20) and (19) reduce in the differential equations obtain as (Chand and Rana [11]):

$$((D^2 - a^2)[Da(D^2 - a^2) - \frac{s}{Va} - (1 + sF)]^2 + TaD^2)W - Raa^2(Da(D^2 - a^2) - \frac{s}{Va} - (1 + Fs))\theta + Rna^2(Da(D^2 - a^2) - \frac{s}{Va} - (1 + Fs))\phi = 0 \tag{26}$$

$$(s - (D^2 - a^2) + \frac{\epsilon NaNb}{Le}D)\theta - W + \frac{\epsilon Nb}{Le}D\phi = 0 \tag{27}$$

$$(\frac{s}{\sigma} - \frac{1}{Le}(D^2 - a^2))\phi + \frac{1}{\epsilon}NaW - \frac{Na}{Le}(D^2 - a^2)\theta = 0 \tag{28}$$

where, $\frac{\partial}{\partial z} \equiv D$ and $k_x^2 + k_y^2 = a^2$

The boundary situation for normal mode investigation are

$$W = 0, \theta = 0, D\phi + NaD\theta = 0 \text{ at } z = 0, z = 1 \tag{29}$$

For the equations θ , ϕ and, W we suppose that the solution has the following format:

$$W = A_1 \sin \pi z, \theta = B_1 \sin \pi z, \phi = C_1 (-Na) \sin \pi z \tag{30}$$

Using Eq. (30), into the linear form of Eqs. (26)–(28) By utilising the orthogonality property, the resulting homogeneous system of equations is what we have:

$$\begin{pmatrix} F_{11} & \frac{a^2 Ra(s+Va+Da\delta Va+FsVa)}{2Va} & \frac{a^2 NaRn(s+Va+Da\delta Va+FsVa)}{2Va} \\ -\frac{1}{2} & \frac{\delta+s}{2} & 0 \\ \frac{Na}{2\epsilon} & \frac{Na\delta}{2Le} & -\frac{Na(Les+\delta\sigma)}{2Le\sigma} \end{pmatrix} \begin{pmatrix} A_1 \\ B_1 \\ C_1 \end{pmatrix} = \begin{pmatrix} 0 \\ 0 \\ 0 \end{pmatrix} \tag{31}$$

where $\delta = (\pi^2 + a^2)$ and $F_{11} = \frac{-\delta s^2 + 2s(1 - Da\delta^2 + Fs)Va - (\delta(Da^2\delta^2 - 2Da(1 + Fs) + (1 + Fs)) + \pi^2 Ta)Va^2}{2Va^2}$

The above homogeneous system’s requirement for the non-zero solution yields the expression for Rayleigh number:

$$Ra = \frac{-NaRn(Le(s + \delta) + \delta\epsilon)\sigma}{\epsilon(Les + \delta\sigma)} - \frac{2Va(s + \delta)F_{11}}{a^2(s + Va + FsVa + DaVa\delta)} \tag{32}$$

3.1 Stationary Mode of Convection

$s = 0$ refers to stationary type of convection; then Eq. (32) reduces to

$$Ra = \frac{-NaRn(Le + \epsilon)}{\epsilon} - \frac{2\delta F_{11}}{a^2(1 + Da\delta)} \tag{33}$$

3.2 Non-linear

We use a stream function $\tilde{\psi}$ to ensure that $\tilde{u} = \frac{\partial \tilde{\psi}}{\partial z}$ and $\tilde{w} = -\frac{\partial \tilde{\psi}}{\partial x}$ put in Eq. (24), (8) and (9) we get:

$$(Da\nabla^2 - \frac{1}{Va} \frac{\partial}{\partial t} - (1 + F \frac{\partial}{\partial t}))^2 \nabla^2 (-\frac{\partial \tilde{\psi}}{\partial x}) + (Ta) \frac{\partial^2}{\partial z^2} (-\frac{\partial \tilde{\psi}}{\partial x}) + Ra \nabla_H^2 \tilde{T} (Da\nabla^2 - \frac{1}{Va} \frac{\partial}{\partial t} - (1 + F \frac{\partial}{\partial t})) - Rn \nabla_H^2 \tilde{\phi} (Da\nabla^2 - \frac{1}{Va} \frac{\partial}{\partial t} - (1 + F \frac{\partial}{\partial t})) = 0 \quad (34)$$

$$\frac{1}{\sigma} \frac{\partial \tilde{\phi}}{\partial t} - \frac{1}{\epsilon} \frac{\partial \tilde{\psi}}{\partial x} \frac{\partial \phi_b}{\partial z} = \frac{1}{Le} \nabla^2 \tilde{\phi} + \frac{Na}{Le} \nabla^2 \tilde{\theta} + \frac{1}{\epsilon} \frac{\partial(\tilde{\psi}, \tilde{\phi})}{\partial(x, z)} \quad (35)$$

$$\frac{\partial \tilde{\theta}}{\partial t} - \frac{\partial \tilde{\psi}}{\partial x} \frac{\partial T_b}{\partial z} = \nabla^2 \tilde{\theta} + \frac{Nb\epsilon}{Le} \left(\frac{\partial \phi_b}{\partial z} \frac{\partial \tilde{\theta}}{\partial z} \right) + \frac{2\epsilon NbNa}{Le} \left(\frac{\partial \tilde{\theta}}{\partial z} \frac{\partial T_b}{\partial z} \right) + \frac{\partial(\tilde{\psi}, \tilde{\theta})}{\partial(x, z)} \quad (36)$$

where, $\nabla^2 = \frac{\partial^2}{\partial x^2} + \frac{\partial^2}{\partial z^2}$. Because all physical quantities are unaffected by y -direction, In Fourier series expansions, we use the following modes for non-linear stability analysis:

$$\tilde{\psi} = \sin(ax) \sin(\pi z) A11(t) \quad (37)$$

$$\tilde{\theta} = B02(t) \sin(2\pi z) + B11(t) \cos(ax) \sin(\pi z) \quad (38)$$

$$\tilde{\phi} = C02(t) \sin(2\pi z) (-N_A) + C11(t) \cos(ax) \sin(\pi z) \quad (39)$$

Where C02(t), B11(t), C11(t), B02(t) and A11(t) are time-dependent functions. Putting the value of (37)–(39) in Eqs. (34)–(36) and taking the orthogonality condition, we have

$$A11'(t) = E11[t] \quad (40)$$

$$B11'(t) = \frac{1}{[3Le(a^2\pi + \sin[a^2\pi])]} [(-A11[t](a + a\pi B02[t]) - \delta B11[t])(3Le(a^2\pi + \sin[a^2\pi])) + 32NaNb\epsilon(B02[t] - C02[t]) \sin[\frac{a^2\pi}{2}]] \quad (41)$$

$$B02'(t) = \frac{1}{[3a^2Le\pi]} \left[(3a^2Le\pi)(-4\pi^2 B02[t] + \frac{1}{2}a\pi A11[t]B11[t]) + 16NaNb\epsilon(-B11[t] + C11[t]) \sin[\frac{a^2\pi}{2}] \right] \quad (42)$$

$$C11'(t) = \frac{a\sigma Le A11[t](1 + \pi C02[t]) + \epsilon(\delta\sigma(B11[t] - C11[t]))}{Le\epsilon} \quad (43)$$

$$C02'(t) = \frac{\pi\sigma(8\pi\epsilon(B02[t] - 8\pi C02[t]) + aLeA11[t]C11[t])}{2Le\epsilon} \quad (44)$$

$$E11'(t) = -\frac{1}{[\delta(1 + Fva)]} [Va((\delta(1 + Da\delta)^2 + \pi^2 Ta)VaA11[t] + a(1 + Da\delta)RavaB11[t] + aNaRnvaC11[t] + a^3DaNaRnvaC11[t] + aDaNa\pi^2 RnvaC11[t] + 2a^2A11'[t] + 2a^4DaA11'[t] + 2\pi^2A11'[t] + 4a^2Da\pi^2A11'[t] + 2Da\pi^4A11'[t] + 2a^2FvaA11'[t] + 2a^4DaFvaA11'[t] + 2F\pi^2vaA11'[t] + 4a^2DaF\pi^2vaA11'[t] + 2DaF\pi^4vaA11'[t] + aRaB11'[t] + FaRavaB11'[t] + aNaRn(1 + Fva)C11'[t])] \quad (45)$$

4 Heat/Nanoparticle Concentration Transport

The heat transport that is represented by Nusselt number, $Nu_T(t)$ is described as:

$$Nu_T(t) = \frac{\text{Heat transport by (conduction+convection)}}{\text{Heat transport by conduction}}$$

$$Nu_T(t) = 1 + \left[\frac{\int_0^{2\pi/a} \left(\frac{\partial \tilde{\theta}}{\partial z} \right) dx}{\int_0^{2\pi/a} \left(\frac{\partial T_b}{\partial z} \right) dx} \right]_{z=0} \tag{46}$$

By using the values of $\tilde{\theta}$ and $T_b(z)$ from Eq. (38) and Eq. (14) into the Eq. (46) we obtain:

$$Nu_T(t) = 1 - 2\pi B02[t] \tag{47}$$

The concentration nanoparticle Nusselt number for the first type of nanoparticles, $Nu_\phi(t)$, can be described as:

$$Nu_\phi(t) = \frac{\text{Mass transport by (diffusion+Advection)}}{\text{mass transport by diffusion}}$$

$$Nu_\phi(t) = 1 + \left[\frac{\int_0^{2\pi/a} \left(\frac{\partial \tilde{\phi}}{\partial z} + N_A \frac{\partial \tilde{\theta}}{\partial z} \right) dx}{\int_0^{2\pi/a} \left(\frac{\partial \phi_b}{\partial z} \right) dx} \right]_{z=0} \tag{48}$$

By using Eqs. (15), (38) and (39) into the Eq. (48) we obtain:

$$Nu_\phi(t) = 1 + 2\pi(B02[t] - C02[t]) \tag{49}$$

5 Results/Discussion

5.1 Linear Stability Analysis

The rotating porous medium layer is examined in this article together with the effects of thermal convection and a heated bottom-up Rivlin-Ericksen elasto-viscous nanofluid, with a finite horizontal layer. The stationary thermal Rayleigh’s number value is enumerated using the Galerkin technique. The following are the parameter values: ($Va = 10, Le = 50, Na = 3, Rn = 5, Ta = 100, Da = 10,$ and $\epsilon = 0.3$ are taken from (Chand and Rana [11]).

For various porosity values of a Rivlin-Ericksen elasto-viscous nanofluid, Fig. 2a displays the difference between the (Ra) with wave number a . The stationary Rayleigh’s number (Ra) increase as a porous medium’s porosity rises, demonstrating the porosity has stabilising effect on the system.

The impact of Darcy number (Da) on the natural curve is displayed in Fig. 2b. As the Darcy number (Da) rises, the stationary Rayleigh’s number (Ra) rises as well, showing that the Darcy number (Da) stabilises the system.

The impact of the Lewis number (Le) on the stability of the system is depicted in Fig. 2c. Based on these figures, we observed that the Lewis number (Le) accelerates the beginning of convection. This may have occurred because thermophoresis with a higher thermophoretic diffusivity is more tolerant of disruption in nanofluids and because Brownian motion/thermophoresis both act as propellants for the motion of nanoparticles.

Figure 2d shows how the modified diffusivity ratio (Na) affects the stability of the system. In these figures, we noticed that the adjusted modified diffusivity ratio (Na) speeds up the commencement of convection. This may have occurred because Brownian motion/thermophoresis, both of which are forces that encourage nanoparticle movement, are more supportive of disturbance in nanofluids at higher thermophoretic diffusivity levels.

Figure 2e illustrates how the concentration Rayleigh number (Rn) affects the stability of the system. The stationary Rayleigh's number (Ra) reduce as the concentration Rayleigh number (Rn) rises, indicating a quicker initiation of convection. This can be discussed as an increment in volumetric fraction, which, by increasing the Brownian motion of the nanoparticles, causes the destabilising impact of concentration Rayleigh number (Rn).

In Fig. 2f we observed the influence of Vadas number (Va) on the system's stability. As increases the value of Vadas number (Va), It has no impact on the system's commencement of convection. Because Vadas number (Va) is vanishes with the growth rate parameter s in the stationary Rayleigh's number (Ra).

The impact of rotation (Ta) Fig. 2g shows Rotation reduces convection because of the existence of centrifugal force acting in the opposite direction of the fluid's movement. The value of stationary Rayleigh's number (Ra) rises as the value rotation terms are increased. Rotation has a stabilising impact on the arrangement.

5.2 Non-linear Stability Analysis

We must look at nonlinear analysis, which involves time-dependent outcomes, to investigate the influence of heat/mass transfer in thermal convection in a porous medium layer that rotates saturated by a Rivlin-Ericksen elastico-viscous nanofluid. To find the numerical values of Nusselt numbers as a function of time t , we applied Mathematica NDSolve to solve Eq. (40)–(45) in Mathematica. Almost all mass/heat transfer outcomes beginning with conduction, however, as t increase, the Nusselt number rises for values of t , indicating convection, then falls and oscillates over time, eventually approaching steady state. Several parameters are used ($Ta = 200$, $Le = 50$, $Rn = 5$, $Na = 2$, $F = 0.3$, $\sigma = 10$, $Va = 10$, $\epsilon = 0.04$, $Nb = 0.01$, and $Da = 1$).

The impact of rotation (Ta) is shown in Fig. 3a and Fig. 4c. Rotation (Ta) decreases mass/heat transfer in the medium due to the existence of centrifugal force operating in the opposite direction of the fluid's velocity. As a result, rotation (Ta) has a system-stabilizing effect.

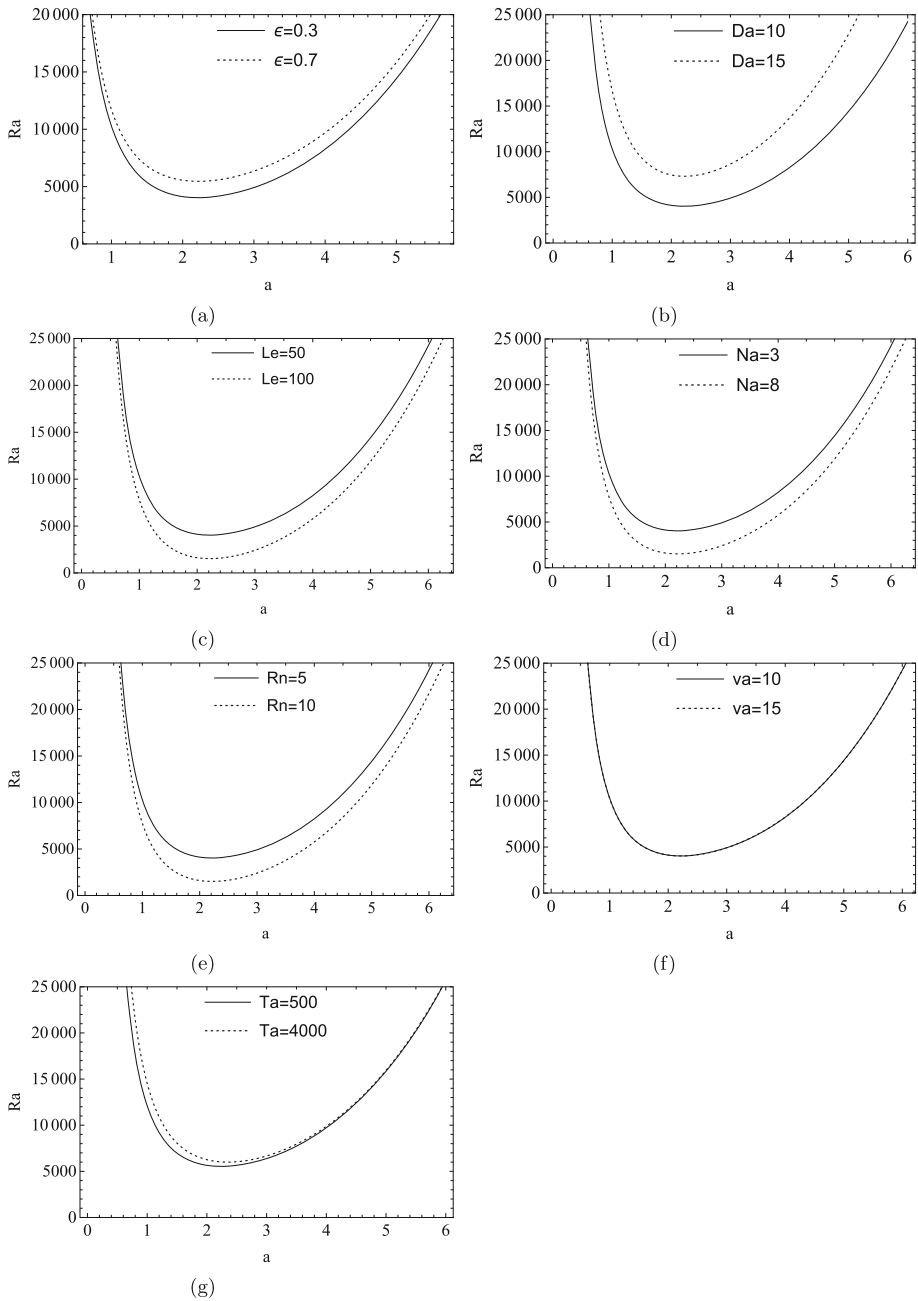


Fig. 2. Marginal stability curves

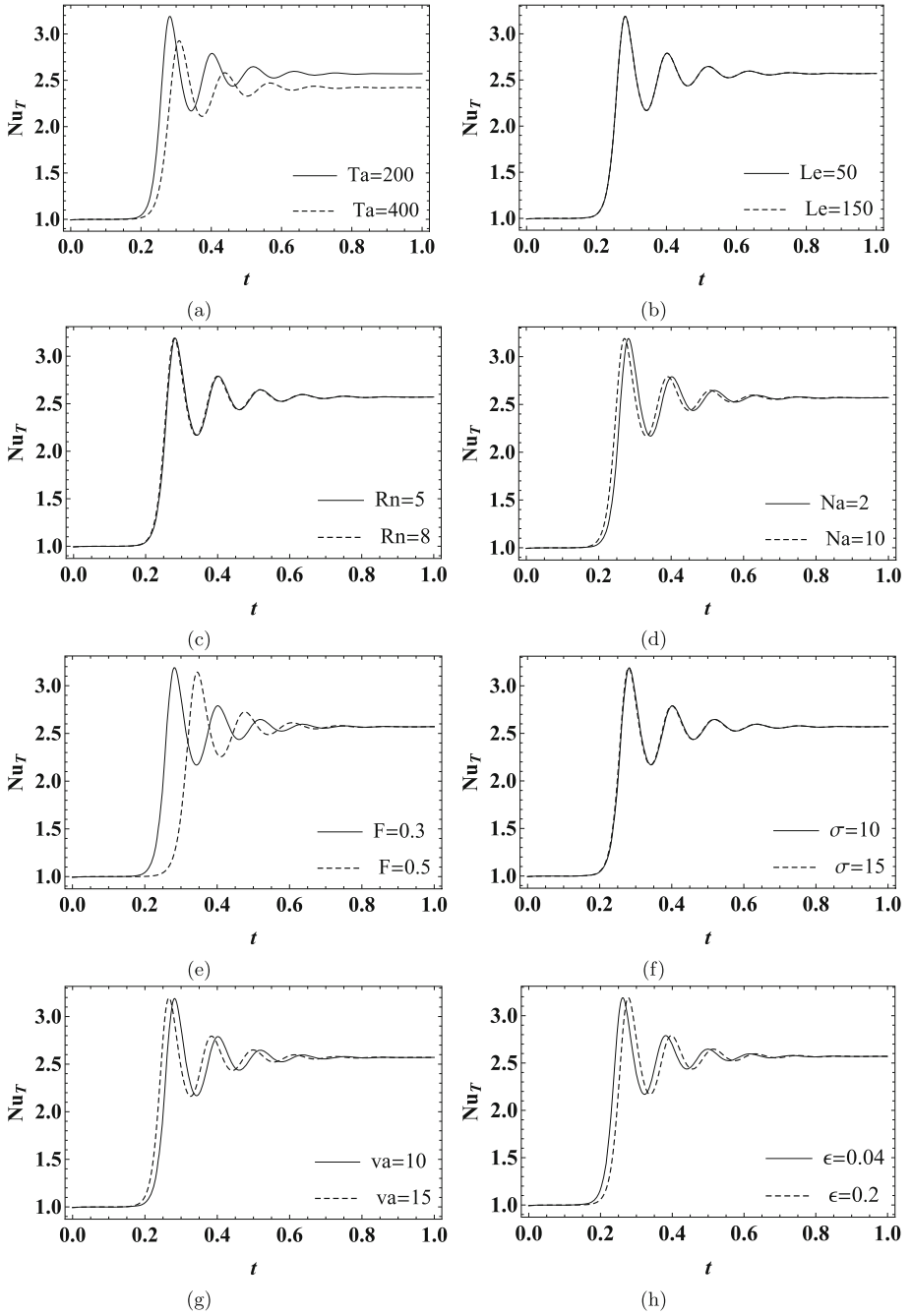


Fig. 3. Graph of thermal Nusselt number with Variation in different parameter

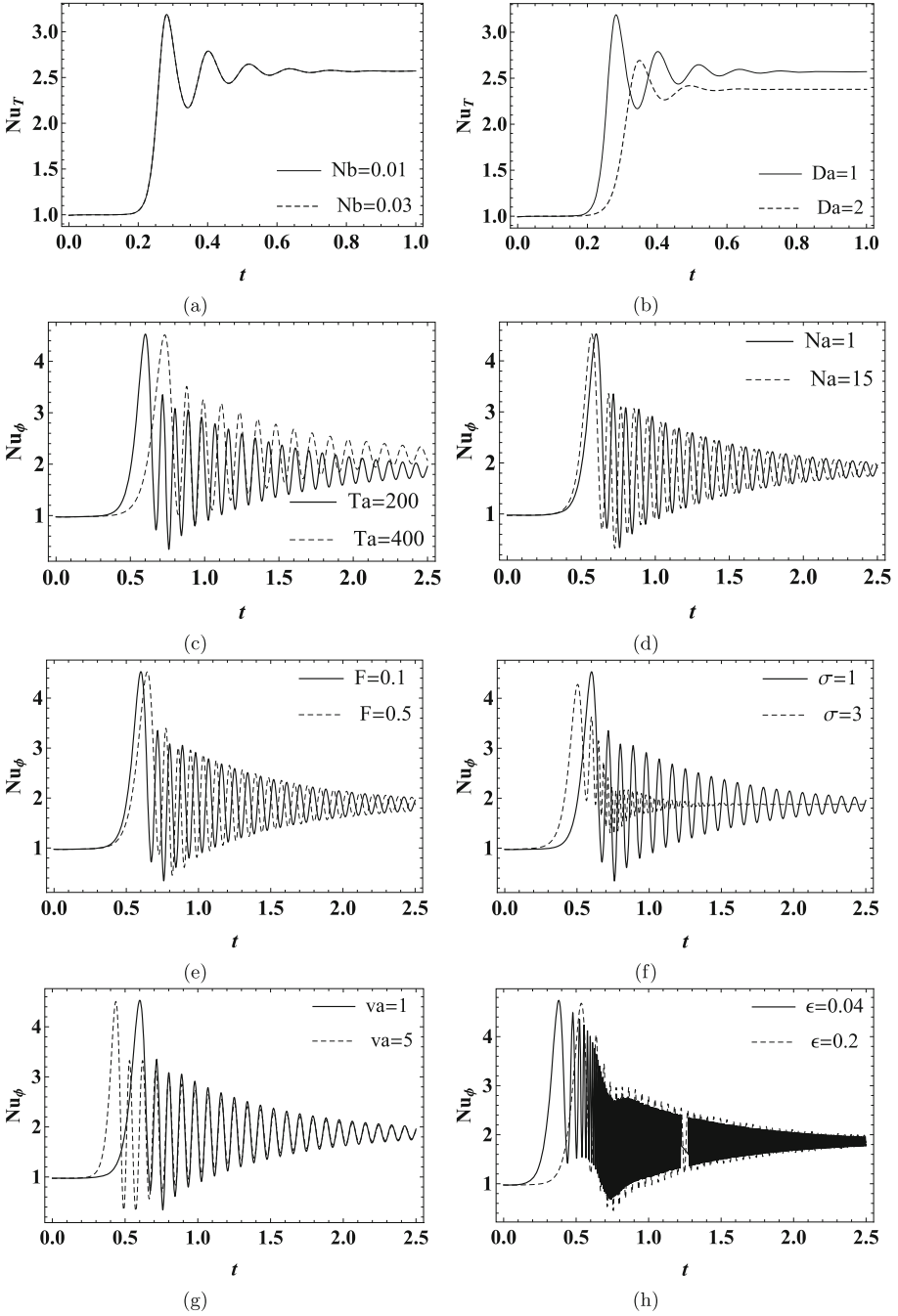


Fig. 4. Graph of thermal Nusselt number with Variation in different parameter

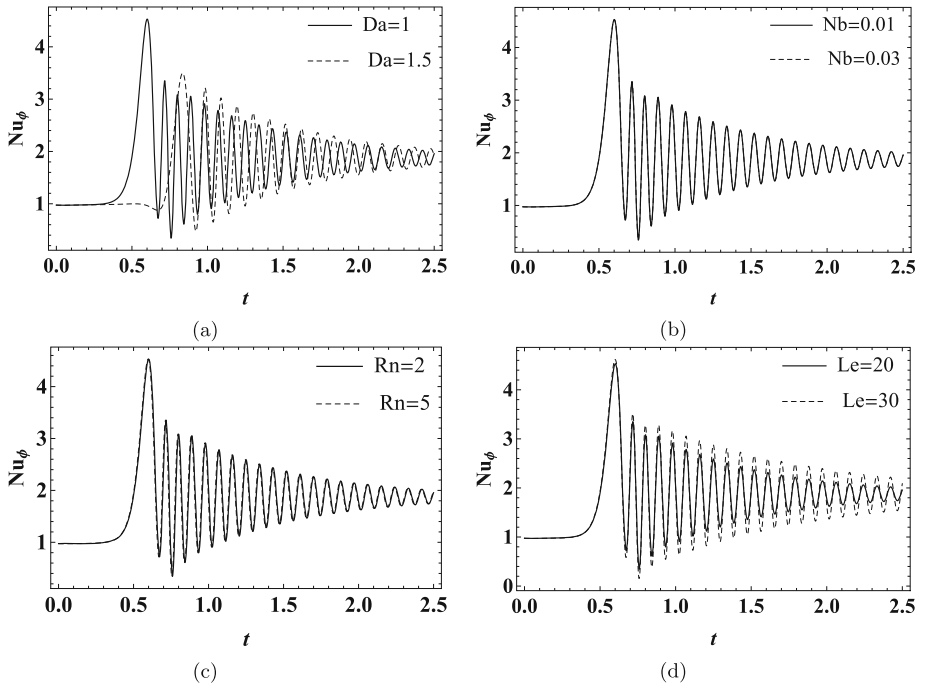


Fig. 5. Graph of Concentration Nusselt number with Variation in different parameter

Figure 3h and Fig. 4h indicate that as the value of the variable (ϵ) rises, the mass transfer as well as heat transfer decreases, indicating that the parameter (ϵ) has a system-destabilizing effect in the system.

Although the value of parameter (Rn) grows in Fig. 3c and Fig. 5c there is no influence on mass/heat transmission in the system.

As the value of parameter (Na) grows, the mass/heat transmission in the system increases, as seen in Fig. 3d and Fig. 4d. This might be the case because Brownian motion/thermophoresis are both forces that propel the motion of nanoparticles, and thermophoresis at higher thermophoretic diffusivity values is more tolerant of disruption in nanofluids. As a result, the (Na) causes the system to become unstable.

As the value of parameter (σ) grows, the mass transfer in the system increases, as shown in Fig. 4f and demonstrating that the parameter (σ) has a system-destabilizing effect, but that heat transport in the system has no effect as shown in Fig. 3f.

Figure 3e and Fig. 4e show the effect of the (F). As a result, Kinematic viscoelasticity parameter (F) reduces mass and heat transport in the medium, and so has a system-stabilizing effect.

Figure 3g and Fig. 4g show the effect of (Va) . It is noticed that Vadas number (Va) rises heat/mass transfer in the medium, therefore it destabilising the system.

There is no effect on mass/heat transfer in the system as the value of parameter Nb and (Le) increases in Fig. 4a, Fig. 3b and Fig. 5b, Fig. 5d.

The effect of (Da) is depicted in Fig. 4b and Fig. 5a. As a result, (Da) decreases heat/mass transmission in the medium, thus it stabilising the system.

6 Conclusions

A porous media saturated with Rivlin-Ericksen elastico-viscous nanofluid with rotation is subject to thermal instability, which we study using linear and non-linear analysis. A graphic explanation of the results has been provided. We get at the major findings listed below:

1. As we increases porosity, it is noticed that the system's convection is delayed as a result of it. This demonstrates that the system is stabilised by the porosity.
2. An improvement in concentration Rayleigh's number (Rn) resulting in a reduction in the stationary Rayleigh number (Ra) , demonstrating that Rn has a system-destabilizing effect.
3. On increasing the value of rotation the value of (Ra) rises. This implies that rotation has a stabilising impact on the arrangement.
4. As we increases the value of Brinkman-Darcy number, it is noticed that it delays the initiation of convection of the system. This demonstrates that the Brinkman-Darcy number stabilises the system.
5. On increasing the value of modified diffusivity ratio, it is observed that decreasing stationary Rayleigh number, this indicating that modified diffusivity ratio has a system-destabilizing effect.
6. Heat/mass transport in the system are both decreased by an increase in rotation.
7. On increasing the porosity, it is noticed that the heat/mass transfer decreases in the system.
8. As the value of Kinematic viscoelasticity increases, it can be noticed that heat/mass transfer of the system decreases.
9. As we increases the value of Vadasz number, It is observed that the system's heat/mass transport have increased.
10. The current problem is studied in infinitely extended horizontal plates, and it can be further extended in various configurations such as cylindrical, Hele-Shaw cell, and spherical. Moreover, the same problem can be investigated with different types of nanofluids in future.

References

1. Rivlin, R.S., Ericksen, J.L.: Stress-deformation relaxations for isotropic materials. *J. Rat. Mech. Anal.* **4**, 323–425 (1955)
2. Srivastava, L.P.: Unsteady flow of Rivlin-Ericksen fluid with uniform distribution of dust particles through channels of different cross sections in the presence of time dependent pressure gradient. *Istanbul Teknil Univer. Bul.* **194**, 19 (1971)
3. Sharma, R.C., Kumar, P.: Effect of rotation on thermal instability in Rivlin-Ericksen elastico-viscous fluid. *Z. Naturforsch.* **51a**, 821–824 (1996)
4. Sharma, R.C., Kumar, P.: Thermal instability in Rivlin-Ericksen elastico-viscous fluid in hydromagnetics. *Z. Naturforsch.* **52a**, 369–371 (1997)
5. Prakash, K., Chand, R.: Effect of kinematic visco-elasticity instability of a Rivlin-Ericksen elastico-viscous fluid in porous medium. *Ganita Sandesh* **14**(1), 1–13 (1999)
6. Sharma, R.C., Kumar, P., Sharma, S.: Rayleigh-taylor instability of Rivlin-Ericksen elastico-viscous fluid through porous medium. *Indian J. Phys. B* **75**(4), 337–340 (2001)
7. Kumar, P., Mohan, H., Lal, R.: Effect of magnetic field on thermal instability of a rotating Rivlin-Ericksen viscoelastic fluid. *Int. J. Math. Math. Sci.* **2006**(3), 1–10 (2006)
8. Sheu, L.J.: Thermal instability in a porous medium layer saturated with a visco-elastic nanofluid. *Transp. Porous Med.* **88**, 461–477 (2011)
9. Rana, G.C., Sharma, V.: Effect of rotation on the onset of convection in Rivlin-Ericksen fluid heated from below in a brinkman porous medium. *Int. J. Fluid Mech. Res.* **39**(6) (2012)
10. Rana, G.C., Thakur, R.C.: Effect of suspended particles on thermal convection in Rivlin-Ericksen elastico-viscous fluid in a brinkman porous medium. *J. Mech. Eng. Sci.* **2**, 162–171 (2012)
11. Chand, R., Rana, G.C.: Thermal instability of Rivlin-Ericksen elastico-viscous nanofluid saturated by a porous medium. *J. Fluids Eng.* **134**(12) (2012)
12. Nield, D.A., Kuznetsov, A.V.: Thermal instability in a porous medium layer saturated by a nanofluid: a revised model. *Int. J. Heat Mass Transf.* **68**, 211–214 (2014)
13. Chand, R., Rana, G.C., Singh, K.: Thermal instability in a Rivlin-Ericksen elastico-viscous nanofluid in a porous medium a revised model. *Int. J. Nanosci. Nanoeng.* **2**(1), 1–5 (2015)
14. Rana, G.C., Chand, R., Sharma, V.: Thermal instability of a Rivlin-Ericksen nanofluid saturated by a Darcy-Brinkman porous medium: a more realistic model. *Eng. Trans.* **64**(3), 271–286 (2016)
15. Saini, S., Sharma, Y.D.: The effect of vertical throughflow in Rivlin-Ericksen elastico-viscous nanofluid in a non-Darcy porous medium. *Nanosyst. Phys. Chem. Math.* **8**(5), 606–612 (2017)
16. Malleswari, D.: Influence of viscoelastic Rivlin-Ericksen fluid on free convective flow past a vertical plate filled in porous medium in presence of transverse magnetic field and double diffusion effects. *IOSR J. Appl. Phys. (IOSRJAP)* **10**(3), 45–62 (2018)
17. Kareem, R.A., Salawu, S.O., Yan, Y.: Analysis of Transient Rivlin-Ericksen Fluid and Irreversibility of Exothermic Reactive Hydromagnetic variable Viscosity. *J. Appl. Comput. Mech.* **6**(1), 26–36 (2020)

18. Choi, S.: Enhancing thermal conductivity of fluids with nanoparticles. In: Signier, D.A., Wang, H.P. (eds.) *Development and Applications of Non-Newtonian Flows*, pp. 99-105. ASME FED, New York (1995)
19. Choi, S.U.S., Eastman, J.A., Yu, W., Thompson, L.J.: Anomalous increased effective thermal conductivities of ethylene glycol-based nanofluids containing copper nanoparticles. *Appl. Phys. Lett.* **78**, 718–720 (2001)
20. Das, S.K., Putra, N., Thiesen, P., Roetzel, W.: Temperature dependence of thermal conductivity enhancement for nanofluids. *ASME J. Heat Transf.* **125**, 567–574 (2003)
21. Buongiorno, J.: Convective transport in nanofluids. *ASME J. Heat Transf.* **128**(3), 240–250 (2006)
22. Tzou, D.Y.: Thermal instability of nanofluids in natural convection. *Int. J. Heat Mass Transf.* **51**, 2967–2979 (2008)
23. Nield, D.A., Kuznetsov, A.V.: Thermal instability in a porous medium layer saturated by a nanofluid. *Int. J. Heat Mass Transf.* **52**, 5796–5801 (2009)
24. Nield, D.A., Kuznetsov, A.V.: The effect of vertical through flow on thermal instability in a porous medium layer saturated by nanofluid. *Transp. Porous Media* **87**, 765–775 (2011)
25. Nield, D.A., Kuznetsov, A.V.: The onset of double-diffusive convection in a nanofluid layer. *Int. J. Heat Fluid Flow* **32**, 771–776 (2011)
26. Bhadauria, B.S., Agarwal, S.: Natural convection in a nanofluid saturated rotating porous layer: a nonlinear study. *Transp. Porous Media* **87**, 585–602 (2011)
27. Bhadauria, B.S., Agarwal, S., Kumar, A.: Non-linear two-dimensional convection in a nanofluid saturated porous. *Media* **90**, 605–625 (2011)
28. Kuznetsov, A.V., Nield, D.A.: Effect of local thermal non-equilibrium on the onset of convection in a porous medium layer saturated by a nanofluid. *Transp. Porous Media* **83**(2), 425–436 (2010)
29. Bhadauria, B.S., Agarwal, S.: Natural convection in a nanofluid saturated rotating porous layer: a nonlinear study. *Transp. Porous Media* **87**(2), 585–602 (2011)
30. Rashidi, M.M., Sheikholeslami, M., Hayat, T., Ganji, D.D.: Free convection of magnetic nanofluid considering MFD viscosity effect. *Int. J. Mol. Liq.* **218**, 393–399 (2016)
31. Rawat, S.K., Mishra, A., Kumar, M.: Numerical study of thermal radiation and suction effects on copper and silver water nanofluids past a vertical Riga plate. *J. MMMS* **15**, 714–736 (2019)
32. Garia, R., Rawat, S.K., Kumar, M., Yaseen, M.: Hybrid nanofluid flow over two different geometries with Cattaneo-Christov heat flux model and heat generation: a model with correlation coefficient and probable error. *Chin. J. Phys.* **74**, 421–439 (2021)
33. Gumber, P., Yaseen, M., Rawat, S.K., Kumar, M.: Heat transfer in micropolar hybrid nanofluid flow past a vertical plate in the presence of thermal radiation and suction/injection effects. *Partial Differ. Eqn. Appl. Math.* **4**, 100240 (2021)
34. Chand, R., Yadav, D., Bhattacharyya, K., Awasthi, M.K.: Thermal convection in a layer of micropolar nanofluid. *Asia-Pac. J. Chem. Eng.* **16**(5), e2681 (2021)
35. Geoffrey, T.: Experiments with rotating fluids. *Proc. R. London A* **100**, 114–21 (1921)
36. Greenspan, H.P.: *The Theory of Rotating Fluid*. Cambridge University Press, Cambridge (1968)
37. Kumar, P., Mohan, H., Lal, R.: The effect of magnetic field on thermal instability of a rotating viscoelastic fluid. *Int. J. Math. Math. Sci.* **28042**, 1–10 (2006)

38. Sunil, Chand, P., Bharti, P.K., Mahajan, A.: Thermal convection in micropolar ferrofluid in the presence of rotation. *J. Magn. Mater.* **320**, 316–324 (2008)
39. Kirillov, O.N., Stefani, F.: The standard and helical magnetorotational instability. *Acta Appl. Math.* **120**, 177–198 (2012)
40. Yadav, D., Bhargava, R., Agrawal, G.S., Hwang, G.S., Lee, J., Kim, M.C.: Magneto-convection in a rotating layer of nanofluid. *Asia-Pac. J. Chem. Eng.* **9**(5), 663–677 (2014)
41. Chand, R., Rana, G.C.: Thermal instability in a rotating porous layer of nanofluid confined within a hele-shaw cell. *J. Nanofluids* **5**(6), 941–948 (2016)
42. Manjula, S.H., Kiran, P., RajReddy, P., Bhadauria, B.S.: The complex Ginzburg Landau model for an oscillatory convection in a rotating fluid layer. *Int. J. Appl. Mech. Eng.* **25**(1), 75–91 (2020)
43. Manjula, S.H., Kiran, P.: Thermo-rheological effect on weak nonlinear rayleigh-benard convection under rotation speed modulation. In: *Boundary Layer Flows*, pp. 01–20. IntechOpen (2022)



Study of the Convective-Radiative Moving Porous Fin with Temperature-Dependent Variables

Parvinder Kaur and Surjan Singh^(✉)

Department of Mathematics, Eternal University, Baru Sahib,
Sirmour 173101, H.P., India
surjan.singhbhu@gmail.com

Abstract. In this article, the temperature in a rectangular moving porous fin with a longitudinal profile has been studied, which involves internal heat generation, variable thermal conductivity, and heat transfer coefficient. In real life, we know that these parameters change with temperature, so in this study, we considered these parameters as temperature function. Darcy's model has been used to form the equation. The heat transfer coefficient is taken as power-law form. A new contribution to this study is adding a porous medium to fin and taking thermal conductivity into four different cases: a constant, a linear, a quadratic, and an exponential form of temperature. The solution to the problem has been carried out by three methods, namely LWCM, LSM, and MM. A comparison of the results obtained by the above-mentioned methods and the exact results has been presented to demonstrate the novelty of the current study. The entire article has been carried out in a non-dimensional form.

Keywords: Darcy model · heat transfer · moving fin · porous medium · numerical methods · temperature · thermal conductivity

Nomenclature

- T : temperature distribution (K)
- T_a : ambient temperature (K)
- T_b : temperature at fin base (K)
- $h(T)$: heat transfer coefficient ($Wm^{-2}K^{-1}$)
- $K(T)$: thermal conductivity ($Wm^{-1}K^{-1}$)
- L : fin length (m)
- P : fin periphery (m)
- \dot{m} : mass flow rate of fluid ($kg s^{-1}$)
- k_a : thermal conductivity at ambient temperature ($Wm^{-1}K^{-1}$)
- h_b : heat transfer coefficient at the fin base ($Wm^{-2}K^{-1}$)
- g : gravitational acceleration (ms^{-2})

R : permeability (m^2)
 Y : thermal expansion coefficient (K^{-1})
 A_c : cross-section area (m^2)
 U : speed of moving fin (ms^{-1})
 q^* : heat generation (Wm^{-3})
 W : fin width (m)
 x : spatial variable
 n : constant

Greek symbols

β : thermal conductivity gradient ($Wm^{-1}K^{-1}$)
 σ : Stefan-Boltzmann constant ($Wm^{-2}K^{-4}$)
 ν : kinematic viscosity (m^2s^{-1})
 ρ : density of material (kgm^{-3})
 ν_w : velocity of fluid (ms^{-1})
 c : specific heat ($JK^{-1}kg^{-1}$)

Dimensionless parameters

θ : temperature
 θ_a : ambient temperature
 X : spatial variable
 k : thermal conductivity
 M : thermo-geometric
 N_r : radiation-conduction
 N_p : porosity parameter
 ε_G : heat generation gradient
 ε : emissivity
 Pe : Peclet number

Abbreviation

ADM : Adomian decomposition method
 DTM : Differential transformation method
 FDM : Finite difference method
 HAM : Homotopy analysis method
 LSM : Least square method
 LSSCM : Least square spectral collocation method
 LWCM : Legendre wavelet collocation method
 LVI : Laplace-variational iterative
 MM : Moment method
 R-K : Runge-Kutta
 WCM : Wavelet collocation method

1 Introduction

Many engineering devices or machines generate heat during their processes, which results in heat being released into the environment. If this generated heat is not released quickly to its surrounding environment, it may cause a temperature rise in system devices, leading to their failure. To prevent this, fins or extended heat surfaces are used. Dongonchi and Ganji [1] evaluated heat transmission in a rectangular moving fin with a heat transfer coefficient, heat generation and thermal conductivity which depends on temperature using DTM. Kraus [2] provided a detailed review of extended surfaces or fins in his book. Gorla and Bakier [3] investigated the influence of convection and radiation in a rectangular porous fin. The performance is investigated in various fins, including the long fin with an insulated tip and the finite-length fin with an exposed tip. Kiwan et al. [4] investigated heat transfer in porous moving fins. A thermal performance study compares porous and solid fins. The effects of parameters and different profiles were studied in detail. Ndlovu and Moitsheki [5] performed the thermal analysis of rectangular and hyperbolic moving fins. DTM was applied to find the solution to the heat transmission equation. Khalaf et al. [6] gave a review on how fins, porous medium and nanofluid materials improve heat transmission in devices. They explained how the world has developed an interest in modern electronics and their applications in science and engineering, which also have a great impact on aspects of life such as optical devices, refrigeration devices, X-rays, etc. Gupta et al. [7] investigated the Cu and Al_2O_3 water-based nanofluid three-dimensional magnetohydrodynamic flow. In the presence of thermal radiation and convective mass and heat transmission boundary conditions, effects of nanoparticles as well as mass and heat transmission were carried out. Ndlovu et al. [8] found the fin efficiency and temperature in a rectangular moving fin with a porous medium using VIM. Unal et al. [9] investigated the temperature distribution in straight and rectangular fins in one dimension. Shateri and Salashour [10] found the heat performance and distribution of temperature in longitudinal fin with porous media using LSM. Fin efficiency and heat flux were also computed for the comparison of fins. Hatami et al. [11] used LSM, CM, and DTM to analyze the energy transfer and distribution of temperature in porous fin. Razzaghi and Yousefi [12] provided a Legendre wavelet-based operational integration P matrix. Singh et al. [13] studied heat transmission in moving fin with heat transfer coefficient, surface emissivity, and thermal conductivity, which is quadratic and linear function of temperature. Sobamowo et al. [14] discussed the performance of convective moving porous fin with different properties of the material and used the LVI method to find an analytical solution. Sobamowo [15] studied a porous moving fin with internal energy generation and thermal conductivity which are temperature function using the finite element method. Singh et al. [16] considered temperature variant parameters and several cases of thermal conductivity to solve heat problem. Fin efficiency was also calculated for the fin. Bhanja et al. [17] used ADM to find fin efficiency and temperature distribution in radiation-convection porous moving fins. LSSCM was used by Chen et al. [18] to predict efficiency and temperature in radiation-convection moving porous fins

under combined convective-radiative and constant temperature boundary conditions. Singh et al. [19] solved a non-linear fin problem whose thermal conductivity is a variable function of temperature by using WCM. Moradi et al. [20] used HAM to find heat transmission in moving porous fin with two boundary conditions. Heat transfer and the impact of parameters on temperature are also discussed. Singh et al. [21] discussed non-Fourier and Fourier energy conduction applying boundary conditions which are periodic in nature. An analytical solution was found using the Laplace transform and its inversion. Wang et al. [22] tested DTM with the Pade approximant as one of the analytical approaches to resolve the ordinary system of heat transport, which is non-linear. For the radiation heat exchange, the Rosseland approximation was taken into consideration. Singh et al. [23] introduced the homotopy analysis transform method, a powerful hybrid computational methodology for analysing Jeffery-Hamel flow. Singh et al. [24] used a method called the homotopy perturbation Elzaki transform to find a solution to the boundary value problem of the non-linear type. With the help of Chebyshev polynomials, Singh et al. [25] solved the fractional version of Bratu's equation, which plays a major role in the vibration-electrospinning and electrospinning processes.

In this present study, the impact of various parameters on temperature of fin is discussed. To find the better method for the study, a percentage error has been computed and a method with the minimum error has been applied for further computation. The formulation of the model is described in Sect. 2. The methodology of the applied methods is provided in Sect. 3. The exact solution is presented in Sect. 4. Section 5 contains a discussion of the findings. Lastly, the conclusion is provided in Sect. 6.

2 Problem Description

We consider a porous moving fin of longitudinal profile in one dimension along with its cross-section area A_c , length L and periphery P which horizontally moves with velocity U which is constant, presented in Fig. 1. The surface of the fin is exposed to a T_a and T_b radiative and convective environment. The radiation role can be more reasonable if the convection force is absent, occurs naturally, or is weak.

For any material, thermal conductivity changes linearly with temperature. Some assumptions have been made about the problem, which are discussed as follows: Darcy's model is used for the interplay in the fluid and porous medium; the porous part is considered to be homogeneous, saturated, and isotropic with single-phase liquids, and the physical properties of the fluid and solid walls depend on temperature. From these assumptions, the equation for moving fin in a porous medium is expressed as:

$$\frac{d}{dx} \left(K(T) \frac{dT}{dx} \right) - \frac{P}{A_c} h(T)(T - T_a) - \frac{\dot{m}c}{A_c dx} (T - T_a) - \frac{\varepsilon\sigma P}{A_c} (T^4 - T_a^4) - \rho c U \frac{dT}{dx} + q^* = 0 \quad (1)$$

$$0 \leq x \leq L$$

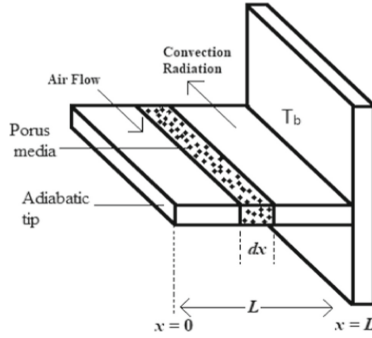


Fig. 1. Schematic diagram of a moving porous fin.

where $K(T)$ is the equivalent thermal conductivity of porous fin, which includes thermal conductivity of the solid part as well as the gas part present in the porous, $h(T)$ is heat transfer coefficient, (\dot{m}) is mass flow of fluid and q^* is energy generation which depends on temperature x is space variable, T is temperature distribution, σ is Boltzmann constant, ε is emissivity, c is specific heat and ρ is density of material. In addition to conduction, convection, and radiative heat flux, Eq. 1 includes terms for internal heat generation and advection. One end of the fin is insulated with a base temperature, while the boundary conditions are specified by [2].

$$T(L) = T_b, \quad \frac{dT}{dx} \Big|_{x=0} = 0. \tag{2}$$

If heat generation change with temperature [1], then we get

$$q^* = q_a^*(1 + \varepsilon_g(T - T_a)) \tag{3}$$

where q_a^* is internal heat generation at ambient temperature.

Mass flow rate of fluid which passes through porous media is [3]

$$\dot{m} = \rho \nu_w W \Delta X$$

Darcy’s model gave the fluid velocity which passes through porous media [4],

$$\nu_w = \frac{gRY}{v} (T - T_a)$$

Heat transfer coefficient is power law form of the temperature given by [5],

$$h(T) = h_b \left(\frac{T - T_a}{T_b - T_a} \right)^n$$

To simplify these equations, introduce non-dimensional parameters as follows [1, 8]:

$$X = \frac{x}{L}, \theta = \frac{T}{T_b}, \theta_a = \frac{T_a}{T_b}, k = \frac{K}{k_a}, h = \frac{h(T)}{h_b}, N_r = \frac{\varepsilon \sigma P L^2 T_b^3}{A_c k_a}, M^2 = \frac{P h_b L^2}{A_c k_a}, N_p = \frac{\rho c g R Y W L^2 T_b}{v k_a A_c}, G = \frac{q_a^* A_c}{h_b P T_b}, Pe = \frac{U L \rho c}{k_a}, \varepsilon_G = \varepsilon_g T_b \tag{4}$$

On applying these parameters, Eq. (1) becomes

$$\begin{aligned} \frac{d}{dX} \left(k(\theta) \frac{d\theta}{dX} \right) - M^2 \frac{(\theta - \theta_a)^{n+1}}{(1 - \theta_a)^n} - N_r(\theta^4 - \theta_a^4) - N_p(\theta - \theta_a)^2 - Pe \frac{d\theta}{dX} \\ + M^2 G(1 + \varepsilon_G(\theta - \theta_a)) = 0, \end{aligned} \tag{5}$$

$$0 \leq X \leq 1.$$

and the boundary conditions becomes

$$\theta(1) = 1, \quad \left. \frac{d\theta}{dX} \right|_{X=0} = 0 \tag{6}$$

where X is dimensionless space variable, θ is dimensionless temperature, M is thermo-geometric, N_r is radiation-conduction, and Pe is Peclet number (speed of fin), when $Pe = 0$ means fin is stationary. In non-dimensional form, heat transfer coefficient is

$$h(T) = h_b \left(\frac{\theta - \theta_a}{1 - \theta_a} \right)^n$$

The constant n can range between -6.6 and 5 . However, in various practical cases, it lies in -3 and 3 [9]. The exponent n describes laminar film boiling at $n = \frac{1}{4}$, laminar natural convection at $n = 3$, and radiation at $n = 3$ [9].

2.1 Particular Cases

The following cases arise when dimensionless thermal conductivity is taken as a different function of temperature as shown below:

Case I

If linear thermal conductivity, $k(\theta) = 1 + \beta\theta$

$$\begin{aligned} (1 + \beta\theta) \frac{d^2\theta}{dX^2} + \beta \left(\frac{d\theta}{dX} \right)^2 - M^2 \frac{(\theta - \theta_a)^{n+1}}{(1 - \theta_a)^n} - N_r(\theta^4 - \theta_a^4) - N_p(\theta - \theta_a)^2 - Pe \frac{d\theta}{dX} \\ + M^2 G(1 + \varepsilon_G(\theta - \theta_a)) = 0, \end{aligned} \tag{7}$$

Case II

If constant thermal conductivity, $k(\theta) = 1$

$$\frac{d^2\theta}{dX^2} - M^2 \frac{(\theta - \theta_a)^{n+1}}{(1 - \theta_a)^n} - N_r(\theta^4 - \theta_a^4) - N_p(\theta - \theta_a)^2 - Pe \frac{d\theta}{dX} + M^2 G(1 + \varepsilon_G(\theta - \theta_a)) = 0, \tag{8}$$

Case III

If thermal conductivity is an exponential function of temperature, $k(\theta) = e^{\beta\theta}$

$$\begin{aligned} e^{\beta\theta} \frac{d^2\theta}{dX^2} + \beta e^{\beta\theta} \left(\frac{d\theta}{dX} \right)^2 - M^2 \frac{(\theta - \theta_a)^{n+1}}{(1 - \theta_a)^n} - N_r(\theta^4 - \theta_a^4) - N_p(\theta - \theta_a)^2 - Pe \frac{d\theta}{dX} \\ + M^2 G(1 + \varepsilon_G(\theta - \theta_a)) = 0, \end{aligned} \tag{9}$$

Case IV

If thermal conductivity is quadratic function of temperature, $k(\theta) = 1 + \beta\theta^2$

$$(1 + \beta\theta^2) \frac{d^2\theta}{dX^2} + 2\beta\theta \left(\frac{d\theta}{dX}\right)^2 - M^2 \frac{(\theta - \theta_a)^{n+1}}{(1 - \theta_a)^n} - N_r(\theta^4 - \theta_a^4) - N_p(\theta - \theta_a)^2 - Pe \frac{d\theta}{dX} + M^2G(1 + \varepsilon_G(\theta - \theta_a)) = 0, \tag{10}$$

3 Computational Methods

3.1 Legendre Wavelet Collocation Method

Let

$$\theta''(X) = c^T \psi(X) \tag{11}$$

here

$$c^T \psi(X) = \sum_{m=1}^{2^{s-1}} \sum_{n=0}^{n-1} c_{m,n} \psi_{m,n}(X)$$

and

$$c_{m,n} = \int_0^1 f(X) \psi_{m,n}(X)$$

The matrices c and $\psi(X)$ are $M \times 1$, expressed as

$$c = \begin{bmatrix} c_{1,0}, c_{1,1}, \dots, c_{1,M-1}, c_{2,0}, c_{2,1}, \dots, c_{2,M-1}, \\ c_{2^{s-1},0}, c_{2^{s-1},1}, \dots, c_{2^{s-1},M-1} \end{bmatrix}^T$$

and

$$\psi(X) = \begin{bmatrix} \psi_{1,0}(X), \psi_{1,1}(X), \dots, \psi_{1,M-1}(X), \psi_{2,0}(X), \\ \psi_{2,1}(X), \dots, \psi_{2,M-1}(X), \psi_{2^{s-1},0}(X), \\ \psi_{2^{s-1},1}(X), \dots, \psi_{2^{s-1},M-1}(X) \end{bmatrix}^T$$

The Legendre wavelet is defined as $\psi_{m,n}(X) = \psi(s, \hat{m}, n, X)$, where s is a positive integer, $m = 1, 2, \dots, 2^{s-1}$, $\hat{m} = 2m - 1$, the order of the Legendre polynomial is n , and in the interval $[0, 1]$, X is defined as:

$$\psi_{m,n}(X) = \begin{cases} \sqrt{(n+1/2)} 2^{s/2} P_n(2^s X - \hat{m}), & \frac{\hat{m}-1}{2^s} \leq X \leq \frac{\hat{m}+1}{2^s} \\ 0, & \text{otherwise} \end{cases} \tag{12}$$

where $m = 1, 2, \dots, 2^{s-1}$ and $n = 0, 1, \dots, M - 1$. $P_n(X)$ is Legendre polynomial of n order as given by [13].

$$P_0(X) = 1, P_1(X) = X, P_{n+1}(X) = \frac{2n+1}{n+1} (X) P_n(X) - \frac{n}{n+1} (X) P_{n-1}(X), n = 1, 2, 3, \dots, M - 1 \tag{13}$$

Now, integrating with respect to X from 0 to X of Eq. (11), we get

$$\theta'(X) = \theta'(0) + c^T P\psi(X), \tag{14}$$

where P is the integration operational matrix, which is $2^{s-1}M \times 2^{s-1}M, s = 1$, given by [12].

Substitute $X = 1$ in Eq. (14), we get

$$\begin{aligned} \theta'(0) &= \theta'(1) - c^T P\psi(1) \\ \Rightarrow \theta'(0) &= -c^T P\psi(1) \end{aligned}$$

From the Eq. (14), we have

$$\theta'(X) = -c^T P\psi(1) + c^T P\psi(X), \tag{15}$$

Again, integrating with respect to X from 0 to X of the Eq. (15), we obtain

$$\theta(X) = 1 - c^T P\psi(1)d'P\psi(X) + c^T P^2\psi(X), \tag{16}$$

Substituting the values of $\theta(X), \theta'(X)$ and $\theta''(X)$ in Eq. 7 to 10. $\theta(X)$ is the approximate solution to these equations. Finding the residual $R(X, c_1, c_2, c_3, \dots, c_n)$ for n collocation points $X_r, r = 1, 2, 3, \dots, n$. There must be equality between the coefficients and collocation points. As a result, the residuals will be obtained.

3.2 Least Square Method

This method is based on residual weighting and minimises the residual of the test function, which is used to solve a non linear differential equation given by [10]. The meaning of this method is to get the minimum continuous summation of squared residuals [11].

$$S = \int_x R(x)R(x)dx = \int_x R^2(x)dx \tag{17}$$

The derivative of the above function with respect to all unfamiliar constants has to be zero in order to obtain the minimum scalar function [11], i.e.

$$\frac{\delta S}{\delta c_i} = 2 \int_x R(x) \frac{\delta R}{\delta c_i} dx = 0 \tag{18}$$

here weight function is

$$W_i = 2 \frac{\delta R}{\delta c_i} \tag{19}$$

the coefficient ‘2’ from this equation can be expelled. Then the weight function of this method will be just derivative of residual with respect to unfamiliar constants i.e.

$$W_i = \frac{\delta R}{\delta c_i} \tag{20}$$

3.3 Moment Method

For this method, the weight function is selected from family of polynomials, expressed as

$$W_i(x) = x^i, \quad i = 0, 1, 2, \dots, n \tag{21}$$

With the residual it is expressed as

$$\int_x W_i(x)R(x)dx = 0, \quad i = 0, 1, 2, \dots, n \tag{22}$$

Using (21), Eq. (22) becomes

$$\int_x x^i R(x)dx = 0, \quad i = 0, 1, 2, \dots, n \tag{23}$$

Now by using this, residual will be obtained.

4 Exact Solution

To calculate exact solution, we consider $\beta = 0$, $n = 0$, $N_r = 0$ and porosity parameter $N_p = 0$ in Eq. (4), then equation reduced in following form i.e.

$$\frac{d^2\theta}{dx^2} - M^2(\theta - \theta_a) - Pe\frac{d\theta}{dx} + M^2G(1 + \varepsilon_G(\theta - \theta_a)) = 0 \tag{24}$$

The boundary conditions are

$$\theta(1) = 1, \quad \left. \frac{d\theta}{dx} \right|_{x=0} = 0$$

After applying boundary conditions to Eq. (24), we get

$$\theta = c_1e^{m_1x} + c_2e^{m_2x} + \frac{M^2G}{Q} \tag{25}$$

where $c_1 = -\frac{m_2(1-\frac{M^2G}{Q})}{m_1e^{m_2} - m_2e^{m_1}}$, $c_2 = \frac{m_1(1-\frac{M^2G}{Q})}{m_1e^{m_2} - m_2e^{m_1}}$ and $Q = M^2 - M^2G\varepsilon_G$.

5 Results and Discussion

We investigate heat transfer in a porous moving fin. Impact of different parameters namely thermal conductivity (β), thermo-geometric (M), radiation-conduction (N_r), Peclet number (Pe), parameter G , heat generation (ε_G), dimensionless ambient temperature (θ_a), porosity parameter (N_p) on temperature distribution is investigated. Thermal conductivity is taken as a variable functions of temperature to study the distribution of temperature in fin. The four different cases for thermal conductivity are (i) linear function of temperature, (ii)

Table 1. Comparison between Exact result, LWCM, LSM and MM

X	Exact result	LWCM	LSM	MM
0.0	0.60736577	0.60736561	0.60736577	0.60736577
0.1	0.60996007	0.60995991	0.60996050	0.60996053
0.2	0.61813073	0.61813058	0.61813085	0.61813089
0.3	0.63254936	0.63254923	0.63254871	0.63254872
0.4	0.65402333	0.65402322	0.65402256	0.65402252
0.5	0.68351841	0.68351832	0.68351836	0.68351831
0.6	0.72218556	0.72218548	0.72218629	0.72218626
0.7	0.77139233	0.77139227	0.77139303	0.77139305
0.8	0.83275995	0.83275990	0.83275985	0.83275991
0.9	0.90820686	0.90820684	0.90820638	0.90820642
1.0	1.00000000	1.0000000	1.00000000	1.00000000

constant, (iii) exponential function of temperature, and (iv) quadratic form of temperature, and heat transfer coefficient is taken as a power-law type. We find the analytic solution to the problem using LWCM, LSM, and MM. A comparison of the exact, LWCM, LSM, and MM is shown in Table 1 to validate the results obtained by these methods when compared to exact results. We can see from the table that the results of these methods are very close to the exact results, which shows the novelty of present work. To determine which method has the highest accuracy, we compute error analysis, as shown in Fig. 2. It has been observed that the error in LWCM is the lowest as compared to LSM and MM. So for further computation, we used LWCM. Reference values for parameters are taken as $\beta = 1, M = 1, Pe = 1, G = 0.1, \varepsilon_G = 0.1, N_r = 1, n = 1, \theta_a = 0.1, N_p = 0.1$.

Figure 3 depicts the impact of thermal conductivity in four cases on temperature. In case III, where thermal conductivity is an exponential form of temperature, a maximum temperature has been observed, whereas in case II, a lower temperature has been observed. As a result, in cases of constant thermal conductivity, cooling is more effective.

Figure 4 describes the impact of thermal conductivity on temperature for cases I, III, and IV, while in case II, thermal conductivity is constant. From the figure, we have noted that by rising the thermal conductivity, fin temperature also rises. Case III has the maximum temperature distribution as compared to the other cases. So when fin has a lower thermal conductivity, cooling becomes more effective in the fin.

Figure 5 depicts the effect of thermo-geometric parameter. It has been noted that as M increases, the temperature in the fin decreases, implying that the enhancement of heat in the environment increases. At a constant value of the heat transfer coefficient, by increasing the fin length, the amount of heat moving through the fin also increases, resulting in a decrease in temperature. Among the cases, in case II temperature is minimum.

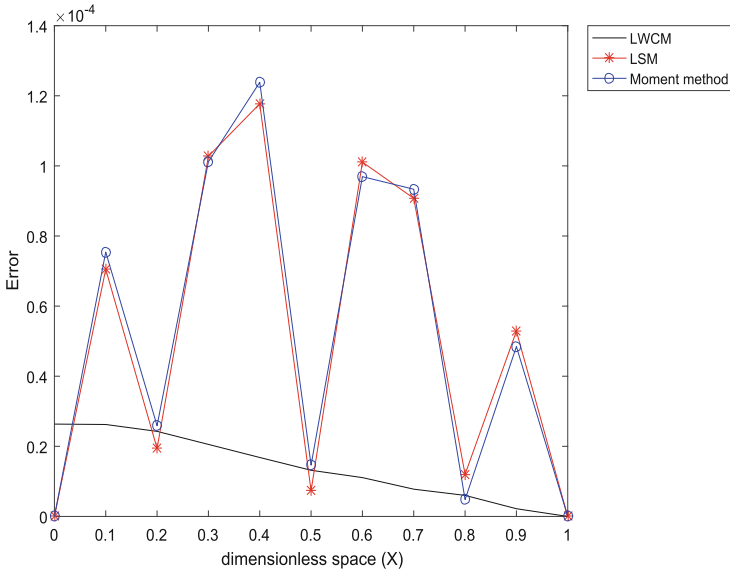


Fig. 2. Error analysis of LWCM, LSM and Moment method

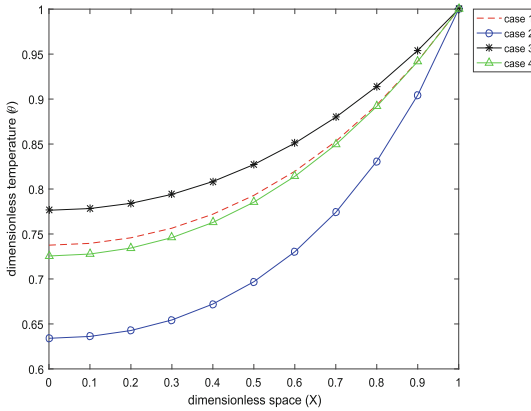


Fig. 3. Temperature distribution in fin for thermal conductivity in cases I, II, III and IV

Figure 6 shows the impact of radiation-conduction. The radiative cooling happens to be more influential if radiative transport is stronger, resulting in lesser the fin temperature. This temperature drop causes the system to cool. We observed that by rising N_r temperature in the fin drops. So case II has a lower temperature compared to other cases.

Figure 7 shows the impact of the Peclet number. We see that by increasing the parameter Pe , fin temperature drops. If Pe increases, then the fin will move

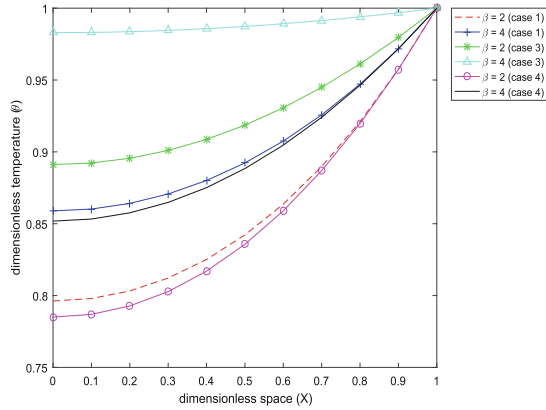


Fig. 4. Effect of β on temperature distribution

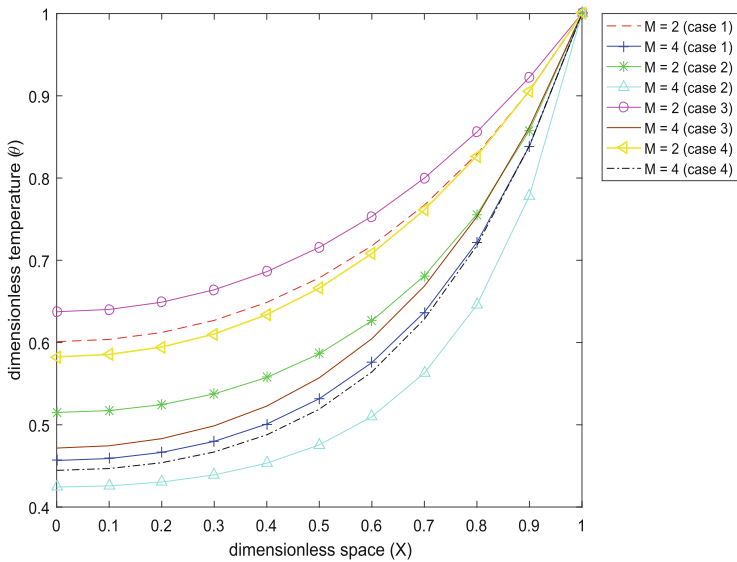


Fig. 5. Effect of M on temperature distribution

faster, and consequently, the temperature in the fin will decrease rapidly because of the increased impact of the adjective on the fin surface. At $Pe = 0$, the fin describes a stationary fin, the fin takes longer to cool down which has been represented by the maximum temperature than a moving fin. The temperature distribution in fin of Case II is lower means cooling process is more effective in this case. The impact of the G parameter is depicted in Fig. 8. It has been seen that by rising the value of G temperature also increases. So case III has a high

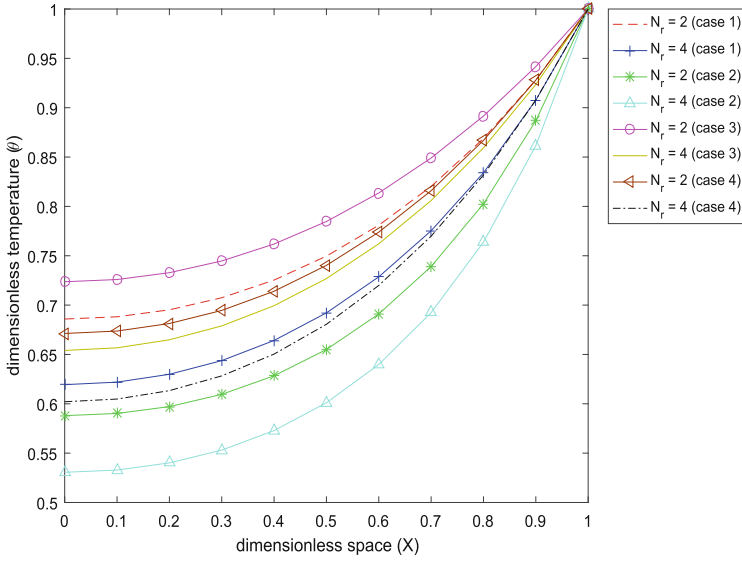


Fig. 6. Effect of N_r on temperature distribution

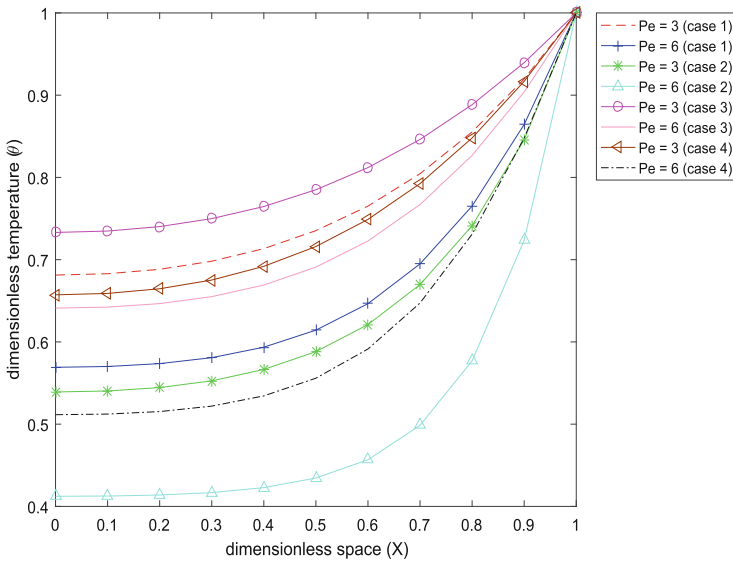


Fig. 7. Effect of Pe on temperature distribution

temperature, whereas case II has a lower temperature. Heat transfer increases when a fin has constant thermal conductivity.

The impact of heat generation is shown in Fig. 9. It demonstrated that increasing the value of the ε_G parameter raises the fin temperature. Among

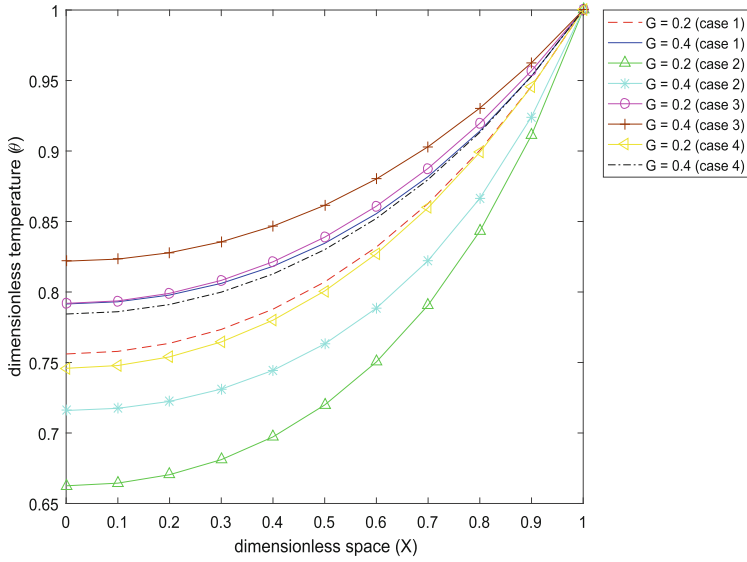


Fig. 8. Effect of G on temperature distribution

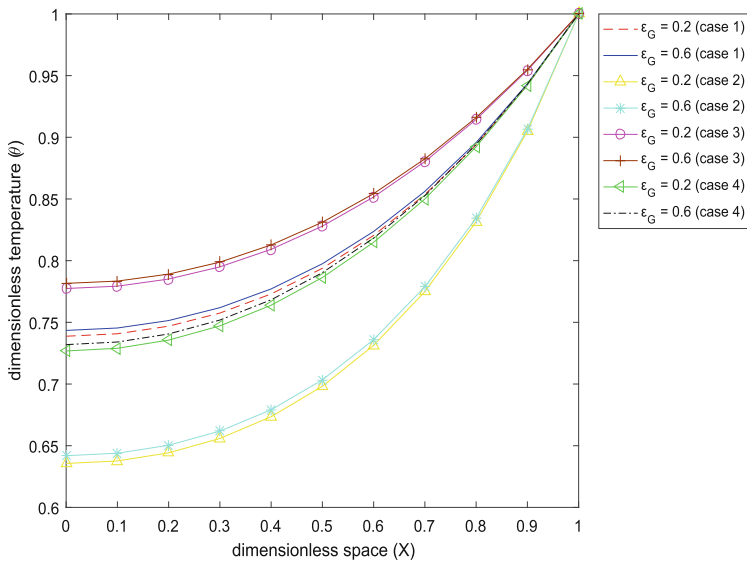


Fig. 9. Effect of ϵ_G on temperature distribution

the cases, case III has a high temperature, and case II has a lower temperature. The physical implementation is that as the heat generation parameter increases, so does the heat transfer in fins.

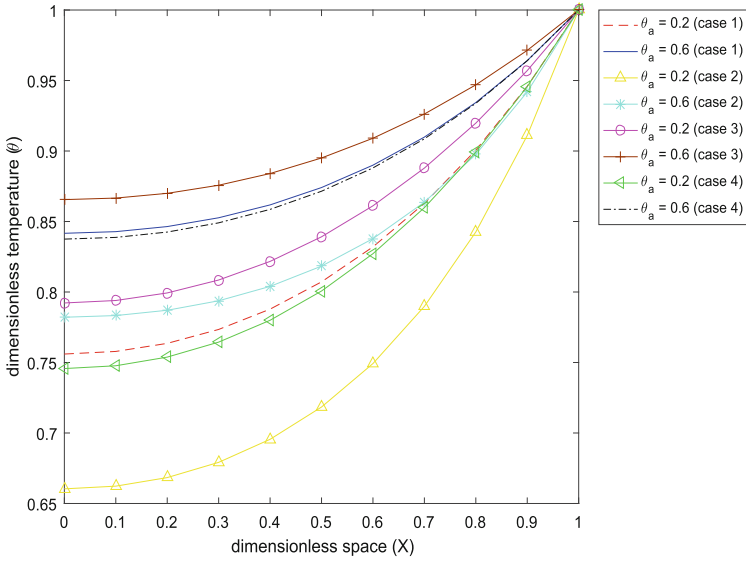


Fig. 10. Effect of θ_a on temperature distribution

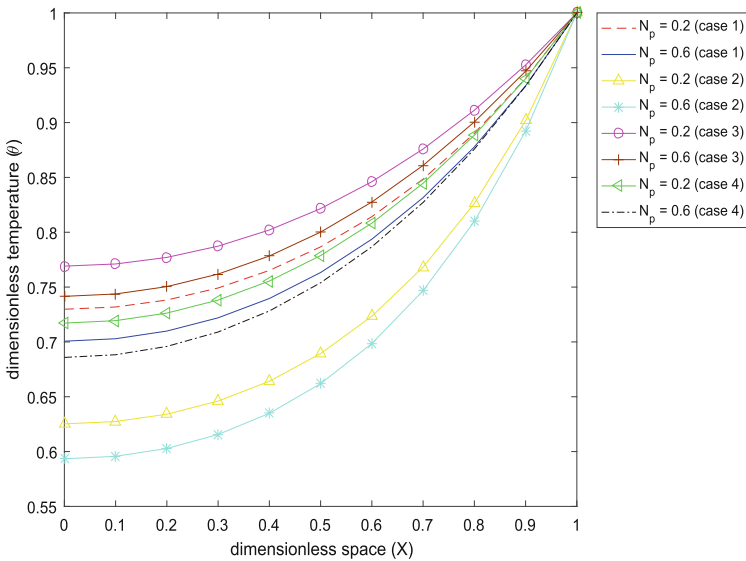


Fig. 11. Effect of N_p on temperature distribution

Figure 10 depicts the impact of ambient temperature. It has been noted that by rising the value of θ_a temperature also rises in the fin. Heat transfer is reduced as the ambient temperature rises. Case III has a high temperature, but Case II

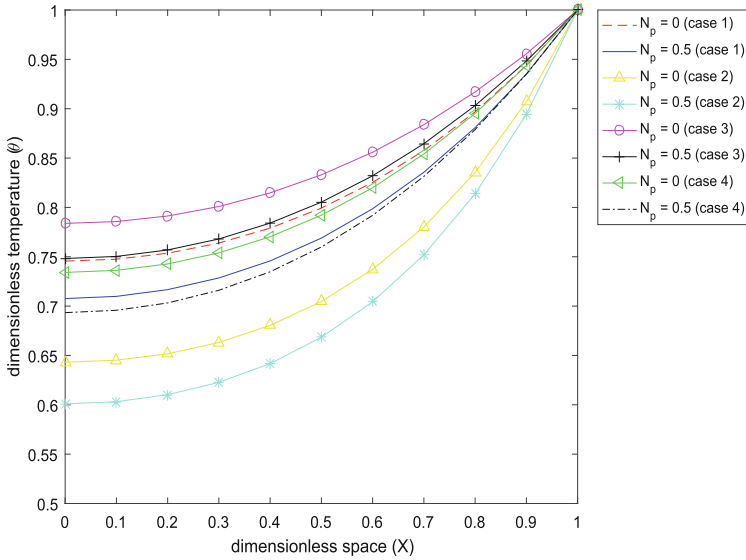


Fig. 12. Temperature distribution in porous and non-porous fin

Table 2. Effect of n on temperature distribution for case I and case II

X	Case I			Case II		
	$n = -1/4$	$n = 1/4$	$n = 3$	$n = -1/4$	$n = 1/4$	$n = 3$
0.0	0.69323516	0.71470983	0.77346094	0.54537012	0.59130005	0.69172816
0.1	0.69570138	0.71694526	0.77512536	0.54813997	0.59370248	0.69341971
0.2	0.70331016	0.72384736	0.78027217	0.5568822	0.60129448	0.6987752
0.3	0.71640567	0.73574874	0.78918116	0.57237481	0.61478202	0.70832539
0.4	0.73537067	0.75303577	0.8022051	0.5956056	0.63508233	0.72278761
0.5	0.76062799	0.77615241	0.81978112	0.627819	0.66337503	0.74311413
0.6	0.79264528	0.80560682	0.84244756	0.67059916	0.70119042	0.77058766
0.7	0.83194463	0.84198195	0.87086785	0.7259869	0.75053383	0.80695858
0.8	0.87911928	0.88595224	0.90586468	0.79666439	0.81407852	0.85466678
0.9	0.93486072	0.9383092	0.94847023	0.88627726	0.89549279	0.91723885
1.0	1.00000000	1.00000000	1.00000000	1.00000000	1.00000000	1.00000000

has a lower temperature. So in this case, cooling will be effective when fin has constant thermal conductivity and a lower ambient temperature.

Figure 11 shows the effect of the porosity parameter. From the figure, it has been seen that as we increased the porosity parameter, the fin temperature decreases. For porosity, Case III has the maximum temperature distribution as compared to other cases. Therefore, in Case II, the heat transfer rate increases, which causes a drop in the fin temperature. Temperature distribution in the

Table 3. Effect of n on temperature distribution for case III and case IV

X	Case III			Case IV		
	$n = -1/4$	$n = 1/4$	$n = 3$	$n = -1/4$	$n = 1/4$	$n = 3$
0	0.74403087	0.75931011	0.80483742	0.67397956	0.69937334	0.76522521
0.1	0.74630373	0.76140001	0.80642881	0.67670894	0.70181414	0.76699524
0.2	0.75326493	0.76780529	0.81131375	0.68515133	0.7093689	0.77247932
0.3	0.76512589	0.7787374	0.81968459	0.69969572	0.72240984	0.78198184
0.4	0.78208927	0.7944145	0.8317691	0.72072724	0.74133192	0.79586672
0.5	0.80434257	0.81505629	0.8478317	0.74860895	0.76653999	0.81455987
0.6	0.83205302	0.84087907	0.8681755	0.78366283	0.79843398	0.83855269
0.7	0.8653644	0.8720917	0.89314549	0.82615455	0.83739441	0.86840696
0.8	0.9043965	0.90889278	0.92313314	0.87628613	0.88377108	0.9047623
0.9	0.94924758	0.95146973	0.95858275	0.9342003	0.93787821	0.9483478
1.0	1.00000000	1.00000000	1.00000000	1.00000000	1.00000000	1.00000000

porous and non-porous fin is shown in Fig. 12. The figure explains that if there is no porous medium, i.e. $N_p = 0$ then the temperature in fin is at its maximum, but if we add a porous medium to the fin, then temperature decreases. We observed that fin temperature is higher in non-porous compared to porous fin. So for higher porosity, heat transfer in the fin also increases, and cooling process in the fin becomes more effective.

Table 2 represents the impact of n on temperature in cases I and II, respectively, and for cases III and IV, it is represented in Table 3. According to the tables, as the value of n rises, so does the fin temperature. So when $n = -1/4 = 1/4$ (i.e., condensation or laminar film boiling), cooling is effective. Case III has a higher temperature as compared to other cases.

6 Conclusion

We have studied a porous moving fin in one-dimension with heat generation, temperature-dependent variable thermal conductivity, and a power-law heat transfer coefficient in this paper. The effect of parameters has been shown using LWCM because it achieves the minimum error among other applied methods. It has been determined that increasing thermal conductivity, heat generation, the parameter G , exponent n , and the ambient temperature raises the temperature in fins. On the other hand, as the temperature in fin decreases, the enhancement of heat increases by increasing the thermo-geometric, radiation-conduction, Peclet number, and porosity parameters. In case III, the fin temperature is high, while in case II, the fin temperature is low. A comparison of porous and non-porous fins revealed that the non-porous fin has a high temperature, whereas adding a porous medium to the fin results in a lower temperature. Because of the porous medium in the fin, heat transmission increases, making cooling more effective.

Future studies may focus on the importance of enhancing heat transmission due to its usefulness in many applications directly affecting human life.

Acknowledgement. The authors are grateful to the Vice-Chancellor of Eternal University, Baru Sahib, India, for providing the necessary facilities. The authors convey their cordial thanks to the reviewers for their valuable suggestions and comments to improve the quality of the manuscript.

References

1. Dogonchi, A.S., Ganji, D.D.: Convection-radiation heat transfer study of moving fin with temperature-dependent thermal conductivity, heat transfer coefficient and heat generation. *Appl. Therm. Eng.* **103**, 705–712 (2016)
2. Kraus, A.D., Aziz, A., Welty, J., Sekulic, D.P.: Extended surface heat transfer. *Appl. Mech. Rev.* **54**(5), B92–B92 (2001)
3. Gorla, R.S.R., Bakier, A.Y.: Thermal analysis of natural convection and radiation in porous fins. *Int. Commun. Heat Mass Transf.* **38**(5), 638–645 (2011)
4. Kiwan, S., Al-Nimr, M.A.: Using porous fins for heat transfer enhancement. *J. Heat Transf.* **123**(4), 790–795 (2001)
5. Ndlovu, P.L., Moitsheki, R.J.: Analysis of transient heat transfer in radial moving fins with temperature-dependent thermal properties. *J. Therm. Anal. Calorim.* **138**(4), 2913–2921 (2019). <https://doi.org/10.1007/s10973-019-08306-5>
6. Khalaf, A.F., et al.: Improvement of heat transfer by using porous media, nanofluid, and fins: a review. *J.* **40**(2), 497–521 (2022). <http://ieta.org/journals/ijht>
7. Gupta, S., Kumar, D., Singh, J.: Magnetohydrodynamic three-dimensional boundary layer flow and heat transfer of water-driven copper and alumina nanoparticles induced by convective conditions. *Int. J. Mod. Phys. B* **33**(26), 1950307 (2019)
8. Ndlovu, P.L., Moitsheki, R.J.: Steady state heat transfer analysis in a rectangular moving porous fin. *Propuls. Power Res.* **9**(2), 188–196 (2020)
9. Unal, H.C.: An analytic study of boiling heat transfer from a fin. *Int. J. Heat Mass Transf.* **30**(2), 341–349 (1987)
10. Shateri, A.R., Salahshour, B.: Comprehensive thermal performance of convection-radiation longitudinal porous fins with various profiles and multiple nonlinearities. *Int. J. Mech. Sci.* **136**, 252–263 (2018)
11. Hatami, M., Hasanpour, A., Ganji, D.D.: Heat transfer study through porous fins (Si₃N₄ and AL) with temperature-dependent thermal conductivity. *Energy Convers. Manag.* **74**, 9–16 (2013)
12. Razzaghi, M., Yousefi, S.: The Legendre wavelets operational matrix of integration. *Int. J. Syst. Sci.* **32**(4), 495–502 (2001)
13. Singh, S., Kumar, D., Rai, K.N.: Convective-radiative fin with temperature dependent thermal conductivity, heat transfer coefficient and wavelength dependent surface emissivity. *Propuls. Power Res.* **3**(4), 207–221 (2014)
14. Sobamowo, M.G., Kamiyo, O.M., Salami, M.O., Yinusa, A.A.: Thermal assessment of a convective porous moving fins of different material properties using Laplace-variational iterative method. *World Sci. News* **139**(2), 135–154 (2020)
15. Sobamowo, G.: Finite element thermal analysis of a moving porous fin with temperature-variant thermal conductivity and internal heat generation. *Rep. Mech. Eng.* **1**(1), 110–127 (2020)

16. Singh, S., Kumar, D., Rai, N.K.: Wavelet collocation solution of non-linear Fin problem with temperature dependent thermal conductivity and heat transfer coefficient. *International J. Nonlinear Anal. Appl.* **6**(1), 105–118 (2015)
17. Bhanja, D., Kundu, B., Aziz, A.: Enhancement of heat transfer from a continuously moving porous fin exposed in convective-radiative environment. *Energy Convers. Manag.* **88**, 842–853 (2014)
18. Chen, H., Ma, J., Liu, H.: Least square spectral collocation method for nonlinear heat transfer in moving porous plate with convective and radiative boundary conditions. *Int. J. Therm. Sci.* **132**, 335–343 (2018)
19. Singh, S., Kumar, D., Rai, K.N.: Wavelet collocation solution for convective radiative continuously moving fin with temperature dependent thermal conductivity. *Int. J. Eng. Adv. Technol.* **2**(4), 10–16 (2013)
20. Moradi, A., Fallah, A.P.M., Hayat, T., Aldossary, O.M.: On solution of natural convection and radiation heat transfer problem in a moving porous fin. *Arab. J. Sci. Eng.* **39**(2), 1303–1312 (2014)
21. Singh, S., Kumar, D., Rai, K.N.: Analytical solution of Fourier and non-Fourier heat transfer in longitudinal fin with internal heat generation and periodic boundary condition (2018)
22. Wang, F., et al.: LSM and DTM-Pade approximation for the combined impacts of convective and radiative heat transfer on an inclined porous longitudinal fin. *Case Stud. Therm. Eng.* **35**, 101846 (2022)
23. Singh, J., Rashidi, M.M., Kumar, D.: A hybrid computational approach for Jeffery-Hamel flow in non-parallel walls. *Neural Comput. Appl.* **31**(7), 2407–2413 (2019)
24. Singh, J., Kumar, D., Baleanu, D.: A hybrid analytical algorithm for thin film flow problem occurring in non-Newtonian fluid mechanics. *Ain Shams Eng. J.* **12**(2), 2297–2302 (2021)
25. Singh, H., Singh, A.K., Pandey, R.K., Kumar, D., Singh, J.: An efficient computational approach for fractional Bratu's equation arising in electrospinning process. *Math. Methods Appl. Sci.* **44**(13), 10225–10238 (2021)



Multi-objective Linear Fractional Transportation Problem Under Uncertainty

Rachana Saini, Vishwas Deep Joshi^(✉), and Jagdev Singh

Department of Mathematics, Faculty of Science, JECRC University, Jaipur, Rajasthan, India
vdjoshi.or@gmail.com

Abstract. This paper proposes a multi-objective linear fractional transportation problem (MOLFTP) with uncertain programming. The fractional transportation problem considers situations where decision-makers are interested in maximizing or minimizing the ratio of certain functions rather than simple functions. All the parameters involved in the problem raised i.e. it is assumed that the availability and demand of the objective function coefficients are uncertain. In addition, an equivalent certainty problem is also raised. Three different methods are the weighted sum method, fuzzy programming, and global criterion method, which are used to obtain the best compromise for the proposed model. A numerical example is also given to support the theory.

Keywords: Multi-objective linear fractional transportation problem · Uncertain programming · Weighted-sum method · Global criterion method

1 Introduction

In recent years, with the globalization of the economy, the issue of freight transportation has received more and more attention from more and more companies and enterprises, especially many multinational corporations. A TP is an optimization problem that seeks to optimize the distribution of quantities from multiple sources to multiple destinations to minimize total cost. Traditional traffic models generally consist of an objective function and two types of constraints: source and destination constraints. It was started by Hitchcock [1] and later it was developed by Coopmans [2].

Some years later, Dantzig [15] proposed the simplex method and applied it to the solution of transport models. Since then, many researchers have started to study the traffic problem. Srinivasan and Thompson [16] proposed an operator theory for the parametric programming of transport problems. In 1991, Vignaux and Michalewicz [17] published a genetic algorithm for linear transport problems. In these classic models, unit prices for transportation, supply, and demand are assumed to be crisp numbers.

Uddin et al. [3] proposed the use of a fuzzy membership function tactic based on goal programming to obtain a desirable compromise for the multi-objective transport problem in uncertain environments where the DM can choose confidence levels for various parameters. Sheng and Yao [4] have shown fixed charge transportation problems based

on uncertainty theory. Javaid et al. [5] presented a model for transportation problems involving uncertain parameters with multiple fractional objectives.

Roy et al. [8] investigate a multi-objective multi-item fixed-charge solid transportation problem (MOMIFCSTP) uses objective functions and constraint coefficients with fuzzy-rough variables. Traffic systems are analyzed in a fuzzy and rough environment. Roy and Midya [9] proposed a multi-objective fixed charge transport problem (MOFCTP). In this problem, the objective function parameters are random rough variables, and the supply and demand parameters are coarse variables. To deal with uncertain (rough and random rough) parameters, the proposed model employs the expectation operator. Midya, S. and Roy, S.K. [10] analyze the MOFCTP using rough programming. To obtain Pareto optimal solutions from deterministic MOFCTP uses Fuzzy programming and linear weighted sum methods. Upmanyu and Saxena [11] discussed fixed-cost problems as a special type of nonlinear programming problem that underlies many industry problems related to cost-related execution activities. It describes a solution algorithm for solving fixed charge problems using multiple fractional objective functions that are all fuzzy. Meity et al. [14] MOTP addresses uncertainty in real-life decision-making problems and incorporates the concept of reliability into transportation cost and effectiveness. The Fuzzy Multiple-Choice Objective and Fuzzy Multiple Choice Goal Planning (FMCGP) of the MOTP objective function are used to select the proper objective for the proposed MOTP. They get compromises and modify the proper objective of the MOTP objective function.

A new approach for solving MOLFTP using uncertain programming is in this paper. This is prepared as follows: Mathematical model in Sect. 2, the definition in Sect. 3, solution methodology in Sect. 4, numerical example in Sect. 5, results in Sect. 6, and conclusion in the last section.

2 Mathematical Model

As a practical result, the transportation problem (TP) habitually understands multiple conflicting objectives related to transportation from multiple origins to different destinations. TP for m sources (origins) and n destinations (demands), the source is a factory or production facility, warehouse, etc., commonly used symbols a_1, a_2, \dots, a_m , the destination is warehouse, outlet, etc., commonly used symbols b_1, b_2, \dots, b_n . If C_{ij} and D_{ij} are the transporting unit cost and unit profit for transporting goods from the i^{th} origin to the j^{th} destination, x_{ij} is the unknown quantity transferred from the i^{th} origin to the j^{th} destination, then the fractional transportation model is following.

(P1)

$$\text{Min } Z = \left(\frac{\sum_{i=1}^m \sum_{j=1}^n C_{ij} x_{ij}}{\sum_{i=1}^m \sum_{j=1}^n D_{ij} x_{ij}} \right),$$

Sub to

$$\sum_{j=1}^n x_{ij} \leq a_i, \quad i = 1, 2, \dots, m,$$

$$\sum_{i=1}^m x_{ij} \geq b_j, \quad j = 1, 2, \dots, n,$$

$$x_{ij} \geq 0, \quad \forall i, j, \quad (1)$$

The feasibility condition of model (P₁) is

$$\sum_{i=1}^m a_i \geq \sum_{j=1}^n b_j \quad (2)$$

In today's highly competitive world, transportation problems have multiple objectives that make it very difficult for decision-makers (DM) to succeed their desired aspirations. In this situation, MOLFTP is a very inspiring working tool for DM, as shown below.

(p₂)

$$\text{Min } Z^k = \left(\frac{\sum_{i=1}^m \sum_{j=1}^n C_{ij}^k x_{ij}}{\sum_{i=1}^m \sum_{j=1}^n D_{ij}^k x_{ij}} \right),$$

Sub to

$$\sum_{j=1}^n x_{ij} \leq a_i, \quad i = 1, 2, \dots, m,$$

$$\sum_{i=1}^m x_{ij} \geq b_j, \quad j = 1, 2, \dots, n,$$

$$x_{ij} \geq 0, \quad \forall i, j, \quad (3)$$

where If C_{ij}^k and D_{ij}^k are the transporting unit cost and unit profit for transporting goods from the i^{th} origin to the j^{th} destination for k objectives, $a_i (i = 1, 2, \dots, m)$ are the supply and $b_j (j = 1, 2, \dots, n)$ are the demand parameter for the k^{th} ($k = 1, 2, \dots, K$) the objective function of the MOLFTP. In general, the quantity C_{ij}^k, D_{ij}^k, a_i and b_j are considered as crisp numbers.

Information about transportation parameters may not be complete, which creates payoff uncertainty. DM can handle converting this situation's uncertain parameters into crisp numbers. In this paper, we developed an algorithm considering the uncertainty of parameters and incorporated the uncertainty scale derived by Liu [6] and [7]. To produce apply an uncertain normal distribution of the corresponding crisp values for the parameters.

3 Definitions

Definition 3.1: Let \bar{h} be an uncertain variable. Then \mathfrak{R} the uncertainty distribution is expressed as \mathfrak{R} of \bar{h} is defined by $\mathfrak{R}(x) = \Omega(\bar{h} \leq x)$ for any real variable x , Ω is the uncertainty measure function [6, 7].

Definition 3.2: The uncertainty parameter φ is a normal uncertainty distribution $\varphi(x) = \left[1 + \exp\left(\frac{\pi(e-x)}{\sqrt{3}\sigma}\right)\right]^{-1}$ for any real number x . It's called regular depends on $N(e, \sigma)$. Where e and σ are real numbers and $\sigma > 0$ [6, 7].

Definition 3.3: Let \bar{h} be an uncertain variable with a generally uncertain distribution $\mathfrak{R}(x)$. Second, the inverse function $\mathfrak{R}^{-1}(x)$ is called the inverse uncertainty distribution of \bar{h} for any real number x [6, 7].

Current research considers transportation parameters such as TP cost, supply, and demand to be uncertain variables, so the model (P₂) uses uncertain measurements.

Theorem 3.1: If \bar{h} is an uncertain variable concerning an uncertain distribution \mathfrak{R} , then for any real number x , $\mathfrak{R}(x) = \Omega(\bar{h} \leq x)$ then $\Omega(\bar{h} \geq x) = 1 - \mathfrak{R}(x)$ (Inverse measure theorem [6, 7]).

Model (P₂) can be written to introduce the inverse measure theorem as follows:

(P₃)

$$\text{Min } Z^k(x) = \sum_{i=1}^m \sum_{j=1}^n \left[\Omega\left(\frac{C_{ij}^k}{D_{ij}^k}\right) \geq \alpha_{ij} \right] x_{ij},$$

Sub to

$$\begin{aligned} \Omega\left(\sum_{j=1}^n x_{ij} \leq a_i\right) &\geq \gamma_i, \quad i = 1, 2, \dots, m, \\ \Omega\left(\sum_{i=1}^m x_{ij} \geq b_j\right) &\geq \delta_j, \quad j = 1, 2, \dots, n, \\ x_{ij} &\geq 0, \forall i, j. \end{aligned} \tag{4}$$

The Normal uncertain variable $N(e, \sigma)$ is defined as $\mathfrak{R}^{-1}(x) = e + \frac{\sqrt{3}\sigma}{\pi} \ln\left(\frac{u}{1-u}\right)$ where ‘ln’ denotes natural logarithm and x is the level of confidence of the DM is called the inverse normal uncertainty distribution.

Due to the presence of uncertain variables the model (P₃) is not a deterministic form.

The uncertainty distributions β_{ij}, θ_i and ψ_j of cost C_{ij}^k and profit D_{ij}^k ($i = 1, 2, \dots, m; j = 1, 2, \dots, n; k = 1, 2, \dots, K$), demand a_i ($i = 1, 2, \dots, m$) and supply parameters b_j ($j = 1, 2, \dots, n$) respectively, the inverse measure shows the following results:

$$\Omega\left(\frac{C_{ij}^k}{D_{ij}^k}\right) \geq \alpha_{ij} \approx \frac{C_{ij}^k}{D_{ij}^k} \geq \beta_{ij}^{-1}(1 - \alpha_{ij})$$

$$\Omega\left(\sum_{j=1}^n x_{ij} \leq a_i\right) \geq \gamma_i \Rightarrow \sum_{j=1}^n x_{ij} \leq \theta_i^{-1}(1 - \gamma_i)$$

and

$$\Omega\left(\sum_{i=1}^m x_{ij} \geq b_j\right) \geq \delta_j \text{ is reduced to } \sum_{j=1}^n x_{ij} \leq \psi_j^{-1}\delta_j$$

The model (P₃) is decrease as follows:

(P₄)

$$\text{Min } Z^k(x) = \sum_{i=1}^m \sum_{j=1}^n \left[\beta_{ij}^{-1}(1 - \alpha_{ij}) \right] x_{ij},$$

Sub to

$$\sum_{j=1}^n x_{ij} \leq \theta_i^{-1}(1 - \gamma_i), \quad i = 1, 2, \dots, m,$$

$$\sum_{j=1}^n x_{ij} \leq \psi_j^{-1}\delta_j, \quad j = 1, 2, \dots, n,$$

$$x_{ij} \geq 0, \forall i, j. \quad (5)$$

Now fuzzy linear membership function $\mu_k(Z^k(x))$ for MOFTP where L^k is the lower bound and U^k is the upper bound of each $Z^k(x)$, as follows:

$$\mu_k\left(Z^k(x)\right) = \begin{cases} 1, & \text{if } Z^k \leq L^k \\ 1 - \frac{Z^k - L^k}{U^k - L^k}, & \text{if } L^k < Z^k < U^k \\ 0, & \text{if } Z^k \geq U^k \end{cases} \quad (6)$$

where $L^k \neq U^k, k = 1, 2, \dots, K$. If $L^k = U^k$, then $\mu_k(Z^k(x)) = 1$ for any value of k. Then model (P₄) can be inscribed as

(P₅)

$$\text{Min } \mu_k\left(Z^k(x)\right).$$

Sub to

$$\sum_{j=1}^n x_{ij} \leq \theta_i^{-1}(1 - \gamma_i), \quad i = 1, 2, \dots, m,$$

$$\sum_{j=1}^n x_{ij} \leq \psi_j^{-1}\delta_j, \quad j = 1, 2, \dots, n,$$

$$x_{ij} \geq 0, \forall i, j. \quad (7)$$

Model (P₅) is converted into introducing an auxiliary variable η , the following traditional LPP:

(P₆)

$$\text{Max } \eta$$

Sub to

$$\begin{aligned} \eta &\leq \mu_k(Z^k(x)) \\ \sum_{j=1}^n x_{ij} &\leq \theta_i^{-1}(1 - \gamma_i), \quad i = 1, 2, \dots, m, \\ \sum_{j=1}^n x_{ij} &\leq \psi_j^{-1}\delta_j, \quad j = 1, 2, \dots, n, \\ 0 &\leq \eta \leq 1, x_{ij} \geq 0, \forall i, j. \end{aligned} \tag{8}$$

4 Solution Methodology

If the information is imperfect, the DM cannot predict the desired optimal target, but it does so by transforming the uncertain parameters into deterministic numbers using the normal distribution $N(e, \sigma)$. You can choose a confidence level ν , where e is the expected value of the uncertainty parameter and σ is the deviation. To achieve the desired goal, the DM considers the following events.

- 1) Use the inverse uncertainty normal distribution $\mathfrak{R}^{-1}(x) = e + \frac{\sqrt{3}\sigma}{\pi} \ln\left(\frac{\nu}{1-\nu}\right)$ to calculate the uncertain unit cost and unit profit (C_{ij}^k and D_{ij}^k) for transporting goods from the i^{th} origins to j^{th} destinations selected confidence level ν for DM selection.
- 2) The inverse uncertain normal distribution $\mathfrak{R}^{-1}(x) = e + \frac{\sqrt{3}\sigma}{\pi} \ln\left(\frac{1-\nu}{\nu}\right)$, calculate the uncertain demand table using the demand for each event choosing the confidence level ν from DM.
- 3) The inverse uncertainty normal distribution $\mathfrak{R}^{-1}(x) = e + \frac{\sqrt{3}\sigma}{\pi} \ln\left(\frac{\nu}{1-\nu}\right)$, compute the supplies listed from the uncertain supply table. A given confidence level ν comes from DM.

4.1 Stepwise Algorithm for Fuzzy Programming Problem

Step 1: The usual uncertain distribution $N(e_i, \sigma_i)$ is used to determine fixed values for uncertain parameters. Where the parameter e represents the expected value and σ represents the standard deviation to which the confidence level ν selected by DM is applied.

Step 2: Formulated a MOFTP using the full value obtained in step 1.

Step 3: If the MOFTP is solved as a single objective TP, all other objectives are ignored. Continue this process for the K objectives k times.

Step 4: Describe the linear membership function $\mu_k(Z^k)$ for the K^{th} objective function.

Step 5: In step 4 obtained by transforming the fuzzy model, into a crisp model follows as:

$$\text{Max } \eta.$$

Sub to

$$\begin{aligned} \eta &\leq \mu_k(Z^k) \\ \sum_{j=1}^n x_{ij} &\leq a_i, \quad i = 1, 2, \dots, m, \\ \sum_{i=1}^m x_{ij} &\geq b_j, \quad j = 1, 2, \dots, n, \\ \eta &\geq 0, \quad x_{ij} \geq 0, \quad \forall i, j. \end{aligned} \quad (9)$$

Step 6: Solve the revised LPP which we get in step 5.

Step 7: The DM presents the feasible solution. If DM is satisfied, then go to step 8. But DM is not satisfied with the repeat process of step 1 to step 6.

Step 8: Stop.

To better understand the calculation algorithm, the flowchart is shown below in Fig. 1:

4.2 Weighted Sum Method (WSM) and Stepwise Solution

By multiplying each objective function by the weight assigned to it and combining multiple objective functions, WSM transforms multi-objective optimization into an objective optimization problem. Here, the weight ω_k ($k = 1, 2, \dots, K$) corresponds to each objective function Z_k ($k = 1, 2, \dots, K$). Here, ω_k can be estimated as the relative importance or value of the objective function evaluated with other objective functions. In other words, the weight can be interpreted as indicating the priority relative to the objective function. The higher the weight ω_k , the more significant the objective function Z_k is. The minor the weight ω_k is, the smaller the importance of the objective function Z_k is. Then combine them into an objective function $\sum_{k=1}^K \omega_k Z_k$ and $\sum_{k=1}^K \omega_k = 1$. Because of its characteristics, this method is called WSM. The process of the WSM [13] is summarized as follows:

Step 1: First, according to the importance of the objective function in the model (P_2), select the weighting coefficients $\omega_1, \omega_2 \dots \omega_K$ to the objective functions ($Z_k, k = 1, 2, \dots, K$) corresponding to the objective function. Must be $\omega_k > 0, k = 1, 2, \dots, K$ and $\sum_{k=1}^K \omega_k = 1$.

Step 2: A single objective problem is solved when the objective function is the weighted sum of all objective functions. A single-objective problem can be expressed as:

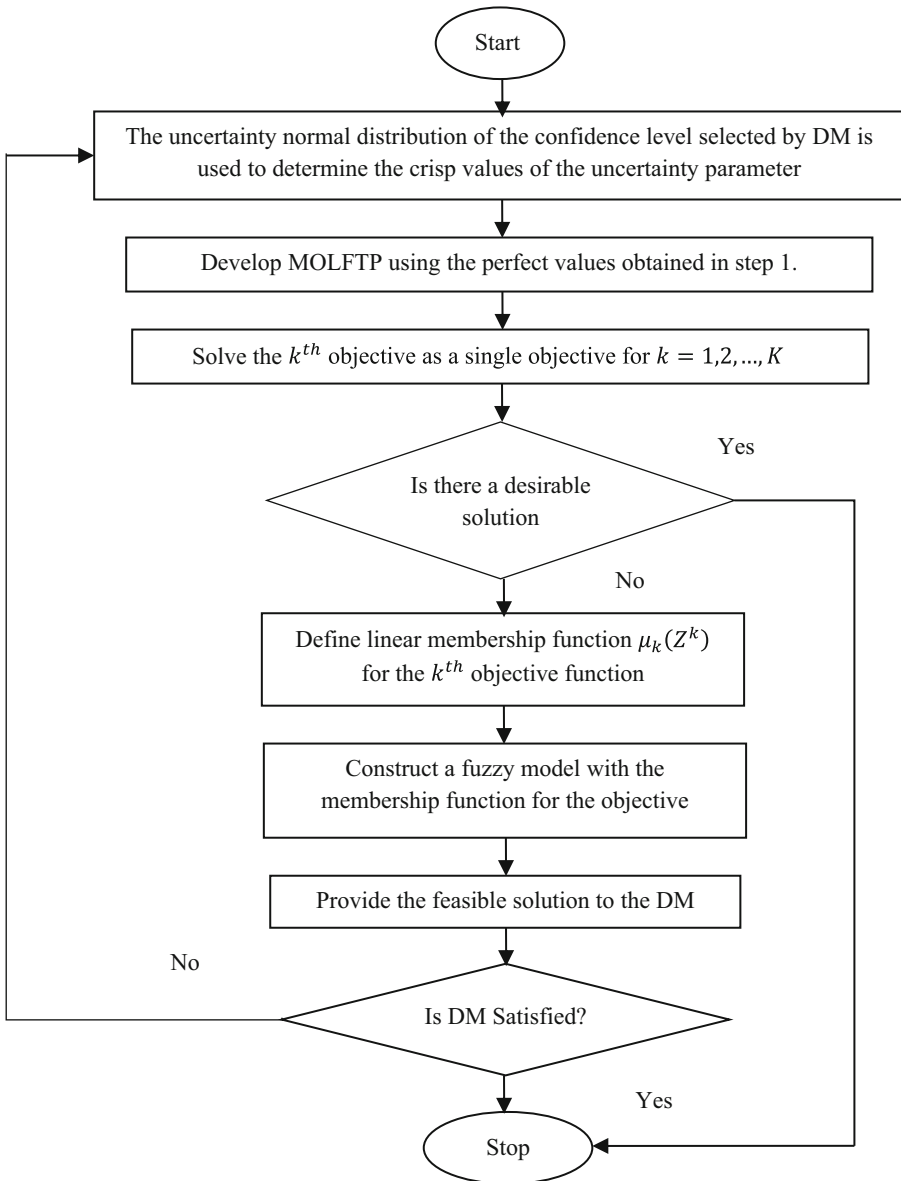


Fig. 1. Flowchart for algorithm

$$\text{Min } \sum_{k=1}^K \omega_k [Z^k(x_{ij})],$$

Sub to

$$\begin{aligned} \sum_{j=1}^n x_{ij} &\leq a_i, \quad i = 1, 2, \dots, m, \\ \sum_{i=1}^m x_{ij} &\geq b_j, \quad j = 1, 2, \dots, n, \\ x_{ij} &\geq 0, \quad \forall i, j \end{aligned} \quad (10)$$

4.3 Global Criterion Method (GSM) and Stepwise Solution

GCM is used to solve MO optimization problems and provide a compromise solution for multi-objective optimization. GCM [12] minimizes the distance between a specific reference point and the feasible objective region. The problems with MOFTP are the following:

$$\text{Min } [Z^1(x), Z^2(x), \dots, Z^K(x)],$$

Sub to

$$\begin{aligned} \sum_{j=1}^n x_{ij} &\leq a_i, \quad i = 1, 2, \dots, m, \\ \sum_{i=1}^m x_{ij} &\geq b_j, \quad j = 1, 2, \dots, n, \\ x_{ij} &\geq 0, \quad \forall i, j. \end{aligned} \quad (11)$$

We can get the solution to the MOFTP problem by following these steps:

Step 1: MOFTP solves the problem of transportation for a single objective. The only single objective function is used at a time, and other objective functions are ignored.

Step 2: Determine the ideal objective point according to the result of step 1, such as $(Z_{min}^1, Z_{min}^2, \dots, Z_{min}^k)$ and the corresponding value $(Z_{max}^1, Z_{max}^2, \dots, Z_{max}^k)$.

Step 3: Formulate the following problem as follows:

$$\text{Min } F(x) = \left[\sum_{k=1}^K \left(\frac{Z^k(x) - Z_{min}^k}{Z_{max}^k - Z_{min}^k} \right)^2 \right]^{\frac{1}{2}},$$

Sub to

$$\begin{aligned} \sum_{j=1}^n x_{ij} &\leq a_i, \quad i = 1, 2, \dots, m, \\ \sum_{i=1}^m x_{ij} &\geq b_j, \quad j = 1, 2, \dots, n, \\ x_{ij} &\geq 0, \quad \forall i, j. \end{aligned} \tag{12}$$

5 Numerical Illustration

To prove the feasibility of the proposed model, MOFTP considers uncertainties in transportation (C_{ij}^k and D_{ij}^k are the transporting unit cost and unit profit for transporting goods from i^{th} origin to the j^{th} destination for k objectives) due to late or early delivery. Market supply and demand are also considered uncertain. DM wants to deliver goods from four origins $O_1, O_2, O_3,$ and O_4 to five destinations $D_1, D_2, D_3, D_4,$ and $D_5,$ and optimizes that objective.

In every case, the inverse uncertainty distributions of the used confidence level $v = 0.1, 0.2, 0.3, 0.4, 0.5, 0.6, 0.7, 0.8, 0.9$ are divided into Tables 1–2 and simplified to Table 3–4.

Table 1. Data for expected value (e) for C_{ij}^k and D_{ij}^k

	D1	D2	D3	D4	D5	a_i
O1	15,21,18 18,19,38	16,25,19 16,20,29	19,27,16 13,23,15	20,28,18 14,26,26	18,22,20 15,27,18	25
O2	13,23,25 19,28,16	12,27,25 12,27,25	13,28,26 13,22,31	14,22,30 18,25,18	16,21,32 14,29,26	28
O3	18,20,38 11,26,23	19,27,27 15,28,39	17,29,21 18,27,38	15,25,21 13,26,21	17,24,33 14,25,27	32
O4	19,29,35 15,25,19	15,23,26 16,22,35	16,24,21 13,23,26	18,26,23 15,27,22	17,28,26 13,29,29	35
b_j	20	25	15	22	18	

Using confidence levels 0.1 to 0.9 get the crisp value represented as in Tables 3 and 4 for the confidence levels 0.1, and 0.2.

Table 2. Data for deviation (σ) C_{ij}^k and D_{ij}^k

	D1	D2	D3	D4	D5	a_i
O1	1,1,1 1,1,2	2,2,2 1,2,1	1,1,1 1.5,1,1	1.5,1,1.5 1,1,1.5	1,1.5,1 2,1.5,1	2
O2	1,1,2 1,1,1	2,1,1 1.5,1,1.5	1.5,2,1 1,2,1	1,1.5,1 2,1.5,1	1,1,1.5 1,1,2	2
O3	2,1.5,1 1,1,1	1,2,1.5 2,1.5,1	1,1,2 1,1,2	1.5,1,2 1.5,2,1	1,1,1 1,1,1.5	1
O4	1.5,1,1 1,2,1.5	2,1.5,2 1,1,2	1,1,1 2,1.5,1	1,1,1.5 1.5,1,1	1,1,2 1,1,1	1
b_j	1.5	1	1	1	1	

Table 3. Using confidence level 0.1, crisp value for uncertain C_{ij}^k and D_{ij}^k

	D1	D2	D3	D4	D5	a_i
O1	13.79,19.79,16.79 16.79,17.79,35.58	13.58,22.58,16.58 14.79,17.58,27.79	17.79,25.79,14.79 11.18,21.79,13.79	18.18,26.79,16.18 12.79,24.79,24.18	15.58,20.18,18.79 12.58,25.18,16.79	27.42
O2	11.79,21.79,22.58 17.79,26.79,14.79	9.58,25.79,23.79 10.18,25.79,23.18	11.18,25.58,24.79 11.79,19.58,29.79	12.79,20.18,28.79 15.58,23.18,16.79	14.79,19.79,30.18 12.79,27.79,23.58	30.42
O3	15.58,18.18,36.79 9.79,24.79,21.79	17.79,24.58,25.18 12.58,26.18,37.79	15.79,27.79,18.58 16.79,25.79,35.58	13.18,23.79,18.58 11.18,23.58,19.79	15.79,22.79,31.79 12.79,23.79,25.18	33.21
O4	17.18,27.79,33.79 13.79,22.58,17.18	12.58,21.18,23.58 14.79,20.79,32.58	14.79,22.79,19.79 10.58,21.18,24.79	16.79,24.79,21.18 13.18,25.79,20.79	15.79,26.79,23.58 11.79,27.79,27.79	36.21
b_j	18.18	23.79	13.79	20.79	16.79	

Table 4. Using confidence level 0.2, crisp value for uncertain C_{ij}^k and D_{ij}^k

	D1	D2	D3	D4	D5	a_i
O1	14.24,20.24,17.24 17.24,18.24,36.47	14.47,23.47,17.47 15.24,18.47,28.24	18.24,26.24,15.24 11.85,22.24,14.24	18.85,27.24,16.85 13.24,25.24,24.85	16.47,20.85,19.24 13.47,25.85,17.24	26.53
O2	12.24,22.24,23.47 18.24,27.24,15.24	10.47,26.24,24.24 10.85,26.24,23.85	11.85,26.47,25.24 12.24,20.47,30.24	13.24,20.85,29.24 16.47,23.85,17.24	15.24,20.24,30.85 13.24,28.24,24.47	29.53
O3	16.47,18.85,37.24 10.24,25.24,22.24	18.24,25.47,25.85 13.47,26.85,38.24	16.24,28.24,19.47 17.24,26.24,36.47	13.85,24.24,19.47 11.85,24.47,20.24	16.24,23.24,32.24 13.24,24.24,25.85	32.76
O4	17.85,28.24,34.24 14.24,23.47,17.85	13.47,21.85,24.47 15.24,21.24,33.47	15.24,23.24,20.24 11.47,21.85,25.24	17.24,25.24,21.85 13.85,26.24,21.24	16.24,27.24,24.47 12.24,28.24,28.24	35.76
b_j	18.85	24.24	14.24	21.24	17.24	

6 Results

This section describes the best results for model P₂ using crisp data extracted from the fuzzy programming method, weighted sum method, and global criterion method using Lingo 17.0 software on a core i3 processor PC.

The value of the fractional objectives as given in the table increases with the increase in the values of the confidence level from (0.1 to 0.9). DMs can define confidence levels based on the relevant organizational context. The DM uses the weight same as 0.3, 0.4, and 0.3 because of different confidence levels in the Weighted sum method (Table 5).

Table 5. Different confidence level values of objectives Z^1, Z^2, Z^3

S.No	Con. Level ν	Z^1			Z^2			Z^3		
		W.S	Fuzzy	G.C.M	W.S	Fuzzy	G.C.M	W.S	Fuzzy	G.C.M
1	0.1	0.90463	0.91064	0.89495	0.96566	0.95607	0.97281	0.75864	0.77408	0.76767
2	0.2	0.92423	0.91334	0.91216	0.96403	0.96548	0.96754	0.76586	0.78525	0.79065
3	0.3	0.93212	0.92107	0.91016	0.9755	0.95778	0.97974	0.75067	0.80795	0.78816
4	0.4	0.93844	0.92577	0.9145	0.97435	0.95897	0.98275	0.75543	0.81583	0.79749
5	0.5	0.94438	0.92993	0.91801	0.9732	0.96022	0.98498	0.75983	0.82263	0.79558
6	0.6	0.93585	0.92643	0.91783	0.99815	0.99054	1.00277	0.76838	0.79755	0.78682
7	0.7	0.9582	0.93858	0.92652	0.97329	0.96325	0.98792	0.76457	0.83389	0.802
8	0.8	0.93899	0.94162	0.92926	1.00037	0.97229	0.99318	0.7714	0.83306	0.80627
9	0.9	0.97893	0.95098	0.94005	0.97568	0.96845	0.98944	0.76995	0.85042	0.82209

7 Conclusion

This paper mainly exploits uncertainty theory to develop a MOLFTP. Given the parameter ambiguity that predominates in the real world, we assume that all parameters are independent and uncertain variables. Uncertain variable problems are often complex to deal with, so apply the expected constraint programming concepts to develop the problem. To solve the resulting MOLFTP, we will explain the weighted sum method, the fuzzy programming method (max-min), and the global criterion method. Finally, numerical examples are also provided to illustrate the applicability of the proposed problem. The results describe the confidence level. Fractional programming has a large scope in modeling various real-world situations, such as information theory problems, inventory management problems, investment allocation problems, segmentation problems, etc. The multi-objective problem can be extended to solve the above practical problems.

References

1. Hitchcock, F.L.: The distribution of a product from several sources to numerous locations. *J. Math. Phys.* **20**, 224–230 (1941)

2. Koopmans, T.C.: Optimum utilization of the transportation system. *Econometrica* **17**, 136–146 (1949)
3. Uddin, M.S., Miah, M., Khan, M.A., Arjani, A.A.: Goal programming tactic for uncertain multi-objective transportation problem using fuzzy linear membership function. *Alex. Eng. J.* **60**, 2525–2533 (2021)
4. Sheng, Y., Yao, K.: Fixed charge transportation problem and its uncertain programming model. *Ind. Eng. Manage. Syst.* **11**(2), 183–187 (2012)
5. Javaid, S., Jalil, S.A., Asim, Z.: A model for uncertain multi-objective transportation problem with fractional objectives. *Int. J. Oper. Res.* **14**(1), 11–25 (2017)
6. Liu, B.: *Uncertainty Theory*, 2nd edn. Springer-Verlag, Berlin (2007)
7. Liu, B.: *Uncertainty Theory: A Branch of Mathematics for Modeling Human Uncertainty*. Springer-Verlag, Berlin (2010)
8. Roy, S.K., Midya, S., Weber, G.-W.: Multi-objective multi-item fixed-charge solid transportation problem under twofold uncertainty. *Neural Comput. Appl.* **31**(12), 8593–8613 (2019). <https://doi.org/10.1007/s00521-019-04431-2>
9. Roy, S.K., Midya, S.: Multi objective fixed-charge transportation problem with random rough variables. *Int. J. Uncertain. Fuzziness Knowl.-Based Syst.* **26**(6), 971–996 (2017)
10. Midya, S., Roy, S.K.: Multi-objective fixed-charge transportation problem using rough programming. *Int. J. Oper. Res.* **37**(3), 377–395 (2020)
11. Upmanyu, M., Saxena, R.R.: On solving a multi-objective fixed charge problem with imprecise fractional objectives. *Appl. Soft Comput.* **40**, 64–69 (2015)
12. Miettinen, K.: *Non-Linear Multi-Objective Optimization*. Kluwer Academic Publishers, USA (1999)
13. Athan, T.W., Papalimberos, P.Y.: A note on weighted criteria methods for compromise solutions in multi-objective optimization. *Eng. Optim.* **27**, 155–176 (1996)
14. Maity, G., Roy, S.K., Verdegay, J.L.: Multi-objective transportation problem with cost reliability under uncertain environment. *Int. J. Comput. Intell. Syst.* **9**(5), 839–849 (2016)
15. Dantzig, G.: Application of the simplex method to a transportation problem. In: *Activity Analysis of Production on Allocation*, New York (1951)
16. Srinivasan, V., Thompsom, G.: An operator theory of parametric programming for the transportation problem. *Naval Res. Logistics Q.* **19**, 227–252 (1972)
17. Vignaux, G., Michalewicz, Z.: A genetic algorithm for the linear transportation problem. *IEEE Trans. Syst. Man Cybern. Syst.* **21**, 445–452 (1991)



Mathematical Model on the Effects of Environmental Pollution on Biological Populations

Sanjay Bhattar, Nishant, and Shyamsunder^(✉)

Department of Mathematics, Malaviya National Institute of Technology Jaipur,
Jaipur, India

sbbhattar.maths@mnit.ac.in, nishantjangra1996@gmail.com,
skumawatmath@gmail.com

Abstract. Partial differential equation (PDE) models are the starting point for developing modeling in various fields, such as mathematics, physics, and engineering. We have developed a mathematical PDE model including the incomplete \aleph -function in this paper. The aim of this paper, study the impact of pollutants on population survival and growth. The results established in this study are general and show different exciting cases in the relevant terms of the parameters involved.

Keywords: Pollution · Incomplete \aleph -function · Population · Partial Differential Equation

1 Introduction and Preliminaries

One of the most significant issues the world is currently experiencing is environmental pollution. Due to rapid industrialization and increasing population on a global scale, natural resources and climate are severely damaged. Rapid population growth brings forth the need for spreading human activities, beautification of cities, the downfall of forests, creation of new industries, etc., ultimately leading to cities' escalation [29]. Urbanization brings many challenges, such as the urban settlement of a growing population, high population density, high-rise buildings, increasing industrialization, and increased traffic [16]. Unchecked urbanization can have a number of negative repercussions, including environmental degradation. Due to unrestricted urbanization, the degradation of the environment is happening very fast, and the pollution problem in cities is getting more serious.

Industrial emissions enter the surrounding environment and affect the local ecosystem [8]. Various sorts of solid waste processing (such as E-waste, debris, plastic, etc.), air pollution, polluted water, industrial discharges, and other factors are contaminating our environment, causing harm to our ecosystem. Environmental pollution is the contamination of normal ecological processes to the point where biological and physical elements of the earth and atmosphere are

contaminated. Aquatic pollution and Industrial emissions have more effect on ecosystems and can abridge the carrying aptitude of fauna and flora. This could result in fatal toxicity, eradication of particular species or communities, or severe pathological abnormalities. Organisms, populations, and sometimes whole ecosystems can change an environment’s anticipating capacity (see [2, 12, 13]) .

Researchers in the 1990s s s developed non-linear mathematical models to study the detrimental impact of environmental contamination on biological populations (see [11, 15, 23]). It has, however, continued to be studied in numerous other modeling studies over the years (see [1, 9, 22, 28]). Different mathematical and experimental studies have been conducted with this approach. To minimize the possible loss of biodiversity, an accurate simulation of the pollution-population system is essential. According to statistics, between 2005 and 2010, more than 3.5 million people per year perished from outdoor air pollution, bringing the global death rate to 4% and to 11% in India [10]. These reports thus imply that to protect the environment and maintain the ecosystem, population growth and environmental pollution issues must be accosted.

Consequently, we propose a non-linear mathematical model to examine how pollutants influence people. Pollution directly affects a species’ rate of development and the ecosystem’s carrying capacity, and both of these characteristics decrease as the concentration of the pollutant grows. It is shown in the mathematical model that we created in this paper by utilizing the incomplete \aleph -function [5].

That is why we choose the incomplete \aleph -function, which consists of the \aleph -function [14], which are extensions and generalizations of higher transcendental functions (see [6, 20]). The most commonly used functions in mathematics, physics, engineering, and mathematical biology are special cases of the incomplete \aleph -function.

The standard definition of the Incomplete \aleph -functions $\gamma \aleph_{r_l, s_l, f_l; k}^{u, v}(\mathcal{V})$ and $\Gamma \aleph_{r_l, s_l, f_l; k}^{u, v}(\mathcal{V})$ follows as define [5]:

$$\begin{aligned} \gamma \aleph_{r_l, s_l, f_l; k}^{u, v}(\mathcal{V}) &= \gamma \aleph_{r_l, s_l, f_l; k}^{u, v} \left[\mathcal{V} \left| \begin{matrix} (\mathcal{A}_1, A_1 : Y), (\mathcal{A}_m, A_m)_{2, v}, [f_m(\mathcal{A}_{ml}, A_{ml})]_{v+1, r_l} \\ (\mathcal{B}_m, B_m)_{1, u}, [f_m(\mathcal{B}_{ml}, B_{ml})]_{u+1, s_l} \end{matrix} \right. \right] \\ &= \frac{1}{2\pi i} \int_{\mathfrak{S}} \Phi(w, Y) \mathcal{V}^{-w} dw, \end{aligned} \tag{1}$$

where

$$\Phi(w, Y) = \frac{\gamma(1 - \mathcal{A}_1 - A_1 w; Y) \prod_{m=1}^u \Gamma(\mathcal{B}_m + B_m w) \prod_{m=2}^v \Gamma(1 - \mathcal{A}_m - A_m w)}{\sum_{l=1}^k f_l \left[\prod_{m=u+1}^{s_l} \Gamma(1 - \mathcal{B}_{ml} - B_{ml} w) \prod_{m=v+1}^{r_l} \Gamma(\mathcal{A}_{ml} + A_{ml}) \right]},$$

and

$$\begin{aligned} \Gamma \aleph_{r_l, s_l, f_l; k}^{u, v}(\mathcal{V}) &= \Gamma \aleph_{r_l, s_l, f_l; k}^{u, v} \left[\mathcal{V} \left| \begin{matrix} (\mathcal{A}_1, A_1 : Y), (\mathcal{A}_m, A_m)_{2, v}, [f_m(\mathcal{A}_{ml}, A_{ml})]_{v+1, r_l} \\ (\mathcal{B}_m, B_m)_{1, u}, [f_m(\mathcal{B}_{ml}, B_{ml})]_{u+1, s_l} \end{matrix} \right. \right] \\ &= \frac{1}{2\pi i} \int_{\mathfrak{S}} \Psi(w, Y) \mathcal{V}^{-w} dw, \end{aligned} \tag{2}$$

where

$$\Psi(w, Y) = \frac{\Gamma(1 - \mathcal{A}_1 - A_1 w; Y) \prod_{m=1}^u \Gamma(\mathcal{B}_m + B_m w) \prod_{m=2}^v \Gamma(1 - \mathcal{A}_m - A_m w)}{\sum_{l=1}^k f_l \left[\prod_{m=u+1}^{s_l} \Gamma(1 - \mathcal{B}_{ml} - B_{ml} w) \prod_{m=v+1}^{r_l} \Gamma(\mathcal{A}_{ml} + A_{ml}) \right]},$$

for $\mathcal{Y} \neq 0, Y \geq 0$, the incomplete \aleph -functions $\gamma_{r_l, s_l, f_l; k}^{\aleph^{u,v}}(\mathcal{Y})$ and $\Gamma_{r_l, s_l, f_l; k}^{\aleph^{u,v}}(\mathcal{Y})$ in (2) and (2) exist under conditions [5]. The following special observations on incomplete \aleph -functions are provided.

Remark 1. On setting $Y = 0$, then Eq. (2) reduces to the \aleph -Function proposed by Sudland at el. [27]:

$$\begin{aligned} \Gamma_{r_l, s_l, f_l; k}^{\aleph^{u,v}} & \left[\mathcal{Y} \left| \begin{array}{l} (\mathcal{A}_1, A_1 : 0), (\mathcal{A}_m, A_m)_{2,v}, [f_m(\mathcal{A}_{ml}, A_{ml})]_{v+1, r_l} \\ (\mathcal{B}_m, B_m)_{1,u}, [f_m(\mathcal{B}_{ml}, B_{ml})]_{u+1, s_l} \end{array} \right. \right] \\ & = \aleph_{r_l, s_l, f_l; k}^{u,v} \left[\mathcal{Y} \left| \begin{array}{l} (\mathcal{A}_m, A_m)_{1,v}, [f_m(\mathcal{A}_{ml}, A_{ml})]_{v+1, r_l} \\ (\mathcal{B}_m, B_m)_{1,u}, [f_m(\mathcal{B}_{ml}, B_{ml})]_{u+1, s_l} \end{array} \right. \right]. \end{aligned} \tag{3}$$

Remark 2. Again, setting $f_l = 1$ in (1) and (2), then it becomes to the Incomplete I -Function suggested by Bansal and Kumar (see [3,4]):

$$\begin{aligned} \gamma_{r_l, s_l, 1; k}^{\aleph^{u,v}} & \left[\mathcal{Y} \left| \begin{array}{l} (\mathcal{A}_1, A_1 : Y), (\mathcal{A}_m, A_m)_{2,v}, [1(\mathcal{A}_{ml}, A_{ml})]_{v+1, r_l} \\ (\mathcal{B}_m, B_m)_{1,u}, [1(\mathcal{B}_{ml}, B_{ml})]_{u+1, s_l} \end{array} \right. \right] \\ & = \gamma_{r_l, s_l; k}^{u,v} \left[\mathcal{Y} \left| \begin{array}{l} (\mathcal{A}_1, A_1 : Y), (\mathcal{A}_m, A_m)_{2,v}, (\mathcal{A}_{ml}, A_{ml})_{v+1, r_l} \\ (\mathcal{B}_m, B_m)_{1,u}, (\mathcal{B}_{ml}, B_{ml})_{u+1, s_l} \end{array} \right. \right], \end{aligned} \tag{4}$$

and

$$\begin{aligned} \Gamma_{r_l, s_l, 1; k}^{\aleph^{u,v}} & \left[\mathcal{Y} \left| \begin{array}{l} (\mathcal{A}_1, A_1 : Y), (\mathcal{A}_m, A_m)_{2,v}, [1(\mathcal{A}_{ml}, A_{ml})]_{v+1, r_l} \\ (\mathcal{B}_m, B_m)_{1,u}, [f_m(\mathcal{B}_{ml}, B_{ml})]_{u+1, s_l} \end{array} \right. \right] \\ & = \Gamma_{r_l, s_l; k}^{u,v} \left[\mathcal{Y} \left| \begin{array}{l} (\mathcal{A}_1, A_1 : Y), (\mathcal{A}_m, A_m)_{2,v}, (\mathcal{A}_{ml}, A_{ml})_{v+1, r_l} \\ (\mathcal{B}_m, B_m)_{1,u}, (\mathcal{B}_{ml}, B_{ml})_{u+1, s_l} \end{array} \right. \right]. \end{aligned} \tag{5}$$

Remark 3. Next, setting $Y = 0$ and $f_l = 1$ in (1) and (2), then it becomes to the I -Function suggested by Saxena [19] :

$$\begin{aligned} \Gamma_{r_l, s_l, 1; k}^{\aleph^{u,v}} & \left[\mathcal{Y} \left| \begin{array}{l} (\mathcal{A}_1, A_1 : 0), (\mathcal{A}_m, A_m)_{2,v}, [1(\mathcal{A}_{ml}, A_{ml})]_{v+1, r_l} \\ (\mathcal{B}_m, B_m)_{1,u}, [f_m(\mathcal{B}_{ml}, B_{ml})]_{u+1, s_l} \end{array} \right. \right] \\ & = I_{r_l, s_l; k}^{u,v} \left[\mathcal{Y} \left| \begin{array}{l} (\mathcal{A}_m, A_m)_{1,v}, (\mathcal{A}_{ml}, A_{ml})_{v+1, r_l} \\ (\mathcal{B}_m, B_m)_{1,u}, (\mathcal{B}_{ml}, B_{ml})_{u+1, s_l} \end{array} \right. \right]. \end{aligned} \tag{6}$$

Remark 4. Further setting $f_l = 1$ and $k = 1$ in (1) and (2), then it becomes to the Incomplete H -Function suggested by Srivastava [26]:

$$\begin{aligned} \gamma \mathbb{N}_{r_l, s_l, 1; 1}^{u, v} & \left[\mathcal{Y} \left| \begin{matrix} (\mathcal{A}_1, A_1 : Y), (\mathcal{A}_m, A_m)_{2, v}, [1(\mathcal{A}_{ml}, A_{ml})]_{v+1, r_l} \\ (\mathcal{B}_m, B_m)_{1, u}, [f_m(\mathcal{B}_{ml}, B_{ml})]_{u+1, s_l} \end{matrix} \right. \right] \\ & = \gamma_{r, s}^{u, v} \left[\mathcal{Y} \left| \begin{matrix} (\mathcal{A}_1, A_1 : Y), (\mathcal{A}_m, A_m)_{2, v} \\ (\mathcal{B}_m, B_m)_{1, u} \end{matrix} \right. \right], \end{aligned} \tag{7}$$

and

$$\begin{aligned} \Gamma \mathbb{N}_{r_l, s_l, 1; 1}^{u, v} & \left[\mathcal{Y} \left| \begin{matrix} (\mathcal{A}_1, A_1 : Y), (\mathcal{A}_m, A_m)_{2, v}, [1(\mathcal{A}_{ml}, A_{ml})]_{v+1, r_l} \\ (\mathcal{B}_m, B_m)_{1, u}, [f_m(\mathcal{B}_{ml}, B_{ml})]_{u+1, s_l} \end{matrix} \right. \right] \\ & = \Gamma_{r, s}^{u, v} \left[\mathcal{Y} \left| \begin{matrix} (\mathcal{A}_1, A_1 : Y), (\mathcal{A}_m, A_m)_{2, v} \\ (\mathcal{B}_m, B_m)_{1, u} \end{matrix} \right. \right]. \end{aligned} \tag{8}$$

Remark 5. Next, we taking $Y = 0$, $f_l = 1$, and $k = 1$ in (2), then it becomes to the H -Function suggested by Srivastava (see, [25], pp. 10):

$$\begin{aligned} \Gamma \mathbb{N}_{r_l, s_l, 1; 1}^{u, v} & \left[\mathcal{Y} \left| \begin{matrix} (\mathcal{A}_1, A_1 : 0), (\mathcal{A}_m, A_m)_{2, v}, [1(\mathcal{A}_{ml}, A_{ml})]_{v+1, r_l} \\ (\mathcal{B}_m, B_m)_{1, u}, [f_m(\mathcal{B}_{ml}, B_{ml})]_{u+1, s_l} \end{matrix} \right. \right] \\ & = H_{r, s}^{u, v} \left[\mathcal{Y} \left| \begin{matrix} (\mathcal{A}_m, A_m)_{1, v} \\ (\mathcal{B}_m, B_m)_{1, u} \end{matrix} \right. \right]. \end{aligned} \tag{9}$$

2 Mathematical Model

In this paper, we use one-dimensional species $0.5z \leq L$ to study the increase in the spread of population density $\zeta_p(z, t)$, ($p = 1, 2$) and their interactions. Due to natural pollution, the growth rate and the environment’s carrying capacity have been decreasing. Environmental pollution those who follow the power behavior law are present in the habitat. The following dynamical equations are among the nonlinear partial differential equations that most accurately describe species evolution:

$$\frac{\partial \zeta_p}{\partial t} = \zeta_p \theta_p(\zeta_1, \zeta_2, h_p(\mathcal{H}(z, t)), g_p(\mathcal{H}(z, t))) + \mathcal{D}_p \frac{\partial^2 \zeta_p}{\partial z^2}, \quad p = 1, 2. \tag{10}$$

Here

- θ_p :- denotes the interaction function of the species,
- h_p :- is the internal growth rate,
- g_p :- denotes the environmental carrying capacity,
- \mathcal{H} :- denotes the concentration of the pollutant,
- \mathcal{D}_p :- is a positive constant that describes the dispersal of species.

The following equation represents the mobility of the concentration \mathcal{H} of the pollutant:

$$\frac{\partial \mathcal{H}}{\partial t} = C - \alpha \mathcal{H} + \mathcal{D}_c \frac{\partial^2 \mathcal{H}}{\partial z^2}. \tag{11}$$

Here

$C > 0$:- is the exogenous rate constant of the pollutant’s entry into the habitat,

$\alpha > 0$:- is a first order constant that indicates decay as an effect of environmental pollution,

$\mathcal{D}_c > 0$:- is the pollutant’s diffusion coefficient.

In developing this model, we have presupposed that an organism’s uptake of a pollutant is proportional to the concentration of the pollutant present in the environment of the population.

It is worth mentioning here that utilizing the Adomians decomposition technique, exact solutions to equation (11) that often appear in mathematical biology may be obtained in both the z and t directions (see for more details, [17]). This technique is well recognized for avoiding linearization and physically inappropriate assumptions while offering an efficient numerical solution with high precision. However, based on the premise of the mathematical demonstration (11), the solution to this mathematical equation will be obtained in the next part of this segment using the incomplete \aleph -function of one variable.

3 Result in Terms of Incomplete \aleph -Functions

We choose the concentration $\mathcal{H}(z, t)$ with reference to the incomplete \aleph -function as follows:

$$\begin{aligned} \mathcal{H}(z, t) &= \Gamma \aleph_{r_l, s_l, f_l; k}^{u, v} \left[\mathcal{Y} z^\nu (t^\varpi - \vartheta)^\ell \right. \\ &\quad \left. \begin{array}{l} (\mathcal{A}_1, A_1 : z), (\mathcal{A}_m, A_m)_{2, v}, [f_m(\mathcal{A}_{ml}, A_{ml})]_{v+1, r_l} \\ (\mathcal{B}_m, B_m)_{1, u}, [f_m(\mathcal{B}_{ml}, B_{ml})]_{u+1, s_l} \end{array} \right] \\ &= \frac{1}{2\pi i} \int_{\mathfrak{S}} \Psi(w, z) \mathcal{Y}^{-w} z^{-w\nu} (t^\varpi - \vartheta)^{-w\ell} dw. \end{aligned} \tag{12}$$

Now, partially differentiating (12) with respect to t and z , we obtain

$$\begin{aligned} \frac{\partial \mathcal{H}}{\partial t} &= \frac{\varpi t^{\varpi-1}}{(t^\varpi - \vartheta)} \Gamma \aleph_{r_l+1, s_l+1, f_l; k}^{u, v+1} \left[\mathcal{Y} z^\nu (t^\varpi - \vartheta)^\ell \right. \\ &\quad \left. \begin{array}{l} (\mathcal{A}_1, A_1 : z), (0, \ell), (\mathcal{A}_m, A_m)_{2, v}, [f_m(\mathcal{A}_{ml}, A_{ml})]_{v+1, r_l} \\ (\mathcal{B}_m, B_m)_{1, u}, (1, \ell), [f_m(\mathcal{B}_{ml}, B_{ml})]_{u+1, s_l} \end{array} \right], \end{aligned} \tag{13}$$

and

$$\frac{\partial^2 \mathcal{H}}{\partial z^2} = \frac{1}{z^2} \Gamma \mathfrak{N}_{r_l+1, s_l+1, f_l; k}^{u, v+1} \left[\mathcal{V} z^\nu (t^\varpi - \vartheta)^\ell \right. \\ \left. \begin{matrix} (\mathcal{A}_1, A_1 : z), (0, \nu), (\mathcal{A}_m, A_m)_{2, v}, [f_m(\mathcal{A}_{ml}, A_{ml})]_{v+1, r_l} \\ (\mathcal{B}_m, B_m)_{1, u}, (2, \nu), [f_m(\mathcal{B}_{ml}, B_{ml})]_{u+1, s_l} \end{matrix} \right], \tag{14}$$

Using (12), (13), and (14) in (11) we obtain following result

$$\frac{\varpi t^{\varpi-1}}{(t^\varpi - \vartheta)} \Gamma \mathfrak{N}_{r_l+1, s_l+1, f_l; k}^{u, v+1} \left[\mathcal{V} z^\nu (t^\varpi - \vartheta)^\ell \right. \\ \left. \begin{matrix} (\mathcal{A}_1, A_1 : z), (0, \ell), (\mathcal{A}_m, A_m)_{2, v}, [f_m(\mathcal{A}_{ml}, A_{ml})]_{v+1, r_l} \\ (\mathcal{B}_m, B_m)_{1, u}, (1, \ell), [f_m(\mathcal{B}_{ml}, B_{ml})]_{u+1, s_l} \end{matrix} \right] \\ = C - \alpha \times \Gamma \mathfrak{N}_{r_l, s_l, f_l; k}^{u, v} \left[\mathcal{V} z^\nu (t^\varpi - \vartheta)^\ell \right. \\ \left. \begin{matrix} (\mathcal{A}_1, A_1 : z), (\mathcal{A}_m, A_m)_{2, v}, [f_m(\mathcal{A}_{ml}, A_{ml})]_{v+1, r_l} \\ (\mathcal{B}_m, B_m)_{1, u}, [f_m(\mathcal{B}_{ml}, B_{ml})]_{u+1, s_l} \end{matrix} \right] + \mathcal{D}_c \\ \times \frac{1}{z^2} \Gamma \mathfrak{N}_{r_l+1, s_l+1, f_l; k}^{u, v+1} \left[\mathcal{V} z^\nu (t^\varpi - \vartheta)^\ell \right. \\ \left. \begin{matrix} (\mathcal{A}_1, A_1 : z), (0, \nu), (\mathcal{A}_m, A_m)_{2, v}, [f_m(\mathcal{A}_{ml}, A_{ml})]_{v+1, r_l} \\ (\mathcal{B}_m, B_m)_{1, u}, (2, \nu), [f_m(\mathcal{B}_{ml}, B_{ml})]_{u+1, s_l} \end{matrix} \right]. \tag{15}$$

Similarly, we can solve $\mathcal{H}(z, t)$ as a term of the incomplete \mathfrak{N} -function ${}^\gamma \mathfrak{N}_{r_l, s_l, f_l; k}^{u, v}$.

4 Special Cases

By correctly describing the parameters involved in the findings obtained, we can easily acquire many more known and unknown (new) results, including many additional highly transcendental functions of interest.

- (i) On taking $z = 0$, $\varpi = 1$, and $\vartheta = 0$ in equation (15), we readily get the result in terms of \mathfrak{N} -Function due to Sharma and Bhargava [21].
- (ii) If setting $z = 0$, $f_l = 1$, $\varpi = 1$, and $\vartheta = 0$ in equations (15), then the outcome is as noted by Bhargava et al. [7].
- (iii) If we set $f_l = 1$, $k = 1$, $\varpi = 1$, and $\vartheta = 0$ in equation (15) then the outcome is as noted by Purohit et al. [18].
- (iv) If we set $z = 0$, $f_l = 1$, $k = 1$, $\varpi = 1$, and $\vartheta = 0$ in equation (15) then the outcome is as noted by Singh and Mehta [24].
- (v) If we substitute $u = 1$, $v = r$, $s = s + 1$, $\mathcal{V} z^\nu (t^\varpi - \vartheta)^\ell = -\mathcal{V} z^\nu (t^\varpi - \vartheta)^\ell$, $B_1 = 1$, $\mathcal{B}_1 = 0$, $\mathcal{A}_m = 1 - \mathcal{A}_m$, $\mathcal{B}_m = 1 - \mathcal{B}_m$ in equation (15), then we obtain the solution that uses the incomplete Fox-Wright function ${}_r\Psi_s^\Gamma$.
- (vi) If we substitute $u = 1$, $v = r$, $s = s + 1$, $\mathcal{V} z^\nu (t^\varpi - \vartheta)^\ell = -\mathcal{V} z^\nu (t^\varpi - \vartheta)^\ell$, $B_1 = 1$, $\mathcal{B}_1 = 0$, $\mathcal{A}_m = 1 - \mathcal{A}_m$, $\mathcal{B}_m = 1 - \mathcal{B}_m$, $A_m = 1$, $B_m = 1$ in equation (15), then we obtain the solution that uses the incomplete generalized hypergeometric function ${}_rF_s$.

5 Conclusion

To study the impact of pollutants on the human population, a non-linear mathematical model has been created. Population growth or population pressure is also accountable for increasing pollution. Still, due to a high increase in pollution concentration, the population will also not be able to survive for long. The atmosphere remains asymptotically stable but at extremely low levels, suggesting that it would not take long for human populations, fauna, and flora to become extinct if concentrations of the pollutant continued to accumulate in the atmosphere. Therefore, controlling pollution is essential for maintaining the human population and ecological balance. Considering the generality of the incomplete \aleph -function, by taking appropriate values of the parameters involved, several exciting results can be derived from the result (15). Thus the results obtained here are general and can be very useful in applied mathematics, environmental science, biochemistry, and other branches.

Acknowledgments. The corresponding author is grateful to the CSIR, MHRD, Govt. of India, New Delhi for funding through grant number (09/843(0006)/2020-EMR-I).

References

1. Agarwal, S., Devi, S.: The effect of environmental tax on the survival of biological species in a polluted environment: a mathematical model. *Nonlinear Anal. Model. Control* **15**(3), 271–286 (2010)
2. Aubert, M., Aubert, J.: Marine pollution and management of shores; pollutions marines et aménagement des rivages. *C.E.R.B.O.M.* 308 (1973)
3. Bansal, M.K., Kumar, D.: On the integral operators pertaining to a family of incomplete I-functions. *AIMS Math.* **5**(2), 1247–1259 (2020)
4. Bansal, M.K., Kumar, D., Harjule, P., Singh, J.: Fractional kinetic equations associated with incomplete I-functions. *Fractal Fract.* **4**(2), 19 (2020)
5. Bansal, M.K., Kumar, D., Nisar, K.S., Singh, J.: Certain fractional calculus and integral transform results of incomplete \aleph -functions with applications. *Math. Methods Appl. Sci.* **43**(8), 5602–5614 (2020)
6. Bansal, M.K., Kumar, D., Singh, J., Nisar, K.S.: On the solutions of a class of integral equations pertaining to incomplete H-function and incomplete \bar{H} -function. *Mathematics* **8**(5), 819 (2020)
7. Bhargava, A., Srivastava, A., Mukherjee, R.: On a mathematical model involving I-Function for studying the effect of environmental pollution. *Proc. Nat. Acad. Sci. India Sec. A: Phys. Sci.* **87**(1), 19–21 (2016). <https://doi.org/10.1007/s40010-016-0319-4>
8. Dubey, B.: A model for the effect of time delay on the dynamics of a population living in a polluted environment. *J. Biol. Syst.* **12**(1), 35–43 (2004)
9. Dubey, B., Narayanan, A.S.: Modelling effects of industrialization, population and pollution on a renewable resource. *Nonlinear Anal. Real World Appl.* **11**(4), 2833–2848 (2010)
10. Emerging, I.: Update, Air, Pollution: World's Worst Environmental Health Risk, UNEP Year Book. Nairobi, Kenya (2014)

11. Freedman, H.I., Shukla, J.B.: Models for the effect of toxicant in single-species and predator-prey systems. *J. Math. Biol.* **30**(1), 15–30 (1991). <https://doi.org/10.1007/BF00168004>
12. Hallam, T.G., De Luna, J.T.: Effects of toxicants on populations: a qualitative: approach III. Environmental and food chain pathways. *J. Theor. Biol.* **109**(3), 411–429 (1984)
13. Hari, P., Raunemaa, T., Hautojärvi, A.: The effects on forest growth of air pollution from energy production. *Atmos. Environ.* **20**(1), 129–137 (1986)
14. Kumar, D., Ayant, F.Y., Uçar, F.: Integral involving aleph-function and the generalized incomplete hypergeometric function. *TWMS J. App. Eng. Math.* **10**(3), 650–656 (2020)
15. Misra, O.P., Saxena, V.P.: Effects of environmental pollution on the growth and existence of biological populations: modelling and stability analysis. *Indian J. Pure Appl. Math.* **22**(10), 805–817 (1991)
16. Munn, R.E., Fedorov, V.: An assessment of environmental impacts of industrial development. With Special Reference to the Doon Valley, India, IIASA, Laxenburg, Austria (1986)
17. Pamuk, S.: An application for linear and nonlinear heat equations by Adomian's decomposition method. *Appl. Math. Comput.* **163**(1), 89–96 (2005)
18. Purohit, S.D., Khan, A.M., Suthar, D.L., Dave, S.: The impact on raise of environmental pollution and occurrence in biological populations pertaining to incomplete H-function. *Natl. Acad. Sci. Lett.* **44**(3), 263–266 (2021). <https://doi.org/10.1007/s40009-020-00996-y>
19. Saxena, V.P.: Formal solution of certain new pair of dual integral equations involving H-functions. *Proc. Nat. Acad. Sci. India Sect. A* **52**, 366–375 (1982)
20. Sharma, R., Singh, J., Kumar, D., Singh, Y.: Certain unified integrals associated with product of the general class of polynomials and incomplete I-functions. *Int. J. Appl. Comput. Math.* **8**(1), 1–11 (2022). <https://doi.org/10.1007/s40819-021-01181-5>
21. Sharma, S.S., Bhargava, A.: On a mathematical model involving aleph-function to study the effects of environmental pollution on biological population. *Int. J. Stat. Appl. Math.* **3**(2), 255–259 (2018)
22. Shukla, J.B., Agrawal, A.K., Dubey, B., Sinha, P.: Existence and survival of two competing species in a polluted environment: a mathematical model. *J. Biol. Syst.* **9**(2), 89–103 (2001)
23. Shukla, J.B., Dubey, B.: Simultaneous effect of two toxicants on biological species: a mathematical model. *J. Biol. Syst.* **4**(1), 109–130 (1996)
24. Singh, S.N., Mehta, R.: Effect of environmental pollution on the growth and existence of biological populations involving H-function. *IOSR J. Math.* **1**(3), 1–2 (2012)
25. Srivastava, H.M., Gupta, K.C., Goyal, S.P.: *The H-Functions of One and Two Variables, with Applications*. South Asian Publishers, New Delhi-Madras, India (1982)
26. Srivastava, H.M., Saxena, R.K., Parmar, R.K.: Some families of the incomplete h-functions and the incomplete \bar{H} -functions and associated integral transforms and operators of fractional calculus with applications. *Russ. J. Math. Phys.* **25**(1), 116–138 (2018). <https://doi.org/10.1134/S1061920818010119>
27. Südland, N., Baumann, B., Nonnenmacher, T.F.: Who knows about the Aleph \aleph -function. *Fract. Calc. Appl. Anal.* **1**(4), 401–402 (1998)

28. Suthar, D.L., Purohit, S.D., Khan, A.M., Dave, S.: Impacts of environmental pollution on the growth and conception of biological populations involving incomplete i-function. In: Sharma, H., Saraswat, M., Kumar, S., Bansal, J.C. (eds.) CIS 2020. LNDECT, vol. 61, pp. 567–575. Springer, Singapore (2021). https://doi.org/10.1007/978-981-33-4582-9_44
29. Rajashekariah, K.: Impact of urbanisation on biodiversity: case Studies From India. WWF-New Delhi, India (2011)



High Gain Calculation & Simulation for Antenna Design for 6G Wireless Applications

Narayan Krishan Vyas^{1,2}(✉) and Mohammad Salim¹

¹ MNIT Jaipur, Jaipur, Rajasthan, India
msalim.ece@mnit.ac.in

² Government Engineering College, Jhalawar, Rajasthan, India
narayankrishanvyas@Rajasthan.gov.in

Abstract. Last few years, mobile communications have been undergoing a drastic evaluation/change for every ten years or so. The technique difference between the communication processes named as “G’s”. As a result, a simulation was conducted after the gain was determined using several mathematical formulae. The sixth generations (6G) of wireless systems, which are systems beyond the fifth generation (5G), are generating a lot of interest as they become commercially available. With the use of formula design and by using determined quantities, this work offers the first mathematical computation for gain. We design/ developed a novel tooth-shaped patch antenna for communication in radar system with better performance. The antenna designed in Tera Hz at 300 GHz frequency. To achieve higher gain, the designed patch antenna exhibits lower mutual coupling effect. Current distribution & gain of designed novel tooth shaped patch antenna having 1.32×10^2 A/m & 9.45 db. The proposed antenna simulated to test the power transferred at the antenna port from the transmission line means impedance bandwidth ($S_{11} < -10$ dB) at frequencies of 326.67 GHz that is, -50.524 dB, allocated to the 6G applications by the Federal Communications Commission. By simulation of proposed patch antenna, visualize the intended output or result, the design of antennas is crucial to achieving the required results for future work. The simulation provides us effects to evaluate various parameters, like as bandwidth, and antenna isolation, for the manufactured device’s superior performance standards. RT/ Duroid 5880 is a low-loss/cost substrate and we used in designs. For 6G frequencies, the required band-width should be more than 20 GHz, which is desirable for future reference/work.

Keywords: Wireless communication · Antenna Gain · 6G · radiation pattern · Bandwidth · impedance matching · mutual coupling effect

1 Introduction

The promise of 5G mobile and wireless technologies to support large data rates and achieve minimal latency is creating issues for the already crowded microwave frequency band. These systems are separated into two categories: Frequency Range 1 (FR1), which includes all frequency bands below 6 GHz, and Frequency Range 2 (FR2), which covers

the so-called 5G millimeter wave (mm-Wave) bands currently being trailed around the world to address these challenges. It is expected that various parts of the lower mm-Wave spectrum, <50 GHz, will be gradually subjugated by 5G systems in the coming decade. However, the data rates are expected to be much higher, on the order of terabits per second (Tbps), as wireless technologies evolve into sixth-generation (6G) systems [1]. The sixth-generation (6G) mobile network is expected to realize and expand the 6G communication system in 2030. The world is currently considering the use of terahertz (THz) frequency bands above 100 GHz because a wider frequency band can be used compared to 5G. At WRC2019, the 275–450 GHz frequency band will be considered for land mobile and fixed services, but the specific specifications are not yet precise because there are many uncertain factors in wireless communication. The U.S. Federal Communications Commission (FCC) decided to open up the electromagnetic wave frequency range from 95 GHz to 3 THz as a test spectrum, and also because 95 GHz to 3 THz covers the terahertz frequency band [2]. This advance will pose even more challenges to the already scarce radio spectrum. In order to meet the increasing demands for data rate in wireless communications, mobile communication systems are evolving toward utilizing higher frequencies such as millimeter wave (mm-Wave) and terahertz (THz) bands. Both mm-Wave and THz communication systems can utilize extremely large bandwidth and can therefore boost peak data rates in 6G.

The 6G applications will need access to an order-of-magnitude more spectrum, utilization of frequencies between 100 GHz and 1 THz becomes of paramount importance. As such, the 6G ecosystem will feature a diverse range of frequency bands, ranging from below 6 GHz up to 1 THz. Some of the characteristics parameters of Microstrip patches are radiation pattern, gain, return loss (RL) bandwidth, efficiency and polarization diversities. Design complexities of a patch antenna increases with the miniaturization of the patch. Patch antennas suffer from different limitations such as impedance mismatch, low gain, and poor return loss performance [3]. Enabled by enhanced mobile broadband (eMBB), new applications in massive machine-type communications (mMTCs) and ultra reliable low-latency communications (uRLLCs) have driven the development toward International Mobile Telecommunications 2020 (IMT-2020) often colloquially called the fifth-generation (5G) of wireless systems [4]. To support such applications, even larger system bandwidths than those seen in 5G are required along with new physical layer (PHY) techniques, as well as higher layer capabilities that are not present today. Significant efforts are underway to characterize and understand wireless systems beyond 5G, which we refer to as the sixth generation (6G) of systems [5]. According to the ITU-T in the three most important driving characteristics linked to the next decade of lifestyle and societal changes, impacting the design and outlook of 6G networks, are:

- i. High-Fidelity Holographic Society
- ii. Connectivity for All Things
- iii. Time Sensitive/Time Engineered Applications [6].

The sub-Terahertz (THz) frequency band (0.1–1 THz) offers a spectrum with a high data rate, wide bandwidth, and lower atmospheric attenuation due to rain and fog. This frequency band is intended to serve terabits per second (Tbps) wireless communication

for the sixth generation (6G) mobile network [7]. The antenna is an indispensable component of any THz wireless communication systems along with active components and associate technologies, the performance of the antennas is directly affected by the communication quality of the entire system. One of THz band frequencies main challenges is a very high path loss, resulting in a major constraint on communication distances. At THz frequencies, the need for high-gain antennas is very important to overcome high atmospheric absorption and high path loss at these frequencies, which will affect the budget of the wireless link. Horn antennas and reflector-based antennas have been proposed at THz frequencies because of their good radiation performance; however, they are bulky in size and have a complex structure, especially with other active compact components in integrating with the circuits [8, 9]. A number of studies focusing on more specific technologies have also been published. For instance, the study in [10] proposes to explore new waveforms for 90–200-GHz frequency bands that offer optimal performance under PHY layer impairments. Haselmayr [11] present a vision of providing an Internet of Bio-nano things using molecular communication. The study in gives an overview of architectures, challenges, and techniques for efficient wireless powering of Internet-of-Things (IoT) networks in 6G [12]. Moreover, Piran and Suh [13] consider the requirements, use cases, and challenges to realize 6G systems with a particular emphasis on artificial intelligence (AI)-based techniques for network management. Sub-Terahertz (Sub-THz) frequencies will be used in the six generation (6G) of mobile communications for high data rate. Its short wavelengths and dielectric loss make antenna in package (AiP) technologies desired for antenna arrays with high radiation gains, where the frequencies are roughly 0.1–0.3 THz [14] to make the wavelength smaller than 1 mm. Such AiP may minimize the physical sizes and lossy transmission lines to integrate the RF devices.

2 Antenna Geometry and Design

Different published papers claim that to achieve good results, a good matching condition of patch can be obtained by cuts in patch with inset feed of patch [15]. By properly control inset position & width, good matching may be achieved. In a spherical shape, an antenna occupying more space in volume will have a wider bandwidth [16]. By increase the height (h) of the substrate it may increase the bandwidth. However by using higher value of substrate height (h) may result in surface waves that travel within the substrate which give results in undesired radiations and issues. For my paper we will explain/described a novel patch antenna design method with inset fed after considering Rogers RO/Duroid 5880 as substrate because it have good relative permittivity of 2.2. The high melting point at 2600 °C of Rogers RO/Duroid 5880 is main advantage. It absorbs moisture very low and has very low loss tangent approx. 0.0009. Along with these properties, Duroid 5880 is easily available and very cheap. For design, we chosen micro strip feed mechanism for better results in performance. As we chosen substrate, now we have to calculate the parameters.

For Patch Length & width,

$$W = \frac{c}{2f_0 \sqrt{\frac{(\epsilon_r + 1)}{2}}} \quad (1)$$

$$L = \frac{C}{2f_0\sqrt{\epsilon_{eff}}} - 2\Delta L \tag{2}$$

ϵ_r is the relative Permittivity of the dielectric substrate.

f_0 is the Resonance Frequency.

C is the Speed of light: 3×10^8 .

By using Eq. 1 & 2, we calculated the value of patch length & width using substrate permittivity for simulation.

Calculation for the Effective Dielectric Constant which is based on the height, dielectric constant of the dielectric and the calculated width of the patch antenna.

$$\epsilon_{eff} = \frac{\epsilon_r + 1}{2} + \frac{\epsilon_r - 1}{2} [1 + 12 \frac{h}{W}]^{-1/2} \tag{3}$$

h is the thickness of substrate.

$$L_{eff} = \frac{c}{2f_0\sqrt{\epsilon_{eff}}} \tag{4}$$

$$\Delta L = 0.412h \frac{(\epsilon_{eff} + 0.3)(\frac{W}{h} + 0.264)}{(\epsilon_{eff} - 0.258)(\frac{W}{h} + 0.8)} \tag{5}$$

Equation 5 gives the calculation of the length extension ΔL & using this we can calculate the actual length of patch, by using Eq. 6,

$$L = L_{eff} - 2\Delta L \tag{6}$$

In CST simulations, we considered many height values of the substrate. At 330 GHz, the substrate height should be less than 0.05 and for design we used height equivalent to 0.194 mm. As we increase the thickness of substrate provides more bandwidth in results but same time it causes the shifting of resonant frequency to lower side [17]. After patch simulation we tried to improve the performance of the patch antenna by insertion of cuts slots with the value of 0.142 mm each and optimizing the patch parameters of the patch antenna, are listed in Table 1. Using Equation from 1 to 6 we simulated novel patch antenna with single antenna is shown in Fig. 1 (Figs. 6 and 8).

Table 1. .

Antenna parameters	Value
Patch Length (L)	2.4 mm
Patch Width (W)	2.90 mm
Substrate Dimensions	L = 4 mm W = 2.90 mm
Ground	L = 4 mm W = 2.90 mm

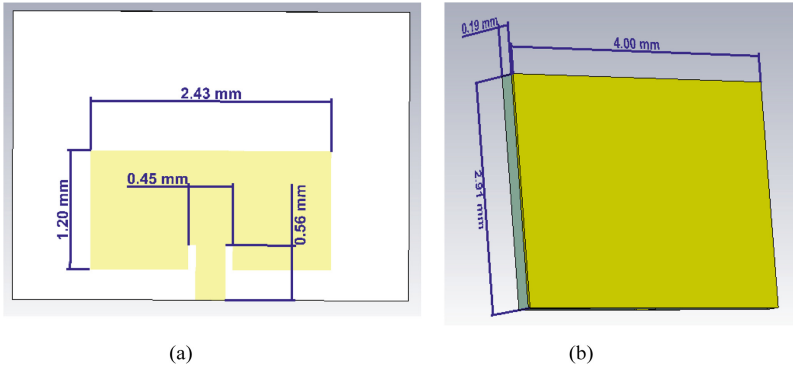


Fig. 1. Conventional Patch antenna with dimensions (a) front view (b) back view

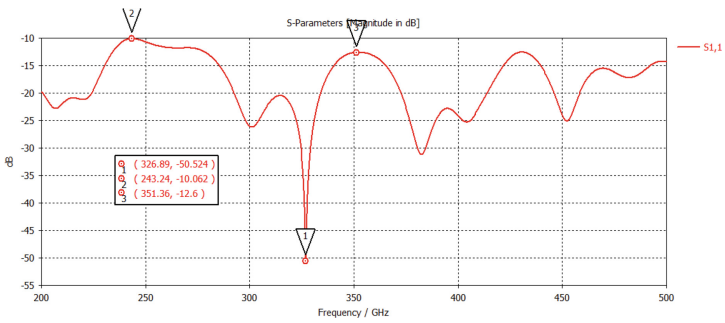


Fig. 2. S-parameter of single antenna

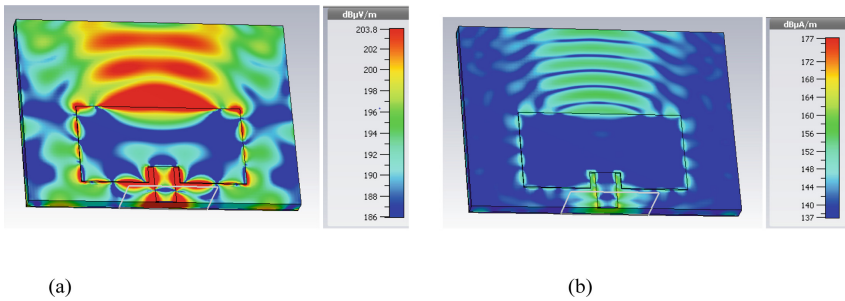


Fig. 3. Top view of E-field (b) Top view of H-field

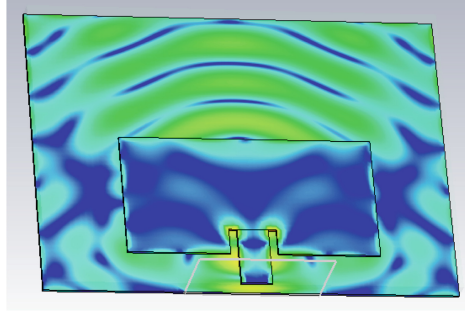


Fig. 4. Surface Current of single antenna

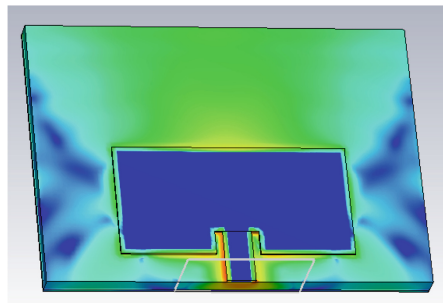


Fig. 5. Power flow

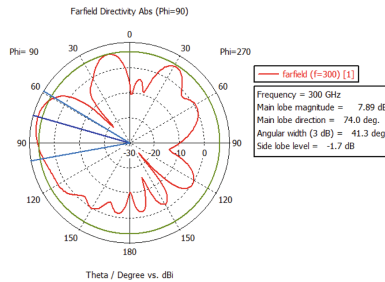


Fig. 6. Far-field of single antenna

The single antenna design is shown in Fig. 1. Simulation done using the CST studio, after simulation Fig. 2 shows the S11 parameter of antenna, Fig. 3(a) & (b) shows E-field & H-Field respectively, Fig. 4 & Fig. 5 shows surface current and power flow. A microstrip patch antenna which will be simulating has width W and length L as 4mm and 2.93 mm, respectively. The patch width, W_p is 1.20 mm, and patch length, L_p of 2.43 mm. The patch antenna is made by pure copper, with the resistivity of $1.68 \Omega\text{m}$ & conductivity of $5.95/\Omega\text{cm}$, and 0.034 mm thick. The substrate used in antenna is a Rogers RO/Duroid 5880. A fully ground planes at the next layer of substrate uses the

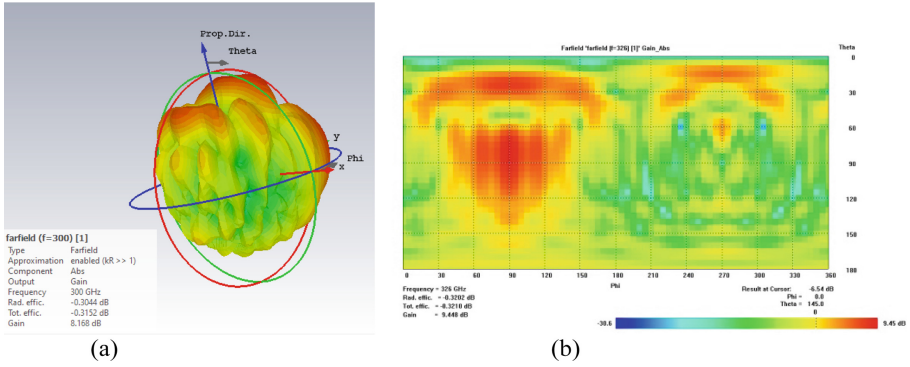


Fig. 7. 3D Far-field (b) 2D far-field with gain

same material as radiating patch. The antenna is fed by 50Ω feed line that has width, W_f of 0.45 mm. At the second stage to get better results, we have tried to improve the performance by changing the parameters of the patch antenna through insertion of cuts slots of equal width & length at top and same time cut slots at patch sides also [18]. To optimizing the result, some parameters used for the patch are summarized as shown in Fig. 7 with inset fed. The designed novel patch antenna along with conventional inset fed patch is shown below,

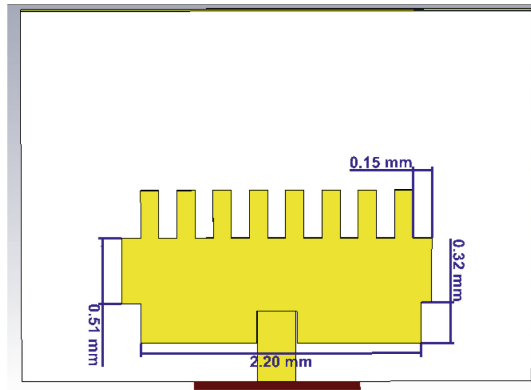


Fig. 8. Shows patch antenna with inset cut slots.

After simulation of inset fed antenna, we received different result parameters which are shown in above figures. Figure 9 shows measurement of power reflected back at the antenna port due to mismatch from the transmission line, having S_{11} parameter as -52.653 dB. Figure 10(a) & 11 shows flows from the positive charge to the negative charge placed on the elements by voltage applied to the antenna & is a vector quantity (has a magnitude and direction) and is measured in Amps/Meter [A/m] respectively. Figure 11 shows surface current & power flow in antenna. Figure 12 & 13 are graphical representation of far-field in 3D & 2D. Similarly Fig. 14 shows the electric field density.

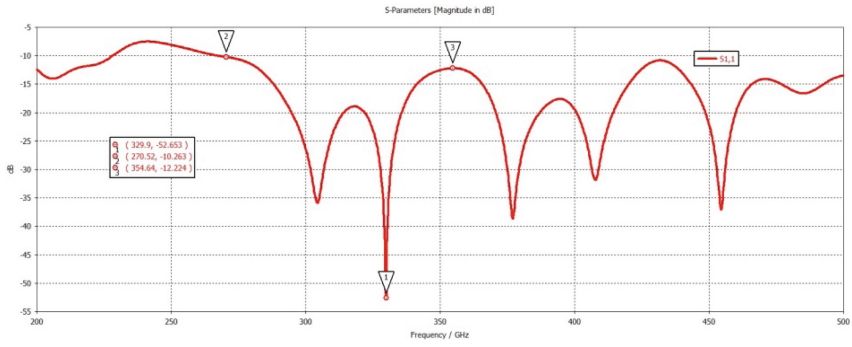


Fig. 9. S-parameter of cut slot patch antenna

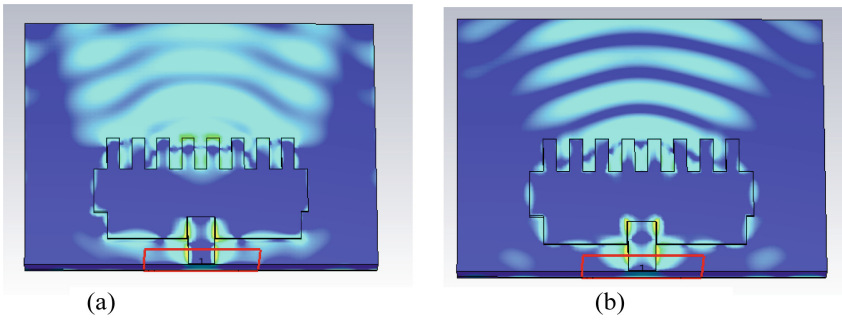


Fig. 10. (a) E-field (b) H-field

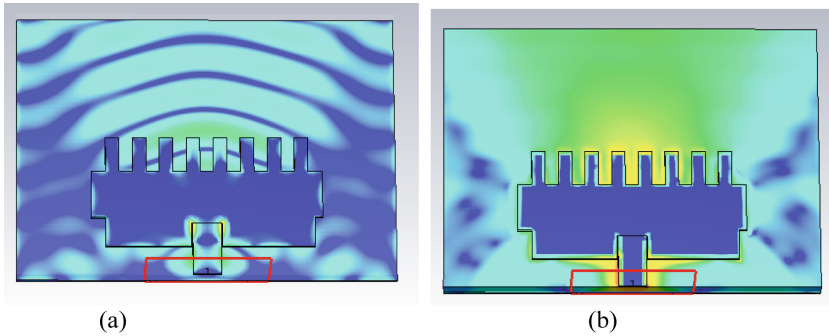


Fig. 11. (a) Surface current (b) Power flow

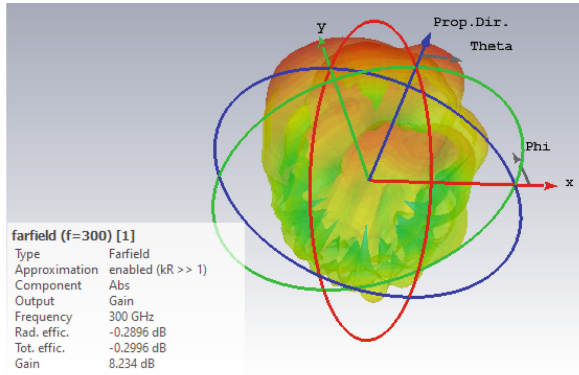


Fig. 12. 3D Far-field with gain

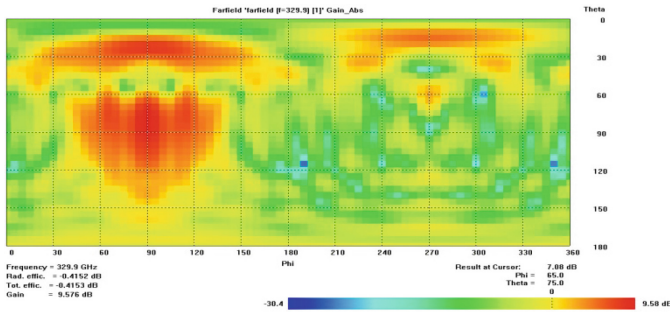


Fig. 13. 2D far-field with gain

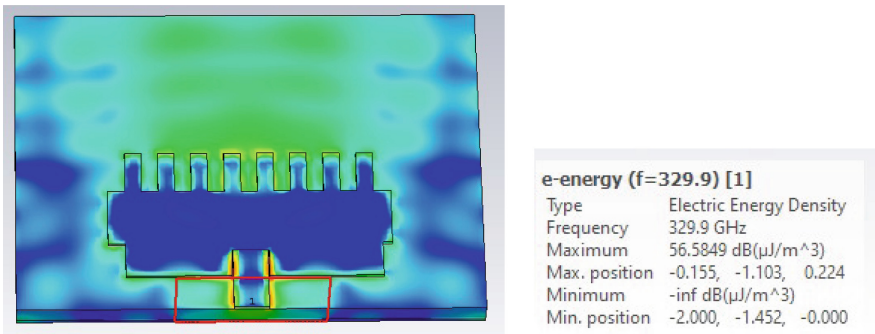


Fig. 14. Electric field Density

3 Conclusion

In the conclusion, the researchers done work previously, for 6G antenna has been reviewed and represented completely. Each researcher work has different objective & results, so by this each used different parameters of height with frequency selection, patch

antenna types, substrate material, fabrication and improvement technique. I designed a novel microstrip patch antenna for 6G application and successfully designed by simulation. The simulated result of inset fed patch has achieved as the operating frequency of 329.9 GHz, and wide bandwidth of 84.12 GHz. Same time, the gain received is 9.58 dB. The gain & the bandwidth can be improved with some more modification in design to get better results.

References

1. Guo, Y.J., Ansari, M., Ziolkowski, R.W., Fonseca, N.J.: Quasi-optical multi-beam antenna technologies for 5G and 6G mmWave and THz networks: a review (2021)
2. Chung, M.A., Chuang, B.R.: Design a broadband u-shaped microstrip patch antenna on silicon-based technology for 6G terahertz (THz) future cellular communication applications
3. Tataria, H., Molisch, A.F., Dohler, M., Sjöland, H., Tufvesson, F.: 6G wireless systems: vision, requirements, challenges, insights, and opportunities. In: Proceedings of the IEEE, vol. 109, no. 7 (2021)
4. Shafi, M.: 5G: a tutorial overview of standards, trials, challenges, deployment, and practice. *IEEE J. Sel. Areas Commun.* **35**(6), 1201–1221 (2017)
5. “White Paper on Broadband Connectivity in 6G”, 6G research visions, No. 10, 6G Flagship Center Univ. Oulu, Oulu, Finland (2020)
6. Network 2030: A Blueprint of Technology, Applications, and Market Drivers Toward the Year 2030, document ITU-T, Focus Group 2030 (2019)
7. Song, H.-J., Nagatsuma, T.: Present and future of terahertz communications. *IEEE Trans. Terahertz Sci. Technol.* **1**(1), 256–263 (2011)
8. Aqlan, B., Himdi, M., Coq, L.L., Vettikalladi, H.: Sub-THz circularly polarized horn antenna using wire electrical discharge machining for 6g wireless communications. *IEEE Access* **8**, 117245–117252 (2020)
9. Llombart, N., Cooper, K.B., Dengler, R.J., Bryllert, T., Siegel, P.H.: Confocal ellipsoidal reflector system for a mechanically scanned active terahertz imager. *IEEE Trans. Antennas Propag.* **58**(6), 1834–1841 (2010)
10. Kraus, J.D., Marhefka, R.J., Khan, A.S.: *Antenna and Wave Propagation*. Tata McGraw Hill Education Pvt. Ltd. (2010)
11. Corre, Y.: Sub-THz spectrum as enabler for 6G wireless communications up to 1 Tbit/s. In Proceedings of 6G Wireless Summit, pp. 1–2 (2019)
12. W. Haselmayr, “Integration of molecular communications into future generation wireless networks,” in Proc. 6G Wireless Summit, Mar. 2019, pp. 1–2
13. Piran, M.J., Suh, D.Y.: Learning-driven wireless communications, towards 6G. In Proceedings of International Conference on Computing, Electronics and Communications Engineering (iCCECE), pp. 219–224 (2019)
14. Federici, J., Moeller, L.: Review of terahertz and subterahertz wireless communications. *J. Appl. Phys.* **107**, 111101 (2010)
15. Baki, A.K.M., Rahman, M.N., Mondal, S.K.: Analysis of performance-improvement of microstrip antenna at 2.45 GHz through inset feed method. In: 2019 1st International Conference on Advances in Science, Engineering and Robotics Technology (ICASERT 2019) May 3–5, Dhaka, Bangladesh (2019)
16. Balanis, C.A.: *Antenna Theory: Analysis and Design*, 3rd edn. Wiley, Hoboken (2005)

17. Chung, M.A., Chuang, B.R.: Design a broadband u-shaped microstrip patch antenna on silicon-based technology for 6G terahertz (THz) future cellular communication applications. In: 2021 10th International Conference on Internet of Everything, Microwave Engineering, Communication and Networks (IEMECON) (2021). <https://doi.org/10.1109/IEMECON53809.2021.9689167>
18. Aqlan, B., Vettikalladi, H., Himdi, M.: A low-cost sub-terahertz circularly polarized antenna for 6g wireless communications. In: 2021 IEEE International Symposium on Antennas and Propagation and USNC-URSI Radio Science Meeting (APS/URSI) (2021). <https://doi.org/10.1109/APS/URSI47566.2021.9704272>



Non-similarity Solutions of MHD Boundary Layer Flow

Abhishek Neemawat¹ and Sushila²(✉)

¹ Department of Mathematics, JECRC University, Jaipur 303905, Rajasthan, India

² Department of Physics, Vivekananda Global University, Jaipur 303012, Rajasthan, India
sushila.jag@gmail.com

Abstract. In this study, we investigated the effects of an imposed uniform transverse magnetic field on the steady 2D viscous flow of an electrically conducting fluid. The governing non-linear PDEs are converted into ODEs using appropriate non-similarity and similarity variables and are then numerically resolved using accepted well-known methods. On the other hand, the values of many parameters regulating the entire flow system, the numerical values of the emerging dimensionless quantities like local Nusselt number and skin-friction coefficient are calculated and presented in tabular form. Computations are performed for velocity and temperature fields for different parameters. The effects of the numerous additional parameters considered in this article on the distribution of temperature (energy) and velocity (momentum) are represented visually by line graphs and described in detail. These characteristics have a considerable impact on the recommended MHD flow.

Keywords: Boundary layer · MHD · Non-similarity · Falkner-Skan equation · viscous dissipation · Görtler Transformation

Nomenclature

x, y	Cartesian co-ordinates
u, v	Velocity components
U_0	Uniform velocity
U_∞	Free flow velocity
T	Fluid temperature
T_w	Temperature at the plate surface
T_∞	Ambient temperature as y tends to infinity
f'	Dimensionless velocity
B_0	Magnetic component
c_p	Specific heat at constant pressure
C_f	Skin friction coefficient
Nu	Local Nusselt number
M	Magnetic parameter
Pr	Prandtl number
Ec	Eckert number
Re_x	Local Reynolds number

Greek Symbols

ρ	Density of the fluid
μ	Dynamic viscosity
ν	Kinematic viscosity
κ	Thermal conductivity
σ_e	Electrical conductivity
η	Dimensionless similarity variable
ψ	Stream function
β	Principal function
θ	Dimensionless temperature

1 Introduction

The most prominent specialties in fluid dynamics are boundary layer flows. Many of these applications in the recent past have been restricted to only one-word similarity estimates. However, the object of this effort was to approximate nonsimilar solutions of MHD boundary layer flow numerically. Problems involving nonsimilar solutions of boundary layer flows are more frequently encountered in industry and have wider applicability. Because the class of “similar” solutions is fairly small, it is necessary to explore the “nonsimilar” solutions, where the momentum of the external flow velocity is regarded as a polynomial and the distance is calculated from the commencement of the boundary layer. Also, the analytical and numerical solutions of “nonsimilar” boundary layer flow problems have never been easy and simple. It’s conceivable that Howarth [1] gave the first appropriate answer for a nonsimilar flow. Tani [2] had significant work on the results of boundary layer flow with nonsimilar solutions (NSS). Later on, Falkner [3], Görtler [4–6], Meksyn [7], and many more researchers made substantial contributions to “nonsimilar” solutions. Some fundamental traits of thermal boundary layer issues were noted by Sparrow et al. [8]. Later, Sparrow and Yu [9] identified the solutions for local non-similarity flow.

There exist many nonsimilar issues with boundary layer flow of surface mass and heat transfer. A variety of factors, including variations in wall heat, free flow velocity, surface mass transfer, the buoyancy force effect, the effect of suction/injection of fluid at the surface, inclination angle effects, etc., can lead to the non-similarity of the boundary layer. The nonsimilarity method was first developed by Sparrow et al. [10], and is the most well-known method of numerical approaches that have been suggested to address these nonsimilar boundary layer problems. Since then, it has been used by numerous researchers to address numerous distinct boundary layer issues. Rogers [11] revealed some significant findings from a comparison of the nonsimilar and the finite difference approach. Gorla and Kumari [12] examined nonsimilar non-Newtonian fluid solutions in permeable material on a vertical plane surface. Duck et al. [13] investigated nonsimilar solutions to the corner boundary layer. Non-similarity solutions for convection boundary layers were studied by Yian and Amin [14]. Cheng and Lin [15] found non-similarity solutions of heat transfer over a wedge. Liao [16] used a highly effective technique called

the homotopy analysis approach to produce analytical results for a non-similarity flow on a flat surface. Fang and Zhong [17] looked at non-identical solutions involving boundary layer flow over a contracting wall. Mureithi and Mason [18] investigated the local nonsimilar solution of viscous dissipation for a forced-free boundary layer flow. Kousar and Liao [19, 20] obtained a series solution over a porous wedge and by an impulsively expanding plane surface by using non-similarity solutions. Elhoucine et al. [21] looked into nonsimilar boundary layer solutions with slip boundary and isothermal wall conditions with positive and negative pressure gradients. Amoo OM et al. [22] focused on a very effective method, named as finite element method (FEM) to solve infinite series equations obtained from the nonsimilar boundary layers. Amoo OM et al. [23] used a comparative examination of numerical techniques to solve the infinite series equation resulting from a nonsimilar boundary layer. MHD flow of Williamson nanofluid having the impacts of variable thickness, thermal radiation and improved Fourier's and Fick's Laws were examined by Gupta et al. [24]. Effects of radiative MHD hybrid-nanofluids flow across a porous extended surface were investigated by Agrawal et al. [25]. In this paper, they formulated heat and mass flux upon Cattaneo-Christov theory. A thin film flow problem having applications in non-Newtonian fluid mechanics was investigated by Sushila et al. [26]. They used optimal homotopy analysis method (OHAM) to find non-dimensional forms of equations. With melting heat transfer, radiation and slip effects on MHD flow of nanofluid along an expanding sheet is explored by Kumar et al. [27].

Because we are conscious of the significance of MHD flow, in the current work, we have developed nonsimilar solutions for a 2D steady boundary layer viscous flow of an electrically conducting fluid with a homogeneous magnetic field. To account for magnetic field effects, the emerging boundary layer equations are converted to the Görtler plane from the physical plane using some standard assumptions and techniques. This process is referred to as the quasi-similarity transformation. For a set of nonsimilar boundary layer flows, a finite difference (central and backward difference) technique has been anticipated to explain the equations on the plane of quasi-similarity. With the aid of a fast computer, the equation's numerical solutions are achieved.

2 Governing Equations

Imagine a semi-infinite 2D plane surface with a continuous flow of viscous incompressible, electrically conducting fluid flowing over it while a uniform transverse magnetic field is applied, as shown in Fig. 1. It is supposed that the magnetic Reynolds number is low enough to allow for the ignoring the induced magnetic field. Also, it is assumed that the fluid's characteristics are both constant and isotropic. As a result, using the standard boundary layer approximations and taking into account viscosity and Joule heating factors, the equations governing the motion are (in the physical plane):

$$\frac{\partial u}{\partial x} + \frac{\partial v}{\partial y} = 0 \quad (1)$$

$$u \frac{\partial u}{\partial x} + v \frac{\partial u}{\partial y} = U_{\infty} \frac{dU_{\infty}}{dx} + \nu \frac{\partial^2 u}{\partial y^2} - \frac{\sigma_e B_0^2 u}{\rho} \quad (2)$$

$$u \frac{\partial T}{\partial x} + v \frac{\partial T}{\partial y} = \frac{\kappa}{\rho c_p} \frac{\partial^2 T}{\partial y^2} + \frac{\mu}{\rho c_p} \left(\frac{\partial u}{\partial y} \right)^2 + \frac{\sigma_e B_0^2 u^2}{\rho c_p} \tag{3}$$

Here velocity components in X and Y directions are given by u and v respectively, $\nu = \mu/\rho$ is called kinematic viscosity; here μ is viscosity coefficient and ρ is taken as fluid density, specific heat at constant pressure is denoted by c_p . σ_e , T and κ are the electrical conductivity, temperature, and thermal conductivity of fluid respectively.

The boundary conditions at the wall and far in the fluid can be expressed mathematically as follows:

$$\begin{aligned} u = 0, \quad v = 0, \quad T = T_w(x) \quad \text{at} \quad y = 0 \\ u \rightarrow U_\infty(x), \quad T \rightarrow T_\infty \quad \text{as} \quad y \rightarrow \infty \end{aligned} \tag{4}$$

where wall temperature is denoted by T_w , free flow velocity and temperature are denoted by U_∞ and T_∞ respectively.

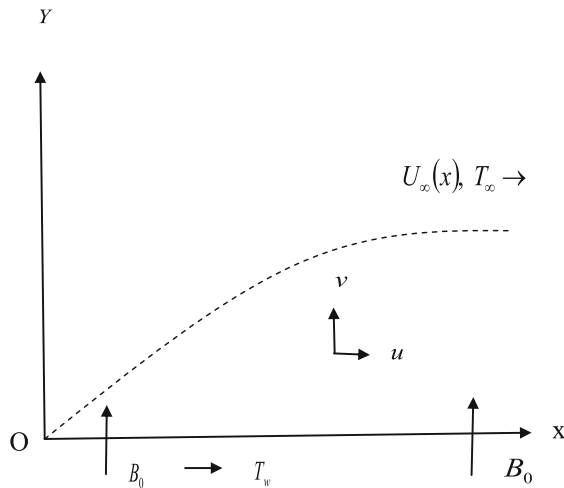


Fig. 1. Schematic flow diagram

3 Görtler Transformation

Görtler [6] changed the dependent and independent variables in ordinary fluid dynamics as follows:

$$\xi = \frac{1}{\nu} \int_0^x U_\infty(x) dx \tag{5}$$

$$\eta = \frac{U_\infty(x)}{\nu \sqrt{2\xi}} y \tag{6}$$

Here stream function ψ and temperature T are defined as follows:

$$\psi = \sqrt{2\xi}vf(\xi, \eta) \tag{7}$$

$$T = T_\infty + (T_w - T_\infty)\theta(\xi, \eta) \tag{8}$$

then, u and v satisfy the equation of continuity and become as

$$u = U_\infty f_\eta \tag{9}$$

and

$$v = -\frac{U_\infty}{\sqrt{2\xi}}[f + 2\xi f_\xi + \eta f_\eta \{\beta(\xi) - 1\}] \tag{10}$$

Equation (1) is known as the continuity equation and it is satisfied identically by the Cauchy-Riemann (C-R) equations ($u = \frac{\partial\psi}{\partial y} = \psi_y, v = -\frac{\partial\psi}{\partial x} = -\psi_x$). After certain simplifications, the momentum (velocity) and energy (temperature) equations provided by (2) and (3) simplify to

$$f_{\eta\eta\eta} + ff_{\eta\eta} - 2\xi f_\eta f_{\xi\eta} + 2\xi f_\xi f_{\eta\eta} - Mf_\eta + \beta(\xi)[1 - f_\eta^2] = 0 \tag{11}$$

$$\theta_{\eta\eta} + Pr[f\theta_\eta + Ec f_\eta^2 + MEc f_\eta^2 - 2\xi f_\eta \theta_\xi + f_\xi \theta_\eta] = 0 \tag{12}$$

The adequate boundary conditions are:

$$\begin{aligned} f(\xi) = 0, \quad f_\eta(\xi) = 0, \quad \theta(\xi) = 1 \quad \text{at } \eta = 0 \\ f_\eta(\xi) \rightarrow 1, \quad \theta(\xi) \rightarrow 0 \quad \text{as } \eta \rightarrow \infty \end{aligned} \tag{13}$$

In the above expression, dimensionless parameters are as follows:

$M = \frac{2\mu\xi\alpha_e B_0^2}{\rho^2 U_\infty^2}$ Magnetic Parameter, $\beta(\xi) = \frac{2U'_\infty(x) \int U_\infty(x) dx}{[U_\infty(x)]^2} = \frac{2\xi(x)\xi''(x)}{\xi'^2(x)}$ Principal Function, $Pr = \frac{\mu c_p}{\kappa}$ Prandtl Number, and $Ec = \frac{U_\infty^2}{c_p(T_w - T_\infty)}$ Eckert Number.

It should be noticed that Eqs. (11) and (12) are dependent on ξ and η . Furthermore, because both equations are non-similar and dimensional, they can be applied to any boundary layer problem.

If ξ is considered as a constant, all derivatives w.r.t. ξ will be zero therefore the Eqs. (11) and (12) become as under:

$$f''' + ff'' + \beta[1 - f'^2] - Mf' = 0 \tag{14}$$

$$\theta'' + Pr(f\theta' + Ec f'^2 + MEc f'^2) = 0 \tag{15}$$

The appropriate boundary conditions are:

$$\begin{aligned} f = f' = 0, \quad \theta = 1 \quad \text{at } \eta = 0 \\ f' \rightarrow 1, \quad \theta \rightarrow 0 \quad \text{as } \eta \rightarrow \infty \end{aligned} \tag{16}$$

Here prime (') denotes the derivative w.r.t. η .

These equations are now self-similar since they solely depend on the dimensionless variable η . For $M = 0$, the Eq. (14) is known as well known Falkner-Skan equation [28].

The physical quantities of engineering interest are skin-friction coefficient C_f and local Nusselt number Nu . Therefore, our task is to investigate how these quantities vary with the other governing parameters. These two quantities are the most important physical parameters in this issue, and these are found proportional to $f''(0)$ and $-\theta'(0)$ respectively, which can be expressed mathematically as follows:

$$C_f = \frac{\mu(u_y)_{y=0}}{\frac{\rho U_\infty^2}{2}} = 2^{1/2} \text{Re}^{-1/2} f''(0) \tag{17}$$

$$Nu = -\frac{x(T_y)_{y=0}}{T_w - T_\infty} = -2^{-1/2} \text{Re}^{1/2} \theta'(0) \tag{18}$$

where $\text{Re}_x = \frac{xU_\infty}{\nu}$ is identified as the local Reynolds number.

The impact of the emerging dimensionless parameters such as skin friction coefficient C_f and local Nusselt number Nu on flow properties is thoroughly examined. The variations of $f''(0)$ with M and β are presented in Table 1 while $-\theta'(0)$ for several values of Pr , M , Ec and β are presented in Table 2.

4 Numerical Solution

An iterative technique is adopted for nonsimilar equations given by (11) and (12) with boundary condition (13) and self-similar equations given by (14) and (15) with boundary condition (16). The R-K 4th order strategy is used to numerically solve these equations on a high-speed computer while employing orderly assumptions for $f''(0)$ and $\theta'(0)$ by using shooting procedure till boundary conditions of similar solutions at infinity are satisfied. While getting numerical solution, the step length of $\Delta\eta = 0.001$ is employed, and the precision is up to the 7th digit of decimal place, i.e. 10^{-7} , that is more than enough for required rate of convergence.

To begin with, a new transformation given by $f_\eta = P$ and $\theta_\eta = Q$ is taken into account and introduced for nonsimilar Eqs. (11) and (12), which transforms these equations to first order in Q and second order in P as

$$P_{\eta\eta} + P_\eta \int_0^\eta Pd\eta + \beta(\xi) [1 - P^2] - MP = 2\xi \left[PP_\xi - P_\eta \frac{\partial}{\partial \xi} \left(\int_0^\eta Pd\eta \right) \right] \tag{19}$$

$$Q_\eta + \text{Pr} \left(\int_0^\eta Pd\eta \right) Q + \text{Pr} Ec P_\eta^2 + M \text{Pr} Ec P^2 = 2 \text{Pr} \left[\xi P \left\{ \frac{\partial}{\partial \xi} \left(\int_0^\eta Qd\eta \right) \right\} - \left(\frac{\partial}{\partial \xi} \int_0^\eta Pd\eta \right) Q \right] \tag{20}$$

Now, backward differences substitute partial derivatives $\frac{\partial}{\partial \xi}$, and central differences replace partial derivatives $\frac{\partial}{\partial \eta}$. A non-uniform grid is utilised for the derivatives w.r.t. η to allow for a better and adequate mesh size close the surface. Non-linear terms

are replaced by reusing terms from earlier calculations. Equations (11) and (12) are translated as follows, with i and j serving as suffixes for the variables ξ and η directions respectively.

$$\frac{2}{\eta_{j+1} - \eta_{j-1}} \left[\frac{P_{i,j+1} - P_{i,j}}{\eta_{j+1} - \eta_j} - \frac{P_{i,j} - P_{i,j-1}}{\eta_j - \eta_{j-1}} \right] + f_{i,j} \frac{P_{i,j+1} - P_{i,j-1}}{\eta_{j+1} - \eta_{j-1}} + \beta(\xi_i) \left[1 - 2P_{i,j}P_{i,jOLD} + P_{i,jOLD}^2 \right] - MP_{i,jOLD} = \tag{21}$$

$$2\xi_i \left[P_{i,jOLD} \frac{P_{i,j} - P_{i-1,j}}{\xi_i - \xi_{i-1}} - \frac{f_{i,j} - f_{i-1,j}}{\xi_i - \xi_{i-1}} \frac{P_{i,j+1} - P_{i,j-1}}{\eta_{j+1} - \eta_{j-1}} \right] \frac{Q_{i,j+1} - Q_{i,j-1}}{\eta_{j+1} - \eta_{j-1}} + Pr f_{i,j} Q_{i,jOLD} + Pr Ec \left(\frac{P_{i,j+1} - P_{i,j-1}}{\eta_{j+1} - \eta_{j-1}} \right)^2 + M Pr Ec P_{i,jOLD} = 2 Pr \left[\xi_i P_{i,jOLD} \left\{ \frac{\theta_{i,j} - \theta_{i-1,j}}{\xi_i - \xi_{i-1}} \right\} - \left\{ \frac{f_{i,j} - f_{i-1,j}}{\xi_i - \xi_{i-1}} \right\} Q_{i,j} \right] \tag{22}$$

The set of Eqs. (21) and (22) that must be solved simultaneously for every value of ξ , i.e. for each i . This method must be repeated a sufficient number of times in the stream-wise direction at a certain grid point ξ . The same method is repeated for next mesh point i.e., $\xi = \xi_{i+1}$, if solution converges.

5 Results and Discussions

Matlab is a programming language that is used to create numerical solvers for both self-similar and nonsimilar situations. Initially, a programme called self-similar was created. It can efficiently resolve Eq. (14) for some fixed values of β and $M = 0$. In next stage, as an addition to the self-similar solution, the Matlab solver for nonsimilar Eqs. (11) and (12) was created. Using the table from White [29], the Matlab coding is verified against Falkner-Skan values. It is feasible to acquire findings precise to at least the 5th figure by taking a step length of similarity variable $\Delta\eta = 10^{-3}$ and a magnification feature for the step length of 1.0001. Tables 1 and 2, respectively, calculate the numerical values for the local Nusselt number and skin friction, and the effects of momentum and temperature field are visually illustrated in Figs. 2, 3, 4, 5, 6, 7 and 8 for distinct values of the non-dimensional parameters taken in the present paper.

According to Table 1, C_f reduces with rising M for some values of β , whereas it grows with growing values of β for some values of M . We also studied effect of various parameters on Nusselt number. Table 2 demonstrates that Nu decreases as M and Ec increases. Principal function β enhances heat transmission at lower Ec but shows opposite phenomenon at larger Ec . At lesser values of Ec , Pr enhances rate of heat transfer i.e. $-\theta'(0)$.

Figures 2, 3 and 4 demonstrate momentum effects plotted for distinct values of parameters such as M and β . Figures 2 and 3 illustrate that velocity increases as β increases in the absence and presence of M . Figure 4 shows that as M reduces, velocity increases. Figures 5, 6, 7 and 8 depict temperature distributions versus similarity variable η for various parameters involved in the present study such as Pr , Ec , M and β . Temperature enhances with increasing M and Ec and increases with reducing values of β and Pr , as shown in these figures.

Table 1. Comparison of $f''(0)$ for several M and β

M	$\beta = 0.0$	$\beta = 0.25$	$\beta = 0.50$	$\beta = 0.75$	$\beta = 1.0$
0.0	0.4693377	0.7319550	0.9276899	1.0905212	1.2325986
0.25	0.2008871	0.5370470	0.7713175	0.9583337	1.1171727
0.5	0.0801791	0.4070924	0.6522242	0.8504977	1.0188785
0.75	0.0369494	0.3244742	0.5632786	0.7633165	0.9355872
1.0	0.0194799	0.2719342	0.4970228	0.6929921	0.8650840

Table 2. Comparison of $-\theta'(0)$ for several Pr , β , Ec and M

β	M	$Pr = 0.023$		$Pr = 0.72$		$Pr = 1.0$	
		$Ec = 0.1$	$Ec = 0.5$	$Ec = 0.1$	$Ec = 0.5$	$Ec = 0.1$	$Ec = 0.5$
0.0	0.0	0.2087364	0.2060060	0.4004292	0.3295523	0.4458530	0.3519092
	0.25	0.2046089	0.2023813	0.3181379	0.2609611	0.3503278	0.2766550
	0.5	0.2022591	0.2006315	0.2621577	0.2170820	0.2815852	0.2223041
	0.75	0.2012265	0.1998842	0.2348586	0.1960952	0.2464834	0.1945894
	1.0	0.2007327	0.1995240	0.2211670	0.1855800	0.2284519	0.1803566
0.25	0.0	0.2101618	0.2063869	0.4292937	0.3275993	0.4794476	0.3432293
	0.25	0.2073652	0.2031986	0.3790027	0.2723981	0.4226134	0.284193
	0.5	0.2053652	0.2015092	0.3386350	0.2367646	0.3759812	0.2439595
	0.75	0.2040134	0.2006438	0.3084840	0.2150850	0.3402677	0.2178736
	1.0	0.2031146	0.2001818	0.2868477	0.2020539	0.3138949	0.2012458
0.5	0.0	0.2109008	0.2062783	0.4439516	0.3169897	0.4962239	0.3253103
	0.25	0.2086183	0.2029447	0.4043143	0.2582247	0.4515910	0.2607218
	0.5	0.2068826	0.2010006	0.3715859	0.2190518	0.4143892	0.2167385
	0.75	0.2055860	0.1999290	0.3451436	0.1941449	0.3838945	0.1878186

(continued)

Table 2. (continued)

β	M	Pr = 0.023		Pr = 0.72		Pr = 1.0	
		$Ec = 0.1$	$Ec = 0.5$	$Ec = 0.1$	$Ec = 0.5$	$Ec = 0.1$	$Ec = 0.5$
0.75	1.0	0.2046224	0.1993622	0.3240899	0.178887	0.3592119	0.1693040
	0.0	0.2113729	0.2060189	0.4531162	0.3042152	0.5064779	0.3054050
	0.25	0.2093580	0.2024546	0.4184627	0.2394709	0.4673890	0.2326230
	0.5	0.2077821	0.2001935	0.3895984	0.1941687	0.4346012	0.1808874
	0.75	0.2065479	0.1988199	0.3655526	0.1633673	0.4071161	0.1451386
	1.0	0.2055851	0.1980320	0.3456591	0.1433200	0.3841351	0.1212439
1.0	0.0	0.2116948	0.2056850	0.4593490	0.2907247	0.5134128	0.2852266
	0.25	0.2098543	0.2019103	0.4275976	0.2203555	0.4773476	0.2045246
	0.5	0.2083724	0.1993363	0.4007010	0.1684300	0.4467020	0.1444928
	0.75	0.2071832	0.1976459	0.3779909	0.1312217	0.4206813	0.1009613
	1.0	0.2062266	0.1965804	0.3588506	0.1052452	0.3986739	0.0700468

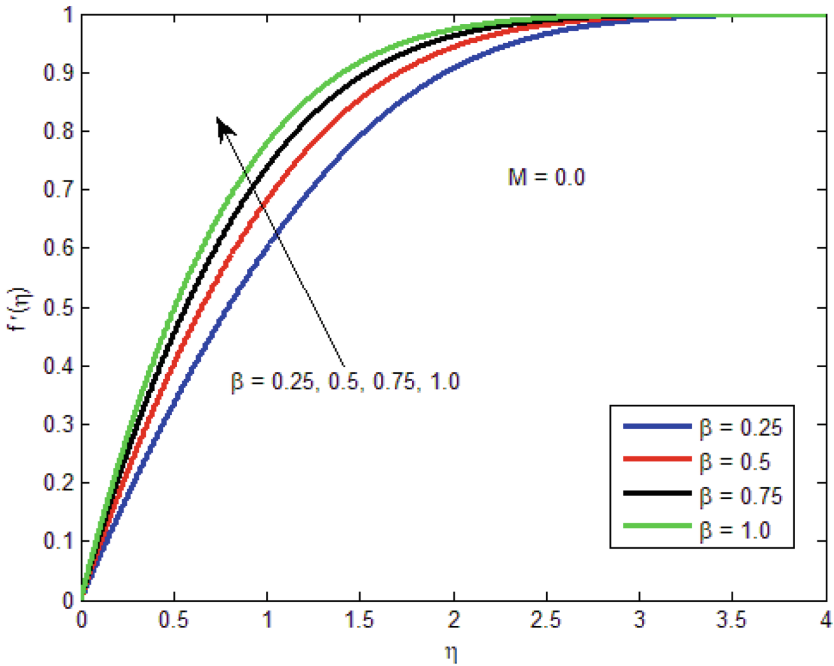


Fig. 2. The axial velocity as a function of η for diverse values of β

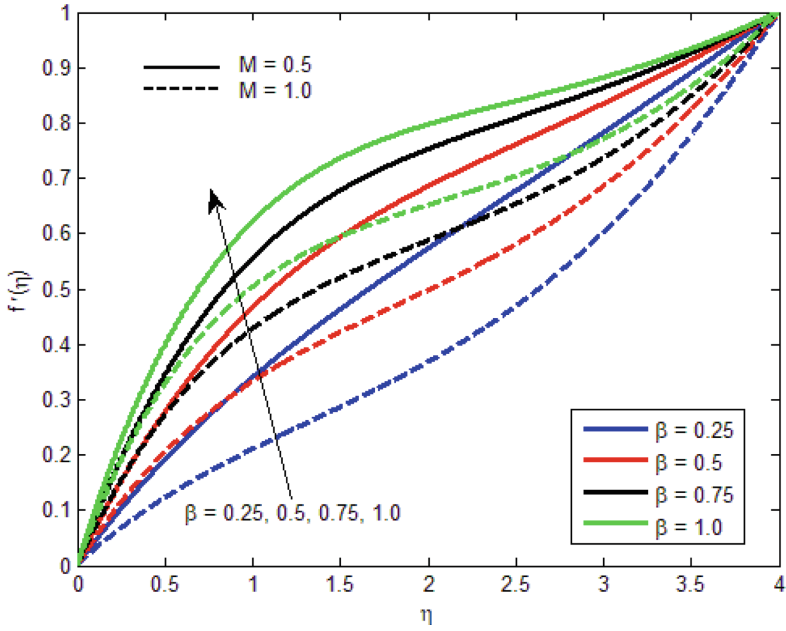


Fig. 3. The axial velocity as a function of η for diverse values of β

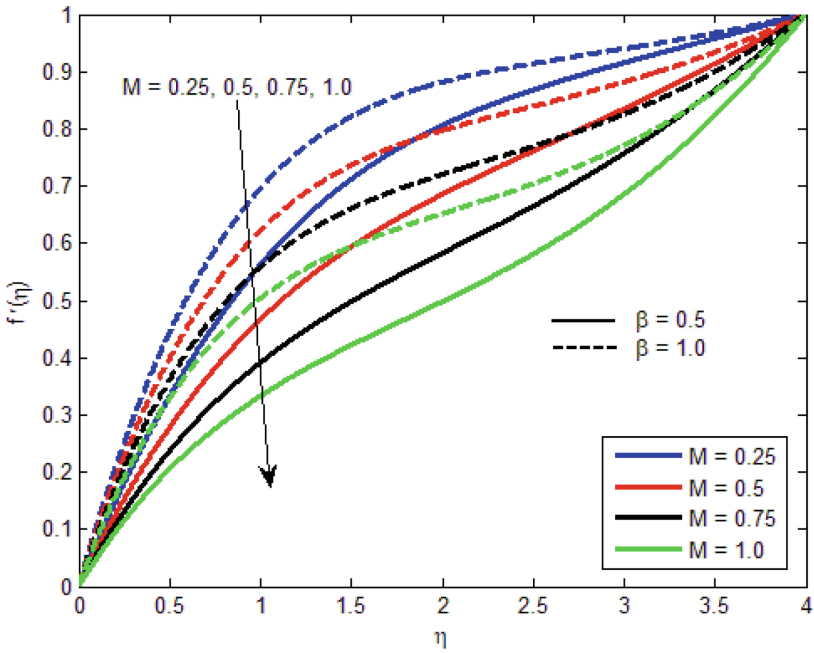


Fig. 4. The axial velocity as a function of η for diverse values of M

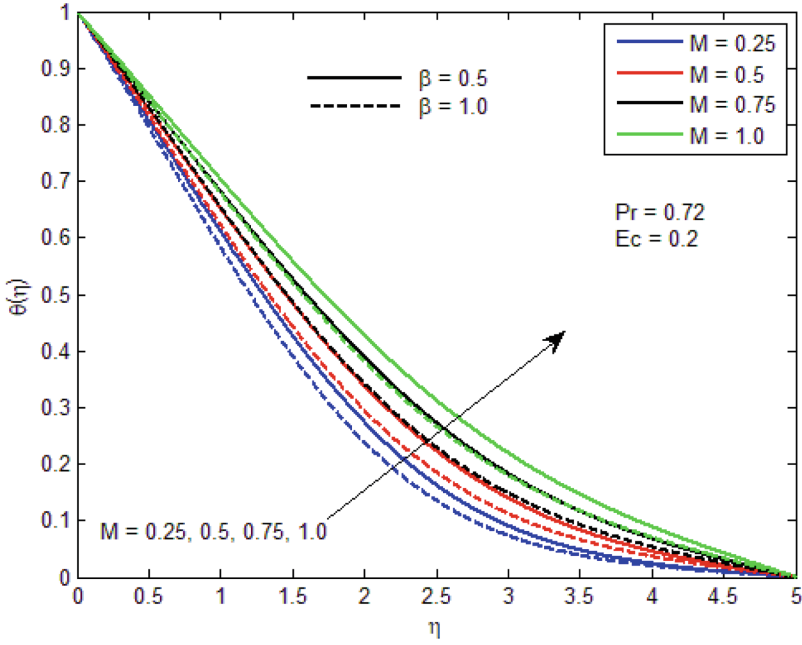


Fig. 5. The temperature distribution $\theta(\eta)$ for diverse values of M

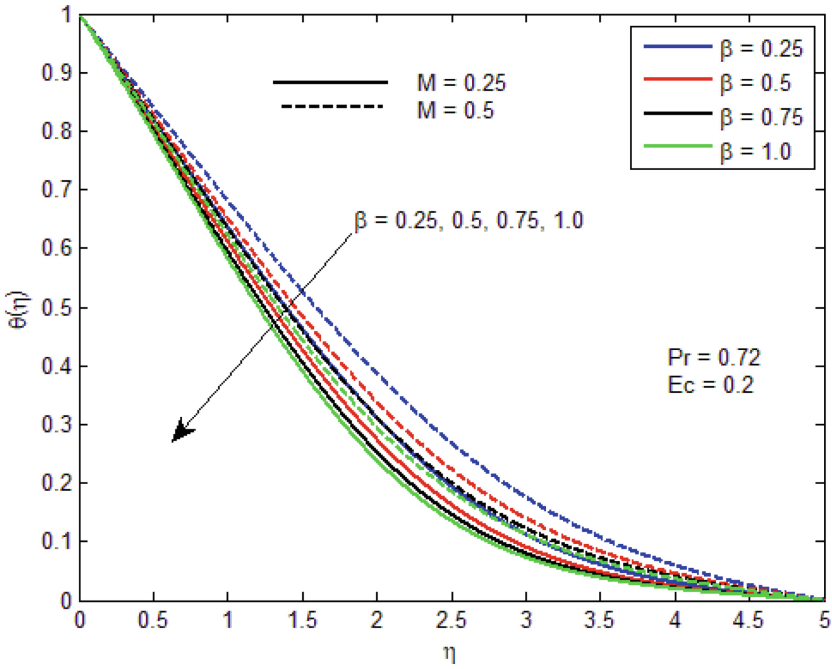


Fig. 6. The temperature distribution $\theta(\eta)$ for diverse values of β

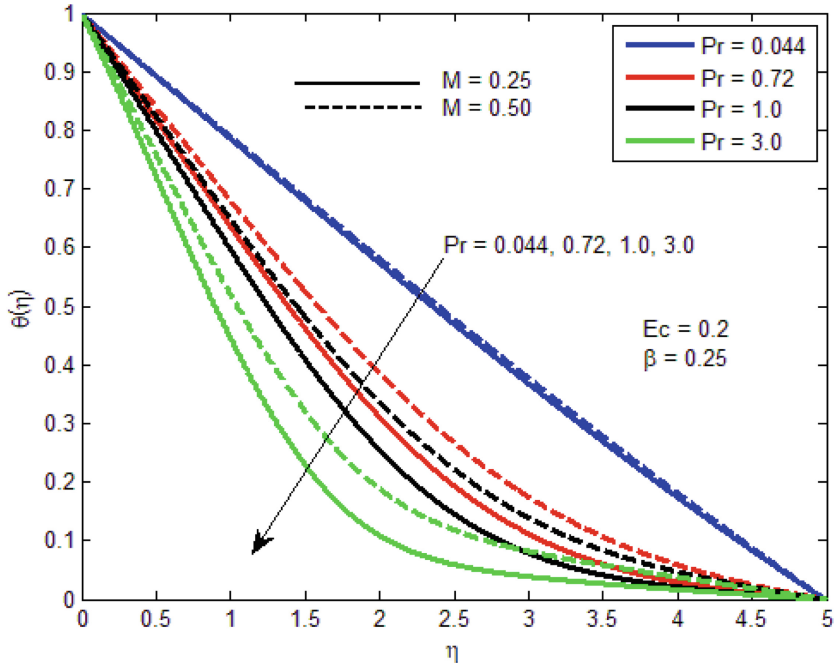


Fig. 7. The temperature distribution $\theta(\eta)$ for diverse values of Pr

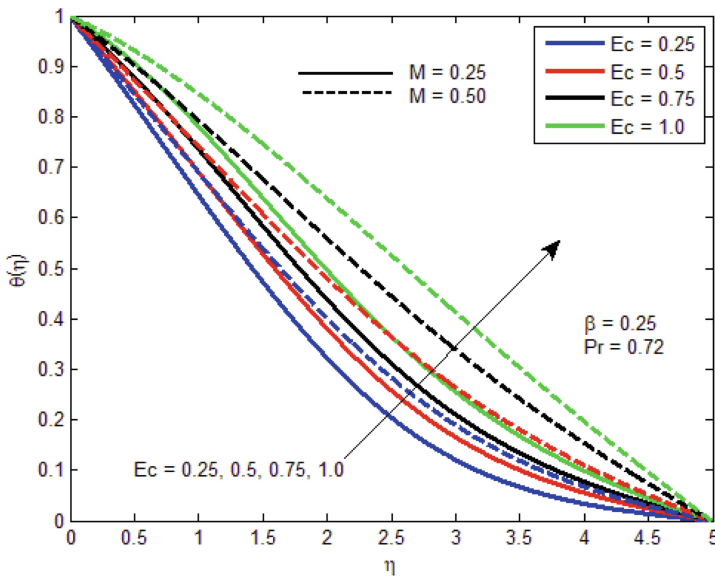


Fig. 8. The temperature distribution $\theta(\eta)$ for diverse values of Ec

6 Conclusions

Present study numerically investigates how an enforced uniform transverse magnetic field affected a fluid that conducts electrically while flowing steadily in two dimensions. Using the proper non-similarity and similarity variables, the governing non-linear PDEs are transformed into ODEs, and they are then numerically resolved using approved, well-established techniques. In the current investigation, the following observations have been made:

- When the magnetic parameter is increased, a resistive force known as the Lorentz force is produced in the flow, which results in a drop in velocity field plots.
- The temperature distribution has been seen to rise when the magnetic field parameter increases. The flow generates some extra heat as a result of the Lorentz force.
- The thermal layer thickness grows when the magnetic field parameter is raised, but the momentum layer thickness decreases.

References

1. Howarth, L.: On the solution of the laminar boundary layer equations. *Proc. Roy. Soc. Ser. A* **164**, 547–579 (1938)
2. Tani, I.: On the solution of the laminar boundary layer equations. *J. Phys. Soc. Japan* **4**, 149 (1949)
3. Falkner, V.M.: *Aeronaut Res. Council Lond.*, RM-1884 (1939)
4. Gortler, H.: A new series for the calculation of steady laminar boundary layer flows. *J. Math. Mech.* **6**, 1–66 (1957)
5. Gortler, H.: Bericht Nr. 34 der Deutschen Versuchsanstalt für Luftfahrt 1957: Zahrentafel universeller Funktionen Zur neuen Reihe für die Berechnung Laminarer Grenzschichten (1957)
6. Gortler, H.: On the calculation of steady laminar boundary layer flows with continuous suction. *J. Math. Mech.* **6**, 323–340 (1957)
7. Meksyn, D.: *New Methods in Laminar Boundary Layer Theory*. Pergamon Press, Oxford (1961)
8. Sparrow, E.M., Husar, R.B., Goldstein, R.J.: Observations and other characteristics of thermals. *J. Fluid Mech.* **41**, 793–800 (1970)
9. Sparrow, E.M., Yu, H.S.: Local non-similar thermal boundary layer solutions. *ASME J. Heat Transf.* **93**(4), 328–334 (1971)
10. Sparrow, E.M., Quack, H., Boerner, C.J.: Local non-similarity boundary layer solutions. *AIAA J.* **8**, 1936–1942 (1970)
11. Rogers, D.F.: *Laminar Flow Analysis*. Cambridge University Press, Cambridge (1992)
12. Gorla, R.S.R., Kumari, M.: Non-similar solutions for mixed convection in non-Newtonian fluids along a vertical plate in a porous medium. *Transp. Porous* **33**, 295–307 (1998)
13. Duck, P.W., Stow, S.R., Dhanak, M.R.: Non-similarity solutions to the corner boundary layer equations (and the effects of wall transpiration). *J. Fluid Mech.* **400**, 125–162 (1999)
14. Yian, L.Y., Amin, N.: Local non-similarity solution for vertical free convection boundary layers. *Matematika* **18**(1), 21–31 (2002)
15. Cheng, W.T., Lin, H.T.: Non-similarity solution and correlation of transient heat transfer in laminar boundary layer flow over a wedge. *Int. J. Eng. Sci.* **40**, 531–548 (2002)

16. Liao, S.J.: *Common Non-linear Sci. Numer. Simul.* **14**, 2144 (2009)
17. Fang, T., Zhong, Y.: *Commun. Non-linear Sci. Numer. Simul.* **15**, 3768 (2010)
18. Mureithi, E.W., Mason, D.P.: Local non-similarity solutions for a forced-free boundary layer flow with viscous dissipation. *Math. Comput. Appl.* **15**(4), 558–573 (2010)
19. Kousar, N., Liao, S.J.: Series solution of non-similarity boundary flows over a porous wedge. *Transp. Porous Media* **83**, 397–412 (2010)
20. Kousar, N., Liao, S.J.: Unsteady non-similarity boundary layer flows caused by an impulsively stretching flat sheet. *Nonlinear Anal. B* **12**, 333–342 (2011)
21. Elhoucine, E., Abdelaziz, O., Jawad, L.: Non-similar solutions of the boundary layers equations with favourable and adverse pressure gradients, isothermal wall and slip boundary conditions: application to Falkner-Skan gaseous flow. *Eur. J. Mech. B/Fluids* **77**, 281–298 (2019)
22. Amoo, O.M., Oyewola, M.O., Fagbenie, R.O.: Application of finite element method to the solution of non-similar boundary layer derived infinite series equations. *Int. J. Heat Mass Transf.* 161 (2020)
23. Amoo, O.M., Fagbenie, R.O., Oyewola, M.O.: A comparative analysis of numerical methods applied to non-similar boundary layer-derived infinite series equation. *Ain Shams Eng. J.* **13**(5), 101713 (2022)
24. Gupta, S., Kumar, D., Singh, J.: Analytical study for MHD flow of Williamson nanofluid with the effects of variable thickness, nonlinear thermal radiation and improved Fourier's and Fick's Laws. *SN Appl. Sci.* **2**(3), 1–12 (2020). <https://doi.org/10.1007/s42452-020-1995-x>
25. Agrawal, P., Dadheech, P.K., Jat, R.N., Baleanu, D., Purohit, S.D.: Radiative MHD hybrid-nanofluids flow over a permeable stretching surface with heat sourcesink embedded in porous medium. *Int. J. Numer. Meth. Heat Fluid Flow* **31**(8), 2818–2840 (2021)
26. Sushila, S.J., Kumar, D., Baleanu, D.: A hybrid analytical algorithm for thin film flow problem occurring in non-Newtonian fluid mechanics. *Ain Shams Eng. J.* **12**(2), 2297–2302 (2021)
27. Kumar, N., et al.: Radiation and slip effects on MHD point flow of nanofluid towards a stretching sheet with melting heat transfer. *Heat Transf.* **51**, 3018–3034 (2022)
28. Falkner, V.M., Skan, S.W.: Some approximate solutions of the boundary layer equations. *Aeronaut Res. Council, London RM-1314 Phil. Mag.* **12**, 865–896 (1931)
29. White, F.M.: *Viscous Fluid Flow*. McGraw-Hill (2006)



Deferred (Δ_v^m, f) -Statistical Convergence of Order α in Normed Space

A. K. Verma and Sudhanshu Kumar^(✉)

Dr. Harisingh Gour Vishwavidyalaya, Sagar 470003, M.P., India
sudhanshukumartomar@gmail.com

Abstract. In this paper, we introduced the space $DS^\alpha(\Delta_v^m, f, X)$ of all deferred (Δ_v^m, f) -statistically convergent sequences of order α in the normed space (X, q) with the help of generalized difference operator Δ_v^m , unbounded modulus function f , $\alpha \in (0, 1]$ and deferred sequences (p_n) , (q_n) of non-negative integers with $p_n < q_n$ for any $n \in \mathbb{N}$, $\lim_{n \rightarrow \infty} (q_n - p_n) = \infty$. We also introduced the space $D\omega^\alpha(\Delta_v^m, f, X)$ of all strongly deferred (Δ_v^m, f) -summable sequences of order α in the normed space (X, q) . Inclusion relations between spaces $DS^\alpha(\Delta_v^m, f, X)$ and $D\omega^\alpha(\Delta_v^m, f, X)$ are established under certain conditions.

Keywords: Statistical convergence · Modulus function · Difference sequence space · Deferred sequences

1 Introduction

In 1951, Steinhaus [22] and Fast [8] introduced the idea of statistical convergence. Later on, Schoenberg [19] reintroduced this concept independently in 1959. After the work of Fridy [10], statistical convergence has been extensively discussed by many researchers in summability theory till now. Statistical convergence depends upon the natural density of subsets of \mathbb{N} . Niven and Zuckerman [17] defined natural density of a subset K of \mathbb{N} , which is given by

$$\delta(K) = \lim_{n \rightarrow \infty} \frac{1}{n} |K(n)|, \text{ provided limit exists,}$$

where $K(n) = \{k \in K : k \leq n\}$ and $|K(n)|$ denotes the cardinality of set $K(n)$.

A sequence $x = (x_k)$ is said to be statistically convergent to l if for each $\epsilon > 0$,

$$\delta(\{k \in \mathbb{N} : |x_k - l| \geq \epsilon\}) = 0, \text{ i.e., } \lim_{n \rightarrow \infty} \frac{1}{n} |\{k \leq n : |x_k - l| \geq \epsilon\}| = 0.$$

Çolak [4] introduced the concept of statistical convergence of order α as follows:

A sequence $x = (x_k)$ is said to be statistically convergent of order α to l if for every $\epsilon > 0$,

$$\lim_{n \rightarrow \infty} \frac{1}{n^\alpha} |\{k \leq n : |x_k - l| \geq \epsilon\}| = 0.$$

Kizmaz [12] introduced difference operator Δ for sequence spaces l_∞ , c and c_0 . Et and Çolak [5] generalized difference operator Δ by introducing m^{th} -order difference operator Δ^m for l_∞ , c , c_0 . Further, Et and Esi [6] generalized space $X(\Delta^m)$ by taking sequence $v = (v_k)$ of non-zero complex numbers. They defined sequence space $X(\Delta_v^m)$ by

$$X(\Delta_v^m) = \{x = (x_k) \in w : \Delta_v^m x \in X\} \text{ for } X = l_\infty, c \text{ and } c_0,$$

where $\Delta_v^0 x_k = (v_k x_k)$ and $\Delta_v^m x_k = \sum_{i=0}^m (-1)^i \binom{m}{i} v_{k+i} x_{k+i}$, for $m \geq 1$.

Nakano [16] was introduced the idea of modulus function in 1953. Ruckle [18] defined a modulus function f is a function from $[0, \infty)$ to $[0, \infty)$ such that

- (i) $f(x) = 0$ if and only if $x = 0$,
- (ii) $f(x + y) \leq f(x) + f(y)$,
- (iii) f is increasing and
- (iv) f is continuous from the right at 0.

In 2014, Aizpuru et al. [2] introduced f -statistical convergence in the normed space by introducing f -density of a subset K of \mathbb{N} with the help of unbounded modulus function f , which is defined as

$$\delta^f(K) = \lim_{n \rightarrow \infty} \frac{f(|K(n)|)}{f(n)}, \text{ provided limit exists.}$$

Obviously, f -density for every finite set is zero.

Let (x_k) be a sequence in the normed space (X, q) . Then the sequence (x_k) is said to be f -statistically convergent to l in X if for each $\epsilon > 0$,

$$\delta^f(\{k \in \mathbb{N} : q(x_k - l) \geq \epsilon\}) = 0.$$

In 1932, Agnew [1] introduced the concept of deferred Cesàro mean of real numbers as follows:

$$(D_{p,q} x)_n = \frac{1}{(q_n - p_n)} \sum_{k=p_{n+1}}^{q_n} x_k,$$

where (p_n) and (q_n) are sequences of non-negative integers with $p_n < q_n$, for any $n \in \mathbb{N}$ and $\lim_{n \rightarrow \infty} q_n = \infty$.

In 2016, Küçükaslan and Yilmaztürk [13] used deferred sequences to define deferred statistical convergence as follows:

A sequence $x = (x_k)$ is said to be deferred statistically convergent to l if for every $\epsilon > 0$,

$$\lim_{n \rightarrow \infty} \frac{1}{(q_n - p_n)} |\{p_n < k \leq q_n : |x_k - l| \geq \epsilon\}| = 0.$$

Later on statistical convergence studied in ([3,7,9–11,21,23]) by using modulus function, difference operator and deferred sequences.

This paper introduced the concept of deferred (Δ_v^m, f) -statistical convergence and strongly deferred (Δ_v^m, f) -summable sequences of order α in the normed space. The study of these concepts unifies most of the earlier work related to f -statistical convergence and deferred statistical convergence.

1.1 Introduced Definitions

We assume that f is an unbounded modulus function, (X, q) is a normed space, m is a non-negative integer, $v = (v_k)$ is a fixed sequence of non-zero complex numbers and $(p_n), (q_n)$ are sequences of non-negative integers with $p_n < q_n$ for any $n \in \mathbb{N}$ and $\lim_{n \rightarrow \infty} (q_n - p_n) = \infty$, and $\alpha, \beta \in (0, 1]$, where $\alpha \leq \beta$. We define

$$W(X) = \{x = (x_k) : x_k \in X \text{ for each } k \in \mathbb{N}\}.$$

The f -deferred density of order α for a subset K of \mathbb{N} is defined by

$$\delta_{p,q}^{f,\alpha}(K) = \lim_{n \rightarrow \infty} \frac{1}{f((q_n - p_n)^\alpha)} f(|\{k \in K : p_n < k \leq q_n\}|), \text{ provided limit exists.}$$

Obviously, f -deferred density of order α is zero for every finite set.

If we take $f(x) = x, \alpha = 1, p_n = 0$ for all n and $q_n = n$, then f -deferred density of order α reduced to natural density. Again, if $\alpha = 1, p_n = 0$ for all n and $q_n = n$, then we get f -density given by Aizpuru et al. [2].

Definition 11. A sequence $x = (x_k)$ in $W(X)$ is called deferred (Δ_v^m, f) -statistically convergent of order α to l in X if for every $\epsilon > 0$,

$$\lim_{n \rightarrow \infty} \frac{1}{f((q_n - p_n)^\alpha)} f(|\{p_n < k \leq q_n : q(\Delta_v^m x_k - l) \geq \epsilon\}|) = 0.$$

In this case, we write $DS^\alpha(\Delta_v^m, f)\text{-lim } x_k = l$. The set of all deferred (Δ_v^m, f) -statistically convergent sequences of order α is denoted by $DS^\alpha(\Delta_v^m, f, X)$. For $p_n = 0$ and $q_n = n$, we denotes $S^\alpha(\Delta_v^m, f, X)$ for set $DS^\alpha(\Delta_v^m, f, X)$. Also, we write $DS^\alpha(\Delta_v^m, X)$ and $DS(\Delta_v^m, f, X)$ in place of set $DS^\alpha(\Delta_v^m, f, X)$ for $f(x) = x$ and $\alpha = 1$, respectively.

Definition 12. A sequence $x = (x_k)$ in $W(X)$ is called deferred (Δ_v^m, f) -summable of order α to l in X if

$$\lim_{n \rightarrow \infty} \frac{1}{f((q_n - p_n)^\alpha)} \sum_{p_n+1}^{q_n} f(q(\Delta_v^m x_k - l)) = 0.$$

In this case, we write $D\omega^\alpha(\Delta_v^m, f)\text{-lim } x_k = l$. The set of all deferred (Δ_v^m, f) -summable sequences of order α is denoted by $D\omega^\alpha(\Delta_v^m, f, X)$. For $p_n = 0$ and $q_n = n$, we denotes $\omega^\alpha(\Delta_v^m, f, X)$ for set $D\omega^\alpha(\Delta_v^m, f, X)$. Also, we write $D\omega^\alpha(\Delta_v^m, X)$ and $D\omega(\Delta_v^m, f, X)$ in place of set $D\omega^\alpha(\Delta_v^m, f, X)$ for $f(x) = x$ and $\alpha = 1$, respectively.

1.2 Particular Cases

By taking particular values of $X, p_n, q_n, f, (v_k), m$ and α , we can obtain some well known previous results in this area. Some of them are as follows:

- (i) If $X = \mathbb{R}$, $f(x) = x$, $m = 0$, $\alpha = 1$, $v_k = 1$ for all k , $q_n = n$ and $p_n = 0$ for all n , then we obtained results given by Fridy [10].
- (ii) If $X = \mathbb{R}$, $f(x) = x$, $m = 0$, $\alpha = 1$, $v_k = 1$ for all k , $q_n = n$ and $p_n = n - \lambda_n$, where (λ_n) is a non-decreasing sequence of positive integers tending to infinity with $\lambda_0 = 1$ and $\lambda_{n+1} \leq \lambda_n + 1$, then we get results discussed by Mursaleen [15].
- (iii) For $X = \mathbb{R}$, $f(x) = x$, $m = 0$, $v_k = 1$ for all k , $q_n = k_n$, $p_n = k_{n-1}$, where (k_n) is lacunary sequence of non-negative integers, we obtained results given by Şengül and Et [20].
- (iv) For $X = \mathbb{R}$, $m = 0$, $v_k = 1$ for all k , $q_n = n$ and $p_n = 0$ for all n , results in this paper coincide with results given by Bhardwaj and Dhawan [3].
- (v) If $X = \mathbb{R}$, $f(x) = x$, $\alpha = 1$, $m = 0$, $v_k = 1$ for all k , then we get results given by Küçükaslan and Yılmaztürk [13].
- (vi) For $X = \mathbb{R}$, $q_n = n$ and $p_n = 0$ for all n , results in this paper coincide with results given by Et and Gidemen [7].

2 Main Results

Theorem 21. Let $x = (x_k)$ and $y = (y_k)$ be any two sequences in $W(X)$.

- (i) If $DS^\alpha(\Delta_v^m, f)\text{-lim } x_k = x_0$ and $c \in \mathbb{C}$, then $DS^\alpha(\Delta_v^m, f)\text{-lim } cx_k = cx_0$.
- (ii) If $DS^\alpha(\Delta_v^m, f)\text{-lim } x_k = x_0$ and $DS^\alpha(\Delta_v^m, f)\text{-lim } y_k = y_0$, then $DS^\alpha(\Delta_v^m, f)\text{-lim}(x_k + y_k) = x_0 + y_0$.

Proof. The proof of this theorem is simple. So, we can omit it.

2.1 Inclusion Relations on $DS^\alpha(\Delta_v^m, f, X)$ and $D\omega^\alpha(\Delta_v^m, f, X)$

Theorem 22. The following inclusion relations hold:

- (i) $DS^\alpha(\Delta_v^m, f, X) \subseteq DS^\beta(\Delta_v^m, f, X)$,
- (ii) $D\omega^\alpha(\Delta_v^m, f, X) \subseteq D\omega^\beta(\Delta_v^m, f, X)$.

Proof. (i) By increasing property of modulus function, we have

$$f((q_n - p_n)^\alpha) \leq f((q_n - p_n)^\beta), \text{ for any } n \in \mathbb{N}.$$

Now, for any $n \in \mathbb{N}$

$$\begin{aligned} \frac{1}{f((q_n - p_n)^\beta)} f(\{p_n < k \leq q_n : q(\Delta_v^m x_k - l) \geq \epsilon\}) \\ \leq \frac{1}{f((q_n - p_n)^\alpha)} f(\{p_n < k \leq q_n : q(\Delta_v^m x_k - l) \geq \epsilon\}). \end{aligned}$$

Taking limit $n \rightarrow \infty$ on both sides, we get the required inclusion.

(ii) Inclusion follows by inequality

$$\frac{1}{f((q_n - p_n)^\beta)} \sum_{p_{n+1}}^{q_n} f(q(\Delta_v^m x_k - l)) \leq \frac{1}{f((q_n - p_n)^\alpha)} \sum_{p_{n+1}}^{q_n} f(q(\Delta_v^m x_k - l)).$$

Corollary 21. (i) $DS^\alpha(\Delta_v^m, f, X) \subseteq DS(\Delta_v^m, f, X)$,
 (ii) $D\omega^\alpha(\Delta_v^m, f, X) \subseteq D\omega(\Delta_v^m, f, X)$.

Theorem 23. Let $\left(\frac{f(q_n^\alpha)}{f((q_n - p_n)^\alpha)}\right)$ be a bounded sequence. Then

- (i) $S^\alpha(\Delta_v^m, f, X) \subseteq DS^\beta(\Delta_v^m, f, X)$,
- (ii) $\omega^\alpha(\Delta_v^m, f, X) \subseteq D\omega^\beta(\Delta_v^m, f, X)$.

Proof. (i) Let $x \in S^\alpha(\Delta_v^m, f, X)$. Then

$$\lim_{n \rightarrow \infty} \frac{1}{f(n^\alpha)} f(|\{k \leq n : q(\Delta_v^m x_k - l) \geq \epsilon\}|) = 0 \Rightarrow \lim_{n \rightarrow \infty} \frac{1}{f(q_n^\alpha)} f(|\{k \leq q_n : q(\Delta_v^m x_k - l) \geq \epsilon\}|) = 0.$$

Now, for any $\epsilon > 0$, we have

$$|\{p_n < k \leq q_n : q(\Delta_v^m x_k - l) \geq \epsilon\}| \leq |\{k \leq q_n : q(\Delta_v^m x_k - l) \geq \epsilon\}|.$$

As modulus function f is increasing, so

$$\begin{aligned} f(|\{p_n < k \leq q_n : q(\Delta_v^m x_k - l) \geq \epsilon\}|) &\leq f(|\{k \leq q_n : q(\Delta_v^m x_k - l) \geq \epsilon\}|) \\ \Rightarrow \frac{1}{f((q_n - p_n)^\beta)} f(|\{p_n < k \leq q_n : q(\Delta_v^m x_k - l) \geq \epsilon\}|) &\leq \frac{f(q_n^\alpha)}{f((q_n - p_n)^\alpha)} \frac{1}{f(q_n^\alpha)} f(|\{k \leq q_n : q(\Delta_v^m x_k - l) \geq \epsilon\}|). \end{aligned}$$

By taking limit $n \rightarrow \infty$ and using given assumption, inclusion follows.

(ii) Let $x \in \omega^\alpha(\Delta_v^m, f, X)$. Then

$$\lim_{n \rightarrow \infty} \frac{1}{f(n^\alpha)} \sum_{k=1}^n f(q(\Delta_v^m x_k - l)) = 0 \Rightarrow \lim_{n \rightarrow \infty} \frac{1}{f(q_n^\alpha)} \sum_{k=1}^{q_n} f(q(\Delta_v^m x_k - l)) = 0.$$

Now, for any n in \mathbb{N} , we can write

$$\begin{aligned} \frac{1}{f((q_n - p_n)^\beta)} \sum_{p_n+1}^{q_n} f(q(\Delta_v^m x_k - l)) &\leq \frac{1}{f((q_n - p_n)^\beta)} \sum_{k=1}^{q_n} f(q(\Delta_v^m x_k - l)) \\ &\leq \frac{f(q_n^\alpha)}{f((q_n - p_n)^\alpha)} \frac{1}{f(q_n^\alpha)} \sum_{k=1}^{q_n} f(q(\Delta_v^m x_k - l)). \end{aligned}$$

Taking limit $n \rightarrow \infty$ and using given assumption, we get the required inclusion.

Corollary 22. Let $\left(\frac{f(q_n^\alpha)}{f((q_n - p_n)^\alpha)}\right)$ be a bounded sequence. Then

- (i) $S^\alpha(\Delta_v^m, f, X) \subseteq DS^\alpha(\Delta_v^m, f, X)$,
- (ii) $\omega^\alpha(\Delta_v^m, f, X) \subseteq D\omega^\alpha(\Delta_v^m, f, X)$.

Theorem 24. For any unbounded modulus function f , $DS^\alpha(\Delta_v^m, f, X) \subseteq DS^\beta(\Delta_v^m, X)$.

Proof. Let $x \in DS^\alpha(\Delta_v^m, f, X)$. Then by definition of limit, for every $p \in \mathbb{N}$, there exists positive integer n_0 such that whenever $n \geq n_0$, we have

$$f(|\{p_n < k \leq q_n : q(\Delta_v^m x_k - l) \geq \epsilon\}|) \leq \frac{1}{p} f((q_n - p_n)^\alpha) = \frac{1}{p} f\left(\frac{p(q_n - p_n)^\alpha}{p}\right).$$

By using sub-additive property of modulus function f , we get

$$\begin{aligned} & f(|\{p_n < k \leq q_n : q(\Delta_v^m x_k - l) \geq \epsilon\}|) \leq \frac{1}{p} p f\left(\frac{(q_n - p_n)^\alpha}{p}\right) \\ \Rightarrow & \quad |\{p_n < k \leq q_n : q(\Delta_v^m x_k - l) \geq \epsilon\}| \leq \frac{(q_n - p_n)^\alpha}{p}, \text{ as } f \text{ is increasing} \\ \Rightarrow & \frac{1}{(q_n - p_n)^\beta} |\{p_n < k \leq q_n : q(\Delta_v^m x_k - l) \geq \epsilon\}| \leq \frac{1}{p}. \end{aligned}$$

Taking limit $n \rightarrow \infty$ on both sides, we get the required inclusion.

Corollary 23. $DS^\alpha(\Delta_v^m, f, X) \subseteq DS^\alpha(\Delta_v^m, X)$.

Result 21. [14] For any modulus function f , $\lim_{t \rightarrow \infty} \frac{f(t)}{t} = \inf \left\{ \frac{f(t)}{t} : t > 0 \right\}$.

Theorem 25. Let modulus function f be such that $\lim_{n \rightarrow \infty} \frac{f(t)}{t} > 0$. Then

$$D\omega^\alpha(\Delta_v^m, f, X) \subseteq D\omega^\beta(\Delta_v^m, X).$$

Proof. Let $\lim_{t \rightarrow \infty} \left[\frac{f(t)}{t} \right] = \gamma$. Then $\gamma = \inf \left\{ \frac{f(t)}{t} : t > 0 \right\}$. This means that $t \leq \gamma^{-1} f(t)$ for all $t \geq 0$. Let $x \in D\omega^\alpha(\Delta_v^m, f, X)$. Now, for any n in \mathbb{N} , we can write

$$\frac{1}{f((q_n - p_n)^\beta)} \sum_{p_{n+1}}^{q_n} q(\Delta_v^m x_k - l) \leq \frac{\gamma^{-1}}{f((q_n - p_n)^\alpha)} \sum_{p_{n+1}}^{q_n} f(q(\Delta_v^m x_k - l)).$$

Taking limit $n \rightarrow \infty$ on both sides, we get the required inclusion.

Corollary 24. Under the assumption of Theorem 25,

$$D\omega^\alpha(\Delta_v^m, f, X) \subseteq D\omega^\alpha(\Delta_v^m, X).$$

2.2 Relationship Between $DS^\alpha(\Delta_v^m, f, X)$ and $D\omega^\alpha(\Delta_v^m, f, X)$

Theorem 26. Let f be an unbounded modulus function satisfying $f(xy) \geq cf(x)f(y)$ for some positive constant c . Then $D\omega^\alpha(\Delta_v^m, f, X) \subseteq DS^\beta(\Delta_v^m, f, X)$.

Proof. Let $x \in D\omega^\alpha(\Delta_v^m, f, X)$ and $\epsilon > 0$. By using sub-additive and increasing property of modulus function f , we can write

$$\begin{aligned} \frac{1}{f((q_n - p_n)^\alpha)} \sum_{p_{n+1}}^{q_n} f(q(\Delta_v^m x_k - l)) &\geq \frac{1}{f((q_n - p_n)^\alpha)} f\left(\sum_{p_{n+1}}^{q_n} q(\Delta_v^m x_k - l)\right) \\ &\geq \frac{1}{f((q_n - p_n)^\beta)} f\left(\sum_{q(\Delta_v^m x_k - l) \geq \epsilon}^{p_{n+1}}^{q_n} q(\Delta_v^m x_k - l)\right) \\ &\geq \frac{1}{f((q_n - p_n)^\beta)} f(|\{p_n < k \leq q_n : q(\Delta_v^m x_k - l) \geq \epsilon\}| \epsilon) \\ &\geq \frac{c}{f((q_n - p_n)^\beta)} f(|\{p_n < k \leq q_n : q(\Delta_v^m x_k - l) \geq \epsilon\}|) f(\epsilon) \end{aligned}$$

Taking limit $n \rightarrow \infty$ on both sides, we have $x \in DS^\beta(\Delta_v^m, f, X)$ and hence inclusion follows.

Corollary 25. Under the assumption of Theorem 26,

$$D\omega^\alpha(\Delta_v^m, f, X) \subseteq DS^\alpha(\Delta_v^m, f, X).$$

Theorem 27. Let $\left(\frac{(q_n - p_n)}{f((q_n - p_n)^\alpha)}\right)$ be a bounded sequence and $\lim_{t \rightarrow \infty} \frac{f(t)}{t} > 0$. Then

$$DS^\alpha(\Delta_v^m, f, X) \cap l_\infty(\Delta_v^m, X) \subseteq D\omega^\beta(\Delta_v^m, f, X) \cap l_\infty(\Delta_v^m, X),$$

where $l_\infty(\Delta_v^m, X) = \{x = (x_k) \in W(X) : \sup_k q(\Delta_v^m x_k) < \infty\}$.

Proof. Let $\lim_{t \rightarrow \infty} \frac{f(t)}{t} = \gamma$. Then $\gamma = \inf \left\{ \frac{f(t)}{t} : t > 0 \right\}$ by Result 21. This means that $t \leq \gamma^{-1} f(t)$ for all $t \geq 0$. Let $x \in DS^\alpha(\Delta_v^m, f, X) \cap l_\infty(\Delta_v^m, X)$. Then there exists $M > 0$ such that $q(\Delta_v^m x_k - l) \leq M$ for all $k \in \mathbb{N}$. For each $\epsilon > 0$, suppose Σ_1 and Σ_2 denote the sums over $p_n < k \leq q_n, q(\Delta_v^m x_k - l) \geq \epsilon$ and $p_n < k \leq q_n, q(\Delta_v^m x_k - l) < \epsilon$, respectively. Now,

$$\begin{aligned} \frac{1}{f((q_n - p_n)^\beta)} \sum_{p_{n+1}}^{q_n} f(q(\Delta_v^m x_k - l)) &\leq \frac{1}{f((q_n - p_n)^\alpha)} (\Sigma_1 f(q(\Delta_v^m x_k - l)) + \Sigma_2 f(q(\Delta_v^m x_k - l))) \\ &\leq \frac{1}{f((q_n - p_n)^\alpha)} \Sigma_1 f(M) + \frac{1}{f((q_n - p_n)^\alpha)} \Sigma_2 f(\epsilon) \\ &\leq \frac{1}{f((q_n - p_n)^\alpha)} |\{p_n < k \leq q_n : q(\Delta_v^m x_k - l) \geq \epsilon\}| f(M) \\ &\quad + \frac{(q_n - p_n)}{f((q_n - p_n)^\alpha)} f(\epsilon) \\ &\leq \frac{\gamma^{-1}}{f((q_n - p_n)^\alpha)} f(|\{p_n < k \leq q_n : q(\Delta_v^m x_k - l) \geq \epsilon\}|) f(M) \\ &\quad + \frac{(q_n - p_n)}{f((q_n - p_n)^\alpha)} f(\epsilon). \end{aligned}$$

Taking limit $n \rightarrow \infty$ and using sequence $\left(\frac{(q_n - p_n)}{f((q_n - p_n)^\alpha)}\right)$ is bounded, inclusion follows.

Corollary 26. Under assumptions of Theorem 27,

$$DS^\alpha(\Delta_v^m, f, X) \cap l_\infty(\Delta_v^m, X) \subseteq D\omega^\alpha(\Delta_v^m, f, X) \cap l_\infty(\Delta_v^m, X).$$

3 Comparison of Inclusion Relations Between Two Deferred Sequences

In this section, we assume (p'_n) and (q'_n) are sequences of non-negative integers such that $p_n \leq p'_n < q'_n \leq q_n$ and $\lim_{n \rightarrow \infty} (q'_n - p'_n) = \infty$ in addition to previous assumptions.

Theorem 31. Let $\{k : p_n < k \leq p'_n\}$ and $\{k : q'_n < k \leq q_n\}$ be finite sets for any $n \in \mathbb{N}$. Then

$$D'S^\alpha(\Delta_v^m, f, X) \subseteq DS^\beta(\Delta_v^m, f, X).$$

Proof. Let $x \in D'S^\alpha(\Delta_v^m, f, X)$. For every $\epsilon > 0$ and any $n \in \mathbb{N}$, we have

$$\begin{aligned} \{p_n < k \leq q_n : q(\Delta_v^m x_k - l) \geq \epsilon\} &= \{p_n < k \leq p'_n : q(\Delta_v^m x_k - l) \geq \epsilon\} \\ &\cup \{p'_n < k \leq q'_n : q(\Delta_v^m x_k - l) \geq \epsilon\} \\ &\cup \{q'_n < k \leq q_n : q(\Delta_v^m x_k - l) \geq \epsilon\}. \end{aligned}$$

By using sub-additive property of modulus function f , we have

$$\begin{aligned} f(|\{p_n < k \leq q_n : q(\Delta_v^m x_k - l) \geq \epsilon\}|) &\leq f(|\{p_n < k \leq p'_n : q(\Delta_v^m x_k - l) \geq \epsilon\}|) \\ &\quad + f(|\{p'_n < k \leq q'_n : q(\Delta_v^m x_k - l) \geq \epsilon\}|) \\ &\quad + f(|\{q'_n < k \leq q_n : q(\Delta_v^m x_k - l) \geq \epsilon\}|). \end{aligned}$$

By given condition on (p'_n) and (q'_n) , we have $(q_n - p_n) \geq (q'_n - p'_n)$, which implies $(q_n - p_n)^\beta \geq (q'_n - p'_n)^\alpha$, and by increasing property of f , $f((q_n - p_n)^\beta) \geq f((q'_n - p'_n)^\alpha)$ for any $n \in \mathbb{N}$. Now,

$$\begin{aligned} \frac{1}{f((q_n - p_n)^\beta)} f(|\{p_n < k \leq q_n : q(\Delta_v^m x_k - l) \geq \epsilon\}|) &\leq \frac{1}{f((q'_n - p'_n)^\alpha)} f(|\{p_n < k \leq p'_n : q(\Delta_v^m x_k - l) \geq \epsilon\}|) \\ &\quad + \frac{1}{f((q'_n - p'_n)^\alpha)} f(|\{p'_n < k \leq q'_n : q(\Delta_v^m x_k - l) \geq \epsilon\}|) \\ &\quad + \frac{1}{f((q'_n - p'_n)^\alpha)} f(|\{q'_n < k \leq q_n : q(\Delta_v^m x_k - l) \geq \epsilon\}|). \end{aligned}$$

Taking limit $n \rightarrow \infty$ on both sides and using finiteness of sets $\{k : p_n < k \leq p'_n\}$ and $\{k : q'_n < k \leq q_n\}$, inclusion follows.

Corollary 31. Under the assumption of Theorem 31,

$$D'S^\alpha(\Delta_v^m, f, X) \subseteq DS^\alpha(\Delta_v^m, f, X).$$

Theorem 32. Let $\{k : p_n < k \leq p'_n\}$ and $\{k : q'_n < k \leq q_n\}$ be finite sets for any $n \in \mathbb{N}$. Then

$$D'\omega^\alpha(\Delta_v^m, f, X) \cap l_\infty(\Delta_v^m, X) \subseteq D\omega^\beta(\Delta_v^m, f, X) \cap l_\infty(\Delta_v^m, X).$$

Proof. For any $x \in D'\omega^\alpha(\Delta_v^m, f, X) \cap l_\infty(\Delta_v^m, X)$, there exists some $M > 0$ such that $q(\Delta_v^m x_k - l) \leq M$ for all $k \in \mathbb{N}$. This implies $f(q(\Delta_v^m x_k - l)) \leq f(M)$ for all $k \in \mathbb{N}$.

By using inequality $f((q_n - p_n)^\beta) \geq f((q'_n - p'_n)^\alpha)$, we can write

$$\begin{aligned} \frac{1}{f((q_n - p_n)^\beta)} \sum_{p_{n+1}}^{q_n} f(q(\Delta_v^m x_k - l)) &\leq \frac{1}{f((q'_n - p'_n)^\alpha)} \sum_{p_{n+1}}^{q_n} f(q(\Delta_v^m x_k - l)) \\ &\leq \frac{1}{f((q'_n - p'_n)^\alpha)} \left[\sum_{p_{n+1}}^{p'_n} f(M) + \sum_{p'_{n+1}}^{q'_n} f(q(\Delta_v^m x_k - l)) + \sum_{q'_{n+1}}^{q_n} f(M) \right] \\ &= \frac{1}{f((q'_n - p'_n)^\alpha)} \sum_{p'_{n+1}}^{q'_n} f(q(\Delta_v^m x_k - l)) \\ &\quad + \frac{1}{f((q'_n - p'_n)^\alpha)} \sum_{p_{n+1}}^{p'_n} f(M) + \frac{1}{f((q'_n - p'_n)^\alpha)} \sum_{q'_{n+1}}^{q_n} f(M). \end{aligned}$$

Taking limit $n \rightarrow \infty$ on both sides and using finiteness of sets $\{k : p_n < k \leq p'_n\}$ and $\{k : q'_n < k \leq q_n\}$, we get the required inclusion.

Corollary 32. Under the assumption of Theorem 32,

$$D'\omega^\alpha(\Delta_v^m, f, X) \cap l_\infty(\Delta_v^m, X) \subseteq D\omega^\alpha(\Delta_v^m, f, X) \cap l_\infty(\Delta_v^m, X).$$

Theorem 33. Suppose (p'_n) and (q'_n) are sequences of non-negative integers such that sequence $\left(\frac{f((q_n - p_n)^\alpha)}{f((q'_n - p'_n)^\alpha)}\right)$ is bounded. Then $DS^\alpha(\Delta_v^m, f, X) \subseteq D'S^\beta(\Delta_v^m, f, X)$.

Proof. Let $x \in DS^\alpha(\Delta_v^m, f, X)$. For every $\epsilon > 0$, it is clear that

$$\{p'_n < k \leq q'_n : q(\Delta_v^m x_k - l) \geq \epsilon\} \subseteq \{p_n < k \leq q_n : q(\Delta_v^m x_k - l) \geq \epsilon\}.$$

By using increasing property of modulus function f , we have

$$f(|\{p'_n < k \leq q'_n : q(\Delta_v^m x_k - l) \geq \epsilon\}|) \leq f(|\{p_n < k \leq q_n : q(\Delta_v^m x_k - l) \geq \epsilon\}|).$$

Thus, for every $\epsilon > 0$ and for any n in \mathbb{N}

$$\begin{aligned} \frac{1}{f((q'_n - p'_n)^\beta)} f(|\{p'_n < k \leq q'_n : q(\Delta_v^m x_k - l) \geq \epsilon\}|) \\ \leq \frac{f((q_n - p_n)^\alpha)}{f((q'_n - p'_n)^\alpha)} \frac{1}{f((q_n - p_n)^\alpha)} f(|\{p_n < k \leq q_n : q(\Delta_v^m x_k - l) \geq \epsilon\}|). \end{aligned}$$

Taking limit $n \rightarrow \infty$ on both sides and using boundedness of sequence $\left(\frac{f((q_n - p_n)^\alpha)}{f((q'_n - p'_n)^\alpha)}\right)$, we get the required inclusion.

Corollary 33. Under the assumption of Theorem 33,

$$DS^\alpha(\Delta_v^m, f, X) \subseteq D'S^\alpha(\Delta_v^m, f, X).$$

Theorem 34. Suppose (p'_n) and (q'_n) are sequences of non-negative integers such that sequence $\left(\frac{f((q_n - p_n)^\alpha)}{f((q'_n - p'_n)^\alpha)}\right)$ is bounded. Then $D\omega^\alpha(\Delta_v^m, f, X) \subseteq D'\omega^\beta(\Delta_v^m, f, X)$.

Proof. Let $x \in D\omega^\alpha(\Delta_v^m, f, X)$. For any $n \in \mathbb{N}$, we can write

$$\begin{aligned} \sum_{p'_{n+1}}^{q'_n} f(q(\Delta_v^m x_k - l)) &\leq \sum_{p_{n+1}}^{q_n} f(q(\Delta_v^m x_k - l)) \\ \Rightarrow \frac{1}{f((q'_n - p'_n)^\beta)} \sum_{p'_{n+1}}^{q'_n} f(q(\Delta_v^m x_k - l)) &\leq \frac{f((q_n - p_n)^\alpha)}{f((q'_n - p'_n)^\alpha)} \frac{1}{f((q_n - p_n)^\alpha)} \sum_{p_{n+1}}^{q_n} f(q(\Delta_v^m x_k - l)). \end{aligned}$$

Taking limit $n \rightarrow \infty$ on both sides and using given assumption, inclusion follows.

Corollary 34. Under the assumption of Theorem 34,

$$D\omega^\alpha(\Delta_v^m, f, X) \subseteq D'\omega^\alpha(\Delta_v^m, f, X).$$

References

1. Agnew, R.P.: On deferred Cesàro means. *Ann. Math.* **33**, 413–421 (1932)
2. Aizpuru, A., Listán-García, M.C., Rambla-Barreno, F.: Density by moduli and statistical convergence. *Quaest. Math.* **37**(4), 525–530 (2014)
3. Bhardwaj, V.K., Dhawan, S.: f -statistical convergence of order α and strong Cesàro summability of order α with respect to a modulus. *J. Inequalities Appl.* **2015**(1), 1–14 (2015)
4. Çolak, R.: Statistical convergence of order α . *Modern Methods in Analysis and Its Applications*, Anamaya Pub, New Delhi, India, pp. 121–129 (2010)
5. Et, M., Çolak, R.: On some generalized difference sequence spaces. *Soochow J. Math.* **21**(4), 377–386 (1995)
6. Et, M., Esi, A.: On Köthe-Toeplitz duals of generalized difference sequence spaces. *Bull. Malays. Math. Sci. Soc.* **23**(1), 25–32 (2000)
7. Et, M., Cinar, M., Şengül, H.: On $\Delta_v^m(f)$ -statistical convergence of order α . *Comm. Statist. Theory Methods* **49**(14), 3521–3529 (2020)
8. Fast, H.: Sur la convergence statistique. *Colloq. Math.* **2**, 241–244 (1951)
9. Fridy, J.A., Orhan, C.: Lacunary statistical convergence. *Pac. J. Math.* **160**(1), 43–51 (1993)
10. Fridy, J.A.: On statistical convergence. *Analysis* **5**, 301–313 (1985)
11. Gupta, S., Bhardwaj, V.K.: On deferred f -statistical convergence. *Kyungpook Math. J.* **58**(1), 91–103 (2018)
12. Kizmaz, H.: On certain sequence spaces. *Can. Math. Bull.* **24**(2), 169–176 (1981)
13. Küçükaslan, M., Yilmaztürk, M.: On deferred statistical convergence of sequences. *Kyungpook Math. J.* **56**, 357–366 (2016)
14. Maddox, I.J.: Inclusions between FK-spaces and Kuttner's theorem. *Math. Proc. Camb. Philos. Soc.* **101**(3), 523–527 (1987)
15. Mursaleen, M.: λ -statistical convergence. *Math. Slovaca* **50**(1), 111–115 (2000)
16. Nakano, H.: Concave modulars. *J. Math. Soc. Jpn.* **5**(1), 29–49 (1953)

17. Niven, I., Zuckerman, H.S.: An Introduction to the Theory of Numbers, 4th edn. Wiley, Hoboken (1980)
18. Ruckle, W.H.: FK spaces in which the sequence of coordinate vectors is bounded. *Can. J. Math.* **25**(5), 973–978 (1973)
19. Schoenberg, I.J.: The integrability of certain functions and related summability methods. *Am. Math. Mon.* **66**, 361–375 (1959)
20. Şengül, H., Et, M.: On lacunary statistical convergence of order α . *Acta Math. Sci.* **34**(2), 473–482 (2014)
21. Şengül, H., Et, M.: f -lacunary statistical convergence and strong f -lacunary summability of order α . *Filomat*, **32**(13), 4513–4521 (2018)
22. Steinhaus, H.: Sur la convergence ordinaire et la convergence asymptotique. *Colloq. Math.* **2**, 73–74 (1951)
23. Tripathy, B.C., Et, M.: On generalized difference lacunary statistical convergence. *Stud. Univ. Babeş-Bolyai, Math.* **50**(1), 119–130 (2005)



Integral Formulae Associated with the S-Function, \overline{H} -Function and the Aleph Function

Sapna Tyagi, Monika Jain^(✉), and Jagdev Singh

Department of Mathematics, JECRC University, Jaipur 303905, Rajasthan, India
monika.jain@jecrcu.edu.in

Abstract. The goal of this paper is to investigate some novel and feasible fractional integrals based on the two operators introduced by Marichev-Saigo in 1974, including the product of S function, \overline{H} -function and Aleph function with $m^\mu(m^\nu + h^\nu)$ as general argument. The fractional integrals established here have very common characteristics. Specializing the parameters of the \overline{H} -function, Aleph and S functions can produce various attractive results. Our findings thus offer remarkable extensions and unifications of a variety of previously known and brand-new findings. Few instances have also been registered.

Keywords: S-Function · Fractional Calculus · Aleph Function · \overline{H} -function · H-Function

1 Introduction

Saxena and Daiya [23] introduced the S-function and investigated its basic aspects and characteristics. According to Prabhakar [17], the S-function is an extension of the Generalized Mittag-Leffler function, which was developed by Srivastava and Tomovski [30].

The definition of S function is as follows:

$$S_{(u,v)}^{(\alpha, \mathfrak{B}, \gamma, \tau, \mathfrak{K})}(\mathfrak{a}_1 \dots \mathfrak{a}_u; \mathbb{l}_1 \dots \mathbb{l}_v; x) = \sum_{n=0}^{\infty} \frac{(\mathfrak{a}_1)_n \dots (\mathfrak{a}_u)_n (\gamma)_{n\tau, \mathfrak{K}}}{(\mathbb{l}_1)_n \dots (\mathbb{l}_v)_n \Gamma_{\mathfrak{K}}(n\alpha + \mathfrak{B})} \frac{x^n}{n!} \quad (1)$$

here $\mathfrak{K} \in \mathbb{R}$, $R(\alpha) > 0$, $\alpha, \mathfrak{B}, \gamma, \tau, \in \mathbb{C}$; $\mathfrak{a}_i (i = 1, 2 \dots f)$, $\mathbb{l}_j (j = 1, 2 \dots g)$, $R(\alpha) > K \mathfrak{K}(\tau)$ and $u < v + 1$.

Inayat–Hussain introduced the \bar{H} -function which is a generalization of H-function [12, 13]. The \bar{H} -function is represented in following way:

$$\begin{aligned} \bar{H}[Z] &= \tilde{H}_{p,q}^{m,n} \left[z \left| \begin{matrix} (e_j, E_j, \alpha_j)_{1,n} \cdots [(e_j, E_j)_{n+1,p}] \\ (\beta_j, F_j)_{1,m} \cdots [(\beta_j, F_j, \beta_j)_{m+1,q}] \end{matrix} \right. \right] \quad (2) \\ &= \frac{1}{2\pi i} \int_{-i\infty}^{i\infty} \omega_{p,q}^{m,n}(\rho) z^{-\rho} d\rho \\ \omega_{p,q}^{m,n}(\rho) &= \frac{\prod_{j=1}^m \Gamma(\beta_j - F_j \rho) \prod_{j=1}^n \Gamma\{(1 - e_j + E_j \rho)\}^{\alpha_j}}{\prod_{j=1+m}^q \Gamma\{(1 - \beta_j + F_j \rho)\}^{\beta_j} \prod_{j=1+n}^p \Gamma(e_j + E_j \rho)} \quad (3) \end{aligned}$$

More details of the \bar{H} -function and its convergence conditions can be studied in the papers [5, 12, 13].

The series representation of $\bar{H}[z]$ function [12, p. 271, Eq. (6)] is as follows:

$$\begin{aligned} \bar{H}_{p,q}^{m,n}[z] &= \tilde{H}_{p,q}^{m,n} \left[z \left| \frac{(e_j, E_j, \alpha_j)_{1,n} \cdots [(e_j, E_j)_{n+1,p}]}{(\beta_j, F_j)_{1,m} \cdots [(\beta_j, F_j, \beta_j)_{m+1,q}]} \right. \right] \quad (4) \\ &= \sum_{g=1}^m \sum_{h=0}^{\infty} \frac{(-1)^h \omega(\rho_{g,h}) z^{\rho_{g,h}}}{h! F_g} \\ \omega_{p,q}^{m,n}(\rho) &= \frac{\prod_{j=1}^m \Gamma(\beta_j - F_j \rho_{g,h}) \prod_{j=1}^n \Gamma(1 - e_j + E_j \rho_{g,h})^{\alpha_j}}{\prod_{j=m+1}^q \Gamma(1 - \beta_j + F_j \rho_{g,h})^{\beta_j} \prod_{j=n+1}^p \Gamma(e_j - E_j \rho_{g,h})} \quad (5) \end{aligned}$$

and

$$\rho_{g,h} = \frac{\beta_g + h}{F_g} \quad (6)$$

The new generalization of the I-function [19, 30] and the H-function [4, 10, 31] is the very well known Aleph-function. In Mellin –Barnes type integral, the Aleph-function is defined in the following terms [7, 14, 32]:

$$\begin{aligned} \aleph[Z] &= \aleph_{P_i, Q_i, \tau_i, r}^{M, N}[Z] = \aleph_{P_i, Q_i, \tau_i, r}^{M, N} \left[z \left| \begin{matrix} (a_j, A_j)_{1, N}, \dots, [\tau_i (a_j, A_j)]_{N+1, P_i} \\ (b_j, B_j)_{1, M}, \dots, [\tau_i (b_j, B_j)]_{M+1, Q_i} \end{matrix} \right. \right] \\ &= \frac{1}{2\pi\omega} \int_L \Phi(\xi) z^{-\xi} d\xi \quad (7) \end{aligned}$$

for all $z \neq 0$, where $\omega = \sqrt{-1}$ and

$$\Phi(\xi) = \frac{\prod_{j=1}^M \Gamma(b_j + B_j \xi) \prod_{j=1}^N \Gamma(1 - a_j - A_j \xi)}{\sum_{i=1}^r \tau_i \prod_{j=N+1}^{P_i} \Gamma(a_{ji} + A_{ji} \xi) \prod_{j=M+1}^{Q_i} \Gamma(1 - b_{ji} - B_{ji} \xi)} \quad (8)$$

The path of integration $L = L_i \gamma_\infty$, $\gamma \in \mathbb{R}$ extends from $\gamma - i\infty$ to $\gamma + i\infty$. The poles of $\Gamma(b_j + B_j \xi)$, $j = \overline{1, M}$. Which do not coincide to the poles of $\Gamma(1 - a_j - A_j \xi)$, $j = \overline{1, N}$ are taken as simple poles. The parameters p_i, q_i are non-negative integers $0 \leq N \leq P_i$, $1 \leq M \leq Q_i$, $\tau_i > 0$ for $i = \overline{1, r}$. The parameters $A_j, B_j, A_{ji}, B_{ji} > 0$ and $a_j, b_j, a_{ji}, b_{ji} \in \mathbb{C}$. The product in (8) is interpreted as unity. The existence conditions for the integral (7) are given as:

$$\theta_\ell > 0, |\arg(z)| < \frac{\pi}{2} \theta_\ell, \ell = \overline{1, r}; \tag{9}$$

$$\theta_\ell > 0, \text{larg}(z) < \frac{\pi}{2} \theta_\ell \text{ and } \text{Re}\{\zeta_\ell\} + 1 < 0, \tag{10}$$

where

$$\theta_\ell = \sum_{j=1}^N A_j + \sum_{j=1}^M B_j - \tau_\ell \left(\sum_{j=N+1}^{P_\ell} A_{j\ell} + \sum_{j=M+1}^{Q_\ell} B_{j\ell} \right) \tag{11}$$

$$\zeta_\ell = \sum_{j=1}^M b_j - \sum_{j=1}^N a_j + \tau_\ell \left(\sum_{j=M+1}^{Q_\ell} b_{j\ell} - \sum_{j=N+1}^{P_\ell} a_{j\ell} \right) + \frac{1}{2}(P_\ell - Q_\ell), \ell = \overline{1, r}, \tag{12}$$

Remark I: Taking $\tau_i = 1, i = 1, \dots, r$, in (2), the I- function is obtained which was defined by Saxena [27] in the following manner:

$$\begin{aligned} I[Y] &= I_{p_i, q_i; r}^{m, n}[Y] = I_{p_i, q_i; r}^{m, n} \left[Y \left| \begin{matrix} [(a_j \alpha_j)_{1, n}], [(a_{ji} \alpha_{ji})_{1+n, p_i}] \\ [(b_j \beta_j)_{1, m}], [(b_{ji} \beta_{ji})_{1+m, q_i}] \end{matrix} \right. \right] \\ &= \frac{1}{2\pi i} \int_L \theta(t) y^t dt, \end{aligned} \tag{13}$$

For the integral (13), the valid conditions are given as in (9)–(12) and the kernel $\theta_{p_i, q_i; r}^{m, n}(t)$ is defined in (8)

Remark II: Putting $r = 1$ and $\tau_1 = \tau_2 = \dots = \tau_3 = 1$, then \aleph -function reduces to the known H-function [9, 11, 31] given by C. Fox.

$$H_{P, Q}^{M, N}[Z] = H_{P, Q}^{M, N} \left[Z \left| \begin{matrix} (a_j, \alpha_j)_{1, P} \\ (b_j, \beta_j)_{1, Q} \end{matrix} \right. \right] = \frac{1}{2\pi i} \int_L \Omega(s) Z^s ds \tag{14}$$

where $i = \sqrt{-1}$, $Z \neq 0$ and

$$\Omega(s) = \frac{\prod_{j=1}^M \Gamma(b_j - \beta_j s) \prod_{j=1}^N \Gamma(1 - a_j + \alpha_j s)}{\prod_{j=N+1}^P \Gamma(a_j - \alpha_j s) \prod_{j=M+1}^Q \Gamma(1 - b_j + \beta_j s)}$$

Remark III: The fractional integration of Aleph function is given by Saxena and Pogány [24]. The papers of Saxena and Pogány [24, 25], Jain [3, 15] have full explanation of Aleph function.

The Aleph function series representation is given in following manner:

$$\aleph_{p_i, q_i, c_i, r}^{M, N}[z] = \aleph_{p_i, q_i, c_i, r}^{M, N} \left[z \left| \begin{matrix} (a_j, A_j)_{1, N} \cdots [c_i(a_j, A_j)_{N+1, p_i, r}] \\ (b_j, B_j)_{1, M} \cdots [c_i(b_j, B_j)_{M+1, q_i, r}] \end{matrix} \right. \right] \tag{15}$$

$$= \sum_{h=1}^M \sum_{k=0}^{\infty} \frac{(-1)^k \Omega(\eta_{h,k}) z^{-\eta_{h,k}}}{B_h k!}$$

$$\Omega(\eta_{h,k}) = \frac{\prod_{j=1}^M \Gamma(b_j + B_{j\eta_{h,k}}) \prod_{j=1}^N \Gamma(1 - a_j - A_{j\eta_{h,k}})}{\sum_{i=1}^r \prod_{j=M+1}^{q_i} \Gamma(1 - b_{ji} - B_{ji\eta_{h,k}}) \prod_{j=N+1}^{p_i} \Gamma(a_{ji} + A_{ji\eta_{h,k}})} \tag{16}$$

and

$$\eta_{h,k} = \frac{b_h + k}{B_h}, p_i < q_i, |z| < 1$$

2 Fractional Integrals

The Marichev-Saigo-Maeda fractional integral operators defined by Marichev [1, 16] for $\alpha, \alpha', \beta, \beta', \eta \in \mathbb{C}$ and $y > 0, Re(\eta) > 0$ are defined as follows:

$$I_{0+}^{\alpha, \alpha', \beta, \beta', \eta}[f(y)] = \frac{y^{-\alpha'}}{\Gamma(\eta)} \int_0^y (y-t)^{\eta-1} t^{-\alpha'} \mathcal{F}_3 \left(\alpha, \alpha', \beta, \beta'; \eta; 1 - \frac{t}{y}; 1 - \frac{y}{t} \right) f(t) dt \tag{17}$$

and

$$I_{0-}^{\alpha, \alpha', \beta, \beta', \eta}[f(y)] = \frac{y^{-\alpha'}}{\Gamma(\eta)} \int_0^y (t-y)^{\eta-1} t^{-\alpha'} \mathcal{F}_3 \left(\alpha, \alpha', \beta, \beta'; \eta; 1 - \frac{y}{t}; 1 - \frac{t}{y} \right) f(t) dt. \tag{18}$$

where \mathcal{F}_3 is Appell function.

The generalized Marichev-Saigo-Maeda fractional integral operator and fractional derivative operator reduce to the Saigo fractional integral and derivative operators involving the hypergeometric function ${}_2F_1$ in their kernel, which was defined by Saigo [21] by replacing the parameter by α by $\alpha + \beta$, and setting $\alpha' = \beta' = 0, \beta = -\eta$ and $\eta = \alpha$ in Eq. (17) and (18).

Take α, β and η and let $x \in \mathbb{R}_+ (0, \infty)$ the fractional integral ($\text{Re}(\alpha) > 0$) and derivative ($\text{Re}(\alpha) > 0$) of the first kind of a function $f(y)$ on \mathbb{R}_+ are defined correspondingly [6, 20, 21] in the following manner

$$\begin{aligned}
 I_{0,y}^{\alpha,\beta,\eta} [f(y)] &= \frac{y^{-\alpha-\beta}}{\Gamma(\alpha)} \int_0^y (y-t)^{\alpha-1} {}_2F_1\left(\alpha + \beta, -\eta; \alpha; 1 - \frac{t}{y}\right) f(t) dt; \text{Re}(\alpha) > 0 \\
 &= \frac{d^r}{dy^r} I_{0,y}^{\alpha+r,\beta-r,\eta-r} f(y); 0 < \text{Re}(\alpha) + r \leq 1 (r = 1, 2, \dots)
 \end{aligned}
 \tag{19}$$

The second kind of fractional integral ($\text{Re}(\alpha) > 0$) and derivatives ($\text{Re}(\alpha) < 0$) are given

$$\begin{aligned}
 J_{y,\infty}^{\alpha,\beta,\eta} [f(y)] &= \frac{1}{\Gamma(\alpha)} \int_y^\infty (t-y)^{\alpha-1} t^{-\alpha-\beta} {}_2F_1\left(\alpha + \beta, -\eta; \alpha; 1 - \frac{y}{t}\right) f(t) dt; \text{Re}(\alpha) > 0 \\
 &= (-1)^r \frac{d^r}{dx^r} I_{0,y}^{\alpha+r,\beta-r,\eta-r} f(y); 0 < \text{Re}(\alpha) + r \leq 1 (r = 1, 2, \dots)
 \end{aligned}
 \tag{20}$$

The use of the next two theorems is demonstrated in the continuation.

Theorem 1: If $\text{Re}(c) > 0, \mu \in \Omega_{a,a',b,b'}$ and h is a positive number and $v = 1, 2, 3, \dots$ and $\sigma, \lambda_1, \lambda_2, \phi_1, \phi_2$ are complex numbers, then

$$\begin{aligned}
 &I_{0,m}^{a,a',b,b',c} \left[m^\mu (m^\nu + h^\nu)^{-\sigma} S_{(u,v)}^{(\alpha,\beta,\gamma,\tau,\delta)} \{ Dm^{\lambda_1} (m^\nu + h^\nu)^{-\phi_1} \} \right. \\
 &\quad \left. \times \bar{H}_{p,q}^{m,n} \left[Z m^{\lambda_2} (m^\nu + h^\nu)^{-\phi_2} \left[\begin{matrix} (e_j, E_j, \alpha_j)_{1,n} \dots [(e_j, E_j)_{n+1,p}] \\ (f_j, F_j)_{1,m} \dots [(f_j, F_j, \beta_j)_{m+1,q}] \end{matrix} \right] \right] \right] \\
 &= \frac{m^{-a-a'-r+\mu+\lambda_1 n+\lambda_2 \delta_{\mathbb{B},\mathbb{A}}}}{h^{(\sigma v+\phi_1 v+\phi_2 \delta_{\mathbb{B},\mathbb{A}} v)}} \sum_{r=0}^\infty \sum_{\mathbb{B}=1}^m \sum_{\mathbb{A}=0}^\infty \frac{(-1)^{\mathbb{A}} \varpi(\delta_{\mathbb{B},\mathbb{A}}) Z^{\delta_{\mathbb{B},\mathbb{A}}}}{\mathbb{A}! F_{\mathbb{B}}} \frac{(\mathbb{A}_n)_n \dots (\mathbb{A}_n)_n (Y)_{n\tau,\delta}}{(\mathbb{B}_1)_n \dots (\mathbb{B}_v)_n \Gamma_{\mathbb{A}}(n\alpha + \mathfrak{P})} \\
 &\quad \times \frac{(a')_r (b')_r}{(a' - \mu - \lambda_1 n - \lambda_2 \delta_{\mathbb{B},\mathbb{A}})_r r! \Gamma(1 - a' - b + c + \mu + \lambda_1 n + \lambda_2 \delta_{\mathbb{B},\mathbb{A}})} \frac{\Gamma(1 - a' + \mu + \lambda_1 n + \lambda_2 \delta_{\mathbb{B},\mathbb{A}})}{\Gamma(1 - a - a' + \mu + c + \lambda_1 n + \lambda_2 \delta_{\mathbb{B},\mathbb{A}} - b)} \\
 &\quad \frac{D^n \Gamma(1 - a - a' + \mu + c + \lambda_1 n + \lambda_2 \delta_{\mathbb{B},\mathbb{A}} - b)}{n! \Gamma(1 - a - a' + \mu + c + \lambda_1 n + \lambda_2 \delta_{\mathbb{B},\mathbb{A}})} {}_{2v+1}F_{2v} \\
 &\quad \left[\frac{\sigma + \phi_1 n + \phi_2 \delta_{\mathbb{B},\mathbb{A}}}{(1 - a - a' - b + c + \mu + \lambda_1 n + \lambda_2 \delta_{\mathbb{B},\mathbb{A}})} \frac{(1 - a' - r + \mu + \lambda_1 n + \lambda_2 \delta_{\mathbb{B},\mathbb{A}})}{(v - a - a' - b + c + \mu + \lambda_1 n + \lambda_2 \delta_{\mathbb{B},\mathbb{A}})} \dots \frac{(v - a' - r + \mu + \lambda_1 n + \lambda_2 \delta_{\mathbb{B},\mathbb{A}})}{(v - a - a' - b + c + \mu + \lambda_1 n + \lambda_2 \delta_{\mathbb{B},\mathbb{A}})} \dots \right] \\
 &\quad \left[\frac{(1 - a - a' + c + \mu + \lambda_1 n + \lambda_2 \delta_{\mathbb{B},\mathbb{A}})}{(v - a - a' + c + \mu + \mathbb{C} + \lambda_1 n + \lambda_2 \delta_{\mathbb{B},\mathbb{A}})} \dots \frac{(v - a - a' + c + \mu + \mathbb{C} + \lambda_1 n + \lambda_2 \delta_{\mathbb{B},\mathbb{A}})}{(v - a' - b + c + \mu + \lambda_1 n + \lambda_2 \delta_{\mathbb{B},\mathbb{A}})} \dots \frac{-m^v}{h^v} \right]
 \end{aligned}
 \tag{21}$$

Proof: First, we compute the fractional integral operator by (17) to obtain Theorem 1 for

$$f(t) = t^\mu (t^u + h^v)^{-\sigma} S_{(u,v)}^{(\alpha, \mathfrak{B}, \gamma, \tau, \mathfrak{R})} [Dt^{\lambda_1} (t^u + h^v)^{-\phi_1}] \times \bar{H}_{p,q}^{m,n} \left[Z m^{\lambda_2} (t^u + h^v)^{-\phi_2} \left[\begin{matrix} (e_j, E_j, \alpha_j)_{1,n} \cdots [(e_j, E_j)_{n+1,p}] \\ (\beta_j, F_j)_{1,m} \cdots [(\beta_j, F_j, \beta_j)_{m+1,q}] \end{matrix} \right] \right] \tag{22}$$

Expressing S function by (1) and defining the common arguments $(m^u + h^v)^{-\sigma}$ argument in series form by the formula

$$(m^u + h^v)^{-\sigma} = h^{-\sigma v} \sum_{\delta=0}^{\infty} \frac{(\sigma)_{\delta}}{\delta!} \left(\frac{-m^u}{h^v} \right)^{\delta} \tag{23}$$

when arranging the order of sum and integral, it is allowed because the process involves absolute convergence, and the integral is calculated using the following result

$$\int_0^y (y-x)^{C-1} x^{\rho-1} {}_2F_1 \left[\mathbb{A}, \mathbb{B}, \mathbb{C}; \left(1 - \frac{x}{y} \right) \right] dx = x^{\rho+C-1} \frac{\Gamma(\mathbb{C})\Gamma(\rho)\Gamma(\rho + \mathbb{C} - \mathbb{A} - \mathbb{B})}{\Gamma(\rho + \mathbb{C} - \mathbb{A})\Gamma(\rho + \mathbb{C} - \mathbb{B})} \tag{24}$$

Then, with some simplification and using the Gauss theorem and the multiplication formula from (Rainville[18], Theo.18), we arrive at the desired consequence stated in (21).

Remark: 1 Replacing a by $a + b$, then setting $a' = b' = 0$, $\beta = -c$ and $c = a$, we get (21) in the following manner

$$I_{0,m}^{a,b,c} \left\{ m^\mu (m^u + h^v)^{-\sigma} S_{(u,v)}^{(\alpha, \mathfrak{B}, \gamma, \tau, \mathfrak{R})} \{ Dm^{\lambda_1} (m^u + h^v)^{-\phi_1} \} \times \bar{H}_{p,q}^{m,n} \left[Z m^{\lambda_2} (m^u + h^v)^{-\phi_2} \left[\begin{matrix} (e_j, E_j, \alpha_j)_{1,n} \cdots [(e_j, E_j)_{n+1,p}] \\ (\beta_j, F_j)_{1,m} \cdots [(\beta_j, F_j, \beta_j)_{m+1,q}] \end{matrix} \right] \right] \right\} \\ = \frac{m^{\mu+\lambda_1 n+\lambda_2 \wp_{\mathfrak{B}, \mathfrak{A}}-b}}{h^{(\sigma v+\phi_1 u+\phi_2 \wp_{\mathfrak{B}, \mathfrak{A}} v)}} \sum_{n=0}^{\infty} \sum_{\mathfrak{g}=1}^m \sum_{\mathfrak{h}=0}^{\infty} \frac{(-1)^{\mathfrak{h}} \varpi(\wp_{\mathfrak{B}, \mathfrak{A}}) Z^{\wp_{\mathfrak{B}, \mathfrak{A}}} (\mathfrak{a}_1)_n \dots (\mathfrak{a}_u)_n (\gamma)_{n\tau, \mathfrak{R}}}{\mathfrak{h}! F_{\mathfrak{B}} (\mathfrak{b}_1)_n \dots (\mathfrak{b}_v)_n \Gamma_{\mathfrak{R}}(n\alpha + \mathfrak{B})} \frac{D^n}{n!} \\ \times \frac{\Gamma(1 + \mu + \lambda_1 n + \lambda_2 \wp_{\mathfrak{B}, \mathfrak{A}}) \Gamma(1 + \mu + c + \lambda_1 n + \lambda_2 \wp_{\mathfrak{B}, \mathfrak{A}} - b)}{\Gamma(1 + \mu + \lambda_1 n + \lambda_2 \wp_{\mathfrak{B}, \mathfrak{A}} - b) \Gamma(1 + \mu + a + c + \lambda_1 n + \lambda_2 \wp_{\mathfrak{B}, \mathfrak{A}})} \times {}_{2u+1}F_{2v} \\ \left[\begin{matrix} \sigma + \phi_1 n + \phi_2 \wp_{\mathfrak{B}, \mathfrak{A}}, \frac{(1 + \mu + \lambda_1 n + \lambda_2 \wp_{\mathfrak{B}, \mathfrak{A}})^u \dots (u + \mu + \lambda_1 n + \lambda_2 \wp_{\mathfrak{B}, \mathfrak{A}})^u \dots (1 + \mu + \lambda_1 n + \lambda_2 \wp_{\mathfrak{B}, \mathfrak{A}} - b)^u \dots}{(u + \mu + \lambda_1 n + \lambda_2 \wp_{\mathfrak{B}, \mathfrak{A}} - b)^u \dots (1 + \mu + c + \lambda_1 n + \lambda_2 \wp_{\mathfrak{B}, \mathfrak{A}} - b)^u \dots (u + \mu + c + \lambda_1 n + \lambda_2 \wp_{\mathfrak{B}, \mathfrak{A}} - b)^u \dots} \dots \\ \frac{(1 + \mu + a + c + \lambda_1 n + \lambda_2 \wp_{\mathfrak{B}, \mathfrak{A}})^u \dots (u + \mu + a + c + \lambda_1 n + \lambda_2 \wp_{\mathfrak{B}, \mathfrak{A}})^u \dots, -m^u}{u, h^v} \end{matrix} \right] \tag{25}$$

Proof: For result (25), we apply the method used in (21).

Theorem 2. If $\text{Re}(c) > 0$, $\mu \in \Omega_{a,a',b,b'}$ and h is a positive number and $v = 1, 2, 3, \dots$ and $\sigma, \lambda_1, \lambda_2, \phi_1, \phi_2$ are complex number, then

$$\begin{aligned}
 & I_{m,\infty}^{a,a',b,b',c} \left\{ m^\mu (m^v + h^v)^{-\sigma} S_{(u,v)}^{(\alpha,\beta,\gamma,\tau,\mathfrak{K})} \{ Dm^{\lambda_1} (m^v \right. \\
 & \quad \left. + h^v)^{-\phi_1} \} \times \bar{H}_{p,q}^{m,n} \left[z m^{\lambda_2} (m^v + h^v)^{-\phi_2} \left[\begin{matrix} (e_j, E_j, \alpha_j)_{1,n} \cdots [(e_j, E_j)_{n+1,p}] \\ (\mathcal{F}_j, F_j)_{1,m} \cdots [(\mathcal{F}_j, F_j, \beta_j)_{m+1,q}] \end{matrix} \right] \right] \right\} \\
 &= \frac{m^{-a-a'-r+c+\mu+\lambda_1 n+\lambda_2 \delta_{\mathbb{R},h}}}{h^{(\sigma v+\phi_1 v+\phi_2 \delta_{\mathbb{R},h} v)}} \sum_{n=r=0}^{\infty} \sum_{\mathfrak{g}=1}^m \sum_{\mathfrak{h}=0}^{\infty} \frac{(-1)^{\mathfrak{h}} \varpi(\delta_{\mathbb{R},h}) z^{\delta_{\mathbb{R},h}}}{\mathfrak{h}! F_{\mathbb{R}}} \frac{(\mathfrak{a}_1)_n \cdots (\mathfrak{a}_u)_n (\gamma)_{n\tau, \mathfrak{K}}}{(\mathfrak{b}_1)_n \cdots (\mathfrak{b}_v)_n \Gamma_{\mathfrak{K}}(n\alpha + \mathfrak{P})} \\
 & \frac{D^u}{n!} \frac{(a')_r (b')_r}{(1-a+\mu+\lambda_1 n+\lambda_2 \delta_{\mathbb{R},h})_r!} \times \frac{\Gamma(a-c-r-\mu-\lambda_1 n-\lambda_2 \delta_{\mathbb{R},h}) \Gamma(-b-\mu-\lambda_1 n-\lambda_2 \delta_{\mathbb{R},h})}{\Gamma(-\mu-\lambda_1 n-\lambda_2 \delta_{\mathbb{R},h}) \Gamma(a-b-\mu-\lambda_1 n-\lambda_2 \delta_{\mathbb{R},h})} \\
 & \times \left[\begin{matrix} \sigma + \phi_1 n + \phi_2 \delta_{\mathbb{R},h}, \frac{(1+\mu+\lambda_1 n+\lambda_2 \delta_{\mathbb{R},h})}{v} \cdots \frac{(v+\mu+\lambda_1 n+\lambda_2 \delta_{\mathbb{R},h})}{v} \cdots \\ \frac{(1-a+b+\mu+\lambda_1 n+\lambda_2 \delta_{\mathbb{R},h})}{v} \cdots \frac{(v-a+b+\mu+\lambda_1 n+\lambda_2 \delta_{\mathbb{R},h})}{v} \cdots \\ \frac{(1-a+c+r+\mu+\lambda_1 n+\lambda_2 \delta_{\mathbb{R},h})}{v} \cdots \frac{(v-a+c+r+\mu+\mathbb{C}+\lambda_1 n+\lambda_2 \delta_{\mathbb{R},h})}{v} \\ \frac{(1+b+\mu+\lambda_1 n+\lambda_2 \delta_{\mathbb{R},h})}{v} \cdots \frac{(v+b+\mu+\lambda_1 n+\lambda_2 \delta_{\mathbb{R},h})}{v}, \frac{-m^v}{h^v} \end{matrix} \right] \tag{26}
 \end{aligned}$$

Proof: To establish Theorem 2, first we compute the fractional integral operator by (18) for

$$\begin{aligned}
 & f(t) = t^\mu (t^v + h^v)^{-\sigma} S_{(u,v)}^{(\alpha,\beta,\gamma,\tau,\mathfrak{K})} [Dt^{\lambda_1} (t^v + h^v)^{-\phi_1}] \\
 & \times \bar{H}_{p,q}^{m,n} \left[z t^{\lambda_2} (t^v + h^v)^{-\phi_2} \left[\begin{matrix} (e_j, E_j, \alpha_j)_{1,n} \cdots [(e_j, E_j)_{n+1,p}] \\ (\mathcal{F}_j, F_j)_{1,m} \cdots [(\mathcal{F}_j, F_j, \beta_j)_{m+1,q}] \end{matrix} \right] \right] \tag{27}
 \end{aligned}$$

Now expand the S-function and explain $(m^v + h^v)^{-\sigma}$ as a general argument in series form by utilize this method

$$(m^v + h^v)^{-\sigma} = h^{-\sigma v} \sum_{\delta=0}^{\infty} \frac{(\sigma)_{\delta}}{\delta!} \left(\frac{-m^v}{h^v} \right)^{\delta}$$

Then interchanging the order of summation and integrations allowed by absolute convergence, the integral is evaluated using the below formula:

$$\int_y^{\infty} (t-y)^{C-1} t^{\rho-1} {}_2F_1 \left[\mathbb{A}, \mathbb{B}, \mathbb{C}; \left(1 - \frac{y}{t} \right) \right] dt = y^{\rho+C-1} \frac{\Gamma(\mathbb{C})\Gamma(1-\rho-\mathbb{C})\Gamma(1-\rho-\mathbb{A}-\mathbb{B})}{\Gamma(1-\rho-\mathbb{A})\Gamma(1-\rho-\mathbb{B})} \quad (28)$$

Applying the relation

$$(a)_{-n} = \frac{(-1)^n}{(1-a)_n} \quad (29)$$

We achieve the desired outcomes by applying the Gauss theorem and the multiplication formula [8, 18], along with some simplification.

Remark 2: Replace a by $a + b$, then setting $a' = b' = 0$, $\beta = -c$ and $c = a$ then we get (26) in this manner.

$$I_{m,\infty}^{a,b,c} \left[\left\{ m^{\mu} (m^v + h^v)^{-\sigma} S_{(u,v)}^{(\alpha, \mathbb{A}, \mathbb{B}, \tau, \mathbb{R})} \{ Dm^{\lambda_1} (m^v + h^v)^{-\phi_1} \} \times \bar{H}_{p,q}^{m,n} \left[\begin{matrix} z m^{\lambda_2} (m^v + h^v)^{-\phi_2} \left[(e_j, E_j, \alpha_j)_{1,n} \cdots [(e_j, E_j)_{n+1,p}] \right] \\ (f_j, F_j)_{1,M} \cdots [(f_j, F_j, \beta_j)_{m+1,q}] \end{matrix} \right] \right\} \right]$$

$$= \frac{m^{\mu+\lambda_1 n+\lambda_2 \rho_{\mathbb{B}, \mathbb{A}}-b}}{h^{(\sigma v+\phi_1 v+\phi_2 \rho_{\mathbb{B}, \mathbb{A}} v)}} \sum_{n=0}^{\infty} \sum_{\mathbb{B}=1}^m \sum_{\mathbb{A}=0}^{\infty} \frac{(-1)^{\mathbb{A}} \varpi(\rho_{\mathbb{B}, \mathbb{A}}) z^{\rho_{\mathbb{B}, \mathbb{A}}}}{\mathbb{A}! F_{\mathbb{B}}} \frac{(\mathbb{A}_1)_n \cdots (\mathbb{A}_u)_n (\gamma)_{n\tau, \mathbb{R}}}{(\mathbb{B}_1)_n \cdots (\mathbb{B}_v)_n \Gamma_{\mathbb{R}}(n\alpha + \mathbb{B})} \frac{D^n}{n!}$$

$$\times \frac{\Gamma(b-\mu-\lambda_1 n-\lambda_2 \rho_{\mathbb{B}, \mathbb{A}}) \Gamma(c-\mu-\lambda_1 n-\lambda_2 \rho_{\mathbb{B}, \mathbb{A}})}{\Gamma(-\mu-\lambda_1 n-\lambda_2 \rho_{\mathbb{B}, \mathbb{A}}) \Gamma(\mathbb{A} + \mathbb{B} + \mathbb{C} - \mu - \lambda_1 n - \lambda_2 \rho_{\mathbb{B}, \mathbb{A}})} \times$$

$$\left[\begin{matrix} \frac{(1 + \mu + \lambda_1 n + \lambda_2 \rho_{\mathbb{B}, \mathbb{A}})}{v} \cdots \frac{(v + \mu + \lambda_1 n + \lambda_2 \rho_{\mathbb{B}, \mathbb{A}})}{v} \cdots \frac{(1 + \mu + \lambda_1 n + \lambda_2 \rho_{\mathbb{B}, \mathbb{A}} - b)}{v} \cdots \\ \frac{(v + \mu + \lambda_1 n + \lambda_2 \rho_{\mathbb{B}, \mathbb{A}} - b)}{v} \cdots \frac{(1 + \mu + \lambda_1 n + \lambda_2 \rho_{\mathbb{B}, \mathbb{A}} - c)}{v} \cdots \frac{(v + \mu + \lambda_1 n + \lambda_2 \rho_{\mathbb{B}, \mathbb{A}} - c)}{v} \cdots \\ \frac{(1 + \mu + \lambda_1 n + \lambda_2 \rho_{\mathbb{B}, \mathbb{A}} - a - b - c)}{v} \cdots \frac{(v + \mu + \lambda_1 n + \lambda_2 \rho_{\mathbb{B}, \mathbb{A}} - a - b - c)}{v} \cdots \frac{-m^v}{h^v} \end{matrix} \right] \quad (30)$$

Proof: The same procedure (26) is used to get the outcome (30).

3 The Fractional Integral Formulae

Taking

$$\begin{aligned}
 f(m) &= [m^\mu (m^\nu + h^\nu)^{-\sigma}] S_{(u,v)}^{(\alpha, \beta, \gamma, \tau, \delta)} [Dm^{\lambda_1} (m^\nu + h^\nu)^{-\phi_1}] \\
 &\times \bar{H}_{\mathcal{P}, \mathcal{Q}}^{m, n} \left[zm^{\lambda_2} (m^\nu + h^\nu)^{-\phi_2} \left[\begin{matrix} (e_j, E_j, \alpha_j)_{1, n} \cdots [(e_j, E_j)_{n+1, \mathcal{P}}] \\ (\ell_j, F_j)_{1, m} \cdots [(\ell_j, F_j)_{m+1, \mathcal{Q}}] \end{matrix} \right] \right] \times \\
 &\mathfrak{K}_{\mathbb{P}_i, \mathbb{Q}_i, \mathbb{C}_i, r}^{M, N} \left[zm^\theta (m^\nu + h^\nu)^{-\rho} \left[\begin{matrix} (a_j, A_j)_{1, \mathbb{N}} \cdots [c_i(a_j, A_j)_{N+1, \mathbb{P}_i, r}] \\ (b_j, B_j)_{1, \mathbb{M}} \cdots [c_i(b_j, B_j)_{M+1, \mathbb{Q}_i, r}] \end{matrix} \right] \right]
 \end{aligned} \tag{31}$$

Then we get

$$\begin{aligned}
 &I_{0, m}^{a, a', b, b', c} \\
 &= \sum_{r=n=0}^{\infty} \sum_{\mathbb{h}=1}^M \sum_{k=0}^{\infty} \sum_{g=1}^m \sum_{\mathbb{h}=0}^{\infty} \varphi(n, \mathbb{h}, k) \frac{(-1)^{\mathbb{h}} \varpi(\wp_{\mathbb{g}, \mathbb{h}}) Z^{\wp_{\mathbb{g}, \mathbb{h}}} m^{\mathbb{X}-a-a'} \Gamma(1-a'+\mathbb{X}) \Gamma(1-a-a'+c+\mathbb{X})}{\mathbb{h}! F_{\mathbb{g}}} \frac{m^{\mathbb{X}-a-a'} \Gamma(1-a'+\mathbb{X}) \Gamma(1-a-a'+c+\mathbb{X})}{h^{\mathbb{Y}} \Gamma(1-a'-b+c+\mathbb{X}) \Gamma(1-a-a'+c+\mathbb{X})} \\
 &\times {}_{2\nu+1}F_{2\nu} \left[\begin{matrix} (\sigma + \phi_1 n + \phi_2 \wp_{\mathbb{g}, \mathbb{h}} - \rho \eta_{\mathbb{h}, k}), \frac{(1-a'-r+\mathbb{X})}{\nu} \dots \frac{(\nu-a'-r+\mathbb{X})}{\nu} \dots \frac{(1-a-a'-b+c+\mathbb{X})}{\nu} \dots \\ \frac{(\nu-a-a'-b+c+\mathbb{X})}{\nu} \dots \frac{(1-a-a'+c+\mathbb{X})}{\nu} \dots \frac{(\nu-a-a'+c+\mathbb{X})}{\nu} \dots \\ \frac{(1-a'-b+c+\mathbb{X})}{\nu} \dots \frac{(\nu-a'-b+c+\mathbb{X})}{\nu} \dots, \frac{-m^\nu}{h^\nu} \end{matrix} \right]
 \end{aligned} \tag{32}$$

where

$$\begin{aligned}
 \varphi(r, n, \mathbb{h}, k) &= \frac{(-1)^k \Omega_{(\eta_{\mathbb{h}, k})} Z^{-\eta_{\mathbb{h}, k}} (\mathbb{a}_1)_n \dots (\mathbb{a}_u)_n (\mathbb{Y})_{n, \mathbb{R}} D^n}{\mathcal{B}_{\mathbb{h}} k! (\mathbb{b}_1)_n \dots (\mathbb{b}_v)_n \Gamma_{\mathbb{R}}(n\alpha + \mathfrak{P}) n!} \\
 &\times \frac{(a')_r (b')_r}{(a' - \mu - \lambda_1 n - \lambda_2 \wp_{\mathbb{g}, \mathbb{h}})_r r!}
 \end{aligned}$$

$$\mathbb{X} = \mu + \lambda_1 n + \lambda_2 \wp_{\mathbb{g}, \mathbb{h}} - \theta \eta_{\mathbb{h}, k}$$

$$\mathbb{Y} = (\sigma + \phi_1 n + \phi_2 \wp_{\mathbb{g}, \mathbb{h}} - \rho \eta_{\mathbb{h}, k}) \nu$$

and

$$\begin{aligned}
 &I_{m, \infty}^{a, a', b, b', c} [f(m)] \\
 &= \sum_{r, n=0}^{\infty} \sum_{\mathbb{h}=1}^M \sum_{k=0}^{\infty} \sum_{g=1}^m \sum_{\mathbb{h}=0}^{\infty} \varphi(r, n, \mathbb{h}, k) \frac{(-1)^{\mathbb{h}} \varpi(\wp_{\mathbb{g}, \mathbb{h}}) Z^{\wp_{\mathbb{g}, \mathbb{h}}} m^{\mathbb{X}-a-a'} \Gamma(a-c-r-\mathbb{X})}{\mathbb{h}! F_{\mathbb{g}}} \frac{m^{\mathbb{X}-a-a'} \Gamma(a-c-r-\mathbb{X})}{h^{\mathbb{Y}} \Gamma(-\mathbb{X})} \\
 &\frac{\Gamma(-b-\mathbb{X})}{\Gamma(a-b-\mathbb{X})} \times {}_{2\nu+1}F_{2\nu} \left[\begin{matrix} (\sigma + \phi_1 n + \phi_2 \wp_{\mathbb{g}, \mathbb{h}} - \rho \eta_{\mathbb{h}, k}), \frac{(1+\mathbb{X})}{\nu} \dots \frac{(\nu+\mathbb{X})}{\nu} \dots \frac{(1-a+b+\mathbb{X})}{\nu} \dots \\ \frac{(\nu-a+b+\mathbb{X})}{\nu} \dots \frac{(1-a+c+r+\mathbb{X})}{\nu} \dots \frac{(\nu-a+c+r+\mathbb{X})}{\nu} \dots \\ \frac{(1+b+\mathbb{X})}{\nu} \dots \frac{(\nu+b+\mathbb{X})}{\nu} \dots, \frac{-m^\nu}{h^\nu} \end{matrix} \right]
 \end{aligned} \tag{33}$$

The conditions for (32) and (33) are given below:

$\text{Re}(c) > 0, (\mu + \lambda n + \theta \frac{a_i}{\mathcal{A}_i}) \in \Omega_{a,a',b,b'}, i = 1, 2 \dots M. |\arg(z)| < \frac{T\pi}{2}, T < 0, \mathbb{h}$ is a positive number and $\sigma, \lambda_1, \lambda_2, \phi_1, \phi_2, \rho$ are complex numbers, $v = 1, 2, 3, \dots n$ are arbitrary positive integers.

Proof: The calculation used in Theorem 1 and Theorem 2 is applied to get the desired results (32) and (33).

Remark: 1 Replace a by $a + b$ and setting $a' = b' = 0, \beta = -c$ and $c = a$, the Marichev-Saigo-Maeda fractional integral operator reduces to Saigo integral operator

$$\begin{aligned}
 & I_{0,m}^{a,b,c} [f(m)] \\
 &= \sum_{n=0}^{\infty} \sum_{\mathbb{h}=1}^M \sum_{k=0}^{\infty} \sum_{g=1}^m \sum_{\mathbb{h}=0}^{\infty} \varphi(n, \mathbb{h}, k) \frac{(-1)^{\mathbb{h}} \varpi(\wp_{g,\mathbb{h}}) \mathbb{Z}^{\wp_{g,\mathbb{h}}} m^{\mathbb{X}-b} \Gamma(1 + \mathbb{X}) \Gamma(1 + \mathbb{X} + c - b)}{\mathbb{h}! F_g} \frac{m^{\mathbb{X}-b} \Gamma(1 + \mathbb{X}) \Gamma(1 + \mathbb{X} + c - b)}{h^{\mathbb{Y}} \Gamma(1 + \mathbb{X} - b) \Gamma(1 + \mathbb{X} + a + c)} \\
 &\times {}_{2v+1}F_{2v} \left[\begin{matrix} \sigma + \phi_1 n + \phi_2 \wp_{g,\mathbb{h}} - \rho \eta_{\mathbb{h},k}, \frac{(1+\mathbb{X})}{v} \dots \frac{(v+\mathbb{X})}{v} \dots \frac{(1+\mathbb{X}-b)}{v} \dots \\ \frac{(v+\mathbb{X}-b)}{v} \dots \frac{(1+\mathbb{X}+c-b)}{v} \dots \frac{(v+\mathbb{X}+c-b)}{v} \dots \\ \frac{(1+\mathbb{X}+a+c)}{v} \dots \frac{(v+\mathbb{X}+a+c)}{v}, \frac{-m^v}{h^v} \end{matrix} \right] \tag{34}
 \end{aligned}$$

where

$$\begin{aligned}
 \varphi(n, \mathbb{h}, k) &= \frac{(-1)^k \Omega_{(\eta_{\mathbb{h},k})} Z^{-\eta_{\mathbb{h},k}}}{\mathcal{B}_{\mathbb{h}} k!} \frac{(\mathbb{a}_1)_n \dots (\mathbb{a}_u)_n (\mathcal{Y})_{n\tau, \mathbb{S}}}{(\mathbb{b}_1)_n \dots (\mathbb{b}_v)_n \Gamma_{\mathbb{S}}(n\alpha + \mathfrak{P})} \frac{D^n}{n!} \\
 \mathbb{X} &= \mu + \lambda_1 n + \lambda_2 \wp_{g,\mathbb{h}} - \theta_{\eta_{\mathbb{h},k}}
 \end{aligned}$$

and $\mathbb{Y} = (\sigma + \phi_1 n + \phi_2 \wp_{g,\mathbb{h}} - \rho \eta_{\mathbb{h},k})v$

$$\begin{aligned}
 & I_{m,\infty}^{a,b,c} [f(m)] = \\
 & \sum_{n=0}^{\infty} \sum_{\mathbb{h}=1}^M \sum_{k=0}^{\infty} \sum_{g=1}^m \sum_{\mathbb{h}=0}^{\infty} \varphi(n, \mathbb{h}, k) \frac{(-1)^{\mathbb{h}} \varpi(\wp_{g,\mathbb{h}}) \mathbb{Z}^{\wp_{g,\mathbb{h}}} m^{\mathbb{X}-b} \Gamma(c - \mathbb{X}) \Gamma(b - \mathbb{X})}{\mathbb{h}! F_g} \frac{m^{\mathbb{X}-b} \Gamma(c - \mathbb{X}) \Gamma(b - \mathbb{X})}{h^{\mathbb{Y}} \Gamma(-\mathbb{X}) \Gamma(a + b + c - \mathbb{X})} \\
 &\times {}_{2v+1}F_{2v} \left[\begin{matrix} (\sigma + \phi_1 n + \phi_2 \wp_{g,\mathbb{h}} - \rho \eta_{\mathbb{h},k}), \frac{(1 + \mathbb{X})}{v} \dots \frac{(v + \mathbb{X})}{v} \dots \frac{(1 + \mathbb{X} - b)}{v} \dots \\ \frac{(v + \mathbb{X} - b)}{v} \dots \frac{(1 + \mathbb{X} - c)}{v} \dots \frac{(v + \mathbb{X} - c)}{v} \dots \\ \frac{(1 + \mathbb{X} - a - b - c)}{v} \dots \frac{(v + \mathbb{X} - a - b - c)}{v}, \frac{-m^v}{h^v} \end{matrix} \right] \tag{35}
 \end{aligned}$$

The conditions for the (34) and (35) are given below:

$\text{Re}(a) > 0, \left(\mu + \lambda n + \theta \frac{a_i}{\mathcal{A}_i}\right) \in \Omega_{\mathbb{B}, \mathbb{C}}, i = 1, 2 \dots M, |\arg(z)| < \frac{T\pi}{2}, T < 0$ is a positive number and $\sigma, \lambda_1, \lambda_2, \phi_1, \phi_2, \rho$ are complex numbers, $v = 1, 2, 3, \dots n$ are arbitrary positive integers.

Proof: For results (34) and (35), we apply the method used in (32) and (33).

4 Special Cases of Theorem 1

1(A)

When $u = v = 0$ the S function reduces to k-Mittag Leffler function defined by Saxena [26], Theorem 1 and 2 reduces in this manner

$$\begin{aligned}
 f(t) &= t^\mu (t^v + h^v)^{-\sigma} S_{(0,0)}^{(\alpha, \mathfrak{B}, \gamma, \tau, \mathfrak{K})} [Dt^{\lambda_1} (t^v + h^v)^{-\phi_1}] \\
 &\times \bar{H}_{p,q}^{m,n} \left[z t^{\lambda_2} (t^v + h^v)^{-\phi_2} \left[\begin{matrix} (e_j, E_j, \alpha_j)_{1,n} \dots [(e_j, E_j)_{n+1,p}] \\ (\mathfrak{f}_j, F_j)_{1,m} \dots [(\mathfrak{f}_j, F_j, \beta_j)_{m+1,q}] \end{matrix} \right] \right] \tag{36} \\
 &I_{0,m}^{a,a',b,b',c} \left[\{m^\mu (m^v + h^v)^{-\sigma} S_{(0,0)}^{(\alpha, \mathfrak{B}, \gamma, \tau, \mathfrak{K})} \{Dm^{\lambda_1} (m^v + h^v)^{-\phi_1}\} \times \bar{H}_{p,q}^{m,n} \left[\begin{matrix} Zm^{\lambda_2} (m^v + h^v)^{-\phi_2} \left[\begin{matrix} (e_j, E_j, \alpha_j)_{1,n} \dots [(e_j, E_j)_{n+1,p}] \\ (\mathfrak{f}_j, F_j)_{1,m} \dots [(\mathfrak{f}_j, F_j, \beta_j)_{m+1,q}] \end{matrix} \right] \end{matrix} \right] \right] \right] \\
 &= \frac{m^{-a-a'-r+\mu+\lambda_1 n+\lambda_2 \rho_{\mathbb{B}, \mathfrak{K}}}}{h^{(\sigma v+\phi_1 v+\phi_2 \rho_{\mathbb{B}, \mathfrak{K}} v)}} \sum_{r=0}^{\infty} \sum_{\mathfrak{g}=1}^m \sum_{\mathfrak{h}=0}^{\infty} \frac{(-1)^{\mathfrak{h}} \varpi(\rho_{\mathbb{B}, \mathfrak{K}}) Z^{\rho_{\mathbb{B}, \mathfrak{K}}} (\gamma)_{n\tau, \mathfrak{K}}}{\mathfrak{h}! F_{\mathbb{B}}} \frac{D^n}{\Gamma_{\mathfrak{K}}(n\alpha + \mathfrak{B}) n!} \\
 &\times \frac{(a')_r (b')_r}{(a' - \mu - \lambda_1 n - \lambda_2 \rho_{\mathbb{B}, \mathfrak{K}})_r r! \Gamma(1 - a' - b + c + \mu + \lambda_1 n + \lambda_2 \rho_{\mathbb{B}, \mathfrak{K}})} \\
 &\frac{\Gamma(1 - a - a' + \mu + c + \lambda_1 n + \lambda_2 \rho_{\mathbb{B}, \mathfrak{K}} - b)}{\Gamma(1 - a - a' + \mu + c + \lambda_1 n + \lambda_2 \rho_{\mathbb{B}, \mathfrak{K}})} {}_{2v+1}F_{2v} \\
 &\left[\begin{matrix} \sigma + \phi_1 n + \phi_2 \rho_{\mathbb{B}, \mathfrak{K}}, \frac{(1-a'-r+\mu+\lambda_1 n+\lambda_2 \rho_{\mathbb{B}, \mathfrak{K}})}{v} \dots \frac{(v-a'-r+\mu+\lambda_1 n+\lambda_2 \rho_{\mathbb{B}, \mathfrak{K}})}{v} \dots \\ \frac{(1-a-a'-b+c+\mu+\lambda_1 n+\lambda_2 \rho_{\mathbb{B}, \mathfrak{K}})}{v} \dots \frac{(v-a-a'-b+c+\mu+\lambda_1 n+\lambda_2 \rho_{\mathbb{B}, \mathfrak{K}})}{v} \dots \\ \frac{(1-a-a'+c+\mu+\lambda_1 n+\lambda_2 \rho_{\mathbb{B}, \mathfrak{K}})}{v} \dots \frac{(v-a-a'+c+\mu+c+\lambda_1 n+\lambda_2 \rho_{\mathbb{B}, \mathfrak{K}})}{v} \\ \frac{(1-a'-b+c+\mu+\lambda_1 n+\lambda_2 \rho_{\mathbb{B}, \mathfrak{K}})}{v} \dots \frac{(v-a'-b+c+\mu+\lambda_1 n+\lambda_2 \rho_{\mathbb{B}, \mathfrak{K}})}{v}, \frac{-m^v}{h^v} \end{matrix} \right] \tag{37}
 \end{aligned}$$

1(B)

If $\tau = \mathfrak{K} = 1$, then the S–function reduces to K–function. The K–function is defined by Sharma [25], we obtain.

$$\begin{aligned}
 & \Gamma_{0,m}^{a,a',b,b',c} \left[\left\{ m^\mu (m^v + h^v)^{-\sigma} S_{(u,v)}^{(\alpha,\mathfrak{B},\gamma,1,1)} \{ Dm^{\lambda_1} (m^v \right. \right. \\
 & \quad \left. \left. + h^v)^{-\phi_1} \} \times \bar{H}_{p,q}^{m,n} \left[z m^{\lambda_2} (m^v + h^v)^{-\phi_2} \left[\begin{matrix} (e_j, E_j, \alpha_j)_{1,n} \cdots [(e_j, E_j)_{n+1,p}] \\ (\mathfrak{f}_j, F_j)_{1,M} \cdots [(\mathfrak{f}_j, F_j, \beta_j)_{m+1,q}] \end{matrix} \right] \right] \right\} \right] \\
 &= \frac{m^{-a-a'}^{-r+\mu+\lambda_1 n+\lambda_2 \delta_{\mathbb{B},\mathfrak{h}}} h^{(\sigma v+\phi_1 v+\phi_2 \delta_{\mathbb{B},\mathfrak{h}} v)}}{\sum_{r=n=0}^{\infty} \sum_{\mathbb{B}=1}^m \sum_{\mathfrak{h}=0}^{\infty} \frac{(-1)^{\mathfrak{h}} \varpi(\delta_{\mathbb{B},\mathfrak{h}}) z^{\delta_{\mathbb{B},\mathfrak{h}}}}{\mathfrak{h}! F_{\mathbb{B}}} \frac{(\mathfrak{a}_1)_n \dots \dots (\mathfrak{a}_u)_n (Y)_n}{(\mathbb{b}_1)_n \dots \dots (\mathbb{b}_v)_n \Gamma(n\alpha + \mathfrak{B})}} \\
 & \quad \times \frac{(a')_r (b')_r}{(a' - \mu - \lambda_1 n - \lambda_2 \delta_{\mathbb{B},\mathfrak{h}})_r r! \Gamma(1 - a' - b + c + \mu + \lambda_1 n + \lambda_2 \delta_{\mathbb{B},\mathfrak{h}})} \frac{\Gamma(1 - a' + \mu + \lambda_1 n + \lambda_2 \delta_{\mathbb{B},\mathfrak{h}})}{D^n \Gamma(1 - a - a' + \mu + c + \lambda_1 n + \lambda_2 \delta_{\mathbb{B},\mathfrak{h}} - b)} \\
 & \quad \frac{2^{v+1} \mathcal{F}_{2v}}{n! \Gamma(1 - a - a' + \mu + c + \lambda_1 n + \lambda_2 \delta_{\mathbb{B},\mathfrak{h}})} \\
 & \left[\frac{\sigma + \phi_1 n + \phi_2 \delta_{\mathbb{B},\mathfrak{h}}}{(1 - a - a' - b + c + \mu + \lambda_1 n + \lambda_2 \delta_{\mathbb{B},\mathfrak{h}})} \dots \frac{(1 - a' - r + \mu + \lambda_1 n + \lambda_2 \delta_{\mathbb{B},\mathfrak{h}})}{(v - a - a' - b + c + \mu + \lambda_1 n + \lambda_2 \delta_{\mathbb{B},\mathfrak{h}})} \dots \right. \\
 & \quad \frac{(1 - a - a' + c + \mu + \lambda_1 n + \lambda_2 \delta_{\mathbb{B},\mathfrak{h}})}{(1 - a' - b + c + \mu + \lambda_1 n + \lambda_2 \delta_{\mathbb{B},\mathfrak{h}})} \dots \frac{(v - a - a' + c + \mu + \mathbb{C} + \lambda_1 n + \lambda_2 \delta_{\mathbb{B},\mathfrak{h}})}{(v - a' - b + c + \mu + \lambda_1 n + \lambda_2 \delta_{\mathbb{B},\mathfrak{h}})} \dots \\
 & \quad \left. \frac{(1 - a' - b + c + \mu + \lambda_1 n + \lambda_2 \delta_{\mathbb{B},\mathfrak{h}})}{v} \dots \frac{(v - a' - b + c + \mu + \lambda_1 n + \lambda_2 \delta_{\mathbb{B},\mathfrak{h}})}{v}, \frac{-m^v}{h^v} \right] \tag{38}
 \end{aligned}$$

1(C)

When $\tau = \gamma = \varkappa = 1$, the S-function reduce to generalized M-series given by Sharma and Jain [2, 29]

$$\begin{aligned}
 & I_{0,m}^{a,a',b,b',c} \left[\{m^\mu (m^v + h^v)^{-\sigma} M_{(u,v)}^{(\alpha,\beta)} \{Dm^{\lambda_1} (m^v + h^v)^{-\phi_1}\} \times \bar{H}_{p,q}^{m,n} \left[zm^{\lambda_2} (m^v + h^v)^{-\phi_2} \left[\begin{matrix} (e_j, E_j, \alpha_j)_{1,n} \cdots [(e_j, E_j)_{n+1,p}] \\ (f_j, F_j)_{1,m} \cdots [(f_j, F_j, \beta_j)_{m+1,q}] \end{matrix} \right] \right] \right] \\
 &= \frac{m^{-a-a'-r+\mu+\lambda_1 n+\lambda_2 \delta_{g,h}}}{h^{(\sigma v+\phi_1 v+\phi_2 \delta_{g,h} v)}} \sum_{r=n=0}^{\infty} \sum_{g=1}^m \sum_{h=0}^{\infty} \frac{(-1)^h \omega(\delta_{g,h}) z^{\delta_{g,h}}}{h! F_g} \frac{(a_1)_n \cdots (a_u)_n}{(b_1)_n \cdots (b_v)_n \Gamma(n\alpha + \beta)} \\
 & \quad \times \frac{(a')_r (b')_r}{(a' - \mu - \lambda_1 n - \lambda_2 \delta_{g,h})_r r! \Gamma(1 - a' - b + c + \mu + \lambda_1 n + \lambda_2 \delta_{g,h})} \frac{\Gamma(1 - a' + \mu + \lambda_1 n + \lambda_2 \delta_{g,h})}{D^n \Gamma(1 - a - a' + \mu + c + \lambda_1 n + \lambda_2 \delta_{g,h} - b)} \\
 & \quad \frac{n!}{\Gamma(1 - a - a' + \mu + c + \lambda_1 n + \lambda_2 \delta_{g,h})} \frac{2_{v+1} \mathcal{F}_{2v}}{2_{v+1} \mathcal{F}_{2v}} \\
 & \quad \left[\frac{\sigma + \phi_1 n + \phi_2 \delta_{g,h}}{(1 - a - a' - b + c + \mu + \lambda_1 n + \lambda_2 \delta_{g,h})} \frac{(1 - a' - r + \mu + \lambda_1 n + \lambda_2 \delta_{g,h})}{v} \cdots \frac{(v - a' - r + \mu + \lambda_1 n + \lambda_2 \delta_{g,h})}{v} \cdots \right] \\
 & \quad \frac{(1 - a - a' - b + c + \mu + \lambda_1 n + \lambda_2 \delta_{g,h})}{v} \cdots \frac{(v - a - a' - b + c + \mu + \lambda_1 n + \lambda_2 \delta_{g,h})}{v} \cdots \\
 & \quad \frac{(1 - a - a' + c + \mu + \lambda_1 n + \lambda_2 \delta_{g,h})}{v} \cdots \frac{(v - a - a' + c + \mu + \mathbb{C} + \lambda_1 n + \lambda_2 \delta_{g,h})}{v} \cdots \\
 & \quad \frac{(1 - a' - b + c + \mu + \lambda_1 n + \lambda_2 \delta_{g,h})}{v} \cdots \frac{(v - a' - b + c + \mu + \lambda_1 n + \lambda_2 \delta_{g,h})}{v} \cdots \frac{-m^v}{h^v} \quad (39)
 \end{aligned}$$

5 Special Cases of Theorem 2

When $u = v = 0$ the S function reduces to k-Mittag Leffler function defined by Saxena [26], Theorem 1 and 2 reduces in this manner.

2(A)

$$\begin{aligned}
 & I_{m,\infty}^{a,a',b,b',c} \left[\{m^\mu (m^\nu + h^\nu)^{-\sigma} S_{(0,0)}^{(\alpha,\mathfrak{B},\gamma,\tau,\mathfrak{K})} \{Dm^{\lambda_1} (m^\nu + h^\nu)^{-\phi_1}\} \right] \\
 & \times \bar{H}_{\rho,q}^{m,n} \left[zm^{\lambda_2} (m^\nu + h^\nu)^{-\phi_2} \left[\begin{matrix} (e_j, E_j, \alpha_j)_{1,n} \cdots [(e_j, E_j)_{n+1,p}] \\ (\ell_j, F_j)_{1,M} \cdots [(\ell_j, F_j)_{m+1,q}] \end{matrix} \right] \right] \\
 & = \frac{m^{-a-a'-r+c+\mu+\lambda_1 n+\lambda_2 \rho_{\mathbb{B},\mathfrak{h}}}}{h^{(\sigma+\phi_1\nu+\phi_2 \rho_{\mathbb{B},\mathfrak{h}}\nu)}} \sum_{n=r=0}^{\infty} \sum_{\mathbb{B}=1}^m \sum_{\mathfrak{h}=0}^{\infty} \frac{(-1)^{\mathfrak{h}} \varpi(\rho_{\mathbb{B},\mathfrak{h}}) z^{\rho_{\mathbb{B},\mathfrak{h}}} \Gamma_{\mathfrak{K}}(\gamma)_{n,r,\mathfrak{K}}}{\mathfrak{h}! F_{\mathbb{B}}} \\
 & \frac{D^n}{n!} \frac{(a')_r (b')_r}{(1-a+\mu+\lambda_1 n+\lambda_2 \rho_{\mathbb{B},\mathfrak{h}})_r \Gamma} \times \frac{\Gamma(a-c-r-\mu-\lambda_1 n-\lambda_2 \rho_{\mathbb{B},\mathfrak{h}}) \Gamma(-b-\mu-\lambda_1 n-\lambda_2 \rho_{\mathbb{B},\mathfrak{h}})}{\Gamma(-\mu-\lambda_1 n-\lambda_2 \rho_{\mathbb{B},\mathfrak{h}}) \Gamma(a-b-\mu-\lambda_1 n-\lambda_2 \rho_{\mathbb{B},\mathfrak{h}})} \\
 & \times \left[\begin{matrix} \sigma + \phi_1 n + \phi_2 \rho_{\mathbb{B},\mathfrak{h}}, \frac{(1+\mu+\lambda_1 n+\lambda_2 \rho_{\mathbb{B},\mathfrak{h}})}{v} \cdots \frac{(v+\mu+\lambda_1 n+\lambda_2 \rho_{\mathbb{B},\mathfrak{h}})}{v} \cdots \\ \frac{(1-a+b+\mu+\lambda_1 n+\lambda_2 \rho_{\mathbb{B},\mathfrak{h}})}{v} \cdots \frac{(v-a+b+\mu+\lambda_1 n+\lambda_2 \rho_{\mathbb{B},\mathfrak{h}})}{v} \cdots \\ \frac{(1-a+c+r+\mu+\lambda_1 n+\lambda_2 \rho_{\mathbb{B},\mathfrak{h}})}{v} \cdots \frac{(v-a+c+r+\mu+\mathbb{C}+\lambda_1 n+\lambda_2 \rho_{\mathbb{B},\mathfrak{h}})}{v} \cdots \\ \frac{(1+b+\mu+\lambda_1 n+\lambda_2 \rho_{\mathbb{B},\mathfrak{h}})}{v} \cdots \frac{(v+b+\mu+\lambda_1 n+\lambda_2 \rho_{\mathbb{B},\mathfrak{h}})}{v} \cdots, \frac{-m^\nu}{h^\nu} \end{matrix} \right]
 \end{aligned}
 \tag{40}$$

2(B)

If $\tau = \mathfrak{K} = 1$, then the S-function reduces to K-function. The K-function is defined by Sharma [28], we obtain

$$\begin{aligned}
 & I_{m,\infty}^{a,a',b,b',c} \left[\{m^\mu(m^\nu + h^\nu)^{-\sigma} S_{(u,v)}^{(\alpha,\mathfrak{B},\gamma,1,1)} \{Dm^{\lambda_1}(m^\nu + h^\nu)^{-\phi_1}\} \times \bar{H}_{p,q}^{m,n} \left[zm^{\lambda_2}(m^\nu + h^\nu)^{-\phi_2} \left[\begin{matrix} (e_j, E_j, \alpha_j)_{1,n} \cdots [(e_j, E_j)_{n+1,p}] \\ (f_j, F_j)_{1,M} \cdots [(f_j, F_j)_{m+1,q}] \end{matrix} \right] \right] \right] \\
 &= \frac{m^{-a-a'-r+c+\mu+\lambda_1 n+\lambda_2 \rho_{\mathfrak{B},\mathfrak{A}}}}{h^{(\sigma v+\phi_1 \nu+\phi_2 \rho_{\mathfrak{B},\mathfrak{A}} \nu)}} \sum_{n=r=0}^{\infty} \sum_{\mathfrak{B}=1}^m \sum_{\mathfrak{A}=0}^{\infty} \frac{(-1)^{\mathfrak{A}} \varpi(\rho_{\mathfrak{B},\mathfrak{A}}) z^{\rho_{\mathfrak{B},\mathfrak{A}}}}{\mathfrak{A}! F_{\mathfrak{B}}} \frac{(\mathfrak{a}_1)_n \cdots \cdots (\mathfrak{a}_u)_n (\mathcal{Y})_n}{(\mathfrak{b}_1)_n \cdots \cdots (\mathfrak{b}_v)_n \Gamma(n\alpha + \mathfrak{B})} \\
 & \frac{D^n}{n!} \frac{(a')_r (b')_r}{(1-a+\mu+\lambda_1 n+\lambda_2 \rho_{\mathfrak{B},\mathfrak{A}})_r r!} \times \frac{\Gamma(a-c-r-\mu-\lambda_1 n-\lambda_2 \rho_{\mathfrak{B},\mathfrak{A}}) \Gamma(-b-\mu-\lambda_1 n-\lambda_2 \rho_{\mathfrak{B},\mathfrak{A}})}{\Gamma(-\mu-\lambda_1 n-\lambda_2 \rho_{\mathfrak{B},\mathfrak{A}}) \Gamma(a-b-\mu-\lambda_1 n-\lambda_2 \rho_{\mathfrak{B},\mathfrak{A}})} \\
 & \times \\
 & {}_{2\nu+1}F_{2\nu} \left[\begin{matrix} \sigma + \phi_1 n + \phi_2 \rho_{\mathfrak{B},\mathfrak{A}}, \frac{(1+\mu+\lambda_1 n+\lambda_2 \rho_{\mathfrak{B},\mathfrak{A}})}{v} \cdots \frac{(v+\mu+\lambda_1 n+\lambda_2 \rho_{\mathfrak{B},\mathfrak{A}})}{v} \cdots \\ \frac{(1-a+b+\mu+\lambda_1 n+\lambda_2 \rho_{\mathfrak{B},\mathfrak{A}})}{v} \cdots \frac{(v-a+b+\mu+\lambda_1 n+\lambda_2 \rho_{\mathfrak{B},\mathfrak{A}})}{v} \cdots \\ \frac{(1-a+c+r+\mu+\lambda_1 n+\lambda_2 \rho_{\mathfrak{B},\mathfrak{A}})}{v} \cdots \frac{(v-a+c+r+\mu+\mathfrak{C}+\lambda_1 n+\lambda_2 \rho_{\mathfrak{B},\mathfrak{A}})}{v} \\ \frac{(1+b+\mu+\lambda_1 n+\lambda_2 \rho_{\mathfrak{B},\mathfrak{A}})}{v} \cdots \frac{(v+b+\mu+\lambda_1 n+\lambda_2 \rho_{\mathfrak{B},\mathfrak{A}})}{v}, \frac{-m^\nu}{h^\nu} \end{matrix} \right]
 \end{aligned}
 \tag{41}$$

2(C)

When $\tau = \gamma = \hat{\kappa} = 1$, the S–function reduce to generalized M–series given by Sharma and Jain [2, 29]

$$\begin{aligned}
 & I_{0,m}^{a,a',b,b',c} \left[m^\mu (m^\nu + h^\nu)^{-\sigma} M_{(u,v)}^{(\alpha,\beta)} \{ Dm^{\lambda_1} (m^\nu + h^\nu)^{-\phi_1} \} \right] \\
 & \times \bar{H}_{p,q}^{m,n} \left[zm^{\lambda_2} (m^\nu + h^\nu)^{-\phi_2} \left[\begin{matrix} (e_j, E_j, \alpha_j)_{1,n} \cdots [(e_j, E_j)_{n+1,p}] \\ (\ell_j, F_j)_{1,M} \cdots [(\ell_j, F_j, \beta_j)_{m+1,q}] \end{matrix} \right] \right] \\
 & = \frac{m^{-a-a'-r+c+\mu+\lambda_1 n+\lambda_2 \rho_{\mathbb{B},\hat{\kappa}}}}{h^{(\sigma\nu+\phi_1\nu+\phi_2\rho_{\mathbb{B},\hat{\kappa}}\nu)}} \sum_{n=r=0}^{\infty} \sum_{\mathbb{G}=1}^m \sum_{\hat{\kappa}=0}^{\infty} \frac{(-1)^{\hat{\kappa}} \varpi(\rho_{\mathbb{B},\hat{\kappa}}) Z^{\rho_{\mathbb{B},\hat{\kappa}}}}{\hat{\kappa}! F_{\mathbb{B}}} \frac{(a_1)_n \dots \dots (a_u)_n}{(b_1)_n \dots \dots (b_v)_n \Gamma(n\alpha + \beta)} \\
 & \frac{D^n}{n!} \frac{(a')_r (b')_r}{(1-a+\mu+\lambda_1 n+\lambda_2 \rho_{\mathbb{B},\hat{\kappa}})_r!} \times \frac{\Gamma(a-c-r-\mu-\lambda_1 n-\lambda_2 \rho_{\mathbb{B},\hat{\kappa}}) \Gamma(-b-\mu-\lambda_1 n-\lambda_2 \rho_{\mathbb{B},\hat{\kappa}})}{\Gamma(-\mu-\lambda_1 n-\lambda_2 \rho_{\mathbb{B},\hat{\kappa}}) \Gamma(a-b-\mu-\lambda_1 n-\lambda_2 \rho_{\mathbb{B},\hat{\kappa}})} \\
 & \times \left[\begin{matrix} \sigma + \phi_1 n + \phi_2 \rho_{\mathbb{B},\hat{\kappa}}, \frac{(1+\mu+\lambda_1 n+\lambda_2 \rho_{\mathbb{B},\hat{\kappa}})}{u} \dots \frac{(\nu+\mu+\lambda_1 n+\lambda_2 \rho_{\mathbb{B},\hat{\kappa}})}{u} \dots \\ \frac{(1-a+b+\mu+\lambda_1 n+\lambda_2 \rho_{\mathbb{B},\hat{\kappa}})}{u} \dots \frac{(\nu-a+b+\mu+\lambda_1 n+\lambda_2 \rho_{\mathbb{B},\hat{\kappa}})}{u} \dots \\ \frac{(1-a+c+r+\mu+\lambda_1 n+\lambda_2 \rho_{\mathbb{B},\hat{\kappa}})}{u} \dots \frac{(\nu-a+c+r+\mu+C+\lambda_1 n+\lambda_2 \rho_{\mathbb{B},\hat{\kappa}})}{u} \\ \frac{(1+b+\mu+\lambda_1 n+\lambda_2 \rho_{\mathbb{B},\hat{\kappa}})}{u} \dots \frac{(\nu+b+\mu+\lambda_1 n+\lambda_2 \rho_{\mathbb{B},\hat{\kappa}})}{u}, \frac{-m^\nu}{h^\nu} \end{matrix} \right] \tag{42}
 \end{aligned}$$

6 Special Cases of the Fractional Integral Formulae

A.1

When $\tau = \gamma = \hat{\kappa} = 1$, the S–function reduce to generalized M–series given by Sharma and Jain [2, 29] and $c_i = r = 1$ the Aleph function reduces in H–function then

$$\begin{aligned}
 f(m) & = [m^\mu (m^\nu + h^\nu)^{-\sigma}] S_{(u,v)}^{(\alpha,\beta,1,1,1)} [Dm^{\lambda_1} (m^\nu + h^\nu)^{-\phi_1}] \\
 & \times \bar{H}_{p,q}^{m,n} \left[zm^{\lambda_2} (m^\nu + h^\nu)^{-\phi_2} \left[\begin{matrix} (e_j, E_j, \alpha_j)_{1,n} \cdots [(e_j, E_j)_{n+1,p}] \\ (\ell_j, F_j)_{1,m} \cdots [(\ell_j, F_j, \beta_j)_{m+1,q}] \end{matrix} \right] \right] \\
 & \times \mathfrak{K}_{\mathbb{P}_i, \mathbb{Q}_i, \mathbb{C}_i, \mathbb{R}}^{M,N} \left[zm^\theta (m^\nu + h^\nu)^{-\rho} \left[\begin{matrix} (a_j, A_j)_{1,N} \cdots [c_i(a_j, A_j)_{N+1,p_i,r}] \\ (b_j, B_j)_{1,M} \cdots [c_i(b_j, B_j)_{M+1,q_i,r}] \end{matrix} \right] \right] \tag{43}
 \end{aligned}$$

Then the result obtained is

$$\begin{aligned}
 & I_{0,m}^{a,a',b,b',c} \\
 &= \sum_{r=n=0}^{\infty} \sum_{\mathbb{h}=1}^M \sum_{k=0}^{\infty} \sum_{g=1}^m \sum_{\mathbb{h}=0}^{\infty} \varphi(r, n, \mathbb{h}, k) \frac{(-1)^{\mathbb{h}} \omega(\wp_{g,\mathbb{h}}) Z^{\wp_{g,\mathbb{h}}} m^{\mathbb{X}-a-a'-r} \Gamma(1-a'+\mathbb{X}) \Gamma(1-a-a'+c+\mathbb{X})}{\mathbb{h}! F_g h^{\mathbb{Y}} \Gamma(1-a'-b+c+\mathbb{X}) \Gamma(1-a-a'+c+\mathbb{X})} \\
 &\times {}_{2\nu+1}\mathcal{F}_{2\nu} \left[\begin{matrix} (\sigma + \phi_1 n + \phi_2 \wp_{g,\mathbb{h}} - \rho \eta_{\mathbb{h},k}), \frac{(1-a'-r+\mathbb{X})}{v} \dots \frac{(v-a'-r+\mathbb{X})}{v} \dots \frac{-(\mathbb{h}+a'-b)+c+\mathbb{X}}{v} \dots \\ \frac{(v-a-a'-b+c+\mathbb{X})}{v} \dots \frac{(1-a-a'+c+\mathbb{X})}{v} \dots \frac{(v-a-a'+c+\mathbb{X})}{v} \dots \\ \frac{(1-a'-b+c+\mathbb{X})}{v} \dots \frac{(v-a'-b+c+\mathbb{X})}{v}, \frac{-m^v}{h^v} \end{matrix} \right] \tag{44}
 \end{aligned}$$

A.2

When $\tau = \gamma = \mathfrak{K} = 1$, the S-function reduce to generalized M-series given by Sharma and Jain [2, 29] and $c_i = r = 1$ the Aleph function reduces in H-function then

$$\begin{aligned}
 & I_{m,\infty}^{a,a',b,b',c} [f(m)] \\
 &= \sum_{r,n=0}^{\infty} \sum_{\mathbb{h}=1}^M \sum_{k=0}^{\infty} \sum_{g=1}^m \sum_{\mathbb{h}=0}^{\infty} \varphi(r, n, \mathbb{h}, k) \frac{(-1)^{\mathbb{h}} \omega(\wp_{g,\mathbb{h}}) Z^{\wp_{g,\mathbb{h}}} m^{\mathbb{X}-a-a'-r+c} \Gamma(a-c-r-\mathbb{X})}{\mathbb{h}! F_g h^{\mathbb{Y}} \Gamma(-\mathbb{X})} \\
 &\frac{\Gamma(-b-\mathbb{X})}{\Gamma(a-b-\mathbb{X})} \\
 &\times {}_{2\nu+1}\mathcal{F}_{2\nu} \left[\begin{matrix} (\sigma + \phi_1 n + \phi_2 \wp_{g,\mathbb{h}} - \rho \eta_{\mathbb{h},k}), \frac{(1+\mathbb{X})}{v} \dots \frac{(v+\mathbb{X})}{v} \dots \frac{(1-a+b+\mathbb{X})}{v} \dots \\ \frac{(v-a+b+\mathbb{X})}{v} \dots \frac{(1-a+c+r+\mathbb{X})}{v} \dots \frac{(v-a+c+r+\mathbb{X})}{v} \dots \\ \frac{(1+b+\mathbb{X})}{v} \dots \frac{(v+b+\mathbb{X})}{v}, \frac{-m^v}{h^v} \end{matrix} \right] \tag{45}
 \end{aligned}$$

where

$$\begin{aligned}
 \varphi(r, n, \mathbb{h}, k) &= \frac{(-1)^k \Omega_{(\eta_{\mathbb{h},k})} Z^{-\eta_{\mathbb{h},k}}}{B_{\mathbb{h}} k!} \frac{(a_1)_n \dots \dots (a_u)_n}{(b_1)_n \dots \dots (b_v)_n} \frac{D^n}{\Gamma(n\alpha + \mathfrak{F}) n!} \\
 &\times \frac{(a')_r (b')_r}{(a' - \mu - \lambda_1 n - \lambda_2 \wp_{g,\mathbb{h}})_r!} \\
 &\mathbb{X} = \mu + \lambda_1 n + \lambda_2 \wp_{g,\mathbb{h}} - \theta_{\eta_{\mathbb{h},k}}
 \end{aligned}$$

and $\mathbb{Y} = (\sigma + \phi_1 n + \phi_2 \wp_{g,\mathbb{h}} - \rho \eta_{\mathbb{h},k})v$.

7 Conclusions

The product of the S-function, \overline{H} -function, and Aleph function with a general argument is just one of the innovative and practical fractional integrals that have been obtained

based on the two operators described by Marichev-Saigo fractional integral in 1974. The fractional integrals presented here are extremely broad in nature, and on specializing the parameter of S- function, \bar{H} -function (or product of several such functions) several results can be obtained from them. As a result, our findings offer fascinating extensions and unifications of a variety of previously reported findings. Additionally, some unique examples have been observed. Also Theorem 1 and 2 gives the unified integral representation of \bar{H} -function and S-function.

References

1. Bansal, M.K., Kumar, D., Jain, R.: A Study of Marichev-saigo Maeda fractional integral operators associated with the S-generalized Gauss hypergeometric function. *Kyungpook Math. J.* **59**, 433–443 (2019)
2. Bansal, M.K., Kumar, D., Khan, I., Singh, J., Nisar, K.S.: Certain unified integrals associated with product of M-series and incomplete H-functions. *Mathematics* **7**(12), 1191 (2019)
3. Bansal, M.K., Kumar, D., Nisar, K.S., Singh, J.: Certain fractional calculus and integral transform results of incomplete functions with applications. *Math. Meth. Appl. Sci.* **43**(8), 5602–5614 (2020)
4. Bansal, M.K., Kumar, D., Singh, J., Nisar, K.S.: Finite and infinite integral Formulas involving the family of Incomplete H-functions. *AAM* **6**, 15–28 (2020)
5. Buschman, R.G., Srivastava, H.M.: The H-function associated with a certain class of Feynman integrals. *J. Phys. A: Math. Gen.* **23**, 4707–4710 (1990)
6. Chaurasia, V.B.L., Dubey, R.S.: Then-dimensional generalized Weyl fractional calculus containing to n-dimensional H-transforms. *Gen. Math. Notes* **6**(1), 61–72 (2011)
7. Dubey, R.S.: An application of Aleph function for detecting glucose supply in human blood. *Int. J. Mod. Math. Sci.* **14**(3), 221–226 (2016)
8. Erdélyi, A., Magnus, W., Oberhettinger, F., Tricomi, F.G.: *Tables of Integral Transforms*, vol. 2. McGraw-Hill, New York-London (1954)
9. Fox, C.: The G and H function as symmetrical Fourier kernels. *Trans. Amer. Math. Soc.* **98**, 395–429 (1961)
10. Gupta, K.C., Gupta, K., Gupta, A.: Generalized fractional integration of the product of two H-function. *J. Raj. Acad. Sci.* **9**(3), 203–212 (2010). ISSN 0716-8446
11. Gupta, K.C., Jain, R., Sharma, A.: A study of unified integral transforms with applications. *J. Raj. Acad. Phys. Sci.* **2**(4), 269–282 (2003)
12. Inayat-Hussain, A.A.: New properties of hypergeometric series derivable from Feynman integrals: 1.Transformation and reduction formulae. *J. Phys. A: Math. Gen.* **20**, 4109–4117 (1987)
13. Inayat-Hussain, A.A.: New properties of hypergeometric series derivable from Feynman integrals: 2.Transformation and reduction formulae. *J. Phys. A: Math. Gen.* **20**, 4119–4128 (1987)
14. Jain, M., Tyagi, S.: An integral relation associated with a general class of polynomials and the aleph function. *Mathematical Modelling, Applied Analysis and Computation. ICMMAAC 2018. Springer Proceedings in Mathematics & Statistics*, vol. 272, pp. 129–136. Springer, Singapore (2019). https://doi.org/10.1007/978-981-13-9608-3_8
15. Jain, M.: Fractional integrals involving \aleph -function and the general class of polynomials. *Int. J. Math. Arch.* **9**(1), 69–76 (2018). ISSN 2229 – 5046
16. Marichev, O.I.: Volterra equation of Mellin convolution type with a Horn function in the kernel, *Izvestiya AkademiiNauk BSSR. Seriya Fiziko-MatematicheskikhNauk* **1**, 128–129 (1974)

17. Prabhakar, T.R.: A singular integral equation with a generalized Mittag-Leffler function in the kernel. *Yokohoma Math. J.* **19**, 7–15 (1971)
18. Rainville, E.D.: *Special function*. Chelsea Publ. Co., Bronx, New York (1971). [First published by Macmillan, New York (1960)]
19. Rathie, A.K.: A new generalization of generalized hypergeometric function. *Le Math. Fasc. Ii* **52**, 297–310 (1997)
20. Saigo, M., Raina, R.K.: Fractional calculus operators associated with a general class of polynomials. *Fukuoka Univ. Sci. Rep.* **18**(1), 15–22 (1988)
21. Saigo, M.: A remark on integral operators involving the Gauss hypergeometric functions. *Math. Rep. College General Ed. Kyushu Univ.* **11**, 135–143 (1978)
22. Saxena, R.K.: Certain properties of generalized Mittag-Leffler function. In: *Conference of the Society of Special Function & Their Applications, Third Annual Conference, Chennai, India*, pp. 78–81 (2002)
23. Saxena, R.K., Daiya, J.: Integral Transform of the S-Functions. *LE MATEMATICHE vol. LXX*, pp.147–159 (2015). Fasc. ii
24. Saxena, R.K., Pogány, T.K.: On fractional integration formulae for Aleph functions. *Appl. Math. Comput.* **218**, 985–990 (2011)
25. Saxena, R.K., Pogány, T.K.: Mathieu-type series for the \aleph -function occurring in Fokker-Planck equation. *EJPAM* **3**(6), 980–988 (2010)
26. Saxena, R.K., Daiya, J., Singh, A.: Intergal transforms of the k-generalized Mittag-Leffler function. *Mat. (Catania)* **69**(2), 7–16 (2014)
27. Saxena, V.P.: Formal solution of certain new pair of dual integral equations involving H-function. *Proc. Nat. Acad. Sci. India Sect. A.* **51**, 366–375 (1982)
28. Sharma, K.: Application of fractional calculus operators to related areas. *Gen. Math. Notes* **7**(1), 33–40 (2011)
29. Sharma, M., Jain, R.: A note on a generalized M-series as a special function of fractional calculus *FCAA.* **12**(4), 449-452 (2009)
30. Srivastava, H.M., Tomovski, Z.: Fractional calculus with an integral operator containing a generalized Mittag-Leffler function in the kernel. *Appl. Math. Comput.* **211**, 198–210 (2009)
31. Srivastava, H.M.: A contour integral involving Fox's H-function. *Indian J. Math.* **14**, 1–6 (1972)
32. Sudland, N., Baumann, B., Nonnenmacher, T.F.: Who knows about the Aleph function? *Fract. Calc. Appl. Anal.* **4**, 401–402 (1998)



Air Quality Index: A Comparative Study of Air Quality in Jaipur When the Pre-lockdown and Post-lockdown Phases Are in Effect

Ronak Khandelwal¹, Suraksha Grewal¹, Ashok K. Kakodia², and Kumud Tanwar¹ (✉)

¹ Department of Chemistry, Kanoria PG Mahila Mahavidyalaya, Jaipur, Rajasthan, India
tanwar.kumud@gmail.com

² Department of Chemistry, Govind Guru Tribal University Banswara, Banswara, Rajasthan, India

Abstract. Excellent air quality is crucial for human health, safety, security, and the environment. Air quality deteriorates as cities and businesses grow, affecting the existence of numerous species as well as the service life and aesthetic appeal of materials. Measuring and evaluating surrounding air quality is the first and most significant step in minimising air toxicity. A large number of water quality surveillance does not always inform the scientific community about the state of the air quality, policymakers, regulating bodies, and, most crucially, the general population. Environmental authorities utilize air quality indexes (AQI) to communicate and interpret information widely due to the health dangers connected with poor air quality. An air quality index is a unique number that represents the air's quality in terms of its impact on human health. In its most sophisticated version, it combines multiple contaminant amounts in some mathematical equations to obtain at a single figure for air quality.

The current study examines into how the COVID-19 pandemic spread affected the quality of the surrounding air during the lockdown and recovery phases. Changes in the air quality index were detected both during phases of the winter period, which lasted from October to January, using data from Adarsh Nagar-Central Pollution Control Board (CPCB) station. The findings found that the city's quality of air had drastically worsened following the lockdown. When compared to the previous years' data during the same era, before to the COVID-19 epidemic, the quantity of particulate and gaseous pollution increased dramatically following the lockdown period. It was noted that, in addition to PM 10, that was the primary pollutants in the air quality index previous to the epidemic, PM 2.5, and PM 10 were all present. This study presents a quick summary of the relatively significant areas that need more focus from lawmakers in order to launch policies targeted at creating adequate air pollution reduction measures.

Keywords: Air Quality index (AQI) · CPCB · COVID-19 Lockdown · Change of air quality · Jaipur city

1 Introduction

Metropolitan areas in developing countries are currently facing significant health concerns as a result of increasing globalisation and urbanisation. Urban clean air is one of

the biggest issues, which is being addressed by both emerging and developed countries. According to research, poor air quality prevails not just in Asia's metropolises, but also smaller cities with a population ranging between 150,000 to 2 million [1]. Numerous epidemiological studies conducted over the last Vicennial have established air pollution outside as a cause of several respiratory ailments such as asthma, early death, and cardiovascular problems [2]. According to the World Health Organization, inhaling dirty air claims the lives of seven million people (UN Environment Programme 2018). This has been named the biggest cause of death in underdeveloped countries. In such instances, the populace residing near major highways in megacity suffers the most. 80% of people in cities live in concentrations that are above the World Health Organization's limits. Due to manufacturing and consumption activities, ozone (O₃), nitrogen oxides (NO_x), carbon monoxide (CO), coarse (PM₁₀), fine (PM_{2.5}), and ultrafine (PM_{0.1}) particle mass, black carbon, benzene and polycyclic aromatic hydrocarbons are all present in huge quantities in urban areas [3]. High levels of air pollution have affected human quality of life and health. Furthermore, studies show that particulate matter and NO₂ levels are greater in cities with increased traffic activity and urban settings [4]. The composition of particulate matter in the environment is a complicated mix of various chemicals species and sources. Particulate matter is emitted directly into the atmosphere by both anthropogenic and natural processes. PM₁₀ and PM_{2.5} are the two major particulate pollutants detected worldwide. Because of its greater retention duration and capacity to enter deep into the lungs and into the circulation, PM_{2.5} poses a larger health hazard than PM₁₀ [5].

At the millennium's turn, developing nations such as India are quickly rapidly developing and modernising, resulting in dangerous levels of air pollution akin to the European Industrial Revolution. Car emissions, industrial pollution, coal burning, forest fires, road dust, and trash burning have been recognized as the key contributors of air pollution in the country [6]. As a result, India is presently the world's sixth most polluted country. Air pollution from transportation and industry is a severe environmental concern in urban areas, with traffic outflow accounting for 50% of PM in the urban air. Elevated concentrations of atmospheric PM_{2.5} and NO₂ have been linked to an increased risk of heart disease and lung cancer among humans [7]. According to the Swiss business IQAir's World Air Quality Report, India's air pollution will worsen in 2021. In 2021, the Rajasthan district of Bhiwadi was named the world's most polluted city. Jaipur, Rajasthan's capital city, is undergoing commercialization, as are a number of India's fastest developing towns, including traffic jams, poor road conditions, inadequate regulation of industrial emissions, population increase, and a reduction in air quality. As a result, local authorities, decision-makers, and stakeholders face increased scrutiny. This has emphasized the significance of geographical and temporal assessment of gaseous and particle pollutants for management and policy action to lower Jaipur's air pollution levels.

SARS-CoV-2, a new corona virus, triggered a highly infectious illness epidemic in December 2019. In reaction to the COVID-19 epidemic, countries all around the have taken extraordinary steps. In India, the Janta Curfew was introduced on March 22, 2020, accompanied by a lockdown, leading in a notable improvement in the nation's air

quality, as evidenced by meteorological department figures and data. One of the mitigation strategies to prevent the disease's spread in the population has surfaced: lockdown enforcement. People were unable to leave their houses due to the lockdown. Transportation systems, comprising road, air, and rail, as well as institutions and industrial sites, were halted, the exception of critical products and services, and were prolonged until May 3, 2020. The air quality of urban centers has improved noticeably as significant anthropogenic activities have been reduced [3]. However, once the limits were eased and business continued as usual, the previously improved air quality began to degrade more rapidly. This research looks at the air quality in Jaipur both before and after the shut-down. The major purpose of this study was to determine how air pollutant concentrations varied during both stages.

2 Research Methodology

2.1 Study Area

Jaipur district is located in the east-central region of Rajasthan, India, and has an area of 11,061.44 Km². It extends within northern latitudes 26° 28' and 27° 51' and eastern longitudes 74° 55' and 76° 15'. It is located on the foothills of the Aravali range, flanked on three sides by hillocks and a broad stretch of plains. The density of population in Jaipur district is 470 persons per square kilometre, with a decennial rate of growth of 26.98%, according to the 2011 census (period 2001–2011). Jaipur, popularly known also as Pink City, is the biggest city in Rajasthan and is situated in the state's centre. It is home to interesting forts and exquisite palaces. The Jaipur district has a semi-arid climate. Winter is moderate and enjoyable, with mean temperature ranging from 10 to 20 °C and humidity levels varying from 30 to 65%. The coolest months are December and January, while temperature vary from 7 to 15 °C [9]. March is a nice month for transitioning from summer to winter. The Jaipur transportation system is mostly dependent on the road. The overall traffic in proportion to the traffic limit means that these routes have a significant volume of traffic during peak hours. Transportation complexity, lane shortage discipline, limited public transit, as well as an exponential increase in personal forms of mobility. Two-wheelers represent the most frequent method of transportation in Jaipur, accounting for 70 percentage points of all registered vehicles, with four-wheelers placing second at 13%, and buses accounting for only 1% of all registered vehicles [10]. The current study investigates the influence of the COVID-19 pandemic outbreak on Jaipur's ambient air quality during the city's pre and post lockdown periods. Data was collected at the Adarsh Nagar-Central Pollution Control Board (CPCB) station <http://www.cpcb.nic.in/>, and changes in the air quality index were noted during both periods of the winter season, which lasted from October to January.

2.2 Air Quality Index

The air quality index (AQI) seems to be a metric that compares pollutant concentrations to ambient air quality in different regions. It condenses complex data regarding air quality produced by several contaminants together into decimal statistic (index value), name,

and colour. The greater the AQI number, the worse the air quality and the more significant the health risk. The AQI is classified into six levels (Table 1). So each category denotes a different gravity of the public health issue. Each group has a unique colour as well. Individuals can immediately tell from the hue whether the air quality in their area has deteriorated to a harmful degree.

Table 1. Various Category of NAQI (National air quality index, CPCB, October 2020)

Category	Range
Excellent	0–50
Tolerable	51–100
Reasonably contaminated	101–200
Dreadful	201–300
Alarming	301–400
Serious	401–500

One of the most important methods for consistently analysing and displaying the status of the air quality is the AQI. In the form of a sub-index, the aggregate impact of individual pollutant concentrations in ambient air is typically reported as a single value. [12]. The AQI index or the sub-index value of the individual pollutant is calculated using the following equation [13]:

$$I_i = \{(I_{GC} - I_{SC}) / (B_{GC} - B_{SC})\} * (C_{pc} - B_{SC}) + I_{SC};$$

where, B_{GC} = Breakpoint concentration greater or equal to given concentration;

B_{SC} = Breakpoint concentration smaller or equal to given concentration; I_{GC} = AQI value corresponding to B_{GC} ; I_{SC} = AQI value corresponding to B_{SC} ; C_{pc} = Concentration of Pollutant (Table 2).

For e.g., Let the Concentration of PM10 pollutant be $85 \mu\text{g}/\text{m}^3$.

So, value of sub-index $I_i = \{(100-50) / [100-50] * [85-50]\} + 50 = 50$.

And finally;

AQI = Max (I_i ; (where $i = 1, 2, 3, \dots, n$; denotes n pollutants).

3 Result and Discussion

3.1 Particulates, Fine (PM2.5)

PM2.5 particles are able to enter the lungs after passing via the respiratory system. Exposure to small particles can cause eye, nose, throat, and respiratory issues as well as coughing, sneezing, nasal congestion, and shortness of breath in the short term. Exposure to fine particles can also compromise lung function and aggravate medical disorders such as asthmatic and cardiovascular disease [22]. As a result, it is deemed critical to explore this clean air parameter, and the findings of both the pre and post closure phases during

Table 2. Break Point concentration of various pollutants (Units: $\mu\text{g}/\text{m}^3$)

AQI Category Array	PM ₁₀ 24- hr	PM _{2.5} 24- hr
Excellent (0–50)	00–50	0–30
Tolerable(51–100)	51–100	31–60
Reasonably polluted (101–200)	101–250	61–90
Dreadful (201–300)	251–350	91–120
Alarming (301–400)	351–430	121–250
Serious (401–500)	>430	>250

the cold weather are shown in Fig. 1. The AQI index in Jaipur city has clearly increased significantly following the lockdown period as shown in the figure. The maximum value observed in the pre lockdown phase for the months of October, November, December, and January was 201,144,113,88, while the maximum value in the post lockdown phase was 289,356,244,226 observed.

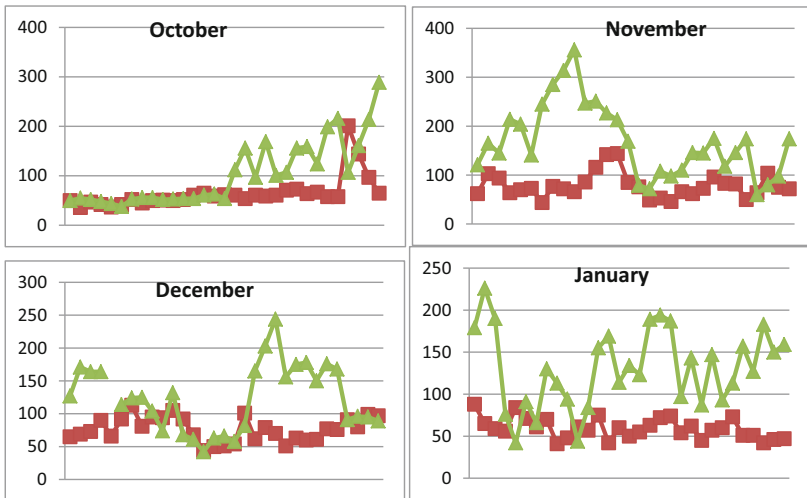


Fig. 1. AQI index Variations of PM_{2.5} in pre and post lockdown phases

Table 3. Shows the average PM2.5 concentration for the months mentioned, both before and after the lockdown phases.

Year	October	November	December	January
2018	83.32	99.53	76.80	97.06
2019	64.30	78.30	76.41	59.35
2020	103.54	169.33	120.16	130.83
2021	89.74	224.93	173.32	131.96

3.2 Coarse Particulate Matter (PM10)

Coarse particulates, which are typically created by processes such as physical grinding, road dust, and agricultural practices, deposit preferentially in the upper and bigger airways. These particles can easily pass thru and settle in the airways of the thoracic region. When these particles are inhaled, they induce lung problems and respiratory difficulties [23]. Figure 2 depicts the air quality index for PM10 throughout the winter season, both before and after lockdown. Again for months of October, November, December, and January, the largest value observed in the pre lockdown period was 233,170,159,127, whereas the maximum value seen in the post lockdown phase was 182,247,220,142.

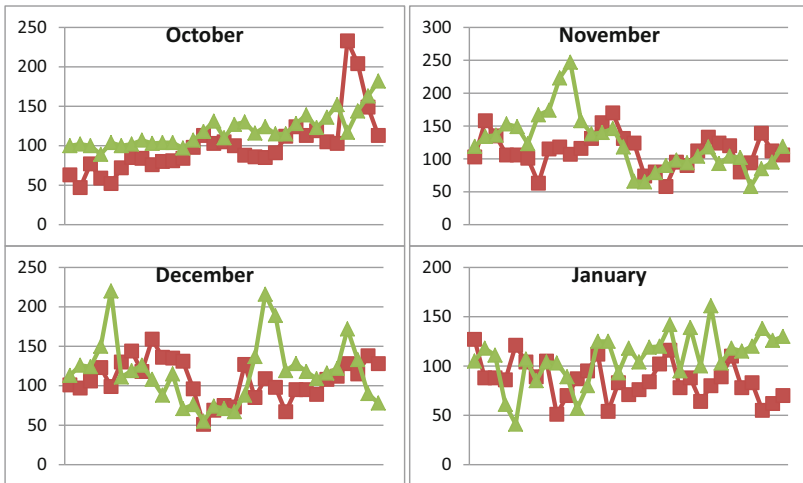


Fig. 2. AQI index Variations of PM10 in pre and post lockdown phases

Table 4. Shows the average PM10 concentration for the months mentioned, both before and after the lockdown phases.

Year	October	November	December	January
2018	137.38	140.60	128.00	116.25
2019	100.12	111.86	107.64	86.00
2020	119.00	123.16	117.06	104.09
2021	89.87	146.96	116.83	101.03

3.3 Major Pollutant

Because the major pollutant determines the AQI, it is critical to understand the major pollutant before and after the pandemic, as illustrated in Fig. 3. Prior to the pandemic, PM10 was the major pollutant, while PM2.5 was the minor pollutant; however, this situation changed dramatically after the pandemic, resulting in an increase in the concentration of PM2.5 pollutant.

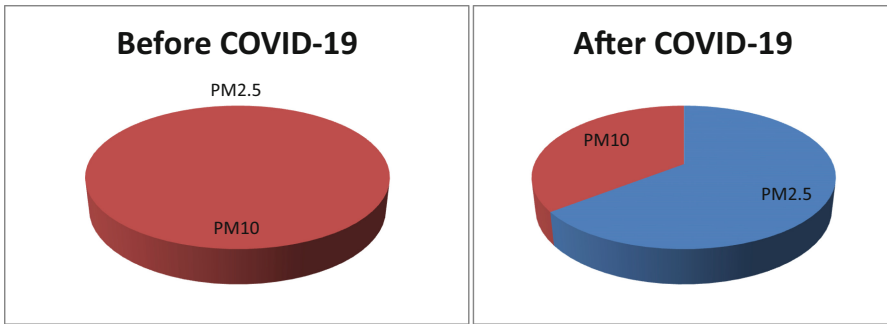


Fig. 3. Major pollutant during both the phases

4 How to Control Air Pollution?

Air pollution can only be controlled if the general public and the government work together as a team to improve air quality. We attempted to illustrate the problem in simple terms so that both parties understand the gravity of the situation and can work together to improve air quality. During the lockdown period, the environment had time to heal itself; now, as we return to our normal routine, we should keep the environment in our minds as well. It is our responsibility to ensure that the air quality does not deteriorate further over time.

4.1 Control Measures to be Taken by the Government

- The government organization should develop strong policies and ensure their implementation.

- Organizations can use this paper to identify the most affected areas and plan accordingly.
- Vehicle emissions are the most major cause of air pollution. Administrators should plan to reduce them by promoting public transportation, carpooling, and other alternatives.
- Cleaner and alternate fuels should be introduced like CNG, LPG, etc.
- In the industrial sector, strict rules and regulations should be put on practice.

4.2 Control Measures to be Taken by the General Public

- RRR- Reduce, reuse and recycle, one of the most important rules that everyone must follow.
- Avoid the burning of garbage, leaves and other items.
- Start using public transport and carpooling
- Avoid the burning of fireworks and spread awareness about their negative consequences
- Practice energy conservation; For ex: Switch off lights when they are not in use

5 Conclusions

Jaipur, Rajasthan's state city, faced significant air pollution following the COVID epidemic. As a result, this study focuses on the airborne pollutants PM10 and PM2.5. According to the findings, the city's quality of air has considerably deteriorated following the lockdown. The particulate matter concentration increased dramatically following the lockdown period when compared with previous years' statistics during the same timeframe prior towards the COVID-19 epidemic. In contrast to PM 10, that was the dominant pollutant in the index of air quality previous to the pandemic, it was revealed that PM 2.5, which is more destructive than PM 10, emerged as a serious worry after the epidemic. According to the data, the greatest concentration of PM10 was 387 g/m³, whereas the maximum concentration of PM2.5 was 306 g/m³. Tables 3 and 4 revealed that, independent of the COVID 19 lockout, the average content of both PM2.5 and PM10 was greatest in November every year.

Before going into the information and data, it is necessary to understand the primary cause of pollution. The use of fossil fuels in automobiles, emissions from different businesses, local dirt, and natural events are the primary sources of increased particulate matter (PM) concentrations. Furthermore, inversion events restrict the distribution of particulates and pollution in major cities with just a growing population and more enterprises. As a result, the city's PM concentration increases. We picked the winter months for our investigation since this phenomena is more widespread during that season. The worldwide shutdown gave us a once-in-a-lifetime chance to identify the reference levels of pollution in numerous big centres throughout the world. COVID- Because to the 19 lockdowns, there was reduced energy consumption and decreased oil demand, which had a substantial impact on industrial and transportation activity. The study's conclusion will assist governmental authorities and decision makers in calibrating an acceptable response plan to reduce Jaipur's ever-increasing pollution levels. This study will also aid administrators in allocating funding and deciding priorities.

References

1. Indonesia: Air Quality Profile - 2010 Edition
2. Parl, S., Allen, R.J., Lim, C.H.: A likely increase in fine particulate matter and premature mortality under future climate change. *Air Qual. Atmos. Health* **13**, 143–151 (2020). <https://doi.org/10.1007/s11869-019-00785-7>
3. Agarwal, A., Kaushik, A., Kumar, S., Mishra, R.K.: Comparative study on air quality status in Indian and Chinese cities before and during the COVID-19 lockdown period. *Air Qual. Atmos. Health* **13**(10), 1167–1178 (2020). <https://doi.org/10.1007/s11869-020-00881-z>
4. Liu, H., Tian, Y.H., Song, J., Huang, C., Li, M.: Effect of ambient air pollution on hospitalization for heart failure in 26 of China's largest cities. *Am. J. Cardiol.* **121**(5), 628–633 (2018)
5. US EPA, Particulate matter (PM) basics (2018). <https://www.epa.gov/pm-pollution/particulate-matter-pm-basics>
6. Pant, P., Harrison, R.M.: Critical review of receptor modelling for particulate matter: a case study of India. *Atmos. Environ.* **49**, 1–12 (2012)
7. Li, S., Feng, K., Li, M.: Identifying the main contributor. *J. Clean. Prod.* **163**, S359–S365 (2017)
8. Indian Meteorological Department (IMD), Climate of Jaipur. Government of India Press, New Delhi (2011)
9. Kumar, A., Garg, A., Pandel, U.: A study of ambient air quality status in Jaipur city (Rajasthan, India), using air quality index. *Nat. Sci.* **9**(6), 38–43 (2011). (ISSN: 1545–0740), <http://www.sciencepub.net/>
10. Kala, J., Sharma, G., Kumar, S., Pipralia, S.: Study of ambient air quality status on urban roads using air quality index -a case of Jaipur city (Rajasthan, India). *Int. J. Theor. Appl. Sci.* **6**(1), 138–147 (2014)
11. National air quality index; Central pollution control board. <http://www.cpcb.nic.in/>
12. Sarella, G., Khambete, A.K.: Ambient air quality analysis using air quality index – a case study of vapi. *Int. J. Innovative Res. Sci. Technol. (IJIRST)* **1**(10), 1–4 (2015)
13. Ott, W.R., Hunt, W.F., Jr.: A quantitative evaluation of the pollutant standards index. *J. Air Pollut. Control Assoc.* **26**, 1051–1054 (1976)
14. Dadhich, A.P., Goyal, R., Dadhich, P.N.: Assessment of spatio-temporal variations in air quality of Jaipur city, Rajasthan, India. *Egypt. J. Remote Sens. Space Sci.* **21**(2), 173–181 (2018). <https://www.sciencedirect.com/journal/the-egyptian-journal-of-remote-sensing-and-space-science>
15. Pandey, M., George, M.P., Gupta, R.K., Gusain, D., Dwivedi, A.: Impact of COVID-19 induced lockdown and unlock down phases on the ambient air quality of Delhi capital city of India. *Urban Clim.* **39**, 100945 (2021)
16. Kumar, A., Mishra, R.K.: Human health risk assessment of major air pollutants at transport corridors of Delhi India. *J. Transp. Health* **10**, 132–143 (2018)
17. Manmeet K.: A Comparative Study to assess the air quality of Ludhiana, India amid COVID-19. In: *IOP Conference Series: Earth and Environmental Science*, vol. 889, p. 012069 (2021)
18. Nigam, S., Rao, B.P.S., Kumar, N., Mhaisalkar, V.A.: Air quality index-A comparative study for assessing the status of air quality. *Res. J. Eng. Technol.* **6**(2), 267–274 (2015)
19. Cheng, W.L., et al.: Revised air quality index derived from an entropy function. *Atmos. Environ.* **38**, 383–391 (2004)
20. Mahato, S., Pal, S., Ghosh, K.G.: Effect of lockdown amid COVID-19 pandemic on air quality of the megacity Delhi India. *Sci. Total Environ.* **730**, 139086 (2020)
21. Dhamaniya, A., Goyal, R.: Use of GIS in transportation planning of Jaipur city. *GIS Dev.* **8**(11), 38–43 (2004)

22. Xing, Y.F., Xu, Y.H., Shi, M.H., Lian, Y.X.: The impact of PM_{2.5} on the human respiratory system. *J. Thorac. Dis.* **8**(1), E69–E74 (2016)
23. Saharsodoudi, H.T.: Statistical modeling approaches for PM₁₀ prediction in urban areas: a review of 21st-century studies. *Atmosphere* **7**(2), 15 (2016). <https://doi.org/10.3390/atmos7020015>



Mathematical Study on Corona-Virus (COVID-19) Disease Transmission and Its Stability Through SEIR Epidemic Model

Krishna Pada Das¹, Sanjukta Pramanik²(✉), Partha Karmakar³,
and Seema Sarkar Mondal⁴

¹ Department of Mathematics, Mahadevananda Mahavidyalaya Monirampore,
Barackpore, West Bengal, India
krishnaisi@yahoo.co.in

² Department of Mathematics, Chakdaha College,
Chakdaha 741222, West Bengal, India
sp.math23@gmail.com

³ West Bengal Board of Primary Education, Salt Lake City, Kolkata 700091, India

⁴ Department of Mathematics, National Institute of Technology Durgapur, Durgapur, West Bengal, India

Abstract. SARS-COV2 being causative agent owing to the potentially fatal malady is identified as Coronavirus Disease (COVID-19) which is a paramount issue for worldwide hygienics. It is hypothesised that this is most likely COVID-19 zoonotic origin due to high aggregate of affected individuals displayed in Wuhan City's wt animal (traditional) market in China. Patients who contracted the COVID-19 infection from another human had to be isolated additionally receiving a range of therapies. The SEIR model, which has four compartments, and the E class—a group of exposed and asymptomatic individuals—have both been covered in this article. Here, a disease-free and endemic equilibrium point is formed, and its local and global stability. Having taken the SEIR epidemic model into consideration we have primarily classified the model into four segments and have started our investigation by determining the existence of equilibrium points, studying their local and global stability. **Here we have established, stability owing to disease equilibrium point being $R_0 < 1$ and stability owing to endemic equilibrium being $R_0 > 1$. Next validity of model taken into account is investigated using the real observations (data) within Italy alongwith estimating merit pertaining to parameters are estimated using the method of least squares so as to observe the dynamics pertaining to the escalation of the virus among the population within Italy. The diagrams have been plotted with the data available and thorough extensive discussions have been carried out thereby emphasizing on the probable date for infection controlling.**

Keywords: Basic reproduction number · COVID-19 · SEIR Model · Global Stability · Compounded Matrix

Classification: 37N25 · 34C23 · 49J15 · 92D30

1 Introduction

World Health Organization (WHO) was illuminated on 31st December, 2019 that coronavirus (SARS-CoV-2)-infected pneumonia (COVID-19) had been found in China's city of Wuhan. This pneumonia has since caused major sickness and death in China [1] as well as elsewhere in the world. As of April 22, 2020 (8:00 PM, GMT+8), there have been 4632 confirmed COVID-19 contaminations and loss of lives in mainland China [2]. Coronaviruses are a wide household of viruses which when viewed under an electron microscope, appear to resemble monarchical crowns and infect both mammals and birds. People who have contracted Corona can exhibit diseases ranging from the upper respiratory infection to considerably increased serious conditions including SARS, Middle East respiratory syndrome, alongwith COVID-19 [3]. Novel coronavirus infection, which started in Wuhan, China, has been reported to have spread to 210 different nations. According to reports dated March 22, 2020, the lethal virus was confirmed to be present in 250,000 instances worldwide, and there were 15,000 fatalities [20]. There were 2,604,718 confirmed cases worldwide as of April 22, 2020, and there were 181,433 fatalities [5]. The entire world had been severely impacted by COVID-19, particularly Italy, the USA, Spain, the UK, and many other nations. To control the COVID-19 outbreak, all the nations have taken exceptional steps, including isolating the infected individuals, preserving social distance, and ultimately implementing a global lockdown policy. The COVID-19 constitutes a menace to the entire civilization because it can cause organ failures, mortality, fever, coughing, shortness of breath, and other breathing issues. On January 30, 2020, WHO designated the coronavirus infestation a global well-being crucial state of affairs [4] due to its rapid global expansion. Despite being a zoonotic illness, it eventually transmits from person to person [12]. Since the coronavirus was first discovered and identified in 1965, three significant outbreaks have been linked to newly circulating, highly pathogenic coronaviruses: the SARS upsurge in mainland China in 2003 [9, 11], the Middle East Respiratory Syndrome (MERS) upsurge in Saudi Arabia in 2012 [7, 8], and the MERS upsurge in South Korea in the year 2015 [6]. In excess of 8000 and 2200 SARS and MERS cases, sequentially, have been confirmed as a result of these epidemics [10]. **Also during 1976, Ebola virus malady was foremost located adjacent to Ebola river in Africa which affected human beings and creatures like monkeys, gorillas, and chimpanzees [18]. Another challenging problem that the world had faced was HIV infection. In the AIDS examination, HIV septicity is a burdensome affair. As a result of this infection CD4+ T-cells are perpetually mutilated within human beings [19]. Just like Corona virus, a major threat to mankind is smoking which affects different organs of human body thus developing complications owing to cardiac arrest in addition to lung carcinoma. For assuring life of human beings several scientists, mathematicians additionally doctors are making efforts to sway smoking [21].**

In present manuscript, a SEIR model has been formulated in order to analyze variability of COVID-19 considering E - class as the exposed and the asymptotic persons. We have established system's positivity and boundedness, local and global stability owing to disease free equilibrium point. Finally our mathematical model is validated

considering the infected cases of Italy from Feb 15 to April 04, 2020 and some important model parameters are estimated. We gave some predictions using the estimated parameters about the controlling of malady.

The manuscript has been structured as follows: Within Sect. 2, proposed model is formulated, model analysis is carried out in Sect. 3 and the validation of model with real data is established within Sect. 4 and ultimately some interpretations are summarized in Sect. 5.

2 Model Formulation

Since COVID-19 spreads throughout the world shortly, it is spreading from human to human when they come closer to one another. The most dangerous characteristic of COVID-19 is that large number of people in this disease are infected but they are on a large scale asymptomatic. Another important side is the incubation period: the infected persons are becoming infectious on an average 2–14 days. It is of utmost importance to dispense additional research based information pertaining to superior apprehension of the novel coronavirus and to a great extent containment owing to the upsurge. For transmission of COVID-19 in company of human race and its stability we have put forward SEIR epidemic model. It incorporates various fundamental and enhanced models, namely SIR, SIS, SEIR, along with others, among which SEIR is a representative example of taking evolution period in record. In this model the used four states namely Susceptible (G), Exposed and asymptomatic (H), infectious (Q), and recovered (U). Total host population is classified into susceptible, exposed and asymptomatic, infectious, and recovered, with the densities, sequentially, denoted by $G(t)$, $H(t)$, $Q(t)$ and $U(t)$. At time t , $M(t)$ denotes size pertaining to total population where $M = G + H + Q + U$. As asymptomatic class spreads, we consider that the G class is becoming infectious when they interact with the H and Q class both. Required mathematical model is professed as follows:

$$\begin{aligned}
 \frac{dG}{dt} &= B - \lambda_{10}GH - \lambda_{20}GQ - \mu_0G \\
 \frac{dH}{dt} &= \lambda_{10}GH + \lambda_{20}GQ - \gamma_0H - \mu_0H \\
 \frac{dQ}{dt} &= \gamma_0H - k_0Q - \beta_0Q - \mu_0Q \\
 \frac{dU}{dt} &= k_0Q - \mu_0U.
 \end{aligned}
 \tag{1}$$

where positive parameter μ_0 is natural death rate. β_0 is non-negative constant, additionally represent rate pertaining to malady resulted demise. Variable γ_0 denotes rate of transfer between uncovered and contagious. Recovery rate pertaining to contagious individuals is preferably represented by k_0 . λ_{10} , λ_{20} are the efficient contact rate in latent, infected and recovered periods. B is constant recruitment of susceptibles. Henceforth $\frac{1}{\gamma_0}$ is mean latent period in addition to $\frac{1}{k_0}$ being mean infectious period.

In order to lessen number of parameters we use the transformation

$$\tau = \mu_0 t, \lambda_1 = \frac{\lambda_{10}}{\mu_0}, \lambda_2 = \frac{\lambda_{20}}{\mu_0}, k = \frac{k_0}{\mu_0}, c = \frac{B}{\mu_0}, \beta = \frac{\beta_0}{\mu_0}$$

and system (1) reduces to the following form:

$$\begin{aligned} \frac{dG}{d\tau} &= c - \lambda_1 GH - \lambda_2 GQ - G \\ \frac{dH}{d\tau} &= \lambda_1 GH + \lambda_2 GQ - \gamma H - H \\ \frac{dQ}{d\tau} &= \gamma H - kQ - \beta Q - Q \\ \frac{dU}{d\tau} &= kQ - U. \end{aligned} \tag{2}$$

3 Model Analysis

3.1 Equilibrium Points: Existence and Stability

Size pertaining to total population $M(t)$ can be determined by $M(t) = G(t) + H(t) + Q(t) + U(t)$, using this in addition to relations in Eq. (2) we have obtained

$$\frac{dM}{d\tau} = c - M - \beta Q$$

It is appropriate in employing H, Q, U and M as variables and swap G by $M(t) = G(t) + H(t) + Q(t) + U(t)$. Henceforth, we arrive at the following mathematical model

$$\begin{aligned} \frac{dH}{d\tau} &= c + (\lambda_1 H + \lambda_2 Q + U)(M - H - Q - U) - \delta e \\ \frac{dQ}{d\tau} &= \gamma H - \omega Q \\ \frac{dU}{d\tau} &= kQ - U \\ \frac{dM}{d\tau} &= c - M - \beta Q. \end{aligned} \tag{3}$$

where $\sigma = \gamma + 1, \omega = k + 1 + \beta$.

System (3) in addition to system (2) are equivalent thereby permitting to attack (2) having analyzed system (3). We studied system (3) within closed set from biological considerations

$$T = \left\{ (H, Q, U, M) \in R_+^4 : 0 \leq H + Q + L \leq M \leq c = \frac{B}{\mu_0} \right\}$$

Positive invariance of T can be examined with reference to system (3).

When $\lambda_1 = \lambda_2 = 0$, it implies exposed & asymptotic and the infected class are absent then we attain non-homogeneous linear system

$$\begin{aligned} \frac{dH}{d\tau} &= c - \delta H \\ \frac{dQ}{d\tau} &= \gamma H - \omega Q \\ \frac{dU}{d\tau} &= kQ - U \\ \frac{dM}{d\tau} &= c - M - \beta Q. \end{aligned} \tag{4}$$

Each solution converges to $L_0 = (H_0, Q_0, U_0, M_0)$ where

$$H_0 = \frac{c}{\delta} = H, \quad Q_0 = \frac{\gamma c}{\delta \omega} = Q, \quad U_0 = \frac{\gamma k c}{\delta \omega} = U, \quad M_0 = \frac{c(\delta \omega - \beta \gamma)}{\delta \omega} = M$$

An equilibrium with $\lambda_1, \lambda_2 > 0$ would be expected satisfying $E \geq E_0, Q \geq Q_0, U \geq U_0, M \leq M_0$. Henceforth we assume right hand side of each of the four differential equations equal to zero in system (3), thereby achieving the following

$$\begin{aligned} c + (\lambda_1 H + \lambda_2 Q + L)(M - H - Q - U) - \delta H &= 0 \\ \gamma H - \omega Q &= 0 \\ kQ - U &= 0 \\ c - M - \beta Q &= 0. \end{aligned} \tag{5}$$

In search of equilibria for $\lambda_1, \lambda_2 > 0, M = c - \beta Q$ is substituted in

$$c + (\lambda_1 H + \lambda_2 Q + U)(M - H - Q - U) - \delta H = 0$$

hence obtaining the polynomial of degree two

$$F(Q) = (\lambda_1 \omega + \lambda_2 \gamma + k \gamma) \delta \omega Q^2 + \gamma [\delta \omega - c(\lambda_1 \omega + \lambda_2 \gamma + k \gamma)] Q - \gamma^2 c = 0$$

If $c = 0, i = 0$ is one root, in addition, second root is given by

$$Q^* = \frac{\gamma [c(\lambda_1 \omega + \lambda_2 \gamma + k \gamma) - \delta \omega]}{(\lambda_1 \omega + \lambda_2 \gamma + k \gamma) \delta \omega}$$

which is positive if and only if $\sigma = c(\lambda_1 \omega + \lambda_2 \gamma + k \gamma) - \delta \omega > 0$.

Owing to $c > 0$, the degree two polynomial $F(Q) = 0$ provides with a positive alongwith a negative root [13]. Positive root is

$$Q^* = \frac{\gamma \sigma + \gamma \sqrt{\sigma^2 + 4c\delta\omega(\lambda_1\omega + \lambda_2\gamma + k\gamma)}}{2\delta\omega(\lambda_1\omega + \lambda_2\gamma + k\gamma)}$$

with

$$\begin{aligned} \lim_{c \rightarrow 0} Q^* &= \frac{\gamma(\sigma + |\sigma|)}{2\delta\omega(\lambda_1\omega + \lambda_2\gamma + k\gamma)} \\ &= 0 \text{ if } \sigma < 0 \\ &= \frac{\gamma[c(\lambda_1\omega + \lambda_2\gamma + k\gamma) - \delta\omega]}{(\lambda_1\omega + \lambda_2\gamma + k\gamma)\delta\omega} \text{ if } \sigma > 0. \end{aligned} \tag{6}$$

Henceforth, threshold estimate is $\sigma = 0$. Moreover, basic reproduction number is

$$R_0 = \frac{c(\lambda_1\omega + \lambda_2\gamma + k\gamma)}{\delta\omega}.$$

In epidemiology, the estimated number of cases that are straightforwardly generated by one case in a community where everyone is vulnerable to infection is symbolised by the letter R_0 . A pathogen’s R_0 is not a biological constant because it is influenced by a variety of other variables, including the environment and the behaviour of the infected population. Epidemiological basic reproduction number and ecological basic reproduction number are the two threshold quantities that make up basic reproduction number.

The Jacobian matrix J of the system (3) at any arbitrary point (G, Q, U, M) is given by

$$\begin{bmatrix} j_{11} & j_{12} & j_{13} & j_{14} \\ j_{21} & j_{22} & j_{23} & j_{24} \\ j_{31} & j_{32} & j_{33} & j_{34} \\ j_{41} & j_{42} & j_{43} & j_{44} \end{bmatrix}. \tag{7}$$

$j_{11} = \lambda_1(M - H - Q - U) - (\lambda_1H + \lambda_2Q + U) - \delta$, $j_{12} = \lambda_2(M - H - Q - U) - (\lambda_1H + \lambda_2Q + U)$, $j_{13} = (M - H - Q - U) - (\lambda_1H + \lambda_2Q + U)$, $j_{14} = \lambda_1$; $j_{21} = \gamma$, $j_{22} = -\omega$, $j_{23} = 0$, $j_{24} = 0$; $j_{31} = 0$, $j_{32} = k$, $j_{33} = -1$, $j_{34} = 0$; $j_{41} = 0$, $j_{42} = -\beta$, $j_{43} = 0$, $j_{44} = -1$.

The system (3) has two equilibrium points $L_0 = (c, 0, 0, 0)$ and $L^* = (H^*, Q^*, U^*, M^*)$, where

$$H^* = \frac{\omega Q^*}{\gamma}, U^* = kQ^*, M^* = c + \beta Q^*$$

and

$$Q^* = \frac{\gamma\sigma + \gamma\sqrt{\sigma^2 + 4c\delta\omega(\lambda_1\omega + \lambda_2\gamma + k\gamma)}}{2\delta\omega(\lambda_1\omega + \lambda_2\gamma + k\gamma)}$$

The disease free equilibrium point L_0 and endemic equilibrium point L^* exists for all parameter values.

Theorem 1. The disease free equilibrium point L_0 is locally as well as globally stable if $R_0 < 1$ and the endemic equilibrium point L^* is locally stable if $R_0 > 1$.

Proof. At disease free equilibrium point L_0 , Jacobian matrix is given by

$$J(L_0) = \begin{bmatrix} \lambda_1 c - \delta & \lambda_2 c & c & \lambda_1 \\ \gamma & -\omega & 0 & 0 \\ 0 & k & -1 & 0 \\ 0 & -\beta & 0 & -1 \end{bmatrix}$$

From this Jacobian Matrix it can be easily shown that the disease free equilibrium point is locally as well as globally stable if

$$R_0 = \frac{c(\lambda_1 \omega + \lambda_2 \gamma + k \gamma)}{\delta \omega} < 1$$

At the equilibrium point L^* , Jacobian matrix corresponding to system (3) is given by

$$J(L^*) = \begin{bmatrix} (m - \frac{c}{n})\lambda_1 - n_0 - \delta & (m - \frac{c}{n_0})\lambda_2 - n_0 & (m - \frac{c}{n_0}) - n_0 & n_0 \\ \gamma & -\omega & 0 & 0 \\ 0 & k & -1 & 0 \\ 0 & -\beta & 0 & -1 \end{bmatrix}$$

with $m = \frac{\delta \omega}{\lambda_1 \omega + \lambda_2 \gamma + k \gamma}$, $n_0 = \lambda_1 e^* + \lambda_2 e^* + r^*$.

Corresponding to the Jacobian matrix $J(L^*)$, characteristic equation is

$$(\rho + 1)(\rho^3 + a_1 \rho^2 + a_2 \rho + a_3) = 0 \tag{8}$$

where

$$\begin{aligned} a_1 &= 1 + \omega + n_0 + \delta + \frac{c\lambda_1}{n_0} - m\lambda_1 \\ &= 1 + \omega + n_0 + \frac{c\lambda_1}{n_0} + \frac{\delta(\gamma\lambda_2 + k\gamma)}{\lambda_1\omega + \lambda_2\gamma + k\gamma} \end{aligned}$$

$$\begin{aligned} a_2 &= \omega + (n_0 + \delta + \frac{c\lambda_1}{n_0})(1 + \omega) + \gamma(n_0 + \frac{c\lambda_2}{n_0}) - m\lambda_1(1 + \omega) - \gamma m \lambda_2 \\ &= \omega + n_0(1 + \omega) + \frac{c\lambda_1}{n_0}(1 + \omega) + \frac{\gamma c \lambda_2}{n_0} + \frac{\delta \gamma [\lambda_2 + k(1 + \omega)]}{\lambda_1 \omega + \lambda_2 \gamma + k \gamma} > 0 \end{aligned}$$

$$\begin{aligned} a_3 &= (1 + n_0)\delta\omega + \frac{k\gamma c}{n} + \frac{\omega c \lambda_1}{n_0} + \frac{\gamma c \lambda_2}{n_0} - m(\lambda_1 \omega + \lambda_2 \gamma + k \gamma) \\ &= n_0 \delta \omega + \frac{k \gamma c}{n_0} + \frac{\omega c \lambda_1}{n_0} + \frac{\gamma c \lambda_2}{n_0} > 0 \end{aligned}$$

It can easily be shown that $a_1 a_2 - a_3 > 0$ for $\lambda_1 > 0$.

Applying Hurwitz criterion, the endemic equilibrium L^* becomes locally asymptotically stable.

Global stability pertaining to L^* can be established by letting $\beta = 0$ in system (2) and we define new parameters

$$X = \frac{\mu_0}{B}G, Y = \frac{\mu_0}{B}H, Z = \frac{\mu_0}{B}Q, U_1 = \frac{\mu_0}{B}U.$$

Employing change of variables, system (2) takes the form

$$\begin{aligned} \frac{dX}{d\tau} &= 1 - c\lambda_1XY - c\lambda_2XZ - cU_1X - X \\ \frac{dY}{d\tau} &= c\lambda_1XY + c\lambda_2XZ + cU_1X - Y \\ \frac{dZ}{d\tau} &= \gamma Y - Z - kZ \\ \frac{dU_1}{d\tau} &= kZ - U_1 \end{aligned} \tag{9}$$

where $M_1(t) = X(t) + Y(t) + Z(t) + U_1(t)$.

Corresponding to total population M_1 we have

$$\frac{dM_1}{d\tau} = 1 - M_1.$$

As $\tau \rightarrow \infty, M_1 \rightarrow 1$ putting $X = 1 - Z - Y - U_1$ in (9) we can achieve limit system

$$\begin{aligned} \frac{dY}{d\tau} &= c(\lambda_1Y + \lambda_2Z + R_1)(1 - Z - Y - U_1) - \gamma Y - Y \\ \frac{dZ}{d\tau} &= \gamma Y - kZ - Z \\ \frac{dU_1}{d\tau} &= kZ - U_1. \end{aligned} \tag{10}$$

We enable change of variables $x = 1 - Z - Y - U_1, y = Y, z = Z$, then system (11) is equivalent to the system (10)

$$\begin{aligned} \frac{dx}{d\tau} &= 1 - x - c[(\lambda_1y - \lambda_2z - (1 - x - y - z)]x \\ \frac{dy}{d\tau} &= c[(\lambda_1y + \lambda_2z + (1 - x - y - z)]x - \gamma y - y \\ \frac{dz}{d\tau} &= \gamma y - z - kz \end{aligned} \tag{11}$$

with

$$\frac{dM_2}{d\tau} = 1 - M_2 - kz.$$

Obviously, feasible region is

$$\Gamma = \{(x, y, z) \in R_+^3 : x, y, z \geq 0, x + y + z = M_2 \leq 1\}.$$

Consider $L^* = (x^*, y^*, z^*)$ be the unique positive equilibrium corresponding to the system (11). Jacobian matrix $J(L^* = (x^*, y^*, z^*))$ is

$$J(L^* = (x^*, y^*, z^*)) = \begin{bmatrix} a_{11} & -c\lambda_1x & -c\lambda_2x \\ a_{21} & c\lambda_1x - \gamma - 1 & c\lambda_2x \\ 0 & \gamma & -1 - k \end{bmatrix}$$

where

$$\begin{aligned} a_{11} &= -1 + cx + c[(\lambda_1y - \lambda_2z - (1 - y - x - z))] \\ a_{21} &= cx + c[(\lambda_1y - \lambda_2z - (1 - y - x - z))] \end{aligned}$$

In the following, employing geometrical approach of Li and Muldowney in [14], we can obtain simple sufficient conditions that disease steady state L^* is globally asymptotically stable. Primarily, a short sketch of this geometrical approach is provided. Let $x \rightarrow f(x) \in R^n$ be a C^1 function for x in an open set $D \subset R^n$. The differential equation considered is

$$\frac{dx}{dt} = f(x). \tag{12}$$

Denoting by $x(t, x_0)$ the solution to (12) such that $x(0, x_0) = x_0$. We make the following two assumptions: (A1) There exists a compact absorbing set $K \subset D$. (A2) Eq. (3.5) has a unique equilibrium \bar{x} in D .

The equilibrium \bar{x} is said to be globally stable in D if it is locally stable and all trajectories in D converge to \bar{x} . For $n \geq 2$, by Bendixson criterion, we mean a condition satisfied by f which precludes the existence of non-constant periodic solutions of (9). The classical Bendixson’s condition $div f(x) < 0$ for $n = 2$ is robust under C^1 local perturbations of f . With reference to higher dimensional systems, the C^1 robust properties are discussed in [7–9]. A point $x_0 \in D$ is wandering for (12) if there exists a neighborhood $N(x_0)$ of x_0 and $T > 0$ such that $N(x_0) \cap x(t, U)$ is empty for all $t > T$. Thus, for example, all equilibria and limit points are non-wandering. In any finite dimension, for autonomous systems, the following global-stability principle is established in Li and Muldowney [14].

Theorem 2. Suppose that assumptions (A1) and (A2) hold. Assume that (12) satisfies a Bendixson criterion that is robust under C^1 local perturbations of f at all non-equilibrium non-wandering points for (12). Then \bar{x} is globally stable in D provided it is stable.

The following Bendixson criterion is given in [14] and shown to have the robustness required by Theorem 3. Let $x \rightarrow P(x)$ be an $\binom{n}{2} \times \binom{n}{2}$ matrix-valued function that is C^1 for $x \in D$. Let us consider $P^{-1}(x)$ exists and is continuous for $x \in K$, the compact absorbing set. A quantity \bar{q}_2 is defined as

$$\bar{q}_2 = \lim_{t \rightarrow \infty} \sup \sup_{x_0 \in K} \frac{1}{t} \int_0^t \mu_0(B_0(x(s, x_0))) ds, \tag{13}$$

where

$$B_0 = P_f P^{-1} + P \frac{\partial f^{[2]}}{\partial x} P^{-1}. \tag{14}$$

the matrix P_f is attained having swaped every entry p of P by its derivative in the direction of f , p_{ijf} , and $\mu_0(B_0)$ is the Lozinskii measure of B with reference to a vector norm $|\cdot|$ in R^N , $N = \binom{n}{2} \times \binom{n}{2}$, defined by [15]

$$\mu_0(B_0) = \lim_{h \rightarrow 0^+} \frac{|i + hB_0| - 1}{h}.$$

It is shown in [14] that, if D is simply connected, the condition $\bar{q}_2 < 0$ eradicates presence of any orbit that gives rise to a simple closed rectifiable curve which is invariant for (12) such as periodic orbits, homoclinic orbits, and heteroclinic cycles. Furthermore, it is robust under C^1 local perturbations of f near any non-equilibrium point that is non-wandering. In particular, the following global-stability result is proved in Li and Muldowney [14].

Theorem 3. Considering simple connectedness of D and that the assumptions (A1) and (A2) hold, the unique equilibrium \bar{x} of (12) is globally stable in D if $\bar{q}_2 < 0$.

Now, we study the global stability of the disease steady state L^* , and obtain

Theorem 4. If $R_0 > 1$, $\lambda_1 > \lambda_2$ and $\gamma + c\lambda_1(1-) < 1$, $c(1-) < 1+$, then the endemic equilibrium L^* of the system (12) is globally asymptotically stable.

Proof: The Jacobian matrix J associated with a general solution to (12) is given by

$$J(L^* = (x^*, y^*, z^*)) = \begin{bmatrix} a_{11} & -c\lambda_1 x & -c\lambda_2 x \\ a_{21} & c\lambda_1 x - \gamma - 1 & c\lambda_2 x \\ 0 & \gamma & -1 - k \end{bmatrix}$$

where

$$a_{11} = -1 + cx + c[(\lambda_1 y - \lambda_2 z - (1 - y - x - z))]$$

$$a_{21} = cx + c[(\lambda_1 y - \lambda_2 z - (1 - y - x - z))]$$

and its second additive compound matrix $J^{[2]}$ is

$$J^{[2]} = \begin{bmatrix} b_{11} & c(\lambda_1)x & c(\lambda_2)x \\ \gamma & cb_{22} & -c(\lambda_1)x \\ 0 & b_{32} & b_{33} \end{bmatrix}$$

where

$$\begin{aligned} b_{11} &= -2 - \gamma + c\lambda_1x - c(\lambda_1y + \lambda_2z) - c(1 - y - x - z) \\ b_{22} &= -2 - k + cx - c(\lambda_1y + z) - c(1 - y - x - z) \\ b_{32} &= -cx + c(\lambda_1y + z) + c(1 - y - x - z) \\ b_{33} &= -2 - \gamma - k + c\lambda_1x. \end{aligned}$$

A comprehensive survey on compound matrix and their relations to differential equations is given by [16]. Set the function

$$P(x, y, z) = \begin{bmatrix} z & x & 0 \\ 0 & y & 0 \\ 0 & y & y \end{bmatrix}.$$

Then $P_f P^{-1} = \text{diag}\{\frac{z'}{z}, \frac{y'}{y}, \frac{y'}{y}\}$ and the matrix

$$B_0 = P_f P^{-1} + P \frac{\partial f^{[2]}}{\partial x} P^{-1}$$

in (14) can be written as block matrix

$$B_0 = \begin{bmatrix} B_{11} & B_{12} \\ B_{21} & B_{22} \end{bmatrix}.$$

where $B_{11} = \frac{z'}{z} - 2 - \gamma + c\lambda_1x - c(\lambda_1y + \lambda_2z) - c(1 - y - x - z)$, $B_{12} = [0, \frac{c(\lambda_2)xz}{y}]$

$$B_{21} = \begin{bmatrix} \frac{\gamma y}{z} \\ \frac{\gamma y}{z} \\ z \end{bmatrix}$$

$$B_{22} = \begin{bmatrix} \frac{y'}{y} - 2 - k + c\lambda_1x - c[\lambda_1y + \lambda_2z + (1 - y - x - z)] & -c(\lambda_1)x \\ \gamma & \frac{y'}{y} - 2 - k - \gamma \end{bmatrix}.$$

Let (u, v, w) denote the vectors in $R^3 \cong R(\frac{n}{2})$. Then we select a norm in R^3 as $|(u, v, w)| = \max |u|, |v| + |w|$ and let μ_0 denote the Lozinskii measure with reference to this norm. Following the method in [17], we have the estimate $\mu_0(B_0) = \sup g_1, g_2$, where $g_1 = \mu_1(B_{11}) + |B_{12}|$; $g_2 = |B_{21}| + \mu_1(B_{22})$.

$|B_{12}|, |B_{21}|$ are matrix norms with respect to the l_1 vector norm, and μ_1 denotes the Lozinskii measure with respect to the l_1 norm, see [15]. More specifically, $\mu_1(B_{11}) = \frac{z'}{z} - 2 - \gamma + c\lambda_1x - c(\lambda_1y + \lambda_2z) - c(1 - y - x - z)$, $|B_{12}| = \frac{c(\lambda_2)xz}{y}$, $|B_{21}| = \frac{\gamma y}{z}$.

To calculate $\mu_1(B_{22})$, add the absolute value of the off-diagonal elements to the diagonal one in each column of B_{22} , and then take the maximum of two sums, see [15]. As $\lambda_1 > \lambda_2$, we get

$$\begin{aligned} \mu_1(B_{22}) &= \max\left\{\frac{y'}{y} - 2 - k + \gamma + c\lambda_1x - c[\lambda_1y + \lambda_2z + (1 - y - x - z)], \right. \\ &\quad \left. \frac{y'}{y} - 2 - k - \gamma + c(\lambda_1)x\right\} \\ &\leq \frac{y'}{y} - 2 - k + \gamma + c\lambda_1x. \end{aligned}$$

From system (12), we get

$$\begin{aligned} x &< 1 - , \\ \frac{y'}{y} &= \frac{y'}{y} + c\lambda_1x - cx + \frac{c(\lambda_2 -)xz}{y} + \frac{c(1 - x)x}{y} - 1 - \gamma, \\ \frac{z'}{z} &= \frac{\gamma y}{z} - k - 1. \end{aligned}$$

$$\begin{aligned} g_1 &= \frac{y'}{y} + \frac{z'}{z} - 1 - \frac{y'}{y} + cx - c(\lambda_1y + \lambda_2z) - c(1 - y - x - z) - \frac{c(1 - x)x}{y} \\ &\leq \frac{y'}{y} + \frac{z'}{z} - 1 + c \end{aligned}$$

$$\begin{aligned} g_2 &= \frac{y'}{y} + \frac{z'}{z} - 1 + \gamma + c\lambda_1x \\ &\leq \frac{y'}{y} + \frac{z'}{z} - 1 + \gamma + c\lambda_1. \end{aligned}$$

We can choose t_1 large enough such that

$$\begin{aligned} g_1 &\leq \frac{y'}{y} + \frac{z'}{z} - 1 + c \\ g_2 &\leq \frac{y'}{y} + \frac{z'}{z} - 1 + \gamma + c\lambda_1 \end{aligned}$$

for $t \geq t_1$, where δ can be chosen arbitrarily small.

Therefore,

$$\mu_0(B_0) \leq \frac{y'}{y} + \frac{z'}{z} - \bar{b}$$

for $t \geq t_1$ where

$$\begin{aligned} \bar{b} &= \min\{1 + c, 1 - \gamma - c\lambda_1\} \\ &= 1 - \gamma - c\lambda_1 > 0 \end{aligned}$$

is a constant.

Along each solution $(x(t), y(t), z(t))$ of (12) with $(x(0), y(0), z(0)) \in \Gamma$, where Γ is the compact absorbing set, we have

$$\begin{aligned} \frac{1}{t} \int_0^t \mu_0(B_0) ds &= \frac{1}{t} \int_0^{t_1} \mu_0(B_0) ds + \frac{1}{t} \int_{t_1}^t \mu_0(B_0) ds \\ &\leq \frac{1}{t} \int_0^{t_1} \mu_0(B_0) ds + \frac{1}{t} \log \frac{y(t)}{y(t_1)} + \frac{1}{t} \log \frac{z(t)}{z(t_1)} - \bar{b}, \end{aligned}$$

which implies that $\bar{q}_2 \leq -\frac{\bar{b}}{2} < 0$ from (13).

4 Model Validation and Parameter Estimation

In this segment, we have estimated parameter values corresponding to the model from real data of COVID-19 disease occurred in Italy. In order to validate model and estimate important model parameters we have fitted the model with real COVID-19 cases of Italy from 15th Feb to 4th April using the non-linear least square principle and software package fmincon. **The statistical method used to estimate parameter is known as “least square method”. By reducing the sum of the residuals of the points from the plotted curve, the least squares method is a statistical technique for determining the best fit for a group of data points. This technique explains the general justification for where to locate the line of greatest fit among the data points being examined. The correlation between a known independent variable and an unknowable dependent variable is represented by each data point.** The least square principle is given below:

Let $\{C_i\}$ be the cumulative number of infected population in real cases and $\{C_i^p\}$ be the cumulative number of model predicted infected population on i^{th} day then our target is to minimize the following

$$F(\Theta) = \sum_{i=1}^n (C_i - C_i^p)^2$$

for all parameters $\theta \in \Theta$. Using this principle we have estimated four important parameters and other parameters are collected from the source (Table 1).

From this estimated parameter values we have observed the dynamics of the spread of infection among the population and compared this observations with data. Figure 1 shows the infected population level in 50 days from model simulation and it also indicates the infection level in 50 days from real data, Fig. 1 (a) presents the spread of infection among population increases exponentially from both model results and data

Table 1. Values of the model parameters and their sensitivity indices for outbreak in Italy

Parameters	Values	Source
β_1	3.640080297324544e-09	Estimated
β_2	3.185862091629136e-08	Estimated
A	1.21	Estimated
γ_1	1/14	[5]
δ	0.37	[5]
μ	0.00001	Estimated
σ_1	0.2	Estimated

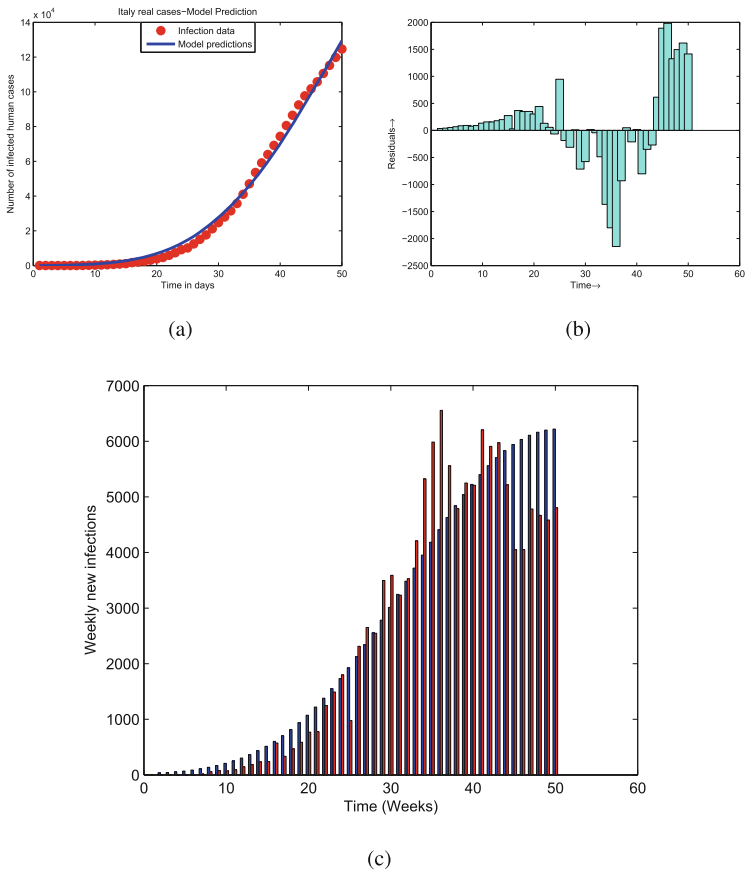


Fig. 1. (a) Fitting model to cumulative cases in Italy, (b) Residuals of the fit, (c) BAR diagram for 50 days.

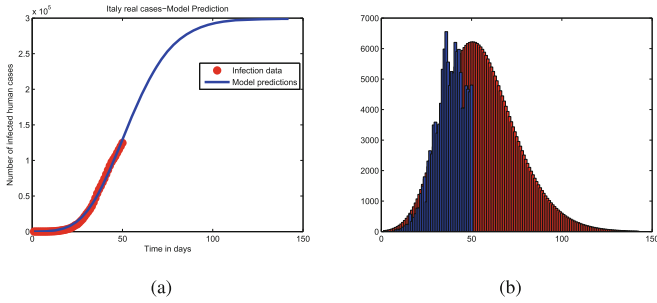


Fig. 2. (a) Cumulative cases prediction in Italy for 140 days, (b) BAR diagramfor 140 days.

results. Figure 1 (b) represents the residuals abundances of the fitted result. From this figure it is observed that in the first 25 days residuals are in positive zone and from 25 days to 45 days some residuals are in negative zone. In last 5 days it is found that residuals are in positive zone that is the residuals are randomly distributed that is the model data fitting is acceptable. However to clear observation we have drawn bar diagram from model simulated data as well as real data of COVID-19 disease occurred in Italy (Fig. 1 (c)).

To predict COVID-19 disease spreading in Italy about the number of per day new infection we have simulated the result for 140 days on basis of data for 50 days. Figure 2(a) shows the cumulative cases prediction in Italy for 140 days. This figure indicates that the prediction of spread of COVID-19 among the populations increases upto 60 days and after 60 days infection will be saturated and stable and the graph of infected population will be Plato. This indicates that the spread of infection becomes saturated and new infection is not be recruited among the community. We have also draw a bar diagram for 140 days prediction results (Fig. 2b). From Fig. 2b it is noticed that in first 60 days height of bar graphs has been increases and after first 60 days the height of bar graph decreases. So from this Figure it is observed that after 130 days i.e. in middle of June 2020 the infection level will be controlled.

5 Conclusion

One of the main infections that primarily affects the human respiratory system is the coronavirus. Both the Middle East respiratory syndrome (MERS)-CoV and the severe acute respiratory syndrome (SARS)-CoV have previously been identified as coronaviruses (CoVs) that pose a serious threat to the public’s health. Fever, coughing, and exhaustion are the most typical initial signs of COVID-19 disease. Other symptoms include sputum production, headache, haemoptysis, diarrhoea, dyspnoea, and lymphopenia. In this study, we take into account a four-dimensional epidemic model to analyse the dynamics of COVID-19 and forecast the corona scenario in Italy. We have first established the existence of the equilibrium points. Under particular threshold conditions, we have also calculated the local and global stability of various equilibrium points. We focused on the fundamental reproduction rate since it is a crucial instrument for halting the spread of disease. We have calculated the fundamental reproduction

number using our suggested model, and we have observed the stability of endemic and disease-free equilibrium both locally and globally. We used the data set for the nation of Italy to validate our suggested model, and we approximated the parameter values and observed illness trends using model outputs and data findings. First, based on data and model simulation findings, we looked at the 50-day results for Italy and discovered that the infection rate in the population had exponentially grown. Both residual fit and bar diagram plots have supported it. The projected outcome for 18 spreading the disease around the community is 140 days. The findings of the model simulations show that the infection will increase for up to 110 days, after which the spread of the disease in the population would decline and become stable after 120 days. However, the outcomes of our model's prediction will be useful to management strategists and policy makers. **In a nutshell, the main goal of this manuscript is to observe the dynamics of Covid-19 virus on the SEIR epidemic model for better understanding of the novel Corona virus and its aftermath in Italy. Our investigation in this manuscript would help to understand to what extent can the spread of the disease be prevented in Italy in due course of time. In future, our model can be modified in different epidemiological point of view for better results. One can extend our model by symptomatic and asymptomatic compartmental part. Our mathematical part can be extended by incorporating delay, stochastic, spatio-temporal effect to get better and realistic results.**

Acknowledgement. We have considered corona based on some biological assumption and the formulation can be adopted from basic idea of SIR model. We have already justified the model result with actual data. We are also grateful to reviewer and editor for valuable comments to improve the papers. We specially thanks to Prof. Jagadev Singh and Prof. Devendra Kumar for support for improving the paper.

References

1. Wang, C., Horby, P.W., Hayden, F.G., et al.: A novel coronavirus outbreak of global health concern. *Lancet* **395**(10223), 470–473 (2020)
2. World Health Organization. Novel Coronavirus (2019-nCoV) Situation Report- 14. https://www.who.int/docs/default-source/coronaviruse/situation-reports/20200203-sitrep-14-ncov.pdf?sfvrsn=f7347413_4. Accessed 3 Feb 2020
3. Tan, W.J., Zhao, X., Ma X.J., et al.: A novel coronavirus genome identified in a cluster of pneumonia cases—Wuhan, China 2019–2020. *China CDC Wkly.* **2**(4), 61–62 2020. <http://weekly.chinacdc.cn/en/article/ccdcw/2020/4/61>
4. World Health Organization. Statement on the Second Meeting of the International Health Regulations. [https://www.who.int/news-room/detail/30-01-2020-statement-on-the-second-meeting-of-the-internationalhealth-regulations-\(2005\)-emergency-committee-regarding-the-outbreak-of-novel-coronavirus-\(2019-ncov\)](https://www.who.int/news-room/detail/30-01-2020-statement-on-the-second-meeting-of-the-internationalhealth-regulations-(2005)-emergency-committee-regarding-the-outbreak-of-novel-coronavirus-(2019-ncov)). Accessed 4 Feb 2020
5. <https://www.worldometers.info/coronavirus/#countries>
6. Cowling, B.J., Park, M., Fang, V.J., Wu, P., Leung, G.M., Wu, J.T.: Preliminary epidemiologic assessment of MERS-CoV outbreak in South Korea, May-June 2015. *Euro. Surveil. Bull. Eur. sur les maladies transmissibles = Eur. Commun. Dis. Bull.* **20**(25), 21163 (2015)
7. De Groot, R.J., et al.: Commentary: middle east respiratory syndrome coronavirus (MERS-CoV): announcement of the coronavirus study group. *J. Virol* **87**(14), 7790–7792 (2013)

8. De Wit, E., Van Doremalen, N., Falzarano, D., Munster, V.J.: SARS and MERS: recent insights into emerging coronaviruses. *Nat. Rev. Microbiol.* **14**(8), 523 (2016)
9. Gumel, A.B., et al.: Modelling strategies for controlling SARS outbreaks. *Proc. Royal Soc. London. Ser. B: Biol. Sci.* **271**(1554), 2223–2232 (2004)
10. Kwok, K.O., Tang, A., Wei, V.W., Park, W.H., Yeoh, E.K., Riley, S.: Epidemic models of contact tracing: systematic review of transmission studies of severe acute respiratory syndrome and middle east respiratory syndrome. *Comput. Struct. Biotechnol J.* **17**, 186–194 (2019)
11. Li, W., et al.: Angiotensin-converting enzyme 2 is a functional receptor for the SARS coronavirus. *Nature* **426**(6965), 450–454 (2003)
12. Chan, J.F.-W., et al.: A familial cluster of pneumonia associated with the 2019 novel coronavirus indicating person-to-person transmission: a study of a family cluster. *Lancet* **395**(10223), 514–523 (2020)
13. Brauer, F., Van den Driessche, P.: Models for transmission of disease with immigration of infectives. *Math. Biosci.* **171**, 143–54 (2001)
14. Li, M.Y., Muldowney, J.S.: A geometric approach to the global-stability problems. *SIAM J. Math. Anal.* **27**, 1070–83 (1996)
15. Coppel, W.A.: *Stability and Asymptotic Behavior of Differential Equation*. Heath, Boston (1965)
16. Muldowney, J.S.: Compound matrices and ordinary differential equations. *Rocky Mount. J. Math.* **20**, 857–72 (1990)
17. Martin, R.H., Jr.: Logarithmic norms and projections applied to linear differential systems. *J. Math. Anal. Appl.* **45**, 432–54 (1974)
18. Singh, H.: Analysis for fractional dynamics of Ebola virus model. *Chaos Solitons Fractals* **138**, 109992 (2020)
19. Singh, H.: Analysis of drug treatment of the fractional HIV infection model of CD4+ T-cells. *Chaos Solitons Fractals* **146**, 110868 (2021)
20. Singh, H., Srivastava, H.M., Hammouch, Z., Nisar, K.S.: Numerical simulation and stability analysis for the fractional-order dynamics of COVID-19. *Results Phys.* **20**, 103722 (2021)
21. Singh, H., Baleanu, D., Singh, J., Dutta, H.: Computational study of fractional order smoking model. *Chaos Solitons Fractals* **142**, 110440 (2020)

Author Index

A

Aeri, Shivani 69
Ali, Atiya 391
Anastassiou, George A. 1

B

Baleanu, Dumitru 53
Baskonus, Haci Mehmet 232
Bhadauria, B. S. 436
Bhatnagar, Anand V. 248
Bhatter, Sanjay 488

C

Chadha, Naresh M. 177
Chaudhary, Susheela 424

D

Das, Krishna Pada 562
Das, Manik 138
Dubey, Ved Prakash 286

F

Fatawat, Kalpana 380

G

Gandhi, Rishu 155
Garg, Manish 100
Gayathri, K. 273
Gomatam, Ravindran 110
Gowrisankar, S. 195
Goyal, Meenu Rani 413
Grewal, Suraksha 552
Gupta, Vinod K. 209

H

Hristov, Jordan 33

I

Ismail 436

J

Jain, Monika 533
Jangid, Sanju 391
Jassim, Hassan Kamil 286
Joshi, Vishwas Deep 475

K

Kakodia, Ashok K. 552
Karmakar, Partha 562
Kasana, Rajesh Kumar 352
Kaur, Harmanjit 413
Kaur, Parvinder 456
Kavita 299
Khandelwal, Ronak 552
Khanduri, Umesh 121
Kulkarni, Vidha 332
Kumar, Ajay 232
Kumar, Arun 371
Kumar, Devendra 82, 286
Kumar, Rakesh 69
Kumar, Sudhanshu 522
Kumbhakar, Bidyasagar 138

L

Lal, Chiman 371

M

Mehta, Ruchika 391
Mehta, Tripti 391
Mondal, Seema Sarkar 562

N

Naheed, Saima 53
Neemawat, Abhishek 508
Nishant 488

P

Pankaj, Ram Dayal 371
Pasayat, T. 317
Pathak, Shivani 380

Patra, A. 317
Prakash, Amit 232
Pramanik, Sanjukta 562

R

Ranjan, Kumar Rajeev 195
Rathie, Arjun K. 332
Raut, Santanu 177

S

Saini, Kezia 100
Saini, Rachana 475
Salim, Mohammad 497
Samraiz, Muhammad 53
Sharma, B. K. 121, 155
Sharma, Poonam 69
Sharma, Shiv Kumar 299
Shobika, K. 273
Shyamsunder 488
Singh, Abhishek 82
Singh, Damini 259

Singh, Jagdev 138, 286, 475, 533
Singh, Pervinder 209
Singh, Sarita 259
Singh, Shubha 82
Singh, Surjan 456
Sunil, Kumar 110
Sushila 508

T

Tanwar, Kumud 552
Tomar, Shruti 177
Tyagi, Sapna 533

U

Umer, Muhammad 53

V

Verma, A. K. 522
Vyas, Narayan Krishan 497
Vyas, Paresh 352
Vyas, Yashoverdhan 248, 332, 380